

MASARYK UNIVERSITY
FACULTY OF SCIENCE

**Molecular Control of Primary
Cilium by Distal Appendages and
Associated Proteins**

HABILITATION THESIS

Lukáš Čajánek

BRNO 2025

Acknowledgement

First and foremost, I want to thank my family for their endless support, tolerance, love, and inspiration.

There have been many people over the years who have shaped my research career. Here, I would like to specifically thank the **BIG four**, whose roles in my scientific life I value the most.

Aleš Hampl offered an undergraduate newbie a chance to get a first glimpse of scientific work in his lab. His laid-back leadership, combined with an emphasis on independence and responsibility, set me on a productive path early on — one that I continue to build on since our paths have crossed again.

Vít'a Bryja played a significant role in daily mentoring during my later undergraduate years and, importantly, after my move to Stockholm (which he helped initiate) during the early days of my Ph.D. training. His supervision — an uncommon blend of top scientific insight and personal warmth — was both a great experience and a lot of fun.

Ernest Arenas welcomed me into his lab at the Karolinska Institute, offering thoughtful mentorship marked by patience, empathy, enthusiasm, and unwavering support. Most importantly, he encouraged me to formulate my own scientific questions and pursue independent research themes. His kind personality is deeply missed.

An interview for a postdoc position in **Erich Nigg's** lab marked my transition from a signaling/stem cell researcher to a cell biologist. His mentorship during my postdoc training set an exceptional example of scientific excellence and efficiency, fair leadership, sharp intellect, and a strong emphasis on scientific independence.

Last but not least, I want to thank all current and former members of my lab. Without your passion for science, scientific rigor, determination to face challenges, and daring to follow your own ideas, there would not be much to include in this thesis.

Table of contents

Acknowledgement.....	ii
List of abbreviations	iv
Thesis commentary	vi
Introduction	1
Primary cilia structure	1
Structure and function of distal appendages	2
Subdistal appendages, their structure and function	3
Axoneme.....	4
Transition zone	4
Ciliary membrane and intraciliary space.....	5
Theme 1: Mechanisms and functions of the CEP164-TTBK2 module	6
Cilia and centrosomes in stem cells	16
Theme 2: Kinesins, IFT, and cell signaling in the regulation of primary cilia	17
Future directions	24
References.....	26
Appendices.....	39
Appendix 1	39
Appendix 2	62
Appendix 3	75
Appendix 4	96
Appendix 5	110
Appendix 6	136
Appendix 7	171
Appendix 8	193
Appendix 9	223
Appendix 10.....	239
Appendix 11.....	261
Appendix 12.....	276
Appendix 13.....	300
Appendix 14.....	347
Appendix 15.....	358

List of abbreviations

AHI	Abelson Helper Integration site	hTERT	Human Telomerase Reverse Transcriptase
ANKRD	Ankyrin Repeat Domain-containing	IFT	Intraflagellar Transport
BBS	Bardet-Biedl Syndrome	INPP5E	Inositol Polyphosphate-5-Phosphatase E
cAMP	Cyclic Adenosine Monophosphate	INTU	Inturned Planar Cell Polarity Protein
APC	Adenomatous Polyposis Coli (WNT-related)/Anaphase-Promoting Complex (cell cycle-related)	KAP	Kinesin Associated Protein
CCDC	Coiled-Coil Domain-Containing	Kd	Dissociation Constant
CEP	Centrosomal Protein	KD	Knockdown
CK	Casein Kinase	KIF	Kinesin Family
CPLANE	Ciliogenesis and Planar Polarity Effector	KLP	Kinesin Like Protein
CP	Ciliary Pocket	LRP	Low-Density Lipoprotein Receptor-Related Protein
CRISPR	Clustered Regularly Interspaced Short Palindromic Repeats	LRRC	Leucine-Rich Repeat-Containing
Cryo-EM	Cryogenic Electron Microscopy	M	Methionine
Cryo-ET	Cryogenic Electron Tomography	MKS	Meckel Syndrome
CV	Ciliary Vesicle	NCS	Neuronal Calcium Sensor
DAVs	Distal Appendage Vesicles	NEK	NIMA (Never In Mitosis A) Related Kinase
DVL	Dishevelled	NMR	Nuclear Magnetic Resonance
DZIP	Deleted In Azoospermia-Interacting Protein	NPHP	Nephrocystin
EHD	EH-Domain Containing Protein	ODF	Outer Dense Fiber
EM	Electron Microscopy	OCT	Octamer-binding Transcription factor
ET	Electron Tomography	P	Proline
FBF	Fas-Binding Factor	PAX	Paired Box Gene Family
FOX	Forkhead Box	PIP	Phosphatidylinositol Phosphate
FZD	Frizzled	PIPKI	Phosphatidylinositol-4-Phosphate 5-Kinase Type I
G	Glycine	PAK	Protein Kinase A
GLI	Glioma-Associated Oncogene	PKD	Polycystic Kidney Disease
GPCR	G Protein-Coupled Receptor	PLK	Polo-Like Kinase
GSK	Glycogen Synthase Kinase	PTCH	Patched
HH	Hedgehog	Q	Glutamine
hPSCs	Human Pluripotent Stem Cells	R	Arginine

RABIN Rab Interacting Protein

RPE Retinal Pigment Epithelium

RPGRIP Retinitis Pigmentosa GTPase
Regulator Interacting Protein

RPGRIP1L RPGRIP1-Like Protein

RSG REM2- and RAB-like small GTPase

S/T Serine/Threonine

SCLT Sodium Channel and Clathrin Linker-
like

SIM Structured Illumination Microscopy

SMO Smoothened

SNAP Synaptosome Associated Protein

STIL SCL/TAL1 Interrupting Locus

TCF/LEF T-Cell Factor/Lymphoid Enhancer
Factor

TCTN Tectonic

TMEM Transmembrane Protein

TTBK Tau Tubulin Kinase

TZ Transition Zone

W Tryptophan

WNT Wingless/Integrated

WW WW Domain

Y Tyrosine

Thesis commentary

Let's imagine a tiny (~several micrometers long), hair-like structure on the surface of nearly every vertebrate cell, carefully orchestrating vital biological processes. These are cilia, evolutionarily conserved organelles with crucial roles in development and tissue homeostasis. Although once overlooked, cilia have gradually captured attention owing to their critical involvement in a wide range of disorders. Given this, a thorough understanding of how cilia are regulated is not merely a scientific pursuit, but it is key to unlocking new therapies for cilia-related diseases and uncovering the hidden mechanisms that drive cilia biology and its associated pathologies. This thesis discusses the regulatory mechanisms and functional consequences of primary cilia biology, along with my contributions to advancing this understanding, with a particular focus on events governed by proteins localized to the distal end of the centriole or its immediate vicinity.

In the first part, I focus on the role of CEP164, a component of the distal appendages of the mother centriole, and its effector, Tau Tubulin Kinase 2 (TTBK2). Together, they form one of the key modules regulating ciliogenesis in vertebrates. The primary contribution of my work to this theme lies in the identification of CEP164-mediated recruitment of TTBK2 to the mother centriole as a trigger for ciliogenesis in human cells. Subsequent follow-up work provided a structural basis for the CEP164–TTBK2 interaction, thereby identifying the underlying mechanism by which CEP164 mutations cause ciliopathies. Significant attention has been devoted to resolving the mechanisms underlying TTBK2 activity in cilia. This led to the identification of several novel substrates of the kinase and numerous phosphorylation sites. Importantly, in selected cases, we were also able to provide functional annotation of the identified phosphosites. Notably, our work linked the inhibitory phosphorylation of a tubulin-depolymerizing kinesin to the regulation of primary cilia length, thus providing a mechanistic foundation for the role of the CEP164–TTBK2 module beyond the initiation of ciliogenesis. In addition, our work capitalizing on the use of human pluripotent stem cells (hPSCs) as a model system established that cilia are not required for self-renewal, in contrast to intact centrosomes. However, primary cilia become critical for fine-tuning the proliferation of hPSC-derived neural progenitors, where ciliogenesis is also controlled by Tau Tubulin Kinase 1 (TTBK1), unlike in most other model systems.

The second part of this thesis is devoted to the regulation of intraflagellar transport (IFT) in cilia and the role of cilia in cell signaling. Regarding the former, the key contribution of my work lies in the identification of the module responsible for the binding and transport of tubulin within the cilium. In additional work, we identified novel ciliary kinesin required for proper cilium assembly and functionality, including the ability of the cilium to act as a signaling organelle. Continuing along the line of ciliary signaling, our work demonstrated that, while the WNT signaling pathway does not appear to play a major role in the regulation of ciliogenesis, TTBK2, a key regulator of ciliogenesis, is able to modulate the activity of Dishevelled (DVL), a key component of the WNT pathway.

The publications listed below represent examples I selected to highlight my contributions to the main theme of my thesis. They comprise 11 original research articles, one methodological paper, and three reviews. My contribution to each manuscript, as well as the journal metrics at the time of publication, is detailed in the tables below. The asterisk (*) indicates publications where I served as the corresponding author. The manuscripts are attached as correspondingly numbered appendices and are highlighted in **blue** in the main text of the thesis for clarity. In situations when the full-text is not freely available from the publishers' websites, original manuscripts deposited to PubMed Central are provided as an open-access alternative.

[1] Čajánek L*, Smite S, Ivashchenko O, Huranova M. Cilia at the crossroad: convergence of regulatory mechanisms to govern cilia dynamics during cell signaling and the cell cycle. *Cell & Bioscience*. 2025 Jun 7;15(1):81. doi: 10.1186/s13578-025-01403-z.(JCR 2024, IF = 6.2, Q1 – Biochemistry & Molecular Biology)

Experimental work (%)	Supervision (%)	Manuscript (%)	Research direction (%)
NA-review article	0	45	50

[2] Lacigová A, Čajánek L*. Phosphorylation at the Helm: Kinase-Mediated Regulation of Primary Cilia Assembly and Disassembly. *Cytoskeleton*. 2025 Mar 10. doi:10.1002/cm.22012. (JCR 2024, IF = 1.6, Q4 – Cell Biology)

Experimental work (%)	Supervision (%)	Manuscript (%)	Research direction (%)
NA-review article	100	40	70

[3] Benk Vysloužil D, Bernatík O, Lánská E, Renzová T, Binó L, Lacigová A, Drahošová T, Lánský Z, Čajánek L*. Tau-tubulin kinase 2 restrains microtubule-depolymerizer KIF2A to support primary cilia growth. *Cell Communication and Signaling*. 2025 Feb 10;23(1):73. doi: 10.1186/s12964-025-02072-8.(JCR 2024, IF = 8.9, Q1 – Cell Biology)

Experimental work (%)	Supervision (%)	Manuscript (%)	Research direction (%)
0	65	35	80

[4] Binó L, Čajánek L*. Tau tubulin kinase 1 and 2 regulate ciliogenesis and human pluripotent stem cells-derived neural rosettes. *Scientific Reports*. 2023 Aug 9;13(1):12884. doi: 10.1038/s41598-023-39887-9. (JCR 2023, IF = 3.8, Q1 – Multidisciplinary Sciences)

Experimental work (%)	Supervision (%)	Manuscript (%)	Research direction (%)
0	100	70	90

[5] Rosa E Silva I, Binó L, Johnson CM, Rutherford TJ, Neuhaus D, Andreeva A, Čajánek L, van Breugel M. Molecular mechanisms underlying the role of the centriolar CEP164-TTBK2 complex in ciliopathies. *Structure*. 2022 Jan 6;30(1):114-128.e9. doi: 10.1016/j.str.2021.08.007.(JCR 2022, IF = 5.7, Q1 – Biochemistry & Molecular Biology)

Experimental work (%)	Supervision (%)	Manuscript (%)	Research direction (%)
-----------------------	-----------------	----------------	------------------------

0	15	10	15
---	----	----	----

[6] Bino L, Mikulenkova E, Stepanek L, Bernatik O, Vyslouzil D, Pejškova P, Gorilak P, Huranova M, Varga V, Čajánek L*. A protocol for generation and live-cell imaging analysis of primary cilia reporter cell lines. *STAR PROTOCOLS*. 2022;3(1). doi:10.1016/j.xpro.2022.101199 Q4.(JCR 2022, IF = 1.3, Q4 – Biochemistry Research Methods)

Experimental work (%)	Supervision (%)	Manuscript (%)	Research direction (%)
0	55	35	65

[7] Bernatik O, Paclikova P, Kotrbova A, Bryja V, Čajánek L*. Primary Cilia Formation Does Not Rely on WNT/ β -Catenin Signaling. *Front Cell Dev Biol*. 2021 Feb 26;9:623753. doi: 10.3389/fcell.2021.623753.(JCR 2021. IF=6.081, Q1 – Developmental Biology)

Experimental work (%)	Supervision (%)	Manuscript (%)	Research direction (%)
0	60	40	75

[8] Pejškova P, Reilly ML, Bino L, Bernatik O, Dolanska L, Ganji RS, Zdrahal Z, Benmerah A, Čajánek L*. KIF14 controls ciliogenesis via regulation of Aurora A and is important for Hedgehog signaling. *Journal of Cell Biology*. 2020 Jun 1;219(6):e201904107. doi: 10.1083/jcb.201904107.(JCR 2020. IF=10.539, Q1- Cell Biology)

Experimental work (%)	Supervision (%)	Manuscript (%)	Research direction (%)
0	70	55	90

[9] Bernatik O, Pejškova P, Vyslouzil D, Hanakova K, Zdrahal Z, Čajánek L*. Phosphorylation of multiple proteins involved in ciliogenesis by Tau Tubulin kinase 2. *Molecular Biology of the Cell*. May 1;31(10):1032-1046. doi: 10.1091/mbc.E19-06-0334. (JCR 2020. IF= 4.138, Q3 – Cell Biology)

Experimental work (%)	Supervision (%)	Manuscript (%)	Research direction (%)
0	60	40	80

[10] Hanáková K, Bernatik O, Kravec M, Micka M, Kumar J, Harnoš J, Ovesná P, Paclíková P, Rádsetoulal M, Potěšil D, Tripsianes K, Čajánek L, Zdrahal Z, Bryja V. Comparative phosphorylation map of Dishevelled 3 links phospho-signatures to biological outputs. *Cell Communication and Signaling*. 2019 Dec 23;17(1):170. doi: 10.1186/s12964-019-0470-z.(JCR 2019. IF=4.344, Q2 – Cell Biology)

Experimental work (%)	Supervision (%)	Manuscript (%)	Research direction (%)
10	0	10	10

[11] Renzova T, Bohaciakova D, Esner M, Pospisilova V, Barta T, Hampl A, Čajánek L*. Inactivation of PLK4-STIL Module Prevents Self-Renewal and Triggers p53-Dependent Differentiation in Human Pluripotent Stem Cells. *Stem Cell Reports*. 2018 Oct 9;11(4):959-972. doi: 10.1016/j.stemcr.2018.08.008. (JCR 2018, IF= 5.499, Q1 – Cell Biology)

Experimental work (%)	Supervision (%)	Manuscript (%)	Research direction (%)
5	70	55	90

[12] Bohaciakova D, Renzova T, Fedorova V, Barak M, Kunova Bosakova M, Hampl A, Čajánek L*. An Efficient Method for Generation of Knockout Human Embryonic Stem Cells Using CRISPR/Cas9 System . *Stem Cells and Development*. 2017 Nov 1;26(21):1521-1527. doi: 10.1089/scd.2017.0058. JCR 2017. IF= 3.315, Q2 – Hematology)

Experimental work (%)	Supervision (%)	Manuscript (%)	Research direction (%)
5	60	50	80

[13] Bryja V, Červenka I, Čajánek L. The connections of Wnt pathway components with cell cycle and centrosome: side effects or a hidden logic. *Crit Rev Biochem Mol Biol*. 2017 Dec;52(6):614-637. doi: 10.1080/10409238.2017.1350135. (JCR 2017. IF=5.279, Q1 - Biochemistry & Molecular Biology)

Experimental work (%)	Supervision (%)	Manuscript (%)	Research direction (%)
NA-review article	0	40	40

[14] Čajánek L, Nigg EA. Cep164 triggers ciliogenesis by recruiting Tau tubulin kinase 2 to the mother centriole. *Proc Natl Acad Sci U S A*. 2014 Jul 15;111(28):E2841-50. doi: 10.1073/pnas.1401777111. (JCR 2014. IF=9.674, Q1 - Multidisciplinary Sciences)

Experimental work (%)	Supervision (%)	Manuscript (%)	Research direction (%)
95	0	75	90

[15] Bhogaraju S, Cajanek L, Fort C, Blisnick T, Weber K, Taschner M, Mizuno N, Lamla S, Bastin P, Nigg EA, Lorentzen E. Molecular basis of tubulin transport within the cilium by IFT74 and IFT81. *Science*. 2013 Aug 30;341(6149):1009-12. doi: 10.1126/science.1240985. JCR 2013. IF= 31.477, Q1 - Multidisciplinary Sciences)

Experimental work (%)	Supervision (%)	Manuscript (%)	Research direction (%)
20	0	10	10

Introduction

The cilium is among the first cellular organelles ever observed, first described in the 17th century by Antonie van Leeuwenhoek, a Dutch pioneer of microbiology and microscopy. Cilia exist in two main forms: motile and non-motile. The non-motile type, which will be the main focus of this thesis, is known as the primary cilium. It derives its name from its early appearance during cellular development, notably observed to emerge before motile cilia in the epithelial cells of mammalian lungs (Sorokin, 1968). Initially dismissed as vestigial due to their inherent lack of motility, primary cilia have since been recognized, particularly over the past three decades, as essential sensory organelles (Čajánek et al., 2025 #Appendix 1; Huangfu et al., 2003; Mill et al., 2023; Satir, 2017). Acting in a way as cellular antennas, they play key roles in processes such as embryogenesis and the maintenance of tissue homeostasis (Bangs and Anderson, 2017; Gopalakrishnan et al., 2023; Ingham, 2022; Pazour et al., 2000). While the complete ablation of cilia is considered incompatible with life (Wallingford, 2019), even subtle defects in their assembly or function can trigger devastating conditions known as ciliopathies and influence the progression of certain cancers (Collinson and Tanos, 2025; Hildebrandt et al., 2011; Reiter and Leroux, 2017).

Primary cilia structure

The cilium comprises the basal body, the transition zone, and the microtubule-based axoneme covered by a ciliary membrane (Satir et al., 2010), **Fig.1**. The basal body is derived from one of the two centrioles that make up the centrosome — specifically, the older (or “mother”) centriole. A centriole is a barrel-shaped structure built with a characteristic nine-fold radial symmetry. Its walls are primarily composed of nine sets of microtubule triplets arranged in a circular fashion, providing the necessary structural stability and integrity (Gönczy and Hatzopoulos, 2019). Toward the distal end, the centriole shifts to a configuration similar to that of an axoneme, featuring microtubule doublets instead of triplets and a reduced diameter compared to its proximal region (Breslow and Holland, 2019; Nigg and Stearns, 2011). Mother centriole differs from the daughter centriole by the presence of two types of appendages, named according to their position at the distal end of the centriole: distal and subdistal appendages, respectively (Bornens, 2012; Nigg and Holland, 2018). Both distal and subdistal appendages rely on the structural integrity and topology of the centriole distal end for their correct assembly (Balestra et al., 2013; Bertiaux et al., 2025; Karasu et al., 2022).

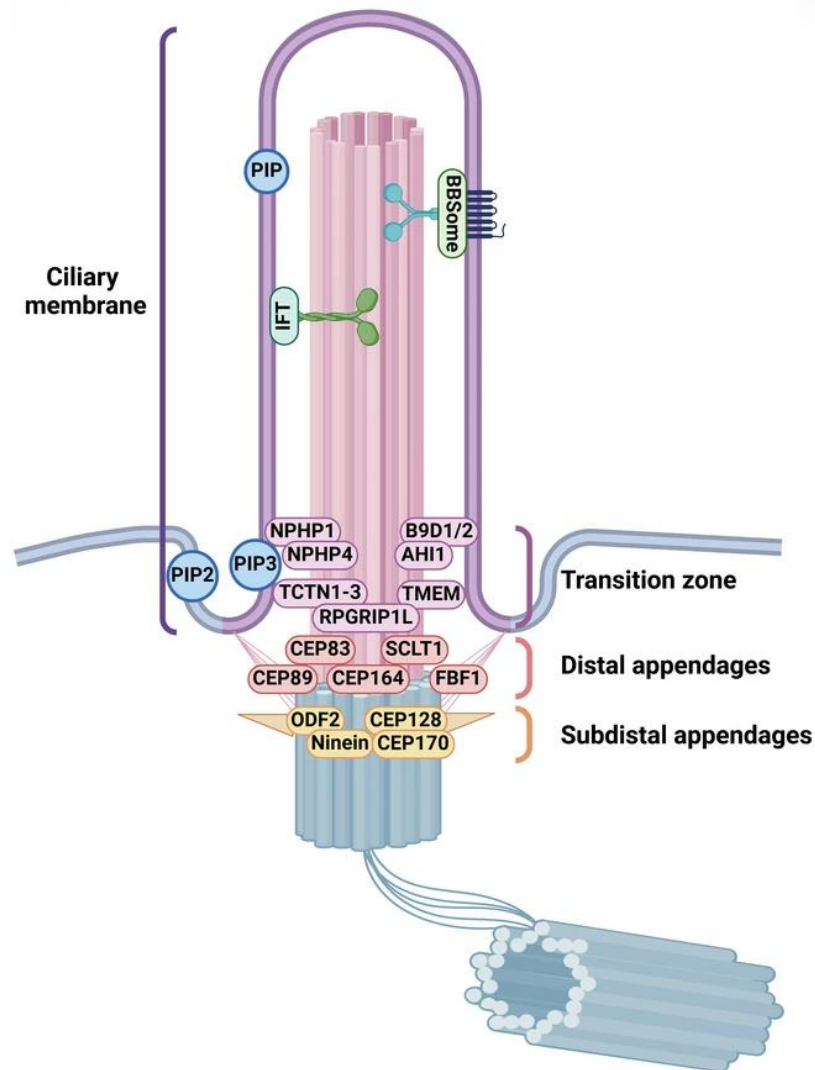


Fig.1: Primary cilium structure. The ciliary axoneme (in pink) is templated by the mother centriole, which, unlike the daughter centriole, possesses distal and subdistal appendages. The transition zone (TZ) acts as a diffusion barrier between the basal body and the ciliary axoneme. Active protein transport is mediated by intraflagellar transport (IFT) machinery, which operates in cooperation with the BBSome (Nachury, 2018; Prasai et al., 2024). Adopted from (Čajánek et al., 2025 #Appendix 1).

Structure and function of distal appendages

It is particularly the distal appendages that are critical for ciliogenesis, as will be discussed in detail in the upcoming chapters. Distal appendages resemble blades attached to two adjacent microtubule triplets on the wall of the mother centriole (Bowler et al., 2019; Chang et al., 2023). Following the transformation of the mother centriole into the basal body, distal appendages are subsequently referred to as transition fibres, mediating the attachment of the basal body to the plasma membrane (Sorokin, 1962, 1968; Tanos et al., 2013). For the sake of simplicity, I will use the term distal appendages when referring to these structures, regardless of the cilia status. The core distal appendage proteins include

CEP83/CCDC41, CEP89/CCDC123, SCLT1, FBF1, and CEP164, all of which have been implicated in the regulation of cilia assembly in numerous studies ([Cajane and Nigg, 2014 #Appendix 14](#); Graser et al., 2007; Joo et al., 2013; Kanie et al., 2025a; Schmidt et al., 2012; Sillibourne et al., 2013; Tanos et al., 2013; Wei et al., 2013). In turn, mutations in genes encoding the core distal appendages components typically give rise to nephronophthisis, a ciliopathy that predominantly affects the kidneys (Chaki et al., 2012; Failler et al., 2014; Gillesse et al., 2024). Additional components identified more recently include NCS1, KIZ, LRRC45, and ANKRD26 (Bowler et al., 2019; Kanie et al., 2025a, 2025b; Kurtulmus et al., 2018), whose roles in cilia biology remain notably less explored. While NCS1 seems to partially mediate the interactions between distal appendages and the membrane (Kanie et al., 2025b), LRRC45 has been implicated in the regulation of centriolar satellites (Kurtulmus et al., 2018); membrane-less assemblies known to contribute to the biogenesis of both centrosomes and cilia (Odabasi et al., 2020; Prosser and Pelletier, 2020).

Distal appendages are assembled in a hierarchical manner. The pioneering work by Barbara Tanos, Bryan Tsou, and colleagues defined CEP83 as the most upstream component, responsible for the recruitment of CEP89 and SCLT1, with the latter subsequently mediating the recruitment of CEP164 and FBF1 (Tanos et al., 2013). Recent work by Tomoharu Kanie, Peter Jackson, and colleagues has proposed an updated model with notably more complex relationships between individual distal appendage components, such as a mutual regulation of CEP83–SCLT1 or the role of SCTL1 upstream of CEP89 recruitment (Kanie et al., 2025a).

The distal appendages mediate recruitment of additional effector proteins to ensure proper cilia formation and function. Tau tubulin kinase 2 (TTBK2) (Goetz et al., 2012), recruited to distal appendages via its interaction with CEP164 ([Cajane and Nigg, 2014 #Appendix 14](#); Oda et al., 2014; [Rosa E Silva et al., 2022 #Appendix 5](#)), is arguably the most prominent example of such an effector, as I will discuss in the upcoming chapters in more detail.

Subdistal appendages, their structure and function

In contrast to the very well-defined and conserved nine-fold symmetry of distal appendages, the structural organization of subdistal appendages exhibits prominent variability (Hall and Hehnly, 2021; Uzbekov and Alieva, 2018). Additionally, subdistal appendages do not appear to directly contribute to the regulation of primary cilium assembly or maintenance. Instead, they primarily function as anchoring sites for centrosomal microtubules, thereby linking the basal body to the cell cytoskeleton (Bornens, 2012; Chong et al., 2020). As a result, subdistal appendages have been associated with the proper positioning of primary cilia (Mazo et al., 2016), although the functional implication of this role remains elusive. Some of the best characterized components of subdistal appendages include ODF2, Ninein, CEP170, and CEP128 (Hall and Hehnly, 2021; Mazo et al., 2016). Notably, super-resolution microscopy

data suggest a structural coupling between several components of distal and subdistal appendages, specifically involving ODF2 and CEP89, which appear to exist in distinct pools associated with both distal and subdistal appendages (Chong et al., 2020).

Axoneme

The microtubule-based axoneme is perhaps the most prominent part of the cilium, typically extending 2–10 micrometers in length, at least in the case of primary cilia in vertebrates (Satir et al., 2010). The axonemal microtubules are arranged in a circumferential array of nine doublets that extend from the basal body, which, as mentioned earlier, also contains nine sets of microtubules, but organized into triplets. While the transition from triplets to doublets likely reflects a shift from the need for high structural stability in the basal body to a combination of stability and flexibility in the axoneme (Mercey et al., 2024; Satir et al., 2008), the precise mechanism that governs this transformation remains unclear. Motile cilia typically contain an additional central pair of singlet microtubules (9+2 arrangement), which in turn enables their motility and characteristic beating dynamics. Conversely, primary cilia are thought to lack these two central microtubules (Mill et al., 2023; Satir et al., 2010). However, the existence of motile cilia — as defined by their axonemal structure (9+2) — with sensory functions, cilia with 9+0 arrangement capable of beating, and immotile cilia with 9+2 configuration has challenged this traditional classification (Cho et al., 2022; Jenkins et al., 2009; Nonaka et al., 1998; Wang and Zhou, 2021). Moreover, primary cilia of several epithelial cell types, including the commonly used hTERT-RPE-1 cell line, follow the 9+0 pattern only in their proximal regions, while the more distal segments of the axoneme display a surprising level of heterogeneity, with microtubules often terminating individually along the ciliary axoneme, well before reaching the ciliary tip (Kiesel et al., 2020; Sun et al., 2019).

Transition zone

The boundary between the basal body and the ciliary axoneme, starting approximately 100 nm above the distal appendages, is termed the transition zone (TZ) (Garcia-Gonzalo and Reiter, 2017; Mercey et al., 2024). The TZ partially overlaps with the so-called ciliary necklace, a structure observed by pioneers of cilia research when examining them using electron microscopy (EM) (Gilula and Satir, 1972). Functionally, the TZ acts as a diffusion barrier/gate at the ciliary base, regulating the entry of both membrane-bound and soluble proteins to maintain the specific micro-environment, distinct from the rest of the cell, within the cilium (Garcia-Gonzalo and Reiter, 2017; Nachury and Mick, 2019; Park and Leroux, 2022). Although the size and organization of the TZ can differ between cell types, a common structural hallmark is the presence of Y-shaped linkers, which connect the axonemal microtubule doublets to the ciliary membrane (Mercey et al., 2024). The identified TZ components are organized in

large complexes with distinct structural, biochemical, and functional characteristics (Garcia-Gonzalo and Reiter, 2017; Park and Leroux, 2022). An example of one such complex is the NPHP complex, which is positioned near the axonemal microtubules and comprises proteins like NPHP1, NPHP4, and RPGRIP1L (Garcia-Gonzalo et al., 2011; Sang et al., 2011). Mutations in the corresponding genes are typically associated with nephronophthisis (Mill et al., 2023; Reiter and Leroux, 2017). Another key TZ component is the MKS complex, composed of proteins either associated with the ciliary membrane or located in its vicinity, such as TCTN1-3, TMEM proteins, AHI1, and B9D1/2 (Garcia-Gonzalo et al., 2011; Sang et al., 2011). Mutations in MKS complex components are often linked to Meckel and Joubert syndromes. These two complexes not only interact with each other but also with other TZ components, namely, a scaffolding protein CEP290. Besides the core TZ complexes just outlined, several additional proteins are associated with the TZ, expected to contribute to ciliary gating regulation via modulation of TZ assembly or function (Park and Leroux, 2022). An example of such a component is the protein DZIP1 (Lapart et al., 2020). Within the complex TZ interactome, CEP290 and RPGRIP1L appear to function as the most upstream regulators in the hierarchical assembly of the TZ (Park and Leroux, 2022; Wiegering et al., 2018).

Ciliary membrane and intraciliary space

The ciliary membrane surrounding the axoneme is continuous with the plasma membrane (Zhao et al., 2023). At the junction where these two membranes meet, an intermediate zone typically forms an inward invagination known as the ciliary pocket, encasing the proximal region of the axoneme. This pocket is notably rich in clathrin-coated pits, indicating a potential role in membrane remodeling and selective cargo recycling specific to the ciliary membrane (Molla-Herman et al., 2010). The composition of the ciliary membrane differs significantly from that of the plasma membrane, particularly in terms of specific lipids and proteins (Conduit and Vanhaesebroeck, 2020). Phosphoinositides (PIPs) serve as a prime example of lipids that exhibit distinct spatial distribution within specialized subdomains of the ciliary membrane. The ciliary membrane is particularly enriched in PIP, while levels of PIP2 and PIP3 are low. In contrast, the plasma membrane contains high levels of both PIP2 and PIP3. Notably, PIP2 accumulates at the intermediate zone near the base of the cilium, whereas PIP3 is specifically enriched in the membrane surrounding the transition zone (Chávez et al., 2015; Conduit et al., 2021; Garcia-Gonzalo et al., 2015; Park et al., 2015). It should be noted that several TZ proteins contain putative PIP binding regions, likely mediating the physical connection between the axoneme and the ciliary membrane via the TZ protein network (Park and Leroux, 2022). The distinct PIP distribution within the cilium is maintained by cilia-residing enzymes such as INPP5E, which converts the PIP2 into PIP within the cilium, thereby preserving the unique lipid boundary at the ciliary base (Chávez et al., 2015; Garcia-Gonzalo et al., 2015; Park et al., 2015).

Analogous to the relationship between the ciliary membrane and the plasma membrane, the soluble content of the cilium, typically termed the cilioplasm, is continuous with the cytoplasm, yet exhibits a distinct composition. Ions and other small molecules, too small to be affected by the gating mechanisms at the ciliary base, can freely diffuse between the cytosol and the cilioplasm (Breslow et al., 2013). However, their concentrations can still vary significantly between these two compartments. A notable example is calcium, which typically reaches much higher steady-state levels within the cilioplasm than in the surrounding cytoplasm (Delling et al., 2013). This discrepancy can be explained by the difference in size: the ciliary volume is several orders of magnitude smaller than the volume of the whole cell. As a result, even minor fluctuations — amounting to just a few molecules — can lead to substantial shifts in ion concentration within the confined space of the cilium. For instance, it has been estimated that a single molecule of cAMP can increase its concentration inside the cilium by approximately 10 nM (Paolocci and Zaccolo, 2023). This extreme sensitivity and compartmentalization underpin the role of primary cilia as highly efficient and responsive signaling organelles (Hilgendorf et al., 2024).

Theme 1: Mechanisms and functions of the CEP164-TTBK2 module

Growing evidence, including my own work ([Benk Vysloužil et al., 2025 #Appendix 3](#); [Bernatik et al., 2020 #Appendix 9](#); [Binó and Čajánek, 2023 #Appendix 4](#); [Cajánek and Nigg, 2014 #Appendix 14](#); [Hanakova et al., 2019 #Appendix 10](#); [Rosa E Silva et al., 2022 #Appendix 5](#)), points to a prominent role for the CEP164–TTBK2 module in regulating key steps of ciliogenesis, reviewed in ([Čajánek et al., 2025 #Appendix 1](#); [Lacigová and Čajánek, 2025 #Appendix 2](#)). Given that, I will start with a brief introduction of both proteins. CEP164 is a structural component of distal appendages, featuring an N-terminal WW domain followed by long intrinsically disordered or coiled-coil regions ([Cajánek and Nigg, 2014 #Appendix 14](#); [Graser et al., 2007](#); [Schmidt et al., 2012](#)). Notably, mutations in *CEP164* lead to nephronophthisis-type of ciliopathy (Chaki et al., 2012). TTBK2 is a S/T kinase and a distant member of the casein kinase 1 (CK1) superfamily, with about 40% identity in the kinase domain with CK1 δ/ϵ and almost 90% kinase domain identity with its sibling kinase, TTBK1 (Flax et al., 2024; Ikezu and Ikezu, 2014; [Lacigová and Čajánek, 2025 #Appendix 2](#)). Mutations in *TTBK2* found in patients generate a premature stop codon around position 450 and lead to spinocerebellar ataxia type 11 (Houlden et al., 2007). Importantly, the loss of either CEP164 or TTBK2 prevents primary cilia assembly, making both proteins crucial regulators of ciliogenesis (Goetz et al., 2012; Graser et al., 2007). The possibility of CEP164–TTBK2 interaction was first suggested by Chaki, Hildebrandt, and colleagues, who identified TTBK2 as a binding partner of CEP164 fragments through a yeast two-hybrid screen (Chaki et al., 2012). The mechanism and functional consequence of this interaction were subsequently explored

during my postdoctoral work, prompted by the observation that ciliogenesis defects in cells depleted of CEP164 resembled those seen following mutation or siRNA-mediated depletion of TTBK2 (Cajane and Nigg, 2014 #Appendix 14; Goetz et al., 2012). These findings defined a model of ciliogenesis in which cilia formation is triggered by the recruitment of TTBK2 to the distal appendages of the mother centriole through its interaction with CEP164. CEP164 (and, in turn, TTBK2) is typically lost from the mother centriole during the rearrangement of distal appendages at G2/M, and brought back with the onset of the G1 phase of the next cell cycle (Cajane and Nigg, 2014 #Appendix 14; Schmidt et al., 2012; Viol et al., 2020). The CEP164–TTBK2 interaction interface comprises the C-terminal part of TTBK2 (Cajane and Nigg, 2014 #Appendix 14), specifically the region 1074-1083 (Oda et al., 2014; Rosa E Silva et al., 2022 #Appendix 5), and the N-terminal WW domain of CEP164 (amino acids 62-84) (Cajane and Nigg, 2014 #Appendix 14; Oda et al., 2014; Rosa E Silva et al., 2022 #Appendix 5). We revealed the binding affinity between CEP164 and TTBK2 moieties *in vitro* to be approximately 60 μ M (Rosa E Silva et al., 2022 #Appendix 5), in line with reports on other WW-domain-mediated interactions (McDonald et al., 2011).

The identification of the instrumental role of the CEP164–TTBK2 module in ciliogenesis has raised a number of outstanding questions regarding the regulation of their interaction, the extent of the module's functions in cilia, and the underlying mechanisms. I will start with the question of how the interaction between CEP164 and TTBK2 is regulated. As already mentioned, our study, done in collaboration with the lab of Mark van Breugel, resolved the structure of the CEP164 interface binding to TTBK2 using crystallography and NMR. The data suggest that the N-terminal part of CEP164 (1-109) comprises an α -helical bundle whose three helices pack together to form a highly conserved hydrophobic core. The WW domain has a canonical three-stranded topology and packs against the α -helical bundle (Rosa E Silva et al., 2022 #Appendix 5). In addition, we identified an intramolecular interaction in CEP164 between Q11 and Y73 that is critical for the stability of the WW domain, and consequently for the ability of CEP164 to bind TTBK2 to promote ciliogenesis. Moreover, we found that R93 was important for the stability of an α -helical bundle located adjacent to the CEP164–TTBK2 binding interface, and its mutation moderately affected the binding *in vitro* and ciliogenesis in cells (Rosa E Silva et al., 2022 #Appendix 5). These findings are particularly intriguing, as they provide an underlying mechanism for the Q11P and R93W mutations described in nephronophthisis patients (Chaki et al., 2012).

CEP164 is not only a binding partner of TTBK2 responsible for its recruitment, but it is also a substrate of the kinase. In fact, we have identified several dozen S/T sites in CEP164 that are regulated by TTBK2 kinase activity, with several of such S/T sites located in the unstructured regions of CEP164, close to the CEP164–TTBK2 binding interface (Bernatik et al., 2020 #Appendix 9; Cajane and Nigg, 2014 #Appendix 14). Intriguingly, mutation of S166, S168, S172, and S201 to alanine showed a moderate effect on TTBK2 levels recruited to the mother centriole, supporting a hypothesis that TTBK2

phosphorylates CEP164 to facilitate its own recruitment (Bernatik et al., 2020 #Appendix 9). Furthermore, both TTBK2 and CEP164 have been found to bind PI4P in proximity to the CEP164–TTBK2 interaction interface. In turn, the PI4P binding has been suggested to compromise the TTBK2–CEP164 complex formation, hence putting the regulation of the interaction under the control of INPP5E and PIPKI γ (Xu et al., 2016). In addition, a recent study has proposed that CEP164 forms dynamic condensates with TTBK2 through a phase separation to facilitate TTBK2 recruitment to the mother centriole (Chou et al., 2025). Nonetheless, while the authors argue for a model in which the phase separation mode cooperates with the WW domain-mediated mode of TTBK2 recruitment, the structural basis for such cooperation and its potential impact on TTBK2 levels at the mother centriole are not entirely clear.

The functions of the CEP164–TTBK2 complex at the mother centriole/ciliary base, and the mechanisms underlying them, arguably represent one of the most fundamental yet not fully resolved questions in the cilium assembly pathway regulation. Work from several labs suggests that TTBK2 recruitment to the distal appendages, initially seen mainly as a 'trigger' to initiate ciliogenesis, serves a more complex role by acting at multiple levels to ensure not only proper cilium assembly, but also its maintenance and function. Given that the kinase activity of TTBK2 is essential for cilia formation (Goetz et al., 2012), identification of its substrates and, in turn, elucidating the structure-function relationship for individual phosphorylations represents a significant milestone in understanding the cilium assembly pathway. Known substrates of TTBK2 include CEP164, CEP83, CEP89, CEP97, CCDC92, MPP9, DVL2/3, KIF2A, RABIN8, and TTBK2 itself through autophosphorylation (Benk Vysloužil et al., 2025 #Appendix 3; Bernatik et al., 2020 #Appendix 9; Cajanek and Nigg, 2014 #Appendix 14; Hanakova et al., 2019 #Appendix 10; Huang et al., 2018; Lo et al., 2019; Oda et al., 2014; Watanabe et al., 2015), **Fig.2**. A shared characteristic among these proteins is the presence of extensive intrinsically disordered regions (IDRs), which lack stable tertiary structures and instead exist as dynamic ensembles of rapidly shifting conformations (Bah and Forman-Kay, 2016; Dyson and Wright, 2005). Phosphorylation of these IDRs can significantly influence their biological roles by reshaping the conformational energy landscape and regulating interactions with other protein domains (Bah et al., 2015; Bah and Forman-Kay, 2016; Cohen, 2000). This suggests that TTBK2-mediated phosphorylation may enable these proteins to adopt specific three-dimensional structures that facilitate their timely interaction and assembly — critical steps in the primary cilia formation.

CEP164–TTBK2 module serves multiple functions during the primary cilium assembly (**Fig.3**). Before discussing these individual functions in detail, I need to outline key steps in the primary cilium assembly pathway. The earliest visible event in ciliogenesis is the appearance of a vesicle at the distal appendages (Sorokin, 1962, 1968; Sotelo and Trujillo-Cenóz, 1958) (**Fig.4**). First, small vesicles, termed distal appendage vesicles (DAVs), attach to the distal appendages. The assembly and transport of the DAVs seems to be under the control of Myosin Va, recruited to the distal appendages at the onset of

ciliogenesis (Wu et al., 2018). Fusion of DAVs, coordinated by the action of two members of EPS15 homology domain (EHD) protein family, EHD1 and EHD3, together with the membrane fusion regulator SNAP29, subsequently gives rise to a large ciliary vesicle (CV) (Lu et al., 2015).

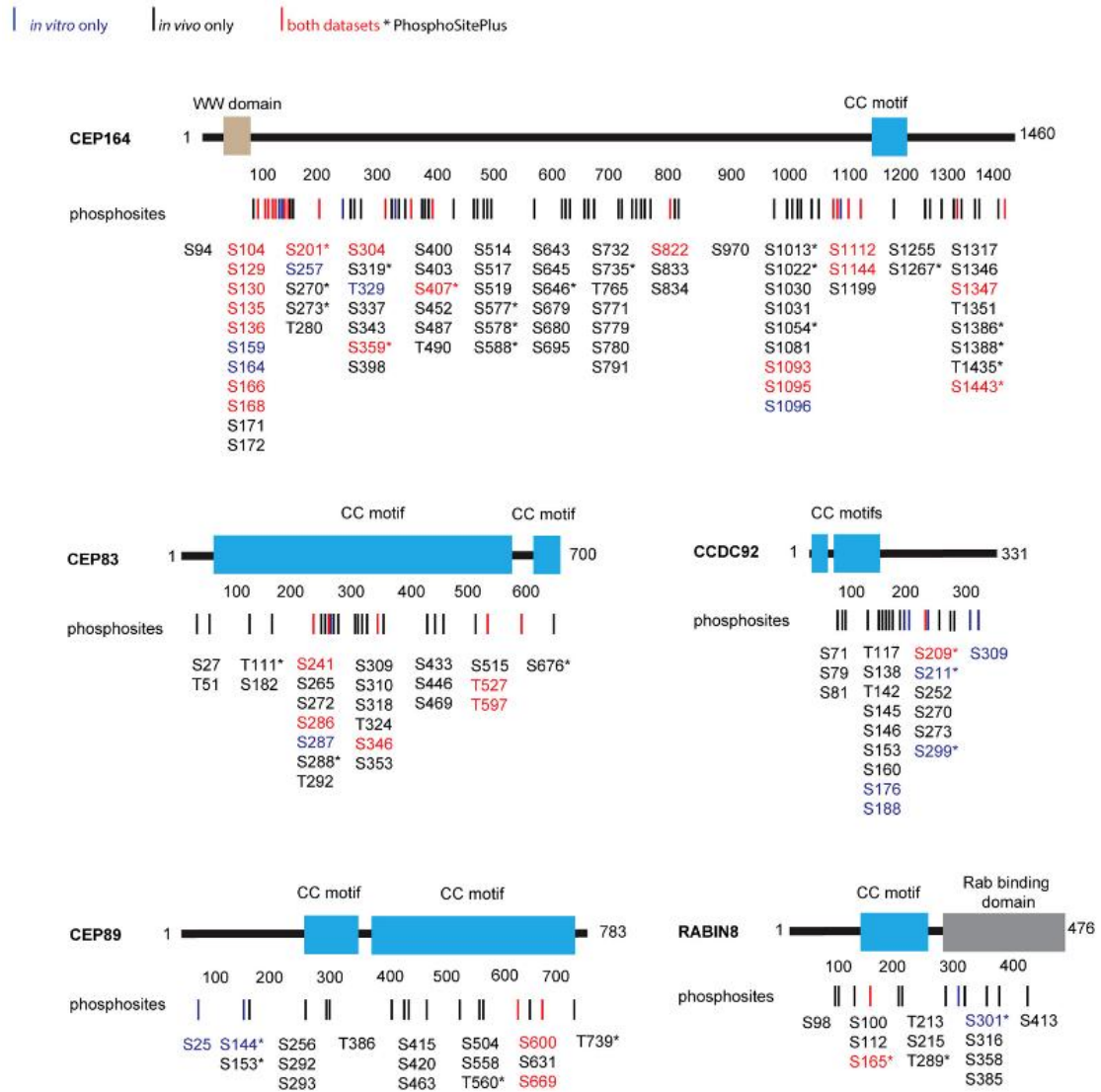


Fig.2: Phosphorylations induced by TTBK2. Each substrate structure is schematized; rectangles represent domains or motifs, and numbers indicate protein length in amino acids. Lines and numbers below each schematic mark TTBK2-induced phosphorylation sites. Red sites were detected both in vitro and in vivo, blue only in vitro, and black only in vivo. An asterisk denotes phosphorylation sites listed in PhosphoSitePlus. Adopted from (Bernatik et al., 2020 #Appendix 9).

In turn, the recruitment of EHD1/EHD3 requires the activity of small GTPase RAB34 (Ganga et al., 2021; Stuck et al., 2021). The CV membrane subsequently elongates to form the ciliary sheath, which develops alongside the growing axoneme and is regulated by the RAB11–RABIN8–RAB8 cascade (Hehnlly et al., 2012; Knodler et al., 2010; Nachury et al., 2007; Saha et al., 2024; Walia et al., 2019; Westlake et al., 2011; Yoshimura et al., 2007). Fusion of the sheath with the plasma membrane

establishes the ciliary membrane, marking the final stage of ciliogenesis by exposing the cilium to the extracellular environment (Zhao et al., 2023). The essential role of CEP164–TTBK2 in distal appendages-mediated vesicle docking and hence the initiation of ciliogenesis is well established (Lacigová and Čajánek, 2025 #Appendix 2). The recruitment of key regulators such as Myosin Va or RAB34 is abrogated, and CV fails to form in cells depleted from CEP164 or TTBK2 (Benk Vysloužil et al., 2025 #Appendix 2; Kanie et al., 2025a; Schmidt et al., 2012; Siller et al., 2017). In agreement, depletion of upstream regulators of distal appendage assembly leads to analogous phenotypes (Joo et al., 2013; Kanie et al., 2025a; Lo et al., 2019).

The mechanism by which DAVs or CV are captured by distal appendages, and the potential role of the CEP164–TTBK2 module in this process, remains poorly understood. Notably, CEP164 and most other distal appendage components lack domains capable of directly interacting with membranes. Interestingly, recent work identified a myristoylation motif in NCS1 and implicated it in CEP89-dependent interactions with DAVs/CV (Kanie et al., 2025b). Yet, as ablation of CEP89 or NCS1 leads to only subtle defects in cilia formation (Kanie et al., 2025a), additional mechanisms mediating interactions with DAVs/DA remain to be identified. On the other hand, available evidence offers initial mechanistic insight into the role of TTBK2-mediated phosphorylation. Specifically, phosphorylation of CEP83 at S29, T292, T527, and S698 by TTBK2 facilitates CV formation (Lo et al., 2019). In addition, our work identified several S/T phosphorylated by TTBK2 in RABIN8, including those within its RAB-binding domain (Bernatik et al., 2020 #Appendix 9). It is tempting to speculate that TTBK2 might in this manner influence the extension of the ciliary membrane; however, direct evidence for this is currently lacking. Moreover, TTBK2 also appears to influence distal appendage assembly, including regulating CEP164 levels at the mother centriole, which are critical for its own recruitment (Cajánek and Nigg, 2014 #Appendix 14; Kanie et al., 2025a). As a result, dissecting the precise roles of TTBK2 and individual distal appendage components in CV formation presents a significant challenge.

To address this, we employed a strategy to separate the function of CEP164 in recruiting TTBK2 from any additional roles it may have. This involved expressing partially active TTBK2 truncation variants that are unable to bind CEP164. Remarkably, partial ciliogenesis still occurred when truncated TTBK2 was expressed in TTBK2 knockout cells, despite the absence of TTBK2 at distal appendages. When CEP164 was subsequently removed in this context — where its TTBK2-recruiting function had already been bypassed — we observed persistent defects in the recruitment of MyosinVa and RAB34

to distal appendages. These findings indicate that CEP164 contributes to CV docking independently of its role in TTBK2 recruitment ([Benk Vysloužil et al., 2025 #Appendix 3](#)).

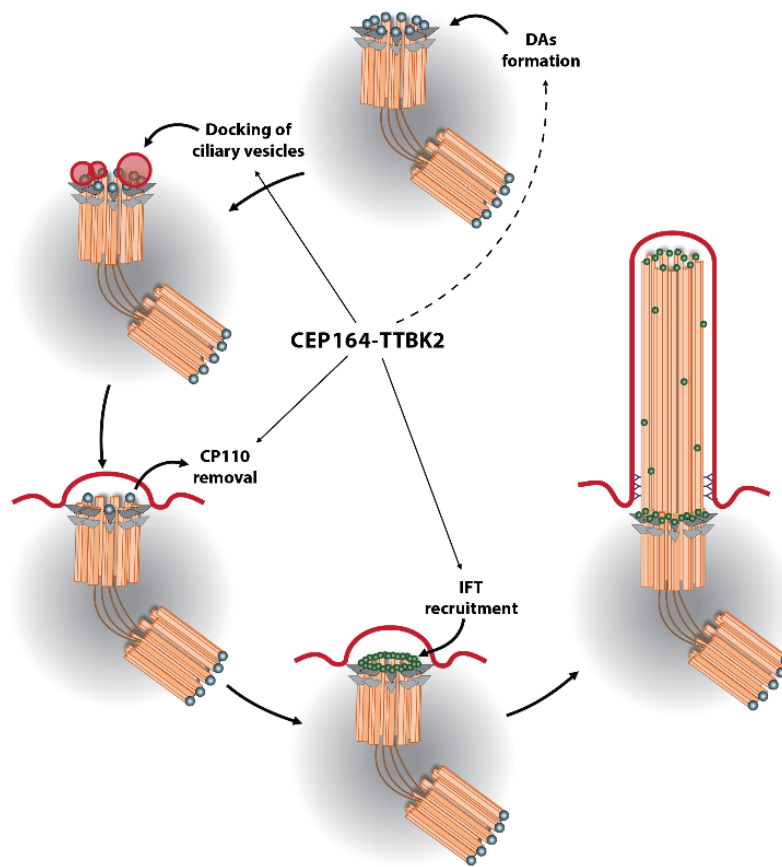


Fig.3: Functions of the CEP164–TTBK2 module in primary cilium assembly. The module plays an instrumental role in regulating CV formation, CP110–CEP97 removal, and IFT recruitment. Furthermore, it is implicated in the modulation of the assembly of distal appendages. Modified from ([Lacigová and Čajánek, 2025 #Appendix 2](#)).

Along the same lines, CEP164 has also been implicated in membrane extension by promoting RAB8–RABIN8 interactions through its C-terminal region (Schmidt et al., 2012; Siller et al., 2017). Of note, while the RABIN8–RAB8 module is essential for ciliary membrane outgrowth, it does not appear to be involved in the actual docking of DAVs or CV (Wu et al., 2018). Therefore, the interaction between CEP164 and the RABIN8–RAB8 module does not account for the role CEP164 has in CV formation, and the molecular basis of this function remains to be elucidated.

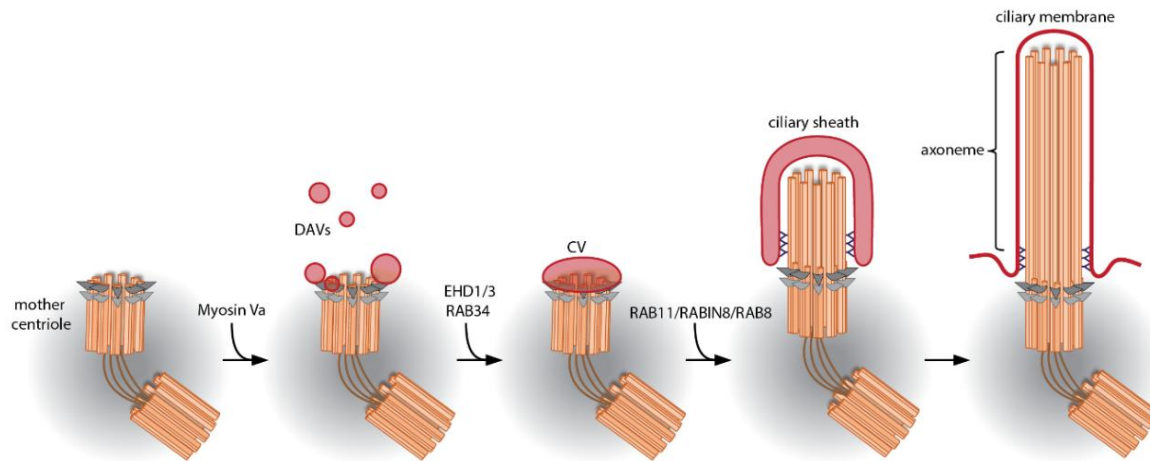


Fig.4: Vesicle docking and membrane extension during primary cilium assembly. Distal appendages are depicted as dark grey triangles, subdistal appendages are shown as light grey triangles. The transition zone (TZ) is indicated by Y linkers. DAVs – distal appendage vesicles, CV – ciliary vesicle.

Cilia growth occurs in parallel with axoneme extension (Čajánek et al., 2025 #Appendix 1). A well-established hallmark of ciliogenesis initiation in vertebrate cells is the removal of the distal end proteins CEP97 and CP110 from the mother centriole (Čajánek et al., 2025 #Appendix 1; Spektor et al., 2007). These proteins form a complex that depends on mutual localization and acts as a steric cap blocking axoneme outgrowth (Iyer et al., 2025; Kobayashi et al., 2011; Spektor et al., 2007). Removal of this cap requires TTBK2 kinase activity, as shown by our work and others (Benk Vysloužil et al., 2025 #Appendix 3; Cajánek and Nigg, 2014 #Appendix 14; Goetz et al., 2012; Tanos et al., 2013). However, how TTBK2 regulates this process is still not fully understood, as discussed in detail in our review (Lacigová and Čajánek, 2025 #Appendix 2). One possibility is that TTBK2 acts directly on the CP110–CEP97 complex, promoting its relocalization or degradation at the mother centriole. Indeed, TTBK2 has been shown to phosphorylate CEP97 (Oda et al., 2014), though the functional impact of this modification is unknown. Alternatively, TTBK2 may act indirectly, a model supported by findings that its phosphorylation of MPP9 facilitates CP110–CEP97 removal (Huang et al., 2018). Moreover, leveraging our previously mentioned model system with truncated TTBK2 points to a TTBK2 recruitment-independent role for CEP164 in regulating CP110 removal from the mother centriole (Benk Vysloužil et al., 2025 #Appendix 3), which warrants further investigation of the underlying mechanism. A plausible explanation may lie in the partial dependence of CP110–CEP97 loss on CV formation in some systems, as was recently discussed (Čajánek et al., 2025 #Appendix 1; Lacigová and Čajánek, 2025 #Appendix 2).

Intriguingly, work from the Goetz lab, together with recent findings from my lab, indicates that the CEP164–TTBK2 module also plays a crucial role in supporting the stability of the axoneme and, in

turn, in regulating cilia maintenance. Expression of truncated TTBK2 in either mice or human cells yields cilia that are notably shorter in length (Benk Vysloužil et al., 2025 #Appendix 3; Bowie et al., 2018; Loukil et al., 2020; Nguyen and Goetz, 2023). Our data suggest that the underlying mechanism lies in aberrant phosphorylation of KIF2A (Benk Vysloužil et al., 2025 #Appendix 3). KIF2A is a kinesin capable of depolymerizing microtubules, which in turn contributes to cilia resorption before mitosis (Miyamoto et al., 2015; Watanabe et al., 2015). KIF2A activity and affinity to microtubules are negatively regulated by TTBK2 phosphorylation, leading to low steady-state KIF2A levels at the cytosolic or axonemal microtubules/mother centriole distal end (Benk Vysloužil et al., 2025 #Appendix 3; Watanabe et al., 2015). Truncated TTBK2 fails to efficiently phosphorylate KIF2A, which consequently exhibits increased microtubule binding affinity and depolymerization activity *in vitro*, leading to aberrant cilia shortening in cells (Benk Vysloužil et al., 2025 #Appendix 3), **Fig.5**.

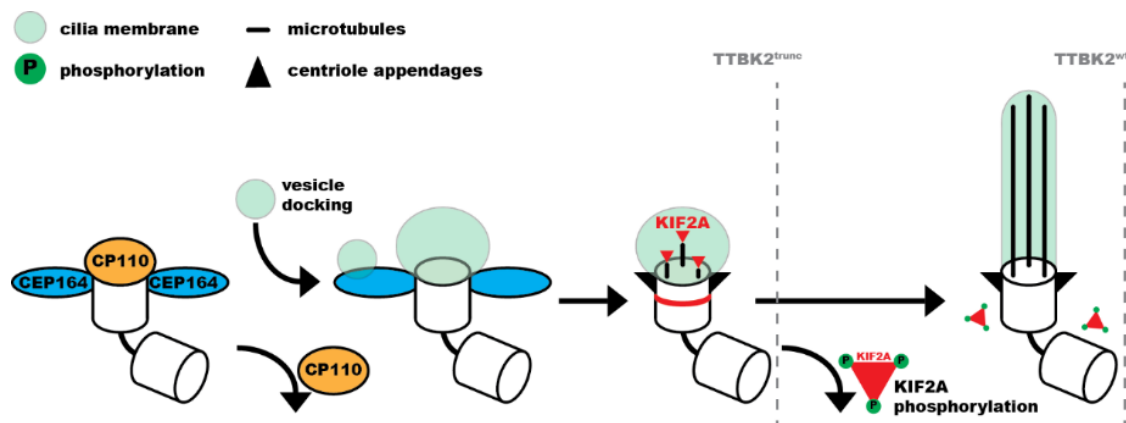


Fig.5: TTBK2 promotes axoneme elongation by phosphorylating KIF2A. TTBK2 activity inhibits KIF2A, reducing its basal body pool and allowing axoneme elongation. In contrast, truncated TTBK2 fails to inhibit KIF2A, resulting in its accumulation at the basal body and shorter cilia. Adopted from (Benk Vysloužil et al., 2025 #Appendix 3).

Another key function of the CEP164–TTBK2 module is regulating the recruitment of IFT protein complexes to the distal end of the mother centriole (Benk Vysloužil et al., 2025 - Appendix 3; Cajanek and Nigg, 2014 - Appendix 14; Goetz et al., 2012; Tanos et al., 2013). Intraflagellar transport (IFT) supports ciliary axoneme growth and maintenance by shuttling cargo between the cilia tip and base, a process driven by IFT complexes in coordination with kinesin and dynein motors (Lacey and Pigino, 2024; Lehtreck et al., 2017; Prevo et al., 2017). While it is well established that loss of CEP164, TTBK2, or CEP83 disrupts IFT protein association with the mother centriole and thereby prevents IFT particle assembly into multiunit trains, the underlying mechanism remains unclear, particularly with respect to relevant substrates of TTBK2.

As shown in my work (Cajánek and Nigg, 2014 #Appendix 14), IFT protein signals largely overlap with the CEP164–TTBK2 module at distal appendages, suggesting a direct association between IFT proteins and distal appendage components, under the regulation of the CEP164–TTBK2 module. This aligns with the established role of the module in IFT recruitment. Moreover, super-resolution microscopy supports this view, indicating that distal appendages might facilitate IFT train assembly and/or entry into the cilium (van den Hoek et al., 2022; Yang et al., 2019, 2018).

In this context, CEP164 emerges as a plausible candidate for directly mediating IFT docking during primary cilium formation, acting as a platform for IFT interaction while also concentrating TTBK2 at the correct site. Rescue experiments with TTBK2–CEP164 chimeras indicate that much of the CEP164 sequence is dispensable for ciliogenesis, as long as TTBK2 is retained at distal appendages via fusion to the C-terminal region of CEP164 (Cajánek and Nigg, 2014 #Appendix 14; Mori et al., 2025), which also binds the RAB8–RABIN8 module (Schmidt et al., 2012). This suggests two possible models: (1) the C-terminal region of CEP164 serves as a shared platform for membrane extension and IFT assembly, or (2) additional proteins mediate these functions. The first model is supported by our observations that IFT recruitment to basal bodies depends on CEP164 even when TTBK2 recruitment is artificially bypassed (Benk Vysloužil et al., 2025 #Appendix 3). The second is backed by studies in multiciliated airway epithelial cells, where CEP164 appears dispensable for IFT recruitment (Siller et al., 2017). Notably, IFT particles can assemble at the distal end of the mother centriole prior to ciliogenesis, likely due to basal TTBK2 activity already present at the site (Cajánek and Nigg, 2014 #Appendix 14; Tasaki et al., 2025).

Regarding the regulation of cilia entry, a study in *C. elegans* suggests that the entry of IFT particles depends on the distal appendage protein FBF1 (Wei et al., 2013). Additionally, TTBK2 has been proposed to regulate the localization of CPLANE proteins RSG1 and INTU (Agbu et al., 2018), which in turn facilitate the entry of a subset of IFT proteins (specifically, the IFT-A subcomplex) into cilia (Toriyama et al., 2016). INPP5E, a phosphoinositide phosphatase involved in regulating ciliary membrane composition, may also be recruited into cilia via transient interaction with CEP164 (Humbert et al., 2012). Moreover, SMO, a key receptor in the Hedgehog signaling pathway, exhibits abnormal ciliary levels in the presence of hypomorphic *TTBK2* alleles in mice (Bowie et al., 2018), suggesting a potential role for the CEP164–TTBK2 module in ciliary gating (Čajánek et al., 2025 #Appendix 1; Lacigová and Čajánek, 2025 #Appendix 2).

As I mentioned earlier, the transition zone (TZ) serves as the primary gating mechanism controlling ciliary entry. Since the loss of CEP164–TTBK2 module components prevents the onset of ciliogenesis, TZ formation is also blocked in such cases (Schmidt et al., 2012; Tanos et al., 2013; Xu et al., 2016). Thus, the current view is that CEP164–TTBK2 may influence TZ indirectly as part of its role

in the ciliogenesis pathway. Any direct involvement of the CEP164–TTBK2 module in regulating gating at the level of TZ remains to be investigated.

Last but not least, the aspect of CEP164–TTBK2 module biology I want to discuss is its function in relation to a specific cell type and cilia type. The role of the CEP164–TTBK2 module as an indispensable element in the cilium assembly pathway is supported by numerous studies using mouse models or human cell lines, although notable exceptions that prove the rule do exist. As shown in our work, human pluripotent stem cells (hPSCs)-derived neural rosette cells are able to assemble primary cilia even in the absence of TTBK2 (albeit with reduced efficiency) (Binó and Čajánek, 2023 #Appendix 4). The mechanism for this rescue seems to lie in the prominent upregulation of expression of TTBK1, a sibling kinase of TTBK2, upon the onset of hPSCs differentiation into neural rosettes. It is important to mention that undifferentiated hPSCs lacking TTBK2 fail to form any primary cilia (Binó and Čajánek, 2023 #Appendix 4). In turn, high levels of TTBK1 appear to partially compensate for the lack of TTBK2 activity in neural rosettes, despite the fact that TTBK1 lacks CEP164 binding motifs and therefore is not recruited to distal appendages (Binó and Čajánek, 2023 #Appendix 4; Lacigová and Čajánek, 2025 #Appendix 2). Similarly, high levels of TTBK2 activity outside of the mother centriole likely mediate the formation of primary cilia by truncated forms of TTBK2 (Benk Vysloužil et al., 2025 #Appendix 3). Intriguingly, while conditional ablation of *CEP164* in mice prevents recruitment of IFT complexes to mother centrioles in specialized cilia of photoreceptor cells in retina (Reed et al., 2022), it leaves IFT protein recruitment intact in airway motile cilia (Siller et al., 2017), indicating a possible customization of CEP164–TTBK2 module functions in different cilia types.

To conclude this chapter, I want to emphasize that while the individual functions of the CEP164–TTBK2 module in the cilium assembly pathway are becoming clearer through work from my lab and others, the main bottleneck remains a lack of mechanistic insight, particularly in establishing clear kinase–substrate relationships. Although we have made solid progress in identifying novel substrates and mapping individual phosphosites, linking specific phosphorylation events to distinct functions to fully resolve the molecular mechanisms still somewhat falls short of expectations. Beyond the common challenges in kinase research, which we have discussed in detail in a recent review, along with potential strategies to address them (Lacigová and Čajánek, 2025 #Appendix 2), most identified TTBK2 phosphosites lack functional validation simply because the roles of the corresponding substrates remain poorly understood. For example, CCDC92, identified as a TTBK2 substrate (Bernatik et al., 2020 #Appendix 9), has been found to interact with CEP164 in several studies (Chaki et al., 2012; Pejskova et al., 2020 #Appendix 8), yet its exact function in ciliogenesis remains unknown. Similarly, the WNT pathway components DVL2/3 (Hanakova et al., 2019 #Appendix 10) are also CEP164 interactors (Chaki et al., 2012), but their role in primary cilia formation is still unclear (Bryja et al., 2017 #Appendix 13; Wallingford and Mitchell, 2011).

Cilia and centrosomes in stem cells

I will use our sortie into hPSC-derived neural rosettes ([Binó and Čajánek, 2023 #Appendix 4](#)) as a proxy to briefly discuss the role of centrioles and cilia in stem cell biology. In mice, primary cilia begin to form in the epiblast, following blastocyst implantation (Bangs et al., 2015). Blastocyst-derived hPSCs, encompassing embryonic stem cells (ESCs) and induced pluripotent stem cells (iPSCs), possess two trademark features — they can self-renew and differentiate into all cell types “in a dish” (Bárta et al., 2021). Interestingly, hPSCs are capable of assembling primary cilia (Banda et al., 2015; Kiprilov et al., 2008), raising questions about the role of these structures in regulating self-renewal and differentiation potential of hPSCs. To address this, we first developed a customized protocol to efficiently generate null alleles using CRISPR/Cas9 gene editing in hPSC cultures ([Bohaciakova et al., 2017 #Appendix 12](#)). Subsequently, we demonstrated that ablation of primary cilia by removal of TTBK2 does not affect the self-renewal properties of hPSCs ([Binó and Čajánek, 2023 #Appendix 4](#)). This is in line with a study reporting the generation of KIF3A/B double knockout hPSCs that lack cilia yet self-renew normally (Cruz et al., 2022). Thus, the study by my postdoc Lucia Binó established that primary cilia do not play a major role in the regulation of undifferentiated hPSCs. In support of this conclusion, overactivation of the cilia-resident HH signaling pathway (Ingham, 2022) fails to prevent hPSCs differentiation induced by FGF2 withdrawal (Wu et al., 2010). Furthermore, our results challenge the proposed model where the acquisition of PAX6 positive neural progenitor fate during hPSC differentiation relies on primary cilia (Jang et al., 2016). Instead, ablation of primary cilia leads to elevated levels of HH signaling, which appears to drive the higher proliferation of neural progenitors at the neural rosette stage, reflected by the larger overall size of neural rosettes ([Binó and Čajánek, 2023 #Appendix 4](#)).

While primary cilia and TTBK2 are dispensable in undifferentiated hPSCs, depletion of centrioles has profoundly more detrimental consequences for stem cell properties, as demonstrated in our work. Specifically, loss of centrioles due to inhibition of PLK4 or depletion of STIL (for more information on the regulation of centriole biogenesis and centrosome formation, please see (Breslow and Holland, 2019; [Bryja et al., 2017 #Appendix 13](#); Nigg and Holland, 2018)) leads to loss of self-renewal potential and induction of differentiation ([Renzova et al., 2018 #Appendix 11](#)). This outcome is likely due to two contributing mechanisms. First, loss of centrioles triggers a p53-dependent surveillance pathway, previously described in somatic cells (Wong et al., 2015), which leads to cell cycle arrest and, concomitantly, induces differentiation in hPSCs (Bárta et al., 2021; [Renzova et al., 2018 #Appendix 11](#)). Second, centriole depletion also activates a p53-independent response that results in proteasome-mediated downregulation of key regulators of the undifferentiated state in hPSCs: OCT4 and Nanog ([Renzova et al., 2018 #Appendix 11](#)). Deciphering the exact mechanism of this protein turnover regulation requires future investigation.

Theme 2: Kinesins, IFT, and cell signaling in the regulation of primary cilia

As I already outlined, IFT represents the key mechanism that ensures the elongation, maintenance, and function of primary cilia by transporting cargo between the ciliary base and tip. The anterograde transport is mediated by kinesin motors, while dynein motors are responsible for the retrograde IFT (Lacey and Pigino, 2024; Rosenbaum and Witman, 2002). Biochemically, IFT proteins can be subdivided into two subcomplexes, IFT-A (comprising IFT144, IFT140, IFT139, IFT122, IFT121 and IFT43) and IFT-B (consisting of IFT172, IFT88, IFT81, IFT80, IFT74, IFT70, IFT57, IFT56, IFT54, IFT52, IFT46, IFT38, IFT27, IFT25, IFT22 and IFT20) (Lacey and Pigino, 2024; Prevo et al., 2017; Taschner and Lorentzen, 2016). The overall structure of the IFT particle (comprising both IFT-A and IFT-B proteins), along with the numerous interactions between individual IFT proteins that support its assembly, has been resolved in recent Cryo-EM studies (Hesketh et al., 2022; Lacey et al., 2023; Meleppattu et al., 2022; van den Hoek et al., 2022). Individual IFT particles/subcomplexes are assembled stepwise into larger polymers termed IFT trains (Lacey and Pigino, 2024; van den Hoek et al., 2022). Both diffusion and vesicle-mediated transport have been implicated in delivering IFT train components to their assembly sites at the mother centriole (Hibbard et al., 2021; Mitra et al., 2025). Regardless of the means of delivery, the recruitment of IFT proteins relies on the CEP164–TTBK2 module, as I discussed earlier in detail. Interestingly, structural studies of *Chlamydomonas* flagella have shown that each microtubule doublet functions as a bidirectional, double-track railway: anterograde IFT trains travel along the B-tubule, while retrograde trains move along the A-tubule (Chhatre et al., 2025; Stepanek and Pigino, 2016).

Additional interactions pertinent to the function of IFT trains include binding to motor proteins, cargo adaptors, and the cargo itself. However, in contrast to the fairly well-characterized interactions between IFT proteins, much less is known about the binding of IFT particles to motor or cargo proteins — partly due to the flexibility of the presumed binding domains, which hinders their analysis by Cryo-EM or Cryo-ET. Notable exception here is the interaction between dynein motor and IFT trains, which is mediated by dynein binding to IFT54 and IFT80 (Lacey et al., 2023). Given that microtubules are the main components of the ciliary axoneme, tubulin represents perhaps the most prominent cargo, transported by IFT (Hao et al., 2011; Rosenbaum and Witman, 2002). To identify potential cargo binding sites in IFT trains, we, in collaboration with the lab of Esben Lorentzen, screened for putative domains in IFT proteins. We identified regions in the N-terminal portions of IFT81 and IFT74 that resemble a tubulin-binding motif. Using structural biology and biochemical approaches, we demonstrated that the N-terminal region of IFT81 binds tubulin, a process facilitated by the N-terminal region of IFT74, resulting in K_d of approximately $0.9 \mu\text{M}$ (Bhogaraju et al., 2013 #Appendix 15). Specifically, binding of the positively charged surface patch on the N-terminal domain of IFT81 to the globular domain of tubulin confers specificity, while IFT74 appears to recognize the tubulin tail to increase the affinity of

the interaction (Bhogaraju et al., 2013 #Appendix 15). In agreement with the role of the N-terminal part of IFT81, tubulin-binding-defective mutants of IFT81 failed to rescue ciliogenesis in IFT81-depleted cells (Bhogaraju et al., 2013 #Appendix 15). Moreover, mutation of the tubulin-binding region leads to the formation of very short flagella and reduced tubulin transport by IFT in *Chlamydomonas* (Kubo et al., 2016). Together, these findings establish that tubulin binding to IFT74-IFT81 represents a mechanism of tubulin delivery inside cilia to support their growth and maintenance.

Heterotrimeric kinesin-2 (composed of KIF3A, KIF3B, and the kinesin-associated protein (KAP)) is considered the key motor driving anterograde IFT (Cole et al., 1998; Engelke et al., 2019; Morris and Scholey, 1997; Nonaka et al., 1998; Rosenbaum and Witman, 2002). Indeed, heterotrimeric kinesin-2 appears to be the sole kinesin driving anterograde IFT in *Chlamydomonas*. However, homodimeric kinesin-2 (OSM-3) takes over IFT just behind the TZ to deliver IFT trains to the cilia tip in *C.elegans* instead of the heterotrimeric kinesin-2 (Ou and Scholey, 2022; Pan et al., 2006; Prevo et al., 2017). Homodimeric kinesin-2 (KIF17) is present in cilia also in vertebrate cells, but current evidence argues against a direct role in IFT. In addition to kinesin-2, cilia contain several other kinesins, some of which play roles in cilium biogenesis (Ou and Scholey, 2022; Reilly and Benmerah, 2019). Specifically, these non-canonical ciliary kinesin motors are thought to function as accessory motors that cooperate with canonical kinesin-2 to regulate axoneme assembly, dynamics, and length (Ou and Scholey, 2022; Scholey, 2008). Since the primary cilia of different cell types exhibit structural and functional specializations (Ott et al., 2024), the activity of non-canonical ciliary kinesin motors may contribute to this diversification. However, experimental evidence supporting this hypothesis is sparse.

Our work identified KIF14 as a novel non-canonical kinesin in primary cilia (Pejskova et al., 2020 #Appendix 8). KIF14 is a member of the kinesin-3 family, with an atypical disordered region found N-terminally to its motor domain. The disordered region and protein dimerization via C-terminal regions are implicated in the regulation of KIF14 processive movement *in vitro* (Zhernov et al., 2020). Before its identification as a ciliary kinesin, KIF14 has been linked to the regulation of chromosome segregation and cytokinesis (Carleton et al., 2006; Gruneberg et al., 2006; Reilly et al., 2018). Our data demonstrate that KIF14 is required for proper primary cilium biogenesis in several vertebrate cell lines. Its depletion reduces the percentage of ciliated cells, and the cilia that do form are significantly shorter. In addition, the cilia fail to respond to HH pathway activation (Pejskova et al., 2020 #Appendix 8). The underlying mechanism appears to involve accumulation of Aurora A, a kinase responsible for cilium disassembly before cell division (Čajánek et al., 2025 #Appendix 1; Pan et al., 2004; Pugacheva et al., 2007). Specifically, cells depleted of KIF14 show increased levels of Aurora A at the cilia base/mother centriole and in their vicinity. In turn, inhibition of Aurora A rescues the cilia formation defect in KIF14-depleted cells, yet does not restore the responsiveness to HH ligand treatment (Pejskova et al., 2020 #Appendix 8). This indicates that while Aurora A acts downstream of KIF14 in primary cilia, an additional Aurora A-independent mechanism underlies its role in ciliary signaling (Fig.6). Our preprinted work suggests

that regulation of ciliary dynamics, and possibly IFT, may represent such a mechanism (Mikulenková et al., 2025). To address this, we optimized workflows for fluorescent tagging of individual ciliary compartments, giving us an important competitive edge to study cilia dynamics and IFT at high spatiotemporal resolution using live-cell imaging in vertebrate cells (Binó et al., 2022 #Appendix 6).

Besides KIF14, an additional member of the kinesin-3 family, KIF13B, has been implicated in the regulation of cilia assembly and function. In *C. elegans*, its ortholog KLP-6 regulates cilia trafficking in a subset of male-specific neurons (Morsci and Barr, 2011). In fact, the authors demonstrated that KLP-6 directly participates in IFT by modulating the velocity of kinesin-2 motors (Morsci and Barr, 2011). This makes KIF13B/KLP-6 the first non-canonical kinesin regulating IFT. Interestingly, vertebrate KIF13B is capable of bidirectional movement in cilia of hTERT-RPE-1 cells, similar to that seen for kinesin-2 (Juhl et al., 2023). However, its possible participation in the modulation of IFT is unclear. Instead, KIF13B has been implicated in regulating the composition of the membrane subdomain surrounding the TZ and, in turn, the HH signaling pathway (Schou et al., 2017). In addition, a recent study has linked KIF13B to the regulation of extracellular vesicle release from cilia (Rezi et al., 2025).

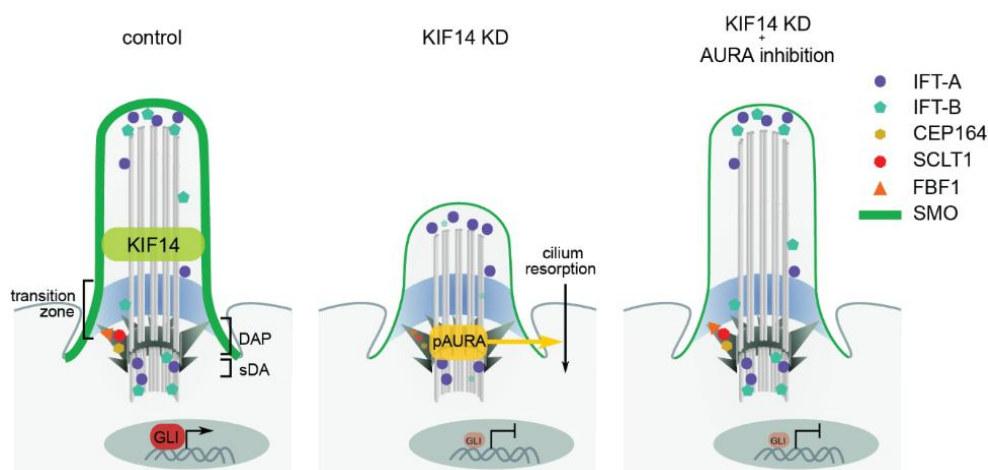


Fig.6: Phenotypes of KIF14 depletion and Aurora A inhibition in primary cilia. DAP–distal appendage proteins, sDA–subdistal appendages, KD–siRNA-mediated knockdown. Adopted from (Pejskova et al., 2020 #Appendix 8).

Primary cilia are highly dynamic organelles, meaning they rely strictly on the continuous transport of cargo in and out (Čajánek et al., 2025 #Appendix 1; Mill et al., 2023). In fact, just a few minutes of pharmacological inhibition of IFT can already lead to visible alterations in ciliary composition (Engelke et al., 2019). A key factor deciding whether a cilium will be assembled, maintained, or disassembled is the cell cycle, thoroughly discussed in several review articles that I co-authored (Bryja et al., 2017 #Appendix 13; Čajánek et al., 2025 #Appendix 1). The most widely used method to induce ciliogenesis in mammalian cell culture involves serum starvation to enrich the G1/G0

population, as exit from the cell cycle/entry into quiescence is considered the most permissive condition for primary cilium assembly (Binó et al., 2022 #Appendix 6; Čajánek et al., 2025 #Appendix 1; Seeley and Nachury, 2010). Conversely, the primary cilium is typically disassembled before the cell enters mitosis (Ford et al., 2018). As a result, primary cilia were initially considered hallmark structures of the quiescent state, potentially even serving a checkpoint function for cell cycle entry (Čajánek et al., 2025 #Appendix 1; Izawa et al., 2015; Seeley and Nachury, 2010). However, it is now recognized that primary cilia are present not only in non-cycling cells but also in proliferating (yet non-mitotic) cells, as demonstrated by live-cell imaging and *in vivo* studies (Bangs et al., 2015; Ford et al., 2018; Ho et al., 2020).

Although direct evidence for a checkpoint role of primary cilia is lacking, their close relationship with the cell cycle is well established (Bryja et al., 2017 #Appendix 13; Čajánek et al., 2025 #Appendix 1; Seeley and Nachury, 2010). One key aspect is the influence of cell cycle regulators on cilia dynamics, particularly proteins known for their mitotic roles. These proteins, such as Aurora A or NEK kinases, and the anaphase-promoting complex (APC), are typically localized at the centrosome or ciliary base, with expression or activity levels low in G1 and peaking in G2/M. In turn, both Aurora A and NEK kinases promote cilia disassembly, and their depletion leads to axoneme elongation (Čajánek et al., 2025 #Appendix 1; Fry et al., 2012; Pan et al., 2004; Pugacheva et al., 2007; Wang et al., 2014). Another well-characterized link between cilia and the cell cycle is the excessive cell proliferation that drives kidney cyst formation — a hallmark of several ciliopathies (Braun and Hildebrandt, 2017; Reiter and Leroux, 2017). Mutations in ciliary proteins such as polycystin-1/2 (PKD1/2) or distal appendage protein CEP164 can cause the formation of cysts, which can be partially suppressed by cyclin-dependent kinase inhibition (Airik et al., 2019; Bukanov et al., 2006). Last but not least, the link between primary cilia and the cell cycle that I want to highlight is the dual role of several proteins in regulating both cilium biogenesis and mitosis (**Fig.7**). Since both processes rely on microtubules, it is unsurprising that ciliary kinesins and other microtubule-associated proteins also contribute to cell division regulation (Čajánek et al., 2025 #Appendix 1; Ou and Scholey, 2022). For example, heterotrimeric kinesin-2 not only drives anterograde IFT but also plays broader roles in intracellular transport (Hirokawa et al., 2009). It associates with the mitotic spindle, and its mutation causes mitotic defects and aneuploidy (Haraguchi et al., 2006). Similarly, KIF14, originally identified as a cytokinesis-regulating kinesin at the midbody, localizes to the ciliary axoneme during interphase, where it regulates cilia growth, IFT, and Hedgehog signaling (Mikulenkova et al., 2025; Pejškova et al., 2020 #Appendix 8). This overlap between mitotic machinery and ciliary regulators also involves IFT (Čajánek et al., 2025 #Appendix 1). Thus, the available evidence suggests that cells repurpose key regulatory proteins, creating a shared toolkit for both cilia and cell cycle control. Classic mitotic regulators like Aurora A, NEKs, and APC drive cilia disassembly to prevent interference with spindle function. Conversely, cilia-residing proteins (e.g., IFT and motor proteins) often take on roles in mitosis or cytokinesis when the cilium is absent (Čajánek et

al., 2025 #Appendix 1). This raises the intriguing possibility that some ciliopathy-related pathologies may in fact arise from non-ciliary functions of these regulators (Lovera and Lüders, 2021; Reiter and Leroux, 2017).

As echoed several times throughout this text, primary cilia serve as crucial signaling organelles. This signaling function is supported by: (1) the compartmentalization of the cilium from the rest of the cell, and (2) the highly dynamic nature of the primary cilium, which allows for rapid changes in its composition to accommodate the specific requirements of a given signaling pathway. The Hedgehog (HH) signaling represents the prototypical pathway decisive for growth and patterning of several organs, critically depending on primary cilia (Bangs and Anderson, 2017; Huangfu et al., 2003; Ingham, 2022). For instance, hyperactive HH signaling due to a defect in IFT-A subcomplex promotes cystogenesis in the kidneys (Tran et al., 2014).

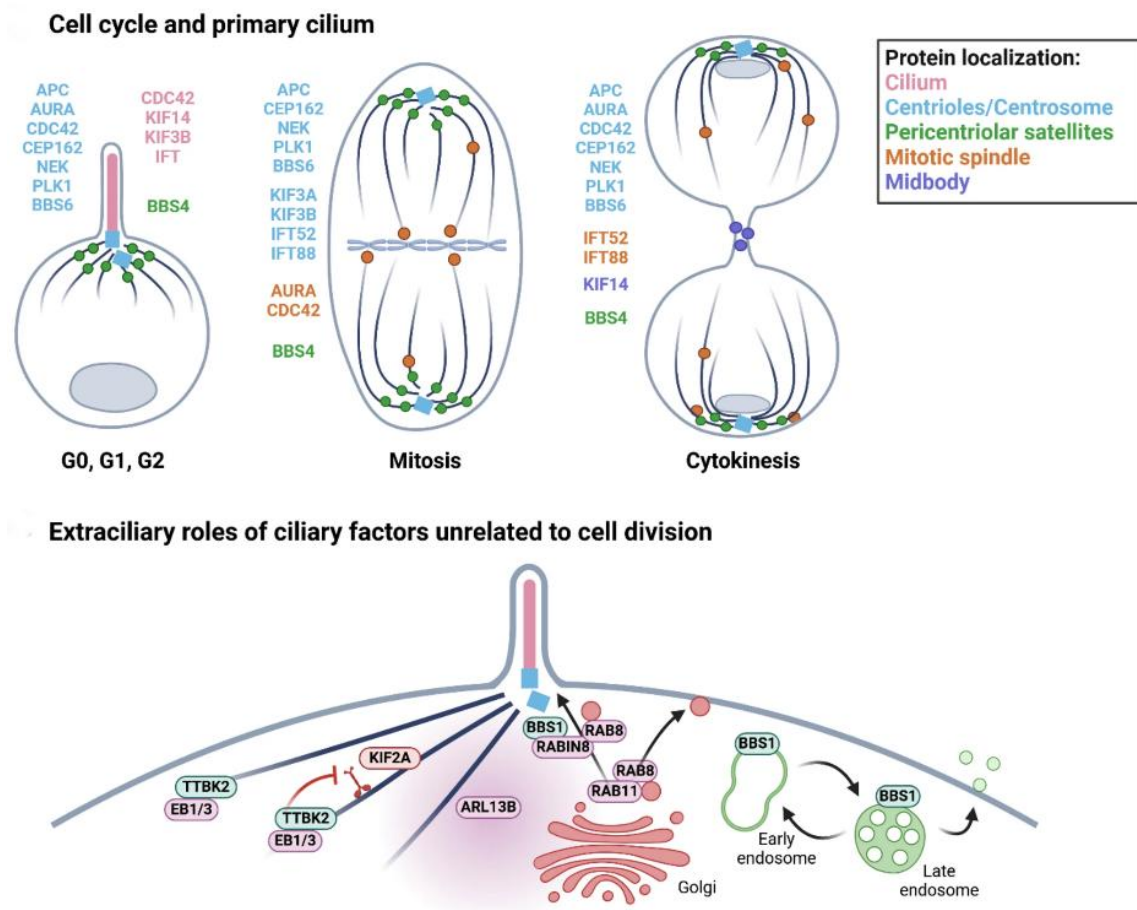


Fig.7: Dual role of cilia regulators. The upper panel illustrates that many regulators of mitosis act as regulators of ciliary function during interphase. The lower panel highlights the contribution of ciliary regulators to the global regulation of intracellular organization and trafficking. Adopted from (Čajánek et al., 2025 #Appendix 1).

In the absence of the HH ligand, receptor SMO is present in the ciliary membrane at very low levels, owing to its repression by another receptor, PTCH, which restricts SMO access to its activating sterol ligands. As a result, SMO is ubiquitinated and removed from the cilium. In this situation, PKA phosphorylates transcriptional regulators GLI2/3, promoting their proteolysis into repressor forms that prevent the transcription of HH target genes. In the presence of HH ligands, the ligand binds to PTCH, which in turn induces the removal of PTCH from cilia. This allows SMO to accumulate in the ciliary membrane and gain access to its activating sterols. Activated SMO promotes the export of receptor GPR161 from the cilium. The removal of GPR161 decreases cAMP levels and leads to reduced PKA activity. In addition, activated SMO also inhibits PKA by directly binding to it. Consequently, the processing of GLI2/3 into the repressor forms is blocked, allowing GLI2/3 to promote the transcription of HH-responsive genes in the nucleus (Hilgendorf et al., 2024; Ingham, 2022; Rohatgi et al., 2007; Shinde et al., 2020). Our finding that KIF14 is required for SMO accumulation in the ciliary membrane following HH ligand stimulation (Pejskova et al., 2020 #Appendix 8) suggests either insufficient import of SMO into cilia or excessive export in the absence of KIF14, warranting further investigation. Primary cilia are not only required for proper HH signaling in vertebrate cells but are also subject to remodeling in response to HH pathway activation. Specifically, acute stimulation with HH ligands leads to shortening of the primary cilium axoneme, likely due to a feedback response (Nager et al., 2017; Phua et al., 2017; Prasai et al., 2024).

WNT signaling is another prominent developmental pathway with ties to primary cilia, yet the relationship between WNT signaling and cilia remains somewhat controversial. The WNT/ β -catenin signaling pathway, like the HH pathway, is a key regulator of cell proliferation with broad roles in development and cancer. Central to this pathway is β -catenin, which translocates from the cytosol to the nucleus upon WNT ligand stimulation, where it partners with TCF/LEF proteins to activate gene expression. WNT ligands bind the Frizzled (FZD) receptor and LRP5/6 co-receptor, triggering a cascade via the scaffolding protein DVL that disrupts the β -catenin degradation complex (APC–AXIN– β -catenin) and inhibits GSK3 β /CK1-mediated phosphorylation. This prevents β -catenin degradation, allowing its stabilization and nuclear import (Maurice and Angers, 2025; Rim et al., 2022). In contrast, the non-canonical WNT pathway operates independently of β -catenin and includes branches such as WNT/PCP and WNT/Ca²⁺ (Bryja et al., 2017 #Appendix 13; Koca et al., 2022; Wallingford and Mitchell, 2011).

The controversy in WNT–cilium relationship lies in the fact that, while some studies argue that the WNT signaling pathway requires functional primary cilia, other reports show no change in WNT signaling following cilia ablation (Bernatik et al., 2021 #Appendix 7; Corbit et al., 2008; Gerdes et al., 2007; Huang and Schier, 2009; Lancaster et al., 2011; Ocbina et al., 2009; Simons et al., 2005; Sugiyama et al., 2011), discussed here (Bryja et al., 2017 #Appendix 13; Čajánek et al., 2025 #Appendix 1; Niehrs et al., 2025). Some of these observed discrepancies can be explained by context-specific activity of the

involved ciliary components (Patnaik et al., 2019) or their possible dual role (Bryja et al., 2017 #Appendix 13; Čajánek et al., 2025 #Appendix 1). As for the latter, compelling evidence indeed suggests that a key step of the WNT/ β -catenin cascade, namely the translocation of β -catenin into the nucleus, is controlled by IFT-A and heterotrimeric kinesin-2, independently of their role in ciliary trafficking (Balmer et al., 2015; Vuong et al., 2018).

Our research has pinpointed DVL as a plausible avenue for WNT signaling–cilium regulators crosstalk by identifying it as a substrate of TTBK2 (Bernatik et al., 2020 #Appendix 9; Hanakova et al., 2019 #Appendix 10). Furthermore, in contrast to CK1 ϵ , an established DVL kinase which promotes WNT/ β -catenin activation, TTBK2 appears to act as a negative regulator of WNT/ β -catenin pathway activation in a kinase activity-dependent manner (Hanakova et al., 2019 #Appendix 10). DVL is able to bind to CEP164 and localize to the centrosome and its vicinity (Bryja et al., 2017 #Appendix 13; Cervenka et al., 2016; Chaki et al., 2012), raising the still unanswered question of whether its phosphorylation by TTBK2 has any functional implications for cilium biology.

Another aspect of the WNT-cilium relationship we chose to explore was the potential impact of WNT signaling on ciliogenesis. It is well established that the transcription factor FOXJ acts upstream of motile cilia formation, and its expression is regulated by the WNT/ β -catenin signaling pathway (Walentek et al., 2012; Yu et al., 2008). However, the potential effects of WNT signaling on the assembly of primary cilia are notably less clear. The WNT/ β -catenin pathway has been shown to act as a negative regulator of ciliogenesis in neural progenitors in the cerebral cortex (Nakagawa et al., 2017). Conversely, treatment with WNT3a, a ligand that typically activates WNT/ β -catenin signaling, has been proposed to promote primary cilia assembly in hTERT-RPE1 (Kyun et al., 2020), while ablation of the LRP5/6 co-receptors has been found to impair ciliogenesis and cilia length maintenance in HEK293T cells (Zhang et al., 2023). On top of that, recent work has proposed that both ablation of WNT signaling and acute treatment with WNT3a ligand lead to impaired ciliogenesis in hTERT-RPE1 (Yuan et al., 2025). Our work — supported by findings from several cell lines, including NIH-3T3 and hTERT-RPE1, and leveraging CRISPR-edited null alleles of key WNT pathway components, treatment with recombinant WNT3a, and pharmacological inhibition of WNT ligand secretion — argues that, while WNT stimulation may have modest negative effects on cilia formation in certain contexts, WNT signaling is not generally required for the assembly of primary cilia (Bernatik et al., 2021 #Appendix 7). In my opinion, the discrepancies reported in the literature may be due to off-target effects of the experimental strategies used or differences in the timing of the applied WNT pathway stimulation/ablation, together indicating possible cell-type-/culture conditions-specific requirements for WNT signaling during ciliogenesis, as discussed previously (Bryja et al., 2017 #Appendix 13; Čajánek et al., 2025 #Appendix 1).

Future directions

While cilia have been known for centuries, the importance of primary cilia for human health was discovered relatively recently — approximately 25 years ago. This discovery has naturally sparked the interest of many cell and developmental biologists, leading to numerous seminal discoveries about the mechanisms and functions of primary cilia. That being said, many fundamental questions concerning primary cilia biology still remain unanswered. I have briefly outlined some of these questions and themes in the previous chapters. Pertinent to the focus of this thesis and the future research of my lab, respectively, I would like to take the opportunity to specifically discuss gaps and unanswered questions related to the CEP164–TTBK2 module and KIF14 in cilia.

Identification of the relevant substrates/phosphosites of TTBK2 and their functional validation to establish a kinase-substrate relationship represents perhaps the most obvious and important direction for moving the mechanistic understanding of cilia assembly regulation forward. However, this often tends to be easier said than done due to several bottlenecks (recently discussed in [\(Lacigová and Čajánek, 2025 #Appendix 2\)](#)). Importantly, thanks to tremendous progress in *in silico* structure biology, one can now model the impact of phosphorylation on protein structure and its subsequent effects on protein-protein interactions. Experiments that were considered science fiction not long ago (e.g., whole proteome *in silico* pulldown) have now become feasible with the latest release of AlphaFold, an AI system that predicts protein 3D structures from amino acid sequences (Abramson et al., 2024) and sufficient computing power (Lange et al., 2025). I am convinced that the right implementation of AlphaFold modeling into cell biology pipelines has the potential to significantly streamline the overall procedure of kinase-substrate relationship validation. Moreover, the possibility to specifically target TTBK2 pharmacologically (Bashore et al., 2023; Halkina et al., 2021) will allow us to study its mechanism in temporal resolution. Furthermore, a pipeline to efficiently isolate centrosomes (Carden et al., 2023) and primary cilia from various models for subsequent downstream applications, including proteomics, should be a significant benefit too.

Additionally, equally important questions relate to the mechanisms by which CEP164 regulates key steps of cilia formation independently of TTBK2 recruitment, as well as how the functions of the CEP164–TTBK2 module may be customized in different cell types and organisms.

It should also be rewarding to pursue the mechanistic basis of the role of KIF14 or any other cilia-residing non-canonical (other than the heterotrimeric kinesin-2) kinesin motors. Notably, recent data indicate that primary cilia of individual cell types display prominent structural and functional customizations. As it is difficult to explain how such diversity arises solely through the use of the “universal” IFT system, it seems plausible that non-canonical or accessory ciliary motors are responsible for tailoring primary cilia in different cell types. It is important to emphasize that understanding the mechanisms by which different ciliary modules regulate cilia dynamics may open avenues for

developing new strategies to restore ciliary function in ciliopathies. For instance, one could consider reducing the accumulation of GPCRs in the cilia of BBSome-defective cells (Prasai et al., 2024) by targeting cargo import regulation. In this context, it is worth noting that our unpublished data suggest a possible interaction between KIF14 and components of the BBSome — an intriguing possibility that warrants further investigation in future studies.

References

- Abramson, J., Adler, J., Dunger, J., Evans, R., Green, T., Pritzel, A., Ronneberger, O., Willmore, L., Ballard, A.J., Bambrick, J., Bodenstein, S.W., Evans, D.A., Hung, C.-C., O'Neill, M., Reiman, D., Tunyasuvunakool, K., Wu, Z., Žemgulytė, A., Arvaniti, E., Beattie, C., Bertolli, O., Bridgland, A., Cherepanov, A., Congreve, M., Cowen-Rivers, A.I., Cowie, A., Figurnov, M., Fuchs, F.B., Gladman, H., Jain, R., Khan, Y.A., Low, C.M.R., Perlin, K., Potapenko, A., Savy, P., Singh, S., Stecula, A., Thillaisundaram, A., Tong, C., Yakneen, S., Zhong, E.D., Zielinski, M., Židek, A., Bapst, V., Kohli, P., Jaderberg, M., Hassabis, D., Jumper, J.M., 2024. Accurate structure prediction of biomolecular interactions with AlphaFold 3. *Nature* 630, 493–500. <https://doi.org/10.1038/s41586-024-07487-w>
- Agbu, S.O., Liang, Y., Liu, A., Anderson, K.V., 2018. The small GTPase RSG1 controls a final step in primary cilia initiation. *J Cell Biol* 217, 413–427. <https://doi.org/10.1083/jcb.201604048>
- Airik, R., Airik, M., Schueler, M., Bates, C.M., Hildebrandt, F., 2019. Roscovitine blocks collecting duct cyst growth in Cep164-deficient kidneys. *Kidney Int* 96, 320–326. <https://doi.org/10.1016/j.kint.2019.04.014>
- Balestra, F.R., Strnad, P., Fluckiger, I., Gonczy, P., 2013. Discovering regulators of centriole biogenesis through siRNA-based functional genomics in human cells. *Dev Cell* 25, 555–71. <https://doi.org/10.1016/j.devcel.2013.05.016>
- Balmer, S., Dussert, A., Collu, G.M., Benitez, E., Iomini, C., Mlodzik, M., 2015. Components of Intraflagellar Transport Complex A Function Independently of the Cilium to Regulate Canonical Wnt Signaling in Drosophila. *Dev Cell* 34, 705–18. <https://doi.org/10.1016/j.devcel.2015.07.016>
- Banda, E., McKinsey, A., Germain, N., Carter, J., Anderson, N.C., Gabel, L., 2015. Cell polarity and neurogenesis in embryonic stem cell-derived neural rosettes. *Stem Cells Dev* 24, 1022–1033. <https://doi.org/10.1089/scd.2014.0415>
- Bangs, F., Anderson, K.V., 2017. Primary Cilia and Mammalian Hedgehog Signaling. *Cold Spring Harb Perspect Biol* 9. <https://doi.org/10.1101/cshperspect.a028175>
- Bangs, F.K., Schrode, N., Hadjantonakis, A.K., Anderson, K.V., 2015. Lineage specificity of primary cilia in the mouse embryo. *Nature Cell Biol* 17, 113–22. <https://doi.org/10.1038/ncb3091>
- Bárta, T., Boháčiková, D., Čajánek, L., 2021. Chapter 7 - Self-renewal in induced pluripotent stem cells, in: Birbrair, A. (Ed.), Recent Advances in iPSC Technology, Advances in Stem Cell Biology. Academic Press, pp. 179–207. <https://doi.org/10.1016/B978-0-12-822231-7.00007-2>
- Bashore, F.M., Marquez, A.B., Chaikuad, A., Howell, S., Dunn, A.S., Beltran, A.A., Smith, J.L., Drewry, D.H., Beltran, A.S., Axtman, A.D., 2023. Modulation of tau tubulin kinases (TTBK1 and TTBK2) impacts ciliogenesis. *Sci Rep* 13, 6118. <https://doi.org/10.1038/s41598-023-32854-4>
- Benk Vysloužil, D., Bernatík, O., Lánská, E., Renzová, T., Binó, L., Lacigová, A., Drahošová, T., Lánský, Z., Čajánek, L., 2025. Tau-tubulin kinase 2 restrains microtubule-depolymerizer KIF2A to support primary cilia growth. *Cell Commun Signal* 23, 73. <https://doi.org/10.1186/s12964-025-02072-8>
- Bernatík, O., Paclíková, P., Kotrbová, A., Bryja, V., Cajanek, L., 2021. Primary Cilia Formation Does Not Rely on WNT/β-Catenin Signaling. *Front Cell Dev Biol* 9, 623753. <https://doi.org/10.3389/fcell.2021.623753>
- Bernatík, O., Pejškova, P., Vysloužil, D., Hanakova, K., Zdrahal, Z., Cajanek, L., 2020. Phosphorylation of multiple proteins involved in ciliogenesis by Tau Tubulin kinase 2. *Mol. Biol. Cell* 31, 1032–1046. <https://doi.org/10.1091/mbc.E19-06-0334>
- Bertiaux, E., Louvel, V., McCafferty, C.L., van den Hoek, H., Batman, U., Mukherjee, S., Bournonville, L., Mercey, O., Mean, I., Müller, A., Van der Stappen, P., Buss, G., Daraspe, J., Genoud, C., Stearns, T., Engel, B.D., Hamel, V., Guichard, P., 2025. The Luminal Ring Protein C2CD3 Acts as a Radial In-to-Out Organizer of the Distal Centriole and Appendages. *bioRxiv* 2025.06.17.660204. <https://doi.org/10.1101/2025.06.17.660204>
- Bhogaraju, S., Cajanek, L., Fort, C., Blisnick, T., Weber, K., Taschner, M., Mizuno, N., Lamla, S., Bastin, P., Nigg, E.A., Lorentzen, E., 2013. Molecular Basis of Tubulin Transport Within the Cilium by IFT74 and IFT81. *Science* 341, 1009–12. <https://doi.org/10.1126/science.1240985>

- Binó, L., Čajánek, L., 2023. Tau tubulin kinase 1 and 2 regulate ciliogenesis and human pluripotent stem cells-derived neural rosettes. *Sci Rep* 13, 12884. <https://doi.org/10.1038/s41598-023-39887-9>
- Binó, L., Mikulenková, E., Štěpánek, L., Bernatík, O., Vysloužil, D., Pejšková, P., Gorilák, P., Huranová, M., Varga, V., Čajánek, L., 2022. A protocol for generation and live-cell imaging analysis of primary cilia reporter cell lines. *STAR Protoc* 3, 101199. <https://doi.org/10.1016/j.xpro.2022.101199>
- Bohaciakova, D., Renzova, T., Fedorova, V., Barak, M., Kunova Bosakova, M., Hampl, A., Cajanek, L., 2017. An Efficient Method for Generation of Knockout Human Embryonic Stem Cells Using CRISPR/Cas9 System. *Stem Cells Dev* 26, 1521–1527. <https://doi.org/10.1089/scd.2017.0058>
- Bornens, M., 2012. The centrosome in cells and organisms. *Science* 335, 422–6. <https://doi.org/10.1126/science.1209037>
- Bowie, E., Norris, R., Anderson, K.V., Goetz, S.C., 2018. Spinocerebellar ataxia type 11-associated alleles of Ttbk2 dominantly interfere with ciliogenesis and cilium stability. *PLoS Genet.* 14, e1007844. <https://doi.org/10.1371/journal.pgen.1007844>
- Bowler, M., Kong, D., Sun, S., Nanjundappa, R., Evans, L., Farmer, V., Holland, A., Mahjoub, M.R., Sui, H., Loncarek, J., 2019. High-resolution characterization of centriole distal appendage morphology and dynamics by correlative STORM and electron microscopy. *Nat Commun* 10, 993. <https://doi.org/10.1038/s41467-018-08216-4>
- Braun, D.A., Hildebrandt, F., 2017. Ciliopathies. *Cold Spring Harb Perspect Biol* 9. <https://doi.org/10.1101/cshperspect.a028191>
- Breslow, D.K., Holland, A.J., 2019. Mechanism and Regulation of Centriole and Cilium Biogenesis. *Annu Rev Biochem* 88, 691–724. <https://doi.org/10.1146/annurev-biochem-013118-111153>
- Breslow, D.K., Koslover, E.F., Seydel, F., Spakowitz, A.J., Nachury, M.V., 2013. An in vitro assay for entry into cilia reveals unique properties of the soluble diffusion barrier. *J Cell Biol* 203, 129–147. <https://doi.org/10.1083/jcb.201212024>
- Bryja, V., Cervenka, I., Cajanek, L., 2017. The connections of Wnt pathway components with cell cycle and centrosome: side effects or a hidden logic? *Crit Rev Biochem Mol Biol* 52, 614–637. <https://doi.org/10.1080/10409238.2017.1350135>
- Bukanov, N.O., Smith, L.A., Klinger, K.W., Ledbetter, S.R., Ibraghimov-Beskrovnaya, O., 2006. Long-lasting arrest of murine polycystic kidney disease with CDK inhibitor roscovitine. *Nature* 444, 949–952. <https://doi.org/10.1038/nature05348>
- Cajanek, L., Nigg, E.A., 2014. Cep164 triggers ciliogenesis by recruiting Tau tubulin kinase 2 to the mother centriole. *Proc Natl Acad Sci U S A* 111, E2841–50. <https://doi.org/10.1073/pnas.1401777111>
- Čajánek, L., Smite, S., Ivashchenko, O., Huranova, M., 2025. Cilia at the crossroad: convergence of regulatory mechanisms to govern cilia dynamics during cell signaling and the cell cycle. *Cell Biosci* 15, 81. <https://doi.org/10.1186/s13578-025-01403-z>
- Carden, S., Vitiello, E., Rosa E Silva, I., Holder, J., Quarantotti, V., Kishore, K., Roamio Franklin, V.N., D'Santos, C., Ochi, T., van Breugel, M., Gergely, F., 2023. Proteomic profiling of centrosomes across multiple mammalian cell and tissue types by an affinity capture method. *Dev Cell* 58, 2393–2410.e9. <https://doi.org/10.1016/j.devcel.2023.09.008>
- Carleton, M., Mao, M., Biery, M., Warren, P., Kim, S., Buser, C., Marshall, C.G., Fernandes, C., Annis, J., Linsley, P.S., 2006. RNA interference-mediated silencing of mitotic kinesin KIF14 disrupts cell cycle progression and induces cytokinesis failure. *Mol Cell Biol* 26, 3853–63. <https://doi.org/10.1128/MCB.26.10.3853-3863.2006>
- Cervenka, I., Valnohova, J., Bernatík, O., Harnos, J., Radsetoulal, M., Sedova, K., Hanakova, K., Potesil, D., Sedlackova, M., Salasova, A., Steinhart, Z., Angers, S., Schulte, G., Hampl, A., Zdrahal, Z., Bryja, V., 2016. Dishevelled is a NEK2 kinase substrate controlling dynamics of centrosomal linker proteins. *Proc Natl Acad Sci U S A* 113, 9304–9309. <https://doi.org/10.1073/pnas.1608783113>
- Chaki, M., Airik, R., Ghosh, A.K., Giles, R.H., Chen, R., Slaats, G.G., Wang, H., Hurd, T.W., Zhou, W., Cluckey, A., Gee, H.Y., Ramaswami, G., Hong, C.J., Hamilton, B.A., Cervenka, I., Ganji, R.S., Bryja, V., Arts, H.H., van Reeuwijk, J., Oud, M.M., Letteboer, S.J., Roepman, R., Husson, H., Ibraghimov-Beskrovnaya, O., Yasunaga, T., Walz, G., Eley, L., Sayer, J.A., Schermer, B., Liebau, M.C., Benzing, T., Le Corre, S., Drummond, I., Janssen, S., Allen, S.J., Natarajan, S.,

- O'Toole, J.F., Attanasio, M., Saunier, S., Antignac, C., Koenekoop, R.K., Ren, H., Lopez, I., Nayir, A., Stoetzel, C., Dollfus, H., Massoudi, R., Gleeson, J.G., Andreoli, S.P., Doherty, D.G., Lindstrad, A., Golzio, C., Katsanis, N., Pape, L., Abboud, E.B., Al-Rajhi, A.A., Lewis, R.A., Omran, H., Lee, E.Y., Wang, S., Sekiguchi, J.M., Saunders, R., Johnson, C.A., Garner, E., Vanselow, K., Andersen, J.S., Shlomei, J., Nurnberg, G., Nurnberg, P., Levy, S., Smogorzewska, A., Otto, E.A., Hildebrandt, F., 2012. Exome Capture Reveals ZNF423 and CEP164 Mutations, Linking Renal Ciliopathies to DNA Damage Response Signaling. *Cell* 150, 533–48. <https://doi.org/10.1016/j.cell.2012.06.028>
- Chang, T.-J.B., Hsu, J.C.-C., Yang, T.T., 2023. Single-molecule localization microscopy reveals the ultrastructural constitution of distal appendages in expanded mammalian centrioles. *Nat Commun* 14, 1688. <https://doi.org/10.1038/s41467-023-37342-x>
- Chávez, M., Ena, S., Van Sande, J., de Kerchove d'Exaerde, A., Schurmans, S., Schiffmann, S.N., 2015. Modulation of Ciliary Phosphoinositide Content Regulates Trafficking and Sonic Hedgehog Signaling Output. *Dev Cell* 34, 338–350. <https://doi.org/10.1016/j.devcel.2015.06.016>
- Chhatre, A., Stepanek, L., Nievergelt, A.P., Alvarez Viar, G., Diez, S., Pigino, G., 2025. Tubulin tyrosination/detyrosination regulate the affinity and sorting of intraflagellar transport trains on axonemal microtubule doublets. *Nat Commun* 16, 1055. <https://doi.org/10.1038/s41467-025-56098-0>
- Cho, J.H., Li, Z.A., Zhu, L., Muegge, B.D., Roseman, H.F., Lee, E.Y., Utterback, T., Woodhams, L.G., Bayly, P.V., Hughes, J.W., 2022. Islet primary cilia motility controls insulin secretion. *Sci Adv* 8, eabq8486. <https://doi.org/10.1126/sciadv.abq8486>
- Chong, W.M., Wang, W.-J., Lo, C.-H., Chiu, T.-Y., Chang, T.-J., Liu, Y.-P., Tanos, B., Mazo, G., Tsou, M.-F.B., Jane, W.-N., Yang, T.T., Liao, J.-C., 2020. Super-resolution microscopy reveals coupling between mammalian centriole subdistal appendages and distal appendages. *Elife* 9, e53580. <https://doi.org/10.7554/eLife.53580>
- Chou, P.-C., Lin, Y.-H., Lin, I.-H., Lin, T.-Y., Huang, Y.-C., Hong, S.-R., Ben Chang, T.-J., Fang, Y., Lin, Y., Yang, T.T., Lin, Y.-C., Huang, J., Wang, W.-J., 2025. Phase separation of TTBK2 and CEP164 is necessary for ciliogenesis. *Cell Reports* 44, 115810. <https://doi.org/10.1016/j.celrep.2025.115810>
- Cole, D.G., Diener, D.R., Himelblau, A.L., Beech, P.L., Fuster, J.C., Rosenbaum, J.L., 1998. Chlamydomonas kinesin-II-dependent intraflagellar transport (IFT): IFT particles contain proteins required for ciliary assembly in Caenorhabditis elegans sensory neurons. *J Cell Biol* 141, 993–1008. <https://doi.org/10.1083/jcb.141.4.993>
- Collinson, R., Tanos, B., 2025. Primary cilia and cancer: a tale of many faces. *Oncogene* 44, 1551–1566. <https://doi.org/10.1038/s41388-025-03416-x>
- Conduit, S.E., Davies, E.M., Fulcher, A.J., Oorschot, V., Mitchell, C.A., 2021. Superresolution Microscopy Reveals Distinct Phosphoinositide Subdomains Within the Cilia Transition Zone. *Front Cell Dev Biol* 9, 634649. <https://doi.org/10.3389/fcell.2021.634649>
- Conduit, S.E., Vanhaesebroeck, B., 2020. Phosphoinositide lipids in primary cilia biology. *Biochem J* 477, 3541–3565. <https://doi.org/10.1042/BCJ20200277>
- Corbit, K.C., Shyer, A.E., Dowdle, W.E., Gaulden, J., Singla, V., Reiter, J.F., 2008. Kif3a constrains β -catenin-dependent Wnt signalling through dual ciliary and non-ciliary mechanisms. *Nat Cell Biol* 10, 70–76. <https://doi.org/10.1038/ncb1670>
- Cruz, N.M., Reddy, R., McFaline-Figueroa, J.L., Tran, C., Fu, H., Freedman, B.S., 2022. Modelling ciliopathy phenotypes in human tissues derived from pluripotent stem cells with genetically ablated cilia. *Nat Biomed Eng* 6, 463–475. <https://doi.org/10.1038/s41551-022-00880-8>
- Delling, M., DeCaen, P.G., Doerner, J.F., Febvay, S., Clapham, D.E., 2013. Primary cilia are specialized calcium signaling organelles. *Nature* 504, 311–314. <https://doi.org/10.1038/nature12833>
- Engelke, M.F., Waas, B., Kearns, S.E., Suber, A., Boss, A., Allen, B.L., Verhey, K.J., 2019. Acute Inhibition of Heterotrimeric Kinesin-2 Function Reveals Mechanisms of Intraflagellar Transport in Mammalian Cilia. *Curr Biol* 29, 1137–1148.e4. <https://doi.org/10.1016/j.cub.2019.02.043>
- Failler, M., Gee, H.Y., Krug, P., Joo, K., Halbritter, J., Belkacem, L., Filhol, E., Porath, J.D., Braun, D.A., Schueler, M., Frigo, A., Alibeu, O., Masson, C., Brochard, K., Hurault de Ligny, B., Novo, R., Pietrement, C., Kayserili, H., Salomon, R., Gubler, M.C., Otto, E.A., Antignac, C., Kim, J., Benmerah, A., Hildebrandt, F., Saunier, S., 2014. Mutations of CEP83 Cause Infantile

- Nephronophthisis and Intellectual Disability. *Am J Hum Genet.* <https://doi.org/10.1016/j.ajhg.2014.05.002>
- Flax, R.G., Rosston, P., Rocha, C., Anderson, B., Capener, J.L., Durcan, T.M., Drewry, D.H., Prinos, P., Axtman, A.D., 2024. Illumination of understudied ciliary kinases. *Front Mol Biosci* 11, 1352781. <https://doi.org/10.3389/fmolb.2024.1352781>
- Ford, M.J., Yeyati, P.L., Mali, G.R., Keighren, M.A., Waddell, S.H., Mjoseng, H.K., Douglas, A.T., Hall, E.A., Sakaue-Sawano, A., Miyawaki, A., Meehan, R.R., Boulter, L., Jackson, I.J., Mill, P., Mort, R.L., 2018. A Cell/Cilia Cycle Biosensor for Single-Cell Kinetics Reveals Persistence of Cilia after G1/S Transition Is a General Property in Cells and Mice. *Dev Cell* 47, 509–523 e5. <https://doi.org/10.1016/j.devcel.2018.10.027>
- Fry, A.M., O'Regan, L., Sabir, S.R., Bayliss, R., 2012. Cell cycle regulation by the NEK family of protein kinases. *J Cell Sci* 125, 4423–33. <https://doi.org/10.1242/jcs.111195>
- Ganga, A.K., Kennedy, M.C., Oguchi, M.E., Gray, S., Oliver, K.E., Knight, T.A., De La Cruz, E.M., Homma, Y., Fukuda, M., Breslow, D.K., 2021. Rab34 GTPase mediates ciliary membrane formation in the intracellular ciliogenesis pathway. *Curr Biol* 31, 2895–2905.e7. <https://doi.org/10.1016/j.cub.2021.04.075>
- Garcia-Gonzalo, F.R., Corbit, K.C., Sirerol-Piquer, M.S., Ramaswami, G., Otto, E.A., Noriega, T.R., Seol, A.D., Robinson, J.F., Bennett, C.L., Josifova, D.J., Garcia-Verdugo, J.M., Katsanis, N., Hildebrandt, F., Reiter, J.F., 2011. A transition zone complex regulates mammalian ciliogenesis and ciliary membrane composition. *Nat Genet* 43, 776–84. <https://doi.org/10.1038/ng.891>
- Garcia-Gonzalo, F.R., Phua, S.C., Roberson, E.C., Garcia, G., Abedin, M., Schurmans, S., Inoue, T., Reiter, J.F., 2015. Phosphoinositides Regulate Ciliary Protein Trafficking to Modulate Hedgehog Signaling. *Dev Cell* 34, 400–409. <https://doi.org/10.1016/j.devcel.2015.08.001>
- Garcia-Gonzalo, F.R., Reiter, J.F., 2017. Open Sesame: How Transition Fibers and the Transition Zone Control Ciliary Composition. *Cold Spring Harb Perspect Biol* 9, a028134. <https://doi.org/10.1101/cshperspect.a028134>
- Gerdes, J.M., Liu, Y., Zaghloul, N.A., Leitch, C.C., Lawson, S.S., Kato, M., Beachy, P.A., Beales, P.L., DeMartino, G.N., Fisher, S., Badano, J.L., Katsanis, N., 2007. Disruption of the basal body compromises proteasomal function and perturbs intracellular Wnt response. *Nat Genet* 39, 1350–60. <https://doi.org/10.1038/ng.2007.12>
- Gillesse, E., Wade, A., Parboosingh, J.S., Au, P.Y.B., Bernier, F.P., C4R Consortium, Lamont, R.E., Innes, A.M., 2024. Genome sequencing identifies biallelic variants in SCLT1 in a patient with syndromic nephronophthisis: Reflections on the SCLT1-related ciliopathy spectrum. *Am J Med Genet A* 194, e63789. <https://doi.org/10.1002/ajmg.a.63789>
- Gilula, N.B., Satir, P., 1972. The ciliary necklace. A ciliary membrane specialization. *J Cell Biol* 53, 494–509. <https://doi.org/10.1083/jcb.53.2.494>
- Goetz, S.C., Liem, K.F., Jr., Anderson, K.V., 2012. The spinocerebellar ataxia-associated gene Tau tubulin kinase 2 controls the initiation of ciliogenesis. *Cell* 151, 847–58. <https://doi.org/10.1016/j.cell.2012.10.010>
- Gönczy, P., Hatzopoulos, G.N., 2019. Centriole assembly at a glance. *J Cell Sci* 132, jcs228833. <https://doi.org/10.1242/jcs.228833>
- Gopalakrishnan, J., Feistel, K., Friedrich, B.M., Grapin-Botton, A., Jurisch-Yaksi, N., Mass, E., Mick, D.U., Müller, R.-U., May-Simera, H., Schermer, B., Schmidts, M., Walentek, P., Wachten, D., 2023. Emerging principles of primary cilia dynamics in controlling tissue organization and function. *EMBO J* 42, e113891. <https://doi.org/10.15252/embj.2023113891>
- Graser, S., Stierhof, Y.D., Lavoie, S.B., Gassner, O.S., Lamla, S., Le Clech, M., Nigg, E.A., 2007. Cep164, a novel centriole appendage protein required for primary cilium formation. *J Cell Biol* 179, 321–30. <https://doi.org/10.1083/jcb.200707181>
- Gruneberg, U., Neef, R., Li, X., Chan, E.H., Chalamalasetty, R.B., Nigg, E.A., Barr, F.A., 2006. KIF14 and citron kinase act together to promote efficient cytokinesis. *J Cell Biol* 172, 363–72. <https://doi.org/10.1083/jcb.200511061>
- Halkina, T., Henderson, J.L., Lin, E.Y., Himmelbauer, M.K., Jones, J.H., Nevalainen, M., Feng, J., King, K., Rooney, M., Johnson, J.L., Marcotte, D.J., Chodaparambil, J.V., Kumar, P.R., Patterson, T.A., Murugan, P., Schuman, E., Wong, L., Hesson, T., Lamore, S., Bao, C., Calhoun, M., Certo, H., Amaral, B., Dillon, G.M., Gilfillan, R., De Turiso, F.G.-L., 2021. Discovery of Potent and

- Brain-Penetrant Tau Tubulin Kinase 1 (TTBK1) Inhibitors that Lower Tau Phosphorylation In Vivo. *J. Med. Chem.* 64, 6358–6380. <https://doi.org/10.1021/acs.jmedchem.1c00382>
- Hall, N.A., Hehnlly, H., 2021. A centriole's subdistal appendages: contributions to cell division, ciliogenesis and differentiation. *Open Biol* 11, 200399. <https://doi.org/10.1098/rsob.200399>
- Hanakova, K., Bernatik, O., Kravec, M., Micka, M., Kumar, J., Harnos, J., Ovesna, P., Paclikova, P., Radsetoulal, M., Potesil, D., Tripsianes, K., Cajanek, L., Zdrahal, Z., Bryja, V., 2019. Comparative phosphorylation map of Dishevelled 3 links phospho-signatures to biological outputs. *Cell Commun Signal CCS* 17, 170. <https://doi.org/10.1186/s12964-019-0470-z>
- Hao, L., Thein, M., Brust-Mascher, I., Civelekoglu-Scholey, G., Lu, Y., Acar, S., Prevo, B., Shaham, S., Scholey, J.M., 2011. Intraflagellar transport delivers tubulin isoforms to sensory cilium middle and distal segments. *Nat Cell Biol* 13, 790–798. <https://doi.org/10.1038/ncb2268>
- Haraguchi, K., Hayashi, T., Jimbo, T., Yamamoto, T., Akiyama, T., 2006. Role of the kinesin-2 family protein, KIF3, during mitosis. *J Biol Chem* 281, 4094–4099. <https://doi.org/10.1074/jbc.M507028200>
- Hehnlly, H., Chen, C.T., Powers, C.M., Liu, H.L., Doxsey, S., 2012. The centrosome regulates the Rab11-dependent recycling endosome pathway at appendages of the mother centriole. *Curr Biol* 22, 1944–50. <https://doi.org/10.1016/j.cub.2012.08.022>
- Hesketh, S.J., Mukhopadhyay, A.G., Nakamura, D., Toropova, K., Roberts, A.J., 2022. IFT-A structure reveals carriages for membrane protein transport into cilia. *Cell* 185, 4971–4985.e16. <https://doi.org/10.1016/j.cell.2022.11.010>
- Hibbard, J.V.K., Vazquez, N., Satija, R., Wallingford, J.B., 2021. Protein turnover dynamics suggest a diffusion-to-capture mechanism for peri-basal body recruitment and retention of intraflagellar transport proteins. *Mol Biol Cell* 32, 1171–1180. <https://doi.org/10.1091/mbc.E20-11-0717>
- Hildebrandt, F., Benzing, T., Katsanis, N., 2011. Ciliopathies. *N Engl J Med* 364, 1533–43. <https://doi.org/10.1056/NEJMr1010172>
- Hilgendorf, K.I., Myers, B.R., Reiter, J.F., 2024. Emerging mechanistic understanding of cilia function in cellular signalling. *Nat Rev Mol Cell Biol* 25, 555–573. <https://doi.org/10.1038/s41580-023-00698-5>
- Hirokawa, N., Noda, Y., Tanaka, Y., Niwa, S., 2009. Kinesin superfamily motor proteins and intracellular transport. *Nature reviews. Mol Cell Biol* 10, 682–96. <https://doi.org/10.1038/nrm2774>
- Ho, E.K., Tsai, A.E., Stearns, T., 2020. Transient Primary Cilia Mediate Robust Hedgehog Pathway-Dependent Cell Cycle Control. *Curr Biol* 30, 2829–2835.e5. <https://doi.org/10.1016/j.cub.2020.05.004>
- Houlden, H., Johnson, J., Gardner-Thorpe, C., Lashley, T., Hernandez, D., Worth, P., Singleton, A.B., Hilton, D.A., Holton, J., Revesz, T., Davis, M.B., Giunti, P., Wood, N.W., 2007. Mutations in TTBK2, encoding a kinase implicated in tau phosphorylation, segregate with spinocerebellar ataxia type 11. *Nat Genet* 39, 1434–6. <https://doi.org/10.1038/ng.2007.43>
- Huang, N., Zhang, D., Li, F., Chai, P., Wang, S., Teng, J., Chen, J., 2018. M-Phase Phosphoprotein 9 regulates ciliogenesis by modulating CP110-CEP97 complex localization at the mother centriole. *Nat Commun* 9, 4511. <https://doi.org/10.1038/s41467-018-06990-9>
- Huang, P., Schier, A.F., 2009. Dampened Hedgehog signaling but normal Wnt signaling in zebrafish without cilia. *Development* 136, 3089–3098. <https://doi.org/10.1242/dev.041343>
- Huangfu, D., Liu, A., Rakeman, A.S., Murcia, N.S., Niswander, L., Anderson, K.V., 2003. Hedgehog signalling in the mouse requires intraflagellar transport proteins. *Nature* 426, 83–7. <https://doi.org/10.1038/nature02061>
- Humbert, M.C., Weihbrecht, K., Searby, C.C., Li, Y., Pope, R.M., Sheffield, V.C., Seo, S., 2012. ARL13B, PDE6D, and CEP164 form a functional network for INPP5E ciliary targeting. *Proc. Natl. Acad. Sci. U.S.A.* 109, 19691–19696. <https://doi.org/10.1073/pnas.1210916109>
- Ikezu, S., Ikezu, T., 2014. Tau-tubulin kinase. *Front Mol Neurosci* 7, 33. <https://doi.org/10.3389/fnmol.2014.00033>
- Ingham, P.W., 2022. Hedgehog signaling. *Curr Top Dev Biol* 149, 1–58. <https://doi.org/10.1016/bs.ctdb.2022.04.003>
- Iyer, S.S., Chen, F., Ogunmolu, F.E., Moradi, S., Volkov, V.A., van Grinsven, E.J., van Hoorn, C., Wu, J., Andrea, N., Hua, S., Jiang, K., Vakonakis, I., Potočnjak, M., Herzog, F., Gigant, B., Gudimchuk, N., Stecker, K.E., Dogterom, M., Steinmetz, M.O., Akhmanova, A., 2025.

- Centriolar cap proteins CP110 and CPAP control slow elongation of microtubule plus ends. *J Cell Biol* 224, e202406061. <https://doi.org/10.1083/jcb.202406061>
- Izawa, I., Goto, H., Kasahara, K., Inagaki, M., 2015. Current topics of functional links between primary cilia and cell cycle. *Cilia* 4. <https://doi.org/10.1186/s13630-015-0021-1>
- Jang, J., Wang, Y., Lalli, M.A., Guzman, E., Godshalk, S.E., Zhou, H., Kosik, K.S., 2016. Primary Cilium-Autophagy-Nrf2 (PAN) Axis Activation Commits Human Embryonic Stem Cells to a Neuroectoderm Fate. *Cell*. <https://doi.org/10.1016/j.cell.2016.02.014>
- Jenkins, P.M., McEwen, D.P., Martens, J.R., 2009. Olfactory Cilia: Linking Sensory Cilia Function and Human Disease. *Chem Senses* 34, 451–464. <https://doi.org/10.1093/chemse/bjp020>
- Joo, K., Kim, C.G., Lee, M.S., Moon, H.Y., Lee, S.H., Kim, M.J., Kweon, H.S., Park, W.Y., Kim, C.H., Gleeson, J.G., Kim, J., 2013. CCDC41 is required for ciliary vesicle docking to the mother centriole. *Proc Natl Acad Sci U S A* 110, 5987–92. <https://doi.org/10.1073/pnas.1220927110>
- Juhl, A.D., Anvarian, Z., Kuhns, S., Berges, J., Andersen, J.S., Wüstner, D., Pedersen, L.B., 2023. Transient accumulation and bidirectional movement of KIF13B in primary cilia. *J Cell Sci* 136, jcs259257. <https://doi.org/10.1242/jcs.259257>
- Kanie, T., Liu, B., Love, J.F., Fisher, S.D., Gustavsson, A.-K., Jackson, P.K., 2025a. A hierarchical pathway for assembly of the distal appendages that organize primary cilia. *Elife* 14, e85999. <https://doi.org/10.7554/eLife.85999>
- Kanie, T., Ng, R., Abbott, K.L., Tanvir, N.M., Lorentzen, E., Pongs, O., Jackson, P.K., 2025b. Myristoylated Neuronal Calcium Sensor-1 captures the preciliary vesicle at distal appendages. *eLife* 14, e85998. <https://doi.org/10.7554/eLife.85998>
- Karasu, O.R., Neuner, A., Atorino, E.S., Pereira, G., Schiebel, E., 2022. The central scaffold protein CEP350 coordinates centriole length, stability, and maturation. *J Cell Biol* 221, e202203081. <https://doi.org/10.1083/jcb.202203081>
- Kiesel, P., Alvarez Viar, G., Tsoy, N., Maraschini, R., Gorilak, P., Varga, V., Honigsmann, A., Pigino, G., 2020. The molecular structure of mammalian primary cilia revealed by cryo-electron tomography. *Nat Struct Mol Biol* 27, 1115–1124. <https://doi.org/10.1038/s41594-020-0507-4>
- Kiprilov, E.N., Awan, A., Desprat, R., Velho, M., Clement, C.A., Byskov, A.G., Andersen, C.Y., Satir, P., Bouhassira, E.E., Christensen, S.T., Hirsch, R.E., 2008. Human embryonic stem cells in culture possess primary cilia with hedgehog signaling machinery. *J Cell Biol* 180, 897–904. <https://doi.org/10.1083/jcb.200706028>
- Knodler, A., Feng, S., Zhang, J., Zhang, X., Das, A., Peranen, J., Guo, W., 2010. Coordination of Rab8 and Rab11 in primary ciliogenesis. *Proc Natl Acad Sci U S A* 107, 6346–51. <https://doi.org/10.1073/pnas.1002401107>
- Kobayashi, T., Tsang, W.Y., Li, J., Lane, W., Dynlacht, B.D., 2011. Centriolar kinesin Kif24 interacts with CP110 to remodel microtubules and regulate ciliogenesis. *Cell* 145, 914–25. <https://doi.org/10.1016/j.cell.2011.04.028>
- Koca, Y., Collu, G.M., Mlodzik, M., 2022. Wnt-frizzled planar cell polarity signaling in the regulation of cell motility. *Curr Top Dev Biol* 150, 255–297. <https://doi.org/10.1016/bs.ctdb.2022.03.006>
- Kubo, T., Brown, J.M., Bellve, K., Craige, B., Craft, J.M., Fogarty, K., Lechtreck, K.F., Witman, G.B., 2016. Together, the IFT81 and IFT74 N-termini form the main module for intraflagellar transport of tubulin. *J Cell Sci* 129, 2106–2119. <https://doi.org/10.1242/jcs.187120>
- Kurtulmus, B., Yuan, C., Schuy, J., Neuner, A., Hata, S., Kalamakis, G., Martin-Villalba, A., Pereira, G., 2018. LRRC45 contributes to early steps of axoneme extension. *J. Cell. Sci.* 131. <https://doi.org/10.1242/jcs.223594>
- Kyun, M.-L., Kim, S.-O., Lee, H.G., Hwang, J.-A., Hwang, J., Soung, N.-K., Cha-Molstad, H., Lee, S., Kwon, Y.T., Kim, B.Y., Lee, K.H., 2020. Wnt3a Stimulation Promotes Primary Ciliogenesis through β -Catenin Phosphorylation-Induced Reorganization of Centriolar Satellites. *Cell Rep* 30, 1447–1462.e5. <https://doi.org/10.1016/j.celrep.2020.01.019>
- Lacey, S.E., Foster, H.E., Pigino, G., 2023. The molecular structure of IFT-A and IFT-B in anterograde intraflagellar transport trains. *Nat Struct Mol Biol* 30, 584–593. <https://doi.org/10.1038/s41594-022-00905-5>
- Lacey, S.E., Pigino, G., 2024. The intraflagellar transport cycle. *Nat Rev Mol Cell Biol* 1–18. <https://doi.org/10.1038/s41580-024-00797-x>

- Lacigová, A., Čajánek, L., 2025. Phosphorylation at the Helm: Kinase-Mediated Regulation of Primary Cilia Assembly and Disassembly. *Cytoskeleton*. <https://doi.org/10.1002/cm.22012>
- Lancaster, M.A., Schroth, J., Gleeson, J.G., 2011. Subcellular spatial regulation of canonical Wnt signalling at the primary cilium. *Nat Cell Biol* 13, 702–9. <https://doi.org/10.1038/ncb2259>
- Lange, S.M., Bennett, J.A., Eisert, R.J., Brown, A., 2025. A conserved mechanism for the retrieval of polyubiquitinated proteins from cilia. *Cell* S0092-8674(25)00865–7. <https://doi.org/10.1016/j.cell.2025.07.043>
- Lapart, J.-A., Billon, A., Duteyrat, J.-L., Thomas, J., Durand, B., 2020. Role of DZIP1-CBY-FAM92 transition zone complex in the basal body to membrane attachment and ciliary budding. *Biochem Soc Trans* 48, 1067–1075. <https://doi.org/10.1042/BST20191007>
- Lehtreck, K.F., Van De Weghe, J.C., Harris, J.A., Liu, P., 2017. Protein transport in growing and steady-state cilia. *Traffic* 18, 277–286. <https://doi.org/10.1111/tra.12474>
- Lo, C.-H., Lin, I.-H., Yang, T.T., Huang, Y.-C., Tanos, B.E., Chou, P.-C., Chang, C.-W., Tsay, Y.-G., Liao, J.-C., Wang, W.-J., 2019. Phosphorylation of CEP83 by TTBK2 is necessary for cilia initiation. *J Cell Biol* 218, 3489–3505. <https://doi.org/10.1083/jcb.201811142>
- Loukil, A., Barrington, C., Goetz, S.C., 2020. A complex of distal appendage-associated kinases linked to human disease regulates ciliary trafficking and stability. *bioRxiv* 2020.08.21.261560. <https://doi.org/10.1101/2020.08.21.261560>
- Lovera, M., Lüders, J., 2021. The ciliary impact of nonciliary gene mutations. *Trends Cell Biol* 31, 876–887. <https://doi.org/10.1016/j.tcb.2021.06.001>
- Lu, Q., Insinna, C., Ott, C., Stauffer, J., Pintado, P.A., Rahajeng, J., Baxa, U., Walia, V., Cuenca, A., Hwang, Y.S., Daar, I.O., Lopes, S., Lippincott-Schwartz, J., Jackson, P.K., Caplan, S., Westlake, C.J., 2015. Early steps in primary cilium assembly require EHD1/EHD3-dependent ciliary vesicle formation. *Nat Cell Biol*. <https://doi.org/10.1038/ncb3109>
- Maurice, M.M., Angers, S., 2025. Mechanistic insights into Wnt- β -catenin pathway activation and signal transduction. *Nat Rev Mol Cell Biol* 26, 371–388. <https://doi.org/10.1038/s41580-024-00823-y>
- Mazo, G., Soplop, N., Wang, W.J., Uryu, K., Tsou, M.B., 2016. Spatial Control of Primary Ciliogenesis by Subdistal Appendages Alters Sensation-Associated Properties of Cilia. *Dev Cell*. <https://doi.org/10.1016/j.devcel.2016.10.006>
- McDonald, C.B., McIntosh, S.K.N., Mikles, D.C., Bhat, V., Deegan, B.J., Seldeen, K.L., Saeed, A.M., Buffa, L., Sudol, M., Nawaz, Z., Farooq, A., 2011. Biophysical analysis of binding of WW domains of the YAP2 transcriptional regulator to PPXY motifs within WBP1 and WBP2 adaptors. *Biochemistry* 50, 9616–9627. <https://doi.org/10.1021/bi201286p>
- Meleppattu, S., Zhou, H., Dai, J., Gui, M., Brown, A., 2022. Mechanism of IFT-A polymerization into trains for ciliary transport. *Cell* 185, 4986–4998.e12. <https://doi.org/10.1016/j.cell.2022.11.033>
- Mercey, O., Mukherjee, S., Guichard, P., Hamel, V., 2024. The molecular architecture of the ciliary transition zones. *Curr Opin Cell Biol* 88, 102361. <https://doi.org/10.1016/j.ceb.2024.102361>
- Mikulenková, E., Pejškova, P., Podhajecky, R., Stepanek, L., Huranova, M., Varga, V., Lansky, Z., Cajánek, L., 2025. Kinesin-3 KIF14 Regulates Intraflagellar Transport Dynamics in Primary Cilia. *bioRxiv*. <https://doi.org/10.1101/2025.03.20.644298>
- Mill, P., Christensen, S.T., Pedersen, L.B., 2023. Primary cilia as dynamic and diverse signalling hubs in development and disease. *Nat Rev Genet* 24, 421–441. <https://doi.org/10.1038/s41576-023-00587-9>
- Mitra, A., Gioukakis, E., Mul, W., Peterman, E.J.G., 2025. Delivery of intraflagellar transport proteins to the ciliary base and assembly into trains. *Sci Adv* 11, eadr1716. <https://doi.org/10.1126/sciadv.adr1716>
- Miyamoto, T., Hosoba, K., Ochiai, H., Royba, E., Izumi, H., Sakuma, T., Yamamoto, T., Dynlacht, B.D., Matsuura, S., 2015. The Microtubule-Depolymerizing Activity of a Mitotic Kinesin Protein KIF2A Drives Primary Cilia Disassembly Coupled with Cell Proliferation. *Cell Rep*. <https://doi.org/10.1016/j.celrep.2015.01.003>
- Molla-Herman, A., Ghossoub, R., Blisnick, T., Meunier, A., Serres, C., Silbermann, F., Emmerson, C., Romeo, K., Bourdoncle, P., Schmitt, A., Saunier, S., Spassky, N., Bastin, P., Benmerah, A., 2010. The ciliary pocket: an endocytic membrane domain at the base of primary and motile cilia. *J Cell Sci* 123, 1785–1795. <https://doi.org/10.1242/jcs.059519>

- Mori, K., Yamazaki, S., Yoshida, K., Shiota, R., Chiba, S., Shin, H.-W., Katoh, Y., Nakayama, K., 2025. Coordinated roles of the CEP164 homodimer and TTBK2 are required for recruitment of the IFT machinery to the mother centriole for ciliogenesis. *Mol Biol Cell* 36, ar79. <https://doi.org/10.1091/mbc.E24-12-0536>
- Morris, R.L., Scholey, J.M., 1997. Heterotrimeric kinesin-II is required for the assembly of motile 9+2 ciliary axonemes on sea urchin embryos. *J Cell Biol* 138, 1009–1022. <https://doi.org/10.1083/jcb.138.5.1009>
- Morsci, N.S., Barr, M.M., 2011. Kinesin-3 KLP-6 Regulates Intraflagellar Transport in Male-Specific Cilia of *Caenorhabditis elegans*. *Curr Biol* 21, 1239–1244. <https://doi.org/10.1016/j.cub.2011.06.027>
- Nachury, M.V., 2018. The molecular machines that traffic signaling receptors into and out of cilia. *Curr Opin Cell Biol* 51, 124–131. <https://doi.org/10.1016/j.ceb.2018.03.004>
- Nachury, M.V., Loktev, A.V., Zhang, Q., Westlake, C.J., Peranen, J., Merdes, A., Slusarski, D.C., Scheller, R.H., Bazan, J.F., Sheffield, V.C., Jackson, P.K., 2007. A core complex of BBS proteins cooperates with the GTPase Rab8 to promote ciliary membrane biogenesis. *Cell* 129, 1201–13. <https://doi.org/10.1016/j.cell.2007.03.053>
- Nachury, M.V., Mick, D.U., 2019. Establishing and regulating the composition of cilia for signal transduction. *Nat Rev Mol Cell Biol* 20, 389–405. <https://doi.org/10.1038/s41580-019-0116-4>
- Nager, A.R., Goldstein, J.S., Herranz-Perez, V., Portran, D., Ye, F., Manuel Garcia-Verdugo, J., Nachury, M.V., 2017. An Actin Network Dispatches Ciliary GPCRs into Extracellular Vesicles to Modulate Signaling. *Cell* 168, 252–+. <https://doi.org/10.1016/j.cell.2016.11.036>
- Nakagawa, N., Li, J., Yabuno-Nakagawa, K., Eom, T.-Y., Cowles, M., Mapp, T., Taylor, R., Anton, E.S., 2017. APC sets the Wnt tone necessary for cerebral cortical progenitor development. *Genes Dev* 31, 1679–1692. <https://doi.org/10.1101/gad.302679.117>
- Nguyen, A., Goetz, S.C., 2023. TTBK2 controls cilium stability by regulating distinct modules of centrosomal proteins. *Mol Biol Cell* 34, ar8. <https://doi.org/10.1091/mbc.E22-08-0373>
- Niehrs, C., Da Silva, F., Seidl, C., 2025. Cilia as Wnt signaling organelles. *Trends Cell Biol* 35, 24–32. <https://doi.org/10.1016/j.tcb.2024.04.001>
- Nigg, E.A., Holland, A.J., 2018. Once and only once: mechanisms of centriole duplication and their deregulation in disease. *Nat Rev Mol Cell Biol*. <https://doi.org/10.1038/nrm.2017.127>
- Nigg, E.A., Stearns, T., 2011. The centrosome cycle: Centriole biogenesis, duplication and inherent asymmetries. *Nat Cell Biol* 13, 1154–60. <https://doi.org/10.1038/ncb2345>
- Nonaka, S., Tanaka, Y., Okada, Y., Takeda, S., Harada, A., Kanai, Y., Kido, M., Hirokawa, N., 1998. Randomization of left-right asymmetry due to loss of nodal cilia generating leftward flow of extraembryonic fluid in mice lacking KIF3B motor protein. *Cell* 95, 829–837. [https://doi.org/10.1016/s0092-8674\(00\)81705-5](https://doi.org/10.1016/s0092-8674(00)81705-5)
- Ocbina, P.J.R., Tuson, M., Anderson, K.V., 2009. Primary Cilia Are Not Required for Normal Canonical Wnt Signaling in the Mouse Embryo. *PLoS One* 4, e6839. <https://doi.org/10.1371/journal.pone.0006839>
- Oda, T., Chiba, S., Nagai, T., Mizuno, K., 2014. Binding to Cep164, but not EB1, is essential for centriolar localization of TTBK2 and its function in ciliogenesis. *Genes Cells* 19, 927–40. <https://doi.org/10.1111/gtc.12191>
- Odabasi, E., Batman, U., Firat-Karalar, E.N., 2020. Unraveling the mysteries of centriolar satellites: time to rewrite the textbooks about the centrosome/cilium complex. *Mol Biol Cell* 31, 866–872. <https://doi.org/10.1091/mbc.E19-07-0402>
- Ott, C.M., Torres, R., Kuan, T.-S., Kuan, A., Buchanan, J., Elabbady, L., Seshamani, S., Bodor, A.L., Collman, F., Bock, D.D., Lee, W.C., da Costa, N.M., Lippincott-Schwartz, J., 2024. Ultrastructural differences impact cilia shape and external exposure across cell classes in the visual cortex. *Curr Biol* 34, 2418–2433.e4. <https://doi.org/10.1016/j.cub.2024.04.043>
- Ou, G., Scholey, J.M., 2022. Motor Cooperation During Mitosis and Ciliogenesis. *Annu Rev Cell Dev Biol* 38, 49–74. <https://doi.org/10.1146/annurev-cellbio-121420-100107>
- Pan, J., Wang, Q., Snell, W.J., 2004. An aurora kinase is essential for flagellar disassembly in *Chlamydomonas*. *Dev Cell* 6, 445–51.
- Pan, X., Ou, G., Civelekoglu-Scholey, G., Blacque, O.E., Endres, N.F., Tao, L., Mogilner, A., Leroux, M.R., Vale, R.D., Scholey, J.M., 2006. Mechanism of transport of IFT particles in *C. elegans*

- cilia by the concerted action of kinesin-II and OSM-3 motors. *J Cell Biol* 174, 1035–1045. <https://doi.org/10.1083/jcb.200606003>
- Paolocci, E., Zacco, M., 2023. Compartmentalised cAMP signalling in the primary cilium. *Front. Physiol.* 14. <https://doi.org/10.3389/fphys.2023.1187134>
- Park, J., Lee, N., Kavoussi, A., Seo, J.T., Kim, C.H., Moon, S.J., 2015. Ciliary Phosphoinositide Regulates Ciliary Protein Trafficking in *Drosophila*. *Cell Rep* 13, 2808–2816. <https://doi.org/10.1016/j.celrep.2015.12.009>
- Park, K., Leroux, M.R., 2022. Composition, organization and mechanisms of the transition zone, a gate for the cilium. *EMBO Rep* 23, e55420. <https://doi.org/10.15252/embr.202255420>
- Patnaik, S.R., Kretschmer, V., Brücker, L., Schneider, S., Volz, A.-K., Oancea-Castillo, L.D.R., May-Simera, H.L., 2019. Bardet-Biedl Syndrome proteins regulate cilia disassembly during tissue maturation. *Cell Mol Life Sci* 76, 757–775. <https://doi.org/10.1007/s00018-018-2966-x>
- Pazour, G.J., Dickert, B.L., Vucica, Y., Seeley, E.S., Rosenbaum, J.L., Witman, G.B., Cole, D.G., 2000. *Chlamydomonas* IFT88 and its mouse homologue, polycystic kidney disease gene *tg737*, are required for assembly of cilia and flagella. *J Cell Biol* 151, 709–18.
- Pejskova, P., Reilly, M.L., Bino, L., Bernatik, O., Dolanska, L., Ganji, R.S., Zdrahal, Z., Benmerah, A., Cajanek, L., 2020. KIF14 controls ciliogenesis via regulation of Aurora A and is important for Hedgehog signaling. *J Cell Biol* 219. <https://doi.org/10.1083/jcb.201904107>
- Phua, S.C., Chiba, S., Suzuki, M., Su, E., Roberson, E.C., Pusapati, G.V., Setou, M., Rohatgi, R., Reiter, J.F., Ikegami, K., Inoue, T., 2017. Dynamic Remodeling of Membrane Composition Drives Cell Cycle through Primary Cilia Excision. *Cell* 168, 264–279 e15. <https://doi.org/10.1016/j.cell.2016.12.032>
- Prasai, A., Ivashchenko, O., Maskova, K., Bykova, S., Schmidt Cernohorska, M., Stepanek, O., Huranova, M., 2024. BBSome-deficient cells activate intraciliary CDC42 to trigger actin-dependent ciliary ectocytosis. *EMBO Rep* 26, 36–60. <https://doi.org/10.1038/s44319-024-00326-z>
- Prevo, B., Scholey, J.M., Peterman, E.J.G., 2017. Intraflagellar transport: mechanisms of motor action, cooperation, and cargo delivery. *FEBS J* 284, 2905–2931. <https://doi.org/10.1111/febs.14068>
- Prosser, S.L., Pelletier, L., 2020. Centriolar satellite biogenesis and function in vertebrate cells. *J Cell Sci* 133, jcs239566. <https://doi.org/10.1242/jcs.239566>
- Pugacheva, E.N., Jablonski, S.A., Hartman, T.R., Henske, E.P., Golemis, E.A., 2007. HEF1-dependent Aurora A activation induces disassembly of the primary cilium. *Cell* 129, 1351–63. <https://doi.org/10.1016/j.cell.2007.04.035>
- Reed, M., Takemaru, K.-I., Ying, G., Frederick, J.M., Baehr, W., 2022. Deletion of CEP164 in mouse photoreceptors post-ciliogenesis interrupts ciliary intraflagellar transport (IFT). *PLoS Genet* 18, e1010154. <https://doi.org/10.1371/journal.pgen.1010154>
- Reilly, M.L., Benmerah, A., 2019. Ciliary kinesins beyond IFT: cilium length, disassembly, cargo transport and signaling. *Biol Cell*. <https://doi.org/10.1111/boc.201800074>
- Reilly, M.L., Stokman, M.F., Magry, V., Jeanpierre, C., Alves, M., Paydar, M., Hellinga, J., Delous, M., Pouly, D., Failler, M., Martinovic, J., Loeuillet, L., Leroy, B., Tantau, J., Roume, J., Evans, C.G., Shan, X., Filges, I., Allingham, J.S., Kwok, B.H., Saunier, S., Giles, R.H., Benmerah, A., 2018. Loss of function mutations in KIF14 cause severe microcephaly and kidney development defects in humans and zebrafish. *Hum Mol Genetic*. <https://doi.org/10.1093/hmg/ddy381>
- Reiter, J.F., Leroux, M.R., 2017. Genes and molecular pathways underpinning ciliopathies. *Nat Rev Mol Cell Biol* 18, 533–547. <https://doi.org/10.1038/nrm.2017.60>
- Renzova, T., Bohaciakova, D., Esner, M., Pospisilova, V., Barta, T., Hampl, A., Cajanek, L., 2018. Inactivation of PLK4-STIL Module Prevents Self-Renewal and Triggers p53-Dependent Differentiation in Human Pluripotent Stem Cells. *Stem Cell Reports*. <https://doi.org/10.1016/j.stemcr.2018.08.008>
- Rezi, C.K., Frei, A., Campestre, F., Boldt, K., Mary, B., Fixdahl, A.M., With Petersen, A.-L., Sicot, A., Berggreen, C.R., Laplace, J., Johansen, S.L., Sørensen, J.K.T., Chamli, M., Berchtold, M.W., Christensen, S.T., Anvarian, Z., May-Simera, H.L., Pedersen, L.B., 2025. KIF13B controls ciliary protein content by promoting endocytic retrieval and suppressing release of large extracellular vesicles from cilia. *Curr Biol* S0960-9822(25)01088–7. <https://doi.org/10.1016/j.cub.2025.08.022>

- Rim, E.Y., Clevers, H., Nusse, R., 2022. The Wnt Pathway: From Signaling Mechanisms to Synthetic Modulators. *Annu Rev Biochem* 91, 571–598. <https://doi.org/10.1146/annurev-biochem-040320-103615>
- Rohatgi, R., Milenkovic, L., Scott, M.P., 2007. Patched1 Regulates Hedgehog Signaling at the Primary Cilium. *Science* 317, 372–376. <https://doi.org/10.1126/science.1139740>
- Rosa E Silva, I., Binó, L., Johnson, C.M., Rutherford, T.J., Neuhaus, D., Andreeva, A., Čajánek, L., van Breugel, M., 2022. Molecular mechanisms underlying the role of the centriolar CEP164-TTBK2 complex in ciliopathies. *Structure* 30, 114–128.e9. <https://doi.org/10.1016/j.str.2021.08.007>
- Rosenbaum, J.L., Witman, G.B., 2002. Intraflagellar transport. *Nat Rev Mol Cell Biol* 3, 813–25. <https://doi.org/10.1038/nrm952>
- Saha, I., Insinna, C., Westlake, C.J., 2024. Rab11-Rab8 cascade dynamics in primary cilia and membrane tubules. *Cell Rep* 43, 114955. <https://doi.org/10.1016/j.celrep.2024.114955>
- Sang, L., Miller, J.J., Corbit, K.C., Giles, R.H., Brauer, M.J., Otto, E.A., Baye, L.M., Wen, X., Scales, S.J., Kwong, M., Huntzicker, E.G., Sfakianos, M.K., Sandoval, W., Bazan, J.F., Kulkarni, P., Garcia-Gonzalo, F.R., Seol, A.D., O'Toole, J.F., Held, S., Reutter, H.M., Lane, W.S., Rafiq, M.A., Noor, A., Ansar, M., Devi, A.R.R., Sheffield, V.C., Slusarski, D.C., Vincent, J.B., Doherty, D.A., Hildebrandt, F., Reiter, J.F., Jackson, P.K., 2011. Mapping the NPHP-JBTS-MKS protein network reveals ciliopathy disease genes and pathways. *Cell* 145, 513–528. <https://doi.org/10.1016/j.cell.2011.04.019>
- Satir, P., 2017. CILIA: before and after. *Cilia* 6, 1. <https://doi.org/10.1186/s13630-017-0046-8>
- Satir, P., Mitchell, D.R., Jékely, G., 2008. How did the cilium evolve? *Curr Top Dev Biol* 85, 63–82. [https://doi.org/10.1016/S0070-2153\(08\)00803-X](https://doi.org/10.1016/S0070-2153(08)00803-X)
- Satir, P., Pedersen, L.B., Christensen, S.T., 2010. The primary cilium at a glance. *J Cell Sci* 123, 499–503. <https://doi.org/10.1242/jcs.050377>
- Schmidt, K.N., Kuhns, S., Neuner, A., Hub, B., Zentgraf, H., Pereira, G., 2012. Cep164 mediates vesicular docking to the mother centriole during early steps of ciliogenesis. *J Cell Biol* 199, 1083–101. <https://doi.org/10.1083/jcb.201202126>
- Scholey, J.M., 2008. Intraflagellar transport motors in cilia: moving along the cell's antenna. *J Cell Biol* 180, 23–29. <https://doi.org/10.1083/jcb.200709133>
- Schou, K.B., Mogensen, J.B., Morthorst, S.K., Nielsen, B.S., Aleliunaite, A., Serra-Marques, A., Furstenberg, N., Saunier, S., Bizet, A.A., Veland, I.R., Akhmanova, A., Christensen, S.T., Pedersen, L.B., 2017. KIF13B establishes a CAV1-enriched microdomain at the ciliary transition zone to promote Sonic hedgehog signalling. *Nat Commun* 8, 14177. <https://doi.org/10.1038/ncomms14177>
- Seeley, E.S., Nachury, M.V., 2010. The perennial organelle: assembly and disassembly of the primary cilium. *J Cell Sci* 123, 511–8. <https://doi.org/10.1242/jcs.061093>
- Shinde, S.R., Nager, A.R., Nachury, M.V., 2020. Ubiquitin chains earmark GPCRs for BBSome-mediated removal from cilia. *J Cell Biol* 219, e202003020. <https://doi.org/10.1083/jcb.202003020>
- Siller, S.S., Sharma, H., Li, S., Yang, J., Zhang, Y., Holtzman, M.J., Winuthayanon, W., Colognato, H., Holdener, B.C., Li, F.-Q., Takemaru, K.-I., 2017. Conditional knockout mice for the distal appendage protein CEP164 reveal its essential roles in airway multiciliated cell differentiation. *PLoS Genet*. 13, e1007128. <https://doi.org/10.1371/journal.pgen.1007128>
- Sillibourne, J.E., Hurbain, I., Grand-Perret, T., Goud, B., Tran, P., Bornens, M., 2013. Primary ciliogenesis requires the distal appendage component Cep123. *Biol Open* 2, 535–45. <https://doi.org/10.1242/bio.20134457>
- Simons, M., Gloy, J., Ganner, A., Bullerkotte, A., Bashkurov, M., Krönig, C., Schermer, B., Benzing, T., Cabello, O.A., Jenny, A., Mlodzik, M., Polok, B., Driever, W., Obara, T., Walz, G., 2005. Inversin, the gene product mutated in nephronophthisis type II, functions as a molecular switch between Wnt signaling pathways. *Nat Genet* 37, 537–543. <https://doi.org/10.1038/ng1552>
- Sorokin, S., 1962. Centrioles and the formation of rudimentary cilia by fibroblasts and smooth muscle cells. *J Cell Biol* 15, 363–77.
- Sorokin, S.P., 1968. Reconstructions of centriole formation and ciliogenesis in mammalian lungs. *J Cell Sci* 3, 207–30.

- Sotelo, J.R., Trujillo-Cenóz, O., 1958. Electron microscope study on the development of ciliary components of the neural epithelium of the chick embryo. *Zellforsch Mikrosk Anat.* 49, 1–12. <https://doi.org/10.1007/BF00335059>
- Spektor, A., Tsang, W.Y., Khoo, D., Dynlacht, B.D., 2007. Cep97 and CP110 suppress a cilia assembly program. *Cell* 130, 678–90. <https://doi.org/10.1016/j.cell.2007.06.027>
- Stepanek, L., Pigino, G., 2016. Microtubule doublets are double-track railways for intraflagellar transport trains. *Science* 352, 721–724. <https://doi.org/10.1126/science.aaf4594>
- Stuck, M.W., Chong, W.M., Liao, J.-C., Pazour, G.J., 2021. Rab34 is necessary for early stages of intracellular ciliogenesis. *Curr Biol* 31, 2887–2894.e4. <https://doi.org/10.1016/j.cub.2021.04.018>
- Sugiyama, N., Tsukiyama, T., Yamaguchi, T.P., Yokoyama, T., 2011. The canonical Wnt signaling pathway is not involved in renal cyst development in the kidneys of inv mutant mice. *Kidney Int* 79, 957–65. <https://doi.org/10.1038/ki.2010.534>
- Sun, S., Fisher, R.L., Bowser, S.S., Pentecost, B.T., Sui, H., 2019. Three-dimensional architecture of epithelial primary cilia. *Proc Natl Acad Sci U S A* 116, 9370–9379. <https://doi.org/10.1073/pnas.1821064116>
- Tanos, B.E., Yang, H.J., Soni, R., Wang, W.J., Macaluso, F.P., Asara, J.M., Tsou, M.F., 2013. Centriole distal appendages promote membrane docking, leading to cilia initiation. *Genes Dev* 27, 163–8. <https://doi.org/10.1101/gad.207043.112>
- Tasaki, K., Satoda, Y., Chiba, S., Shin, H.-W., Katoh, Y., Nakayama, K., 2025. Mutually independent and cilia-independent assembly of IFT-A and IFT-B complexes at mother centriole. *Mol Biol Cell* 36, ar48. <https://doi.org/10.1091/mbc.E24-11-0509>
- Taschner, M., Lorentzen, E., 2016. The Intraflagellar Transport Machinery. *Cold Spring Harb Perspect Biol* 8, a028092. <https://doi.org/10.1101/cshperspect.a028092>
- Toriyama, M., Lee, C., Taylor, S.P., Duran, I., Cohn, D.H., Bruel, A.L., Tabler, J.M., Drew, K., Kelly, M.R., Kim, S., Park, T.J., Braun, D., Pierquin, G., Biver, A., Wagner, K., Malfroot, A., Panigrahi, I., Franco, B., Al-Lami, H.A., Yeung, Y., Choi, Y.J., University of Washington Center for Mendelian, G., Duffourd, Y., Faivre, L., Riviere, J.B., Chen, J., Liu, K.J., Marcotte, E.M., Hildebrandt, F., Thauvin-Robinet, C., Krakow, D., Jackson, P.K., Wallingford, J.B., 2016. The ciliopathy-associated CPLANE proteins direct basal body recruitment of intraflagellar transport machinery. *Nat Genet.* <https://doi.org/10.1038/ng.3558>
- Tran, P.V., Talbott, G.C., Turbe-Doan, A., Jacobs, D.T., Schonfeld, M.P., Silva, L.M., Chatterjee, A., Prysak, M., Allard, B.A., Beier, D.R., 2014. Downregulating hedgehog signaling reduces renal cystogenic potential of mouse models. *J Am Soc Nephrol* 25, 2201–2212. <https://doi.org/10.1681/ASN.2013070735>
- Uzbekov, R., Alieva, I., 2018. Who are you, subdistal appendages of centriole? *Open Biol* 8, 180062. <https://doi.org/10.1098/rsob.180062>
- van den Hoek, H., Klena, N., Jordan, M.A., Alvarez Viar, G., Righetto, R.D., Schaffer, M., Erdmann, P.S., Wan, W., Geimer, S., Plitzko, J.M., Baumeister, W., Pigino, G., Hamel, V., Guichard, P., Engel, B.D., 2022. In situ architecture of the ciliary base reveals the stepwise assembly of intraflagellar transport trains. *Science* 377, 543–548. <https://doi.org/10.1126/science.abm6704>
- Viol, L., Hata, S., Pastor-Pedro, A., Neuner, A., Murke, F., Wuchter, P., Ho, A.D., Giebel, B., Pereira, G., 2020. Nek2 kinase displaces distal appendages from the mother centriole prior to mitosis. *J Cell Biol* 219. <https://doi.org/10.1083/jcb.201907136>
- Vuong, L.T., Iomini, C., Balmer, S., Esposito, D., Aaronson, S.A., Mlodzik, M., 2018. Kinesin-2 and IFT-A act as a complex promoting nuclear localization of β -catenin during Wnt signalling. *Nat Commun* 9, 5304. <https://doi.org/10.1038/s41467-018-07605-z>
- Walentek, P., Beyer, T., Thumberger, T., Schweickert, A., Blum, M., 2012. ATP4a is required for Wnt-dependent Foxj1 expression and leftward flow in Xenopus left-right development. *Cell Rep* 1, 516–527. <https://doi.org/10.1016/j.celrep.2012.03.005>
- Walia, V., Cuenca, A., Vetter, M., Insinna, C., Perera, S., Lu, Q., Ritt, D.A., Semler, E., Specht, S., Stauffer, J., Morrison, D.K., Lorentzen, E., Westlake, C.J., 2019. Akt Regulates a Rab11-Effector Switch Required for Ciliogenesis. *Dev. Cell* 50, 229–246.e7. <https://doi.org/10.1016/j.devcel.2019.05.022>

- Wallingford, J.B., 2019. We Are All Developmental Biologists. *Dev Cell* 50, 132–137. <https://doi.org/10.1016/j.devcel.2019.07.006>
- Wallingford, J.B., Mitchell, B., 2011. Strange as it may seem: the many links between Wnt signaling, planar cell polarity, and cilia. *Genes Dev* 25, 201–13. <https://doi.org/10.1101/gad.2008011>
- Wang, D., Zhou, J., 2021. The Kinocilia of Cochlear Hair Cells: Structures, Functions, and Diseases. *Front Cell Dev Biol* 9, 715037. <https://doi.org/10.3389/fcell.2021.715037>
- Wang, W., Wu, T., Kirschner, M.W., 2014. The master cell cycle regulator APC-Cdc20 regulates ciliary length and disassembly of the primary cilium. *eLife* 3, e03083. <https://doi.org/10.7554/eLife.03083>
- Watanabe, T., Kakeno, M., Matsui, T., Sugiyama, I., Arimura, N., Matsuzawa, K., Shirahige, A., Ishidate, F., Nishioka, T., Taya, S., Hoshino, M., Kaibuchi, K., 2015. TTBK2 with EB1/3 regulates microtubule dynamics in migrating cells through KIF2A phosphorylation. *J Cell Biol* 210, 737–751. <https://doi.org/10.1083/jcb.201412075>
- Wei, Q., Xu, Q., Zhang, Y., Li, Y., Zhang, Q., Hu, Z., Harris, P.C., Torres, V.E., Ling, K., Hu, J., 2013. Transition fibre protein FBF1 is required for the ciliary entry of assembled intraflagellar transport complexes. *Nat Commun* 4, 2750. <https://doi.org/10.1038/ncomms3750>
- Westlake, C.J., Baye, L.M., Nachury, M.V., Wright, K.J., Ervin, K.E., Phu, L., Chalouni, C., Beck, J.S., Kirkpatrick, D.S., Slusarski, D.C., Sheffield, V.C., Scheller, R.H., Jackson, P.K., 2011. Primary cilia membrane assembly is initiated by Rab11 and transport protein particle II (TRAPP II) complex-dependent trafficking of Rabin8 to the centrosome. *Proc Natl Acad Sci U S A* 108, 2759–64. <https://doi.org/10.1073/pnas.1018823108>
- Wiegering, A., Dildrop, R., Kalfhues, L., Spychala, A., Kuschel, S., Lier, J.M., Zobel, T., Dahmen, S., Leu, T., Struchtrup, A., Legendre, F., Vesque, C., Schneider-Maunoury, S., Saunier, S., Rüther, U., Gerhardt, C., 2018. Cell type-specific regulation of ciliary transition zone assembly in vertebrates. *EMBO J* 37, e97791. <https://doi.org/10.15252/embj.201797791>
- Wong, Y.L., Anzola, J.V., Davis, R.L., Yoon, M., Motamedi, A., Kroll, A., Seo, C.P., Hsia, J.E., Kim, S.K., Mitchell, J.W., Mitchell, B.J., Desai, A., Gahman, T.C., Shiau, A.K., Oegema, K., 2015. Reversible centriole depletion with an inhibitor of Polo-like kinase 4. *Science* 348, 1155–1160. <https://doi.org/10.1126/science.aaa5111>
- Wu, C.-T., Chen, H.-Y., Tang, T.K., 2018. Myosin-Va is required for preciliary vesicle transportation to the mother centriole during ciliogenesis. *Nat. Cell Biol.* 20, 175–185. <https://doi.org/10.1038/s41556-017-0018-7>
- Wu, S.M., Choo, A.B., Yap, M.G., Chan, K.K., 2010. Role of Sonic hedgehog signaling and the expression of its components in human embryonic stem cells. *Stem Cell Res* 4, 38–49. <https://doi.org/10.1016/j.scr.2009.09.002>
- Xu, Q., Zhang, Y., Wei, Q., Huang, Y., Hu, J., Ling, K., 2016. Phosphatidylinositol phosphate kinase PIPKγ and phosphatase INPP5E coordinate initiation of ciliogenesis. *Nat Commun* 7, 10777. <https://doi.org/10.1038/ncomms10777>
- Yang, T.T., Chong, W.M., Wang, W.-J., Mazo, G., Tanos, B., Chen, Z., Tran, T.M.N., Chen, Y.-D., Weng, R.R., Huang, C.-E., Jane, W.-N., Tsou, M.-F.B., Liao, J.-C., 2018. Super-resolution architecture of mammalian centriole distal appendages reveals distinct blade and matrix functional components. *Nature Commun* 9, 2023. <https://doi.org/10.1038/s41467-018-04469-1>
- Yang, T.T., Tran, M.N.T., Chong, W.M., Huang, C.-E., Liao, J.-C., 2019. Single-particle tracking localization microscopy reveals nonaxonemal dynamics of intraflagellar transport proteins at the base of mammalian primary cilia. *Mol Biol Cell* 30, 828–837. <https://doi.org/10.1091/mbc.E18-10-0654>
- Yoshimura, S., Egerer, J., Fuchs, E., Haas, A.K., Barr, F.A., 2007. Functional dissection of Rab GTPases involved in primary cilium formation. *J Cell Biol* 178, 363–9. <https://doi.org/10.1083/jcb.200703047>
- Yu, X., Ng, C.P., Habacher, H., Roy, S., 2008. Foxj1 transcription factors are master regulators of the motile ciliogenic program. *Nat Genet* 40, 1445–1453. <https://doi.org/10.1038/ng.263>
- Yuan, C., Neuner, A., Streubel, J., Bhanushali, A., Simons, M., Acebrón, S.P., Pereira, G., 2025. The interplay between Wnt and mTOR signaling modulates ciliogenesis in human retinal epithelial cells. *PLoS Biol* 23, e3003369. <https://doi.org/10.1371/journal.pbio.3003369>

- Zhang, K., Silva, F.D., Seidl, C., Wilsch-Bräuninger, M., Herbst, J., Huttner, W.B., Niehrs, C., 2023. Primary cilia are WNT-transducing organelles whose biogenesis is controlled by a WNT-PP1 axis. *Devl Cell* 58, 139-154.e8. <https://doi.org/10.1016/j.devcel.2022.12.006>
- Zhao, H., Khan, Z., Westlake, C.J., 2023. Ciliogenesis membrane dynamics and organization. *Semin Cell Dev Biol* 133, 20–31. <https://doi.org/10.1016/j.semcdb.2022.03.021>
- Zhernov, I., Diez, S., Braun, M., Lansky, Z., 2020. Intrinsically Disordered Domain of Kinesin-3 Kif14 Enables Unique Functional Diversity. *Curr Biol* 30, 3342-3351.e5. <https://doi.org/10.1016/j.cub.2020.06.039>

Appendices

Selected publications contributing to this thesis. * – corresponding authorship

Appendix 1

Čajánek L*, Smite S, Ivashchenko O, Huranova M. Cilia at the crossroad: convergence of regulatory mechanisms to govern cilia dynamics during cell signaling and the cell cycle. *Cell & Bioscience*. 2025 Jun 7;15(1):81. doi: 10.1186/s13578-025-01403-z.(JCR 2024, IF = 6.2, Q1 – Biochemistry & Molecular Biology)

REVIEW

Open Access



Cilia at the crossroad: convergence of regulatory mechanisms to govern cilia dynamics during cell signaling and the cell cycle

Lukáš Čajánek^{1,2*} , Sindija Smite³, Olha Ivashchenko³ and Martina Huranova^{3*}

Abstract

Cilia are versatile, microtubule-based organelles that facilitate cellular signaling, motility, and environmental sensing in eukaryotic cells. These dynamic structures act as hubs for key developmental signaling pathways, while their assembly and disassembly are intricately regulated along cell cycle transitions. Recent findings show that factors regulating ciliogenesis and cilia dynamics often integrate their roles across other cellular processes, including cell cycle regulation, cytoskeletal organization, and intracellular trafficking, ensuring multilevel crosstalk of mechanisms controlling organogenesis. Disruptions in these shared regulators lead to broad defects associated with both ciliopathies and cancer. This review explores the crosstalk of regulatory mechanisms governing cilia assembly, disassembly, and maintenance during ciliary signaling and the cell cycle, along with the broader implications for development, tissue homeostasis, and disease.

Keywords Cilia, Ciliary dynamics, Ciliary signaling, Cell cycle regulation, Tissue development, Ciliopathies, Cancer

Current model of primary cilia assembly and disassembly

Cilia are hair-like organelles composed of microtubules that extend from the cell surface of most eukaryotic cells. Cilia are probably the first ever observed cellular organelles, already described in the 17th century by a Dutch pioneer of microbiology and microscopy, Antonie van Leeuwenhoek [1]. Cilia can be motile or non-motile, with non-motile cilia referred to as primary cilia. The “primary” aspect of primary cilia relates to the time of their appearance, as primary cilium was noted to appear before the motile cilia in cells of rat lung epithelium [2]. Initially, primary cilia were thought to be vestigial, owing to their lack of motility. However, research over the past two decades has significantly twisted this perspective, revealing that primary cilia serve as crucial cellular antennas with essential roles in embryogenesis and tissue

*Correspondence:

Lukáš Čajánek
cajanek@med.muni.cz

Martina Huranova
martina.huranova@img.cas.cz

¹Laboratory of Cilia and Centrosome Biology, Department of Histology and Embryology, Faculty of Medicine, Masaryk University, Kamenice 3, Brno 62500, Czech Republic

²Section of Animal Physiology and Immunology, Department of Experimental Biology, Faculty of Science, Masaryk University, Kamenice 5, Brno 62500, Czech Republic

³Laboratory of Cilia Genetics and Pathology, Institute of Molecular Genetics of the Czech Academy of Sciences, Vídeňská 1083, Prague 142 00, Czech Republic



© The Author(s) 2025. **Open Access** This article is licensed under a Creative Commons Attribution 4.0 International License, which permits use, sharing, adaptation, distribution and reproduction in any medium or format, as long as you give appropriate credit to the original author(s) and the source, provide a link to the Creative Commons licence, and indicate if changes were made. The images or other third party material in this article are included in the article's Creative Commons licence, unless indicated otherwise in a credit line to the material. If material is not included in the article's Creative Commons licence and your intended use is not permitted by statutory regulation or exceeds the permitted use, you will need to obtain permission directly from the copyright holder. To view a copy of this licence, visit <http://creativecommons.org/licenses/by/4.0/>.

homeostasis [3, 4], [5]. Cilia significance has become even more evident with the discovery that a variety of human diseases, collectively termed ciliopathies, are linked to defects in ciliary structure and/or function [6, 7, 8]. In our review, we discuss primary cilia as dynamic organelles responding to various regulatory clues during their assembly, disassembly, and maintenance and, in turn, how the dynamic nature of primary cilia influences fundamental biological processes, including cell fate determination, tissue patterning, signal transduction, and cellular homeostasis.

Primary cilia and their structure

The primary cilium consists of the basal body, the transition zone (TZ), and the membrane-enclosed microtubule-based ciliary axoneme (Fig. 1A) [9]. The basal body originates from the older of the two centrioles of the centrosome, termed the mother centriole. Centrioles are barrel-like structures typically assembled according to radial nine-fold symmetry. A major part of their walls is made of nine microtubule triplets arranged in a circular pattern, which contributes to the structural integrity and overall stability of centrioles. The centriole's most distal part transitions to a geometry reminiscent of an axoneme by containing microtubule doublets instead of

triplets and being of smaller diameter than the proximal centriole part [10]. Only a fully matured mother centriole can serve as a basal body, having acquired two sets of appendages [11]. The structural integrity of the centriole distal part is critical for both distal (DAs) and subdistal (SDAs) appendages formation [12, 13].

DAs are present as blades that attach to two adjacent microtubule triplets of the mother centriole wall, forming a structure resembling a nine-fold pinwheel [14]. The DAs blades consist of CEP83/CCDC41, CEP89/CCDC123, SCLT1, and CEP164, which are crucially involved with primary cilia assembly initiation [15, 16] and protein FBF1, involved in regulating ciliary gating [17, 18]. DAs are assembled in a hierarchical manner, with CEP83 being responsible for the recruitment of SCLT1 and CEP89. SCLT1 successively mediates FBF1 and CEP164 recruitment [15]. Mutations in DAs genes (demonstrated for *CEP164*, *CEP83*, and *SCLT1*) typically lead to nephronophthisis, a ciliopathy manifesting in kidneys [5, 6, 19]. Unlike DAs nine-fold symmetry arrangement, SDAs structure does not seem well conserved. Moreover, SDAs are not directly decisive in the regulation of cilium assembly or maintenance; instead, they act as anchorage points for centrosomal microtubules, hence connecting the basal body to the rest of the cell [20]. In

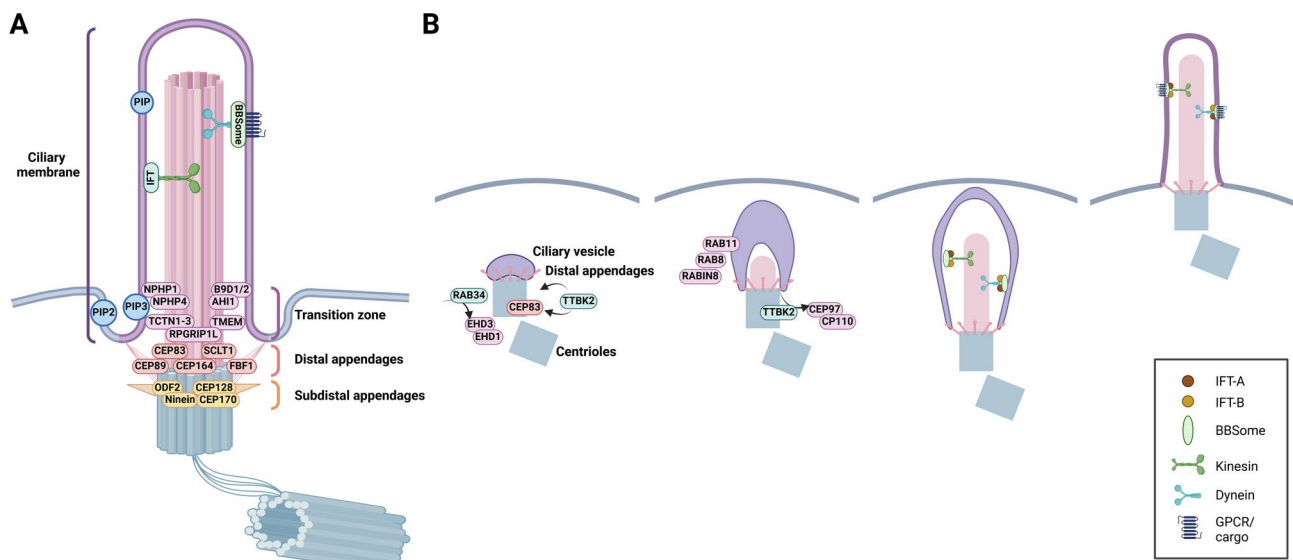


Fig. 1 Primary cilium structure and mechanism of intracellular ciliogenesis. **A** Primary cilium originates from the basal body (grey), modified centriole, which possesses two sets of appendages – distal (DAs) and subdistal (SDAs). The central structure is the membrane-enclosed microtubule-based ciliary axoneme (pink). The transition zone (TZ) acts as a diffusion barrier between the basal body and the ciliary axoneme. The ciliary membrane is rich in phosphoinositides (PIP), while phosphatidylinositol 4,5-bisphosphate (PIP2) levels are increased in the periciliary membrane at the cilium base; the phosphatidylinositol (3,4,5)-trisphosphate (PIP3) seems specifically enriched in the membrane surrounding the TZ. Active protein transport is facilitated by intraflagellar transport (IFT) machinery, which works in cooperation with the BBSome – cargo adapter complex. IFT is a bidirectional movement of complexes along the microtubules from the base of the cilium to its tip (anterograde transport) by kinesin motors and from the tip back to the ciliary base (retrograde transport) by dynein motors. **B** Intracellular ciliogenesis begins with the formation of the ciliary vesicle at the distal appendages, a process facilitated by EHD1/EHD3 and RAB34. TTBK2 phosphorylates CEP83 and other DAs components, enabling the ciliary vesicle to dock to the mother centriole. Ciliary vesicle membrane expansion is regulated by the RAB11/RABIN8/RAB8 cascade, driving the development and elongation of the ciliary membrane. Simultaneously, IFT mediates the growth of the axoneme, coordinating its assembly with the extension of the ciliary membrane. This image was created with BioRender.com

turn, they have been implicated in the correct positioning of primary cilia [21], yet functional consequences are not clear. SDAs components include ODF2, Ninein, CEP170, CEP128, and others [20, 22]. Vertebrate cells typically contain only one fully matured mother centriole at a time, allowing for the formation of a single cilium [11]. However, multiciliated cells, including those found in the lung airway epithelium or kidneys, are an exception. During their differentiation, these cells generate up to hundreds of centrioles, which then serve as basal bodies [23].

The transition zone (TZ) delineates the transition between the basal body and the ciliary axoneme [24, 25]. Super-resolution studies have positioned the TZ approximately 100 nm above the DAs [26, 27, 28]. The TZ serves as a diffusion barrier for both membrane and soluble proteins to ensure the unique composition of the intra-ciliary milieu and, consequently, is essential for primary cilia function [25, 29]. Its arrangement and size may vary between different cell types, the common structural feature being the presence of Y-shaped linkers (termed Y-links) that crosslink axonemal microtubule doublets with the ciliary membrane [24, 26]. Many TZ proteins have already been identified [30, 31], most of which are linked to ciliopathies [8], which has then raised even more interest in studying the TZ. Nevertheless, the exact composition of Y-links remains elusive. TZ components cluster into several structurally and functionally distinct protein complexes [32]. One of them is the NPHP complex, which resides in the proximity of axonemal microtubules and consists of proteins such as NPHP1, NPHP4, and RPGRIP1L [25], [32]. Their mutations typically lead to nephronophthisis [8]. A second complex, termed MKS, comprises proteins located in or near the ciliary membrane (e.g., TCTN1-3, several TMEM proteins, AHI1, B9D1/2, etc.) [25], [32]. Corresponding mutations in MKS members are typically involved with Meckel and Joubert syndromes [5], [8]. Both complexes are engaged in several interactions, including mutual ones, interactions with CEP290 (a large protein commonly annotated as another MKS member), and proteins of the so-called Inversin compartment [25]. CEP290 and RPGRIP1L seem to act as the most upstream components in the hierarchy of individual TZ components recruitment [33].

The most common view of axonemal microtubule arrangement in primary cilia is the “9+0” configuration, where the central microtubule doublet, typical for the motile cilia with their “9+2” arrangement, is missing. While this simplistic model still holds credibility, it is apparent that the spectrum of different configurations is broader than originally anticipated, since the list of reported “exceptions from the rule” is rapidly enlarging. For instance, cilia found in olfactory neurons are immotile, albeit with “9+0” configuration [34]. Conversely, beta-cell “primary” cilia, with the typical “9+0”

configuration, show movement in response to glucose stimulation, likely to facilitate insulin secretion [35]. Moreover, epithelial cell primary cilia seem to follow the “9+0” rule only in their proximal parts, while more distal regions of the axoneme exhibit a surprising level of heterogeneity and “disorganization”, with several individual microtubules often ending well before reaching the tip of the cilium [36], [37].

The ciliary membrane is continuous with the plasma membrane, the intermediate zone between them termed the periciliary membrane, which sometimes invaginates to form a ciliary pocket surrounding the proximal part of the axoneme [38], [39]. The ciliary membrane has a unique content of lipids and proteins, critical for correct ciliary functions [29], [40]. Phosphoinositides (PIPs) are perhaps the best example of lipids displaying a precise spatial organization within the cilium membrane. Specifically, the ciliary membrane is rich in PIP, while low in PIP2 and PIP3. Conversely, the plasma membrane has a high content of PIP2 and PIP3. PIP2 levels are increased in the periciliary membrane at the cilium base, while the PIP3 seems specifically enriched in the membrane surrounding the TZ [41]. This particular configuration is maintained by cilia-residing enzymes such as INPP5E, which converts the PIP2 into PIP inside the cilium to maintain the boundary [42], [43].

The soluble content of cilia (recently referred to as cilioplasm [44]) also evinces substantial differences from the composition of cytoplasm. Whereas soluble small molecules easily diffuse between the cilioplasm and cytosol, their concentrations can significantly differ between these two compartments. One such example is calcium, whose steady-state levels can be much higher in the cilioplasm than in the cytoplasm of the same cell [45]. Given that cilium volume is smaller than cell volume by several orders of magnitude, the effects of ciliary ions on cytosol can be safely considered negligible. Conversely, relatively subtle changes (by as little as “a few molecules”) can in fact mean dramatic differences in ion concentration in the context of cilia [46, 47]. For instance, it is estimated that a single molecule of cAMP translates into a 10 nM concentration increase of cAMP inside cilia [44]. This compartmentalization provides a conceptual base for primary cilia as sensitive and efficient signaling organelles [44, 47].

Primary cilia assembly regulation

Ciliogenesis activation is typical for postmitotic cells, as the cilium is accordingly disassembled prior to the entry of another round of mitosis [9]. Exit from the cell cycle and entry into quiescence is considered the most permissive condition for the assembly of a primary cilium [9]. Commensurate with that, perhaps the most commonly used protocol to facilitate ciliogenesis in mammalian

cell culture is based on enriching the G1/G0 cell population via serum starvation [48]. Consequently, primary cilia were considered specific hallmarks of quiescent state [49]. Moreover, certain evidence suggests that primary cilia may even have a checkpoint function - guarding against cell cycle re-entry [50]. Nevertheless, based on data from live cell imaging and in vivo models, primary cilia apparently can be readily found not only in non-cycling but also in proliferating (yet non-mitotic) cells [51], [52]. Actually, vertebrate cells seem capable of assembling primary cilium throughout the cell cycle (except mitosis) [51]. Therefore, the timing of the onset of cilium assembly can be heterogeneous, and factors responsible for such asynchrony within a cell population are currently unknown. The earliest observed event in ciliogenesis, as documented in transmission electron microscopy (TEM) experiments, is the docking of the basal body DAs to the ciliary vesicle (CV) [2, 38] or directly to the apical cell membrane [53]. The former is a feature of the intracellular pathway of cilia assembly, where ciliogenesis already initiates in the cytoplasm, before the mother centriole attachment to the plasma membrane [54], [55]. The latter is common for the extracellular cilia assembly pathway of polarized cells, where ciliogenesis commences following mother centriole docking to the plasma membrane surface. This paper focuses on mechanisms of intracellular ciliogenesis, which is a more broadly used mechanism (Fig. 1B). Specific aspects of the extracellular cilium assembly pathway have previously been thoroughly addressed [56].

The large CV forms from the fusion of smaller vesicles, termed distal appendage vesicles (DAVs), attached to the DAs. Myosin-Va, implicated in the assembly and transport of DAVs, appears to be the earliest vesicle trafficking regulator recruited to the basal body [57]. Large CV formation depends on the coordinated action of two members of the EHD protein family, EHD1 and EHD3 [58]. Recruitment of EHD1/EHD3 to cilia base relies on the activity of small GTPase RAB34, localizing to ciliary sheath transiently forming during the assembly of primary cilia [59, 60]. When these proteins are depleted, DAVs can still dock, but the smaller vesicles fail to fuse, hence halting ciliogenesis [57], [58]. The CV membrane's subsequent expansion, controlled by the RAB11/RABIN8/RAB8 cascade, leads to the formation and extension of the ciliary membrane, assembled in parallel with the growing axoneme. The small GTPase RAB11 is crucial for delivering vesicles containing RABIN8, a RAB8 guanine nucleotide exchange factor (GEF), to the mother centriole and for regulating RABIN8 activity. Locally enriched RABIN8 ensures the timely activation of small GTPase RAB8, promoting the extension of the ciliary membrane [61], [62], [63, 64]. Noteworthy, very few reports have documented an uncoupling of the growth of

the primary cilium membrane and axoneme, suggesting tight cooperation of both processes by yet unclear mechanism [65].

The mother centriole-membrane interaction critically relies on intact DAs [15]. Meticulous TEM analyses showed that DAVs/CV docking is severely compromised when CEP164 [66, 67], CEP83/CCDC41 [68], CEP89/CEP123 [69], and to a lesser extent LRRC45 [70], are depleted. While the roles of SCLT1 and ANKRD26 in DAVs/CV docking have not been directly examined by TEM, SCLT1 is required for the recruitment of RAB34 [60, 71]. One open question concerns the mechanism regulating the DAs-CV interactions. It is plausible that individual DAs components and their domains directly mediate the interactions with CV regulators EHD1/3, Myosin-Va, or RAB34 to support efficient CV formation [71]. Certain aspects of such regulation are under the control of effector protein Tau Tubulin Kinase 2 (TTBK2) [72], recruited to DAs by interaction with CEP164 [73, 74]. The absence of TTBK2 prevents CV-mother centriole interactions, which seems to be partly mediated by its phosphorylation of CEP83 [75]. TTBK2 phosphorylates additional proteins involved in CV- mother centriole interactions (i.e. CEP164, CEP89, RABIN8) [73, 76], however, the functional relevance of this remains unclear.

Cilium growth occurs concurrently with the extension of the microtubule-based axoneme. However, the mechanism that triggers the outgrowth of microtubules from the mother centriole distal end is not entirely clear. A widely accepted hallmark of the onset of ciliogenesis in vertebrate cells is the removal of the centriole distal end proteins CEP97 and CP110 specifically from the mother centriole [77]. CEP97 and CP110 depend on each other for proper localization to the centriole distal end and form a complex that is commonly viewed as a "cap," possibly sterically hindering the outgrowth of microtubules to form the axoneme [77, 78]. The removal of this "cap" depends on TTBK2 kinase activity [15, 72, 73], [79]. While it is not fully resolved how TTBK2 controls this process, one possibility is that TTBK2 directly acts on the CP110-CEP97 complex to induce its relocation or destruction. Accordingly, TTBK2 has been shown to phosphorylate CEP97 [80]. Alternatively, TTBK2 might indirectly facilitate the removal of CP110-CEP97 by phosphorylating MPP9 [81].

Although CP110-CEP97 loss from the mother centriole serves as a reliable sign of ciliogenesis initiation in numerous studies, the function of these proteins appears more complex. For instance, depletion of CP110 or CEP97 was reported to cause artificially elongated centrioles [52, 78, 82] or facilitate primary cilia formation in certain cell types [81, 83]. Conversely, some evidence suggests these proteins play a positive role in cilia formation [84, 85, 86]. Therefore, the "cap to prevent microtubule

growth” model seems overly simplistic for the emerging context-dependent role of CP110-CEP97.

Axoneme outgrowth is mediated by Intraflagellar Transport (IFT) proteins. IFT is a bidirectional movement of complexes along the axonemal doublet microtubules from the cilium base to its tip (anterograde transport) by kinesin motors (typically kinesin-II) and then from the tip back to the ciliary base (retrograde transport) by dynein 2 motors [87, 88]. The main IFT function is to deliver various cargo (e.g., ciliary components such as tubulin, receptors, etc.) into the cilia and back to promote cilium growth and maintenance. Cargo proteins can interact with IFT complexes directly (e.g. tubulin [89]) or via adaptor proteins [90]. Fully assembled IFT complexes comprise individual IFT proteins forming IFT-A and IFT-B subcomplexes, coupled with respective motor proteins [91]. Cryo-EM work in flagella of *Chlamydomonas* revealed that each microtubule doublet is used as a bidirectional double-track railway - anterograde IFT trains move along B-microtubules, and retrograde trains use A-microtubules for transport [92]. IFT complexes localize to two distinct pools at the ciliary base – one that overlaps with the DAs and the other within the TZ [93]. Their recruitment requires kinase activity of TTBK2 and intact DAs [71, 72], [73], however, exactly which DAs component(s) serve a physical docking platform for the interaction with IFTs is not clear. While IFTs are recruited to DAs even in nonciliated cells [73], their assembly into fully functional “trains” seems to be completed within TZ, to be subsequently loaded inside the cilium [94, 95].

The transport of molecules inside and outside of cilium is critical for cilium growth, maintenance, and function. The current model posits that TZ together with DAs transformed into so-called transition fibers form a selective barrier between the cilium and the rest of a cell to control the ciliary entrance and exit [5, 20], [25]. Numerous studies have documented the existence of such a gating barrier at the ciliary base, yet the actual mechanism of sorting and transporting selected molecules across the barrier is not fully resolved. According to some evidence, the ciliary entry of various cargo is mediated by IFT activity. In this case, the cargo is simply dragged through the sorting barrier by the activity of IFT motors [5, 29]. In agreement with this model, anterograde IFT trains (likely cargo-loaded) are assembled at TZ, and inactivation of their motors impairs TZ localization of IFT trains and, successively, cilium elongation [5], [90], [95]. This mechanism likely ensures the ciliary entry of tubulin subunits, in cooperation with their free diffusion across the TZ [89, 96]. In addition, membrane-associated proteins and transmembrane receptors seem to enter the cilium independently of IFT motor activity. They rely instead on interactions with IFT-A subcomplex and adaptor protein

TULP3 [97, 98]. TULP3 is a PIP2-binding protein, and its ciliary localization is restricted by the PIP2/PIP3 boundary, maintained by INPP5E (which itself is recruited to cilia in a TULP3-dependent manner) [97, 99].

The ciliary exit of many receptors is accordingly facilitated by the BBSome, an octameric cargo adaptor protein complex comprised of BBS1, BBS2, BBS4, BBS5, BBS7, BBS8, BBS9, and BBS18 subunits [64]. Mutations in any of the BBSome subunits lead to ciliopathy termed Barder-Biedl syndrome [100], albeit with various severity across tissues [101]. BBSome formation occurs in a step-wise fashion and is spatially governed by the BBS4 and BBS1 subunits [102, 103]. BBS4 localizes to pericentriolar satellites and recruits here the other subunits to form the pre-BBSome. BBS1 resides at the centrosome and facilitates pre-BBSome translocation and BBSome completion at the ciliary base. Moreover, BBS1 binds RABIN8 and thus serves as a bridge between RAB8/RAB11 dependent vesicular trafficking and the ciliary transport machinery [63, 64].

BBSome seems to be associated with IFT trains in many organisms. As Max Nachury stated, the BBSome may have been easily called IFT-C if not for historical reasons [98]. In fact, BBSome directly regulates IFT machinery movement in *C.elegans* [104]. Whether the analogous function is conserved in vertebrates is currently unclear. Nevertheless, the key function of BBSome, well documented across various model organisms, probably resides in regulating the ciliary exit of membrane receptors (e.g., SSTR3, GPR161, etc.) [98]. According to the current model, BBSome travels together with IFT particles in both anterograde and retrograde directions to retrieve ciliary receptors. Their ciliary exit, namely the passing through the TZ barrier, is subsequently facilitated by interactions with adaptor protein ARL6 (BBS3) [105].

DAs transformed into transition fibers are considered as another module regulating ciliary gating [40]. Such gating function is well expected, considering the intimate association of DAs and the membrane, implied by TEM or super-resolution microscopy studies [2, 17], [28, 38]. However, direct evidence of such function is lacking (and long-awaited), including the details on the interactions between individual DAs proteins and the membrane. One of the limitations is the critical role of several DAs proteins (namely CEP83, CEP164, and SCLT1) and TTBK2 in the initiation of the cilium assembly pathway (see earlier), hence the absence of any of these proteins halts ciliogenesis before any gating mechanism has a chance to step in. There is one exception though - FBF1. Deletion of FBF1 leads to moderate ciliogenesis defect [18, 71], allowing a careful analysis of primary cilia forming independently of FBF1. Indeed, lack of FBF1 in *C. elegans* or human cells causes defective cilia entry of IFT

particles [18], together with reduced ciliary localization of SMO, PKD2, and SSTR3 receptors [17, 106]. The exact mechanism(s) that compromise the IFT/receptor recruitment here awaits to be identified.

Primary cilia disassembly regulation

It is well documented that primary cilium needs to be disassembled prior to the onset of mitosis, most likely to free the mother centriole for centrosome-mediated spindle organization and positioning [9], [107]. Serum-starved NIH3T3, hTERT-RPE1, or IMCD3 cells gradually lose cilia following serum addition [48, 49], [108], and asynchronous NIH3T3 (with ARL13B/Fucci sensor) were shown to disassemble primary cilia at G2/M [51]. An intriguing exception to this otherwise strictly followed rule is the Ptk1 cell line, in which primary cilium is able to persist even during early mitosis [109]. There are at least two modes for disassembling primary cilium. Consistent with the gradual shortening of flagella in *Chlamydomonas* before cell division [110], primary cilia of vertebrate cells can be slowly resorbed by axoneme depolymerization [108]. Moreover, the flagella of many protists can be lost in a process of rapid deciliation, which involves

cutting off the ciliary axoneme by the microtubule-severing enzyme Katanin [111]. A similar mode of action also mediates primary cilia disassembly in vertebrate cells. Furthermore, both these modes of primary cilia removal can act separately as well as in combination [108]. While the identification of “switch factors”, controlling which mode of cilia assembly will be used requires additional work, it is becoming clear that the precise timing of cilia disassembly has significant physiological consequences. For instance, primary cilia of neuronal progenitors in developing chick neural tubes undergo timely remodeling of ciliary axoneme, which permits switching between specific branches of the Hedgehog (HH) signaling pathway crucial in neuronal patterning and differentiation [112] (see more on that in the HH signaling pathway chapter).

Gradual cilium disassembly requires destabilization and depolymerization of axonemal microtubules (Fig. 2). The upstream controlling mechanism involves mitotic kinase Aurora A (AURA), whose activity increases during the cell cycle, together with the size of the AURA pool at the base of primary cilia [113]. While the function of AURA upstream of cilia disassembly is well documented

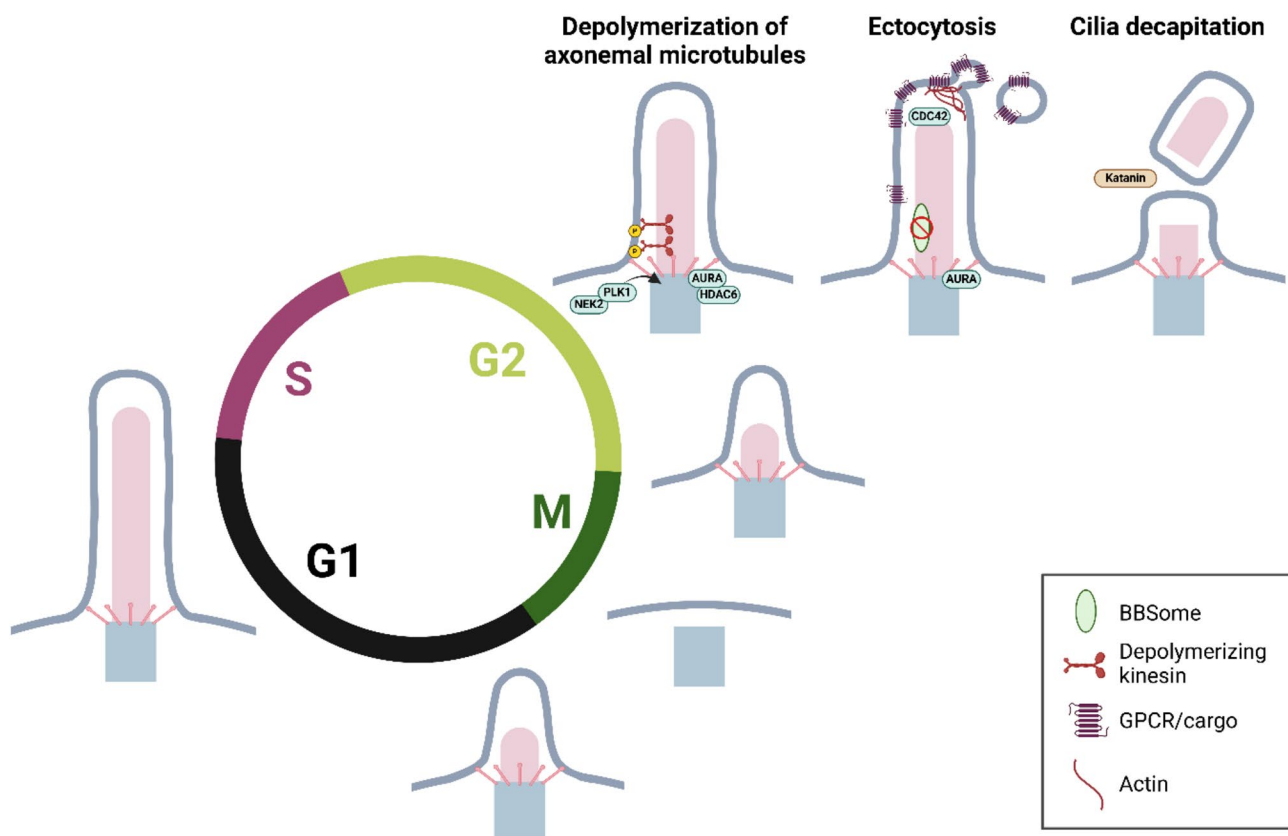


Fig. 2 Primary cilium dynamics during cell cycle. Primary cilia are disassembled before mitosis and reassembled after cell division during the early G1 phase. Cilium disassembly occurs through several potentially overlapping mechanisms, including gradual resorption mediated by AURA kinase and HDAC6, CDC42 and actin-dependent ectocytosis, and Katanin-dependent ciliary decapitation. Axoneme (light pink), basal body (grey) with distal appendages (DAs; pink). This image was created with BioRender.com

and conserved from *Chlamydomonas* to vertebrates [113, 114], the underlying mechanism is less clear. Available evidence from cell culture-based experiments suggests that a subset of histone deacetylases including HDAC6 or HDAC2, able to deacetylate tubulin, acts downstream of AURA to mediate the destabilization of axonemal microtubules [113, 115]. However, genetic ablation of HDAC6 or other HDACs does not lead to major ciliary phenotypes in vivo, indicating the involvement of compensatory actions and/or cell type specificity of the outlined mechanism [116, 117]. Still, considering both AURA and HDAC6 are enriched at the cilia base (with currently no evidence of their localization in the ciliary axoneme), one of the outstanding questions is how the signal from AURA/HDAC6 passes to the axonemal microtubules. A possible (though highly speculative) explanation may relate to the fact that HDAC6 prefers tubulin dimers over polymerized microtubules [118]. In such a scenario, HDAC6 would primarily act on tubulin subunits transported through the barrier at the cilia base.

Disassembly of the primary cilium before mitosis is further controlled by several members of the kinesin 13 family (e.g., KIF2A, and KIF24). Unlike conventional kinesin motor proteins, kinesin 13 proteins do not “walk” along microtubules but possess the unique activity of ATP-dependent microtubule depolymerization to promote resorption of ciliary axoneme [119]. KIF2A is enriched at the base of primary cilia in the close vicinity of DAs/SDAs, and can also be found in the axoneme [79], [120]. The ability of kinesin 13 proteins to depolymerize microtubules is tightly controlled by upstream kinases. Phosphorylation by mitotic kinases such as PLK1 promotes its activity [120], while phosphorylation by TTBK2 counteracts KIF2A recruitment to the ciliary base and hampers its microtubule-depolymerizing activity [79, 121]. Similarly, the activity of axoneme-depolymerizing kinesin KIF24 is promoted by phosphorylation by NEK2 [122].

Another phenomenon, termed ectocytosis or cilia decapitation, has been recently linked to the regulation of primary cilia dynamics, eventually leading to their disassembly [123], [124] (Fig. 2). Here, events like the defective exit of ciliary receptors owing to impaired BBSome function [124], [125], or mitogen-induced INPP5E removal from primary cilia [123], trigger remodeling of ciliary actin and, accordingly, myosin-mediated abscission of the ciliary membrane and its release from the tip of cilia in a form of a small vesicle. Consequently, this may cause gradual resorption of the whole ciliary axoneme. Intriguingly, INPP5E removal from cilia and, successively, the shortening of ciliary axoneme requires AURA activity [123, 126], providing another means of how AURA activation contributes to primary cilia disassembly. Here, the shortening of primary cilia caused by BBSome deficiency

can be reversed through both AURA and the intraciliary RHO GTPase CDC42 [125, 127], suggesting a close interplay between axoneme resorption and ciliary membrane turnover.

Crosstalk of cilia assembly and disassembly pathways with other regulatory mechanisms

The previous paragraphs have illustrated that primary cilia are highly dynamic organelles. In fact, as little as 5 min of halted IFT is enough to detect changes in primary cilia composition. Therefore, perhaps unexpected heterogeneity and asynchrony related to the initiation of their assembly and disassembly, respectively [51, 108], possibly reinforce a notion that having/not having a cilium is a result of counteracting interactions of pro-assembly and pro-resorption pathways. In this section, we plan to discuss some of these interactions thoroughly, including the relationship between cilia formation/resorption and cell cycle, the crosstalk between individual regulatory modules in cilium biology, along with the possible dual (non-ciliary) role of primary cilia regulators.

Cell cycle and primary cilia

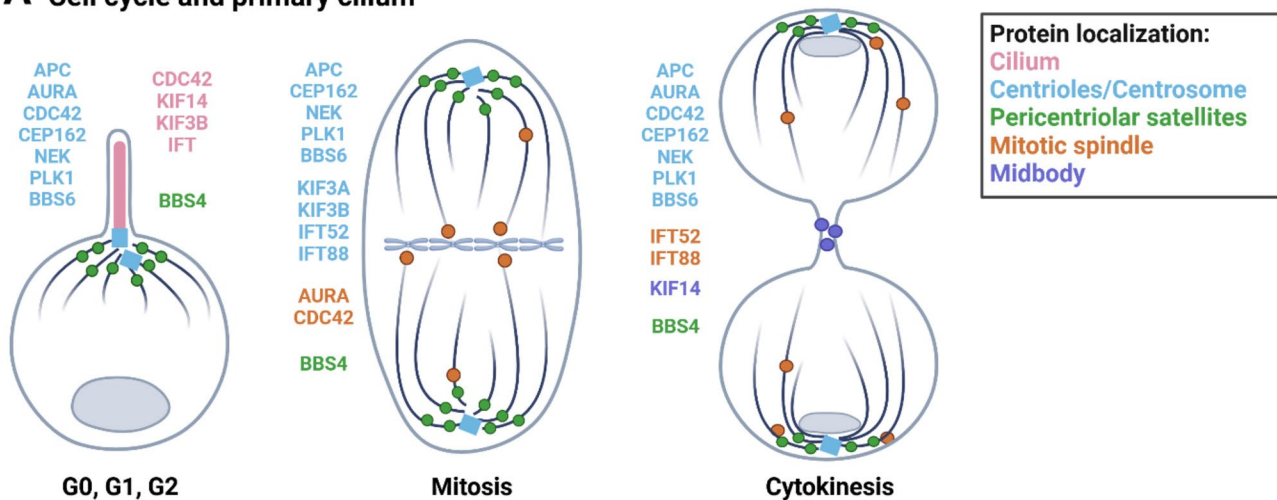
As previously noted, primary cilia were originally viewed as hallmarks of quiescence, perhaps even having a checkpoint function. According to this model, primary cilium had to be resorbed before cell cycle re-entry and, conversely, a block of primary cilia disassembly led to cell cycle arrest [50]. While this model has gained some attention, especially when considering the possibility of halting tumor growth by inducing ciliogenesis in cancer cells, it remains controversial, with conflicting data in the literature. Actually, this raises a conundrum: How can organelle, resorbed prior to cell cycle re-entry, still convey proliferative signals (e.g. by HH ligands) important for G1-S transition? [9] Specifically, scaffolding protein trichoplein (TCHP) has been proposed to promote G1-S transition in ciliated cells by activating AURA and then disassembling cilia [128]. This model, however, has been challenged in a report indicating that TCHP regulates cell cycle progression independently of cilia status [129]. With the wide adaptation of live cell imaging microscopy, many reports have subsequently demonstrated the presence of primary cilia in cycling cells [9], [51, 130]. Still, considering the heterogeneity in the timing of primary cilia assembly/disassembly, the possibility of some feedback mechanism between primary cilia and cell cycle, eventually leading to cell cycle alterations between ciliated and non-ciliated cells cannot be completely dismissed.

While direct evidence for the checkpoint role of primary cilia is currently lacking, the intimate relationship between primary cilia and the cell cycle is well

documented (Fig. 3A). One aspect of this interconnection is the effect of cell cycle regulators on primary cilia dynamics. The key players here are proteins well known for their prominent roles in mitosis. They are typically associated with the centrosome/ciliary base throughout the cell cycle, starting with very low abundance at G1 and peaking their levels/activity in the G2 or M phase. These include, for instance, AURA (see above) and NEK kinases [131], as well as an anaphase-promoting factor (APC) [132]. Similarly to AURA, the activities of NEK kinases have been shown to promote cilia shortening/disassembly, while their depletion leads to ciliary axoneme elongation. These effects were observed in several models,

including *Chlamydomonas* and *Tetrahymena*, as well as in mammalian cells, suggesting the role of NEKs is well conserved [131]. Mechanisms underlying the effects of NEK kinase activity include destabilization of microtubules [131] or, in the case of NEK2, disassembly of DAs [133]. The ciliary role of APC seems to be mediated by targeting NEK1 for degradation [132]. Interestingly, some mitotic regulators can act as ciliogenesis-promoting factors, e.g., by facilitating centriole maturation. One such example is PLK1, whose ectopic activation in interphase erases differences between mother and daughter centrioles (the daughter prematurely assembles DAs), and then, allows the formation of two primary cilia per cell

A Cell cycle and primary cilium



B Extraciliary roles of ciliary factors unrelated to cell division

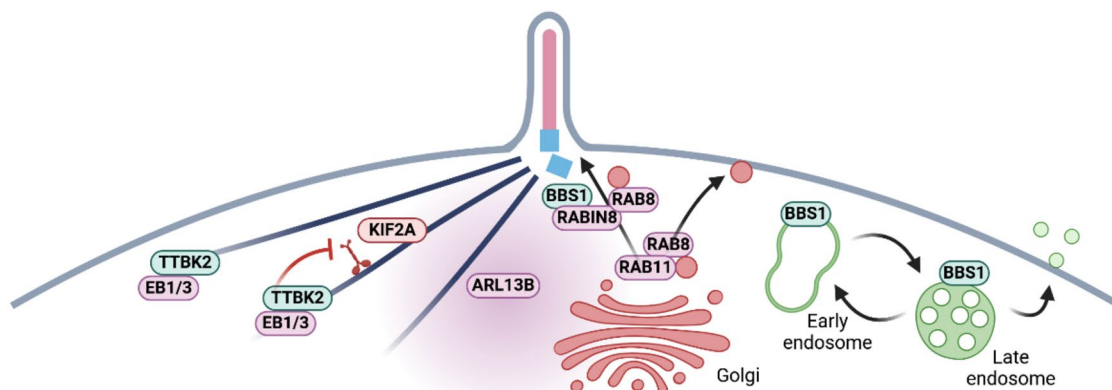


Fig. 3 Dual roles of cilia regulators in cell cycle and intracellular organization. **A** Established mitotic regulators such as AURA, NEKs, APC, CDC42, and PLK1 also play critical roles in regulating cilium disassembly. Common ciliary factors such as IFTs (e.g. IFT52 and IFT88), KIF3A/B, KIF14, CEP162, BBS4, and BBS6 also facilitate the formation of the mitotic spindle, chromosome alignment, and the progression of cytokinesis. **B** The factors involved in ciliogenesis and cilia function are vital to intracellular organization. TTBK2 binds to EB1/3 and promotes microtubule growth by suppressing depolymerizing activity of the KIF2A kinesin. ARL13B regulates the non-canonical Hedgehog (HH) pathway and is key in controlling actin organization. The RAB11/RABIN8/RAB8 cascade controls polarized vesicular trafficking to the plasma and ciliary membrane, where the latter is mediated by the BBS1-RABIN8 module. BBS1 is also involved in the endomembrane vesicular trafficking between the early and late endosomes. This image was created with BioRender.com

[134]. Considering the orderly nature of the cell cycle, heterogeneity in the timing of primary cilia assembly/disassembly seen in several time-lapse experiments is somewhat unexpected. It implies that rather than providing an instructive signal coupled to a specific checkpoint, the cell cycle creates a permissive window for cilia assembly, fine-tuned by (potentially stochastic) fluctuations in the activities of key regulators.

Perhaps the best-described functional connection between cilia and cell cycle is the extensive proliferation leading to cyst formation in kidneys – a hallmark feature of several ciliopathies[6]. In fact, kidney cyst formation, caused by mutation of cilia residing receptor polycystin 1/2 (PKD1/2) or DAs protein CEP164, can be mitigated by inhibition of cyclin-dependent kinases[19], [135]. Aberrant proliferation related to PKD1/2 mutations seems to be caused by deregulated Ca^{2+} signaling and cAMP production[136]. Another prominent driver of cell proliferation in kidneys is the Hedgehog (HH) signaling pathway. The causative relationship between cilia defects, deregulated HH signaling, and kidney cyst formation has been indicated for mutation of the IFT-A component, IFT139, that leads to bulbous cilia and an overactivated HH pathway[137], [138].

Another aspect of primary cilia–cell cycle connection is the role of several cilia components in cell cycle regulation, particularly during mitosis and cytokinesis. These effects appear to represent additional functions of these proteins, independent of primary cilia. Both mitosis and cytokinesis rely on the action of microtubules and associated proteins associated. Kinesins and other microtubule-binding proteins therefore represent a group where such cilia-unrelated function is anticipated[139]. KIF3A and KIF3B constitute the kinesin-II heterodimer, which, besides participating in the anterograde IFT in cilia, represents one of the most ubiquitously expressed kinesins, implicated in many forms of intracellular transport [140]. Furthermore, KIF3A/3B is associated with mitotic spindle in both *Chlamydomonas* and vertebrate cells, and expression of a mutated form of KIF3B leads to mitotic abnormalities and aneuploidy [141]. A different example is another microtubule-plus end motor, KIF14, originally identified as cytokinesis-regulating kinesin associated with the midbody [142, 143]. However, during interphase, KIF14 localizes to the axoneme of primary cilia to regulate cilia growth, IFT, and competence to convey HH pathway activation [144, 145]. The association between mitotic apparatus and cilia regulators extends to IFT and BBS proteins (see Table 1 for a detailed overview). This is perhaps the best documented for IFT88 (member of IFT-B complex). In dividing cells, IFT88 localizes to the mitotic spindle, where it takes part in a dynein1-driven complex to ensure the correct formation of astral microtubule arrays and spindle orientation. Consequently,

IFT88 depletion leads to mitotic defects in cell culture cell lines, mice, and zebrafish [146]. Moreover, IFT88 has been implicated in the re-localization of AURB during cytokinesis [147], and, together with another IFT-B component, IFT52, in the clustering of supernumerary centrosomes in cancer cells [148]. Also, IFT proteins from both IFT-B and IFT-A subcomplex re-localize from basal bodies/cilia to cleavage furrow in dividing *Chlamydomonas* [149]. Interestingly, IFT-A and KIF3A have another way to affect the cell cycle independently of cilia – via regulation of the WNT/ β -catenin pathway [150], [151]. Our WNT signaling chapter has further details. Other important primary cilia biology regulators with ties to proliferation control are BBS proteins. One of the initial BBS studies, which linked BBS4 to primary cilia and centriolar satellites, actually reported that BBS4 depletion leads to cell cycle arrest and prominent cytokinesis defects [152]. This proposed mechanism involves BBS4-PCM1 interaction in centriolar satellites and, accordingly, defective anchoring of microtubules in BBS4-depleted cells. Similarly, chaperonin BBS6 exhibits prominent localization to centrosome and centriolar satellites, and its depletion induces cytokinesis defects and the appearance of multinucleated cells [153]. One more example of a ciliary component with a cilia-unrelated role during cell division is CEP162, a protein with microtubule-binding ability residing at the centriole distal end to promote and restrict the TZ formation [154]. Additionally, CEP162 localizes to spindle microtubules and centrosomes in dividing cells, and its loss leads to abnormal mitosis and chromosome segregation defects [154], [155].

Summarily, available evidence suggests that cells are efficiently re-purposing their regulatory elements, leading to a shared toolkit of regulators of cilia and cell cycle. Proteins commonly viewed as mitotic regulators (AURA, NEKs, APC) mediate the cilia disassembly to ensure cilia do not intervene with spindle function during cell division. Conversely, proteins involved in cilia biogenesis (IFT, BBS, KIF3A/3B, KIF14, etc.) often take over new tasks during mitosis or cytokinesis, as there is no cilium to care about at the moment. This opens an interesting possibility that some of the many pathologies found across different “ciliopathies” may in fact stem from non-ciliary functions of cilia regulators [156].

Extraciliary roles of ciliary factors

TTBK2 represents an example of a critical regulator of primary cilia assembly, with an additional role outside of cilia, not directly linked to cell division (Fig. 3B; Table 1). Outside of the basal body, TTBK2 interacts with microtubule plus-end tracking proteins (+TIPs) such as EB1/3 to localize to cytoskeletal microtubules and regulate their dynamics and successive cell migration [121]. Interestingly, at least some activities of TTBK2, both inside and

Table 1 Cilia regulators with dual roles

Protein(s)	Centrosome/cilia -related function	Extraciliary functions - cell cycle	Extraciliary functions- other
AURA	cilia disassembly [113, 114]	mitotic entry, spindle assembly, chromosome alignment [157]	
HDAC6	cilia disassembly [113, 115]		microtubule deacetylation [116, 117]
CDC42	cilia shortening, actin-dependent ectocytosis [125]	chromosome alignment [157]	regulator of cell polarity and actin-based morphogenesis [158]
NEK kinases	cilia shortening/disassembly [131]	destabilization of MTs [131] disassembly of DAs [133]	
APC	stability of axonemal microtubules through targeting NEK1 [132]	anaphase promoting complex [157]	
PLK1	centriole maturation [134]	mitosis progression [157]	
KIF3A KIF3B	anterograde IFT [140]	intracellular transport [140] mutations in KIF3B - mitotic abnormalities and aneuploidy [141]	intracellular transport [140]
KIF14	cilia growth and trafficking, HH activation [144]	localization to midbody, cytokinesis progression [142, 143]	
IFT88	ciliogenesis, IFT transport [87]	spindle orientation, AURB positioning during cytokinesis [147]	clustering of centrosomes in cancer cells [148]
BBS4	BBSome-dependent trafficking [152]	cell cycle progression and cytokinesis [152]	pre-BBSome assembly [102] exosome release [235]
BBS1	BBSome-dependent trafficking, ciliary gating by supporting TZ structure [102]		endomembrane trafficking [162, 163]
BBS6	BBSome assembly [153]	progression of cytokinesis [153]	CCT/TRiC-chaperonin complex [153] exosome release [235]
CEP162	TZ formation [154]	chromosome segregation during mitosis [155]	
TTBK2	primary cilia assembly [73–77, 80, 173, 174]		MTs dynamics and cell migration [121]
RAB11 RAB8 RABIN8	polarized trafficking of ciliary vesicles, outgrowth of ciliary membrane and ciliogenesis [61, 62, 64]		endosomal recycling, polarized transport of Golgi-derived vesicles [63, 159, 160]
ARL13B	ciliary membrane composition; ciliary targeting of INPP5E and HH pathway components [165–167]		non-canonical HH signaling essential for the axon guidance [168, 169]

outside of primary cilia, rely on a common mechanism - phosphorylation and subsequent inactivation of microtubule-depolymerizing kinesin KIF2A [79], [121].

RAB11/RABIN8/RAB8 pathway activity is not restricted to primary cilia and is also involved in several aspects of vesicular trafficking in the cytosol, including endosomes recycling or transport of Golgi-derived vesicles to the cell membrane [63], [159], [160]. The BBS1 subunit of the BBSome interacts with RABIN8, linking the BBSome to the vesicular trafficking of ciliary proteins to the primary cilium base [64], [161]. BBS1 has also been detected on early and late endosomes in HEK293 cells [162], suggesting that BBSome is more broadly involved in the endomembrane system beyond its function in ciliary transport [163].

A surprising non-ciliary function has also been identified for ARL13B, which is perhaps the most commonly used marker to visualize primary cilia in microscopy-based experiments, and its mutations cause Joubert syndrome [48], [164]. ARL13B is a membrane-associated small GTPase of the ARF/ARL family, important for correct ciliary targeting and localization of INPP5E and

several HH pathway components [165], [166], [167]. Recent work from the Caspary lab described ARL13B^{V358A} mutant, which is unable to localize to primary cilia, and the cilia are shorter and show diminished INPP5E levels. Notably, ARL13B^{V358A} still seems fully capable of rescuing major HH phenotypes related to ARL13b loss in mice [168], [169]. While ARL13B^{V358A} is missing in primary cilia, it could be identified in axons and growth cones of commissural neurons, where it probably mediates non-canonical HH signaling relevant for axon guidance [169]. Considering the prominent role of ARL13B in disease and the well-supported model of HH pathway dependence on primary cilia in vertebrates, it would be very interesting to test the ability of ARL13B^{V358A} to mediate HH signaling in a model with ablated ciliogenesis.

Interactions between individual modules of primary cilia

In the following section, we will discuss how individual cilia compartments affect each other to control the dynamics of the fully assembled organelle. We begin with the basal body, which is typically viewed as an inseparable

part of cilium, and, via the DAs-associated activities previously noted, is critically involved in primary cilia assembly initiation (Figs. 1A and 4A). In the primary cilia of sensory neurons of the nematode *C. elegans*, the basal body is degraded following cilium assembly [170]. In fact, centrioles are lost in most cells in *C. elegans*, coinciding with the cessation of proliferation. Even though the basal body is lost, transition fiber-like structures still connect the proximal axoneme end with the membrane [170], indicating a function of this compartment exceeding ciliogenesis initiation. Indeed, emerging evidence from mice and cell culture cell lines has established DAs kinase TTBK2 capacity in primary cilia maintenance. TTBK2 activity ablation after cilia assembly effectuates their shortening, perturbed localization of IFT proteins and HH pathways components, and axonemal microtubules glutamylation reduction [171, 172]. Proposed mechanisms downstream from TTBK2 involve KIF2A inhibitory effects [79] and centriolar satellite remodeling [172].

Dynamic interactions are also typical for the IFT. As noted earlier, disruption of IFT-dynein or IFT-A complexes results in short, bulged primary cilia due to the accumulation of IFT proteins and their cargo. Conversely, mutations in IFT-B components typically result in complete axoneme assembly failure [87]. Interestingly, while

the general phenotypes of anterograde and retrograde defects, respectively, are well distinguishable, emerging evidence also suggests “crosstalk” between anterograde and retrograde transport (Fig. 4B). The putative sites for such interactions are the ciliary base and tip, respectively, where IFT trains rearrange to switch motors [87]. Acute inhibition of heteromeric KIF3A/3B kinesin II, for instance, completely halts both anterograde and retrograde transport in primary cilia in NIH3T3 cells within minutes [173]. However, dynein motor inhibition by ciliobrevin D halts anterograde IFT trains within 30 min of stalled retrograde transport [174]. Furthermore, CHE-3, the *C. elegans* orthologue of the retrograde IFT-dynein-2 motor DYNC2H1 demonstrably affects both retrograde and anterograde transport [175]. Similar observations were reported in WDR60 and WDR34 dynein-2 mutants using mammalian cell lines [176]. One possible explanation for these phenotypes is the roadblock/traffic jam model, where stalled IFT trains impair “opposing” IFT train movement indirectly, by sterically limiting the “free road” available. Considering IFT-A and IFT-B trains show direction-specific usage of the two microtubules in a doublet to avoid collisions, at least in *Chlamydomonas* [92], reported reciprocal interactions between anterograde and retrograde transport machinery may indicate

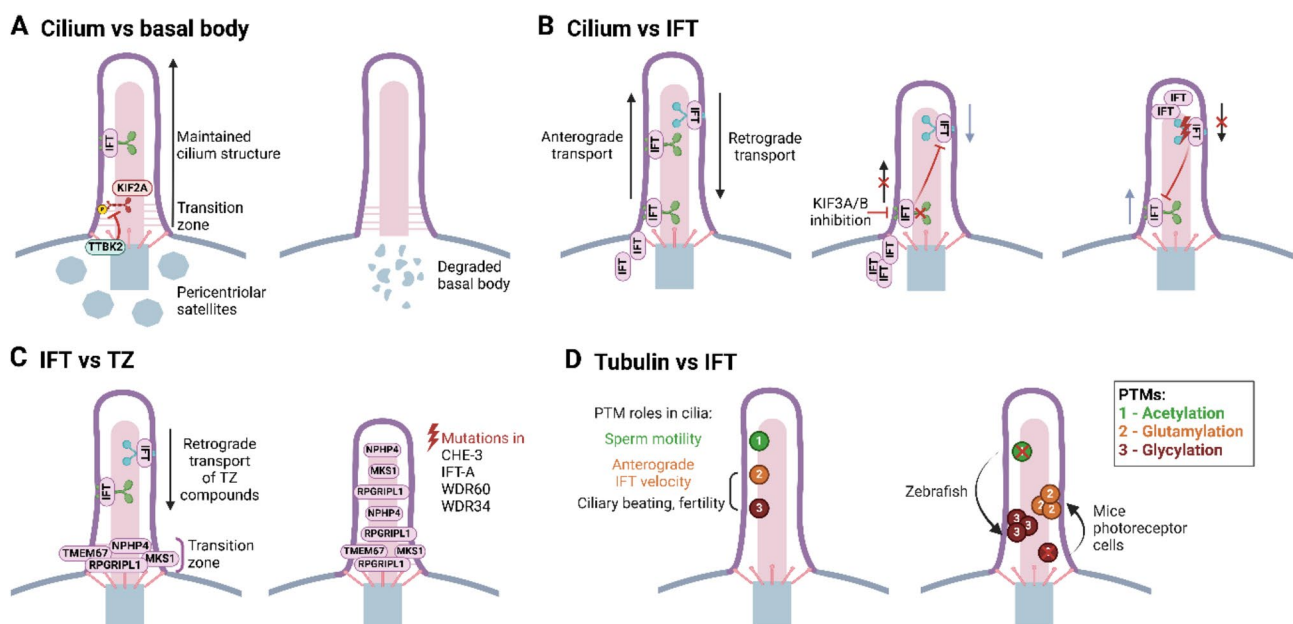


Fig. 4 Interactions between individual modules of primary cilia. **A** The basal body and pericentriolar satellites are crucial for the growth and maintenance of the ciliary axoneme. TTBK2 at the basal body promotes cilium growth by suppressing the depolymerizing kinesin KIF2A. In *C. elegans*, the basal body is degraded once the cilium is assembled. **B** Anterograde and retrograde IFT display functional crosstalk in cilium length control. Inhibition of the heteromeric KIF3A/3B kinesin II disrupts anterograde IFT and indirectly halts retrograde IFT, causing IFT particles to accumulate at the ciliary base. Inhibition of the dynein motor by ciliobrevin D or mutation in IFT-A complexes indirectly abrogates anterograde IFT. **C** Retrograde IFT is crucial for correct TZ establishment. Mutations in components of retrograde IFT lead to the mislocalization of TZ components inside the cilium, and the shortening of cilia. **D** Posttranslational modifications (PTMs) of axonemal tubulin are crucial for cilia function. Axoneme acetylation, glutamylation, and glycylation are involved in cilia beating and sperm motility, likely modulating the velocity of the anterograde IFT. PTMs can also compensate for each other; axoneme hyper-glycylation can compensate for axoneme deacetylation in zebrafish cilia, while axoneme hyper-glutamylation can compensate for axoneme deglycylation in murine photoreceptors. This image was created with BioRender.com

a more complex relationship. The modeling of IFT motor capacity to walk through crowded environments or pass obstacles warrants future investigation.

We have previously discussed the IFT trains being assembled at TZ and noted that IFT-A proteins participate in the import of membrane receptors through the TZ gate. Interestingly, IFT-TZ interactions seem to be even more complex with available evidence further implying IFT involvement in TZ assembly/maintenance regulation (Fig. 4C). The initial evidence of IFT involvement in TZ formation comes from *Trypanosoma*, where IFT mutations precipitate TZ shortening [177]. The requirement of functional IFT for correct TZ function is conserved in metazoan. Ablation of WDR60 or WDR34 in hTERT-RPE1 cells affects the expansion of RPGRIP1 from the TZ inside the cilium and reduces the TMEM67 pool in the TZ [176]. Similarly, ectopic localization (expansion from the TZ into the proximal axoneme) of several TZ components is connected to the ablation of dynein motor CHE-3 in *C. elegans* [175]. Furthermore, such ectopic localization of several TZ components has also been established for several IFT-A mutants in *C. elegans* [170]. The functional consequence of IFT-TZ interactions is the prominent worsening of gating function in worms with ablated IFT and MKS over the single mutants [178]. One possible explanation of IFT effects on TZ is that TZ proteins begin their assembly in the most proximal region of the axoneme following ciliogenesis onset, yet a portion of these proteins can become mis-localized to distal ciliary regions and potentially create ectopic axoneme–membrane connections. The IFT retrograde machinery purpose may therefore be to assist in the retrieval of mis-localized TZ proteins [175], [178]. Interestingly, the antithesis of IFT-TZ interaction is that disrupting the TZ NPHP module restores the ciliary exit of “underpowered” retrograde trains in WDR-60 mutant, which otherwise accumulate inside the cilium [179]. The model of mutual regulation of IFT-TZ has support in association (though rare) of eye and kidney phenotypes, typical for TZ defects, with IFT mutations [8], [180].

New paradigms are emerging on possible mutual interactions of the ciliary axoneme and IFT motor proteins. Modulation of microtubule tracks in the ciliary axoneme, which fine-tunes the motor proteins walking on them, could be explained by the so-called “tubulin code”. The overall concept behind this term is that molecular patterns generated by combinations of tubulin isoforms and their posttranslational modifications (PTMs) such as acetylation, (poly)glutamylation, (poly)glycylation, detyrosination, etc., control the functions of microtubules [181], [182]. Almost all of the amino acid and length variation between different tubulin isoforms is confined to their unstructured C-terminal tails (CCTs). Consequently, the presence and absence of

the CCT, respectively, and the type of its modification have substantial effects on the motility of several kinesin motors (including kinesin II) on purified microtubules in vitro [181]. Ciliary axonemes of both primary and motile cilia are rich in several tubulin PTMs [181], [184], which has been commonly associated (although not yet completely proved) with their considerably higher stability over the cytosolic microtubules. Thus, “guilt by association” evidence suggests that tubulin PTMs play a role in cilia biology (Fig. 4D). Indeed, several of these PTMs show non-uniform, pattern-like distribution in the axoneme [184]. The function of tubulin PTMs is reasonably well-documented for the motile cilia, where the glycylation and glutamylation are particularly enriched in the B microtubule of the doublet [184]. However, the role of tubulin modifications in primary cilia biology is less clear [181]. Polyglycylation of tubulin CCT is almost exclusively found in ciliary axonemes over cytosolic microtubules [181], and is essential for ciliogenesis, at least in protists. *Tetrahymena* strains with defective polyglycylation (where tubulin encoding genes were replaced with variants lacking corresponding glycylation sites) have profound defects in axoneme structure and exhibit impaired movement of flagella [182]. The situation seems to be different in mammals. Elimination of enzymes responsible for tubulin glycylation (TTLL3 and TTLL8) results in the absence of glycylation in cilia, albeit without a penetrant cilia-related phenotype (mice are viable and of normal morphology). Glycylation, therefore, does not seem to be critically involved in the assembly or maintenance of primary cilia. Instead, the defects in TTLL3/TTLL8 double knockout are restricted to the sperm flagella, inducing altered beating dynamics and then reduced fertility [185]. Similarly, aberrant (poly)glutamylation is linked to defective cilia beating in both *Tetrahymena* and mammals (where it often manifests in fertility and respiratory defects) [181], [186]. Significantly, axoneme glutamylation has been implicated in the regulation of the velocity of several ciliary motors and the release of cilia-derived extracellular vesicles in *C. elegans* [187]. Moreover, chemically-induced cilia deglutamylation led to a slower anterograde movement of IFT88 containing trains in primary cilia of NIH3T3 cells [188]. If confirmed in other model systems, the glutamylation-IFT link could provide long-anticipated, yet currently lacking evidence of the functional impact of glutamylation/tubulin code on primary cilia biology. The purpose of acetylation in cilia is currently unclear, despite the fact that tubulin acetylation was the first described tubulin PTM [181]. Enzyme α TAT1 has been identified as the major regulator of tubulin acetylation, its ablation causing a loss of this PTM in mice, however excepting moderate fertility defects related to sperm motility, the mice are viable and develop normally [189]. Surprisingly,

the cytosolic microtubules exhibited higher stability in the absence of α TAT1 [189]. We use this observation as a proxy to present another emerging phenomenon in tubulin PTMs regulation – compensatory mechanisms at the level of “writers”, “erasers”, or even between individual types of tubulin PTMs, which likely contribute to the lack of gross cilia phenotypes in various models. Loss of tubulin glycylation in mouse photoreceptors is accompanied by an increased glutamylation, perhaps due to competition of the corresponding enzymes for the same modification sites in the CTT [181]. Mutation of three enzymes responsible for tubulin deacetylation (SIRT2, HDAC6, and HDAC10) brings about the anticipated reduction of tubulin acetylation in cytosolic microtubules, yet concurrently decreased acetylation and increased glycylation of ciliary axonemes in zebrafish, and, furthermore, without a notable impact on ciliary function [117]. Clearly, resolving the nature of compensatory mechanisms is a crucial step in assessing the functional impact of tubulin PTMs on primary cilia biology. Since we have now discussed means in which the axoneme may affect walking motor proteins, it is worthwhile noting a rather hypothetical, yet very intriguing possibility that motor protein may communicate back to the cilium MT tracks. This new concept, currently demonstrated on prototypical cytosolic kinesins, kinesin 1 and 4, suggests that motors can not only induce conformational changes in tubulin owing to their walk, but the stepping may actually induce damage in the microtubule, which can be subsequently repaired by incorporation of free tubulins in the damage sites [190].

Substantively, three areas await further consideration: Whether this phenomenon additionally applies to ciliary kinesins, its potential impact for IFT, and whether the cilium developed efficient countermeasures to compensate/eliminate kinesin-induced changes in microtubule tracks.

Adaptive changes in primary cilium structure and composition to cell signaling pathways

Cilia are typically categorized into primary cilia (which are immotile and serve to sense and transduce signals), and motile cilia (which move extracellular fluids). However, increasing research reveals that both primary and motile cilia can modulate key developmental signaling pathways, such as HH, and WNT [191], [192]. Likewise, certain primary cilia can exhibit limited or specialized motility under specific conditions. As previously noted, pancreatic beta cells possess so-called hybrid cilia, which move to sense glucose levels and promote insulin production in the pancreas [35]. A temporally regulated change in primary cilia motility has been observed during the perinatal period of the choroid plexus development [193]. This transient motility shift was accompanied by changes in gene expression, suggesting a unique role

in choroid plexus formation at this stage [193]. During tissue and organ development, cilia can change their identity and also undergo retraction and reassembly [127], [194], [195]. Moreover, emerging evidence suggests that cilia physically interact with neuronal axons via synapse-like connections [196]. These and other findings emphasize the need to view cilia as dynamic organelles with complex, context-specific adaptations in homeostasis, development, and regeneration. Recently, cilium's involvement in developmental signaling pathway transduction was reviewed in great detail [3], [5]. At this juncture, we will explore how specific signals shape cilium composition and structure and accordingly, how cilia are associated with key signaling pathway regulations, crucial for cell differentiation and tissue morphogenesis.

Hedgehog signaling

Hedgehog (HH) signaling is a prototype of a cilia-dependent pathway decisive for growth and patterning of different tissues and organs during embryogenesis. Key molecular players comprise the transmembrane receptors PTCH, SMO, and GPR161, along with soluble factors including PKA, GLI proteins and the second messenger cAMP [197]. The pathway is induced via HH ligand binding to PTCH and its removal from cilia allowing SMO to enter. Recent studies indicate HH is transported in the neural tube to recipient cells with the help of cytonemes – specialized cellular actin-based extensions that facilitate targeted delivery [198]. SMO accumulation in cilia induces inhibitory receptor GPR161 export by β -arrestin-BBSome-IFT retrograde trains [105]. GPR161 removal decreases cAMP levels and leads to reduced PKA activity [199]. Consequently, GLI3FL (full-length) processing into its repressor form, GLI3R, is inhibited, permitting the transcription of HH-responsive genes. The cilium compartment provides spatial and temporal control over HH signaling, thereby differentiating the effects of ciliary versus non-ciliary cAMP and GPR161 activity [200], [201]. Changes in primary cilia composition induced by HH signaling are rapid and detectable within minutes upon HH pathway activation [202]. Several mechanisms have been proposed to mediate dynamic rearrangements of primary cilia in response to HH pathway activation. HH-mediated SMO activation promotes interactions of GPR161 and PTCH with β -arrestin, which results in the retrieval of both receptors from cilia by endocytosis [203], [204]. Acute HH pathway activation supports primary cilia shortening [125], [205], likely via activation of the ectocytosis/cilia decapitation feedback response [123], [124], [125](Fig. 5A). Certainly, the “heterogeneity/ plasticity” in the timing of the assembly/disassembly of primary cilia noted earlier likely mediates the robustness of HH pathway effects on cell proliferation. In this case, HH pathway activity in either G1-S of the previous

cell cycle or the G1 phase of the cell cycle, when the decision is made, is sufficient to drive cell cycle entry [206]. This model is consistent with the remarkable finding that a decision “to divide” could have been made in virtually any phase of the previous cell cycle [207]. HH-induced signaling is thus propagated in a robust manner into the progeny to promote fate decisions within complex tissues.

In muscles, HH signaling promotes the myogenic differentiation of the muscle stem cells [208], at the expense of fibrosis and inflammation [209]. Cilia of these stem cells maintain them in a quiescent state, preserving their ability to generate new myoblasts both during development and in response to stimuli, such as injury [195], [208], [210] (Fig. 5A). During aging, muscle stem cells lose their cilia, causing a decline in regenerative capacity [210]. The primary cilium of muscle stem cells transduces the HH pathway to ensure the proper timing of myoblast differentiation and proliferation [208]. Interestingly, defective cilia formation seems to drive these stem cells into premature proliferation, which can ultimately result in rhabdomyosarcoma [208]. Differentiated myoblasts lose their capacity to assemble primary cilia (hence to respond to HH pathway activation) during myofibrillar transition as they migrate and form myofibers [195]. Regenerative capacity of skeletal muscles is also dependent on fibro/adipogenic progenitors (FAPs) that dynamically modulate their ciliation during muscle regeneration. Preventing FAPs to ciliate blocks adipogenesis and promotes myogenesis following muscle injury [211]. Intriguingly, the mechanism involves the activation of HH target genes, due to the inability of FAPs with ablated primary cilia to generate GLI3R, which otherwise represses the HH target genes [211].

Furthermore, regulation of primary cilia length to fine-tune the responsiveness to HH pathway activation has been proposed to play a key role during the establishment of the dorsolateral axis in the forming neural tube (Fig. 5A). Here, primary cilia of the neural plate HH-responding cells (before the neural tube closure) are relatively short. Intriguingly, following the neural tube closure, HH-producing cells located in the floorplate elongate their cilia and concomitantly attenuate their responsiveness to HH pathway activation [212]. While the attenuation of the HH pathway in the floor plate depends on these elongating cilia, mechanisms driving their elongation and the HH pathway shutdown are still awaiting full determination [212]. One possibility is that the elongation is a consequence of the structural transformation of these cilia to become motile [213]. Cilia remodeling is also occurring during neurogenic divisions of progenitors in the neural tube, in a process termed apical abscission, which physically separates the axoneme and the basal body, hence rendering the cilium

temporarily dysfunctional [214]. Remarkably, disrupting the cilium formation during or after its remodeling during the apical abscission impairs axonogenesis in newly born neurons, possibly via a non-canonical HH signaling pathway (not involving regulation of gene expression) [112].

In ciliopathy conditions, such as BBS, cells lack the retrograde adaptor BBSome for retrieval of GPR161 and additional receptors. Activation of the HH pathway in BBSome deficient cells also leads to cilia shortening [125], although the mechanism differs from that in wild-type conditions (Fig. 5A). HH induces hyperactivation here of intraciliary GTPase CDC42, which promotes actin-dependent ectocytosis of the ciliary content, including GPR161, and successively, shortens the ciliary axoneme [125]. Despite these alterations, HH signaling is not entirely suppressed in the BBS context [124], [215]. The GPR161 might likely be removed in ectosomes together with SMO in a bipartite complex [203] or additional HH modifiers, such as PKA [216]. In such cases, the ectocytosis-dependent decrease in cAMP and PKA activity might alleviate GLI3 phosphorylation and sustain low levels of HH signaling.

In Joubert syndrome, upon loss of INPP5E, cilia become shorter and HH signaling increases [123], [217]. INPP5E controls cilium dynamics via regulating ciliary PIP levels and TULP3-dependent import of receptors (e.g. GPR161) to cilia [42], [126]. AURA, as one of the key regulators of primary cilia disassembly, has been depicted to drive cilia shortening via depleting cilia of INPP5E [123]. It remains to be seen if AURA activity also mediates some of the reported effects of the HH pathway on primary cilia length. Overactive HH signaling and short cilia have been also identified in PINK1-deficient human and mouse models of familial Parkinson's disease [218].

WNT signaling

Canonical (WNT/ β -catenin) and non-canonical WNT (WNT/ β -catenin-independent) signaling belong to the major developmental pathways with a somewhat controversial relationship to primary cilium. WNT/ β -catenin signaling pathway, similar to the HH signaling pathway, is a potent driver of cell proliferation, with numerous implications for development and cancer [130], [219]. As the name suggests, its key element is the protein β -catenin, which is in response to WNT ligand stimulation translocated from the cytosol into the nucleus, where it, in cooperation with TCF/LEF proteins, drives gene expression [219]. Upon a WNT ligand binding to receptor Frizzled (FZD) and co-receptor LRP5/6, the signal is via activities of scaffolding protein DVL transduced to a complex of APC-AXIN- β -catenin, and kinases such as GSK3 β and CK1. This causes the disassembly of this so-called degradation complex, β -catenin escapes

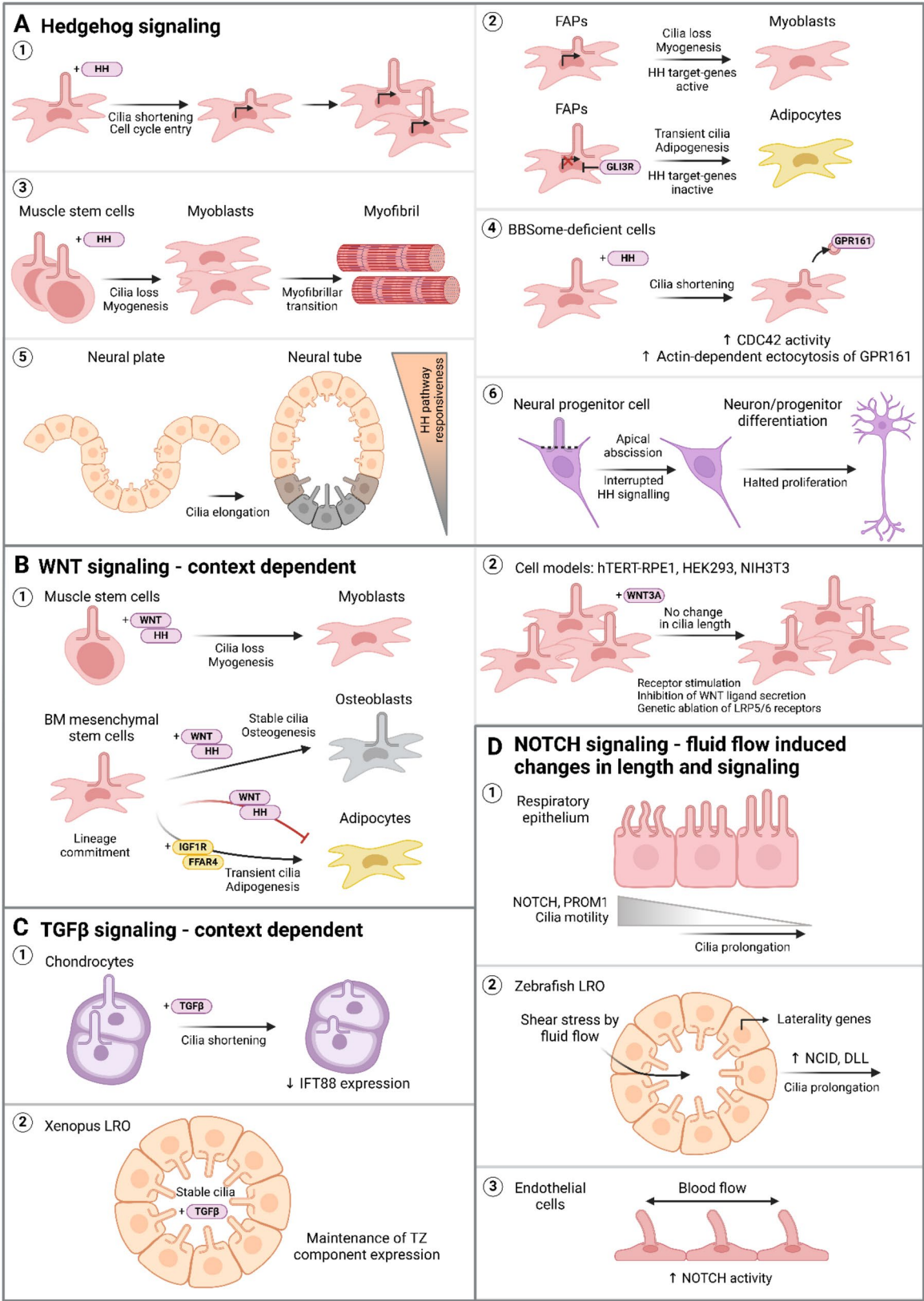


Fig. 5 (See legend on next page.)

(See figure on previous page.)

Fig. 5 Adaptive changes to cilia dynamics during cell signaling. **A** Activation of HH signaling triggers cilia shortening and promotes cell cycle entry, passing on this effect to the subsequent progeny (1). In fibro/adipogenic progenitors (FAPs), the length of cilia modulates muscle regeneration. Short or absent cilia on FAPs block adipogenesis and promote myogenesis, while long cilia favor adipogenesis (2). Similarly, HH signaling induces myoblast differentiation from muscle stem cells, where myoblasts lose cilia to form myofibrils (3). In BBSome deficiency, HH signaling triggers CDC42/actin-dependent ectocytosis of ciliary GPR161, leading to subsequent cilia shortening (4). After neural tube closure, HH-producing cells elongate cilia to attenuate their responsiveness to the HH pathway (5). During differentiation of neural progenitors, apical abscission of the ciliary axoneme from the basal body leads to a temporary cilia dysfunction. **B** The effects of WNT signaling on primary cilia dynamics are context-dependent. During tissue differentiation, WNT functions together with HH to either stimulate cilia disassembly in myoblasts or sustain cilia dependent signaling in bone marrow mesenchymal stem cells (BM MSCs) during osteogenesis (1). In MSCs, WNT and HH act inhibitory on adipo-commitment, leading to the emergence of adipocytes through IGF1R/FFAR4 cilia-dependent signaling and eventual cilia disassembly (1). In cell culture systems, activation of WNT with WNT3a ligand or pharmacological inhibition of WNT ligands secretion, does not alter number or length of cilia (2). **C** The effects of TGF β signaling on cilia dynamics exhibit a context- and cell type-specific dependency. Activation of the TGF β signaling pathway leads to the shortening of primary cilia in cultured chondrocytes (1), whereas it maintains cilia length in cilia of *Xenopus* left-right organizer (LRO) (2). **D** NOTCH signaling is primarily triggered by the fluid flow-induced alterations in cilia dynamics, which in turn promotes cilia function in diverse cellular systems, such as respiratory epithelium (1), zebrafish left-right organizer (LRO) (2) and endothelial cells in the myocardium (3). This image was created with BioRender.com

GSK3 β /CK1-mediated phosphorylation marking it for degradation, which then leads to the stabilization of β -catenin levels and import into the nucleus [219]. The non-canonical pathway is characterized by its β -catenin-independent status and typically involves branches such as WNT/PCP and WNT/Ca²⁺ [130, 220]. Discussion here is focused on the links between WNT/ β -catenin signaling and primary cilia, as the connections between cilia and WNT/ β -catenin-independent pathways (in particular the WNT/PCP) have been previously identified and thoroughly covered in several reviews [220], [221]. Several components of WNT signaling have been identified associated with basal body/centrosome (e.g. β -catenin, DVL, AXIN, APC) [130] and/or ciliary axoneme (e.g. LRP5/6, FZD) [222]. This evidence alone clearly argues for a link between primary cilia/centrosomes and the components of the WNT/ β -catenin signaling pathway. However, functional consequences of such a link for cilia or WNT/ β -catenin signaling are considerably less clear. Deregulation of cilia formation/function by acute depletion of some of its regulators (e.g. INVS, BBS1, BBS4, BBS6/MKS, etc.) [223], [224] or mutation of KIF3A in mouse fibroblast [225] leads to concomitant defects in WNT/ β -catenin signaling. Conversely, mutation of ciliary regulators in vivo (e.g. IFT88, IFT172, INVS, DYNC2H1, and KIF3A) does not seem to cause major defects in WNT/ β -catenin signaling, even though ciliogenesis and/or HH pathway are severely dysregulated [226], [227], [228]. One plausible explanation for these contradicting reports is the activation of compensatory mechanisms that lower the penetrance of the WNT-related phenotypes (in contrast to acute depletion/inhibition by siRNA or morpholino) in models with permanent gene deletion/mutation (e.g. owing to transcriptional adaptation following CRISPR/Cas9 gene editing [229]). Alternatively, some of these effects could be explained by the dual role of some of the cilia components previously discussed (Table 1). Interestingly, compelling evidence suggests that a key step of the WNT/ β -catenin cascade, namely the translocation of β -catenin into the nucleus

is controlled by IFT-A and kinesin II (KIF3A) proteins. Specifically, lack of IFT140 or KIF3A, though not IFT88, prevents nuclear accumulation of β -catenin following WNT ligand stimulation, independently of their role in primary cilia [150], [151]. Furthermore, reported effects (or their lack of) may reflect the high complexity of the cilia – WNT/ β -catenin signaling relationship (e.g., context-dependent effects, non-cell autonomous functions). The WNT/ β -catenin signaling pathway is well established in the specification of motile cilia, via regulation of expression of transcription factor FOXJ, acting upstream of the induction of motile cilia formation [230], [231]. WNT signaling effects on primary cilia dynamics seem to be context-dependent (Fig. 5B). Analysis of cell lines such as hTERT-RPE1, HEK293, and NIH3T3 established that stimulation with WNT3a ligand, pharmacological inhibition of WNT ligands secretion, or genetic ablation of LRP5/6 receptors did not alter the number nor length of primary cilia [232], while ablation or knockdown of LRP5/6 impaired primary cilia formation in HEK293T cells [222]. The explanation may be the cell type-specific activation of a cilia-residing WNT signaling branch, independent of β -catenin and regulation of transcription, yet utilizing LRP5/6 and GSK3 β , capable of modulating primary cilia dynamics [222]. The exact mechanism of how the ciliary WNT/GSK3 β pathway contributes to cilia dynamics as well as the overall outcome of WNT signaling in ciliopathy conditions remains to be elucidated. In BBS, loss of BBSome stimulates premature cilia disassembly via ectocytosis/cilia decapitation [123], [124], [125]. Simultaneously, it disrupts WNT signaling and leads to altered differentiation of multiple tissues, including the retinal pigment epithelium (RPE) layer in the retina [127], [223], [233], [234]. It is not yet known whether the BBSome regulates the ciliary WNT/GSK pathway. Nevertheless, loss of the BBSome results in dysregulation of the cellular endomembrane system, causing increased exocytosis of the small secretory vesicles containing WNT regulators [235]. An intriguing possibility is that the BBSome may act to balance intraciliary

and extraciliary WNT signaling, though this hypothesis needs to be thoroughly tested. It will now be crucial to explore how this WNT/GSK3 β signaling route contributes to the overall WNT signaling outcome in ciliopathy models and examine its potential crosstalk with the HH pathway in relevant cases such as cancer and embryogenesis. In fact, considering that dysregulation of either the HH signaling pathway or signaling downstream of LRP5/6 induces neural tube closure defects [220], [236], a developing neural tube could represent a suitable model system to probe for HH pathway alternations in conditions with hampered WNT/(LRP5/6)/GSK3 β signaling.

Another system offering room for HH-WNT interactions is mesenchymal cells (Fig. 5B). In mesenchymal cells of the soft palate, WNT/ β -catenin signaling has been proposed to facilitate cilium disassembly and proliferation during myogenesis [237]. The WNT signaling is here likely accompanied by the HH pathway activation, which is essential for the proper myogenic differentiation as well [208, 210]. WNT and HH pathways are vital for driving the osteo-lineage commitment of mesenchymal stem cells (MSCs) during bone growth and upon mechanical loading [238, 239], [240]. Loss of IFT20 skews the osteo-/adipo-commitment of MSCs toward the adipogenic lineage [239], emphasizing the critical role of functional cilia in this process while still leaving open the possibility for IFT20 extraciliary functions. In contrast, the commitment of MSCs to adipogenic lineage is suppressed by WNT and HH pathways and driven by the IGF-1R and FFAR4 signaling [241], [242]. The primary cilium here is present only on committed pre-adipocytes to secure the onset of the adipogenic program and then disappears in mature adipocytes [242, 243], [244]. WNT signaling in MSCs also regulates the production of chemokines, such as CXCL12, being essential to maintaining hematopoiesis in bone marrow [245]. BBS patients and mouse models exhibit altered blood parameters, with a notable decrease in CXCL12 production observed in the bone marrow of BBS mouse models [246]. This indicates that ciliary factors, IFT20, BBS4, and BBS18 in MSCs regulate both the intrinsic and extrinsic functions of MSCs in bone tissue. However, it remains unclear whether BBSome deficiency influences the production of extracellular vesicles in MSCs, as seen in cell lines [235], and how this, consequently, impacts bone marrow homeostasis.

TGF β signaling

The TGF β signaling pathway regulates a wide range of cellular processes, including cell proliferation and differentiation. Upon stimulation with the TGF β ligand, the cilia localized receptors TGF β IR and TGF β IIR become internalized via the clathrin-mediated endocytosis [247], [248]. Ciliary pocket (CiPo) is considered prominently decisive in TGF β receptor retrieval, hence acting

upstream of the phosphorylation of key effector proteins, SMAD2/3, to promote their transport into the nucleus to drive gene expression (reviewed in greater detail in [249]). Noteworthy, the involvement of CiPo in clathrin-mediated endocytosis of TGF β receptors in vertebrates is pursuant to the function of the analogous region, the flagellar pocket, which serves as the sole site of endocytosis in protists [39]. A defect in TGF β signaling has been reported following the ablation of IFT88 and CEP128 (a component of SDAs), causing defects in dorsoventral patterning in early embryogenesis [247], [248]. Surprisingly, depletion of CEP128 impairs ciliary TGF β signaling while leaving primary cilia largely intact (in fact, its depletion facilitates cilia formation and promotes their length), leaving the contributing mechanism expected to hamper receptor trafficking at CiPo to be found.

Similar to the WNT signaling pathway, the effects of TGF β signaling on cilia dynamics are context- and cell type-dependent (Fig. 5C). While activation of the TGF β signaling pathway triggers shortening of primary cilia in cultured chondrocytes [250], cilia of *Xenopus* left-right organizer and other tissues reveal reduced length following the blocking of TGF β pathway [251], and cilia remain largely intact in human mesenchymal stem cells in response to deregulated TGF β signaling [252]. Underlying mechanisms involve the regulation of gene expression of key regulators of cilia assembly. Specifically, TGF β signaling suppresses IFT88 expression in chondrocytic cells, resulting in a reduction in both the number and length of cilia [250]. Conversely, TGF β signaling in *Xenopus* is required to sustain the expression of TZ components, and hence cilia maintenance [251].

Aberrant TGF β signaling is linked to congenital heart diseases and skeletal anomalies, which are common features of ciliopathies and has been recently associated with Alstrom syndrome [223], [224], [225]. In mesenchymal stem cells, TGF β signaling drives the differentiation of myogenic, chondrogenic, and adipogenic lineages [239], [253], [254]. Loss of IFT20 decreases TGF β driven SMAD2/3 phosphorylation, impairs glucose metabolic homeostasis, and promotes adipolineage commitment of the bone marrow MSCs [239]. TGF β signaling is critical for bone regeneration during fracture healing by regulating the expression of angiogenic and chondrogenic genes in chondrocytes and recruitment of the bone marrow MSCs to the site of injury [252], [253].

Decrease in primary cilia frequency or length upon loss of IFTs or by upregulation of cilia disassembly factors can be also linked to altered TGF β -mediated extracellular matrix protein expression, which is a common prerequisite of fibrosis and cancer in many tissues, such as atrial fibrosis [254], lung pulmonary fibrosis [255], polycystic liver disease [256], liver fibrosis [257], cholangiocarcinoma [258], or colon cancer [259].

NOTCH signaling

NOTCH signaling is a developmental pathway controlling intercellular communication during tissue morphogenesis [260], its correct regulation relying on functional basal body/cilium, for instance, in developing skin [261] or in liver [262]. NOTCH signaling is transduced by the interaction of two cells, where one cell provides one of the DELTA-like (DLL1, DLL3, and DLL4) or JAGGED ligands (JAGGED1, JAGGED2) and the second one the receptors (NOTCH 1–4). Ligand–receptor interaction triggers γ -secretase-dependent cleavage of the NOTCH intracellular domain (NICD), which then translocates from the cytoplasm to the nucleus, where it promotes expression of key transcription factors *Hes* and *Hey* regulating the expression of downstream genes [263]. NOTCH pathway components, including the NOTCH receptor, were detected at the basal body and/or ciliary axoneme [163, 264]. The spatial organization of NOTCH signaling is regulated by the polarized trafficking module involving ARF4-RAB11 GTPases [264], [265]. Once at the membrane, the NOTCH receptor is continuously recycled through the endomembrane system back to the surface to maintain signaling capacity. Loss of BBS1, BBS4, or ALMS results in overactivation of the NOTCH pathway, likely owing to NOTCH retention in sorting endosomes [163].

Cilia-deficient keratinocytes *in vitro* and in mice embryonic epidermis have defects in NOTCH signaling [261]. Similarly, cKO of IFT88 leads to an increased proliferation yet decreased NOTCH signaling in corneal epithelial cells [266]. Furthermore, ablation of cilia-localized PKD2 in the liver induces increased NOTCH signaling and formation of cysts [262]. The primary cilium is also needed for hematogenic endothelial cell (HE) differentiation through the regulation of NOTCH signaling. HE cells give rise to hematopoietic stem and progenitor cells (HSPC). Reduced expression of HSPC markers, RUNX1 and CYMB, was observed in cilia-impaired zebrafish embryos due to reduced protein levels of NICD [267].

Studies examining the relationship between cilia dynamics and NOTCH signaling primarily focus on fluid flow-induced changes in cilia length and signal transduction, revealing an apparent interdependence between these two processes (Fig. 5D). Hyper-activation of the NOTCH pathway by overexpressing the NICD or DELTA-like ligand results in prolongation of cilia in the left-right organizer in zebrafish embryo. Here, the fluid flow-induced change in the cilium length triggered NOTCH signaling for transcriptional activation of laterality genes [268]. Similarly, in the endocardium, the mechanical shear stress signals via cilia activate the NOTCH pathway and regulate regeneration in zebrafish hearts [269]. During airway differentiation, NOTCH activity regulates levels of PROM1, a stem cell marker,

to establish multiciliated cell diversity in the respiratory tract and modulate mucociliary clearance [270]. High NOTCH and PROM1 levels produce multiciliated cells with fast-beating cilia, whereas low levels result in cells with longer, low-beating cilia. It will be interesting to investigate whether increased mucociliary shear stress, induced e.g. by infections, increases cilia beating and further NOTCH activation similar to the shear stress in the endocardium or the fluid flow in the LRO [268], [269].

While not covered in this review, additional regulatory signaling circuits are involved in ciliogenesis control, including the tyrosine kinase signaling receptor, and HIPPO -YAP/TAZ pathway. Several excellent reviews concerning ciliogenesis control circuits may be referenced here [249], [271].

Managing cilia length and function: therapeutic strategies for converging mechanisms

Disruptions in ciliary dynamics are implicated in both ciliopathies and cancer progression, underscoring the therapeutic potential of targeting cilium-related processes. On one hand, strategies aimed at restoring cilium length and function show considerable promise in reducing cancer cell division and tumor growth [255], [258]. On the other hand, stabilization of the primary cilium helps cancer cells adopt a quiescent, stem-like state, which shields them from treatments based on kinase inhibitors [272]. In this part, we highlight small-molecule compounds that effectively modulate specific pathological mechanisms, including the regulation (both upregulation and down-regulation) of the Hedgehog signaling pathway and the assembly and disassembly of primary cilia - processes closely associated with cancer development. Some of these inhibitors are already approved for specific conditions, and their use, either alone or in combination, holds the potential for addressing a broader range of cilia-associated disorders.

Targeting the HH signaling pathway

A key characteristic of cilium dysfunction is the disruption of signaling pathways, such as HH, which is commonly observed in conditions like Joubert syndrome, polycystic kidney disease, and Bardet-Biedl syndrome [5]. SMO inhibitors, such as cyclopamine or purmorphamine, have demonstrated potential in regulating excessive HH signaling caused by shortened or malformed cilia. This has been observed in conditions like Parkinson's disease [218], in nephronophthisis associated with CEP290 mutations in Joubert syndrome [273], [274], and abnormal brain ventralization linked to dysfunctional INPP5E [217].

Increased HH signaling is also linked to the development of basal cell carcinoma and medulloblastoma [275], [276]. Here, the tumor growth can be driven by

hyperactivated SMO in the presence of primary cilium and also by active GLI2, independent of the primary cilium. This indicates that the role of primary cilium is determined by the specific oncogene driving HH-triggered cancers, emphasizing the need for accurate diagnostics to select the most effective compounds or HH inhibitors to target pathogenic HH signaling [275], [276], [277]. In the case of brain tumors dependent on cilia, employment of TTBK1/2 inhibitors could represent a promising strategy to mitigate cilia-dependent HH upregulation [278], [279].

Activation of HH signaling plays a critical role in osteoarthritis [280] and can be suppressed by LiCl-mediated cilia prolongation in chondrocytes [281]. Similarly, LiCl treatment inhibits HH signaling in pancreatic ductal carcinoma cells leading to suppression of their tumorigenic phenotype [282]. Since LiCl is widely used for the treatment of people with bipolar disorders, it remains to be elucidated whether LiCl modulates the neuronal ciliary signaling pathway involving GPCRs, such as the dopamine receptor. Disrupted ciliary signaling, especially the HH pathway, could therefore serve as an ideal therapeutic target for ciliopathies, neurodegenerative disorders, and cancers driven by its dysfunction or exploitation.

Targeting the cilia disassembly factors HDAC6 and AURA

As previously noted, the mechanisms of the AURA/HDAC6 module in regulation cilia dynamics leave several questions unanswered. Importantly, however, strategies based on small molecules targeting those regulators seem to restore cilia homeostasis in several cilia dysfunction-related pathologies. In conditions like BBS and renal anomalies, including polycystic kidney disease and nephronophthisis, defects in cilia dynamics were mitigated using HDAC6 inhibitors [283], [284], such as tubacin [127], ACY-1215 [285] or tubastatin [286]. Similarly, in Rett syndrome, mutations in the MECP2 gene lead to microtubule instability, and tubacin treatment restored impaired HH signaling [287].

Another phenotype associated with ciliopathies like Bardet-Biedl, Alstrom, and MORM syndromes, is obesity [8]. Obese adipose-derived MSCs possess dysfunctional cilia with compromised HH signaling [288]. Notably, treatment with HDAC6 or AURA inhibitors, such as MLN8054, restored cilium length and expression of genes associated with osteogenic and adipogenic lineage commitment in these cells [244], [288]. This is in agreement with the view that primary cilia maintain stem cells in a quiescent state while preserving their capacity to differentiate, as noted earlier [208], [210], [239], [244].

HDAC6 inhibitors are also effective in cancer therapies, as many cancer cells rely on deregulated cilia dynamics for rapid cell division. In cholangiocytes, overexpression of HDAC6 drives increased cell proliferation,

contributing to cystogenesis and tumor progression [258]. Thus, by stabilizing cilia and disrupting the timing of ciliary disassembly needed for mitotic entry, these inhibitors impair cancer cell proliferation. Furthermore, combining HDAC6 or AURA inhibitors with inhibitors of other pathways overactive in cancer cells, such as WNT or GFR (growth factor receptor) signaling [255], can more effectively halt cancer progression and potentially overcome resistance to single-pathway inhibitors.

Altogether, numerous studies underscore the importance of stabilizing cilia not only to address ciliopathies and cancer but also to preserve the regenerative potential of tissues. This highlights the therapeutic promise of HDAC6 and AURA inhibitors, which modulate ciliary dynamics and help restore normal cellular signaling in these conditions. An advantage of HDAC6 inhibitors is they are non-toxic to healthy tissues, and HDAC6-deficient mice do not exhibit any pathological phenotype under normal conditions [116]. However, mutations in HDAC6 lead to an increase in axoneme glycylation [117], suggesting that HDAC6 inhibitors may similarly activate compensatory mechanisms to preserve axoneme stability. HDAC6 is part of a large family, and certain HDAC6-selective inhibitors lack specificity, potentially causing off-target effects. Furthermore, HDACs are involved in various cellular processes, and off-target effects could lead to unexpected adverse phenotypes. Further research is therefore necessary to design more selective and effective HDAC6 inhibitors.

Therapeutical potential in compensatory mechanisms of ciliary modules

Understanding the mechanisms by which ciliary modules regulate cilia dynamics opens new avenues for developing new strategies to restore cilia function in ciliopathies. In BBS, cilia shortening is promoted by increased F-actin polymerization [125], [289] and elevated PIP2 within cilia [289]. Accumulation of PIP2 and F-actin in cilia phenocopies the loss of function INPP5E phenotype in Joubert syndrome [123]. Here, overexpressing INPP5E in olfactory neurons lacking BBSome restored cilia length and rescued odor detection and perception in BBS mice [289]. Another strategy to restore cilia length in BBS could involve suppressing the overactivated ciliary CDC42, thereby reducing excessive intraciliary actin polymerization and preventing ectocytosis to stabilize and elongate cilia [125]. One might potentially aim to target cargo import regulation [97], [144] to reduce the accumulation of GPCRs (SMO, GPR161, etc.) in cilia of BBSome-deficient cells, mitigating ectocytosis and overall cilia destabilization.

Challenges and future directions

Addressing shared mechanisms offers considerable potential for developing therapies applicable across multiple disorders, creating a framework for targeted and tailored treatment strategies. Combining inhibitors of ciliary disassembly, such as HDAC6 or AURA inhibitors, with approaches to modulate the activity of INPP5E, CDC42, or cargo import, could synergistically enhance cilia stabilization. Reducing actin polymerization might, for example, improve the effectiveness of disassembly inhibitors by mitigating another destabilizing force within cilia. By focusing on both structural (axonemal and F-actin dynamics) and functional (cargo trafficking and signaling) aspects of ciliary maintenance, these approaches offer a dual mechanism to restore cilia length and function, particularly in diseases where multiple pathways are disrupted.

Acknowledgements

We acknowledge BioRender.com for the creation of all figures included within this review.

Author contributions

LC and MH conceptualized and wrote the review. SS and OI designed and prepared the figures and table. All authors read and approved the final manuscript.

Funding

LC and MH acknowledge support from the Czech Science Foundation (grant 21–21612 S).

Data availability

Not applicable.

Declarations

Ethics approval and consent to participate

Not applicable.

Consent for publication

Not applicable.

Competing Interests.

The authors declare that they have no competing interests.

Received: 9 January 2025 / Accepted: 28 April 2025

Published online: 07 June 2025

References

- Beales P, Jackson PK. Cilia - the prodigal organelle. *Cilia*. 2012;1:1–3.
- Sorokin SP. Reconstructions of centriole formation and ciliogenesis in mammalian lungs. *J Cell Sci*. 1968;3:207–30.
- Gopalakrishnan J, et al. Emerging principles of primary cilia dynamics in controlling tissue organization and function. *EMBO J*. 2023;42:e113891.
- Bangs F, Anderson KV. Primary cilia and mammalian Hedgehog signaling. *Cold Spring Harb Perspect Biol*. 2017. <https://doi.org/10.1101/cshperspect.a028175>
- Mill P, Christensen ST, Pedersen LB. Primary cilia as dynamic and diverse signalling hubs in development and disease. *Nat Rev Genet*. 2023;24:421–41.
- Braun DA, Hildebrandt F. Ciliopathies. *Cold Spring Harb Perspect Biol*. 2017. <https://doi.org/10.1101/cshperspect.a028191>
- Mitchison HM, Valente EM. Motile and non-motile cilia in human pathology: from function to phenotypes. *J Pathol*. 2017;241:294–309.
- Reiter JF, Leroux MR. Genes and molecular pathways underpinning ciliopathies. *Nat Rev Mol Cell Biol*. 2017. <https://doi.org/10.1038/nrm.2017.60>
- Seeley ES, Nachury MV. The perennial organelle: assembly and disassembly of the primary cilium. *J Cell Sci*. 2010;123:511–8.
- Bornens M, Gonczy P. Centrosomes back in the limelight. *Philos Trans R Soc Lond B Biol Sci*. 2014. <https://doi.org/10.1098/rstb.2013.0452>
- Nigg EA, Holland AJ. Once and only once: mechanisms of centriole duplication and their deregulation in disease. *Nat Rev Mol Cell Biol*. 2018;19:297–312.
- Ishikawa H, Kubo A, Tsukita S. Odf2-deficient mother centrioles lack distal/subdistal appendages and the ability to generate primary cilia. *Nat Cell Biol*. 2005;7:517–24.
- Balestra FR, Strnad P, Fluckiger I, Gonczy P. Discovering regulators of centriole biogenesis through siRNA-based functional genomics in human cells. *Dev Cell*. 2013;25:555–71.
- Bowler M, et al. High-resolution characterization of centriole distal appendage morphology and dynamics by correlative STORM and electron microscopy. *Nat Commun*. 2019;10:993.
- Tanos BE, et al. Centriole distal appendages promote membrane docking, leading to cilia initiation. *Genes Dev*. 2013;27:163–8.
- Chang T-JB, Hsu JC-C, Yang TT. Single-molecule localization microscopy reveals the ultrastructural constitution of distal appendages in expanded mammalian centrioles. *Nat Commun*. 2023;14:1688.
- Yang TT, et al. Super-resolution architecture of mammalian centriole distal appendages reveals distinct blade and matrix functional components. *Nat Commun*. 2018;9:2023.
- Wei Q, et al. Transition fibre protein FBF1 is required for the ciliary entry of assembled intraflagellar transport complexes. *Nat Commun*. 2013;4:2750.
- Airik R, Airik M, Schueler M, Bates CM, Hildebrandt F. Roscovitine blocks collecting duct cyst growth in Cep164-deficient kidneys. *Kidney Int*. 2019;96:320–6.
- Ma D, Wang F, Teng J, Huang N, Chen J. Structure and function of distal and subdistal appendages of the mother centriole. *J Cell Sci*. 2023;136:jcs260560.
- Mazo G, Soplop N, Wang WJ, Uryu K, Tsou MB. Spatial control of primary ciliogenesis by subdistal appendages alters Sensation-Associated properties of cilia. *Dev Cell*. 2016. <https://doi.org/10.1016/j.devcel.2016.10.006>
- Chong WM, et al. Super-resolution microscopy reveals coupling between mammalian centriole subdistal appendages and distal appendages. *eLife*. 2020;9:e53580.
- Brooks ER, Wallingford JB. Multiciliated cells. *Curr Biol CB*. 2014;24:R973–982.
- Gilula NB, Satir P. The ciliary necklace. A ciliary membrane specialization. *J Cell Biol*. 1972;53:494–509.
- Garcia-Gonzalo FR, Reiter JF. Open Sesame: how transition fibers and the transition zone control ciliary composition. *Cold Spring Harb Perspect Biol*. 2017;9:a028134.
- Mercey O, Mukherjee S, Guichard P, Hamel V. The molecular architecture of the ciliary transition zones. *Curr Opin Cell Biol*. 2024;88:102361.
- Yang T. Superresolution pattern recognition reveals the architectural map of the ciliary transition zone. *Sci Rep*. 2015;5:14096.
- Shi X, et al. Super-resolution microscopy reveals that disruption of ciliary transition-zone architecture causes Joubert syndrome. *Nat Cell Biol*. 2017;19:1178–88.
- Nachury MV, Mick DU. Establishing and regulating the composition of cilia for signal transduction. *Nat Rev Mol Cell Biol*. 2019;20:389–405.
- Gupta GD, et al. A dynamic protein interaction landscape of the human centrosome-cilium interface. *Cell*. 2015;163:1484–99.
- Diener DR, Lupetti P, Rosenbaum JL. Proteomic analysis of isolated ciliary transition zones reveals the presence of ESCRT proteins. *Curr Biol CB*. 2015;25:379–84.
- Sang L, et al. Mapping the NPHP-JBTS-MKS protein network reveals ciliopathy disease genes and pathways. *Cell*. 2011;145:513–28.
- Wiegand A, et al. Cell type-specific regulation of ciliary transition zone assembly in vertebrates. *EMBO J*. 2018;37:e97791.
- Jenkins PM, McEwen DP, Martens JR. Olfactory cilia: linking sensory cilia function and human disease. *Chem Senses*. 2009;34:451–64.
- Cho JH, et al. Islet primary cilia motility controls insulin secretion. *Sci Adv*. 2022;8:eabq8486.
- Sun S, Fisher RL, Bowser SS, Pentecost BT, Sui H. Three-dimensional architecture of epithelial primary cilia. *Proc Natl Acad Sci U S A*. 2019;116:9370–9379.
- Kiesel P, et al. The molecular structure of mammalian primary cilia revealed by cryo-electron tomography. *Nat Struct Mol Biol*. 2020;27:1115–24.

38. Sorokin S. Centrioles and the formation of rudimentary cilia by fibroblasts and smooth muscle cells. *J Cell Biol.* 1962;15:363–77.
39. Molla-Herman A, et al. The ciliary pocket: an endocytic membrane domain at the base of primary and motile cilia. *J Cell Sci.* 2010;123:1785–95.
40. Garcia G, Raleigh DR, Reiter JF. How the ciliary membrane is organized Inside-Out to communicate Outside-In. *Curr Biol.* 2018;28:R421–34.
41. Conduit SE, Davies EM, Fulcher AJ, Oorschot V, Mitchell CA. Superresolution microscopy reveals distinct phosphoinositide subdomains within the cilia transition zone. *Front Cell Dev Biol.* 2021;9:634649.
42. Garcia-Gonzalo FR, et al. Phosphoinositides regulate ciliary protein trafficking to modulate Hedgehog signaling. *Dev Cell.* 2015;34:400–9.
43. Conduit SE, Vanhaesebroeck B. Phosphoinositide lipids in primary cilia biology. *Biochem J.* 2020;477:3541–65.
44. Hilgendorf KJ, Myers BR, Reiter JF. Emerging mechanistic understanding of cilia function in cellular signalling. *Nat Rev Mol Cell Biol.* 2024;25:555–73.
45. Delling M, DeCaen PG, Doerner JF, Febvay S, Clapham DE. Primary cilia are specialized calcium signaling organelles. *Nature.* 2013;504:311–4.
46. Paolucci E, Zaccolo M. Compartmentalised cAMP signalling in the primary cilium. *Front Physiol.* 2023. <https://doi.org/10.3389/fphys.2023.1187134>
47. Nachury MV. How do cilia organize signalling cascades? *Philos Trans R Soc B Biol Sci.* 2014;369:20130465.
48. Binó L, et al. A protocol for generation and live-cell imaging analysis of primary cilia reporter cell lines. *STAR Protoc.* 2022;3:101199.
49. Tucker RW, Pardee AB, Fujiwara K. Centriole ciliation is related to quiescence and DNA synthesis in 3T3 cells. *Cell.* 1979;17:527–35.
50. Izawa I, Goto H, Kasahara K, Inagaki M. Current topics of functional links between primary cilia and cell cycle. *Cilia.* 2015. <https://doi.org/10.1186/s13630-015-0021-1>
51. Ford MJ, et al. A cell/cilia cycle biosensor for single-cell kinetics reveals persistence of cilia after G1/S transition is a general property in cells and mice. *Dev Cell.* 2018;47:509–e5235.
52. Bangs FK, Schrodde N, Hadjantonakis A-K, Anderson K. V. Lineage specificity of primary cilia in the mouse embryo. *Nat Cell Biol.* 2015;17:113–22.
53. Sotelo JR, Trujillo-Cenóz, O. Electron microscope study on the development of ciliary components of the neural epithelium of the chick embryo. *Z Für Zellforsch Mikrosk Anat.* 1958;49:1–12.
54. Kumar D, Reiter J. How the centriole builds its cilium: of mothers, daughters, and the acquisition of appendages. *Curr Opin Struct Biol.* 2021;66:41–8.
55. Wang L, Dynlacht BD. The regulation of cilium assembly and disassembly in development and disease. *Development.* 2018. <https://doi.org/10.1242/dev.151407>
56. Labat-de-Hoz L, et al. A model for primary cilium biogenesis by polarized epithelial cells: role of the midbody remnant and associated specialized membranes. *Front Cell Dev Biol.* 2020;8:622918.
57. Wu C-T, Chen H-Y, Tang TK. Myosin-Va is required for preciliary vesicle transportation to the mother centriole during ciliogenesis. *Nat Cell Biol.* 2018;20:175–85.
58. Lu Q, et al. Early steps in primary cilium assembly require EHD1/EHD3-dependent ciliary vesicle formation. *Nat Cell Biol.* 2015. <https://doi.org/10.1038/ncb3109>
59. Ganga AK, et al. Rab34 GTPase mediates ciliary membrane formation in the intracellular ciliogenesis pathway. *Curr Biol.* 2021;31:2895–e29057.
60. Stuck MW, Chong WM, Liao J-C, Pazour GJ. Rab34 is necessary for early stages of intracellular ciliogenesis. *Curr Biol CB.* 2021;31:2887–e28944.
61. Yoshimura S-I, Egerer J, Fuchs E, Haas AK, Barr FA. Functional dissection of Rab GTPases involved in primary cilium formation. *J Cell Biol.* 2007;178:363–9.
62. Westlake CJ, et al. Primary cilia membrane assembly is initiated by Rab11 and transport protein particle II (TRAPP II) complex-dependent trafficking of Rabin8 to the centrosome. *Proc Natl Acad Sci U S A.* 2011;108:2759–64.
63. Knödler A, et al. Coordination of Rab8 and Rab11 in primary ciliogenesis. *Proc Natl Acad Sci U S A.* 2010;107:6346–51.
64. Nachury MV, et al. A core complex of BBS proteins cooperates with the GTPase Rab8 to promote ciliary membrane biogenesis. *Cell.* 2007;129:1201–13.
65. Shkya S, Westlake CJ. Recent advances in understanding assembly of the primary cilium membrane. *Fac Rev.* 2021;10:16.
66. Schmidt KN, et al. Cep164 mediates vesicular docking to the mother centriole during early steps of ciliogenesis. *J Cell Biol.* 2012;199:1083–101.
67. Siller SS, et al. Conditional knockout mice for the distal appendage protein CEP164 reveal its essential roles in airway multiciliated cell differentiation. *PLOS Genet.* 2017;13:e1007128.
68. Joo K, et al. CCDC41 is required for ciliary vesicle docking to the mother centriole. *Proc Natl Acad Sci U S A.* 2013;110:5987–92.
69. Sillibourne JE, et al. Primary ciliogenesis requires the distal appendage component Cep123. *Biol Open.* 2013;2:535–45.
70. Kurtulmus B, et al. LRRC45 contributes to early steps of axoneme extension. *J Cell Sci.* 2018;131:jcs223594.
71. Kanie T, et al. A hierarchical pathway for assembly of the distal appendages that organize primary cilia. *eLife.* 2025;14:e85999.
72. Goetz SC, Liem KF Jr., Anderson K. V. The spinocerebellar ataxia-associated gene Tau tubulin kinase 2 controls the initiation of ciliogenesis. *Cell.* 2012;151:847–58.
73. Cajanek L, Nigg EA. Cep164 triggers ciliogenesis by recruiting Tau tubulin kinase 2 to the mother centriole. *Proc Natl Acad Sci U S A.* 2014;111:E2841–50.
74. Rosa E, Silva I, et al. Molecular mechanisms underlying the role of the centriolar CEP164-TTBK2 complex in ciliopathies. *Struct Lond Engl* 1993. 2022;30:114–e1289.
75. Lo C-H, et al. Phosphorylation of CEP83 by TTBK2 is necessary for cilia initiation. *J Cell Biol.* 2019;218:3489–505.
76. Bernatik O, et al. Phosphorylation of multiple proteins involved in ciliogenesis by Tau tubulin kinase 2. *Mol Biol Cell.* 2020;31:1032–46.
77. Spektor A, Tsang WY, Khoo D, Dynlacht BD. Cep97 and CP110 suppress a cilia assembly program. *Cell.* 2007;130:678–90.
78. Kobayashi T, Tsang WY, Li J, Lane W, Dynlacht B. D. Centriolar Kinesin Kif24 interacts with CP110 to remodel microtubules and regulate ciliogenesis. *Cell.* 2011;145:914–25.
79. Benk Vysloužil D, et al. Tau-tubulin kinase 2 restrains microtubule-depolymerizer KIF2A to support primary cilia growth. *Cell Commun Signal.* 2025;23:73.
80. Oda T, Chiba S, Nagai T, Mizuno K. Binding to Cep164, but not EB1, is essential for centriolar localization of TTBK2 and its function in ciliogenesis. *Genes Cells.* 2014;19:927–40.
81. Huang N, et al. M-Phase phosphoprotein 9 regulates ciliogenesis by modulating CP110-CEP97 complex localization at the mother centriole. *Nat Commun.* 2018;9:4511.
82. Schmidt TJ, et al. Control of centriole length by CPAP and CP110. *Curr Biol CB.* 2009;19:1005–11.
83. Prosser SL, Morrison CG. Centrin2 regulates CP110 removal in primary cilium formation. *J Cell Biol.* 2015;208:693–701.
84. Dobbelaere J, Schmidt Cernohorska M, Huranova M, Slade D, Dammermann A. Cep97 is required for centriole structural integrity and cilia formation in *Drosophila*. *Curr Biol CB.* 2020;30:3045–e30567.
85. Yadav SP, et al. Centrosomal protein CP110 controls maturation of the mother centriole during cilia biogenesis. *Dev Camb Engl.* 2016;143:1491–501.
86. Walentek P et al. Ciliary transcription factors and miRNAs precisely regulate Cp110 levels required for ciliary adhesions and ciliogenesis. *eLife* 2016;5:e17557.
87. Pedersen LB, Rosenbaum JL. Intraflagellar transport (IFT) role in ciliary assembly, resorption and signalling. *Curr Top Dev Biol.* 2008;85:23–61.
88. Kozminski KG, Johnson KA, Forscher P, Rosenbaum JL. A motility in the eukaryotic flagellum unrelated to flagellar beating. *Proc Natl Acad Sci U S A.* 1993;90:5519–23.
89. Bhogaraju S, et al. Molecular basis of tubulin transport within the cilium by IFT4 and IFT81. *Science.* 2013;341:1009–12.
90. Lehtreck K. Cargo adapters expand the transport range of intraflagellar transport. *J Cell Sci.* 2022;135:jcs260408.
91. Pigino G. Intraflagellar transport. *Curr Biol CB.* 2021;31:R530–6.
92. Stepanek L, Pigino G. Microtubule doublets are double-track railways for intraflagellar transport trains. *Science.* 2016;352:721–4.
93. Yang TT, et al. Superresolution pattern recognition reveals the architectural map of the ciliary transition zone. *Sci Rep.* 2015;5:14096.
94. Yang TT, Tran MNT, Chong WM, Huang C-E, Liao J-C. Single-particle tracking localization microscopy reveals nonaxonemal dynamics of intraflagellar transport proteins at the base of mammalian primary cilia. *Mol Biol Cell.* 2019;30:828–37.
95. van den Hoek H, et al. In situ architecture of the ciliary base reveals the stepwise assembly of intraflagellar transport trains. *Science.* 2022;377:543–8.
96. Van De Craft J, Harris JA, Kubo T, Witman GB, Lehtreck KF. Diffusion rather than intraflagellar transport likely provides most of the tubulin required for axonemal assembly in *Chlamydomonas*. *J Cell Sci.* 2020;133:jcs249805.
97. Mukhopadhyay S, et al. TULP3 bridges the IFT-A complex and membrane phosphoinositides to promote trafficking of G protein-coupled receptors into primary cilia. *Genes Dev.* 2010;24:2180–93.

98. Nachury MV. The molecular machines that traffic signaling receptors into and out of cilia. *Curr Opin Cell Biol*. 2018;51:124–31.
99. Han S, et al. TULP3 is required for localization of membrane-associated proteins ARL13B and INPP5E to primary cilia. *Biochem Biophys Res Commun*. 2019;509:227–34.
100. Ansley SJ, et al. Basal body dysfunction is a likely cause of pleiotropic Bardet-Biedl syndrome. *Nature*. 2003;425:628–33.
101. Niederlova V, Modrak M, Tsyklauri O, Huranova M, Stepanek O. Meta-analysis of genotype-phenotype associations in Bardet-Biedl syndrome uncovers differences among causative genes. *Hum Mutat*. 2019;40:2068–87.
102. Prasai A, et al. The BBSome assembly is spatially controlled by BBS1 and BBS4 in human cells. *J Biol Chem*. 2020;295:14279–90.
103. Zhang Q, Yu D, Seo S, Stone EM, Sheffield VC. Intrinsic protein-Protein Interaction-mediated and Chaperonin-assisted sequential assembly of stable Bardet-Biedl syndrome protein complex, the BBSome. *J Biol Chem*. 2012;287:20625–35.
104. Blacque OE, et al. Loss of *C. elegans* BBS-7 and BBS-8 protein function results in cilia defects and compromised intraflagellar transport. *Genes Dev*. 2004;18:1630–42.
105. Ye F, Nager AR, Nachury MV. BBSome trains remove activated GPCRs from cilia by enabling passage through the transition zone. *J Cell Biol*. 2018;217:1847–68.
106. Yan H, et al. TALPID3 and ANKRD26 selectively orchestrate FBF1 localization and cilia gating. *Nat Commun*. 2020;11:2196.
107. Nigg EA, Stearns T. The centrosome cycle: centriole biogenesis, duplication and inherent asymmetries. *Nat Cell Biol*. 2011;13:1154–60.
108. Mirvis M, Siemers KA, Nelson WJ, Stearns TP. Primary cilium loss in mammalian cells occurs predominantly by whole-cilium shedding. *PLOS Biol*. 2019;17:e3000381.
109. Rieder CL, Jensen CG, Jensen LCW. The resorption of primary cilia during mitosis in a vertebrate (PtK1) cell line. *J Ultrastruct Res*. 1979;68:173–85.
110. Liang Y, Meng D, Zhu B, Pan J. Mechanism of ciliary disassembly. *Cell Mol Life Sci*. 2016;73:1787–802.
111. Quarumby LM. Cellular deflagellation. *Int Rev Cytol*. 2004;233:47–91.
112. Toro-Tapia G, Das RM. Primary cilium remodeling mediates a cell signaling switch in differentiating neurons. *Sci Adv*. 2020;6:eabb0601.
113. Pugacheva EN, Jablonski SA, Hartman TR, Henske EP, Golemis E. A. HEF1-dependent Aurora A activation induces disassembly of the primary cilium. *Cell*. 2007;129:1351–63.
114. Pan J, Wang Q, Snell WJ. An aurora kinase is essential for flagellar disassembly in *Chlamydomonas*. *Dev Cell*. 2004;6:445–51.
115. Kobayashi T, et al. HDAC2 promotes loss of primary cilia in pancreatic ductal adenocarcinoma. *EMBO Rep*. 2017;18:334–43.
116. Zhang Y, et al. Mice lacking histone deacetylase 6 have hyperacetylated tubulin but are viable and develop normally. *Mol Cell Biol*. 2008;28:1688–701.
117. Łysyganicz PK, et al. Loss of deacetylation enzymes Hdac6 and Sirt2 promotes acetylation of cytoplasmic tubulin, but suppresses axonemal acetylation in zebrafish cilia. *Front Cell Dev Biol*. 2021;9:676214.
118. McKenna ED, Sarbanes SL, Cummings SW, Roll-Mecak A. The tubulin code, from molecules to health and disease. *Annu Rev Cell Dev Biol*. 2023;39:331–61.
119. Reilly ML, Benmerah A. Ciliary kinesins beyond IFT: cilium length, disassembly, cargo transport and signaling. *Biol Cell*. 2019. <https://doi.org/10.1111/boc.201800074>
120. Miyamoto T, et al. The Microtubule-Depolymerizing activity of a mitotic Kinesin protein KIF2A drives primary cilia disassembly coupled with cell proliferation. *Cell Rep*. 2015. <https://doi.org/10.1016/j.celrep.2015.01.003>
121. Watanabe T, et al. TTBK2 with EB1/3 regulates microtubule dynamics in migrating cells through KIF2A phosphorylation. *J Cell Biol*. 2015;210:737–51.
122. Kim S, Lee K, Choi J-H, Ringstad N, Dynlacht BD. Nek2 activation of Kif24 ensures cilium disassembly during the cell cycle. *Nat Commun*. 2015;6:8087.
123. Phua SC, et al. Dynamic remodeling of membrane composition drives cell cycle through primary cilia excision. *Cell*. 2017;168:264–e27915.
124. Nager AR, et al. An actin network dispatches ciliary GPCRs into extracellular vesicles to modulate signaling. *Cell*. 2017;168:252–e26314.
125. Prasai A, et al. BBSome-deficient cells activate intraciliary CDC42 to trigger actin-dependent ciliary ectocytosis. *EMBO Rep*. 2024. <https://doi.org/10.1038/s44319-024-00326-z>
126. Stilling S, Kalliakoudas T, Benninghoven-Frey H, Inoue T, Falkenburger BH. PIP2 determines length and stability of primary cilia by balancing membrane turnovers. *Commun Biol*. 2022;5:93.
127. Patnaik SR, et al. Bardet-Biedl syndrome proteins regulate cilia disassembly during tissue maturation. *Cell Mol Life Sci CMLS*. 2019;76:757–75.
128. Inoko A, et al. Trichoplein and Aurora A block aberrant primary cilia assembly in proliferating cells. *J Cell Biol*. 2012;197:391–405.
129. Huang M, et al. Cell cycle arrest induced by trichoplein depletion is independent of cilia assembly. *J Cell Physiol*. 2022;237:2703–12.
130. Bryja V, Cervenka I, Cajanek L. The connections of Wnt pathway components with cell cycle and centrosome: side effects or a hidden logic? *Crit Rev Biochem Mol Biol*. 2017;52:614–37.
131. Fry AM, O'Regan L, Sabir SR, Bayliss R. Cell cycle regulation by the NEK family of protein kinases. *J Cell Sci*. 2012;125:4423–33.
132. Wang W, Wu T, Kirschner MW. The master cell cycle regulator APC-Cdc20 regulates ciliary length and disassembly of the primary cilium. *eLife*. 2014;3:e03083.
133. Viol L et al. Nek2 kinase displaces distal appendages from the mother centriole prior to mitosis. *J Cell Biol*. 2020. <https://doi.org/10.1083/jcb.201907136>
134. Kong D, et al. Centriole maturation requires regulated Plk1 activity during two consecutive cell cycles. *J Cell Biol*. 2014;206:855–65.
135. Bukanov NO, Smith LA, Klingner KW, Ledbetter SR. Ibraghimov-Beskrovnaya, O. Long-lasting arrest of murine polycystic kidney disease with CDK inhibitor roscovitine. *Nature*. 2006;444:949–52.
136. Chebib FT, Sussman CR, Wang X, Harris PC, Torres VE. Vasopressin and disruption of calcium signalling in polycystic kidney disease. *Nat Rev Nephrol*. 2015;11:451–64.
137. Tran PV, et al. THM1 negatively modulates mouse Sonic Hedgehog signal transduction and affects retrograde intraflagellar transport in cilia. *Nat Genet*. 2008;40:403–10.
138. Tran PV, et al. Downregulating Hedgehog signaling reduces renal cystogenic potential of mouse models. *J Am Soc Nephrol JASN*. 2014;25:2201–12.
139. Ou G, Scholey JM. Motor Cooperation during mitosis and ciliogenesis. *Annu Rev Cell Dev Biol*. 2022;38:49–74.
140. Hirokawa N, Noda Y, Tanaka Y, Niwa S. Kinesin superfamily motor proteins and intracellular transport. *Nat Rev Mol Cell Biol*. 2009;10:682–96.
141. Haraguchi K, Hayashi T, Jimbo T, Yamamoto T, Akiyama T. Role of the Kinesin-2 family protein, KIF3, during mitosis. *J Biol Chem*. 2006;281:4094–9.
142. Gruneberg U, et al. KIF14 and Citron kinase act together to promote efficient cytokinesis. *J Cell Biol*. 2006;172:363–72.
143. Carleton M, et al. RNA interference-mediated Silencing of mitotic Kinesin KIF14 disrupts cell cycle progression and induces cytokinesis failure. *Mol Cell Biol*. 2006;26:3853–63.
144. Pejškova P et al. KIF14 controls ciliogenesis via regulation of Aurora A and is important for Hedgehog signaling. *J Cell Biol*. 2020. <https://doi.org/10.1083/jcb.201904107>
145. Mikulenkova E et al. Kinesin-3 KIF14 Regulates Intraflagellar Transport Dynamics in Primary Cilia. 2025;644298 Preprint at <https://doi.org/10.1101/2025.03.20.644298> (2025).
146. Delaval B, Bright A, Lawson ND, Doxsey S. The cilia protein IFT88 is required for spindle orientation in mitosis. *Nat Cell Biol*. 2011;13:461–8.
147. Taulet N, et al. IFT proteins spatially control the geometry of cleavage furrow ingression and lumen positioning. *Nat Commun*. 2017;8:1928.
148. Vitre B, et al. IFT proteins interact with HSET to promote supernumerary centrosome clustering in mitosis. *EMBO Rep*. 2020;21:e49234.
149. Wood CR, et al. IFT proteins accumulate during cell division and localize to the cleavage furrow in *Chlamydomonas*. *PLoS ONE*. 2012;7:e30729.
150. Vuong LT, et al. Kinesin-2 and IFT-A act as a complex promoting nuclear localization of β -catenin during Wnt signalling. *Nat Commun*. 2018;9:5304.
151. Balmer S, et al. Components of intraflagellar transport complex A function independently of the cilium to regulate canonical Wnt signaling in *Drosophila*. *Dev Cell*. 2015;34:705–18.
152. Kim JC, et al. The Bardet-Biedl protein BBS4 targets cargo to the pericentriolar region and is required for microtubule anchoring and cell cycle progression. *Nat Genet*. 2004;36:462–70.
153. Kim JC, et al. MKKS/BBS6, a divergent chaperonin-like protein linked to the obesity disorder Bardet-Biedl syndrome, is a novel centrosomal component required for cytokinesis. *J Cell Sci*. 2005;118:1007–20.
154. Wang W-J, et al. CEP162 is an axoneme-recognition protein promoting ciliary transition zone assembly at the cilia base. *Nat Cell Biol*. 2013;15:591–601.
155. Leon A, Omri B, Gely A, Klein C, Crisanti P. QN1/KIAA1009: a new essential protein for chromosome segregation and mitotic spindle assembly. *Oncogene*. 2006;25:1887–95.
156. Lovera M, Lüders J. The ciliary impact of nonciliary gene mutations. *Trends Cell Biol*. 2021;31:876–87.

157. Wieser S, Pines J. The biochemistry of mitosis. *Cold Spring Harb Perspect Biol*. 2015. <https://doi.org/10.1101/cshperspect.a015776>
158. Pichaud F, Walther RF, Nunes de Almeida F. Regulation of Cdc42 and its effectors in epithelial morphogenesis. *J Cell Sci*. 2019. <https://doi.org/10.1242/jcs.217869>
159. Hehnly H, Chen C-T, Powers CM, Liu H-L, Dossy S. The centrosome regulates the Rab11-dependent recycling endosome pathway at appendages of the mother centriole. *Curr Biol*. 2012;22:1944–50.
160. Ang AL, et al. Recycling endosomes can serve as intermediates during transport from the golgi to the plasma membrane of MDCK cells. *J Cell Biol*. 2004;167:531–43.
161. Jin H, et al. The conserved Bardet-Biedl syndrome proteins assemble a coat that traffics membrane proteins to cilia. *Cell*. 2010;141:1208–19.
162. Guo D-F, et al. The BBSome in POMC and AgRP neurons is necessary for body weight regulation and sorting of metabolic receptors. *Diabetes*. 2019;68:1591–603.
163. Leitch CC, Lodh S, Prieto-Echagüe V, Badano JL, Zaghloul, N. A. Basal body proteins regulate Notch signaling through endosomal trafficking. *J Cell Sci*. 2014;127:2407–19.
164. Cantagrel V, et al. Mutations in the cilia gene ARL13B lead to the classical form of Joubert syndrome. *Am J Hum Genet*. 2008;83:170–9.
165. Caspary T, Larkins CE, Anderson KV. The graded response to Sonic Hedgehog depends on cilia architecture. *Dev Cell*. 2007;12:767–78.
166. Larkins CE, Aviles GDG, East MP, Kahn RA, Caspary T. ARL13b regulates ciliogenesis and the dynamic localization of Shh signaling proteins. *Mol Biol Cell*. 2011;22:4694–703.
167. Humbert MC, et al. ARL13B, PDE6D, and CEP164 form a functional network for INPP5E ciliary targeting. *Proc Natl Acad Sci U S A*. 2012;109:19691–6.
168. Gigante ED, Taylor MR, Ivanova AA, Kahn RA, Caspary T. ARL13B regulates Sonic Hedgehog signaling from outside primary cilia. *eLife*. 2020. <https://doi.org/10.7554/eLife.50434>
169. Ferent J, et al. The ciliary protein ARL13b functions outside of the primary cilium in Shh-mediated axon guidance. *Cell Rep*. 2019;29:3356–e33663.
170. Serwas D, Su TY, Roessler M, Wang S, Dammermann A. Centrioles initiate cilia assembly but are dispensable for maturation and maintenance in *C. elegans*. *J Cell Biol*. 2017;216:1659–71.
171. Bowie E, Norris R, Anderson KV, Goetz SC. Spinocerebellar ataxia type 11-associated alleles of Ttbk2 dominantly interfere with ciliogenesis and cilium stability. *PLoS Genet*. 2018;14:e1007844.
172. Nguyen A, Goetz SC. TTBK2 controls cilium stability by regulating distinct modules of centrosomal proteins. *Mol Biol Cell*. 2023;34:ar8.
173. Engelke MF, et al. Acute inhibition of heterotrimeric Kinesin-2 function reveals mechanisms of intraflagellar transport in mammalian cilia. *Curr Biol*. 2019;29:1137–e11484.
174. Ye F, et al. Single molecule imaging reveals a major role for diffusion in the exploration of ciliary space by signaling receptors. *eLife*. 2013;2:e00654.
175. Jensen VL, et al. Role for intraflagellar transport in building a functional transition zone. *EMBO Rep*. 2018;19:e45862.
176. Vuolo L, Stevenson NL, Heesom KJ, Stephens DJ. Dynein-2 intermediate chains play crucial but distinct roles in primary cilia formation and function. *eLife*. 2018;7:e39655.
177. Absalon S, et al. Intraflagellar transport and functional analysis of genes required for flagellum formation in trypanosomes. *Mol Biol Cell*. 2008;19:929–44.
178. Scheidel N, Blaque OE. Intraflagellar transport complex A genes differentially regulate cilium formation and transition zone gating. *Curr Biol CB*. 2018;28:3279–e32872.
179. De-Castro ARG, et al. WDR60-mediated dynein-2 loading into cilia powers retrograde IFT and transition zone crossing. *J Cell Biol*. 2021;221:e202010178.
180. Bujakowska KM, et al. Mutations in IFT172 cause isolated retinal degeneration and Bardet-Biedl syndrome. *Hum Mol Genet*. 2015;24:230–42.
181. Janke C, Magiera MM. The tubulin code and its role in controlling microtubule properties and functions. *Nat Rev Mol Cell Biol*. 2020;21:307–26.
182. Verhey KJ, Gaertig J. The tubulin code. *Cell Cycle*. 2007;6:2152–60.
183. Sirajuddin M, Rice LM, Vale RD. Regulation of microtubule motors by tubulin isotypes and post-translational modifications. *Nat Cell Biol*. 2014;16:335–44.
184. Viar GA, Pigino G. Tubulin posttranslational modifications through the lens of new technologies. *Curr Opin Cell Biol*. 2024;88:102362.
185. Gadadhar S, et al. Tubulin glycylation controls axonemal dynein activity, flagellar beat, and male fertility. *Science*. 2021;371:eabd4914.
186. Suryavanshi S, et al. Tubulin glutamylation regulates ciliary motility by altering inner dynein arm activity. *Curr Biol CB*. 2010;20:435–40.
187. O'Hagan R, et al. Glutamylation regulates transport, specializes function, and sculpts the structure of cilia. *Curr Biol*. 2017;27:3430–e34416.
188. Hong S-R, et al. Spatiotemporal manipulation of ciliary glutamylation reveals its roles in intraciliary trafficking and Hedgehog signaling. *Nat Commun*. 2018;9:1732.
189. Kalebic N, et al. α TAT1 is the major α -tubulin acetyltransferase in mice. *Nat Commun*. 2013;4:1962.
190. Verhey KJ, Ohi R. Causes, costs and consequences of kinesin motors communicating through the microtubule lattice. *J Cell Sci*. 2023;136:jcs260735.
191. Mao S, et al. Motile cilia of human airway epithelia contain Hedgehog signaling components that mediate noncanonical Hedgehog signaling. *Proc Natl Acad Sci U S A*. 2018;115:1370–5.
192. Seidl C, et al. Mucociliary Wnt signaling promotes cilia biogenesis and beating. *Nat Commun*. 2023;14:1259.
193. Nonami Y, Narita K, Nakamura H, Inoue T, Takeda S. Developmental changes in ciliary motility on choroid plexus epithelial cells during the perinatal period. *Cytoskeleton*. 2013;70:797–803.
194. Ott CM, et al. Permanent Deconstruction of intracellular primary cilia in differentiating granule cell neurons. *J Cell Biol*. 2024;223:e202404038.
195. Rozycki M, et al. The fate of the primary cilium during myofibroblast transition. *Mol Biol Cell*. 2014;25:643–57.
196. Müller A, et al. Structure, interaction and nervous connectivity of beta cell primary cilia. *Nat Commun*. 2024;15:9168.
197. Ingham PW. Hedgehog signaling. *Curr Top Dev Biol*. 2022;149:1–58.
198. Hall ET, et al. Cytoneme signaling provides essential contributions to mammalian tissue patterning. *Cell*. 2024;187:276–e29323.
199. Mukhopadhyay S, et al. The ciliary G-protein-coupled receptor Gpr161 negatively regulates the Sonic Hedgehog pathway via cAMP signaling. *Cell*. 2013;152:210–23.
200. Truong ME, et al. Vertebrate cells differentially interpret ciliary and extraciliary cAMP. *Cell*. 2021;184:2911–e292618.
201. Hwang S-H, Somatilaka BN, White K, Mukhopadhyay S. Ciliary and extraciliary Gpr161 pools repress Hedgehog signaling in a tissue-specific manner. *eLife*. 2021. <https://doi.org/10.7554/eLife.67121>
202. May EA, et al. Time-resolved proteomics profiling of the ciliary Hedgehog response. *J Cell Biol*. 2021;220:e202007207.
203. Pal K, et al. Smoothened determines β -arrestin-mediated removal of the G protein-coupled receptor Gpr161 from the primary cilium. *J Cell Biol*. 2016;212:861–75.
204. Yue S, et al. Requirement of Smurf-mediated endocytosis of Patched1 in Sonic Hedgehog signal reception. *eLife*. 2014;3:e02555.
205. Ansari SS, et al. Sonic Hedgehog activates prostaglandin signaling to stabilize primary cilium length. *J Cell Biol*. 2024;223:e202306002.
206. Ho EK, Tsai AE, Stearns T. Transient primary cilia mediate robust Hedgehog Pathway-Dependent cell cycle control. *Curr Biol CB*. 2020;30:2829–e28355.
207. Min M, Rong Y, Tian C, Spencer SL. Temporal integration of mitogen history in mother cells controls proliferation of daughter cells. *Science*. 2020;368:1261–5.
208. Fu W, Asp P, Canter B, Dynlacht B D. Primary cilia control Hedgehog signaling during muscle differentiation and are deregulated in rhabdomyosarcoma. *Proc Natl Acad Sci U S A*. 2014;111:9151–6.
209. Straface G, et al. Sonic Hedgehog regulates angiogenesis and myogenesis during post-natal skeletal muscle regeneration. *J Cell Mol Med*. 2009;13:2424–35.
210. Palla AR, et al. Primary cilia on muscle stem cells are critical to maintain regenerative capacity and are lost during aging. *Nat Commun*. 2022;13:1439.
211. Kopinke D, Roberson EC, Reiter JF. Ciliary Hedgehog signaling restricts Injury-Induced adipogenesis. *Cell*. 2017;170:340–e35112.
212. Cruz C, et al. Foxj1 regulates floor plate cilia architecture and modifies the response of cells to Sonic Hedgehog signalling. *Dev Camb Engl*. 2010;137:4271–82.
213. Hagenlocher C, Walentek P, Ller M, Thumberger C, T., Feistel K. Ciliogenesis and cerebrospinal fluid flow in the developing *Xenopus* brain are regulated by foxj1. *Cilia* 2013;2:12.
214. Das RM, Storey KG. Apical abscission alters cell polarity and dismantles the primary cilium during neurogenesis. *Science*. 2014;343:200–4.
215. Zhang Q, Seo S, Bugge K, Stone EM, Sheffield V. C. BBS proteins interact genetically with the IFT pathway to influence SHH-related phenotypes. *Hum Mol Genet*. 2012;21:1945–53.
216. Bachmann VA, et al. Gpr161 anchoring of PKA consolidates GPCR and cAMP signaling. *Proc. Natl. Acad. Sci. U. S. A.* 2016;113:7786–7791.

217. Schembs L, et al. The ciliary gene INPP5E confers dorsal telencephalic identity to human cortical organoids by negatively regulating Sonic Hedgehog signaling. *Cell Rep.* 2022;39:110811.
218. Schmidt S, et al. Primary cilia and SHH signaling impairments in human and mouse models of Parkinson's disease. *Nat Commun.* 2022;13:4819.
219. Nusse R, Clevers H. Wnt/ β -Catenin signaling, disease, and emerging therapeutic modalities. *Cell.* 2017;169:985–99.
220. Wallingford JB, Mitchell B. Strange as it May Seem: the many links between Wnt signaling, planar cell polarity, and cilia. *Genes Dev.* 2011;25:201–13.
221. May-Simera HL, Kelley MW. Cilia. Wnt signaling, and the cytoskeleton. *Cilia.* 2012;1:7.
222. Zhang K, et al. Primary cilia are WNT-transducing organelles whose biogenesis is controlled by a WNT-PP1 axis. *Dev Cell.* 2023;58:139–e1548.
223. Gerdes JM, et al. Disruption of the basal body compromises pro-teasomal function and perturbs intracellular Wnt response. *Nat Genet.* 2007;39:1350–60.
224. Simons M, et al. Inversin, the gene product mutated in nephronophthisis type II, functions as a molecular switch between Wnt signaling pathways. *Nat Genet.* 2005;37:537–43.
225. Corbit KC, et al. Kif3a constrains β -catenin-dependent Wnt signalling through dual ciliary and non-ciliary mechanisms. *Nat Cell Biol.* 2008;10:70–6.
226. Huang P, Schier AF. Dampened Hedgehog signaling but normal Wnt signaling in zebrafish without cilia. *Development.* 2009;136:3089–98.
227. Ocbina PJR, Tuson M, Anderson KV. Primary cilia are not required for normal canonical Wnt signaling in the mouse embryo. *PLoS ONE.* 2009. <https://doi.org/10.1371/journal.pone.0006839>
228. Sugiyama N, Tsukiyama T, Yamaguchi TP, Yokoyama T. The canonical Wnt signaling pathway is not involved in renal cyst development in the kidneys of Inv mutant mice. *Kidney Int.* 2011;79:957–65.
229. El-Brolosy MA, et al. Genetic compensation triggered by mutant mRNA degradation. *Nature.* 2019;568:193–7.
230. Walentek P, Beyer T, Thumberger T, Schweickert A, Blum M. ATP4a is required for Wnt-dependent Foxj1 expression and leftward flow in *Xenopus* Left-Right development. *Cell Rep.* 2012;1:516–27.
231. Yu X, Ng CP, Habacher H, Roy S. Foxj1 transcription factors are master regulators of the motile ciliogenic program. *Nat Genet.* 2008;40:1445–53.
232. Bernatik O, Paclikova P, Kotrova A, Bryja V, Cajánek L. Primary cilia formation does not rely on WNT/ β -Catenin signaling. *Front Cell Dev Biol.* 2021;9:623753.
233. Freke GM, et al. De-Suppression of mesenchymal cell identities and variable phenotypic outcomes associated with knockout of Bbs1. *Cells.* 2023;12:2662.
234. Horvitz A, Levi-Carmel N, Shnaider O, Birk R. BBS genes are involved in accelerated proliferation and early differentiation of BBS-related tissues. *Differ Res Biol Divers.* 2024;135:100745.
235. Volz A-K, et al. Bardet-Biedl syndrome proteins modulate the release of bioactive extracellular vesicles. *Nat Commun.* 2021;12:5671.
236. Bryja V, et al. The extracellular domain of Lrp5/6 inhibits noncanonical Wnt signaling in vivo. *Mol Biol Cell.* 2009;20:924–36.
237. Janečková E, et al. Canonical Wnt signaling regulates soft palate development by mediating ciliary homeostasis. *Development.* 2023;150:dev201189.
238. Holmen SL, et al. Essential role of β -Catenin in postnatal bone acquisition. *J Biol Chem.* 2005;280:21162–8.
239. Li Y, Yang S, Liu Y, Qin L, Yang S. IFT20 governs mesenchymal stem cell fate through positively regulating TGF- β -Smad2/3-Glut1 signaling mediated glucose metabolism. *Redox Biol.* 2022;54:102373.
240. Johnson GP, Fair S, Hoey DA. Primary cilium-mediated MSC mechanotransduction is dependent on Gpr161 regulation of Hedgehog signalling. *Bone.* 2021;145:115846.
241. Hilgendorf KI, et al. Omega-3 fatty acids activate ciliary FFAR4 to control adipogenesis. *Cell.* 2019;179:1289–e130521.
242. Zhu D, Shi S, Wang H, Liao K. Growth arrest induces primary-cilium formation and sensitizes IGF-1-receptor signaling during differentiation induction of 3T3-L1 preadipocytes. *J Cell Sci.* 2009;122:2760–8.
243. Marion V, et al. Transient ciliogenesis involving Bardet-Biedl syndrome proteins is a fundamental characteristic of adipogenic differentiation. *Proc Natl Acad Sci U S A.* 2009;106:1820–5.
244. Ritter A, et al. Restoration of primary cilia in obese adipose-derived mesenchymal stem cells by inhibiting Aurora A or extracellular signal-regulated kinase. *Stem Cell Res Ther.* 2019;10:255.
245. Tamura M, Sato MM, Nashimoto M. Regulation of CXCL12 expression by canonical Wnt signaling in bone marrow stromal cells. *Int J Biochem Cell Biol.* 2011;43:760–7.
246. Tsyklauri O, et al. Bardet-Biedl syndrome ciliopathy is linked to altered hematopoiesis and dysregulated self-tolerance. *EMBO Rep.* 2021;22:e50785.
247. Clement CA, et al. TGF- β signaling is associated with endocytosis at the pocket region of the primary cilium. *Cell Rep.* 2013;3:1806–14.
248. Mönnich M, et al. CEP128 localizes to the subdistal appendages of the mother centriole and regulates TGF- β /BMP signaling at the primary cilium. *Cell Rep.* 2018;22:2584–92.
249. Christensen ST, Morthorst SK, Mogensen JB, Pedersen LB. Primary cilia and coordination of receptor tyrosine kinase (RTK) and transforming growth factor β (TGF- β) signaling. *Cold Spring Harb Perspect Biol.* 2017;9:a028167.
250. Kawasaki M, et al. TGF- β suppresses Ift88 expression in chondrocytic ATDC5 cells: TGF- β REGULATES IFT88. *J Cell Physiol.* 2015;230:2788–95.
251. Tözer J, et al. TGF- β signaling regulates the differentiation of motile cilia. *Cell Rep.* 2015;11:1000–7.
252. Labour M-N, Riffault M, Christensen ST, Hoey DA. TGF β 1 - induced recruitment of human bone mesenchymal stem cells is mediated by the primary cilium in a SMAD3-dependent manner. *Sci Rep.* 2016;6:35542.
253. Liu M, Alharbi M, Graves D, Yang S. IFT80 is required for fracture healing through controlling the regulation of TGF- β signaling in chondrocyte differentiation and function. *J Bone Min Res Off J Am Soc Bone Min Res.* 2020;35:571–82.
254. Kawasaki M, et al. Primary cilia suppress the fibrotic activity of atrial fibroblasts from patients with atrial fibrillation in vitro. *Sci Rep.* 2024;14:12470.
255. Zhang W, et al. Dual Inhibition of HDAC and tyrosine kinase signaling pathways with CUDC-907 attenuates TGF β 1 induced lung and tumor fibrosis. *Cell Death Dis.* 2020;11:765.
256. Waddell SH, et al. A TGF β -ECM-integrin signaling axis drives structural reconfiguration of the bile duct to promote polycystic liver disease. *Sci Transl Med.* 2023;15:eabq5930.
257. Hong R, et al. XIAP-mediated degradation of IFT88 disrupts HSC cilia to stimulate HSC activation and liver fibrosis. *EMBO Rep.* 2024;25:1055–74.
258. Gradilone SA, et al. HDAC6 Inhibition restores ciliary expression and decreases tumor growth. *Cancer Res.* 2013;73:2259–70.
259. Paul C, et al. Loss of primary cilia promotes inflammation and carcinogenesis. *EMBO Rep.* 2022;23:e55687.
260. Zhou B, et al. Notch signaling pathway: architecture, disease, and therapeutics. *Signal Transduct Target Ther.* 2022;7:95.
261. Ezratty EJ, et al. A role for the primary cilium in Notch signaling and epidermal differentiation during skin development. *Cell.* 2011;145:1129–41.
262. Wang W, et al. IFT-A deficiency in juvenile mice impairs biliary development and exacerbates ADPKD liver disease. *J Pathol.* 2021;254:289–302.
263. Andersson ER, Sandberg R, Lendahl U. Notch signaling: simplicity in design, versatility in function. *Dev Camb Engl.* 2011;138:3593–612.
264. Ezratty EJ, Pasolli HA, Fuchs EA. Presenilin-2-ARF4 trafficking axis modulates Notch signaling during epidermal differentiation. *J Cell Biol.* 2016;214:89–101.
265. Mazelova J, et al. Ciliary targeting motif VxPx directs assembly of a trafficking module through Arf4. *EMBO J.* 2009;28:183–92.
266. Grisanti L, Revenkova E, Gordon RE, Iomini C. Primary cilia maintain corneal epithelial homeostasis by regulation of the Notch signaling pathway. *Dev Camb Engl.* 2016;143:2160–71.
267. Liu Z, et al. Primary cilia regulate hematopoietic stem and progenitor cell specification through Notch signaling in zebrafish. *Nat Commun.* 2019;10:1839.
268. Lopes SS, et al. Notch signalling regulates left-right asymmetry through ciliary length control. *Dev Camb Engl.* 2010;137:3625–32.
269. Li X, et al. Primary cilia mediate Klf2-dependant Notch activation in regenerating heart. *Protein Cell.* 2020;11:433–45.
270. Serra CFH, et al. Prolaminin 1 and Notch regulate ciliary length and dynamics in multiciliated cells of the airway epithelium. *iScience.* 2022;25:104751.
271. Rausch V, Hansen CG. The Hippo pathway, YAP/TAZ, and the plasma membrane. *Trends Cell Biol.* 2020;30:32–48.
272. Jenks AD, et al. Primary cilia mediate diverse kinase inhibitor resistance mechanisms in cancer. *Cell Rep.* 2018;23:3042–55.
273. Srivastava S, et al. A human patient-derived cellular model of Joubert syndrome reveals ciliary defects which can be rescued with targeted therapies. *Hum Mol Genet.* 2017;26:4657–67.
274. Hynes AM, et al. Murine Joubert syndrome reveals Hedgehog signaling defects as a potential therapeutic target for nephronophthisis. *Proc Natl Acad Sci U S A.* 2014;111:9893–8.
275. Wong SY, et al. Primary cilia can both mediate and suppress Hedgehog pathway-dependent tumorigenesis. *Nat Med.* 2009;15:1055–61.

276. Han Y-G, et al. Dual and opposing roles of primary cilia in medulloblastoma development. *Nat Med*. 2009;15:1062–5.
277. Wu VM, Chen SC, Arkin MR, Reiter JF. Small molecule inhibitors of Smoothed ciliary localization and ciliogenesis. *Proc. Natl. Acad. Sci.* 109, 13644–13649 (2012).
278. Halkina T, et al. Discovery of potent and brain-penetrant Tau tubulin kinase 1 (TTBK1) inhibitors that lower Tau phosphorylation in vivo. *J Med Chem*. 2021;64:6358–80.
279. Bashore FM, et al. Modulation of Tau tubulin kinases (TTBK1 and TTBK2) impacts ciliogenesis. *Sci Rep*. 2023;13:6118.
280. Lin AC, et al. Modulating Hedgehog signaling can attenuate the severity of osteoarthritis. *Nat Med*. 2009;15:1421–5.
281. Thompson CL, Wiles A, Poole CA, Knight MM. Lithium chloride modulates chondrocyte primary cilia and inhibits Hedgehog signaling. *FASEB J Off Publ Fed Am Soc Exp Biol*. 2016;30:716–26.
282. Peng Z, et al. Lithium inhibits tumorigenic potential of PDA cells through targeting hedgehog-Gli signaling pathway. *PLoS ONE*. 2013;8:e61457.
283. Cao Y, et al. Chemical modifier screen identifies HDAC inhibitors as suppressors of PKD models. *Proc Natl Acad Sci U S A*. 2009;106:21819–24.
284. Mergen M, et al. The nephronophthisis gene product NPHP2/Inversin interacts with Aurora A and interferes with HDAC6-mediated cilia disassembly. *Nephrol Dial Transpl Off Publ Eur Dial Transpl Assoc - Eur Ren Assoc*. 2013;28:2744–53.
285. Yanda MK, Liu Q, Cebotaru V, Guggino WB, Cebotaru L. Histone deacetylase 6 inhibition reduces cysts by decreasing cAMP and Ca²⁺ in knock-out mouse models of polycystic kidney disease. *J Biol Chem*. 2017;292:17897–908.
286. Cebotaru L, et al. Inhibition of histone deacetylase 6 activity reduces cyst growth in polycystic kidney disease. *Kidney Int*. 2016;90:90–9.
287. Frasca A, et al. MECP2 mutations affect ciliogenesis: a novel perspective for Rett syndrome and related disorders. *EMBO Mol Med*. 2020;12:e10270.
288. Ritter A, et al. Primary cilia are dysfunctional in obese adipose-derived mesenchymal stem cells. *Stem Cell Rep*. 2018;10:583–99.
289. Xie C, et al. Reversal of ciliary mechanisms of disassembly rescues olfactory dysfunction in ciliopathies. *JCI Insight*. 2022;7:e158736.

Publisher's note

Springer Nature remains neutral with regard to jurisdictional claims in published maps and institutional affiliations.

Appendix 2

Lacigová A, Čajánek L*. Phosphorylation at the Helm: Kinase-Mediated Regulation of Primary Cilia Assembly and Disassembly. *Cytoskeleton*. 2025 Mar 10. doi:10.1002/cm.22012. (JCR 2024, IF = 1.6, Q4 – Cell Biology)

REVIEW ARTICLE OPEN ACCESS

Phosphorylation at the Helm: Kinase-Mediated Regulation of Primary Cilia Assembly and Disassembly

Andrea Lacigová¹  | Lukáš Čajánek^{1,2} 

¹Laboratory of Cilia and Centrosome Biology, Department of Histology and Embryology, Faculty of Medicine, Masaryk University, Brno, Czech Republic | ²Section of Animal Physiology and Immunology, Department of Experimental Biology, Faculty of Science, Masaryk University, Brno, Czech Republic

Correspondence: Lukáš Čajánek (cajANEK@med.muni.cz)

Received: 20 November 2024 | **Revised:** 11 February 2025 | **Accepted:** 28 February 2025

Funding: LC acknowledges the support from the Czech Science Foundation (22-13277S).

Keywords: kinase | phosphorylation | primary cilium | substrate

ABSTRACT

The primary cilium serves as an antenna of most vertebrate cells and is important for conveying cues from several signaling pathways into appropriate cellular responses during development and homeostasis. Cilia assembly and disassembly processes are thought to be strictly controlled; however, the precise nature of molecular events underlying this control still awaits full resolution. Through their enzymatic activity, kinases function as flexible yet highly controllable regulators of a vast variety of cellular processes. Their activity ranges from cell cycle control to regulation of cell motility, signal transduction, and metabolism. This review focuses on the emerging role of kinases in primary cilia biology. We underscore their functions in primary cilia formation, maintenance, and resorption while examining available models and the respective mechanisms of their actions.

1 | Introduction

1.1 | Structure

Cilia are rod-like organelles that extend from the surface of most eukaryotic cells. They can be either motile (also called flagella) or non-motile, with the latter variety referred to as primary cilia. It was their lack of movement that led to the initial erroneous view of primary cilia as vestigial structures without a clear physiological function. Significantly, this notion has shifted during the past two decades, as evidence demonstrating the vital roles of primary cilia in embryogenesis and tissue homeostasis has emerged (Anvarian et al. 2019; Gopalakrishnan et al. 2023). Nowadays, primary cilia can be depicted in simple terms as a cellular antenna, integrating the ability to sense and respond to both biochemical and physical stimuli coming from the extracellular milieu. In fact, the primary cilium accommodates

receptors and effectors of several signaling pathways and serves as a prominent signaling hub. Its role in cell-to-cell communication is perhaps best portrayed within the Hedgehog signaling pathway (Anvarian et al. 2019; Bangs and Anderson 2017; Bryja et al. 2017). Primary cilia's crucial role in cell signaling is highlighted by numerous reports linking defects in primary cilia biogenesis and function to a wide range of human diseases, collectively known as ciliopathies. Correctly assembled and functional primary cilia's significance is substantiated by the diversity of organ systems affected by ciliopathies, ranging from kidneys or liver to the central nervous system, and the frequently lethal developmental abnormalities caused by disrupted ciliogenesis (Amack 2022; Mill et al. 2023; Reiter and Leroux 2017). The specific aspects of cilia-related signaling and their impact on cilia dynamics were thoroughly covered in several recent reviews (Gopalakrishnan et al. 2023; Hilgendorf et al. 2024; Mill et al. 2023) and will not be discussed in detail here.

The figures were made using Adobe Illustrator 2021.

This is an open access article under the terms of the [Creative Commons Attribution-NonCommercial](https://creativecommons.org/licenses/by-nc/4.0/) License, which permits use, distribution and reproduction in any medium, provided the original work is properly cited and is not used for commercial purposes.

© 2025 The Author(s). *Cytoskeleton* published by Wiley Periodicals LLC.

The distinct structural aspects of primary cilia attracted the attention of researchers even before their functional relevance was recognized. Among the cells capable of forming primary cilia, each contains only a single cilium consisting of the basal body (BB) and the axoneme that is covered by the ciliary membrane (Figure 1A). The BB is derived from the mature centriole (also called mother centriole, MC) of the centriolar pair of

the centrosome and is decorated with two sets of appendages at its distal (surface-oriented) end (Sorokin 1962). Centrioles are barrel-like structures made of nine microtubule triplets arranged in a circular pattern (nine-fold symmetry) (Nigg et al. 2014). The BB function is to template the ciliary axoneme. The distal part of the BB adopts an arrangement reminiscent of an axoneme, by containing microtubule doublets instead of triplets. Successively,

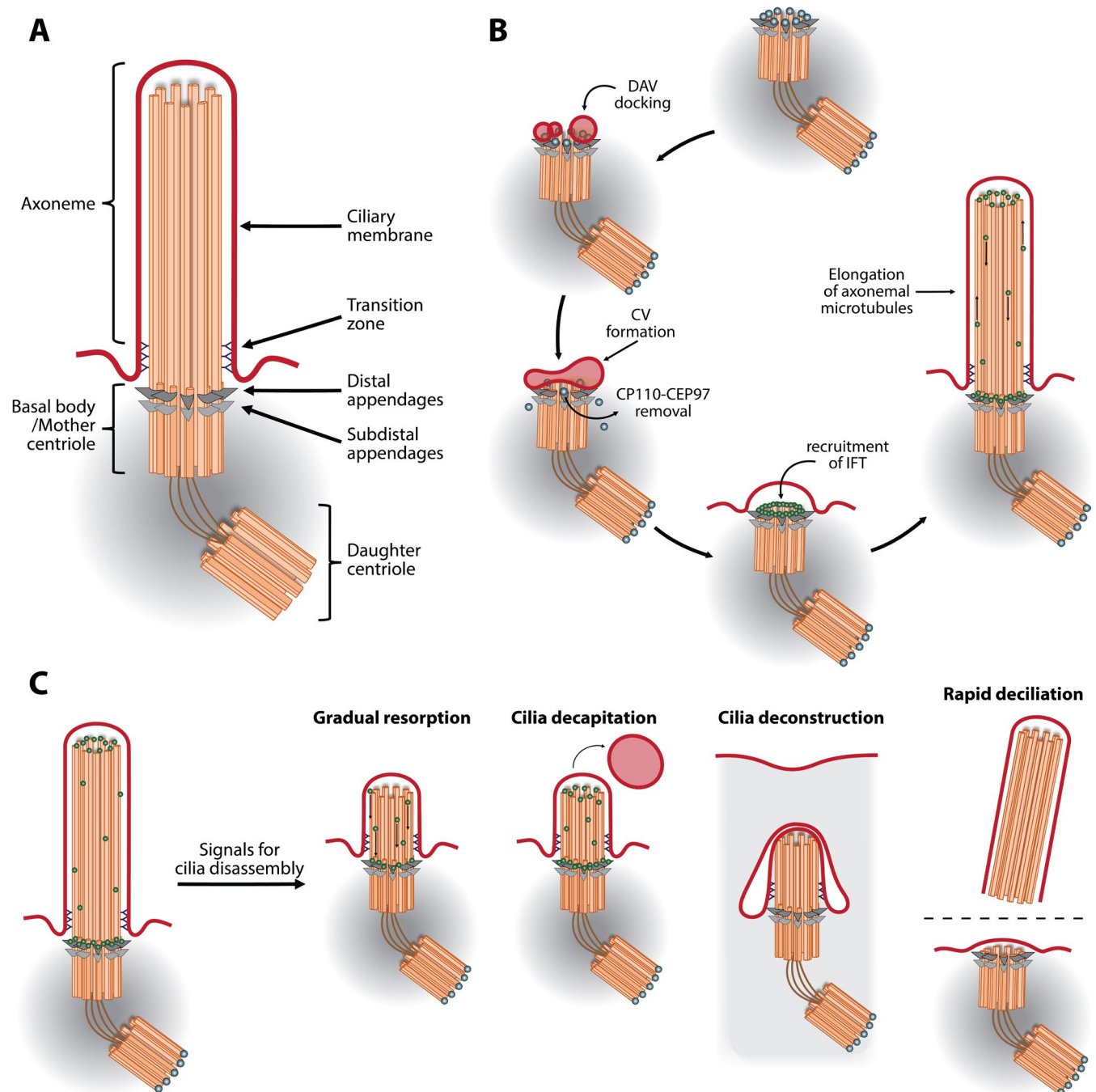


FIGURE 1 | Structure of primary cilia, ciliogenesis, and cilia disassembly (A) Primary cilium consists of a basal body (BB) and axoneme covered by the ciliary membrane. At its distal end, the BB is decorated with distal and subdistal appendages (DAs and SDAs, respectively). The proximal part of the axoneme creates the transition zone. (B) Primary cilia formation starts by docking distal appendage vesicles (DAVs) to the DAs. DAVs later fuse to form the ciliary vesicle (CV). Removal of the CP110-CEP97 complex is thought to be a prerequisite for the subsequent elongation of axonemal microtubules. To ensure directed transport of cargo within the cilium, IFT needs to be recruited to the BB. Synchronized elongation of axonemal microtubules and the ciliary membrane results in the growth of the cilium. (C) Upon receiving respective signals, the cells are believed to dispatch cilia by one of the following mechanisms—either through degradation of axonemal microtubules and gradual resorption of the cilium, through cilia decapitation, through rapid deciliation resulting in shedding of the axoneme, or through cilia deconstruction.

the axoneme represents the extension of those nine microtubule doublets at the distal end of the BB, acting as a skeleton of the cilium. Axonemal microtubules exhibit several post-translation modifications (PTMs), including acetylation, glutamylation, glycylation, and detyrosination, which are thought to help regulate their stability (Deretic et al. 2023). Axonemal microtubules serve as tracks for the movement of ciliary motor proteins such as kinesins and dyneins (Lacey and Pigino 2024). Intriguingly, tyrosination/detyrosination of axonemal tubulin has recently been envisioned as crucial for collision-free transport inside the cilium (Chhatre et al. 2025). The compartment between the BB and the axoneme, termed the transition zone, contains so-called Y-links connecting the membrane with the microtubules. This arrangement permits the transition zone to serve as a semipermeable sorting barrier regulating trafficking to/from the cilium to ensure distinct ciliary composition and, hence, the signaling function (Garcia-Gonzalo and Reiter 2017; Mill et al. 2023). The transition zone comprises two main functional complexes—the NPHP module and the MKS module, which contribute to the transition zone functionality via a network of mutual interactions (Park and Leroux 2022).

The two sets of appendages are termed according to their position as distal (DAs) and subdistal (SDAs) appendages, respectively. They are both assembled during centriole maturation in the G2/M phase of the cell cycle. The DAs are arranged as blade-like structures attached to the microtubules of the MC wall, with respect to the nine-fold symmetry of the centriole (Chang et al. 2023; Nigg et al. 2014). The DAs are indispensable for ciliogenesis (Ma et al. 2023; Tanos et al. 2013). They are assembled in a hierarchical manner with the protein CEP83/CCDC41 recruiting proteins CEP89/CCDC123 and SCLT1. SCLT1, in turn, mediates the correct localization of FBF1 and CEP164 to the centriole distal end (Tanos et al. 2013). Unlike the nine-fold symmetrical arrangement of DAs, the structure of SDAs is notably less conserved. SDAs serve as anchoring points for microtubules nucleated by the centrosome, hence connecting the BB to the cytoskeleton, and they do not seem to have a major role in primary cilium assembly (Ma et al. 2023).

Classical perception defines the primary cilia axoneme to have a “9+0” arrangement of microtubule doublets, with the central pair, typically defining the motile cilia (“9+2” arrangement), missing in primary cilia. However, deviations from this canonical ciliary architecture exist across various cell types. This also applies to the length of individual microtubules in primary cilia, exhibiting unexpected heterogeneity (Kiesel et al. 2020; Sun et al. 2019).

1.2 | Ciliogenesis

Ciliogenesis typically occurs in postmitotic cells. Originally, primary cilia were regarded as indicators of quiescence and considered, in fact, to have a checkpoint function regulating cell cycle re-entry (Seeley and Nachury 2010). However, data from live cell imaging and in vivo studies show that primary cilia can be found in both non-cycling and proliferating (non-mitotic) cells and that the timing of cilium assembly initiation may vary (Ford et al. 2018; Seeley and Nachury 2010). This variability in timing reflects differences in cellular states or specific requirements for

cilium function across cell types. The earliest visible step in the intracellular assembly pathway of ciliogenesis involves the docking of the MC to a ciliary vesicle (CV) (Figure 1B). Trafficking of vesicles to the pericentriolar area is regulated on several levels, with the actin network a vital factor (J. Kim et al. 2010). The alternative extracellular assembly pathway, active in polarized cells, involves the MC's direct docking to the plasma membrane.

The CV forms from the fusion of smaller distal appendage vesicles (DAVs). Myosin-Va, involved in the assembly and transport of DAVs, is considered the first vesicle regulator recruited to the MC with the onset of ciliogenesis (Wu et al. 2018). The subsequent formation of the large CV relies on the coordinated actions of EHD1, EHD3, and small GTPase Rab34 (Ganga et al. 2021; Lu et al. 2015; Stuck et al. 2021). CV membrane expansion, regulated by the Rab11/Rabin8/Rab8 cascade, facilitates the formation and elongation of the ciliary membrane alongside the growing axoneme (Shakya and Westlake 2021). Specifically, small GTPase Rab11 regulates the trafficking of CVs containing Rabin8, a Rab8 guanine nucleotide exchange factor (GEF), to the MC in order to activate Rab8 to stimulate ciliary membrane growth (Shakya and Westlake 2021). Both CV docking and expansion require intact DAs.

The cilium grows by simultaneously extending its membrane and the microtubule-based axoneme. However, the mechanism that initiates microtubule outgrowth from the MC distal end remains unclear. A well-established step of ciliogenesis onset is the removal of distal end proteins CP110, also involved in the regulation of centrosomal duplication and separation, and CEP97 from the MC. These proteins rely on each other for proper localization and form a complex that is thought to act as a “cap” hindering axoneme microtubule outgrowth (Chen et al. 2002; Spektor et al. 2007). In line with that, CP110 activity at the microtubule ends also restricts the length of centrioles (Iyer et al. 2025; Schmidt et al. 2009). Although the loss of CP110-CEP97 from the MC is a reliable marker for the initiation of ciliogenesis, their roles appear to be more complex and, perhaps, context-dependent, as the loss of CP110 has also been linked to defects in cilia assembly (Walentek et al. 2016; Yadav et al. 2016).

The later stage of ciliogenesis is regulated by Intraflagellar Transport (IFT) proteins. IFT represents a bidirectional movement of multiprotein particles along ciliary microtubules, with anterograde transport to the cilium tip driven by kinesin motors (typically kinesin 2) and retrograde transport back to the base supported by dynein 2 motors. The primary role of IFT is to transport cargo (ciliary components such as tubulin and receptors) to support cilium growth and maintenance (Lacey and Pigino 2024; Pedersen and Rosenbaum 2008; Scholey 2008).

1.3 | Cilia Resorption

Primary cilium must be disassembled before mitosis to permit the MC to facilitate centrosome-mediated spindle organization and positioning. Serum starvation is commonly used to promote the formation of cilia in cultured cells and, consequently, the serum-starved cells gradually lose their cilia upon serum re-addition. Data from live-cell imaging experiments indicate

the loss of primary cilia at the G/M transition (Ford et al. 2018; Seeley and Nachury 2010).

One way to remove cilium is gradual resorption through axoneme depolymerization (Figure 1C). Considering the role of tubulin PTMs such as glycylation, (poly)glutamylation, and acetylation in the regulation of microtubule lattice stability (Janke and Magiera 2020), dynamic changes in ciliary tubulin PTMs are thought to represent one of the driving mechanisms mediating axoneme disassembly (Seeley and Nachury 2010). This disassembly is also regulated by kinesin 13 family members, including KIF2A and KIF24. Unlike conventional kinesin motors, these kinesin proteins promote ATP-dependent microtubule depolymerization, facilitating the resorption of the ciliary axoneme (Reilly and Benmerah 2019).

Ectocytosis or cilia decapitation has recently been associated with the regulation of primary cilia dynamics, ultimately leading to their disassembly (Nager et al. 2017; Phua et al. 2017). When triggered by events such as the defective exit of ciliary receptors, subsequent remodeling of ciliary actin leads to myosin-mediated abscission of the ciliary membrane, which is then released from the ciliary tip as a vesicle. This mechanism may lead to the gradual resorption of the entire ciliary axoneme.

Another means for cells to dispose of their cilia is via rapid deciliation, which involves severing the ciliary axoneme with the microtubule-severing enzyme katanin (Mirvis et al. 2019; Quarmby 2004).

Notably, cilia deconstruction has recently been identified as a unique and rapid cilia resorption mechanism *in vivo*, described in cerebellar granule cells during the process of their differentiation (Constable et al. 2024; Ott et al. 2024). The underlying mechanism seems to reside in the downregulation of key regulators of cilia assembly and maintenance at the level of mRNA transcript (Constable et al. 2024) or protein (Lin et al. 2024).

2 | Kinases Regulating Primary Cilia

2.1 | Role of Kinases in Cilia Assembly and Maintenance

As outlined above, ciliogenesis is a multistep and time-regulated process. The employment of kinases is emerging as a key mechanism allowing robust and stepwise control of the cilium assembly pathway. The role of individual kinases ranges from specific control of one aspect of primary cilia assembly to a position of central regulator orchestrating multiple events (Figure 2). Tau Tubulin Kinase 2 (TTBK2), a member of the CK1 superfamily, is an example of a kinase with arguably the most critical and complex role in ciliogenesis. TTBK2, through its kinase activity, is indispensable for primary cilia formation in mice and human cells, and its ablation leads to complete failure of ciliogenesis (Bernatik et al. 2020; Goetz et al. 2012). Interestingly, TTBK2 activity can be partially compensated by its sibling kinase, TTBK1, in hPCS-derived neural progenitors (Binó and Čajánek 2023).

To successfully carry out its functions in primary cilia, correct localization is essential. To initiate the cilium assembly

pathway, TTBK2 is recruited to DAs via the interaction of its C-terminus with the N-terminal region of CEP164 (Čajánek and Nigg 2014). Despite being tethered at the C-terminus, recent data suggest CEP164-bound TTBK2 may be able to extend its N-terminal kinase domain over 100 nm, thanks to disordered regions spanning both TTBK2 and CEP164 (Silva et al. 2022). This would give TTBK2 a reasonable reach to target substrates beyond the DAs.

The formation of CV and its interaction with DAs require TTBK2 activity, which seems to be partially mediated by TTBK2 phosphorylation of CEP83 (Lo et al. 2019). TTBK2 also phosphorylates additional proteins implicated in CV/membrane regulation (e.g., CEP164, CEP89, Rabin8), yet the role of these phosphorylations is not known (Bernatik et al. 2020). Pursuant to the notion that TTBK2 can phosphorylate several DA components (namely CEP83, CEP89, and CEP164) (Bernatik et al. 2020), TTBK2 also promotes their MC localization (Čajánek and Nigg 2014). Moreover, a recent preprint (Kanie et al. 2025) linked the ablation of TTBK2 to alterations in the recruitment of several DA components. Thus, TTBK2 could fine-tune the assembly of DAs, possibly via a positive feedback loop. The critical role of TTBK2 in the initiation of ciliogenesis is further highlighted by its requirement for the removal of the CEP97-CP110 complex from the MC and the recruitment of IFT proteins to the newly forming BB (Goetz et al. 2012).

Recently, several other kinases have emerged as regulators of ciliogenesis at the level of TTBK2. The CEP164–TTBK2 interaction has been slated for regulation by PtdIns(4)P, binding to specific motives in CEP164 and TTBK2, thus hampering their interaction (Xu et al. 2016). According to this model, Phosphatidylinositol Phosphate Kinase 1 γ (PIPK1 γ) and phosphatase INPP5E modulate the CEP164–TTBK2 interaction by controlling the levels of PtdIns(4)P at the BB (Xu et al. 2016). PIPK1 γ phosphorylates PtdIns(4)P, changing it to PtdIns(4,5)P₂, an action counteracted by INPP5E activity.

Conditional primary cilia ablation (e.g., by removing TTBK2 in adult mice) induces progressive degeneration of the cerebellum (Bowie and Goetz 2020). Conversely, primary cilia disassembly mediated by TTBK2 degradation triggers the differentiation of granule neuron progenitors (Lin et al. 2024), further indicating that TTBK2 acts as a crucial regulator during neurodevelopment. TTBK2 was originally studied for its involvement in Tau-related proteinopathies, hinting at its possible multifaceted involvement in neurodegeneration (Taylor et al. 2019). Notably, a correlation between primary cilia/TTBK2 defects and neurodegeneration has further support in the work of Steger et al. 2017, which confirmed that Parkinson's disease (PD) related mutation of Leucine Rich Repeat Kinase 2 (LRRK2) results in a hyperactive product that attenuates primary cilia formation. The defect in ciliogenesis caused by the LRRK2 mutation is accompanied by reduced MC levels of TTBK2, signifying the role of LRRK2 upstream of TTBK2 (Sobu et al. 2021). Furthermore, LRRK2 has been reported to phosphorylate several Rab GTPases and in turn affect Myosin-Va, which might point to additional mechanisms of how LRRK2 affects cilia (Dhekne et al. 2021; Steger et al. 2017). Whether LRRK2-related cilia defects could be rescued by increased TTBK2 activity has not been tested. Remarkably, ciliogenesis defects linked to PD-related LRRK2

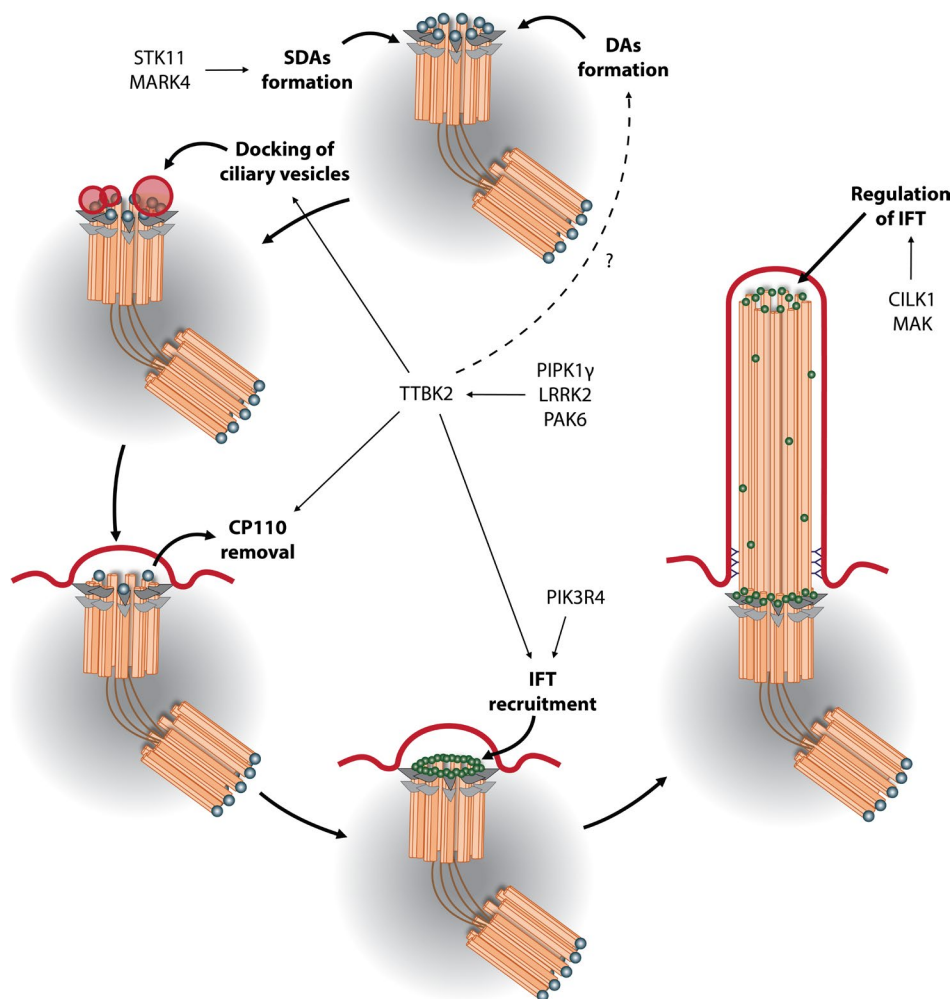


FIGURE 2 | Kinases involved in the regulation of primary cilia assembly several ciliogenesis steps are controlled by kinases. TTBK2 plays a central role by promoting CV docking, CP110 removal, and IFT recruitment. Furthermore, TTBK2 is suggested to promote the correct assembly of distal appendages (DAs). PIPK1 γ , LRRK2, and PAK6 act upstream of TTBK2, regulating its localization at the basal body. STK11 and MARK4 have been shown to enable the release of a negative regulator, CP110, from the distal end of the mother centriole through the recruitment of ODF2 to the sub-distal appendages (SDAs). PIK3R4 enables IFT20 recruitment to the basal body by triggering its release from the Golgi apparatus. CILK1 and MAK regulate IFT within the ciliary axoneme and thus affect cilia maintenance.

mutations could be rescued by a LRRK2-interacting kinase, P21 Activated Kinase 6 (PAK6) (Civiero et al. 2015; Iannotta et al. 2024), known for its role as an effector protein for small GTPases RAC and CDC42 in the regulation of the cytoskeleton (Wells and Jones 2010). Nevertheless, PAK6 is unable to rescue defects caused by LRRK2 mutations that interfere with LRRK2-PAK6 affinity (Iannotta et al. 2024). While it is unclear whether PAK6 kinase activity is required to observe ciliogenesis rescue effects, further investigation of LRRK2 and PAK6 involvement in cilia formation, either through regulation of TTBK2 or by some other mechanism (e.g., involving Rab GTPases), might uncover novel pathways relevant for the biogenesis of these organelles.

Apart from being controlled by TTBK2, ciliogenesis initiation and CEP97-CP110 removal from the MC distal end also rely on the activity of Microtubule Affinity Regulating Kinase 4 (MARK4). MARK4 promotes MC localization of the SDA protein ODF2, which is subsequently required for CEP97-CP110 loss and effective axoneme extension (Kuhns et al. 2013).

Given that IFT88 recruitment was not disrupted by MARK4 or ODF2 depletion (Kuhns et al. 2013), MARK4 presumably does not act upstream of TTBK2 (an absence of which impairs both CEP97-CP110 and IFT), but more likely functions in a parallel pathway. Significantly, MARK4 is positively regulated by Serine/Threonine Kinase 11 (STK11) (Lizcano et al. 2004), which has been previously reported to promote ciliogenesis (Jacob et al. 2011).

IFT and its ability to transport cargo within the axoneme are crucial for both cilia assembly and maintenance (Ishikawa and Marshall 2011; Pedersen and Rosenbaum 2008). Several kinases regulate IFT by controlling protein recruitment to cilia, as well as through modulating IFT-motor or IFT-cargo interactions. Here again, TTBK2 is prominently involved in recruiting IFT proteins. In its absence, IFT proteins fail to localize to the MC distal end (Goetz et al. 2012), yet the underlying mechanism is not known. Other kinases have been attributed to more specific roles. For example, Phosphoinositide-3-kinase Regulatory Subunit 4 (PIK3R4), which in its mutated forms induces ciliopathy defects,

triggers the release of IFT20 from the Golgi, hence promoting its ciliary base recruitment (Stoetzel et al. 2016). Moreover, Male Germ Cell Associated Kinase (MAK) represents an example of a kinase regulating IFT inside the cilium. The interaction with IFT74–81 subunits helps to load tubulin onto the IFT complexes to allow its ciliary import (Bhogaraju et al. 2013). MAK is particularly enriched in the cilia tip, and its phosphorylation of IFT74 has been linked to a reduction of tubulin affinity toward IFT74–81. Thus, MAK activity in the tip of primary cilia is believed to promote the release of IFT cargo (tubulin) in the cilia tip (Jiang et al. 2022). Besides effecting IFT-cargo interactions, MAK is also thought to be involved in the regulation of the stability of axonemal microtubules (Maurya et al. 2019), the motility of ciliary kinesins (Yi et al. 2018), and the docking and undocking of kinesin motors and IFT particles (Burghoorn et al. 2007). While these diverse functions help to explain cilia length control deregulation observed after MAK ablation (Berman et al. 2003; Hilton et al. 2013), the underlying mechanisms (relevant substrates) are unclear. Deregulated cilia length, often accompanied by the accumulation of IFT proteins and other ciliary components in the tip of the cilium, is also characteristic of the ablation of Ciliogenesis Associated Kinase 1 (CILK1/ICK) (Chaya et al. 2014). Similarly to MAK, CILK1 resides in ciliary axonemes, is able to interact with IFT and act as its cargo (Nakamura et al. 2020). Loss of CILK1 seems to accelerate anterograde IFT (Broekhuis et al. 2014; Kunova Bosakova et al. 2018). One of the proposed mechanisms downstream of CILK1 involves phosphorylation of KIF3A, a subunit of the ciliary kinesin II complex (Chaya et al. 2014). However, homozygous knockin mice carrying Ala instead of the corresponding phosphosite of CILK1 in KIF3A (T674) lack any visible cilia defects, likely owing to a compensatory mechanism and/or the contribution of additional substrates to CILK1 phenotypes (Gailey et al. 2021).

Essentially, kinases involved in the modulation of IFT properties are expected to impact both the initial phase of cilia formation and cilia maintenance. Related defects are thought to shift the balance between the promotion of ciliogenesis/cilium growth and the induction of gradual cilia resorption, subsequently causing abnormalities in cilia length. Indeed, a function in the regulation of primary cilia length and axoneme stability has recently been identified for TTBK2 (Bowie et al. 2018; Nguyen and Goetz 2023). One proposed mechanism involves the counteraction of the MT-depolymerizing activity of kinesin 13 proteins. In this case, TTBK2 phosphorylates the N-terminal region of KIF2A at the MC, which impairs its ability to bind and depolymerize axonemal microtubules (Vysloulzil et al. 2025; Watanabe et al. 2015).

2.2 | Role of Kinases in Cilia Disassembly

One of the central functions in the network of kinases involved in the regulation of cilia disassembly is effected by Aurora kinase A (AURKA) (Figure 3), where a BB pool of AURKA promotes primary cilia resorption (Pugacheva et al. 2007; Yin et al. 2022). Based on evidence from various cell lines, AURKA is believed to carry out this function by enhancing histone deacetylase HDAC6 activity, ultimately resulting in the destabilization of axonemal microtubules (Pugacheva et al. 2007). While the prominent role of AURKA in primary cilia disassembly is well established and conserved from Chlamydomonas to vertebrates (Pan et al. 2004; Pugacheva et al. 2007), we recognize that the proposed model is not without limitations.

Firstly, genetic ablation of HDAC6 (or any other HDAC) does not produce significant ciliary phenotypes in vivo, suggesting that compensatory mechanisms take place and/or cell type specificity plays

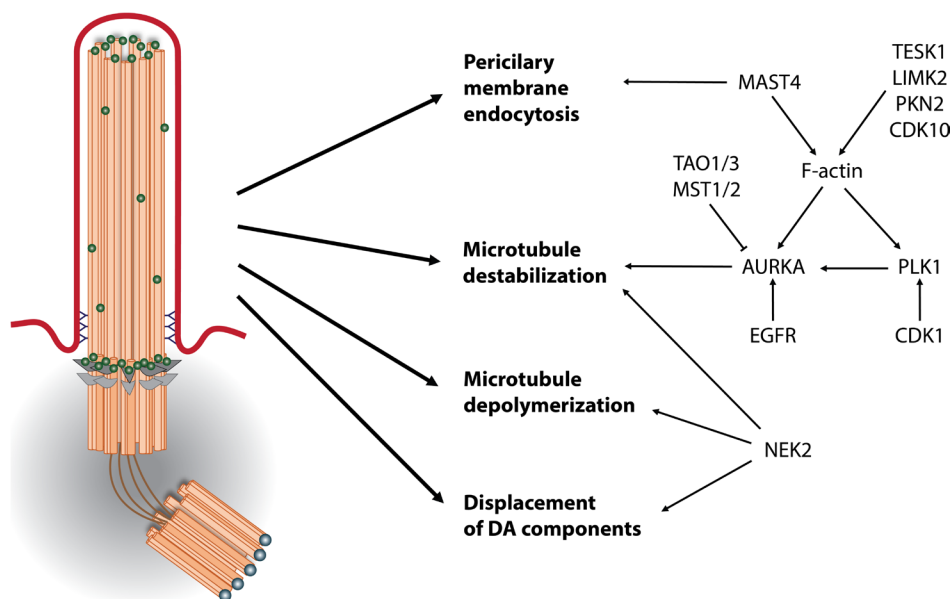


FIGURE 3 | Kinases involved in the regulation of primary cilia disassembly. Cilia resorption is thought to be driven by several simultaneous processes. NEK2 has been associated with the destabilization of axonemal microtubules, with their depolymerization through KIF24 activity and with the displacement of several DA components. AURKA is believed to promote cilia resorption through the destabilization of axonemal microtubules. EGFR, PLK1, and CDK1 were identified as factors promoting cilia resorption-related activity of AURKA, while MST1/2 and TAO1/3 evince a negative effect on this AURKA activity. Increased levels of F-actin result in upregulated AURKA and PLK1 expression and are enhanced by the activity of TESK1, LIMK2, PKN2, CDK10, and MAST4, while MAST4 appears to simultaneously promote periciliary membrane endocytosis.

a role (Łysyganicz et al. 2021; Y. Zhang et al. 2008). Additionally, since both AURKA and HDAC6 are concentrated at the base of the cilia (with no current evidence of their presence in the ciliary axoneme), an important question remains: How does the signal from AURKA/HDAC6 reach the axonemal microtubules?

AURKA, besides its prominent impact on primary cilia dynamics, plays a key role in mitosis regulation. Several mechanisms responsible for the tight control of its activity have been identified (Figure 4). Interaction with Ca^{2+} -regulated multifunctional protein calmodulin stimulates AURKA activity at the ciliary base (Plotnikova et al. 2012). Furthermore, trichoplein (TCHP), a keratin filament-binding protein with a scaffolding function, has been shown to bind and activate AURKA to promote cilia resorption (Inoko et al. 2012). TCHP levels are regulated by Epidermal Growth Factor Receptor (EGFR), a kinase shown to phosphorylate and activate USP8 deubiquitinase, inducing an increase in TCHP steady-state levels and, in turn, AURKA activation (Kasahara et al. 2018).

Another suggested mechanism for regulating AURKA activity is through interaction with a scaffolding protein HEF1/NEDD9, which subsequently promotes activating auto-phosphorylation. Another regulatory pathway acting on AURKA is based on suppression of HEF1/NEDD9 via negative feedback to limit its own activity (Pugacheva and Golemis 2005). HEF1/NEDD9 is subjected to regulation by additional upstream kinases, including its stabilization through the activity of the well-established mitotic kinase, Polo-like kinase 1 (PLK1) (Doornbos and Roepman 2021; Lee et al. 2012). Notably, the PLK1–AURKA relationship is rather complex, as AURKA is responsible for the activation of PLK1 before mitotic entry (Seki et al. 2008). In order to carry out its

function, PLK1 is recruited to the pericentriolar matrix (PCM) by interaction with PCM1. This interaction is facilitated by Cyclin-Dependent Kinase 1 (CDK1)-mediated phosphorylation of PCM1 (Wang et al. 2013). Along with its effects on AURKA activity, PLK1 has been proposed to counteract ciliogenesis by preventing correct localization of TZ component DZIP1 (B. Zhang et al. 2017) and by phosphorylating and activating microtubule-depolymerizing kinesins from the kinesin 13 family (Miyamoto et al. 2015). To illustrate the complexity and context-dependent role of PLK1 in cilia, it should be noted that PLK1 may also act as a ciliogenesis-promoting factor. PLK1 activity is required for MC maturation, including the assembly of DAs. In fact, ectopic PLK1 activation precipitates the premature assembly of DAs and, consequently, the formation of two primary cilia per cell (Kong et al. 2014).

Another mechanism proposed to regulate cilia resorption at the level of AURKA-HDAC6 involves two kinases, Macrophage Stimulating 1 and 2 (MST1 and 2), together with the SAV1 scaffolding protein. This complex, upon its activation during ciliogenesis, promotes the dissociation of the AURKA-HDAC6 complex (M. Kim et al. 2014). Another kinase, TAO Kinase 1 (TAO1), has been shown to activate this complex (Boggiano et al. 2011; Poon et al. 2011) and its depletion impairs ciliogenesis in RPE1 cells, as does the depletion of TAO3 (M. Kim et al. 2014). Another suggested mechanism for MST1/2 to foster cilia formation is through the promotion of Rab8a recruitment to the cilium (M. Kim et al. 2014). The biological relevance of MST2 for cilia biology is supported by its localization at the BB, as well as its identification as a candidate ciliopathy gene (Reiter and Leroux 2017).

Another mitotic kinase with a prominent function in primary cilia disassembly is NIMA-related Kinase 2 (NEK2). Similar to AURKA and PLK1, NEK2 promotes cilia disassembly before mitosis (Spalluto et al. 2012). Contrary to the effects of HEF1 on AURKA, HEF1 seems to act as a negative regulator of NEK2 activity (Pugacheva and Golemis 2005). Several distinct mechanisms have been proposed to mediate the NEK2 effects on primary cilia dynamics, including through HDAC6 activity regulation (Endicott et al. 2015). Another suggested mechanism is via activation of kinesin 13 member KIF24, which depolymerizes microtubules, resulting in destabilization of the axoneme and cilium resorption (Kim, Lee, et al. 2015). Furthermore, NEK2 promotes the displacement of a subset of DA components (namely CEP123/CEP89, CEP164, and LRRC45) from the MC, hence hampering ciliogenesis (Viol et al. 2020). Several other members of the NIMA-related kinase family, namely NEK1 in the context of short-rib polydactyly syndrome type Majewski (Thiel et al. 2011), NEK8 in nephronophthisis (Otto et al. 2008), and NEK9 in relation to lethal skeletal dysplasia (Casey et al. 2016), are linked to cilia regulation via their described ciliopathy mutations. While the phenotypes of the corresponding mouse models include deregulated cilia numbers and kidney cyst formation, the exact roles of these NEKs in primary cilia dynamics remain elusive (Otto et al. 2008; Quarmby and Mahjoub 2005; Upadhyaya et al. 2000).

Several kinases have been indicated to indirectly promote cilia resorption via their effects on actin polymerization and, thus, the levels of F-actin within the cell. While there is currently no report of direct modulation of ciliary actin by kinases, compelling evidence links kinase-mediated regulation of the actin cytoskeleton to the regulation of primary cilia (Guen et al. 2016; Kim,

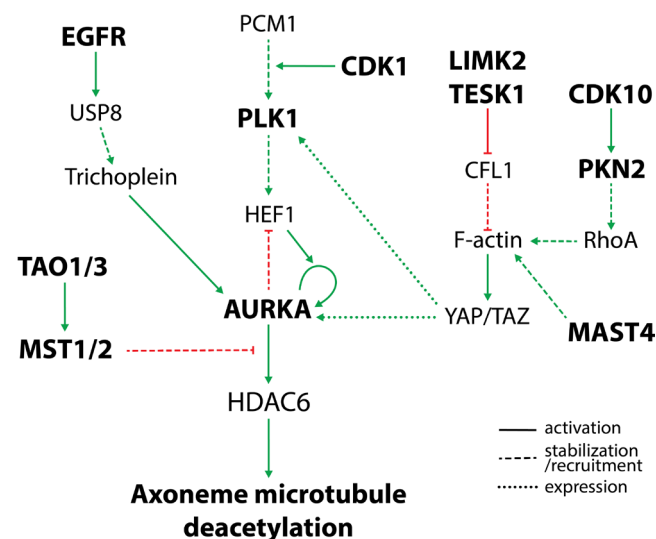


FIGURE 4 | Proposed pathways of AURKA-mediated cilia disassembly regulation several kinases have been linked to the regulation of AURKA activity in the context of cilia resorption. EGFR and PLK1 aid AURKA activity through the stabilization of its activating effectors (TCHP in the case of EGFR and HEF1 in the case of PLK1) and PLK1 activity is enhanced by CDK1-facilitated recruitment to the pericentriolar region. Both AURKA and PLK1 expression levels are upregulated in response to higher F-actin levels, which are enhanced by LIMK2, TESK1, PKN2, CDK10, and MAST4 activity.

Jo, et al. 2015; Sakaji et al. 2023). There are two main mechanisms by which the actin cytoskeleton is thought to affect primary cilia formation. First, a high level of actin polymerization seems to interfere with vesicular trafficking, possibly preventing DAVs and CVs formation/docking and membrane delivery to the growing cilium (Cao et al. 2012; J. Kim et al. 2010). In addition to this negative effect on ciliogenesis, actin polymerization promotes cilia resorption through regulating the expression of at least two kinases driving cilia disassembly—AURKA and PLK1. This second mechanism is mediated by the Hippo signaling pathway, which drives the relocalization of transcription co-activators YAP/TAZ from the cytoplasm into the nucleus (and subsequently the expression of target genes encoding AURKA and PLK1) in cells with increased levels of F-actin (J. Kim, Jo, et al. 2015).

There are several mechanisms for kinases to regulate actin polymerization and, consequently, cilia stability. Kinases LIM Domain Kinase 2 (LIMK2) and Testis Associated Actin Remodeling Kinase 1 (TESK1) positively regulate actin polymerization by inhibiting an actin-cleaving protein, CFL1, which then effectively blocks primary cilia formation in unciliated cells or facilitates cilia resorption in ciliated cells. Conversely, the depletion of LIMK2 or TESK1 promotes ciliogenesis (J. Kim, Jo, et al. 2015). Similarly, Cyclin-Dependent Kinase 10 (CDK10) in a heterodimer with cyclin M phosphorylates Protein Kinase N2 (PKN2), which in turn stabilizes small GTPase RhoA, one of the key regulators of actin polymerization (Guen et al. 2016). Ablation of CDK10-cyclin M activity produces developmental defects in vivo and elongated cilia axonemes in mouse fibroblasts (Guen et al. 2016). Moreover, the activity of Microtubule Associated Serine/Threonine Kinase Family Member 4 (MAST4) facilitates cilia disassembly through the activation of another key regulator of actin polymerization, small GTPase CDC42, and its downstream effector Arp2/3. Intriguingly, CDC42 has recently been identified as the main regulator of ciliary actin and a trigger of ciliary ectocytosis (Prasai et al. 2024), which might suggest an additional mechanism for MAST4 to promote cilia disassembly. In addition to regulating actin branching, MAST4 also activates Rab5-modulated periciliary membrane endocytosis to further promote cilia resorption (Sakaji et al. 2023). It is worth noting that all of these kinases were recognized as residing at the centrosome or in cilia (Guen et al. 2016; J. Kim, Jo, et al. 2015; Patel et al. 2020; Sakaji et al. 2023), suggesting that their involvement in regulating cilia resorption might not be restricted to actin network remodeling, and other regulatory mechanisms, potentially more prominent, await identification.

2.3 | Conclusions and Future Outlook

Our noted examples of kinase involvement in primary cilia assembly and disassembly only represent a partial picture. A dozen or more kinases found to be mutated in ciliopathies are expected to impact primary cilia status (Reiter and Leroux 2017). While genetic evidence linking particular genes and cilia-associated pathologies is well manifested, the underlying mechanism is often, unfortunately, completely lacking. Expository, as previously stated, several NEK kinases family members (namely NEK1 (Thiel et al. 2011), NEK2 (Fakhro et al. 2011), NEK8 (Otto et al. 2008) and NEK9 (Casey et al. 2016)) have been identified

as ciliopathy genes. However, in contrast to the established role of NEK2, mechanisms mediating the roles of the other NEKs remain largely unclear. Other kinases involved in ciliopathies, such as Protein Kinase A (PKA) or STK36/Fused, have well-defined roles in ciliary signaling (particularly in the Hedgehog pathway) rather than in primary cilium biogenesis, hence were not addressed here. We guide our readers instead to recent reviews devoted to the ciliary function of these kinases (Flax et al. 2024; Hilgendorf et al. 2024). Moreover, several screens hinted at possible cilia roles of a number of kinases (Breslow et al. 2018; Kuhns et al. 2013; Loukil et al. 2021), however functional validation and identification of corresponding mechanisms await resolving for most of these putative cilia-regulating kinases. Thus, we envision that our current understanding of ciliary kinases represents the infamous “tip of the iceberg” and that more kinases and kinase-related mechanisms highly relevant to primary cilia biology still await discovery.

As exemplified here by examining the roles of TTBK2 and AURKA, kinases represent prominent regulators of primary cilia assembly, maintenance, and resorption. Yet, the field of ciliary kinases remains relatively understudied. Many open questions persist concerning the exact cascade of events downstream of a particular kinase. When considering sub-cellular/sub-ciliary localization of cilia-regulating kinases, there is clearly some degree of compartmentalization. In certain cases, the link between localization and function seems straightforward (e.g., CILK1/ICK and MAK localize inside primary cilia to regulate IFT), while in others the connection is less obvious (e.g., TTBK2 or AURKA are enriched at the cilia base, yet missing from intraciliary milieu, where events affecting axoneme stabilization/destabilization presumably take place). The main bottleneck with any kinase study has always been establishing a kinase-substrate relationship and the target-specific function of a given kinase, including elucidation of functional consequences of the phosphorylation of a given substrate specifically for cilia biology. Current biochemical and bioinformatic approaches are estimated to have only identified upstream kinases for less than 5% of the whole phosphoproteome, and functional assignments of identified phosphosites are almost negligible (Needham et al. 2019). Furthermore, progress has been hampered by challenges with specifically perturbing target-specific functions of kinases or, in general, cilia-specific functions of examined proteins. The identification of substrates and individual phosphosites of ciliary kinases will no doubt benefit from recent advances in kinome profiling (Johnson et al. 2023) and high-sensitivity (phospho)proteomics approaches (Needham et al. 2019). Wet lab-based experimental validation of substrates/phosphosites should be facilitated by rapidly developing gene editing techniques, along with the recent surge in AI-based protein structure prediction algorithms, soon likely capable of modeling the impact of PTMs such as phosphorylation.

Acknowledgments

Open access publishing facilitated by Masarykova univerzita, as part of the Wiley - CzechELib agreement.

Conflicts of Interest

The authors declare no conflicts of interest.

Data Availability Statement

The authors have nothing to report.

References

- Amack, J. D. 2022. "Structures and Functions of Cilia During Vertebrate Embryo Development." *Molecular Reproduction and Development* 89, no. 12: 579–596. <https://doi.org/10.1002/mrd.23650>.
- Anvarian, Z., K. Mykityn, S. Mukhopadhyay, L. B. Pedersen, and S. T. Christensen. 2019. "Cellular Signalling by Primary Cilia in Development, Organ Function and Disease." *Nature Reviews. Nephrology* 15, no. 4: 199–219. <https://doi.org/10.1038/s41581-019-0116-9>.
- Bangs, F., and K. V. Anderson. 2017. "Primary Cilia and Mammalian Hedgehog Signaling." *Cold Spring Harbor Perspectives in Biology* 9, no. 5: a028175. <https://doi.org/10.1101/cshperspect.a028175>.
- Berman, S. A., N. F. Wilson, N. A. Haas, and P. A. Lefebvre. 2003. "A Novel MAP Kinase Regulates Flagellar Length in Chlamydomonas." *Current Biology* 13, no. 13: 1145–1149. [https://doi.org/10.1016/S0960-9822\(03\)00415-9](https://doi.org/10.1016/S0960-9822(03)00415-9).
- Bernatik, O., P. Pejškova, D. Vysloulzil, K. Hanakova, Z. Zdrahal, and L. Cajanek. 2020. "Phosphorylation of Multiple Proteins Involved in Ciliogenesis by Tau Tubulin Kinase 2." *Molecular Biology of the Cell* 31, no. 10: 1032–1046. <https://doi.org/10.1091/mbc.E19-06-0334>.
- Bhogaraju, S., L. Cajanek, C. Fort, et al. 2013. "Molecular Basis of Tubulin Transport Within the Cilium by IFT74 and IFT81." *Science* 341, no. 6149: 1009–1012. <https://doi.org/10.1126/science.1240985>.
- Binó, L., and L. Čajánek. 2023. "Tau Tubulin Kinase 1 and 2 Regulate Ciliogenesis and Human Pluripotent Stem Cells-Derived Neural Rosettes." *Scientific Reports* 13, no. 1: 12–884. <https://doi.org/10.1038/s41598-023-39887-9>.
- Boggiano, J. C., P. J. Vanderzalm, and R. G. Fehon. 2011. "Tao-1 Phosphorylates Hippo/MST Kinases to Regulate the Hippo-Salvador-Warts Tumor Suppressor Pathway." *Developmental Cell* 21, no. 5: 888–895. <https://doi.org/10.1016/j.devcel.2011.08.028>.
- Bowie, E., and S. C. Goetz. 2020. "TTBK2 and Primary Cilia Are Essential for the Connectivity and Survival of Cerebellar Purkinje Neurons." *eLife* 9: e51166. <https://doi.org/10.7554/eLife.51166>.
- Bowie, E., R. Norris, K. V. Anderson, and S. C. Goetz. 2018. "Spinocerebellar Ataxia Type 11-Associated Alleles of Ttbk2 Dominantly Interfere With Ciliogenesis and Cilium Stability." *PLoS Genetics* 14, no. 12: e1007844. <https://doi.org/10.1371/journal.pgen.1007844>.
- Breslow, D. K., S. Hoogendoorn, A. R. Kopp, et al. 2018. "A CRISPR-Based Screen for Hedgehog Signaling Provides Insights Into Ciliary Function and Ciliopathies." *Nature Genetics* 50, no. 3: 460–471. <https://doi.org/10.1038/s41588-018-0054-7>.
- Broekhuis, J. R., K. J. Verhey, and G. Jansen. 2014. "Regulation of Cilium Length and Intraflagellar Transport by the RCK-Kinases ICK and MOK in Renal Epithelial Cells." *PLoS One* 9, no. 9: e108470. <https://doi.org/10.1371/journal.pone.0108470>.
- Bryja, V., I. Cervenka, and L. Cajanek. 2017. "The Connections of Wnt Pathway Components With Cell Cycle and Centrosome: Side Effects or a Hidden Logic?" *Critical Reviews in Biochemistry and Molecular Biology* 52, no. 6: 614–637. <https://doi.org/10.1080/10409238.2017.1350135>.
- Burghoorn, J., M. P. J. Dekkers, S. Rademakers, T. de Jong, R. Willemsen, and G. Jansen. 2007. "Mutation of the MAP Kinase DYF-5 Affects Docking and Undocking of Kinesin-2 Motors and Reduces Their Speed in the Cilia of Caenorhabditis Elegans." *Proceedings of the National Academy of Sciences* 104, no. 17: 7157–7162. <https://doi.org/10.1073/pnas.0606974104>.
- Čajánek, L., and E. A. Nigg. 2014. "Cep164 Triggers Ciliogenesis by Recruiting Tau Tubulin Kinase 2 to the Mother Centriole." *Proceedings of the National Academy of Sciences of the United States of America* 111, no. 28: E2841–E2850. <https://doi.org/10.1073/pnas.1401777111>.
- Cao, J., Y. Shen, L. Zhu, et al. 2012. "Mir-129-3p Controls Cilia Assembly by Regulating CP110 and Actin Dynamics." *Nature Cell Biology* 14, no. 7: 697–706. <https://doi.org/10.1038/ncb2512>.
- Casey, J. P., K. Brennan, N. Scheidel, et al. 2016. "Recessive NEK9 Mutation Causes a Lethal Skeletal Dysplasia With Evidence of Cell Cycle and Ciliary Defects." *Human Molecular Genetics* 25, no. 9: 1824–1835. <https://doi.org/10.1093/hmg/ddw054>.
- Chang, T.-J. B., J. C.-C. Hsu, and T. T. Yang. 2023. "Single-Molecule Localization Microscopy Reveals the Ultrastructural Constitution of Distal Appendages in Expanded Mammalian Centrioles." *Nature Communications* 14, no. 1: 1688. <https://doi.org/10.1038/s41467-023-37342-x>.
- Chaya, T., Y. Omori, R. Kuwahara, and T. Furukawa. 2014. "ICK Is Essential for Cell Type-Specific Ciliogenesis and the Regulation of Ciliary Transport." *EMBO Journal* 33, no. 11: 1227–1242. <https://doi.org/10.1002/embj.201488175>.
- Chen, Z., V. B. Indjeian, M. McManus, L. Wang, and B. D. Dynlacht. 2002. "CP110, a Cell Cycle-Dependent CDK Substrate, Regulates Centrosome Duplication in Human Cells." *Developmental Cell* 3, no. 3: 339–350. [https://doi.org/10.1016/s1534-5807\(02\)00258-7](https://doi.org/10.1016/s1534-5807(02)00258-7).
- Chhatre, A., L. Stepanek, A. P. Nievergelt, G. Alvarez Viar, S. Diez, and G. Pigino. 2025. "Tubulin Tyrosination/Detyrosination Regulate the Affinity and Sorting of Intraflagellar Transport Trains on Axonemal Microtubule Doublets." *Nature Communications* 16, no. 1: 1055. <https://doi.org/10.1038/s41467-025-56098-0>.
- Civiero, L., M. D. Cirnar, A. Beilina, et al. 2015. "Leucine-Rich Repeat Kinase 2 Interacts With p21-Activated Kinase 6 to Control Neurite Complexity in Mammalian Brain." *Journal of Neurochemistry* 135, no. 6: 1242–1256. <https://doi.org/10.1111/jnc.13369>.
- Constable, S., C. M. Ott, A. L. Lemire, et al. 2024. "Permanent Cilia Loss During Cerebellar Granule Cell Neurogenesis Involves Withdrawal of Cilia Maintenance and Centriole Capping." *Proceedings of the National Academy of Sciences of the United States of America* 121, no. 52: e2408083121. <https://doi.org/10.1073/pnas.2408083121>.
- Deretic, J., E. Odabasi, and E. N. Firat-Karalar. 2023. "The Multifaceted Roles of Microtubule-Associated Proteins in the Primary Cilium and Ciliopathies." *Journal of Cell Science* 136, no. 23: jcs261148. <https://doi.org/10.1242/jcs.261148>.
- Dhekne, H. S., I. Yanatori, E. G. Vides, et al. 2021. "LRRK2-Phosphorylated Rab10 Sequesters Myosin Va With RILPL2 During Ciliogenesis Blockade." *Life Science Alliance* 4, no. 5: e202101050. <https://doi.org/10.26508/lsa.202101050>.
- Doornbos, C., and R. Roepman. 2021. "Moonlighting of Mitotic Regulators in Cilium Disassembly." *Cellular and Molecular Life Sciences* 78, no. 11: 4955–4972. <https://doi.org/10.1007/s00018-021-03827-5>.
- Endicott, S. J., B. Basu, M. Khokha, and M. Brueckner. 2015. "The NIMA-Like Kinase Nek2 Is a Key Switch Balancing Cilia Biogenesis and Resorption in the Development of Left-Right Asymmetry." *Development* 142, no. 23: 4068–4079. <https://doi.org/10.1242/dev.126953>.
- Fakhro, K. A., M. Choi, S. M. Ware, et al. 2011. "Rare Copy Number Variations in Congenital Heart Disease Patients Identify Unique Genes in Left-Right Patterning." *Proceedings of the National Academy of Sciences of the United States of America* 108, no. 7: 2915–2920. <https://doi.org/10.1073/pnas.1019645108>.
- Flax, R. G., P. Rosston, C. Rocha, et al. 2024. "Illumination of Understudied Ciliary Kinases." *Frontiers in Molecular Biosciences* 11: 1352781. <https://doi.org/10.3389/fmolb.2024.1352781>.
- Ford, M. J., P. L. Yeyati, G. R. Mali, et al. 2018. "A Cell/Cilia Cycle Biosensor for Single-Cell Kinetics Reveals Persistence of Cilia After

- G1/S Transition Is a General Property in Cells and Mice." *Developmental Cell* 47, no. 4: 509–523. <https://doi.org/10.1016/j.devcel.2018.10.027>.
- Gailey, C. D., E. J. Wang, L. Jin, et al. 2021. "Phosphosite T674A Mutation in Kinesin Family Member 3A Fails to Reproduce Tissue and Ciliary Defects Characteristic of CILK1 Loss of Function." *Developmental Dynamics* 250, no. 2: 263–273. <https://doi.org/10.1002/dvdy.252>.
- Ganga, A. K., M. C. Kennedy, M. E. Oguchi, et al. 2021. "Rab34 GTPase Mediates Ciliary Membrane Formation in the Intracellular Ciliogenesis Pathway." *Current Biology* 31, no. 13: 2895–2905. <https://doi.org/10.1016/j.cub.2021.04.075>.
- Garcia-Gonzalo, F. R., and J. F. Reiter. 2017. "Open Sesame: How Transition Fibers and the Transition Zone Control Ciliary Composition." *Cold Spring Harbor Perspectives in Biology* 9, no. 2: a028134. <https://doi.org/10.1101/cshperspect.a028134>.
- Goetz, S. C., K. F. Liem, and K. V. Anderson. 2012. "The Spinocerebellar Ataxia-Associated Gene Tau Tubulin Kinase 2 Controls the Initiation of Ciliogenesis." *Cell* 151, no. 4: 847–858. <https://doi.org/10.1016/j.cell.2012.10.010>.
- Gopalakrishnan, J., K. Feistel, B. M. Friedrich, et al. 2023. "Emerging Principles of Primary Cilia Dynamics in Controlling Tissue Organization and Function." *EMBO Journal* 42, no. 21: e113891. <https://doi.org/10.15252/embj.2023113891>.
- Guen, V. J., C. Gamble, D. E. Perez, et al. 2016. "Star Syndrome-Associated CDK10/Cyclin M Regulates Actin Network Architecture and Ciliogenesis." *Cell Cycle* 15, no. 5: 678–688. <https://doi.org/10.1080/15384101.2016.1147632>.
- Hilgendorf, K. I., B. R. Myers, and J. F. Reiter. 2024. "Emerging Mechanistic Understanding of Cilia Function in Cellular Signalling." *Nature Reviews Molecular Cell Biology* 25, no. 7: 555–573. <https://doi.org/10.1038/s41580-023-00698-5>.
- Hilton, L. K., K. Gunawardane, J. W. Kim, M. C. Schwarz, and L. M. Quarumby. 2013. "The Kinases LF4 and CNK2 Control Ciliary Length by Feedback Regulation of Assembly and Disassembly Rates." *Current Biology: CB* 23, no. 22: 2208–2214. <https://doi.org/10.1016/j.cub.2013.09.038>.
- Iannotta, L., R. Fasiczka, G. Favetta, et al. 2024. "PAK6 Rescues Pathogenic LRRK2-Mediated Ciliogenesis and Centrosomal Cohesion Defects in a Mutation-Specific Manner." *Cell Death & Disease* 15, no. 10: 1–14. <https://doi.org/10.1038/s41419-024-07124-4>.
- Inoko, A., M. Matsuyama, H. Goto, et al. 2012. "Trichoplein and Aurora A Block Aberrant Primary Cilia Assembly in Proliferating Cells." *Journal of Cell Biology* 197, no. 3: 391–405. <https://doi.org/10.1083/jcb.201106101>.
- Ishikawa, H., and W. F. Marshall. 2011. "Ciliogenesis: Building the Cell's Antenna." *Nature Reviews Molecular Cell Biology* 12, no. 4: 222–234. <https://doi.org/10.1038/nrm3085>.
- Iyer, S. S., F. Chen, F. E. Ogunmolu, et al. 2025. "Centriolar Cap Proteins CP110 and CPAP Control Slow Elongation of Microtubule Plus Ends." *Journal of Cell Biology* 224, no. 3: e202406061. <https://doi.org/10.1083/jcb.202406061>.
- Jacob, L. S., X. Wu, M. E. Dodge, et al. 2011. "Genome-Wide RNAi Screen Reveals Disease-Associated Genes That Are Common to Hedgehog and Wnt Signaling." *Science Signaling* 4, no. 157: 2001225. <https://doi.org/10.1126/scisignal.2001225>.
- Janke, C., and M. M. Magiera. 2020. "The Tubulin Code and Its Role in Controlling Microtubule Properties and Functions." *Nature Reviews. Molecular Cell Biology* 21, no. 6: 307–326. <https://doi.org/10.1038/s41580-020-0214-3>.
- Jiang, X., W. Shao, Y. Chai, et al. 2022. "DYF-5/MAK-Dependent Phosphorylation Promotes Ciliary Tubulin Unloading." *Proceedings of the National Academy of Sciences of the United States of America* 119, no. 34: e2207134119. <https://doi.org/10.1073/pnas.2207134119>.
- Johnson, J. L., T. M. Yaron, E. M. Huntsman, et al. 2023. "An Atlas of Substrate Specificities for the Human Serine/Threonine Kinome." *Nature* 613, no. 7945: 759–766. <https://doi.org/10.1038/s41586-022-05575-3>.
- Kanie, T., B. Liu, J. F. Love, S. D. Fisher, A.-K. Gustavsson, and P. K. Jackson. 2025. "A Hierarchical Pathway for Assembly of the Distal Appendages That Organize Primary Cilia." *eLife* 14: e85999. <https://doi.org/10.7554/eLife.85999>.
- Kasahara, K., H. Aoki, T. Kiyono, et al. 2018. "EGF Receptor Kinase Suppresses Ciliogenesis Through Activation of USP8 Deubiquitinase." *Nature Communications* 9, no. 1: 758. <https://doi.org/10.1038/s41467-018-03117-y>.
- Kiesel, P., G. Alvarez Viar, N. Tsoy, et al. 2020. "The Molecular Structure of Mammalian Primary Cilia Revealed by Cryo-Electron Tomography." *Nature Structural & Molecular Biology* 27, no. 12: 1115–1124. <https://doi.org/10.1038/s41594-020-0507-4>.
- Kim, J., H. Jo, H. Hong, et al. 2015. "Actin Remodelling Factors Control Ciliogenesis by Regulating YAP/TAZ Activity and Vesicle Trafficking." *Nature Communications* 6, no. 1: 6781. <https://doi.org/10.1038/ncomm57781>.
- Kim, J., J. E. Lee, S. Heynen-Genel, et al. 2010. "Functional Genomic Screen for Modulators of Ciliogenesis and Cilium Length." *Nature* 464, no. 7291: 1048–1051. <https://doi.org/10.1038/nature08895>.
- Kim, M., M. Kim, M.-S. Lee, C.-H. Kim, and D.-S. Lim. 2014. "The MST1/2-SAV1 Complex of the Hippo Pathway Promotes Ciliogenesis." *Nature Communications* 5, no. 1: 5370. <https://doi.org/10.1038/ncomm56370>.
- Kim, S., K. Lee, J.-H. Choi, N. Ringstad, and B. D. Dynlacht. 2015. "Nek2 Activation of Kif24 Ensures Cilium Disassembly During the Cell Cycle." *Nature Communications* 6: 8087. <https://doi.org/10.1038/ncomms9087>.
- Kong, D., V. Farmer, A. Shukla, et al. 2014. "Centriole Maturation Requires Regulated Plk1 Activity During Two Consecutive Cell Cycles." *Journal of Cell Biology* 206, no. 7: 855–865. <https://doi.org/10.1083/jcb.201407087>.
- Kuhns, S., K. N. Schmidt, J. Reymann, et al. 2013. "The Microtubule Affinity Regulating Kinase MARK4 Promotes Axoneme Extension During Early Ciliogenesis." *Journal of Cell Biology* 200, no. 4: 505–522. <https://doi.org/10.1083/jcb.201206013>.
- Kunova Bosakova, M., M. Varecha, M. Hampl, et al. 2018. "Regulation of Ciliary Function by Fibroblast Growth Factor Signaling Identifies FGFR3-Related Disorders Achondroplasia and Thanatophoric Dysplasia as Ciliopathies." *Human Molecular Genetics* 27, no. 6: 1093–1105. <https://doi.org/10.1093/hmg/ddy031>.
- Lacey, S. E., and G. Pigino. 2024. "The Intraflagellar Transport Cycle." *Nature Reviews Molecular Cell Biology* 26, no. 3: 1–18. <https://doi.org/10.1038/s41580-024-00797-x>.
- Lee, K. H., Y. Johmura, L.-R. Yu, et al. 2012. "Identification of a Novel Wnt5a-CK1ε-Dvl2-Plk1-Mediated Primary Cilia Disassembly Pathway." *EMBO Journal* 31, no. 14: 3104–3117. <https://doi.org/10.1038/emboj.2012.144>.
- Lin, I.-H., Y.-R. Li, C.-H. Chang, et al. 2024. "Regulation of Primary Cilia Disassembly Through HUWE1-Mediated TTBK2 Degradation Plays a Crucial Role in Cerebellar Development and Medulloblastoma Growth." *Cell Death and Differentiation* 31, no. 10: 1349–1361. <https://doi.org/10.1038/s41418-024-01325-2>.
- Lizcano, J. M., O. Göransson, R. Toth, et al. 2004. "LKB1 Is a Master Kinase That Activates 13 Kinases of the AMPK Subfamily, Including MARK/PAR-1." *EMBO Journal* 23, no. 4: 833–843. <https://doi.org/10.1038/sj.emboj.7600110>.
- Lo, C.-H., I.-H. Lin, T. T. Yang, et al. 2019. "Phosphorylation of CEP83 by TTBK2 Is Necessary for Cilia Initiation." *Journal of Cell Biology* 218, no. 10: 3489–3505. <https://doi.org/10.1083/jcb.201811142>.

- Loukil, A., C. Barrington, and S. C. Goetz. 2021. "A Complex of Distal Appendage-Associated Kinases Linked to Human Disease Regulates Ciliary Trafficking and Stability." *Proceedings of the National Academy of Sciences of the United States of America* 118, no. 16: e2018740118. <https://doi.org/10.1073/pnas.2018740118>.
- Lu, Q., C. Insinna, C. Ott, et al. 2015. "Early Steps in Primary Cilium Assembly Require EHD1/EHD3-Dependent Ciliary Vesicle Formation." *Nature Cell Biology* 17, no. 3: 228–240. <https://doi.org/10.1038/ncb3109>.
- Łysyganicz, P. K., N. Pooranachandran, X. Liu, et al. 2021. "Loss of Deacetylation Enzymes Hdac6 and Sirt2 Promotes Acetylation of Cytoplasmic Tubulin, but Suppresses Axonemal Acetylation in Zebrafish Cilia." *Frontiers in Cell and Developmental Biology* 9: 676214. <https://doi.org/10.3389/fcell.2021.676214>.
- Ma, D., F. Wang, J. Teng, N. Huang, and J. Chen. 2023. "Structure and Function of Distal and Subdistal Appendages of the Mother Centriole." *Journal of Cell Science* 136, no. 3: jcs260560. <https://doi.org/10.1242/jcs.260560>.
- Maurya, A. K., T. Rogers, and P. Sengupta. 2019. "A CCRK and a MAK Kinase Modulate Cilia Branching and Length via Regulation of Axonemal Microtubule Dynamics in *Caenorhabditis Elegans*." *Current Biology: CB* 29, no. 8: 1286–1300. <https://doi.org/10.1016/j.cub.2019.02.062>.
- Mill, P., S. T. Christensen, and L. B. Pedersen. 2023. "Primary Cilia as Dynamic and Diverse Signalling Hubs in Development and Disease." *Nature Reviews. Genetics* 24, no. 7: 421–441. <https://doi.org/10.1038/s41576-023-00587-9>.
- Mirvis, M., K. A. Siemers, W. J. Nelson, and T. P. Stearns. 2019. "Primary Cilium Loss in Mammalian Cells Occurs Predominantly by Whole-Cilium Shedding." *PLoS Biology* 17, no. 7: e3000381. <https://doi.org/10.1371/journal.pbio.3000381>.
- Miyamoto, T., K. Hosoba, H. Ochiai, et al. 2015. "The Microtubule-Depolymerizing Activity of a Mitotic Kinesin Protein KIF2A Drives Primary Cilia Disassembly Coupled With Cell Proliferation." *Cell Reports* 10: 664–673. <https://doi.org/10.1016/j.celrep.2015.01.003>.
- Nager, A. R., J. S. Goldstein, V. Herranz-Pérez, et al. 2017. "An Actin Network Dispatches Ciliary GPCRs Into Extracellular Vesicles to Modulate Signaling." *Cell* 168, no. 1–2: 252–263. <https://doi.org/10.1016/j.cell.2016.11.036>.
- Nakamura, K., T. Noguchi, M. Takahara, et al. 2020. "Anterograde Trafficking of Ciliary MAP Kinase-Like ICK/CILK1 by the Intraflagellar Transport Machinery Is Required for Intraciliary Retrograde Protein Trafficking." *Journal of Biological Chemistry* 295, no. 38: 13363–13376. <https://doi.org/10.1074/jbc.RA120.014142>.
- Needham, E. J., B. L. Parker, T. Burykin, D. E. James, and S. J. Humphrey. 2019. "Illuminating the Dark Phosphoproteome." *Science Signaling* 12, no. 565: eaau8645. <https://doi.org/10.1126/scisignal.aau8645>.
- Nguyen, A., and S. C. Goetz. 2023. "TTBK2 Controls Cilium Stability by Regulating Distinct Modules of Centrosomal Proteins." *Molecular Biology of the Cell* 34, no. 1: ar8. <https://doi.org/10.1091/mbc.E22-08-0373>.
- Nigg, E. A., L. Čajánek, and C. Arquint. 2014. "The Centrosome Duplication Cycle in Health and Disease." *FEBS Letters* 588, no. 15: 2366–2372. <https://doi.org/10.1016/j.febslet.2014.06.030>.
- Ott, C. M., S. Constable, T. M. Nguyen, et al. 2024. "Permanent Deconstruction of Intracellular Primary Cilia in Differentiating Granule Cell Neurons." *Journal of Cell Biology* 223, no. 10: e202404038. <https://doi.org/10.1083/jcb.202404038>.
- Otto, E. A., M. L. Trapp, U. T. Schultheiss, J. Helou, L. M. Quarmbly, and F. Hildebrandt. 2008. "NEK8 Mutations Affect Ciliary and Centrosomal Localization and May Cause Nephronophthisis." *Journal of the American Society of Nephrology: JASN* 19, no. 3: 587. <https://doi.org/10.1681/ASN.2007040490>.
- Pan, J., Q. Wang, and W. J. Snell. 2004. "An Aurora Kinase Is Essential for Flagellar Disassembly in *Chlamydomonas*." *Developmental Cell* 6, no. 3: 445–451. [https://doi.org/10.1016/s1534-5807\(04\)00064-4](https://doi.org/10.1016/s1534-5807(04)00064-4).
- Park, K., and M. R. Leroux. 2022. "Composition, Organization and Mechanisms of the Transition Zone, a Gate for the Cilium." *EMBO Reports* 23, no. 12: e55420. <https://doi.org/10.15252/embr.202255420>.
- Patel, H., J. Li, A. Herrero, et al. 2020. "Novel Roles of PRK1 and PRK2 in Cilia and Cancer Biology." *Scientific Reports* 10, no. 1: 3902. <https://doi.org/10.1038/s41598-020-60604-3>.
- Pedersen, L. B., and J. L. Rosenbaum. 2008. "Chapter Two Intraflagellar Transport (IFT): Role in Cilium Assembly, Resorption and Signalling." In *Current Topics in Developmental Biology*, vol. 85, 23–61. Academic Press. [https://doi.org/10.1016/S0070-2153\(08\)00802-8](https://doi.org/10.1016/S0070-2153(08)00802-8).
- Phua, S. C., S. Chiba, M. Suzuki, et al. 2017. "Dynamic Remodeling of Membrane Composition Drives Cell Cycle Through Primary Cilia Excision." *Cell* 168, no. 1–2: 264–279. <https://doi.org/10.1016/j.cell.2016.12.032>.
- Plotnikova, O. V., A. S. Nikonova, Y. V. Loskutov, P. Y. Kozyulina, E. N. Pugacheva, and E. A. Golemis. 2012. "Calmodulin Activation of Aurora-A Kinase (AURKA) Is Required During Ciliary Disassembly and in Mitosis." *Molecular Biology of the Cell* 23, no. 14: 2658–2670. <https://doi.org/10.1091/mbc.e11-12-1056>.
- Poon, C. L. C., J. I. Lin, X. Zhang, and K. F. Harvey. 2011. "The Sterile 20-Like Kinase Tao-1 Controls Tissue Growth by Regulating the Salvador-Warts-Hippo Pathway." *Developmental Cell* 21, no. 5: 896–906. <https://doi.org/10.1016/j.devcel.2011.09.012>.
- Prasai, A., O. Ivashchenko, K. Maskova, et al. 2024. "Bbsome-Deficient Cells Activate Intraciliary CDC42 to Trigger Actin-Dependent Ciliary Ectocytosis." *EMBO Reports* 26, no. 1: 36–60. <https://doi.org/10.1038/s44319-024-00326-z>.
- Pugacheva, E. N., and E. A. Golemis. 2005. "The Focal Adhesion Scaffolding Protein HEF1 Regulates Activation of the Aurora-A and Nek2 Kinases at the Centrosome." *Nature Cell Biology* 7, no. 10: 937–946. <https://doi.org/10.1038/ncb1309>.
- Pugacheva, E. N., S. A. Jablonski, T. R. Hartman, E. P. Henske, and E. A. Golemis. 2007. "HEF1-Dependent Aurora A Activation Induces Disassembly of the Primary Cilium." *Cell* 129, no. 7: 1351–1363. <https://doi.org/10.1016/j.cell.2007.04.035>.
- Quarmbly, L. M. 2004. "Cellular Deflagellation." *International Review of Cytology* 233: 47–91. [https://doi.org/10.1016/S0074-7696\(04\)33002-0](https://doi.org/10.1016/S0074-7696(04)33002-0).
- Quarmbly, L. M., and M. R. Mahjoub. 2005. "Caught Nek-Ing: Cilia and Centrioles." *Journal of Cell Science* 118, no. 22: 5161–5169. <https://doi.org/10.1242/jcs.02681>.
- Reilly, M. L., and A. Benmerah. 2019. "Ciliary Kinesins Beyond IFT: Cilium Length, Disassembly, Cargo Transport and Signalling." *Biology of the Cell* 111, no. 4: 79–94. <https://doi.org/10.1111/boc.201800074>.
- Reiter, J. F., and M. R. Leroux. 2017. "Genes and Molecular Pathways Underpinning Ciliopathies." *Nature Reviews. Molecular Cell Biology* 18, no. 9: 533–547. <https://doi.org/10.1038/nrm.2017.60>.
- Sakaji, K., S. Ebrahimiazar, Y. Harigae, et al. 2023. "MAST4 Promotes Primary Ciliary Resorption Through Phosphorylation of Tctex-1." *Life Science Alliance* 6, no. 11: e202301947. <https://doi.org/10.26508/lsa.202301947>.
- Schmidt, T. I., J. Kleylein-Sohn, J. Westendorf, et al. 2009. "Control of Centriole Length by CPAP and CP110." *Current Biology: CB* 19, no. 12: 1005–1011. <https://doi.org/10.1016/j.cub.2009.05.016>.
- Scholey, J. M. 2008. "Intraflagellar Transport Motors in Cilia: Moving Along the Cell's Antenna." *Journal of Cell Biology* 180, no. 1: 23–29. <https://doi.org/10.1083/jcb.200709133>.

- Seeley, E. S., and M. V. Nachury. 2010. "The Perennial Organelle: Assembly and Disassembly of the Primary Cilium." *Journal of Cell Science* 123, no. 4: 511–518. <https://doi.org/10.1242/jcs.061093>.
- Seki, A., J. A. Coppinger, C.-Y. Jang, J. R. Yates III, and G. Fang. 2008. "Bora and Aurora A Cooperatively Activate Plk1 and Control the Entry Into Mitosis." *Science* 320, no. 5883: 1655. <https://doi.org/10.1126/science.1157425>.
- Shakya, S., and C. J. Westlake. 2021. "Recent Advances in Understanding Assembly of the Primary Cilium Membrane." *Faculty Reviews* 10: 16. <https://doi.org/10.12703/r/10-16>.
- Silva, I. R. e., L. Binó, C. M. Johnson, et al. 2022. "Molecular Mechanisms Underlying the Role of the Centriolar CEP164-TTBK2 Complex in Ciliopathies." *Structure* 30, no. 1: 114. <https://doi.org/10.1016/j.str.2021.08.007>.
- Sobu, Y., P. S. Wawro, H. S. Dhekne, W. M. Yeshaw, and S. R. Pfeffer. 2021. "Pathogenic LRRK2 Regulates Ciliation Probability Upstream of Tau Tubulin Kinase 2 via Rab10 and RILPL1 Proteins." *Proceedings of the National Academy of Sciences* 118, no. 10: e2005894118. <https://doi.org/10.1073/pnas.2005894118>.
- Sorokin, S. 1962. "Centrioles and the Formation of Rudimentary Cilia by Fibroblasts and Smooth Muscle Cells." *Journal of Cell Biology* 15: 363–377.
- Spalluto, C., D. I. Wilson, and T. Hearn. 2012. "Nek2 Localises to the Distal Portion of the Mother Centriole/Basal Body and Is Required for Timely Cilium Disassembly at the G2/M Transition." *European Journal of Cell Biology* 91, no. 9: 675–686. <https://doi.org/10.1016/j.ejcb.2012.03.009>.
- Spektor, A., W. Y. Tsang, D. Khoo, and B. D. Dynlacht. 2007. "Cep97 and CP110 Suppress a Cilia Assembly Program." *Cell* 130, no. 4: 678–690. <https://doi.org/10.1016/j.cell.2007.06.027>.
- Steger, M., F. Diez, H. S. Dhekne, et al. 2017. "Systematic Proteomic Analysis of LRRK2-Mediated Rab GTPase Phosphorylation Establishes a Connection to Ciliogenesis." *eLife* 6: e31012. <https://doi.org/10.7554/eLife.31012>.
- Stoetzel, C., S. Bär, J.-O. De Craene, et al. 2016. "A Mutation in VPS15 (PIK3R4) Causes a Ciliopathy and Affects IFT20 Release From the Cis-Golgi." *Nature Communications* 7, no. 13: 586. <https://doi.org/10.1038/ncomms13586>.
- Stuck, M. W., W. M. Chong, J.-C. Liao, and G. J. Pazour. 2021. "Rab34 Is Necessary for Early Stages of Intracellular Ciliogenesis." *Current Biology: CB* 31, no. 13: 2887–2894. <https://doi.org/10.1016/j.cub.2021.04.018>.
- Sun, S., R. L. Fisher, S. S. Bowser, B. T. Pentecost, and H. Sui. 2019. "Three-Dimensional Architecture of Epithelial Primary Cilia." *Proceedings of the National Academy of Sciences of the United States of America* 116, no. 19: 9370–9379. <https://doi.org/10.1073/pnas.1821064116>.
- Tanos, B. E., H. J. Yang, R. Soni, et al. 2013. "Centriole Distal Appendages Promote Membrane Docking, Leading to Cilia Initiation." *Genes & Development* 27, no. 2: 163–168. <https://doi.org/10.1101/gad.207043.112>.
- Taylor, L. M., P. J. McMillan, B. C. Kraemer, and N. F. Liachko. 2019. "Tau Tubulin Kinases in Proteinopathy." *FEBS Journal* 286, no. 13: 2434–2446. <https://doi.org/10.1111/febs.14866>.
- Thiel, C., K. Kessler, A. Giessler, et al. 2011. "NEK1 Mutations Cause Short-Rib Polydactyly Syndrome Type Majewski." *American Journal of Human Genetics* 88, no. 1: 106–114. <https://doi.org/10.1016/j.ajhg.2010.12.004>.
- Upadhyay, P., E. H. Birkenmeier, C. S. Birkenmeier, and J. E. Barker. 2000. "Mutations in a NIMA-Related Kinase Gene, Nek1, Cause Pleiotropic Effects Including a Progressive Polycystic Kidney Disease in Mice." *Proceedings of the National Academy of Sciences* 97, no. 1: 217–221. <https://doi.org/10.1073/pnas.97.1.217>.
- Viol, L., S. Hata, A. Pastor-Pedro, et al. 2020. "Nek2 Kinase Displaces Distal Appendages From the Mother Centriole Prior to Mitosis." *Journal of Cell Biology* 219, no. 3: e201907136. <https://doi.org/10.1083/jcb.201907136>.
- Vysloužil, B. D., O. Bernatík, E. Lánská, et al. 2025. "Tau-Tubulin Kinase 2 Restrains Microtubule-Depolymerizer KIF2A to Support Primary Cilia Growth." *Cell Communication and Signaling* 23, no. 1: 73. <https://doi.org/10.1186/s12964-025-02072-8>.
- Walentek, P., I. K. Quigley, D. I. Sun, U. K. Sajjan, C. Kintner, and R. M. Harland. 2016. "Ciliary Transcription Factors and miRNAs Precisely Regulate Cp110 Levels Required for Ciliary Adhesions and Ciliogenesis." *eLife* 5: e17557. <https://doi.org/10.7554/eLife.17557>.
- Wang, G., Q. Chen, X. Zhang, et al. 2013. "PCM1 Recruits Plk1 to Pericentriolar Matrix to Promote Primary Cilia Disassembly Before Mitotic Entry." *Journal of Cell Science* 126, no. 6: 1355–1365. <https://doi.org/10.1242/jcs.114918>.
- Watanabe, T., M. Kakeno, T. Matsui, et al. 2015. "TTBK2 With EB1/3 Regulates Microtubule Dynamics in Migrating Cells Through KIF2A Phosphorylation." *Journal of Cell Biology* 210, no. 5: 737–751. <https://doi.org/10.1083/jcb.201412075>.
- Wells, C. M., and G. E. Jones. 2010. "The Emerging Importance of Group II PAKs." *Biochemical Journal* 425, no. 3: 465–473. <https://doi.org/10.1042/BJ20091173>.
- Wu, C.-T., H.-Y. Chen, and T. K. Tang. 2018. "Myosin-Va Is Required for Preciliary Vesicle Transportation to the Mother Centriole During Ciliogenesis." *Nature Cell Biology* 20, no. 2: 175–185. <https://doi.org/10.1038/s41556-017-0018-7>.
- Xu, Q., Y. Zhang, Q. Wei, Y. Huang, J. Hu, and K. Ling. 2016. "Phosphatidylinositol Phosphate Kinase PIPKIγ and Phosphatase INPP5E Coordinate Initiation of Ciliogenesis." *Nature Communications* 7: 10777. <https://doi.org/10.1038/ncomms10777>.
- Yadav, S. P., N. K. Sharma, C. Liu, L. Dong, T. Li, and A. Swaroop. 2016. "Centrosomal Protein CP110 Controls Maturation of the Mother Centriole During Cilia Biogenesis." *Development (Cambridge, England)* 143, no. 9: 1491–1501. <https://doi.org/10.1242/dev.130120>.
- Yi, P., C. Xie, and G. Ou. 2018. "The Kinases Male Germ Cell-Associated Kinase and Cell Cycle-Related Kinase Regulate Kinesin-2 Motility in Neuronal Cilia." *Traffic* 19, no. 7: 522–535. <https://doi.org/10.1111/tra.12572>.
- Yin, F., Q. Chen, Y. Shi, et al. 2022. "Activation of EGFR-Aurora A Induces Loss of Primary Cilia in Oral Squamous Cell Carcinoma." *Oral Diseases* 28, no. 3: 621–630. <https://doi.org/10.1111/odi.13791>.
- Zhang, B., G. Wang, X. Xu, et al. 2017. "DAZ-Interacting Protein 1 (Dzip1) Phosphorylation by Polo-Like Kinase 1 (Plk1) Regulates the Centriolar Satellite Localization of the BBSome Protein During the Cell Cycle." *Journal of Biological Chemistry* 292, no. 4: 1351–1360. <https://doi.org/10.1074/jbc.M116.765438>.
- Zhang, Y., S. Kwon, T. Yamaguchi, et al. 2008. "Mice Lacking Histone Deacetylase 6 Have Hyperacetylated Tubulin but Are Viable and Develop Normally." *Molecular and Cellular Biology* 28, no. 5: 1688–1701. <https://doi.org/10.1128/MCB.01154-06>.

Appendix 3

Benk Vysloužil D, Bernatík O, Lánská E, Renzová T, Binó L, Lacigová A, Drahošová T, Lánský Z, **Čajánek L***. Tau-tubulin kinase 2 restrains microtubule-depolymerizer KIF2A to support primary cilia growth. *Cell Communication and Signaling*. 2025 Feb 10;23(1):73. doi: 10.1186/s12964-025-02072-8.(JCR 2024, IF = 8.9, Q1 – Cell Biology)

RESEARCH

Open Access



Tau-tubulin kinase 2 restrains microtubule-depolymerizer KIF2A to support primary cilia growth

David Benk Vyslouchil^{1,2}, Ondřej Bernatík^{1,2}, Eva Lánská^{3,4}, Tereza Renzová¹, Lucia Binó¹, Andrea Lacigová¹, Tereza Drahošová¹, Zdeněk Lánský³ and Lukáš Čajánek^{1,2*}

Abstract

Background Primary cilia facilitate cellular signalling and play critical roles in development, homeostasis, and disease. Their assembly is under the control of Tau-Tubulin Kinase 2 (TTBK2), a key enzyme mutated in patients with spinocerebellar ataxia. Recent work has implicated TTBK2 in the regulation of cilia maintenance and function, but the underlying molecular mechanisms are not understood.

Methods To dissect the role of TTBK2 during cilia growth and maintenance in human cells, we examined disease-related TTBK2 truncations. We used biochemical approaches, proteomics, genetic engineering, and advanced microscopy techniques to unveil molecular events triggered by TTBK2.

Results We demonstrate that truncated TTBK2 protein moieties, unable to localize to the mother centriole, create unique semi-permissive conditions for cilia assembly, under which cilia begin to form but fail to elongate. Subsequently, we link the defects in cilia growth to aberrant turnover of a microtubule-depolymerizing kinesin KIF2A, which we find restrained by TTBK2 phosphorylation.

Conclusions Together, our data imply that the regulation of KIF2A by TTBK2 represents an important mechanism governing cilia elongation and maintenance. Further, the requirement for concentrating TTBK2 activity to the mother centriole to initiate ciliogenesis can be under specific conditions bypassed, revealing TTBK2 recruitment-independent functions of its key partner, CEP164.

Keywords Cilia, Ciliogenesis, TTBK2, KIF2A, Basal body

*Correspondence:

Lukáš Čajánek
cajanek@med.muni.cz

¹Laboratory of Cilia and Centrosome Biology, Department of Histology and Embryology, Faculty of Medicine, Masaryk University, Kamenice 3, Brno 62500, Czech Republic

²Department of Experimental Biology, Faculty of Science, Masaryk University, Kamenice 5, Brno 62500, Czech Republic

³Institute of Biotechnology, Czech Academy of Sciences, BIOCEV, Průmyslová 595, Vestec, Prague 252 50, Czech Republic

⁴Department of Cell Biology, Faculty of Science, Charles University, Viničná 7, Prague 12800, Czech Republic



© The Author(s) 2025, corrected publication 2025. **Open Access** This article is licensed under a Creative Commons Attribution-NonCommercial-NoDerivatives 4.0 International License, which permits any non-commercial use, sharing, distribution and reproduction in any medium or format, as long as you give appropriate credit to the original author(s) and the source, provide a link to the Creative Commons licence, and indicate if you modified the licensed material. You do not have permission under this licence to share adapted material derived from this article or parts of it. The images or other third party material in this article are included in the article's Creative Commons licence, unless indicated otherwise in a credit line to the material. If material is not included in the article's Creative Commons licence and your intended use is not permitted by statutory regulation or exceeds the permitted use, you will need to obtain permission directly from the copyright holder. To view a copy of this licence, visit <http://creativecommons.org/licenses/by-nc-nd/4.0/>.

Background

Primary cilia are evolutionarily conserved signalling organelles found on the surface of a broad spectrum of vertebrate cells [1, 2]. They play a major role in intercepting extracellular stimuli, which helps to govern complex processes in multicellular organisms, including humans [3, 4]. Even though these organelles have not attracted much attention in the past, their biomedical importance became apparent following the discovery of ciliopathies, an expanding group of human diseases caused by ciliary dysfunction [5, 6].

The primary cilium typically appears as a hair-like protrusion of the cell membrane. It consists of the mother centriole (MC)-derived basal body, the transition zone allowing sorting of ciliary components, and the microtubule-based axoneme enclosed within an ARL13B-rich ciliary membrane [7, 8]. The MC distal end is decorated by two sets of appendage proteins. The distal set of appendages is especially important for the initiation of cilia formation – it helps to dock the MC to preciliary vesicles and/or cell membrane and recruits pro-ciliogenesis factors to the base of the growing cilium [9, 10]. To initiate the outgrowth of ciliary axoneme, capping complexes consisting of CP110 and CEP97 proteins are removed from MC distal end [11]. Subsequently, the axoneme extends with the assistance of intraflagellar transport (IFT) machinery [12].

Perhaps the most prominent regulator of the cilium assembly pathway outlined above is Tau-Tubulin Kinase 2 (TTBK2) [13], a serine/threonine kinase from the CK1 superfamily [14, 15]. To initiate ciliogenesis, TTBK2 is recruited to MC distal appendages via interaction with CEP164 [16]. Thus, TTBK2 gets in a prime position to govern key events at the base of the future cilium by its kinase activity [13]. The processes regulated by TTBK2 include the recruitment of Golgi-derived preciliary vesicles [17] and IFT proteins [13], or the removal of CP110/CEP97 [13]. However, the full scope of TTBK2-regulated mechanisms and their relation to ciliogenesis remains to be discovered.

TTBK2 has been shown to phosphorylate a number of MC-related (e.g. CEP164, CEP83, CEP89 [17, 18]) or cell signalling-related proteins (e.g. Dishevelled, a component of the WNT signaling pathway [18, 19]), but the functional relevance of these interactions is often not clear. Furthermore, recent work highlights the possibility of TTBK2 maintaining the length and integrity of primary cilia [20, 21], but molecular mechanisms that would link TTBK2 to axoneme length control remain elusive. Finally, truncating mutations in TTBK2 have been shown to trigger the onset of spinocerebellar ataxia 11 (SCA11), a rare progressive neurodegenerative disease [21–23]. While the genetic link between TTBK2 and SCA11 has

been well described, the molecular pathology of SCA11 is unclear.

In this study, we aimed to elucidate the role TTBK2 plays beyond initiating cilia formation in human cells. As targeting TTBK2 through conventional loss-of-function approaches completely blocks cilia formation [13, 18], we examined TTBK2 variants similar in length and sequence to SCA11 mutants [22]. We show that expressing truncated TTBK2 in hTERT RPE-1 TTBK2 KO cells creates unique semi-permissive conditions for ciliogenesis, bypassing TTBK2 recruitment to the MC. In turn, we utilize this model system to reveal a TTBK2-mediated regulatory mechanism involving kinesin KIF2A, a member of kinesin-13 family with microtubule-depolymerizing activity [24, 25]. KIF2A has been previously shown to aid the resorption of primary cilia following cell cycle re-entry [26], but its role during cilia assembly was not clear. Here, we demonstrate that the interplay between KIF2A and TTBK2 represents an important regulatory mechanism governing primary cilia formation in human cells.

Materials and methods

RPE-1 cell culture and stable line derivation

All hTERT RPE-1 cell lines were cultivated in DMEM/F12 cultivation media (Thermo Fisher Scientific, Cat.N.31331028), supplemented by 10% fetal bovine serum (Biosera), 1% penicillin/streptomycin and 1% L-glutamine. When performing 12/24-well format experiments, culture media was changed daily. To induce primary cilia formation, the cells were cultivated in serum-free complete media for the last 24 h of the experiment. Plasmid transfection (200ng plasmid DNA/well in a 24-well format) was carried out using the Lipofectamine 3000 Transfection Reagent (Thermo Fisher Scientific, Cat.N. L3000001, 0.2 µl P3000 / 100ng DNA, 0.3 µl Lipofectamine / 100ng DNA) and following the manufacturer's manual. Paclitaxel treatment was carried out by adding paclitaxel (Merck, Cat.N. T7402, final concentration 5µM) to culture media 4 h prior to fixation.

To generate DOX-inducible transgenic cell lines, hTERT RPE-1 Flp-In T-Rex cells (a gift from Erich A. Nigg) or hTERT RPE-1 Flp-In T-REX TTBK2 KO cells [18] were seeded on 5 cm dishes, grown to 90% confluency, and co-transfected with pOG44 (5µg total DNA) and a donor vector (pgLap1/2, 500ng total DNA) containing the gene of interest (GOI) coupled to a G418-resistance gene. Transfectants with stably integrated GOI were then selected based on their resistance to G418 (0.5 mg/ml, 1–2 weeks, Merck, Cat.N. G8168). To induce the expression of the GOI the cells were treated with doxycycline (2 µg/ml, Merck, Cat.N. 3072) for the duration of the experiment. For a list of plasmids used in this work see Supplementary Table 1.

For lentiviral transduction of hTERT RPE-1 cells with TTBK2 constructs we used plasmids listed in Supplementary Tables 1 and followed a previously published protocol [27].

For KIF2A knockdown, the cells were seeded on glass coverslips in a 24-well format and cultivated in complete media. After 24 h, the cells were transfected with KIF2A siRNA (50nM final concentration, for siRNA details, see Supplementary Table 1) using Lipofectamine RNAiMAX (Thermo Fisher Scientific, Cat.N.13778100). Culture media was changed on the next day, the cells were cultivated for 48 h in complete media, serum-starved for 24 h, fixed, and analyzed.

HEK293T cell culture and transfection

HEK293T cells were cultivated in DMEM cultivation media (Thermo Fisher Scientific, Cat.N.31966047), supplemented by 10% fetal bovine serum (Biosera) and 1% penicillin/streptomycin. When performing 12/24-well format experiments, culture media was changed daily. To induce primary cilia formation, the cells were cultivated in serum-free complete media for the last 24 h of the experiment.

Transfection of HEK293T cells was carried out using polyethyleneimine (PEI, 2 mg/ml stock solution) in the following way: PEI was incubated in serum-free DMEM media for 10 min, plasmids (Supplementary Table 1) were equilibrated in serum-free DMEM media and then mixed with PEI in a 3 µl of PEI to 1 µg of plasmid ratio. The resulting mixes of plasmid and PEI in DMEM were then added to cells and left in the culture overnight, the media was changed for a fresh complete media on the next day. 48 h after transfection, the cells were processed (fixed with MetOH or lysed) and analyzed.

Western blot

Cells were lysed in 1x Laemli lysis buffer (62.5 mM Tris-HCl pH 6.8, 2% 2-mercaptoethanol, 10% glycerol, 0.01% bromophenol blue, 2% sodium dodecyl sulfate (SDS). SDS-PAGE and membrane transfer were performed using instrumentation by BioRad (Mini-PROTEAN tetra vertical electrophoresis cell, Mini Trans-blot module). Cell lysates were loaded to a 5% stacking gel combined with an 8% running gel and ran at 150 V in a running buffer (0.1% SDS, 0.192 M glycine, 0.025 M Tris-base). The proteins were transferred to an Immobilon-PVDF membrane (Merck, Cat.N. IEVH00005) at 100 V for 75 min in a transfer buffer (20% methanol, 0.192 M glycine, 0.025 M Tris-base). The membranes were then blocked in 5% solution of skimmed milk in wash buffer (20 mM Tris-base, 0.1% Tween 20, 150 mM NaCl) and incubated with primary antibodies (see Supplementary Table 1) diluted in the same solution overnight at 4 °C. The next day the membranes were washed 3 times for 10 min in

wash buffer, incubated with secondary antibodies (Supplementary Table 2) diluted in 5% milk/wash buffer for 2 h at room temperature, and then washed in wash buffer 3 times for 10 min. The membranes were then developed using ECL Prime (Merck, Cat.N. GERPN2236) and Chemidoc Imaging System (BioRad, Cat.N. 12003154). For an easier analysis of membranes, a labelled protein ladder (Thermo Fisher Scientific, Cat.N. 26625) was used in every SDS-PAGE performed.

Immunoprecipitation and MS/MS analysis

To isolate KIF2A for MS/MS analysis, HEK293T cells grown on 15 cm plates were transfected with 2 µg of Flag-KIF2A plasmid + 8 µg of the corresponding GFP-TTBK2 construct. 48 h post-transfection the cells were scraped into lysis buffer (0.5% Triton X-100, 0.5% NP40, 150mM NaCl, 20mM Tris-HCl pH 7.4) containing PhosSTOP (Roche, Cat.N. 4906837001, 1 tablet/10 ml buffer), Complete Mini Protease Inhibitor Cocktail (Roche, Cat.N. 11836153001, 1 tablet/10 ml buffer) and lysed for 15 min on ice. The cell lysates were centrifuged at 16,000x g for 10 min at 4 °C and the supernatants were then incubated overnight at 4 °C with anti-Flag M2 affinity gel beads (Merck, Cat.N. A2220). M2 beads were then pelleted and washed three times with lysis buffer containing protease inhibitors, resuspended in 1x Laemli lysis buffer, and boiled at 95 °C for 10 min. The resulting samples were separated in an 8% acrylamide gel and stained with Coomassie stain. Prominent bands of the correct size were cut out and subjected to protein extraction followed by MS/MS analysis [16]. The final plotted values represent mean relative phosphointensities from 3 independent experiments, only phosphosites detected with an absolute intensity above 10⁶ units were taken into consideration.

Software and data analysis

All statistical analyses were performed in GraphPad Prism software (version 8.0.1), standard deviations (SDs) are shown in all graphs, unless otherwise stated in the figure legend. The ACDC [28] Matlab script (version 0.9) or the CiliaQ [29] Fiji plugin (version 0.1.4) were used for measuring cilia number and length. 3D reconstructions of expansion microscopy images were generated using Imaris software (version 9.8.2). AlphaFold structure predictions were generated using the AlphaFold multimer model (AlphaFold version 2.3.1, DB preset: full DBS, model preset: multimer, 5 predictions per seed with model relaxation), protein structures were visualized using ChimeraX (version 1.8).

Immunofluorescence microscopy

hTERT RPE-1 cells were grown on glass coverslips in a 24-well format, washed with PBS, and fixed using ice-cold

methanol at -20 °C for 20 min. The coverslips were then briefly washed 2 times with PBS, incubated with primary antibodies overnight at 4 °C, washed 3×10 min with PBS before being incubated with secondary antibodies for 2 h in a dark chamber at room temperature, washed 3×10 min with PBS again and mounted using glycer-gel (Dako, Cat.N.C0563) or the ProLong Glass Antifade Mountant (ThermoFisher, Cat.N. P36980). The imaging was performed with the use of ZEISS microscopes, either with AxImager A2 (Plan-Apochromat 100x/1.40 Oil DIC, Hamatsu camera) or LSM-800 (Plan-Apochromat 63x/1.40 Oil DIC M27, Hamatsu camera). Raw images (.czi files) were acquired as z-stacks, processed with the maximum intensity projection feature in Fiji, saved as 16-bit.tif files, and analysed further (e.g. signal measurements). For a list of antibodies used during imaging see Supplementary Table 2.

Image analysis and signal intensity measurements were done in Fiji (version 2.0). Centriolar signal intensity of the protein of interest (POI) and the corresponding centriolar marker (CAP350, CETN1, gTUB) was measured by drawing an ellipsoidal region of interest (ROI) around the centrioles and measuring mean signal intensities inside the ROI (=centriolar signal), then slightly moving the ROI next to the centrioles and measuring mean signal intensities again (=background signal). The final plotted values are equal to:

$$\frac{(\text{centriolar POI signal} - \text{background POI})}{(\text{centriolar marker signal} - \text{background marker signal})}$$

Expansion microscopy

Following cultivation on glass slides in a 24-well format, the cells were briefly washed with PBS and fixed with fixation buffer (PBS, 4% paraformaldehyde, 4% acrylamide) for 48 hours at room temperature, then briefly washed 2 times with PBS. For each sample, a droplet of polymerizing acrylamide gel (PBS, 19% sodium acrylate, 10% acrylamide, 0.1% N, N'-Methylenebisacrylamide, 0.5% ammonium persulfate, 0.5% temed) was prepared, the coverslips were quickly put on top of the gel droplet, with the cells facing the droplet. The samples were then incubated at 4 °C for 10 min, then at 37 °C for 30 min. The resulting coverslips covered in polymerized gel were transferred to a denaturation buffer (50mM Tris-base, 200mM NaCl, 200mM SDS) and the glass coverslips were gently removed from the gels using flat forceps. The gels were then incubated in denaturation buffer at 95 °C for 2 h and let to expand for 1 h in ddH₂O at room temperature. The gels were then cut into smaller pieces and incubated overnight at room temperature in primary antibodies (Supplementary Table 2) diluted 1:50 in blocking buffer (PBS, 2% BSA, 0.02% sodium azide). The next

day the samples were washed 2×30 min with ddH₂O and then incubated at room temperature overnight in secondary antibodies (Supplementary Table 2) diluted 1:500 in blocking buffer. The following day the samples were washed 2×30 min with ddH₂O, placed in a glass-bottom microscopy dish (Ibidi), and imaged using the LSM-880 Airy2 microscope (alpha Plan-Apochromat 100x/1.46 Oil DIC M27 Elyra, AiryScan detector) by ZEISS. Raw images (.czi files) were processed with the AiryScan and Orthogonal Projection (maximum intensity) post-processing features in ZenBlack.

Centriole/axoneme lengths (3C) were measured by first reconstructing the AcTUB signal in 3D using the Surfaces function in Imaris, then using the Elipsoid Axis Length function in Imaris to calculate the length of 3D-reconstructed centrioles/axonemes.

Transmission electron microscopy

hTERT RPE-1 cells were grown on 5 cm dishes for 48 h, then fixed with 3% glutaraldehyde solution (G5882-100mL, Sigma Aldrich) in 0.1 M cacodylate buffer (C0250-100G, Sigma Aldrich) at 4 °C. After rinsing in 0.1 M cacodylate buffer, the samples were postfixed by 1% OsO₄ (05500-1G Sigma Aldrich), dehydrated using ascending ethanol grade (50, 70, 96, and 100% 71250-11002 Penta), embedded in LR White resin (AGR1281 Agar Scientific), polymerized 3 days at 65 °C, and processed by the standard protocol for electron microscopy. Ultrathin sections were imaged using transmission electron microscope (Morgagni 268D, ThermoFisher Scientific, Netherlands).

CEP164 phosphoantibody generation

Antibody against pS201 in CEP164 was custom-derived by Moravia Biotechnology Ltd (<https://www.moravia-n-biotech.com>). In brief, rabbits were immunized using a 13mer peptide TKGLLGpSIYEDKT during 3 rounds of immunization, the IgG was then purified using a gel matrix.

Live-cell imaging

Reporter hTERT-RPE-1 Flp-In T-Rex TTBK2 KO cell lines with DOX-inducible expression of Flag-TTBK2 constructs and constitutive mNeonGreen-ARL13B reporter expression were prepared as described before [27]. For the time-lapse live imaging experiment cells were seeded in DMEM/F12 medium, 10%FBS, 1%L-glutamine, and Penicilin/streptomycin, supplemented with 1 µg/mL DOX on a 10-well glass-bottom CELLVIEW CELL CULTURE SLIDE, PS, 75/25 MM (Greiner Bio-One) at a high density (~30.000 cells per well). 72 h after seeding the medium was replaced with FluoroBrite DMEM with 1%L-glutamine and Penicilin/Streptomycin supplemented with 1 µg/mL DOX to start the starvation

of cells and induce cilia growth. Slides with cells were equilibrated in the microscope environmental chamber for at least 30 min before imaging started. We used Elyra7 inverted microscope equipped with super-resolution structured illumination microscopy (SIM) module with Plan-Apochromat 40x/1.4 Oil DIC M27. Z-stack images were taken every 15 min, the resulting multi-scene.czi file was processed in Zen Black Software by the SIM² Method. The processed z-stacks were projected in one layer by Maximal Orthogonal Projection in Zen Blue Software and individual scenes were saved as.tif files using Bio-Formats Importer plugin in Fiji. Cilia length was measured with the Segmented line tool in Fiji.

FRAP

hTERT RPE-1 TTBK2 KO cells DOX-inducibly expressing Flag-tagged TTBK2 constructs were seeded in μ Slide 8 Well High (Ibidi) chambers. The next day the cells were transfected with GFP-KIF2A^{wt}, cultivated for another 24 h, and then subjected to FRAP analysis using the LSM-880 microscope system by Zeiss – centriolar GFP signal was bleached with a strong laser pulse (100% laser intensity, 500ms) and the region of interest was imaged over the following 60s before measuring GFP signal intensity using the ZenBlack software. T_{half} was calculated from individual FRAP recovery curves (single-fit algorithm) using the EasyFRAP web tool [30].

RT-qPCR

hTERT RPE-1 cell lines were seeded in a 12-well format, cultivated for 48 h (with 2 μ g/ml DOX where indicated), washed with PBS and immediately stored at -80 °C overnight. The samples were then processed with the RNAeasy kit (QIAGEN, Cat.N. 74104) in compliance with the manufacturer's protocol to isolate mRNA. cDNA synthesis was performed using the Transcriptor First Strand cDNA Synthesis Kit (Roche, Cat.N. 04379012001). To compare gene expression (cDNA level), real-time PCR was performed with the use of primers listed in Supplementary Tables 1 and LightCycler SYBR Green I Master (Roche, Cat.N. 04887352001). Relative gene expression was then calculated using the delta-delta Ct method [31].

Site-directed mutagenesis

Site-directed mutagenesis of TTBK2 and KIF2A constructs was performed using the Agilent QUIKChange II XL kit (Agilent Technologies, cat.n. 200522) according to manufacturer's instructions, except 25ng (instead of 10ng) of parental template/plasmid was used in each PCR reaction. PCR reaction products were used to transform XL10 Gold chemo-competent bacteria (Agilent Technologies, cat.n. 200315) and successful mutagenesis of target sequences was confirmed by DNA sequencing.

GFP-KIF2A lysates preparation

HEK293T cells were seeded on 15 cm dishes, transfected with 15ug of plasmid DNA / dish, 30 h post transfection they were scraped down into PBS and centrifuged at 200g / 5 min. Cell pellets were resuspended in 0.5 pellet volumes of lysis buffer (BRB20 (20mM PIPES pH 6.9, 1mM EGTA, 1mM MgCl₂) supplemented with 1x phosphatase inhibitors (4906845001, Sigma Aldrich), 1x protease inhibitors (04693159001, Sigma Aldrich) and 0.05% Triton X-100 (# X100, Sigma). The mixture was sonicated on ice with three short pulses using the MS1 sonotrode (Hielscher Ultrasonics), setting "cycle" 1, "amplitude" 100% (30 kHz). The solution was then transferred to 270 μ l Beckman ultracentrifuge tubes and ultra-centrifuged in the Beckman 42.2 Ti rotor at 35000 x g, 4 °C for 30 min in the Beckman Coulter Optima XPN-90 ultracentrifuge. The supernatant was used directly for experiments or snap frozen in liquid nitrogen and stored at -80 °C.

Microtubule Assembly

Tubulin, Biotin-labelled tubulin as well as HiLyte647-labelled tubulin were purchased from Cytoskeleton Inc. (T240, T333P and TL670M, respectively). Biotinylated HiLyte647-labelled microtubules were polymerized from 4 mg/ml tubulin in the BRB80 (80mM PIPES, 1mM EGTA, 1mM MgCl₂, pH 6.9) supplemented with 1 mM MgCl₂ and 1 mM GTP (Jena Bioscience, Jena, Germany) for 30 min at 37 °C. The polymerized microtubules were diluted in BRB80T (BRB80 with 10 μ M taxol) and centrifuged for 30 min at 21380g and room temperature in a Hettich® Universal 320R centrifuge, rotor 1420-A. After centrifugation, the pellet was resuspended and kept in BRB80T at room temperature.

TIRF Microscopy

Total internal reflection fluorescent (TIRF) microscopy experiments were performed on Zeiss Elyra PS.1 microscope using 100x/1.46 oil immersion objective and EM CCD Andor PALM camera. Fluorescence-labelled microtubules and KIF2A proteins were visualized using 647 nm and 488 nm lasers, respectively. The microscope was controlled by ZEN software (black edition). All experiments were performed at room temperature. For the TIRF experiments, the chambers were prepared by attaching two cleaned and silanized (0.05% dichlorodimethylsilane - DDS, Sigma Aldrich, 440272) glass coverslips (22 \times 22 mm² and 18 \times 18 mm²; Corning, Inc.) with melted thin strips of parafilm. Chambers were incubated with 20 μ g/mL anti-biotin antibody (Sigma Aldrich, B3640) in PBS for 5 min followed by incubation with 1% Pluronic (F127, Sigma Aldrich, P2443) for at least 30 min. The chambers were then washed with BRB80T, 5 μ L of in vitro prepared microtubules were added to the chamber and allowed to

adhere to the antibodies for 30 s. Unbound microtubules were washed away with BRB80T and chambers were pre-incubated with TIRF assay buffer (BRB20 supplemented with 1 mM EGTA, 2mM MgCl₂, 75mM KCl, 10mM dithiothreitol, 0.02 mg/ml casein, 10μM taxol, 1mM Mg-ATP, 20mM D-glucose, 1% Tween, 0.22 mg/ml glucose oxidase and 20 μg/ml catalase) before the experiments. All experiments were performed in TIRF assay buffer (AB). All experiments were quantified by pooling data from three different days.

KIF2A lysate imaging

Chambers were prepared as described above. For intensity and depolymerisation rate analysis, KIF2A lysates were diluted in AB buffer as follows: the WT lysate was diluted 1000x and the other lysates were all diluted to match the intensity of WT GFP signal in the epifluorescence (indicating similar concentration of GFP). For experiments shown in supplementary data, 10x higher concentrations were used to confirm the observed effects. Diluted lysates were added to surface-immobilized microtubules and imaged for 3 min with 5 s intervals. Microscopy data were analyzed using ImageJ 2.3.0/1.53q (FIJI). KIF2A density on the microtubules was measured by drawing a line through the entire microtubule and measuring the Mean Grey Value. For background subtraction, the line was then moved to an area close to the microtubule where no microtubule is present, and the Mean Grey Value was measured again and subtracted from the Mean Grey Value on the microtubule. To measure the depolymerisation rate, the length of the microtubule was measured at the beginning and then at the end of the video. The depolymerisation rate was calculated and normalized to wild-type KIF2A.

Results

Truncated TTBK2 proteins display reduced biochemical activity (Fig. 1)

As outlined above, a complete lack of TTBK2 activity blocks the cilium assembly cascade at the very beginning. This poses a considerable challenge when studying molecular events that only occur later, after cilium assembly has been triggered by TTBK2 (1A). To tackle this issue, we aimed to establish a system with reduced TTBK2 activity, rather than completely blocking this key kinase. To this end, we focused on *TTBK2* truncating mutations which lead to SCA11 pathology in human [22], while the corresponding truncated protein moieties showed significantly reduced or no activity in mice [13, 21]. We prepared two truncated TTBK2 constructs (1B, see also Supplementary Table 1): TTBK2^{trunc1} (1-450 AA protein truncated shortly after the kinase domain) and TTBK2^{trunc2} (adenosine insertion at nucleotide 1329 shifts the reading frame in the last

6 AAs and creates a premature STOP codon [22]) and examined their biochemical activity. CEP164, a *bona fide* substrate of TTBK2, undergoes a mobility shift in response to TTBK2-induced phosphorylation [16, 18]. Indeed, we observed that Flag-tagged wild-type TTBK2 (Flag-TTBK2^{wt}) induced a mobility shift of Myc-tagged N-terminal part of CEP164 (1-467 AA, CEP164^{NT}) when co-expressed in HEK293T cells. In contrast, the expression of Flag-TTBK2^{trunc1} (1C) or Flag-TTBK2^{trunc2} (1D) showed no effect on Myc-CEP164^{NT} mobility, indicating that phosphorylation of Myc-CEP164^{NT} was hampered upon TTBK2 truncation. To corroborate our findings, we generated an antibody against the TKGLLGpSIYEDKT peptide of CEP164 corresponding to the phosphorylated S201 residue targeted by TTBK2 [18] (we termed the antibody „pCEP164“, see S1A-B for antibody validation). Having confirmed the specificity of the pCEP164 antibody to CEP164 protein, we in turn examined pCEP164 levels at MCs in hTERT RPE-1 TTBK2 KO cells DOX-inducibly expressing individual Flag-tagged variants of TTBK2 (see S1C for cell lines validation). Using this system, we found pCEP164 MC signal markedly increased in cells expressing Flag-TTBK2^{wt}, compared to Flag-tagged kinase-dead TTBK2 (Flag-TTBK2^{kd}), Flag-TTBK2^{trunc1}, or Flag-TTBK2^{trunc2} (1E-F), in agreement with our WB data. We note that while the results clearly show the induction of the pCEP164 antibody epitope by TTBK2^{wt}, the ability of this antibody to recognize specifically the phosphorylated S201 needs to be confirmed in the future.

Next, we examined the phosphorylation status of Dishevelled-3 (DVL3), another TTBK2 substrate [18]. As expected, DVL3 was phosphorylated and up-shifted when co-expressed with Flag-TTBK2^{wt}, but not Flag-TTBK2^{kd}. However, we observed a mobility shift of DVL3 when co-expressed with Flag-TTBK2^{trunc1} (1G) or GFP-TTBK2^{trunc2} (1H). We titrated TTBK2 plasmids and confirmed that both TTBK2^{wt} and TTBK2^{trunc1} also induced DVL3 mobility shift when expressed at comparable levels (1I). This intriguing result suggested that truncated TTBK2 proteins indeed possessed a residual biochemical activity towards a subset of TTBK2 substrates rather than being completely inactive.

Truncated TTBK2 triggers cilia assembly (Fig. 2)

If the diminished activity of TTBK2^{trunc1} (we elected it over TTBK2^{trunc2} due to slightly more pronounced defects in phosphorylating CEP164) was to be considered to model the role of TTBK2 in later stages of ciliogenesis/cilia maintenance, it had to support at least some degree of cilia formation. To test this, we again turned to hTERT RPE-1 TTBK2 KO cells DOX-inducibly expressing TTBK2 constructs. First, we found that TTBK2 KO RPE-1 cells were devoid of ARL13B-positive primary cilia altogether and expressing Flag-TTBK2^{wt} rescued the

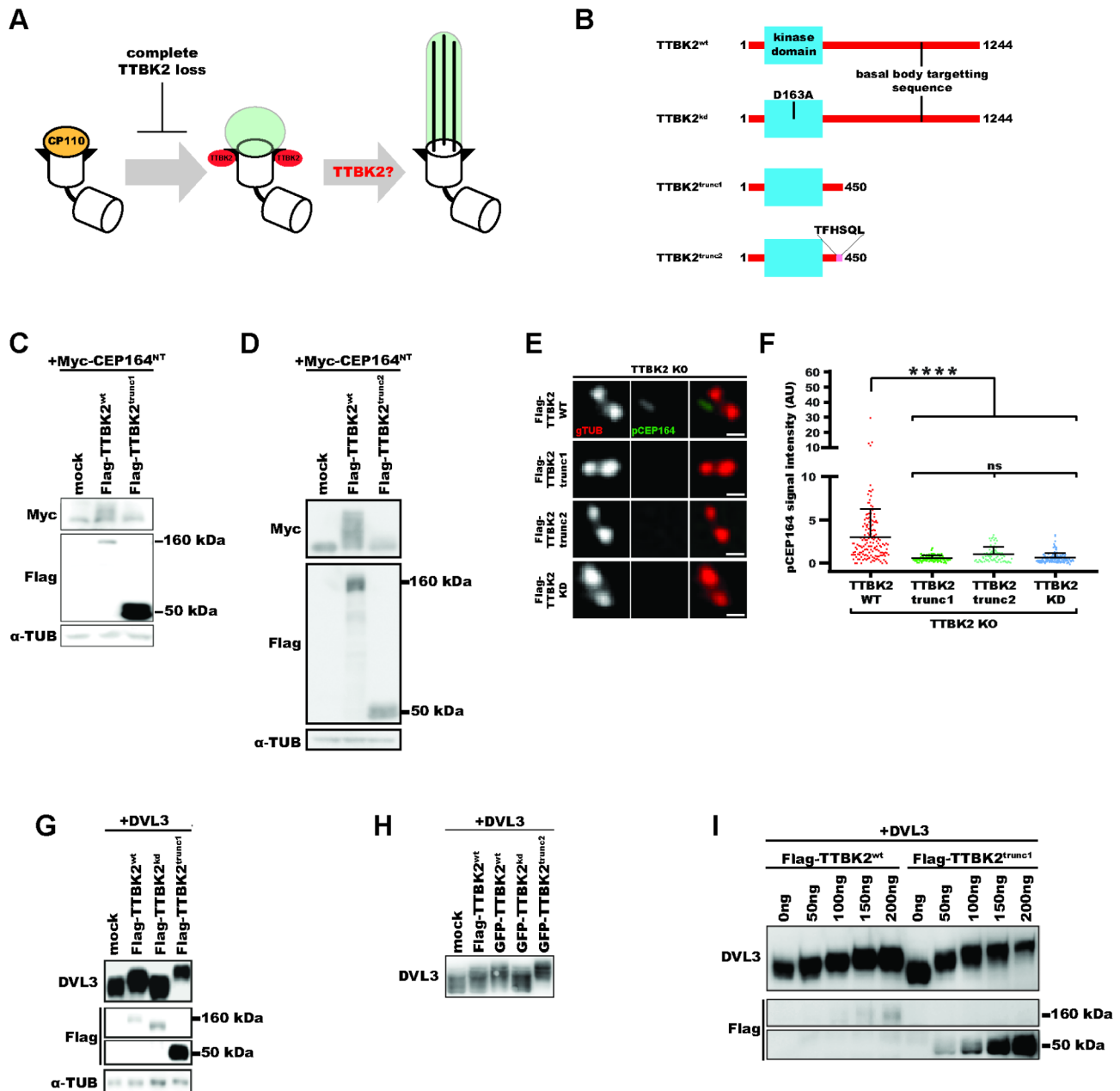


Fig. 1 Truncated TTBK2 proteins display reduced biochemical activity (1A) study outline; (1B) TTBK2 constructs used in this study; (1C-D) Western blot analysis of lysates from HEK293T cells transfected with Myc-CEP164^{NT} and Flag-TTBK2 constructs; (1E-F) hTERT RPE-1 TTBK2 KO cells DOX-inducibly expressing Flag-TTBK2 constructs were fixed and stained for pCEP164 (scale bars: 0.5 μm); (1F) The intensity of pCEP164 centriolar signal was quantified from the images (4 independent experiments, n≥79 cells per condition, normalized to gTUB, one-way ANOVA, ****P<0.0001); (1G-I) Western blot analysis of lysates from HEK293T cells transfected with DVL3 and Flag-TTBK2 constructs

frequency of ciliated cells to ~34% (2A-B), as expected. Remarkably, expressing Flag-TTBK2^{trunc1} rescued cilia formation in ~11% of cells, in contrast to Flag-TTBK2^{kd} which completely failed to rescue (2A-B). At the same time, we noticed a marked reduction of cilia length in cells expressing Flag-TTBK2^{trunc1} compared to Flag-TTBK2^{wt}, hinting at a possible defect in cilia assembly and/or maintenance (2C). The C-terminal part of wild-type TTBK2 interacts with CEP164, which targets TTBK2 to

the MC [16]. As expected, Flag-TTBK2^{trunc1}, which lacks the CEP164-binding region (1B), failed to be recruited to the MC and instead localized dispersely throughout the cytoplasm (2A, S2A). Interestingly, re-targeting TTBK2^{trunc1} to the MC by fusing it to the C-terminal part of CEP164 (468–1460 AA, we termed the construct „CEP164 chimera”) rescued both cilia number and cilia length to the level of TTBK2^{wt} (2A-C), suggesting that the observed defects in cilia assembly were caused by

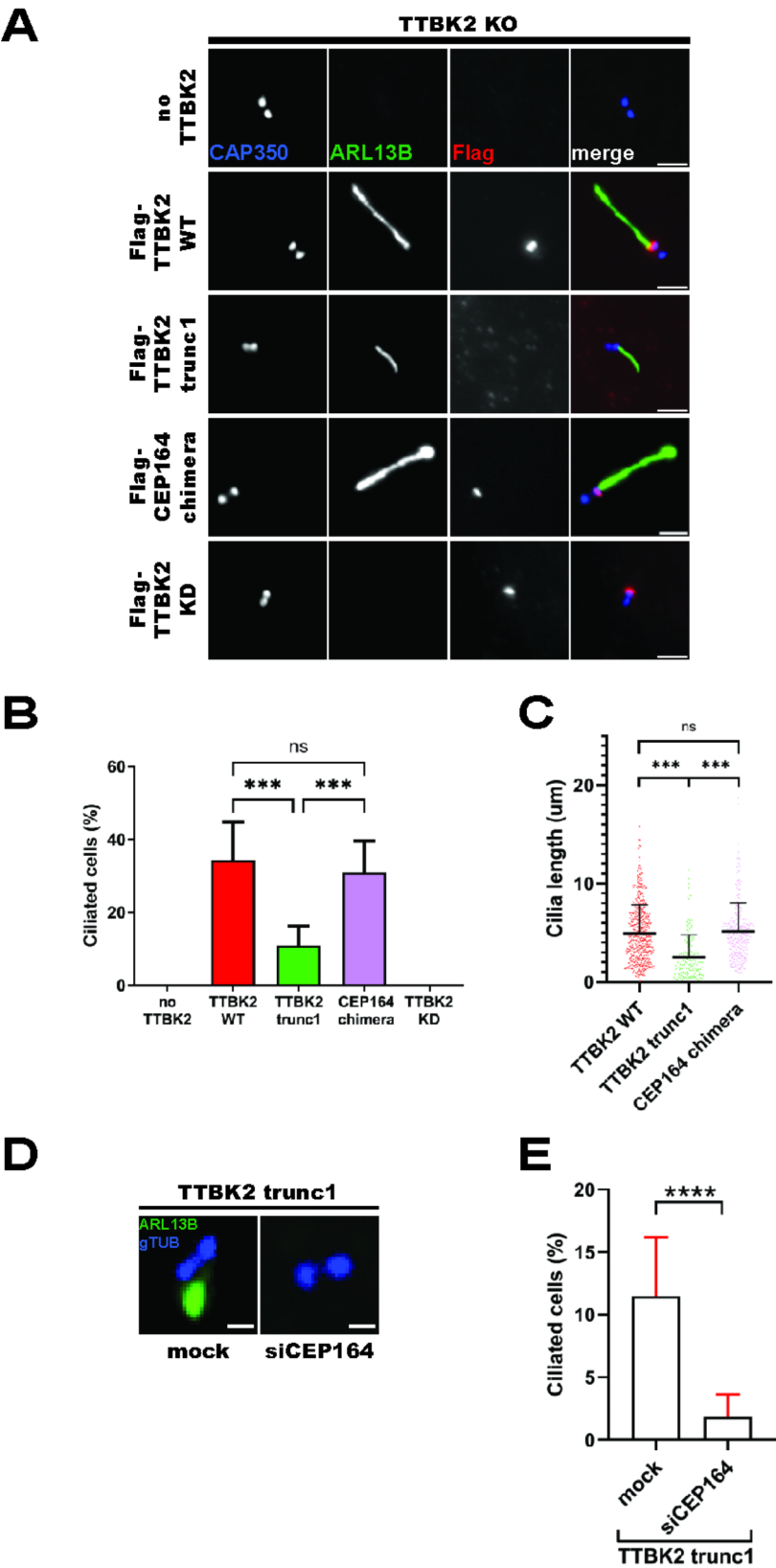


Fig. 2 (See legend on next page.)

(See figure on previous page.)

Fig. 2 Truncated TTBK2 triggers cilia assembly (2A-C) hTERT RPE-1 TTBK2 KO cells DOX-inducibly expressing Flag-TTBK2 constructs were fixed and stained for ARL13B and the indicated antibodies (scale bars: 2µm); **(2B)** shows percentage of ciliated cells in the corresponding cell line (n=4 independent experiments, one-way ANOVA, ***P<0.001); **(2C)** shows cilia length quantification (4 independent experiments, n≥153 cilia per condition, one-way ANOVA, ***P<0.001); **(2D-E)** hTERT RPE-1 TTBK2 KO cells DOX-inducibly expressing Flag-TTBK2^{trunc1} were transfected with siRNA targeting CEP164 **(2E)** shows cilia number upon siCEP164 treatment (n=3 independent experiments, unpaired T-test, ****P<0.0001)

TTBK2^{trunc1} mislocalization. Noteworthy, we confirmed that different cilia length in cells expressing Flag-TTBK2^{wt} vs Flag-TTBK2^{trunc1} stemmed from qualitative differences between these constructs, rather than different expression levels (S2B-F).

Further, the partial rescue of cilia formation by Flag-TTBK2^{trunc1} (2B) suggested that TTBK2 enrichment at the MC was not strictly necessary for triggering cilia assembly. To test this, we examined hTERT RPE-1 CEP164 KO cells (a kind gift from Ciaran Morrison), which displayed prominent ciliogenesis defects, yet occasionally formed primary cilia [32]. First, we confirmed that CEP164 and TTBK2 signals were absent from the MCs of CEP164 KO cells (S2G-J), in line with the reported role of CEP164 in TTBK2 recruitment [16]. Remarkably, the rare primary cilia we found forming in the absence of CEP164 lacked the CEP164-recruited TTBK2 pools at their MCs (S2K). This data supports the notion that TTBK2 might trigger cilia formation even when localizing outside the MC, albeit with very low efficiency.

Considering the established role of CEP164 in ciliogenesis and TTBK2 recruitment, it was interesting to see that Flag-TTBK2^{trunc1} could trigger cilia assembly despite lacking the CEP164-interacting motif, prompting us to ask whether CEP164 was required for cilia formation in these cells. We found that depleting MC-associated CEP164 through siRNA (see S2L-M for siRNA validation) disrupted cilia assembly in Flag-TTBK2^{trunc1} cells (2D-E), suggesting that CEP164 mediated additional processes besides recruiting TTBK2 to the MC.

TTBK2^{trunc1} cilia are short, but display normal architecture (Fig. 3)

Having established that truncated TTBK2 could not rescue ciliogenesis as effectively as wild-type TTBK2 (2B-C), we wanted to distinguish early and late defects in cilia formation. Cilia assembly in RPE-1 cells starts with the formation of a preciliary vesicle at the distal end of the MC, which later elongates into a ciliary sheath once ciliary microtubules extend towards it [33]. Using transmission electron microscopy (TEM), we detected various, consecutive stages of preciliary vesicle formation in Flag-TTBK2^{trunc1} cells, including cells with an elongated ciliary sheath (3A). In contrast to Flag-TTBK2^{wt}, we struggled to detect fully assembled cilia in Flag-TTBK2^{trunc1}, in agreement with their lower occurrence in our IF microscopy experiment (2B).

To corroborate our findings, we took advantage of expansion microscopy, which offered vastly improved cilia detection over TEM. Primary cilia formed in the Flag-TTBK2^{wt} condition showed a typical arrangement of acetylated tubulin (AcTUB)-positive axonemal microtubules, enclosed within a ciliary membrane labelled by ARL13B (3B, left panel). Many cilia found in the Flag-TTBK2^{trunc1} condition were similar to that but with a shorter axoneme (3B, middle panel). Further, in Flag-TTBK2^{trunc1} we often noticed structures consisting of ARL13B-positive vesicles docked to the MC but with no apparent sign of axonemal microtubules extending (3B, right panel).

To quantify this phenotype, we measured the length of AcTUB signal of both centrioles in a pair. Using these measurements, we determined the ratio of combined MC + axoneme length relative to the length of the daughter centriole (3C, see left panel). ARL13B was used simply to determine whether a given cell initiated cilium assembly. For centriole pairs with no ARL13B signal the MC/DC length ratio was around 1 (3C, red datapoints), indicating that no ciliary axoneme was extending. In ARL13B-positive centriole pairs (3C, green datapoints), the MC/DC length ratio shifted towards higher values, as the corresponding mother centrioles templated cilia. However, the average MC/DC length ratio was smaller in Flag-TTBK2^{trunc1} compared to Flag-TTBK2^{wt} (3C), in agreement with the observed cilia length defect (2C). What is more, ARL13B-positive Flag-TTBK2^{trunc1} centriole pairs frequently displayed a length ratio between 1 and 1.5 (3C, grey area in the graph), indicating that their axonemal microtubules did not extend (14/45 cells in Flag-TTBK2^{trunc1} compared to 3/19 cells in Flag-TTBK2^{wt}).

In sum, our data show that cilia forming in Flag-TTBK2^{trunc1} cells displayed no obvious ultrastructural defects, but were simply shorter than their Flag-TTBK2^{wt} counterparts.

Early ciliogenesis progression in TTBK2^{trunc1} (Fig. 4)

To examine how efficiently the truncated TTBK2 triggered individual early steps of ciliogenesis, we first stained for CP110, a protein removed from the MC in response to TTBK2 activity [13]. We found both Flag-TTBK2^{wt} and Flag-TTBK2^{trunc1}, but not Flag-TTBK2^{kd}, to efficiently induce the MC removal of CP110 in TTBK2 KO background (4A-B).

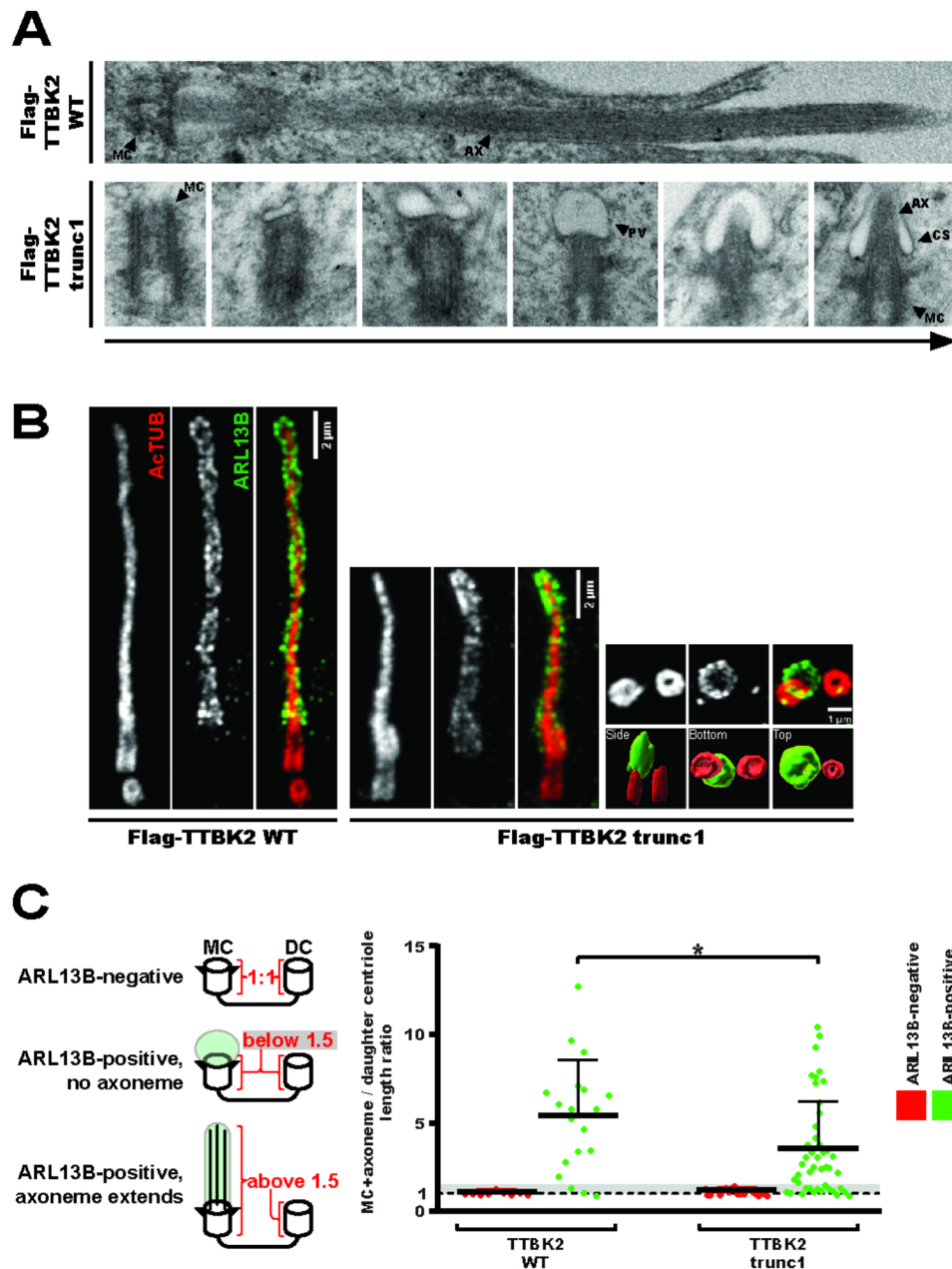


Fig. 3 *TTBK2*^{trunc1} cilia are short, but display normal architecture **(3A)** hTERT RPE-1 *TTBK2* KO cells DOX-inducibly expressing Flag-*TTBK2* constructs were analyzed using TEM, upper panel shows a mature cilium in Flag-*TTBK2*^{wt}, bottom panels show consecutive stages of early ciliogenesis in Flag-*TTBK2*^{trunc1} (MC=mother centriole, PV=preciliary vesicle, CS=ciliary sheath, AX=axoneme); **(3B)** expansion microscopy reveals ARL13B-positive ciliary membrane (green channel) and ActTUB-positive ciliary microtubules (red channel), 6 small panels on the right show an ARL13B-positive vesicle docked to the MC with the bottom panels showing 3D-reconstruction of the same image viewed from different perspectives **(3C)** MC+axoneme and DC lengths were measured using the ActTUB signal from expansion microscopy images, the ratio of each MC+axoneme to DC was quantified (4 independent experiments, n=19 for *TTBK2*^{wt}, n=45 for *TTBK2*^{trunc1}, unpaired T-test, *P<0.05), grey area in the graph indicates values between 1 and 1.5

Next, we examined the MC recruitment of IFT88, a protein involved in shuttling of molecules inside cilia [12]. We found that while Flag-*TTBK2*^{kd} failed to promote IFT88 recruitment to the MC, Flag-*TTBK2*^{wt} and to a lesser extent also Flag-*TTBK2*^{trunc1} showed a rescue effect on IFT88 MC levels (4C-D).

Finally, we tested if MyosinVa and RAB34, two markers of early membrane structures [34–36], localized to the MC in *TTBK2*^{trunc1}. Flag-*TTBK2*^{wt} and Flag-*TTBK2*^{trunc1} showed comparable frequencies of MyosinVa- and RAB34-positive MCs, whereas Flag-*TTBK2*^{kd} did not rescue the MC recruitment of these two markers (4E-H).

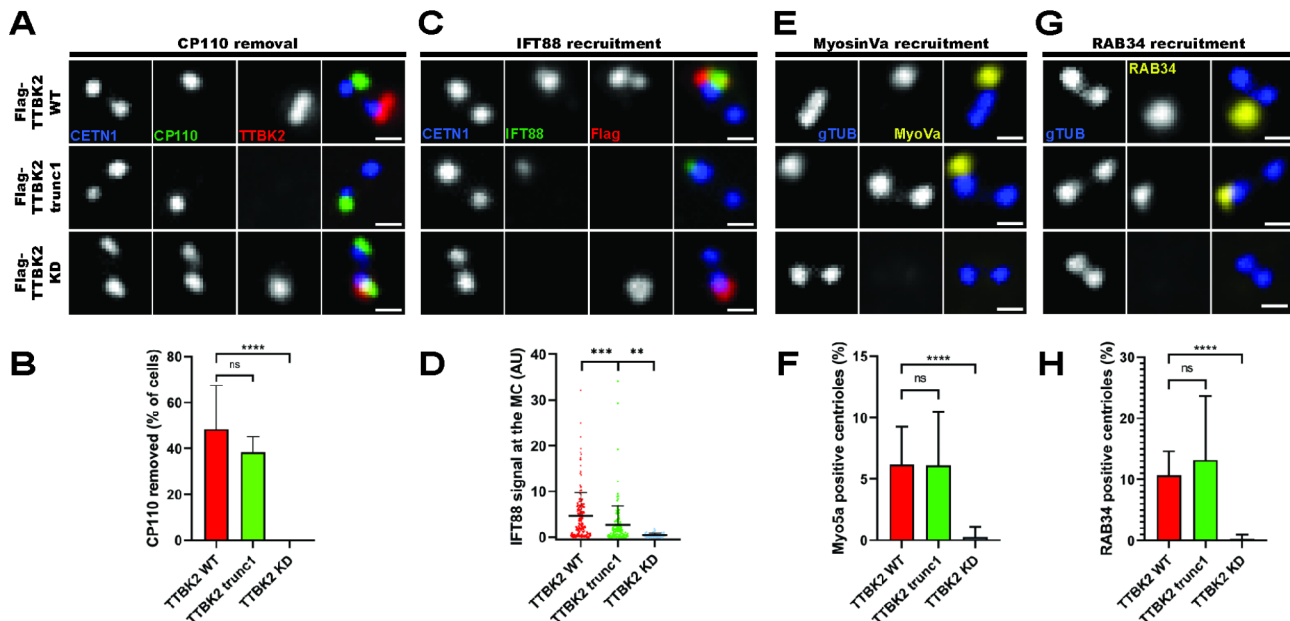


Fig. 4 Early ciliogenesis progression in *TTBK2^{trunc1}* (4A, 4C, 4E, 4G) hTERT RPE-1 *TTBK2* KO cells DOX-inducibly expressing Flag-*TTBK2* constructs were stained with the indicated antibodies (scale bars: 0.5μm) (4B) shows percentage of cells with CP110 removed from the MC (n=3 independent experiments, one-way ANOVA, ****P<0.0001); (4D) shows IFT88 signal intensity at the MC (normalized to CETN1, 6 independent experiments, n≥59 for each condition, one-way ANOVA, ***P<0.001, **P<0.01); (4F) shows percentage of cells with MyosinVa signal present at the MC (n=4 independent experiments, one-way ANOVA, ****P<0.0001); and (4H) shows percentage of cells with RAB34 signal present at the MC (n=4 independent experiments, one-way ANOVA, ****P<0.0001)

To capitalize on the ability of *TTBK2^{trunc1}* to trigger cilia formation in a CEP164-dependent manner (2D), but independently of CEP164-mediated *TTBK2* recruitment to the MC (2A), we examined the effects of CEP164 depletion on the above-tested markers. Intriguingly, our data revealed a clear dependency of all markers on CEP164 presence (S3A-D). To our knowledge, our model system is the first to decouple the role of CEP164 in recruiting *TTBK2* from its other roles during cilia assembly, which warrants further investigation.

To conclude, our results showed that truncated *TTBK2* could indeed reasonably well trigger canonical early steps of the cilium assembly cascade.

Short cilia in *TTBK2^{trunc1}* are linked to KIF2A accumulation (Fig. 5)

Given that Flag-*TTBK2^{trunc1}* cells could initiate ciliogenesis (Figs. 3 and 4), we speculated that the observed defects in cilia formation (2A-C) might arise later, during axoneme extension. To test our hypothesis, we examined cilia growth dynamics using live-cell imaging of cells expressing mNeonGreen-ARL13B. Of note, the expression of exogenous ARL13B led to an overall increase in cilia length (if compared to experiments without exogenous ARL13B), in agreement with previous observations [27, 37]. We found that RPE-1 cells expressing Flag-*TTBK2^{wt}* formed steadily growing cilia during the 5 h period of the experiment (5A-B). In contrast, cilia in

Flag-*TTBK2^{trunc1}*-expressing cells elongated very slowly, sometimes even shortened towards the end of the experiment. Moreover, we noted an increase in cilia breakage events (5C) in the Flag-*TTBK2^{trunc1}* condition (0.355 breaks per cilium) compared to Flag-*TTBK2^{wt}* (0.222 breaks per cilium). Taken together with the rather modest defect in IFT88 MC levels in *TTBK2^{trunc1}*-expressing cells (4C-D), we hypothesized that *TTBK2* might regulate axoneme length by an additional, unknown mechanism and sought to identify it.

We focused on KIF2A, a microtubule(MT)-depolymerizing kinesin implicated in cilia resorption upon cell cycle re-entry [26], which interacts with *TTBK2* [24]. We found that KIF2A MC levels were elevated in RPE-1 cells expressing Flag-*TTBK2^{trunc1}* compared to Flag-*TTBK2^{wt}* (5D-E), confirming and extending previous observations from mutant mouse embryonic fibroblasts [13]. In addition, we found a modest negative correlation between KIF2A basal body presence and cilia length (S4A). Given that KIF2A acts as a negative regulator of cilia length [26], we next tested the possible causality between KIF2A MC accumulation and axoneme extension defects in Flag-*TTBK2^{trunc1}* cells by depleting KIF2A through siRNA (see S4B-C for depletion efficiency validation). Remarkably, even though KIF2A depletion did not significantly change the percentage of ciliated cells (S4D), it fully rescued the cilia length defect in Flag-*TTBK2^{trunc1}*-expressing cells (5F-G). Importantly, KIF2A depletion showed no

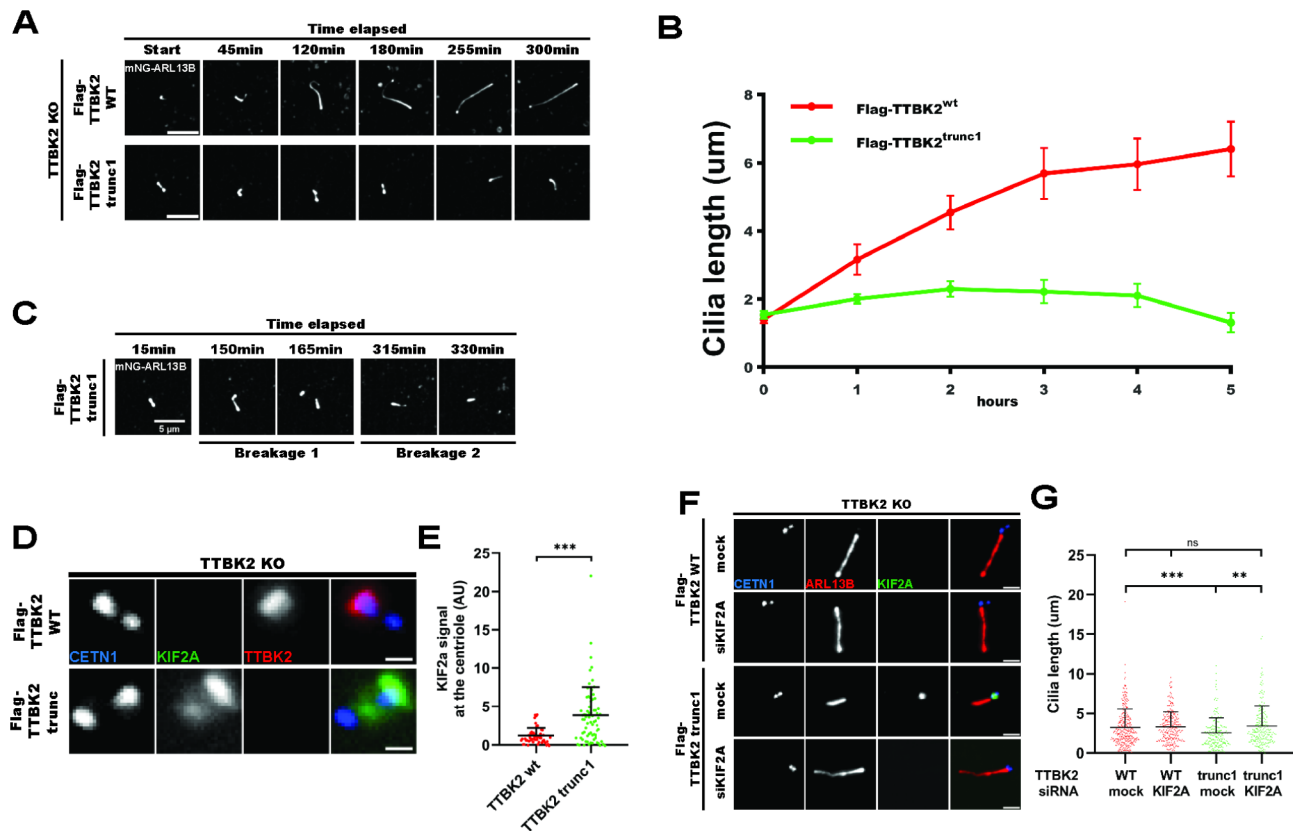


Fig. 5 Short cilia in TTBK2^{trunc1} are linked to KIF2A accumulation (5A-C) hTERTPE-1 TTBK2 KO cells expressing mNeonGreen-ARL13B and Flag-TTBK2 constructs were subjected to live-cell imaging (images show the NeonGreen signal, scale bars: 5μm); (5B) shows the mean length of cilia measured over the course of 5 hours (+/- standard error of mean, 4 independent experiments, n≥90 cilia per condition); (5C) Flag-TTBK2^{trunc1} cells exhibited frequent cilia breakage events; (5D-E) hTERT RPE-1 TTBK2 KO cells DOX-inducibly expressing Flag-TTBK2 constructs were fixed and stained for KIF2A and the indicated antibodies (scale bars: 0.5μm); (5E) shows KIF2A signal intensity at the MC (4 independent experiments, n≥54 cells per condition, normalized to CETN1, one-way ANOVA, ****P<0.0001). (5F-G) hTERT RPE-1 TTBK2 KO cells DOX-inducibly expressing Flag-TTBK2 constructs were transfected with mock or KIF2A siRNA (scale bars: 2μm); (5G) shows cilia length quantification (4 independent experiments, n≥189 cilia per condition, one-way ANOVA, **P<0.01, ***P<0.001)

additive effect on cilia length in Flag-TTBK2^{wt}, suggesting that KIF2A-mediated inhibition of axoneme growth was specific to Flag-TTBK2^{trunc1} cells.

KIF2A overactivation phenocopies TTBK2 truncation (Fig. 6)

Having established the functional link between truncated TTBK2 and KIF2A, we examined in detail the effects of KIF2A on cilia length. First, we generated hTERT RPE-1 cell lines DOX-inducibly expressing GFP-KIF2A^{wt} or GFP-KIF2A^{KVD}, a mutant defective in MT depolymerization [26, 38]. We found both constructs to preferentially localize to centrioles and/or their proximity (6A-B). Intriguingly, we could detect GFP-KIF2A^{KVD} decorating the ciliary axoneme, suggesting that KIF2A could localize directly inside cilia (6A). In addition, we resolved the signal of GFP-KIF2A^{wt} using expansion microscopy and found it to form ring-like structures near the MC distal end, closely resembling the localization pattern of distal or subdistal appendage proteins (6B). Furthermore, our

expansion microscopy protocol revealed a faint signal of GFP-KIF2A^{wt} decorating the ciliary axoneme. We also detected endogenous KIF2A localizing to centrioles and their proximity and its centriolar localization was abolished by paclitaxel treatment (5μM, 4 h), suggesting a dependency on intact microtubules (S5A-B).

Upon investigating KIF2A localization pattern, we examined its effects on primary cilia formation. Following DOX-induced expression of GFP-KIF2A^{wt}, but not GFP-KIF2A^{KVD}, we could readily observe a reduction of cilia length (6C-D), in line with previous work [26]. In addition, we found that GFP-KIF2A^{wt}, but not GFP-KIF2A^{KVD}, reduced the percentage of ciliated cells (6E).

To conclude, our data established that the activity of KIF2A in primary cilia interferes with cilia assembly and phenocopies the defects seen in Flag-TTBK2^{trunc1} cells.

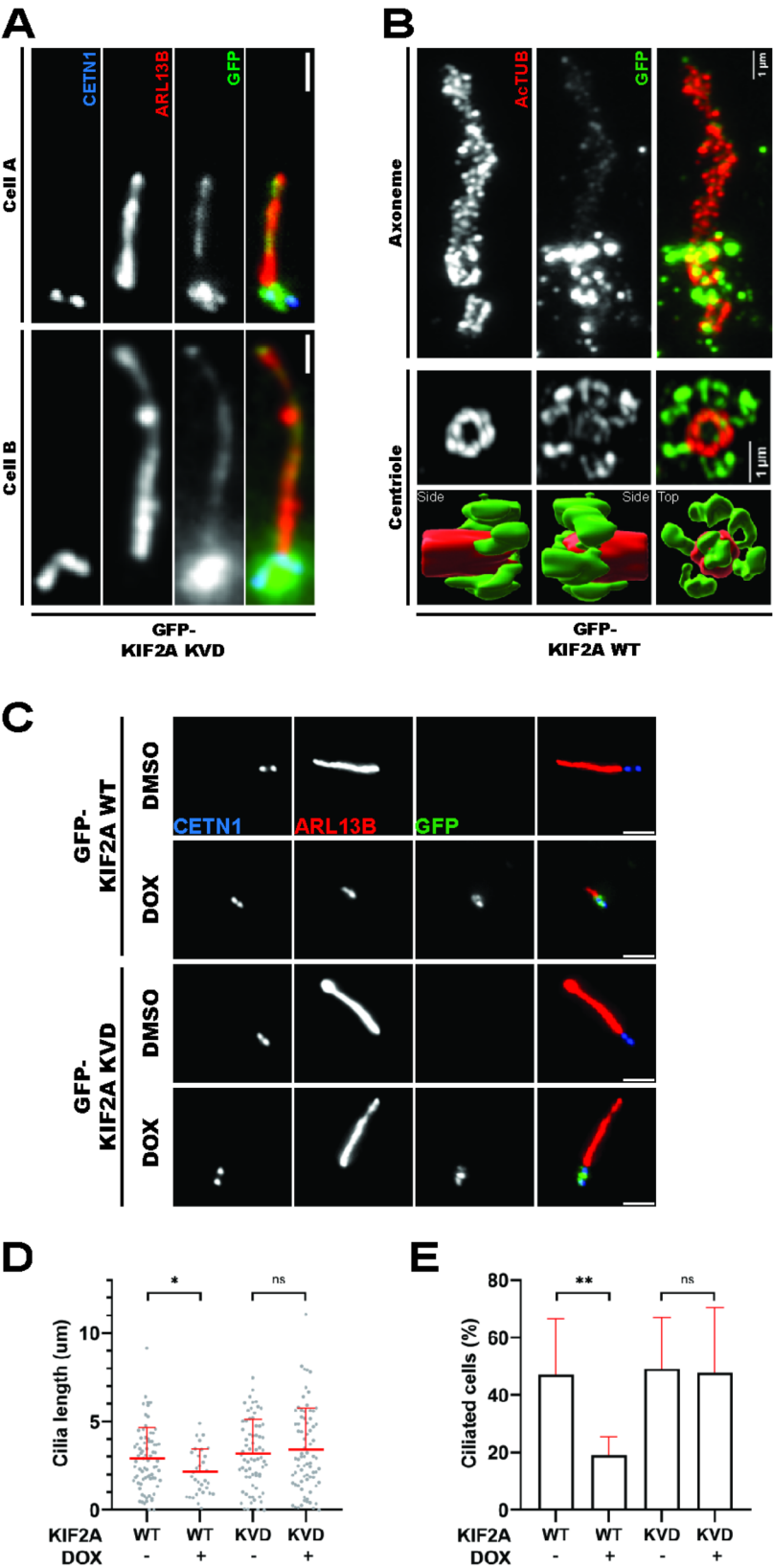


Fig. 6 (See legend on next page.)

(See figure on previous page.)

Fig. 6 KIF2A overactivation phenocopies TTBK2 truncation (6A) hTERT RPE-1 cells expressing GFP-KIF2A^{KVD} were fixed and stained for ARL13B and CETN1 (scale bars: 1 μ m), the images show two representative cells with GFP-KIF2A^{KVD} signal decorating the cilium (**6B**) hTERT RPE-1 cells expressing GFP-KIF2A^{wt} were fixed, subjected to expansion microscopy, and stained for ActUB and GFP, GFP-KIF2A^{wt} (green channel) localized to the basal body and also showed a faint axonemal signal, bottom panels show Imaris 3D reconstructions of a centriole viewed from different perspectives (**6C–E**) hTERT RPE-1 cells expressing GFP-KIF2A constructs were treated with DMSO or DOX, fixed, and stained for ARL13B and the indicated antibodies (scale bars: 2 μ m); (**6D**) shows cilia length quantification (2 independent experiments, $n \geq 32$ cilia per condition, unpaired T-test, * $P < 0.05$); (**6E**) shows percentage of ciliated cells ($n = 2$ independent experiments, unpaired T-test, ** $P < 0.01$)

TTBK2-induced phosphorylations inhibit KIF2A MT binding and depolymerization in vitro (Fig. 7)

To reveal how TTBK2 regulates KIF2A, we first examined KIF2A phosphorylation induced by TTBK2. Following co-expression of Flag-KIF2A^{wt} with GFP-tagged TTBK2 variants in TTBK2 KO HEK293T, we immunopurified Flag-KIF2A^{wt}, subjected the isolates to MS/MS analysis and identified several TTBK2-induced S/T phospho-sites (S6A). We further focused on S137 and S140 (7A) as phospho-sites that were specifically induced by GFP-TTBK2^{wt}, but not by GFP-TTBK2^{trunc2} (we selected it over TTBK2^{trunc1} in this experiment due to its slightly higher activity towards CEP164) or GFP-TTBK2^{kd}. Together with the closely neighbouring S135 which was identified, but not functionally characterized, in a study by Watanabe *et al.* [24], these 3 serine residues are located in an unstructured loop near the N-terminus of KIF2A, according to predicted KIF2A structure found in the AlphaFold DB [39] (7A, marked in yellow).

To test if phosphorylation of the S135-140 cluster regulated KIF2A function, we mutated the entire cluster to alanine (A) or glutamate (E) to block or mimic phosphorylation, respectively. Then, we incubated lysates from HEK293T cells transfected with GFP-tagged KIF2A phosphomutants with in vitro reconstituted and stabilized MTs and used total internal reflection fluorescence (TIRF) microscopy to examine KIF2A-MT interaction dynamics (7B). We found that mimicking phosphorylation of the S135-140 cluster (in GFP-KIF2A^{S135-140E}) reduced the amount of KIF2A bound to MTs (7C, S6B).

Given that, we used a similar TIRF assay to examine whether S135-140 phosphorylation regulated MT depolymerization (7D). Intriguingly, mimicking phosphorylation of the S135-140 cluster inhibited MT depolymerization by GFP-KIF2A^{S135-140E} (7E, S6C). Taken together, our data established that TTBK2-mediated phosphorylation of S135-140 regulates the ability of KIF2A to bind and depolymerize MTs in vitro.

In addition to the S135-140 cluster, we tested if phosphorylation of KIF2A residues S586/S604 (identified by MS/MS in S6A) regulated KIF2A function. Surprisingly, we found that both mimicking and blocking S586/S604 phosphorylation (in GFP-KIF2A^{S586/604E} and GFP-KIF2A^{S586/604A} respectively) enhanced KIF2A MT affinity (S6D) and depolymerization (S6E). Our modeling using AlphaFold [40] showed that both mutants display stabilized alpha-helical structures in regions involved in

KIF2A dimerization [38] (S6F). We note that while our in silico modelling results might explain the phenotype of S586/S604 mutants, we could not conclusively address the possible role of TTBK2-mediated phosphorylation of S586 and S604. Further work will be required to determine if these C-terminal phosphorylations truly regulate KIF2A under physiological conditions.

TTBK2 regulates KIF2A in cells to support cilia formation (Fig. 8)

Next, we examined the consequences of TTBK2-mediated KIF2A phosphorylation for its localization and effects on cilia. Since we observed changes in KIF2A MC levels between our RPE-1 cell lines (5D–E), but no difference in total levels of KIF2A (S4A), we reasoned that TTBK2 might specifically regulate KIF2A recruitment to MC rather than whole-cell KIF2A protein levels. To probe for changes in MC-associated KIF2A, we carried out a fluorescence recovery after photobleaching (FRAP) analysis of GFP-KIF2A^{wt} MC pools in Flag-TTBK2^{wt} and Flag-TTBK2^{trunc1} RPE-1 cells. We observed a small, but consistent reduction in recovery halftime (T_{half}) of GFP-KIF2A^{wt} MC signal in Flag-TTBK2^{wt} compared to Flag-TTBK2^{trunc1} cells (8A–B), suggesting a faster KIF2A MC turnover in Flag-TTBK2^{wt}.

Next, to examine if KIF2A MC recruitment was regulated by phosphorylation of the S135-140 cluster, we expressed GFP-KIF2A^{wt}, GFP-KIF2A^{S135-140E} or GFP-KIF2A^{S135-140A} in RPE-1 cells. Remarkably, we found that mimicking S135-140 phosphorylation strongly diminished KIF2A MC localization in GFP-KIF2A^{S135-140E}, whereas GFP-KIF2A^{wt} and GFP-KIF2A^{S135-140A} localized normally (8C–D). This result suggested that TTBK2 phosphorylation of S135-140 likely facilitates ciliogenesis by preventing the accumulation of KIF2A at MCs. However, our results also hinted at possible limitations of our experimental setup, as we were not able to resolve a difference in MC levels between GFP-KIF2A^{wt} and GFP-KIF2A^{S135-140A} (see also Discussion).

Finally, to test if phosphorylation of KIF2A at S135-140 regulated cilia formation, we compared ciliogenesis in hTERT RPE-1 cells DOX-inducibly expressing GFP-tagged KIF2A phosphomutants. We observed that cells overexpressing GFP-KIF2A^{S135-140E} formed cilia that were longer compared to cells expressing GFP-KIF2A^{S135-140A} (8E–F), indicating that phosphorylation of KIF2A at S135-140 supported axoneme elongation.

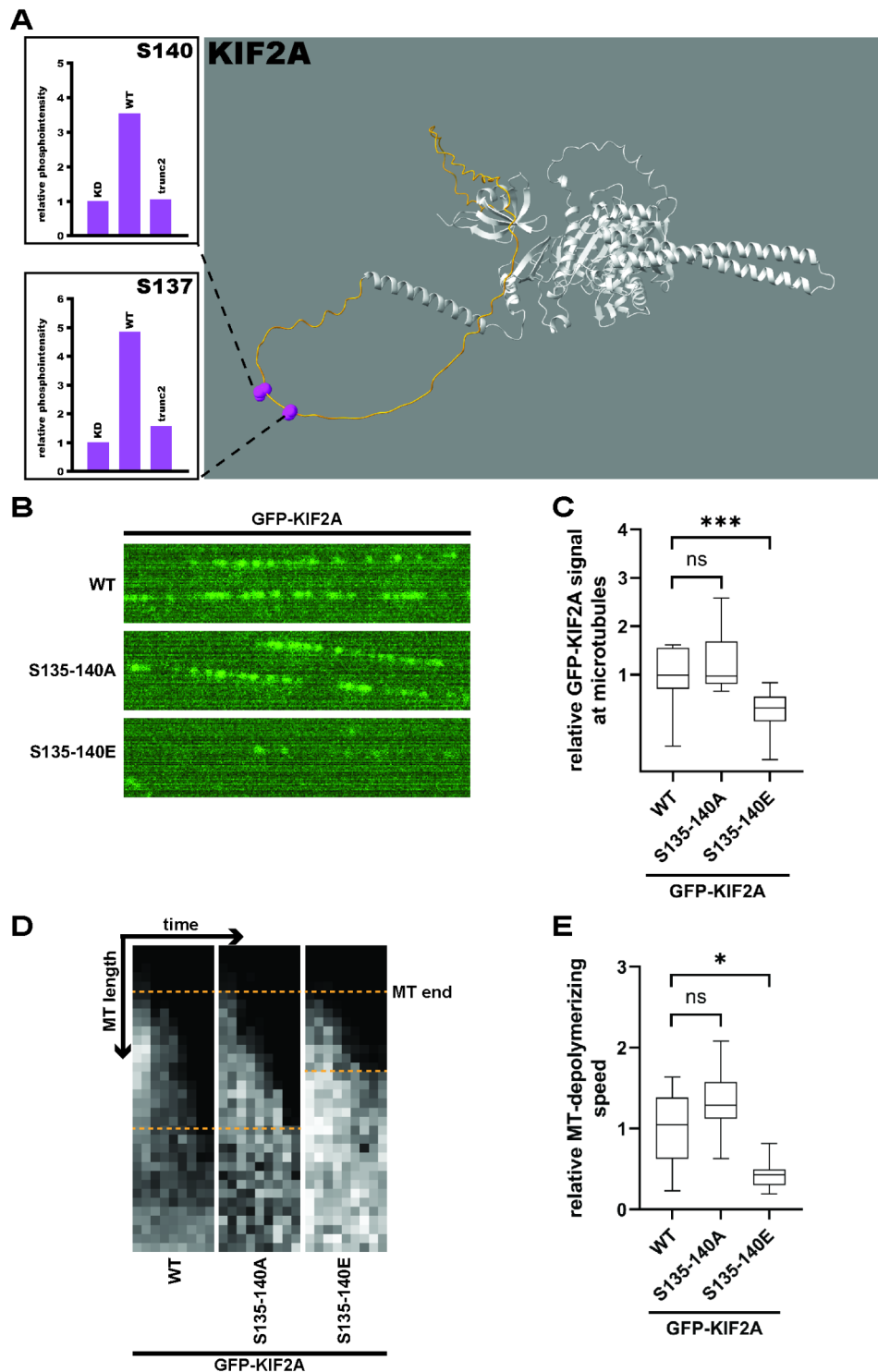


Fig. 7 TTBK2-induced phosphorylations inhibit KIF2A MT binding and depolymerization in vitro **(7A)** HEK293T cells were transfected with Flag-KIF2A and GFP-TTBK2 constructs, lysed, incubated with anti-Flag affinity beads, and the isolates were subjected to MS/MS analysis. Phosphorylation intensities between TTBK2 WT, KD, and trunc2 were quantified as means of 3 independent experiments and normalized to TTBK2 KD (see S6A for complete phosphomap), TTBK2^{wt} induced phosphorylation of KIF2A serines S137 and S140; **(7B-E)** lysates of HEK293T cells transfected with GFP-KIF2A constructs were incubated with *in vitro* stabilized microtubules; **(7B)** shows a representative picture of MT-bound GFP-KIF2A molecules; **(7C)** shows KIF2A signal intensity at MTs (n=3 independent experiments, normalised to GFP-KIF2A^{wt}, Kruskal-Wallis test, ***P<0.001); **(7D)** representative kymographs showing MT shortening by different KIF2A constructs, gray signal shows biotinylated tubulin; **(7E)** shows the rate of MT depolymerization by KIF2A as a measure of MT shortening over time (n=3 independent experiments, normalised to GFP-KIF2A^{wt}, Welch ANOVA test, *P<0.05)

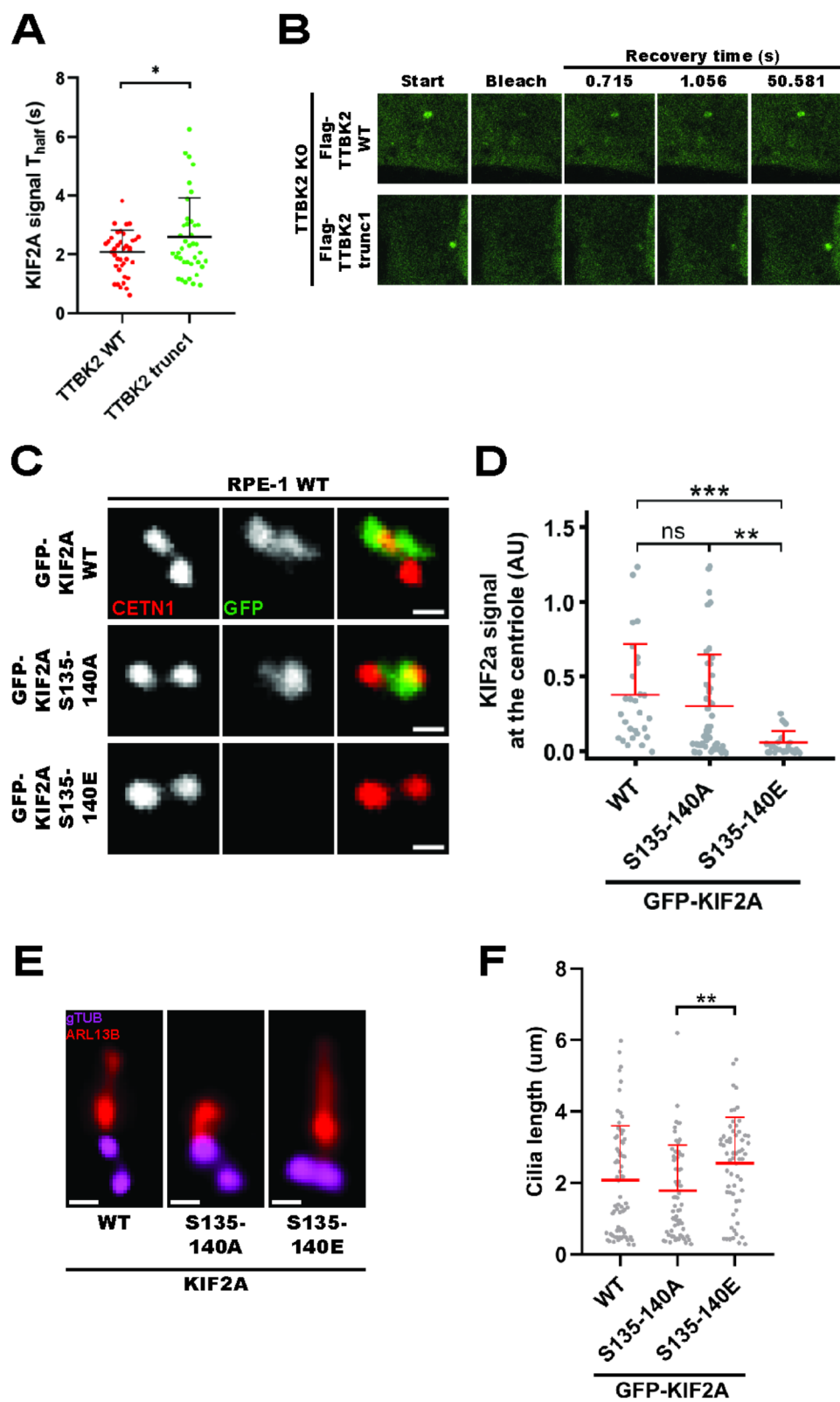


Fig. 8 (See legend on next page.)

(See figure on previous page.)

Fig. 8 TTBK2 regulates KIF2A in cells to support cilia formation (8A-B) hTERT RPE-1 TTBK2 KO cells DOX-inducibly expressing Flag-TTBK2 constructs were transfected with GFP-KIF2A^{wt} and subjected to FRAP analysis; **(8A)** shows individual T_{half} values calculated using the EasyFRAP web algorithm (3 independent experiments, $n \geq 38$ cells per condition, unpaired T-test, $*P < 0.05$); **(8C-D)** hTERT RPE-1 cells were transfected with GFP-KIF2A constructs, fixed, and stained for CETN1 (scale bars: 0.5 μm); **(8D)** shows GFP-KIF2A signal intensity at the mother centriole (3 independent experiments, $n \geq 25$ cells per condition, normalized to CETN1, one-way ANOVA, $**P < 0.01$, $***P < 0.001$); **(8E-F)** hTERT RPE-1 cells DOX-inducibly expressing GFP-KIF2A constructs were fixed and stained with the indicated antibodies; **(8F)** shows cilia length quantification (3 independent experiments, $n \geq 61$ cilia per condition, one-way ANOVA, $**P < 0.01$)

Taken together, our results suggest that TTBK2 phosphorylation destabilizes KIF2A basal body pools and prevents its accumulation at the base of the cilium, which supports efficient axoneme growth. In contrast, truncated TTBK2 inefficiently phosphorylates KIF2A, which seems to alter its turnover, leading to increased KIF2A levels at the ciliary base, and in turn to reduced ciliary length (Fig. 9).

Discussion

We and others have demonstrated that the C-term region of TTBK2 is essential for its interaction with CEP164 [16, 41, 42]. Still, we were initially surprised to see the difference in TTBK2^{trunc1/2}-induced phosphorylation between CEP164 and DVL3. We speculate that such selectivity in targeting individual TTBK2 substrates may be explained by hampered interaction capabilities of truncated TTBK2. Interestingly, our rescue experiment using the TTBK2-CEP164 chimera demonstrates that the diminished ciliogenesis-promoting activity of TTBK2^{trunc1} resides in its spatial properties (mislocalization), rather than a defective kinase activity per se. Importantly, the expression of TTBK2^{trunc1} in hTERT RPE-1 TTBK2 KO allowed for semi-permissive conditions for cilia assembly. Intriguingly, we found that initial events of primary cilia formation (CP110 removal, IFT recruitment, formation of a membrane vesicle), were rather moderately affected. In contrast, TTBK2^{trunc1} was not able to effectively mediate KIF2A turnover and support axoneme elongation. Based on these observations, we hypothesize that individual steps of ciliogenesis likely differ in their requirements for TTBK2 activity.

Earlier work established that the MC-associated pool of KIF2A is phosphorylated by mitotic kinase PLK1 to trigger primary cilia resorption [26]. Our data demonstrate that in addition to its MC-associated pool, KIF2A can also be detected along axonemal microtubules inside the cilium. This observation raises several intriguing possibilities. First, our expansion microscopy data suggest that the MC-associated pool of KIF2A is well within the reach of TTBK2 kinase activity at the MC [43, 44], given the flexibility of TTBK2's long, highly unstructured C-terminal part [42]. Thus, KIF2A seems to be in a suitable position for direct regulation by TTBK2 phosphorylation, analogous to their interactions at microtubule plus ends [24]. Further, the presence of KIF2A inside the cilium helps to explain how KIF2A microtubule-depolymerizing

activity mediates the resorption of primary cilia observed earlier [26]. However, we cannot exclude a contribution of additional mechanisms, e.g. KIF2A action towards microtubules anchored to the subdistal appendages of the MC [45, 46]. We also noted that the axoneme-associated pool of KIF2A was somewhat easier to detect in the case of KIF2A^{KVD}, perhaps due to altered dynamics of tubulin-KIF2A^{KVD} interaction [47, 48]. Furthermore, our data suggest that altered KIF2A turnover contributes to primary cilia defects related to the activities of truncated TTBK2 moieties. We showed that KIF2A accumulated at the MC of TTBK2 KO hTERT RPE-1 cells expressing Flag-TTBK2^{trunc1}, and that primary cilia length can be rescued by KIF2A depletion. Noteworthy, a similar accumulation of KIF2A has also been observed in *Ttbk2* hypomorphic mutant mice [21]. Nonetheless, differential phosphorylation of additional substrates by TTBK2^{wt} vs. truncated TTBK2 may also play a role here – this notion is further supported by our observation that KIF2A depletion fully restored primary cilia length, but only showed a partial rescue on the number of cilia in TTBK2 KO hTERT RPE-1 Flag-TTBK2^{trunc1} cells (5G, S4B).

Our data demonstrate that TTBK2-induced phosphorylation of the S135-140 cluster in KIF2A represents a key regulatory mechanism, which inhibits KIF2A binding to microtubules and reduces KIF2A MC pools. Interestingly, the interaction between microtubules, which are negatively charged, and the positively charged neck region in KIF2C (MCAK), another member of the kinesin-13 family, has been shown to aid KIF2C microtubule binding [49]. It is therefore tempting to speculate that phosphorylation of the S135-140 cluster in KIF2A creates a local negative charge that inhibits KIF2A binding to microtubules by increasing the initial energy barrier between free-in-solution and MT-bound KIF2A states. Lastly, our in vitro and cell-based assays could not resolve a difference between KIF2A^{wt} and KIF2A^{S135-140A}, likely due to altered substrate-to-kinase stoichiometry caused by KIF2A overexpression used in those experiments.

Our earlier work demonstrated that a CEP164 mutant defective in binding TTBK2 fails to rescue ciliogenesis following CEP164 depletion [16]. Indeed, in several systems TTBK2 is essential for the onset of ciliogenesis, with no alternative pathway available to compensate for TTBK2 MC recruitment defect [21, 23]. However, in light of our current data we speculate that concentrating TTBK2 activity at the MC is not strictly necessary

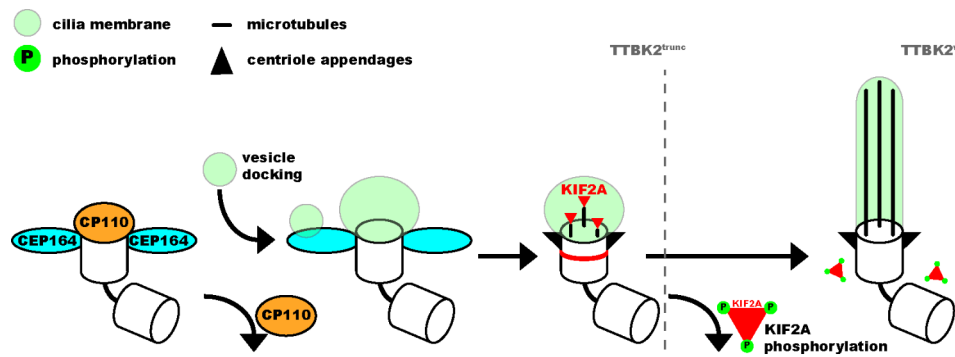


Fig. 9 TTBK2 supports axoneme elongation by phosphorylation-mediated inhibition of KIF2A In our model, TTBK2 kinase activity is needed to prime the basal body for cilia outgrowth by removing CP110 and mediating the docking of ciliary vesicles to the mother centriole. Both wild-type and truncated TTBK2 are sufficient to support these initial processes. TTBK2 activity is then required to inhibit KIF2A and diminish its basal body pool, enabling full elongation of the ciliary axoneme in wild-type TTBK2. In contrast, truncated TTBK2 fails to inhibit KIF2A, leading to KIF2A accumulation at the basal body and shorter cilia

for the phosphorylation of at least some of its basal body substrates, provided the levels and activity of the kinase outside of the MC are sufficiently high (e.g. in TTBK2^{trunc1}-expressing TTBK2 KO hTERT RPE-1 cells). Under such conditions, there seems to be a way to bypass the requirement for MC-concentrated TTBK2 activity when triggering ciliogenesis. This hypothesis is further supported by our observations in CEP164 KO cells, which can form cilia (though rarely) even in the absence of detectable TTBK2 MC pools. The obvious question is if such regulation has any physiological relevance or merely represents a peculiarity of one particular cell culture system. We think the former is indeed a plausible scenario. In fact, our recent work has demonstrated that TTBK1, a kinase highly similar to TTBK2 but lacking the CEP164-binding motif, does not localize to the MC. Remarkably, we found TTBK1 expression upregulated during human pluripotent stem cell neuronal differentiation, in turn allowing it to exert a rescue effect on cilia formation in differentiated, but not undifferentiated TTBK2 KO cells [50], which is in line with the activities of truncated TTBK2 reported here.

Further, previous work by Schmidt et al. [51] demonstrated that CEP164 depletion severely disrupted docking of vesicles to the MC. However, it remained to be discovered if vesicles failed to dock due to TTBK2 misslocalization or because CEP164 played a more direct role during the docking process. Our data support the latter possibility, as cells expressing TTBK2^{trunc1} showed no defects in preciliary vesicle formation (3A-C). Moreover, depleting CEP164 from TTBK2^{trunc1} cells inhibited MC recruitment of membrane markers MyosinVa and RAB34 (S3C-D), and of IFT88 (S3B), favoring the notion that CEP164 might act as a common docking platform at the MC, independently of its TTBK2-recruitment function.

The last (but not least) observation we find pertinent to discuss relates to the TTBK2-mediated removal of

CP110. As TTBK2^{trunc1} does not interact with CEP164, in principle it has no means of “distinguishing” between MC- and DC-associated CP110. However, while elevated levels of TTBK2^{trunc1} may compensate for its absence from the MC, our data clearly show that TTBK2^{trunc1} can specifically remove the MC-pool of CP110, but not the DC-pool of CP110. This decoupling of TTBK2 activity from the recruiting role of CEP164 challenges some of the recently proposed models of TTBK2-induced removal of CP110 [52] and suggests the existence of an additional mechanism ensuring MC-specific CP110 loss. We speculate that distal appendages may be plausible candidates for that function. In fact, depleting CEP164 from TTBK2^{trunc1} cells inhibited CP110 removal from the MC (S3A). Intriguingly, docking of vesicles to the distal appendages has been proposed to act upstream of CP110 removal [10, 17, 53, 54]. However, other studies reporting defective vesicle docking have found no concomitant defect in the removal of CP110 [34, 36]. Thus, the cooperation of distal appendages and TTBK2 to regulate primary cilia assembly warrants further investigation.

Conclusions

TTBK2 has emerged as a crucial regulator of primary cilia formation, but the full scope of its activities and the underlying mechanisms are only starting to become apparent. Herein, we present evidence that (i) TTBK2 supports axoneme growth by restraining KIF2A levels at the mother centriole – to the best of our knowledge, our work provides the first functional validation of a TTBK2-mediated phosphorylation of a ciliary kinesin in the context of primary cilia assembly; and (ii) TTBK2 enrichment at the mother centriole, important to trigger ciliogenesis, might be under specific conditions bypassed.

Supplementary Information

The online version contains supplementary material available at <https://doi.org/10.1186/s12964-025-02072-8>.

Supplementary Material

Acknowledgements

We thank Erich Nigg, Peter Jackson, Randall Moon, Ciaran Morrison, Vítězslav Bryja, and Stephan Angers for sharing reagents with us. We are also grateful to Naděžda Vašková for assistance with TEM. We acknowledge the core facility CELLIM supported by the Czech-Biolmaging large RI project (LM2023050 funded by MEYS CR) for their support with obtaining scientific data presented in this paper. Furthermore, CEITEC Proteomics Core Facility is gratefully acknowledged for obtaining the scientific data presented in this paper. CIISB, Instruct-CZ Centre of Instruct-ERIC EU consortium, funded by MEYS CR infrastructure project LM2023042 and European Regional Development Fund-Project „UP CIISB“ (No. CZ.02.1.01/0.0/0.0/18_046/00159 74), is acknowledged for the financial support of the measurements at the CEITEC Proteomics Core Facility. We also acknowledge the Centre of Imaging Methods core facility, Faculty of Science, Charles University, supported by the Czech-Biolmaging through MEYS CR (LM2015062 and CZ.02.1.01/0.0/0.0/16_013/0001775). Lastly, computational resources were provided by the e-INFRA CZ project (ID:90254), supported by the Ministry of Education, Youth and Sports of the Czech Republic.

Author contributions

D.V. - performed and analyzed most of the experiments and assembled the figures, O.B. - contributed to stable cell lines generation and performed initial experiments, E.L. - performed in vitro TIRF experiments, T.R. - carried out experiments with pCEP164 antibody, L.B. - performed time lapse experiment with ARL13B reporter cell line in Fig. 5, A.L. - contributed to analysis of KIF2A mutants in Fig. 8, T.D. - contributed to WB analysis in Fig. 1, Z.L. - supervised in vitro TIRF experiments, L.C. - conceptualized and supervised the study and together with D.V. wrote the paper. All authors approved the final version of the manuscript.

Funding

This work was supported by grant 22–132775 from Czech Science Foundation to LC, the institutional support of the Czech Academy of Sciences (RVO: 86652036), and project LX22NPO5107 (MEYS): Financed by European Union – Next Generation EU. DV was supported by grant MUNI/C/0026/2020 from Masaryk University. TD was supported by grant MUNI/A/1738/2024 from Masaryk University. TR was supported by grant MUNI/R/1148/2021 from Masaryk University.

Data availability

No datasets were generated or analysed during the current study.

Declarations

Ethics approval and consent to participate

N/A.

Consent for publication

N/A.

Competing interests

The authors declare no competing interests.

Received: 11 November 2024 / Accepted: 29 January 2025

Published online: 10 February 2025

References

1. Satir P, Christensen ST. Overview of structure and function of mammalian cilia. *Annu Rev Physiol*. 2007;69:377–400. <https://doi.org/10.1146/annurev.physiol.69.040705.141236>

2. Anvarian Z, Mykityn K, Mukhopadhyay S, Pedersen LB, Christensen ST. Cellular signalling by primary cilia in development, organ function and disease. *Nat Rev Nephrol*. 2019;15(4):199–219. <https://doi.org/10.1038/s41581-019-0116-9>
3. Huangfu D, Liu A, Rakeman AS, Murcia NS, Niswander L, Anderson KV. Hedgehog signalling in the mouse requires intraflagellar transport proteins. *Nature*. 2003;426(6962):83–87. <https://doi.org/10.1038/nature02061>
4. Basu B, Brueckner M. Cilia multifunctional organelles at the center of vertebrate left-right asymmetry. *Curr Top Dev Biol*. 2008;85:151–174. [https://doi.org/10.1016/S0070-2153\(08\)00806-5](https://doi.org/10.1016/S0070-2153(08)00806-5)
5. Braun DA, Hildebrandt F. Ciliopathies. *Cold Spring Harb Perspect Biol*. 2017;9(3):a028191. Published 2017 Mar 1. <https://doi.org/10.1101/cshperspect.a028191>
6. Reiter JF, Leroux MR. Genes and molecular pathways underpinning ciliopathies. *Nat Rev Mol Cell Biol*. 2017;18(9):533–547. <https://doi.org/10.1038/nrm.2017.60>
7. Seeley ES, Nachury MV. The perennial organelle: assembly and disassembly of the primary cilium. *J Cell Sci*. 2010;123(Pt 4):511–518. <https://doi.org/10.1242/jcs.061093>
8. Caspari T, Larkins CE, Anderson KV. The graded response to Sonic Hedgehog depends on cilia architecture. *Dev Cell*. 2007;12(5):767–778. <https://doi.org/10.1016/j.devcel.2007.03.004>
9. Tanos BE, Yang HJ, Soni R, et al. Centriole distal appendages promote membrane docking, leading to cilia initiation. *Genes Dev*. 2013;27(2):163–168. <https://doi.org/10.1101/gad.207043.112>
10. Kanie T, Liu B, Love JF, Fisher SD, Gustavsson AK, Jackson PK. A hierarchical pathway for assembly of the distal appendages that organize primary cilia. *Elife*. Published online January 30, 2025. <https://doi.org/10.7554/eLife.85999>
11. Spektor A, Tsang WY, Khoo D, Dynlacht BD. Cep97 and CP110 suppress a cilia assembly program. *Cell*. 2007;130(4):678–690. <https://doi.org/10.1016/j.cell.2007.06.027>
12. Lechtreck KF, Van De Weghe JC, Harris JA, Liu P. Protein transport in growing and steady-state cilia. *Traffic*. 2017;18(5):277–286. <https://doi.org/10.1111/tra.12474>
13. Goetz SC, Liem KF Jr, Anderson KV. The spinocerebellar ataxia-associated gene Tau tubulin kinase 2 controls the initiation of ciliogenesis. *Cell*. 2012;151(4):847–858. <https://doi.org/10.1016/j.cell.2012.10.010>
14. Takahashi M, Tomizawa K, Sato K, Ohtake A, Omori A. A novel tau-tubulin kinase from bovine brain. *FEBS Lett*. 1995;372(1):59–64. [https://doi.org/10.1016/0014-5793\(95\)00955-9](https://doi.org/10.1016/0014-5793(95)00955-9)
15. Qi H, Yao C, Cai W, Girtan J, Johansen KM, Johansen J. Asator, a tau-tubulin kinase homolog in *Drosophila* localizes to the mitotic spindle. *Dev Dyn*. 2009;238(12):3248–3256. <https://doi.org/10.1002/dvdy.22150>
16. Čajánek L, Nigg EA. Cep164 triggers ciliogenesis by recruiting Tau tubulin kinase 2 to the mother centriole. *Proc Natl Acad Sci U S A*. 2014;111(28):E2841–E2850. <https://doi.org/10.1073/pnas.1401777111>
17. Lo CH, Lin IH, Yang TT, et al. Phosphorylation of CEP83 by TTBK2 is necessary for cilia initiation. *J Cell Biol*. 2019;218(10):3489–3505. <https://doi.org/10.1083/jcb.201811142>
18. Bernatik O, Pejškova P, Vysloulžil D, Hanáková K, Zdrahal Z, Čajánek L. Phosphorylation of multiple proteins involved in ciliogenesis by Tau Tubulin kinase 2. *Mol Biol Cell*. 2020;31(10):1032–1046. <https://doi.org/10.1091/mbc.E19-06-0334>
19. Hanáková K, Bernatik O, Kravec M, et al. Comparative phosphorylation map of Dishevelled 3 links phospho-signatures to biological outputs. *Cell Commun Signal*. 2019;17(1):170. Published 2019 Dec 23. <https://doi.org/10.1186/s12964-019-0470-z>
20. Nguyen A, Goetz SC. TTBK2 controls cilium stability by regulating distinct modules of centrosomal proteins. *Mol Biol Cell*. 2023;34(1):ar8. doi:10.1091/mbc.E22-08-0373
21. Bowie E, Norris R, Anderson KV, Goetz SC. Spinocerebellar ataxia type 11-associated alleles of Ttbk2 dominantly interfere with ciliogenesis and cilium stability. *PLoS Genet*. 2018;14(12):e1007844. Published 2018 Dec 10. <https://doi.org/10.1371/journal.pgen.1007844>
22. Houlden H, Johnson J, Gardner-Thorpe C, et al. Mutations in TTBK2, encoding a kinase implicated in tau phosphorylation, segregate with spinocerebellar ataxia type 11 [published correction appears in *Nat Genet*. 2008 Feb;40(2):255. Giunti, Paolo [corrected to Giunti, Paola]]. *Nat Genet*. 2007;39(12):1434–1436. <https://doi.org/10.1038/ng.2007.43>
23. Bouskila M, Esoof N, Gay L, et al. TTBK2 kinase substrate specificity and the impact of spinocerebellar-ataxia-causing mutations on expression, activity,

- localization and development. *Biochem J.* 2011;437(1):157–167. <https://doi.org/10.1042/BJ20110276>
24. Watanabe T, Kakeno M, Matsui T, et al. TTBK2 with EB1/3 regulates microtubule dynamics in migrating cells through KIF2A phosphorylation. *J Cell Biol.* 2015;210(5):737–751. <https://doi.org/10.1083/jcb.201412075>
25. Desai A, Verma S, Mitchison TJ, Walczak CE. Kin I kinesins are microtubule-depolymerizing enzymes. *Cell.* 1999;96(1):69–78. [https://doi.org/10.1016/S0092-8674\(00\)80960-5](https://doi.org/10.1016/S0092-8674(00)80960-5)
26. Miyamoto T, Hosoba K, Ochiai H, et al. The Microtubule-Depolymerizing Activity of a Mitotic Kinesin Protein KIF2A Drives Primary Cilia Disassembly Coupled with Cell Proliferation. *Cell Rep.* 2015;10(5):664–673. <https://doi.org/10.1016/j.celrep.2015.01.003>
27. Binó L, Mikulenková E, Štěpánek L, et al. A protocol for generation and live-cell imaging analysis of primary cilia reporter cell lines. *STAR Protoc.* 2022;3(1):101199. Published 2022 Mar 2. <https://doi.org/10.1016/j.xpro.2022.101199>
28. Lauring MC, Zhu T, Luo W, Wu W, Yu F, Toomre D. New software for automated cilia detection in cells (ACDC). *Cilia.* 2019;8:1. Published 2019 Aug 1. <https://doi.org/10.1186/s13630-019-0061-z>
29. Hansen JN, Rassmann S, Stüven B, Jurisch-Yaksi N, Wachten D. CiliaQ: a simple, open-source software for automated quantification of ciliary morphology and fluorescence in 2D, 3D, and 4D images. *Eur Phys J E Soft Matter.* 2021;44(2):18. Published 2021 Mar 8. <https://doi.org/10.1140/epje/s10189-021-00031-y>
30. Koulouras G, Panagopoulos A, Rapsomaniki MA, Giakoumakis NN, Taraviras S, Lygerou Z. EasyFRAP-web: a web-based tool for the analysis of fluorescence recovery after photobleaching data. *Nucleic Acids Res.* 2018;46(W1):W467–W472. <https://doi.org/10.1093/nar/gky508>
31. Livak KJ, Schmittgen TD. Analysis of relative gene expression data using real-time quantitative PCR and the 2⁻(Delta Delta C(T)) Method. *Methods.* 2001;25(4):402–408. <https://doi.org/10.1006/meth.2001.1262>
32. Daly OM, Gaboriau D, Karakaya K, et al. CEP164-null cells generated by genome editing show a ciliation defect with intact DNA repair capacity. *J Cell Sci.* 2016;129(9):1769–1774. <https://doi.org/10.1242/jcs.186221>
33. Sorokin S. Centrioles and the formation of rudimentary cilia by fibroblasts and smooth muscle cells. *J Cell Biol.* 1962;15(2):363–377. <https://doi.org/10.1083/jcb.15.2.363>
34. Wu CT, Chen HY, Tang TK. Myosin-Va is required for preciliary vesicle transportation to the mother centriole during ciliogenesis. *Nat Cell Biol.* 2018;20(2):175–185. <https://doi.org/10.1038/s41556-017-0018-7>
35. Stuck MW, Chong WM, Liao JC, Pazour GJ. Rab34 is necessary for early stages of intracellular ciliogenesis. *Curr Biol.* 2021;31(13):2887–2894.e4. <https://doi.org/10.1016/j.cub.2021.04.018>
36. Ganga AK, Kennedy MC, Oguchi ME, et al. Rab34 GTPase mediates ciliary membrane formation in the intracellular ciliogenesis pathway. *Curr Biol.* 2021;31(13):2895–2905.e7. <https://doi.org/10.1016/j.cub.2021.04.075>
37. Larkins CE, Aviles GD, East MP, Kahn RA, Caspary T. Arl13b regulates ciliogenesis and the dynamic localization of Shh signaling proteins. *Mol Biol Cell.* 2011;22(23):4694–4703. <https://doi.org/10.1091/mbc.E10-12-0994>
38. Walczak CE, Gayek S, Ohi R. Microtubule-depolymerizing kinesins. *Annu Rev Cell Dev Biol.* 2013;29:417–441. <https://doi.org/10.1146/annurev-cellbio-101512-122345>
39. Varadi M, Anyango S, Deshpande M, et al. AlphaFold Protein Structure Database: massively expanding the structural coverage of protein-sequence space with high-accuracy models. *Nucleic Acids Res.* 2022;50(D1):D439–D444. <https://doi.org/10.1093/nar/gkab1061>
40. Jumper J, Evans R, Pritzel A, et al. Highly accurate protein structure prediction with AlphaFold. *Nature.* 2021;596(7873):583–589. <https://doi.org/10.1038/s41586-021-03819-2>
41. Oda T, Chiba S, Nagai T, Mizuno K. Binding to Cep164, but not EB1, is essential for centriolar localization of TTBK2 and its function in ciliogenesis. *Genes Cells.* 2014;19(12):927–940. <https://doi.org/10.1111/gtc.12191>
42. Rosa E Silva I, Binó L, Johnson CM, et al. Molecular mechanisms underlying the role of the centriolar CEP164-TTBK2 complex in ciliopathies. *Structure.* 2022;30(1):114–128.e9. <https://doi.org/10.1016/j.str.2021.08.007>
43. Yang TT, Chong WM, Wang WJ, et al. Super-resolution architecture of mammalian centriole distal appendages reveals distinct blade and matrix functional components. *Nat Commun.* 2018;9(1):2023. Published 2018 May 22. <https://doi.org/10.1038/s41467-018-04469-1>
44. Bowler M, Kong D, Sun S, et al. High-resolution characterization of centriole distal appendage morphology and dynamics by correlative STORM and electron microscopy. *Nat Commun.* 2019;10(1):993. Published 2019 Mar 1. <https://doi.org/10.1038/s41467-018-08216-4>
45. Hall NA, Hehnyly H. A centriole's subdistal appendages: contributions to cell division, ciliogenesis and differentiation. *Open Biol.* 2021;11(2):200399. <https://doi.org/10.1098/rsob.200399>
46. Mazo G, Soplop N, Wang WJ, Uryu K, Tsou MF. Spatial Control of Primary Ciliogenesis by Subdistal Appendages Alters Sensation-Associated Properties of Cilia. *Dev Cell.* 2016;39(4):424–437. <https://doi.org/10.1016/j.devcel.2016.10.006>
47. Trofimova D, Paydar M, Zara A, Talje L, Kwok BH, Allingham JS. Ternary complex of Kif2A-bound tandem tubulin heterodimers represents a kinesin-13-mediated microtubule depolymerization reaction intermediate. *Nat Commun.* 2018;9(1):2628. Published 2018 Jul 6. <https://doi.org/10.1038/s41467-018-05025-7>
48. Wang W, Shen T, Guerois R, et al. New Insights into the Coupling between Microtubule Depolymerization and ATP Hydrolysis by Kinesin-13 Protein Kif2C. *J Biol Chem.* 2015;290(30):18721–18731. <https://doi.org/10.1074/jbc.M115.646919>
49. Cooper JR, Wagenbach M, Asbury CL, Wordeman L. Catalysis of the microtubule on-rate is the major parameter regulating the depolymerase activity of MCAK. *Nat Struct Mol Biol.* 2010;17(1):77–82. <https://doi.org/10.1038/nsmb.1728>
50. Binó L, Čajánek L. Tau tubulin kinase 1 and 2 regulate ciliogenesis and human pluripotent stem cells-derived neural rosettes. *Sci Rep.* 2023;13(1):12884. Published 2023 Aug 9. <https://doi.org/10.1038/s41598-023-39887-9>
51. Schmidt KN, Kuhns S, Neuner A, Hub B, Zentgraf H, Pereira G. Cep164 mediates vesicular docking to the mother centriole during early steps of ciliogenesis. *J Cell Biol.* 2012;199(7):1083–1101. <https://doi.org/10.1083/jcb.201202126>
52. Huang N, Zhang D, Li F, et al. M-Phase Phosphoprotein 9 regulates ciliogenesis by modulating CP110-CEP97 complex localization at the mother centriole. *Nat Commun.* 2018;9(1):4511. Published 2018 Oct 30. <https://doi.org/10.1038/s41467-018-06990-9>
53. Lu Q, Insinna C, Ott C, et al. Early steps in primary cilium assembly require EHD1/EHD3-dependent ciliary vesicle formation. *Nat Cell Biol.* 2015;17(4):531. <https://doi.org/10.1038/ncb3155>
54. Walia V, Cuenca A, Vetter M, et al. Akt Regulates a Rab11-Effector Switch Required for Ciliogenesis. *Dev Cell.* 2019;50(2):229–246.e7. <https://doi.org/10.1016/j.devcel.2019.05.022>

Publisher's note

Springer Nature remains neutral with regard to jurisdictional claims in published maps and institutional affiliations.

Appendix 4

Binó L, Čajánek L*. Tau tubulin kinase 1 and 2 regulate ciliogenesis and human pluripotent stem cells-derived neural rosettes. *Scientific Reports*. 2023 Aug 9;13(1):12884. doi: 10.1038/s41598-023-39887-9. (JCR 2023, IF = 3.8, Q1 – Multidisciplinary Sciences)



OPEN Tau tubulin kinase 1 and 2 regulate ciliogenesis and human pluripotent stem cells–derived neural rosettes

Lucia Binó¹ & Lukáš Čajánek^{1,2}

Primary cilia are key regulators of embryo development and tissue homeostasis. However, their mechanisms and functions, particularly in the context of human cells, are still unclear. Here, we analyzed the consequences of primary cilia modulation for human pluripotent stem cells (hPSCs) proliferation and differentiation. We report that neither activation of the cilia-associated Hedgehog signaling pathway nor ablation of primary cilia by CRISPR gene editing to knockout Tau Tubulin Kinase 2 (TTBK2), a crucial ciliogenesis regulator, affects the self-renewal of hPSCs. Further, we show that TTBK1, a related kinase without previous links to ciliogenesis, is upregulated during hPSCs-derived neural rosette differentiation. Importantly, we demonstrate that while TTBK1 fails to localize to the mother centriole, it regulates primary cilia formation in the differentiated, but not the undifferentiated hPSCs. Finally, we show that TTBK1/2 and primary cilia are implicated in the regulation of the size of hPSCs-derived neural rosettes.

Cilia are hair-like organelles protruding from the surface of most cells. While the motile cilia are perhaps the oldest organelles ever known¹, the function of the single non-motile primary cilium has for a long time been enigmatic. It is now appreciated that primary cilium contains receptors and effectors of several signaling pathways, such as the Hedgehog (HH) pathway^{2,3}. Conversely, primary cilia govern important aspects of embryonic development and tissue homeostasis^{3,4}. Defects in the assembly and function of primary cilia cause diseases such as Bardet-Biedel syndrome, Joubert syndrome, or nephronophthisis, collectively termed ciliopathies⁵. Cilia status also affects certain types of cancer, such as medulloblastoma or basal cell carcinoma⁶. Therefore, targeting cilium-related pathways may represent a propitious therapeutic strategy.

The fully grown primary cilium is composed of the mother centriole-derived basal body, the transition zone, and the microtubule-based axoneme enclosed within a ciliary membrane⁷. The cilium assembly is initiated at the distal end of the mother centriole, by the coordinated action of distal appendage components (such as CEP83 and CEP164) and Tau Tubulin kinase 2 (TTBK2)^{8–11}. TTBK2 kinase activity is essential for ciliogenesis—no cilia are formed in cells devoid of the active kinase. Following the delivery and docking of vesicles to the distal appendages, components of Intraflagellar transport (IFT) are recruited in a TTBK2-dependent manner^{8,10} to facilitate the growth of the ciliary axoneme by transporting various cargoes between the cilia base and tip¹². Noteworthy, no evidence for a role in cilia formation has yet been provided for TTBK1, with its kinase domain highly similar to that of TTBK2¹³.

The Hedgehog pathway is perhaps the best-characterized signaling pathway relying on primary cilia. In the absence of HH ligand, the Patched (PTCH) receptor localizes inside the primary cilium and prevents ciliary accumulation of the receptor Smoothened (SMO). The binding of the HH ligand to PTCH initiates the removal of PTCH from the cilium, in turn leading to the accumulation of SMO inside cilia. SMO then interacts with cholesterol inside the cilium to switch the processing of GLI from its repressive form (GLI-R) to the active (GLI-A) form. Both GLI-R and GLI-A are translocated from primary cilia to the cell nucleus to repress and induce HH target genes, respectively^{2,4,14}. The transcripts regulated by HH include components of the pathway (i.e. *PTCH1*, *GLI1*), as well as transcription factors regulating proliferation and cell fate decisions³.

The HH signaling pathway plays a prominent role in neural development. Its activity is critical for the establishment of the floor plate (the source of HH ligand in the ventral part of the neural tube) and the specification of individual neuronal types^{15,16}. This activity is opposed by WNT/beta-catenin and BMP pathways. Thus, the neural tube pattern formation results from counteracting activities of HH, WNT, and BMP, regulated both spatially and

¹Laboratory of Cilia and Centrosome Biology, Department of Histology and Embryology, Faculty of Medicine, Masaryk University, Kamenice 3, 62500 Brno, Czech Republic. ²Section of Animal Physiology and Immunology, Department of Experimental Biology, Faculty of Science, Masaryk University, Kamenice 5, 62500 Brno, Czech Republic. ✉email: cajanek@med.muni.cz

Figure 1. HH signaling increases the size of neural rosettes. **(A)** Experimental design of neural rosettes early phase differentiation experiments. Cells were seeded on D0, SAG treatment started on D1 and cultures were analyzed on D9. **(B)** Representative image of cilia IF staining in early phase differentiation of CCTL14 rosettes on D9, ARL13B staining was used to detect primary cilia, γ -TUBULIN staining indicates centrioles; scalebar = 20 μ m. **(C)** SHH target gene *GLI1* and *PTCH1* mRNA expression (qRT-PCR) in mock- and SAG-treated early phase of differentiation CCTL14 rosettes (D9); n = 5, t-test. **(D)** Experimental design of neural rosettes later phase differentiation experiments. D0—start of the experiment, D9—patches of neural rosettes were transferred in a fresh culture plate, D10—start of daily SAG treatment, D15/20—analysis. **(E)** Representative images of mock- or SAG-treated later stage differentiation CCTL14 rosettes on D15 in phase contrast (top) and IF (bottom), PAX6 staining was used to show ongoing neural differentiation, ZO1 staining indicates polarization in the lumen of neural rosettes; scalebar = 100 μ m. **(F)** Measurement of the rosette area in mock- or SAG-treated later stage differentiation CCTL14 rosettes on D15; n = 3, t-test. **(G)** Representative images of mock- or SAG-stimulated later stage differentiation Neo1 rosettes on D15 in phase contrast; scalebar = 100 μ m. **(H)** Measurement of the rosette area in mock- or SAG-treated later stage differentiation Neo1 rosettes on D15; n = 4, t-test.

temporally^{17,18}. In addition, HH signaling drives cell proliferation during neurodevelopment in mice¹⁹ and can promote cell division in both neural and non-neural cell types^{20,21}.

A major obstacle to the understanding of the role of the primary cilium and cilium-associated pathways has been the absence of a suitable cellular system to model human phenotypes and mechanisms. Human pluripotent stem cells (hPSCs), encompassing embryonic stem cells (ESCs) and induced pluripotent stem cells (iPSCs), can self-renew and differentiate into all cell types of the human body^{22,23}. Consequently, they hold great promise for modeling both physiological and pathophysiological aspects of human embryogenesis “in a dish”^{24,25}. Interestingly, undifferentiated hPSCs can assemble primary cilia and express HH pathway components^{26–28}. In mice, primary cilia start to appear in the epiblast, following embryo implantation²⁹. However, the relevance of primary cilia for hPSCs self-renewal or differentiation capabilities is incompletely understood, with contradictions in the literature. While primary cilia have been proposed as instrumental for neural differentiation of hPSCs³⁰, their ablation, either in mouse embryos or in hPSCs, leads to surprisingly subtle neural differentiation defects^{31,32}.

Events of neural differentiation and neural tube development can be modeled using hPSCs-derived neural rosettes, assemblies of radially organized neuroepithelial cells with a central lumen^{33,34}. The neural rosettes, typically expressing early neuronal markers such as SOX2 and PAX6, can be readily specified into individual region-specific neuronal subtypes as well as serve as a progenitor niche^{35–37}. HH pathway, together with Notch signaling, has been implicated in the maintenance of neural rosettes³³.

Here, we combine the pharmacological activation of the HH signaling pathway with the CRISPR/Cas9-mediated ablation of TTBK2, to investigate the role of primary cilia in the proliferation and neural differentiation of hPSCs. We demonstrate that while TTBK2 and primary cilia are not required for the self-renewal of hPSCs, primary cilia and HH signaling regulate the size of hPSCs-derived neural rosettes. In addition, our data identify an unexpected role for TTBK1 in the cilium assembly pathway.

Results

HH signaling increases the size of neural rosettes. To examine the role of primary cilia-related HH signaling in hPSCs (human pluripotent stem cells), we treated CCTL14 hPSC line with Smoothened Agonist (SAG) (5 nM, day (D)1–9) during neural rosettes differentiation (Fig. 1A). First, we observed ARL13B positive primary cilia pointing out of the apical cell surface (lumen) of the neural rosette (Fig. 1B), in agreement with a previous report²⁷. Next, we found that SAG treatment led to an induction of mRNA expression of HH target genes *GLI1* and *PTCH1* (Fig. 1C). In contrast, while SAG or mock treated rosettes showed expected changes in mRNA levels of pluripotency (NANOG, OCT4) and differentiation (PAX6, and ISL1) markers over undifferentiated control, SAG did not have a notable effect on the expression of any of those makers (Suppl. Fig. 1A).

Next, we examined the effects of HH pathway activation in a later stage of neural rosette differentiation. To this end, we dissected patches of CCTL14-derived neural rosettes on D9 and cultured them in the presence of SAG/vehicle until D15 or D20 (Fig. 1D). On D15, cells forming the rosettes expressed neuronal marker PAX6 and showed tight junction protein ZO-1 highly enriched at the apical membrane (Fig. 1E), as expected³⁸. Consistent with the role of the HH pathway in neural tube patterning¹⁸ we also observed increased expression of *SHH* mRNA and reduced expression of *WNT1* mRNA following the SAG treatment (Suppl. Fig. 1B). Interestingly, we found the SAG-treated rosettes were notably larger than their mock-treated controls (Fig. 1E,F). Importantly, we confirmed the effect of SAG treatment on the neural rosette size using iPSC line Neo1 (Fig. 1G,H). In sum, our data confirm and extend the previous observation of a positive effect of HH pathway activation on neural rosette size³³.

TTBK2 is crucial for ciliogenesis but dispensable for self-renewal in hPSCs. Having validated our model system, we used CRISPR gene editing to establish TTBK2 knockout (KO) in CCTL14 hPSCs. We hypothesized that TTBK2 null hPSCs should be devoid of primary cilia. In line with that, we observed that WT (mock transfected) hPSCs formed ARL13B + primary cilia in about 50% of cells, while hPSCs transfected with TTBK2 gRNA (we termed this mixed cell population “TTBK2 low”) showed notable reduction in ciliation (Fig. 2A). In turn, we isolated individual clonal lines. First, we verified that CRISPR-Cas9 successfully disrupted ORF of the TTBK2 locus in exon 4, which encodes a part of the kinase domain (Fig. 2B and Suppl. Fig. 2A). In total, we obtained 4 TTBK2 KO and 3 WT counterparts (WT1 and WT2 clones were derived from mock transfected population, while WT3 represents “unedited” clone isolated from the “TTBK2 low” mixed population), which

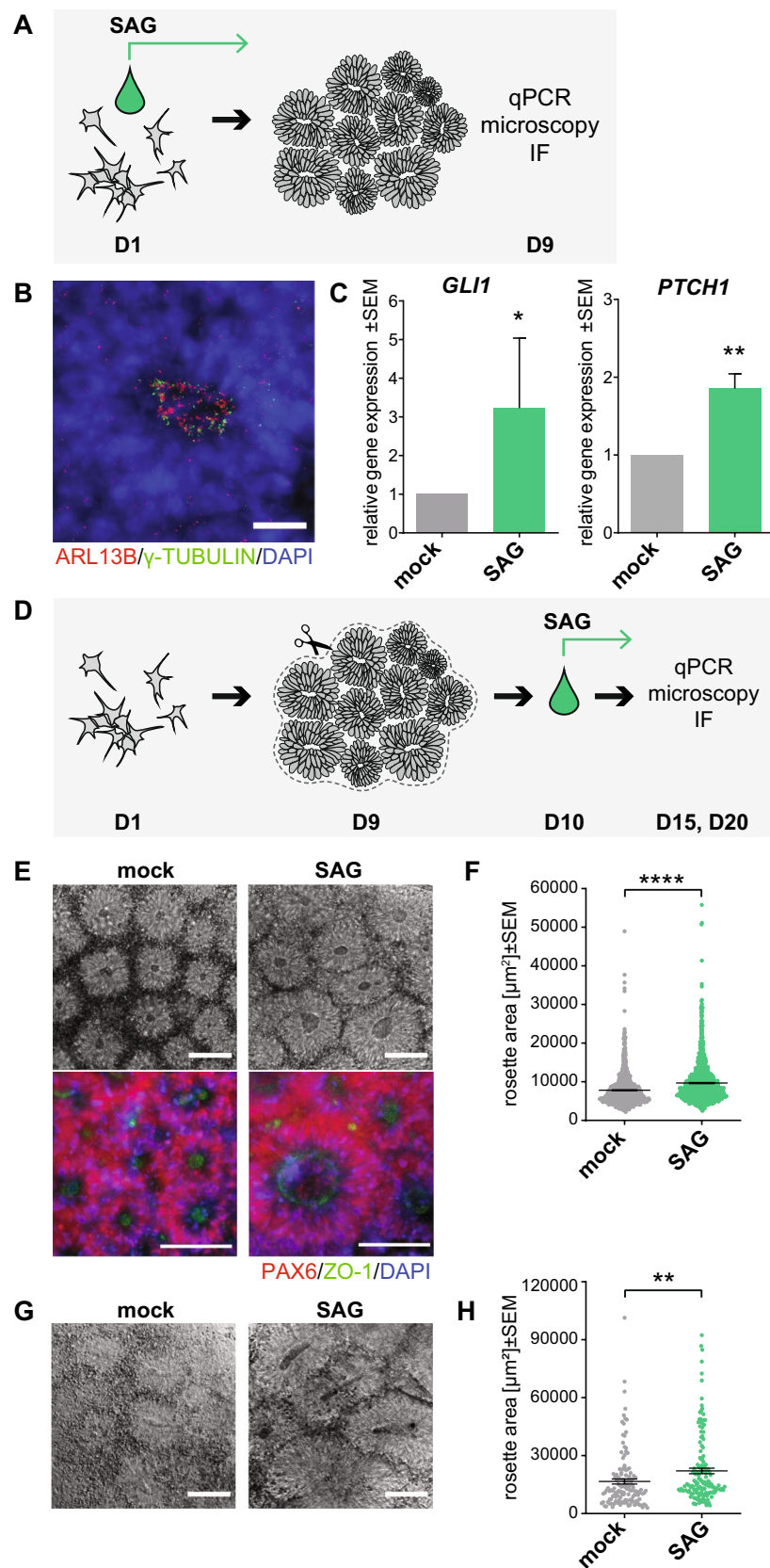


Figure 2. TTBK2 is crucial for ciliogenesis but dispensable for self-renewal in hPSCs. (A) Percentage of cells with ARL13B + primary cilium in WT (mock transfected) and “TTBK2 low” populations of CCTL14 hPSCs. 40 cells per image from 6 images analyzed for each condition. (B) Schematic of the TTBK2 exon 4 sequence detail in representative WT and TTBK2 CRISPR cell lines, purple = insertion/deletion. (C) Representative images of IF detection of TTBK2 (top) and cilia presence (bottom; visualized by ARL13B staining) in undifferentiated WT and TTBK2 KO. γ -TUBULIN staining was used to detect centrioles; scalebar = 5 μ m. (D) Representative images of colony morphology of undifferentiated cells in WT1 and TTBK2 KO1. (E) Percentage of cells with ARL13B + primary cilium in individual clonal cell lines. 20 cells in 1–3 ROIs per image from 2–3 images for each condition were analyzed. (F) Relative growth comparison of indicated undifferentiated WT and TTBK2 KO lines assessed by crystal violet absorption measurement, centrinone treatment previously shown to impair the proliferation capacity was used as a control; n = 3. (G) mRNA expression (qRT-PCR) of pluripotency markers *NANOG* and *OCT4* in undifferentiated WT1 and TTBK2 KO1. Parental CCTL14 differentiated into neural rosettes was included for reference; n = 4, one way ANOVA with Holm-Sidak’s multiple comparisons test.

we used as controls in our following experiments. Of note, we also obtained one heterozygote line, with one allele disrupted and the other containing in-frame deletion within the kinase domain (Suppl. Fig. 2A), which we termed TTBK2 “mutant” (TTBK2 MUT). Next, we confirmed the lack of detectable levels of TTBK2 protein in total cell lysate (Suppl. Fig. 2B.) and at the mother centriole in TTBK2 KO/MUT lines (Fig. 2C and Suppl. Fig. 2C). Importantly, the lines lacking TTBK2 expression failed to form ARL13B + primary cilia (Fig. 2C,E, and Suppl. Fig. 2C).

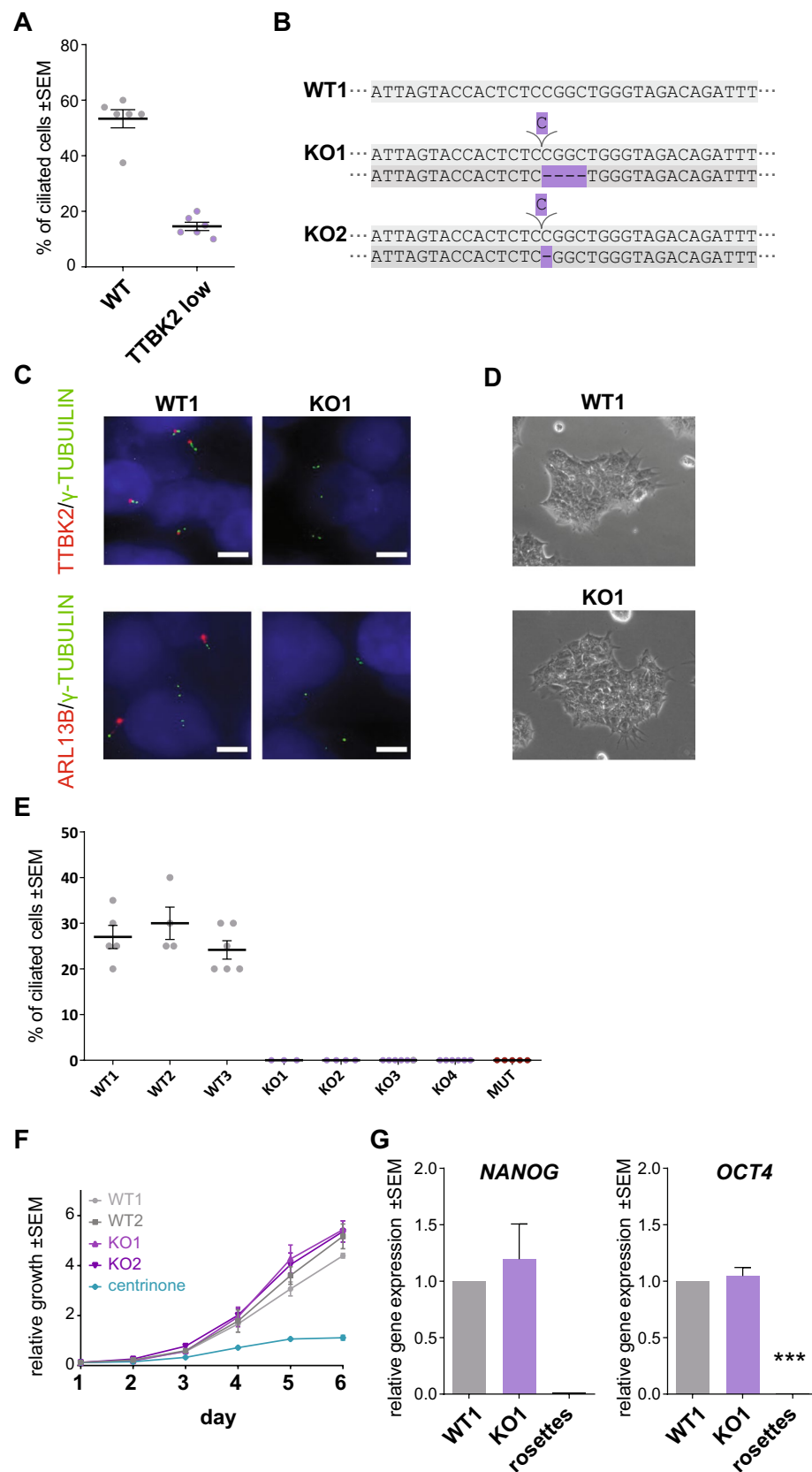
Both TTBK2 WT and TTBK2 KO/MUT hPSCs grew in flat smooth-edged colonies with proto-typical hPSCs morphology (Fig. 2D, Suppl. Fig. 2D), which remained stable and self-renewing with no apparent signs of spontaneous differentiation in over 20 + passages. In line with that, we found that while depletion of centrioles by centrinone (150 nM) treatment^{39,40} significantly impaired the proliferation capacity of hPSCs, the ablation of TTBK2/primary cilia showed no such effect (Fig. 2F and Suppl. Fig. 2E). Moreover, TTBK2 WT and KO expressed comparable levels of pluripotency markers *OCT4* and *NANOG* (Fig. 2G, and Suppl. Fig. 2B and F). Similarly, we found no effect of SAG treatment on the proliferation of CCTL14 and Neo1 hPSCs (Suppl. Fig. 2G,H), the expression of pluripotency markers *OCT4* and *NANOG* (Suppl. Fig. 2I,J), and protein level of *OCT4* (Suppl. Fig. 2K). These results confirm and extend recent observations on the primary cilia—self-renewal relationship^{32,41} and suggest that TTBK2 and primary cilia are dispensable for self-renewal of hPSCs.

Lack of TTBK2 increases the size of neural rosettes. Primary cilia are required for the correct activity of both the positive and negative HH pathway regulators³. As a result, primary cilia mutants show a loss of function HH phenotypes in some cell types and a gain of function HH phenotypes in others⁴. Given that, we asked what specific function TTBK2/primary cilia serve in the regulation of the size of hPSC-derived neural rosettes. To this end, we adopted the protocol used earlier (Fig. 1D). First, we confirmed that TTBK2 was absent from mother centrioles (Suppl. Fig. 3) and the primary cilia formation was impaired in TTBK2 KO neural rosettes (Fig. 3A,B). Next, we found both WT and KO TTBK2 lines were able to efficiently form neural rosettes expressing PAX6, with ZO-1 recruited to the apical membrane (Fig. 3C,D). Remarkably, we noticed that neural rosettes were notably larger in mock-treated TTBK2 KOs than in the corresponding WT controls. In addition, while SAG treatment promoted the rosette size increase in WT, it failed to show an additive effect in TTBK2 KO (Fig. 3D,E). Next, we asked if altered cell proliferation may explain the observed effects on neural rosette size. To this end, we examined the number of phospho histone 3 (pH3) positive cells in neural rosettes on D15. Indeed, we found the relative number of pH3 + cells was elevated in TTBK2 KO and MUT cells, respectively (Fig. 3F,G).

In sum, these results demonstrate that while TTBK2 and primary cilia are required for the response to HH pathway stimulation in neural rosettes, their ablation mimics the HH pathway activation phenotype. However, as we have not been able to unambiguously determine the status of HH pathway activation in differentiating WT and TTBK2 KO neural rosettes, contribution of other pathways to the rosette size phenotype is formally possible.

Tau tubulin kinase 1 (TTBK1) regulates cilia formation. Our data indicated that TTBK2 is indispensable for ciliogenesis in undifferentiated hPSCs (Fig. 2B, Suppl. Fig. 2C), in agreement with its role in primary cilia formation in other biological systems^{8,42}. Surprisingly, our data also revealed that even when TTBK2 was absent (Suppl. Fig. 3), some primary cilia still formed with the ongoing differentiation of TTBK2 KO-derived neural rosettes (Fig. 3A), albeit at a much-reduced rate over WT (Fig. 3B). We hypothesized that the absence of TTBK2 may be partially rescued specifically during neural differentiation. In turn, we considered Tau tubulin kinase 1 (TTBK1) as a plausible mediator of such rescue effect. As we already mentioned, TTBK1 had no previous links to the regulation of ciliogenesis, but shared a high degree of sequence homology in its kinase domain with TTBK2 (Suppl. Fig. 4C), and showed high expression levels in the CNS¹³.

First, we examined the expression of *TTBK1* and found its mRNA levels significantly upregulated in differentiating CCTL14 hPSC—derived neural rosettes (Fig. 4A), and in neuro-differentiated cultures and organoids of i3N iPSCs (Suppl. Fig. 4A). Next, we used TTBK1/2 inhibitor⁴¹ (1 μ M) during neural rosette differentiation (D12–15) of TTBK2 WT and KO hPSCs, respectively. We found that the treatment not only reduced ciliogenesis in TTBK2 WT but almost fully eliminated cilia formation in TTBK2 KO (Fig. 4C). Importantly, the inhibition of TTBK1/2 led to an additional increase of the rosette size in TTBK2 KO (Fig. 4D). To corroborate this observation, we transiently expressed TTBK1-Halo in TTBK2 KO hPSCs and hTERT-RPE-1 TTBK2 KO cells. Remarkably, we found that while transiently expressed GFP-TTBK2 localized to basal bodies, TTBK1-Halo failed to do so, nevertheless its expression partially supported the formation of ARL13b + primary cilia in TTBK2 KO cells.



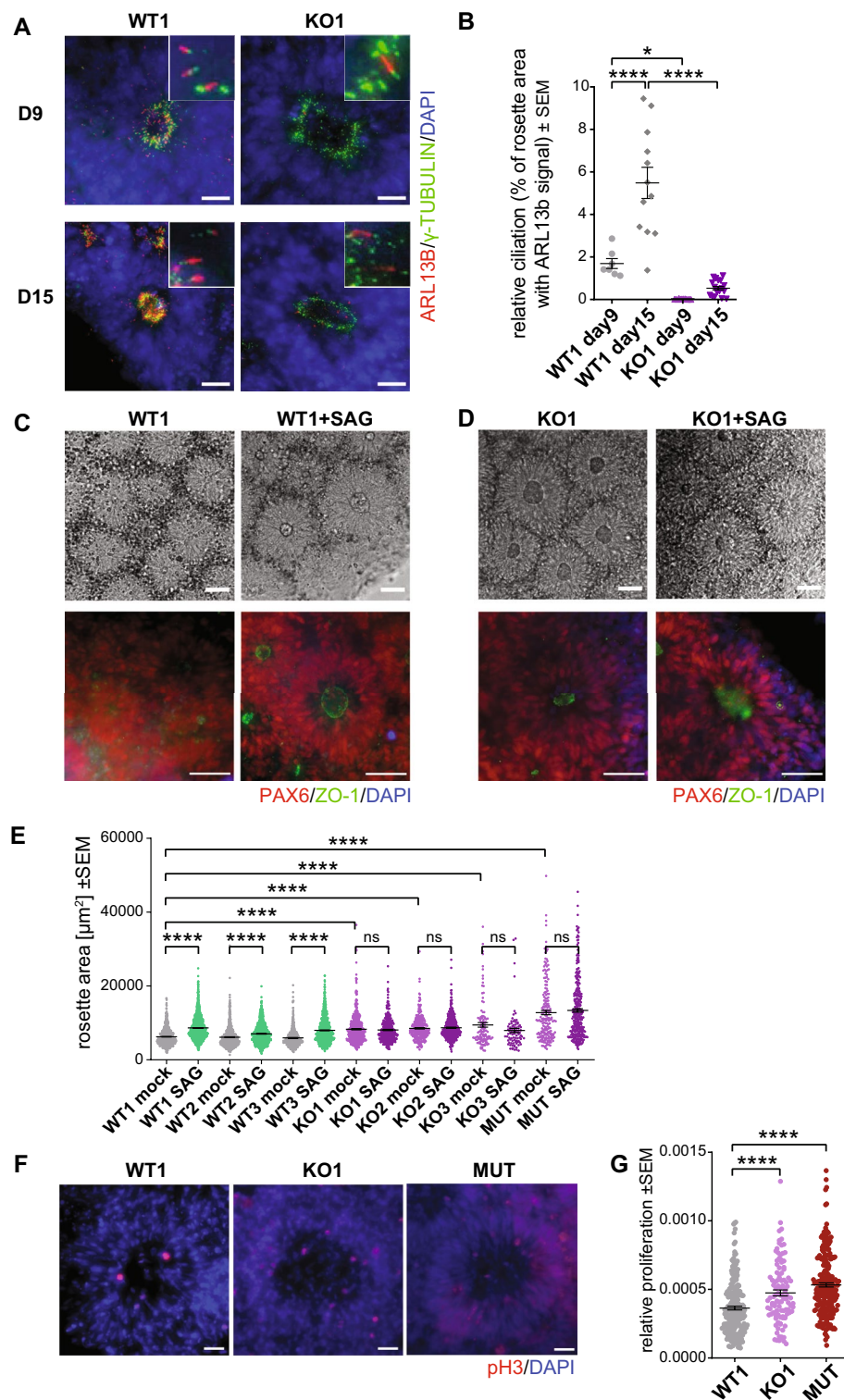


Figure 3. Lack of TTBK2 increases the size of neural rosettes. **(A)** Representative images of IF detection of primary cilia (visualized by ARL13B staining) in WT1- and TTBK2 KO1-derived neural rosettes at D9 (top) and D15 (bottom), γ -TUBULIN was used to indicate centrioles; scalebar = 20 μm . **(B)** Relative ciliation (measured as ARL13B positive rosette area fraction) in WT1- or TTBK2 KO1-derived neural rosettes at D9 and D15; $n = 2$, one-way ANOVA with Holm-Sidak's multiple comparisons test. **(C)** Mock- or SAG-treated WT1-derived neural rosettes visualized in phase contrast (top) or IF (bottom). PAX6 staining was used to monitor ongoing neural differentiation, ZO1 staining visualizes polarization of the lumen; scalebar = 50 μm . **(D)** Mock- or SAG-treated TTBK2 KO1-derived neural rosettes visualized in phase contrast (top) and IF (bottom), PAX6 staining was used to monitor ongoing neural differentiation, ZO1 staining visualizes polarization of the lumen; scalebar = 50 μm . **(E)** Measurement of the rosette area in mock- or SAG-treated WT- and TTBK2 KO-derived neural rosettes, respectively, on D15; $n = 3$, one-way ANOVA with Holm-Sidak's multiple comparisons test. **(F)** Representative images of Phospho-histone3 (pH3) IF detection in the indicated conditions on D15; scalebar = 20 μm . **(G)** Relative proliferation as a ratio of pH3 positive cells number per rosette area on D15; $n = 3$, one-way ANOVA with Holm-Sidak's multiple comparisons test.

Specifically, while transfection and in turn rescue effect of TTBK1/2 on cilia formation (Fig. 4E, Suppl. Fig. 4B) were rather inefficient in TTBK2 KO hPSCs, the rescue was more pronounced in TTBK2 KO hTERT-RPE-1 cells. Here, TTBK1-Halo transient expression rescued ciliogenesis in ~10% of cells, while GFP-TTBK2 supported primary cilia formation in ~15% of transfected cells (Fig. 4G). In sum, these data suggest that TTBK1 participates in the regulation of primary cilia assembly and that ciliogenesis in hPSC-derived neural rosettes is under the control of both TTBK1 and TTBK2, with TTBK2 likely playing more prominent role.

Discussion

Both primary cilia and stem cells have emerged as key regulators of embryo development and tissue homeostasis. Here we have explored the functions of primary cilia using a panel of WT and CRISPR/Cas9-edited hPSCs devoid of TTBK2 and, in turn, primary cilia. While we found no major function for TTBK2/primary cilia in hPSCs self-renewal, we identified a role for primary cilia and HH pathway in the regulation of hPSCs-derived neural rosettes. In addition, our data implicated TTBK1 in the regulation of ciliogenesis in human cells (Fig. 5).

Primary cilia, capable to transduce HH signal, were reported in hPSCs previously, but with unclear biological significance^{26,27}. Our data indicate that TTBK2 and primary cilia do not play a major role in the regulation of undifferentiated hPSCs. In support of our observation, activation of the HH pathway failed to prevent hPSCs spontaneous differentiation following FGF2-withdrawal²⁸. While we cannot completely rule out the impact of specific culture conditions, we conclude that hPSCs lacking primary cilia can be efficiently propagated without notable changes in the morphology of individual colonies or pluripotency markers expression. When finalizing this manuscript, similar results have been reported using KIF3A/KIF3B knockout hPSCs³² or TTBK2 knockout iPSCs⁴¹.

So why would hPSCs invest their resources to assemble the primary cilium, if this organelle is not crucial at this particular cell stage? We speculate the presence of primary cilia in the undifferentiated cell state may facilitate the later execution of a specific differentiation program⁴³. In a way, this may be conceptually similar to the poised state of many gene promoters in hPSCs, thus subsequently allowing an efficient response upon appropriate stimuli⁴⁴.

Our data indicate that ablation of primary cilia in hPSCs leads to a similar phenotype as the activation of the HH pathway—increased size of neural rosette. This observation is in agreement with a different dependency of individual HH activators and inhibitors on the presence of primary cilia. Interestingly, while various HH “gain of function” phenotypes have been reported following the disruption of primary cilia⁴, loss of primary cilia due to TTBK2 ablation in the neural tube in mice has been associated with HH “loss of function” defects⁸. In addition, disruption of ciliogenesis in OFD1 KO mouse embryonic stem cells led to reduced activation of the HH pathway in the course of neural differentiation⁴⁵. It remains to be determined what factors underlay such differences between mouse and human cells. Interestingly, recent work has postulated that hPSCs-derived neural rosettes are formed by a mechanism of secondary neurulation, which is in mice restricted to the most caudal parts of the developing neural tube³⁴.

Primary cilia were proposed as essential for hPSCs conversion into PAX6 + neural progenitors, hence for the neural fate acquisition³⁰. Our data challenge such a model and suggest that TTBK2 and primary cilia are not critical for the acquisition of PAX6 + neural progenitor fate during hPSC differentiation. Instead, primary cilia seem to regulate the proliferation of neural progenitors at the neural rosette stage. This observation is in agreement with a reported accumulation of SOX2 + neural progenitors in KIF3A and KIF3B KO hPSCs³² and with the absence of early neurodifferentiation phenotypes in mice with primary cilia defects^{8,31,46}. Moreover, given the recent progress in the development of inhibitors of TTBK1/2^{41,47}, temporal ablation of primary cilia could be exploited to tweak the yield of neurodifferentiation protocols.

TTBK1 and TTBK2 share almost 60% identity and 70% similarity in their kinase domains, making them the closest relatives within the CK1 kinase family¹³. Previous data, including our own, established that TTBK2 is essential for primary cilia formation in several systems—no other kinase seemed able to compensate for a complete loss of TTBK2^{8,42}. Similarly, our current data show that the ablation of TTBK2 in undifferentiated hPSCs leads to a complete loss of primary cilia. Intriguingly, however, our results further suggest that TTBK1 can partially compensate for the absence of TTBK2 in hPSCs-derived neural rosettes. This is quite surprising, as the Proline-rich motif implicated in TTBK2-CEP164 interaction^{9,48,49} and, in turn, the recruitment of the kinase to the mother centriole, is poorly conserved in TTBK1 (Suppl. Fig. 4D). One plausible explanation is that concentrating the kinase activity at mother centriole is not strictly necessary for the efficient phosphorylation of its key substrates, provided the levels and activity of the kinase outside of the mother centriole are sufficiently high. Indeed, undifferentiated hPSCs have low levels of TTBK1, not sufficient for any noticeable contribution to primary cilia assembly. In contrast, TTBK1 expression is significantly upregulated during neural rosette formation, and, consequently, TTBK1 becomes competent to affect ciliogenesis. Importantly, our rescue experiment with transient TTBK1 transfection represents proof of concept that TTBK1 is able to regulate primary cilia. Our model is attractive also from the point of TTBK2 frame-shift mutations, associated with spinocerebellar ataxia 11⁵⁰. Here, the resulting truncated protein moieties lack the C-terminal CEP164 binding motif and hence are considered unable to support ciliogenesis^{8,51}. In addition, primary cilia are emerging as critical regulators of CNS functionality^{52–54}. Given that TTBK1 has been considered a plausible therapeutic target for the treatment of Alzheimer's disease (AD)^{47,55–57}, its direct involvement in primary cilia regulation may significantly hamper these efforts in AD targeting. Therefore, future studies should address in which cell types is TTBK1 able to regulate ciliogenesis and the exact mechanism of its action.

Figure 4. Tau tubulin kinase 1 (TTBK1) regulates cilia formation. **(A)** mRNA expression (qRT-PCR) of *TTBK1* in undifferentiated parental cell line CCTL14, and WT1- or TTBK2 KO1-derived neural rosettes on D15; $n=2-3$, one-way ANOVA with Holm-Sidak's multiple comparisons test. **(B)** IF detection of primary cilia (visualized by ARL13B staining) in mock- or TTBK1/2 inhibitor-treated WT1 and TTBK2 KO1, respectively, on D15; γ -TUBULIN was used to detect centrioles; scalebar = 50 μm . **(C)** Relative ciliation (measured as ARL13B positive rosette area fraction) in WT1- or TTBK2 KO1-derived neural rosettes, treated as indicated, on D15; $n=2$, one-way ANOVA with Holm-Sidak's multiple comparisons test. **(D)** Rosette area measurement in WT1- or TTBK2 KO1-derived neural rosettes, treated as indicated, on D15; $n=2$, one-way ANOVA with Holm-Sidak's multiple comparisons test. **(E)** IF detection of primary cilia (visualized by ARL13B staining) in TTBK2 KO1 transfected with TTBK1-Halo (left) or not transfected (right). CETN1 staining was used to detect centrioles; scalebar = 5 μm . **(F)** IF detection of primary cilia (visualized by ARL13B staining) in hTERT RPE-1 TTBK2 KO cells transfected with TTBK1-Halo (left) or not transfected (right), CETN1 was used to indicate centrioles; scalebar = 5 μm . **(G)** Summary of the rescue effect of TTBK1 or TTBK2 expression in hTERT RPE-1 TTBK2 KO on ciliogenesis; $n=3$, one-way ANOVA with Holm-Sidak's multiple comparisons test.

Material and methods

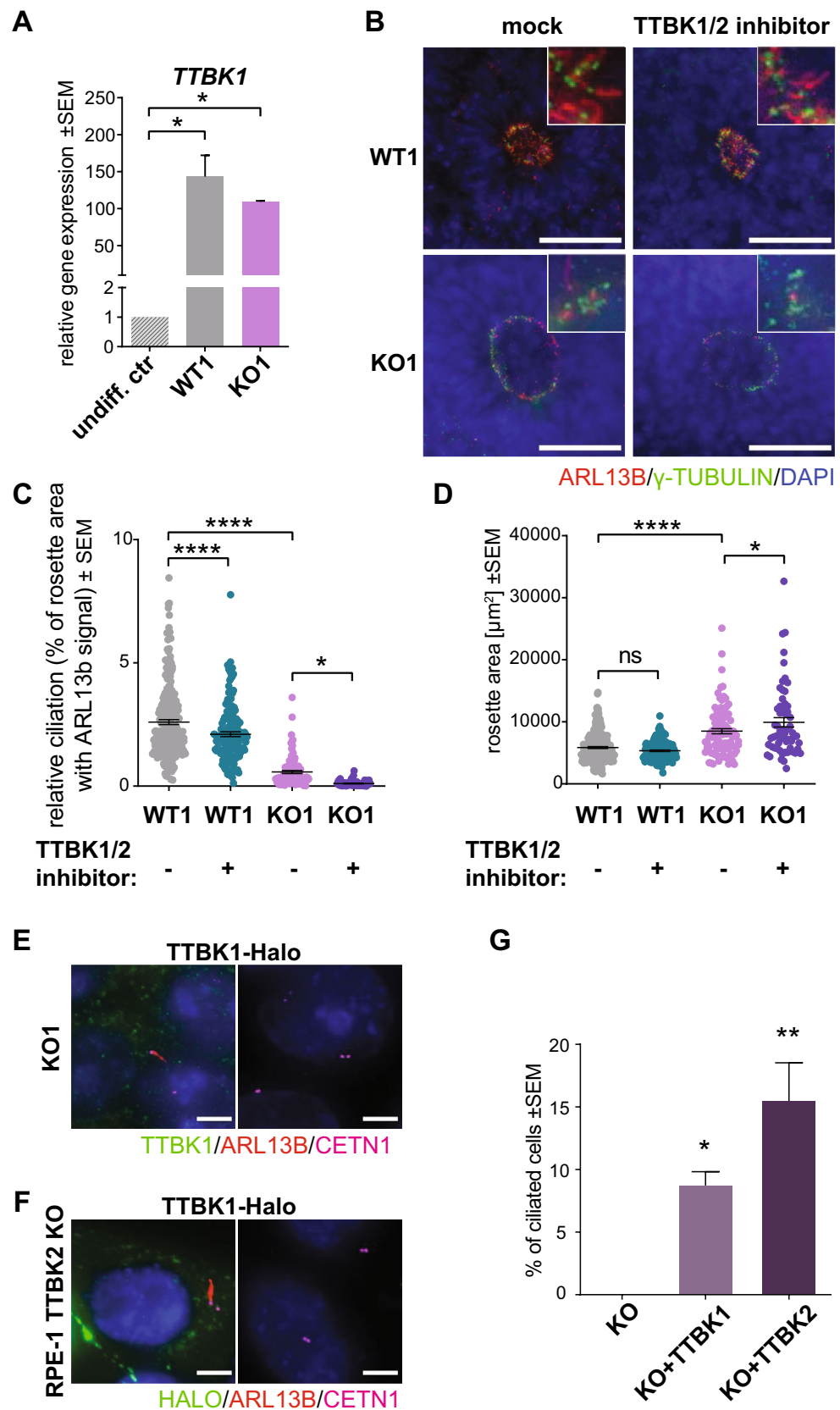
Cell culture and transfection. CCTL14 cells (<https://hpscreg.eu/cell-line/MUNIE007-A>) were cultured in the undifferentiated state as a feeder-free monolayer on Matrigel (Corning)-coated plastic in daily changed MEF-conditioned hESC medium ((DMEM/F12, 15% Knockout serum replacement (both from Gibco), 2 mM L-glutamine, 1 \times nonessential amino acids (NEAA) (both from Biosera), 1/2x Zell Shield (Minerva Biolabs), 100 $\mu\text{mol/L}$ β -mercaptoethanol (Sigma-Aldrich) and 10 ng/ml hFGF2 (Invitrogen)). Conditioned medium was enriched with 2 mM L-glutamine, 1/2x Zell Shield, and 10 ng/ml hFGF2 before use. iPSC Neo1 w1 cells⁴⁰ were cultured in the undifferentiated state as a feeder-free monolayer on Matrigel (Corning)-coated plastic in daily changed complete mTeSR medium (StemCell Technologies) with 1/2x Zell Shield. Cells were regularly passaged using Tryple Express (Thermo Fisher Scientific). Where indicated, undifferentiated cells were treated with 500 nM SAG (Sigma) on D1 and D2 after seeding and analyzed on D3. i3N cells were maintained and differentiated as described in detail in⁵⁸. hTERT RPE-1 KO cells were cultured in DMEM/F12, 10% FBS, and 2 mM L-glutamine as described before⁴².

For transient transfection experiments, TTBK2 KO cell lines were seeded on glass coverslips (Matrigel-coated for hPSCs) and the next day transfected with 0.5 μg TTBK1-HaloTag human ORF in pFN21A (FHC12512, Promega) or pglap1-TTBK2 ("GFP-TTBK2"⁴²) using Lipofectamine 3000 (Invitrogen). The medium was changed 4 h after transfection for fresh culture medium. To promote ciliogenesis, hTERT RPE-1 were starved in serum-free DMEM/F12 with 2 mM L-glutamine 24 h after transfection for 24 h. For quantification, at least 40 transfected cells were analyzed per condition and experiment.

Neural rosette differentiation. Cells were seeded in density 4000–6000 cells/ cm^2 in a complete growth medium with 20 μM ROCK1 inhibitor Y-27632 (Selleckchem). On the next day (D1) medium was changed for Rosette differentiation medium (DMEM/F12:Neurobasal 1:1 (both from Gibco), N2, B27 with vitamin A (both from ThermoFisher), 2 mM L-Glutamine, 1 \times NEAA, 1/2x Zell Shield) with 20 μM Y-27632, and 20 μM TGF- β inhibitor SB 431542 (Sigma). Where indicated, 5 nM SAG (Sigma) treatment started on D1. On D4 the medium was changed for Rosette differentiation medium (without inhibitors), the medium was changed daily until D9. Around D6 rosettes started to appear. For the early stage of the differentiation experiment (Fig. 1A), the cells were fixed/harvested on D9. For later stages of neural rosette differentiation (Fig. 1D), clusters of rosettes were cut out on D9 and transferred on a Matrigel-coated plate (for immunostaining glass coverslips were inserted in the wells and coated with Matrigel) with fresh Rosette differentiation medium. On D10, the medium was changed, and 5 nM SAG was added, where indicated. Half of the medium (with vehicle/SAG) volume was replaced daily until D15. Where indicated, rosette cultures were treated with TTBK1/2 inhibitor (1 μM) (gift from Alison Axtman⁴¹) daily on D12–D15.

Phase contrast imaging and rosette area measurement. Phase contrast images of differentiated rosettes were acquired on D15 using inverted microscope LEICA DM IL LED equipped with Leica DFC295 camera (Leica Microsystems), Leica Application Suite (LAS) Version 3.8.0, and HI PLAN I 10x/0.22 objective. Freehand selection tool in Fiji (version 2.1.0⁵⁹) was employed to outline the rosette outer border, and the area inside the selected outline was measured as the Rosette area.

Immunofluorescence (IF) imaging. For cilia staining, the cultures were fixed by $-20\text{ }^{\circ}\text{C}$ methanol, washed in PBS, blocked in blocking buffer (1% BSA in PBS), and stained 1 h/RT or overnight/ $4\text{ }^{\circ}\text{C}$ with the following primary antibodies in blocking buffer: ARL-13B (rabbit, 17711-1-AP, Proteintech, 1:1000), ARL13B (mouse, sc-515784, Santa-Cruz, 1:200), γ -tubulin (mouse, T6557, Sigma, 1:1000), TTBK1 (mouse, HPA031736, Sigma, 1:500), TTBK2 (rabbit, HPA018113, Sigma, 1:500), Halo-tag (mouse, 28a8 ChromoTek, 1:200), Alexa Fluor 647-direct labeled CETN1 (rabbit, 12794-1-AP, Proteintech/ A20186, Invitrogen, 1:50). For neural rosette markers and phosphoH3 staining, the cultures were fixed in 4% PFA 20 min/ $4\text{ }^{\circ}\text{C}$, washed 2 \times in PBS, permeabilized in 0.2% Triton-X100 in PBS 5 min/RT, and stained 1 h/RT or overnight/ $4\text{ }^{\circ}\text{C}$ with following primary antibodies in 0.2% Triton-X100 in PBS: PAX6 (rabbit, #60433, Cell Signaling, 1:300), ZO-1-1A12 (mouse, 33-9100, Invitrogen, 1:800), Phospho-Histone H3 Thr11 (rabbit, #9764 Cell Signaling, 1:300). Coverslips were then washed 3 \times 5 min in PBS and stained with donkey-raised secondary antibodies in either blocking buffer or



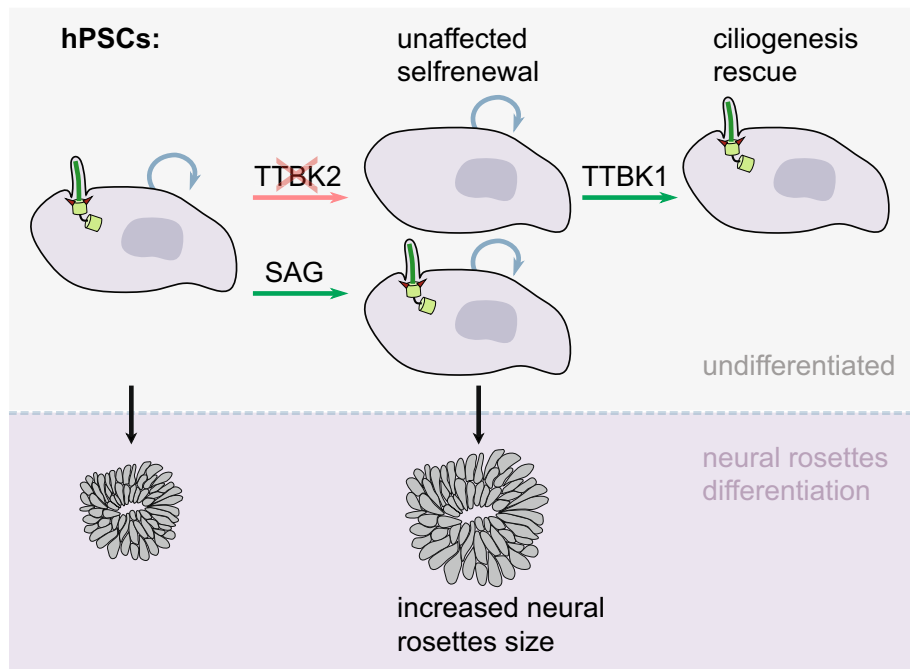


Figure 5. Graphical summary of the main results. Ablation of TTBK2 in hPSCs prevents primary cilia formation, which can be rescued by the expression of TTBK1. Ablated ciliogenesis, or SAG-mediated activation of the HH pathway, does not affect the self-renewal of hPSCs. Removal of TTBK2/primary cilia increases the size of neural rosettes during hPSCs neural differentiation, similar to the effect of HH pathway activation.

0,2% Triton-X100 in PBS, 1 h/RT; anti-mouse or anti-rabbit Alexa Fluor 488, 568 or 647 (all Invitrogen, 1:1000). Nuclei were stained with DAPI or Hoechst 5 min/RT. After washing, coverslips were mounted using Glycergel (Agilent) or ProLong™ Glass Antifade Mountant (Invitrogen).

Z-stack images were acquired on Zeiss AxioImager.Z2, with Hamamatsu ORCA Flash 4.0 camera, using 40x/1.3 Plan Apochromat OIL or 63x/1.4 Plan-Apochromat OIL objective controlled by Zen Blue Software.

Image analysis. Z-slices were projected in one layer by Maximal Intensity Z-projection, a Color composite image was created in Fiji. To approximate the amount of the cilia (high density of the cilia in rosette lumen hampers counting their exact numbers), we measured the ARL13B positive rosette area fraction (defined as % of rosette area with ARL13b signal, termed “relative ciliation” in the figures). Freehand selection tool in Fiji employed to outline the rosettes outer borders, which were then added to the ROI manager. The image was split into separate color channels and in the channel where the ARL13B signal was acquired a threshold mask was applied and adjusted manually to represent the area with the ARL13B-stained cilia. For each rosette analyzed, the fraction of the rosette (%) covered by the mask was then determined. To quantify the proliferation of the cells in rosettes, we counted phospho-histon3 (pH3)-positive cells per rosette. The freehand selection tool in Fiji was again used to outline the rosette outer borders. The pH3-positive cells within the selected outline were manually counted and a ratio of the pH3 cell number to the rosette area was obtained.

qRT-PCR. Total RNA was isolated using RNA blue reagent according to the manufacturer’s recommendations. 0.3–1 µg RNA was used for cDNA synthesis using Transcriptor First Strand cDNA Synthesis Kit (Roche). 2 µl of 8 × diluted cDNA was used in 10 µl qPCR reactions with LightCycler® 480 SYBR Green I Master with primers listed in Table 1. according to the manufacturer’s protocol and monitored in real-time using LightCycler® 480 Instrument II (Roche). Relative gene expression was calculated using $2^{-\Delta\Delta C_q}$ method; GAPDH was used as the reference gene.

Western blot. Protein expression was analyzed by western blotting as described before⁴⁰. Briefly, cells were lysed in SDS lysis buffer (50 mM Tris–HCl pH 6.8, 10% glycerol, 1% SDS). Protein concentration was measured using DC Protein Assay Kit (Bio-Rad) and an equal amount of protein was loaded in 8% gel. The following primary antibodies were used: TTBK2 (rabbit, HPA018113, Sigma, 1:250), NANOG (rabbit, #3580, Cell Signaling, 1:1000), OCT4 (mouse, SC-5279, Santa Cruz, 1:4000), α -TUBULIN (mouse, 6631–1 Proteintech, 1:2000) was used as a loading control. To detect the signal, anti-rabbit (#7074, Cell Signaling, 1:3000), or anti-mouse (A4461, Sigma, 1:3000) secondary HRP-conjugated antibodies were used. The chemiluminescent signal was revealed using ECL Prime (GE Healthcare) and ChemiDoc Imaging System (BioRad).

Growth curves. The relative growth rate was determined using a crystal violet assay as described before⁴⁰. Briefly, cells were seeded on 96 well plates, and mock- or SAG (500 nM) treated from D1. Cultures were fixed on D1-6 in 4% formaldehyde, PBS washed, and incubated in 0.5% crystal violet (1 h). Following 3 × H₂O wash, they were incubated in 33% acetic acid (20 min/shaking). Relative growth was determined as an increase in absorbance at 570 nm.

CRISPR/Cas9 knock-out. TTBK2 gRNA⁴² cloned into pSpCas9 (BB)-2A-GFP vector or vehicle were repeatedly transfected into CCT14 line, as described before⁶⁰. pSpCas9(BB)-2A-GFP vector was a gift from Feng Zhang (<https://www.addgene.org/4813861>). GFP-positive cells were single-cell sorted using BD FACS ARIA II to matrigel-coated 96-well plates. Selected clones were verified for TTBK2 presence by immunostaining, expanded, and sequenced to verify the disruption of the TTBK2 locus.

Sequence alignment. Jalview software (version 2.11.2.5)⁶² was used for TTBK1 and TTBK2 sequence alignment visualization.

Statistical analysis. Quantitative data are presented as the mean ± SEM. When relevant, individual data points are shown to illustrate the sample size of each analyzed condition (Figs. 1E,H, 3B,E,G, 4C and D: one dot—one analyzed rosette; Fig. 2A: one dot—% of ciliated cells per image (40 cells per image, 6 images); Fig. 2E: one dot—% of ciliated cells in one ROI of 20 cells (several ROIs per image were measured). Statistical differences among groups were evaluated by t-test or one-way analysis of variance (ANOVA) followed by Holm-Sidak's or Tukey's multiple comparisons tests. For all statistical analyses, P value < 0.05 was considered significant (*P < 0.05, **P < 0.01, ***P < 0.001, and ****P < 0.0001). All statistical analyses were performed with GraphPad Prism (GraphPad Software; www.graphpad.com). All experiments were performed at least in triplicate (n = number of biological replicates) unless stated otherwise.

Data availability

The datasets generated during and/or analyzed during the current study are available from the corresponding author upon reasonable request.

Received: 27 February 2023; Accepted: 1 August 2023

Published online: 09 August 2023

References

- Beales, P. & Jackson, P. K. Cilia—The prodigal organelle. *Cilia* **1**, 1 (2012).
- Anvarian, Z., Mykityn, K., Mukhopadhyay, S., Pedersen, L. B. & Christensen, S. T. Cellular signalling by primary cilia in development, organ function and disease. *Nat. Rev. Nephrol.* **15**, 199–219 (2019).
- Ingham, P. W. Chapter One—Hedgehog signaling. In *Current Topics in Developmental Biology* Vol. 149 (ed. Soriano, P. M.) 1–58 (Academic Press, 2022).
- Bangs, F. & Anderson, K. V. Primary cilia and mammalian hedgehog signaling. *Cold Spring Harb. Perspect. Biol.* **9**, a028175 (2017).
- Reiter, J. F. & Leroux, M. R. Genes and molecular pathways underpinning ciliopathies. *Nat. Rev. Mol. Cell Biol.* **18**, 533–547 (2017).
- Han, Y.-G. & Alvarez-Buylla, A. Role of primary cilia in brain development and cancer. *Curr. Opin. Neurobiol.* **20**, 58–67 (2010).
- Satir, P., Pedersen, L. B. & Christensen, S. T. The primary cilium at a glance. *J. Cell Sci.* **123**, 499–503 (2010).
- Goetz, S. C., Liem, K. F. & Anderson, K. V. The spinocerebellar ataxia-associated gene Tau Tubulin Kinase 2 (TTBK2) controls the initiation of ciliogenesis. *Cell* **151**, 847–858 (2012).
- Čajánek, L. & Nigg, E. A. Cep164 triggers ciliogenesis by recruiting Tau tubulin kinase 2 to the mother centriole. *Proc. Natl. Acad. Sci. U. S. A.* **111**, E2841–E2850 (2014).
- Tanos, B. E. *et al.* Centriole distal appendages promote membrane docking, leading to cilia initiation. *Genes Dev.* **27**, 163–168 (2013).
- Graser, S. *et al.* Cep164, a novel centriole appendage protein required for primary cilium formation. *J. Cell Biol.* **179**, 321–330 (2007).
- Prevo, B., Scholey, J. M. & Peterman, E. J. G. Intraflagellar transport: mechanisms of motor action, cooperation, and cargo delivery. *FEBS J.* **284**, 2905–2931 (2017).
- Ikezu, S. & Ikezu, T. Tau-tubulin kinase. *Front. Mol. Neurosci.* **7**, 33 (2014).
- Radhakrishnan, A., Rohatgi, R. & Siebold, C. Cholesterol access in cellular membranes controls Hedgehog signaling. *Nat. Chem. Biol.* **16**, 1303–1313 (2020).
- Chiang, C. *et al.* Cyclopia and defective axial patterning in mice lacking Sonic hedgehog gene function. *Nature* **383**, 407–413 (1996).
- Briscoe, J. *et al.* Homeobox gene Nkx2.2 and specification of neuronal identity by graded Sonic hedgehog signalling. *Nature* **398**, 622–627 (1999).
- Jessell, T. M. Neuronal specification in the spinal cord: Inductive signals and transcriptional codes. *Nat. Rev. Genet.* **1**, 20–29 (2000).
- Ulloa, F. & Briscoe, J. Morphogens and the control of cell proliferation and patterning in the spinal cord. *Cell Cycle* **6**, 2640–2649 (2007).
- Blaess, S., Corrales, J. D. & Joyner, A. L. Sonic hedgehog regulates Gli activator and repressor functions with spatial and temporal precision in the mid/hindbrain region. *Development* **133**, 1799–1809 (2006).
- Liu, A., Joyner, A. L. & Turnbull, D. H. Alteration of limb and brain patterning in early mouse embryos by ultrasound-guided injection of Shh-expressing cells. *Mech. Dev.* **75**, 107–115 (1998).
- Rowitch, D. H. *et al.* Sonic hedgehog regulates proliferation and inhibits differentiation of CNS precursor cells. *J. Neurosci.* **19**, 8954–8965 (1999).
- Thomson, J. A. *et al.* Embryonic stem cell lines derived from human blastocysts. *Science* **282**, 1145–1147 (1998).
- Takahashi, K. *et al.* Induction of pluripotent stem cells from adult human fibroblasts by defined factors. *Cell* **131**, 861–872 (2007).
- Park, I.-H. *et al.* Disease-specific induced pluripotent stem cells. *Cell* **134**, 877–886 (2008).
- Shahbazi, M. N. *et al.* Self-organization of the human embryo in the absence of maternal tissues. *Nat. Cell Biol.* **18**, 700–708 (2016).
- Kiprilov, E. N. *et al.* Human embryonic stem cells in culture possess primary cilia with hedgehog signaling machinery. *J. Cell Biol.* **180**, 897–904 (2008).

27. Banda, E. *et al.* Cell polarity and neurogenesis in embryonic stem cell-derived neural rosettes. *Stem Cells Dev.* **24**, 1022–1033 (2015).
28. Wu, S. M., Choo, A. B. H., Yap, M. G. S. & Chan, K. K.-K. Role of Sonic hedgehog signaling and the expression of its components in human embryonic stem cells. *Stem Cell Res.* **4**, 38–49 (2010).
29. Bangs, F. K., Schrode, N., Hadjantonakis, A.-K. & Anderson, K. V. Lineage specificity of primary cilia in the mouse embryo. *Nat. Cell Biol.* **17**, 113–122 (2015).
30. Jang, J. *et al.* Primary cilium-autophagy-Nrf2 (PAN) axis activation commits human embryonic stem cells to a neuroectoderm fate. *Cell* **165**, 410–420 (2016).
31. Tong, C. K. *et al.* Primary cilia are required in a unique subpopulation of neural progenitors. *Proc. Natl. Acad. Sci. U. S. A.* **111**, 12438–12443 (2014).
32. Cruz, N. M. *et al.* Modelling ciliopathy phenotypes in human tissues derived from pluripotent stem cells with genetically ablated cilia. *Nat. Biomed. Eng.* **6**, 463–475 (2022).
33. Elkabetz, Y. *et al.* Human ES cell-derived neural rosettes reveal a functionally distinct early neural stem cell stage. *Genes Dev.* **22**, 152–165 (2008).
34. Fedorova, V. *et al.* Differentiation of neural rosettes from human pluripotent stem cells in vitro is sequentially regulated on a molecular level and accomplished by the mechanism reminiscent of secondary neurulation. *Stem Cell Res.* **40**, 101563 (2019).
35. Kelava, I. & Lancaster, M. A. Stem cell models of human brain development. *Cell Stem Cell* **18**, 36–748 (2016).
36. Wilson, P. G. & Stice, S. S. Development and differentiation of neural rosettes derived from human embryonic stem cells. *Stem Cell Rev.* **2**, 67–77 (2006).
37. Elkabetz, Y. & Studer, L. Human ESC-derived neural rosettes and neural stem cell progression. *Cold Spring Harb. Symp. Quant. Biol.* **73**, 377–387 (2008).
38. Hříbková, H., Grabiec, M., Klemová, D., Slaninová, I. & Sun, Y.-M. Calcium signaling mediates five types of cell morphological changes to form neural rosettes. *J. Cell Sci.* **131**, 206896 (2018).
39. Wong, Y. L. *et al.* Reversible centriole depletion with an inhibitor of Polo-like kinase 4. *Science* **348**, 1155–1160 (2015).
40. Renzova, T. *et al.* Inactivation of PLK4-STIL module prevents self-renewal and triggers p53-dependent differentiation in human pluripotent stem cells. *Stem Cell Rep.* **11**, 959–972 (2018).
41. Bashore, F. M. *et al.* Modulation of tau tubulin kinases (TTBK1 and TTBK2) impacts ciliogenesis. *Sci. Rep.* **13**, 6118 (2023).
42. Bernatik, O. *et al.* Phosphorylation of multiple proteins involved in ciliogenesis by Tau Tubulin kinase 2. *MBoC* **31**, 1032–1046 (2020).
43. Anderson, C. T. & Stearns, T. Centriole age underlies asynchronous primary cilium growth in mammalian cells. *Curr. Biol.* **19**, 1498–1502 (2009).
44. Macrae, T. A., Fothergill-Robinson, J. & Ramalho-Santos, M. Regulation, functions and transmission of bivalent chromatin during mammalian development. *Nat. Rev. Mol. Cell Biol.* **24**, 6–26 (2022).
45. Hunkapiller, J., Singla, V., Seol, A. & Reiter, J. F. The ciliogenic protein Oral-Facial-Digital 1 regulates the neuronal differentiation of embryonic stem cells. *Stem Cells Dev.* **20**, 831–841 (2011).
46. Huangfu, D. *et al.* Hedgehog signalling in the mouse requires intraflagellar transport proteins. *Nature* **426**, 83–87 (2003).
47. Halkina, T. *et al.* Discovery of potent and brain-penetrant Tau Tubulin Kinase 1 (TTBK1) inhibitors that lower Tau phosphorylation on vivo. *J. Med. Chem.* **64**, 6358–6380 (2021).
48. Oda, T., Chiba, S., Nagai, T. & Mizuno, K. Binding to Cep164, but not EB1, is essential for centriolar localization of TTBK2 and its function in ciliogenesis. *Genes Cells* **19**, 927–940 (2014).
49. Rosa e Silva, I. *et al.* Molecular mechanisms underlying the role of the centriolar CEP164-TTBK2 complex in ciliopathies. *Structure* **30**, 114–1289 (2022).
50. Houlden, H. *et al.* Mutations in TTBK2, encoding a kinase implicated in tau phosphorylation, segregate with spinocerebellar ataxia type 11. *Nat. Genet.* **39**, 1434–1436 (2007).
51. Bowie, E., Norris, R., Anderson, K. V. & Goetz, S. C. Spinocerebellar ataxia type 11-associated alleles of Ttbk2 dominantly interfere with ciliogenesis and cilium stability. *PLoS Genet.* **14**, e1007844 (2018).
52. Bowie, E. & Goetz, S. C. TTBK2 and primary cilia are essential for the connectivity and survival of cerebellar Purkinje neurons. *eLife* **9**, e51166 (2020).
53. Schmidt, S. *et al.* Primary cilia and SHH signaling impairments in human and mouse models of Parkinson's disease. *Nat. Commun.* **13**, 4819 (2022).
54. Sheu, S.-H. *et al.* A serotonergic axon-cilium synapse drives nuclear signaling to alter chromatin accessibility. *Cell* **185**, 3390–3407. e18 (2022).
55. Ikezu, S. *et al.* Tau-tubulin kinase 1 and amyloid- β peptide induce phosphorylation of collapsin response mediator protein-2 and enhance neurite degeneration in Alzheimer disease mouse models. *Acta Neuropathol. Commun.* **8**, 12 (2020).
56. Nozal, V. & Martinez, A. Tau Tubulin Kinase 1 (TTBK1), a new player in the fight against neurodegenerative diseases. *Eur. J. Med. Chem.* **161**, 39–47 (2019).
57. Taylor, L. M. *et al.* Pathological phosphorylation of tau and TDP-43 by TTBK1 and TTBK2 drives neurodegeneration. *Mol. Neurodegener.* **13**, 7 (2018).
58. Fernandopulle, M. S. *et al.* Transcription factor-mediated differentiation of human iPSCs into neurons. *Curr. Protoc. Cell Biol.* **79**, e51 (2018).
59. Schindelin, J. *et al.* Fiji: An open-source platform for biological-image analysis. *Nat. Methods* **9**, 676–682 (2012).
60. Bohaciakova, D. *et al.* An efficient method for generation of knockout human embryonic stem cells using CRISPR/Cas9 system. *Stem Cells Dev.* **26**, 1521–1527 (2017).
61. Ran, F. A. *et al.* Genome engineering using the CRISPR-Cas9 system. *Nat. Protoc.* **8**, 2281–2308 (2013).
62. Waterhouse, A. M., Procter, J. B., Martin, D. M. A., Clamp, M. & Barton, G. J. Jalview Version 2—A multiple sequence alignment editor and analysis workbench. *Bioinformatics* **25**, 1189–1191 (2009).

Acknowledgements

We thank Alison Axtman, Jan Raška, and Tomáš Bárta for sharing reagents or samples, Tomáš Loja for help with FACS, and Hana Hříbková with Dáša Bohačiková for advice on neural rosette differentiation protocol. The work was supported by grants from the Czech Science Foundation (22-13277S) and the Faculty of Medicine (MUNI/11/SUP/03/2022) to L.C. We acknowledge the core facility CELLIM supported by the Czech-BioImaging large RI project (LM2018129 funded by MEYS CR) for their support with obtaining scientific data presented in this article.

Author contributions

L.B.—performed experiments and analyzed data, L.C.—conceived and supervised the project, and together with L.B. wrote the paper.

Competing interests

The authors declare no competing interests.

Additional information

Supplementary Information The online version contains supplementary material available at <https://doi.org/10.1038/s41598-023-39887-9>.

Correspondence and requests for materials should be addressed to L.Č.

Reprints and permissions information is available at www.nature.com/reprints.

Publisher's note Springer Nature remains neutral with regard to jurisdictional claims in published maps and institutional affiliations.



Open Access This article is licensed under a Creative Commons Attribution 4.0 International License, which permits use, sharing, adaptation, distribution and reproduction in any medium or format, as long as you give appropriate credit to the original author(s) and the source, provide a link to the Creative Commons licence, and indicate if changes were made. The images or other third party material in this article are included in the article's Creative Commons licence, unless indicated otherwise in a credit line to the material. If material is not included in the article's Creative Commons licence and your intended use is not permitted by statutory regulation or exceeds the permitted use, you will need to obtain permission directly from the copyright holder. To view a copy of this licence, visit <http://creativecommons.org/licenses/by/4.0/>.

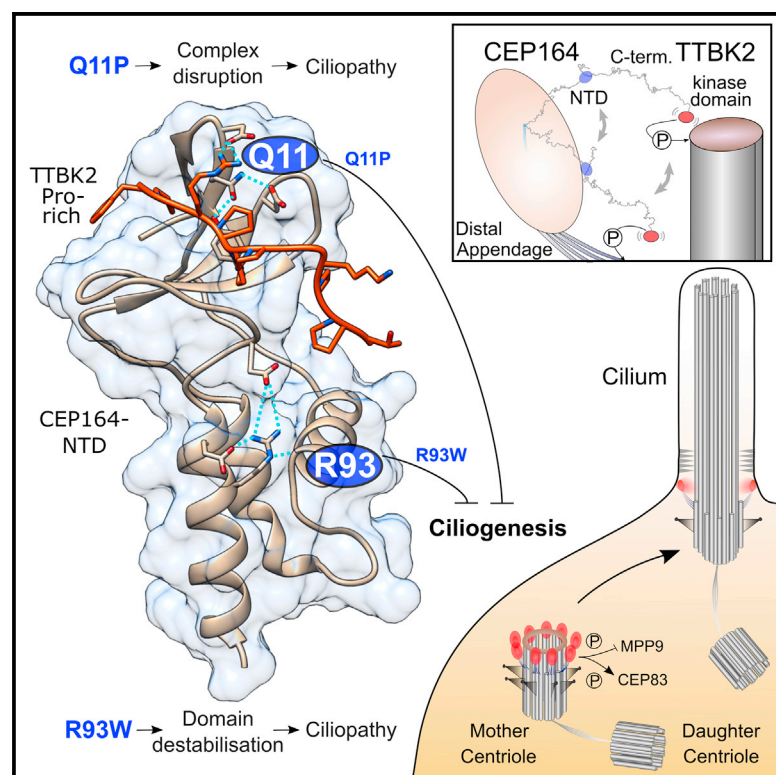
© The Author(s) 2023

Appendix 5

Rosa E Silva I, Binó L, Johnson CM, Rutherford TJ, Neuhaus D, Andreeva A, **Čajánek L**, van Breugel M. Molecular mechanisms underlying the role of the centriolar CEP164-TTBK2 complex in ciliopathies. *Structure*. 2022 Jan 6;30(1):114-128.e9. doi: 10.1016/j.str.2021.08.007.(JCR 2022, IF = 5.7, Q1 – Biochemistry & Molecular Biology)

Molecular mechanisms underlying the role of the centriolar CEP164-TTBK2 complex in ciliopathies

Graphical abstract



Authors

Ivan Rosa e Silva, Lucia Binó, Christopher M. Johnson, ..., Antonina Andreeva, Lukáš Čajánek, Mark van Breugel

Correspondence

m.vanbreugel@qmul.ac.uk (M.v.B.),
ivan.silva@alumni.usp.br (I.R.e.S.)

In brief

Rosa e Silva et al. report the structural characterization of the centriolar CEP164-TTBK2 complex that is essential for cilia formation. The authors show how ciliopathic mutations in CEP164 compromise complex formation and shed light on how CEP164 binding is coordinated with TTBK2 activities such as substrate access and EB1/3 association.

Highlights

- CEP164-NTD contains a TTBK2-binding WW domain inserted into an α -helical bundle
- CEP164-Q11P and R93W mutants cause ciliopathies by disrupting complex formation
- CEP164-NTD binding does not stimulate TTBK2 activity but impairs its EB1 engagement
- Disordered regions in TTBK2 and CEP164 might facilitate substrate access by TTBK2



Article

Molecular mechanisms underlying the role of the centriolar CEP164-TTBK2 complex in ciliopathies

Ivan Rosa e Silva,^{1,2,*} Lucia Binó,³ Christopher M. Johnson,² Trevor J. Rutherford,² David Neuhaus,² Antonina Andreeva,² Lukáš Cajánek,³ and Mark van Breugel^{1,2,4,*}

¹Queen Mary University of London, School of Biological and Chemical Sciences, 2 Newark Street, London E1 2AT, UK

²Medical Research Council – Laboratory of Molecular Biology, Francis Crick Avenue, Cambridge CB2 0QH, UK

³Department of Histology and Embryology, Faculty of Medicine, Masaryk University, Kamenice 5, Brno 62500, Czech Republic

⁴Lead contact

*Correspondence: m.vanbreugel@qmul.ac.uk (M.v.B.), ivan.silva@alumni.usp.br (I.R.e.S.)

<https://doi.org/10.1016/j.str.2021.08.007>

SUMMARY

Cilia formation is essential for human life. One of the earliest events in the ciliogenesis program is the recruitment of tau-tubulin kinase 2 (TTBK2) by the centriole distal appendage component CEP164. Due to the lack of high-resolution structural information on this complex, it is unclear how it is affected in human ciliopathies such as nephronophthisis. Furthermore, it is poorly understood if binding to CEP164 influences TTBK2 activities. Here, we present a detailed biochemical, structural, and functional analysis of the CEP164-TTBK2 complex and demonstrate how it is compromised by two ciliopathic mutations in CEP164. Moreover, we also provide insights into how binding to CEP164 is coordinated with TTBK2 activities. Together, our data deepen our understanding of a crucial step in cilia formation and will inform future studies aimed at restoring CEP164 functionality in a debilitating human ciliopathy.

INTRODUCTION

Cilia are hair-like cell projections that extend outward from the cell surface. They are found on most human cell types and are strictly required for human life (Bettencourt-Dias et al., 2011; Ishikawa and Marshall, 2011; Werner et al., 2017). Cilia are involved in cell motility and fluid flow generation. They also act as sensors that respond to physical and chemical stimulation and thereby play crucial roles in critical signaling pathways during development and in tissue homeostasis (Bettencourt-Dias et al., 2011; Ishikawa and Marshall, 2011; Singla and Reiter, 2006; Werner et al., 2017).

Centrioles are cylindrical cell organelles that are typically found as a pair in the center of centrosomes in interphase cells (Joukov and De Nicolo, 2019; Werner et al., 2017). The two centrioles differ in age, with the older (mother) centriole distinguished from the younger (daughter) centriole by the presence of distal and subdistal appendages (Bowler et al., 2019; Chong et al., 2020; Tanos et al., 2013; Yang et al., 2018). During cilia formation, mother centrioles become basal bodies that template cilia through the elongation of the plus ends of the doublet microtubules that constitute parts of their wall structure (Ishikawa and Marshall, 2011; Pedersen et al., 2008; Werner et al., 2017). The distal appendages play crucial roles during ciliogenesis by mediating membrane docking and providing a platform on which essential steps in cilia formation take place (Kumar and Reiter, 2021).

The initiation of ciliogenesis is tightly regulated both temporally and spatially (Werner et al., 2017; Kumar and Reiter, 2021). One of the earliest steps in cilia formation is the recruitment of tau-

tubulin kinase 2 (TTBK2) to the distal appendages of centrioles through CEP164 that is located at their tip structure (Bowler et al., 2019; Cajanek and Nigg, 2014; Oda et al., 2014; Goetz et al., 2012; Yang et al., 2018). TTBK2 recruitment requires a conserved WW domain in the N-terminal region of CEP164 and a proline-rich region in TTBK2 (Cajanek and Nigg, 2014; Oda et al., 2014; Schmidt et al., 2012). CEP164-TTBK2 complex formation facilitates TTBK2-mediated phosphorylation of both CEP83 at the base of distal appendages (Bernatik et al., 2020; Lo et al., 2019) and MPHOSP9 (MPP9) at the distal end of the mother centriole (Huang et al., 2018). As a consequence, MPP9 and the associated CP110-CEP97 complex that caps the distal ends of mother centrioles are removed, promoting ciliary axoneme growth (Huang et al., 2018).

In agreement with this model, lack of CEP164 or TTBK2 impairs ciliogenesis in mammalian tissue culture cells and mouse models without otherwise affecting centriole structure (Bowie and Goetz, 2020; Cajanek and Nigg, 2014; Goetz et al., 2012; Graser et al., 2007; Humbert et al., 2012; Kobayashi et al., 2020; Lo et al., 2019; Oda et al., 2014; Schmidt et al., 2012; Slaats et al., 2014). Furthermore, CEP164 or TTBK2 truncations that lack their respective TTBK2- or CEP164-interacting region do not support ciliogenesis *in vivo* (Bowie et al., 2018; Cajanek and Nigg, 2014; Goetz et al., 2012; Kobayashi et al., 2020; Oda et al., 2014). Consistently, overexpression of the WW domain-containing N-terminal region of CEP164 in tissue culture cells results in a dominant-negative effect on cilia formation, probably by competing with TTBK2 association with CEP164 at distal



appendages (Cajane et al., 2014; Chaki et al., 2012; Slaats et al., 2014; Schmidt et al., 2012). Importantly, a chimera between CEP164, lacking its TTBK2-interacting N-terminal region, and a kinase domain containing part of TTBK2 is sufficient to rescue the ciliogenesis defect in CEP164-depleted cells (Cajane et al., 2014). Together, these data argue that recruitment of TTBK2 to the distal appendages by CEP164 is the main function of CEP164's N-terminal region and that this step is critical for the initiation of ciliogenesis.

Despite the strong evidence that functionally links CEP164 and TTBK2, many questions remain open concerning this complex. Most of the functional insights rest on the use of truncation constructs, and biochemical analyses on this complex, including its binding affinity, are largely missing. Importantly, despite the crucial importance for ciliogenesis of TTBK2 recruitment to CEP164, the mechanisms by which this step is regulated are currently largely unknown. Phosphatidylinositol-4-phosphate binding to TTBK2 and CEP164 has been suggested to compromise TTBK2-CEP164 complex formation (Xu et al., 2016), but the structural basis of this proposed mechanism is unclear and other regulatory mechanisms might act in parallel. Directly in the vicinity of the proposed CEP164-binding motif in TTBK2 is located an EB1/3 binding motif important for TTBK2 recruitment to microtubules (Oda et al., 2014; Watanabe et al., 2015; Jiang et al., 2012). Thus, EB1/3 and CEP164 binding to TTBK2 might be sterically mutually exclusive, a mechanism that could contribute to the regulation of TTBK2 recruitment. Other cellular factors might directly compete with TTBK2 binding to CEP164 by mimicking its WW domain-binding motif. The identification of TTBK2's critical CEP164-binding motif might therefore facilitate the identification of putative TTBK2 regulating factors.

There are currently no high-resolution structural data available that could shed light on the molecular basis of CEP164-TTBK2 complex formation. The lack of structural information hampers our ability to derive the binding motif for the interaction with the WW domain of CEP164 and prevents insight into the structural constraints and plausibility of the proposed regulatory mechanism of TTBK2 recruitment. Importantly, high-resolution structural information on the CEP164-TTBK2 complex is also crucial to understand its involvement in human disease. Mutations in centriole components such as CEP164 that impair cilia formation or function are either incompatible with human life or result in disorders referred to as ciliopathies (Fliegauf et al., 2008; Mitchison and Valente, 2017; Braun and Hildebrandt, 2017). Nephronophthisis is an autosomal recessive ciliopathy that constitutes the most frequent genetic cause of kidney failure in children (Hildebrandt et al., 2009). Probably due to compromised signaling pathways that affect planar cell polarity, cysts and fibrosis progressively arise in the kidney, leading to kidney failure (Braun and Hildebrandt, 2017; Fischer et al., 2006; Hildebrandt et al., 2009; Stokman et al., 2021). To date, there is no treatment available to slow the progressive loss of kidney function, and patients ultimately require dialysis or kidney transplantation to survive (Hildebrandt et al., 2009; Stokman et al., 2021).

A structural understanding of how ciliopathy mutations affect CEP164 function might therefore inform translational research approaches aimed at alleviating disease progression in patients. The two missense mutations Q11P (homozygous) and R93W (compound heterozygous with a Q525X truncation mutation) in

CEP164 are associated with nephronophthisis, while a homozygous CEP164 R93W mutation also has been identified in a patient with BBS (Bardet-Biedl syndrome)-like syndrome (Chaki et al., 2012; Maria et al., 2016). It is currently not known whether and how these mutations affect the interaction between CEP164 and TTBK2 to give rise to the underlying ciliopathy. Furthermore, it is unclear what potential strategies could be used to address CEP164 dysfunction in these ciliopathies. While both mutations fall within the N-terminal region of CEP164, its WW domain is located between residues 56 and 89 (Cajane et al., 2014) and therefore is not directly targeted by the Q11P and the R93W mutations.

In this paper, we present a detailed biochemical, functional, and high-resolution structural analysis of the complex between the N-terminal domain (NTD) of CEP164 and its TTBK2-binding motif. Our data unambiguously demonstrate that the Q11P and R93W ciliopathic mutations compromise complex formation, reveal the structural basis of the underlying processes, and suggest possible approaches to mitigate their deleterious effects. Furthermore, our data and analyses provide insight into how TTBK2 recruitment to CEP164 affects TTBK2 activities and also allow us to propose a model of how TTBK2 is able to reach its substrates while bound at the distal appendages. Together, our data provide high-resolution structural information on a distal appendage complex and deepen our understanding of a critical step in cilia formation in human health and disease.

RESULTS

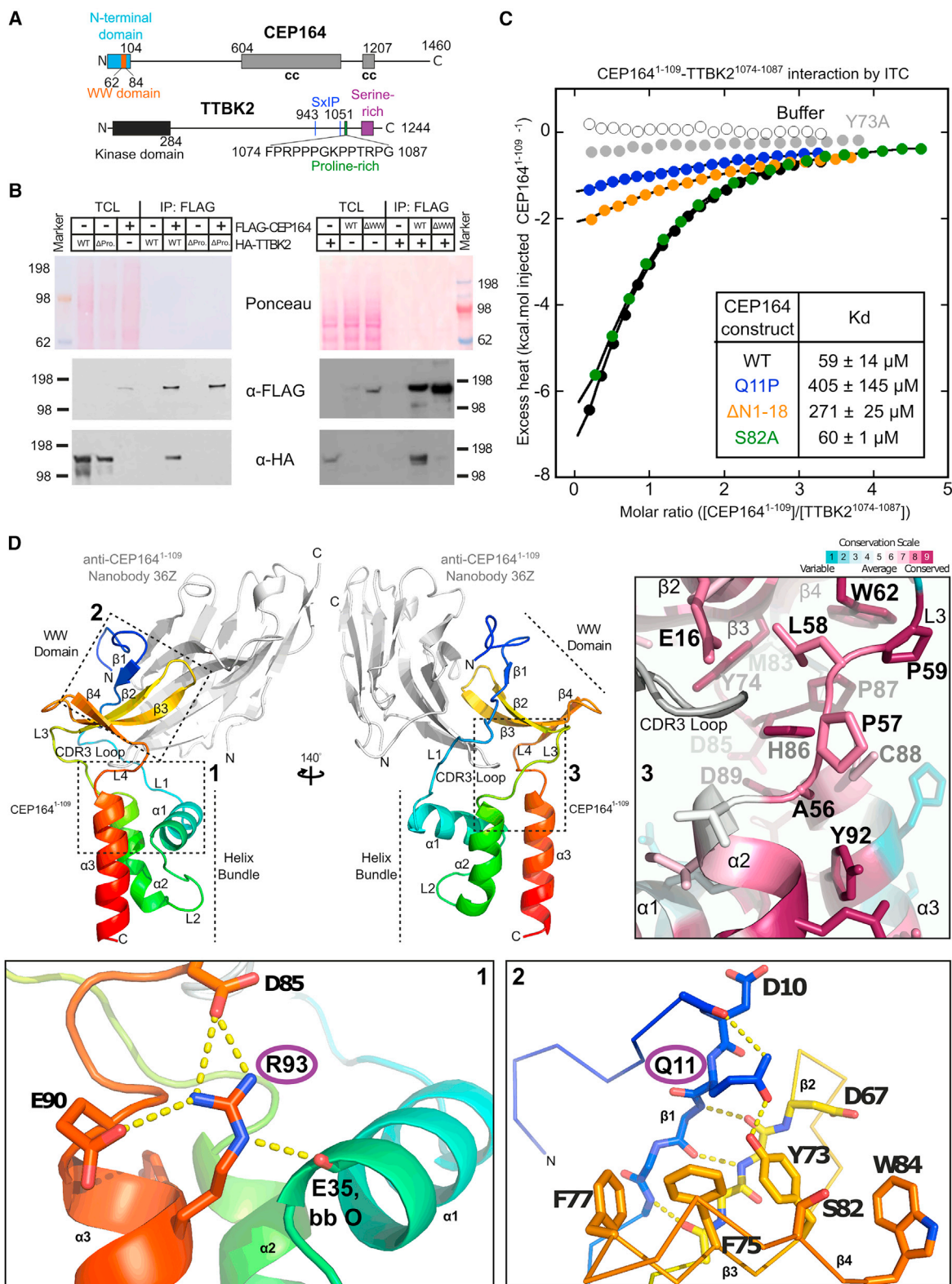
Unraveling the TTBK2-CEP164 interaction

TTBK2 interacts through a proline-rich C-terminal region (TTBK2^{1074–1085}) with a predicted WW domain (CEP164^{62–84}) in the N-terminal part of CEP164 (Cajane et al., 2014; Oda et al., 2014). Consistent with these findings, we established that the ability of FLAG-tagged CEP164 to pull down hemagglutinin (HA)-tagged TTBK2 depended on both elements (Figures 1A and 1B). Furthermore, pull-down experiments with recombinantly produced GST-CEP164^{1–109} and cell extracts from tissue culture cells expressing TTBK2^{1074–1087}-GFP also established that CEP164^{1–109} and TTBK2^{1074–1087} are sufficient to bind to each other (Figures S1A and S1F). Similar experiments, but with TTBK2^{1074–1087} constructs carrying alanine mutations in consecutive blocks of four amino acids, suggested that the residues within TTBK2^{1074–1083} (the first three mutated blocks) contribute strongly to CEP164 binding, while the effect of those residues within TTBK2^{1084–1087} (the last mutated block) is limited (Figure S1A).

To determine the corresponding binding affinity of the TTBK2-CEP164 complex, we performed isothermal titration calorimetry (ITC) with purified recombinant CEP164^{1–109} (Figure S1H) and synthetically produced TTBK2^{1074–1087} (Figure 1C; Table 1). Analysis of the ITC data suggested a binding affinity of ~60 μ M, which is in agreement with the binding affinities observed for other WW domain-proline-rich binding motif (PRBM) interactions (Iglesias-Bexiga et al., 2015; McDonald et al., 2011; Verma et al., 2018).

Structure and dynamics of the NTD of CEP164

To gain insight into the structural basis of TTBK2 binding by CEP164, we first determined the high-resolution structure of



the NTD of CEP164 (CEP164^{1–109}) from two different crystal forms by X-ray crystallography to a resolution of 1.6 and 1.7 Å (Table 2; Figures 1D and S2). These crystal forms were obtained by co-crystallization with two different camelid nanobodies (10Z and 36Z) that were raised against CEP164^{1–109}.

The CEP164^{1–109} (CEP164-NTD) structure from the first crystal form (Figure 1D, co-crystallized with nanobody 36Z) revealed a globular shape composed of a head, neck, and body delineating the WW domain, connecting linkers and an α -helical domain. The WW domain has a canonical three-stranded topology (β 2–4 in Figure 1D) and is inserted into the helical domain. The N-terminal region of CEP164-NTD preceding the helical domain is partly unstructured with the exception of residues 12–14 that form a short fourth strand (β 1 in Figure 1D) stabilized by mainchain-mainchain hydrogen bonds to β 2 of the WW domain. The β 1-strand is also held in place by additional contacts, including a sidechain-mainchain hydrogen bond between R7 and D67, and a sidechain-sidechain hydrogen bond between Y73 and Q11 (Figure 1D; magnified view, panel 2, Figure S2B). Intriguingly, Q11 is mutated to proline in a CEP164 allele that is associated with the human ciliopathy nephronophthisis (Chaki et al., 2012).

As expected, the CEP164^{1–109} structure derived from the second crystal form (obtained by co-crystallization with nanobody 10Z) is very similar to the first structure (root-mean-square deviation [RMSD]: 0.86Å over 87 aligned CEP164 residues), including the position of the bound nanobody (Figure S2). Surprisingly, the very N terminus, including the short additional β 1-strand of the WW domain, is highly divergent in both structures. While such a strand is observed at a comparable place in the second CEP164^{1–109} structure, it is formed by residues 4–6 (not residues 12–14) and is held in place only through mainchain interactions with β 2 of CEP164. The structural promiscuity of this region might argue that the short β 1-strand is only weakly bound. In agreement with this notion, NMR experiments with ¹⁵N-labeled purified, recombinant CEP164^{1–109} confirm the high flexibility of the very N-terminal region of CEP164 in solution (residues 1–23) (Figure S3A, (Berjanskii and Wishart, 2005)). Residues 7–14 show marginally higher {¹H}¹⁵N heteronuclear Overhauser effect (het-NOE) values (~0.5) than their flanking residues but a lower degree of order than residues in the folded helical and WW domains. het-NOE data for the ¹⁵N-labeled ciliopathic Q11P mutant did not reveal an increased flexibility of this N-terminal region. We conclude that the first 23 residues of the CEP164-NTD appear to associate only weakly with the WW domain.

The body of the CEP164^{1–109} structure comprises an α -helical bundle whose three helices pack together to form a highly

conserved hydrophobic core (Figure S4). The WW domain packs against the α -helical bundle and is held in place by the interconnecting linkers L3 and L4 (Figure 1D; magnified view, panel 3). In both crystal structures, the bound nanobodies are partially sandwiched between the WW domain and the helical bundle, allowing the complementary determining region 3 (CDR3) loop of the nanobodies to interact with residues at the interface between helical bundle and WW domain (Figures S2 and 1D).

To gain insight into the dynamics of both parts of the CEP164-NTD in the absence of nanobodies, we also determined the CEP164^{1–109} structure by NMR (Figures 2A and 2B; Table 3). The obtained NMR ensemble structures, superposed to the helical bundle or WW domain, demonstrated that both parts of CEP164-NTD were highly similar in the 20 NMR ensemble structures and were also highly similar to the crystal structure of the nanobody-bound CEP164-NTD (Figures 2A and 2B). However, the relative orientation between both parts showed some variability due to slight rotation movements in the interconnecting linkers L3+4. As a result, the angle between α -helical bundle and WW domain in the NMR ensemble structures (see Figure 2A for definition) varied in the approximate range 97°–117°. The corresponding angle in the crystal structure of nanobody-bound CEP164^{1–109} was ~83° (Figure 2C). This decrease is due to the CDR3 loop of the nanobody, which makes several bridging interactions between helical bundle and WW domain that pull both together (Figure 2A). We conclude that CEP164^{1–109} displays some inter-domain flexibility and that the overall CEP164^{1–109} structure is largely unaffected by the bound nanobodies.

Stability of the CEP164-NTD

Sequence analysis of the CEP164 homologs demonstrated that sequence conservation of CEP164-NTD is mainly found in the interior of the α -helical bundle and the solvent-exposed side of the WW domain (Figure S4) as well as in linker L3+4, which connects both domains (Figure 1D, magnified view - panel 3). Two nearly invariant proline residues, P59 and P87, in this linker region make hydrophobic contacts with the highly conserved W62. In addition, the invariant H86 in the vicinity forms a hydrogen bond with the A56 mainchain. The high conservation of this linker region suggests that inter-domain packing might be functionally important (for example, in stabilizing the WW domain fold).

To test this hypothesis, we deleted either WW domain or helical bundle from CEP164^{1–109} by recombinantly joining the loops connecting them. Subsequently, we purified these constructs and examined their fold and thermostability using circular

3xHA-TTBK2 or 3xHA-TTBK2 carrying a deletion of its proline-rich region 1,074–1,087 (Δ Pro). Right: pull-down with 3xFLAG-CEP164 or 3xFLAG-CEP164 carrying a deletion containing its WW domain (Δ WW) and 3xHA-TTBK2. TCL, total cell lysate.

(C) Recombinant CEP164^{1–109} and TTBK2^{1074–1087} interact with low micromolar affinity. Typical ITC of a synthetic TTBK2^{1074–1087} peptide and recombinant human CEP164^{1–109} constructs carrying the indicated mutations, at 25°C. The resulting dissociation constants (K_D) are indicated as an average (\pm SD) from three to five independent measurements.

(D) Top left: ribbon representation of the structure of CEP164^{1–109}, rainbow-colored from N- to C-terminus, in complex with a camelid nanobody (in gray). Rotation, as indicated. Consecutive alpha helices (α), beta sheets (β), and linkers (L) are labeled. Dotted boxes labeled from 1 to 3 indicate the regions shown magnified in the three panels below (1 and 2) or to the right (3). Bottom: detailed view of the CEP164^{1–109} regions containing residues R93 (box 1) or Q11 (box 2). These residues are mutated to W or P, respectively, in ciliopathies. Yellow dotted lines indicate hydrogen bonds. Selected residues are shown as sticks and are labeled. bb, backbone. Top right, ribbon representation of the region indicated by box 3, colored according to ConSurf (Ashkenazy et al., 2016) conservation scores from variable (cyan) to conserved (burgundy). Key residues in the interface region between the WW domain and the helical bundle are shown as sticks and are labeled.

Table 1. ITC analysis of the interaction between CEP164^{1–109} constructs and TTBK2^{1074–1087}

CEP164 ^{1–109} construct	N (±SD)	K _D (μM, ±SD)	ΔH (kcal/mol, ±SD)	n
WT	0.7 ± 0.2	59 ± 14	–17 ± 7	5
Q11P	1 (fixed)	405 ± 145	–9 ± 4	3
S82A	0.7 ± <0.1	60 ± 1	–14 ± <1	3
ΔN1–18	1 (fixed)	271 ± 25	–10 ± 1	3

dichroism (CD) spectroscopy (Figures 2D and S1I). Our results showed that CEP164^{1–109} has a mixed α/β fold and unfolds with a T_m of approximately 55°C. The helical domain alone (CEP164^{19–62,80–109}) had a CD spectrum consistent with a highly α -helical structure, as expected, and displayed a thermostability similar to CEP164^{1–109}, while the spectrum and the lack of a cooperative denaturation transition for the WW domain alone (CEP164^{1–28,50–94}) indicated that it had a largely unfolded conformation. Furthermore, a deletion of the helical bundle from full-length FLAG-tagged CEP164 largely abolished its ability to pull down HA-tagged TTBK2 from lysates of cells expressing these constructs (Figure 2E). Thus, our data suggest that the CEP164 WW domain requires the intramolecular interaction with the helical bundle to fold stably and function *in vivo*.

Structural basis for TTBK2 binding by the CEP164-NTD

To understand in more detail how CEP164 and TTBK2 interact, we determined the high-resolution structure of the CEP164-NTD in complex with TTBK2^{1074–1087} by X-ray crystallography to a resolution of 2.4 Å (Table 2, Figures 3A and S1E). Due to the low micromolar affinity of this complex ($K_D \sim 60 \mu\text{M}$, Figure 1C), we fused TTBK2^{1074–1087} recombinantly to the N terminus of CEP164^{1–109} to obtain diffraction-quality protein crystals of this complex. For crystallization, we again utilized nanobody 36Z as a crystallization chaperone. In the structure, neither the WW domain nor the α -helical bundle of the CEP164-NTD revealed significant conformational changes upon binding to TTBK2^{1074–1087} (apo- and TTBK2-bound structures superposed with an RMSD of 1.03 Å over 99 structurally equivalent residues) (Figure S3B). The main difference resided in the N-terminal region of CEP164^{1–109} where residues 6–8 form a second short strand in addition to the β 1-strand of residues 12–14.

WW domains are categorized into four groups that differ in their ligand-binding specificity. Class I and IV WW domains recognize PPxY and phosphorylated (S/T)P motifs by accommodating their Xaa-P residues into a single, so-called XP groove defined by two highly conserved aromatic residues. In contrast, class II and III WW domains utilize two XP grooves, XP and XP2, to bind to PPLP and PxxGMxPP motifs, respectively (Kato et al., 2004; Zarrinpar and Lim, 2000). The CEP164^{1–109}-TTBK2^{1074–1087} complex revealed a strong similarity to class II/III WW domains (Figure S5). Like these, it contains two XP grooves with the aromatic residues CEP164 Y73 and W84 defining the XP, and F75 and F77 the XP2 groove. TTBK2^{1074–1087} adopts a polyproline helix II conformation and packs with core prolines against both grooves: P1075, P1077, P1078, and P1082 stack against CEP164 F75, F77, Y73, and W84, respectively, with P1075 occupying the XP2 and P1077–P1078 the XP groove (Figures 3A and

S5A). P1079 and G1080 allow the backbone between residues P1078 and P1082 to bend like an arch over W84 to sandwich it. An additional contact between TTBK2 and CEP164 is made by R1076, which forms a salt bridge with residue D10 of CEP164, probably facilitating P1075 docking into the XP2 groove. D10 positioning is enabled by Q11 (mutated to proline in nephronophthisis), which hydrogen bonds with residues Y73 and D10. Finally, CEP164 residue S82 hydrogen bonds to the mainchain of the TTBK2 peptide. Residues TTBK2^{1085–1087} were not visible in our structure, arguing that they do not make significant contact with CEP164 (Figure S1A). NMR-based binding experiments with purified ¹⁵N-labeled CEP164^{1–109} and unlabeled TTBK2^{1074–1087} revealed an excellent agreement with our crystallographic analyses of this complex (Figure S3C).

Determinants of TTBK2 recognition by CEP164-NTD and the impact of nephronophthisis mutation Q11P

To dissect the importance of these interactions, we performed pull-down assays with purified GST-CEP164^{1–109} and cell extracts from cells expressing TTBK2^{1074–1087}-GFP constructs containing individual alanine mutations. The results shown in Figure 3C suggest that residues F1074, R1076, P1077, P1078, and G1080 are particularly important for CEP164 binding. We confirmed the importance of the core residues in the context of the full-length proteins by pull-down experiments with FLAG-tagged CEP164 and HA-tagged TTBK2 (wild-type [WT] and mutant) (Figure S1C). Our structural data (Figure 3A) rationalize these biochemical findings with the exception of the strong impact of the F1074A mutant. While F1074 is well placed to make hydrophobic contacts with CEP164 residues F75 and F77, its electron density was poorly defined, arguing against a tight binding of this residue *in crystallo*.

To establish the importance of the interface residues Q11, Y73, and S82 in the CEP164-NTD, we purified recombinant CEP164^{1–109}, the ciliopathy mutant Q11P, and the S82A and Y73A mutants (Figure S1H). To ascertain the role of the N-terminal, flexible (Figure S3A) region of CEP164^{1–109}, we also purified a corresponding deletion construct (CEP164^{19–109}, Δ1–18). CD spectra analyses of these constructs suggested that their fold is not significantly perturbed compared with the WT protein with only very minor changes evident in the Y73A mutant (Figure S1D). Next, we determined the binding affinity of these mutants to synthetically produced TTBK2^{1074–1087} by ITC (Figure 1C). Analysis of the ITC data suggested that the S82A mutation does not affect TTBK2 binding affinity. In contrast, Q11P and CEP164-NTD Δ1–18 both showed a strong drop in binding strength to $\sim 400 \mu\text{M}$ and $\sim 270 \mu\text{M}$, respectively, while the Y73A mutant did not show any significant binding activity. These results confirm the crucial role of Y73 and of the ciliopathic residue Q11 for the TTBK2 interaction. In contrast, the contribution of S82 to TTBK2 binding in solution appears negligible.

We extended the mutational analysis of CEP164 interface residues further by performing pull-down assays with recombinantly produced GST-CEP164^{1–109} WT, Q11P, Y73A, F75A, F77A, S82A, W84A, and Δ1–18 mutants (Figure S1F) and cell extracts from cells expressing TTBK2^{1074–1087}-GFP. In agreement with our previous data, S82A bound to TTBK2^{1074–1087} similar to the WT protein, while mutations Q11P, Y73A, F77A, W84A, and Δ1–18 resulted in a strongly reduced and F75A in a moderately

Table 2. X-ray crystallography dataset analysis and refinement statistics

Protein complex	Nanobody 10Z-CEP164 ^{1–109}	Nanobody 36Z-CEP164 ^{1–109}	Nanobody 36Z-TTBK2 ^{1074–1087} -CEP164 ^{1–109}
PDB accession code	7O06	7O0S	7O3B
Beamline	I04 (Diamond)	I04 (Diamond)	I03 (Diamond)
Space group	P12 ₁ 1	I121	C222 ₁
Wavelength (Å)	0.97942	0.97942	0.97625
Monomers in the asymmetric unit	2	1	3
Unit cell dimensions (Å, °)	a = 50.9, b = 70.7, c = 62.0, α = 90.00, β = 90.09, γ = 90.00	a = 38.3, b = 50.6, c = 119.9, α = 90.0, β = 99.0, γ = 90.00	a = 70.6, b = 127.7, c = 218.9, α = 90.0, β = 90.0, γ = 90.0
Resolution (Å)	62.0–1.6	59.2–1.7	61.8–2.4
Completeness (overall/inner/outer shell) (%)	99.4/99.9/98.9	100.0/99.7/100.0	98.7/95.7/99.4
Rmerge (overall/inner/outer shell)	0.097/0.059/1.463	0.146/0.105/1.658	0.091/0.035/0.705
Rpim (overall/inner/outer shell)	0.040/0.025/0.627	0.061/0.047/0.700	0.052/0.018/0.436
Mean I/σ (overall/inner/outer shell)	9.9/27.0/1.7	6.1/18.2/1.0	8.6/17.0/2.1
Multiplicity (overall/inner/outer shell)	6.7/6.1/6.3	6.6/5.9/6.5	3.8/3.7/3.8
Wilson B-factor (Å ²)	19.2	24.9	33.5
Number of reflections (used in refinement)	57,658 (57,454)	25,042 (24,957)	38,541 (38,506)
Number of atoms	3,796	1,909	5,678
Waters	275	150	104
Rwork/Rfree (% data used)	0.1804/0.2108 (5%)	0.2019/0.2411 (5%)	0.1894/0.2395 (5%)
RMSD from ideal values: bond length/angles (Å/°)	0.006/0.797	0.006/0.813	0.004/0.623
Mean B value (Å ²)	28.06	31.80	55.0
Overall correlation coefficient Fo-Fc/Fo-Fc free	0.963/0.956	0.959/0.936	0.933/0.911
Molprobrity score	1.21	1.34	1.71
Clashscore, all atoms	2.73	3.48	4.50
Poor rotamers (%)	1.83	1.05	3.34
Ramachandran outliers (%)	0.00	0.00	0.00
Ramachandran favored (%)	98.34	97.22	97.54

reduced TTBK2 binding (Figure 3B). We further confirmed these findings in the context of full-length proteins in a pull-down experiment with HA-tagged TTBK2 and FLAG-tagged CEP164, WT, Y73A, S82A, W84, and Q11P mutants (Figure S1B) that corroborated a strong (Y73A and W84A) or a significant reduction (ciliopathy mutation Q11P) of the TTBK2-CEP164 interaction, while no binding defect was observed for the S82A mutant. The apparently stronger binding of the Q11P mutant in the full-length context is probably explained by the fact that both CEP164 and TTBK2 are capable of self-interacting (Bowie et al., 2018; Sivasubramaniam et al., 2008), thereby increasing their binding affinity due to avidity effects. Together, our data confirm the structural model of the CEP164-TTBK2 complex, define its critical interactions, and establish the nephronophthisis-associated mutation Q11P as directly compromising the complex interface and binding affinity.

CEP164-NTD destabilization by nephronophthisis mutant R93W

In contrast to Q11P, the other CEP164-NTD-linked nephronophthisis-associated mutation R93W is not located near the TTBK2-

CEP164 interface. Instead, R93 is located in the helical bundle, where it forms several hydrogen bonds predicted to stabilize it (Figure 1D; magnified view, panel 1). Thus, the R93W mutation might destabilize the helical bundle that is required for the TTBK2-interacting WW domain to fold stably (Figures 2D and 2E). To test whether this mutation indeed affects the CEP164-NTD stability, we purified the CEP164^{1–109} R93W mutant and assessed its fold and thermostability by CD spectroscopy (Figures 3D and 3E). As a control, we also performed this experiment with the Q11P nephronophthisis mutant that structurally is not predicted to affect CEP164^{1–109} stability (Figure 1D). Our results (Figures 3D and 3E) show that the R93W but not the Q11P mutation indeed strongly lowered the thermostability of the CEP164-NTD. Signs of destabilization were already evident around room temperature, while the mutant structure appeared largely unaffected at 7°C. Transverse relaxation optimized spectroscopy (TROSY) NMR experiments with ¹⁵N-labeled CEP164^{1–109} WT and R93W mutant corroborate the temperature-dependent structural instability of the R93W mutant but also indicate that the mutant structure is already compromised at 4°C (Figure S6A). We conclude that the ciliopathic R93W mutation destabilizes the CEP164-NTD fold.

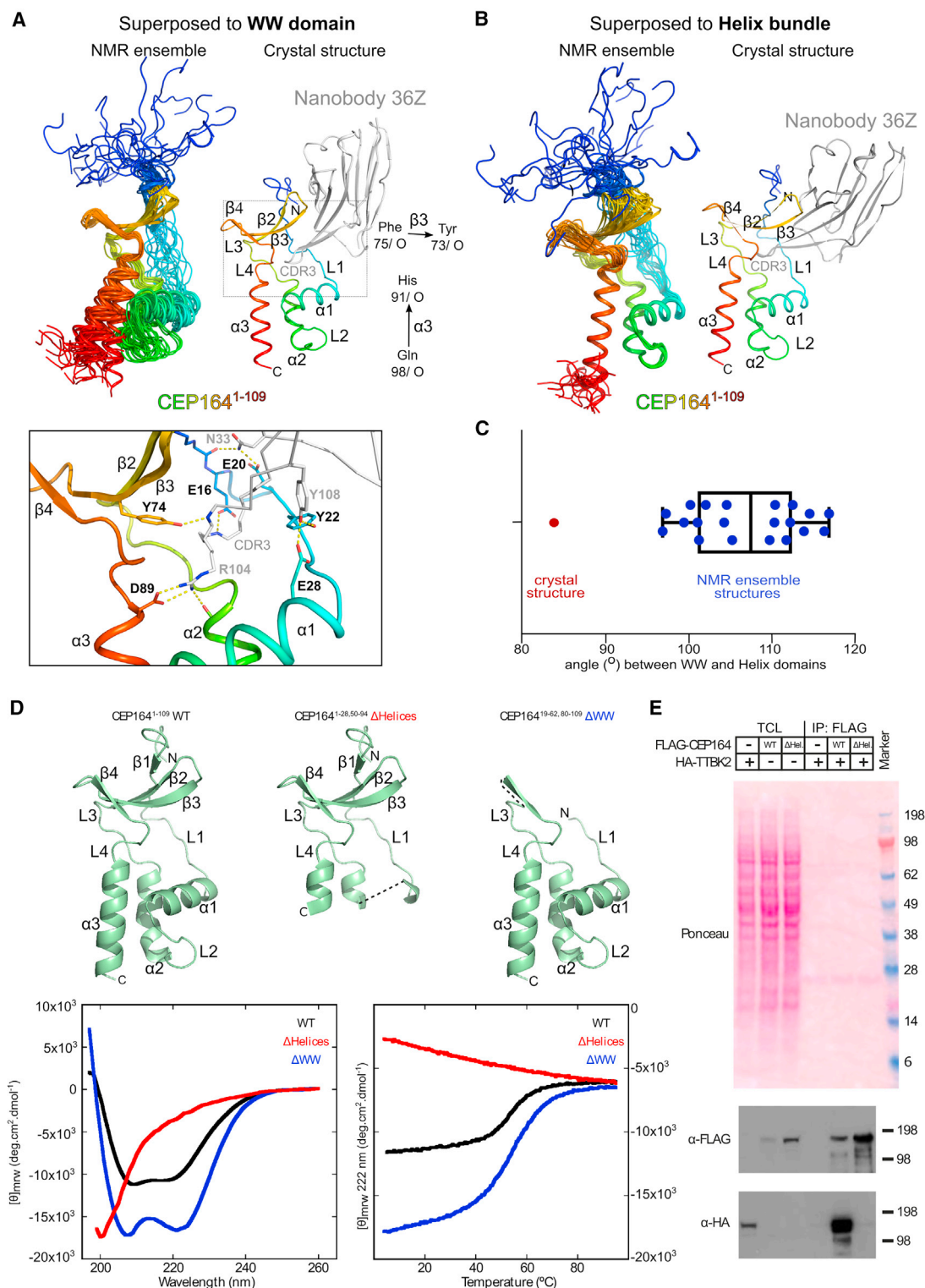


Figure 2. The isolated helical bundle but not the WW domain of CEP164¹⁻¹⁰⁹ folds stably in solution

(A) Left, NMR structure ensemble of CEP164¹⁻¹⁰⁹ superposed to its WW domain (CEP164⁶²⁻⁸³), rainbow-colored from N (blue) to C terminus (red). Right, corresponding view of the superposed crystal structure of nanobody-bound CEP164¹⁻¹⁰⁹ (nanobody in gray). The corresponding RMSD values (±SD) were 0.7 ± 0.2 Å and 0.9 ± 0.1 Å, respectively. Consecutive alpha-helices (α), beta-sheets (β), and linkers (L) are labeled. The vectors used to calculate the helical bundle-WW domain orientation angles (in C) are indicated. The dotted box designates the region shown magnified below. Bottom, detailed view of the CEP164¹⁻¹⁰⁹ region contacted by the nanobody CDR3 loop.

(legend continued on next page)

To establish the impact of the R93W mutation on TTBK2 binding, we employed pull-down assays with recombinantly produced GST-CEP164^{1–109} WT, Q11P, and R93W (Figure S1G) and cell extracts from cells expressing TTBK2^{1074–1087}-GFP (Figure 3F). As seen before, the CEP164 Q11P mutation strongly diminished TTBK2 binding (to 7% of the WT level). In contrast, the impact of the R93W mutant was weaker but still significant, with the amount of pulled down TTBK2^{1074–1087}-GFP reduced to 60% of the WT level. This experiment had to be performed at 4°C, a temperature at which the impact of the R93W mutation on the stability of the NTD of CEP164 is small (Figure 3D). We also performed ITC experiments with the TTBK2^{1074–1087} peptide and the CEP164^{1–109} R93W mutant at 25°C, and these experiments indicated a moderate reduction in binding affinity compared with the WT. However, the ITC data were complicated by the coupling of peptide binding and refolding of a fraction of the CEP164^{1–109} R93W mutant, since the CEP164 construct is destabilized and partially unfolded at 25°C (Figures 3D and S6A), so we are unable to assign a more precise value to the effect on binding. Together, our data suggest that the ciliopathic R93W mutation negatively affects the CEP164-TTBK2 interaction through CEP164-NTD destabilization.

CEP164 Q11P and R93W mutants affect cilia formation in RPE-1 cells

Since the ciliopathy-associated Q11P and R93W CEP164 mutants showed reduced binding to TTBK2 in our pull-down assays, we asked whether they would also have an impact on ciliogenesis in rescue experiments with human, serum-starved CEP164-null telomerase reverse transcriptase-immortalized retina pigmentation epithelial (hTERT RPE-1) cells (Daly et al., 2016). Both CEP164 mutations did not interfere with CEP164 localization to the mother centriole but showed a significant reduction in ARL13b-positive cilia formation compared with the WT construct (Figures 3G and 3H). Consistent with our biochemical data, the CEP164 R93W mutation resulted in a less strong effect than the Q11P mutation in this assay (Figure 3H). Thus, our data confirm the genetic data in patients (Chaki et al., 2012; Maria et al., 2016) and suggest that two CEP164 mutations that give rise to ciliopathies with comparable strength in patients show differential impacts on ciliogenesis in tissue culture cells.

CEP164-NTD binding inhibits EB1 engagement by TTBK2

TTBK2 is not only recruited to centriole distal appendages but also to microtubule ends through a SxIP motif-mediated interaction with the end binding protein EB1/3 (Watanabe et al., 2015;

Jiang et al., 2012). Of the two SxIP motifs present in TTBK2, the second motif (TTBK2^{1051–1054}) contributes the most strongly to EB1/3 binding (Watanabe et al., 2015) and is located in the vicinity of the CEP164-interacting motif of TTBK2 (TTBK2^{1074–1084}). To check whether EB1 and CEP164-NTD can engage this part of TTBK2 simultaneously, we performed pull-down experiments with purified MBP-TTBK2^{1033–1087} (WT, TTBK2^{1051–1054} SKIP to AAA, or TTBK2^{1076–1078} RPP to AAA) and EB1 in the presence of an excess of CEP164^{1–109}. The results shown in Figure 4A demonstrate that the presence of CEP164-NTD strongly decreased EB1 binding to TTBK2^{1033–1087} compared with the TTBK2^{1076–1078} RPP to AAA mutant that is unable to engage CEP164-NTD. In contrast, excess EB1-GFP does not efficiently compete with CEP164-NTD binding to MBP-TTBK2^{1033–1087} (Figure S7B), probably due to its lower binding affinity. Further pull-down experiments with 3xFLAG-EB1 and full-length 3xHA-TTBK2 (WT or CEP164-binding-deficient ΔPro-rich [Δ1,074–1,087] mutant) in the presence of GST-CEP164^{1–109} (WT or TTBK-binding deficient Y73A mutant) confirm our findings (Figure S7A). We conclude that CEP164-NTD binding inhibits EB1 engagement of the major EB1 binding site in TTBK2.

CEP164-NTD binding does not stimulate TTBK2 autophosphorylation

Many kinases exist in an auto-inhibited state that is relieved by an activating event such as phosphorylation or protein binding. Thus, we wanted to test whether CEP164-NTD binding to TTBK2 activates its kinase activity. To this end, we recombinantly produced dephosphorylated N-terminally 3xFLAG- and C-terminally STREP-tagged TTBK2 kinase (WT and kinase dead D163A mutant). The WT but not the D163A mutant TTBK2 kinase efficiently phosphorylated itself, as judged by its strong upward mobility in SDS-PAGE gels after incubation with ATP. Incubation with an excess of purified CEP164^{1–109}, WT, or TTBK2-binding-deficient Y73A mutant did not stimulate TTBK2 phosphorylation levels compared with the corresponding buffer control (Figure S7C). Thus, TTBK2 binding to CEP164 does not strongly activate TTBK2 kinase activity.

CEP164 and TTBK2 contain long regions predicted to be unstructured

Short binding motifs are often found in extended, open conformation, such as regions of disorder. To evaluate TTBK2 for the presence of such regions, we analyzed its sequence using several different disorder prediction algorithms (MFDp2, Mizianty et al., 2013; SPOT-Disorder, Hanson et al., 2017, 2019; or

(B) Similar to (A), but CEP164^{1–109} NMR structures superposed to their helical bundle (CEP164^{26–55}, 87–103). The corresponding RMSD values (±SD) were 0.5 ± 0.1 Å and 0.8 ± 0.1 Å, respectively.

(C) Measured angles between the helical bundle and the WW domain in the NMR and crystal structures as indicated in (A). The average value across the NMR ensemble was 107° ± 7°. The individual angle values in each ensemble member are overlaid to a box-and-whisker plot. The whiskers represent the maximum and the minimum measured values, while the box ranges between the first and the third quartiles; the median value is also indicated.

(D) Top: ribbon representation of the CEP164^{1–109} structure (in green). The ΔHelices and ΔWW panels indicate the construct deletions of the helical bundle or WW domain, respectively, by omitting the corresponding structural regions. Dotted black lines highlight the parts that were directly spliced together in the constructs. Alpha helices (α), beta sheets (β), and linkers (L) are labeled. Bottom: CD analyses of recombinant CEP164^{1–109} WT as well as the corresponding ΔHelices and ΔWW constructs. Left: buffer-subtracted CD spectra at 25°C. Right: CD-based thermal melting analysis recorded at 222 nm.

(E) The helical bundle of CEP164 is necessary for the CEP164-TTBK2 interaction. Western blot showing a pull-down experiment with lysates from cells expressing 3xHA-TTBK2 and 3xFLAG tagged CEP164 or 3xFLAG-CEP164 carrying a deletion of its helical bundle. ΔHel., construct as indicated by ΔHelices in (D). TCL, total cell lysate.

Table 3. Structural statistics for the NMR solution structure of CEP164^{1–109}

Structural restraints			
NOE-derived distance restraints			
intraresidue	668	very strong (0–2.5 Å)	27
sequential	483	strong (0–3.0 Å)	36
medium ($2 \leq i-j \leq 4$)	339	medium (0–4.0 Å)	118
long ($ i-j > 4$)	365	weak (0–5.5 Å)	1674
total	1855	total	1855
Dihedral restraints			
ϕ	81		
ψ	82		
ω	113		
H-bond restraints			
distances	72		
H bonds	36		
Statistics for accepted structures			
Number of accepted structures	20		
Mean AMBER energy terms (kcal/mol \pmSD)			
E (total)	–5,431.4 \pm 21.2		
E (van der Waals)	–797.8 \pm 12.9		
E (distance restraints)	15.9 \pm 3.6		
Distance restraint violations >0.2 Å (average number per structure)	4.7 \pm 2.1		
Angle restraint violations $>5^\circ$ (average number per structure)	12.1 \pm 3.6		
RMSDs from the ideal geometry used within AMBER			
bond lengths	0.0102 Å		
bond angles	2.11°		
Ramachandran statistics			
most favored	94.2%		
additionally allowed	5.4%		
generously allowed	0.2%		
disallowed	0.2%		
Average atomic RMSDs from average structure (\pmSD) residues 26–36, 44–53, 90–103			
N, C α , C backbone atoms	0.27 \pm 0.06 Å		
all heavy atoms	0.91 \pm 0.07 Å		

AUCpred, Wang et al., 2016) that have ranked highly in a recent experimental benchmarking (Nielsen and Mulder, 2019). The results shown in Figure 4B suggest that, outside its N-terminal kinase domain, TTBK2 contains large regions of disorder. Thus, TTBK2 probably has a high level of flexibility between its kinase domain and its C-terminal CEP164-binding region. This flexibility might facilitate its access to its known substrates (Bernatik et al., 2020; Huang et al., 2018; Lo et al., 2019) at or around the centriole wall.

DISCUSSION

Ciliopathies are genetic diseases that arise when mutations impair cilia formation or function. Elucidation of the correspond-

ing molecular mechanisms can lead to a deepened understanding of the underlying biological processes and is an important first step toward the development of targeted therapeutic strategies. The recruitment of TTBK2 by the centriole distal appendage component CEP164 is one of the crucial early events in cilia formation (Cajane and Nigg, 2014; Oda et al., 2014; Huang et al., 2018).

The structures of CEP164-NTD revealed a two-domain organization in which a WW domain is inserted into an α -helical bundle consisting of three α helices. Despite an element of inter-domain flexibility, these two domains act as a single unit whose stability critically depends on the core interactions within the helical bundle. CEP164-NTD accommodates the TTBK2 proline-rich peptide into two non-continuous hydrophobic grooves (XP and

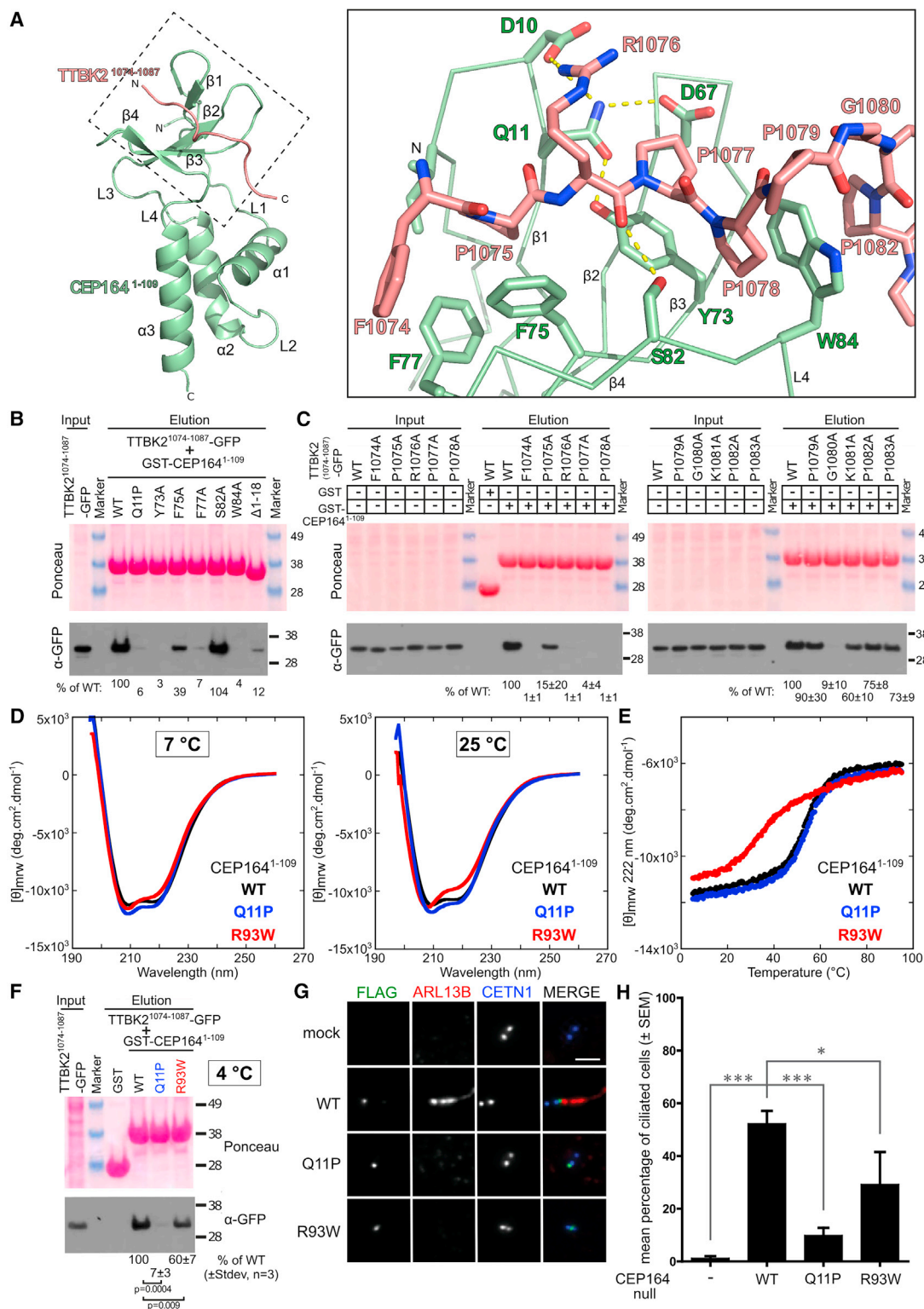


Figure 3. High-resolution structure of the CEP164¹⁻¹⁰⁹-TTBK2¹⁰⁷⁴⁻¹⁰⁸⁷ complex that is compromised by the ciliopathy-associated mutations Q11P and R93W in CEP164

(A) Left: ribbon representation of the structure of CEP164¹⁻¹⁰⁹ (green) in complex with TTBK2¹⁰⁷⁴⁻¹⁰⁸⁷ (red). The structure of the bound camelid nanobody used for co-crystallization is omitted for optical clarity. Consecutive alpha-helices (α), beta-sheets (β), and linkers (L) are labeled. The dotted box is shown magnified to the right. Right: detailed view of the interface region between CEP164¹⁻¹⁰⁹ and TTBK2¹⁰⁷⁴⁻¹⁰⁸⁷. Key interface residues are shown as sticks and are labeled. Yellow dotted lines indicate hydrogen bonds.

(legend continued on next page)

XP2). While both ligand-binding interface and ligand orientation in the complex structure showed striking similarities to class II/III WW domain complexes (Kato et al., 2004), there are also features unique to the CEP164-NTD-TTBK2 interaction. In CEP164-NTD, the XP2 groove is formed by two phenylalanines (F75, F77) and a tyrosine (Y73) instead of a tryptophan and tyrosine or two tyrosines as observed in FE65 and FBP11 WW domains, respectively. Furthermore, the CEP164-NTD contains a flexible N-terminal region that complements the WW domain in the complex structure with an additional two-stranded β -hairpin that directly contributes to ligand binding. The side-chains of I8 and V13 in this region contribute to the shape of the XP2 groove. As a result, this groove is considerably smaller and deeper than the grooves of other class II/III WW domains and accommodates a single proline residue instead of a pair of prolines. This difference might also explain the importance of F1074 in providing additional hydrophobic contacts that contribute to complex stability.

The mutations Q11P and R93W in CEP164 are associated with ciliopathies (Chaki et al., 2012; Maria et al., 2016; Slaats et al., 2014). Q11P was identified as a homozygous mutation and R93W as a compound heterozygous mutation with the Q525X truncation in nephronophthisis patients that displayed early kidney failure and retinal degeneration (Chaki et al., 2012). The Q525X mutation probably results in a strongly dysfunctional CEP164 truncation, as it is unable to localize to the mother centriole. Consistent with this notion, patients with the similar but homozygous truncation mutation R576X show more severe phenotypes with additional features typical for motile ciliopathies, such as primary ciliary dyskinesia (Chaki et al., 2012). A homozygous R93W CEP164 mutation was also found in a patient with BBS (Bardet-Biedl syndrome)-like syndrome with hypogonadism, retinal phenotypes, and obesity but without renal anomalies (Maria et al., 2016).

Our data show that the CEP164 Q11P and R93W mutants localize normally to the mother centriole but are defective in rescuing cilia formation in human, CEP164-null hTERT RPE-1 cells, confirming the genetic data in human patients (Chaki et al., 2012; Maria et al., 2016). Although both mutations are located away from the WW domain of CEP164 (residues 62–84), they affect its ability to engage TTBK2 in pull-down assays. Structurally, the R93W mutation reduces the thermostability of

the CEP164-NTD by impairing the folding of the WW domain-stabilizing helical bundle. In contrast, residue Q11 is part of a short β -strand that associates with the WW domain and contributes to the placement of several side chains that directly contact TTBK2. The Q11P mutation compromises these interactions. Intriguingly, the removal of the first 18 residues of CEP164-NTD has a less strong effect on TTBK2 binding than Q11P. Thus, we speculate that the Q11P proline partly occupies the XP grooves of CEP164-NTD and thereby also acts to compete with TTBK2 binding. Our data suggest that the corresponding CEP164-NTD region is flexible enough to allow these movements. In terms of therapeutic potential, our data suggest that reagents that stabilize the CEP164-NTD fold in the R93W mutant, or prevent the WW domain association of the Q11P region, would hold promise in alleviating disease manifestation in the corresponding patients.

Our *in vitro* and *in vivo* data suggest that the R93W mutation affects TTBK2 binding and cilia formation less strongly than the Q11P mutation. Nevertheless, in patients, no corresponding clear-cut genotype-phenotype relationship is obvious (Chaki et al., 2012; Maria et al., 2016). CEP164 might have functions outside ciliogenesis that contribute to disease manifestations to account for this observation. Thus, CEP164 was suggested to function in cell cycle progression and its dysfunction, for example in the R93W mutant, to contribute to the pathogenesis of nephronophthisis through DNA damage-induced replicative stress, although this mutant was also found to have some negative effect on cilia formation (Slaats et al., 2014). However, in another study, CEP164 was not found to influence cell proliferation or the DNA damage response (Daly et al., 2016). Thus, as suggested for two closely related ciliopathy mutations in CEP120 (Joseph et al., 2018), the genetic backgrounds of the affected patients might modify the exact clinical manifestation of these ciliopathy mutations instead.

Our data also give insights into how TTBK2 binding to CEP164 might influence other TTBK2 activities. Located close to the CEP164-NTD binding region of TTBK2 is one of two EB1-binding SxIP motifs. This motif is responsible for the majority of the EB1-binding affinity of TTBK2 (Watanabe et al., 2015, Figure S7A). EB1-dependent TTBK2 recruitment to microtubules is important for microtubule regulation (Watanabe et al., 2015), and we show here that CEP164-NTD binding inhibits EB1 engagement by

(B) Several interfacial residues of the CEP164 WW domain are critical for its interaction with TTBK2. Western blot showing a pull-down experiment with recombinant GST or GST-CEP164^{1–109}, WT or the indicated mutants, and lysates from cells expressing C-terminally GFP-tagged TTBK2^{1074–1087}. Below the blot, the band intensities of the eluates (as percentage of the WT level) are shown.

(C) Several residues within the CEP164-binding region of TTBK2 are essential for its interaction with CEP164 and define a CEP164-binding motif. Western blot showing a pull-down experiment with recombinant GST or GST-CEP164^{1–109} and lysates from cells expressing C-terminally GFP-tagged TTBK2^{1074–1087} constructs. TTBK2 constructs carried single alanine mutations as indicated above the blot. Below the blot, the band intensities of the eluates (as percentage of the WT level) are shown (\pm SD, $n = 3$).

(D and E) The R93W, but not the Q11P mutation decrease the thermostability of the NTD of CEP164. (D) Buffer-subtracted CD spectra of recombinant CEP164^{1–109} WT as well as its Q11P and R93W mutants at 7°C and 25°C. (E) CD-based thermal melting analysis of CEP164^{1–109} WT, Q11P, and R93W at 222 nm.

(F) Both Q11P and R93W nephronophthisis mutations in CEP164^{1–109} compromise the interaction with TTBK2^{1074–1087} at 4°C. Western blot showing a pull-down experiment with recombinant GST or GST-CEP164^{1–109}, WT, Q11P, or R93W and lysates from cells expressing C-terminally GFP-tagged TTBK2^{1074–1087}. Below the blot, the band intensities of the eluates (as percentage of the WT level) are shown (\pm SD, $n = 3$).

(G and H) The CEP164 Q11P and R93W ciliopathy mutants localize to mother centrioles but do not efficiently rescue cilia formation in CEP164-null cells. (G) Immunofluorescence staining of hTERT RPE-1 CEP164-null cells rescued with the indicated, transfected 3xFLAG-tagged CEP164 constructs (green). Primary cilia were detected by ARL13b staining (red). CETN1 was used to visualize centrosomes (blue). Scale bar: 5 μ m. (H) Quantification of the percentage of ciliated cells (mean percentage of ciliated cells \pm SEM). Statistical significance between the groups was analyzed by one-way ANOVA with a Holm-Sidak multiple comparison post hoc test; number of cells, $N_{WT} = 66$, $N_{Q11P} = 58$, $N_{R93W} = 55$, and $N_{untransfected} = 57$; * $p = 0.02$, *** $p \leq 0.0005$.

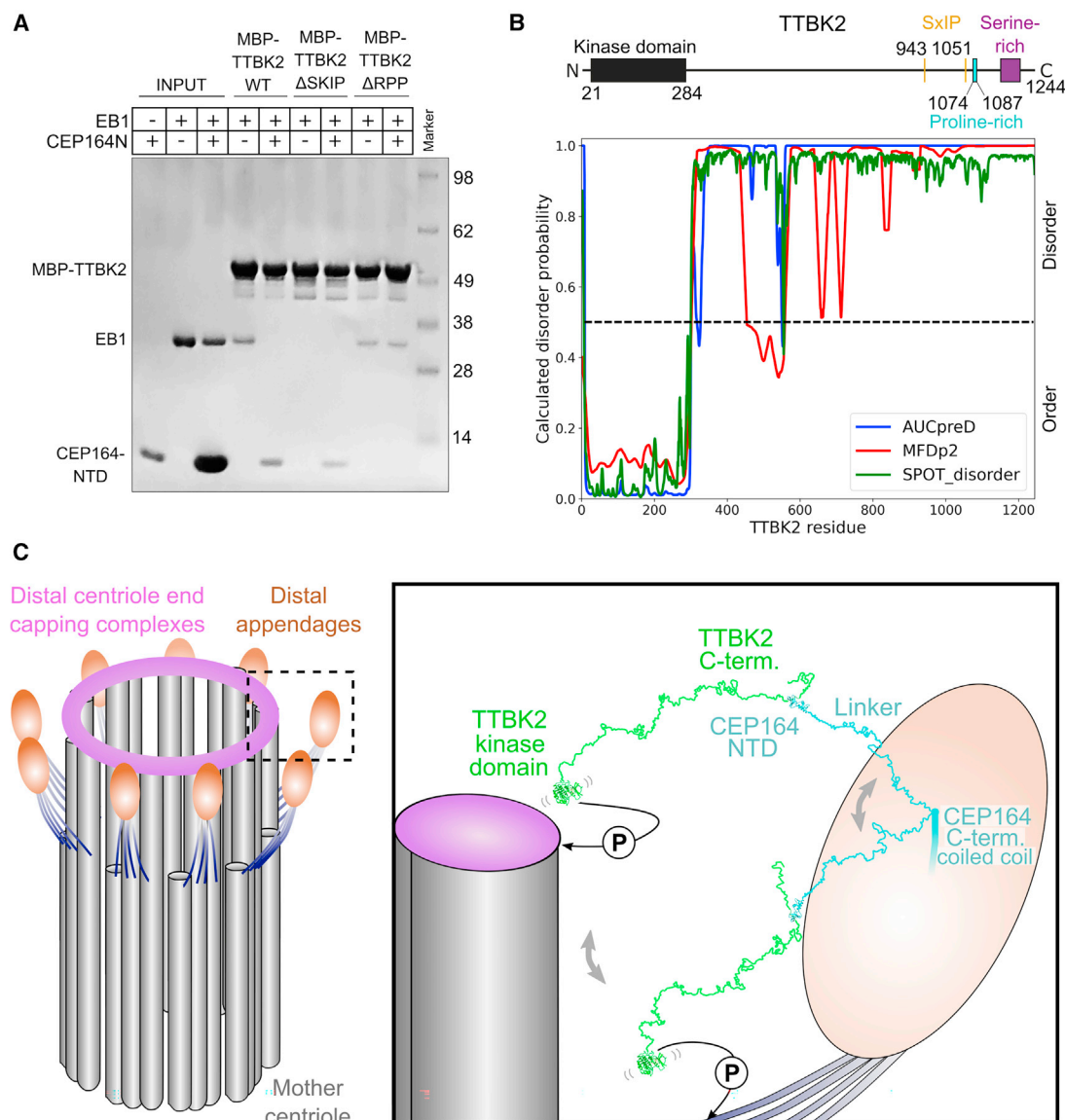


Figure 4. CEP164-NTD binding to TTBK2 inhibits the TTBK2-EB1 interaction

(A) CEP164^{1–109} and EB1 compete for binding to MBP-TTBK2^{1033–1087}. Coomassie-stained SDS-PAGE gel showing pull-down experiments with purified MBP-TTBK2^{1033–1087} (WT, EB1-binding-deficient TTBK2^{1051–1054 SKIP to AAAA} or CEP164-NTD-binding-deficient TTBK2^{1076–1078 RPP to AAA}) with EB1 in the presence of an excess of CEP164^{1–109}.

(B) Per-residue disorder probabilities of TTBK2 as calculated by different disorder prediction algorithms. Values above 0.5 (dashed line) indicate disorder. The location of the kinase domain and selected sequence features of TTBK2 are indicated above the plot.

(C) Model of the TTBK2-CEP164 architecture at the distal appendages. Left: scheme of the mother centriole with distal appendages based on electron microscopy tomography segmentation analysis (Bowler et al., 2019). Subdistal appendages are omitted for clarity. Right: close-up view of a single distal appendage region. CEP164 is indicated in cyan, the bound TTBK2 is shown in green. The connecting linkers between CEP164-NTD and the CEP164 coiled-coil domain and between the CEP164-bound TTBK2^{1074–1084} region and the N-terminal TTBK2 kinase domain (PDB: 6vrf) (Bao et al., 2021) are drawn in an extended and open conformation. Based on disorder predictions and the paucity of predicted secondary structure elements, we propose that these linkers are largely flexible (Figures 4B and S6B). This flexibility would allow the TTBK2-CEP164-NTD complex to sample larger areas of the distal appendage region and would enable TTBK2 to reach its phosphorylation substrates at (MPP9) or close to (CEP83) the distal centriole end. A circled “P” indicates a phosphorylation event by TTBK2.

TTBK2 *in vitro*. This argues that microtubule end association and CEP164 binding of TTBK2 might be mutually exclusive *in vivo* such that distal appendage-associated TTBK2 interacts with CEP164, while the non-centriolar TTBK2 fraction can interact with EB1/3 in the same cell. Preventing EB1/3 engagement and microtubule regulation by distal appendage-bound TTBK2 might

be important for efficient cilia formation, but the functional importance of this putative mechanism in cells remains to be established. Intriguingly, the structural footprint of CEP164-NTD and EB1 on their TTBK2-binding regions (this study; PDB: 3gjo; Honnappa et al., 2009) is not large enough to directly account for the observed competition. Thus, CEP164-NTD and EB1 probably

engage larger regions of TTBK2 than their core binding motifs alone.

There are currently conflicting data concerning whether TTBK2 binding to CEP164 activates its kinase domain (Oda et al., 2014). To address this question, we performed TTBK2 phosphorylation assays with recombinantly produced TTBK2 (WT or kinase dead D163A mutant) in the presence of either binding-competent (WT) or -incompetent (Y73A mutant) CEP164-NTD. Our data did not reveal a stimulation of TTBK2 activity by CEP164-NTD binding. Thus, CEP164 might not be involved in activating an otherwise inactive TTBK2 but possibly recruits TTBK2 in an already activated form.

One of the puzzles concerning TTBK2 function after CEP164 binding is that its effector substrates CEP83 and MPP9 are located close to or at the centriole microtubule wall at a significant distance away from CEP164. While the N-terminal region of CEP164 *in vivo* is found at a radius of 121–284 nm from the centriole center (Bowler et al., 2019), CEP83 and MPP9 are found at a radius of 106–194 nm and ~113 nm, respectively (Bowler et al., 2019; Huang et al., 2018). Thus, TTBK2 would need to span a significant distance to reach these substrates.

While it has been suggested that TTBK2 might redistribute to a site closer to the centriole center (Lo et al., 2019), we favor an alternative explanation. Our bioinformatics analyses suggest that the TTBK2 region downstream of its N-terminal kinase domain (residues 21–284) and upstream of its CEP164-binding region (residues 1,074–1,084) contains large stretches of unfolded regions (Figure 4B). CEP164 also contains a region of ~500 residues downstream of its TTBK2-binding NTD and upstream of its first coiled-coil region, which appears largely unstructured (Figure S6B). Such regions, even with interspersed folded islands, can behave with random coil characteristics (Fitzkee and Rose, 2004). Our theoretical calculations suggest that a region of this combined length would display an average (root mean square) end-to-end distance of ~30 nm but could span much larger distances when extended. Thus, the kinase domain of (CEP164-bound) TTBK2 would probably be able to reach its substrates without relocation and CEP164-NTD, and its bound TTBK2 might be highly mobile around the distal appendages. In agreement with this notion, Bowler et al. (2019) recently showed that the N-terminal part of CEP164 displays a wider distribution at distal appendages that extends beyond their electron dense head structure. These findings accord well with our proposal that the CEP164 NTD is separated by a flexible linker from the appendage-anchored part of CEP164. We propose that the ability of distal appendage components to sample the wider area around them might be important for many different aspects of distal appendage function (Figure 4C).

STAR★METHODS

Detailed methods are provided in the online version of this paper and include the following:

- **KEY RESOURCES TABLE**
- **RESOURCE AVAILABILITY**
 - Lead contact
 - Materials availability
 - Data and code availability

● EXPERIMENTAL MODEL AND SUBJECT DETAILS

- Cell lines

● METHOD DETAILS

- Recombinant protein purification
- Nanobody generation
- Protein crystallization
- X-ray crystallography data processing
- Pull-down assays
- Autophosphorylation assay
- Bioinformatics
- Circular dichroism (CD)
- Isothermal titration calorimetry (ITC)
- NMR
- NMR structure calculations
- Ciliogenesis rescue experiments

● QUANTIFICATION AND STATISTICAL ANALYSIS

SUPPLEMENTAL INFORMATION

Supplemental information can be found online at <https://doi.org/10.1016/j.str.2021.08.007>.

ACKNOWLEDGMENTS

We acknowledge M. Mazzorana (I04, MX15916-82) and N. Paterson (I03, MX21426-1) at the Diamond Light Source (UK), and M. Yu and J. O'Donnell (MRC-LMB) for dataset collection. We thank C. Morrison (NUI Galway), R. Williams, O. Perisic, and M. Hegde (MRC-LMB) for reagents. We thank M. van Roon (MRC-LMB) for technical support and helpful scientific discussions. We acknowledge the laboratory management staff from the School of Biological and Chemical Sciences and the Blizard Institute, Queen Mary University of London; the crystallization, X-ray crystallography, and NMR facilities from the MRC-LMB; and the CELLIM of CEITEC supported by the Czech-Biolmaging large RI project (MEYS CR grant LM2018129). This work was supported by the Medical Research Council (file reference MC_UP_1201/3 to M.v.B. and a Cesar Milstein Fellowship for I.R.S.), the Queen Mary University of London (start-up grant to M.v.B.), the Czech Science Foundation (grant 19-05244S), and the Swiss National Science Foundation (grant IZ11Z0_166533 to L.C.).

AUTHOR CONTRIBUTIONS

I.R.S. and M.v.B. determined the crystal structures and performed the biochemical experiments. C.M.J. performed ITC. T.J.R. performed the NMR experiments. T.J.R. and D.N. solved the NMR structure. L.B. and L.C. performed the immunofluorescence experiments. A.A. contributed bioinformatics and structural analyses. M.v.B. supervised the project. I.R.S. and M.v.B. wrote the original draft of the manuscript. All authors contributed to the reviewing and editing of the manuscript. L.C. and M.v.B. secured funding.

DECLARATION OF INTERESTS

The authors declare no competing interests.

Received: April 30, 2021

Revised: July 19, 2021

Accepted: August 17, 2021

Published: September 8, 2021

REFERENCES

- Afonine, P.V., Grosse-Kunstleve, R.W., Echols, N., Headd, J.J., Moriarty, N.W., Mustyakimov, M., Terwilliger, T.C., Urzhumtsev, A., Zwart, P.H., and Adams, P.D. (2012). Towards automated crystallographic structure refinement with phenix.refine. *Acta Crystallogr. D Biol. Crystallogr.* 68, 352–367.
- Aragón, E., Goerner, N., Zaromytidou, A.I., Xi, Q., Escobedo, A.I., Massague, J., and Macias, M.J. (2011). A Smad action turnover switch operated by WW

domain readers of a phosphoserine code. *Genes Dev.* 25, 1275–1288. <https://doi.org/10.1101/gad.206081>.

Argentaro, A., Yang, J.C., Chapman, L., Kowalczyk, M.S., Gibbons, R.J., Higgs, D.R., Neuhaus, D., and Rhodes, D. (2007). Structural consequences of disease-causing mutations in the ATRX-DNMT3-DNMT3L (ADD) domain of the chromatin-associated protein ATRX. *Proc. Natl. Acad. Sci. U S A* 104, 11939–11944.

Ashkenazy, H., Abadi, S., Martz, E., Chay, O., Mayrose, I., Pupko, T., and Ben-Tal, N. (2016). ConSurf 2016: an improved methodology to estimate and visualize evolutionary conservation in macromolecules. *Nucleic Acids Res.* 44, W344–W350.

Bao, C., Bajrami, B., Marcotte, D.J., Chodaparambil, J.V., Kerns, H.M., Henderson, J., Wei, R., Gao, B., and Dillon, G.M. (2021). Mechanisms of regulation and diverse activities of tau-tubulin kinase (TTBK) isoforms. *Cell. Mol. Neurobiol.* 41, 669–685. <https://doi.org/10.1007/s10571-020-00875-6>.

Berjanskii, M.V., and Wishart, D.S. (2005). A simple method to predict protein flexibility using secondary chemical shifts. *J. Am. Chem. Soc.* 127, 14970–14971. <https://doi.org/10.1021/ja054842f>.

Bernatik, O., Pejškova, P., Vyslouliz, D., Hanakova, K., Zdrahal, Z., and Cajanek, L. (2020). Phosphorylation of multiple proteins involved in ciliogenesis by Tau Tubulin kinase 2. *Mol. Biol. Cell* 31, 1032–1046.

Bettencourt-Dias, M., Hildebrandt, F., Pellman, D., Woods, G., and Godinho, S.A. (2011). Centrosomes and cilia in human disease. *Trends Genet.* 27, 307–315.

Bowie, E., and Goetz, S.C. (2020). TTBK2 and primary cilia are essential for the connectivity and survival of cerebellar Purkinje neurons. *eLife* 9, e51166.

Bowie, E., Norris, R., Anderson, K.V., and Goetz, S.C. (2018). Spinocerebellar ataxia type 11-associated alleles of Ttbk2 dominantly interfere with ciliogenesis and cilium stability. *PLoS Genet.* 14, e1007844.

Bowler, M., Kong, D., Sun, S.F., Nanjundappa, R., Evans, L., Farmer, V., Holland, A., Mahjoub, M.R., Sui, H.X., and Loncarek, J. (2019). High-resolution characterization of centriole distal appendage morphology and dynamics by correlative STORM and electron microscopy. *Nat. Commun.* 10, 993.

Braun, D.A., and Hildebrandt, F. (2017). Ciliopathies. *Cold Spring Harb. Perspect. Biol.* 9. <https://doi.org/10.1101/cshperspect.a028191>.

van Breugel, M., Wilcken, R., McLaughlin, S.H., Rutherford, T.J., and Johnson, C.M. (2014). Structure of the SAS-6 cartwheel hub from *Leishmania major*. *eLife* 3, e01812.

Cajanek, L., and Nigg, E.A. (2014). Cep164 triggers ciliogenesis by recruiting Tau tubulin kinase 2 to the mother centriole. *Proc. Natl. Acad. Sci. U S A* 111, E2841–E2850.

Case, D.A., Cheatham, T.E., Darden, T., Gohlke, H., Luo, R., Merz, K.M., Onufriev, A., Simmerling, C., Wang, B., and Woods, R.J. (2005). The Amber biomolecular simulation programs. *J. Comput. Chem.* 26, 1668–1688.

Chaki, M., Airik, R., Ghosh, A.K., Giles, R.H., Chen, R., Slaats, G.G., Wang, H., Hurd, T.W., Zhou, W.B., Cluckey, A., et al. (2012). Exome capture reveals ZNF423 and CEP164 mutations, linking renal ciliopathies to DNA damage response signaling. *Cell* 150, 533–548.

Chen, V.B., Arendall, W.B., III, Headd, J.J., Keedy, D.A., Immormino, R.M., Kapral, G.J., Murray, L.W., Richardson, J.S., and Richardson, D.C. (2010). MolProbity: all-atom structure validation for macromolecular crystallography. *Acta Crystallogr. D Biol. Crystallogr.* 66, 12–21.

Chong, W.M., Wang, W.J., Lo, C.H., Chiu, T.Y., Chang, T.J., Liu, Y.P., Tanos, B., Mazo, G., Tsou, M.F.B., Jane, W.N., et al. (2020). Super-resolution microscopy reveals coupling between mammalian centriole subdistal appendages and distal appendages. *eLife* 9, e53580.

Daly, O.M., Gaboriau, D., Karakaya, K., King, S., Dantas, T.J., Lalor, P., Dockery, P., Kramer, A., and Morrison, C.G. (2016). CEP164-null cells generated by genome editing show a ciliation defect with intact DNA repair capacity. *J. Cell Sci.* 129, 1769–1774.

Diamond, R. (1995). COORDINATE-BASED CLUSTER-analysis. *Acta Crystallogr. D Biol. Crystallogr.* 51, 127–135.

Emsley, P., and Cowtan, K. (2004). Coot: model-building tools for molecular graphics. *Acta Crystallogr. D Struct. Biol.* 60, 2126–2132.

Evans, P.R., and Murshudov, G.N. (2013). How good are my data and what is the resolution? *Acta Crystallogr. D Biol. Crystallogr.* 69, 1204–1214.

Fischer, E., Legue, E., Doyen, A., Nato, F., Nicolas, J.F., Torres, V., Yaniv, M., and Pontoglio, M. (2006). Defective planar cell polarity in polycystic kidney disease. *Nat. Genet.* 38, 21–23.

Fitzkee, N.C., and Rose, G.D. (2004). Reassessing random-coil statistics in unfolded proteins. *Proc. Natl. Acad. Sci. U S A* 101, 12497–12502.

Fliegauf, M., Benzing, T., and Omran, H. (2008). When cilia go bad: cilia defects and ciliopathies (vol 8, pg 880, 2007). *Nat. Rev. Mol. Cell Biol.* 9, 88.

Goetz, S.C., Liem, K.F., and Anderson, K.V. (2012). The spinocerebellar ataxia-associated gene tau tubulin kinase 2 controls the initiation of ciliogenesis. *Cell* 151, 847–858.

Graser, S., Stierhof, Y.D., Lavoie, S.B., Gassner, O.S., Lamla, S., Le Clech, M., and Nigg, E.A. (2007). Cep164, a novel centriole appendage protein required for primary cilium formation. *J. Cell Biol.* 179, 321–330.

Hanson, J., Yang, Y., Paliwal, K., and Zhou, Y. (2017). Improving protein disorder prediction by deep bidirectional long short-term memory recurrent neural networks. *Bioinformatics* 33, 685–692.

Hanson, J., Paliwal, K.K., Litfin, T., and Zhou, Y.Q. (2019). SPOT-Disorder2: improved protein intrinsic disorder prediction by ensembled deep learning. *Genomics Proteomics Bioinformatics* 17, 645–656.

Hildebrandt, F., Attanasio, M., and Otto, E. (2009). Nephronophthisis: disease mechanisms of a ciliopathy. *J. Am. Soc. Nephrol.* 20, 23–35.

Hommel, U., Harvey, T.S., Driscoll, P.C., and Campbell, I.D. (1992). Human epidermal growth-factor - high-resolution solution structure and comparison with human transforming growth factor- α . *J. Mol. Biol.* 227, 271–282.

Honnappa, S., Gouveia, S.M., Weisbrich, A., Damberger, F.F., Bhavesh, N.S., Jawhari, H., Grigoriev, I., van Rijssel, F.J., Buey, R.M., Lawera, A., et al. (2009). An EB1-binding motif acts as a microtubule tip localization signal. *Cell* 138, 366–376. <https://doi.org/10.1016/j.cell.2009.04.065>.

Huang, N., Zhang, D.H., Li, F.Y., Chai, P.Y., Wang, S., Teng, J.L., and Chen, J.G. (2018). M-Phase Phosphoprotein 9 regulates ciliogenesis by modulating CP110-CEP97 complex localization at the mother centriole. *Nat. Commun.* 9, 4511.

Humbert, M.C., Weihbrecht, K., Searby, C.C., Li, Y.L., Pope, R.M., Sheffield, V.C., and Seo, S. (2012). ARL13B, PDE6D, and CEP164 form a functional network for INPP5E ciliary targeting. *Proc. Natl. Acad. Sci. U S A* 109, 19691–19696.

Iglesias-Bexiga, M., Castillo, F., Cobos, E.S., Oka, T., Sudol, M., and Luque, I. (2015). WW domains of the yes-kinase-associated protein (YAP) transcriptional regulator behave as independent units with different binding preferences for PPxY motif-containing ligands. *PLoS One* 10. <https://doi.org/10.1371/journal.pone.0113828>.

Ishikawa, H., and Marshall, W.F. (2011). Ciliogenesis: building the cell's antenna. *Nat. Rev. Mol. Cell Biol.* 12, 222–234.

Jiang, K., Toedt, G., Montenegro Gouveia, S., Davey, N.E., Hua, S., van der Vaart, B., Grigoriev, I., Larsen, J., Pedersen, L.B., Bezstarosti, K., et al. (2012). A proteome-wide screen for mammalian SxIP motif-containing microtubule plus-end tracking proteins. *Curr. Biol.* 22, 1800–1807.

Joseph, N., Al-Jassar, C., Johnson, C.M., Andreeva, A., Barnabas, D.D., Freund, S.M.V., Gergely, F., and van Breugel, M. (2018). Disease-associated mutations in CEP120 destabilize the protein and impair ciliogenesis. *Cell Rep.* 23, 2805–2818.

Joukov, V., and De Nicolo, A. (2019). The centrosome and the primary cilium: the yin and yang of a hybrid organelle. *Cells* 8. <https://doi.org/10.3390/cells8070701>.

Kato, Y., Nagata, K., Takahashi, M., Lian, L.B., Herrero, J.J., Sudol, M., and Tanokura, M. (2004). Common mechanism of ligand recognition by group II/III WW domains - redefining their functional classification. *J. Biol. Chem.* 279, 31833–31841.

Kobayashi, T., Tanaka, K., Mashima, Y., Shoda, A., Tokuda, M., and Itoh, H. (2020). CEP164 deficiency causes hyperproliferation of pancreatic cancer cells. *Front. Cell Dev. Biol.* 8, 1–12.

- Kumar, D., and Reiter, J. (2021). How the centriole builds its cilium: of mothers, daughters, and the acquisition of appendages. *Curr. Opin. Struct. Biol.* 66, 41–48.
- Laskowski, R.A., MacArthur, M.W., Moss, D.S., and Thornton, J.M. (1993). Procheck - a program to check the stereochemical quality of protein structures. *J. Appl. Crystallogr.* 26, 283–291.
- Laskowski, R.A., Rullmann, J.A.C., MacArthur, M.W., Kaptein, R., and Thornton, J.M. (1996). AQUA and PROCHECK-NMR: programs for checking the quality of protein structures solved by NMR. *J. Biomol. NMR* 8. <https://doi.org/10.1007/BF00228148>.
- Lee, W., Tonelli, M., and Markley, J.L. (2015). NMRFAM-SPARKY: enhanced software for biomolecular NMR spectroscopy. *Bioinformatics* 31, 1325–1327.
- Lo, C.H., Lin, I.H., Yang, T.T., Huang, Y.C., Tanos, B.E., Chou, P.C., Chang, C.W., Tsay, Y.G., Liao, J.C., and Wang, W.J. (2019). Phosphorylation of CEP83 by TTBK2 is necessary for cilia initiation. *J. Cell Biol.* 218. <https://doi.org/10.1083/jcb.201811142>.
- Maria, M., Lamers, I.J.C., Schmidts, M., Ajmal, M., Jaffar, S., Ullah, E., Mustafa, B., Ahmad, S., Nazmutdinova, K., Hoskins, B., et al. (2016). Genetic and clinical characterization of Pakistani families with Bardet-Biedl syndrome extends the genetic and phenotypic spectrum. *Sci. Rep.* 6, 34764.
- Markley, J.L., Bax, A., Arata, Y., Hilbers, C.W., Kaptein, R., Sykes, B.D., Wright, P.E., and Wuthrich, K. (1998). Recommendations for the presentation of NMR structures of proteins and nucleic acids - (IUPAC Recommendations 1998). *Pure Appl. Chem.* 70, 117–142.
- McCoy, A.J., Grosse-Kunstleve, R.W., Adams, P.D., Winn, M.D., Storoni, L.C., and Read, R.J. (2007). Phaser crystallographic software. *J. Appl. Crystallogr.* 40, 658–674.
- McDonald, C.B., McIntosh, S.K.N., Mikles, D.C., Bhat, V., Deegan, B.J., Seldeen, K.L., Saeed, A.M., Buffa, L., Sudol, M., Nawaz, Z., et al. (2011). Biophysical analysis of binding of WW domains of the YAP2 transcriptional regulator to PPXY motifs within WBP1 and WBP2 adaptors. *Biochemistry* 50, 9616–9627.
- Meiyappan, M., Birrane, G., and Ldias, J.A. (2007). Structural basis for proline recognition by the FE65 WW domain. *J. Mol. Biol.* 372, 970–980. <https://doi.org/10.1016/j.jmb.2007.06.064>.
- Mitchison, H.M., and Valente, E.M. (2017). Motile and non-motile cilia in human pathology: from function to phenotypes. *J. Pathol.* 241, 294–309.
- Mizianty, M.J., Peng, Z., and Kurgan, L. (2013). MFDp2: accurate predictor of disorder in proteins by fusion of disorder probabilities, content and profiles. *Intrinsically Disord. Proteins* 1. <https://doi.org/10.4161/idp.24428>.
- Murshudov, G.N., Skubak, P., Lebedev, A.A., Pannu, N.S., Steiner, R.A., Nicholls, R.A., Winn, M.D., Long, F., and Vagin, A.A. (2011). REFMAC5 for the refinement of macromolecular crystal structures. *Acta Crystallogr. D Biol. Crystallogr.* 67, 355–367.
- Nielsen, J.T., and Mulder, F.A.A. (2019). Quality and bias of protein disorder predictors. *Sci. Rep.* 9, 5137.
- Oda, T., Chiba, S., Nagai, T., and Mizuno, K. (2014). Binding to Cep164, but not EB1, is essential for centriolar localization of TTBK2 and its function in ciliogenesis. *Genes Cells* 19, 927–940.
- Pedersen, L.B., Veland, I.R., Schroder, J.M., and Christensen, S.T. (2008). Assembly of primary cilia. *Dev. Dyn.* 237. <https://doi.org/10.1002/dvdy.21521>.
- Pires, J.R., Parthier, C., Aido-Machado, R., Wiedermann, U., Otte, L., Bohm, G., Rudolph, R., and Oschkinat, H. (2005). Structural basis for APPTPPPLPP peptide recognition by FBP11WW1 domain. *J. Mol. Biol.* 348, 399–408. <https://doi.org/10.1016/j.jmb.2005.02.056>.
- Schmidt, K.N., Kuhns, S., Neuner, A., Hub, B., Zentgraf, H., and Pereira, G. (2012). Cep164 mediates vesicular docking to the mother centriole during early steps of ciliogenesis. *J. Cell Biol.* 199, 1083–1101.
- Schneider, C.A., Rasband, W.S., and Eliceiri, K.W. (2012). NIH Image to ImageJ: 25 years of image analysis. *Nat. Methods* 9, 671–675. <https://doi.org/10.1038/nmeth.2089>.
- Schwieters, C.D., Kuszewski, J.J., Tjandra, N., and Clore, G.M. (2003). The Xplor-NIH NMR molecular structure determination package. *J. Magn. Reson.* 160, 65–73.
- Shen, Y., Delaglio, F., Cornilescu, G., and Bax, A. (2009). TALOS plus : a hybrid method for predicting protein backbone torsion angles from NMR chemical shifts. *J. Biomol. NMR* 44, 213–223.
- Singla, V., and Reiter, J.F. (2006). The primary cilium as the cell's antenna: signaling at a sensory organelle. *Science* 313, 629–633.
- Sivasubramanian, S., Sun, X., Pan, Y.R., Wang, S., and Lee, E.Y. (2008). Cep164 is a mediator protein required for the maintenance of genomic stability through modulation of MDC1, RPA, and CHK1. *Genes Dev.* 22, 587–600.
- Slaats, G.G., Ghosh, A.K., Falke, L.L., Le Corre, S., Shaltiel, I.A., van de Hoek, G., Klasson, T.D., Stokman, M.F., Logister, I., Verhaar, M.C., et al. (2014). Nephronophthisis-associated CEP164 regulates cell cycle progression, apoptosis and epithelial-to-mesenchymal transition. *PLoS Genet.* 10, e1004594.
- Stokman, M.F., Saunier, S., and Benmerah, A. (2021). Renal ciliopathies: sorting out therapeutic approaches for nephronophthisis. *Front. Cell Dev. Biol.* 9, 653138.
- Tabares da Rosa, S., Wogulis, L.A., Wogulis, M.D., González-Sapienza, G., and Wilson, D.K. (2019). Structure and specificity of several trilocarban-binding single domain camelid antibody fragments. *J. Mol. Recognit.* 32, e2755. <https://doi.org/10.1002/jmr.2755>.
- Tanos, B.E., Yang, H.J., Soni, R., Wang, W.J., Macaluso, F.P., Asara, J.M., and Tsou, M.F. (2013). Centriole distal appendages promote membrane docking, leading to cilia initiation. *Genes Dev.* 15, 163–168.
- Verma, A., Jing-Song, F., Finch-Edmondson, M.L., Velazquez-Campoy, A., Balasegaran, S., Sudol, M., and Sivaraman, J. (2018). Biophysical studies and NMR structure of YAP2 WW domain - LATS1 PPxY motif complexes reveal the basis of their interaction. *Oncotarget* 9, 8068–8080.
- Wang, S., Ma, J.Z., and Xu, J.B. (2016). AUCpred: proteome-level protein disorder prediction by AUC-maximized deep convolutional neural fields. *Bioinformatics* 32, 672–679.
- Watanabe, T., Kakeno, M., Matsui, T., Sugiyama, I., Arimura, N., Matsuzawa, K., Shirahige, A., Ishidate, F., Nishioka, T., Taya, S., et al. (2015). TTBK2 with EB1/3 regulates microtubule dynamics in migrating cells through KIF2A phosphorylation. *J. Cell Biol.* 210, 737–751.
- Werner, S., Pimenta-Marques, A., and Bettencourt-Dias, M. (2017). Maintaining centrosomes and cilia. *J. Cell Sci.* 130, 3789–3800.
- Winter, G., Waterman, D.G., Parkhurst, J.M., Brewster, A.S., Gildea, R.J., Gerstel, M., Fuentes-Montero, L., Vollmar, M., Michels-Clark, T., Young, I.D., et al. (2018). DIALLS: implementation and evaluation of a new integration package. *Acta Crystallogr. D Struct. Biol.* 74, 85–97.
- Xia, B., Tsui, V., Case, D.A., Dyson, H.J., and Wright, P.E. (2002). Comparison of protein solution structures refined by molecular dynamics simulation in vacuum, with a generalized Born model, and with explicit water. *J. Biomol. NMR* 22, 317–331.
- Xu, Q.W., Zhang, Y.X., Wei, Q., Huang, Y., Hu, J.H., and Ling, K. (2016). Phosphatidylinositol phosphate kinase PIPKI gamma and phosphatase INPP5E coordinate initiation of ciliogenesis. *Nat. Commun.* 7, 10777.
- Yang, T.T., Chong, W.M., Wang, W.J., Mazo, G., Tanos, B., Chen, Z.M., Tran, T.M.N., Chen, Y.D., Weng, R.R., Huang, C.E., et al. (2018). Super-resolution architecture of mammalian centriole distal appendages reveals distinct blade and matrix functional components. *Nat. Commun.* 9, 2023.
- Zarrinpar, A., and Lim, W.A. (2000). Converging on proline: the mechanism of WW domain peptide recognition. *Nat. Struct. Biol.* 7, 611–613.

STAR★METHODS

KEY RESOURCES TABLE

REAGENT or RESOURCE	SOURCE	IDENTIFIER
Antibodies		
Monoclonal ANTI-FLAG M2 antibody produced in mouse	Sigma-Aldrich/Merck	Cat# F1804
Polyclonal ANTI-HA antibody produced in rabbit	Gift from R. Hegde (MRC-LMB)	N/A
Polyclonal ANTI-GFP antibody produced in rabbit	Invitrogen/ThermoFisher Scientific	Cat# A11122
Polyclonal ANTI-ARL13B antibody produced in rabbit	Proteintech	Cat# 17711-1
ANTI-CENT1 – Alexa Fluor 647	Proteintech/Invitrogen	Cat# 12794-1-AP/ A20186
Donkey anti-Mouse IgG (H+L) Secondary Antibody, Alexa Fluor 488	Invitrogen/ThermoFisher Scientific	Cat# R37114
Donkey anti-Rabbit IgG (H+L) Highly Cross-Adsorbed Secondary Antibody, Alexa Fluor 568	Invitrogen/ThermoFisher Scientific	Cat# A10042
Normal Rabbit IgG	Santa Cruz Biotechnology	Cat# sc-2027
Bacterial Strains		
Rosetta (DE3)	Gift from J. Kilmartin (MRC-LMB)	N/A
Chemicals, Peptides, and Recombinant Proteins		
Glycerol Mounting Media	Agilent	Cat# C056330-2
Lipofectamine 3000	Thermo Fisher Scientific	Cat# L3000001
D-MEM/F-12, supplied, GlutaMAX, sodium carbonate	Thermo Fisher Scientific	Cat# 31331028
D-MEM Glutamax	Thermo Fisher Scientific	Cat# 10566016
Expi293 Expression Medium	Thermo Fisher Scientific	Cat# A1435101
Glutathione sepharose 4B	GE Healthcare Life Sciences	Cat# 17075601
Amylose resin	New England Biolabs	Cat# E8021S
anti-FLAG M2 magnetic beads	Sigma-Aldrich/Merck	Cat# M8823
NuPAGE 4-12% Bis-Tris 1.0mm 15-well	ThermoFisher Scientific	Cat# NP0323BOX
PEI	Polysciences	Cat# 24765
TTBK2 ¹⁰⁷⁴⁻¹⁰⁸⁷ peptide	Biomatik	N/A
Wizard Classic 2 screen	Rigaku/ Molecular Dimensions	Cat# MD15-W2-T
JCSG screen	Qiagen/ NeXtal	Cat# 130920
Wizard Cryo 2 screen	Rigaku/ Molecular Dimensions	Cat# MD15-C2-T
Deposited Data		
Crystal structure of <i>Homo sapiens</i> CEP164 ¹⁻¹⁰⁹ in complex with camelid nanobody 10Z	This paper	PDB accession code 7O06
Crystal structure of <i>Homo sapiens</i> CEP164 ¹⁻¹⁰⁹ in complex with camelid nanobody 36Z	This paper	PDB accession code 7O0S
Crystal structure of <i>Homo sapiens</i> TTBK2 ¹⁰⁷⁴⁻¹⁰⁸⁷ -CEP164 ¹⁻¹⁰⁹ in complex with camelid nanobody 36Z	This paper	PDB accession code 7O3B
NMR structure ensemble of <i>Homo sapiens</i> CEP164 ¹⁻¹⁰⁹	This paper	PDB accession code 7NWJ
NMR data	This paper	BMRB accession code 50793

(Continued on next page)

Continued

REAGENT or RESOURCE	SOURCE	IDENTIFIER
Crystal structure of the camelid nanobody VHH T9	Tabares da Rosa et al. (2019)	PDB accession code 5VLV
Crystal structure of human EB1 in complex with microtubule Tip localization signal peptide of MACF	Honnappa et al. (2009)	PDB accession code 3GJO
Crystal structure of ADP bound TTBK2 kinase domain	Bao et al. (2021)	PDB accession code 6VRF
NMR structure of Smurf1 WW domain in complex with a Smad1 derived peptide	Aragón et al. (2011)	PDB accession code 2LAZ
NMR structure of YAP WW domain in complex with a Smad1 derived peptide	Aragón et al. (2011)	PDB accession code 2LAW
NMR structure of FBP11WW1 domain in complex with a proline-rich peptide	Pires et al. (2005)	PDB accession code 1YWI
Crystal structure of FE65 WW domain in complex with hMena peptide	Meiyappan et al. (2007)	PDB accession code 2HO2

Experimental Models: Cell Lines

hTERT RPE-1	Gift from C. Morrison (NUI Galway) (Daly et al., 2016)	N/A
CEP164 null hTERT RPE-1	Gift from C. Morrison (NUI Galway) (Daly et al., 2016)	N/A
Flp-In T-REx 293	Gift from R. Hegde (MRC-LMB) (Joseph et al., 2018)	N/A
Expi293	Gift from O. Perisic, R. Williams group (MRC-LMB)	N/A

Recombinant DNA

pGEX6P1-CEP164 ¹⁻¹⁰⁹ (BamH1 and EcoR1 sites)	This paper	N/A
pGEX6P1-TTBK2 ¹⁰⁷⁴⁻¹⁰⁸⁷ -CEP164 ¹⁻¹⁰⁹ (BamH1 and EcoR1 sites)	This paper	N/A
pGEX6P1-CEP1641-28,50-94 (=ΔHelices)-TEV-HIS6 (BamH1-EcoR1 sites)	This paper	N/A
pGEX6P1-camelid nanobody 10Z (BamH1 and EcoR1 sites)	This paper	N/A
pGEX6P1-camelid nanobody 36Z (BamH1 and EcoR1 sites)	This paper	N/A
pOPTM -TTBK2 ¹⁰⁷⁴⁻¹⁰⁸⁷ (Nde1 and BamH1 sites)	This paper	N/A
pGEX6P1- EB1 (BamH1 and EcoR1 sites)	This paper	N/A
pSKB2LNB-EB1-GFP (Nde1 and BamH1 sites)	This paper	N/A
pGEX6P1-CEP164N-GFP (BamH1 and EcoR1 sites)	This paper	N/A
pcDNA 3.1 derivative – 3xFLAG-TTBK2-3xSTREP (WT or D163A mutant) (BamH1 and EcoR1 sites)	This paper	N/A
pcDNA 3.1 derivative – 3xFLAG-CEP164 (WT or Q11P, or R93W, or kinase dead) (BamH1 and EcoR1 sites)	This paper	N/A
pcDNA 3.1 derivative – 3xHA-TTBK2 (or mutant) (BamH1 and EcoR1 sites)	This paper	N/A

Software and Algorithms

DIALS	(Winter et al., 2018)	https://dials.github.io/
AIMLESS	(Evans and Murshudov, 2013)	http://www.ccp4.ac.uk/download

(Continued on next page)

Continued

REAGENT or RESOURCE	SOURCE	IDENTIFIER
PHASER	(McCoy et al., 2007)	http://www.ccp4.ac.uk/download
REFMAC	(Murshudov et al., 2011)	http://www.ccp4.ac.uk/download
COOT	(Emsley and Cowtan, 2004)	http://www.ccp4.ac.uk/download
PHENIX.REFINE	(Afonine et al., 2012)	http://www.phenix-online.org/download/
MolProbity	(Chen et al., 2010)	http://molprobity.manchester.ac.uk/
The PyMOL Molecular Graphics System	Schrödinger, LLC	Version 2.0 / https://pymol.org/2/#download
GraphPad Prism Software	GraphPad Software	Version 6.0 / https://www.graphpad.com/
AUCpreD	(Wang et al., 2016)	http://raptorx.uchicago.edu/StructurePropertyPred/predict/
Multilayered Fusion-based Disorder predictor (MFDp2)	(Mizianty et al., 2013)	http://biomine.cs.vcu.edu/servers/MFDp2/
SPOT-Disorder2	(Hanson et al., 2019)	https://sparks-lab.org/server/spot-disorder2/
Malvern Panalytical PEAQ software	Malvern	N/A
TopSpin	Bruker	Version 3
NMRFAM-SPARKY	(Lee et al., 2015)	https://nmrfam.wisc.edu/nmrfam-sparky-distribution/
XPLOR-NIH	(Schwieters et al., 2003)	https://nmr.cit.nih.gov/xplor-nih/
TALOS+	(Shen et al., 2009)	https://spin.niddk.nih.gov/bax/nmrserver/talos/
AMBER 11	(Case et al., 2005)	https://ambermd.org/GetAmber.php
CLUSTERPOSE	(Diamond, 1995)	https://www.ccpn.ac.uk/v2-software/software/extras/contributions
PROCHECK-NMR	(Laskowski et al., 1993; Laskowski et al., 1996)	https://www.ebi.ac.uk/thornton-srv/software/PROCHECK/
DeltaVision softWoRx	GE Healthcare Life Sciences	N/A
Other		
Sephacryl S-300 column	GE Healthcare Life Sciences	Cat# GE17-0599-01
Hi-Trap Q-FF column	GE Healthcare Life Sciences	Cat# 17515601
Hi-Trap Q-HP column	GE Healthcare Life Sciences	Cat# 17115401
Superdex S75 HR 10/30 column	GE Healthcare Life Sciences	Cat# 17-1047-01
Hi-Trap SP-FF column	GE Healthcare Life Sciences	Cat# 17-5157-01
Ni-NTA	Qiagen	Cat# 30210
Complete Protease Inhibitor cocktail (EDTA free)	Roche/Merck	Cat# 11873580001
Malvern Panalytical autoITC	Malvern	MRC-LMB
Jasco 815 Spectropolarimeter	JASCO	MRC-LMB
Bruker Avance-III spectrometers operating at 1H frequencies of 600, 700 or 800 MHz	Bruker	MRC-LMB
DeltaVision Elite microscope	GE Healthcare Life Sciences	National Centre for Biomolecular Research, Faculty of Science, Masaryk University

RESOURCE AVAILABILITY

Lead contact

Further information and requests for resources and reagents should be directed to and will be fulfilled by M. van Breugel (m.vanbreugel@qmul.ac.uk).

Materials availability

All unique reagents generated in this study are available from the Lead Contact.

Data and code availability

Coordinates and structure factors of crystal structures that are presented in this paper are available in the Protein Data Bank (PDB, accession codes: Nanobody 10Z-CEP164¹⁻¹⁰⁹ - 7O06, Nanobody 36Z-CEP164¹⁻¹⁰⁹ - 7O0S, Nanobody 36Z-TTBK2¹⁰⁷⁴⁻¹⁰⁸⁷-CEP164¹⁻¹⁰⁹ - 7O3B). NMR data are deposited in the Biological Magnetic Resonance Bank (BMRB, accession code 50793). NMR structure ensemble of CEP164¹⁻¹⁰⁹ coordinates are deposited in PDB (accession code 7NWJ). This paper does not report original code. Any additional information required to reanalyse the data reported in this paper is available from the lead contact upon request.

EXPERIMENTAL MODEL AND SUBJECT DETAILS

Cell lines

Human cell culture

Flp-In T-REx 293 cells (gift from R. Hegde, MRC-LMB, Cambridge, UK) were grown in D-MEM, GlutaMAX (Thermo Fisher Scientific) supplied with 10% FBS. CEP164-null hTERT RPE-1 (gift from C. Morrison, NUI Galway, Ireland) cells were grown in D-MEM/F-12 (Thermo Fisher Scientific), GlutaMAX, sodium carbonate (ThermoFisher Scientific) supplied with 0, 0.5 or 10% FBS. Expi293 cells (gift from O. Perisic from R. Williams lab, MRC-LMB, Cambridge, UK) were grown in Expi293 medium (ThermoFisher). All cell lines were grown at 37°C with 5% CO₂.

Bacterial cell culture

Escherichia coli Rosetta (DE3) (gift from J. Kilmartin, MRC-LMB, Cambridge, UK) were grown in LB or 2xTY media and used for protein expression and purification.

METHOD DETAILS

Recombinant protein purification

DNA encoding human CEP164¹⁻¹⁰⁹ (Uniprot Q9UPV0) was cloned into vector pGEX6P1 cut by BamH1-EcoR1 restriction enzyme digestion, giving rise to an ORF with an N-terminal GST-tag that can be removed by cleavage with PreScission protease. Mutations or deletions were introduced into this construct by site-directed mutagenesis. Constructs (or empty pGEX6P1) were expressed in *E. coli* Rosetta (DE3) cells at 18°C by IPTG induction overnight. Subsequently, the proteins were purified from cell lysates (prepared by sonication and centrifugational clearing) by chromatography with Glutathione-Sepharose 4B (GE Healthcare) and eluted with reduced Glutathione using standard methods. Unlike for the preparation of the GST-tagged versions, for the preparation of the untagged CEP164 constructs, purified GST-PreScission protease was added and the eluates dialysed against 10 mM Tris-Cl pH 8.0, 50 mM NaCl, 2 mM DTT. Subsequently, the eluates were subjected to gel-filtration on a Sephacryl S-300 column (GE Healthcare) run in 10 mM Tris-Cl pH 8.0, 50 mM NaCl, 2 mM DTT. Peak fractions were pooled and subjected to ion-exchange chromatography on a Hi-Trap Q-FF or -HP column (GE Healthcare) run using a linear salt gradient from 10 mM Tris-Cl, pH 8.0, 2 mM DTT (buffer A) to buffer A, 1M NaCl over 25 column volumes. Peak fractions were concentrated, snap frozen in small aliquots and stored at -80°C. For the untagged CEP164 constructs that were used in ITC or thermostability experiments or for crystallisations, a final gel-filtration step was performed on a Superdex S75 column (Pharmacia) either run in ITC buffer (PBS, 2 mM DTT, ITC or thermostability assay) or in 10 mM Na-Hepes pH 7.2, 50 mM NaCl, 2 mM DTT (crystallisation). The proteins were concentrated, snap frozen in aliquots and stored at -80°C.

¹⁵N- or ¹⁵N¹³C-labelled CEP164¹⁻¹⁰⁹ proteins were expressed as above, but in supplemented M9 medium (van Breugel et al., 2014) containing ¹⁵NH₄Cl and optionally ¹³C Glucose. Proteins were purified by Glutathione-Sepharose 4B (GE Healthcare) chromatography, followed by GST-PreScission protease addition, an optional gel-filtration step on a Sephacryl S-300 column (GE Healthcare) run in 10 mM Tris-Cl pH 8.0, 50 mM NaCl, 2 mM DTT, followed by ion-exchange chromatography on a Hi-Trap Q-FF or Q-HP column (GE Healthcare) run using a linear salt gradient from 10 mM Tris-Cl, pH 8.0, 4 mM DTT (buffer A) to buffer A, 1M NaCl over 25 column volumes. Peak fractions were concentrated and a final gel-filtration step performed on a Superdex S75 column (Pharmacia) run in NMR buffer (PBS, 4 mM DTT, supplemented with Complete Protease Inhibitor cocktail (EDTA free, Roche)). The proteins were concentrated, snap frozen in aliquots and stored at -80°C.

The fusion construct TTBK2¹⁰⁷⁴⁻¹⁰⁸⁷-CEP164¹⁻¹⁰⁹ (Uniprot Q6IQ55 / Q9UPV0 respectively) was cloned into vector pGEX6P1 cut by BamH1-EcoR1 restriction enzyme digestion, giving rise to an ORF with an N-terminal GST-tag that can be removed by cleavage with PreScission protease. This construct had the linker AGSGAGS placed between TTBK2¹⁰⁷⁴⁻¹⁰⁸⁷ and CEP164¹⁻¹⁰⁹. Expression and Glutathione-Sepharose purification were as described above, but instead of elution with Glutathione, the protein was eluted by on-beads cleavage with GST-PreScission protease in 50 mM Tris-Cl, pH 7.4, 2 mM DTT. This was followed by ion-exchange chromatography on a Hi-Trap Q-FF column (GE Healthcare) run using a linear salt gradient from 10 mM Tris-Cl, pH 8.0, 2 mM DTT (buffer A) to buffer A, 1M NaCl over 25 column volumes. Peak fractions were concentrated and a final gel-filtration step performed on a Superdex S75 column (Pharmacia) run in 10 mM Na-Hepes pH 7.2, 50 mM NaCl, 2 mM DTT. The proteins were concentrated, snap frozen in aliquots and stored at -80°C.

Construct CEP164^{1-28,50-94} (=ΔHelices)-TEV-HIS6 was cloned into vector pGEX6P1 cut by BamH1-EcoR1 restriction enzyme digestion, giving rise to an ORF with an N-terminal GST-tag that can be removed by cleavage with PreScission protease and a C-terminal His-tag that can be removed by cleavage with TEV protease. The construct was expressed in *E. coli* Rosetta (DE3) cells at 18°C by IPTG induction overnight. Subsequently, the protein was purified from cell lysates (prepared by sonication and centrifugational

clearing) by Ni-NTA (Qiagen) chromatography using standard methods. After elution, the eluate was dialysed overnight against cleavage buffer (50 mM Tris-HCl, pH 8.0, 500 mM NaCl, 5 mM imidazole, pH 7.5, 2 mM DTT) in the presence of TEV protease. Subsequently, the reactions were allowed to bind to Glutathione-Sepharose 4B (GE Healthcare) beads, the beads washed with cleavage buffer, and the protein eluted by on-beads cleavage with GST-PreScission protease in PBS, 2 mM DTT. After a gel-filtration step on a Superdex S75 column (Pharmacia) in PBS, 2 mM DTT, the peak fractions were concentrated and the protein snap frozen and stored at -80°C .

Camelid Nanobodies 10Z and 36Z were cloned into vector pGEX6P1 cut by BamH1-EcoR1 restriction enzyme digestion, giving rise to an ORF with an N-terminal GST-tag that can be removed by cleavage with PreScission protease. Expression and Glutathione-Sepharose purification were as described above. Purified GST-PreScission protease was added and the eluates dialysed against 10 mM Tris-Cl pH 7.4. Na-Acetate pH 5.3 (10Z) or (optionally) Na-Bicine pH 9.0 (36Z) were added to 10 mM followed by ion-exchange chromatography on a Hi-Trap S-FF (10Z) or Q-FF (36Z) column (GE Healthcare) run using a linear salt gradient from 10 mM Na-Hepes pH 7.2 (buffer A) (10Z) or 10 mM Tris-Cl, pH 8.0 or pH 8.5 (buffer A) (36Z) to buffer A, 1M NaCl over 25 column volumes. Peak fractions were concentrated and a final gel-filtration step performed on a Superdex S75 column (Pharmacia) run in 10 mM Na-Hepes pH 7.2, 50 mM NaCl, (optionally) 2 mM DTT. The proteins were concentrated, snap frozen in aliquots and stored at -80°C .

The peptide corresponding to TTBK2¹⁰⁷⁴⁻¹⁰⁸⁷ was synthesised by Biomatik (Wilmington, Delaware, 19809 USA) to a purity of 98% as judged by HPLC analysis and was reconstituted with Millipore dH₂O. Amino acid analysis (New England Peptide, Gardner, MA 01440 USA) was used in duplicate to determine the accurate concentration of the peptide stock in solution (4.844 mM).

MBP-TTBK2¹⁰³³⁻¹⁰⁸⁷ (wild-type, EB1-binding deficient TTBK2¹⁰⁵¹⁻¹⁰⁵⁴ SKIP to AAA or CEP164-NTD-binding deficient TTBK2¹⁰⁷⁶⁻¹⁰⁷⁸ RPP to AAA) in vector pOPTM (R. Williams lab, MRC-LMB) were expressed in *E. coli* Rosetta (DE3) cells at 18°C by IPTG induction and purified from cell lysates by chromatography with Amylose resin (NEB, E8021) and eluted with Maltose using standard methods. Eluates were subjected to ion-exchange chromatography on a Hi-Trap Q-HP column (GE Healthcare) run using a linear salt gradient from 10 mM Tris-Cl, pH 8.0, 2 mM DTT (buffer A) to buffer A, 1M NaCl over 25 column volumes. Finally, the eluates were run in PBS, 2 mM DTT on a Superdex 200 column (GE Healthcare). Peak fractions were concentrated, snap frozen in small aliquots and stored at -80°C .

EB1 (in vector pGEX6P1) was expressed in *E. coli* Rosetta (DE3) cells at 18°C by IPTG induction, purified by chromatography with Glutathione-Sepharose 4B (GE Healthcare) and eluted with reduced Glutathione using standard methods. EB1-GFP (in a modified pET28 vector) was expressed similarly and purified by chromatography with NiNTA resin (Qiagen) and eluted with Imidazole using standard methods. Purified GST-PreScission protease was added to the eluates and eluates dialysed against 10 mM Tris-Cl pH 8.0, 2 mM DTT. Subsequently, the eluates were subjected to ion-exchange chromatography on a Hi-Trap Q-HP column (GE Healthcare) run using a linear salt gradient from 10 mM Tris-Cl, pH 8.0, 2 mM DTT (buffer A) to buffer A, 1M NaCl over 25 column volumes. Finally, the eluates were run in PBS, 2 mM DTT on a Superdex 200 column (GE Healthcare). Peak fractions were concentrated, snap frozen in small aliquots and stored at -80°C . CEP164-NTD (CEP164¹⁻¹⁰⁹, optionally C-terminally tagged with GFP, both constructs in vector pGEX6P1) that was used in the competition assay was purified as described above and equally subjected to a final gel-filtration step in PBS, 2 mM DTT on a Superdex 200 column (GE Healthcare).

Full-length 3xFLAG-TTBK2-2xStrep-tag II (Uniprot Q6IQ55, natural variant L8P) was expressed in Expi293 cells by transient transfection for 48h, and purified from cells lysates (prepared by sonication and centrifugational clearing) by chromatography with anti-FLAG M2 Affinity gel (Sigma, A2220) and eluted with 3xFLAG peptide (Sigma, F4799) in 50 mM HEPES pH 8.0, 100 mM NaCl, 0.1% IGEPAL CA-630, 0.5 mM DTT. Eluates were incubated in the presence of Lambda-Protein-Phosphatase (Santa Cruz) with Strep-Tactin Sepharose (IBA) beads, beads washed with 50 mM HEPES pH 8.0, 100 mM NaCl, 0.1% IGEPAL CA-630, 2 mM DTT and then eluted with 6 mM D-Desthiobiotin (IBA) in 50 mM HEPES, 100 mM NaCl, 0.1% IGEPAL CA-630, 2 mM DTT, pH 7.8. The eluted proteins were snap frozen in small aliquots and stored at -80°C .

Nanobody generation

Nanobodies against recombinant, purified human CEP164¹⁻¹⁰⁹ were supplied by VIB Nanobody Core (Vrije Universiteit Brussel (VUB), 1050 Brussels). They were raised by injections of purified CEP164¹⁻¹⁰⁹ into a llama, followed by construction of a VHH library from peripheral blood lymphocytes for phage display, phage display panning against CEP164¹⁻¹⁰⁹ and analysis of clones by anti-CEP164¹⁻¹⁰⁹ ELISA and sequencing.

Protein crystallization

Nanobody 10Z/36Z and CEP164¹⁻¹⁰⁹ were mixed equimolar to a final concentration of 0.81 mM (Nanobody 10Z-CEP164¹⁻¹⁰⁹ complex) or 1.16 mM (Nanobody 36Z-CEP164¹⁻¹⁰⁹ complex). Crystals of the corresponding protein-complexes were obtained in the Wizard 2 screen (Emerald BioStructures, reservoir solution: 0.1 M Hepes, pH 7.5, 1.26 M ammonium sulfate) (10Z-CEP164¹⁻¹⁰⁹) or in the JCSG+ suite (Qiagen, reservoir solution: 0.18 M tri-ammonium citrate, 20 % (w/v) PEG 3350) (36Z-CEP164¹⁻¹⁰⁹) by the vapour diffusion method at 19°C using 100 nl protein solution and 100 nl of reservoir solution. Crystals were mounted after six days in the mother liquor, to which PEG-400 was added to 30%, and frozen in liquid nitrogen.

Nanobody 36Z and the TTBK2¹⁰⁷⁴⁻¹⁰⁸⁷-CEP164¹⁻¹⁰⁹ fusion protein were mixed equimolar to a final concentration of 1.38 mM. Crystals of the corresponding protein-complex were obtained in the Emerald BioStructures Cryo 2 Screen (reservoir

solution: 100 mM Acetate, pH 4.5, 100 mM NaCl, 30 % PEG-200) by the vapour diffusion method at 19°C using 100 nl protein solution and 100 nl of reservoir solution. Crystals were mounted after seven days in the mother liquor and frozen in liquid nitrogen.

X-ray crystallography data processing

Datasets were integrated using DIALS (Winter et al., 2018) and were scaled using AIMLESS (Evans and Murshudov, 2013). The structure of the Nanobody 10Z-CEP164¹⁻¹⁰⁹ complex was solved by molecular replacement with PHASER (McCoy et al., 2007) using the nanobody of PDB 5VLV (with removed loops and as poly-alanine model, Tabares da Rosa et al., 2019) as a search model. Cycles of refinement in REFMAC (Murshudov et al., 2011) and manual building in COOT (Emsley and Cowtan, 2004) allowed the complete building of the nanobody 10Z structure. The electron density maps showed clear electron densities in regions not occupied by the nanobody that tentatively could be assigned to CEP164¹⁻¹⁰⁹ residues. Placement of these residues and further refinement in REFMAC (Murshudov et al., 2011) and PHENIX.REFINE (Afonine et al., 2012) and manual building cycles in COOT (Emsley and Cowtan, 2004) allowed the successive building of a complete model of CEP164¹⁻¹⁰⁹ with high confidence.

The structure of the Nanobody 36Z-CEP164¹⁻¹⁰⁹ complex was solved by molecular replacement with PHASER (McCoy et al., 2007) using the nanobody of PDB 5VLV (with removed loops and as poly-alanine model, Tabares da Rosa et al., 2019) and the CEP164¹⁻¹⁰⁹ structure as search models. Cycles of refinement in REFMAC (Murshudov et al., 2011) and PHENIX.REFINE (Afonine et al., 2012) and manual building in COOT (Emsley and Cowtan, 2004) were used to build the structure of the Nanobody 36Z-CEP164¹⁻¹⁰⁹ complex.

The structure of the complex between Nanobody 36Z and the TTBK2¹⁰⁷⁴⁻¹⁰⁸⁷-CEP164¹⁻¹⁰⁹ fusion protein was solved by molecular replacement with PHASER (McCoy et al., 2007) using the nanobody 36Z and the CEP164¹⁻¹⁰⁹ structure as search models. Cycles of refinement in REFMAC (Murshudov et al., 2011) and PHENIX.REFINE (Afonine et al., 2012) and manual building in COOT (Emsley and Cowtan, 2004) were used to build the structures of nanobody 36Z and of CEP164¹⁻¹⁰⁹. The electron density maps showed clear electron densities close to the surface of the WW domain of CEP164¹⁻¹⁰⁹ that were not occupied by the nanobody or CEP164¹⁻¹⁰⁹. Due to a high connectivity and clear side-chain densities for TTBK2 R1076 and most of the TTBK2¹⁰⁷⁴⁻¹⁰⁸⁷ proline residues, these electron densities allowed the confident building of TTBK2 residues 1074-1084 in further refinement and building cycles.

Structure visualization and measurement of the angle between CEP164¹⁻¹⁰⁹ head and body structures were done in PyMOL (The PyMOL Molecular Graphics System, Version 2.0 Schrödinger, LLC). GraphPad Prism Software v. 6.0 (GraphPad Software; www.graphpad.com) was used to plot the result.

Pull-down assays

Pull-downs with full-length 3xFLAG CEP164 constructs

Flp-In T-REx 293 cells were transfected with a pcDNA 3.1 derivative vector (gift from R. Hegde, MRC-LMB) expressing (from a CMV promoter) 3xFLAG tagged human CEP164 (Uniprot Q9UPV0, natural variant T988S) or 3xHA tagged human TTBK2 (Uniprot Q6IQ55, natural variant L8P) constructs using Polyethylenimine (PEI MAX, MW 40000, Polysciences). Cells were lysed by sonication in lysis buffer (PBS, 0.1% (v/v) IGEPAL CA-630, supplemented with Complete Protease Inhibitor (EDTA free, Roche)) and lysates were cleared by centrifugation. Cleared lysates containing the 3xFLAG-tagged CEP164 constructs were added to anti-FLAG M2 magnetic beads (M8823, Sigma). After incubation on a rotator for 1h at 4°C, beads were washed with lysis buffer and the cleared lysates containing the 3xHA-tagged human TTBK2 constructs were added to the beads. After another incubation on a rotator for 1h at 4°C, beads were washed with lysis buffer, eluted with SDS and eluates subjected to Western blotting using a mouse monoclonal anti-FLAG antibody (F1804, Sigma) or a polyclonal rabbit antibody against the HA-tag (gift from R. Hegde, MRC-LMB, Cambridge, UK).

Pull-downs with GST-CEP164¹⁻¹⁰⁹

Flp-In T-REx 293 cells were transfected with vector pEGFP-N1 containing TTBK2¹⁰⁷⁴⁻¹⁰⁸⁷ constructs (cloned into pEGFP-N1 utilising the Xho1-BamH1 restriction sites) using Polyethylenimine (PEI MAX, MW 40000, Polysciences). Cells were lysed by sonication in lysis buffer (PBS, 0.1% (v/v) IGEPAL CA-630, 2 mM DTT, supplemented with Complete Protease Inhibitor (EDTA free, Roche)) and lysates were cleared by centrifugation. Cleared lysates were added to Glutathione-Sepharose 4B beads (GE Healthcare) onto which 60 µg of purified GST or GST-CEP164¹⁻¹⁰⁹ constructs had been bound beforehand (in lysis buffer). After incubation on a rotator for 1h at 4°C, beads were washed with lysis buffer and eluted with Laemmli Buffer. Eluates were subjected to Western blotting using a polyclonal GFP antibody (Invitrogen, A11122).

Pull-downs with 3xFLAG EB1 constructs

Flp-In T-REx 293 cells were transfected with a pcDNA 3.1 derivative vector expressing (from a CMV promoter) 3xFLAG only, 3xFLAG tagged human EB1 or 3xHA tagged human TTBK2 (WT or ΔPro-rich (Δ1074-1087)) constructs, using Polyethylenimine (PEI MAX, MW 40000, Polysciences). Cells were lysed by sonication in lysis buffer (PBS, 0.1% (v/v) IGEPAL CA-630, 0.1 mM DTT, supplemented with Complete Protease Inhibitor (EDTA free, Roche)) and lysates were cleared by centrifugation. Cleared lysates containing the 3xFLAG or the 3xFLAG tagged EB1 construct were added to anti-FLAG M2 affinity gel (A2220, Sigma). After incubation on a rotator for 1h at 4°C, beads were washed with lysis buffer and the centrifugationally cleared cell lysates containing the 3xHA-tagged human TTBK2 constructs, mixed with ~ 0.4 mg/ml recombinant GST-CEP164¹⁻¹⁰⁹ (WT or Y73A, expressed in *E.coli* Rosetta, purified by glutathione affinity chromatography and dialysed against PBS, 1 mM DTT), were added to the beads. After incubation on a rotator for 1h at 4°C, beads were washed with lysis buffer, eluted with SDS and eluates subjected to Western blotting using a mouse monoclonal anti-FLAG antibody (F1804, Sigma) or a polyclonal rabbit antibody against the HA-tag (gift of R. Hegde, MRC-LMB, Cambridge, UK).

Pull-downs with MBP-TTBK2 constructs

A total of 100 μ g of purified CEP164-NTD-GFP or 100 μ g of purified EB1 (optionally in the presence of a 10X molar excess of purified CEP164-NTD) was added in 300 μ l lysis buffer (PBS, 0.1% IGEPAL CA-630, 2 mM DTT) to Amylose resin (New England Biolabs) onto which 30 μ g of purified MBP-TTBK2 constructs (MBP-TTBK2¹⁰³³⁻¹⁰⁸⁷ wild-type, EB1-binding deficient TTBK2¹⁰⁵¹⁻¹⁰⁵⁴ SKIP to AAA, or CEP164-NTD-binding deficient TTBK2¹⁰⁷⁶⁻¹⁰⁷⁸ RPP to AAA) had been bound beforehand. After incubation on a rotator for 1h at 4°C, beads were washed with lysis buffer and eluted with Laemmli Buffer. Eluates were subjected to electrophoresis in a NuPAGE 4-12% gel (Invitrogen) and stained with Coomassie brilliant blue. In a similar set-up, we tested whether the presence of purified EB1-GFP (in 10X molar excess) would affect CEP164-NTD-GFP binding to these MBP-TTBK2 constructs.

Autophosphorylation assay

Purified dephosphorylated full-length 3xFLAG-TTBK2-2xStrep-tag II (wild-type or kinase dead (KD, D163A)) produced in Expi293 cells were submitted to an auto-phosphorylation assay. A total of 30 μ g of recombinant kinase was incubated with 2.0 mM ATP and 2.0 mM MgCl₂ in a buffer containing 50 mM HEPES pH 8.0, 100 mM NaCl, 2 mM DTT (total reaction volume of 35 μ l) for 10 minutes on ice in the presence or in the absence of 120 μ g of purified CEP164-NTD WT or Y73A mutant. The reaction was quenched by adding 10 μ l Laemmli buffer and the product was analysed in a 8% SDS-PAGE (Tris-Glycine) gel stained with Coomassie brilliant blue.

Bioinformatics

Intrinsically disordered regions were predicted using the following methods: AUCpreD (Wang et al., 2016), Multilayered Fusion-based Disorder predictor (MFDp2, (Mizianty et al., 2013)) and SPOT-Disorder v1.0 (Hanson et al., 2017, 2019). The theoretical mean end-to-end distance of protein intrinsically disordered regions was calculated based on the method described in (Fitzkee and Rose, 2004).

Circular dichroism (CD)

Measurements were made using a Jasco 815 Spectropolarimeter with a 0.1 cm cuvette and in PBS buffer. Spectra were recorded at 0.2 mg/ml concentration using a scan rate of 50 nm/min, bandwidth 1nm and were the average of 8 scans. Mean residue ellipticity was calculated using

$$\Theta_{mrw} = 0.1 \times \Theta / ([\text{conc.}] \times N \times PL)$$

where Θ is the measured signal in millidegree, N is the number of residues and PL the pathlength in cm, thereby allowing direct comparison of the constructs of differing sequence lengths.

Thermal denaturation was followed at 222 nm with a bandwidth of 4 nm between 4 and 95°C and using a scan rate of 1°C/min. Sample concentration was 0.2 mg/ml and Θ_{mrw} was calculated as above.

Isothermal titration calorimetry (ITC)

Binding interactions were studied using a Malvern Panalytical autoITC instrument at 25°C and in PBS buffer. The ITC method is particularly sensitive to errors in the concentration of the ligand titrated from the instrument syringe added in excess of the binding partner in the cell. For this reason, we chose to perform ITC experiments with the CEP164¹⁻¹⁰⁹ protein in the syringe and with the target binding peptide (which contains no aromatics that would allow its quantification using UV absorbance) in the cell. We were able to concentrate the protein up to the 1-3 mM stock concentrations required for the syringe with no evidence of aggregation.

ITC experiments were performed with 19 injections of 2 μ L preceded by a small 0.5 μ L pre-injection that was not used during curve fitting. Control measurements of injections of CEP164¹⁻¹⁰⁹ protein into buffer were performed (WT and mutants where stocks of materials permitted) and these control heats were close to the values seen for buffer into buffer blank runs. All ITC binding data were corrected with the appropriate control heats of dilution of CEP164¹⁻¹⁰⁹ and fitted using the one set of binding sites' model in Malvern Panalytical PEAQ software.

In our ITC experiments, the binding stoichiometry of the TTBK2-CEP164 (wild-type) complex was 0.7 (\pm 0.2 SD, n=5) across different batches of CEP164¹⁻¹⁰⁹ preparations. This stoichiometry is lower than 1, the value expected for the 1:1 complexes typically formed between WW domains and proline-rich binding motifs (PRBMs) and seen in the crystal structure of the TTBK2-CEP164 complex (Figure 3A). This discrepancy is not large and may simply result from the fact that the fitted stoichiometry is poorly constrained where titrations are performed with material in the ITC cell at or below the K_D concentration (ITC c-value \sim 1). It was not possible to perform experiments at higher concentrations due to sample limitation and concerns over aggregation. However, we also note the preponderance of prolines in the TTBK2 peptide that will be present in various combinations of cis-trans isomerization states in this unstructured peptide. Some fraction of these states may be unable to bind CEP164 and their re-isomerization may be slow on the timescale of ITC measurement thereby resulting in the underestimated binding stoichiometry that then reflects binding competent fraction of peptide.

Stock peptide solution in the ITC cell was prepared by weight of lyophilized material to a notional 100 μ M. This stock used for all ITC measurements was then quantified using a commercial amino acid analysis service provided by New England Peptide (Gardner, MA 01440 USA).

NMR

NMR spectra were recorded using Bruker Avance-III spectrometers operating at ^1H frequencies of 600, 700 or 800 MHz, each equipped with 5 mm inverse cryogenically cooled probes, and with a sample temperature of 293 K unless otherwise stated. All samples were prepared in physiological ionic strength buffer (25 mM aqueous sodium phosphate, 125 mM sodium chloride, at pH 7.4, supplemented with 4 mM DTT and 1 pill of Complete Protease Inhibitor cocktail (EDTA free, Roche) per 250 ml) and degassed by repeated cycles of vacuum or argon in the head space. Backbone and $\text{C}\beta$ resonance assignments were obtained for a 120 μM sample of ^{13}C - and ^{15}N -labelled protein, using standard triple resonance techniques and unmodified Bruker pulse programs. Aliphatic sidechain resonance assignments were recorded from a 2D ^1H - ^{13}C -HSQC, aided by 3D (H)CCH- and H(C)CH-TOCSY spectra. Side-chain resonances of Tyr and Phe residues were assigned using 2D ^1H - ^{13}C -HSQC selective for the aromatic region, and (HB)CB(CGCD)HD and (HB)CB(CGCC-TOCSY)H spectra, and Trp sidechain assignments from 2D NOESY and DQF-COSY. Chemical shifts were referenced to the ^1H frequency of internal 210 μM dimethylsilapentanesulfonate (DSS) added to a 250 μM ^{15}N -labelled sample, with X-nuclei referenced according to IUPAC recommendations (Markley et al., 1998).

For structure determination NOE intensities were recorded for 500 μM ^{15}N -labelled protein using a 2D ^1H - ^1H -NOESY with 120 ms NOE mixing time (τ_m) and excitation sculpting water suppression, with 1.5 seconds repetition delay, 512 and 2048 data points in t_1 and t_2 , respectively and spectral widths of 8.4 kHz in both dimensions. Assignment was supported by 3D ^{13}C -edited and ^{15}N -edited ^1H - ^1H -NOESY-HSQC spectra recorded with 100 ms τ_m , 800 MHz ^1H .

Steady state $\{^1\text{H}\}^{15}\text{N}$ -NOE data were acquired in duplicate as pseudo-3D spectra at 600 MHz ^1H , interleaving rows with or without 120 ^1H pulses applied at 5 ms intervals throughout the 7 seconds recycle delay. Samples were ^{15}N -labelled, at concentrations of 500 μM for WT protein, 320 μM for the Q11P mutant.

All NMR datasets were processed using TopSpin version 3 (Bruker) and analysed using NMRFAM-SPARKY (Lee et al., 2015).

NMR structure calculations

Initial structures were calculated using XPLOR-NIH (Schwieters et al., 2003). Distance restraints were categorised as strong (0–2.2 Å), medium (0–3.0 Å), weak (0–4.0 Å) or very weak (0–5.5 Å), based on NOE intensity. Since the XPLOR-NIH calculations employed r^{-6} summation for all groups of equivalent protons and non-stereospecifically assigned prochiral groups, and since no stereoassignments were made (and the assignment-swapping protocol within XPLOR-NIH for deriving stereoassignments indirectly during the structure calculation itself was not applied), all distance restraints involving protons within such groups were converted to group restraints (by using wildcards such as HB*). All lower bounds were set to zero (Hommel et al., 1992). Backbone ϕ and ψ torsion angle restraints were derived from chemical shift indices, using the program TALOS+ (Shen et al., 2009). H-bond restraints with distance ranges 0–2.2 Å for H...O and 0–3.2 Å for N...O, were included in the secondary structural elements identified in the initial structures and confirmed empirically from the TALOS+ analysis. Structures were calculated from polypeptide chains with randomized ϕ and ψ torsion angles using a two-stage simulated annealing protocol within the program XPLOR-NIH, essentially as described in (Argentaro et al., 2007).

The structures calculated in XPLOR-NIH were then subjected to a further stage of refinement using a full force field and an implicit water-solvent model as implemented in the program AMBER 11 (Case et al., 2005). Calculations comprised initial minimization (200 steps steepest descent then 1800 steps conjugate gradient), then two rounds of 20 ps of simulated annealing (each comprising 5000 x 1 fs-steps heating from 0–500 K; 13000 x 1 fs-steps cooling to 100 K; 2000 x 1 fs-steps cooling to 0 K) and final minimization (200 steps steepest descent then 1800 steps conjugate gradient). The experimental distance and torsion angle restraints were applied throughout, and force constants for the distance restraints were increased during the simulated annealing to final values of 20 kcal mol $^{-1}$ Å $^{-2}$ for distance restraints, 20 kcal mol $^{-1}$ rad $^{-2}$ for ϕ and ψ torsion angle restraints and 50 kcal mol $^{-1}$ rad $^{-2}$ for ω torsion angle restraints. Implicit solvent representation using the generalized Born method (Xia et al., 2002) was employed throughout (igb=1), and Langevin temperature control was used (ntt=3; gamma_ln=5).

The program CLUSTERPOSE (Diamond, 1995) was used to calculate the mean rmsd of ensembles to their mean structures, Ramachandran statistics were evaluated using PROCHECK-NMR (Laskowski et al., 1993; Laskowski et al., 1996) and structures were visualized using the program PyMOL (The PyMOL Molecular Graphics System, Version 1.8 (Schrödinger, LLC, 2015)).

Ciliogenesis rescue experiments

hTERT RPE-1 CEP164 knockout cells (gift from C. Morrison, (Daly et al., 2016)) were cultured in DMEM/F12 supplemented with 10% FBS, 1% L-Glutamine (all from ThermoFisher), and 1 x penicillin/streptomycin (Biosera). 24h after seeding cells on glass coverslips, they were transfected with 0.5 μg of indicated plasmid (3XFLAG-CEP164 WT, 3XFLAG-CEP164 Q11P or 3XFLAG-CEP164 R93W) using Lipofectamine 3000 (ThermoFisher). The culture medium was exchanged 3h after transfection. To induce ciliogenesis, the cells were starved in 0.1% FBS medium 48h after transfection for 24 h. Cells were then fixed by ice-cold MeOH, 2x washed in PBS, blocked in blocking buffer (1% BSA in PBS), and stained with following primary and secondary antibodies: anti-FLAG (mouse, F1804, Sigma), anti-ARL-13B (rabbit, 17711-1-AP, Proteintech) directly labeled anti-CETN1-Alexa Fluor 647 (12794-1-AP, Proteintech labeled using Alexa FluorTM 647 Antibody Labeling Kit A20186, Invitrogen), anti-mouse Alexa Fluor 488 (R37114, Invitrogen), anti-rabbit Alexa Fluor 568 (A10042, Invitrogen). Prior to the incubation with anti-CETN1 Alexa Fluor 647, blocking with normal rabbit IgG (sc-2027, Santa Cruz Biotechnology) was done. Coverslips were mounted using Glycergel (Agilent).

Microscopy analysis was done on DeltaVision Elite microscope (GE Healthcare) with a 100×/Zeiss Plan-ApoChromat 1.4 objective and DeltaVision softWoRx acquisition software. Flag-positive cells as well as control untransfected cells were counted and inspected for ARL-13B signal. The image stacks were deconvolved with three cycles of conservative ratio deconvolution algorithm using softWoRx, and directly projected as maximal intensity images.

QUANTIFICATION AND STATISTICAL ANALYSIS

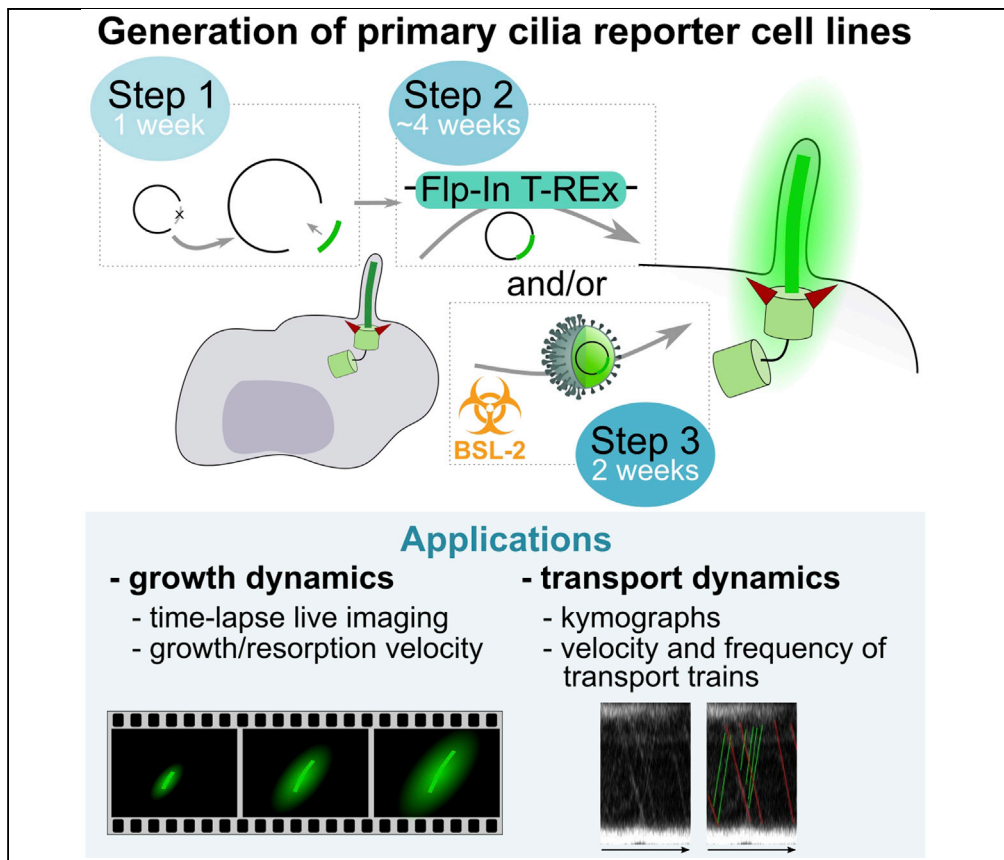
For ITC, dissociation constant (K_D) data are presented as mean \pm SD of n independent experiments, as indicated in Table 1. For Western blot experiments, band intensity was quantified in ImageJ software (Schneider et al., 2012). Band intensity data are presented as mean \pm SD of $n=3$ independent replicates (Figures 3D, 3F, S1A, and S1B). Statistical significance between WT and mutants was analysed by a paired, two-tailed t -test in Microsoft Excel (Figure 3F). For ciliogenesis rescue assays (Figure 3H), data are presented as mean percentage of ciliated cells \pm SEM. Statistical significance between the groups was analysed by one way ANOVA with Holm-Sidak post-hoc test using GraphPad Prism Software v. 6.0 (GraphPad Software; www.graphpad.com) from $n=5$ independent experiments, with $N=10$ -20 cells per condition (total number of cells: $N_{WT}=66$, $N_{Q11P}=58$, $N_{R93W}=55$, and $N_{untransfected}=57$).

Appendix 6

Bino L, Mikulenkova E, Stepanek L, Bernatik O, Vyslouzil D, Pejiskova P, Gorilak P, Huranova M, Varga V, Čajánek L*. A protocol for generation and live-cell imaging analysis of primary cilia reporter cell lines. *STAR PROTOCOLS*. 2022;3(1). doi:10.1016/j.xpro.2022.101199 Q4.(JCR 2022, IF = 1.3, Q4 – Biochemistry Research Methods)

Protocol

A protocol for generation and live-cell imaging analysis of primary cilia reporter cell lines



Primary cilia are hair-like sensory organelles protruding from the surface of most human cells. As cilia are dynamic, several aspects of their biology can only be revealed by real-time analysis in living cells. Here we describe the generation of primary cilia reporter cell lines. Furthermore, we provide a detailed protocol of how to use the reporter cell lines for live-cell imaging microscopy analysis of primary cilia to study their growth as well as intraciliary transport.

Lucia Binó, Erika Mikulenková, Luděk Štěpánek, ..., Martina Huranová, Vladimír Varga, Lukáš Čajánek

cajanek@med.muni.cz

Highlights

Constructing expression vector for preparation of primary cilia reporter cell lines

Generation of stable cell lines using Flp-In™ T-REx™ and viral transduction

Analysis of primary cilia growth dynamics in time-lapse live cell imaging

Imaging and analysis of ciliary transport in living cells

Binó et al., STAR Protocols 3, 101199

March 18, 2022 © 2022 The Author(s).

<https://doi.org/10.1016/j.xpro.2022.101199>



Protocol

A protocol for generation and live-cell imaging analysis of primary cilia reporter cell lines

Lucia Binó,^{1,6} Erika Mikulenková,^{1,6} Luděk Štěpánek,² Ondřej Bernatík,¹ David Vysloužil,^{1,3} Petra Pejšková,¹ Peter Gorilák,^{2,4} Martina Huranová,⁵ Vladimír Varga,² and Lukáš Čajánek^{1,3,7,8,*}

¹Laboratory of Cilia and Centrosome Biology, Department of Histology and Embryology, Faculty of Medicine, Masaryk University, Kamenice 3, 62500 Brno, Czechia

²Laboratory of Cell Motility, Institute of Molecular Genetics of the Czech Academy of Sciences, Vídeňská 1083, 14220 Prague, Czechia

³Department of Experimental Biology, Faculty of Science, Masaryk University, Kamenice 5, 62500 Brno, Czechia

⁴Charles University, Faculty of Science, Albertov 6, 128 00 Prague, Czechia

⁵Laboratory of Adaptive Immunity, Institute of Molecular Genetics of the Czech Academy of Sciences, Vídeňská 1083, 14220 Prague, Czechia

⁶These authors contributed equally

⁷Technical contact

⁸Lead contact

*Correspondence: cajanek@med.muni.cz
<https://doi.org/10.1016/j.xpro.2022.101199>

SUMMARY

Primary cilia are hair-like sensory organelles protruding from the surface of most human cells. As cilia are dynamic, several aspects of their biology can only be revealed by real-time analysis in living cells. Here we describe the generation of primary cilia reporter cell lines. Furthermore, we provide a detailed protocol of how to use the reporter cell lines for live-cell imaging microscopy analysis of primary cilia to study their growth as well as intraciliary transport.

For complete details on the use and execution of this protocol, please refer to Bernatík et al. (2020) and Pejškova et al. (2020).

BEFORE YOU BEGIN

In this protocol, we describe live-cell imaging analysis of primary cilia in the human cell line hTERT-RPE-1. For this purpose, appropriate ciliary markers, such as a small GTPase ARL13b (Caspary et al., 2007) or an intraflagellar transport (IFT) protein IFT74 (Bhogaraju et al., 2013) are coupled to a fluorescent tag. We begin with a brief outline of a suitable cloning strategy. Subsequently, we describe two approaches for the derivation of cell lines stably expressing mNeonGreen-ARL13b or mNeonGreen-IFT74 cilia reporters. The first strategy is based on Flp-InTM T-RExTM system (developed by Invitrogen / Thermo Fisher Scientific), allowing stable integration of gene of interest (GOI) specifically into a defined locus. The second one utilizes retroviral transduction. If your goal is to prepare a system with two different transgenes, consider using a combination of “Flp-InTM T-RExTM and virus” or “two viruses”. The whole procedure described here is easily adaptable as a “complete pipeline”, from its beginning to the end. Alternatively, only specific parts may be selected, depending on the available tools and the experimental question tested. When planning the experiments, it should be noted that preparation of the reporter cell lines and their validation will require at least several weeks. Importantly, the work involving the production of retroviral particles has to be carried out in a lab suitable for the production of viruses (biosafety level 2 (BSL-2)). The protocol below describes the specific steps using the human cell line hTERT-RPE-1. However, we have also carried out parts of this protocol in HEK293T, NIH3T3, and IMCD3 cells. Before starting, all reagents should be prepared as described below.



Cloning of GOI into expression vectors

⌚ Timing: ~ one week

Cloning of gene of interest (GOI), such as ARL13b or IFT74, into an expression vector suitable for the generation of cilia reporter cell line using either the Flp-InTM T-RExTM system (e.g., pgLAP1_Neo) or retroviral transduction (e.g., Murine stem cell virus pMSCV-N-mNeonGreen-IRES-PURO), is in both cases best achieved by using the Gateway cloning system (Thermo Fisher Scientific). Other cloning methods might also work fine. For the Gateway cloning please follow the manufacturer's guidelines (www.thermofisher.com). Importantly, one has to consider whether the N- or C-terminal tagging of the selected protein interferes with its function (localization). Therefore, please bear in mind that the vectors mentioned above only allow for the N-terminal tagging.

Note: The mNeonGreen tag offers several advantages over GFP in terms of stability, brightness, and resistance to photobleaching, even when using regular GFP microscopy filters. It has an excitation maximum at 506 nm and an emission maximum at 517 nm ([Shaner et al., 2013](#)). However, the use of mNeonGreen is subjected to a license from Allele Biotechnology (Allelebiotechnology.com), while the use of other fluorescent tags, such as GFP or mCherry, is not restricted.

Note: The expression and the correct ciliary localization of the tagged protein of interest should be always verified. Consider using immunofluorescence (IF) microscopy, Western blotting (WB), or ideally both. In the case of both ARL13b and IFT74, we have used their N-terminally tagged variants that displayed subcellular localization identical to their endogenous counterparts. We observed, however, that ARL13b over-expression in hTERT-RPE-1 leads to slightly longer primary cilia if compared to non-transfected cells, in agreement with an earlier report ([Larkins et al., 2011](#)). To assess the functionality of the tagged protein, a gold standard is a rescue experiment using knockout (KO) cells ([Prasai et al., 2020](#)) or following RNAi-mediated depletion.

Generation of stable cell lines using Flp-InTM T-RExTM system

⌚ Timing: typically 3–4 weeks

The following paragraph describes a generation of a reporter cell line expressing a protein of interest from a specific genomic locus under the control of a doxycycline (DOX)-inducible promoter ([Figure 1](#)). The Flp-InTM T-RExTM system (www.thermofisher.com) works very well for that purpose. The main advantage of this approach is that the stable cell lines derived from the same parental cells have the GOI integrated in the same site ([Ward et al., 2011](#)). This typically leads to a more uniform level of expression across the population, in contrast to random, multiple site integrations of viral vectors. In turn, typically only polyclonal selection of stable Flp-InTM T-RExTM transfectants is required. The main limitation of this system is the need for the Flp-InTM T-RExTM parental cell line. To study ciliogenesis, the hTERT-immortalized retinal pigment epithelial cell line, hTERT-RPE-1 (available from ATCC), is probably the most commonly used cell line. In our experience, this cell line is well suitable for live-cell imaging experiments, as their cilia are typically oriented in the imaging plane. Its Flp-InTM T-RExTM derivative has been recently published ([Bernatik et al., 2020](#); [Pejskova et al., 2020](#)). Alternatively, the Flp-InTM T-RExTM parental cell line can be derived from the hTERT-RPE-1 cells or any other cell line suitable to study ciliogenesis (e.g., NIH3T3, IMCD3, etc.) by following these instructions (www.thermofisher.com). It is important to bear in mind that most Flp-InTM T-RExTM – compatible expression vectors (e.g., pgLAP1 (Addgene plasmid #19702) or pgLAP2 (Addgene plasmid #19703)) use hygromycin resistance as a selection marker, which is not suitable for use in hTERT-RPE-1; hygromycin was used for selection of hTERT expressing clones when this cell line was originally established. As PURO resistance (PAC gene) was introduced into

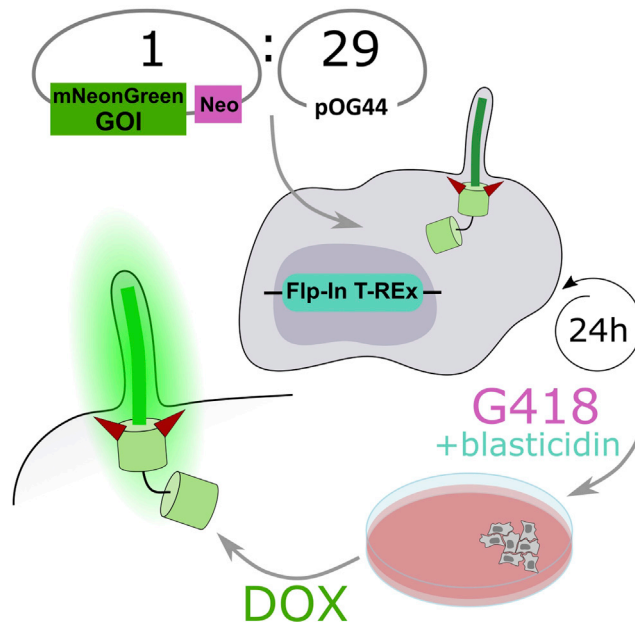


Figure 1. Schematic of the generation of stable cell lines using the Flp-In™ T-REx™ system

Generation of a reporter cell line expressing a protein of interest (in our case IFT74) from a specific genomic locus under the control of a doxycycline (DOX)-inducible promoter. Flp-In™ T-REx™ parental cell line (e.g., hTERT-RPE-1 Flp-In™ T-REx™) is co-transfected with pgLAP1_Neo/pgLAP2_Neo or derivatives encoding the GOI, and pOG44 plasmid, encoding the Flp recombinase. Due to the low activity of the Flp recombinase in typical cell culture conditions, we recommend the ratio of pgLAP1_Neo-GOI to pOG44 plasmid to be at least 1:29. The selection of stably transfected cells should start no earlier than 24 h post-transfection, by replacing the medium with a fresh one supplemented with G418 and blasticidin (blasticidin resistance comes with the Flp-In™ T-REx™ cassette). The expression of the integrated transgene in the generated reporter cell line is then induced by addition of DOX in the culture medium.

the cells on the same plasmid as hygromycin resistance (“PURO resistance”), we highly recommend using expression vectors with neomycin resistance (G418-based selection), such as pgLAP1_Neo (Pejskova et al., 2020), pgLAP2_Neo (Bernatik et al., 2020), or pGFT1.1 (mNeonGreen derivative of pgLAP1_Neo vector).

1. hTERT-RPE-1 Flp-In™ T-REx™ cells are seeded on two or more 6 cm culture dishes ($\sim 45 \times 10^3$ cells per cm^2). The cells are grown for 1–2 days to $\sim 80\%$ confluency. This typically gives the best performance in terms of the transfection efficiency and survival.

Note: Prepare one dish per each planned stable cell line, and one additional dish to serve as negative control.

2. Cells are then co-transfected with pgLAP1_Neo/pgLAP2_Neo or derivatives encoding the GOI, and pOG44 plasmid, encoding the Flp recombinase (Ward et al., 2011). Negative control is transfected only with pOG44 plasmid.

Note: We have derived most of our cell lines following transfection using Lipofectamine 3000 (https://tools.thermofisher.com/content/sfs/manuals/lipofectamine3000_protocol.pdf), but other methods might work just as well.

△ CRITICAL: Due to the low activity of the Flp recombinase in typical cell culture conditions, we recommend the ratio of pgLAP1_Neo-GOI to pOG44 plasmid to be at least 1:29. For

optimal performance, we suggest the total amount of transfected DNA per 80% confluent 6 cm culture dish (with surface area $\sim 21.5 \text{ cm}^2$) not to exceed 3 μg (2.9 μg of pOG44: 0.1 μg of pgLAP1_Neo).

3. The selection of stably transfected cells should start no earlier than 24 h post-transfection
 - a. Replace the medium with a fresh one supplemented with G418 (typically 400 $\mu\text{g}/\text{mL}$, please see notes below), and blasticidin (10 $\mu\text{g}/\text{mL}$, to keep selection pressure for the integrated pcDNA6/TR plasmid of the T-REx system).
 - b. The medium is initially replaced every 3 days until all cells in the negative control condition die out, then the intervals can be prolonged to 5 days. Note that 1–2 weeks after the selection start most of the cells should die and small colonies of resistant cells should be visible upon visual inspection of the plate. Consider marking the position of the colonies on the bottom of the dish.
 - c. Within additional 5–10 days the colonies of resistant cells are usually sufficiently large (\sim hundreds of tightly packed cells), so can be trypsinized and transferred to a new growth vessel (1 well of 24-well plate or 6-well plate, depending on the total number of cells).

[Troubleshooting 1](#)

Optional: Consider freezing down a backup sample for cryopreservation when passaging the cells.

4. During the expansion of the cells
 - a. the expression of the integrated transgene should be verified by WB or IF microscopy.
 - b. Cryopreserve the expanded cells with verified transgene expression.
 - c. Keeping the selection pressure (G418 and blasticidin) after thawing a frozen vial is recommended, but not strictly necessary. Let the cells recover for about 24 h post-thawing before the selection antibiotics are added.

Note: Searching the literature will give an estimate of a working dose for a given antibiotic and cell line, respectively (e.g., $\sim 400 \mu\text{g}/\text{mL}$ G418 for hTERT-RPE-1). As the effectiveness of antibiotics selection depends on several factors, we recommend determining its optimal concentration in your particular cell line and culture conditions before the actual experiment. Generally, at least 3–4 different concentrations are tested to ensure complete killing within 5–7 days.

Note: Always consider including a condition transfected only with pOG44 plasmid to serve as a negative control for the subsequent selection of stable transfectants. We suggest visually inspecting the cells about 4–6 h post-transfection, in case of pronounced signs of post-transfection toxicity, we recommend replacing the medium with a fresh one immediately.

Note: DOX typically induces sufficient expression at dose range 0.01–1 $\mu\text{g}/\text{mL}$ within 24–48 h, however, the optimal time window will always reflect the used GOI and the actual experimental question.

Preparation of viral particles

⌚ Timing: 4 days

In the following section, we describe the production of viral particles based on the pMSCV retroviral backbone (pMSCV-mNeonGreen vector with GOI of choice (e.g., ARL13b)) (Figure 2). Viral transduction is a fast and efficient way to generate stable transfectants in virtually any cell line. The limitation is typically heterogeneous expression levels of the transgene across the population (multiple integration sites, silencing over time), so we highly recommend enriching the population with the desired expression level by cell sorting or eventually isolating individual clones.

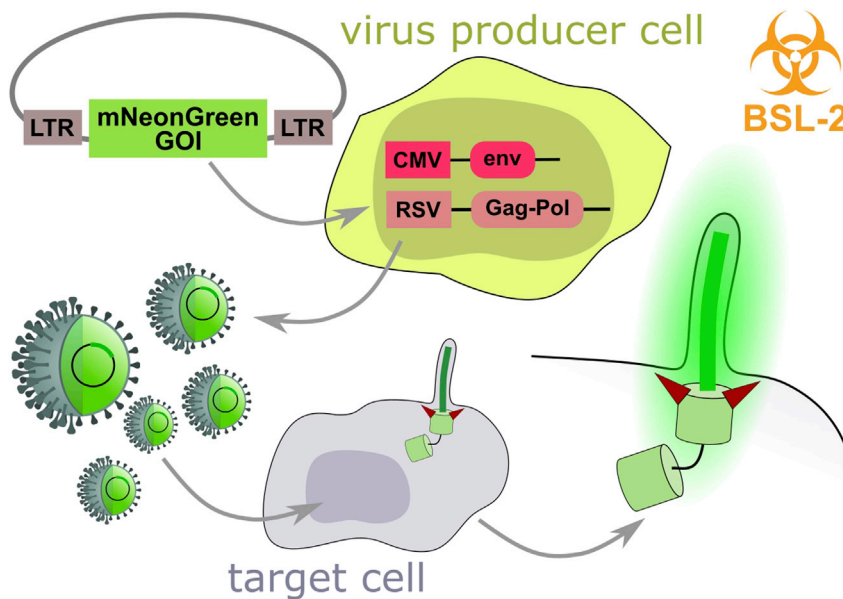


Figure 2. Schematic of the generation of stable cell lines using viral transduction

Note, that significant part of this procedure needs to be performed in Biosafety level (BSL)-2 lab. pMSCV-mNeonGreen retroviral backbone with the GOI (e.g., ARL13b) is transfected into virus producer cells (here we used Phoenix-Ampho cell line, capable of producing Gag-Pol and envelope protein). Viral particles-enriched medium is subsequently collected and used to infect the target cells (e.g., hTERT-RPE-1) thus generating a stable reporter cell line.

For the production of retroviruses, we have used Phoenix-Ampho cell line, a second-generation retrovirus producer cell line derived from HEK 293T, which is capable of producing Gag-Pol and envelope protein. The viral particles generated by this cell line can infect most mammalian cell lines. Alternatively, Phoenix-Eco producer cell line can be used in situations when Phoenix-Ampho is not optimal (e.g., mouse fibroblasts). Both Phoenix-Ampho and Phoenix-Eco cell lines, derived by the Nolan lab (Swift et al., 1999), can be obtained from ATCC. Other suitable packaging systems might work as well.

The following protocol describes the preparation of 9 mL of viral particles-enriched medium, which is sufficient for subsequent transduction of target cells in 9 wells on a 12-well plate or 4–5 wells of a 6-well plate.

5. Day 1: Seed the production cell line Phoenix-Ampho in HEK complete medium in a 25 cm² culture flask. We have obtained the best transfection efficiency when transfecting the cells the next day when ~80% confluent.
6. Day 2:
 - a. Before the transfection, carefully change the medium for the Phoenix transfection medium. 3 mL media is typically sufficient to fully cover the surface of the 25 cm² cell culture flask.
 - b. Prepare a transfection mix to transfect the cells using polyethylenimine (PEI) - mix 300 μ L OPTIMEM, 8 μ g of pMSCV-mNeonGreen vector with GOI of choice (e.g., ARL13b), and 20 μ L PEI solution.
 - c. Briefly vortex and spin down using a tabletop centrifuge (10.000 g, 10 s, RT).
 - d. Following incubation (10 min, RT), add the transfection mixture dropwise to the medium in the flask and mix carefully by gently swaying the flask.

IMPORTANT: All the following steps need to be PERFORMED IN THE VIRAL PRODUCTION SUITABLE LAB (BSL-2), see "CRITICAL" section of this part of the protocol.

7. Transfer the cells to viral production suitable lab (equipped with a laminar flow hood, centrifuge, and cell culture CO₂ incubator). After ~3 h replace the medium for a Viral particles production medium (3 mL, pre-heated).
8. Day 3:
 - a. We recommend collecting the viral particles-enriched medium every 12 h for 36 h (getting in total 9 mL of virus-containing medium). Keep the falcon tube with the collected viral particles-containing medium at 4°C in between the collection steps.
 - b. Add Viral particles production medium (3 mL, pre-heated) after each collection.
9. Day 4:
 - a. Pool the collected viral particles-enriched medium.
 - b. Filter the pre-cleared media using 0.45 µm low-binding syringe filters. [Troubleshooting 2](#)

Optional: If your viral particles-enriched medium has a lot of debris, consider a short spin (3,000 g, 5 min, 4°C) before the filtration step (9b).

▮▮ Pause Point: The collected viral particles-enriched medium may be used immediately, or stored at –80°C, aliquoted in cryotubes. Try to avoid multiple freezing-thawing cycles.

△ CRITICAL: Work carefully with the Phoenix-Ampho retrovirus producer cell line, when collecting/replacing the medium. The cells tend to easily detach from the surface of a culture plastic when handled harshly. The cells detach immediately in case a cold medium is used, therefore usage of the preheated medium is essential.

△ CRITICAL: Perform all the viral particles-related work in an accordingly equipped cell culture lab suitable for viral production (BSL-2). Use appropriate personal protective equipment at all times. Avoid sharing equipment (such as micropipettes) with “non-viral” labs, always use filter tips. All virus-containing waste has to be treated with appropriate disinfectant (e.g., Alcohol-based rapid disinfectant Bacillol), put in a sealed plastic bag, and discarded in a biohazard waste container. The workspace (i.e., laminar flow cell culture hood) needs to be disinfected using appropriate disinfectant and UV light after each use. Take into account that viral particles-related work rules can differ in your institution/country.

Note: We typically employ PEI-based transfection ([Longo et al., 2013](#)), to transfect the Phoenix-Ampho cells, step 6b. Other transfection vehicles such as Calcium phosphate or lipid-based reagents are also suitable.

Note: Cells producing large quantities of the virus will typically stop proliferating and change their morphology. Consider monitoring that as a sign the procedure proceeds as expected.

Generation of reporter cell lines using viral transduction

⌚ **Timing:** ~1 week

This section covers the production of cilia reporter hTERT-RPE-1 cell line using retroviral particles (we use here pMSCV-mNeonGreen-ARL13b retrovirus, please see the previous section). The choice of the appropriate cell line to transduce depends on the design of the planned experiment and the experimental question tested. If you are aiming to prepare a system with two different transgenes, consider using a combination of “Flp-InTM T-RExTM and virus” or “two viruses” (please see the Notes further). Alternatively, any suitable cell line can be used (e.g., hTERT-RPE-1, NIH3T3, IMCD3, MDCKII). Again, all virus-related work needs to be carried out in VIRAL PRODUCTION SUITABLE LAB (BSL-2).

10. Following trypsinization, prepare the appropriate volume of target cell suspension (here we used about 50,000 cells/well of the 12-well plate) and centrifuge (200 g, 4 min) in a 1.5 mL tube.
11. Resuspend the cell pellet in 1 mL of the collected viral particles-enriched medium (either freshly prepared or thawed in a water bath at 37°C, see the previous part of the protocol) with the addition of 5 µg/mL polybrene (1 mg/mL stock) and transfer the cell suspension to the plate.
12. Following the transduction (minimum 4 h, maximum overnight), wash the cells with PBS and add preheated cultivation medium. Longer incubation may improve transduction efficiency. Consider PBS washing and replacing the medium daily, passage the cells when ~80% confluent.
[Troubleshooting 3](#)

Note: We recommend replacing the medium at least 5 times and passage the cells at least once (including the change of the culture plastic) before they can be considered free of any remaining virus particles (bear in mind the biosafety rules at your institute may differ). Until then it is advised to work with the cells as if they still contained the virus – so they should be handled only in **VIRAL PRODUCTION SUITABLE LAB (BSL2)**.

13. During the expansion of the transduced cells, the expression of the integrated transgene should be verified by WB or IF microscopy. Cryopreserve the expanded cells with verified transgene expression and correct localization.

Optional: If your vector carries a suitable resistance marker, you may choose to apply selection antibiotics (e.g., G418, Puromycin, etc.) to enrich for the transduced cells. Do not forget to have one extra well as “non-transduced control”, which will be used to assess the selection efficiency. Searching the literature will give an estimate of a working dose for a given antibiotic and cell line, respectively. As several factors are affecting the efficient dose of the antibiotic, we recommend determining the optimal concentration of the antibiotic of choice in your particular cell line and culture conditions before the actual experiment. In the case of G418, at least 3–4 different concentrations should be tested to ensure complete killing within 5–7 days. Note that the pMSCV vector has a selection marker for Puromycin, which is suitable for efficient selection of transductants in e.g., NIH3T3 or IMCD3 cells, but not so much for hTERT-RPE-1 (see before).

Note: Retroviral transduction and Flp-InTM T-RExTM technology can be combined. This is particularly handy in experiments such as live-cell imaging microscopy when a versatile system allowing simultaneous expression of several transgenes (one “marker” and one “tested” gene) is needed (e.g., loss-of-function rescue type of experiment or functional testing of potential dominant-negative effects of a transgene of choice). To give a specific example, we have recently described Flp-InTM T-RExTM hTERT-RPE-1 cells lacking Tau tubulin kinase 2 (TTBK2) ([Bernatik et al., 2020](#)), a key regulator of primary cilia assembly ([Goetz et al., 2012](#)). Subsequently, pgLAP2_Neo-TTBK2 was used to express FLAG-TTBK2 in a DOX-inducible manner from the Flp-InTM locus. In turn, these cells were transduced by pMSCV-mNeonGreen-ARL13b retrovirus. Inducible expression of FLAG-TTBK2 restored formation of mNeonGreen positive primary cilia, which can be monitored directly in living cells, as described in detail in the following section (see [Figure 16](#) for expected outcome).

Note: It is also possible to transduce the same cell line with two or more pMSCVs with spectrally distinct fluorescent tags. In the case of using multiple pMSCV vectors bearing the same antibiotic resistance gene, the resulting cell line must be sorted for positive cells based on the signal of the fluorescent tags. Using this approach, we successfully generated multiple double-tagged cell lines with the combination of mNeonGreen and mCherry fluorescent tags (unpublished data).

△ **CRITICAL:** The population of cells after transduction typically shows a rather heterogeneous expression of a transgene. Moreover, the majority of loci used for the integration by retroviruses are silenced (Mok et al., 2007). Given that, we strongly recommend enriching for cells with the desired level of transgene expression, for instance by fluorescence-activated cell sorting (FACS). Alternatively, patches of cells expressing the transgene can be also isolated from culture plates manually. Once isolated, these cells should be quickly expanded and cryopreserved in sufficient numbers for later use. Sorting out the desired cell population is even more pertinent if no efficient antibiotic selection is available. We emphasize occasional monitoring of the level of expression of the transgene when routinely propagating these cells. If a notable drop in the number of transgene-positive cells is observed (when compared to the starting point) we suggest thawing a low passage vial of these transductants or to re-sort the cell population by FACS to again enrich for cells expressing the transgene at a sufficient level.

KEY RESOURCES TABLE

REAGENT or RESOURCE	SOURCE	IDENTIFIER
Antibodies		
Polyclonal Anti-ARL13B antibody produced in rabbit	Proteintech	Cat# 17711-1
Monoclonal Anti-γ-Tubulin antibody produced in mouse	Sigma-Aldrich/Merck	Cat# T6557
Donkey anti-Rabbit IgG Secondary Antibody, Alexa Fluor 568	Thermo Fisher Scientific	Cat# A10042
Donkey anti-Mouse Secondary Antibody, Alexa Fluor 647	Thermo Fisher Scientific	Cat# A-31571
Chemicals, peptides, and recombinant proteins		
Bacillol AF	Hartmann	Cat# 975075
Blasticidin S	Sigma-Aldrich/Merck	Cat# 15205
DMEM, high glucose, GlutaMAX™ Supplement, pyruvate	Gibco/Thermo Fisher Scientific	Cat# 31966021
DMEM/F-12, no glutamine	Gibco/Thermo Fisher Scientific	Cat# 21331020
Doxycycline Hydrochloride, Ready-Made Solution	Sigma-Aldrich/Merck	Cat# D3072-1ML
FBS Ultra-low endotoxin	Biosera	Cat# FB-1101/500
FluoroBrite DMEM	Thermo Fisher Scientific	Cat# A1896701
G418	Roche	Cat# 4727878001
L-glutamine	Biosera	Cat# XC-T1715/100
Lipofectamine 3000	Invitrogen/Thermo Fisher Scientific	Cat# L3000-008
OPTIMEM	Gibco/Thermo Fisher Scientific	Cat# 31985070
Penicillin/Streptomycin	Biosera	Cat# XC-A4122/100
Polybrene	Sigma-Aldrich/Merck	Cat# H9268
Polyethylenimine (PEI)	Sigma-Aldrich/Merck	Cat# 408727
Trypsin-EDTA Solution 0.05%	Serana	Cat# RTL-003-100ML
Zeiss Immersol Immersion oil 518 F	Carl Zeiss	Cat# 444960-0000-000
Zeiss Immersol Immersion oil W 2010	Carl Zeiss	Cat# 444969-0000-000
Experimental models: Cell lines		
hTERT-RPE-1 Flp-In™ T-REx™ (human)	a gift from E. Nigg (University of Basel)	Bernatik et al., 2020
Phoenix-Ampho (human)	ATCC	Cat# CRL-3213
Recombinant DNA		
pGFT1.1	Derivative of the pgLAP1_Neo with EGFP tag replaced by mNeonGreen.	N/A

(Continued on next page)

Continued

REAGENT or RESOURCE	SOURCE	IDENTIFIER
pgLAP1_Neo	Derivative of the pgLAP1 (a gift from P. Jackson, Stanford University School of Medicine; addgene Plasmid #19702) with Hygromycin resistance gene replaced by G418 (Neomycin) resistance gene for selection of RPE-1 cells	(Bernatik et al., 2020; Pejskova et al., 2020)
pgLAP2_Neo	Derivative of the pgLAP2 (a gift from P. Jackson, Stanford University School of Medicine; addgene Plasmid #19703) with Hygromycin resistance gene replaced by G418 (Neomycin) resistance gene for selection of RPE-1 cells	(Bernatik et al., 2020; Pejskova et al., 2020)
pMSCV-N-mNG-IRES-PURO	The plasmid MSCV-N-FLAG-HA-IRES-PURO (a gift from W. Harper, Harvard Medical School; addgene plasmid #41033 (Sowa et al., 2009)), was modified by replacing FLAG-HA with mNeonGreen.	(Kiesel et al., 2020)
pOG44	Thermo Fisher Scientific	V600520
Software and algorithms		
Fiji	(Schindelin et al., 2012)	version 2.1.0; https://imagej.net
ZEN Black	Carl Zeiss	version 2.3 SP1
ZEN Blue	Carl Zeiss	version 2.6
NIS Elements Advanced Research (Ar)	Nikon	version 5.02
Other		
biosafety level 2 flow box + centrifuge and microscope	N/A	N/A
CELLVIEW CELL CULTURE SLIDE, PS, 75/25 MM,	Greiner Bio-One	Cat# 543079
glass bottom dish with 20 mm micro-well	Cellvis	Cat# D35-20-1.5-N
μ-Slide 8 well chamber slide	IBidi	ibiTreat; Cat# 80826
table top centrifuge	N/A	N/A

MATERIALS AND EQUIPMENT

HEK complete medium

Reagent	Final concentration	Amount
DMEM	89%	445 mL
FBS	10%	50 mL
P/S	1%	5 mL
Total	n/a	500 mL

RPE-1 complete medium

Reagent	Final concentration	Amount
DMEM/F-12	88%	440 mL
10% FBS	10%	50 mL
L-glutamine	1%	5 mL
P/S	1%	5 mL
Total	n/a	500 mL

Phoenix transfection medium

Reagent	Final concentration	Amount
DMEM	99.50%	49.75 mL
FBS	0.50%	0.25 mL
Total	n/a	50 mL

Imaging medium		
Reagent	Final concentration	Amount
FluoroBrite DMEM	98%	490 mL
L-glutamine	1%	5 mL
P/S	1%	5 mL
Total	n/a	500 mL

Viral particles production medium		
Reagent	Final concentration	Amount
DMEM	90%	45 mL
FBS	10%	5 mL
Total	n/a	50 mL

Note: All prepared media can be stored in a fridge (4°C) for several months.

PEI Solution		
Reagent	Final concentration	Amount
PEI	2 mg/mL	80 µL
PBS (pH 7.2)	n/a	40 mL
Total	n/a	80 mL

Note: Prepared solution can be stored in a fridge (4°C) for several months.

Phoenix transfection mixture		
Reagent	Final concentration	Amount
OPTIMEM	n/a	300 µL
pMSCV-mNeonGreen with GOI of choice (ARL13b)	n/a	8 µg
PEI Solution	n/a	20 µL
Total	n/a	n/a

△ **CRITICAL:** Antibiotics (such as Penicillin/Streptomycin, G418, etc.) are considered harmful, use appropriate protection when working with them (wear gloves, use cell culture hood).

STEP-BY-STEP METHOD DETAILS

Analysis of time-lapse videos to study primary cilia dynamics

⌚ **Timing:** 3–4 days

Here we describe in detail the analysis of primary cilia growth/resorption in living cells on the example of mNeonGreen-ARL13b cell line prepared in the previous steps.

1. Day 1: Seed the cells (here we used hTERT-RPE-1 Flp-In T-REx TTBK2 KO cells (Bernatik et al., 2020) with DOX-inducible expression of FLAG-TTBK2 and constitutive mNeonGreen-ARL13b reporter) in a RPE-1 complete medium supplemented with DOX on a 10-well glass-bottom CELL-VIEW CELL CULTURE SLIDE, PS, 75/25 MM at a high density (~25.000–30.000 cells per well).

Note: Typically we use DOX in 1 $\mu\text{g}/\text{mL}$ final concentration, please see DOX optimization step in the section “[Generation of stable cell lines using Flp-InTM T-RexTM system](#)”.

Note: Other types of chamber slides can also be used here. Throughout this protocol we used CELLVIEW CELL CULTURE SLIDE or IBidi μ -Slide. We recommend choosing CELLVIEW CELL CULTURE SLIDE for long-term experiments such as cilia growth/resorption analysis. Their black chambers offer better protection from light during adjacent well imaging. Moreover, the area of the chamber is smaller and volume of the medium higher, thus decreasing the risk of medium evaporation compared to IBidi μ -Slide.

Note: For the imaging setup using LSM800 (described below) it is advised to use adjacent wells and limit the analysis to 3 conditions (3 wells) maximum to reduce the movement of the slide during imaging. Increasing the number of wells/conditions comes hand in hand with increased time the microscope needs to move between each condition/well and increasing the chance the immersion runs dry.

2. Day 2 (the exact timing may differ in respect to your experimental treatment): Depending on the biological question, this is probably the time to treat the cells as needed (e.g., small molecules, siRNA transfection, etc.).
3. Day 3 (the exact timing may differ in respect to your experimental treatment):
 - a. Wash the cells with PBS or serum-free low auto-fluorescence FluoroBrite medium (imaging medium) to remove the remnants of the previous media.
 - b. Add Imaging medium (supplemented with 1 $\mu\text{g}/\text{mL}$ of DOX) to the cells to promote ciliogenesis. Add as much medium as possible in the well to prevent its evaporation during the long imaging (we typically use about 300 $\mu\text{L}/\text{well}$).
 - c. Depending on the experimental question either proceed directly to live-cell imaging to monitor the growth of the cilia.
 - d. Or starve the cells for 24 h to promote cilia formation, and before imaging add Imaging medium with 10% FBS (supplemented with 1 $\mu\text{g}/\text{mL}$ of DOX, see above) to monitor cilia resorption.

Time-lapse live imaging of cilia dynamics acquisition

Given that live cells growing on the surface of the slide are to be imaged in this setup, an inverted microscope system is required. To keep the cells in optimal conditions throughout the whole imaging session (in our case up to 16 h), it is necessary to use a microscope equipped with an environmental chamber, which allows precise control of temperature, humidity, and CO_2 levels. The confocal microscope compared to a widefield microscope offers a better signal-to-background noise ratio which might be helpful to extract the specific signal in cells with a higher background signal as seen in our reporter cell line. Inside living tissue, the important events can occur deep within the specimen, further away from the cover glass. Water immersion objectives typically overcome spherical aberrations better than oil immersion objectives, as it better matches the sample refractive index. Due to the increased evaporation it is recommended to use water oil immersion e.g., Zeiss Immersol Immersion oil W 2010 (Carl Zeiss, 444969-0000-000). Moreover, it is very helpful and convenient if the microscope – operating software allows multi-position acquisition with easy position list setup, which will enable to add specific positions of the cells with cilia.

Here we used Inverted (Axio Observer.Z1) laser scanning confocal and epifluorescence microscope LSM800 equipped with an environmental chamber for live-cell imaging (controlled temperature, humidity, CO_2). We opted for C-Apochromat 63 \times /1.20 Korr UV VIS IR water immersion objective. Solid state laser 488 in combination with high-sensitivity GaAsP detector were used to acquire images and the microscope was controlled by ZEN Blue software. Data acquisition was performed in 1024 \times 1024 pixel format, with pixel time around 1 μs and pixel size 0.10 μm in bidirectional mode with

2× averaging and 8-bit bit depth. Images were taken as Z-stacks thickness 0.6 μm with 0.5 μm slices spacing (see the note below) every 10–15 min for up to 16 h.

Note: Being aware that the optimal Z-slice spacing according to the Nyquist criterion would be lower (0.28 μm) we opted for 0.5 μm slice spacing. This allowed us to keep around 10% overlap between the slices, while significantly reducing the time of acquisition and in turn sample bleaching. Importantly, this setting also allows to use of wider range in the Z-axis, which is particularly relevant for imaging cilia, as they typically spread across the Z-axis. We did not observe any loss of information when using the maximal projection image for the final cilia length analysis.

4. Open the ZEN Blue Software.
5. Turn on the temperature and atmosphere control in the “Incubation” window (Figure 3A) at least 20 min before starting the microscope setup for the chamber to reach the set incubation conditions. After sample insertion in the holder the microscope setup will take another 30–40 min, thus the whole system is equilibrated at least for one hour before the actual start of the imaging.
6. Put a drop of the appropriate immersion medium (here we used a Zeiss Immersol Immersion oil W 2010 with a refractive index of water) on the selected objective and insert the slide with the cells in the slide holder, close the chamber with the lid.
7. In the “Locate” tab (Figure 3B) turn on the fluorescence (represented by “GFP” button) and find the focus looking on the specimen through the eyepiece. You can search specifically for a cell with cilium here. Make sure to close the shutter as soon as you find the sample focus, to avoid sample bleaching.
8. Switch to “Acquisition” tab (Figure 3C), select “Z-stack”, “Tiles” and “Time series” and “Auto Save” to add the particular windows with setup options.
9. In the “Imaging Setup” window (Figure 3C) add “+LSM Confocal”, add “Tracks” in a “Frame” mode, here we only use one channel, thus one Track. Select the “Dye” (here we used the preset EGFP) and the “Color code”.
10. In the “Acquisition Mode” window (Figure 4A) set the “Scan Speed” to get the “Pixel speed” around 1 μs. Bidirectional “Direction” of scanning will make the imaging faster and 2× “Averaging” reduces noise and improves image quality.
11. In the “Channels” window (Figure 4B) select one Track at a time, turn on the appropriate laser (here 488 nm for GFP and its derivatives such as mNeonGreen), start with the “Master Gain” on ~650 V, and in the Live mode increase the laser % to see your cells and/or your cilia signal. Keep in mind to leave the laser intensity as low as possible, considering the possible bleaching effect or even cell death over time.
12. Find the position with the cells of interest either in “Locate” or “Live” mode and add them in “Positions” list in the “Tiles” window by clicking on a “+” button until all positions to be imaged are added to the list. Uncheck the “Tile Regions/Position – Sort by Y then X”, so the positions stay in the order added also for the imaging (Figure 5).

Note: When planning the experiment, keep in mind that only a limited number of positions can be imaged in one experiment, depending on the number of conditions/wells, number of channels, and number of the Z-slices to fit into the selected time between the timepoints. This is also highly dependent on the microscope system of your choice. With our setting with imaging two conditions in one channel, 10–15 Z-slices each and 10–15 min between the steps we used up to 20 positions in total.

13. In the “Definite Focus” window (Figure 6A) in “Live” mode click “Find Surface”, if necessary fine-tune the focus on the center of the cell/cilium and click Store Focus. This creates an offset value, which will be used to set the focus plane in the same distance from the automatically found focus before each timepoint. It is also possible to do this step right at the beginning of the imaging to

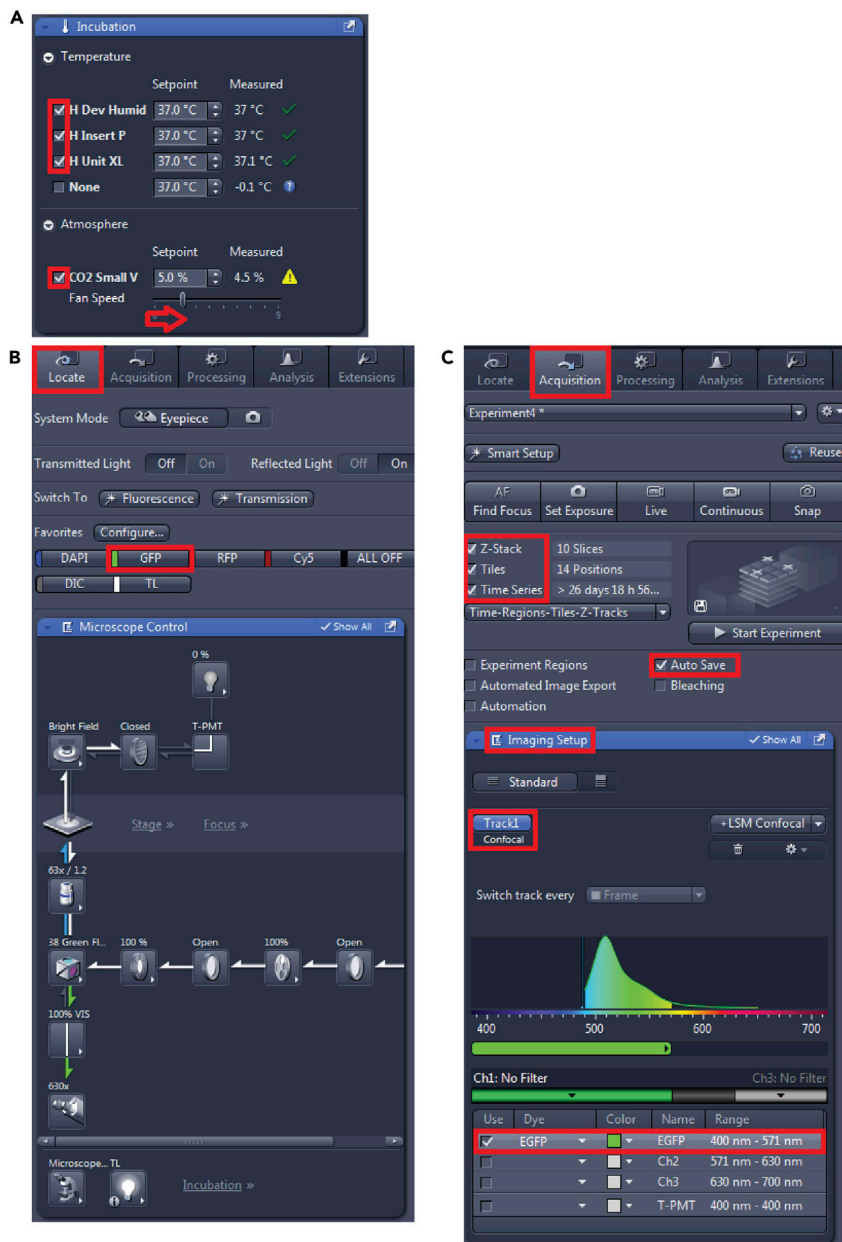


Figure 3. Setup of the Zeiss LSM800 in ZEN Blue, steps 18, 20–22

(A) Incubation conditions, (B) localizing the cells using the eyepiece and (C) Imaging Setup details.

find the focus plane of the cells and thus eliminating the need for the manual search of the focus plane.

14. In the “Focus Strategy” window (Figure 6B) choose:
 - a. “Use Focus Surface/Z Values Defined by Tiles Setup”.
 - b. In “Focus Surface” choose “Local (per Region/Position)”.
 - c. Check “Adapt Focus Surface/Z values” with “Definite focus”, “Update with Multiple Offsets”.
 - d. In “Initial Definition of Support Points/Positions/Tile Regions” choose “By Definite Focus: Recall Focus”.
 - e. With this setting before each new timepoint, the software will find the surface and update the focus plane, which would help with the loss of focus during the long-term imaging.

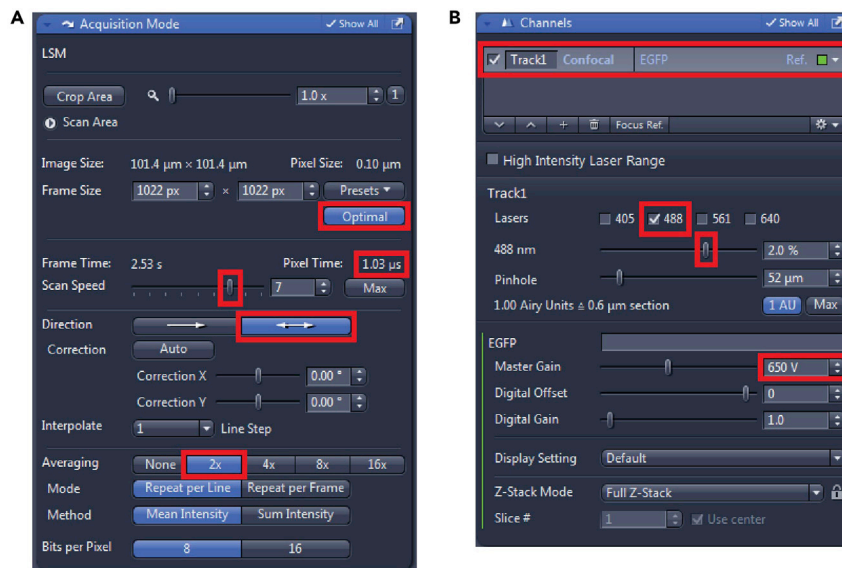


Figure 4. Setup of the Zeiss LSM800 in ZEN Blue, steps 23, 24

(A) Details of Acquisition setup and (B) Laser power and Gain setup of Channels.

15. In the "Z-stack" window (Figure 6C) in the "Center" mode set the desired number of slices, and the interval between them, the center position will be taken from the "Tiles setup", as set in the "Focus Strategy" above.
16. In "Time Series" window (Figure 6D) set "Duration" to "As Long as Possible" so the scanning will continue until manually stopped or set a precise number of cycles. Set an interval between the individual time points and the units – here we used 10 or 15 min.
17. In "AutoSave" window fill in the file name and the saving path.
18. Click "Start Experiment" which will start imaging. [Troubleshooting 4, 5, and 6](#)
19. For further analysis, the Z-slices can be projected in one layer by Orthogonal maximal projection. This is particularly useful when imaging objects like cilia, which spread through several Z slices. To do so:
 - a. Have your Z-stack *.czi file to be processed in the active tab.
 - b. Go to "Processing" tab.
 - c. In "Method" find "Orthogonal Projection".
 - d. Set "Projection Plane" to "Frontal (XY)", set "Method" to "Maximum" and click "Apply".
 - e. This will create a maximum intensity projection of all the Z planes into a single XY image.
20. The resulting file contains all the positions as "Scenes" in one large *.czi file. To export individual positions to individual TIFF files:
 - a. Have the *.czi file to be processed in the active tab (it can be either the original Z-stack or processed Orthogonal Projection file).
 - b. Go to "Processing" tab.
 - c. In "Method" find OME/TIFF export.
 - d. In the "Method Parameters" unselect "Merge All Scenes" and set the path for the exported TIFF images, click "Apply".

Imaging of intraflagellar transport (IFT) in primary cilia of living cells

⌚ **Timing:** ~4 days (according to the type of treatment)

This section covers live-cell imaging analysis of IFT, namely the measurement of transport frequency and velocity, in primary cilia of hTERT-RPE-1 cells stably expressing mNeonGreen-tagged protein IFT74 (pGFT1.1 - mNeonGreen-IFT74).



Figure 5. Setup of the Zeiss LSM800 in ZEN Blue, step 25

Creating a list of Positions for the subsequent imaging.

21. Day 1: Seed the hTERT-RPE-1 mNeonGreen-IFT74 reporter cell line in RPE-1 complete medium supplemented with DOX (typically 1 µg/mL, please see DOX optimization step in the section “[Generation of stable cell lines using Flp-In™ T-REx™ system](#)”) on IBidi ibiTreat µ-Slide 8 well chamber slide (see note after step 14 in the previous section of this protocol) at a high density (~25.000 cells per well). We used 300 µL of the media per well.
22. Day 2 (the exact timing may differ in respect to your experimental treatment): Depending on the biological question, this is probably the time to treat the cells as needed (e.g., small molecules, siRNA transfection, etc.).
23. Day 3 (the exact timing may differ in respect to your experimental treatment):
 - a. Aspirate the medium from the cells grown in µ-Slide 8 well chamber slide.
 - b. Wash the cells with PBS or imaging medium to remove the remnants of the previous media. Aspirate the solution for each well.

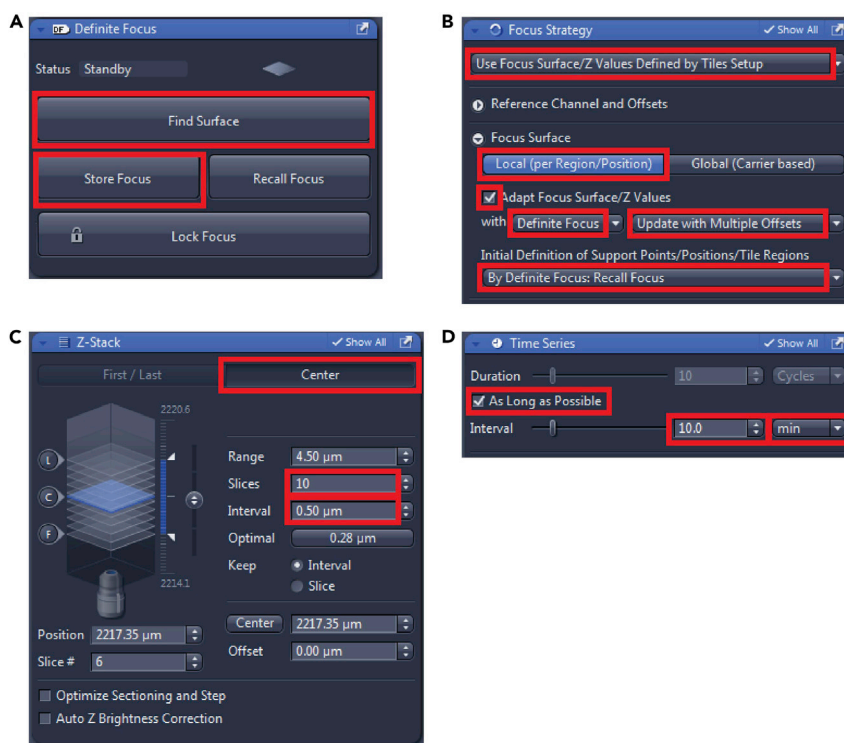


Figure 6. Setup of the Zeiss LSM800 in ZEN Blue, steps 26–29

(A) Definite Focus and Offset setup (B) Focusing strategy details (C) Setup of the Z-stack and (D) Time Series.

- c. Add Imaging medium (supplemented with 1 µg/mL of DOX, see above) to the cells to promote ciliogenesis.
- d. After 24 h proceed directly to live-cell imaging to monitor the transport of IFT trains.

Note: If your experimental setup is based on the use of small molecule(s), do not forget to add them to the media. If you want to study more rapid response to your intervention, it is probably better to start the treatment just before the imaging (see below).

Time-lapse live imaging of IFT in primary cilia acquisition

As the copy number of each IFT protein in a given train is rather low (Ishikawa and Marshall, 2015), the signal emitted by mNeonGreen-tagged IFT protein per each train is weak. Typically, this could be circumvented by using long exposures to increase the signal-to-noise, but imaging the IFT trains requires taking images at a fast enough rate that the movement of the trains does not cause blurring in the image. Thus, it is necessary to use both fast and sensitive instrumentation. For this purpose, we have employed an inverted Zeiss LSM880 laser scanning confocal microscope mounted on an Axio Observer.7 stand and equipped with an Airyscan detector. We opted for alpha Plan-Apochromat 100×/1.46 oil differential interference contrast M27 immersion objective. Compact light source HXP120V mercury lamp was used for the ocular observation. Images were acquired using Multiline Argon laser 35 mW in combination with a ZEISS Airyscan detector and the microscope was controlled by ZEN Black acquisition software. Data acquisition was performed using the confocal in super resolution mode, with the Airyscan detector, Pixel Dwell Time below 1 µs and Scan Time below 200 ms (depending on scan speed), 16 Bit Depth (8 bit depth can also be used, it could actually help for dim the sample) and Zoom 8–11 (depending on the length of imaged cilia). Images were taken as Time Series taking an image every 200 ms, with 150 images in total. The Airyscan detector allows acquisition with increased resolution and signal-to-noise ratio compared to conventional confocal scanning. A spinning disk confocal microscopy, Total Internal Reflection Fluorescent (TIRF), or “TIRF-like” microscopy (see the section “Imaging IFT using variable-angle

epifluorescence microscopy" for details) is also suitable for the IFT imaging due to reduced bleaching of the fluorescence signal and very good signal-to-background noise ratio, in comparison to e.g., standard wide-field microscopy.

Note: Using an oil objective with a higher numerical aperture (NA) will allow for higher resolution imaging, especially in combination with the Airyscan detector (in comparison to the water objective used in the previous section).

24. Before beginning the imaging, prepare the microscope of your choice (here Zeiss LSM 880 with Airyscan detector, operated via ZEN Black acquisition software according to your needs (e.g., preheat the chamber to 37°C and equilibrate it with CO₂ (see step 18 in the previous section), switch on argon laser, etc.).
25. Open the ZEN Black acquisition software.
26. Put a drop of the appropriate immersion medium on the selected objective and insert the μ -Slide 8 well coverslips with the cells in the slide holder.
27. In the "Locate" tab turn on the fluorescence (represented by "GFP" button) (Figure 7A) and find the focus with the eyepiece. You can search specifically for a cell with cilium here.
28. In the "Acquisition" tab in "Imaging Setup" window (Figure 7B) add "+LSM Confocal", add "Tracks" in a "Frame mode", here we only use one channel, thus one Track. Select the "Dye" and a "Color code".
29. Select the "Acquisition" tab (Figure 8A) and tick "Time Series". The recommended settings of key parameters of the "Acquisition Mode" window (Figure 8B) to start with is the following:
 - a. Pixel Dwell Time: typically below 1 μ s - depending on scan speed,
 - b. Scan Time: typically below 200 ms - depending on scan speed)
 - c. Bit Depth: 16 Bit,
 - d. Zoom: typically 8–11, depending on the length of imaged cilia.

Note: For our imaging setup it was sufficient to acquire images in one focus plane in "Airyscan super resolution" module. However, in case the use of Z-stack is desirable the "Fast module" could be used instead of the "Airyscan super resolution" to shorten the time of individual acquisition steps.

30. Set laser line attenuator transmission (for 488 nm: 0.5%) and select the "Airyscan Mode / SR" (superresolution) in "Channels" window (Figure 8C).
31. Set "Cycles" (up to 150) and "Intervals" (to 200 ms) in "Time Series" window (Figure 8D).
32. While being in "Live mode", adjust focus on primary cilia and select a region of interest with the cilium you want to analyze, click on "Start Experiment" (Figure 8A). [Troubleshooting 7](#)
33. Following the time-lapse acquisition, a *.czi file is created and saved locally.
34. Go to the "Processing" window and select "Airyscan Processing", "Select" and then Apply (Figure 9). Airyscan processing is a type of post-acquisition processing, which allows for simultaneous improvement in resolution and signal-to-noise. This generates a processed *.czi file with better resolution than the unprocessed *.czi file. For illustration of the processed file see [Methods Video S1](#).

Note: For the analysis of IFT74 dynamics in primary cilia we used auto setting of Airyscan processing. For the analysis of molecule movement it is sufficient to use the auto setting when the strength of the filter is calculated for each image separately, which results in different Airyscan processing values. However, when comparing structure sizes or intensities between different samples, the same optimized Airyscan processing setting (with manually adjusted strength of the processing) should be reused in the whole set of images which are to be compared.

35. Repeat the steps 45–47 to obtain a sufficient number of recordings of primary cilia per each condition of your experiment. We recommend measuring at least 20 primary cilia per experimental condition to get sufficiently robust data for the subsequent analysis.

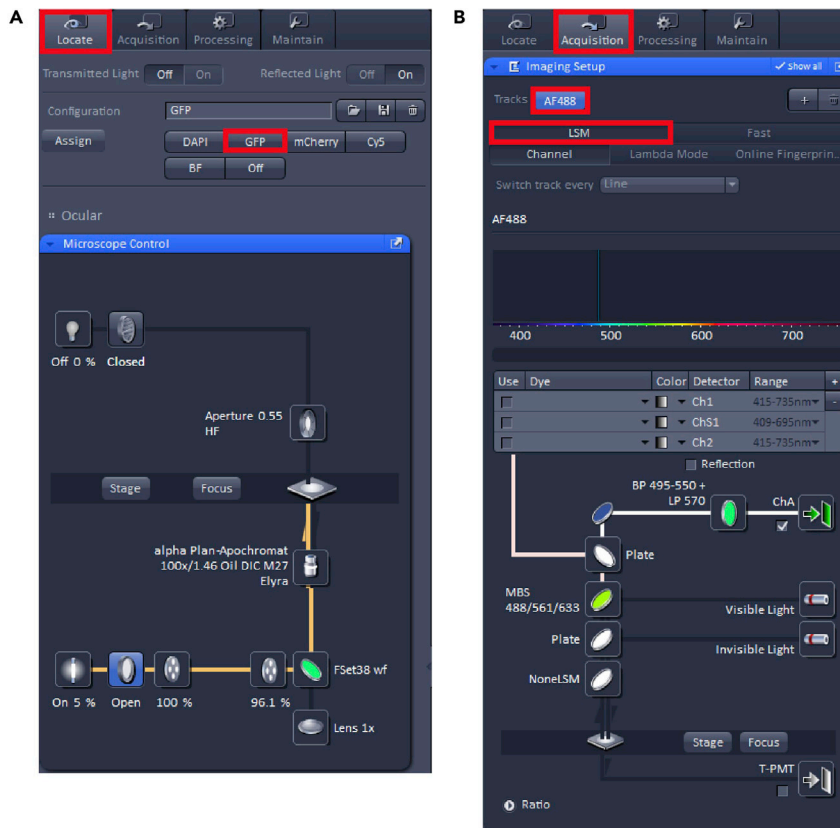


Figure 7. Setup of the Zeiss LSM880 in ZEN Black, steps 40–41

(A) Localizing the cells using the eyepiece and (B) Imaging Setup details.

Note: The speed of IFT movement is typically between 0.25 and 1 $\mu\text{m/s}$ (Ishikawa and Marshall, 2015). The settings described above allow taking an image every 200 ms, with 150 images in total, which is typically sufficient to detect the movement of IFT trains. We try to minimize the bleaching of IFT trains by setting laser power to minimal levels. Please consider adjusting these parameters according to your needs to get optimal results.

Note: Primary cilia in non-polarized cells (e.g., hTERT-RPE-1) are typically confined in a deep narrow pit created by membrane invagination (Mazo et al., 2016; Sorokin, 1962). While response of such “submerged” primary cilia to clues, such as fluid flow, is limited (Mazo et al., 2016), their imaging and IFT analysis is, in turn, fairly straightforward (as they do not significantly move).

Pause Point: The subsequent computer analysis can be done at any time.

36. Here we describe how to assemble obtained images into a kymograph (a very convenient tool to visualize time-lapse data in a single image) and to determine the velocity and frequency of IFT trains. To analyze the obtained data for IFT movement dynamics we suggest using Fiji software (2.1.0 version or newer, no specific plug-ins are required).

Note: Commercial image analysis software packages (e.g., MetaMorph) are also suitable.

- a. Start the Fiji software to open an Airyscan processed *.czi file (i.e., drag and drop the file to Fiji toolbar or click on File → Open...) (Methods Video S2, steps 49a–c).

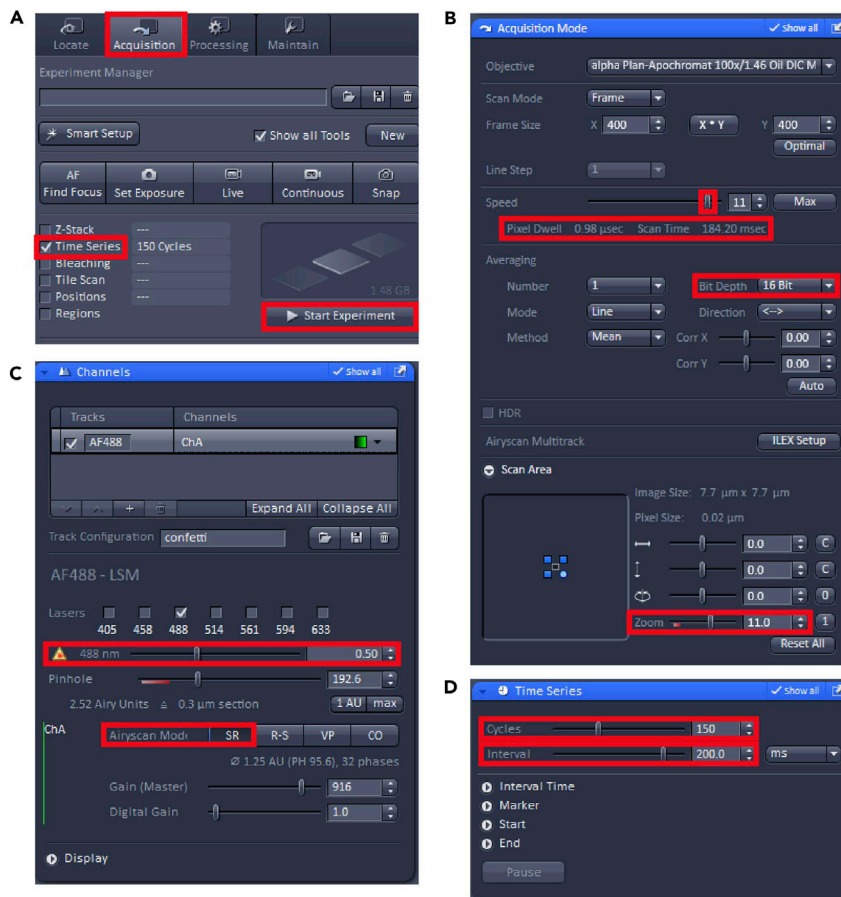


Figure 8. Setup of the Zeiss LSM880 in ZEN Black, steps 42–45

Setup details of Acquisition tab (A) Acquisition Mode (B), Channels (C), and Time Series (D).

- b. Click on Image → Adjust → Brightness/Contrast for adjustment of brightness and contrast to create an optimal image display for analysis.
 - c. Right-click on a straight line in the Fiji toolbar and choose Segmented Line. Draw a segmented line from the base to the tip of the primary cilium (left-click to start drawing and adding points, right-click to finish the drawing) and measure the length of the cilium by selecting the panel “Analyze” → “Measure” or keyboard shortcut Ctrl+M. The measured length will be displayed as µm in “Results” window.
- All steps of time-lapse imaging analysis of IFT transport dynamics using Fiji software can also be found in the tutorial videos ([Methods Videos S2](#) and [S3](#), and [4](#)).

△ **CRITICAL:** Draw the line from base to tip of the primary cilium. To position the cilium correctly, pay attention to the signal difference between the base and the tip (the foci of IFT protein signal at the ciliary base is typically more prominent and also of different shape over the IFT pool in the tip, [Figure 10](#)). Alternatively, detection of the cilia orientation can be facilitated by expressing additional markers, such as a basal body protein fused with a red fluorescent tag (e.g., mCherry-TTBK2). In a situation the orientation is not clear, exclude such primary cilium from the analysis.

- d. Open the “ROI Manager” in Fiji by selecting “Analyze” → “Tools” → “ROI Manager” ([Methods Video S3](#), steps 49d-51).

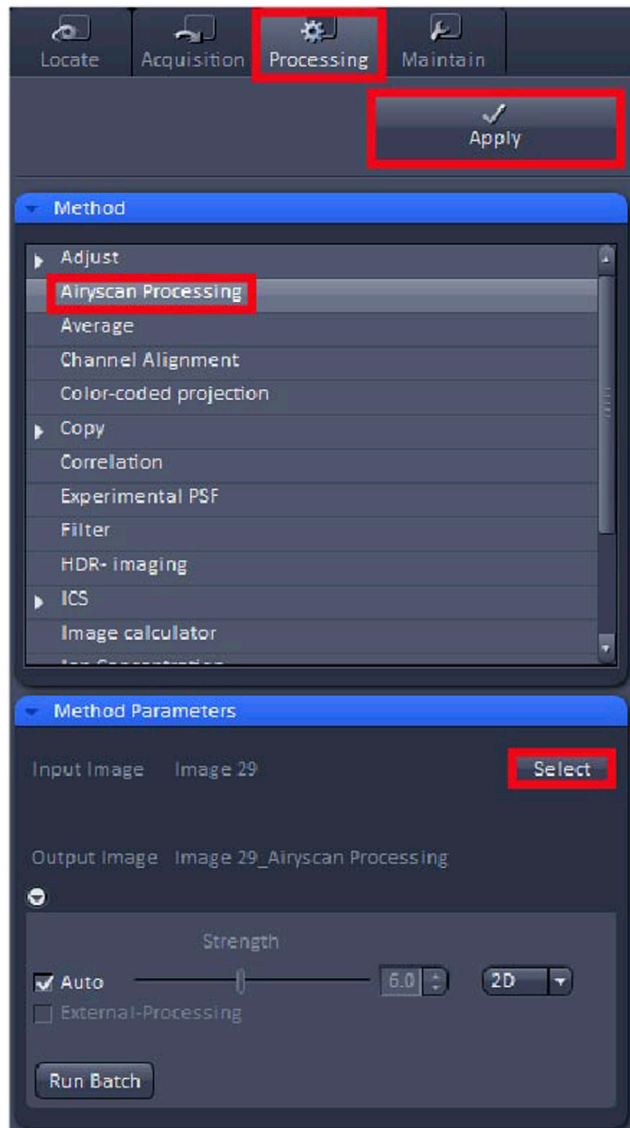


Figure 9. Setup of the Zeiss LSM880 in ZEN Black, step 47

Setup details of Airyscan processing.

- e. Click on “Analyze” → “Multi Kymograph” → “Multi Kymograph” (with Linewidth 1) to create a kymograph from the time-lapse data.

37. Rotate the image 90 degrees by left-clicking on “Image” → “Transform” → “Rotate 90 Degrees Left”.

Optional: You can enlarge the kymograph by pressing the “+” on the keyboard and also adjust brightness and contrast if needed.

Note: Note that the base of the imaged cilium is now at the bottom of the obtained kymograph, while the ciliary tip is at its top (Figure 11A). Consequently, the first image of time-lapse is situated on the very left side of the obtained kymograph, which can in turn be used to track any detected movement of mNeonGreen-IFT74 particles inside the cilium.

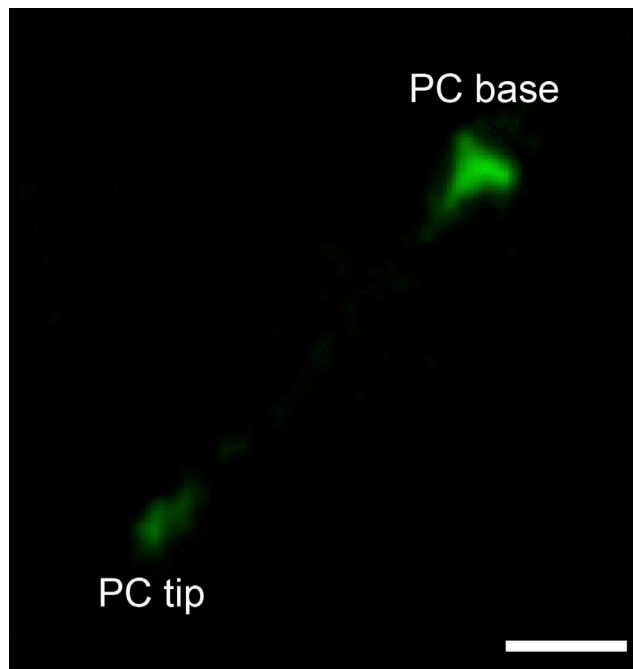


Figure 10. Primary cilium orientation

IFT signal (green; mNeonGreen) at the base is more distinct and also of a different shape compared to the IFT protein signal at the tip of the primary cilium (PC). Scale bar=1 μ m.

38. IFT trains inside cilia use either anterograde or retrograde type of transport ([Rosenbaum and Witman, 2002](#)). To track the movement of individual IFT trains, draw straight lines (right-click on a Segmented line in Fiji toolbar and choose Straight Line) through all visible tracks of IFT74 trains in the kymograph and add them to the "ROI manager".

Note: Note that we track only trajectories clearly distinguishable from the background signal (in turn the drawn lines sometimes do not fully span from the tip to the base).

39. Select the "ROI Manager" panel and click "Measure" ([Methods Video S4](#)).

Note: Remember that only the IFT train trajectories tracked in the kymograph in step 49c will be measured. The obtained values represent an angle between each measured trajectory and the horizontal axis, the speed of IFT train is calculated by $\tan(\text{angle})$ ([Ishikawa and Marshall, 2015](#)). Because the unit of $\tan(\text{angle})$ is given in pixel, this can be converted into $\mu\text{m/s}$ by multiplying pixel size and frequency (frames per second), see step 54. The positive angle values represent the anterograde transport while the negative values represent the retrograde transport.

Note: Keep in mind that only IFT trains "passing through" the drawn line (step 49c) will be included in kymograph analysis. Consequently, it may be necessary to draw an additional line to "cover" all IFT particles recorded in the time-lapse Movie.

Optional: To add a color code in the kymograph for better orientation, click on the line or the number in "ROI Manager", select "Properties" in "ROI Manager", and change the color ([Video 3](#)). In [Figure 11B](#) shown as an example, the anterograde transport lines are shown in green while the lines representing the retrograde transport are in red (see for details). The

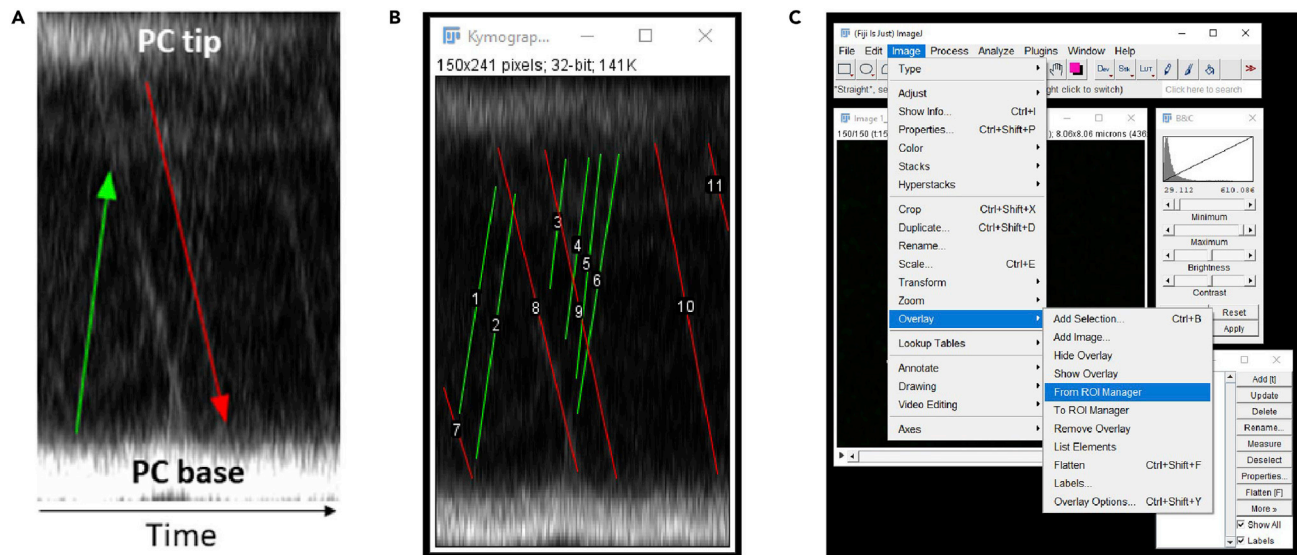


Figure 11. Tracking of movement in kymograph

(A) The kymograph represents the movement of IFT74 particles inside the primary cilium (PC). The primary cilium base and tip are at the bottom and top of the kymograph, respectively. The first image of the time-lapse is located on the left side of the kymograph. The green arrow shows the anterograde transport going from the base to the tip of the cilium while the red arrow indicates the retrograde transport going from the tip to the base of the cilium. (B) Tracks in the kymograph can be distinguished by color and numbers. Green lines represent the anterograde transport while red lines depict retrograde transport. (C) The visualized tracks in the kymograph have to be overlaid from ROI manager before you save the image.

numbering of lines is done automatically, but you can hide the numbers by checking off “Labels” in “ROI Manager” (Methods Video S4).

Optional: To save the kymograph with overlaid track visualization, select “Image” → “Overlay” → “From ROI Manager” (Figure 11C), and save as usual.

△ CRITICAL: Keep in mind that the position of the signal in the kymograph corresponds to the time when the individual images were recorded. As the time axis goes from left to right, the lines representing detected IFT tracks are also oriented from left to right. In turn, the tracks going from the base of the cilium (bottom of the kymograph) to the tip of the cilium (top of the kymograph) visualize the anterograde transport, while the tracks going from the tip to the base belong to the retrograde transport. The direction of drawing the straight lines in the kymograph is critical for the correct calculation of IFT trains’ velocity. Therefore, the individual lines need to be drawn in the proper direction: anterograde from the bottom of the kymograph; retrograde from the top of the kymograph; and in chronological order, i.e., from left to right (Figure 11A).

⏸ Pause Point: The subsequent determination of frequency and velocity of measured IFT trains can be done at any time.

Determination of frequency and velocity of IFT trains using mNeonGreen-IFT74:

40. The frequency of trains directly corresponds to the number of green (anterograde) and red (retrograde) lines per used period of time.
41. Calculate the velocity of individual IFT trains:

$$\text{Velocity } (\mu\text{m/s}) = \tan(\text{angle}) * \text{pixel size} * \text{frames per second}$$

Note: As mentioned earlier, the determined angle values for retrograde transport will be negative, which in this case reflects the fact the trains are moving in the opposite direction (to the anterograde transport). However, as velocity cannot be negative, simply use absolute values for its calculation in the case of the IFT trains moving via the retrograde route.

Note: The used pixel size and number of frames can be determined in Fiji, click on Image → Properties ([Methods Video S4](#)).

Alternative: Imaging IFT transport using variable-angle epifluorescence (VAEM) microscopy

Experiments focused on detailed study of IFT train trajectories require high time resolution and signal-to-noise ratio. If these parameters are critical, wide-field techniques such as TIRF microscopy can be a preferred alternative to confocal microscopy. TIRF microscopy uses critical angle illumination, where incident light is totally internally reflected at the glass-sample interface and only ~300 nm deep evanescent field penetrates into the sample ([Martin-Fernandez et al., 2013](#)). This way, most of the background fluorescence is suppressed and contrast sufficient to image single molecules is achieved in the illuminated part of the cells. Most primary cilia are, unfortunately, located in cells such that they are out of the range of a true TIRF microscopy. However, modifications of the TIRF microscopy, sometimes referred to as “pseudo TIRF”, such as highly inclined and laminated optical sheet (HILO) or variable-angle epifluorescence microscopy (VAEM) can be used to illuminate fluorophores deeper in the sample while still gaining significant improvement in signal-to-noise ratio ([Tokunaga et al., 2008](#)) ([Figure 12](#)). VAEM illuminates a sample at a sub-critical angle, at which light does not undergo total internal reflection, but enters the sample at a high inclination. It can be set up on any microscope equipped with a TIRF condenser. Here we demonstrate its use to visualize IFT in primary cilia with high time resolution.

We use an inverted widefield microscope Nikon Eclipse Ti-E equipped with a motorized XY stage, Perfect Focus System, H-TIRF module, Nikon CFI Apo TIRF 60× Oil NA 1.4 objective, 488 nm laser diode illumination and Quad Band Filter Set 405/488/561/640 nm (TRF89901, Chroma). Temperature, humidity and CO₂ concentration were maintained by module for environmental control (Okolab). Images were recorded by an EMCCD Andor iXon Ultra DU888 camera (Andor Technologies) with 1024 × 1024 sensor format, 13 μm × 13 μm pixel size and 16-bit bit depth, controlled by NIS elements Ar 5.02 software.

42. Prepare ciliated hTERT-RPE-1 cells with mNeonGreen-IFT74 marker as described in previous sections.
43. Switch on the microscope, camera, and 488 nm laser illumination.
44. Install the objective-heating collar and environmental control stage insert, allow at least 20 min for the temperature, CO₂ and humidity to stabilize before inserting the sample (see step 18 in the previous section).
45. Start the NIS Elements software.
46. Apply immersion oil to the objective, insert a glass bottom dish with the cells and switch on the “Perfect Focus” system. As the glass/buffer interface has not been detected yet, the “Perfect Focus” button on the microscope will be flashing green.
47. Slowly raise the objective until the immersion oil makes contact with the glass bottom of the dish. Keep raising the objective until the microscope emits a beep and the “Perfect Focus” button stops flashing. This means that the glass/buffer interface has been detected and the “Perfect Focus” is now in control of the objective-sample distance. The focusing knobs on the microscope are no longer active and focus adjustments must be made through the offset control wheel of the “Perfect Focus” system.
48. Switch on 488 nm laser illumination, start “Live” acquisition in NIS Elements, and position the sample to have at least one cilium in the field of view.

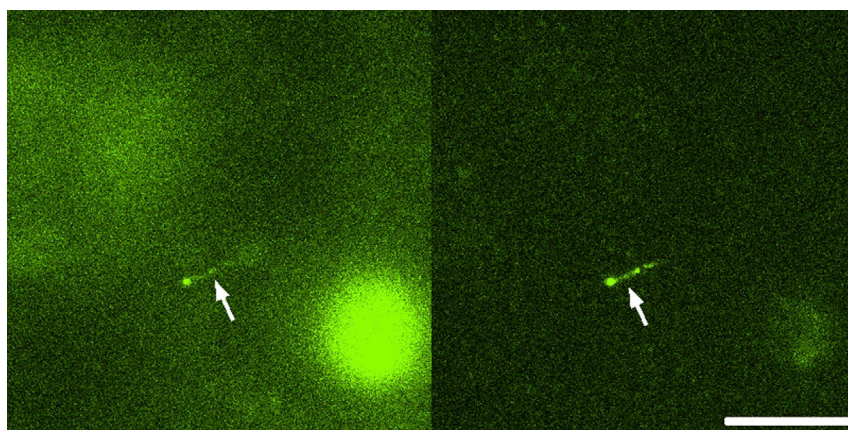


Figure 12. Comparison of epifluorescence microscopy (left) and VAEM (right)

A cilium is marked with an arrow. Note the difference in the background fluorescence signal. Scale bar=10 μ m.

49. You need to set up one microscope configuration with a low laser power for sample screening and another one with a higher laser power for acquisition. There are three main parameters to set (Figure 13): (a) exposure time, (b) illumination angle, and (c) laser power, and optionally also (d) region of interest. Signal-to-background ratio above 1.5 (typically 1,500 gray value background and 2,250 gray value IFT fluorescence) allows reliable tracking of IFT trains, therefore it should be the minimum target for high laser power acquisition.
 - a. Exposure time will be determined by the experimental question. The minimum time we use is 10 ms. Using shorter exposure times does not improve the time resolution much, but reduces the signal-to-noise ratio significantly. Select an appropriate value in the “DU-888 Settings” window (Figure 13A).
 - b. Illumination angle needs to be adjusted for each experiment individually. The position of cilia in individual cells varies, which affects their distance from the glass surface. Hence, the optimal illumination angle also varies and needs to be determined empirically. We recommend adjusting the angle each time the sample dish is replaced, or a dish is moved by a significant distance (more than 2 mm). The illumination angle is set by moving the beam position in X and Y in the “Lapp H-TIRF XY-F Pad” window (Figure 13B). When both values are set to 0, the microscope is in epifluorescence mode.

Note: To find an optimal illumination angle, first determine the critical angle of a true TIRF illumination. At the critical angle, no cilia will be visible, only the cell regions in direct contact with the glass surface. Subsequently, reduce the angle step-by-step towards the epi-illumination mode until cilia start to be visible. Stop when the signal from the ciliary marker starts to be eclipsed by the fluorescence background. As the cilium in focus is partially bleached at this point, move to a different field of view and verify that the signal-to-background ratio is at its optimal level.

Note: The illumination angle will not be consistent across the entire field of view and the optimization and subsequent acquisition should be performed in the same region (usually center) of the field of view.

- c. We typically use laser power of 50%–75% for no more than 40 s of acquisition. When screening samples the laser power should be set to the lowest level which allows localizing the cilia (e.g., 10%) (Figure 13C).

Note: The laser power increases both the signal-to-noise ratio and cell damage significantly and should be set with respect to the intended duration of the acquisition. Several experimental

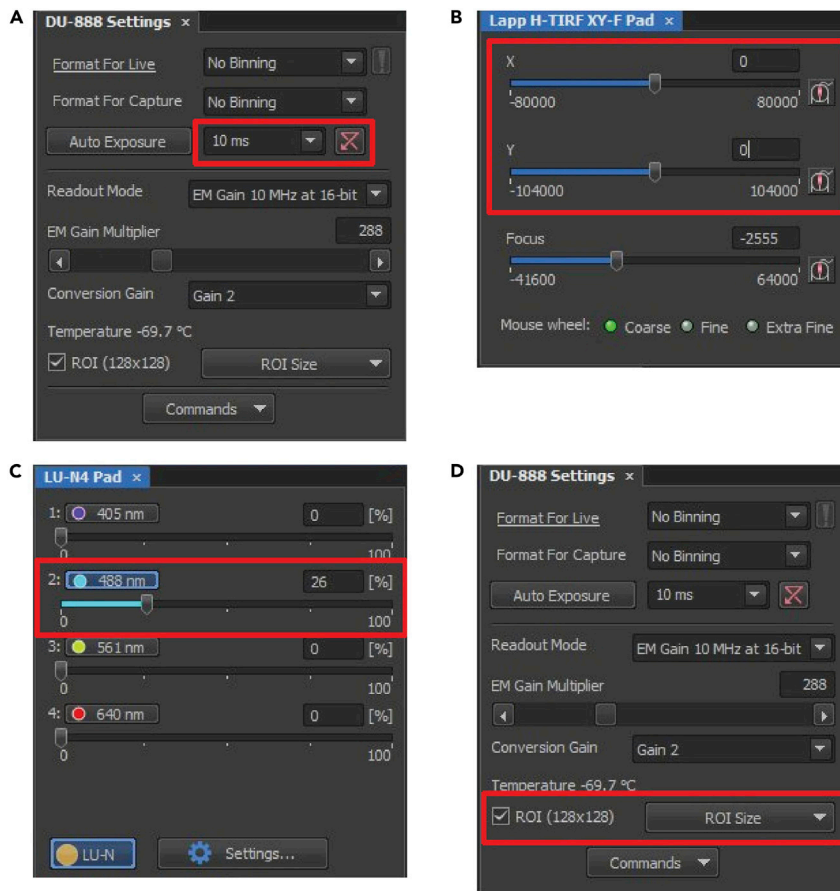


Figure 13. Imaging settings for VAEM, step 62

(A) Exposure time (B) Illumination angle. X and Y sliders set the position of a focused laser beam at the back focal plane of the objective, determining the angle at which light enters the sample. Zero position (shown here) places the beam at the center of the back focal plane, which leads to conventional epifluorescence illumination. Position above 55,000 displaces the beam enough to generate TIRF illumination. (C) Laser intensity setting (D) Region of interest setting.

movies should be recorded first to determine if there is significant bleaching of the fluorophores or cell damage (recognizable by IFT trains slowing down) during the recording.

- d. The full field of view of our camera is 1024×1024 pixels ($88 \mu\text{m}^2$ with our optical setup), which can accommodate several cells and cilia.

Optional: While imaging multiple cells at once can be an advantage, recording full-frame movies comes with significant time overhead in addition to the selected exposure time and reduces the resulting frame rate. For very fast single cilium acquisitions, check "ROI" box at the "DU-888 Settings" panel (Figure 13D) and using "ROI size / Define ROI" define the region of interest of 128×128 pixels (resulting in a $11 \times 11 \mu\text{m}$ field of view with our setup).

50. Once the desired parameters are set for the screening configuration:
 - a. Create a button (Figure 14) for a new configuration in the OC panel, preferably by duplicating an existing TIRF configuration,
 - b. right-click on it and choose "Assign current microscope settings".
 - c. Then change the microscope settings to the desired acquisition configuration,
 - d. again create a new button,
 - e. right-click on it and choose "Assign current microscope settings".

51. Define the experiment flow in the “ND Acquisition” window. For a simple time-lapse experiment, two variables need to be defined: time and optical configuration (Figure 15).
 - a. In the “Time” panel, check “Phase 1” only, set “Interval” to “No Delay” and “Duration” to the desired value.
 - b. In the “Lambda” panel, check the first “Opt. Conf.” option and set it to the optical configuration prepared for acquisition. Set the path for saving movies and appropriate filename base. Software will automatically add incrementing numbers to the filename base if multiple movies are recorded in the same experiment.
52. Switch to the low-power screening configuration and start searching for a suitable cilium to image. Once found, move it to the center of the field of view and bring it into focus with the “Perfect Focus” offset control. If you are using the region of interest option, switch on the “ROI” in the “Camera panel” and reposition the cilium to be fully contained in the visible area.
53. Press the “Run now” button in the “ND Acquisition” window. The optical configuration will switch to the high-power illumination configuration and the movie is recorded.

△ CRITICAL: Time spent on previewing the cell and switching from searching to acquisition should be kept to a minimum to prevent cell damage and photobleaching. It is a good practice to organize the microscope workplace and software layout to have all necessary knobs and buttons at an easy reach.

54. Switch back to the low-power screening configuration and repeat the process with more cilia.

Optional: Review the recorded movie using NIS elements or Fiji to ascertain that the image quality is satisfactory.

EXPECTED OUTCOMES

Analysis of time-lapse videos to study primary cilia dynamics

To assess cilia resorption dynamics using the described protocol, the cells hTERT-RPE-1 Flp-In T-REx TTBK2 KO cells (Bernatik et al., 2020) with DOX-inducible expression of FLAG-TTBK2 and constitutive mNeonGreen-ARL13b reporter, were serum-starved for 24 h, and 10% FBS was added just before the imaging to induce cilium resorption. The primary cilium length was measured using a segmented-line tool for selection of the fluorescence signal of the ciliary marker in maximum Z intensity projected images in Fiji (see step 49c and Methods Video S2). Representative images were acquired every 1 h (Figure 16). Alternatively, starting the experiment right after the serum starvation step will allow to image the cilia growth in time. From the measured lengths, it is also possible to calculate cilia growth/resorption speed, as described e.g., in (Pejskova et al., 2020).

Imaging of IFT transport in primary cilia of living cells

Following the protocol in the section “Imaging of IFT transport in primary cilia of living cells”, we obtained a time-lapse movie (150 images, 1 image per 200 ms), which shows the movement of IFT trains (Methods Video S1).

Based on the kymograph analysis of the time-lapse image sequence, we can determine the length of the primary cilium (see step 49c), frequency (see step 53) of the anterograde and retrograde IFT74 trains, and also their velocity (see step 54). The length of our measured primary cilium is 4.366 μm (Figure 17A). We detected 6 anterograde trains and 5 retrograde trains within 30 s of recording (Figure 17B). The velocities of the individual IFT74 trains were calculated in step 54, giving 0.54 $\mu\text{m/s}$ on average for anterograde transport and 0.32 $\mu\text{m/s}$ on average for retrograde transport (Figure 17C).

Imaging IFT transport using variable-angle epifluorescence (VAEM) microscopy

VAEM microscopy is particularly suited for detailed study of individual IFT trajectories. The high temporal resolution achieved by this technique allows quantifying not only the average velocity of an IFT train, but also any changes in speed, pausing, or collisions (Figure 18).

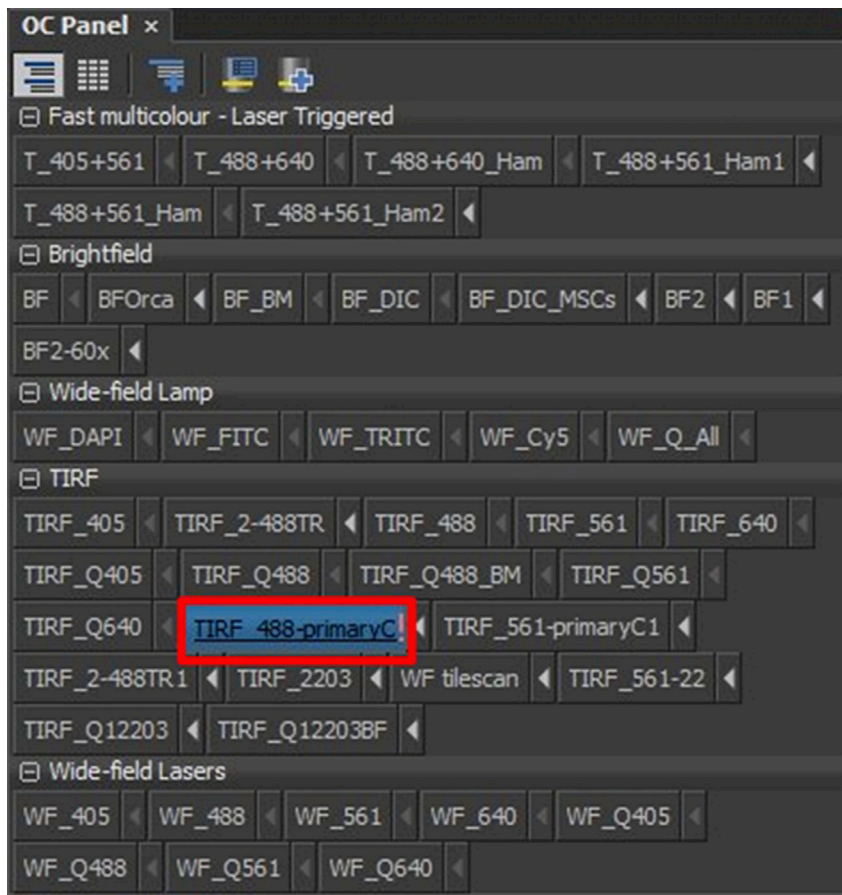


Figure 14. Selection of optical configuration, step 63

Highlighted button sets up the high-power illumination configuration. Right-click on the button offers the option "Assign current microscope settings" to update the configuration.

LIMITATIONS

We have combined two strategies to generate primary cilia reporter cell lines to study the cilia dynamics, namely the rate of cilia assembly/disassembly as well as the IFT transport, using high time resolution live-cell imaging microscopy. We consider the described protocol sufficiently robust, as it represents a joined effort of three labs where it has been successfully implemented. Nonetheless, certain inherent limitations need to be considered. Some of them have been already discussed in the protocol or are mentioned in the [troubleshooting](#) section.

Probably the most critical factor for successful analysis of primary cilia using time-lapse microscopy (and even more so in the case of IFT analysis) is the signal-to-background noise ratio. This parameter is typically affected by several factors, such as properties and position (N-terminal or C-terminal) of the selected fluorescent tag, the level of expression of the cilium reporter in a given cell line, relative enrichment of the reporter in the cilium compartment over the cytoplasm, as well as the abilities and settings of the microscope used for the analysis. Thus, it is important to bear in mind that trade-offs often need to be considered (sufficient signal intensity vs. signal bleaching over time, high speed of imaging vs. phototoxicity, etc.). For example, the laser power increases both the signal and cell damage significantly. Therefore, it should be always set with respect to the planned duration of the acquisition.

Additional point we want to mention relates to an automated image analysis. Various tools have been recently described ([Bansal et al., 2021](#); [Hansen et al., 2021](#); [Lauring et al., 2019](#)) and

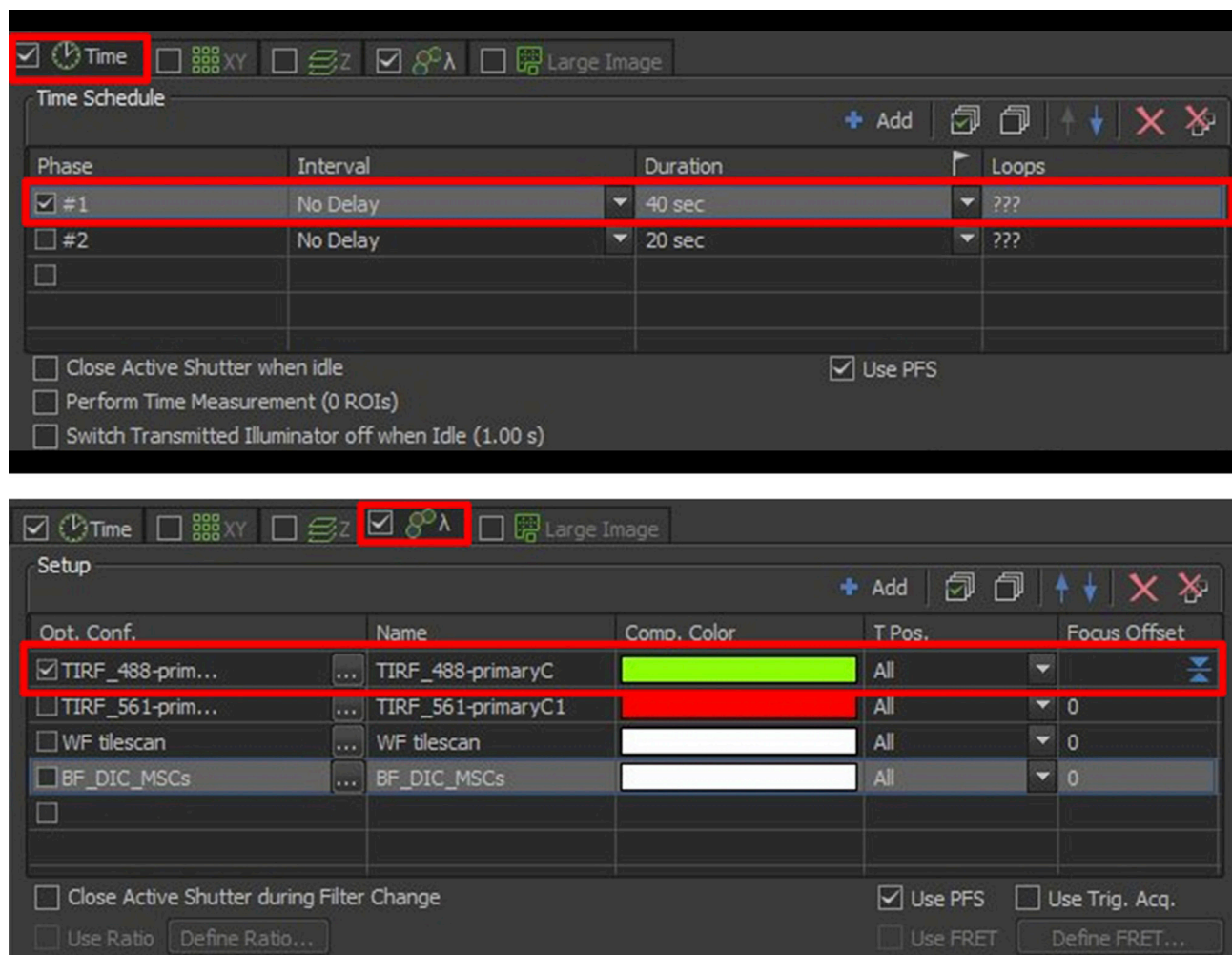


Figure 15. Setting up an experiment acquisition, step 64

In the "Time" panel, select one phase with interval option "No delay". In the "Lambda" panel select one optical configuration and set to the high-power illumination configuration.

successfully implemented by us as well as others to unbiasedly determine cilia properties (e.g., cilia number, length, signal intensity, etc.) from the acquired images. Similarly, tools for automated kymograph analysis are becoming available (Jakobs et al., 2019; Mangeol et al., 2016) and thus could be used for IFT analysis. We have not tested automated segmentation or automatic kymograph analysis in our IFT analysis experiments. These approaches offer to significantly speed up the process, in contrast to analysis done "manually". On the other hand, they might struggle with correct detection of the IFT signal in cilia (as the IFT signal in cilia is typically "non-static", not forming a full line).

Limitation of any reporter-based system, including the one described here, is that a reporter might alter properties of the system. As already mentioned, we and others noted that ARL13b overexpression has positive effect on cilia length. Such factors need to be taken in account when planning your experiments (e.g., by examining possible effect of particular cilia reporter on length/dynamics of cilia in newly established stable cell line). Gene editing to insert a fluorescence reporter into the locus of suitable gene ("endogenous tagging" (Bauer et al., 2016; Cho et al., 2021)) may bypass the "overexpression" problem, but with a risk of insufficient signal strength for planned live-cell imaging experiments.

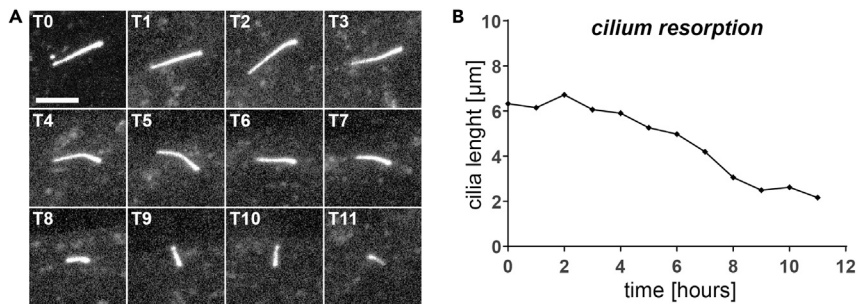


Figure 16. Outcome of analysis of the time-lapse videos

(A) maximum Z intensity projected representative images of resorbing cilium.

(B) Cilium length (μm) as measured over time. Scale bar=5 μm.

When implementing this protocol for your needs (especially when you need to adapt it for your particular cell line or protein of choice) always perform small-scale pilot experiments first to determine if there is significant bleaching of the fluorophores or cell damage. A visible slowdown of IFT movements during the acquisition is typically a sign of extensive cell damage by the applied laser illumination.

In general, low expression plasmids are preferred as reporters, as you reduce the chance of getting overexpression artifacts. On the other hand, this may cause problems when trying to get a sufficient signal-to-background noise ratio during the imaging.

TROUBLESHOOTING

Problem 1

Generation of stable cell line Flp-InTM T-RExTM gives either no surviving clones following the antibiotics selection or obtained clones show no expression of the used transgene (step 3).

Potential solution

No surviving colony typically indicates too harsh selection pressure. Consider carefully optimizing the effective concentration and time of the selection of antibiotics for your cell line before starting. An outgrowth of “empty” clones (no detectable expression of the transgene) typically indicates toxicity of the used transgene in the given cell line, so there is a negative selection pressure among the stable transfectants. A solution to that is to either use a different transgene or a different cell line, if possible.

Problem 2

Inefficient production of viral particles (low yield) (steps 5–9).

Potential solution

The production of viral particles can be improved by several factors. First, we recommend using the low passage of the Phoenix-Ampho cells. Prolonged cultivation of these cells (>3 weeks) in our hands typically leads to a drop in the virus production efficiency. In addition, prolonged transfection time generally gives higher transfection efficiency and in turn higher virus titer. We also observed that co-transfection with pCL-Ampho plasmid (Naviaux et al., 1996) may further increase the efficiency of virus production. Consider upscaling the protocol (increase the target cell number, amount of viral particle medium, etc. accordingly) to get more transduced cells to start with.

Problem 3

Low efficiency of viral transduction (steps 10–12).

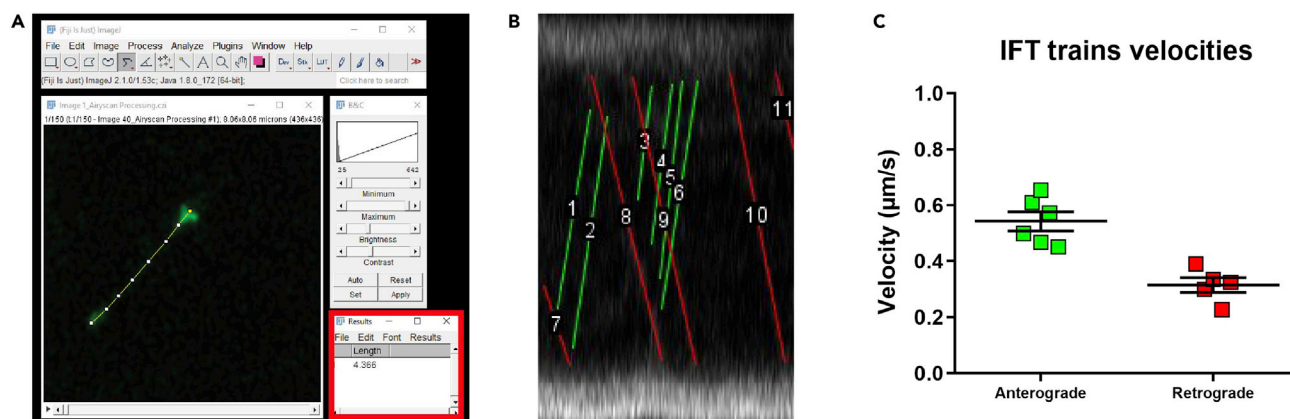


Figure 17. Outcomes of IFT74 transport in primary cilium of living cells analysis

(A–C) Length of the primary cilium (A), number (B) and velocity (C) of the anterograde and retrograde IFT74 trains were determined. Error bars represent mean with SEM.

Potential solution

In many situations, simple upscaling of the protocol helps to get a sufficient number of transduced cells for their subsequent isolation by cell sorting. In addition, we use Polybrene (Hexadimethrine bromide) in our protocol, a small, positively charged molecule that binds to cell surfaces and facilitates binding between virus particles and the cellular membrane. As the doses of Polybrene used typically differ between labs/protocols, optimizing the concentration of Polybrene is expected to improve transduction efficiency. There are alternatives to Polybrene such as dextran which may be also considered.

Problem 4

No or only very few cilia were detected in the live-cell imaging experiment (steps 14–16, 34–36, 55).

Potential solution

A low number of cilia seen in live-cell imaging experiments can be caused by several different problems. First, determine whether the problem stems from a suboptimal cilia formation or suboptimal signal detection of the used cilia reporter (cilia are formed, but hard to detect). In the former case, use healthy cells, consider thawing a low passage aliquot of the cells, and check routinely for Mycoplasma. In addition, to promote ciliogenesis, try to optimize the cell density, length of serum starvation period, or consider using small molecules promoting cilia formation (e.g., Cytochalasin D (Bernatik et al., 2021; Kim et al., 2010)). In case the cilia presence is DOX-inducible (i.e., in the case of rescue experiment), we observed that adding DOX already 1–2 days prior to seeding the cells for imaging experiment results in a better rescue effect. If the absence of cilia is rather a detection problem, consider fine-tuning the settings of your imaging system. Bear in mind that boosting your signal often comes with the cost of increased cytotoxicity or photobleaching. See also [troubleshooting 5](#) and [7](#).

Problem 5

Extensive cytotoxicity in a live-cell imaging experiment (steps 14–16, 29, 34–36, 55).

Potential solution

Consider shortening the starvation period, also always try to keep the laser intensity as low as possible. For long time-lapse experiments, make sure there is a sufficient amount of medium (even its partial evaporation often leads to stress that may affect cell survival). In addition, consider increasing the time between taking individual images during the time-lapse session.

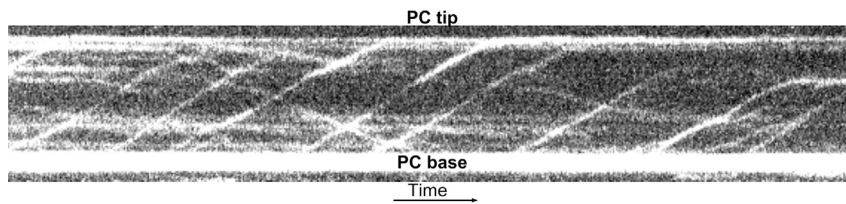


Figure 18. Outcome of the variable angle epifluorescence microscopy imaging of intraflagellar transport in the primary cilium of an RPE-1 cell

Total duration of the movie is 40 s, the length of the cilium is 8 μm .

Problem 6

Cells move out of the imaged area during time-lapse recording (see LSM800 microscope parameters in chapter “Analysis of time-lapse videos to study primary cilia dynamics” and steps 14, 24).

Potential solution

Try to increase cell density, as cells tend to migrate and thus can “escape” from the field of view more at lower densities. A further strategy to reduce the impact of cell migration during long time-lapse experiments is to try to increase the imaged area or eventually to use an objective with lower magnification. Using lower laser power helps here as well, as we have often observed that cells tend to escape from the illuminated area when the laser power is set too high.

Problem 7

Weak signal/fast bleaching during measurement of the IFT transport (steps 43, 62c).

Potential solution

A very common problem when analyzing cilia by live-cell imaging approaches, which is not easy to solve and is one of the reasons we have included two protocols describing how to measure IFT transport in mammalian cilia. In general, try to use as low laser power as possible in your experiments. If the problem is at the reporter side, consider to FACS sort a cell population with sufficient expression of your reporter and try to use cells with the low passage as the reporter expression may be silenced in higher passages. If none of that helps, consider using a different reporter and/or cell line for your experiments. Using several copies of the same fluorescent protein for tagging (e.g., triple mNeon-Green) will boost the signal, but bear in mind large tags might affect the function of your tagged protein.

RESOURCE AVAILABILITY

Lead contact

Further information and requests for resources and reagents should be directed to and will be fulfilled by the lead contact, Lukáš Čajánek (cajanek@med.muni.cz).

Materials availability

Unique reagents (i.e., plasmids or cell lines) generated in this study can be requested from the lead contact.

Data and code availability

This study did not generate datasets/code.

SUPPLEMENTAL INFORMATION

Supplemental information can be found online at <https://doi.org/10.1016/j.xpro.2022.101199>.

ACKNOWLEDGMENTS

This work was supported by grants from the Czech Science Foundation (19-05244S, 21-21612S, and 22-13277S) and the Swiss National Science Foundation (IZ11Z0_166533) to L.C. L.S. was supported by the European Union's Horizon 2020 research and innovation program under the Marie Skłodowska-Curie grant agreement no. 846796 and P.G. by the Charles University project GA UK no. 972120. We acknowledge the core facility CELLIM at Masaryk University and the Imaging Methods Core Facility at BIOCEV, both supported by the Czech-BioImaging large RI project (LM2018129 funded by MEYS CR), for their assistance with obtaining scientific data presented in this article.

AUTHOR CONTRIBUTIONS

L.B. acquired data and prepared figures related to viral transduction and live-cell imaging microscopy. E.M. acquired data and prepared figures related to viral transduction and live-cell imaging microscopy. L.S. acquired data and prepared figures related to live-cell imaging microscopy. O.B. acquired data related to stable cell lines generation. D.V. acquired data related to stable cell lines generation. P.P. and P.G. generated reagents and optimized protocols. L.C. coordinated the study. All authors wrote and edited the manuscript.

DECLARATION OF INTERESTS

The authors declare no competing interests.

REFERENCES

- Bansal, R., Engle, S.E., Kamba, T.K., Brewer, K.M., Lewis, W.R., and Berbari, N.F. (2021). Artificial intelligence approaches to assessing primary cilia. *J. Vis. Exp.* e62521. <https://doi.org/10.3791/62521>.
- Bauer, M., Cubizolles, F., Schmidt, A., and Nigg, E.A. (2016). Quantitative analysis of human centrosome architecture by targeted proteomics and fluorescence imaging. *EMBO J.* 35, 2152–2166. <https://doi.org/10.15252/embj.201694462>.
- Bernatik, O., Paclikova, P., Kotrbova, A., Bryja, V., and Cajanek, L. (2021). Primary cilia formation does not rely on WNT/ β -catenin signaling. *Front. Cell Dev. Biol.* 9, 623753. <https://doi.org/10.3389/fcell.2021.623753>.
- Bernatik, O., Pejškova, P., Vyslouzil, D., Hanakova, K., Zdrahal, Z., and Cajanek, L. (2020). Phosphorylation of multiple proteins involved in ciliogenesis by Tau Tubulin kinase 2. *Mol. Biol. Cell* 31, 1032–1046. <https://doi.org/10.1091/mbc.E19-06-0334>.
- Bhogaraju, S., Cajanek, L., Fort, C., Blisnick, T., Weber, K., Taschner, M., Mizuno, N., Lamla, S., Bastin, P., Nigg, E.A., and Lorentzen, E. (2013). Molecular basis of tubulin transport within the cilium by IFT14 and IFT181. *Science* 341, 1009–1012. <https://doi.org/10.1126/science.1240985>.
- Caspary, T., Larkins, C.E., and Anderson, K.V. (2007). The graded response to Sonic Hedgehog depends on cilia architecture. *Dev. Cell* 12, 767–778. <https://doi.org/10.1016/j.devcel.2007.03.004>.
- Cho, N.H., Cheveralls, K.C., Brunner, A.-D., Kim, K., Michaelis, A.C., Raghavan, P., Kobayashi, H., Savy, L., Li, J.Y., Canaj, H., et al. (2021). OpenCell: proteome-scale endogenous tagging enables the cartography of human cellular organization. <https://doi.org/10.1101/2021.03.29.437450>.
- Goetz, S.C., Liem, K.F., Jr., and Anderson, K.V. (2012). The spinocerebellar ataxia-associated gene Tau tubulin kinase 2 controls the initiation of ciliogenesis. *Cell* 151, 847–858. <https://doi.org/10.1016/j.cell.2012.10.010>.
- Hansen, J.N., Rassmann, S., Stüven, B., Jurisch-Yaksi, N., and Wachten, D. (2021). CiliaQ: a simple, open-source software for automated quantification of ciliary morphology and fluorescence in 2D, 3D, and 4D images. *Eur. Phys. J. E Soft Matter* 44, 18. <https://doi.org/10.1140/epje/s10189-021-00031-y>.
- Ishikawa, H., and Marshall, W.F. (2015). Efficient live fluorescence imaging of intraflagellar transport in mammalian primary cilia. *Methods Cell Biol.* 127, 189–201. <https://doi.org/10.1016/bs.mcb.2015.01.002>.
- Jakobs, M.A., Dimitracopoulos, A., and Franze, K. (2019). KymoButler, a deep learning software for automated kymograph analysis. *eLife* 8, e42288. <https://doi.org/10.7554/eLife.42288>.
- Kiesel, P., Alvarez Viar, G., Tsoy, N., Maraschini, R., Gorilak, P., Varga, V., Honigsmann, A., and Pigino, G. (2020). The molecular structure of mammalian primary cilia revealed by cryo-electron tomography. *Nat. Struct. Mol. Biol.* 27, 1115–1124. <https://doi.org/10.1038/s41594-020-0507-4>.
- Kim, J., Lee, J.E., Heynen-Genel, S., Suyama, E., Ono, K., Lee, K., Ideker, T., Aza-Blanc, P., and Gleeson, J.G. (2010). Functional genomic screen for modulators of ciliogenesis and cilium length. *Nature* 464, 1048–1051. <https://doi.org/10.1038/nature08895>.
- Larkins, C.E., Aviles, G.D.G., East, M.P., Kahn, R.A., and Caspary, T. (2011). Arl13b regulates ciliogenesis and the dynamic localization of Shh signaling proteins. *MBio* 22, 4694–4703. <https://doi.org/10.1091/mbc.e10-12-0994>.
- Lauring, M.C., Zhu, T., Luo, W., Wu, W., Yu, F., and Toomre, D. (2019). New software for automated cilia detection in cells (ACDC). *Cilia* 8, 1. <https://doi.org/10.1186/s13630-019-0061-z>.
- Longo, P.A., Kavran, J.M., Kim, M.-S., and Leahy, D.J. (2013). Transient mammalian cell transfection with polyethylenimine (PEI). *Methods Enzymol.* 529, 227–240. <https://doi.org/10.1016/B978-0-12-418687-3.00018-5>.
- Mangeol, P., Prevo, B., and Peterman, E.J.G. (2016). KymographClear and KymographDirect: two tools for the automated quantitative analysis of molecular and cellular dynamics using kymographs. *MBio* 27, 1948–1957. <https://doi.org/10.1091/mbc.e15-06-0404>.
- Martin-Fernandez, M., Tynan, C., and Webb, S. (2013). A 'pocket guide' to total internal reflection fluorescence. *J. Microsc.* 252, 16–22. <https://doi.org/10.1111/jmi.12070>.
- Mazo, G., Soplop, N., Wang, W.J., Uryu, K., and Tsou, M.B. (2016). Spatial control of primary ciliogenesis by subdistal appendages alters sensation-associated properties of cilia. *Dev. Cell* 39, 424–437. <https://doi.org/10.1016/j.devcel.2016.10.006>.
- Mok, H.P., Javed, S., and Lever, A. (2007). Stable gene expression occurs from a minority of integrated HIV-1-based vectors: transcriptional silencing is present in the majority. *Gene Ther.* 14, 741–751. <https://doi.org/10.1038/sj.gt.3302923>.
- Naviaux, R.K., Costanzi, E., Haas, M., and Verma, I.M. (1996). The pCL vector system: rapid production of helper-free, high-titer, recombinant retroviruses. *J. Virol.* 70, 5701–5705. <https://doi.org/10.1128/JVI.70.8.5701-5705.1996>.
- Pejšková, P., Reilly, M.L., Bino, L., Bernatik, O., Dolanska, L., Ganji, R.S., Zdrahal, Z., Benmerah, A., and Cajanek, L. (2020). KIF14 controls ciliogenesis via regulation of Aurora A and is important for Hedgehog signaling. *J. Cell Biol.* 219, e201904107. <https://doi.org/10.1083/jcb.201904107>.
- Prasai, A., Schmidt Cernohorska, M., Ruppova, K., Niederlova, V., Andelova, M., Draber, P., Stepanek, O., and Huranova, M. (2020). The BBSome

assembly is spatially controlled by BBS1 and BBS4 in human cells. *J. Biol. Chem.* 295, 14279–14290. <https://doi.org/10.1074/jbc.RA120.013905>.

Rosenbaum, J.L., and Witman, G.B. (2002). Intraflagellar transport. *Nat. Rev. Mol. Cell Biol.* 3, 813–825. <https://doi.org/10.1038/nrm952>.

Schindelin, J., Arganda-Carreras, I., Frise, E., Kaynig, V., Longair, M., Pietzsch, T., Preibisch, S., Rueden, C., Saalfeld, S., Schmid, B., et al. (2012). Fiji: an open-source platform for biological-image analysis. *Nat. Methods* 9, 676–682. <https://doi.org/10.1038/nmeth.2019>.

Shaner, N.C., Lambert, G.G., Chammas, A., Ni, Y., Cranfill, P.J., Baird, M.A., Sell, B.R., Allen, J.R., Day,

R.N., Israelsson, M., et al. (2013). A bright monomeric green fluorescent protein derived from *Branchiostoma lanceolatum*. *Nat. Methods* 10, 407–409. <https://doi.org/10.1038/nmeth.2413>.

Sorokin, S. (1962). Centrioles and the formation of rudimentary cilia by fibroblasts and smooth muscle cells. *J. Cell Biol.* 15, 363–377.

Sowa, M.E., Bennett, E.J., Gygi, S.P., and Harper, J.W. (2009). Defining the human deubiquitinating enzyme interaction landscape. *Cell* 138, 389–403. <https://doi.org/10.1016/j.cell.2009.04.042>.

Swift, S., Lorens, J., Achacoso, P., and Nolan, G.P. (1999). Rapid production of retroviruses for efficient

gene delivery to mammalian cells using 293T cell-based systems. *Curr. Protoc. Immunol.* 31, 10.17.14–10.17.29. <https://doi.org/10.1002/0471142735.im1017cs31>.

Tokunaga, M., Imamoto, N., and Sakata-Sogawa, K. (2008). Highly inclined thin illumination enables clear single-molecule imaging in cells. *Nat. Methods* 5, 159–161. <https://doi.org/10.1038/nmeth1171>.

Ward, R.J., Alvarez-Curto, E., and Milligan, G. (2011). Using the Flp-InTM T-RexTM system to regulate GPCR expression. *Methods Mol. Biol.* 746, 21–37. https://doi.org/10.1007/978-1-61779-126-0_2.

Appendix 7

Bernatik O, Paclikova P, Kotrbova A, Bryja V, **Cajane L***. Primary Cilia Formation Does Not Rely on WNT/ β -Catenin Signaling. *Front Cell Dev Biol.* 2021 Feb 26;9:623753. doi: 10.3389/fcell.2021.623753.(JCR 2021. IF=6.081, Q1 – Developmental Biology)



Primary Cilia Formation Does Not Rely on WNT/ β -Catenin Signaling

Ondrej Bernatik¹, Petra Paclikova², Anna Kotrbova², Vitezslav Bryja² and Lukas Cajanek^{1*}

¹ Department of Histology and Embryology, Faculty of Medicine, Masaryk University, Brno, Czechia, ² Section of Animal Physiology and Immunology, Department of Experimental Biology, Faculty of Science, Masaryk University, Brno, Czechia

OPEN ACCESS

Edited by:

Francesc R. Garcia-Gonzalo,
Autonomous University of Madrid,
Spain

Reviewed by:

Helen Louise May-Simera,
Johannes Gutenberg University
Mainz, Germany
Colin Anfimov Johnson,
University of Leeds, United Kingdom

*Correspondence:

Lukas Cajanek
cajanek@med.muni.cz;
lukas.cajanek@gmail.com

Specialty section:

This article was submitted to
Cell Adhesion and Migration,
a section of the journal
Frontiers in Cell and Developmental
Biology

Received: 30 October 2020

Accepted: 04 January 2021

Published: 26 February 2021

Citation:

Bernatik O, Paclikova P,
Kotrbova A, Bryja V and Cajanek L
(2021) Primary Cilia Formation Does
Not Rely on WNT/ β -Catenin
Signaling.
Front. Cell Dev. Biol. 9:623753.
doi: 10.3389/fcell.2021.623753

Primary cilia act as crucial regulators of embryo development and tissue homeostasis. They are instrumental for modulation of several signaling pathways, including Hedgehog, WNT, and TGF- β . However, gaps exist in our understanding of how cilia formation and function is regulated. Recent work has implicated WNT/ β -catenin signaling pathway in the regulation of ciliogenesis, yet the results are conflicting. One model suggests that WNT/ β -catenin signaling negatively regulates cilia formation, possibly via effects on cell cycle. In contrast, second model proposes a positive role of WNT/ β -catenin signaling on cilia formation, mediated by the re-arrangement of centriolar satellites in response to phosphorylation of the key component of WNT/ β -catenin pathway, β -catenin. To clarify these discrepancies, we investigated possible regulation of primary cilia by the WNT/ β -catenin pathway in cell lines (RPE-1, NIH3T3, and HEK293) commonly used to study ciliogenesis. We used WNT3a to activate or LGK974 to block the pathway, and examined initiation of ciliogenesis, cilium length, and percentage of ciliated cells. We show that the treatment by WNT3a has no- or lesser inhibitory effect on cilia formation. Importantly, the inhibition of secretion of endogenous WNT ligands using LGK974 blocks WNT signaling but does not affect ciliogenesis. Finally, using knock-out cells for key WNT pathway components, namely DVL1/2/3, LRP5/6, or AXIN1/2 we show that neither activation nor deactivation of the WNT/ β -catenin pathway affects the process of ciliogenesis. These results suggest that WNT/ β -catenin-mediated signaling is not generally required for efficient cilia formation. In fact, activation of the WNT/ β -catenin pathway in some systems seems to moderately suppress ciliogenesis.

Keywords: primary cilia, Wnt/ β -catenin, ciliogenesis, cell signaling, Wnt3a, RPE-1, HEK293, NIH3T3

INTRODUCTION

Primary cilia are tubulin-based rod-shaped organelles on the surface of most mammalian cells. They play a fundamental role in embryo development and tissue homeostasis. Importantly, defects in primary cilia structure and function lead to variety of developmental disorders collectively called ciliopathies (Hildebrandt et al., 2011; Mitchison and Valente, 2017; Reiter and Leroux, 2017). Moreover, primary cilia defects have been related to cancer (Han et al., 2009; Wong et al., 2009; Jenks et al., 2018).

Cilium formation is organized by the mother centriole (MC)-derived basal body, the older centriole of the pair that makes up the centrosome. While centrosome is best known as microtubule

organizing center coordinating mitosis, primary cilium formation is tightly connected with G1/G0 phase (Ford et al., 2018; Mirvis et al., 2018). The growth of primary cilium itself is preceded by the accumulation of vesicles at MC distal appendages (Sorokin, 1962; Westlake et al., 2011; Schmidt et al., 2012; Lu et al., 2015; Wu et al., 2018) and by the removal of CEP97/CP110 capping complex specifically from MC distal end (Spektor et al., 2007). Major role in the cilia initiation is linked to the Tau tubulin kinase 2 (TTBK2) activity (Goetz et al., 2012). Once recruited to MC by distal appendage protein CEP164 (Čajánek and Nigg, 2014; Oda et al., 2014), TTBK2 seems to control both the process of vesicle docking and the CP110/CEP97 removal (Goetz et al., 2012; Lo et al., 2019). In turn, this allows the extension of tubulin-based axoneme sheathed by ciliary membrane from MC-derived basal body. The formed cilium is physically separated from the rest of a cell by ciliary transition zone, a selective barrier ensuring only specific proteins to enter the cilium (García-Gonzalo and Reiter, 2017; Gonçalves and Pelletier, 2017; Nachury, 2018). Such compartmentation and hence specific protein composition of primary cilium is the basis for its instrumental role in the Hedgehog signaling pathway in vertebrates (Bangs and Anderson, 2017; Nachury and Mick, 2019). In addition, several links between primary cilia and other signaling pathways such as WNT or TGF- β have recently emerged (Anvarian et al., 2019).

WNT signaling pathways are developmentally important signaling routes regulating cell differentiation, migration, and proliferation and their activity controls shaping of the embryo (Nusse and Clevers, 2017). WNT signaling pathways can be distinguished based on whether they use β -catenin as an effector protein. The pathway relying on stabilization of β -catenin is termed the WNT/ β -catenin pathway and regulates stemness, cell differentiation and proliferation, while the β -catenin-independent or non-canonical WNT pathways regulate cytoskeleton, cell polarity, and cell movements (Humphries and Mlodzik, 2018; Steinhart and Angers, 2018). These two branches of WNT pathways are activated by a distinct set of extracellularly secreted WNT ligand proteins (Angers and Moon, 2009). WNTs are posttranslationally palmitoylated by O-Acyl-transferase Porcupine, and only after the lipid modification are the WNT proteins fully active (Willert et al., 2003; Zhai et al., 2004). Following their secretion, WNTs bind to seven-pass transmembrane receptors from Frizzled family that form heterodimeric complexes with various coreceptors. WNT/ β -catenin pathway uses LRP5/6 coreceptors (Pinson et al., 2000; Tamai et al., 2000; Wehrli et al., 2000). Signal received by the receptor-coreceptor pair on the cell membrane is then relayed to Dishevelled (DVL) proteins that, following phosphorylation by CK1- δ/ϵ and other kinases (Bernatik et al., 2011; González-Sancho et al., 2013; Hanáková et al., 2019), are used both by the non-canonical and the WNT/ β -catenin pathways (Sokol, 1996; Wallingford et al., 2000). β -catenin destruction complex, composed of proteins Adenomatous polyposis coli (APC), AXIN and two kinases; GSK3- β and CK1- α , is then inactivated by DVL sequestration of AXIN proteins (Tamai et al., 2004). Then β -catenin phosphorylation by GSK3- β and CK1- α on its N-terminal degron is terminated and the non-phosphorylated

Active β -catenin (ABC) accumulates, translocates to the nucleus where it binds transcription factors of TCF-LEF family to trigger transcription of target genes (Behrens et al., 1996; Molenaar et al., 1996). Not surprisingly, many developmental disorders and cancers are directly caused by WNT pathways deregulation (Zhan et al., 2017; Humphries and Mlodzik, 2018).

Whilst the connections between primary cilia and hedgehog signaling are well documented (Huangfu et al., 2003; Corbit et al., 2005; Rohatgi et al., 2007), the relationship between cilia and WNT signaling is still rather controversial. The exception here seems to be the WNT/PCP pathway [one of the non-canonical WNT pathways (Butler and Wallingford, 2017)], which was described to affect cilia formation and functions via effects on cytoskeleton and basal body positioning (Wallingford and Mitchell, 2011; May-Simera and Kelley, 2012; Carvajal-Gonzalez et al., 2016; Bryja et al., 2017). As for the WNT/ β -catenin pathway, there are reports showing that primary cilia loss or disruption leads to upregulation of the pathway activity (Corbit et al., 2008; McDermott et al., 2010; Wiens et al., 2010; Lancaster et al., 2011; Liu et al., 2014; Zingg et al., 2018; Patnaik et al., 2019), but also studies that deny any involvement of primary cilia in WNT/ β -catenin signaling (Huang and Schier, 2009; Ocbina et al., 2009). Some of these discrepancies can perhaps be explained by context-specific activity of involved ciliary components (Lancaster et al., 2011; Patnaik et al., 2019) or effects directly on WNT/ β -catenin pathway independently of the role in cilia formation (Balmer et al., 2015; Kim et al., 2016), or the requirement for intact basal bodies rather than cilia (Vertii et al., 2015; Vora et al., 2020).

To make the matters even more puzzling, two opposing models have recently emerged regarding possible function of WNT/ β -catenin pathway in cilia formation. Activation of the WNT/ β -catenin pathway in neural progenitors of the developing cerebral cortex was reported to hamper cilia formation in mice (Nakagawa et al., 2017), arguing for a negative role of the excessive WNT/ β -catenin signaling in ciliogenesis. In contrast, a recent report described a direct involvement of WNT/ β -catenin signaling pathway in promotion of primary cilia formation through β -catenin driven stabilization of centriolar satellites in RPE-1 cell line (Kyun et al., 2020). We approached this conundrum using cell lines that commonly serve as ciliogenesis model systems (RPE-1, NIH3T3, and HEK293). Using either pharmacological or genetic means to manipulate the WNT/ β -catenin pathway, we found no evidence of facilitated ciliogenesis in response to the activation of WNT/ β -catenin signaling.

MATERIALS AND METHODS

Cell Culture

RPE-1 cells were grown in DMEM/F12 (Thermo Fisher Scientific, 11320033) supplemented by 10% FBS (Biosera, cat. No. FB-1101/500), 1% Penicillin/Streptomycin (Biosera, cat. No. XC-A4122/100) and 1% L-glutamine (Biosera, cat. No. XC-T1715/100), HEK293 T-Rex (referred to as HEK293, cat.no. R71007, Invitrogen) and NIH3T3 cells were grown in DMEM

Glutamax® (Thermo Fisher Scientific, 10569069) supplemented by 10% FBS and 1% Penicillin/Streptomycin. Where indicated, RPE-1 cells were starved by serum free medium, NIH3T3 cells were starved by 0.1% FBS containing medium, and HEK293 cells were starved by serum free medium for 24 h. Cells were seeded at 50,000/well (RPE-1 and NIH3T3) or 120000/well (HEK293) of 24 well plate. Treatments by small molecules were done for indicated times: LGK974 (0.4 μ M) (Sellck, cat. No. S7143) for 72 h (LGK974 was re-added to the starvation medium as indicated in **Figure 2A**), Cytochalasin D (500nM) (Merck Cat. No. C8273) for 16 h, PF670462 (1 μ M) (Merck, SML0795) for 24 h. WNT3a (90 ng/ml) (R&D systems, Cat.no. 5036-WN) for 2 h or 24 h.

Western Blot and Quantification

Western blot was performed as previously described (Bernatik et al., 2020). Antibodies used: LRP6 (Cell signaling, Cat.no. #2560), Phospho-LRP5/6 (Ser1493/Ser1490; Cell signaling, Cat.no. #2568), AXIN1 (Cell signaling, Cat.no. #3323) DVL2 (Cell signaling, Cat.no. #3216), Active- β -catenin (Merck, Cat. no. 05-665-25UG), and α -tubulin (Proteintech, Cat.no. 66031-1-Ig). Quantifications were performed using Fiji distribution of ImageJ. Intensity of pLRP5/6 and ABC band was measured and normalized to mean value from all conditions of given experiment. Intensity of LRP6 and DVL2 was calculated as the ratio of the upper to lower band intensity (the bands are indicated by arrows in the corresponding Figures) and normalized to mean value from all conditions of given experiment. Quantification was performed on $n = 3$. Statistical analyses by students t -test or one-way ANOVA were performed using Graphpad Prism, $P < 0.05$ (*), $P < 0.01$ (**), $P < 0.001$ (***), and $P < 0.0001$ (****).

Immunocytochemistry

RPE-1, NIH3T3 and HEK293 cells were seeded on glass coverslips, treated as indicated, washed by PBS and fixed for 10 min in -20°C methanol, washed 3 \times by PBS, blocked (2% BSA in PBS with 0.01% NaN_3), 3 \times washed by PBS, incubated with primary antibodies for 1 h, 3 \times washed by PBS, incubated with secondary antibodies (Goat anti-Rabbit IgG Alexa Fluor 488 Secondary Antibody, Cat.no. A11008; Goat anti-Mouse IgG Alexa Fluor 568 Secondary Antibody, Cat.no. A11031, all from Thermo Fisher Scientific) for 2 h in dark, washed 3 \times by PBS, incubated 5 min with DAPI, 2 \times washed by PBS and mounted to glycerol (DAKO #C0563). Microscopy analysis was done using Zeiss AxioImager.Z2 with Hamamatsu ORCA Flash 4.0 camera, 63 \times Apo oil immersion objective, and ZEN Blue 2.6 acquisition SW (Zeiss). Image stacks acquired using Zeiss AxioImager.Z2 were projected as maximal intensity images by using ImageJ distribution FIJI (Schindelin et al., 2012). Where appropriate, contrast and/or brightness of images were adjusted by using Photoshop CS5 (Adobe) or FIJI. To assess effects on ciliogenesis or cilia length, at least 4–5 fields of vision (approximately 200–400 cells per experiment) were analyzed per experimental condition, on at least $n = 3$. Cilia present on HEK293 cells were counted manually. Cilia present on RPE-1 or NIH3T3 were counted in ACDC software semiautomatic mode, all cilia present were verified and adjusted manually as recommended (Lauring et al., 2019). For the experiments in **Supplementary Figures 1D–G**

(analysis of CP110 and TTBK2 presence on the MC), 3–4 fields of vision (200–400 cells) were analyzed per experimental run, $n = 3$. Statistical analyses by one-way ANOVA were performed using Graphpad Prism, $P < 0.05$ (*), $P < 0.01$ (**), $P < 0.001$ (***), and $P < 0.0001$ (****). Results are presented as mean plus SEM. Primary antibodies used: Arl13b (Proteintech, Cat.no. 17711-1-AP), γ -tubulin (Merck, T6557), CP110 (Proteintech, 12780-1-AP), and TTBK2 (Merck, Cat.no. HPA018113).

Dual Luciferase (TopFLASH) Assay, Transfection of HEK293

Transfection and dual luciferase assay of HEK293 WT and KO cells was carried out as previously described (Pačlíková et al., 2017). In brief, in 0.1 μ g of the pRLtkLuc plasmid and 0.1 μ g of the Super8X TopFlash plasmid per well of 24 well plate were cotransfected, on the next day cells were treated by 90ng/ml WNT3a and signal was measured after 24 h treatment.

CRISPR/Cas9 Generation of LRP5/6 Double Knock-Out and AXIN1/2 Double Knock-Out HEK293 Cells

Used guide RNAs were following: LRP5 gRNA gagcgggcccagaagactag, LRP6 gRNA ttgccttagatcctcaagt, AXIN1 gRNA cgaacttctgaggtccacg, and AXIN2 gRNA tccttattggcgatcaaga. gRNAs were cloned into pSpCas9 (BB)-2A-GFP (PX458) (Addgene plasmid, 41815) or pU6-(BbsI)-CBh-Cas9-T2A-mCherry (Addgene plasmid, 64324) plasmids. Following transfection by Lipofectamine 2000 (Thermo Fisher Scientific) the transfected cells were FACS sorted [FACS Aria Fusion (BD Biosciences)] and clonally expanded. Genotyping of LRP5 KO and AXIN2 KO mutants was done following genomic DNA isolation (DirectPCR Lysis Reagent; 301-C, Viagen Biotech) by PCR using DreamTaq DNA Polymerase (Thermo Fisher Scientific). Used primers: LRP5 forward: gtctggtctgacgcagtaca, LRP5 reversed: aggatggcctcaatgactgt, AXIN2 forward: cagtgcagggaagaag, and AXIN2 reversed: gtcttggtggcaggcttc. PCR products were cut by BfaI (R0568S, NEB) in case of LRP5 KO and Hpy188III (R0622S, NEB) for AXIN2 KO screening, respectively. Successful disruption of individual ORFs was confirmed by sequencing, **Supplementary Figures 2A,D, 3A–E**.

RESULTS

Treatment by Recombinant WNT3a Induces WNT/ β -Catenin Pathway Activation but Not Ciliogenesis

First, we tested if primary ciliogenesis can be modulated by activation of WNT/ β -catenin pathway in RPE-1 by recombinant WNT3a. Experiment outline is schematized (**Figure 1A**). We initially treated the cells for 2 h. While we observed the expected accumulation of active β -catenin (ABC), phosphorylation and shift of LRP5/6 coreceptors (LRP6, pLRP5/6, S1490/S1493), and phosphorylation and upshift of DVL2 (**Figures 1B–E** and **Supplementary Figure 1A**), WNT3a did not alter the length

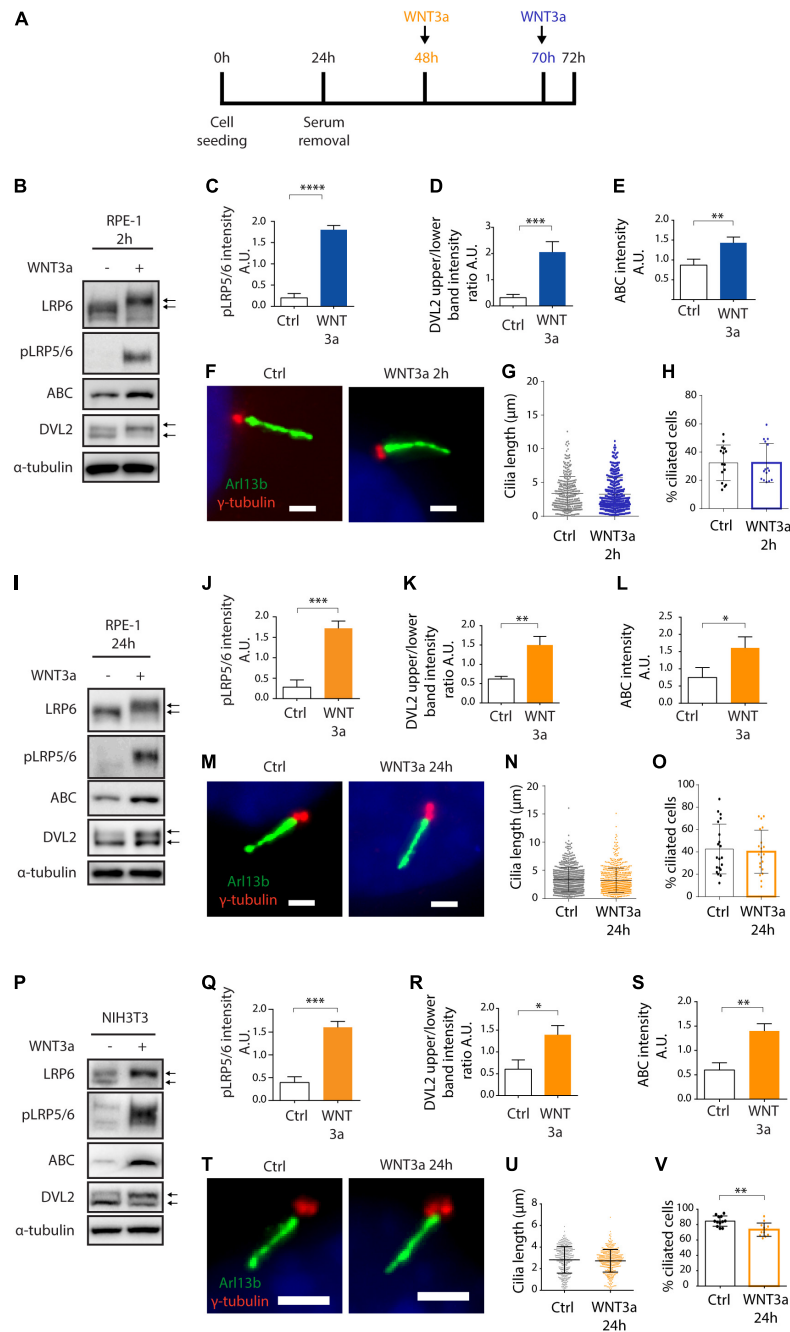


FIGURE 1 | WNT3a does not promote ciliogenesis or cilia length. **(A)** Experimental scheme of WNT3a treatment experiment. Cells were seeded and grown for 24 h, then starved for additional 48 h. A 2 h treatment (RPE-1) by WNT3a is indicated in blue, 24 h treatment is indicated in orange (RPE-1 and NIH3T3). **(B)** Western blot analysis of 2 h WNT3a treatment of RPE-1. The treatment leads to LRP6 shift and increased LRP5/6 phosphorylation, DVL2 phosphorylation and upshift, and accumulation of ABC. The quantification of relative ABC levels is shown in **(E)** $n = 3$, DVL2 band intensities (upper to lower band intensity ratio, the bands are indicated by arrows) is shown in **(D)** $n = 3$, the quantification of pLRP5/6 intensity is presented in **(C)** $n = 3$. **(F)** Representative images of RPE-1 cells treated by WNT3a or vehicle (control) for 2 h and stained for Arl13b (green) and γ -tubulin (red). Scale bar = 2 μ m. DAPI (blue) was used to counter stain nuclei. The corresponding quantification of the cilia length **(G)** and the percentage of cells with Arl13+ cilium **(H)**. Each dot indicates either length of a single primary cilium **(G)** or percentage of ciliated cells in a single image **(H)**. **(I)** Western blot analysis of 24 h WNT3a treatment of RPE-1. The treatment leads to LRP6 shift, increased LRP5/6 phosphorylation, DVL2 phosphorylation and upshift, and accumulation of ABC. The quantification of pLRP5/6 intensity is shown in **(J)** $n = 3$, DVL2 bands (indicated by arrows) intensity ratio is shown in **(K)** $n = 3$, quantification of relative ABC levels is presented in **(L)** $n = 3$. **(M)** Representative images of RPE-1 cells treated by WNT3a or vehicle (control) for 24 h and stained for Arl13b (green) and γ -tubulin (red). Scale bar = 2 μ m. DAPI (blue) was used to counter stain nuclei. The corresponding quantification of the cilia length and the percentage of cells with Arl13+ cilium is shown in **(N,O)**, respectively. Each dot indicates either length of a single primary cilium **(N)** or percentage of ciliated cells in a single image **(O)** $n = 4$. **(P)** Western blot analysis of NIH3T3 cells treated by WNT3a for 24 h shows LRP6

(Continued)

FIGURE 1 | Continued

shift and LRP5/6 phosphorylation, DVL2 phosphorylation and upshift, and accumulation of ABC. The quantification of pLRP5/6 intensity is shown in **(Q)** $n = 3$, DVL2 band intensities (upper to lower band intensity ratio, the bands are indicated by arrows) is shown in **(R)** $n = 3$, quantification of relative ABC intensity **(S)** $n = 3$. **(T)** Representative images of NIH3T3 cells treated by WNT3a for 24 h, stained for Arl13b (green), and γ -tubulin (red). Scale bar = 2 μ m. DAPI (blue) was used to counter stain nuclei. The corresponding quantification of the cilia length **(U)** and the percentage of cells with Arl13+ cilium **(V)**. Each dot indicates either length of a single primary cilium **(U)** or percentage of ciliated cells in one image frame **(V)** $n = 3$.

or number of Arl13b positive cilia (**Figures 1F–H**). Next, we examined effects of prolonged treatment of RPE-1 cells by WNT3a. Importantly, we were able to detect that WNT/ β -catenin pathway is still active after 24 h, as visible from the mobility shift of LRP6 (**Figure 1I** and **Supplementary Figure 1B**) or the elevated levels of ABC, pLRP5/6 or DVL2 phosphorylation (**Figures 1I–L**), but the treatment did not show any notable effects on cilia length or numbers (**Figures 1M–O**). In agreement with these data, WNT3a treatment failed to alter either TTBK2 recruitment to MC (**Supplementary Figures 1D,E**) or MC-specific loss of CP110 (**Supplementary Figures 1F,G**). To corroborate these findings, we also tested the influence of WNT3a in NIH3T3 cell line. Similarly, to RPE-1, WNT3a treatment for 24 h was able to activate the WNT/ β -catenin pathway in NIH3T3 cells (**Figures 1P–S** and **Supplementary Figure 1C**), but the length of cilia was not affected (**Figures 1T,U**). Intriguingly, we detected a decrease in the percentage of ciliated cells following the WNT3a treatment (**Figure 1V**).

Inhibition of WNT Secretion Halts WNT Signaling but Not Ciliogenesis

Having found WNT3a-activated WNT/ β -catenin signaling is not sufficient to promote cilia formation, we tested a possibility that steady state WNT signaling is required for effective ciliogenesis. WNT/ β -catenin pathway is intensively studied as a driver of oncogenic growth, thus there are currently available various small molecules that inhibit WNT ligand secretion. To this end, we used a Porcupine inhibitor LGK974 to block the secretion of endogenous WNT ligands and in turn block the steady state WNT signaling (Jiang et al., 2013). As a positive control in these experiments we used cytochalasin D (CytoD), an actin polymerization inhibitor known to facilitate ciliogenesis and promote cilia elongation (Kim et al., 2015). Experiment outline is schematized (**Figure 2A**). While we observed no visible change in pLRP5/6 levels following the LGK974 treatment (**Figures 2B,C**), perhaps because the basal levels of pLRP5/6 were at our detection limit, we detected downshift of DVL2 (**Figures 2B,D**) confirming the endogenous WNT signaling was successfully ablated. Importantly, however, the LGK974 treatment did not alter primary ciliogenesis, in contrast to CytoD that facilitated CP110 removal from MC (**Supplementary Figures 1F,G**), cilia elongation (**Figures 2E,F**), and formation (**Figures 2E,G**). In addition, we inhibited WNT signaling at the level of CK1- δ/ϵ using small molecule PF670462 (Badura et al., 2007; Janovska et al., 2018), and found no effect on ciliogenesis (**Supplementary Figures 1H–J**). Next, we applied the approach outlined in **Figure 2A** also to NIH3T3 cells, with very similar results - LGK974 caused no visible change in pLRP5/6 levels but inhibited WNT signaling on the level of DVL2 (**Figures 2H–J**),

but LGK974 treatment failed to show any effect on cilia length, in contrast to CytoD treatment (**Figures 2K,L**). We noted the CytoD treatment in NIH3T3 did not increase the cilia numbers (**Figure 2M**), possibly due to high basal ciliation rate of NIH3T3 compared to RPE-1. In sum, these data imply that signaling mediated by endogenous WNT ligands is not required for primary ciliogenesis.

Genetic Ablation of WNT/ β -Catenin Pathway Does Not Alter Primary Ciliogenesis

To corroborate our findings, we established a panel of HEK293 cells devoid of critical components of WNT signaling pathways. To specifically block the course of WNT/ β -catenin pathway we used LRP5/6 double knock out HEK293 cells, to block the course of any WNT signaling pathway we used DVL1/2/3 triple knock out HEK293 cells (Paclíková et al., 2017) and to overactivate WNT/ β -catenin pathway we used AXIN1/2 double knock out HEK293 cells.

First, we have verified successful disruption of LRP5 gene by sequencing (**Supplementary Figures 2A, 3A**), and lack of LRP6 and pLRP5/6 signals in LRP5/6 null cells by western blot (**Figure 3A** and **Supplementary Figure 2B**). Furthermore, we confirmed these cells cannot activate WNT/ β -catenin signaling (**Supplementary Figure 2C**). Similarly, we confirmed disruption of AXIN1 and AXIN2 genes in AXIN1/2 dKO by sequencing (**Supplementary Figures 2D, 3B–E**), and lack of AXIN1 by western blot (**Supplementary Figure 2E**). In addition, we observed that loss of AXIN1/2 function leads to excessive ABC accumulation (**Figure 3A**) and in turn to overactivation of WNT/ β -catenin signaling in AXIN1/2dKO cells (**Supplementary Figure 2F**), as expected.

Having characterized our model system, we examined cilia formation in those cells. Consistently with previous work, HEK293 cells form cilia less frequently than RPE-1 or NIH3T3 cells (Lancaster et al., 2011; Bernatik et al., 2020). We were able to detect about 5% of cells with Arl13b+ primary cilium in WT HEK293. The percentage of ciliated cells, but not the cilia length, was reduced in DVL1/2/3 tKO cells (**Figures 3B–D**). This observation is in agreement with the role of DVL and WNT/PCP pathway in the regulation of basal body positioning and ciliogenesis (Park et al., 2008; Shnitsar et al., 2015; Sampilo et al., 2018). Systemic activation of WNT/ β -catenin pathway by AXIN1/2 removal produced a somewhat mixed result. Using AXIN1/2 dKO clone 3D2 we initially observed a non-significant negative trend on the cilia formation. However, this was not confirmed using an independent clone 3H2 (**Figure 3D**). Importantly, the ablation of WNT/ β -catenin pathway in LRP5/6 dKO cells had no effect on either the percentage of ciliated cells

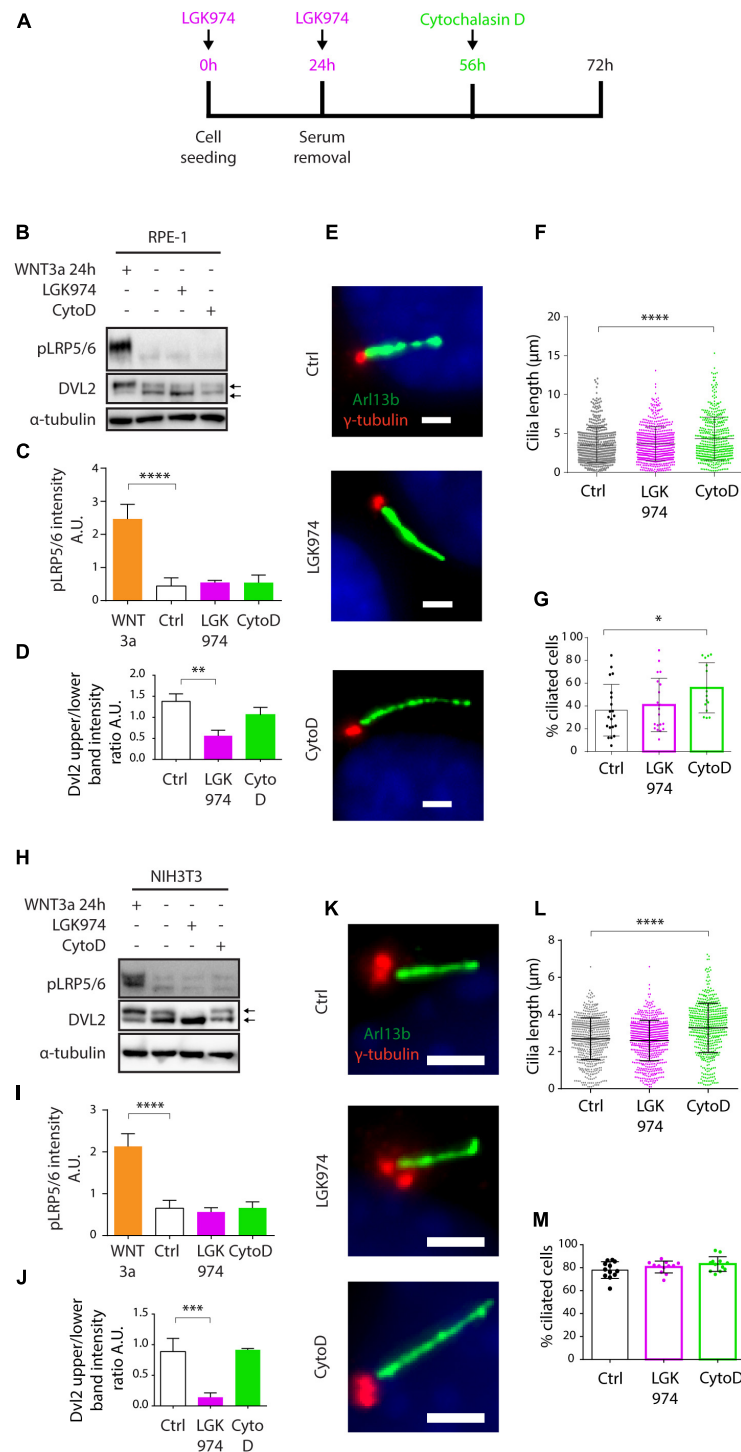


FIGURE 2 | Inhibition of WNT secretion has no effect on ciliogenesis or cilia length. **(A)** Experimental scheme illustrating the time points of LGK974 (Purple) or CytoD (Green) treatments. **(B)** Western blot analysis of RPE-1 treated by LGK974 or CytoD. WNT3a was used as positive control to activate WNT/ β -catenin pathway. pLRP5/6 intensity is quantified in **(C)** $n = 3$, DVL2 shift (upper to lower band intensity ratio) is quantified in **(D)** $n = 3$. **(E)** Representative images of RPE-1 cells following the indicated treatment, stained for Arl13b (green) and γ -tubulin (red). Scale bar = 2 μ m. DAPI (blue) was used to counter stain nuclei. Quantification of the cilia length **(F)** and the percentage of cells with Arl13+ cilium **(G)**. Each dot indicates either length of a single primary cilium **(F)** or percentage of ciliated cells in one image frame **(G)** $n \geq 3$. **(H)** Western blot analysis NIH3T3 treated by LGK974 or CytoD. pLRP5/6 intensity is quantified in **(I)** $n = 3$, **(J)** Quantification of DVL2 band intensities (upper to lower band intensity ratio) $n = 3$. **(K)** Representative images of NIH3T3 cells following treatment with LGK974 or CytoD, stained for Arl13b (green) and γ -tubulin (red). Scale bar = 2 μ m. DAPI (blue) was used to counter stain nuclei. Quantification of the cilia length **(L)** and the percentage of cells with Arl13+ cilium **(M)**. Each dot indicates either length of a single primary cilium **(L)** or percentage of ciliated cells in one image frame **(M)** $n = 3$.

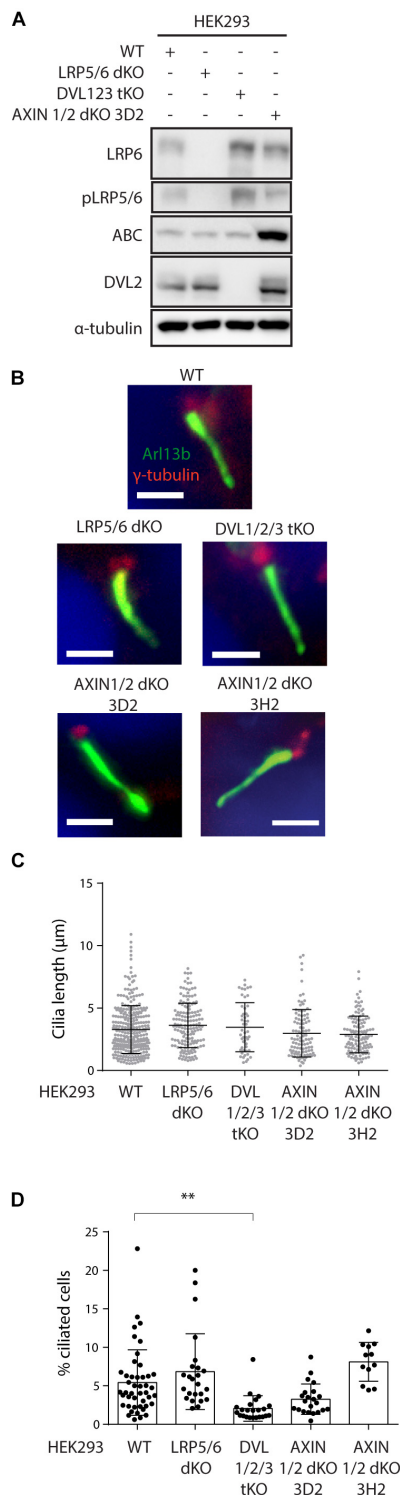


FIGURE 3 | Ablation of WNT β -catenin pathway does not alter primary ciliogenesis. **(A)** Western blot analysis of individual HEK293 KO cell lines using the indicated antibodies. Note that LRP5/6 dKO cells lack LRP6 and phospho LRP5/6 (pSer1493/pSer1490), DVL1/2/3 tKO cell do not have detectable levels of DVL2. AXIN1/2 dKO cells shown elevated level of ABC. **(B–D)** HEK293 Cells were starved for 48 h, stained for Arl13b (green), γ -tubulin (red), (Continued)

FIGURE 3 | Continued

and DAPI (blue), and analyzed by IF microscopy. Representative images are shown in **(B)**. Scale bar = 2 μ m. Quantification of cilia length and percentage of ciliated cells is shown in **(C,D)**, respectively. Each dot indicates either length of a single primary cilium **(C)** or percentage of ciliated cells in one image **(D)**. $n = 4$.

or cilia length (**Figures 3B–D**), in agreement with our earlier observations based on pharmacological inhibition of endogenous WNT signaling in RPE-1 or NIH3T3. In sum, from these data we conclude that WNT/ β -catenin signaling is not required for effective ciliogenesis.

DISCUSSION

Regulation of ciliogenesis is a complex process involving multiple factors directly or indirectly influencing cilia initiation and elongation. The regulators of cilium formation encompass a wide range of molecules such as components of centrioles, regulators of vesicular trafficking, intraflagellar transport proteins, membrane proteins, and components of cytoskeleton (Seeley and Nachury, 2010; Ishikawa and Marshall, 2017; Wang and Dynlacht, 2018; Conkar and Firat-Karalar, 2020).

WNT3a is considered a prototypical “canonical” WNT ligand that activates WNT/ β -catenin pathway (Willert et al., 2003). Moreover, WNT3a and hence the WNT/ β -catenin pathway are well known for their mitogenic potential in many experimental systems (Niehrs and Acebron, 2012). In addition, WNT/ β -catenin pathway has been shown to act mainly during G2/M phase of the cell cycle (Davidson et al., 2009), while primary cilia form during G0/G1 and during the G2/M they disassemble (Rieder et al., 1979; Ford et al., 2018). Furthermore, mitogenic signals typically promote cilium disassembly (Rieder et al., 1979; Tucker et al., 1979; Pugacheva et al., 2007). From this perspective, the recently reported positive role of WNT3a and WNT/ β -catenin signaling on primary cilia formation (Kyun et al., 2020) is counterintuitive and puzzling.

Principally, there are several important methodological differences between our work and the previous results (Kyun et al., 2020) which may account for the different outcomes. (1) In our experiments we activated the WNT/ β -catenin pathway by recombinant WNT3a, in contrast to WNT3a conditioned medium often used in the previous study (Kyun et al., 2020). Thus, some of the reported effects of WNT3a conditioned medium may be a result of secondary effects. (2) We applied up to 24 h stimulation by WNT3a to activate or 72 h LGK974 to block the pathway, respectively. We cannot formally exclude that the longer WNT3a treatments used by Kyun et al., could account for the observed differences. However, we argue this seems unlikely, given that full activation of the WNT/ β -catenin pathway or cilium formation typically happens within several hours following the proper stimuli (Bryja et al., 2007; Naik and Piwnicka-Worms, 2007; Pitaval et al., 2010; Lu et al., 2015; Wu et al., 2018; Pejškova et al., 2020). In fact, prolonged WNT/ β -catenin pathway stimulation increases a chance for indirect secondary effects. Indeed, WNT signaling has been shown to regulate expression of

a number of ligands from FGF (Kratochwil et al., 2002; Barrow et al., 2003; Shimokawa et al., 2003; Chamorro et al., 2005; Hendrix et al., 2006) or BMP (Baker et al., 1999; Kim et al., 2002; Shu et al., 2005) families that might in turn affect ciliogenesis (Neugebauer et al., 2009; Komatsu et al., 2011; Cibois et al., 2015; Bosakova et al., 2018). 3. Finally, we visualized cilia by staining for Arl13b, a small GTPase from Arf/Arl-family highly enriched in the ciliary membrane (Caspary et al., 2007; Cantagrel et al., 2008; Hori et al., 2008; Duldulao et al., 2009; Cevik et al., 2010; Li et al., 2010). In the report by Kyun et al., acetylated α -tubulin antibody staining was used to assess the cilia length, thickness, and numbers. From this perspective, it is plausible some of the reported changes in cilia length or thickness in fact reflect changes in the acetylation of ciliary tubulin rather than changes in cilium size. That being said, there is an evidence that individual cilia differ significantly in the levels of tubulin post-translation modifications and the levels of tubulin modifications may dramatically change in response to the appropriate stimuli (Piperno et al., 1987; Berbari et al., 2013; He et al., 2018).

Our data show that while WNT3a consistently activates the WNT/ β -catenin pathway, it has no or minor negative effects on ciliogenesis. Elevated β -catenin levels following APC ablation have been related to reduced ciliogenesis and cell cycle defects in the developing cortex in mice (Nakagawa et al., 2017). Indeed, we detected modest decrease in the percentage of ciliated NIH3T3 cells following WNT3a induced β -catenin accumulation. We speculate we did not observe comparable negative effect on cilia following the WNT/ β -catenin pathway activation after AXIN1/2 loss due to abnormal cell cycle regulation in HEK293, which hampers detection of relatively subtle deviations in their cell cycle progression (Löber et al., 2002; Stepanenko and Dmitrenko, 2015). These data are in contrast to Kyun et al., where accumulation of β -catenin by WNT3a conditioned medium treatment or by expression of S45A non-degradable oncogenic mutant variant of β -catenin (Liu et al., 2002) facilitates ciliogenesis.

In sum, we found no evidence that endogenous WNT/ β -catenin signaling, while ablated either pharmacologically in RPE-1 or NIH3T3 by LGK974, or genetically by removal of LRP5/6 in HEK293, is required for primary cilia to form. Our findings presented in this article challenge some of the published evidence and argue against positive role of WNT3a or WNT/ β -catenin pathway in ciliogenesis or cilia length regulation.

REFERENCES

- Angers, S., and Moon, R. T. (2009). Proximal events in Wnt signal transduction. *Nat. Rev. Mol. Cell Biol.* 10, 468–477. doi: 10.1038/nrm2717
- Anvarian, Z., Mykityn, K., Mukhopadhyay, S., Pedersen, L. B., and Christensen, S. T. (2019). Cellular signalling by primary cilia in development, organ function and disease. *Nat. Rev. Nephrol.* 15, 199–219. doi: 10.1038/s41581-019-0116-9
- Badura, L., Swanson, T., Adamowicz, W., Adams, J., Cianfroga, J., Fisher, K., et al. (2007). An inhibitor of casein kinase I ϵ induces phase delays in circadian rhythms under free-running and entrained conditions. *J. Pharmacol. Exp. Ther.* 322, 730–738. doi: 10.1124/jpet.107.122846
- Baker, J. C., Beddington, R. S. P., and Harland, R. M. (1999). Wnt signaling in *Xenopus* embryos inhibits Bmp4 expression and activates neural development. *Genes Dev.* 13, 3149–3159. doi: 10.1101/gad.13.23.3149
- Balmer, S., Dussert, A., Collu, G. M., Benitez, E., Iomini, C., and Mlodzik, M. (2015). Components of intraflagellar transport complex a function independently of the cilium to regulate canonical Wnt signaling in *Drosophila*. *Dev. Cell* 34, 705–718. doi: 10.1016/j.devcel.2015.07.016

DATA AVAILABILITY STATEMENT

The original contributions presented in the study are included in the article/**Supplementary Material**, further inquiries can be directed to the corresponding author.

AUTHOR CONTRIBUTIONS

OB designed and performed the experiments, and wrote and edited the manuscript. PP and AK performed selection and verification of CRISPR edited HEK293 cell lines. VB edited the manuscript. LC designed the experiments, and wrote and edited the manuscript. All authors contributed to the article and approved the submitted version.

FUNDING

This work was supported by grants from the Czech Science Foundation (19-05244S) and the Swiss National Science Foundation (IZ11Z0_166533) to LC. OB was supported by funds from the Faculty of Medicine MU to junior researcher (Ondrej Bernatik, ROZV/28/LF/2020). VB was supported from European Structural and Investment Funds, Operational Program Research, Development and Education – Preclinical Progression of New Organic Compounds with Targeted Biological Activity” (Preclinprogress) – CZ.02.1.01/0.0/0.0/16_025/0007381.

ACKNOWLEDGMENTS

We acknowledge the core facility CELLIM supported by the Czech-BioImaging large RI project (LM2018129 funded by MEYS CR) for their support with obtaining scientific data presented in this article. hCas9 (BB)-2A-GFP was a gift from George Church (Addgene plasmid #41815) and pU6-(BbsI)_CBh-Cas9-T2A-mCherry was a gift from Ralf Kuehn (Addgene plasmid # 64324).

SUPPLEMENTARY MATERIAL

The Supplementary Material for this article can be found online at: <https://www.frontiersin.org/articles/10.3389/fcell.2021.623753/full#supplementary-material>

- Bangs, F., and Anderson, K. V. (2017). Primary cilia and mammalian hedgehog signaling. *Cold Spring Harb. Perspect. Biol.* 9:a028175. doi: 10.1101/cshperspect.a028175
- Barrow, J. R., Thomas, K. R., Boussadia-Zahui, O., Moore, R., Kemler, R., Capecchi, M. R., et al. (2003). Ectodermal Wnt3 β -catenin signaling is required for the establishment and maintenance of the apical ectodermal ridge. *Genes Dev.* 17, 394–409. doi: 10.1101/gad.1044903
- Behrens, J., Von Kries, J. P., Kühl, M., Bruhn, L., Wedlich, D., Grosschedl, R., et al. (1996). Functional interaction of β -catenin with the transcription factor LEF-1. *Nature* 382, 638–642. doi: 10.1038/382638a0
- Berbari, N. F., Sharma, N., Malarkey, E. B., Pieczynski, J. N., Boddu, R., Gaertig, J., et al. (2013). Microtubule modifications and stability are altered by cilia perturbation and in cystic kidney disease. *Cytoskeleton* 70, 24–31. doi: 10.1002/cm.21088
- Bernatik, O., Pejškova, P., Vyslouzil, D., Hanakova, K., Zdrahal, Z., and Cajanek, L. (2020). Phosphorylation of multiple proteins involved in ciliogenesis by Tau Tubulin kinase 2. *Mol. Biol. Cell* 31, 1032–1046. doi: 10.1091/MBC.E19-06-0334
- Bernatik, O., Sri Ganji, R., Dijksterhuis, J. P., Konik, P., Cervenka, I., Polonio, T., et al. (2011). Sequential activation and inactivation of dishevelled in the Wnt/ β -catenin pathway by casein kinases. *J. Biol. Chem.* 286, 10396–10410. doi: 10.1074/jbc.M110.169870
- Bosakova, M. K., Varecha, M., Hampl, M., Duran, I., Nita, A., Buchtova, M., et al. (2018). Regulation of ciliary function by fibroblast growth factor signaling identifies FGFR3-related disorders achondroplasia and thanatophoric dysplasia as ciliopathies. *Hum. Mol. Genet.* 27, 1093–1105. doi: 10.1093/hmg/ddy031
- Bryja, V., Červenka, I., and Čajánek, L. (2017). The connections of Wnt pathway components with cell cycle and centrosome: side effects or a hidden logic? *Crit. Rev. Biochem. Mol. Biol.* 52, 614–637. doi: 10.1080/10409238.2017.1350135
- Bryja, V., Schulte, G., and Arenas, E. (2007). Wnt-3a utilizes a novel low dose and rapid pathway that does not require casein kinase 1-mediated phosphorylation of Dvl to activate β -catenin. *Cell. Signal.* 19, 610–616. doi: 10.1016/j.cellsig.2006.08.011
- Butler, M. T., and Wallingford, J. B. (2017). Planar cell polarity in development and disease. *Nat. Rev. Mol. Cell Biol.* 18, 375–388. doi: 10.1038/nrm.2017.11
- Čajánek, L., and Nigg, E. A. (2014). Cep164 triggers ciliogenesis by recruiting Tau tubulin kinase 2 to the mother centriole. *Proc. Natl. Acad. Sci. U. S. A.* 111:E2841–50. doi: 10.1073/pnas.1401777111
- Cantagrel, V., Silhavy, J. L., Bielas, S. L., Swistun, D., Marsh, S. E., Bertrand, J. Y., et al. (2008). Mutations in the cilia gene ARL13B lead to the classical form of Joubert syndrome. *Am. J. Hum. Genet.* 83, 170–179. doi: 10.1016/j.ajhg.2008.06.023
- Carvajal-Gonzalez, J. M., Mulero-Navarro, S., and Mlodzik, M. (2016). Centriole positioning in epithelial cells and its intimate relationship with planar cell polarity. *BioEssays* 38, 1234–1245. doi: 10.1002/bies.201600154
- Caspary, T., Larkins, C. E., and Anderson, K. V. (2007). The graded response to sonic hedgehog depends on cilia architecture. *Dev. Cell* 12, 767–778. doi: 10.1016/j.devcel.2007.03.004
- Cevik, S., Hori, Y., Kaplan, O. I., Kida, K., Toivenon, T., Foley-Fisher, C., et al. (2010). Joubert syndrome ARL13b functions at ciliary membranes and stabilizes protein transport in *Caenorhabditis elegans*. *J. Cell Biol.* 188, 953–969. doi: 10.1083/jcb.200908133
- Chamorro, M. N., Schwartz, D. R., Vonica, A., Brivanlou, A. H., Cho, K. R., and Varmus, H. E. (2005). FGF-20 and DKK1 are transcriptional targets of β -catenin and FGF-20 is implicated in cancer and development. *EMBO J.* 24, 73–84. doi: 10.1038/sj.emboj.7600460
- Cibois, M., Luxardi, G., Chevalier, B., Thomé, V., Mercey, O., Zaragosi, L. E., et al. (2015). BMP signalling controls the construction of vertebrate mucociliary epithelia. *Development* 142, 2352–2363. doi: 10.1242/dev.118679
- Conkar, D., and Firat-Karalar, E. N. (2020). Microtubule-associated proteins and emerging links to primary cilium structure, assembly, maintenance, and disassembly. *FEBS J.* doi: 10.1111/febs.15473 Online ahead of print
- Corbit, K. C., Aanstad, P., Singla, V., Norman, A. R., Stainier, D. Y. R., and Reiter, J. F. (2005). Vertebrate smoothened functions at the primary cilium. *Nature* 437, 1018–1021. doi: 10.1038/nature04117
- Corbit, K. C., Shyer, A. E., Dowdle, W. E., Gaulden, J., Singla, V., and Reiter, J. F. (2008). Kif3a constrains β -catenin-dependent Wnt signalling through dual ciliary and non-ciliary mechanisms. *Nat. Cell Biol.* 10, 70–76. doi: 10.1038/ncb1670
- Davidson, G., Shen, J., Huang, Y. L., Su, Y., Karaulanov, E., Bartscherer, K., et al. (2009). Cell cycle control of Wnt receptor activation. *Dev. Cell* 17, 788–799. doi: 10.1016/j.devcel.2009.11.006
- Duldulao, N. A., Lee, S., and Sun, Z. (2009). Cilia localization is essential for in vivo functions of the Joubert syndrome protein ARL13b/Scorpion. *Development* 136, 4033–4042. doi: 10.1242/dev.036350
- Ford, M. J., Yeyati, P. L., Mali, G. R., Keighren, M. A., Waddell, S. H., Mjoseng, H. K., et al. (2018). A cell/cilia cycle biosensor for single-cell kinetics reveals persistence of cilia after G1/S transition is a general property in cells and mice. *Dev. Cell* 47, 509.e5–523.e5. doi: 10.1016/j.devcel.2018.10.027
- Garcia-Gonzalo, F. R., and Reiter, J. F. (2017). Open sesame: how transition fibers and the transition zone control ciliary composition. *Cold Spring Harb. Perspect. Biol.* 9:a028134. doi: 10.1101/cshperspect.a028134
- Goetz, S. C., Liem, K. F., and Anderson, K. V. (2012). The spinocerebellar ataxia-associated gene tau tubulin kinase 2 controls the initiation of ciliogenesis. *Cell* 151, 847–858. doi: 10.1016/j.cell.2012.10.010
- Gonçalves, J., and Pelletier, L. (2017). The ciliary transition zone: finding the pieces and assembling the gate. *Mol. Cells* 40, 243–253. doi: 10.14348/molcells.2017.0054
- González-Sancho, J. M., Greer, Y. E., Abrahams, C. L., Takigawa, Y., Baljinnyam, B., Lee, K. H., et al. (2013). Functional consequences of Wnt-induced dishevelled 2 phosphorylation in canonical and noncanonical Wnt signaling. *J. Biol. Chem.* 288, 9428–9437. doi: 10.1074/jbc.M112.448480
- Han, Y. G., Kim, H. J., Dlugosz, A. A., Ellison, D. W., Gilbertson, R. J., and Alvarez-Buylla, A. (2009). Dual and opposing roles of primary cilia in medulloblastoma development. *Nat. Med.* 15, 1062–1065. doi: 10.1038/nm.2020
- Hanáková, K., Bernatik, O., Kravec, M., Micka, M., Kumar, J., Harnoš, J., et al. (2019). Comparative phosphorylation map of Dishevelled 3 links phospho-signatures to biological outputs. *Cell Commun. Signal.* 17:170. doi: 10.1186/s12964-019-0470-z
- He, K., Ma, X., Xu, T., Li, Y., Hodge, A., Zhang, Q., et al. (2018). Axoneme polyglutamylation regulated by Joubert syndrome protein ARL13B controls ciliary targeting of signaling molecules. *Nat. Commun.* 9:3310. doi: 10.1038/s41467-018-05867-1
- Hendrix, N. D., Wu, R., Kuick, R., Schwartz, D. R., Fearon, E. R., and Cho, K. R. (2006). Fibroblast growth factor 9 has oncogenic activity and is a downstream target of Wnt signaling in ovarian endometrioid adenocarcinomas. *Cancer Res.* 66, 1354–1362. doi: 10.1158/0008-5472.CAN-05-3694
- Hildebrandt, F., Benzing, T., and Katsanis, N. (2011). Ciliopathies. *N. Engl. J. Med.* 364, 1533–1543. doi: 10.1056/nejmra1010172
- Hori, Y., Kobayashi, T., Kikko, Y., Kontani, K., and Katada, T. (2008). Domain architecture of the atypical Arf-family GTPase ARL13b involved in cilia formation. *Biochem. Biophys. Res. Commun.* 373, 119–124. doi: 10.1016/j.bbrc.2008.06.001
- Huang, P., and Schier, A. F. (2009). Dampened Hedgehog signaling but normal Wnt signaling in zebrafish without cilia. *Development* 136, 3089–3098. doi: 10.1242/dev.041343
- Huangfu, D., Liu, A., Rakeman, A. S., Murcia, N. S., Niswander, L., and Anderson, K. V. (2003). Hedgehog signalling in the mouse requires intraflagellar transport proteins. *Nature* 426, 83–87. doi: 10.1038/nature02061
- Humphries, A. C., and Mlodzik, M. (2018). From instruction to output: Wnt/PCP signaling in development and cancer. *Curr. Opin. Cell Biol.* 51, 110–116. doi: 10.1016/j.ceb.2017.12.005
- Ishikawa, H., and Marshall, W. F. (2017). Intraflagellar transport and ciliary dynamics. *Cold Spring Harb. Perspect. Biol.* 9:a021998. doi: 10.1101/cshperspect.a021998
- Janovska, P., Verner, J., Kohoutek, J., Bryjova, L., Gregorova, M., Dzimkova, M., et al. (2018). Casein kinase 1 is a therapeutic target in chronic lymphocytic leukemia. *Blood* 131, 1206–1218. doi: 10.1182/blood-2017-05-786947
- Jenks, A. D., Vyse, S., Wong, J. P., Kostaras, E., Keller, D., Burgoyne, T., et al. (2018). Primary cilia mediate diverse kinase inhibitor resistance mechanisms in cancer. *Cell Rep.* 23, 3042–3055. doi: 10.1016/j.celrep.2018.05.016
- Jiang, X., Hao, H. X., Growney, J. D., Woolfenden, S., Bottiglio, C., Ng, N., et al. (2013). Inactivating mutations of RNF43 confer Wnt dependency in pancreatic ductal adenocarcinoma. *Proc. Natl. Acad. Sci. U.S.A.* 110, 12649–12654. doi: 10.1073/pnas.1307218110

- Kim, J., Jo, H., Hong, H., Kim, M. H., Kim, J. M., Lee, J. K., et al. (2015). Actin remodelling factors control ciliogenesis by regulating YAP/TAZ activity and vesicle trafficking. *Nat. Commun.* 6:6781. doi: 10.1038/ncomms7781
- Kim, J. S., Crooks, H., Dracheva, T., Nishanian, T. G., Singh, B., Jen, J., et al. (2002). Oncogenic β -catenin is required for bone morphogenetic protein 4 expression in human cancer cells. *Cancer Res.* 62, 2744–2748.
- Kim, M., Suh, Y. A., Oh, J. H., Lee, B. R., Kim, J., and Jang, S. J. (2016). KIF3A binds to β -arrestin for suppressing Wnt/ β -catenin signalling independently of primary cilia in lung cancer. *Sci. Rep.* 6:32770. doi: 10.1038/srep32770
- Komatsu, Y., Kaartinen, V., and Mishina, Y. (2011). Cell cycle arrest in node cells governs ciliogenesis at the node to break left-right symmetry. *Development* 138, 3915–3920. doi: 10.1242/dev.068833
- Kratochwil, K., Galceran, J., Tontsch, S., Roth, W., and Grosschedl, R. (2002). FGF4, a direct target of LEF1 and Wnt signaling, can rescue the arrest of tooth organogenesis in *Left1*^{-/-} mice. *Genes Dev.* 16, 3173–3185. doi: 10.1101/gad.1035602
- Kyun, M. L., Kim, S. O., Lee, H. G., Hwang, J. A., Hwang, J., Soung, N. K., et al. (2020). Wnt3a stimulation promotes primary ciliogenesis through β -catenin phosphorylation-induced reorganization of centriolar satellites. *Cell Rep.* 30, 1447.e5–1462.e5. doi: 10.1016/j.celrep.2020.01.019
- Lancaster, M. A., Schroth, J., and Gleeson, J. G. (2011). Subcellular spatial regulation of canonical Wnt signalling at the primary cilium. *Nat. Cell Biol.* 13, 700–708. doi: 10.1038/ncb2259
- Lauring, M. C., Zhu, T., Luo, W., Wu, W., Yu, F., and Toomre, D. (2019). New software for automated cilia detection in cells (ACDC). *Cilia* 8:1. doi: 10.1186/s13630-019-0061-z
- Li, Y., Wei, Q., Zhang, Y., Ling, K., and Hu, J. (2010). The small GTPases ARL-13 and ARL-3 coordinate intraflagellar transport and ciliogenesis. *J. Cell Biol.* 189, 1039–1051. doi: 10.1083/jcb.200912001
- Liu, B., Chen, S., Cheng, D., Jing, W., and Helms, J. A. (2014). Primary cilia integrate hedgehog and Wnt signaling during tooth development. *J. Dent. Res.* 93, 475–482. doi: 10.1177/0022034514528211
- Liu, C., Li, Y., Semenov, M., Han, C., Baeg, G. H., Tan, Y., et al. (2002). Control of β -catenin phosphorylation/degradation by a dual-kinase mechanism. *Cell* 108, 837–847. doi: 10.1016/S0092-8674(02)00685-2
- Lo, C. H., Lin, I. H., Yang, T. T., Huang, Y. C., Tanos, B. E., Chou, P. C., et al. (2019). Phosphorylation of CEP83 by TTBK2 is necessary for cilia initiation. *J. Cell Biol.* 218, 3489–3505. doi: 10.1083/JCB.201811142
- Löber, C., Lenz-Stöppler, C., and Döbelstein, M. (2002). Adenovirus E1-transformed cells grow despite the continuous presence of transcriptionally active p53. *J. Gen. Virol.* 83, 2047–2057. doi: 10.1099/0022-1317-83-8-2047
- Lu, Q., Insinna, C., Ott, C., Stauffer, J., Pintado, P. A., Rahajeng, J., et al. (2015). Early steps in primary cilium assembly require EHD1/EHD3-dependent ciliary vesicle formation. *Nat. Cell Biol.* 17, 228–240. doi: 10.1038/ncb3109
- May-Simera, H., and Kelley, M. W. (2012). Planar cell polarity in the inner ear. *Curr. Top. Dev. Biol.* 101, 111–140. doi: 10.1016/B978-0-12-394592-1.00006-5
- McDermott, K. M., Liu, B. Y., Tlsty, T. D., and Pazour, G. J. (2010). Primary cilia regulate branching morphogenesis during mammary gland development. *Curr. Biol.* 20, 731–737. doi: 10.1016/j.cub.2010.02.048
- Mirvis, M., Stearns, T., and Nelson, W. J. (2018). Cilium structure, assembly, and disassembly regulated by the cytoskeleton. *Biochem. J.* 475, 2329–2353. doi: 10.1042/BCJ20170453
- Mitchison, H. M., and Valente, E. M. (2017). Motile and non-motile cilia in human pathology: from function to phenotypes. *J. Pathol.* 241, 294–309. doi: 10.1002/path.4843
- Molenaar, M., Van De Wetering, M., Oosterwegel, M., Peterson-Maduro, J., Godsave, S., Korinek, V., et al. (1996). XTcf-3 transcription factor mediates β -catenin-induced axis formation in xenopus embryos. *Cell* 86, 391–399. doi: 10.1016/S0092-8674(00)80112-9
- Nachury, M. V. (2018). The molecular machines that traffic signaling receptors into and out of cilia. *Curr. Opin. Cell Biol.* 51, 124–131. doi: 10.1016/j.cob.2018.03.004
- Nachury, M. V., and Mick, D. U. (2019). Establishing and regulating the composition of cilia for signal transduction. *Nat. Rev. Mol. Cell Biol.* 20, 389–405. doi: 10.1038/s41580-019-0116-4
- Naik, S., and Piwnica-Worms, D. (2007). Real-time imaging of β -catenin dynamics in cells and living mice. *Proc. Natl. Acad. Sci. U.S.A.* 104, 17465–17470. doi: 10.1073/pnas.0704465104
- Nakagawa, N., Li, J., Yabuno-Nakagawa, K., Eom, T. Y., Cowles, M., Mapp, T., et al. (2017). APC sets the Wnt tone necessary for cerebral cortical progenitor development. *Genes Dev.* 31, 1679–1692. doi: 10.1101/gad.302679.117
- Neugebauer, J. M., Amack, J. D., Peterson, A. G., Bisgrove, B. W., and Yost, H. J. (2009). FGF signalling during embryo development regulates cilia length in diverse epithelia. *Nature* 458, 651–654. doi: 10.1038/nature07753
- Niehrs, C., and Acebron, S. P. (2012). Mitotic and mitogenic Wnt signalling. *EMBO J.* 31, 2705–2713. doi: 10.1038/emboj.2012.124
- Nusse, R., and Clevers, H. (2017). Wnt/ β -catenin signaling, disease, and emerging therapeutic modalities. *Cell* 169, 985–999. doi: 10.1016/j.cell.2017.05.016
- Ocbina, P. J. R., Tuson, M., and Anderson, K. V. (2009). Primary cilia are not required for normal canonical Wnt signaling in the mouse embryo. *PLoS One* 4:e6839. doi: 10.1371/journal.pone.0006839
- Oda, T., Chiba, S., Nagai, T., and Mizuno, K. (2014). Binding to Cep164, but not EB1, is essential for centriolar localization of TTBK2 and its function in ciliogenesis. *Genes to Cells* 19, 927–940. doi: 10.1111/gtc.12191
- Paclíková, P., Bernatik, O., Radaszkiewicz, T. W., and Bryja, V. (2017). The N-terminal part of the dishevelled DEP domain is required for Wnt/ β -catenin signaling in mammalian cells. *Mol. Cell. Biol.* 37:e145-17. doi: 10.1128/mcb.00145-17
- Park, T. J., Mitchell, B. J., Abitua, P. B., Kintner, C., and Wallingford, J. B. (2008). Dishevelled controls apical docking and planar polarization of basal bodies in ciliated epithelial cells. *Nat. Genet.* 40, 871–879. doi: 10.1038/ng.104
- Patnaik, S. R., Kretschmer, V., Brücker, L., Schneider, S., Volz, A. K., Oancea-Castillo, L., et al. (2019). Bardet-Biedl Syndrome proteins regulate cilia disassembly during tissue maturation. *Cell. Mol. Life Sci.* 76, 757–775. doi: 10.1007/s00018-018-2966-x
- Pejskova, P., Reilly, M. L., Bino, L., Bernatik, O., Dolanska, L., Ganji, R. S., et al. (2020). KIF14 controls ciliogenesis via regulation of Aurora A and is important for Hedgehog signaling. *J. Cell Biol.* 219:e201904107. doi: 10.1083/JCB.201904107
- Pinson, K. I., Brennan, J., Monkley, S., Avery, B. J., and Skarnes, W. C. (2000). An LDL-receptor-related protein mediates Wnt signalling in mice. *Nature* 407, 535–538. doi: 10.1038/35035124
- Piperno, G., LeDizet, M., and Chang, X. J. (1987). Microtubules containing acetylated alpha-tubulin in mammalian cells in culture. *J. Cell Biol.* 104, 289–302. doi: 10.1083/jcb.104.2.289
- Pitaval, A., Tseng, Q., Bornens, M., and Théry, M. (2010). Cell shape and contractility regulate ciliogenesis in cell cycle-arrested cells. *J. Cell Biol.* 191, 303–312. doi: 10.1083/jcb.201004003
- Pugacheva, E. N., Jablonski, S. A., Hartman, T. R., Hensley, E. P., and Golemis, E. A. (2007). HEF1-dependent aurora a activation induces disassembly of the primary cilium. *Cell* 129, 1351–1363. doi: 10.1016/j.cell.2007.04.035
- Reiter, J. F., and Leroux, M. R. (2017). Genes and molecular pathways underpinning ciliopathies. *Nat. Rev. Mol. Cell Biol.* 18, 533–547. doi: 10.1038/nrm.2017.60
- Rieder, C. L., Jensen, C. G., and Jensen, L. C. W. (1979). The resorption of primary cilia during mitosis in a vertebrate (PtK1) cell line. *J. Ultrastructure Res.* 68, 173–185. doi: 10.1016/S0022-5320(79)90152-7
- Rohatgi, R., Milenkovic, L., and Scott, M. P. (2007). Patched1 regulates hedgehog signaling at the primary cilium. *Science* 317, 372–376. doi: 10.1126/science.1139740
- Sampilo, N. F., Stepicheva, N. A., Zaidi, S. A. M., Wang, L., Wu, W., Wikramanayake, A., et al. (2018). Inhibition of microRNA suppression of dishevelled results in Wnt pathway-associated developmental defects in sea urchin. *Development* 145:dev167130. doi: 10.1242/dev.167130
- Schindelin, J., Arganda-Carreras, I., Frise, E., Kaynig, V., Longair, M., Pietzsch, T., et al. (2012). Fiji: an open-source platform for biological-image analysis. *Nat. Methods* 9, 676–682. doi: 10.1038/nmeth.2019
- Schmidt, K. N., Kuhns, S., Neuner, A., Hub, B., Zentgraf, H., and Pereira, G. (2012). Cep164 mediates vesicular docking to the mother centriole during early steps of ciliogenesis. *J. Cell Biol.* 199, 1083–1101. doi: 10.1083/jcb.201202126

- Seeley, E. S., and Nachury, M. V. (2010). The perennial organelle: assembly and disassembly of the primary cilium. *J. Cell Sci.* 123, 511–518. doi: 10.1242/jcs.061093
- Shimokawa, T., Furukawa, Y., Sakai, M., Li, M., Miwa, N., Lin, Y. M., et al. (2003). Involvement of the FGF18 gene in colorectal carcinogenesis, as a novel downstream target of the β -catenin/T-cell factor complex. *Cancer Res.* 63, 6116–6120.
- Shnitsar, I., Bashkurov, M., Masson, G. R., Ogunjimi, A. A., Mosessian, S., Cabeza, E. A., et al. (2015). PTEN regulates cilia through dishevelled. *Nat. Commun.* 6:8388. doi: 10.1038/ncomms9388
- Shu, W., Guttentag, S., Wang, Z., Andl, T., Ballard, P., Lu, M. M., et al. (2005). Wnt/ β -catenin signaling acts upstream of N-myc, BMP4, and FGF signaling to regulate proximal-distal patterning in the lung. *Dev. Biol.* 283, 226–239. doi: 10.1016/j.ydbio.2005.04.014
- Sokol, S. Y. (1996). Analysis of dishevelled signalling pathways during *Xenopus* development. *Curr. Biol.* 6, 1456–1467. doi: 10.1016/S0960-9822(96)00750-6
- Sorokin, S. (1962). Centrioles and the formation of rudimentary cilia by fibroblasts and smooth muscle cells. *J. Cell Biol.* 15, 363–377. doi: 10.1083/jcb.15.2.363
- Spektor, A., Tsang, W. Y., Khoo, D., and Dynlacht, B. D. (2007). Cep97 and CP110 suppress a cilia assembly program. *Cell* 130, 678–690. doi: 10.1016/j.cell.2007.06.027
- Steinhart, Z., and Angers, S. (2018). Wnt signaling in development and tissue homeostasis. *Development* 145:dev146589. doi: 10.1242/dev.146589
- Stepanenko, A. A., and Dmitrenko, V. V. (2015). HEK293 in cell biology and cancer research: phenotype, karyotype, tumorigenicity, and stress-induced genome-phenotype evolution. *Gene* 569, 182–190. doi: 10.1016/j.gene.2015.05.065
- Tamai, K., Semenov, M., Kato, Y., Spokony, R., Liu, C., Katsuyama, Y., et al. (2000). LDL-receptor-related proteins in Wnt signal transduction. *Nature* 407, 530–535. doi: 10.1038/35035117
- Tamai, K., Zeng, X., Liu, C., Zhang, X., Harada, Y., Chang, Z., et al. (2004). A Mechanism for Wnt coreceptor activation. *Mol. Cell* 13, 149–156. doi: 10.1016/S1097-2765(03)00484-2
- Tucker, R. W., Pardee, A. B., and Fujiwara, K. (1979). Centriole ciliation is related to quiescence and DNA synthesis in 3T3 cells. *Cell* 17, 527–535. doi: 10.1016/0092-8674(79)90261-7
- Vertii, A., Bright, A., Delaval, B., Hehnl, H., and Doxsey, S. (2015). New frontiers: discovering cilia-independent functions of cilia proteins. *EMBO Rep.* 16, 1275–1287. doi: 10.15252/embr.201540632
- Vora, S. M., Fassler, J. S., and Phillips, B. T. (2020). Centrosomes are required for proper β -catenin processing and Wnt response. *Mol. Biol. Cell* 31, 1951–1961. doi: 10.1091/mbc.E20-02-0139
- Wallingford, J. B., and Mitchell, B. (2011). Strange as it may seem: the many links between Wnt signaling, planar cell polarity, and cilia. *Genes Dev.* 25, 201–213. doi: 10.1101/gad.2008011
- Wallingford, J. B., Rowning, B. A., Vogell, K. M., Rothbächer, U., Fraser, S. E., and Harland, R. M. (2000). Dishevelled controls cell polarity during *Xenopus* gastrulation. *Nature* 405, 81–85. doi: 10.1038/35011077
- Wang, L., and Dynlacht, B. D. (2018). The regulation of cilium assembly and disassembly in development and disease. *Development* 145:dev151407. doi: 10.1242/dev.151407
- Wehrli, M., Dougan, S. T., Caldwell, K., O'Keefe, L., Schwartz, S., Valzel-Ohayon, D., et al. (2000). Arrow encodes an LDL-receptor-related protein essential for Wingless signalling. *Nature* 407, 527–530. doi: 10.1038/35035110
- Westlake, C. J., Baye, L. M., Nachury, M. V., Wright, K. J., Ervin, K. E., Phu, L., et al. (2011). Primary cilia membrane assembly is initiated by Rab11 and transport protein particle II (TRAPP-II) complex-dependent trafficking of Rabin8 to the centrosome. *Proc. Natl. Acad. Sci. U.S.A.* 108, 2759–2764. doi: 10.1073/pnas.1018823108
- Wiens, C. J., Tong, Y., Esmail, M. A., Oh, E., Gerdes, J. M., Wang, J., et al. (2010). Bardet-biedl syndrome-associated small GTPase ARL6 (BBS3) functions at or near the ciliary gate and modulates Wnt signaling. *J. Biol. Chem.* 285, 16218–16230. doi: 10.1074/jbc.M109.070953
- Willert, K., Brown, J. D., Danenberg, E., Duncan, A. W., Weissman, I. L., Reya, T., et al. (2003). Wnt proteins are lipid-modified and can act as stem cell growth factors. *Nature* 423, 448–452. doi: 10.1038/nature01611
- Wong, S. Y., Seol, A. D., So, P. L., Ermilov, A. N., Bichakjian, C. K., Epstein, E. H., et al. (2009). Primary cilia can both mediate and suppress Hedgehog pathway-dependent tumorigenesis. *Nat. Med.* 15, 1055–1061. doi: 10.1038/nm.2011
- Wu, C. T., Chen, H. Y., and Tang, T. K. (2018). Myosin-Va is required for preciliary vesicle transportation to the mother centriole during ciliogenesis. *Nat. Cell Biol.* 20, 175–185. doi: 10.1038/s41556-017-0018-7
- Zhai, L., Chaturvedi, D., and Cumberledge, S. (2004). Drosophila Wnt-1 undergoes a hydrophobic modification and is targeted to lipid rafts, a process that requires porcupine. *J. Biol. Chem.* 279, 33220–33227. doi: 10.1074/jbc.M403407200
- Zhan, T., Rindtorff, N., and Boutros, M. (2017). Wnt signaling in cancer. *Oncogene* 36, 1461–1473. doi: 10.1038/onc.2016.304
- Zingg, D., Debbache, J., Peña-Hernández, R., Antunes, A. T., Schaefer, S. M., Cheng, P. F., et al. (2018). EZH2-mediated primary cilium deconstruction drives metastatic melanoma formation. *Cancer Cell* 34, 69.e14–84.e14. doi: 10.1016/j.ccell.2018.06.001

Conflict of Interest: The authors declare that the research was conducted in the absence of any commercial or financial relationships that could be construed as a potential conflict of interest.

Copyright © 2021 Bernatik, Paclikova, Kotrbova, Bryja and Cajanek. This is an open-access article distributed under the terms of the Creative Commons Attribution License (CC BY). The use, distribution or reproduction in other forums is permitted, provided the original author(s) and the copyright owner(s) are credited and that the original publication in this journal is cited, in accordance with accepted academic practice. No use, distribution or reproduction is permitted which does not comply with these terms.

Appendix 8

Pejskova P, Reilly ML, Bino L, Bernatik O, Dolanska L, Ganji RS, Zdrahal Z, Benmerah A, **Cajane L***. KIF14 controls ciliogenesis via regulation of Aurora A and is important for Hedgehog signaling. *Journal of Cell Biology*. 2020 Jun 1;219(6):e201904107. doi: 10.1083/jcb.201904107.(JCR 2020. IF=10.539, Q1- Cell Biology)

ARTICLE

KIF14 controls ciliogenesis via regulation of Aurora A and is important for Hedgehog signaling

Petra Pejskova¹, Madeline Louise Reilly^{2,3}, Lucia Bino¹, Ondrej Bernatik¹, Linda Dolanska¹, Ranjani Sri Ganji⁴, Zbynek Zdrahal⁴, Alexandre Benmerah², and Lukas Cajanek¹

Primary cilia play critical roles in development and disease. Their assembly and disassembly are tightly coupled to cell cycle progression. Here, we present data identifying KIF14 as a regulator of cilia formation and Hedgehog (HH) signaling. We show that RNAi depletion of KIF14 specifically leads to defects in ciliogenesis and basal body (BB) biogenesis, as its absence hampers the efficiency of primary cilium formation and the dynamics of primary cilium elongation, and disrupts the localization of the distal appendage proteins SCLT1 and FBF1 and components of the IFT-B complex. We identify deregulated Aurora A activity as a mechanism contributing to the primary cilium and BB formation defects seen after KIF14 depletion. In addition, we show that primary cilia in KIF14-depleted cells are defective in response to HH pathway activation, independently of the effects of Aurora A. In sum, our data point to KIF14 as a critical node connecting cell cycle machinery, effective ciliogenesis, and HH signaling.

Introduction

The primary cilium is an antenna-like structure typically present on the surface of nondividing cells. While it was originally described as a vestigial organelle, and hence largely neglected, recent years have indisputably proven its status as a seminal structure for sensing various extracellular stimuli (Anvarian et al., 2019; Bangs and Anderson, 2017). In vertebrates, primary cilia govern many important aspects of embryonic development as well as tissue homeostasis in adulthood (Gerdes et al., 2009; Goetz and Anderson, 2010; Reiter and Leroux, 2017). Consequently, deregulation of primary cilia assembly, maintenance, or function is linked to numerous human diseases, collectively termed “ciliopathies” (Badano et al., 2006; Baker and Beales, 2009; Braun and Hildebrandt, 2017; Mitchison and Valente, 2017).

Primary cilium assembly, as well as disassembly, is intimately connected to cell cycle progression and in turn to the centrosome duplication cycle. In cultured cells, primary cilia formation generally occurs after exiting mitosis, in G₀, and conversely, resorption of primary cilia starts upon entry into the new cell cycle (Sánchez and Dynlacht, 2016). Cells in the G₀/G₁ phase typically contain one centrosome with two centrioles. A hallmark of the older, fully mature, so-called mother centriole is a set of distal and subdistal appendages, which decorate its distal

end (Bowler et al., 2019; Yang et al., 2018). As the immature, daughter centriole lacks those structures, only a mother centriole is capable of serving as the basal body (BB) to allow ciliogenesis (Firat-Karalar and Stearns, 2014; Kobayashi and Dynlacht, 2011; Nigg and Holland, 2018). However, the picture of the mutual interactions between primary cilia and the cell cycle still remains far from complete (Seeley and Nachury, 2010).

The fully grown primary cilium is composed of the BB, a mother centriole anchored to the plasma membrane via its distal appendages (Anderson, 1972; Kobayashi and Dynlacht, 2011); the transition zone, a specialized domain at the ciliary base involved in targeting and sorting of proteins to and from the ciliary compartment (Reiter et al., 2012); and the axoneme, a microtubule-based structure protruding into the extracellular space and enclosed within the ciliary membrane (Garcia-Gonzalo and Reiter, 2017; Satir et al., 2010).

The molecular aspects of primary cilium formation have started to emerge only recently, yet many questions remain to be answered. Ciliogenesis seems to be initiated by the docking of small vesicles to the distal appendages of a mother centriole and their subsequent fusion into one large ciliary vesicle (Lu et al., 2015; Sorokin, 1962; Wu et al., 2018). Correct assembly and

¹Department of Histology and Embryology, Masaryk University, Faculty of Medicine, Brno, Czech Republic; ²Laboratory of Hereditary Kidney Diseases, Institut National de la Santé et de la Recherche Médicale UMR 1163, Paris University, Imagine Institute, Paris, France; ³Paris Diderot University, Paris, France; ⁴Central European Institute of Technology, Brno, Czech Republic.

Correspondence to Lukas Cajanek: cajanek@med.muni.cz.

© 2020 Pejskova et al. This article is distributed under the terms of an Attribution–Noncommercial–Share Alike–No Mirror Sites license for the first six months after the publication date (see <http://www.rupress.org/terms/>). After six months it is available under a Creative Commons License (Attribution–Noncommercial–Share Alike 4.0 International license, as described at <https://creativecommons.org/licenses/by-nc-sa/4.0/>).

composition of the distal appendages is essential here, as the absence of many individual distal appendage components (CEP164, CEP83, CEP89, and SCLT1) prevents vesicle docking (Schmidt et al., 2012; Sillibourne et al., 2013; Tanos et al., 2013). A further step in ciliogenesis and mother centriole to BB transition resides in the removal of CP110 and CEP97 from the distal end of the mother centriole (Huang et al., 2018; Spektor et al., 2007). This process requires the activity of TTBK2, recruited to the BB by CEP164 (Čajánek and Nigg, 2014; Goetz et al., 2012; Oda et al., 2014). TTBK2 and the distal appendage protein FBF1 are also involved in the recruitment of components of the intraflagellar transport (IFT) system (Čajánek and Nigg, 2014; Goetz et al., 2012; Wei et al., 2013). In turn, IFT particles are responsible for moving cargos to the tip (anterograde IFT-B complex) of the axoneme and back (retrograde IFT-A complex). IFT-based transport is crucial for not only ciliogenesis but also primary cilium maintenance and sensory function (Lechtreck, 2015; Rosenbaum and Witman, 2002; Scholey, 2003).

Primary cilia seem to be implicated in the modulation of several pathways in vertebrates (Anvarian et al., 2019; Bryja et al., 2017), but it is indisputably Hedgehog (HH) signaling where the importance of primary cilia is best characterized (Bangs and Anderson, 2017; Mukhopadhyay and Rohatgi, 2014). In the absence of a ligand, the Patched receptor localizes to the primary cilium and is thought to inhibit the entry of the Smoothened (SMO) receptor into the primary cilium. Following ligand binding to Patched, SMO moves to the ciliary membrane and promotes the accumulation and activation of GLI proteins at the tip of the primary cilia. Activated GLIs are then transported out of the primary cilia by IFT complexes, and, in turn, regulate proliferation, migration, and differentiation via the induction of target gene expression in the cell nucleus (Bangs and Anderson, 2017; Briscoe and Théron, 2013).

As we have already mentioned, cell cycle machinery is thought to be connected to primary cilium formation, maintenance, and disassembly (Izawa et al., 2015). The exact mechanisms underlying this relationship are only beginning to emerge. It is generally accepted that cells initiate primary cilium resorption upon cell cycle reentry (G1/S) and that primary cilia are fully resorbed before the onset of mitosis (late G2). Thus, primary cilium formation can be readily triggered by serum starvation of various cultured cell lines, and conversely, primary cilium resorption can be induced by the addition of serum. Molecules implicated in controlling primary cilium disassembly seem to include many well-established regulators of mitotic progression (Plotnikova et al., 2012; Sánchez and Dynlacht, 2016; Seeley and Nachury, 2010). Among these, mitotic kinase Aurora A (AURA) has turned out to be a key regulatory element of primary cilium disassembly (Inoko et al., 2012; Pan et al., 2004; Plotnikova et al., 2012; Pugacheva et al., 2007). Activation of AURA in the context of primary cilium resorption is at least in part mediated by the adaptor protein HEF1/NEDD9 (Gradilone et al., 2013; Pugacheva et al., 2007) and in turn leads to the promotion of primary cilium disassembly by a mechanism expected to involve the deacetylase HDAC6 (Gradilone et al., 2013; Pugacheva et al., 2007). Additional levels of mutual crosstalk between the cell cycle tool kit and primary cilium assembly/

disassembly are likely to exist. Indeed, recent evidence has implied the possibility of a connection at the level of regulation and/or regulators of cytokinesis (Bernabé-Rubio et al., 2016; Smith et al., 2011).

Here, we report on a new role of kinesin KIF14 in primary cilium formation. Kinesins are molecular motors capable of binding microtubules through their motor domain, and they are involved in various aspects of intracellular transport, including ciliogenesis (Hirokawa et al., 2009; Reilly and Benmerah, 2019; Silverman and Leroux, 2009). They may serve different functions in primary cilia. While kinesin II complex is important for driving anterograde transport of IFT particles from the base of the cilium to its tip (Cole et al., 1998; Marszałek et al., 1999; Morris and Scholey, 1997), KIF7 seems to organize the HH signaling platform at the tip of the primary cilium (Endoh-Yamagami et al., 2009; He et al., 2014), and it has been proposed that KIF24 negatively regulates the early steps of primary cilium formation (Kobayashi et al., 2011) and mediates cilium disassembly (Kim et al., 2015). KIF14, a member of the kinesin-3 subfamily, has been previously implicated in the regulation of chromosome segregation (Zhu et al., 2005) and cytokinesis and midbody formation (Bassi et al., 2013; Carleton et al., 2006; Gruneberg et al., 2006; Moawia et al., 2017; Ohkura et al., 1997). Interestingly, recent reports have suggested a possible link between KIF14 mutations and ciliopathies (Filges et al., 2014; Makrythanasis et al., 2018; Reilly et al., 2019), yet no evidence that KIF14 is involved in ciliogenesis has been provided. In this work, we demonstrate through various means that KIF14 depletion is associated with primary cilium defects and hence KIF14 is important for primary cilium formation and primary cilium-related signaling. Moreover, we identify deregulated AURA as a mediator of at least some of the KIF14 depletion phenotypes.

Results

To find novel regulators of primary cilium formation, we used proteomics and literature data mining. In our proteomics approaches, we focused on the identification of CEP164 interactome. We have combined two independent strategies to obtain our candidates: coimmunoprecipitation (coIP) of endogenous CEP164 in hTERT RPE-1 (retinal pigment epithelium cells immortalized with human telomerase reverse transcriptase) cells and proximity-dependent biotinylation by inducibly expressed CEP164-BirA* in HEK293 (human embryonic kidney) cells. By combining the results from both experiments (Table S1 and Table S2) with literature data mining, we selected five candidates to focus on: CCDC92, LUZP1, SCYL2, KIF7, and KIF14 (Fig. 1 A).

KIF14 knockdown causes ciliogenesis defects

To assess the potential role of our candidates in ciliogenesis, we used siRNA to knock down their expression in the hTERT RPE-1 cell line (Fig. S1 A). Having confirmed efficient depletion of individual mRNAs, we next examined the possible impact of RNAi on the formation of ARL13B⁺ primary cilium (Fig. 1 B). Interestingly, while knockdown of SCYL2, LUZP1, CCDC92, or

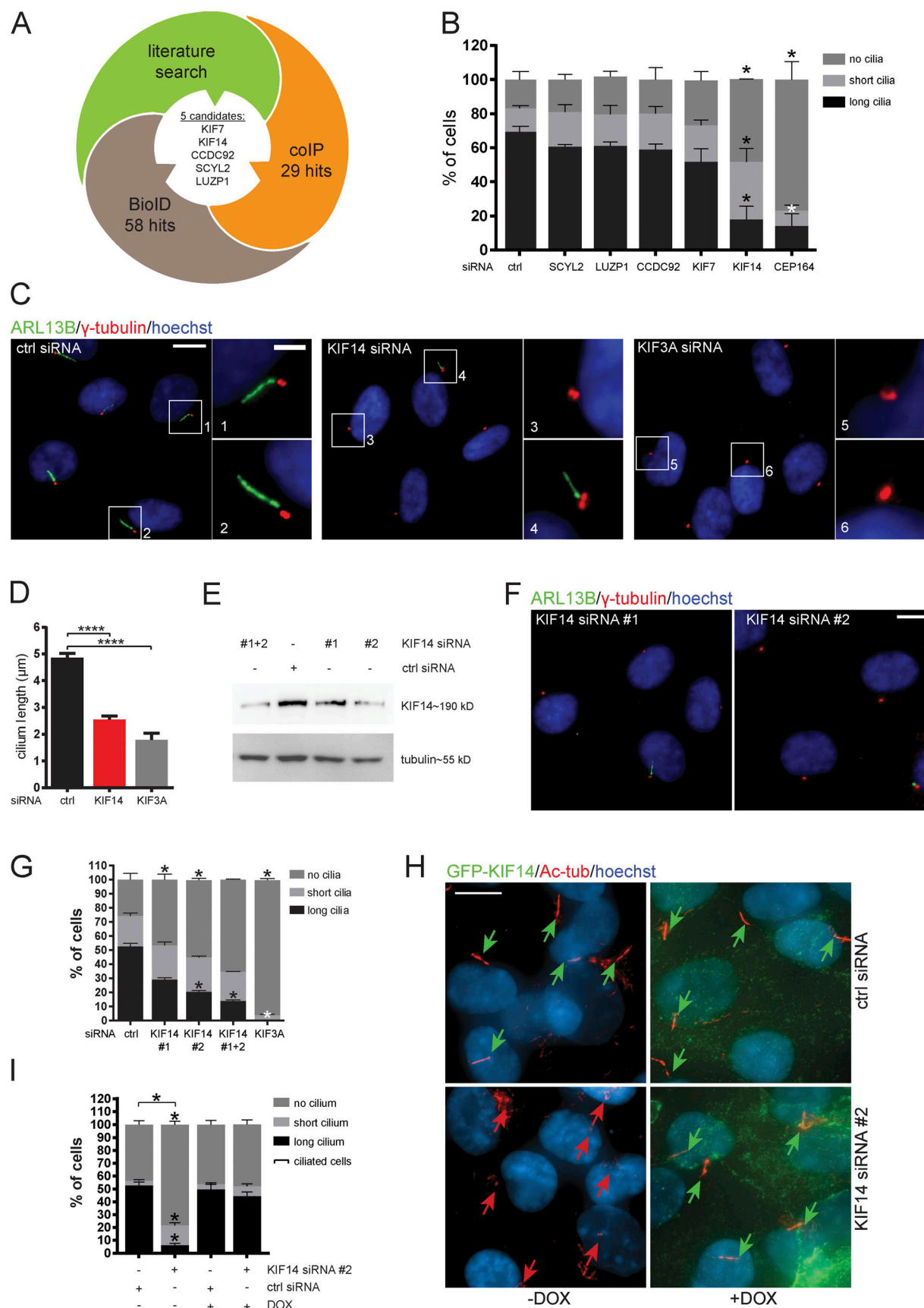


Figure 1. KIF14 knockdown causes ciliogenesis defects. (A) Graphical summary illustrating rational behind the selection of candidates. (B–H) hTERT RPE-1 cells were transfected with indicated siRNA and 24 h serum starved. (B) Quantification of ARL13B⁺ primary cilia formation. CEP164 siRNA was used as a

positive control. For SCYL2 and CEP164 silencing, we used single siRNA oligos; for LUZP1, CCDC92, KIF7, and KIF14, we used a 50 nM mix of oligos 1 and 2 (Table S3). **(C)** Representative images of immunofluorescent staining of ARL13B (green), γ -tubulin (red), and DNA (blue); scale bar, 10 μ m (crops 1 and 2 show examples of “long” primary cilia; crop 3 shows “no” cilium; and crop 4 shows a “short” primary cilium; scale bar, 2 μ m). Silencing of KIF3A was used as a positive control. **(D)** Graph of cilia length (only cells with ciliary axoneme are included). **(E–G)** Test of KIF14 knockdown efficiency using different siRNA oligos. **(E)** Western blot analysis of protein expression in total hTERT RPE-1 cell lysates. **(F)** Representative images of IF staining of ARL13B (green), γ -tubulin (red), and DNA (blue); scale bar, 10 μ m. **(G)** Quantification of ARL13B⁺ primary cilia formation after KIF14 knockdown using different siRNA oligos. KIF3A siRNA was used as a positive control. **(H)** IF staining of ciliogenesis defects rescue, caused by KIF14 siRNA #2-mediated depletion, by expression of GFP-KIF14si2res upon DOX induction (GFP-KIF14, green; Ac-tub, red; and DNA, blue); scale bar, 10 μ m. Green arrows point to long primary cilia (>3.3 μ m), and red arrows point to short primary cilia (<3.3 μ m). **(I)** Quantification of ciliogenesis rescue. Note that ciliated cells here refer to a sum of short-cilium and long-cilium cells. Asterisks indicate statistical significance determined using an unpaired *t* test (D and I; ciliated cells = short + long) or the Holm–Sidak method (B, G, and I; categories).

KIF7 showed no apparent effect on primary cilium formation, KIF14 depletion led to prominent ciliogenesis defects (Fig. 1, B and C). Specifically, the proportion of cells forming fully grown primary cilia (“long”; >3.3 μ m) after KIF14 knockdown was reduced compared with the control, while populations of cells with short (\leq 3.3 μ m) or no primary cilia were increased (Fig. 1, B and C). We subsequently examined the effect on primary cilium length more closely and found that primary cilia were on average ~50% shorter in KIF14-depleted cells than in controls (Fig. 1, C and D). To further corroborate these findings, obtained using a mix of two siRNAs, we tested the effects of KIF14 siRNA on ciliogenesis in hTERT RPE-1 cells using three individual KIF14 siRNA oligos. KIF14 siRNA #1 and #2 were used in our original experiments; KIF14 siRNA #3 had previously been shown to efficiently deplete KIF14 levels (Carleton et al., 2006). We tested their KD efficiency on protein (Fig. 1 E and Fig. S1 B) and mRNA (Fig. S1 C) levels and in turn examined their effects on the formation of ARL13B⁺ primary cilia. Importantly, all tested KIF14 siRNAs led to a similar defect in the formation of ARL13B⁺ primary cilia (Fig. 1, F and G; and Fig. S1, D–F). Furthermore, we confirmed the defect in primary cilium formation following KIF14 depletion using another marker of primary cilia, acetylated tubulin (Ac-tub) in hTERT RPE-1 (Fig. S1, G–I). Finally, to fully prove the specificity of ciliogenesis defects detected in the KIF14 siRNA condition, we established a stable hTERT RPE-1 cell line inducibly expressing a GFP-KIF14 mutant resistant to KIF14 siRNA #2 (GFP-KIF14siRNA2res; Fig. S1 J). Importantly, the expression of GFP-KIF14siRNA2res, following the depletion of endogenous KIF14, was able to fully restore the formation of primary cilia to levels comparable to controls (Fig. 1, H and I).

Having established that KIF14 is needed for efficient formation of primary cilia in hTERT RPE-1, we next examined its implication in ciliogenesis in several other cell lines. Importantly, we observed similar phenotypes following the depletion of KIF14 in neonatal human dermal fibroblasts (nHDFs; Fig. S1, K–M), human embryonic stem cells (hESCs; Fig. S1, N–P), human induced pluripotent stem cells (hiPSCs; Fig. S1, Q–S), and IMCD3s (a mouse inner medullary collecting duct cell line; Fig. S1, T–V). We conclude that the function of KIF14 in ciliogenesis is not restricted to one particular cell type.

KIF14 localizes to primary cilia in interphase cells

KIF14 was reported to localize to midbody during cytokinesis (Carleton et al., 2006; Gruneberg et al., 2006), which we also observed in our models (not shown). Given the effects of KIF14

depletion we found, we examined KIF14 localization in cells in interphase, when the cells can form primary cilia. First, we transiently expressed GFP-KIF14 and untagged KIF14, respectively, in hTERT RPE-1 and found that both proteins could localize to primary cilia (Fig. 2, A and B). To corroborate this observation, we examined the localization of endogenous KIF14. Importantly, while we detected the signal of the KIF14 antibody in primary cilia in hTERT RPE-1, the signal was diminished in cells transfected with KIF14 siRNA, thereby demonstrating the specificity of the KIF14 staining (Fig. 2 C).

Mutations in *KIF14* have been implicated in the etiology of microcephaly and kidney development defects (Filges et al., 2014; Makrythanasis et al., 2018; Moawia et al., 2017; Reilly et al., 2019). Given the observation of ciliary localization of KIF14, we in turn examined KIF14 mutants described by Reilly and colleagues (Reilly et al., 2019; Fig. 2 D), in terms of their ability to localize to BB and axoneme, respectively. We found that following transient transfection in hTERT RPE-1, all tested variants could be readily detected at centrin⁺ centrioles (Fig. 2, E and F). Intriguingly, KIF14 mutations leading to truncated protein moieties (Q1380x, Q1304x, and R1189x) showed a strong enrichment in the ciliary tip compartment (Fig. 2, E–G), in contrast to N-terminal motor domain mutants (R364C and T456M; previously demonstrated as being defective in the motor domain function (Reilly et al., 2019), which showed diminished signal intensity in the ciliary tip (Fig. 2, E–G). These results suggest that both N-terminal and C-terminal parts of KIF14 are implicated in the correct transport of KIF14 molecules in primary cilium axoneme.

KIF14 affects dynamics of cilia growth

Given the phenotypes we found, we next examined the dynamics of ciliogenesis defects following KIF14 depletion by tracking primary cilium growth using time-lapse microscopy (Fig. 3 A). First, we confirmed the consistency of the primary cilium formation defects after KIF14 depletion in the hTERT RPE-1 cell line expressing GFP-ARL13B upon doxycycline (DOX) induction (Fig. S2, A and B). Next, we tracked GFP-ARL13B⁺ cilia growth over time. We examined changes in the length of primary cilia within a period of 9 h post primary cilium induction and found that primary cilia after KIF14 knockdown were notably shorter than controls, with the differences becoming more pronounced at the later time points of our time-lapse experiment (Fig. 3 B). In agreement with this observation, our measurements further revealed that the initial speed of primary cilium elongation was

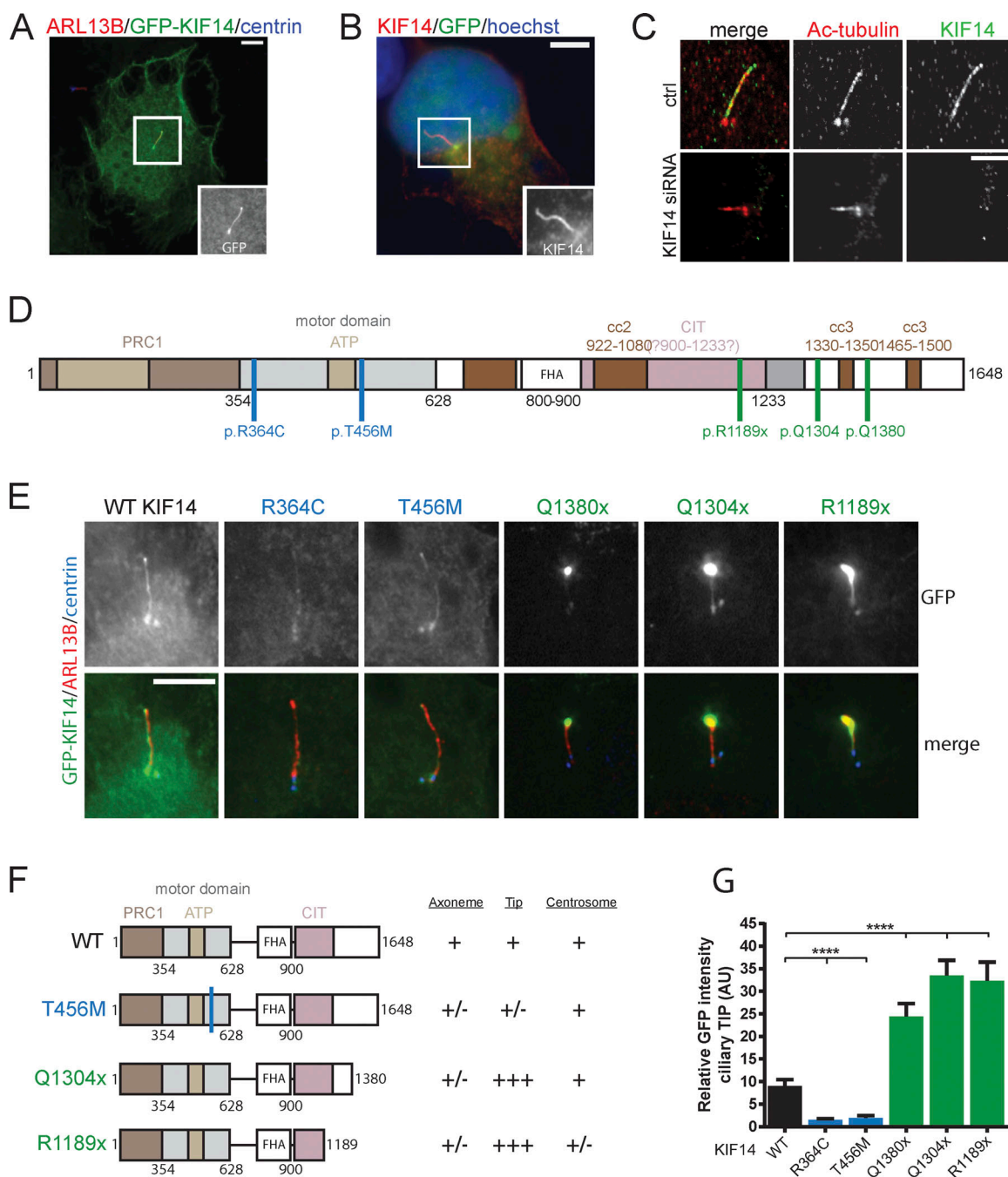


Figure 2. KIF14 localizes to primary cilia in interphase cells. (A) Representative image of IF staining detecting GFP-KIF14 (green) localization to the ciliary axoneme after overexpression in hTERT RPE-1, ARL13B (red), or centrin (blue); scale bar, 10 μ m. (B) Representative image of IF staining detecting untagged KIF14 (red) localization to the ciliary axoneme after overexpression in hTERT RPE-1, GFP (green), or DNA (blue); scale bar, 10 μ m. (C) Representative images of high-resolution microscopy analyses of endogenous KIF14 (green) localization to the ciliary axoneme and Ac-tub (red) in control vs. KIF14-depleted hTERT RPE-1 cells; scale bar, 5 μ m. (D) Scheme of KIF14 mutants (Reilly et al., 2018) transfected into hTERT RPE-1 cells. PRC1, Protein Regulator of Cytokinesis 1 - binding domain; CIT, Citron Kinase - binding domain; FHA, forkhead-associated domain. (E) Representative images of IF microscopy analysis of KIF14 truncated mutant localization, ARL13B (red), GFP-KIF14 (green), and centrin (blue); scale bar, 20 μ m. Note the accumulation of GFP-KIF14 in the ciliary tip upon transfection of C-terminally truncated mutants. (F) Graphical overview of GFP-KIF14 mutant localization. (G) Quantification of the GFP-KIF14 ciliary tip accumulation for different KIF14 mutants (relative fluorescent signal, arbitrary units). Asterisks indicate statistical significance determined using an unpaired t test, $n = 2$, $N \geq 55$. AU, arbitrary units.

comparable between controls and KIF14-depleted cells, but the growth in the KIF14 siRNA condition dramatically dropped at later time points and subsequently completely stopped (please note the effects on average and current speed of cilia

growth, respectively (Fig. 3, C and D). Together, these results have established that the depletion of KIF14 hampers the dynamics of primary cilium growth, mainly at the later stage of axoneme elongation.

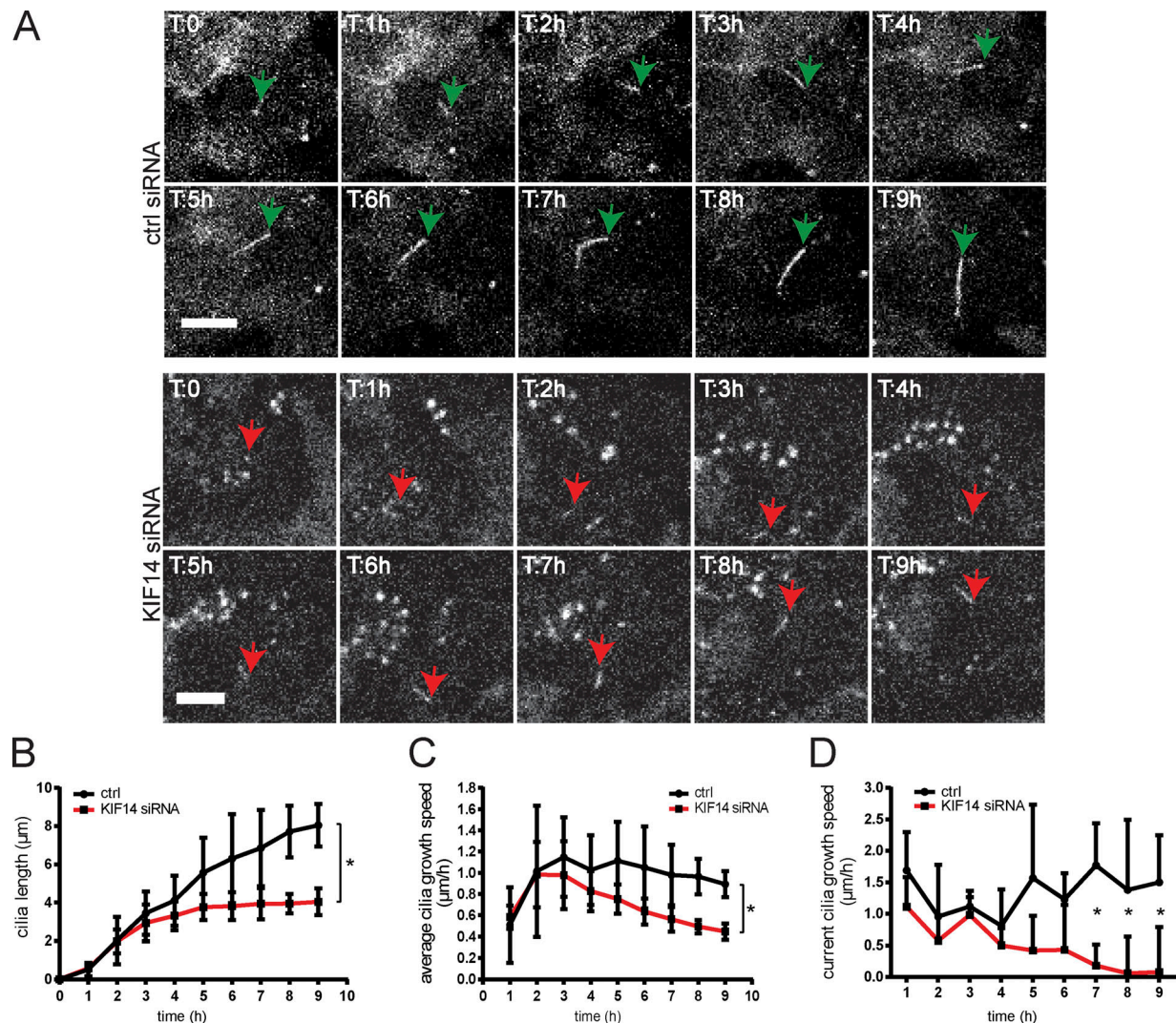


Figure 3. KIF14 depletion affects dynamics of primary cilia growth. (A–D) Time-lapse imaging microscopy analyses of ciliogenesis in stable GFP-ARL13B hTERT RPE-1 during 9 h after serum starvation. **(A)** Representative stills of control or KIF14 siRNA-transfected cells; scale bars, 20 μm (ctrl siRNA) and 10 μm (KIF14 siRNA). Green arrows point to long (control) primary cilia, and red arrows point to short primary cilia. T indicates time in hours. **(B)** Quantification of cilia length during time-lapse microscopy of GFP-ARL13B⁺ primary cilia. Note the increasing difference between control and KIF14-depleted cells at later time points. **(C and D)** Measurements of the speed of ciliary axoneme elongation. The average primary cilia growth speed (μm/h) reflects actual PC length reached at the indicated time (C), and the current primary cilia speed of growth (μm/h) represents an increment of length per hour (D). Asterisks indicate statistical significance determined using an unpaired *t* test.

KIF14 knockdown affects BB components and IFT-B anterograde transport

To better understand the function of KIF14 in primary cilium formation, we performed a series of IF microscopy analyses of BB and/or primary cilium components, previously implicated in key steps of ciliogenesis. First, we confirmed that tested markers of centriole or primary cilium (CAP350 [Yan et al., 2006], γ-tubulin, ARL13B, and Ac-tub) were not affected in terms of either localization or intensity by KIF14 KD (Fig. S2, C–F), and hence can be used for subsequent normalization to accurately determine the relative abundance of any further tested component in hTERT RPE-1. Next, we examined the BB components TTBK2 (Fig. 4, A and B), CP110 (Fig. S2 G), and CEP164 (Fig. S2, H and I), implicated in the early steps of primary cilium formation (Čajánek and Nigg, 2014; Goetz et al., 2012; Graser et al., 2007;

Schmidt et al., 2012; Spektor et al., 2007), and found their levels at BB not affected by KIF14 knockdown (Fig. 4, A and B; and Fig. S2, G–I). Interestingly, FBF1, a protein localizing between distal appendage sheets (Wei et al., 2013; Yang et al., 2018), and SCLT1, localizing to distal appendage sheets together with CEP164 (Tanos et al., 2013; Yang et al., 2018), were present at BB in significantly lower levels in KIF14-depleted cells than in controls (Fig. 4, C–F). In addition, levels of ODF2, a component of sub-distal appendages (Ishikawa et al., 2005), were also modestly decreased after KIF14 depletion (Fig. 4, G and H). Additional proteins tested (CEP290, INVS, and CEP97) were not affected by KIF14 siRNA knockdown (data not shown).

The primary cilium defects we observed following KIF14 depletion (observation of short cilia with altered axoneme elongation) implied possible perturbation of IFT machinery.

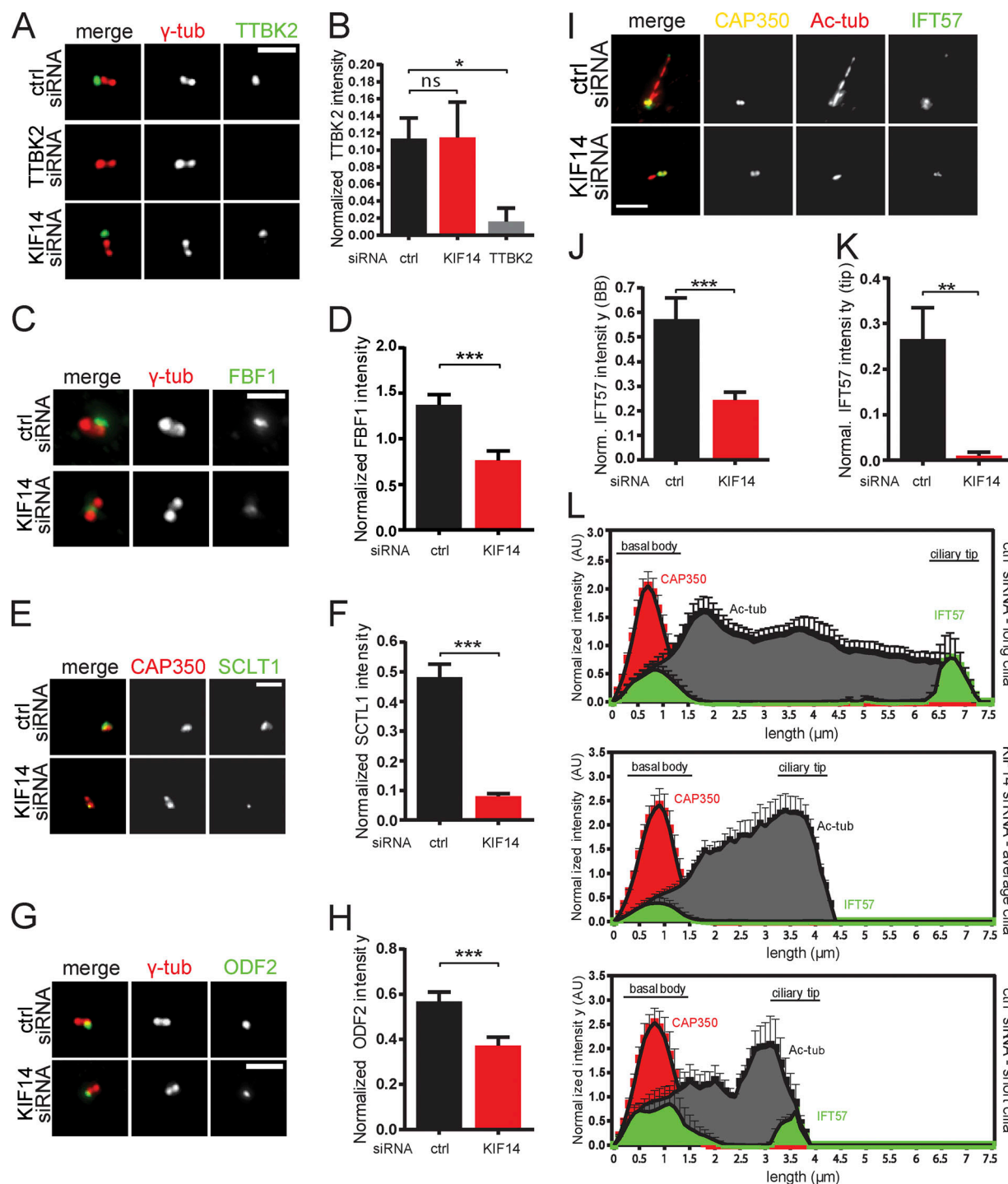


Figure 4. KIF14 knockdown affects BB components and IFT-B anterograde transport. hTERT RPE-1 cells were transfected with the indicated siRNA, serum starved for 24 h, and analyzed by IF microscopy. γ -tubulin or CAP350 staining was used to visualize centrosomes, and Ac-tub staining detected primary cilia. **(A)** TTBK2 localization (green) is not affected by KIF14 depletion (TTBK2 siRNA knockdown was used as a positive control); γ -tubulin, red; scale bar, 2 μ m. **(B)** Quantification of TTBK2 signal (normalized to γ -tubulin). **(C)** FBF1 protein intensity (green) is significantly affected by KIF14 depletion; γ -tubulin, red; scale bar, 2 μ m. **(D)** Quantification of FBF1 signal (normalized to γ -tubulin). **(E)** SCLT1 protein intensity (green) is significantly affected by KIF14 depletion; CAP350, red; scale bar, 2 μ m. **(F)** Quantification of SCLT1 signal (normalized to CAP350). **(G)** ODF2 protein intensity (green) is significantly affected by KIF14 depletion; γ -tubulin, red; scale bar, 2 μ m. **(H)** Quantification of ODF2 signal (normalized to γ -tubulin). **(I)** Localization of IFT57 (green) is significantly different after KIF14 depletion (CAP350, yellow; Ac-tubulin, red); scale bar, 3 μ m. **(J and K)** Quantification of IFT57 signal at BBs (J; "norm." means normalized to CAP350) and in the ciliary tip (K; "normal." means normalized to CAP350). **(L)** Histograms showing distribution of IFT57 (green), CAP350 (red), and Ac-tub (gray) and its signal intensities along primary cilia. Quantification was done for typical "control long" cilia and "short" defective cilia after KIF14 siRNA (N = 10) and for additional control also within a subset of short primary cilia in controls (N = 5). Asterisks or "ns" indicates statistical significance determined by unpaired t test (ns, not significant).

Indeed, microscopy analysis revealed that IFT57 normalized signal intensities at the base of primary cilia (Fig. 4, I and J) and in the ciliary tip (Fig. 4, I and K) were both significantly decreased upon KIF14 depletion. Importantly, this seems to be specifically related to KIF14 deficiency rather than the length of primary cilia, as we observed similar behavior when comparing primary cilia of KIF14 depleted cells to control primary cilia of comparable length (Fig. 4 L). Further, IFT88, another component of IFT-B complex, also showed reduced levels after KIF14 depletion, both at the BB (Fig. S2, J, K, and P) and the tip (Fig. S2, J, L, and P), while the levels of IFT140, a member of IFT-A complex, were found to be unchanged by the lack of KIF14 (Fig. S2, M–O and Q).

Together, these data suggest that KIF14 knockdown leads to changes in BB and IFT-B within the primary cilia.

KIF14 and CIT knockdown leads to minor effects on cell cycle in RPE-1

Given that KIF14 was described as playing a role in mitosis, particularly during cytokinesis (Carleton et al., 2006; Gruneberg et al., 2006; Reilly et al., 2019), we examined possible links between phenotypes we found and cell cycle/cytokinesis. Surprisingly, we found no evidence of defective cytokinesis in serum-starved hTERT RPE-1, as tested by immunofluorescence microscopy analyses of binucleated cells (Fig. 5 A). Next, we examined the cell cycle distribution after KIF14 knockdown by FACS or phospho-histone H3 (ph-H3; marker of G2/M cells) immunofluorescence staining. The results from nonstarved cells, depleted of KIF14 by siRNA, revealed a slight increase in S- and G2/M-cells, respectively (Fig. S3, A–D), in line with the reported mitotic role of KIF14 (Carleton et al., 2006; Gruneberg et al., 2006; Reilly et al., 2019). Importantly, we did not observe any alterations of cell cycle distribution after KIF14 knockdown at the endpoint phase of our experimental setup (cells after 24 h serum starvation), as examined by FACS (Figs. 5 B and S3 E) or ph-H3 immunofluorescence staining (Fig. 5, C and D). To corroborate these data further, we used siRNA targeting Citron Rho-interacting kinase (CIT; Fig. S3, F–H), an additional regulator of cytokinesis and KIF14 interactor (Bassi et al., 2011; Gruneberg et al., 2006). Importantly, we found that CIT siRNA had similar effects to the depletion of KIF14 in RPE-1 (Fig. S3, I–O).

Role of KIF14 in primary cilium formation seems independent of its role in mitosis

As the lack of binucleated cells following KIF14/CIT depletion is evidence, but not proof, of mitosis/cytokinesis occurring correctly, we sought other means to corroborate our results.

Prolonged mitosis typically leads to up-regulation of p53, which in turn triggers apoptosis, differentiation, or cell cycle arrest (Bazzi and Anderson, 2014; Orth et al., 2012; Renzova et al., 2018). To probe for any possible contribution of mitotic stress to the effect of KIF14 depletion on primary cilium formation, we first tested whether KIF14 siRNA could possibly elevate p53 levels. However, we found no evidence of such an effect (Fig. S3 P). Next, we examined the effects of prolonged mitosis, induced by 10 μ M monastrol for 2–4 h, on primary

cilium formation in hTERT RPE-1 (please see the scheme of the experiment in Fig. 5 E). We found that monastrol-mediated mitotic arrest and subsequent release had only a modest effect on primary cilium formation (please compare the first column in the “leftover” condition to the first column in the “M-arrest” condition; Fig. 5 F), and showed no effect on ciliary length (Fig. S3 Q). Importantly, however, the depletion of KIF14 led to a significantly lower percentage of ciliated cells, both in controls (“leftover”) and cells that experienced temporal mitotic arrest from monastrol treatment (Fig. 5 F). Based on these results, we conclude that any stress generated during mitotic arrest is unlikely to mediate the effects of KIF14 depletion on primary cilium formation.

Further, we aimed to test whether going through mitosis is required for the primary cilium phenotypes related to KIF14 knockdown. First, we depleted KIF14 by siRNA in hTERT RPE-1 cells that were serum starved for 24 h before transfection (Fig. 5 G). As expected, 24 h serum starvation showed a profound negative effect on the number of KI-67⁺ (marker of active cell cycle) cells (Fig. S3, R and S). Importantly, however, the cells transfected with KIF14 siRNA following the serum starvation still showed impaired primary cilium formation (Fig. 5, H–J) in a manner comparable to our initial observations (Fig. 1). To strengthen this observation further, we used the cyclin-dependent kinases inhibitor (R)-roscovitine (Meijer et al., 1997) to halt any remaining proliferation before the transfection with siRNA (Fig. 5 K). As shown in Fig. 5 L and quantified in Fig. 5, M and N, KIF14 depletion in hTERT RPE-1, cultured in serum-free medium + 20 μ M roscovitine, again demonstrated negative effects on the proportion of cells with primary cilium (in Fig. 5 M) and the primary cilium length (Fig. 5 N). From these experiments, we conclude that impaired ciliogenesis following KIF14 depletion is not a simple reflection of mitotic delay or long-term effects on cell cycle; rather, KIF14 has a novel function in primary cilium formation, which seems to be independent of its role during mitosis/cytokinesis. This prompted us to examine alternative explanations for KIF14 action toward primary cilium formation.

KIF14 depletion deregulates AURA

AURA is a kinase known for its function in centrosome maturation and mitotic progression. Intriguingly, recent studies have also implicated AURA in the resorption of primary cilia (Inaba et al., 2016; Inoko et al., 2012; Plotnikova et al., 2012; Pugacheva et al., 2007). In light of our data, we hypothesized that abrogated AURA activity might explain some of the defects observed in KIF14-depleted cells.

To this end, we examined levels of AURA phosphorylated at Thr288 within its kinase domain T-loop (phospho-AURA [pAURA]), which typically indicates increased activity of the kinase (Littlepage et al., 2002; Walter et al., 2000). Our Western blot analysis (Fig. S4 A) suggested an up-regulation of pAURA and hence its increased activity in the KIF14 siRNA condition. We confirmed this intriguing observation through immunofluorescence microscopy analyses of pAURA levels (Fig. 6, A and B; and Fig. S4 B). As these data were not able to resolve whether there is indeed an increase of pAURA at BB, we turned to high-

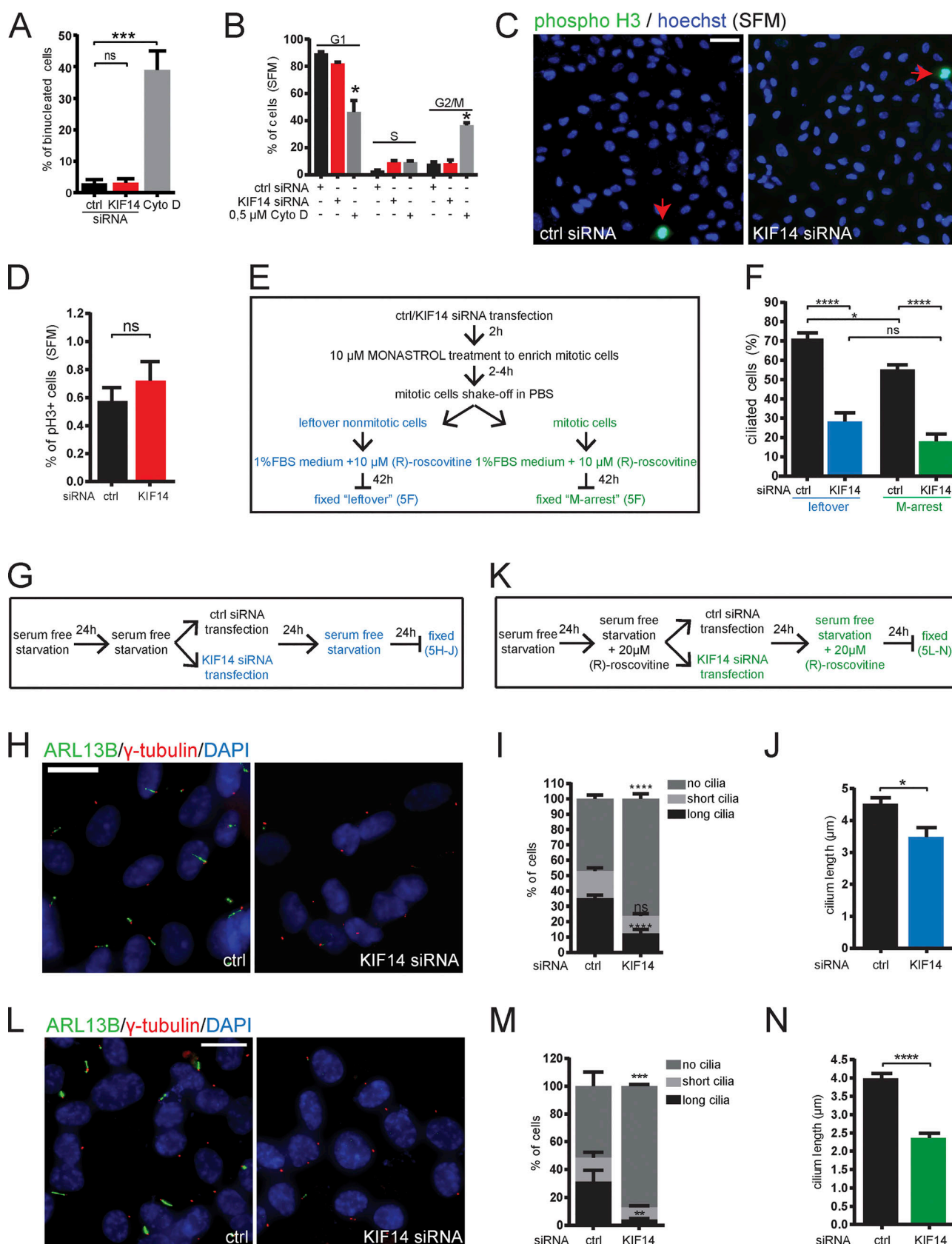


Figure 5. KIF14 function in primary cilia formation is related to interphase. (A–D) hTERT RPE-1 cells were transfected with the indicated siRNA, serum starved (SFM) for 24 h, and analyzed. (A) Quantification of proportion of binucleated cells by microscopy analysis. Treatment with 0.5 μM cytochalasin D (Cyto D) was used as a positive control. (B) Cell cycle distribution analysis of control or KIF14 siRNA-transfected cells with a comparable proportion of cells in G2/M

phase. **(C)** Representative images of detection of ph-H3^+ cells (green and pointed out with arrows; DNA, blue); scale bar, 50 μm . **(D)** Quantification of the percentage of ph-H3^+ cells, where a total of 40,000 nuclei were counted. **(E and F)** Examination of the effects of prolonged mitosis, induced by 10 μM monastrol for 2–4 h, on primary cilia formation in hTERT RPE-1 cells (please see the scheme of the experiment in E). **(F)** Monastrol-mediated mitotic arrest and subsequent release into 10 μM (R)-roscovitine (a cyclin-dependent kinase inhibitor) had only a modest effect on primary cilia formation (please compare black columns). Depletion of KIF14 leads to a significantly lower percentage of ciliated cells, both in controls (“leftover”) and cells that experienced temporal mitotic arrest from monastrol treatment. **(G–J)** hTERT RPE-1 cells were synchronized in G0 by serum starvation (24 h before siRNA transfection), transfected by the indicated siRNA, and serum starved for an additional 48 h before fixation (please see the scheme of the experiment in G). **(H)** Representative images (ARL13B in green, γ -tubulin in red, and DNA in blue; scale bar, 20 μm) show a significant effect of KIF14 depletion on ciliogenesis independent of mitosis, quantified as a decreased percentage of ciliated cells (I) and cilia length (J). **(K–N)** Same experimental setup as in G–J, with an additional 20 μM (R)-roscovitine to halt any proliferation before the transfection with siRNA (please see the scheme of the experiment in K, representative images in L; scale bar, 20 μm , and quantifications in M and N). Asterisks or “ns” indicates statistical significance determined using an unpaired *t* test (A, B, D, F, J, and N) or the Holm–Sidak method (I and M).

resolution confocal microscopy to specifically examine pAURA levels in this compartment. Importantly, as shown in Fig. 6, C and D, we detected a significant elevation of activated pAURA at BB after depletion of KIF14.

Having established a link between KIF14 depletion and AURA activation, we analyzed the effects of increased pAURA levels on primary cilium formation in our model (Fig. 6 E). In agreement with previous reports (Inoko et al., 2012; Plotnikova et al., 2012; Pugacheva et al., 2007), we found that overexpression of MYC-AURA decreased the proportion of hTERT RPE-1 cells able to build primary cilia (Fig. 6, E and F) and that those primary cilia formed were shorter than controls (Fig. 6 E and Fig. S4 C). Interestingly, we further found that MYC-AURA expression led to reduced BB levels of FBF1 (Fig. 6, G and H), SCLT1 (Fig. 6, I and J), IFT57 (Fig. 6, K and L), and IFT88 (Fig. S4, D and E), but not ODF2 (Fig. S4, F and G). These data not only indicated that AURA may play a role in recruitment of the examined BB components but importantly also suggested that there is not only a phenotypic correlation but probably also a causality between KIF14 depletion, AURA activation, and defective ciliogenesis.

AURA activity mediates effects of KIF14 depletion on primary cilia formation

To fully prove this hypothesis, we treated control or KIF14 siRNA-transfected hTERT RPE-1 cells with 100 nM AURA inhibitor TCS7010 (Fig. 7 A). First, we examined the effect of the KIF14 depletion in combination with AURA inhibition on the recruitment of FBF1 and found that while its levels at BB decreased in KIF14-depleted cells, treatment with AURA inhibitor restored its levels to that of controls (Fig. 7, B and C). Interestingly, we observed a similar rescue effect on KIF14 depletion for BB levels of SCLT1 (Fig. 7, D and E). Next, we examined possible rescue effects of KIF14 siRNA by AURA inhibitor on levels of IFT-B proteins. In line with earlier observations, KIF14 siRNA led to lower levels of IFT57 at the BB and ciliary tip (Fig. 7, F and G). Importantly, the addition of AURA inhibitor restored IFT57 ciliary levels in KIF14-depleted cells (Fig. 7, F and G), although we noted that distribution of the IFT57 signal along the axoneme was still somewhat different than in controls. A similar rescue effect was observed in the case of IFT88 (Fig. S5 A). Remarkably, the use of TCS7010 inhibitor also led to the rescue of two key phenotypes associated with KIF14 depletion in serum-starved cells: the reduction of the proportion of cells forming primary cilia (Fig. 7, H and I) and the defective cilia length (Fig. 7 J).

Activation of AURA is typically tightly controlled, with a number of proteins proposed to act as activators of AURA activity (Hirota et al., 2003; Hutterer et al., 2006; Inaba et al., 2016; Kinzel et al., 2010; Kozyreva et al., 2014; Kufer et al., 2002; Plotnikova et al., 2012; Ran et al., 2015). Having established elevated AURA activity as a mediator of several primary cilium and BB defects in KIF14-depleted cells, we in turn asked to what extent individual AURA activators contributed to the KIF14 depletion defects we observed. To this end, we transfected hTERT RPE-1 with KIF14 siRNA, together with either additional siRNA targeting the individual AURA activator or in combination with small-molecule calmidazolium chloride treatment (4 μM) to inhibit calmodulin. Interestingly, we found that targeting individual candidate activators had only modest rescue effects on the KIF14 depletion phenotypes; NEDD9 and PIFO siRNA conditions partially rescued the percentage of ciliated cells (Fig. S5 B), as well as the cilium length (Fig. S5 C). Depletion of the remaining candidates showed modest rescue of the primary cilium length defect (Fig. S5 C) but failed to produce statistically significant effects for the percentage of ciliated cells (Fig. S5 B). This implies that the mechanism of AURA activation in KIF14-depleted cells is rather complex and that in this case, the participation of several regulators of its activity seems more plausible than a scenario with one “master regulator.”

Together, these data have demonstrated a connection between KIF14 depletion and the up-regulation of the resorption pathway caused by elevated activation of AURA, which results in a short cilia phenotype and defects in ciliogenesis.

KIF14 regulates HH signaling independently of AURA activity

To examine any functional consequences of the observed defects in primary cilium formation, we tested the ability of KIF14-depleted cells to respond to HH pathway activation. As expected, when KIF14 was depleted, nHDF cells failed to induce expression of *GLII*, an HH pathway target gene (Lee et al., 1997), in response to a treatment with the agonist of the SMO receptor, smoothened agonist (SAG; Fig. 8 A). Furthermore, we examined the translocation of SMO into the primary cilia, which is a prerequisite for the activation of the expression of the target gene *GLII*. Interestingly, while in control nHDF cells SMO readily translocated into primary cilia upon SAG treatment, the SMO translocation was impaired in KIF14-depleted nHDF cells able to form primary cilia (Fig. 8, B and C; and Fig. S5 D). These data suggest that a deficiency of KIF14 protein leads not only to a somewhat expected defect in response to HH pathway

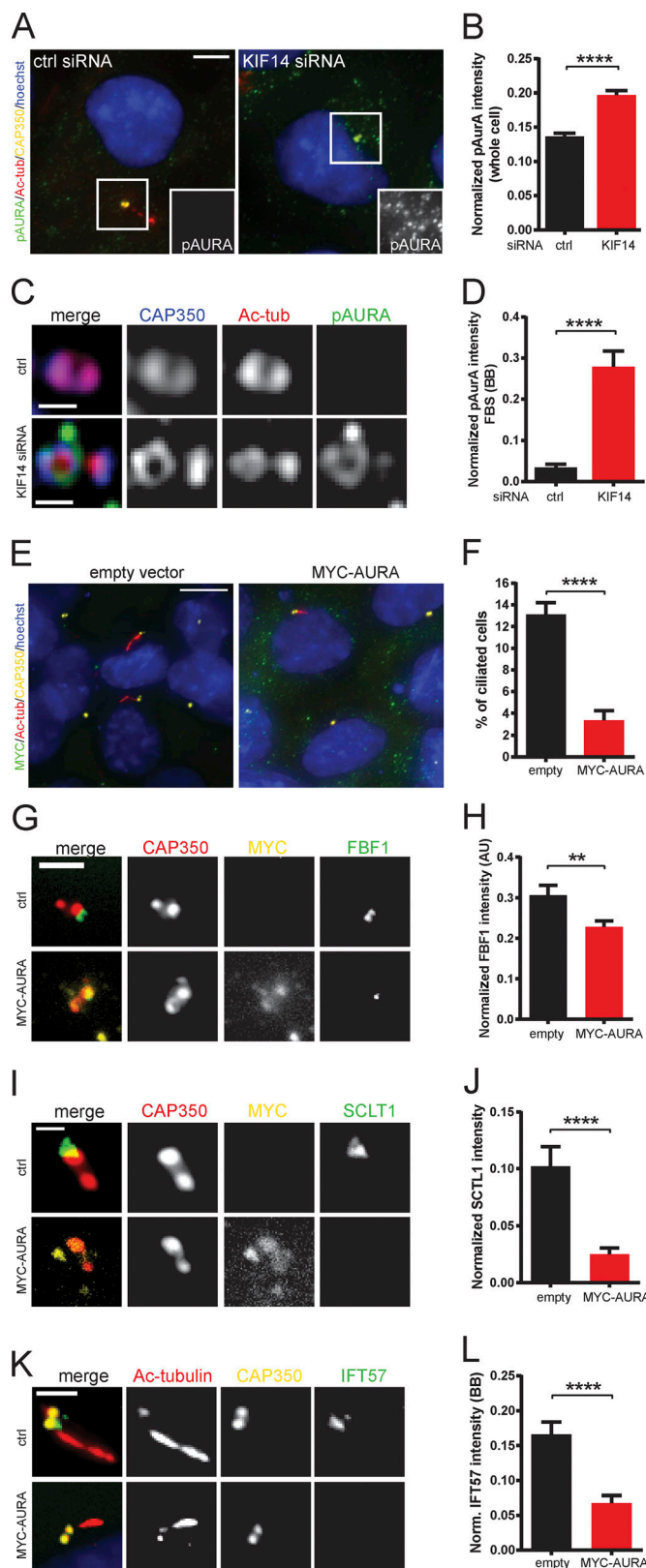


Figure 6. KIF14 depletion deregulates AURA. (A) Representative images of IF detection of pAURA (green), Ac-tub (red), CAP350 (yellow), and DNA (blue) in serum-starved hTERT RPE-1 cells; scale bar, 5 μ m. (B) Quantification of pAURA fluorescent intensity (normalized to Hoechst signal intensity) in serum-starved whole cells. (C) Detection of a BB-specific pool of pAURA

stimulation on the cell population level (in line with the observed reduction in the number of cells forming primary cilia) but intriguingly also to HH activation response abnormalities in short primary cilia formed upon KIF14 depletion.

Next, we asked whether the defect in SMO localization we found is also mediated by elevated AURA, as we observed for the ciliogenesis phenotypes. Remarkably, however, the accumulation of SMO in primary cilia in KIF14-depleted cells treated with AURA inhibitor was still impaired, even though the AURA inhibition showed prominent rescue effects on the percentage of ciliated cells and the primary cilium length (Fig. 8, D and E; and Fig. 7, H-J). In agreement with this result, we found that KIF14-depleted cells treated with AURA inhibitor were not able to respond to SAG agonist treatment through the induction of *GLII* mRNA (Fig. 8 F).

Together, those data propose that KIF14 has a dual role in relation to primary cilia formation and function, with the elevated AURA activity responsible for the ciliogenesis defects, but not the HH signaling abnormalities found.

Discussion

Cell cycle regulation and ciliogenesis are intimately interconnected via a regulatory network, the extent of which is only starting to become apparent. Here, we have explored this connection by examining the role of KIF14, a protein hinted at during our initial proteomics experiments, in primary cilium formation. We have found that KIF14 is required for correct BB biogenesis and primary cilium formation in several cell lines, as well as for proper response of primary cilia to HH pathway activation. Further, we have pinpointed deregulated AURA activity as a downstream mediator of KIF14 deficiency responsible for BB and primary cilium defects (Fig. 9).

Our testing of five putative regulators of primary cilium formation has revealed that depletion of KIF14 leads to a penetrant decrease in the proportion of cells with primary cilia and reduced ciliary length, in contrast to depletion of SCYL2, LUZP1, CCDC92, or KIF7, which shows no apparent effect on ciliogenesis. In a similar vein, and in line with reports on connections

(green) in nonstarved cells using high-resolution microscopy (CAP350, blue; Ac-tub, red); scale bar, 0.4 μ m. (D) Quantification of pAURA signal intensity on BB (normalized to CAP350 signal intensity). (E-L) Effect of MYC-AURA overexpression on 24 h serum-starved hTERT RPE-1 cells. (E) Representative images of IF detection of MYC-tagged (green), Ac-tub⁺ primary cilia (red; CAP350, yellow; DNA, blue) in mock- or MYC-AURA-transfected cells; scale bar, 10 μ m. (F) Graph quantifying statistically significant decrease of ciliated cells percentage after MYC-AURA overexpression. (G and H) Examination of FBF1 (green) localization and decreased intensity after MYC-AURA overexpression. Representative images (CAP350 in red, MYC in yellow) are shown in G (scale bar, 2 μ m) and intensity quantification (normalized to CAP350) in H. (I and J) Examination of SCLT1 (green) localization and decreased intensity after MYC-AURA overexpression. Representative images (CAP350 in red, MYC in yellow) are shown in I (scale bar, 1 μ m) and intensity quantification (normalized to CAP350) in J. (K and L) Examination of IFT57 (green) localization and decreased intensity at BBs after MYC-AURA overexpression. Representative images (Ac-tub in red, CAP350 in yellow) are shown in K (scale bar, 2 μ m) and BB intensity quantification (normalized to CAP350) in L. Asterisks indicate statistical significance determined using an unpaired *t* test.

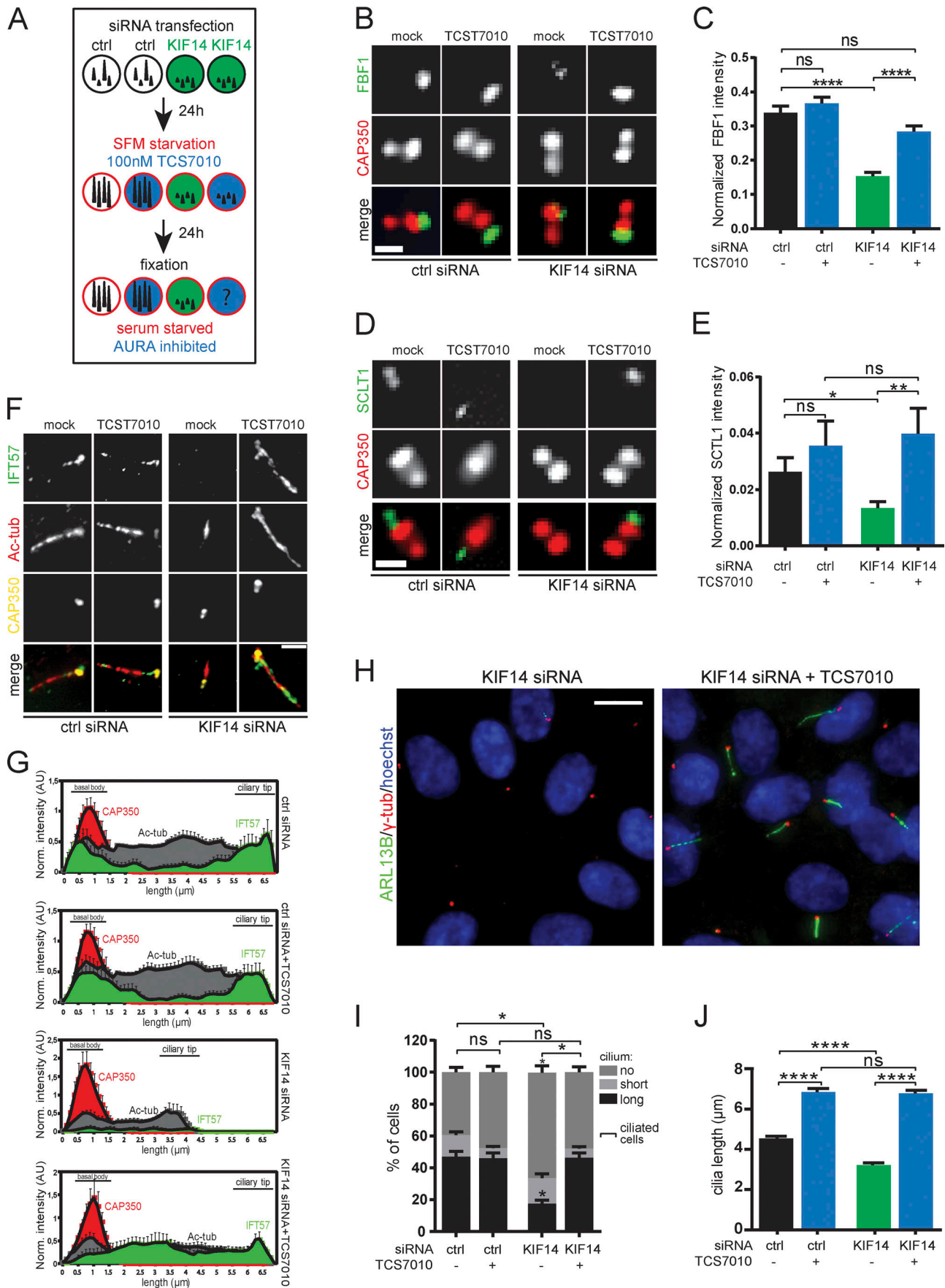


Figure 7. AURA activity mediates effects of KIF14 depletion on primary cilia formation. (A) Experimental design of KIF14 siRNA effects rescue using 100 nM TCS7010 (AURA inhibitor). (B–J) hTERT RPE-1 cells were transfected with indicated siRNA 48 h before fixation and last 24 h serum starved and AURA inhibited by TCS7010. (B and C) Examination of FBF1 (green) localization and intensity. Representative images (CAP350 in red; scale bar, 1 μ m) are shown in B and intensity quantification (normalized to CAP350) in C. (D and E) Examination of SCLT1 (green) localization and intensity. Representative images (CAP350 in red; scale bar, 1 μ m) are shown in D and intensity quantification (normalized to CAP350) in E. (F and G) Examination of IFT57 (green) localization and intensity. Representative images (CAP350 in yellow, Ac-tub in red; scale bar, 2 μ m) are shown in F and intensity quantification histograms (normalized to CAP350; N = 5) in G ("norm." means normalized to CAP350). (H) Representative images of AURA inhibition rescue experiment of ciliogenesis defect caused by KIF14 knockdown. Detection of ARL13B⁺ primary cilia (green; γ -tubulin, red; DNA, blue); scale bar, 10 μ m. (I) Quantification of ARL13B⁺ primary cilia formation. (J) Effects on ARL13B⁺ primary cilia length. Asterisks or "ns" indicates statistical significance determined using Tukey's multiple comparisons test (C, E, and J), an unpaired t test (I; ciliated cells = short + long), or the Holm–Sidak method (I; categories).

between KIF7 and ciliopathies (Ali et al., 2012; Dafinger et al., 2011), the absence of KIF7 does not seem to lead to major ciliogenesis defects related to IFT or trafficking of HH pathway proteins into primary cilia; instead, KIF7 has been demonstrated to reside in ciliary tips, where it is responsible for fine-tuning the response to HH pathway activation (Endoh-Yamagami et al., 2009; He et al., 2014). It should be noted that the absence of KIF7 led to increased primary cilium length in mouse embryonic fibroblasts (He et al., 2014), which we did not observe in hTERT RPE-1 cells following KIF7 depletion. SCYL2, LUZP1, and CCDC92 have previously been found to be associated with centrioles/BBs (Chaki et al., 2012; Gupta et al., 2015), but as the absence of obvious primary cilium formation phenotypes implies, if they somehow function in primary cilium formation, their role is likely modulatory and/or redundant.

Previous studies established KIF14 as a regulator of cytokinesis (Carleton et al., 2006; Gruneberg et al., 2006; Makrythanasis et al., 2018; Moawia et al., 2017; Ohkura et al., 1997; Reilly et al., 2019) and, given the reported developmental kidney and brain defects linked to *KIF14* mutations, also suggested its possible participation in the pathophysiology of ciliopathies (Filges et al., 2014; Heidet et al., 2017; Reilly et al., 2019). Reilly and colleagues showed that a lower incidence of primary cilia following KIF14 ablation in zebrafish is a consequence of the accumulation of cells blocked in mitosis, which in turn prevents primary cilium formation, as mitotic cells are not able to make a primary cilium. However, our data suggest that the relationship between KIF14 and primary cilium formation is more complex. First, we (this study) and others have detected KIF14 associated with BB components (Gupta et al., 2015; Jakobsen et al., 2011) or localized to primary cilium axoneme. Second, in agreement with the reports on the mitotic role of KIF14, we have also detected alterations in the cell cycle progression of KIF14-depleted cells. However, as those changes are restricted to serum-cultured cells and are somewhat modest, we argue that they do not explain the prominent defects in ciliogenesis and HH pathway activation we detected following serum starvation of those cells. Third, the presence of binucleated cells, a hallmark of dysfunctional cytokinesis, showed very low to no phenotypic penetrance in our models, in line with a report of a very modest incidence of binucleation in nontransformed cell lines over cancerous cell lines (McKenzie and D'Avino, 2016). With all that said, our data clearly indicate the requirement of KIF14 for effective ciliogenesis in several cell types we tested, encompassing human cells of embryonic origin (hPSCs), hTERT RPE-1, nHDF-1, and the murine cell line IMCD3.

There might be several reasons as to why the primary cilium formation phenotypes related to KIF14 deficiency were not detected in previous studies. Even though we consistently observed the KIF14 depletion-linked primary cilium defects in several cell lines, we cannot formally exclude it plays a cell-type-specific role in vivo. In fact, this possibility has support in earlier reports describing cell-type-restricted requirement of KIF14 or CIT for efficient cytokinesis in *Drosophila* (Ohkura et al., 1997), mouse embryos (Di Cunto et al., 2000), and humans (Filges et al., 2014; Reilly et al., 2019). In addition, the role of KIF14 in primary cilium formation may be redundant with a yet-unknown factor. In turn, its deficit may not be sufficiently penetrant in a model of constitutive knockout (Reilly et al., 2019) due to genetic compensation (El-Brolosy and Stainier, 2017). In fact, striking phenotypic differences between the acute depletion and the long-term loss have been reported for several regulators of primary cilium formation (Hall et al., 2013; Yadav et al., 2016).

Both cytokinesis and ciliogenesis rely on strict coordination of microtubule organization and directed membrane trafficking; both have been intensively studied, yet evidence of a "shared" regulatory toolbox is surprisingly sparse. The first indication that such crosstalk might indeed be plausible came from a study showing the localization of a set of central spindle/midbody proteins (PRC1, MKLP-1, INCENP, and centriolin) to BBs in vertebrate ciliated epithelial cells and in turn reporting primary cilium phenotypes for the aforementioned mutants in *Caenorhabditis elegans* (Smith et al., 2011). Conversely, it was also shown that IFT88 depletion leads to mitotic defects in HeLa cells, mouse kidney cells, and zebrafish embryos (Delaval et al., 2011). Furthermore, Bernabé-Rubio and colleagues (Bernabé-Rubio et al., 2016, 2019 Preprint) showed that the midbody is required for primary cilia formation. In addition, CIT mutations in rats were reported to cause alterations in primary cilium length (Anastas et al., 2011), and CIT protein was found to be associated with primary cilia in mice (Mick et al., 2015). Intriguingly, both CIT and KIF14 siRNA were observed to have an effect on primary cilium formation in recent large-scale screens (Kuhns et al., 2013; Wheway et al., 2015), and the proteins were found to be associated with centrosomes (Jakobsen et al., 2011). Our experiments have demonstrated that KIF14 depletion impairs primary cilium formation even if the cells have been starved and chemically arrested before siRNA transfection. This indicates that primary cilium phenotypes linked to the depletion of KIF14 are not a mere consequence of impaired mitosis but rather that KIF14

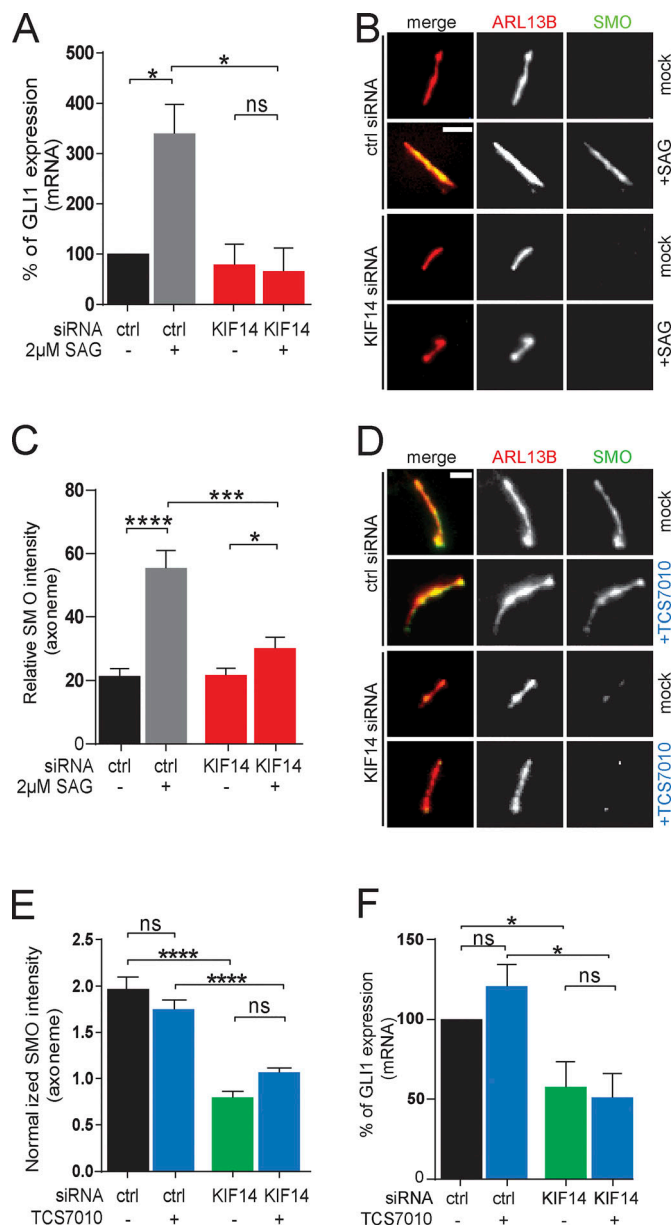


Figure 8. KIF14 regulates HH signaling independently of AURA activity. (A–C) Functional analyses of HH pathway activation following control or KIF14 silencing and mock or 2 μM SAG treatment in nHDFs. (A) Quantitative RT-PCR quantification of the effect of *GLI1* on mRNA levels. (B and C) Analysis of the effect of KIF14 depletion on SMO translocation to the ciliary axoneme and its intensity. (B) Representative images of SMO (green) and ARL13B (red) IF detection; scale bar, 2 μm. (C) Quantification of changes in relative SMO intensity. (D–F) Examination of effect of TCS7010 AURA inhibition on response of nHDF cells transfected with the indicated siRNA to HH pathway activation. Experimental setup was the same as in Fig. 7 A, but with an additional 0.5 μM SAG treatment for the last 24 h. (D) Representative images of SMO (green) and ARL13B (red) IF detection in nHDF cells transfected with ctrl or KIF14 siRNA and treated with mock or AURA inhibitor; scale bar = 2 μm. Quantification of changes in SMO intensity (normalized to ARL13B) is shown in E and quantitative RT-PCR quantification of effect on mRNA level of *GLI1* in F. Asterisks or “ns” indicate statistical significance determined using Tukey’s multiple comparisons test.

has a novel role in interphase cells. Given that, it should be rewarding to explore in detail the extent of cooperation between regulators of cytokinesis and ciliogenesis, respectively.

Additional evidence of a specific, interphase-related role for KIF14 relates to its ability to localize to primary cilia. In this regard, our data suggest that both the N-terminal motor domain and the C-terminal part of KIF14 are required for its efficient transport in primary cilium axoneme. The fact that the motor domain mutants R364C and T456M were to some extent able to get inside the primary cilia, albeit with reduced efficiency, suggests a possible participation of a different motor protein. One point to bear in mind is that these experiments were performed in the KIF14 WT background, so it is plausible that the presence of WT KIF14 is somewhat responsible for this observation. Alternatively, although the mutations R364C and T456M lead to several impairments of KIF14 motor function (Reilly et al., 2019), we cannot exclude the possibility that some residual motor activity is still retained.

C-terminal KIF14 mutations (Q1380*, Q1304*, and R1189*) used in our study give rise to truncated protein moieties, with functional motor domain. Nonetheless, their ability to participate in either intermolecular or intramolecular interactions is expected to be hampered (Reilly et al., 2019; Verhey et al., 2011). In agreement with this prediction, all these mutants showed prominent accumulation in the tip of primary cilium (at microtubule ends), which we suspect relates to their constitutively active character in terms of microtubule binding (see also Reilly et al., 2019) and in turn the inability to reload on retrograde transport complexes to be transported back to ciliary base.

Activation of AURA is typically linked to resorption of primary cilia (Inaba et al., 2016; Inoko et al., 2012; Plotnikova et al., 2012; Pugacheva et al., 2007). Primary cilium phenotypes related to KIF14 depletion in our models include hampered speed of primary cilium elongation, hindered responsiveness of primary cilium to HH pathway stimulation, and defective recruitment and/or distribution of a subset of components of BB appendages (FBF1, SCLT1, and ODF2) or IFTs (IFT88 and IFT57). Our data imply that aberrant AURA activity is responsible for the defects in BB biogenesis and dynamics of primary cilium formation. Indeed, altered distribution of IFT88 along the axoneme, reminiscent of what we see following KIF14 depletion, was observed upon inhibition of AURA (Pugacheva et al., 2007). In addition, we speculate that FBF1, which is involved in the assembly of IFT complexes (Wei et al., 2013) and that we found regulated by KIF14 and AURA, might also be implicated in the observed alterations in the distribution of IFT components. Furthermore, SCLT1 and FBF1 are incorporated into distal appendages during centriole maturation in the G2 phase of the cell cycle (Tanos et al., 2013), and FBF1 undergoes temporal removal from distal appendages during mitosis (Bowler et al., 2019), when AURA activity peaks. Importantly, our data represent the first evidence implicating AURA in the control of distal appendage components in human cells, in line with the recently reported role of AURA in the regulation of mitotic removal of CEP164 from distal appendages in the murine IMCD3 cell line (Bowler et al., 2019). Of note, previous work by Tanos and colleagues (Tanos et al., 2013) showed that CEP164 requires SCLT1 for its localization to distal appendage. As our data demonstrate that elevated AURA activity affects SCLT1, but not CEP164, we speculate the residual SCLT1 present in distal appendage suffices for the correct localization of CEP164.

FINAL SCHEME

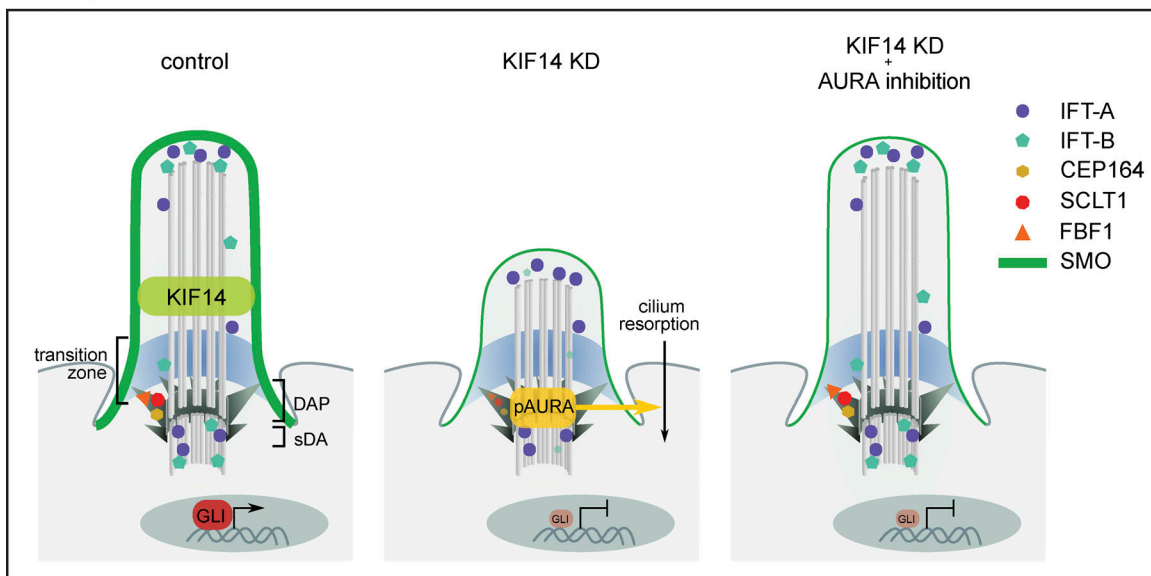


Figure 9. **Final scheme.** Graphic summary of prominent phenotypes observed after KIF14 depletion and effects AURA inhibition. DAP, distal appendage proteins; KD, siRNA knockdown; sDA, subdistal appendage. KIF14 localizes to the ciliary axoneme. KIF14-depleted cells have increased pAURA levels on BBs, decreased intensities of distal appendage proteins FBF1 and SCLT1, and changed distribution of IFT57 and IFT88. This in turn leads to lower proportion of ciliated cells, reduced ciliary length, and failure to respond to HH pathway activation (reduced SMO ciliary localization and diminished expression of target gene *Gli1*). Treatment of KIF14-depleted cells by AURA inhibitor rescues the localization defects of FBF1, SCLT1, IFT57, and IFT88; defective cilia formation; and reduced ciliary length but fails to restore competence of KIF14-depleted primary cilia to respond to HH pathway activation.

Our data suggest that the role of KIF14 in primary cilium formation is related to the activation of AURA in interphase by a currently unknown mechanism. AURA activity is typically regulated by interactions with adaptor proteins, with TPX2, AJUBA, and BORA playing the most prominent roles in the activation of AURA during mitosis (Carmena et al., 2009). Recent studies hinted that nonmitotic activation of AURA in the context of primary cilium resorption is at least in part mediated by the adaptor protein HEF1/NEDD9 (Korobeynikov et al., 2017; Pugacheva et al., 2007). Additional proteins implicated in AURA activation in interphase include PIFO (Kinzel et al., 2010), Trichoplein (Inoko et al., 2012), and CPAP (Gabriel et al., 2016). We have attempted to pinpoint a key factor responsible for AURA activation in KIF14-depleted cells. Nonetheless, our data argue against a model with one “master” activator mediating AURA activation in our models and rather suggest the participation of several regulators, which we speculate might act in a synergistic fashion. A detailed examination of the mechanism of how KIF14 regulates AURA should not only bring the necessary mechanistic insight but could also provide a means for possible future therapy to mitigate defects related to KIF14 mutations. Importantly, not all KIF14 depletion phenotypes seem to be linked to elevated AURA activity. Our data clearly show that inhibition of AURA in KIF14-depleted cells is able to almost completely rescue the defective localization of SCLT1, FBF1, IFT88, and IFT57, and, in turn, the proportion of cells able to assemble a fully grown primary cilium. However, although the primary cilia form in numbers and lengths similar to controls, these primary cilia fail to respond accordingly to the stimulation of the HH pathway with SAG. Thus, these data imply that KIF14 also plays a specific

role in the activation of the HH signaling pathway, which is distinct from the effects on primary cilium formation mediated by the elevated AURA activity.

In sum, our study demonstrates a novel function for KIF14 in the regulation of primary cilium formation dynamics and responsiveness to HH signaling in human cells. It identifies AURA activity as a downstream mediator of at least some of the KIF14 depletion-related primary cilium defects and points toward KIF14 as an important element connecting cell cycle machinery, effective ciliogenesis, and HH signaling.

Materials and methods

Cell culture, transfections, and treatments

All cell lines were cultured at 5% CO₂ at 37°C. hTERT RPE-1 (Čajánek and Nigg, 2014) and Flp-In T-REx RPE-1 (both kind gifts from E. Nigg, Biozentrum, University of Basel, Basel, Switzerland) and mouse innermedullary collecting duct cells (IMCD-3; kind gift from G. Jansen, Erasmus University Medical Center, Rotterdam, Netherlands) were cultured in DMEM/F12 supplemented with 10% FBS, 1% L-Glutamine (all from ThermoFisher), and 1× penicillin/streptomycin (Biosera). HEK293T and Flp-In T-REx 293 cells (#R78007; Invitrogen) were cultured in GlutaMax DMEM supplemented with 10% FBS (both from ThermoFisher) and 1× penicillin/streptomycin (Biosera). Inducible cell lines were cultivated in standard medium, with tetracycline-free FBS, for induction and media supplemented with 1 µg/ml DOX. nHDFs (#C0045C; Gibco) were cultivated in knockout DMEM supplemented with 10% heat-inactivated FBS, 1% L-Glutamine (all from ThermoFisher), 1× nonessential amino

acids, 1× penicillin/streptomycin (both from Biosera), and 1% β-mercaptoethanol (Sigma-Aldrich). hESCs (CCTL14; <https://hpscreg.eu/cell-line/MUNIE007-A>) were cultured in feeder-free conditions on Matrigel-coated cell culture plastic in daily exchanged mouse embryonic fibroblast-conditioned hESC medium (DMEM/F12, 15% knockout serum replacement; both from ThermoFisher), 2 mM L-glutamine, 1× nonessential amino acids, 0.5% Pen/Strep (all from Biosera) + 0.5× ZellShield (Minerva Biolabs), 100 μmol/L β-mercaptoethanol (Sigma-Aldrich), and 10 ng/ml hFGF2 (ThermoFisher). hiPSCs (Neo1, derived as described previously; Barta et al., 2016) were cultured in feeder-free conditions on Matrigel-coated plastic in daily exchanged mTeSR medium (StemCell Technologies).

Cells were transfected 24 h after seeding at 60% confluency (both human stem cell lines were seeded in high density to reach full confluency at the end of the experiment). DNA transfections of RPE-1 cells were done with Lipofectamine 3000 (ThermoFisher) or FuGENE HD Transfection (Promega) 24 h before analysis, and siRNAs were transfected with Lipofectamine RNAiMAX (ThermoFisher) 48 h before analysis. HEK293 cells were transfected using polyethylenimine (Sigma-Aldrich) 24 h before analysis. For knockdowns of KIF14, CIT, KIF7, SCYL2, LUZP1, CCDC92, AJUBA, BORA, NEDD9, PIFO, TCHP, or TPX2, the cells were transfected using different siRNA oligos (25 nM #1, 25 nM #2, or 25 nM #3 separately, where indicated) or 50 nM mix (50 nM mix of 25 nM #1 and 25 nM #2, where indicated). For a list of all siRNA sequences used, see Table S3.

For cilia analysis, cells were starved in serum-free medium for 24 h before analysis. To induce HH pathway activity, nHDF cells were starved in serum-free media and treated with 0.5–2 μM SAG (SMO agonist; Sigma-Aldrich) for 24 h before analysis (Fig. 8, A–C; and Fig. S5 D). Where indicated, cells were treated for indicated time period with either vehicle (DMSO) or the following compounds at the indicated dose: 100 nM TCS7010 (AURA inhibitor; Tocris Bioscience; Fig. 7, A–J; Fig. S5 A; and Fig. 8, D–F), 10–20 μM (R)-roscovitine (Bukanov et al., 2006; Fig. 5, E, F, and K–N), or 10 μM monastrol (Fig. 5, E and F).

DNA constructs and stable cell lines

To generate destination vector with N-terminal MYC-BirA* tag, MYC-BirA* was amplified by PCR from pcDNA3.1 MYC-BirA* (43920; Addgene) using forward primer NO°1 and reverse primer NO°2 (Table S4) to create AflII and BstBI site-containing overhangs and cloned into TOPO entry vector (using TOPO TA Cloning Kit, K450001; ThermoFisher) sites. Next, following digest with AflII and BstBI (enzymes from NEB) the MYC-BirA* fragment was ligated (K1422; ThermoFisher) into AflII and BstBI sites of pgLAP2 vector (19703; Addgene). MYC-BirA*-CEP164 construct was generated from pDONOR-CEP164 (Čajánek and Nigg, 2014) and MYC-BirA* destination vector described above by LR Gateway cloning reaction (ThermoFisher), and subsequently validated for correct expression and localization by Western blot and immunofluorescence microscopy analyses following transfection of HEK293T cells.

MYC-AURA was kind gift from E. Nigg (Meraldi et al., 2002). pcDNA3.1 (Invitrogen) empty vector was used as transfection control for AURA overexpression experiments.

KIF14 construct resistant to KIF14 siRNA #2 sequence: 5'-TTT AATAGTCAACATTGCT-3' was generated by site-directed mutagenesis of pENTR KIF14 vector (generated by Gateway cloning from KIF14 plasmid kindly provided by F. Barr, University of Oxford, Oxford, UK; Gruneberg et al., 2006) in seven nucleotides (t2536a, a2539g, a2542c, c2545a, c2548t, t2551c, and t2554c) using PCR with mutagenesis forward NO°3 and reverse NO°4 primers (Table S4). Expression vector for KIF14siRNA2res was generated using LR Gateway cloning (ThermoFisher) of pENTR KIF14siRNA2res into pgLAP1_Neo destination vector. KIF14siRNA2res-pgLAP1_Neo (GFP-KIF14siRNA2res) was subsequently used for cotransfection with pOG44 FLP-recombinase expression vector (V600520; ThermoFisher) at a 1:30 ratio (total amount of DNA 2 μg/10-cm-diameter dish) by Lipofectamine 3000 (ThermoFisher) to create stable inducible RPE-1 FLP-in T-REx (kind gift from E. Nigg; Čajánek and Nigg, 2014). Cells were selected with 700 μg/ml G418 and 5 μg/ml of blasticidin S (both from Sigma-Aldrich).

To generate pgLAP1_Neo vector, Neomycin ORF was amplified by PCR from pcDNA3.1 (ThermoFisher) and cloned into TOPO entry vector (using TOPO TA Cloning Kit K450001; ThermoFisher) with SacII and NheI site-containing overhangs using primers NO°5 and NO°6 (Table S4). Next, following digest with SacII and NheI (NEB) the Neomycin ORF fragment was cloned using Rapid DNA Ligation Kit (K1422; ThermoFisher) into SacII and NheI sites of modified pgLAP1 vector; the NheI site was generated by site-directed mutagenesis of pgLAP1 (19702; Addgene) using primers NO°7 and NO°8 (Table S4).

Plasmids encoding WT, 1–356, 1–718, and 800–1648 human KIF14 GFP-fusions were kind gifts from F. Barr and U. Gruneberg (University of Oxford, Oxford, UK; Gruneberg et al., 2006). Mutant forms (R364C, T456M, Q1380*, Q1304*, and R1189*) corresponding to mutations identified in fetuses with syndromic microcephaly were described previously (Reilly et al., 2019). The lentiviral vector, pReceiver-Lv225, encoding for untagged human KIF14, EX-T0642-Lv225, was obtained from GeneCopoeia.

The ARL13B-GFP FLP-in RPE-1 cell line was kind gift from V. Varga (Institute of Molecular Genetics of the Czech Academy of Sciences, Prague, Czech Republic).

Stable inducible FLP-In T-REx 293 cell lines were selected by 500 μg/ml hygromycin and 5 μg/ml blasticidin S (both from Sigma-Aldrich) selection of cells cotransfected with BioID construct (MYC-BirA*-CEP164 or MYC-BirA* empty vector) and pOG44 FLP-recombinase expression vector (V600520; ThermoFisher) at a 1:9 ratio (total amount of DNA 12 μg/10-cm-diameter dish) using polyethylenimine.

All stable cell lines were validated by Western blot analysis and immunofluorescence staining.

Rescue experiments

A hTERT RPE-1 cell line inducibly (1 μg/ml DOX for 5 d before analysis) expressing GFP-KIF14 resistant to siRNA 2 (GFP-KIF14si2res) was transfected with 50 nM KIF14 siRNA #2 or control siRNA 48 h prior to analysis (Fig. 1, H and I). For rescue experiments with AURA inhibition, hTERT RPE-1 cells were seeded to 50% confluency, transfected 72 h prior to analysis with control or KIF14 siRNA, starved with serum-free medium 48 h

prior analysis, and treated with 100 nM TCS7010 AURA inhibitor for 24 h (Fig. 7, A–J; Fig. S5 A; and Fig. 8, D–F).

Cells were then fixed with ice-cold MeOH and analyzed by immunofluorescence staining.

Antibodies

For complete list of antibodies used, see Table S5. MYC antibody was described previously (Evan et al., 1985), as was CAP350 antibody (Yan et al., 2006).

Immunofluorescence staining

Cells were washed with PBS and fixed by either ice-cold MeOH or 3.7% PFA (Fig. 1, C and D; and Fig. S3, C, D, N, and O) followed by permeabilization by PBS + 0.1% TRITON X-100, blocked in blocking buffer (1% BSA in PBS), and subjected to incubation with primary and secondary antibodies, respectively. Cell nuclei were stained with 1 µg/ml Hoechst (Life Technologies) or DAPI (Sigma-Aldrich), and coverslips were mounted using Glycergel (Agilent) or Mowiol (Sigma-Aldrich).

Microscopes, image acquisition, measurements, quantifications, and time-lapse microscopy analyses

Microscopy analyses of fixed cells were done in 25°C on microscopes DeltaVision Elite (GE Healthcare) with a 100×/Zeiss Plan-ApoChromat 1.4 objective and DeltaVision softWoRx acquisition software (here, the image stacks were taken with a Z distance of 0.2 µm, deconvolved with three to five cycles of conservative ratio deconvolution algorithm, and directly projected as maximal intensity images), Zeiss Axio Observer.Z1 with confocal unit LSM 800 with 63×/Zeiss Plan-ApoChromat 1.4 objective, and Zeiss AxioImager.Z2 with Hamamatsu ORCA Flash 4.0 camera and 63×/Plan-ApoChromat 1.4 objective (both with ZEN Blue acquisition software). For acquisition, a Zeiss Axio Observer.Z1 and AxioCam 503 charge-coupled device camera in widefield mode was used (ZEN Blue software). For higher resolution microscopy (Fig. 2 C; Fig. 6, C and D; and Fig. S4 B), a laser scanning confocal microscope was used (Zeiss LSM 880 with Airyscan Fast module and 100×/M27 oil differential interference contrast Plan-ApoChromat 1.46 objective and ZEN Black acquisition software). Time-lapse microscopy analyses were done in 37°C/5% CO₂/FluorBright DMEM media (Thermo-Fisher) on Zeiss Axio Observer.Z1 with 10×/0.3 EC Plan-Neofluar, 25×/LCI Plan-Neofluar 0.8, and 40×/Plan-ApoChromat 1.3 objectives using ZEN Blue software for acquisition.

All images within given experiment were acquired with the same laser intensities and exposition times and projected to maximum Z intensity (ranging from 0.1- to 0.25-µm interval and total Z ranging from 2 to 50 slices) before analysis in ImageJ (National Institutes of Health). Where appropriate, contrast and/or brightness adjustment and cropping of final images were done using ZEN Black software (Zeiss) or ImageJ, with identical settings applied to all images from the given experiment.

For Fig. 2, A, B, and E–G, stained cells were imaged using an epi-illumination microscope (DMR; Leica) with a cooled charge-coupled device camera (DFC3000G; Leica). Images were acquired with LAS (V4.6; Leica) and processed with ImageJ and Photoshop CS2 (Adobe Systems).

Cilia lengths were measured using straight- or segmented-line tool for selection of fluorescent signal of ciliary marker in maximum Z intensity projected images in ImageJ. Cilia were categorized as follows: no cilia (no ARL13B/Ac-tub signal); hTERT RPE-1: short cilia, ≤3.3 µm; long cilia, ≥3.3 µm; nHDF, hESC CCTL14, and hiPSC: short cilia, ≤2.2 µm; long cilia, ≥2.2 µm; IMCD-3: short cilia, ≤4 µm; long cilia, ≥4 µm.

Time-lapse imaging analyses of GFP-ARL13B⁺ primary cilium were done within period of 10 h after primary cilium induction (serum starvation) and KIF14 depletion (24 h), the imaging interval was 10 min, and representative images were acquired every 1 h (Fig. 3 A). Primary cilium length were measured using straight- or segmented-line tool for selection of fluorescent signal of ciliary marker in single Z plane in ImageJ software. Average primary cilium growth speed (Fig. 3 C) was calculated and plotted as

$$\text{AVG cilia growth speed } (\mu\text{m/h}) = \frac{\text{actual length } (\mu\text{m})}{\text{total growth time (hours)}}$$

Current cilia growth speed (Fig. 3 D) was calculated and plotted as 1 h long term increase of primary cilium length:

$$\text{current cilia growth speed } (\mu\text{m/h}) = \frac{\text{actual length} - \text{length 1 h ago } (\mu\text{m})}{1 \text{ h}}$$

Where indicated, quantification of fluorescent signal intensities within selected regions was performed using ImageJ. Quantification of relative intensity of centriolar markers was performed using maximum Z intensity projected images, exported to the .tiff format, by mean gray value of the region of interest (ROI), circling mother centriole fluorescent signal, after subtraction of background mean gray value of the same-sized ROI, shifted horizontally next to the mother centriole (Fig. 2 G; and Fig. S2, C and D):

$$\text{CM relative intensity (a.u.)} = (\text{ROI mean grey value}) - (\text{background ROI mean grey value})$$

Quantification of normalized intensity of proteins localized to the mother centriole (MC) or ciliary tip were performed as calculation of protein of interest (POI) relative fluorescent signal after subtraction of background mean gray value of the same-sized ROI, shifted horizontally and centriolar markers (CM) relative fluorescent signal ratio (Fig. 4, B, D, F, H, J, and K; Fig. S2, G, I, K–L, N, and O; Fig. 6, D, H, J, and L; Fig. 7, C and E; and Fig. S4, G and E):

$$\text{Normalized MC intensity} = \frac{\text{POI relative fluorescent signal}}{\text{CM relative fluorescent signal}}$$

Quantification of relative intensity of proteins localized to the ciliary axoneme (PCA) was performed using maximum Z intensity projected images, exported to the .tiff format, by mean gray value of the ROI, freehand selecting fluorescent signal of

ciliary axoneme, after subtraction of background mean gray value of the same ROI, shifted horizontally next to the ciliary axoneme (Fig. S2, E and F; and Fig. 8 C):

$$\text{PCA relative intensity (a.u.)} = (\text{ROI mean grey value}) - (\text{background ROI mean grey value})$$

Quantification of normalized intensity of proteins localized to the ciliary axoneme (PCA) was performed as calculation of protein of interest (POI) relative fluorescent signal after subtraction of background mean gray value of the same-sized ROI, shifted horizontally, and PCA relative fluorescent signal ratio (Fig. 8 E):

$$\text{Normalized PCA intensity} = \frac{\text{POI relative fluorescent signal}}{\text{PCA relative fluorescent signal}}$$

Quantification of whole cell normalized intensity of AURA was performed using maximum Z intensity projected images, exported to the .tiff format. Final values were calculated as mean gray value of fluorescent signal of AURA in the ROI, circling nuclei, centrosome, and major part of cytosol with the same area for every analyzed cell, and Hoechst signal in the same ROI (Fig. 6 B and Fig. S4 B):

$$\text{Normalized AURA intensity (whole cell)} = \frac{\text{AURA mean gray value in the ROI}}{\text{Hoechst mean gray value in the ROI}}$$

Histograms (Fig. S2, P and Q; and Fig. 4 L, Fig. 7 G, and Fig. S5 A) of proteins, localized to the BB and ciliary axoneme with the same length for all analyzed cells in the indicated group, were generated using Plot Profile tool after segmented line selection of fluorescent signal of indicated protein marker in maximum Z intensity projected images in ImageJ. Plot Profiles of at least 10 cells per each category were then converted to the numbers using Plot Profile-list tool, and means + SEM for each point were calculated. Ac-tub and IFT intensities were aligned to CAP350 signal and plotted to the histograms using GraphPad Prism 6 software.

SDS-PAGE and Western blotting

Cells were washed in PBS and lysed in SDS lysis buffer (50 mM Tris-HCl, pH 6.8, 10% glycerol, and 1% SDS). Protein concentration was measured using the DC Protein Assay Kit (Bio-Rad). Samples were adjusted to equal concentration, mixed with bromophenol blue (0.01%) and β -mercaptoethanol (2.5%), boiled, and sonicated. Proteins were separated by SDS-PAGE, transferred onto polyvinylidene fluoride membranes (Millipore), and blocked with 5% milk in TBS-Tween buffer (10 mM Tris-HCl, pH 7.4, 100 mM NaCl, and 0.05% Tween). Membranes were incubated with primary and secondary antibodies, respectively (Table S5). Chemiluminescent signal was revealed by ECL Prime (GE Healthcare) and film (Agfa Healthcare) or Image Reader LAS-4000 (GE Healthcare). Subsequent crops and quantification analysis were done using ImageJ software.

BioID

For affinity capturing of biotinylated proteins, we adopted protocol published by Roux et al. (2012). Briefly, cells were incubated for 24 h in complete media supplemented with 1 μ g/ml DOX and 50 μ M biotin. After three PBS washes (all following

steps on ice), cells (4×10^7) were washed with wash buffer (50 mM Tris-HCl, pH 7.4), lysed in 1 ml lysis buffer (50 mM Tris, pH 7.4, 250 mM NaCl, 0.4% SDS, 1 mM DTT, 2% Triton X-100, and 1 \times Complete protease inhibitor [4693132001; Roche]) and sonicated. Then, an equal volume of ice-cold wash buffer was added, and samples were centrifuged at 16,000 relative centrifugal force. Supernatants were incubated with 40 μ l Strep-tactin Sepharose High Performance beads (#28935599; GE Healthcare) overnight at 4°C. Beads were collected and washed three times with 25 mM Tris-HCl (pH 7.4), three times with wash buffer, and twice with 50 mM NH_4HCO_3 . Samples were analyzed by mass spectrometry.

Immunoprecipitation

hTERT RPE-1 cells (3×15 -cm plates per condition) were grown to confluency, washed in PBS, scraped, pelleted by centrifugation (400 g/5 min/4°C), resuspended in immunoprecipitation (IP) lysis buffer (20 mM Tris-Cl, pH 7.4, 150 mM NaCl, 0.5% NP-40, 0.5% Triton-X-100, 0.1 mM DTT [43815; Merck], and 1 \times Complete proteasome inhibitors [4693132001; Roche]) and lysed (15 min on ice). Following centrifugation (15,000 g for 10 min at 4°C), cleared extracts were incubated 2–6 h at 4°C in an orbital shaker with either anti-CEP164 antibody (Graser et al., 2007) or control IgG antibody (sc-66931; Santa Cruz), coupled to protein G Sepharose beads (17-0618-01; GE Healthcare). Bound protein complexes were washed four times with IP lysis buffer and four times with wash buffer (20 mM Tris-Cl, pH 7.4, and 150 mM NaCl).

Protein digest and liquid chromatography with tandem mass spectrometry (LC-MS/MS) analysis of peptides

On-beads digestion

Following IP washes, bead-bound protein complexes were digested directly on beads by addition of 0.75 μ g (1 μ g/ μ l) trypsin (sequencing grade; Promega) in 50 mM NaHCO_3 buffer. Beads were gently tapped to ensure even suspension of trypsin solution and incubated at 37°C with mild agitation for 2 h. Beads were then vortexed to ensure the complex falls off the beads and the partially digested complex was transferred to the clean tubes to separate it from the beads and incubated at 37°C for 16 h without agitation. Resulting peptides were extracted into LC-MS vials by 2.5% formic acid (FA) in 50% acetonitrile (ACN) and 100% ACN with addition of polyethylene glycol (20,000; final concentration 0.001%; Stejskal et al., 2013) and concentrated in a SpeedVac concentrator (ThermoFisher).

LC-MS/MS analysis of peptides

LC-MS/MS analyses of peptide mixture were done using the RSLCnano system connected to an Orbitrap Elite hybrid spectrometer (ThermoFisher). Prior to LC separation, tryptic digests were online concentrated and desalted using trapping column (100 μ m \times 30 mm; flow rate of 4 μ l/min) filled with 3.5- μ m X-Bridge BEH 130 C18 sorbent (Waters). After washing of trapping column with 0.1% FA, the peptides were eluted (flow 300 nl/min) from the trapping column onto an analytical column (Acclaim Pepmap100 C18, 3 μ m particles, 75 μ m \times 500 mm; ThermoFisher) by a 100-min nonlinear gradient program (1–56% of mobile phase B; mobile phase A: 0.1% FA in water;

mobile phase B: 0.1% FA in 80% ACN). Equilibration of the trapping column and the column was done before sample injection to sample loop. The analytical column outlet was directly connected to the Digital PicoView 550 (New Objective) ion source with PicoTip emitter SilicaTip (FS360-20-15-N-20-C12; New Objective). ABIRD (active background ion reduction device) was installed.

MS data were acquired in a data-dependent strategy selecting up to top 10 precursors based on precursor abundance in the survey scan (350–2,000 *m/z*). The resolution of the survey scan was 60,000 (400 *m/z*) with a target value of 1×10^6 ions, one microscan and maximum injection time of 200 ms. HCD MS/MS spectra were acquired with a target value of 50,000 and resolution of 15,000 (400 *m/z*). The maximum injection time for MS/MS was 500 ms. Dynamic exclusion was enabled for 45 s after one MS/MS spectra acquisition and early expiration was disabled. The isolation window for MS/MS fragmentation was set to 2 *m/z*.

The analysis of the mass spectrometric RAW data files was performed using the Proteome Discoverer software (version 1.4; ThermoFisher) with in-house Mascot (version 2.6; Matrixscience) and Sequest search engines utilization. MS/MS ion searches were done at first against modified cRAP database (based on <http://www.thegpm.org/crap/>; 111 sequences in total) containing protein contaminants like keratin and trypsin. MS/MS spectra assigned by the Mascot search engine to any cRAP protein peptide with a Mascot ion score >30 were excluded from the next database searches. Remaining filtered MS/MS ions were further searched against UniProtKB proteome database for *Homo sapiens* (taxonomy ID 9606), downloaded on January 17, 2017 (number of proteins, 21,031). Mass tolerance for peptides and MS/MS fragments were 10 ppm and 0.05 D, respectively. Oxidation of methionine, deamidation (N, Q), and acetylation (protein N terminus) as optional modification and two-enzyme missed cleavages were set for all searches. Percolator was used for post-processing of the search results. Only peptides with *q*-value <0.01, rank 1, and at least six amino acids were considered. Proteins matching the same set of peptides were reported as protein groups. Protein groups/proteins were reported only if they had at least one unique peptide. Label-free quantification using protein area calculation in Proteome Discoverer was used (top three protein quantification; Silva et al., 2006).

Obtained lists of candidate binding partners were manually curated to remove false-positive hits and nonspecific binders. For coIP experiments, hits commonly detected in both mock (IP/IgG) and IP/CEP164 were deleted, and hits with a CRAPome ratio (number of entries/total entries $\times 100\%$; <https://www.crapome.org/>) >10% were also deleted. Only candidates detected at least in two biological replicates were considered (Table S1). For BioID experiments, only candidates with an identified peptide ratio in CEP164/control ≥ 2 in two consecutive experiments and with ≥ 10 identified peptides in CEP164 sample in at least one experiment at the same time were considered (Table S2).

Quantitative RT-PCR

1 μ g RNA, isolated using the RNeasy Mini Kit (Qiagen), was used for cDNA synthesis using the Transcriptor First Strand cDNA Synthesis Kit (Roche). Reactions were done in triplicates with

LightCycler 480 SYBR Green I Master according to the manufacturer's protocol and monitored in real time using LightCycler 480 Instrument II (Roche). Relative gene expression was calculated using the $2^{-\Delta\Delta CT}$ method; GAPDH was used as reference gene (for primer sequences, see Table S4).

Cell cycle distribution and flow cytometry

Cells were siRNA transfected for 48 h (0.5 μ M Cytochalasin D; 24-h treatment was used as positive control to enrich the proportion of G2/M cells) and serum starved for 24 h where indicated. Cells were fixed (30 min, ice-cold 70% ethanol), washed with PBS + 0.5% BSA, and treated with RNase A (0.016 mg/ml, 30 min, 37°C). DNA was stained by propidium iodide (20 μ g/ml; both from Sigma-Aldrich). The cell cycle profile was determined using FACS CANTO II (BD Biosciences) and FlowJo software (www.flowjo.com); at least 40,000 events per sample were analyzed. For graph creation, doublets were excluded. Quantification in histograms indicates increased ploidy (cells with >G2/M DNA content).

Mitotic shake-off

To increase the proportion of mitotic cells, 24 h after seeding, cells were transfected by KIF14 or control siRNA; 2 h after siRNA transfection, cells were treated for additional 2–4 h with 10 μ M monastrol (Sigma-Aldrich). Following treatment, mitotic cells were shaken off in PBS. Leftover nonmitotic cells were also passaged by trypsin. All conditions were counted and seeded in the same density. Cells were further maintained in 1% serum medium and, where indicated, supplemented with 10–20 μ M (R)-roscovitine (an inhibitor of cyclin-dependent kinases; Bukanov et al., 2006) for 2 d to induce ciliogenesis and block the cell cycle progression. Cells were then fixed and analyzed by immunofluorescence (see illustrative scheme in Fig. 5 E).

Statistics

All statistical analyses were done and graphically visualized in GraphPad Prism Software v. 6.0 (GraphPad Software; www.graphpad.com). All data are presented as mean \pm SEM from at least three independent experiments ($n \geq 3$), unless otherwise stated in the figure legends. In all experiments, at least 100 cells/cilia were counted or measured per condition ($N \geq 100$), unless otherwise stated in the figure legends. *P* values < 0.05 were considered significant (*, *P* < 0.05; **, *P* < 0.005; ***, *P* < 0.001; ****, *P* < 0.0001), and asterisks indicate statistical significance when compared with controls, unless otherwise stated. To determine statistical significance between two categories (simple data groups), an unpaired *t* test was used. To determine statistical significance between more than two groups, Tukey's multiple comparisons test was used (comparing the mean of each column with the mean of every other column). For group data with more than one category in columns, statistical significance was determined using the Holm-Sidak method ($\alpha = 5\%$), and each category was analyzed individually, without assuming a consistent SD.

Online supplemental material

Fig. S1 shows that KIF14 knockdown causes ciliogenesis defects in different cell types. Fig. S2 shows that KIF14 knockdown

affects localization of BB components and IFT-B machinery. Fig. S3 shows that KIF14 and CIT knockdown leads to minor effects on cell cycle in RPE-1. Fig. S4 shows that KIF14 depletion de-regulates AURA. Fig. S5 shows that AURA activity mediates effects of KIF14 depletion on primary cilia formation. Table S1 lists candidate binding partners for CEP164 coIP. Table S2 lists the candidate binding partners from CEP164 BioID experiments, showing proximity-dependent biotinylation by CEP164-BirA*. Table S3 lists all siRNA sequences used in this study. Table S4 lists the primers used in this study. Table S5 lists the antibodies used in this study.

Acknowledgments

We thank Erich Nigg (Biozentrum, University of Basel, Basel, Switzerland), Vladimir Varga (Institute of Molecular Genetics of the Czech Academy of Sciences, Prague, Czech Republic), Stjepan Uldrijan (Masaryk University, Brno, Czech Republic), Francis Barr (University of Oxford, Oxford, UK), Ulrike Grunberg (University of Oxford, Oxford, UK), Lumir Krejci (Masaryk University, Brno, Czech Republic), Pavel Krejci (Masaryk University, Brno, Czech Republic), Gert Jansen (Erasmus University Medical Center, Rotterdam, Netherlands), Peter Jackson (Stanford University School of Medicine, Stanford, CA), Kyle Roux (Stanford University School of Medicine, Stanford, CA), and Vladimir Rotrekl (Masaryk University, Brno, Czech Republic) for sharing reagents or instruments.

This work was supported by the Czech Science Foundation (grants 16-03269Y and 19-05244S to L. Cajanek), the Swiss National Science Foundation (grant IZ11Z0_166533 to L. Cajanek), and the Fondation pour la Recherche Médicale (grant DEQ20130326532 to A. Benmerah). O. Bernatik was supported by Faculty of Medicine MU junior researcher funds. Z. Zdrahal was supported by the Ministry of Education, Youth and Sports of the Czech Republic (MEYS CR; project CEITEC 2020, LQ1601). M.L. Reilly was supported by a Paris Diderot University fellowship. We acknowledge the core facility CELLIM of CEITEC supported by the Czech-BioImaging large RI project (MEYS CR grant LM2018129) for their support with obtaining scientific data presented in this paper. CIISB research infrastructure project (MEYS CR grant LM2018127) is gratefully acknowledged for the financial support of the LC-MS/MS measurements at the Proteomics Core Facility.

The authors declare no competing financial interests.

Author contributions: P. Pejškova performed and analyzed most of the experiments and assembled figures. M.L. Reilly performed and analyzed experiments in Fig. 2, A, B, and D–G. L. Bino performed and analyzed experiments in Fig. S1, N–V and assembled Fig. 9. O. Bernatik constructed cell line for experiment in Fig. 1, H and I, and Fig. S1 J. L. Dolanska performed and analyzed experiments in Fig. 8, A and C and Fig. S5 D. R.S. Ganji and Z. Zdrahal performed the proteomics analysis. A. Benmerah conceptualized and supervised work related to Fig. 2, A, B, and D–G. L. Cajanek conceptualized and supervised the study and, together with P. Pejškova, Z. Zdrahal, and A. Benmerah, wrote the paper. All authors approved the final version of the manuscript.

Submitted: 18 April 2019

Revised: 20 December 2019

Accepted: 26 March 2020

References

- Ali, B.R., J.L. Silhavy, N.A. Akawi, J.G. Gleeson, and L. Al-Gazali. 2012. A mutation in KIF7 is responsible for the autosomal recessive syndrome of macrocephaly, multiple epiphyseal dysplasia and distinctive facial appearance. *Orphanet J. Rare Dis.* 7:27. <https://doi.org/10.1186/1750-1172-7-27>
- Anastas, S.B., D. Mueller, S.L. Semple-Rowland, J.J. Breunig, and M.R. Sarkisian. 2011. Failed cytokinesis of neural progenitors in citron kinase-deficient rats leads to multiciliated neurons. *Cereb. Cortex.* 21:338–344. <https://doi.org/10.1093/cercor/bhq099>
- Anderson, R.G.W.. 1972. The three-dimensional structure of the basal body from the rhesus monkey oviduct. *J. Cell Biol.* 54:246–265. <https://doi.org/10.1083/jcb.54.2.246>
- Anvarian, Z., K. Mykytyn, S. Mukhopadhyay, L.B. Pedersen, and S.T. Christensen. 2019. Cellular signalling by primary cilia in development, organ function and disease. *Nat. Rev. Nephrol.* 15:199–219. <https://doi.org/10.1038/s41581-019-0116-9>
- Badano, J.L., N. Mitsuma, P.L. Beales, and N. Katsanis. 2006. The ciliopathies: an emerging class of human genetic disorders. *Annu. Rev. Genomics Hum. Genet.* 7:125–148. <https://doi.org/10.1146/annurev.genom.7.080505.115610>
- Baker, K., and P.L. Beales. 2009. Making sense of cilia in disease: the human ciliopathies. *Am. J. Med. Genet. C. Semin. Med. Genet.* 151C:281–295. <https://doi.org/10.1002/ajmg.c.30231>
- Bangs, F., and K.V. Anderson. 2017. Primary Cilia and Mammalian Hedgehog Signaling. *Cold Spring Harb. Perspect. Biol.* 9. a028175. <https://doi.org/10.1101/cshperspect.a028175>
- Barta, T., L. Peskova, J. Collin, D. Montaner, I. Neganova, L. Armstrong, and M. Lako. 2016. Brief Report: Inhibition of miR-145 Enhances Reprogramming of Human Dermal Fibroblasts to Induced Pluripotent Stem Cells. *Stem Cells.* 34:246–251. <https://doi.org/10.1002/stem.2220>
- Bassi, Z.I., K.J. Verbrughe, L. Capalbo, S. Gregory, E. Montembault, D.M. Glover, and P.P. D'Avino. 2011. Sticky/Citron kinase maintains proper RhoA localization at the cleavage site during cytokinesis. *J. Cell Biol.* 195: 595–603. <https://doi.org/10.1083/jcb.201105136>
- Bassi, Z.I., M. Audusseau, M.G. Riparbelli, G. Callaini, and P.P. D'Avino. 2013. Citron kinase controls a molecular network required for midbody formation in cytokinesis. *Proc. Natl. Acad. Sci. USA.* 110:9782–9787. <https://doi.org/10.1073/pnas.1301328110>
- Bazzi, H., and K.V. Anderson. 2014. Acentriolar mitosis activates a p53-dependent apoptosis pathway in the mouse embryo. *Proc. Natl. Acad. Sci. USA.* 111:E1491–E1500. <https://doi.org/10.1073/pnas.1400568111>
- Bernabé-Rubio, M., G. Andrés, J. Casares-Arias, J. Fernández-Barrera, L. Rangel, N. Reglero-Real, D.C. Gershlick, J.J. Fernández, J. Millán, I. Correia, et al. 2016. Novel role for the midbody in primary ciliogenesis by polarized epithelial cells. *J. Cell Biol.* 214:259–273. <https://doi.org/10.1083/jcb.201601020>
- Bernabé-Rubio, M., M. Bosch-Fortea, E. García, J.B. de la Serna, and M.A. Alonso. 2019. The ciliary membrane of polarized epithelial cells stems from a midbody remnant-associated membrane patch with condensed nanodomains. *bioRxiv.* doi: (Preprint posted June 11, 2019). <https://doi.org/10.1101/667642>
- Bowler, M., D. Kong, S. Sun, R. Nanjundappa, L. Evans, V. Farmer, A. Holland, M.R. Mahjoub, H. Sui, and J. Lencarek. 2019. High-resolution characterization of centriole distal appendage morphology and dynamics by correlative STORM and electron microscopy. *Nat. Commun.* 10:993. <https://doi.org/10.1038/s41467-018-08216-4>
- Braun, D.A., and F. Hildebrandt. 2017. Ciliopathies. *Cold Spring Harb. Perspect. Biol.* 9. a028191. <https://doi.org/10.1101/cshperspect.a028191>
- Briscoe, J., and P.P. Théron. 2013. The mechanisms of Hedgehog signalling and its roles in development and disease. *Nat. Rev. Mol. Cell Biol.* 14: 416–429. <https://doi.org/10.1038/nrm3598>
- Bryja, V., I. Červenka, and L. Čajánek. 2017. The connections of Wnt pathway components with cell cycle and centrosome: side effects or a hidden logic? *Crit. Rev. Biochem. Mol. Biol.* 52:614–637. <https://doi.org/10.1080/10409238.2017.1350135>
- Bukanov, N.O., L.A. Smith, K.W. Klinger, S.R. Ledbetter, and O. Ibraghimov-Beskrovnaia. 2006. Long-lasting arrest of murine polycystic kidney disease with CDK inhibitor roscovitine. *Nature.* 444:949–952. <https://doi.org/10.1038/nature05348>

- Čajánek, L., and E.A. Nigg. 2014. Cep164 triggers ciliogenesis by recruiting Tau tubulin kinase 2 to the mother centriole. *Proc. Natl. Acad. Sci. USA*. 111:E2841–E2850. <https://doi.org/10.1073/pnas.1401777111>
- Carleton, M., M. Mao, M. Biery, P. Warrenner, S. Kim, C. Buser, C.G. Marshall, C. Fernandes, J. Annis, and P.S. Linsley. 2006. RNA interference-mediated silencing of mitotic kinesin KIF14 disrupts cell cycle progression and induces cytokinesis failure. *Mol. Cell. Biol.* 26:3853–3863. <https://doi.org/10.1128/MCB.26.10.3853-3863.2006>
- Carmena, M., S. Ruchaud, and W.C. Earnshaw. 2009. Making the Auroras glow: regulation of Aurora A and B kinase function by interacting proteins. *Curr. Opin. Cell Biol.* 21:796–805. <https://doi.org/10.1016/j.cob.2009.09.008>
- Chaki, M., R. Airik, A.K. Ghosh, R.H. Giles, R. Chen, G.G. Slaats, H. Wang, T.W. Hurd, W. Zhou, A. Cluckey, et al. 2012. Exome capture reveals ZNF423 and CEP164 mutations, linking renal ciliopathies to DNA damage response signaling. *Cell*. 150:533–548. <https://doi.org/10.1016/j.cell.2012.06.028>
- Cole, D.G., D.R. Diener, A.L. Himelblau, P.L. Beech, J.C. Fuster, and J.L. Rosenbaum. 1998. Chlamydomonas kinesin-II-dependent intraflagellar transport (IFT): IFT particles contain proteins required for ciliary assembly in *Caenorhabditis elegans* sensory neurons. *J. Cell Biol.* 141:993–1008. <https://doi.org/10.1083/jcb.141.4.993>
- Dafinger, C., M.C. Liebau, S.M. Elsayed, Y. Hellenbroich, E. Boltshauser, G.C. Korenke, F. Fabretti, A.R. Jancke, I. Ebermann, G. Nürnberg, et al. 2011. Mutations in KIF7 link Joubert syndrome with Sonic Hedgehog signaling and microtubule dynamics. *J. Clin. Invest.* 121:2662–2667. <https://doi.org/10.1172/JCI43639>
- Delaval, B., A. Bright, N.D. Lawson, and S. Doherty. 2011. The cilia protein IFT88 is required for spindle orientation in mitosis. *Nat. Cell Biol.* 13:461–468. <https://doi.org/10.1038/ncb2202>
- Di Cunto, F., S. Imarisio, E. Hirsch, V. Broccoli, A. Bulfone, A. Migheli, C. Atzori, E. Turco, R. Triolo, G.P. Dotto, et al. 2000. Defective neurogenesis in citron kinase knockout mice by altered cytokinesis and massive apoptosis. *Neuron*. 28:115–127. [https://doi.org/10.1016/S0896-6273\(00\)00090-8](https://doi.org/10.1016/S0896-6273(00)00090-8)
- El-Brolosy, M.A., and D.Y.R. Stainier. 2017. Genetic compensation: A phenomenon in search of mechanisms. *PLoS Genet.* 13: e1006780. <https://doi.org/10.1371/journal.pgen.1006780>
- Endoh-Yamagami, S., M. Evangelista, D. Wilson, X. Wen, J.-W. Theunissen, K. Phamluong, M. Davis, S.J. Scales, M.J. Solloway, F.J. de Sauvage, et al. 2009. The mammalian Cos2 homolog Kif7 plays an essential role in modulating Hh signal transduction during development. *Curr. Biol.* 19:1320–1326. <https://doi.org/10.1016/j.cub.2009.06.046>
- Evan, G.I., G.K. Lewis, G. Ramsay, and J.M. Bishop. 1985. Isolation of monoclonal antibodies specific for human c-myc proto-oncogene product. *Mol. Cell. Biol.* 5:3610–3616. <https://doi.org/10.1128/MCB.5.12.3610>
- Filges, I., E. Nosova, E. Bruder, S. Tercanli, K. Townsend, W.T. Gibson, B. Röthlisberger, K. Heinemann, J.G. Hall, C.Y. Gregory-Evans, et al. 2014. Exome sequencing identifies mutations in KIF14 as a novel cause of an autosomal recessive lethal fetal ciliopathy phenotype. *Clin. Genet.* 86:220–228. <https://doi.org/10.1111/cge.12301>
- Firat-Karalar, E.N., and T. Stearns. 2014. The centriole duplication cycle. *Philos. Trans. R. Soc. Lond. B Biol. Sci.* 369: 20130460. <https://doi.org/10.1098/rstb.2013.0460>
- Gabriel, E., A. Wason, A. Ramani, L.M. Gooi, P. Keller, A. Pozniakovsky, I. Poser, F. Noack, N.S. Telugu, F. Calegari, et al. 2016. CPAP promotes timely cilium disassembly to maintain neural progenitor pool. *EMBO J.* 35:803–819. <https://doi.org/10.15252/embj.201593679>
- García-González, F.R., and J.F. Reiter. 2017. Open Sesame: How Transition Fibers and the Transition Zone Control Ciliary Composition. *Cold Spring Harb. Perspect. Biol.* 9: a028134. <https://doi.org/10.1101/cshperspect.a028134>
- Gerdes, J.M., E.E. Davis, and N. Katsanis. 2009. The vertebrate primary cilium in development, homeostasis, and disease. *Cell*. 137:32–45. <https://doi.org/10.1016/j.cell.2009.03.023>
- Goetz, S.C., and K.V. Anderson. 2010. The primary cilium: a signalling centre during vertebrate development. *Nat. Rev. Genet.* 11:331–344. <https://doi.org/10.1038/nrg2774>
- Goetz, S.C., K.F. Liem, Jr., and K.V. Anderson. 2012. The spinocerebellar ataxia-associated gene Tau tubulin kinase 2 controls the initiation of ciliogenesis. *Cell*. 151:847–858. <https://doi.org/10.1016/j.cell.2012.10.010>
- Gradilone, S.A., B.N. Radtke, P.S. Bogert, B.Q. Huang, G.B. Gajdos, and N.F. LaRusso. 2013. HDAC6 inhibition restores ciliary expression and decreases tumor growth. *Cancer Res.* 73:2259–2270. <https://doi.org/10.1158/0008-5472.CAN-12-2938>
- Graser, S., Y.-D. Stierhof, S.B. Lavoie, O.S. Gassner, S. Lamla, M. Le Clech, and E.A. Nigg. 2007. Cep164, a novel centriole appendage protein required for primary cilium formation. *J. Cell Biol.* 179:321–330. <https://doi.org/10.1083/jcb.200707181>
- Gruneberg, U., R. Neef, X. Li, E.H.Y. Chan, R.B. Chalamalasetty, E.A. Nigg, and F.A. Barr. 2006. KIF14 and citron kinase act together to promote efficient cytokinesis. *J. Cell Biol.* 172:363–372. <https://doi.org/10.1083/jcb.200511061>
- Gupta, G.D., É. Coyaudo, J. Gonçalves, B.A. Mojarad, Y. Liu, Q. Wu, L. Gheiratmand, D. Comartin, J.M. Tkach, S.W.T. Cheung, et al. 2015. A Dynamic Protein Interaction Landscape of the Human Centrosome-Cilium Interface. *Cell*. 163:1484–1499. <https://doi.org/10.1016/j.cell.2015.10.065>
- Hall, E.A., M. Keighren, M.J. Ford, T. Davey, A.P. Jarman, L.B. Smith, I.J. Jackson, and P. Mill. 2013. Acute versus chronic loss of mammalian Azil/Cep131 results in distinct ciliary phenotypes. *PLoS Genet.* 9: e1003928. <https://doi.org/10.1371/journal.pgen.1003928>
- He, M., R. Subramanian, F. Bangs, T. Omelchenko, K.F. Liem, Jr., T.M. Kapoor, and K.V. Anderson. 2014. The kinesin-4 protein Kif7 regulates mammalian Hedgehog signalling by organizing the cilium tip compartment. *Nat. Cell Biol.* 16:663–672. <https://doi.org/10.1038/ncb2988>
- Heidet, L., V. Morinière, C. Henry, L. De Tomasi, M.L. Reilly, C. Humbert, O. Alibeu, C. Fourrage, C. Bole-Feysot, P. Nitschké, et al. 2017. Targeted Exome Sequencing Identifies PBX1 as Involved in Monogenic Congenital Anomalies of the Kidney and Urinary Tract. *J. Am. Soc. Nephrol.* 28:2901–2914. <https://doi.org/10.1681/ASN.2017010043>
- Hirokawa, N., Y. Noda, Y. Tanaka, and S. Niwa. 2009. Kinesin superfamily motor proteins and intracellular transport. *Nat. Rev. Mol. Cell Biol.* 10:682–696. <https://doi.org/10.1038/nrm2774>
- Hirota, T., N. Kunitoku, T. Sasayama, T. Marumoto, D. Zhang, M. Nitta, K. Hatakeyama, and H. Saya. 2003. Aurora-A and an interacting activator, the LIM protein Ajuba, are required for mitotic commitment in human cells. *Cell*. 114:585–598. [https://doi.org/10.1016/S0092-8674\(03\)00642-1](https://doi.org/10.1016/S0092-8674(03)00642-1)
- Huang, N., D. Zhang, F. Li, P. Chai, S. Wang, J. Teng, and J. Chen. 2018. M-Phase Phosphoprotein 9 regulates ciliogenesis by modulating CP110-CEP97 complex localization at the mother centriole. *Nat. Commun.* 9:4511. <https://doi.org/10.1038/s41467-018-06990-9>
- Hutterer, A., D. Berndt, F. Wirtz-Peitz, M. Zigman, A. Schleiffer, and J.A. Knoblich. 2006. Mitotic activation of the kinase Aurora-A requires its binding partner Bora. *Dev. Cell*. 11:147–157. <https://doi.org/10.1016/j.devcel.2006.06.002>
- Inaba, H., H. Goto, K. Kasahara, K. Kumamoto, S. Yonemura, A. Inoko, S. Yamano, H. Wanibuchi, D. He, N. Goshima, et al. 2016. Ndel1 suppresses ciliogenesis in proliferating cells by regulating the trichoplein-Aurora A pathway. *J. Cell Biol.* 212:409–423. <https://doi.org/10.1083/jcb.201507046>
- Inoko, A., M. Matsuyama, H. Goto, Y. Ohmuro-Matsuyama, Y. Hayashi, M. Enomoto, M. Ibi, T. Urano, S. Yonemura, T. Kiyono, et al. 2012. Trichoplein and Aurora A block aberrant primary cilia assembly in proliferating cells. *J. Cell Biol.* 197:391–405. <https://doi.org/10.1083/jcb.201106101>
- Ishikawa, H., A. Kubo, S. Tsukita, and S. Tsukita. 2005. Odf2-deficient mother centrioles lack distal/subdistal appendages and the ability to generate primary cilia. *Nat. Cell Biol.* 7:517–524. <https://doi.org/10.1038/ncb1251>
- Izawa, I., H. Goto, K. Kasahara, and M. Inagaki. 2015. Current topics of functional links between primary cilia and cell cycle. *Cilia*. 4:12. <https://doi.org/10.1186/s13630-015-0021-1>
- Jakobsen, L., K. Vanselow, M. Skogs, Y. Toyoda, E. Lundberg, I. Poser, L.G. Falkenberg, M. Benneken, J. Westendorf, E.A. Nigg, et al. 2011. Novel asymmetrically localizing components of human centrosomes identified by complementary proteomics methods. *EMBO J.* 30:1520–1535. <https://doi.org/10.1038/emboj.2011.63>
- Kim, S., K. Lee, J.-H. Choi, N. Ringstad, and B.D. Dynlacht. 2015. Nek2 activation of Kif24 ensures cilium disassembly during the cell cycle. *Nat. Commun.* 6:8087. <https://doi.org/10.1038/ncomms9087>
- Kinzel, D., K. Boldt, E.E. Davis, I. Bartscher, D. Trümbach, B. Diplas, T. Attié-Bitach, W. Wurst, N. Katsanis, M. Ueffing, et al. 2010. Pitchfork regulates primary cilia disassembly and left-right asymmetry. *Dev. Cell*. 19:66–77. <https://doi.org/10.1016/j.devcel.2010.06.005>
- Kobayashi, T., and B.D. Dynlacht. 2011. Regulating the transition from centriole to basal body. *J. Cell Biol.* 193:435–444. <https://doi.org/10.1083/jcb.201101005>
- Kobayashi, T., W.Y. Tsang, J. Li, W. Lane, and B.D. Dynlacht. 2011. Centriolar kinesin Kif24 interacts with CP110 to remodel microtubules and regulate ciliogenesis. *Cell*. 145:914–925. <https://doi.org/10.1016/j.cell.2011.04.028>
- Korobeynikov, V., A.Y. Deneka, and E.A. Golemis. 2017. Mechanisms for nonmitotic activation of Aurora-A at cilia. *Biochem. Soc. Trans.* 45:37–49. <https://doi.org/10.1042/BST20160142>

- Kozyreva, V.K., S.L. McLaughlin, R.H. Livengood, R.A. Calkins, L.C. Kelley, A. Rajulapati, R.J. Ice, M.B. Smolkin, S.A. Weed, and E.N. Pugacheva. 2014. NEDD9 regulates actin dynamics through cortactin deacetylation in an AURKA/HDAC6-dependent manner. *Mol. Cancer Res.* 12:681–693. <https://doi.org/10.1158/1541-7786.MCR-13-0654>
- Kufer, T.A., H.H.W. Silljé, R. Körner, O.J. Gruss, P. Meraldi, and E.A. Nigg. 2002. Human TPX2 is required for targeting Aurora-A kinase to the spindle. *J. Cell Biol.* 158:617–623. <https://doi.org/10.1083/jcb.200204155>
- Kuhns, S., K.N. Schmidt, J. Reymann, D.F. Gilbert, A. Neuner, B. Hub, R. Carvalho, P. Wiedemann, H. Zentgraf, H. Erfle, et al. 2013. The microtubule affinity regulating kinase MARK4 promotes axoneme extension during early ciliogenesis. *J. Cell Biol.* 200:505–522. <https://doi.org/10.1083/jcb.201206013>
- Lechtreck, K.F.. 2015. IFT-cargo interactions and protein transport in cilia. *Trends Biochem. Sci.* 40:765–778. <https://doi.org/10.1016/j.tibs.2015.09.003>
- Lee, J., K.A. Platt, P. Censullo, and A. Ruiz i Altaba. 1997. Gli1 is a target of Sonic hedgehog that induces ventral neural tube development. *Development.* 124:2537–2552.
- Littlepage, L.E., H. Wu, T. Andresson, J.K. Deanehan, L.T. Amundadottir, and J.V. Ruderman. 2002. Identification of phosphorylated residues that affect the activity of the mitotic kinase Aurora-A. *Proc. Natl. Acad. Sci. USA.* 99:15440–15445. <https://doi.org/10.1073/pnas.202606599>
- Lu, Q., C. Insinna, C. Ott, J. Stauffer, P.A. Pintado, J. Rahajeng, U. Baxa, V. Walia, A. Cuenca, Y.-S. Hwang, et al. 2015. Early steps in primary cilium assembly require EHD1/EHD3-dependent ciliary vesicle formation. *Nat. Cell Biol.* 17:228–240. <https://doi.org/10.1038/ncb3109>
- Makrythanasis, P., R. Maroofian, A. Stray-Pedersen, D. Musaev, M.S. Zaki, I.G. Mahmoud, L. Selim, A. Elbadawy, S.N. Jhangiani, Z.H. Coban Akdemir, et al. 2018. Biallelic variants in KIF14 cause intellectual disability with microcephaly. *Eur. J. Hum. Genet.* 26:330–339. <https://doi.org/10.1038/s41431-017-0088-9>
- Marszalek, J.R., P. Ruiz-Lozano, E. Roberts, K.R. Chien, and L.S.B. Goldstein. 1999. Situs inversus and embryonic ciliary morphogenesis defects in mouse mutants lacking the KIF3A subunit of kinesin-II. *Proc. Natl. Acad. Sci. USA.* 96:5043–5048. <https://doi.org/10.1073/pnas.96.9.5043>
- McKenzie, C., and P.P. D'Avino. 2016. Investigating cytokinesis failure as a strategy in cancer therapy. *Oncotarget.* 7:87323–87341. <https://doi.org/10.18632/oncotarget.13556>
- Meijer, L., A. Borgne, O. Mulner, J.P. Chong, J.J. Blow, N. Inagaki, M. Inagaki, J.G. Delcros, and J.P. Moulinoux. 1997. Biochemical and cellular effects of roscovitine, a potent and selective inhibitor of the cyclin-dependent kinases cdc2, cdk2 and cdk5. *Eur. J. Biochem.* 243:527–536. <https://doi.org/10.1111/j.1432-1033.1997.t01-2-00527.x>
- Meraldi, P., R. Honda, and E.A. Nigg. 2002. Aurora-A overexpression reveals tetraploidization as a major route to centrosome amplification in p53-/- cells. *EMBO J.* 21:483–492. <https://doi.org/10.1093/emboj/21.4.483>
- Mick, D.U., R.B. Rodrigues, R.D. Leib, C.M. Adams, A.S. Chien, S.P. Gygi, and M.V. Nachury. 2015. Proteomics of Primary Cilia by Proximity Labeling. *Dev. Cell.* 35:497–512. <https://doi.org/10.1016/j.devcel.2015.10.015>
- Mitchison, H.M., and E.M. Valente. 2017. Motile and non-motile cilia in human pathology: from function to phenotypes. *J. Pathol.* 241:294–309. <https://doi.org/10.1002/path.4843>
- Moawia, A., R. Shaheen, S. Rasool, S.S. Waseem, N. Ewida, B. Budde, A. Kawalia, S. Motameny, K. Khan, A. Fatima, et al. 2017. Mutations of KIF14 cause primary microcephaly by impairing cytokinesis. *Ann. Neurol.* 82:562–577. <https://doi.org/10.1002/ana.25044>
- Morris, R.L., and J.M. Scholey. 1997. Heterotrimeric kinesin-II is required for the assembly of motile 9+2 ciliary axonemes on sea urchin embryos. *J. Cell Biol.* 138:1009–1022. <https://doi.org/10.1083/jcb.138.5.1009>
- Mukhopadhyay, S., and R. Rohatgi. 2014. G-protein-coupled receptors, Hedgehog signaling and primary cilia. *Semin. Cell Dev. Biol.* 33:63–72. <https://doi.org/10.1016/j.semcdb.2014.05.002>
- Nigg, E.A., and A.J. Holland. 2018. Once and only once: mechanisms of centriole duplication and their deregulation in disease. *Nat. Rev. Mol. Cell Biol.* 19:297–312. <https://doi.org/10.1038/nrm.2017.127>
- Oda, T., S. Chiba, T. Nagai, and K. Mizuno. 2014. Binding to Cep164, but not EBI1, is essential for centriolar localization of TTBK2 and its function in ciliogenesis. *Genes Cells.* 19:927–940. <https://doi.org/10.1111/gtc.12191>
- Ohkura, H., T. Török, G. Tick, J. Hoheisel, I. Kiss, and D.M. Glover. 1997. Mutation of a gene for a Drosophila kinesin-like protein, Klp38B, leads to failure of cytokinesis. *J. Cell Sci.* 110:945–954.
- Orth, J.D., A. Loewer, G. Lahav, and T.J. Mitchison. 2012. Prolonged mitotic arrest triggers partial activation of apoptosis, resulting in DNA damage and p53 induction. *Mol. Biol. Cell.* 23:567–576. <https://doi.org/10.1091/mbc.e11-09-0781>
- Pan, J., Q. Wang, and W.J. Snell. 2004. An aurora kinase is essential for flagellar disassembly in Chlamydomonas. *Dev. Cell.* 6:445–451. [https://doi.org/10.1016/S1534-5807\(04\)00064-4](https://doi.org/10.1016/S1534-5807(04)00064-4)
- Plotnikova, O.V., A.S. Nikonova, Y.V. Loskutov, P.Y. Kozyulina, E.N. Pugacheva, and E.A. Golemis. 2012. Calmodulin activation of Aurora-A kinase (AURKA) is required during ciliary disassembly and in mitosis. *Mol. Biol. Cell.* 23:2658–2670. <https://doi.org/10.1091/mbc.e11-12-1056>
- Pugacheva, E.N., S.A. Jablonski, T.R. Hartman, E.P. Henske, and E.A. Golemis. 2007. HEF1-dependent Aurora A activation induces disassembly of the primary cilium. *Cell.* 129:1351–1363. <https://doi.org/10.1016/j.cell.2007.04.035>
- Ran, J., Y. Yang, D. Li, M. Liu, and J. Zhou. 2015. Deacetylation of α -tubulin and cortactin is required for HDAC6 to trigger ciliary disassembly. *Sci. Rep.* 5:12917. <https://doi.org/10.1038/srep12917>
- Reilly, M.L., and A. Benmerah. 2019. Ciliary kinesins beyond IFT: Cilium length, disassembly, cargo transport and signalling. *Biol. Cell.* 111:79–94. <https://doi.org/10.1111/boc.201800074>
- Reilly, M.L., M.F. Stokman, V. Magry, C. Jeanpierre, M. Alves, M. Paydar, J. Hellinga, M. Delous, D. Pouly, M. Failler, et al. 2019. Loss of function mutations in KIF14 cause severe microcephaly and kidney development defects in humans and zebrafish. *Hum. Mol. Genet.* 28:778–795. <https://doi.org/10.1093/hmg/ddy381>
- Reiter, J.F., and M.R. Leroux. 2017. Genes and molecular pathways underpinning ciliopathies. *Nat. Rev. Mol. Cell Biol.* 18:533–547. <https://doi.org/10.1038/nrm.2017.60>
- Reiter, J., O. Blacque, and M. Leroux. 2012. The base of the cilium: Roles for transition fibres and the transition zone in ciliary formation, maintenance and compartmentalization. *EMBO Rep.* 13:608–618.
- Renzova, T., D. Bohaciakova, M. Esner, V. Pospisilova, T. Barta, A. Hampl, and L. Cajanek. 2018. Inactivation of PLK4-STIL Module Prevents Self-Renewal and Triggers p53-Dependent Differentiation in Human Pluripotent Stem Cells. *Stem Cell Reports.* 11:959–972. <https://doi.org/10.1016/j.stemcr.2018.08.008>
- Rosenbaum, J.L., and G.B. Witman. 2002. Intraflagellar transport. *Nat. Rev. Mol. Cell Biol.* 3:813–825. <https://doi.org/10.1038/nrm952>
- Roux, K.J., D.I. Kim, M. Raida, and B. Burke. 2012. A promiscuous biotin ligase fusion protein identifies proximal and interacting proteins in mammalian cells. *J. Cell Biol.* 196:801–810. <https://doi.org/10.1083/jcb.201112098>
- Sánchez, I., and B.D. Dynlacht. 2016. Cilium assembly and disassembly. *Nat. Cell Biol.* 18:711–717. <https://doi.org/10.1038/ncb3370>
- Satir, P., L.B. Pedersen, and S.T. Christensen. 2010. The primary cilium at a glance. *J. Cell Sci.* 123:499–503. <https://doi.org/10.1242/jcs.050377>
- Schmidt, K.N., S. Kuhns, A. Neuner, B. Hub, H. Zentgraf, and G. Pereira. 2012. Cep164 mediates vesicular docking to the mother centriole during early steps of ciliogenesis. *J. Cell Biol.* 199:1083–1101. <https://doi.org/10.1083/jcb.201202126>
- Scholey, J.M.. 2003. Intraflagellar transport. *Annu. Rev. Cell Dev. Biol.* 19:423–443. <https://doi.org/10.1146/annurev.cellbio.19.111401.091318>
- Seeley, E.S., and M.V. Nachury. 2010. The perennial organelle: assembly and disassembly of the primary cilium. *J. Cell Sci.* 123:511–518. <https://doi.org/10.1242/jcs.061093>
- Sillibourne, J.E., I. Hurbain, T. Grand-Perret, B. Goud, P. Tran, and M. Bornens. 2013. Primary ciliogenesis requires the distal appendage component Cep123. *Biol. Open.* 2:535–545. <https://doi.org/10.1242/bio.20134457>
- Silva, J.C., M.V. Gorenstein, G.-Z. Li, J.P.C. Vissers, and S.J. Geromanos. 2006. Absolute quantification of proteins by LCMSE: a virtue of parallel MS acquisition. *Mol. Cell. Proteomics.* 5:144–156. <https://doi.org/10.1074/mcp.M500230-MCP200>
- Silverman, M.A., and M.R. Leroux. 2009. Intraflagellar transport and the generation of dynamic, structurally and functionally diverse cilia. *Trends Cell Biol.* 19:306–316. <https://doi.org/10.1016/j.tcb.2009.04.002>
- Smith, K.R., E.K. Kieserman, P.I. Wang, S.G. Basten, R.H. Giles, E.M. Marcotte, and J.B. Wallingford. 2011. A role for central spindle proteins in cilia structure and function. *Cytoskeleton (Hoboken)*. 68:112–124. <https://doi.org/10.1002/cm.20498>
- Sorokin, S. 1962. Centrioles and the formation of rudimentary cilia by fibroblasts and smooth muscle cells. *J. Cell Biol.* 15:363–377. <https://doi.org/10.1083/jcb.15.2.363>
- Spektor, A., W.Y. Tsang, D. Khoo, and B.D. Dynlacht. 2007. Cep97 and CP110 suppress a cilia assembly program. *Cell.* 130:678–690. <https://doi.org/10.1016/j.cell.2007.06.027>

- Stejskal, K., D. Potěšil, and Z. Zdráhal. 2013. Suppression of peptide sample losses in autosampler vials. *J. Proteome Res.* 12:3057–3062. <https://doi.org/10.1021/pr400183v>
- Tanos, B.E., H.-J. Yang, R. Soni, W.-J. Wang, F.P. Macaluso, J.M. Asara, and M.-F.B. Tsou. 2013. Centriole distal appendages promote membrane docking, leading to cilia initiation. *Genes Dev.* 27:163–168. <https://doi.org/10.1101/gad.207043.112>
- Verhey, K.J., N. Kaul, and V. Soppina. 2011. Kinesin assembly and movement in cells. *Annu. Rev. Biophys.* 40:267–288. <https://doi.org/10.1146/annurev-biophys-042910-155310>
- Walter, A.O., W. Seghezzi, W. Korver, J. Sheung, and E. Lees. 2000. The mitotic serine/threonine kinase Aurora2/AIK is regulated by phosphorylation and degradation. *Oncogene*. 19:4906–4916. <https://doi.org/10.1038/sj.onc.1203847>
- Wei, Q., Q. Xu, Y. Zhang, Y. Li, Q. Zhang, Z. Hu, P.C. Harris, V.E. Torres, K. Ling, and J. Hu. 2013. Transition fibre protein FBF1 is required for the ciliary entry of assembled intraflagellar transport complexes. *Nat. Commun.* 4:2750. <https://doi.org/10.1038/ncomms3750>
- Wheway, G., M. Schmidts, D.A. Mans, K. Szymanska, T.T. Nguyen, H. Racher, I.G. Phelps, G. Toedt, J. Kennedy, K.A. Wunderlich, et al; University of Washington Center for Mendelian Genomics. 2015. An siRNA-based functional genomics screen for the identification of regulators of ciliogenesis and ciliopathy genes. *Nat. Cell Biol.* 17:1074–1087. <https://doi.org/10.1038/ncb3201>
- Wu, C.-T., H.-Y. Chen, and T.K. Tang. 2018. Myosin-Va is required for preciliary vesicle transportation to the mother centriole during ciliogenesis. *Nat. Cell Biol.* 20:175–185. <https://doi.org/10.1038/s41556-017-0018-7>
- Yadav, S.P., N.K. Sharma, C. Liu, L. Dong, T. Li, and A. Swaroop. 2016. Centrosomal protein CP110 controls maturation of the mother centriole during cilia biogenesis. *Development*. 143:1491–1501. <https://doi.org/10.1242/dev.130120>
- Yan, X., R. Habedanck, and E.A. Nigg. 2006. A complex of two centrosomal proteins, CAP350 and FOP, cooperates with EB1 in microtubule anchoring. *Mol. Biol. Cell*. 17:634–644. <https://doi.org/10.1091/mbc.e05-08-0810>
- Yang, T.T., W.M. Chong, W.-J. Wang, G. Mazo, B. Tanos, Z. Chen, T.M.N. Tran, Y.-D. Chen, R.R. Weng, C.-E. Huang, et al. 2018. Super-resolution architecture of mammalian centriole distal appendages reveals distinct blade and matrix functional components. *Nat. Commun.* 9:2023. <https://doi.org/10.1038/s41467-018-04469-1>
- Zhu, C., J. Zhao, M. Bibikova, J.D. Leverson, E. Bossy-Wetzel, J.-B. Fan, R.T. Abraham, and W. Jiang. 2005. Functional analysis of human microtubule-based motor proteins, the kinesins and dyneins, in mitosis/cytokinesis using RNA interference. *Mol. Biol. Cell*. 16:3187–3199. <https://doi.org/10.1091/mbc.e05-02-0167>

Supplemental material

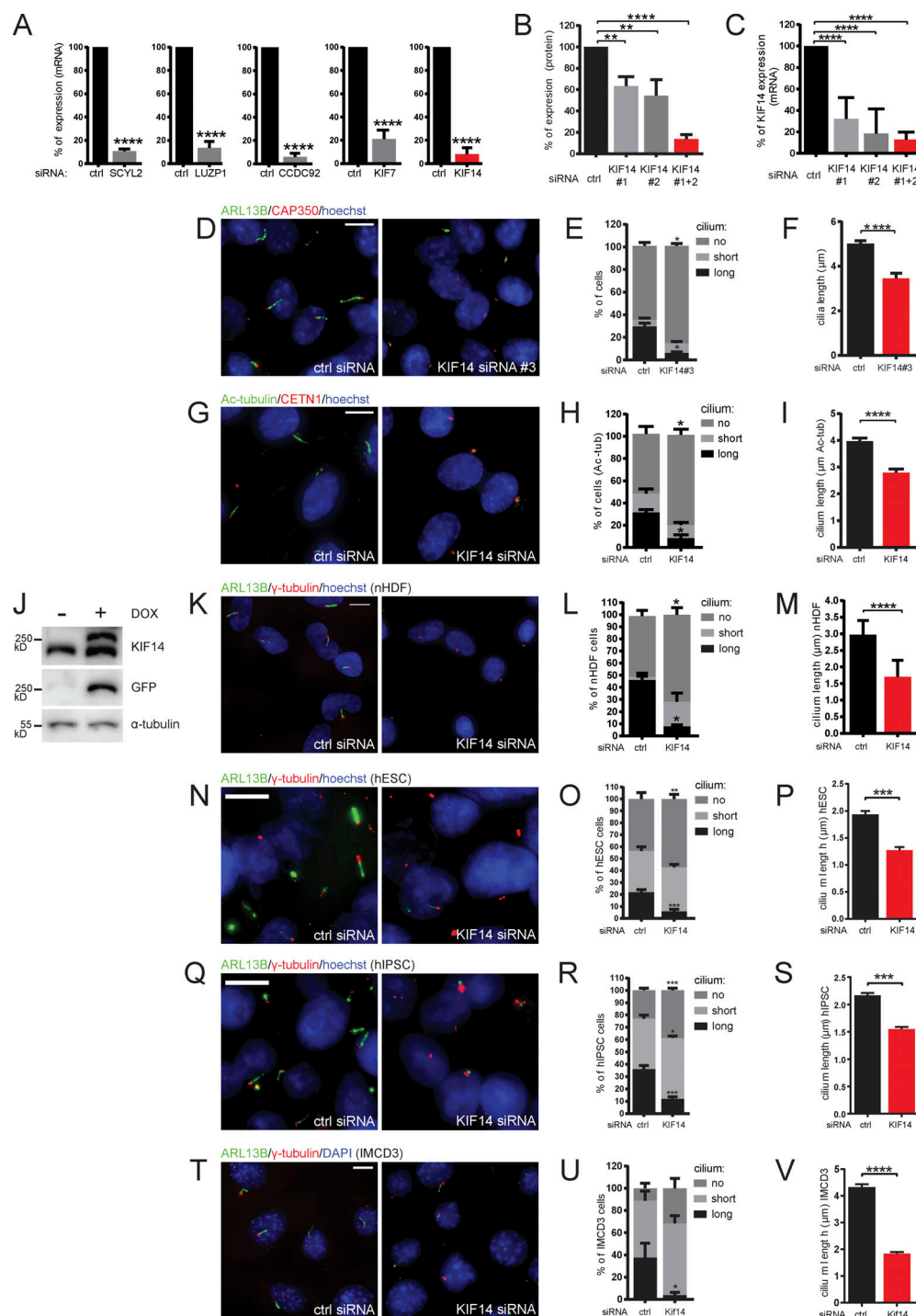


Figure S1. KIF14 knockdown causes ciliogenesis defects in different cell types. (A) Quantitative RT-PCR mRNA expression analysis for validation of siRNA knockdown efficiency (related to Fig. 1B). For SCYL2 silencing, we used a single siRNA oligo; for LUZP1, CCDC92, KIF7, and KIF14, we used a 50 nM mix of oligos 1 and 2 (Table S3). (B and C) Test of KIF14 knockdown efficiency using different siRNA oligos in hTERT RPE-1 cells. (B) Quantification of Fig. 1E. Western blot analysis of protein expression in total cell lysates using two different siRNA KIF14 oligos. (C) Quantitative RT-PCR expression analysis of KIF14 mRNA. (D–F) Test of the effect of KIF14 siRNA oligo #3 (Carleton et al., 2006; Table S3) on hTERT RPE-1 cells. (D) Representative image of IF staining of ARL13B (green), CAP350 (red), and DNA (blue); scale bar, 10 μ m. (E and F) Graphs of primary cilia formation ability after KIF14 siRNA #3 knockdown (E) and the effect on ARL13B⁺ cilia length (F). (G–I) Validation of the effect of KIF14 knockdown on ciliogenesis in hTERT RPE-1 cells using Ac-tub as a ciliary marker. (G) Representative images of IF staining of Ac-tub (green), CETN1 (red), and DNA (blue); scale bar, 10 μ m. Quantification of the experiment is shown as a percentage of ciliated cells (H) and by Ac-tub⁺ cilia length (I). (J) Validation of Flp-in T-REx RPE-1 cell line by Western blot analysis upon DOX induction expressing GFP-KIF14 mutant resistant to KIF14 siRNA 2 (GFP-KIF14siRNA2res; related to Fig. 1, H and I). (K–V) Examination of phenotypes after KIF14 depletion in nHDFs (K–M), hESCs (N–P), hiPSCs (Q–S), and IMCD3s (T–V). (K, N, Q, and T) Representative images of experiments detecting IF staining of ARL13B (green), γ -tubulin (red), DNA (blue); scale bars, 10 μ m. Quantifications of experiments (by percentage of ciliated cells) are shown in L, O, R, and U, and graphs showing ARL13B⁺ ciliary lengths are shown in M, P, S, and V. Asterisks indicate statistical significance using an unpaired *t* test.

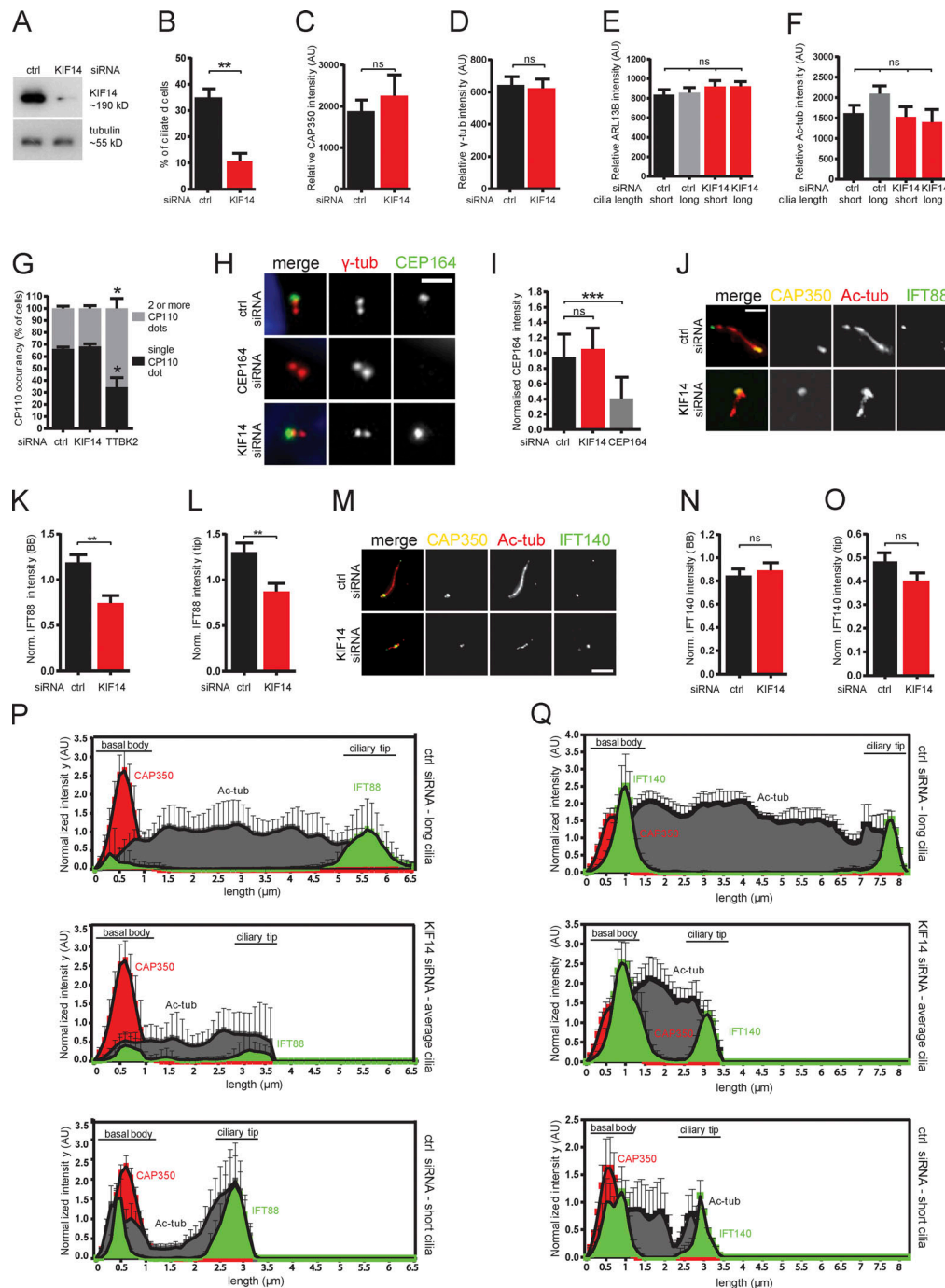


Figure S2. KIF14 knockdown affects localization of BB components and IFT-B machinery. (A) Validation of KIF14 siRNA knockdown efficiency by Western blot protein expression analysis in Flp-in T-Rex RPE-1 cell line (referring to time-lapse imaging experiments in Fig. 3) upon doxycycline (DOX) induction expression GFP-ARL13B. (B) Quantification of ciliogenesis ability in GFP-ARL13B inducible RPE-1 cells after KIF14 siRNA knockdown. hTERT RPE-1 cells were transfected with the indicated siRNA, serum starved for 24 h, and analyzed by IF microscopy (related to Fig. 4, C–Q). γ -tubulin or CAP350 staining were used to visualize centrosomes, Ac-tubulin or ARL13B staining detected primary cilia. (C–F) Examination of protein levels of BB and ciliary markers used for normalization; levels are not affected by KIF14 siRNA. Relative CAP350 (C) and γ -tubulin (D) BB intensities and relative ARL13B (E) and Ac-tubulin (F) ciliary intensity are quantified in arbitrary units (AU) after background subtraction. (G) KIF14 depletion does not affect process of CP110 removal from the distal end of mother centriole as quantified by number of CP110 dots. TTBK2 knockdown was used as positive control. (H) Representative images of IF staining detects CEP164 (green), γ -tubulin (red), and DNA (blue); scale bar, 2 μ m. Quantification of CEP164 intensity on BB (normalized to γ -tubulin) in I (CEP164 siRNA was used as positive control). (J) Representative images of IF staining of IFT88 (green), CAP350 (yellow), and Ac-tub (red); scale bar, 3 μ m. (K and L) Quantification of IFT88 intensity (normalized to CAP350) at BBs (K) and a decrease of IFT88 in the ciliary tip (L) are shown. (M) Representative images of IF staining of IFT140 (green), CAP350 (yellow), and Ac-tub (red); scale bar, 3 μ m. (N and O) IFT140 intensity (normalized to CAP350) at BBs (N) or in the ciliary tip (O) was not affected by KIF14 depletion. (P–Q) Histograms demonstrate distribution of CAP350 (red), Ac-tub (gray), and IFT (green) proteins along the ciliary axoneme (N = 20). Quantification was done for typical control long cilia and short defective cilia after KIF14 siRNA and for additional control also within a subset of short primary cilia in controls. Asterisks or ns indicates statistical significance determined by an unpaired *t* test.

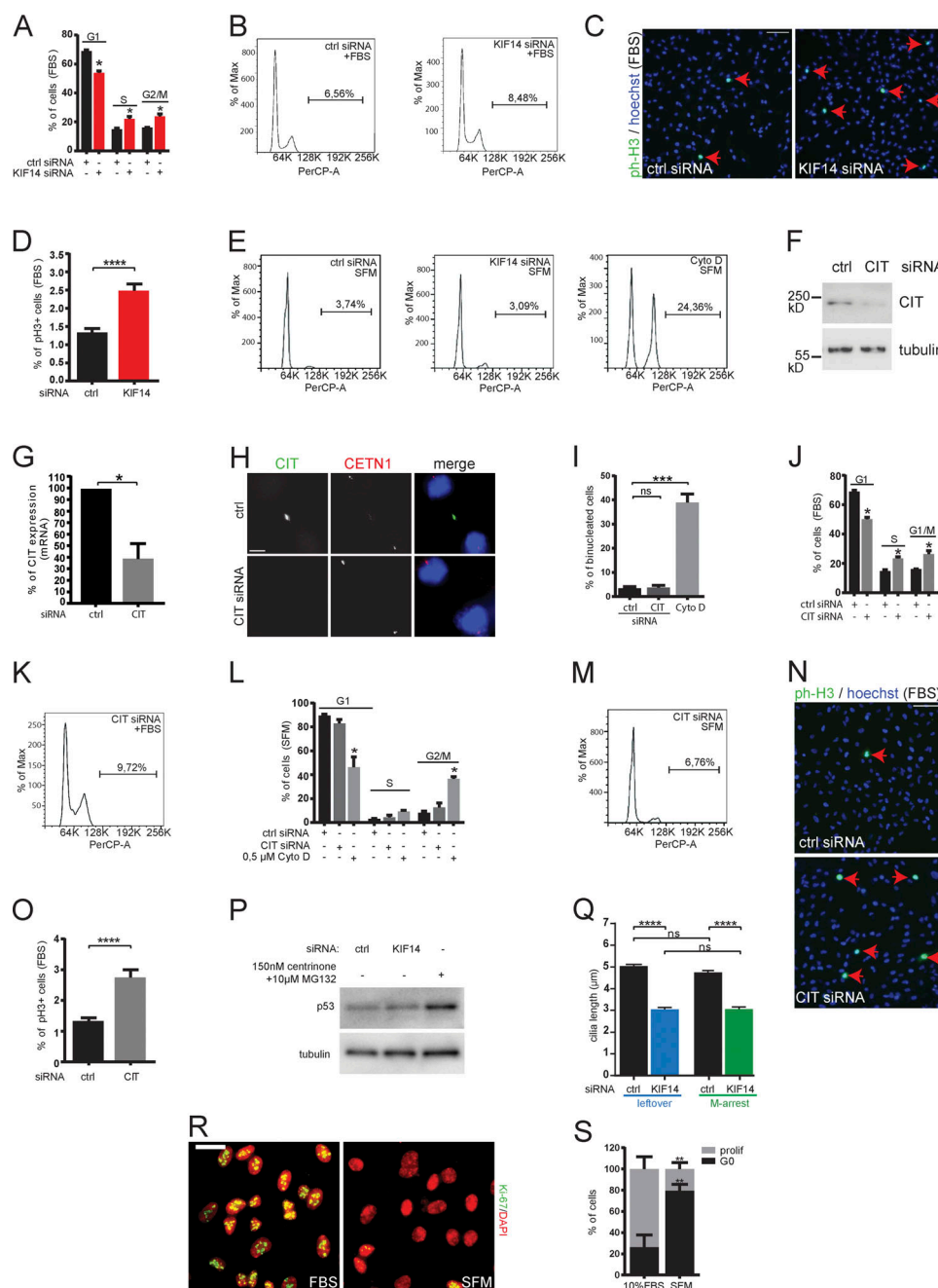


Figure S3. KIF14 and CIT knockdown leads to minor effects on cell cycle in RPE-1, related to Fig. 5, A–E. Cell cycle analyses demonstrating distribution of hTERT RPE-1 cells 48 h transfected with control or KIF14 siRNA and 24 h proliferating in normal 10% FBS medium (A–D) or serum starved (E). **(A and B)** Graph (A) and histograms (B) of flow cytometry analysis of cycling cells show minor increase in G2/M cells (quantification indicates increased ploidy = cells with >G2/M DNA content). **(C and D)** Representative images (C; phospho-histone H3 in green and DNA in blue; scale bar, 100 μm) and graph of quantification (D) show minor increment of phospho-histone H3 positive (ph-H3⁺) proliferating cells. **(E)** Histograms of flow cytometry analyses quantified in Fig. 5 B graph. **(F–H)** Validation of CIT siRNA knockdown efficiency in hTERT RPE-1 cells by Western blot analysis on protein level (F) and quantitative RT-PCR analysis of CIT mRNA depletion (G). **(H)** Representative images of IF microscopy detecting CIT (green), CETN1 (red), and DNA (blue); scale bar, 5 μm. **(I–O)** Cell cycle analyses demonstrating distribution of hTERT RPE-1 cells 48 h transfected with control or CIT siRNA and proliferating for 24 h in normal 10% FBS medium (J, K, N, and O) or serum starved (I and L–M). **(I)** Quantification of percentage of binucleated cells (cytochalasin D treatment was used as positive control). **(J–M)** Flow cytometry cell cycle analyses demonstrating minor increase in proportion of G2/M phase in 10% FBS and unaffected G2/M proportion in serum-starved conditions (quantification indicates increased ploidy = cells with >G2/M DNA content). **(N and O)** Representative images of ph-H3 (green) and DNA (blue) IF staining show minor increase of proliferating cells after CIT depletion in 10% FBS condition; scale bar, 100 μm (quantified in O). **(P)** P53 Western blot analysis of whole hTERT RPE-1 cell lysates transfected for 48 h with control or KIF14 siRNA (150 nM centrinone + 10 μM MG132 treatment was used as positive control). **(Q)** Graph showing ARL13B⁺ cilia length (related to Fig. 5, E and F; please see scheme of the experiment in Fig. 5 E). **(R and S)** Analysis of effectiveness of serum starvation to synchronize hTERT RPE-1 cells in G0 phase (related to Fig. 5, G–J). **(R)** Representative images show IF staining detecting the proliferation marker Ki-67 (green) and DNA (red); scale bar, 20 μm. **(S)** Quantification of proportion of cells synchronized in G0 (Ki-67⁺). Asterisks or "ns" indicate statistical significance determined using an unpaired *t* test.

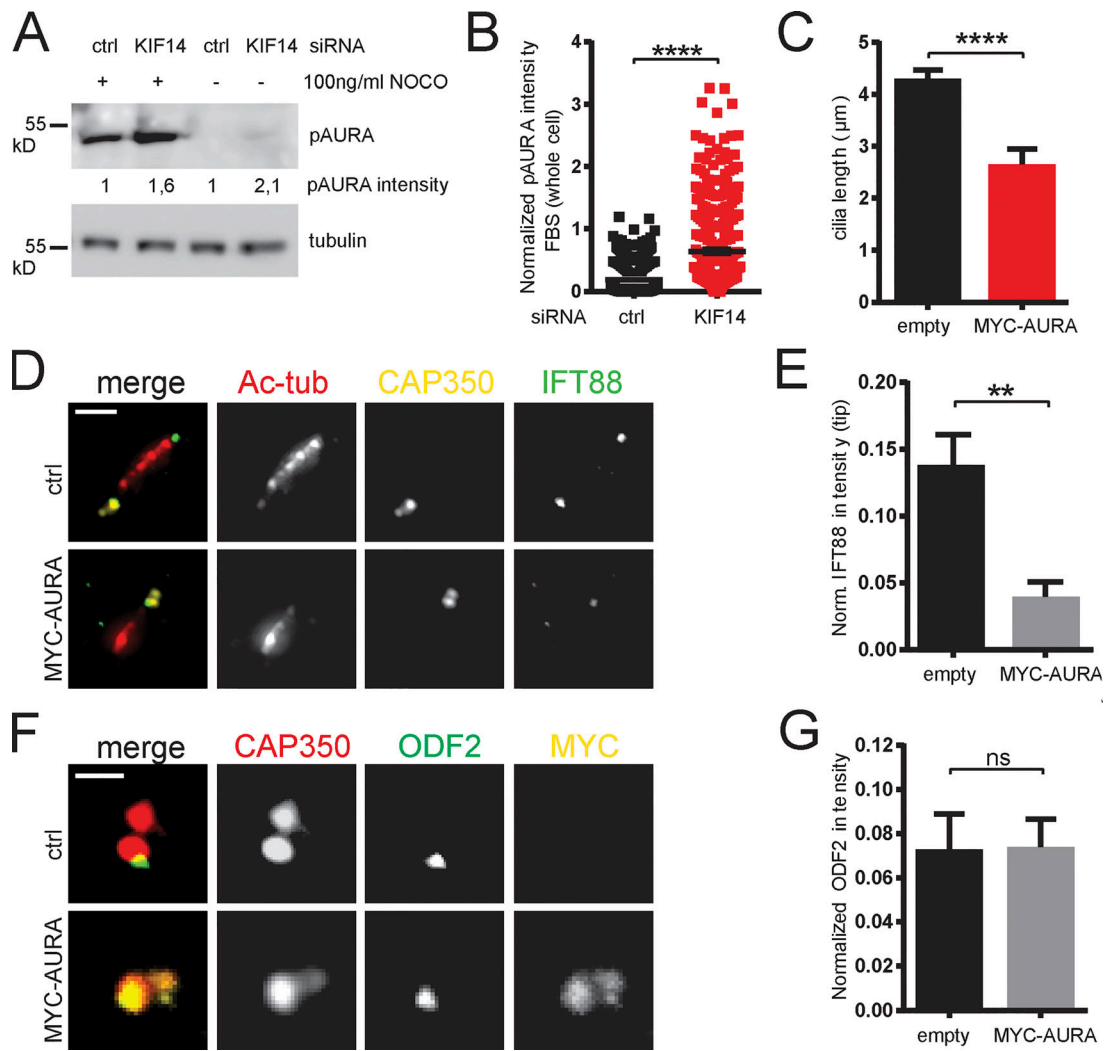
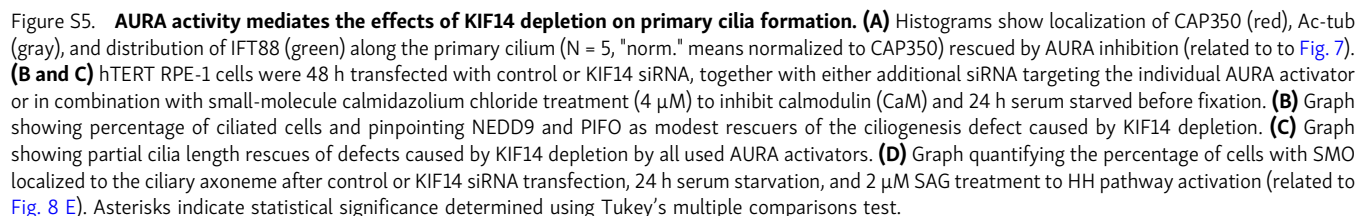


Figure S4. **KIF14 depletion deregulates AURA.** (A) Western blot analysis of whole hTERT RPE-1 cell lysates to detect an increase in pAURA protein levels after KIF14 depletion (100 ng/ml nocodazole treatment was used to enrich for mitotic cells). (B) Quantification of pAURA fluorescence intensity (normalized to Hoechst signal intensity) in nonstarved hTERT RPE-1 cells after control or KIF14 siRNA transfection. (C) Graph showing cilia lengths after MYC-AURA overexpression in hTERT RPE-1 cells (related to Fig. 6, E and F). (D–G) Related to Fig. 6, G–L. (D) Representative images of IFT88 (green), Ac-tub (red), and CAP350 (yellow) IF staining of hTERT RPE-1 cells transfected with mock or MYC-AURA (scale bar, 2 μ m), where the proportion of ciliated cells is decreased, as quantified in E. (F) Representative images of ODF2 (green), CAP350 (red), and MYC (yellow) IF staining of hTERT RPE-1 cells transfected with mock or MYC-AURA (scale bar, 1 μ m), where the proportion of ciliated cells is not changed (as quantified in G). Asterisks or "ns" indicates statistical significance compared with control determined using an unpaired t test.



Pejskova et al.
KIF14 regulates ciliogenesis

Appendix 9

Bernatik O, Pejškova P, Vysloužil D, Hanáková K, Zdrahal Z, **Cajanek L***. Phosphorylation of multiple proteins involved in ciliogenesis by Tau Tubulin kinase 2. *Molecular Biology of the Cell*. May 1;31(10):1032-1046. doi: 10.1091/mbc.E19-06-0334. (JCR 2020. IF= 4.138, Q3 – Cell Biology)

Phosphorylation of multiple proteins involved in ciliogenesis by Tau Tubulin kinase 2

Ondrej Bernatik^a, Petra Pejškova^a, David Vyslouzil^a, Katerina Hanakova^{b,c}, Zbynek Zdrahal^{b,c}, and Lukas Cajanek^{a,*}

^aDepartment of Histology and Embryology, Faculty of Medicine; ^bCentral European Institute of Technology and

^cNational Centre for Biomolecular Research, Faculty of Science, Masaryk University, 62500 Brno, Czech Republic

ABSTRACT Primary cilia are organelles necessary for proper implementation of developmental and homeostasis processes. To initiate their assembly, coordinated actions of multiple proteins are needed. Tau tubulin kinase 2 (TTBK2) is a key player in the cilium assembly pathway, controlling the final step of cilia initiation. The function of TTBK2 in ciliogenesis is critically dependent on its kinase activity; however, the precise mechanism of TTBK2 action has so far not been fully understood due to the very limited information about its relevant substrates. In this study, we demonstrate that CEP83, CEP89, CCDC92, Rabin8, and DVL3 are substrates of TTBK2 kinase activity. Further, we characterize a set of phosphosites of those substrates and CEP164 induced by TTBK2 in vitro and in vivo. Intriguingly, we further show that identified TTBK2 phosphosites and consensus sequence delineated from those are distinct from motifs previously assigned to TTBK2. Finally, we show that TTBK2 is also required for efficient phosphorylation of many S/T sites in CEP164 and provide evidence that TTBK2-induced phosphorylations of CEP164 modulate its function, which in turn seems relevant for the process of cilia formation. In summary, our work provides important insight into the substrates–TTBK2 kinase relationship and suggests that phosphorylation of substrates on multiple sites by TTBK2 is probably involved in the control of ciliogenesis in human cells.

Monitoring Editor

Yixian Zheng
Carnegie Institution

Received: Jun 19, 2019

Revised: Dec 23, 2019

Accepted: Feb 25, 2020

INTRODUCTION

Primary cilia (PCs) are organelles fundamental for proper development and homeostasis. Malfunctioning of PCs leads to ciliopathies, a group of diseases with a broad span of phenotypic manifestations, such as obesity, blindness, polycystic kidneys, and polydactyly (Mitchison and Valente, 2017; Reiter and Leroux, 2017). In addition,

PCs abnormalities have been recently related to cancer (Wong *et al.*, 2009; Jenks *et al.*, 2018; Wang and Dynlacht, 2018), further affirming the importance of correctly functioning PCs for tissue homeostasis.

PCs are usually assembled on postmitotic cells, with their formation being triggered at the distal end of the matured (mother) centrioles (MCs). They consist of a microtubule-based axoneme enclosed within a ciliary membrane, and transformed MC (basal body) (Ishikawa and Marshall, 2011; Nigg and Stearns, 2011). MCs differ from daughter centrioles by the presence of two sets of proteinaceous appendages named distal appendages (DA) and sub-DA (SDA) according to their position on MCs (Nigg and Stearns, 2011). The earliest sign of ciliogenesis seems to be the accumulation of small Golgi-derived vesicles in the vicinity of DA (Sorokin, 1962; Lu *et al.*, 2015; Wu *et al.*, 2018), depending on the activity of the Rab11-Rab8a-Rabin8 cascade (Knödler *et al.*, 2010; Westlake *et al.*, 2011; Hehnlly *et al.*, 2012; Schmidt *et al.*, 2012). Disruption of DA structure prevents vesicle docking and in turn leads to a failure of cilium assembly (Schmidt *et al.*, 2012; Chang *et al.*, 2013; Sillibourne *et al.*, 2013; Tanos *et al.*, 2013). Initially, five DA proteins, CEP164 (Graser *et al.*, 2007), CEP83 (Joo *et al.*, 2013), CEP89 (Sillibourne *et al.*, 2013), FBF1 (Tanos *et al.*, 2013; Wei *et al.*, 2013), and SCLT1

This article was published online ahead of print in MBoc in Press (<http://www.molbiolcell.org/cgi/doi/10.1091/mbc.E19-06-0334>) on March 4, 2020.

The authors declare that they have no conflicts of interest with the contents of this article.

*Address correspondence to: Lukas Cajanek (lukas.cajanek@gmail.com).

Abbreviations used: AA, amino acid; CEP164 N-term, N-terminal part of CEP164; CK1, casein kinase 1; DA, distal appendage; DEPP, Disorder Enhanced Phosphorylation Predictor; FA, formic acid; FBS, fetal bovine serum; FL, full length; IDR, intrinsically disordered region; KD, kinase dead; L, leucine; MC, mother centriole; PBS, phosphate-buffered saline; PC, primary cilia; PEG, polyethylene glycol; PEI, Polyethyleneimine; PONDR, Predictor of Natural Disordered Region; SCA11, spinocerebellar ataxia type 11; SDA, subdistal appendage; TBS, Tris-buffered saline; TTBK2, Tau tubulin kinase 2.

© 2020 Bernatik *et al.* This article is distributed by The American Society for Cell Biology under license from the author(s). Two months after publication it is available to the public under an Attribution–Noncommercial–Share Alike 3.0 Unported Creative Commons License (<http://creativecommons.org/licenses/by-nc-sa/3.0>).

“ASCB®,” “The American Society for Cell Biology®,” and “Molecular Biology of the Cell®” are registered trademarks of The American Society for Cell Biology.

(Tanos *et al.*, 2013), were identified. Recent identification of new DA components suggests the list might not be complete (Kurtulmus *et al.*, 2018; Bowler *et al.*, 2019).

Cilia initiation turns to the cilia extension process when the centriolar distal end capping proteins CP110, CEP97, and MPP9 are removed and ciliary axoneme begins to elongate (Spektor *et al.*, 2007; Huang *et al.*, 2018). This key step in the cilium assembly pathway is controlled by Tau Tubulin kinase 2 (TTBK2) (Goetz *et al.*, 2012; Čajánek and Nigg, 2014). TTBK2 is recruited to DA by CEP164 (Čajánek and Nigg, 2014; Oda *et al.*, 2014), and their mutual interaction is fine-tuned by INNPP5E and PI3K γ (Xu *et al.*, 2016). In addition, TTBK2 seems uniquely positioned among the DA-associated proteins—its depletion still allows cilia initiation to proceed, but the axoneme does not extend and ciliogenesis in turn fails, implying that TTBK2 may function as a switch in the cilia assembly pathway, turning the cilia initiation program to cilia elongation and maintenance (Goetz *et al.*, 2012; Čajánek and Nigg, 2014; Oda *et al.*, 2014; Bowie *et al.*, 2018).

From an evolutionary perspective, TTBK2 is a member of the casein kinase 1 (CK1) superfamily; its kinase domain shows 38% identity with CK1 δ (Ikezu and Ikezu, 2014; Liao *et al.*, 2015). Apart from TTBK2, the additional kinase MARK4 has been implicated in cilium initiation and assembly, although it seems to control the processes via SDA rather than DA of the MCs (Kuhns *et al.*, 2013).

TTBK2 mutations are causative for development of the neurodegenerative disorder spinocerebellar ataxia type 11 (SCA11) (Houlden *et al.*, 2007; Bauer *et al.*, 2010; Lindquist *et al.*, 2017). Interestingly, SCA11-associated mutant variants of TTBK2, typically truncated around amino acid (AA) 450, are unable to interact with CEP164, fail to localize to DA (Goetz *et al.*, 2012; Čajánek and Nigg, 2014), and instead seem to act in a dominant negative manner to disturb PC formation (Goetz *et al.*, 2012; Bowie *et al.*, 2018). As no other kinase can compensate for defects caused by TTBK2 mutations in SCA11, it again can be argued that TTBK2 has nonredundant functions in ciliogenesis. Previous work proved that ciliogenesis critically depends on TTBK2 kinase activity (Goetz *et al.*, 2012). However, information about bona fide substrates and/or S/T sites that are subjected to TTBK2 phosphorylation is very limited. So far, TTBK2 has been demonstrated to phosphorylate five substrates—Tau (Takahashi *et al.*, 1995; Tomizawa *et al.*, 2001), KIF2A (Watanabe *et al.*, 2015), CEP164 (Čajánek and Nigg, 2014), CEP97 (Oda *et al.*, 2014), and MPP9 (Huang *et al.*, 2018)—and only 11 S/T sites, namely S208 and S210 of Tau, S135 of KIF2A, S629 and S636 of MPP9, and T1309, S1317, S1346, S1347, S1434, and S1443 of CEP164 (Kitano-Takahashi *et al.*, 2007; Oda *et al.*, 2014; Watanabe *et al.*, 2015; Huang *et al.*, 2018).

Here, we report on novel TTBK2 substrates and an extensive set of TTBK2-induced phosphorylation sites determined and verified using a combination of *in vitro*, *in vivo*, and *in silico* approaches. Using our datasets of phosphorylated peptide sequences, we delineated a set of kinase motifs for TTBK2. For the functional validation we focused on CEP164 and through a combination of CRISPR editing, mass spectrometry and structure–function experiments provide evidence that phosphorylation by TTBK2 modulates functions of CEP164.

RESULTS

TTBK2 acts on multiple candidate substrates

To identify novel TTBK2 substrates, we focused our effort on a set of candidate proteins that localize to DA or interact with CEP164 and have been implicated in cilia initiation. These include the DA

components CEP83 and CEP89, Rab8a, Rabin8, DVL3, CCDC92, and CP110 (Chaki *et al.*, 2012; Schmidt *et al.*, 2012; Tanos *et al.*, 2013; Cervenka *et al.*, 2016; Huang *et al.*, 2018). First, given that the reported TTBK2 substrates CEP164 and MPP9 respond to elevated TTBK2 levels with a profound mobility shift (Čajánek and Nigg, 2014; Huang *et al.*, 2018), we examined the behavior of individual candidates following their coexpression with TTBK2 in HEK293T WT cells. Interestingly, while we found no response to FLAG-TTBK2 coexpression in the case of HA-CP110 and GFP-Rab8a, we observed a mobility shift of MYC-CEP83, MYC-CEP89, GFP-Rabin8, and GFP-DVL2 similar to that of MYC-CEP164 (Figure 1A), indicating that these proteins are modified in a TTBK2-dependent manner. Next, to corroborate our observations, we included the TTBK2 D163A mutant with disabled kinase domain activity (KD) (Bouskila *et al.*, 2011) in our experiments. Importantly, as depicted in Figure 1B, GFP-CEP164, GFP-CEP89, GFP-CEP83, GFP-CCDC92, and GFP-Rabin8, but not GFP-Rab8a, specifically responded to TTBK2, but not TTBK2 KD, suggesting that the observed shifts in protein mobility reflect a modification of the given protein mediated by kinase activity of TTBK2.

TTBK2 directly phosphorylates CEP83, CEP89, Rabin8, CCDC92, and DVL3

Having found that TTBK2 might phosphorylate several proteins necessary for the process of cilia initiation, we performed *in vitro* kinase assays of individual candidate substrates in the presence of TTBK2, followed by MS/MS identification and quantification of detected phosphorylations. To ensure proper protein folding and functionality, individual candidate substrates and TTBK2, respectively, were purified by immunoprecipitation from HEK293T cells. TTBK2 KD was used as a control condition to account for actions of endogenous kinases possibly copurifying with immunoprecipitated TTBK2. In addition, in the second repetition we included λ phosphatase treatment in our workflow to reduce the impact of any already present phosphorylation. The experimental workflow is summarized in Supplemental Figure S1A. In brief, the criteria to assign any identified phosphorylation to TTBK2 were as follows (please see *Materials and Methods* for additional details): 1) the intensity of phosphopeptide was higher than 2×10^6 ; 2) phosphopeptide intensity was at least twice that of the corresponding phosphopeptide intensity in control samples (TTBK2 KD). By applying these criteria, we detected 45 phosphorylated S/T sites induced by TTBK2 in the tested proteins (CEP164, CEP83, CEP89, Rabin8, CCDC92, DVL3) (Figure 2, A and B, blue and red color coded). The total number of identified phosphorylations was ~120 (Supplemental Figure S2A; Figure 2B; Supplemental Table S1).

In a similar manner, we examined autophosphorylation of TTBK2. Here we analyzed four experimental conditions: 1) purified TTBK2, 2) purified TTBK2 treated with λ phosphatase, 3) TTBK2 treated with λ phosphatase subsequently subjected to an *in vitro* kinase assay, and 4) TTBK2 KD treated with λ phosphatase, subjected to an *in vitro* kinase assay (schematized in Supplemental Figure S1B). We compared phosphosites identified in condition 3 with control conditions 2 and 4. Phosphorylations that were induced at least twofold over both controls were considered to be TTBK2 induced. Condition 1 was included to assess the efficiency of the λ phosphatase treatment. This analysis led to the identification of approximately 110 phosphorylations, of which 79 were found to be induced by TTBK2. The induced phosphorylations are found along the whole sequence of TTBK2, with a significant portion of the sites residing at the C-terminus (Figure 2C; Supplemental Figure S2B; Supplemental Table S1).

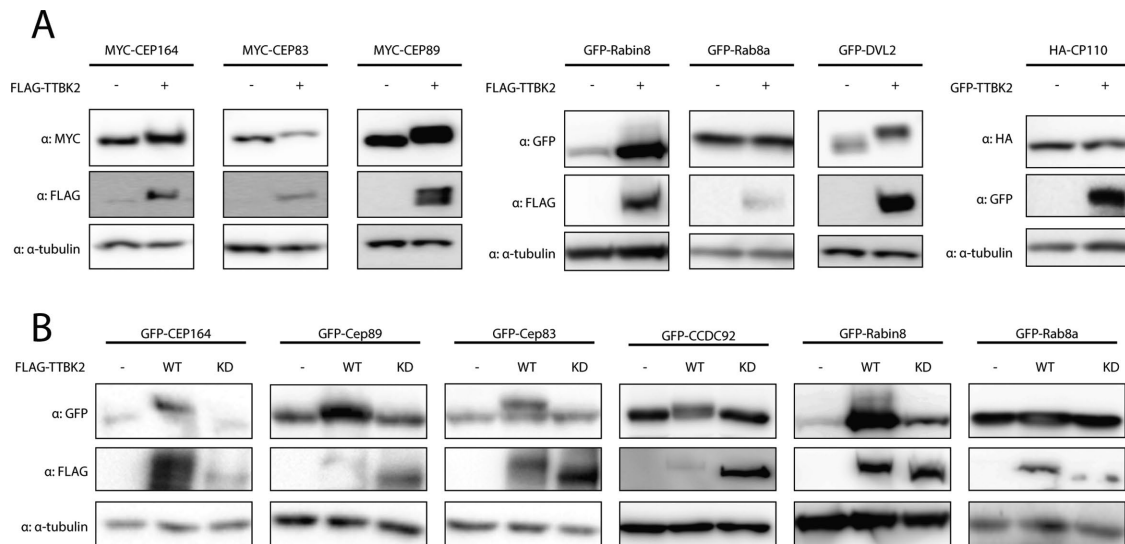


FIGURE 1: TTBK2 induces mobility shift of CEP164, CEP89, CEP83, CCDC92, Rabin8, and DVL2. HEK293T cells were transfected by indicated plasmids, lysed 24 h posttransfection and analyzed by WB using indicated antibodies. (A) Electrophoretic mobility of MYC-CEP164, MYC-CEP83, MYC-CEP89, GFP-Rabin8, and GFP-DVL2 is decelerated by FLAG-TTBK2 expression. HA-CP110 and GFP-Rab8a do not change their mobility on FLAG-TTBK2 or GFP-TTBK2 expression. (B) Detection of mobility shift of GFP-CEP164, GFP-CEP89, GFP-CEP83, GFP-CCDC92, and GFP-Rabin8 induced by FLAG-TTBK2 but not FLAG-TTBK2 KD. Note that TTBK2 WT undergoes profound mobility shift compared with TTBK2 KD, indicating autophosphorylation. Depicted experiments were performed at least twice.

The detection of phosphorylation of a specific S/T residue using an *in vitro* kinase assay typically suffices to assume a direct kinase–substrate relationship for individual proteins tested but might not fully reflect phosphorylation of a given protein *in vivo*. To this end, we set out to analyze phosphorylations of individual substrates coexpressed with TTBK2 and subsequently purified from HEK293T cells. The experiment workflow is summarized in Supplemental Figure S1C. The criteria for *in vivo* TTBK2-induced phosphorylations were more stringent than in the case of *in vitro* analysis to account for the higher complexity of the samples and in turn for the potential influence of other protein kinases (please refer to *Materials and Methods* for details). This *in vivo* approach identified approximately 230 phosphorylations (Supplemental Table S1; Supplemental Figure S3) of which 133 were induced by TTBK2 (Figure 2A, black and red color coded). Importantly, a comparison of induced phosphorylation sites identified *in vivo* and *in vitro* not only showed a fairly extensive overlap between the datasets for individual proteins (phosphorylations common for both datasets are in red, Figure 2A; Supplemental Figure S3) but also revealed many phosphosites localized in clusters or pairs, often dispersed through the entire protein sequence (Figure 2A).

Specifically, in the case of CEP164, 18 individual S/T sites were found to be induced by TTBK2 by both approaches; for CEP83, it was five S/T residues; for CEP89, it was two S/T; and for CCDC92 and Rabin8, both showed one S/T phosphorylation in common between *in vitro* and *in vivo*. Of note, analysis of DVL3 *in vivo* phosphorylations induced in the context of several kinases, including TTBK2, has been recently reported (Hanáková *et al.*, 2019). Overall, 27 (64%) induced phosphorylations detected through an *in vitro* approach were also found induced *in vivo*, thereby confirming a role of TTBK2 in the phosphorylation of tested proteins (Figure 2A). Additionally, six sites identified as being induced *in vitro* were occasionally also detected *in vivo* but did not pass the set threshold to be considered induced (Supplemental Table S1; Supplemental Figure S2A; Supplemental Figure S3). It is worth noting that the

majority of sites detected by *in vivo* analyses (in total 106 phosphorylated S/T residues, Supplemental Table S1) were not detected using the *in vitro* approach.

TTBK2 shows motif similarities to CK1

Given the number of phosphorylations we identified and the reports on preferential phosphorylation of intrinsically disordered regions (IDRs) over folded protein regions (Iakoucheva *et al.*, 2004; Xie *et al.*, 2007; Bah *et al.*, 2015; Bah and Forman-Kay, 2016), we analyzed TTBK2 substrates using the Predictor of Natural Disordered Regions (PONDR) (Peng *et al.*, 2005; Peng and Zhang, 2006) and the Disorder Enhanced Phosphorylation Predictor (DEPP) (Iakoucheva *et al.*, 2004) to check the extent of IDRs and the overlap between the identified and the predicted phosphosites, respectively. The analysis carried out using the PONDR algorithms VSL-2 (Figure 3, A and B; Supplemental Figure S4, violet line) and VL3-BA (Figure 3, A and B; Supplemental Figure S4, blue line) revealed long IDRs in all the proteins tested (Figure 3, A and B, and Supplemental Figure S4). In addition, comparing our experimental data to DEPP-predicted phosphorylations revealed many examples of extensive overlap (Figure 3, A and B; Supplemental Figure S4). Specifically, experimentally identified CEP164 phosphorylations were found distributed throughout the protein sequence in a pattern resembling that of DEPP prediction (Figure 3A). Further, DEPP predicted extensive phosphorylation of the TTBK2 C-terminal part in line with our experimental data (Figure 3A). In addition, we observed similarity between the experimentally detected and the predicted phosphorylation sites also in the case of the remaining examined substrates of TTBK2 (Supplemental Figure S4). In light of these findings, we examined previously identified substrates of TTBK2, namely, CEP97, Tau, KIF2a, and MPP9 by PONDR and DEPP. As expected, all previously identified phosphosites were localized within long IDRs, which were predicted to contain many additional phosphorylation sites (Supplemental Figure S5).

Next, we compared our experimental results with the data available in the PhosphoSitePlus database. For the purpose of

A | *in vitro* only | *in vivo* only | both datasets * PhosphoSitePlus

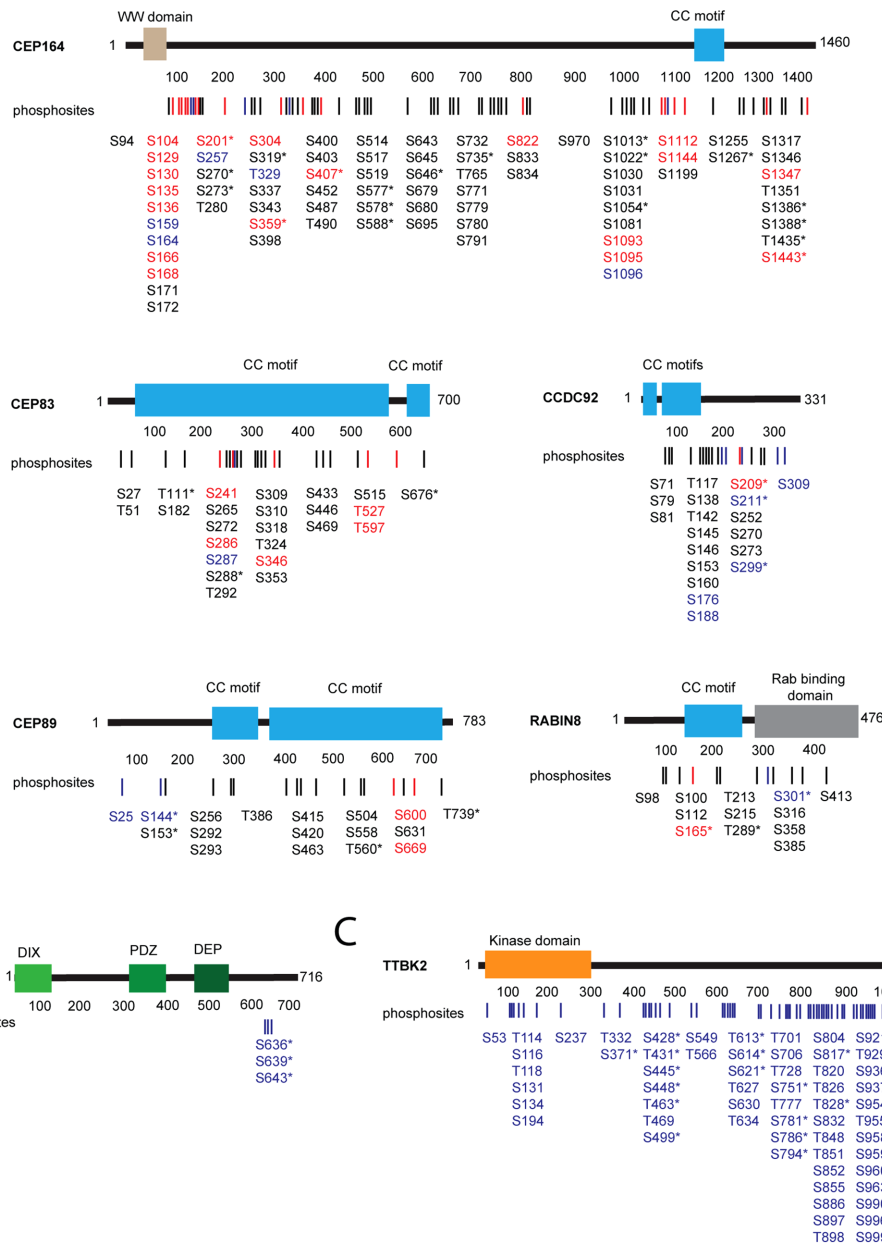


FIGURE 2: TTBK2 phosphorylates its substrates on multiple serines and threonines. Map of identified phosphorylations induced by TTBK2 on tested substrates. (A, B) Structure of each TTBK2 substrate is schematized, rectangles indicate the presence of a domain or motif, and numbers indicate the length of given protein in amino acids. Lines and numbers, respectively, below the schematic protein structure indicate positions of each phosphorylation induced by TTBK2. Sites shown in red were detected both *in vitro* and *in vivo*, sites in blue were detected only *in vitro*, and sites in black were detected only *in vivo*. The asterisk indicates that given phosphorylation is covered in PhosphoSitePlus. (A) TTBK2-induced phosphorylation of CEP164, CEP89, CEP83, CCDC92, or Rabin8 identified *in vitro* and *in vivo*. (B) TTBK2 phosphorylation of DVL3 identified *in vitro*. (C) TTBK2 autophosphorylations identified *in vitro*.

this comparison, we did not discriminate here between induced and noninduced phosphorylations or between individual datasets of our analysis. Interestingly, we found that 99/133 (74%) phosphorylations reported for the substrate proteins on PhosphoSitePlus were also detected in our experiments (Figure 2, A–C; Supplemental Table S1, marked by an asterisk). Although we cannot rule out the possibility that some of phosphosites

identified by our analyses are a result of overexpression, many of the identified sites seem physiological as they were previously detected in endogenous proteins. Importantly, however, only 53/229 (23%) of TTBK2-induced phosphorylations were previously identified by large-scale proteomic studies. This implies that phosphorylation of some of these residues might be limited to a specific cellular context.

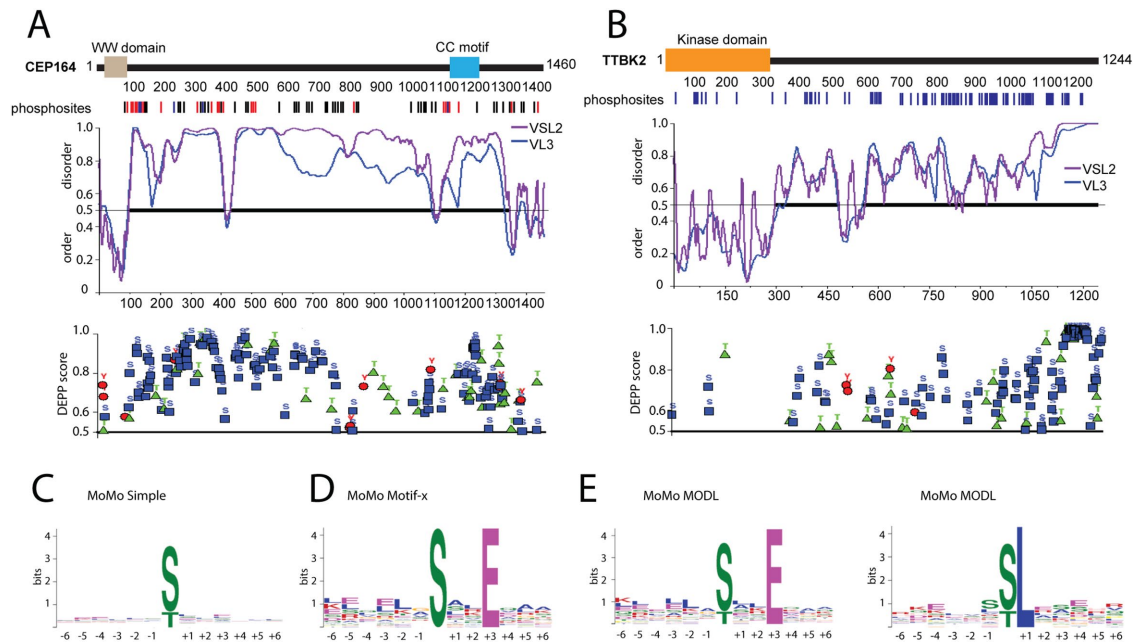


FIGURE 3: TTBK2 shows motif similarities to CK1. (A, B) Protein disorder and phosphorylation prediction for CEP164 and TTBK2. Structure of CEP164 and TTBK2 is schematized as described in Figure 2. The first graph below the schematized structure of CEP164 and TTBK2, respectively, depicts prediction of disorder/order (with cut-off score 0.5) determined by PONDR using VSL2 (violet line) and VL3-BA (blue line) algorithms. The second graph plots DEPP score (with cut-off score 0.5) and individual phosphosites thereby predicted (phosphoS as blue rectangle, phosphoT as green triangle, and phosphoY as red circle). (C–E) Determination of TTBK2 kinase motifs using indicated algorithms. Size of depicted symbols indicates relative abundance of each amino acid at given position within a set of phosphorylated peptides. Kinase motif search was performed by C, MoMo simple; D, Motif-x; and E, MODL algorithms.

As it was previously reported that TTBK2 preferentially phosphorylated S/T sites with pY at the +2 position (Bouskila *et al.*, 2011), we examined our datasets for the presence of this motif. However, we identified only two phosphorylations (S201 in CEP164; S316 in Rabin8) with Y at the +2 position, which could in principle fit into the proposed consensus sequence. Next, we manually searched the dataset for priming sites at the –3 position (pS/pT-x-x-S/T motif) reported for the CK1 family (Cheong and Virshup, 2011) and found 28 phosphorylations fitting this criterion (CEP164: S171, S273, S403, S455, T490, S517, S646, S735, S1096, S1255, S1258; CDC92: S145, S179, S273; Rabin8: S100; DVL3: S639; TTBK2: S134, T431, S448, T820, T851, S855, S958, S963, S999, S1033, S1042, S1243). Thus, the majority of phosphorylation sites we found were without any kinase motif assigned. To probe for possible unrecognized TTBK2 consensus sites, we pooled data from *in vitro* and *in vivo* datasets and used them for an unbiased kinase motif search by the MeMe suite tool MoMo (Bailey *et al.*, 2009; Cheng *et al.*, 2017). Initial analysis by a “simple” algorithm, which plots the relative abundance of individual AA residues at the indicated position within the whole dataset, did not reveal any enrichment (Figure 3C). Given that, we subsequently performed analysis by Motif-x and MODL algorithms, respectively, that can resolve consensus motif sequences present only in a subset of peptides (Chou and Schwartz, 2011; Cheng *et al.*, 2017). Intriguingly, both algorithms detected a preference for glutamic acid (E) at the +3 position (MODL, 32 peptides; Motif-x, 27 peptides) (Figure 3, D and E). In addition, analysis using MODL detected a preference for leucine (L) at the +1 position (MODL, 30 peptides) (Figure 3E). Sequences of peptides with the identified motifs are listed in Supplemental Table S2.

CEP164 phosphorylation is largely dependent on TTBK2

To further study TTBK2 phosphorylations, we decided to derive HEK293T and RPE1 cells devoid of TTBK2. First, we verified that CRISPR-Cas9 successfully disrupted ORF of the TTBK2 locus by indels in exon 4, which encodes part of the kinase domain of TTBK2 (Figure 4A). Next, we confirmed that CRISPR/Cas9-edited cells lacked any detectable levels of TTBK2 (Figure 4B; Supplemental Figure S6, A–C), while MC localization of CEP164 or CEP83 was not affected (Supplemental Figure 6, B and C). Functionally, TTBK2-deficient cells fail to form cilia. Subsequent reintroduction of WT, but not the KD form of TTBK2, allowed PCs formation in TTBK2 KO HEK293T or RPE1, as expected (Figure 4D; Supplemental Figure S6D). Additionally, we found that CEP164 migrated faster on PAA gel when TTBK2 was depleted (Figure 4B; Supplemental Figure S6A), implying that posttranslational modifications of CEP164 were diminished in TTBK2 KO cells. Reintroduction of the WT form of TTBK2 to TTBK2 KO RPE1 rescued CEP164 PAA mobility, in contrast to TTBK2 KD (Figure 4C). These results confirm and extend previous observations (Goetz *et al.*, 2012; Lo *et al.*, 2019). We also examined the behavior of CEP83, CEP89, and CEP97, substrates of TTBK2 reported here or previously, in response to TTBK2 ablation. However, in contrast to CEP164, we failed to detect any difference in the PAA mobility of these proteins (Figure 4B).

Our observations suggesting that TTBK2 is a main driving force of CEP164 phosphorylation prompted us to narrow down our validation attempts to CEP164. First, we examined the importance of TTBK2 for phosphorylation of endogenous CEP164. We isolated CEP164 by immunoprecipitation from TTBK2 WT and KO HEK293T cells, respectively, and subjected the protein complexes to MS/MS analysis of phosphorylation. We detected approximately 37 phosphorylations, with 27 of those being twice or more

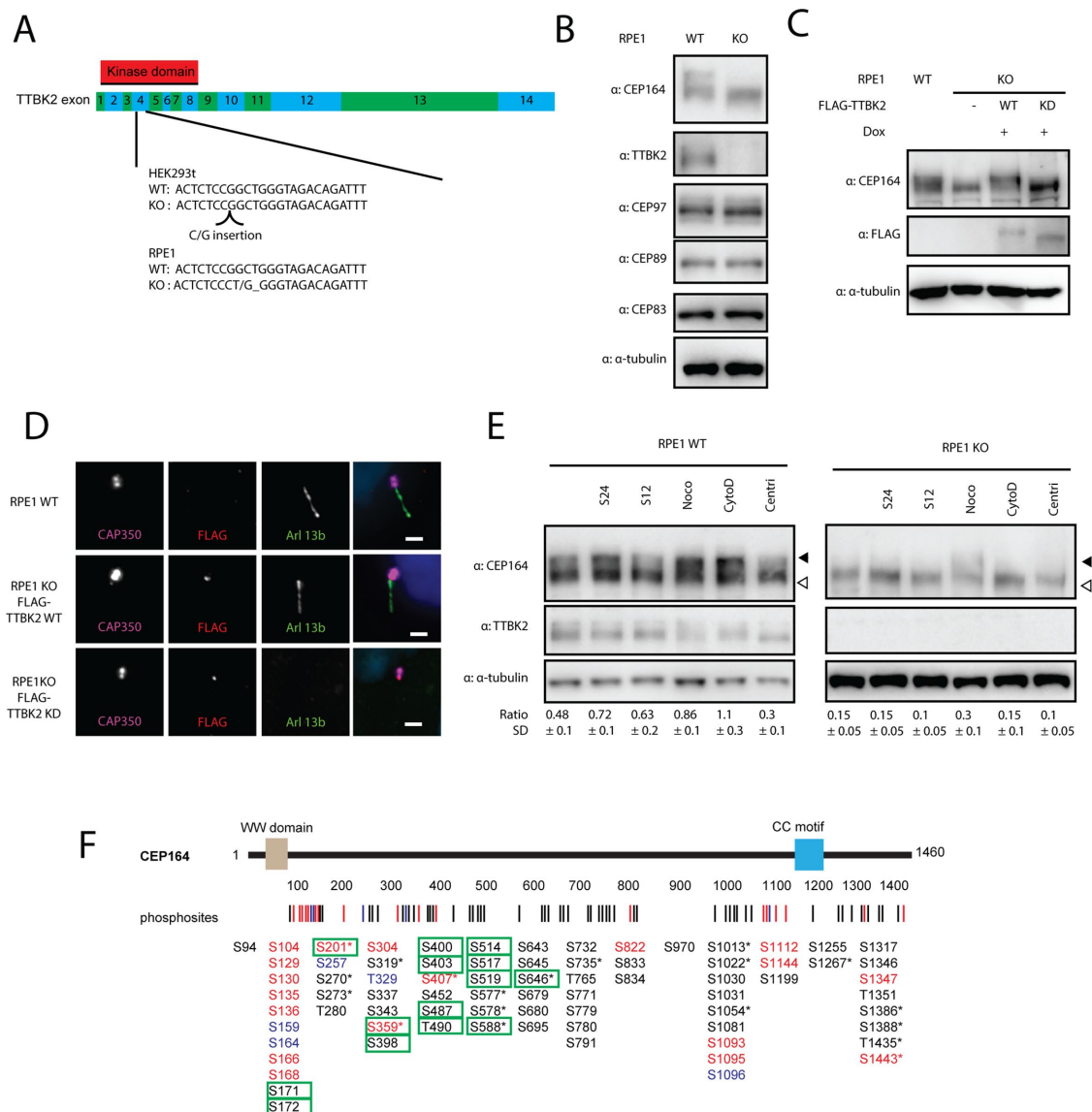


FIGURE 4: TTBK2 is required for phosphorylation of CEP164 during induction of ciliogenesis. (A) Scheme of TTBK2 editing by CRISPR-Cas9. TTBK2 exons are coded in green and blue, kinase domain position is marked by a red rectangle. gRNA targets Exon4, Cas9-edited sequences of TTBK2 for RPE1 are indicated. (B) WB analysis of RPE1 WT and TTBK2 KO cells. TTBK2 protein is missing in RPE1 TTBK2 KO cells, CEP164 is migrating faster in TTBK2 KO RPE1, while no changes in migration pattern were detected for CEP89, CEP83, and CEP97. (C, D) FLAG TTBK2 WT and KD versions were reintroduced in RPE1 TTBK2 KO cells. (C) CEP164 migration pattern is rescued by FLAG-TTBK2 WT but not by FLAG-TTBK2 KD reintroduction in RPE1 TTBK2 KO cells. (D) Ciliogenesis is rescued by FLAG-TTBK2 WT but not by FLAG-TTBK2 KD reintroduction in RPE1 TTBK2 KO cells. (E) RPE1 WT and TTBK2 KO cells were treated as indicated and CEP164 migration was analyzed. Starvation for 12 or 24 h and nocodazole (100 ng/ml, overnight) and cytochalasin D (2 μ M, overnight) treatment lead to slower CEP164 migration, while treatment by PLK4 inhibitor centrinone (150 μ M, 72 h) enhances CEP164 migration in RPE1 WT cells. Treatment of RPE1 TTBK2 KO cells by nocodazole leads to slower CEP164 migration. Ratio indicates relative abundance of the top band (indicated by full arrowhead) of CEP164 divided by the bottom band (indicated by empty arrowhead). WB was quantified for $N = 4$ for WT and $n = 3$ for TTBK2 KO cells; SD indicates SD. (F) Structure of CEP164 is schematized, rectangles indicate domains or motifs, and numbers indicate length in amino acids. Lines and numbers, respectively, below the schematic protein structure indicate positions of each phosphorylation induced by TTBK2. Sites shown in red were detected both in vitro and in vivo, sites in blue were detected only in vitro, and sites in black were detected only in vivo. Green rectangle marks phosphorylations more intensive in WT compared with TTBK2 KO HEK293T cells. The asterisk indicates that given phosphorylation is covered in PhosphoSitePlus.

as intensive in WT HEK293T (Supplemental Figure S6F; Supplemental Table S1). Importantly, 14 phosphosites matched the TTBK2-induced phosphorylations detected by our previous in vitro or in vivo approaches (Figure 4F, marked by a green rectangle).

From the rest of the S/T identified here as being regulated by endogenous TTBK2, 10 sites were assigned as not being targeted by TTBK2, while three sites were new (not identified in any of our previous experiments) (Supplemental Figure S6F and

Supplemental Table S1). Together with our previous data, these findings establish that TTBK2 is both sufficient and required for efficient CEP164 phosphorylation.

Next, we attempted to relate TTBK2 phosphorylation of CEP164 to a particular event, for example, the induction of PC formation by serum starvation or treatment by cytochalasin D, nocodazole-induced mitotic arrest, or centrinone-induced centriole ablation (Wong *et al.*, 2015). Thus, we examined the extent of CEP164 phosphorylation by monitoring the ratio between slower (hyperphosphorylated) and faster (hypophosphorylated) migrating forms of CEP164 (Čajánek and Nigg, 2014). As shown in Figure 4E, we observed the accumulation of slower migrating CEP164 forms in nocodazole-treated cells, in line with previous results (Schmidt *et al.*, 2012). Interestingly, we detected that 12 h of serum starvation induced a moderate shift of CEP164, which became more prominent 24 h poststarvation. In addition, treatment by another compound promoting ciliogenesis, actin polymerisation inhibitor cytochalasin D (Kim *et al.*, 2010), also showed a pronounced effect on CEP164 PAA mobility. Of note, the bitor centrinone caused a modest decrease in CEP164 phosphorylation. Remarkably, the effects of ciliogenesis-inducing agents (serum starvation, cytochalasin D), but not of nocodazole, on the relative increase of slow (hyperphosphorylated) forms of CEP164 were markedly reduced in TTBK2-deficient cells (Figure 4E). These data imply that TTBK2 is responsible for efficient phosphorylation of CEP164 during ciliogenesis.

CEP164 N-terminus phosphorylation leads to altered function

The functional relevance of a phosphorylation is usually tested by mutating detected phosphorylated sites to nonphosphorylatable variants and subsequent examination of whether this alters the function of tested protein (Sieracki and Komarova, 2013). Our analysis detected a significant number of induced phosphorylation sites, implying possible complex regulation, as multiple phosphorylations typically act in a combinatorial manner (Cohen, 2000; Bah and Forman-Kay, 2016). In addition, the majority of the identified phosphosites resided in IDRs with a currently unknown impact on the biology of a given protein. On the other hand, our experiments also revealed several TTBK2 phosphosites within the N-terminal part of CEP164 (CEP164 N-term, AA 1–467), which, via its WW domain (predicted to contain AA 56–89; Schmidt *et al.*, 2012; Čajánek and Nigg, 2014), interacts with TTBK2 and in turn regulates ciliogenesis (Schmidt *et al.*, 2012; Čajánek and Nigg, 2014; Oda *et al.*, 2014). Bearing this in mind, we decided to test the functional consequences of TTBK2 phosphorylation of the CEP164 N-term. First, we examined the role of endogenous TTBK2 by analyzing phosphorylations of the FLAG-CEP164 N-term, transiently expressed in TTBK2 WT or KO HEK293T cells. We found that four phosphorylated S/T (S166, S168, S172, and S201) of 14 identified were at least two times more intensive in TTBK2 WT than in TTBK2 KO samples (Figure 5A; Supplemental Figure S6G; Supplemental Table S1).

Next, we examined all CEP164 phosphorylation data and selected seven TTBK2 phosphorylation sites (S129, S130, S135, S136, S166, S168, and S201) located in the proximity of the WW domain of the CEP164 N-term and mutated those to A in the CEP164 full-length (FL) protein and CEP164 N-term, naming the obtained mutants the “CEP164 FL-A” and “CEP164 N-A term.” It is worth noting that *in silico* modeling of introduced mutations in CEP164 N-term using PONDR did not reveal any major impact on protein folding (Figure 5B). First, we examined exogenously expressed CEP164 FL-A and CEP164 N-A term in terms of mobility

shift after serum starvation and noted that FL-A and N-A term did not produce slow migrating forms on serum starvation, in contrast to their corresponding WT counterparts (Supplemental Figure S6E). Next, to resolve whether the introduced mutations in any way changed the CEP164–TTBK2 relationship, we tested whether the CEP164 N-A term and TTBK2 can coimmunoprecipitate. However, we did not detect any notable difference between the FLAG-CEP164 N-term and the FLAG-CEP164 N-A term to coimmunoprecipitate with MYC-TTBK2 when overexpressed in HEK293T cells (Figure 5C). We reasoned that our failure to see any difference meant the changes were too subtle to be revealed by the used approach and decided to test the CEP164–TTBK2 relationship by other means. Interestingly, we observed that while ciliogenesis was efficiently induced in mock (51%) or FLAG-CEP164 M-part (468–1135 AA) (43%) transfected RPE-1 cells, in line with previous reports (Schmidt *et al.*, 2012; Čajánek and Nigg, 2014; Oda *et al.*, 2014), FLAG-CEP164 N-term expression almost completely abrogated the formation of PCs (below 5% of ciliated cells) in contrast to the FLAG-CEP164 N-A term that still allowed the formation of PCs in about 20% of transfected RPE-1 cells (Figure 5D). The CEP164 N-term fails to localize to the MCs (Schmidt *et al.*, 2012; Čajánek and Nigg, 2014); in turn, its expression leads to the sequestration of endogenous TTBK2 from MCs and hence to profound inhibition of ciliogenesis (Čajánek and Nigg, 2014). Based on our observations, we hypothesized that the ability of the CEP164 N-term to sequester endogenous TTBK2 (Čajánek and Nigg, 2014) might be affected in the CEP164 N-A term. Intriguingly, we found that the FLAG-CEP164 N-A term was still able to sequester TTBK2 from MC, but to a lesser extent than the FLAG-CEP164 N-term (Figure 5, E and F). Next, we found levels of IFT88, but not of CEP83, located on the MCs significantly more reduced in cells expressing the FLAG-CEP164 N-term than in cells expressing the FLAG-CEP164 N-A term (Figure 5, G–J). This observation is in line with previous reports as well as our observations showing that MC localization of IFT88, but not of CEP83, is dependent on TTBK2 activity (Supplemental Figure S6, B and C) (Goetz *et al.*, 2012). Taken together, these results imply that phosphorylation of the given residues (S129, S130, S135, S136, S166, S168, and S201) modulates CEP164 function which in turn may be functionally important for TTBK2 recruitment to MC and ciliogenesis.

DISCUSSION

TTBK2 seems to have a unique position among other regulators of ciliogenesis, as its action marks the “end of the beginning” by pushing cilia initiation toward cilia extension. However, how TTBK2 regulatory function is implemented is still only partially understood. To gain insight into this process, we set out to identify its substrates. In this study, we have demonstrated that several proteins either directly binding to CEP164 or localizing to its proximity, namely, CEP83, CEP89, CCDC92, Rabin8, and DVL2/3, as well as CEP164 itself, are subjected to TTBK2 phosphorylation primarily in their IDRs. We further revealed a previously undetected consensus motif similarity of TTBK2 to that of CK1, at least for a subset of phosphorylated sites.

Our observation that TTBK2 is able to phosphorylate components of DA and proteins associated with the centriole distal end does not come as a complete surprise, given its proposed role in the assembly of the appendages (Čajánek and Nigg, 2014). Moreover, thanks to the recently detailed description of DA structure and organization (Yang *et al.*, 2018; Bowler *et al.*, 2019), it is tempting to speculate that TTBK2 might be able to target additional basal body proteins besides those included in our screen. In our initial

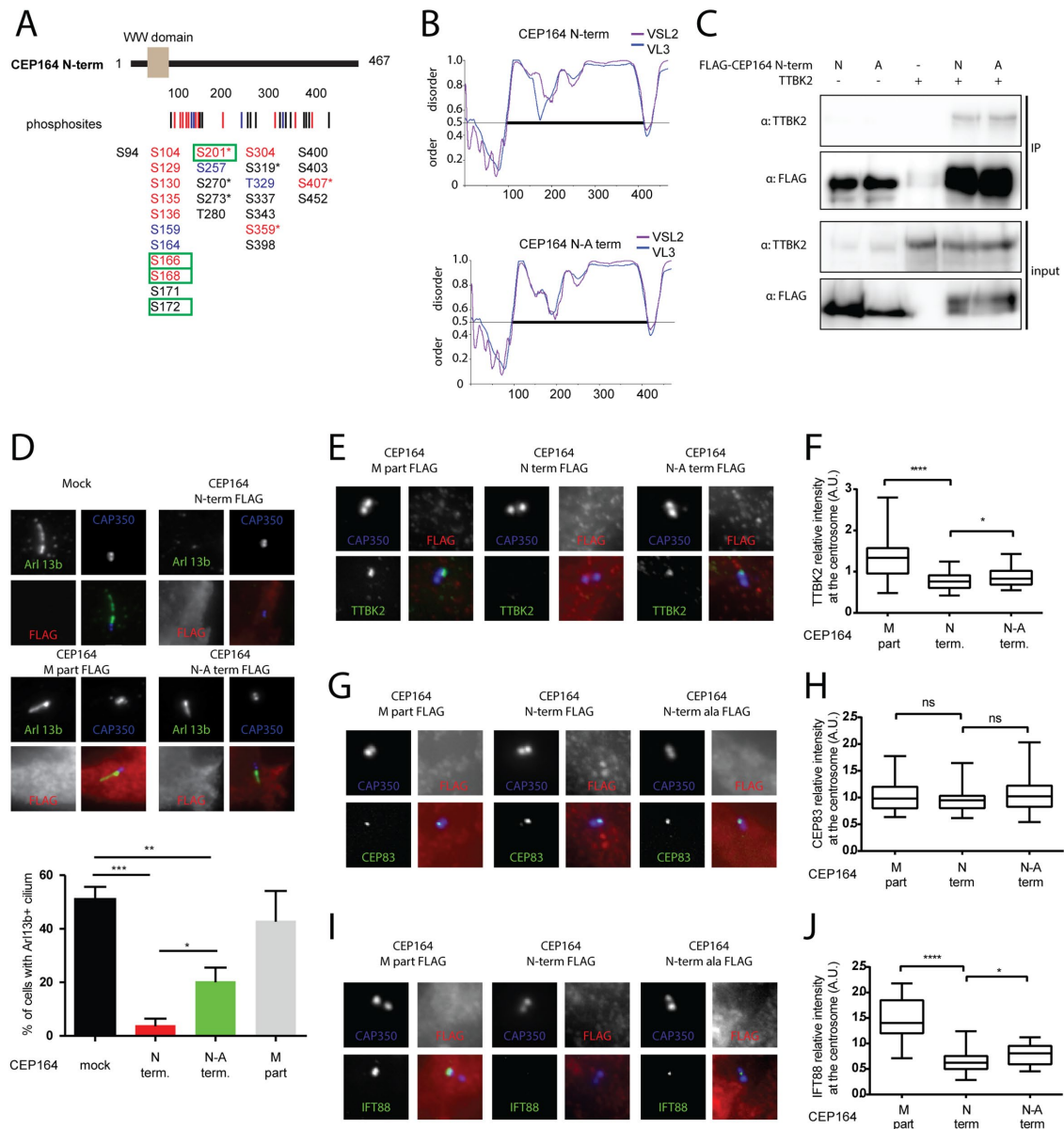


FIGURE 5: Phosphorylation of CEP164 N-terminus by TTBK2 affects its function and ciliogenesis. (A) Structure of CEP164 N-term is schematized, rectangle indicates WW domain, and numbers indicate length in amino acids. Lines and numbers, respectively, below the schematic protein structure indicate positions of each phosphorylation induced by TTBK2. Sites shown in red were detected both in vitro and in vivo, sites in blue were detected only in vitro, and sites in black were detected only in vivo. Green rectangle marks phosphorylations more intensive in WT compared with TTBK2 KO HEK293T cells. The asterisk indicates that given phosphorylation is covered in PhosphoSitePlus. (B) In silico analysis of protein folding by PONDR VSL2 (violet line) and VL3-BA (blue line) algorithms; the numbers indicate length of given protein in amino acids. Note that mutation of seven TTBK2 phosphorylated sites (S129, S130, S135, S136, S166, S168, S201) to Alanines (CEP164 N-A term) is not expected to change protein folding over control (CEP164 N-term). (C) HEK293T cells were transfected by indicated plasmids and 24 h posttransfection were subjected to immunoprecipitation by anti-FLAG antibody. No difference was observed between FLAG-CEP164 N term and FLAG-CEP164 N-A term in their ability of to coimmunoprecipitate MYC-TTBK2. (D–J) RPE1 cells were transfected by indicated FLAG-tagged CEP164 truncation constructs and, following 24 h, starved for an additional 24 h to induce ciliogenesis, or ON to evaluate TTBK2, IFT88, or CEP83 on MC. (D) ARL13b (green) and CAP350 (blue, inset) staining was used to detect PCs and centrosomes, respectively, and expression of indicated CEP164 variants was detected by FLAG antibody (red). The graph summarizes effects on PC formation from four independent experiments, and RPE-1 cells transfected with empty vector (mock) or CEP164 M part were used as controls and analyzed by Student's t test; *** $p < 0.001$, ** $p < 0.01$, * $p < 0.05$; SEM. (E–J) Following fixation, RPE-1 cells were stained for TTBK2, CEP83, or IFT88 (green); FLAG (red); and CAP350 (blue) to examine differences in localization of tested proteins to MC. The graph summarizes the effects protein intensity on MC (TTBK2 $n = 5$, IFT88 $n = 3$, CEP83 $n = 4$, 30–40 cells analyzed per condition) and analyzed by Student's t test; **** $p < 0.0001$, * $p < 0.05$; SEM.

screening, CP110 and Rab8a did not shift on TTBK2 coexpression, hence we did not include them in the subsequent detailed analysis. However, as a lack of mobility shift does not necessarily mean a lack of phosphorylation, it would be premature to rule them out as TTBK2 substrates. Interestingly, two of the CP110 binding partners, CEP97 and MPP9, have already been reported as TTBK2 substrates and their phosphorylation has been implicated in CP110/CEP97 complex removal from the distal end of the MCs (Oda et al., 2014; Huang et al., 2018).

The extent of the mobility shift we observed for CEP164, CEP83, CEP89, CCDC92, Rabin8, and DVL3 suggested modification by multiple phosphates rather than by single phosphorylation, which we subsequently confirmed with MS-based experiments. Importantly, our analysis detected not only the majority of sites previously assigned as targets of TTBK2 activity (Čajánek and Nigg, 2014), namely, the CEP164 sites T1309, S1317, S1347, and S1443 in both datasets and S1346 in vivo, but also many new ones, thereby demonstrating the robustness and sensitivity of our workflow. Furthermore, in the example of CEP164, we demonstrated that TTBK2 regulates phosphorylation of a fairly large number of S/T sites on the endogenous level.

The majority (64%) of TTBK2 phosphorylation sites we detected in vitro were subsequently confirmed in vivo. A significant portion of the sites detected by in vivo analysis (in total 106 phosphorylated S/T residues) was not revealed using the in vitro approach. Importantly, we managed to validate the role of TTBK2 in phosphorylation of several in vivo-induced S/T sites in CEP164 using TTBK2 WT and KO cells. Several factors may account for the differences we see between individual analyzed datasets, such as the different activity of the kinase in vitro and in vivo, different preferences for substrates, or the presence/absence of priming phosphorylations or compensating kinase(s) and counteracting phosphatases (Hunter, 1995).

TTBK2 is considered a distant member of the CK1 kinase family. However, it was previously shown that its truncated variant (TTBK2 1–450) preferentially phosphorylates peptides with priming phosphorylation residue at the +2 position (Bouskila et al., 2011). This unusual substrate preference, unique among CK1 family members which typically favor the stretch of acidic residues or pS/pT around the –3 position (Flotow et al., 1990; Flotow and Roach, 1991; Knippschild et al., 2005; Cheong and Virshup, 2011), was related to differences in the putative phosphate-binding groove between TTBK1/2 and all remaining CK1 isoforms (Bouskila et al., 2011). Although it has been found that several Y kinases reside at the centrosome and MCs, respectively (Tsun et al., 2011; Jay et al., 2015), the significance of that for centriole biogenesis or ciliogenesis is unclear. Importantly, this study and others (Kitano-Takahashi et al., 2007; Čajánek and Nigg, 2014; Watanabe et al., 2015; Huang et al., 2018) failed to detect any significant presence of Y at +2 at verified TTBK2 substrates, raising the question of whether TTBK2 extensively utilized such a motif in vivo. Additionally, although we detected several phosphorylations that fit the canonical consensus motif pS/pT-x-x-**S/T** of CK1, our unbiased motif search analysis implies that TTBK2 may in addition favor glutamic acid (E) at the +3 position and L at the +1 position, respectively, at least in a subset of its targets. These motifs resemble the noncanonical CK1 motif **SLS** and to some extent also a motif with an acidic stretch of residues located C-terminally from the target S/T reported before (Marin et al., 2003; Ferrarese et al., 2007; Borgal et al., 2014; Bowie et al., 2018). Importantly, one must bear in mind that delineation of kinase motifs has been typically carried out using rather reduced libraries of synthetic peptides that lack a secondary or tertiary structure of bona fide physiological substrates of a given kinase. In fact, it has

been demonstrated that the phosphorylation of a substrate by CK1 isoforms does not strictly depend on the consensus sequence, but there is a significant effect of a tertiary structure of the substrate (Cegielska et al., 1998). From this point, FL TTBK2 does not seem to use the motif with pY at the +2 position in substrates we examined; instead, our data suggest it may use motifs resembling noncanonical motifs reported for CK1. Of note, detailed inspection of the assay that identified pY+2 as the preferred motif for TTBK2 also show that TTBK2 can phosphorylate peptides carrying noncanonical CK1-like motifs in vitro, albeit to a lesser extent than pY+2 (Bouskila et al., 2011). To further analyze the preference for motif usage by TTBK2, cocrystallization of the kinase domain of TTBK2 with some of its physiological substrates would help in defining the molecular mechanism mediating their mutual interactions.

Using a model system of HEK293T and RPE1 cells that lack TTBK2, we showed that TTBK2 extensively modified CEP164, while a similar effect was not observed in the case of the other confirmed TTBK2 substrates (CEP83, CEP89, or CEP97), possibly due to the insufficient sensitivity of used readout. This suggests that CEP164 might be the main target of TTBK2 phosphorylation. This prediction is further supported by the observation that a majority of TTBK2 phosphosites we identified using the MS approaches indeed resided to CEP164.

The PCs formation in cultured cells can be readily induced by a serum withdrawal or treatment by cytochalasin D (Kim et al., 2010; Seeley and Nachury, 2010). Intriguingly, our data imply not only that CEP164 is phosphorylated following the induction of the PCs formation but also importantly that TTBK2 is involved in the phosphorylation. Previous work postulated that CEP164 is heavily phosphorylated in mitosis, perhaps in relation to its disappearance from the DA (Schmidt et al., 2012). Our data support this observation and in addition suggest that the mitotic phosphorylation of CEP164 does not depend on TTBK2.

The amino acid sequences of intrinsically disordered proteins determine their inability to fold into stable tertiary structures and instead enable them to rapidly interconvert between distinct conformations to mediate their biological functions (Dyson and Wright, 2005; Bah and Forman-Kay, 2016). Consequently, this allows the intrinsically disordered proteins to expose a significant part of their primary sequence for binding and posttranslational modification (Iakoucheva et al., 2004; Xie et al., 2007; Bah and Forman-Kay, 2016) and hence provides them with the ability to act as hubs in protein complexes that typically facilitate the assembly of various organelles (Cohen, 2000; Hegyi et al., 2007; Bah and Forman-Kay, 2016). In line with these reports, all proteins we identified as substrates of TTBK2 modified by multiple phosphorylations are predicted to have long IDRs suitable for such extensive modification. Given that phosphorylation of IDRs might affect protein structure and hence binding properties (Cohen, 2000; Bah et al., 2015), it is tempting to speculate that TTBK2 phosphorylation allows basal body DA proteins to achieve a novel quality that ensures their timely interactions and assembly to complexes necessary for the formation of PCs.

We provided experimental evidence supporting this hypothesis on the example of CEP164–TTBK2 interactions. We admit that the observed effects of the introduced S to A mutations of the CEP164 N-term on sequestration of TTBK2, MCs levels of IFT88, and ciliogenesis are modest. However, this is to be expected, as the mutated residues lie within IDR outside of the reported TTBK2 binding region (Čajánek and Nigg, 2014), but still in the vicinity to possibly mediate the effect on CEP164–TTBK2 interaction. From this perspective, our data suggest that at least some of the mutated

residues participate in WW domain-mediated CEP164–TTBK2 interaction. Interestingly, recent incisive work by Xu and colleagues (Xu *et al.*, 2016) pinpointed a regulatory role of a short, basic AA stretch (110–122) of CEP164 for the CEP164–TTBK2 interaction via phosphatidylinositol-4 phosphate binding. As the cluster S129–S136, phosphorylated by TTBK2, localizes very close to the described PI binding stretch, it is tempting to speculate that phosphorylation of this cluster might represent a mechanism of how TTBK2 modulates its own interaction with CEP164 via cross-talk with the INPP5E/PIP3K γ regulatory element, possibly by hampering the binding of the acidic phosphoinositol head group to its basic binding site (Xu *et al.*, 2016). It should be rewarding to explore whether there is indeed any functional interaction between TTBK2 sites we identified and the activity of PIP3K/INPP5E implied in the regulation of CEP164–TTBK2 binding (Xu *et al.*, 2016).

There is one more aspect related to our validation experiments. Three of the sites we identified in our initial screening experiments, and subsequently chose to target (S166, S168, and S201) in structure–function experiments, also clearly showed regulation by endogenous TTBK2. It is not clear whether this is also true for the S129–S136 cluster, as we were not able to recover the corresponding peptides during the phosphoenrichment step, thereby indicating that their overall abundance is not sufficient to be detected by the applied instrumentation.

While this paper was being revised, a study identifying CEP83 as a target of TTBK2 phosphorylation at S29, T292, T527, and S698 was published (Lo *et al.*, 2019). Intriguingly, the authors related the TTBK2 phosphorylation of CEP83 to the docking of vesicles to DA. The authors also showed that CEP164-induced TTBK2 recruitment to MC is necessary for CEP83 phosphorylation. Our data confirm and extend this work, as we detected not only three of four sites reported by Lo and colleagues (although S698 did not pass our criteria to be considered as TTBK2 induced) but also several additional TTBK2-induced phosphosites in CEP83. Interestingly, since several members of DA seem to be direct targets of TTBK2 kinase activity, it would be of great interest to investigate possible mutual dependencies of individual phosphorylations and their impact on the functions of DA components in future. Additionally, we confirmed and extended a recent report on TTBK2 phosphorylation of DVL3 (Hanáková *et al.*, 2019), a component of WNT signaling pathways known to reside at the centrosome (Cervenka *et al.*, 2016; Młodzik, 2016; Bryja *et al.*, 2017). This may have several biological implications, as TTBK2 seems to phosphorylate a small cluster of S/T residues in the C-terminus of DVL3, which is important for regulating DVL3 oligomerization (Bernatík *et al.*, 2014), which is in turn essential for DVL-mediated signal transduction via the formation of signalosomes (Schwarz-Romond *et al.*, 2007). In addition, the C-terminus of DVL is typically phosphorylated by CK1 ϵ (Bernatík *et al.*, 2014), thereby opening an intriguing window for a cross-talk at the level of TTBK2–CK1 ϵ , possibly through differential phosphorylation of the DVL3 C-terminus as CK1 ϵ phosphorylates DVL3 at many additional sites to those targeted by TTBK2 (Hanáková *et al.*, 2019). Clearly, additional work will be necessary to fully examine the implications of TTBK2-mediated DVL phosphorylation for WNT signaling pathways as well as basal body-related aspects of DVL biology.

In summary, our findings expand the current knowledge about TTBK2 substrates and provide an important insight into the extent and character of TTBK2-mediated phosphorylations in the context of basal body proteins and PC initiation, respectively. Underpinning the functions of TTBK2 phosphorylations, as well as its interactions with other kinases implicated in ciliogenesis, will undoubtedly be vital for a mechanistic understanding of cilium assembly.

MATERIALS AND METHODS

Cell culture and transfection

RPE-1 Flp-In T-Rex (a gift from Erich Nigg) and TTBK2 KO cells and RPE1 WT were grown in DMEM F12 (Thermo Fisher Scientific, 11320033) supplemented by 10% fetal bovine serum (FBS), 1% penicillin/streptomycin, and 1% L-glutamine. HEK293T wt, and TTBK2 KO Flp-In T-Rex (Thermo Fisher Scientific, R78007) cells were grown in DMEM Glutamax (Thermo Fisher Scientific, 10569069) supplemented by 10% FBS and 1% penicillin/streptomycin. Transfection of RPE1 was carried out by Lipofectamine 3000 (Invitrogen) according to manufacturer's instructions (up to 0.5 μ g DNA per condition/well, 24-well plate format). HEK293T were transfected by Polyethyleneimine (PEI) as follows: PEI was incubated in DMEM for 10 min and then mixed with plasmid equilibrated in DMEM in ratio 3 μ l PEI/1 μ g plasmid; the mixture was incubated for 15 min and then added to cells. Growth medium was changed 4 h after transfection. To induce formation of PC, 24 h following the transfection, RPE-1 cells were starved by serum-free medium for 24 h to assess ciliogenesis or ON for TTBK2 removal measurement. Centrinone (150 μ M) (Wong *et al.*, 2015) treatment was carried out for 72 h. Cytochalasine (2 μ M) (Merck, Sigma Aldrich, C8273) and Nocodazole (100 ng/ml) (Merck, Sigma-Aldrich, M1404) treatment was carried out overnight.

Western blot

To analyze electrophoretic migration of the proteins after TTBK2 coexpression, HEK293T cells were transfected by the indicated plasmids and 24 h posttransfection directly lysed in 1 \times sample buffer (2% SDS, 62.5 mM Tris, pH 6.8, 10% glycerol, 2% 2-Mercaptoethanol, 0.01% bromophenol blue). RPE1 cells were treated as indicated. Western blot was carried out by using Bio-Rad apparatus (Mini-PROTEAN Tetra Vertical Electrophoresis Cell, Mini Trans-Blot Module) for the SDS–PAGE run and transfer. The samples were loaded to discontinuous SDS–PAGE (5% stacking; 7, 8, or 10% running gel; percentage used based on analyzed protein MW) and run at 150 V. Proteins were transferred to immobilon PVDF (Merck, IPVH20200) membranes at 100 V. ELFO Running buffer (0.025 M Tris, 0.192 M glycine, 0.1% SDS), WB Transfer buffer (0.025 M Tris, 0.192 M glycine, 20% Methanol). Membranes were blocked in 5% skimmed milk in Tris-buffered saline (TBS)–Tween (20 mM Tris, 150 mM NaCl, 0.1% Tween 20, pH 7.6) and incubated with the primary antibodies at 4°C ON. Then membranes were washed in TBS–Tween twice, incubated with the secondary antibodies for 1 h at RT, washed by TBS–Tween twice, and developed using ECL prime (Merck, GERPN2232). For the concentration of antibodies used, please refer to Supplemental Table S3.

WB quantification was done using FIJI distribution of ImageJ; the number of the experiments used for the quantification is stated in the corresponding figure legend.

Immunoprecipitation

To analyze binding of TTBK2 to CEP164 N term or CEP164 N-A term, 10-cm plates of HEK293T cells were transfected (in total 6 μ g of DNA mixed with 18 μ l of PEI in plain DMEM). Cells were washed by phosphate-buffered saline (PBS) 24 h posttransfection, scraped to Lysis buffer (20 mM Tris–Cl, pH 7.4, 150 mM NaCl, 0.5% NP40, 0.5% Triton X-100 [Merck, X100], and 1 \times Complete proteasome inhibitors [Roche, 4693132001]), and lysed (15 min on ice). Following centrifugation (15,000 \times g for 10 min at +4°C), cleared extracts were incubated ON at +4°C in an orbital shaker with anti-FLAG sepharose beads (M2 clone, Merck, A2220). Bound complexes were pelleted, washed, and analyzed by SDS–PAGE and Western blotting.

Where appropriate, contrast and/or brightness of images were adjusted by using Photoshop CS5 (Adobe).

Purification of proteins from HEK293T cells

Cep164 N-, M-, and C- terminal fragment and CEP83, CEP89, CCDC92, Rabin8, and DVL3 coding plasmids fused to FLAG tag and FLAG-TTBK2 WT and kinase dead variant (KD) were used for production of proteins for in vitro or TTBK2 autophosphorylation experiments. GFP-TTBK2 WT was coexpressed for in vivo experiments. To purify the protein of interest, each expression plasmid (please see detailed list of used plasmids in Supplemental Table S3) was transfected to HEK293T cells (2 × 15 cm plate per condition, 20 µg DNA), either individually (in vitro kinase assay) or in combination with TTBK2 expression vector (in vivo). For the MS/MS analysis of samples of the endogenous CEP164 phosphorylations 2 × 15 (run 1) or 4 × 15 (run 2) cm 90% confluent plates of HEK293T WT or TTBK2 KO cells were used. Analysis of CEP164 N-term phosphorylations in WT and TTBK2 KO HEK293T was done as follows: 1 × 15 cm dish of HEK293T WT or TTBK2 KO cells was transfected by 10 µg of FLAG-CEP164 N-term. Posttransfection (36–48 h), the proteins of interest were immunoprecipitated; briefly: cells were washed in PBS, scraped, pelleted by centrifugation (400 × g/5 min/+4°C), resuspended in Lysis buffer (20 mM Tris-Cl, pH 7.4, 150 mM NaCl, 0.5% NP40, 0.5% Triton-X-100, 0.1 mM DTT [Merck, 43815], 1× Complete proteasome inhibitors [Merck, 4693132001], and 1× phosphoSTOP [Merck, PHOSS-RO]), sonicated (2 × 20 s on ice), and lysed (10 min on ice). Following centrifugation (15,000 × g for 10 min at +4°C), cleared extracts were incubated 2–6 h at +4°C in an orbital shaker with anti-FLAG sepharose beads (M2 clone, Merck, A2220). Bound complexes were pelleted and 5× washed (Lysis buffer with 1M NaCl). Samples for in vitro kinase assay were additionally 2× washed with kinase buffer (50 mM Tris-Cl, pH = 7.4, 10 mM MgCl₂, 0.1 M EGTA + 0.1 mM DTT), resuspended in kinase buffer + 0.1% DTT + 10% glycerol, and stored as 25% slurry at –80°C until used. Where indicated, samples were treated with λ-phosphatase (New England BioLabs [NEB], P0753S) (30°C for 20 min) according to manufacturer's instructions, and λ-phosphatase was then removed by 2× wash with kinase buffer + phosphoSTOP (Merck, PHOSS-RO), 50 mM NaF (NEB, P0759S), and 10 mM sodium orthovanadate (NEB, P0758S). Samples were subsequently subjected to in vitro kinase assay (in vitro samples) or directly analyzed by MS/MS (in vivo dataset, samples of endogenous CEP164 and CEP164 N-term immunoprecipitated from WT and TTBK2 KO HEK293T).

Immunocytofluorescence microscopy

RPE1 cells were seeded on glass coverslips, fixed for 10 min in –20°C Methanol, washed 3× with PBS, blocked (2% bovine serum albumin in PBS with 0.01% NaN₃), 3× PBS washed, incubated with primary antibodies for 1 h, 3× washed by PBS, incubated with secondary antibodies for 1 h in dark, washed 3× with PBS, incubated with DAPI, washed by PBS 2×, and mounted by glycerol (DAKO #C0563). Microscopy analyses were done using either DeltaVision Elite (GE Healthcare) with 100×/Zeiss Plan-ApoChromat 1.4 objective and DeltaVision softWoRx acquisition SW (here the image stacks were taken with a Z distance of 0.2 µm, deconvolved with one cycle of conservative ratio deconvolution algorithm, and directly projected as maximal intensity images) or Zeiss AxioImager.Z2 with Hamamatsu ORCA Flash 4.0 camera, 100× Apo oil immersion objective, and ZEN Blue 2.6 acquisition SW (Zeiss). Image stacks acquired using Zeiss AxioImager.Z2 were projected as maximal intensity images by using ImageJ distribution FIJI

(Schindelin et al., 2012). Where appropriate, contrast and/or brightness of images were adjusted by using Photoshop CS5 (Adobe) or FIJI. For ciliogenesis experiment (Figure 4C), at least 50 cells were analyzed per each condition. For the experiment in Figure 4D, a densitometry analysis within selected regions of interest was performed in 16-bit TIFF images by using FIJI analyzing 30–40 cells per condition. Data are presented as relative staining intensity (staining intensity of a protein of interest normalized to the staining intensity of the centriolar marker CAP350). Statistical analysis by unpaired Student's *t* test was performed using Graphpad Prism; *P* < 0.05 (*), *P* < 0.01 (**), *P* < 0.001 (***), and *P* < 0.0001 (****) were considered significant. Results are presented as mean plus SEM.

In vitro kinase assay

Beads-bound proteins were washed with kinase buffer (50 mM Tris, pH 7.4, 10 mM MgCl₂, and 0.1 mM EGTA), mixed according to experimental scheme (Supplemental Figure S1), and incubated in the kinase buffer supplemented with 1 mM ATP, 5× Complete proteasome inhibitors (Merck, 4693132001), 1× phosphoSTOP (Merck, PHOSS-RO), 50 mM NaF (NEB, P0759S) and 10 mM sodium orthovanadate (NEB, P0758S), and incubated for 30 min/30°C. The kinase reaction was terminated by the addition of 4× sample buffer, and the resulting samples were analyzed by MS/MS.

CRISPR TTBK2 RPE1 and HEK293T cells

TTBK2 targeting gRNA oligos FWD: CaccgCATTAGTACCACTCTCCGCGC REV: aaacGCCGGAGAGTGGTACTAATGc were cloned into pSpCas9 (BB)-2A-GFP (PX458) <https://www.addgene.org/48138/> according to published protocol (Ran et al., 2013), and the resulting construct was sequenced to verify successful gRNA integration. HEK293T WT Flp-in T-Rex were transfected using Lipofectamine 3000. Single clones of HEK293T cells were produced using serial dilution method and were screened for TTBK2 presence by WB and PCR; clones were sequenced to verify disruption of TTBK2 locus. RPE1 WT Flp-in T-Rex cells were nucleofected by Neon transfection system (1350 V, 20 ms, 2 pulses) (Thermo Fisher Scientific) and GFP-positive cells were sorted using BD FACS ARIA II to 96-well plates. Clones were screened for TTBK2 presence by WB and PCR; clones were sequenced to verify disruption of TTBK2 locus.

Establishment of TTBK2 overexpressing stable RPE1 Flp-In T-Rex

RPE1 TTBK2 KO Flp-In T-Rex cells were transfected by pgLAP2 NEO containing TTBK2 WT or KD variant and pOG44 (ratio 1:29, 0.1 µg of pgLAP2 NEO with transgene and 2.9 µg of pOG44 per 6-cm dish) by Lipofectamine 3000. Transfection was carried out overnight, medium was changed, and selection antibiotics (G418 c = 0.5 mg/ml, Blastidicine c = 25 µg/ml) were added. Selection continued until colonies appeared. Expression of the transgene was verified by WB and IC.

MS/MS analysis

In-gel digestion. Immunoprecipitates were separated on SDS-PAGE gel electrophoresis, fixed with acetic acid in methanol and stained with Coomassie brilliant blue G250 (EZBlue, G1041, Merck) for 1 h. Corresponding 1D bands were excised. After destaining, the proteins in-gel pieces were incubated with 10 mM DTT at 56°C for 45 min. After removal of DTT excess, samples were incubated with 55 mM IAA at room temperature in darkness for 30 min, then alkylation solution was removed and gel pieces were hydrated for 45 min at 4°C in digestion solution (5 ng/µl trypsin, sequencing grade, Promega, in 25 mM AB). The trypsin digestion proceeded for

2 h at 37°C on Thermomixer (750 rpm; Eppendorf). Digested peptides were extracted from gels using 50% ACN solution with 2.5% formic acid (FA) and concentrated in a speedVac concentrator (Eppendorf). The aliquot (1/10) of concentrated sample was transferred to a LC-MS vial with already added polyethylene glycol (PEG; final concentration 0.001%) and directly analyzed by LC-MS/MS for protein identification.

Phosphopeptide enrichment. The rest of the sample (9/10) was used for phosphopeptide analysis. Sample was diluted with acidified acetonitrile solution (80% ACN, 2% FA). Phosphopeptides were enriched using Pierce Magnetic Titanium Dioxide Phosphopeptide Enrichment Kit (Thermo Fisher Scientific, Waltham, MA) according to manufacturer protocol and eluted into LC-MS vial with already added PEG (final concentration 0.001%). Eluates were concentrated under vacuum and then dissolved in water and 0.6 µl of 5% FA to get 12 µl of peptide solution before LC-MS/MS analysis.

LC-MS/MS analysis. LC-MS/MS analyses of peptide mixture were done using RSLCnano system connected to Orbitrap Elite hybrid spectrometer (Thermo Fisher Scientific) with ABIRD (Active Background Ion Reduction Device; ESI Source Solutions) and Digital PicoView 550 (New Objective) ion source (tip rinsing by 50% acetonitrile with 0.1% FA) installed. Prior to LC separation, peptide samples were online concentrated and desalted using trapping column (100 µm × 30 mm) filled with 3.5 µm X-Bridge BEH 130 C18 sorbent (Waters). After washing of trapping column with 0.1% FA, the peptides were eluted (flow rate 300 nL/min) from the trapping column onto Acclaim Pepmap100 C18 column (3-µm particles, 75 µm × 500 mm; Thermo Fisher Scientific) by 65 min-long gradient. Mobile phase A (0.1% FA in water) and mobile phase B (0.1% FA in 80% acetonitrile) were used. The gradient elution started at 1% of mobile phase B and increased from 1% to 56% during the first 50 min (30% in the 35th and 56% in 50th min), then increased linearly to 80% of mobile phase B in the next 5 min and remained at this state for the next 10 min. Equilibration of the trapping column and the column was done prior to sample injection to sample loop. The analytical column outlet was directly connected to the Digital PicoView 550 ion source. MS data were acquired in a data-dependent strategy selecting up to top 10 precursors based on precursor abundance in the survey scan (350–2000 m/z). The resolution of the survey scan was 60,000 (400 m/z) with a target value of 1×10^6 ions, one microscan, and maximum injection time of 1000 ms. High resolution (15,000 at 400 m/z) HCD MS/MS spectra were acquired with a target value of 50,000. Normalized collision energy was 32% for HCD spectra. The maximum injection time for MS/MS was 500 ms. Dynamic exclusion was enabled for 45 s after one MS/MS spectra acquisition and early expiration was disabled. The isolation window for MS/MS fragmentation was set to 2 m/z.

Data analysis

The analysis of the mass spectrometric RAW data was carried out using the Proteome Discoverer software (Thermo Fisher Scientific; version 1.4) with in-house Mascot (Matrixscience; version 2.4.1 or higher) search engine utilization. MS/MS ion searches were done against in-house database containing expected protein of interest with additional sequences from cRAP database (downloaded from <http://www.thegpm.org/crap/>). Mass tolerance for peptides and MS/MS fragments was 7 ppm and 0.03 Da, respectively. These post-translational modifications were considered as possible: Oxidation of methionine, deamidation (N, Q), and phosphorylation (S, T, Y) as optional modification; carbamidomethylation of C as fixed modification;

no enzyme specificity was selected. The phosphoRS (version 3.1) feature was used for preliminary phosphorylation localization. Final phosphosite assignment (including inspection of phosphorylations with ambiguous localization) was performed by manual evaluation of the fragmentation spectra of the individual phosphopeptides. Quantitative information was assessed and manually validated in Skyline software (Skyline daily 3.6.1.10230). Normalization of the data was performed using a set of phosphopeptide standards (added to the sample prior phosphoenrichment step; MS PhosphoMix 1, 2, 3 Light, Sigma) in combination with summed peak area of nonphosphorylated peptides identified in analyses of samples without phosphoenrichment. The mass spectrometry proteomics data have been deposited to the ProteomeXchange Consortium via the PRIDE (Perez-Riverol *et al.*, 2019) partner repository URL: <https://www.ebi.ac.uk/pride/archive/projects/PXD014199>.

Identification of phosphorylations

Average intensity for individual phosphosites or clusters was calculated from MS/MS data as a sum of intensities of all phosphorylated peptides containing the particular pS/pT. Data are summarized in Supplemental Table S1 and graphically represented in Supplemental Figures S2, A and B, S3, and S6, F and G. Induction of phosphosites by TTBK2, summarized for individual substrates in Figure 2, was evaluated using individual phosphorylated peptides intensities to allow careful curation of the data. We used the following criteria to assess induction of phosphosite by TTBK2.

In vitro dataset, 1: the intensity of at least one phosphorylated peptide of a given phosphosite must have been equal to or higher than 2×10^6 threshold. 2: The sum of intensities of all phosphopeptides detected for a given phosphosite in an individual experiment must have been at least twofold of total intensity of the corresponding phosphosite in the control sample (substrate incubated with TTBK2 KD). If the exact position of the phosphorylated residue could not be resolved, each of the S/T residues of a given cluster was considered as phosphorylated. If the phosphopeptide containing such a cluster met criteria 1 and 2, the cluster was considered induced (in total, six peptides with 15 individual phosphorylations).

In the case of TTBK2 autophosphorylation analysis, two reference samples (controls) were used: 1, TTBK2 WT + λ-phosphatase; and 4, TTBK2 KD + λ-phosphatase + kinase assay) as shown in Supplemental Figure S1B. Thus, the individual phosphorylation must have fulfilled the above described criteria for both controls to be considered TTBK2 induced.

In vivo dataset, 1: the intensity of at least one phosphorylated peptide must have been equal to or higher than 2×10^6 threshold if identified repeatedly, or equal to or higher than 2×10^7 threshold if detected in a single experiment. 2: The sum of intensities of all phosphopeptides detected for a given phosphosite in an individual experiment must have been at least twofold of intensity of the corresponding phosphosite in the control sample (Mock). If the exact position of the phosphorylated residue could not be resolved, each of the S/T residues of a given cluster was considered as phosphorylated. If a phosphopeptide containing such a cluster met criteria 1 and 2, the cluster was considered induced (in total, two peptides with four individual phosphorylations).

CEP164 endogenous phosphorylations: CEP164 was immunoprecipitated from HEK293T wt or TTBK2 KO. Listed are phosphorylations with intensity of at least one phosphorylated peptide equal to or higher than 1×10^6 .

Phosphorylation of CEP164 N-term in HEK293T wt or TTBK2 KO. 1: The intensity of at least one phosphorylated peptide must have been equal to or higher than 2×10^6 . 2: The sum of intensities

of phosphopeptides detected for given phosphosite must have been at least twofold of intensity of the corresponding phosphosite in the control sample.

The graphs in Supplemental Figures S2, A and B, S3, and S6, F and G show comparison of the average intensity for individual S/T phosphosites. Cases where the exact position could not be assigned are indicated as (/) for two possible positions or (–) for clusters. In Supplemental Figure S2A, every S/T phosphosite average intensity detected in samples with Mock (black bar), TTBK2 WT induced (red bar), Mock + λ phosphatase (gray bar), and TTBK2 WT + λ phosphatase (blue bar) is indicated on the y-axis. To allow better visualization of intensity of individual phosphosites in one graph, note that the scale of the y-axis is in log₁₀. In Supplemental Figure 2B, every S/T phosphosite average intensity detected in samples with 1, TTBK2 WT (black bar); 2, CTRL#1: TTBK2 WT + λ phosphatase (gray bar); 3, TTBK2 WT + λ phosphatase + kinase assay (red bar), and 4, CTRL#2: TTBK2 KD + λ phosphatase + kinase assay (Brown bar) is indicated on the y-axis, log₁₀ scale. In Supplemental Figure 3, every S/T phosphosite average intensity detected in samples with Mock (black bar) and TTBK2 WT induced (red bar) is indicated on the y-axis, log₁₀ scale. In Supplemental Figure 6F, every S/T phosphosite of endogenous CEP164 average intensity detected in HEK293T WT (red bar) or HEK293T TTBK2 KO (black bar) is indicated on the y-axis, log₁₀ scale. In Supplemental Figure 6E, every S/T phosphosite of FLAG-CEP164 N-term average intensity detected in HEK293T WT (red bar) or HEK293T TTBK2 KO (black bar) is indicated on the y-axis, log₁₀ scale.

Kinase motif determination

Kinase motifs were delineated using a dataset of 13 AA long peptides with central S/T, which we identified as TTBK2-induced in vitro and in vivo datasets. For the purpose of this analysis, the in vitro and in vivo datasets were cross-correlated, and phosphorylations identified as TTBK2 induced in one dataset and not induced in the other were excluded from the kinase motif determination peptide dataset. Peptide sequences were loaded to MeMe suite phosphorylation motif finder MoMo and analyzed using simple Motif-x and MODL algorithms (Bailey et al., 2009; Chou and Schwartz, 2011). The minimal number of occurrences for kinase motif to be considered was set to 10 for all algorithms. Specific setting for Motif-x algorithms was $p < 0.001$; motifs with central S/T were considered separately. Default MODL settings were used (maximum number of iterations = 50, maximum number of iterations with no decrease in MDL = 10, with central S/T combined onto one motif). Peptides used and those identified by individual algorithms are listed in Supplemental Table S2.

In silico analyses

Depiction of domains or motifs in Figures 2, A–C and 3, A and B and Supplemental Figures S4 and S5 was based on uniprot.org. Canonical protein sequences from uniprot.org were used for disorder and phosphorylation prediction (Figure 3, A and B; Supplemental Figures S4 and S5), protein identifiers used are as follows: CEP164 (Q9UPV0), CEP83 (Q9Y592), CEP89 (Q96ST8), CCDC92 (Q53HC0), Rabin8 (Q96QF0), DVL3 (Q92997), TTBK2 (Q6IQ55), MPP9 (Q99550), KIF2a (O00139), Tau (P10636), and CEP97 (Q8IW35). Prediction of protein disorder was performed by POND (http://www.pondr.com/) algorithms VSL-2 (Peng and Zhang, 2006) and VL3-BA (Peng et al., 2005). A score above 0.5 for disorder prediction suggests an unstable or none secondary structure; a score below 0.5 suggests this protein part has defined a secondary structure. Prediction of protein phosphorylation was performed by the DEPP

(Iakoucheva et al., 2004) (http://www.pondr.com/cgi-bin/depp.cgi). Only phosphorylations with a DEPP score above 0.5 were considered as possibly phosphorylated, with the highest scoring phosphorylations being the most probable.

ACKNOWLEDGMENTS

We thank Erich Nigg, Gislene Pereira, Vitezslav Bryja, Peter Jackson, Robert Lefkowitz, Stephane Angers, Joon Kim, Andrew K. Shiau, and Lumir Krejci for sharing reagents or instruments and Tomas Loja for help with cell sorting. The work was supported by grants from the Czech Science Foundation (16-03269Y, 19-05244S) and the Swiss National Science Foundation (IZ11Z0_166533) to L.C. O.B. was supported by funds from the Faculty of Medicine, Masaryk University, to junior researcher Ondrej Bernatik. K.H. and Z.Z. were supported by project CEITEC 2020 (LQ1601) funded by the Ministry of Education, Youth and Sports of the Czech Republic (MEYS). We acknowledge the core facility CELLIM of CEITEC, supported by the MEYS CR (LM2018129 Czech-Bio-Imaging). CIISB research infrastructure project LM2018127 funded by MEYS CR is gratefully acknowledged for the financial support of the LC-MS/MS measurements at the Proteomics Core Facility.

REFERENCES

- Bah A, Forman-Kay JD (2016). Modulation of intrinsically disordered protein function by post-translational modifications. *J Biol Chem* 291, 6696–6705.
- Bah A, Vernon RM, Siddiqui Z, Krzeminski M, Muhandiram R, Zhao C, Sonenberg N, Kay LE, Forman-Kay JD (2015). Folding of an intrinsically disordered protein by phosphorylation as a regulatory switch. *Nature* 519, 106–109.
- Bailey TL, Boden M, Buske FA, Frith M, Grant CE, Clementi L, Ren J, Li WW, Noble WS (2009). MEME Suite: Tools for motif discovery and searching. *Nucleic Acids Res* 37, https://doi.org/10.1093/nar/gkp335.
- Bauer P, Stevanin G, Beetz C, Synofzik M, Schmitz-Hübsch T, Wüllner U, Berthier E, Ollagnon-Roman E, Riess O, Forlani S, et al. (2010). Spinocerebellar ataxia type 11 (SCA11) is an uncommon cause of dominant ataxia among French and German kindreds. *J Neurol Neurosurg Psychiatry* 81, 1229–1232.
- Bernatik O, Sedová K, Schille C, Ganji RS, Červenka I, Trantírek L, Schambony A, Zdráhal Z, Bryja V (2014). Functional analysis of dishevelled-3 phosphorylation identifies distinct mechanisms driven by casein kinase 1 ϵ and Frizzled5. *J Biol Chem* 289, 23520–23533.
- Borgal L, Rinschen MM, Dafinger C, Hoff S, Reinert MJ, Lamkemeyer T, Lienkamp SS, Benzing T, Schermer B (2014). Casein kinase 1 α phosphorylates the Wnt regulator Jade-1 and modulates its activity. *J Biol Chem* 289, 26344–26356.
- Bouskila M, Essof N, Gay L, Fang EH, Deak M, Begley MJ, Cantley LC, Prescott A, Storey KG, Alessi DR (2011). TTBK2 kinase substrate specificity and the impact of spinocerebellar ataxia-causing mutations on expression, activity, localization and development. *Biochem J* 437, 157–167.
- Bowie E, Norris R, Anderson KV, Goetz SC (2018). Spinocerebellar ataxia type 11-associated alleles of Ttbk2 dominantly interfere with ciliogenesis and cilium stability. *PLoS Genet* 14, https://doi.org/10.1371/journal.pgen.1007844.
- Bowler M, Kong D, Sun S, Nanjundappa R, Evans L, Farmer V, Holland A, Mahjoub MR, Sui H, Loncarek J (2019). High-resolution characterization of centriole distal appendage morphology and dynamics by correlative STORM and electron microscopy. *Nat Commun* 10, 993.
- Bryja V, Červenka I, Čajánek L (2017). The connections of Wnt pathway components with cell cycle and centrosome: side effects or a hidden logic? *Crit Rev Biochem Mol Biol* 52, 614–637.
- Čajánek L, Nigg EA (2014). Cep164 triggers ciliogenesis by recruiting Tau tubulin kinase 2 to the mother centriole. *Proc Natl Acad Sci USA* 111, E2841–E2850.
- Cegielska A, Gietzen KF, Rivers A, Virshup DM (1998). Autoinhibition of casein kinase 1 ϵ (CK1 ϵ) is relieved by protein phosphatases and limited proteolysis. *J Biol Chem* 273, 1357–1364.
- Cervenka I, Valnohova J, Bernatik O, Harnos J, Radsetoual M, Sedova K, Hanakova K, Potesil D, Sedlackova M, Salasova A, et al. (2016). Dishevelled is a NEK2 kinase substrate controlling dynamics of centrosomal linker proteins. *Proc Natl Acad Sci USA* 113, 9304–9309.

- Chaki M, Airik R, Ghosh AK, Giles RH, Chen R, Slaats GG, Wang H, Hurd TW, Zhou W, Cluckey A, et al. (2012). Exome capture reveals ZNF423 and CEP164 mutations, linking renal ciliopathies to DNA damage response signaling. *Cell* 150, 533–548.
- Chang J, Seo SG, Lee KH, Nagashima K, Bang JK, Kim BY, Erikson RL, Lee KW, Lee HJ, Park JE, et al. (2013). Essential role of Cenexin1, but not Odf2, in ciliogenesis. *Cell Cycle* 12, 655–662.
- Cheng A, Grant C, Bailey TL, Noble W (2017). MoMo: Discovery of post-translational modification motifs. *BioRxiv* 153882.
- Cheong JK, Virshup DM (2011). Casein kinase 1: Complexity in the family. *Int J Biochem Cell Biol* 43, 465–469.
- Chou MF, Schwartz D (2011). Biological sequence motif discovery using motif-x. *Curr Protoc Bioinforma*, <https://doi.org/10.1002/0471250953.bi1315s35>.
- Cohen P (2000). The regulation of protein function by multisite phosphorylation - A 25 year update. *Trends Biochem Sci* 25, 596–601.
- Dyson HJ, Wright PE (2005). Intrinsically unstructured proteins and their functions. *Nat Rev Mol Cell Biol* 6, 197–208.
- Ferrarese A, Marin O, Bustos VH, Venerando A, Antonelli M, Allende JE, Pinna LA (2007). Chemical dissection of the APC repeat 3 multistep phosphorylation by the concerted action of protein kinases CK1 and GSK3. *Biochemistry* 46, 11902–11910.
- Flotow H, Graves PR, Wang A, Fiol CJ, Roeske RW, Roach PJ (1990). Phosphate groups as substrate determinants for casein kinase I action. *J Biol Chem* 265, 14264–14269.
- Flotow H, Roach PJ (1991). Role of acidic residues as substrate determinants for casein kinase I. *J Biol Chem* 266, 3724–3727.
- Goetz SC, Liem KF, Anderson KV. (2012). The spinocerebellar ataxia-associated gene tau tubulin kinase 2 controls the initiation of ciliogenesis. *Cell* 151, 847–858.
- Graser S, Stierhof YD, Lavoie SB, Gassner OS, Lamla S, Le Clech M, Nigg EA (2007). Cep164, a novel centriole appendage protein required for primary cilium formation. *J Cell Biol* 179, 321–330.
- Hanákova K, Bernatik O, Ovesná P, Kravec M, Micka M, Rádsetoual M, Potěšil D, Čajánek L, Zdráhal Z, Bryja V (2019). Comparative phosphorylation map of Dishevelled3 (DVL3). *BioRxiv* 621896.
- Hegyi H, Schad E, Tompa P (2007). Structural disorder promotes assembly of protein complexes. *BMC Struct Biol* 7, <https://doi.org/10.1186/1472-6807-7-65>.
- Hehnl H, Chen CT, Powers CM, Liu HL, Doxsey S (2012). The centrosome regulates the Rab11-dependent recycling endosome pathway at appendages of the mother centriole. *Curr Biol* 22, 1944–1950.
- Houlden H, Johnson J, Gardner-Thorpe C, Lashley T, Hernandez D, Wort P, Singleton AB, Hilton DA, Holton J, Revesz T, et al. (2007). Mutations in TTBK2, encoding a kinase implicated in tau phosphorylation, segregate with spinocerebellar ataxia type 11. *Nat Genet* 39, 1434–1436.
- Huang N, Zhang D, Li F, Chai P, Wang S, Teng J, Chen J (2018). M-Phase Phosphoprotein 9 regulates ciliogenesis by modulating CP110-CEP97 complex localization at the mother centriole. *Nat Commun* 9, 4511.
- Hunter T (1995). Protein kinases and phosphatases: The Yin and Yang of protein phosphorylation and signaling. *Cell* 80, 225–236.
- Iakoucheva LM, Radivojac P, Brown CJ, O'Connor TR, Sikes JG, Obradovic Z, Dunker AK (2004). The importance of intrinsic disorder for protein phosphorylation. *Nucleic Acids Res* 32, 1037–1049.
- Ikezu S, Ikezu T (2014). Tau-tubulin kinase. *Front Mol Neurosci* 7, <https://doi.org/10.3389/fnmol.2014.00033>.
- Ishikawa H, Marshall WF (2011). Ciliogenesis: Building the cell's antenna. *Nat Rev Mol Cell Biol* 12, 222–234.
- Jay J, Hammer A, Nestor-Kalinowski A, Diakonova M (2015). JAK2 tyrosine kinase phosphorylates and is negatively regulated by centrosomal protein ninein. *Mol Cell Biol* 35, 111–131.
- Jenks AD, Vyse S, Wong JP, Kostaras E, Keller D, Burgoyne T, Shoemark A, Tsalikis A, de la Roche M, Michaelis M, et al. (2018). Primary cilia mediate diverse kinase inhibitor resistance mechanisms in cancer. *Cell Rep* 23, 3042–3055.
- Joo K, Kim CG, Lee MS, Moon HY, Lee SH, Kim MJ, Kweon HS, Park WY, Kim CH, Gleeson JG, et al. (2013). CCDC41 is required for ciliary vesicle docking to the mother centriole. *Proc Natl Acad Sci USA* 110, 5987–5992.
- Kim J, Lee JE, Heynen-Genel S, Suyama E, Ono K, Lee K, Ideker T, Aza-Blanc P, Gleeson JG (2010). Functional genomic screen for modulators of ciliogenesis and cilium length. *Nature* 464, 1048–1051.
- Kitano-Takahashi M, Morita H, Kondo S, Tomizawa K, Kato R, Tanio M, Shirota Y, Takahashi H, Sugio S, Kohno T (2007). Expression, purification and crystallization of a human tau-tubulin kinase 2 that phosphorylates tau protein. *Acta Crystallogr Sect F Struct Biol Cryst Commun* 63, 602–604.
- Knippschild U, Gocht A, Wolff S, Huber N, Löhler J, Stöter M (2005). The casein kinase 1 family: Participation in multiple cellular processes in eukaryotes. *Cell Signal* 17, 675–689.
- Knödler A, Feng S, Zhang J, Zhang X, Das A, Peränen J, Guo W (2010). Coordination of Rab8 and Rab11 in primary ciliogenesis. *Proc Natl Acad Sci USA* 107, 6346–6351.
- Kuhns S, Schmidt KN, Reymann J, Gilbert DF, Neuner A, Hub B, Carvalho R, Wiedemann P, Zentgraf H, Erfle H, et al. (2013). The microtubule affinity regulating kinase MARK4 promotes axoneme extension during early ciliogenesis. *J Cell Biol* 200, 505–522.
- Kurtulmus B, Yuan C, Schuy J, Neuner A, Hata S, Kalamakis G, Martin-Villalba A, Pereira G (2018). LRRC45 contributes to early steps of axoneme extension. *J Cell Sci* 131, <https://doi.org/10.1242/jcs.223594>.
- Liao JC, Yang TT, Weng RR, Kuo CTe, Chang CW (2015). TTBK2: A tau protein kinase beyond tau phosphorylation. *Biomed Res Int* 2015, <https://doi.org/10.1155/2015/575170>.
- Lindquist SG, Møller LB, Dali CI, Marner L, Kamsteeg EJ, Nielsen JE, Hjermind LE (2017). A novel TTBK2 de novo mutation in a Danish family with early-onset spinocerebellar ataxia. *Cerebellum* 16, 268–271.
- Lo CH, Lin IH, Yang TT, Huang YC, Tanos BE, Chou PC, Chang CW, Tsay YG, Liao JC, Wang WJ (2019). Phosphorylation of CEP83 by TTBK2 is necessary for cilia initiation. *J Cell Biol* 218, 3489–3505.
- Lu Q, Insinna C, Ott C, Stauffer J, Pintado PA, Rahajeng J, Baxa U, Walia V, Cuenca A, Hwang YS, et al. (2015). Early steps in primary cilium assembly require EHD1/EHD3-dependent ciliary vesicle formation. *Nat Cell Biol* 17, 228–240.
- Marin O, Bustos VH, Cesaro L, Meggio F, Pagano MA, Antonelli M, Allende CC, Pinna LA, Allende JE (2003). A noncanonical sequence phosphorylated by casein kinase 1 in β -catenin may play a role in casein kinase 1 targeting of important signaling proteins. *Proc Natl Acad Sci USA* 100, 10193–10200.
- Mitchison HM, Valente EM (2017). Motile and non-motile cilia in human pathology: from function to phenotypes. *J Pathol* 241, 294–309.
- Mlodzik M (2016). The dishevelled protein family: still rather a mystery after over 20 years of molecular studies. *Curr Top Dev Biol* 117, 75–91.
- Nigg EA, Stearns T (2011). The centrosome cycle: Centriole biogenesis, duplication and inherent asymmetries. *Nat Cell Biol* 13, 1154–1160.
- Oda T, Chiba S, Nagai T, Mizuno K (2014). Binding to Cep164, but not EB1, is essential for centriolar localization of TTBK2 and its function in ciliogenesis. *Genes to Cells* 19, 927–940.
- Peng K, Vucetic S, Radivojac P, Brown CJ, Dunker AK, Obradovic Z (2005). Optimizing long intrinsic disorder predictors with protein evolutionary information. *J Bioinform Comput Biol* 3, 35–60.
- Peng QY, Zhang QF (2006). Precise positions of Phoebe determined with CCD image-overlapping calibration. *Mon Not R Astron Soc* 366, 208–212.
- Perez-Riverol Y, et al. (2019). The PRIDE database and related tools and resources in 2019: Improving support for quantification data. *Nucleic Acids Res* 47, D442–D450.
- Ran FA, Hsu PD, Wright J, Agarwala V, Scott DA, Zhang F (2013). Genome engineering using the CRISPR-Cas9 system. *Nat Protoc* 8, 2281–2308.
- Reiter JF, Leroux MR (2017). Genes and molecular pathways underpinning ciliopathies. *Nat Rev Mol Cell Biol* 18, 533–547.
- Schindelin J, et al. (2012). Fiji: An open-source platform for biological-image analysis. *Nat Methods* 9, 676–682.
- Schmidt KN, Kuhns S, Neuner A, Hub B, Zentgraf H, Pereira G (2012). Cep164 mediates vesicular docking to the mother centriole during early steps of ciliogenesis. *J Cell Biol* 199, 1083–1101.
- Schwarz-Romond T, Fiedler M, Shibata N, Butler PJG, Kikuchi A, Higuchi Y, Bienz M (2007). The DIX domain of Dishevelled confers Wnt signaling by dynamic polymerization. *Nat Struct Mol Biol* 14, 484–492.
- Seeley ES, Nachury MV (2010). The perennial organelle: Assembly and disassembly of the primary cilium. *J Cell Sci* 123, 511–518.
- Sieracki NA, Komarova YA (2013). Studying cell signal transduction with biomimetic point mutations. <https://doi.org/10.5772/35029>.
- Sillibourne JE, Hurbain I, Grand-Perret T, Goud B, Tran P, Bornens M (2013). Primary ciliogenesis requires the distal appendage component Cep123. *Biol Open* 2, 535–545.
- Sorokin S (1962). Centrioles and the formation of rudimentary cilia by fibroblasts and smooth muscle cells. *J Cell Biol* 15, 363–377.
- Spektor A, Tsang WY, Khoo D, Dynlacht BD (2007). Cep97 and CP110 suppress a cilia assembly program. *Cell* 130, 678–690.
- Takahashi M, Tomizawa K, Sato K, Ohtake A, Omori A (1995). A novel tau-tubulin kinase from bovine brain. *FEBS Lett* 372, 59–64.

- Tanos BE, Yang HJ, Soni R, Wang WJ, Macaluso FP, Asara JM, Tsou MFB (2013). Centriole distal appendages promote membrane docking, leading to cilia initiation. *Genes Dev* 27, 163–168.
- Tomizawa K, Omori A, Ohtake A, Sato K, Takahashi M (2001). Tau-tubulin kinase phosphorylates tau at Ser-208 and Ser-210, sites found in paired helical filament-tau. *FEBS Lett* 492, 221–227.
- Tsun A, Qureshi I, Stinchcombe JC, Jenkins MR, De La Roche M, Kleczkowska J, Zamoyska R, Griffiths GM (2011). Centrosome docking at the immunological synapse is controlled by Lck signaling. *J Cell Biol* 192, 663–674.
- Wang L, Dynlacht BD (2018). The regulation of cilium assembly and disassembly in development and disease. *Dev* 145.
- Watanabe T, Kakeno M, Matsui T, Sugiyama I, Arimura N, Matsuzawa K, Shirahige A, Ishidate F, Nishioka T, Taya S, et al. (2015). TTBK2 with EB1/3 regulates microtubule dynamics in migrating cells through KIF2A phosphorylation. *J Cell Biol* 210, 737–751.
- Wei Q, Xu Q, Zhang Y, Li Y, Zhang Q, Hu Z, Harris PC, Torres VE, Ling K, Hu J (2013). Transition fibre protein FBF1 is required for the ciliary entry of assembled intraflagellar transport complexes. *Nat Commun* 4, <https://doi.org/10.1038/ncomms3750>.
- Westlake CJ, Baye LM, Nachury MV, Wright KJ, Ervin KE, Phu L, Chalouni C, Beck JS, Kirkpatrick DS, Slusarski DC, et al. (2011). Primary cilia membrane assembly is initiated by Rab11 and transport protein particle II (TRAPP2) complex-dependent trafficking of Rabin8 to the centrosome. *Proc Natl Acad Sci USA* 108, 2759–2764.
- Wong SY, Seol AD, So PL, Ermilov AN, Bichakjian CK, Epstein EH, Dlugosz AA, Reiter JF (2009). Primary cilia can both mediate and suppress Hedgehog pathway-dependent tumorigenesis. *Nat Med* 15, 1055–1061.
- Wong YL, Anzola JV, Davis RL, Yoon M, Motamedi A, Kroll A, Seo CP, Hsia JE, Kim SK, Mitchell JW, et al. (2015). Reversible centriole depletion with an inhibitor of Polo-like kinase 4. *Science* (80-) 348, 1155–1160.
- Wu CT, Chen HY, Tang TK (2018). Myosin-Va is required for preciliary vesicle transportation to the mother centriole during ciliogenesis. *Nat Cell Biol* 20, 175–185.
- Xie H, Vucetic S, Iakoucheva LM, Oldfield CJ, Dunker AK, Obradovic Z, Uversky VN (2007). Functional anthology of intrinsic disorder. 3. Ligands, post-translational modifications, and diseases associated with intrinsically disordered proteins. *J Proteome Res* 6, 1917–1932.
- Xu Q, Zhang Y, Wei Q, Huang Y, Hu J, Ling K (2016). Phosphatidylinositol phosphate kinase PIPKγ and phosphatase INPP5E coordinate initiation of ciliogenesis. *Nat Commun* 7, 10777.
- Yang TT, et al. (2018). Super-resolution architecture of mammalian centriole distal appendages reveals distinct blade and matrix functional components. *Nat Commun* 9, <https://doi.org/10.1038/s41467-018-04469-1>.

Appendix 10


Hanáková K, Bernatík O, Kravec M, Micka M, Kumar J, Harnoš J, Ovesná P, Paclíková P, Rádsetoulal M, Potěšil D, Tripsianes K, **Čajánek L**, Zdráhal Z, Bryja V. Comparative phosphorylation map of Dishevelled 3 links phospho-signatures to biological outputs. *Cell Communication and Signaling*. 2019 Dec 23;17(1):170. doi: 10.1186/s12964-019-0470-z.(JCR 2019. IF=4.344, Q2 – Cell Biology)

RESEARCH

Open Access



Comparative phosphorylation map of Dishevelled 3 links phospho-signatures to biological outputs

Kateřina Hanáková^{1,2†}, Ondřej Bernatík^{3,4†}, Marek Kravec³, Miroslav Micka³, Jitender Kumar¹, Jakub Harnoř³, Petra Ovesná⁵, Petra Paclíková³, Matěj Rádsetoulal³, David Potěřil¹, Konstantinos Tripsianes¹, Lukáš Čajánek⁴, Zbyněk Zdráhal^{1,2*} and Vítězslav Bryja^{3,6*} 

Abstract

Background: Dishevelled (DVL) is an essential component of the Wnt signaling cascades. Function of DVL is controlled by phosphorylation but the molecular details are missing. DVL3 contains 131 serines and threonines whose phosphorylation generates complex barcodes underlying diverse DVL3 functions. In order to dissect the role of DVL phosphorylation we analyzed the phosphorylation of human DVL3 induced by previously reported (CK1 ϵ , NEK2, PLK1, CK2 α , RIPK4, PKC δ) and newly identified (TTBK2, Aurora A) DVL kinases.

Methods: Shotgun proteomics including TiO₂ enrichment of phosphorylated peptides followed by liquid chromatography tandem mass spectrometry on immunoprecipitates from HEK293T cells was used to identify and quantify phosphorylation of DVL3 protein induced by 8 kinases. Functional characterization was performed by in-cell analysis of phospho-mimicking/non-phosphorylatable DVL3 mutants and supported by FRET assays and NMR spectroscopy.

Results: We used quantitative mass spectrometry and calculated site occupancies and quantified phosphorylation of > 80 residues. Functional validation demonstrated the importance of CK1 ϵ -induced phosphorylation of S268 and S311 for Wnt-3a-induced β -catenin activation. S630–643 cluster phosphorylation by CK1, NEK2 or TTBK2 is essential for even subcellular distribution of DVL3 when induced by CK1 and TTBK2 but not by NEK2. Further investigation showed that NEK2 utilizes a different mechanism to promote even localization of DVL3. NEK2 triggered phosphorylation of PDZ domain at S263 and S280 prevents binding of DVL C-terminus to PDZ and promotes an open conformation of DVL3 that is more prone to even subcellular localization.

Conclusions: We identify unique phosphorylation barcodes associated with DVL function. Our data provide an example of functional synergy between phosphorylation in structured domains and unstructured IDRs that together dictate the biological outcome.

Keywords: Dishevelled, DVL3, Phosphorylation, Kinase, Mass spectrometry, CK1, TTBK2, NEK2, Wnt

Background

Wnt signaling pathway has been linked to an etiology of multiple developmental defects, inherited diseases and many types of cancer [1]. Wnt pathways can be divided into several main “branches”. The best studied (canonical) pathway

depends on β -catenin and members of the TCF/LEF (T-cell factor/lymphoid enhancer-binding factor) family of transcriptional factors. In the absence of Wnt ligand, the intracellular level of free β -catenin is constantly low due to the activity of a degradation complex including adenomatous polyposis coli, Axin and glycogen synthase kinase (GSK) 3 β . Upon Wnt binding, the destruction complex is inhibited allowing accumulation and nuclear activity of β -catenin. However, Wnts can also activate other, so-called non-canonical Wnt pathways, which are β -catenin-independent and biochemically distinct from canonical Wnt signaling. There is strong

* Correspondence: zdrahal@sci.muni.cz; bryja@sci.muni.cz

[†]Kateřina Hanáková and Ondřej Bernatík contributed equally to this work.

¹CEITEC—Central European Institute of Technology, Masaryk University, Kamenice 5, 625 00 Brno, Czech Republic

³Department of Experimental Biology, Faculty of Science, Masaryk University, Kotlářská 2, 611 37 Brno, Czech Republic

Full list of author information is available at the end of the article



evidence that several such pathways exist (for complete overview see [2]).

All known Wnt-induced pathways are transduced through Frizzled transmembrane receptors [3] and intracellular protein Dishevelled (Dsh in *Drosophila*, DVL1–3 in human). DVL proteins consist of three structured domains: N-terminally located DIX domain, centrally located PDZ domain and C-terminally located DEP domain. The individual domains are linked by intrinsically disordered regions followed by approximately 200 amino acid long, also intrinsically disordered, C-terminal tail.

There is a general agreement based on genetic experiments that DVL plays a crucial role as a signaling hub in both Wnt/ β -catenin and non-canonical Wnt pathways [4]. In addition DVL has been reported to have multiple other functions such as docking of basal body [5, 6], function and maintenance of primary cilia [7], cytokinesis [8], or positioning of the mitotic spindle [9]; all of them possibly linked to its role in the regulation of centrosomal cycle [10].

Despite the well documented role of DVL in the Wnt signaling and the growing evidence for its participation in additional cellular processes, the molecular mechanisms that regulate DVL action in the cell are almost unknown. However, it is believed that post-translational modifications (PTM), particularly phosphorylation, represent a key component of such regulatory mechanisms. DVL proteins are very rich in serine (S) and threonine (T); for example, DVL3 contains 131 S/T residues, which can be potentially phosphorylated. The best described consequence of the activation of both Wnt/ β -catenin as well as non-canonical Wnt pathway is phosphorylation of DVL by the Wnt-induced Casein kinase 1 ϵ (CK1 ϵ) [11–14]. In addition to CK1 ϵ , multiple other kinases have been reported to phosphorylate DVL in different contexts. For example, CK2 α in both Wnt signaling pathways [14–16], Polo-like kinase (PLK) 1 in the control of mitotic spindle [9], Nima-related kinase (NEK) 2 in the centrosome [10, 17], protein kinase C (PKC) δ in non-canonical Wnt signaling [18], and receptor-interacting protein kinase (RIPK) 4 in the Wnt/ β -catenin signaling [19]. Recent work using mass spectrometry [10, 20, 21] has identified more than 50 S/T of DVL that are indeed phosphorylated. However, the functional significance of these phosphorylation sites in DVL remains unclear. With respect to the current understanding of PTMs in the intrinsically disordered proteins, it is reasonable to speculate that the physiological function is achieved by a combination (“barcode”) of phosphorylated sites rather than by mere phosphorylation of individual sites.

In this study we analyzed and compared the phosphorylation of DVL3 induced by eight S/T kinases. We have selected DVL3 as a candidate because its absence shows

the strong phenotypes in vivo [22]. We have studied the phosphorylation of this DVL isoform earlier [10, 16, 23, 24], which allows for a direct comparison. The studied kinases included six previously reported DVL kinases, Aurora A that was reported with DVL in the same complex [25] and TTBK2, a DVL kinase identified in this study. We have applied complementary proteomic approaches to describe in detail and in a quantitative manner how individual kinases modify DVL3. The phosphorylation barcoding unveiled unique but also common phosphorylation patterns that represent a reference point for the interpretation of existing and any future data analyzing phosphorylation of DVL. Last but not least, our work provides an example of universal pipelines for the phosphoanalysis of proteins modified in complex patterns at dozens of residues.

Materials and methods

Cell culture, transfection, and treatments

HEK293T, HEK293 T-REx and DVL1/2/3-null HEK293 T-REx cells were propagated in DMEM, 10% FCS, 2 mM L-glutamine, 50 units/ml penicillin, 50 units/ml streptomycin. CK1 ϵ inhibitor PF-670462 was used at 10 μ M. Cells were seeded on appropriate culture dishes (15 cm diameter dish for IP, 24-well plate for WB, dual luciferase assay, ICC) and the next day were transfected using polyethylenimine (PEI) in a stoichiometry of 3 μ l PEI (0.1% w/v in MQ water) per 1 μ g of DNA. Cells were harvested for immunoblotting or immunocytofluorescence 24 h after transfection, for immunoprecipitation after 48 h. The following plasmids have been published previously: FLAG-DVL3 [26], CK1 ϵ [27], Myc-NEK2 [28], FLAG-PLK1 [29], Myc-Aurora A [30], HA-CK2 α [31], YFP-PKC δ [32], VSV-RIPK4 [33] and GFP-TTBK2 WT and KD [34].

Dual luciferase TopFlash/Renilla reporter assay

For the luciferase reporter assay, cells were transfected with 0.1 μ g of Super8X TopFlash construct, 0.1 μ g of pRLTKluc (Renilla) luciferase construct and other plasmids as indicated (50 ng of DVL3 in Fig. 1d, 200 ng of DVL3 in Fig. 9b) in a 24-well plate and processed 24 h after transfection. For the TopFlash assay, a Promega dual luciferase assay kit was used according to the manufacturer's instructions. Relative luciferase units of firefly luciferase were measured and normalized to the Renilla luciferase signal.

Coimmunoprecipitation and Western blotting

For MS/MS-based identification of phosphorylation, HEK293T cells were seeded on 15 cm dishes and transfected with corresponding plasmids (8 μ g of DVL3 plasmid plus 8 μ g of pCDNA3 or plasmid encoding the kinase per dish) 24 h after seeding. Two ml of ice-cold lysis buffer supplemented with protease inhibitors

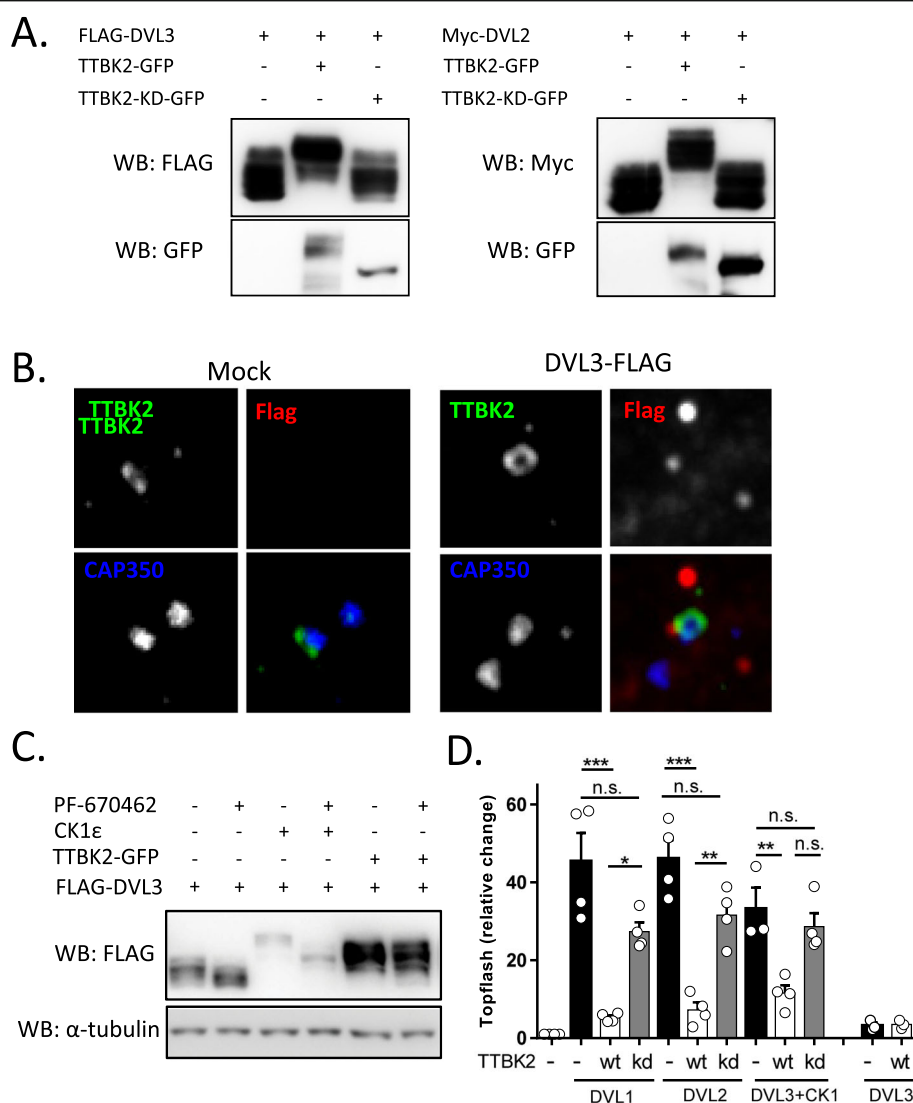


Fig. 1 Identification of TTBK2 as a novel DVL kinase. **a:** HEK293 cells were transfected with FLAG-DVL3 and Myc-DVL2 plasmids with wild type (wt) or kinase dead (KD) TTBK2-GFP. Active TTBK2 promoted phosphorylation-dependent mobility shift of DVL3 on Western blotting. **b:** Endogenous TTBK2 (green) localized into distal appendages of the mother centriole in hTERT-RPE1 cells (left). Overexpression of FLAG-DVL3 (stained in red) was not able to displace TTBK2 from the centriole (right). Centrioles were stained with CAP350 (blue). **c:** HEK293 cells were transfected with indicated plasmids, treated with CK1 ϵ inhibitor PF-670462 (10 μ M) and subsequently analyzed by Western blotting. TTBK2-induced electrophoretic mobility shift of DVL3 was not diminished upon CK1 ϵ inhibition unlike the mobility shift induced by CK1 ϵ . **d:** HEK293 cells were transfected with indicated plasmids and by the TopFLASH reporter system. Luminescence in the cell lysates was measured 24 h after transfection. Mean, SD and individual data points are indicated. Statistical differences were tested by One-way ANOVA and Tukey's post test (* $p < 0.05$, ** $p < 0.01$, *** $p < 0.001$)

(Roche Applied Science, 11,836,145,001), phosphatase inhibitors (Calbiochem, 524,625), 0.1 mM DTT, and 10 mM N-ethylmaleimide (Sigma E3876) was used for lysis of one 15 cm dish. Lysate was collected after 20 min of lysis on 4°C and was cleared by centrifugation at 18000×g for 20 min. Three µg of anti-FLAG M2 (F1804; Sigma) antibody were used per sample. Samples were incubated with the antibody for 40 min, then 25 µl of G protein-Sepharose beads (GE Healthcare, 17-0618-05) equilibrated in the lysis buffer were added to each sample. Samples were incubated on the carousel overnight,

washed 6 times with lysis buffer and finally, 40 μ l of 2 \times Laemmli buffer was added and samples were subsequently boiled.

The samples were loaded to 8% SDS-PAGE gels. Electrophoresis was performed through the stacking gel at 100 V and through the separating gel at 150 with PageRuler Prestained Protein Ladder (ThermoFisher, Cat. No. 26620) as a marker. Gels were then processed for mass spectrometry or the proteins were transferred to the polyvinylidene difluoride membrane (Merck Millipore, Cat. No. IPVH00010) by Western Blotting (WB). Subsequently, the membrane was blocked

in 5% defatted milk or 3% BSA for 1 h with shaking. After the blocking step, the membrane was incubated with corresponding primary and secondary antibodies. Proteins were visualized by ECL (Enhanced chemiluminescence; Merck Millipore, Cat. No. WBKLS0500). The signal was detected using Vilber FUSION-SL system. Western blot was quantified using ImageJ software.

The antibodies used were: anti-FLAG M2 (Sigma-Aldrich, #F1804) for WB and IP, anti-CK1 ϵ (Santa Cruz, #sc-6471), anti-GFP (Fitzgerald, #20R-GR-011), HA11 (Covance #MMS-101R), VSV (Sigma-Aldrich #V 5507), c-Myc (Santa Cruz, #sc-40), α -tubulin (Proteintech, 66, 031-1-Ig), anti-DVL3 (sc-8027, Santa Cruz Biotechnology) and anti- β -actin (cs4970, Cell Signalling). Following phospho-specific antibodies have been published previously – pS280-DVL3 (pS280) [10], pS643 [20], and pS697 [10]. Anti phospho-S192 antibody was prepared by immunizing rabbits by TTSFFDS(p) DEDDST peptide on a service basis by Moravian Biotechnology (<http://www.moravian-biotech.com>).

Immunofluorescence

Cells were seeded onto glass coverslips and next day transfected according to the scheme. 24 h post transfection medium was removed, cells were washed by PBS and fixed by 4% PFA for 10 min or ice-cold MetOH (5 min/–20°C, Fig. 1b). Coverslips were then washed in PBS and incubated with primary antibodies for 1 h, washed three times with PBS and then incubated with secondary antibodies conjugated to Alexa Fluor 488 (Invitrogen A11001) or/and Alexa Fluor 594 (Invitrogen A11058), washed with PBS and stained with DAPI (1:5000); all coverslips were mounted on microscopic slides. Cells were then visualized on Olympus IX51 fluorescent microscope using 40 \times air or 100 \times oil objectives and/or Olympus Fluoview 500 confocal laser scanning microscope IX71 using 100 \times oil objective. 200 positive cells per experiment ($N=3$) were analyzed and scored according to their phenotype into two categories (punctae/even). The antibodies used were as follows: anti-FLAG M2 (Sigma-Aldrich, #F1804), anti-DVL3 (Santa Cruz, #sc-8027), anti-CK1 ϵ (Santa Cruz, #sc-6471), HA11 (Covance #MMS-101R), VSV (Sigma-Aldrich #V 5507), c-Myc (Santa Cruz, #sc-40) and anti-GFP (Fitzgerald, #20R-GR-011), CAP350 [35], TTBK2 (Sigma-Aldrich, #HPA018113). Images presented in Fig. 1b were acquired using DeltaVision-Elite system (Applied Precision/GE) with a 100 \times /1.4 Apo plan oil immersion objective. Image stacks were taken with a z distance of 0.2 μ m, deconvolved (conservative ratio, three cycles), and projected as maximal intensity images by using SoftWoRX (Applied Precision/GE).

FIAsH FRET

The HEK293 cells were seeded onto round 24-mm coverslips, which were previously placed in six-well plates and coated with 200 μ l of poly-D-lysine (1 mg/ml) for 20 min.

Cells were transfected 16–18 h later using Effectene (Qiagen), according to the manufacturer's instructions. DMEM was replaced 6 h later and the analysis was done 24 h after transfection.

FIAsH labeling of the DVL3 FIAsH III sensor was performed as previously described [24]. Shortly, transfected cells were washed once with Hank's Balanced Salt Solution (HBSS) containing 1.8 g/l glucose and then incubated at 37°C for 1 h with HBSS supplemented with 500 nM FIAsH; 12.5 μ M 1,2-ethanedithiol (EDT). In order to reduce non-specific labeling, cells were then rinsed once with HBSS and incubated for 10 min with HBSS containing 250 μ M EDT and corresponding inhibitors. Finally, cells were washed twice with HBSS and maintained in DMEM medium.

To determine the FRET efficiency of the DVL3 FIAsH III sensor, coverslips with the cells were mounted using an Attofluor holder (Molecular Probes) and placed on a Zeiss inverted microscope (Axiovert200), equipped with 63 \times oil objective lens and a dual-emission photometric system (Till Photonics). Cells were excited at 436 ± 10 nm using a frequency of 10 Hz with 40 ms illumination time out of a total of 100 ms. Emission of ECFP (480 ± 20 nm) and FIAsH (535 ± 15 nm), and the FRET ratio (FIAsH/ECFP) were monitored simultaneously. Fluorescence signals were detected by photodiodes and digitalized using an analogue-digital converter (Digidata 1440A, Axon Instruments). Fluorescence intensities data were acquired using Clampex software (Axon Instruments). During measurements, cells were maintained in imaging buffer; 5 mM of 2,3-dimercapto-1-propanol (also called British anti-Lewisite – BAL) was added to the cells approximately 40 s after the recording started. Recovery of ECFP fluorescence was monitored over time and FRET efficiency was calculated as described [36]. One independent experiment represents approximately 4–6 repeats (i.e. single-cell FRET signals) for each condition.

Site directed mutagenesis

The mutagenesis reactions were performed using the QuikChange II XL Site-Directed Mutagenesis Kit following the manufacturer's instructions (Agilent Technologies, #200521). All mutations described in this study were verified by Sanger sequencing. Following primers were used:

DVL3 S268A forw	ATCTCCATTGTGGACCAAGCCAACGAGCGTGGTGACGGC
DVL3 S268A rev	GCCGTCACCACGCTCGTTGGCTTGGTCCACAATGGAGAT
DVL3 S311A for	ATCAACTTTGAGAACATGGCTAATGACGATGCAGTCCGG
DVL3 S311A rev	CCGGACTGCATCGTCATTAGCCATGTTCTCAAAGTTGAT
DVL3 S268E forw	ATCTCCATTGTGGACCAAGAGAACGAGCGTGGTGACGGC
DVL3 S268E rev	GCCGTCACCACGCTCGTTCTTGGTCCACAATGGAGAT
DVL3 S311E	ATCAACTTTGAGAACATGGAGAATGACGATGCAG

Materials and methods (Continued)

forw	TCCGG
DVL3 S311E rev	CCGGACTGCATCGTCATTCTCCATGTTCTCAAAGTTGAT
Dvl2 S281E forw	TACAACTTCCTGGGTATCGAGATTGTTGGCCAGAGCAAT
Dvl2 S281E rev	ATTGCTCTGGCCAACAATCTCGATACCCAGGAAGTTGTA
Dvl2 S298E forw	GGCGGCATCTACATTGGCGAGATCATGAAGGGTG GGGCC
Dvl2 S298E rev	GGCCCCACCTTCATGATCTCGCCAATGTAGATGCCGCC

Rescue assays

For transfection HEK293 T-REx (WT) and DVL1/2/3-null HEK293 T-REx cells (D1/2/3 TKO HEK293 T-REx) cells were seeded at 200000 cell/well in 24 well plate density. Next day, the cells were transfected using polyethylenimine (PEI) in concentration 1 µg/ml and pH 7.4 and the PEI ratio 6 µl of PEI/ 1 µg DNA. Mixture of transfected plasmids (10 ng of indicated DVL3 plasmid, 100 ng of Super8X TopFlash construct and 100 ng of pRLTKluc (Renilla) luciferase construct per well, the total amount of DNA was equalized by pcDNA3.1 to 400 ng DNA/well) and PEI was diluted separately in plain DMEM (DMEM without FBS, L-glutamine and antibiotics). After 6 h, medium containing transfection mix was removed and exchanged by complete DMEM medium. In all experiments cells were treated by 1 µM porcupine inhibitor LGK974 (Stem RD, 974–02) to reduce the autocrine secretion of all Wnt ligands and recombinant human R-spondin1 250 ng/ml (PeproTech, 120–38). For stimulation of the cells, Wnt3a recombinant protein was used for 14 h in concentration 80 ng/ml (R&D Systems, 5036-WN-CF). Control stimulations were done with 0.1% BSA in PBS. Samples were then analyzed by TopFlash reporter assay and WB.

Protein expression and purification

Human DVL2 PDZ domain (aa 265–361) and its phosphomimicking mutant (S281E + S298E) were cloned into pET vector with N-terminal His₆-tag, a lipoyl domain tag and a TEV cleavage site. All proteins were expressed in BL21-DE3(RIL) cells. For NMR studies, cells were grown in minimal medium (M9) supplemented by ¹⁵NH₄Cl (1 g/l) and/or ¹³C₆ glucose (2 g/l) and induced with 0.5 mM IPTG for 24 h at 16 °C. Proteins were purified as described before [24] and stored in 20 mM Hepes (pH 6.8) and 50 mM KCl for NMR studies. The DVL3_C peptide 698–716 with phosphorylated S700 (DVL_C) used in NMR studies was purchased from KareBay Biochem, Inc. (New Jersey, USA).

NMR spectroscopy

NMR experiments were carried out at CEITEC Josef Dadok National NMR Centre on a 700 MHz Bruker

Avance III spectrometers equipped with ¹H/¹³C/¹⁵N TCI cryogenic probe head with z-axis gradients. Chemical shift assignments of the phosphomimicking PDZ mutant (S281E + S298E) were obtained automatically using 4D-CHAINS technology [37] as described before for the wt PDZ domain [24]. NMR titrations were performed in series of ¹H-¹⁵N HSQC spectra using 100 µM of ¹⁵N-labeled protein (wild type or phosphomimicking mutant) and increasing amounts of DVL_C (stock concentration of 800 µM).

Mass spectrometry**In gel digestion**

Immunoprecipitates were separated on SDS-PAGE gel electrophoresis, fixed with acetic acid in methanol and stained with Coomassie brilliant blue for 1 h. Corresponding 1D bands were excised. After destaining, the proteins in gel pieces were incubated with 10 mM DTT at 56 °C for 45 min. After removal of DTT excess samples were incubated with 55 mM IAA at room temperature in darkness for 30 min, then alkylation solution was removed and gel pieces were hydrated for 45 min at 4 °C in digestion solution (5 ng/µl trypsin, sequencing grade, Promega, in 25 mM AB). The trypsin digestion proceeded for 2 h at 37 °C on Thermomixer (750 rpm; Eppendorf). Subsequently, the tryptic digests were cleaved by chymotrypsin (5 ng/µl, sequencing grade, Roche, in 25 mM AB) for 2 h at 37 °C. Digested peptides were extracted from gels using 50% ACN solution with 2.5% formic acid (FA) and concentrated in speedVac concentrator (Eppendorf). The aliquot (1/10) of concentrated sample was transferred to LC-MS vial with already added polyethylene glycol (PEG; final concentration 0.001%, [38] and directly analyzed by LC-MS/MS for protein identification.

Phosphopeptide enrichment

The rest of the sample (9/10) was used for phosphopeptide analysis. Sample was diluted with acidified acetonitrile solution (80% ACN, 2% FA). Phosphopeptides were enriched using Pierce Magnetic Titanium Dioxide Phosphopeptide Enrichment Kit (Thermo Scientific, Waltham, Massachusetts, USA) according to manufacturer protocol and eluted into LC-MS vial with already added PEG (final concentration 0.001%). Eluates were concentrated under vacuum and then dissolved in water and 0.6 µl of 5% FA to get 12 µl of peptide solution before LC-MS/MS analysis.

LC-MS/MS analysis

LC-MS/MS analyses of peptide mixture were done using RSLCnano system connected to Orbitrap Elite hybrid spectrometer (Thermo Fisher Scientific) with ABIRD (Active Background Ion Reduction Device; ESI Source Solutions) and Digital PicoView 550 (New Objective) ion

source (tip rinsing by 50% acetonitrile with 0.1% formic acid) installed. Prior to LC separation, peptide samples were online concentrated and desalted using trapping column (100 $\mu\text{m} \times 30\text{ mm}$) filled with 3.5 μm X-Bridge BEH 130 C18 sorbent (Waters). After washing of trapping column with 0.1% FA, the peptides were eluted (flow 300 nl/min) from the trapping column onto Acclaim Pepmap100 C18 column (3 μm particles, 75 $\mu\text{m} \times 500\text{ mm}$; Thermo Fisher Scientific) by 65 min long gradient. Mobile phase A (0.1% FA in water) and mobile phase B (0.1% FA in 80% acetonitrile) were used in both cases. The gradient elution started at 1% of mobile phase B and increased from 1 to 56% during the first 50 min (30% in the 35th and 56% in 50th min), then increased linearly to 80% of mobile phase B in the next 5 min and remained at this state for the next 10 min. Equilibration of the trapping column and the column was done prior to sample injection to sample loop. The analytical column outlet was directly connected to the Digital PicoView 550 ion source.

MS data were acquired in a data-dependent strategy selecting up to top 10 precursors based on precursor abundance in the survey scan (350–2000 m/z). The resolution of the survey scan was 60,000 (400 m/z) with a target value of 1×10^6 ions, one microscan and maximum injection time of 200 ms. High resolution (15,000 at 400 m/z) HCD MS/MS spectra were acquired with a target value of 50,000. Normalized collision energy was 32% for HCD spectra. The maximum injection time for MS/MS was 500 ms. Dynamic exclusion was enabled for 45 s after one MS/MS spectra acquisition and early expiration was disabled. The isolation window for MS/MS fragmentation was set to 2 m/z .

Data analysis

The analysis of the mass spectrometric RAW data was carried out using the Proteome Discoverer software (Thermo Fisher Scientific; version 1.4) with in-house Mascot (Matrixscience; version 2.4.1) search engine utilization. MS/MS ion searches were done against in-house database containing expected protein of interest with additional sequences from cRAP database (downloaded from <http://www.thegpm.org/crap/>). Mass tolerance for peptides and MS/MS fragments were 7 ppm and 0.03 Da, respectively. Oxidation of methionine, deamidation (N, Q) and phosphorylation (S, T, Y) as optional modification, carbamidomethylation of C as fixed modification, TrypChymo enzyme specificity and three enzyme miss cleavages were set for all searches. The phosphoRS (version 3.1) feature was used for preliminary phosphorylation localization. Final localization of all phosphorylations (including those with ambiguous localization) was performed by manual evaluation of the fragmentation spectra of the

individual phosphopeptides. Based on the presence of individual fragments in the peptide sequence, it was decided whether the localization was accurate or not.

Quantitative information was assessed and manually validated in Skyline software (Skyline daily 3.6.1.10230). Normalization of the data was performed using the set of phosphopeptide standards (added to the sample prior phosphoenrichment step; MS PhosphoMix 1, 2, 3 Light, Sigma-Aldrich) and by non-phosphorylated peptides identified in direct analyses.

All quantitative data (peptide intensities) were processed by two approaches (see Fig. 3a). In the first approach (pipeline #1 and #3) that often resulted in the formation of phosphorylated clusters all identified phosphorylated peptides were considered. This has resulted in three categories of identification: (i) one peptide or set of peptides with one clearly localized phosphorylated site, (ii) one or set of overlapping peptides covering sequence region with two or more clearly localized phosphorylated sites (phosphorylated sites separated by a comma in the Figures) and (iii) one or set of overlapping peptides covering sequence region with two or more phosphorylated sites, but some of them are not clearly localized (phosphorylated sites separated by a dash in the Figures). Sum of intensities of phosphorylated peptides (includes different peptide sequences, charges and peptides with other modifications) was calculated for each cluster. In case of direct analysis (pipeline #1), we calculated site occupancies as percentage ratio of phosphorylated peptide intensity (summed if more than one) to total intensity (summed intensities of phosphorylated peptide(s) + corresponding non-phosphorylated peptide(s)). Sites/clusters with the site occupancy > 5% at least in one experiment are shown in Fig. 4. For pipeline #3, the difference between the phosphorylated peptide summed intensity in the kinase-induced sample and the control (in log10 scale) was calculated for each replicate and the mean from all three replicates was used for the heat map (see in Additional file 2: Figure S2). In the second approach (pipeline #2), only phosphorylated peptides with the clearly localized phosphorylation site (based on manual inspection) were considered. In case of the multiphosphorylated peptides the total intensity of the peptide was assigned to each phosphorylated site. Sum of intensities of phosphorylated peptides was calculated for each phosphorylated site. The heat map (Fig. 5) was build-up in the same way as for pipeline #3 described above. For the production of phosphoplots the sum of intensities for each phosphorylated site (pipeline #2) were log-transformed (log10) and average from 3 replicates was calculated (values under the detection limit were not included in the calculation).

Numerical data & statistics

Cluster analysis

Data of absolute peptide intensities were log-transformed (log10) because of their log-normal distribution. Log-transformed data of each replicate were standardized to control (kinase subtracted from “no kinase” control) and averaged from 3 replicates. Cluster analysis was applied both for kinases and for phosphosites; Ward’s minimum variance method based on the Lance-Williams recurrence and Euclidean distance were used. Circular plot accompanied by heat map was used for visualization of complex relation among phosphosites and kinases. All analyses were performed using R software.

Other analyses

One-way ANOVA and Tukey Post tests were calculated by GraphPad Prism (GraphPad Software Inc.).

Results

Identification of TTBK2 as a kinase acting upstream of DVL

Our previous work identified interactions between DVL3, CEP164, and TTBK2 kinase [34, 39]. To examine the possible regulation of DVL by TTBK2, we tested whether this poorly characterized centrosomal kinase phosphorylates DVL3 and DVL2 in HEK293 cells. As shown in Fig. 1a, TTBK2 co-expression induced a prominent electrophoretic mobility shift for both DVL3 and DVL2 in a kinase activity-dependent manner, suggesting that TTBK2 is capable to efficiently promote phosphorylation of DVL. TTBK2 also gets auto-phosphorylated as described earlier [34]. TTBK2 has been described as a kinase that primarily resides on the mother centriole where it regulates ciliogenesis [34, 40–45]. Given the previous reports on DVL centrosomal localization and the possible DVL implication in ciliogenesis [6, 7, 10, 46] we tested whether overexpressed DVL has the capacity to displace TTBK2 from the centriole. As shown in Fig. 1b (left panel), we confirmed, in line with earlier reports, the localization of TTBK2 to the mother centriole, which is however not affected by overexpression of DVL3 (Fig. 1b, right).

Mobility-shift of DVL2 and DVL3 induced by TTBK2 (Fig. 1a) can be in principle a consequence of direct phosphorylation of DVL by TTBK2 or a consequence of activation of other DVL kinases by TTBK2. In the second scenario, the well-established DVL kinase CK1 ϵ represents the most obvious candidate target of TTBK2. To address whether TTBK2 acts directly on DVL or rather acts as CK1 ϵ activator we treated cells with the CK1 inhibitor PF-670462 and subsequently analyzed the electrophoretic mobility shift of DVL3. As shown in Fig. 1c, PF-670462 efficiently reduced phosphorylation induced by CK1 ϵ but not by TTBK2, hence demonstrating that

TTBK2 phosphorylation of DVL does not require CK1 ϵ activity.

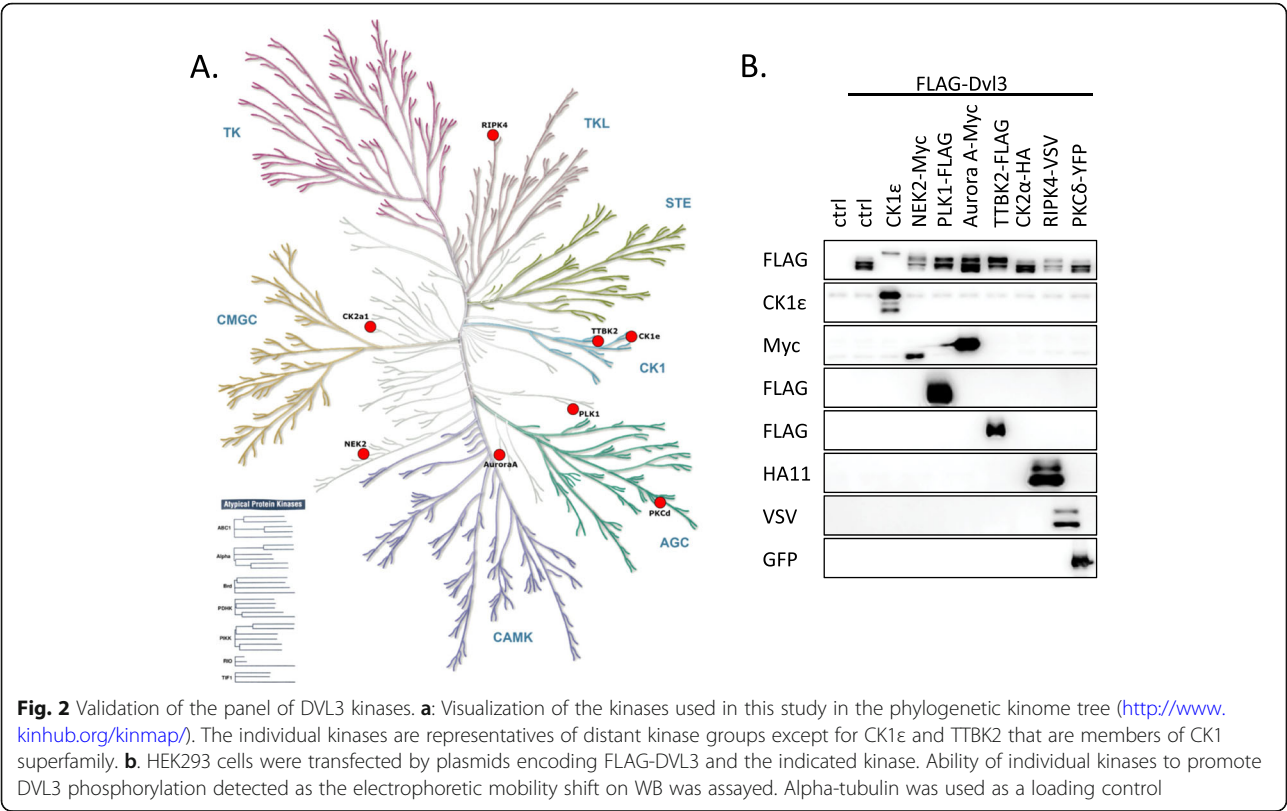
The best-defined role of DVL is the positive regulation of the Wnt/ β -catenin pathway. In order to address if TTBK2 modulates this DVL function we analyzed the ability of TTBK2 to promote or to inhibit DVL-induced TCF/LEF-dependent luciferase reporter (TopFlash) in HEK293 cells. Interestingly, TTBK2 did inhibit efficiently DVL1- and DVL2-induced TopFlash activation in a kinase activity-dependent manner. Because DVL3 alone induces TopFlash very poorly (Fig. 1d, right; see also [47]) we co-transfected CK1 ϵ and DVL3 and even in this case TTBK2 co-expression reduced TopFlash activation (Fig. 1d). In summary, we demonstrate that the robust phosphorylation of DVL mediated by TTBK2 is associated with the decreased capacity of DVL to act in the Wnt/ β -catenin pathway.

Design and validation of DVL kinase panel

TTBK2 represents an additional kinase to the ever-growing list of DVL kinases. Currently, multiple kinases from diverse families have been reported to phosphorylate at least one of DVL isoforms. From the fragmented published results, it is not possible to find out the unique/general or constitutive/induced phosphorylation events and patterns that are associated with various functions of DVL in connection to individual kinases. This prompted us to perform a direct comparison of DVL phosphorylation by individual kinases. We chose human HEK293 cells, a common model for the analysis of Wnt signaling, and human DVL3 as a representative DVL protein. Previously reported DVL kinases – CK1 ϵ [11], CK2 α [15], PLK1 [9], NEK2 [10, 17], PKC δ [18], RIPK4 [19] and the newly identified TTBK2 were added to the panel. We also included mitotic kinase Aurora A that has been reported to act in the same complex with DVL [25]. These S/T kinases represent very diverse members of the protein kinase family as visualized on the kinome tree (Fig. 2a). Most kinases – except for CK2 α and PKC δ – could trigger electrophoretic mobility shift of DVL3 when co-expressed with DVL3 (Fig. 2b).

Pipelines for the generation of the phosphorylation map of DVL3

Following validation of our experimental system (Fig. 2) we performed a global analysis of DVL3 phosphorylation events. In three independent experiments, FLAG-DVL3 was overexpressed in HEK293 cells, with or without the studied kinase, immunoprecipitated using anti-FLAG antibody, separated on SDS-PAGE and stained with Coomassie Brilliant Blue (see Additional file 1: Figure S1 for the gels used in this study). Bands corresponding to DVL3 were cut out and after Tryp-Chymo digestion 1/10 of the sample was analyzed directly (see pipeline #1 in Fig. 3a) and the remaining 9/10 of the



peptide mixture was enriched for the phosphorylated peptides by TiO₂ (see pipelines #2 and #3). All samples were subsequently analyzed by liquid chromatography coupled to mass spectrometry (LC-MS/MS).

Peptides with accurately characterized phosphorylated site(s) were identified alongside with peptides of ambiguous phospholocalization, as it is common to proteomic studies. Therefore, in the accurate position focused analysis (pipeline #2) only a subgroup of peptides with clearly identified phosphorylated positions (based on manual inspection) were included. In the overall quantitative analysis (pipeline #3) all phosphorylated peptides were processed despite the uncertainty of phosphoresidues and as such were presented as “phosphorylated clusters”. For the detailed information on the quantification in these two pipelines see Materials and Methods.

Combination of the above-mentioned approaches allowed us to cover more than 95% of the DVL3 sequence across all experiments (Fig. 3b); for sequence coverage in individual samples see Additional file 6: Table S2.

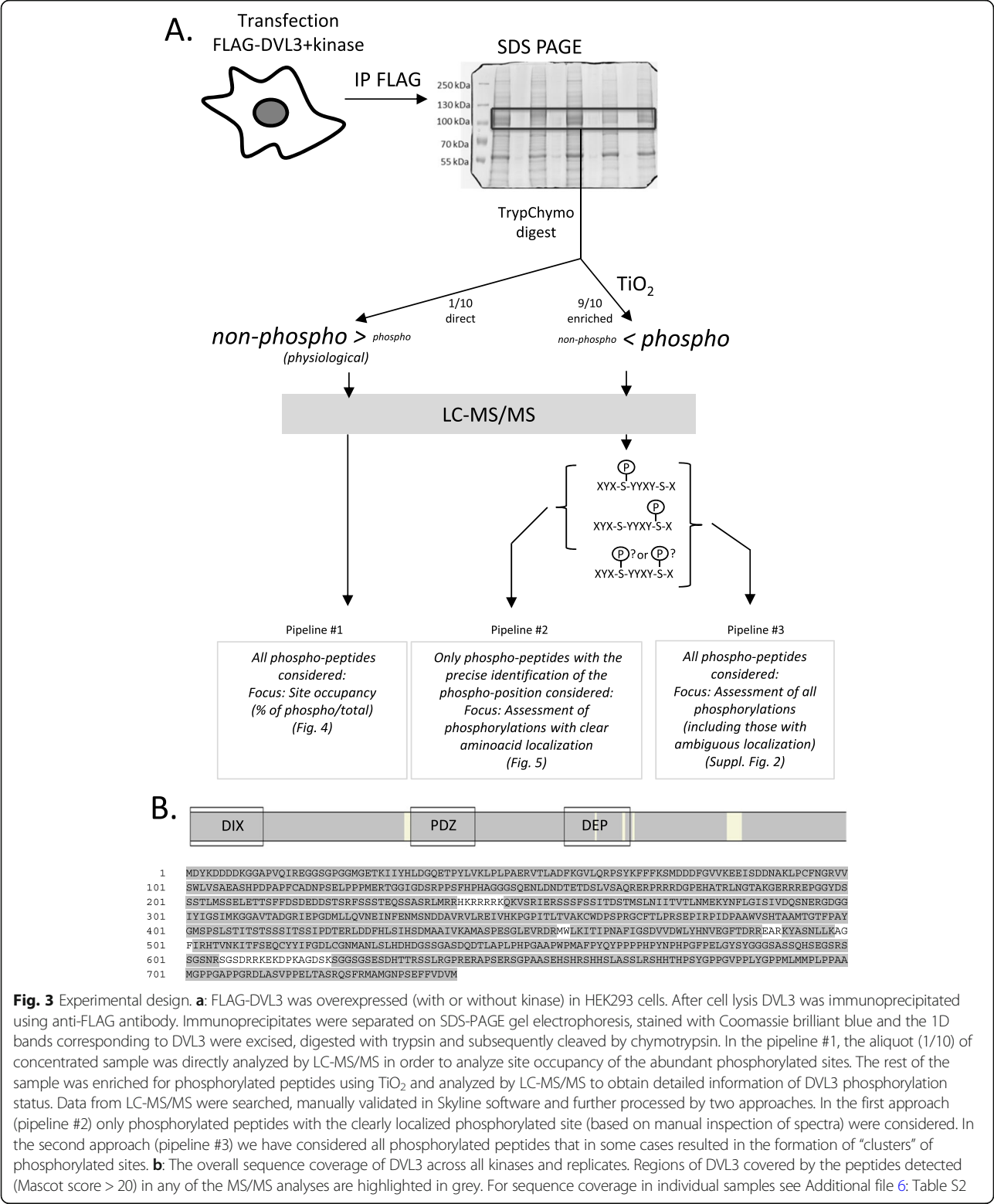
Phosphorylation map of DVL3: site occupancy of phosphorylated sites

To assess the site occupancy, we utilized direct analysis of the samples without any enrichment (the experimental pipeline #1, Fig. 3a) which allowed us to

detect phosphorylated and non-phosphorylated peptides corresponding to the same position(s). Subsequently we calculated the approximate occupancy of the selected phosphorylated sites, i.e. % of DVL3 molecules phosphorylated at given S or T residue(s).

We calculated site occupancies as the percentage ratio of phosphorylated peptide intensity (or sum of intensities if more than one) covering individual phosphosites or clusters to total intensity (phosphorylated peptide(s) + corresponding non-phosphorylated peptide(s)). Phosphorylated sites/clusters with >5% site occupancy in one sample are plotted in Fig. 4. For three clusters (S232–S244, T608–S612, S622–S630) we were not able to detect matching non-phosphorylated peptides and therefore these sites were not included in the site occupancy calculations.

We observed an increase in the phosphorylated site occupancy (above 5%) after overexpression of at least one protein kinase in all but one [14] cases (Fig. 4). The notable exception was the phosphorylated cluster S192, S197, whose phosphorylation decreased in the presence of CK1ε and to a lesser extent in the presence of TTBK2, PLK1 and NEK2. Phosphorylation of three sites was induced selectively only by one kinase; S280 and S407 were induced only by NEK2, and S268 was induced only by CK1ε. In the remaining 11 sites/clusters, two or three kinases were capable to trigger



phosphorylation: CK1ε/TTBK2 at S350 and at the cluster S512, S513, S516; NEK2/PLK1 at S263; NEK2/Aurora A at S469 (in the single replicate); NEK2/PLK1/CK1ε at S505; NEK2/CK1ε/TTBK2 (and to some extent PLK1) at S311, and at the clusters S203–S209 and S633–S643. Three other clusters – cluster S125, T133, S135, S137, cluster S175, S176 and cluster S559, S566, S567, S570 showed relatively high occupancy in the

control but were further phosphorylated by several kinases, including NEK2, CK1 ϵ , TTBK2 and PLK1.

Phosphorylation map of DVL3: detailed analysis after phospho-enrichment

In order to analyze phosphorylation of DVL3 in depth, we enriched the phosphorylated peptides by TiO₂. This approach, commonly utilized for detailed screening of protein phosphorylation, allows detection of less abundant phosphopeptides. Phospho-enrichment data were processed in two ways (Fig. 3a). Primarily, we assessed qualitatively and quantitatively only phosphopeptides with clearly identified (validated by manual inspection of MS/MS data) phosphorylation site(s) (the experimental pipeline #2, Fig. 3a). By this approach we detected 88 unique phosphorylation sites in DVL3. Peptide intensities (Additional file 5: Table S1) were compared with the DVL3-only control dataset in order to express the relative increase/decrease in the phosphorylation of each site. Data from all three replicates presenting the relative change to control are summarized as a heat map in Fig. 5. Most phosphorylated sites with the largest relative increase were identified after induction by NEK2, CK1 ϵ and TTBK2.

In order to assess the impact of excluding phosphopeptides with ambiguous phosphosite localization on quantitative changes, we processed all phosphorylated peptides according to the pipeline #3 (Fig. 3a). Intensities of the phosphorylated clusters using this approach are shown as a heat map in Additional file 2: Figure S2, and illustrate that for 15 clusters analyzed, they match very well the intensities of individual phosphorylated sites presented in Fig. 5. Comparison of results in Fig. 5 and Additional file 2: Figure S2, however, also identified cases where individual phosphorylated sites within the cluster displayed a distinct behavior. Namely, in the cluster T106–S140 the NEK2-induced phosphorylation of T106, S112 and S116 was masked by high intensity constitutive phosphorylation of S125, T133 and S137. In the phosphorylated cluster S202–S209, phosphorylation was decreased for three sites – S202, S203 and S204 – in case of CK1 ϵ and TTBK2 whereas NEK2, on the contrary, induced further phosphorylation of S204. Similarly, for the cluster S598–S612 induced by NEK2, CK1 ϵ , TTBK2 and PKC δ we mapped the activity of NEK2 predominantly to S601, S603 and S605 whereas CK1 ϵ phosphorylated mainly to S611 and S612.

The quantitative data presented in Fig. 5 (accurate positions) and Additional file 2: Figure S2 (clusters) have been combined and analyzed in order to correlate individual kinases with individual phosphorylated sites/clusters. Unbiased cluster analysis (Additional file 3: Figure S3) groups CK1 ϵ and TTBK2, both from the CK1 family, with NEK2, whereas all the remaining kinases

form a second group. There are multiple residues that are phosphorylated only by NEK2, which further distinguishes it from CK1 ϵ and TTBK2. Interestingly, CK1 ϵ and TTBK2 behave very similarly and they can be best resolved by the phosphorylation at position S268 that is CK1 ϵ -specific. This is in very good agreement with the site occupancy analysis shown in Fig. 4.

Phosphorylation map of DVL3: analysis of the phosphorylated clusters

The phosphorylated clusters visualized in Additional file 2: Figure S2 can, in principle, represent mixtures of peptides phosphorylated at distinct sites or true multiphosphorylated signatures with possible biological function. To get a better insight, we analyzed in detail the peptides phosphorylated at 3 or more sites. We found 9 peptide families fulfilling these requirements (Fig. 6). Out of these only one cluster – S112, S116, S125, T133, S135, S137 – was not induced by any of the kinases. The remaining 8 clusters were induced by one or several kinases – 3 only by NEK2, 2 mainly by CK1 ϵ and TTBK2 and 3 by NEK2 and one or more additional kinases.

These phosphorylated clusters were detected only in the intrinsically disordered regions of DVL3. The phosphorylated motifs are well conserved and found also in DVL1 and DVL2 except for S622–630 and S636–S643 (Fig. 6, right). This may suggest that the function of multisite phosphorylation of these motifs in the regulation of DVL is also conserved.

Comparison of individual pipelines and validation by phospho-specific antibodies

In our study, we used several sample and data processing pipelines (see Fig. 3). As the last step we compared the individual pipelines (i) between each other and (ii) with several phosphorylation-specific antibodies raised against phosphorylated DVL3 peptides. We probed the samples described in Fig. 2b with antibodies against phosphorylated-S280-DVL3 (pS280) [10], pS643 [20], pS697 [10] and the newly generated anti-pS192. As shown in Fig. 7 a-d that combines Western blots and MS/MS data from pipelines #1 and #2, the signal of phospho-specific antibodies partially matches the changes observed by mass spectrometry. The signal of pS192-DVL3 decreased after CK1 ϵ , PLK1 and TTBK2 co-expression whereas pS280, pS643 and pS697 increased mostly by NEK2. However, some discrepancies were observed, especially for low intensity signals, namely, all three previously validated antibodies pS280, pS643 and pS697 do detect higher phosphorylation after Aurora A co-expression that was not detected by LC-MS/MS. On the other hand, increase in S643 phosphorylation probed for TTBK2 by all MS/MS pipelines was not detected by anti-pS643-DVL3 antibody.

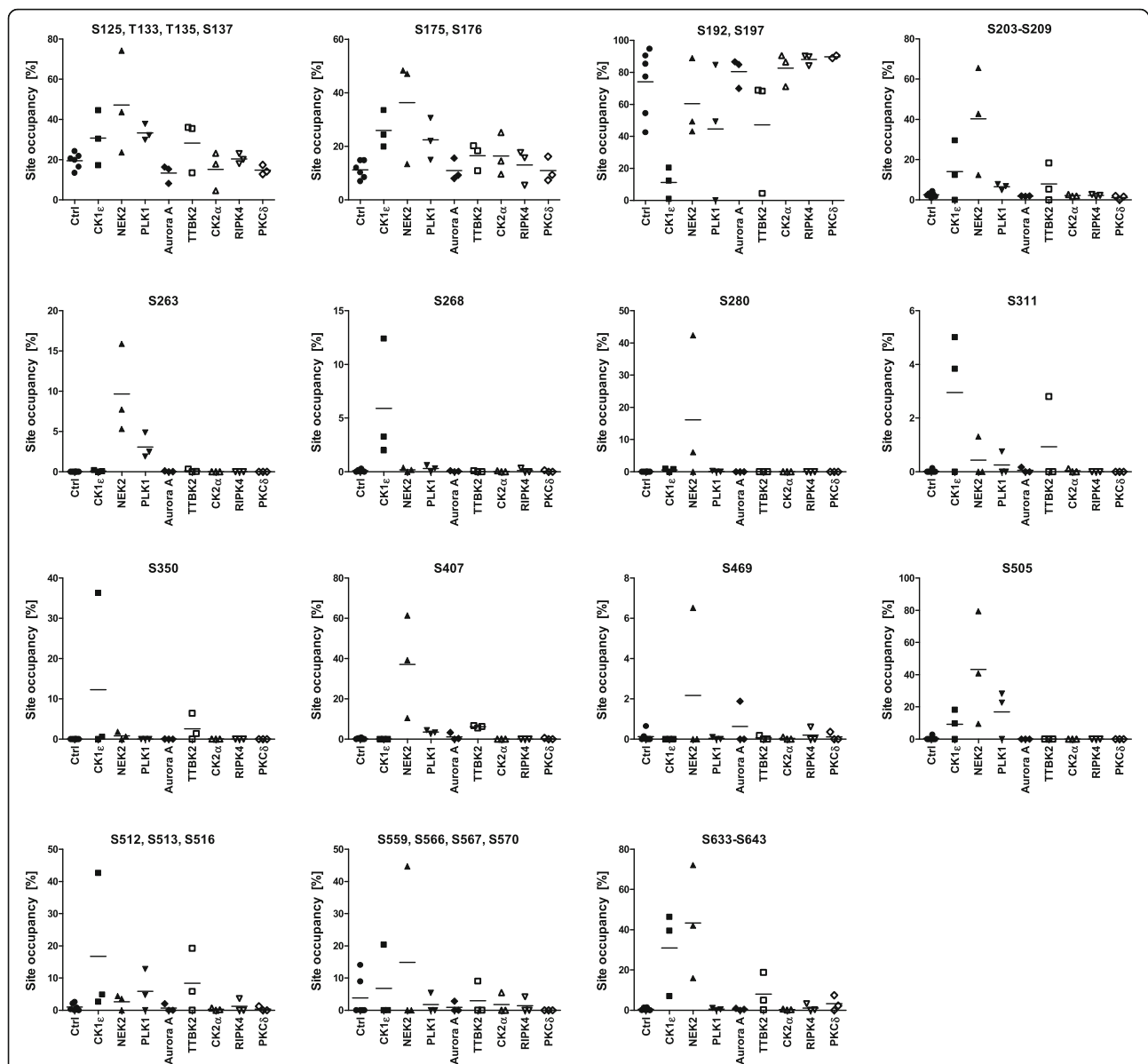


Fig. 4 Site occupancy of the abundant phosphorylated sites. Site occupancy analysis was performed according to the pipeline #1 in Fig. 3a. Fifteen phosphorylated peptides or clusters that were phosphorylated in more than 5% at least in one replicate are plotted. Graphs present individual data points from three biological replicates (two controls/biological sample) and the mean values (horizontal line)

Phosphoplot – a tool for visualization of complex phosphorylation patterns

The heat map data visualization highlights phosphorylation differences in comparison to control but does not provide a full and intuitive picture combining absolute intensities, their changes and position of individual phosphorylated peptides. To address this, we designed a visualization diagram, that we refer to as “phosphoplot”. In the phosphoplot all S/T from the primary sequence of the analyzed protein are shown. The intensities of phosphorylated peptides in the control and experimental conditions are plotted. As such, the

phosphoplot combines information on absolute peptide intensities, experimental differences and positional information, including non-phosphorylated sites. The phosphoplots of DVL3 for individual kinases based on data from pipeline #2 are shown in Fig. 8. Phosphoplot inspection identified regions of DVL3 without detected phosphorylation despite being S/T rich – such as T365–T392 between PDZ and DEP domains, and on the contrary, regions between DIX and PDZ domains that are highly constitutively phosphorylated. It also clearly identifies the uniquely phosphorylated sites for each kinase.

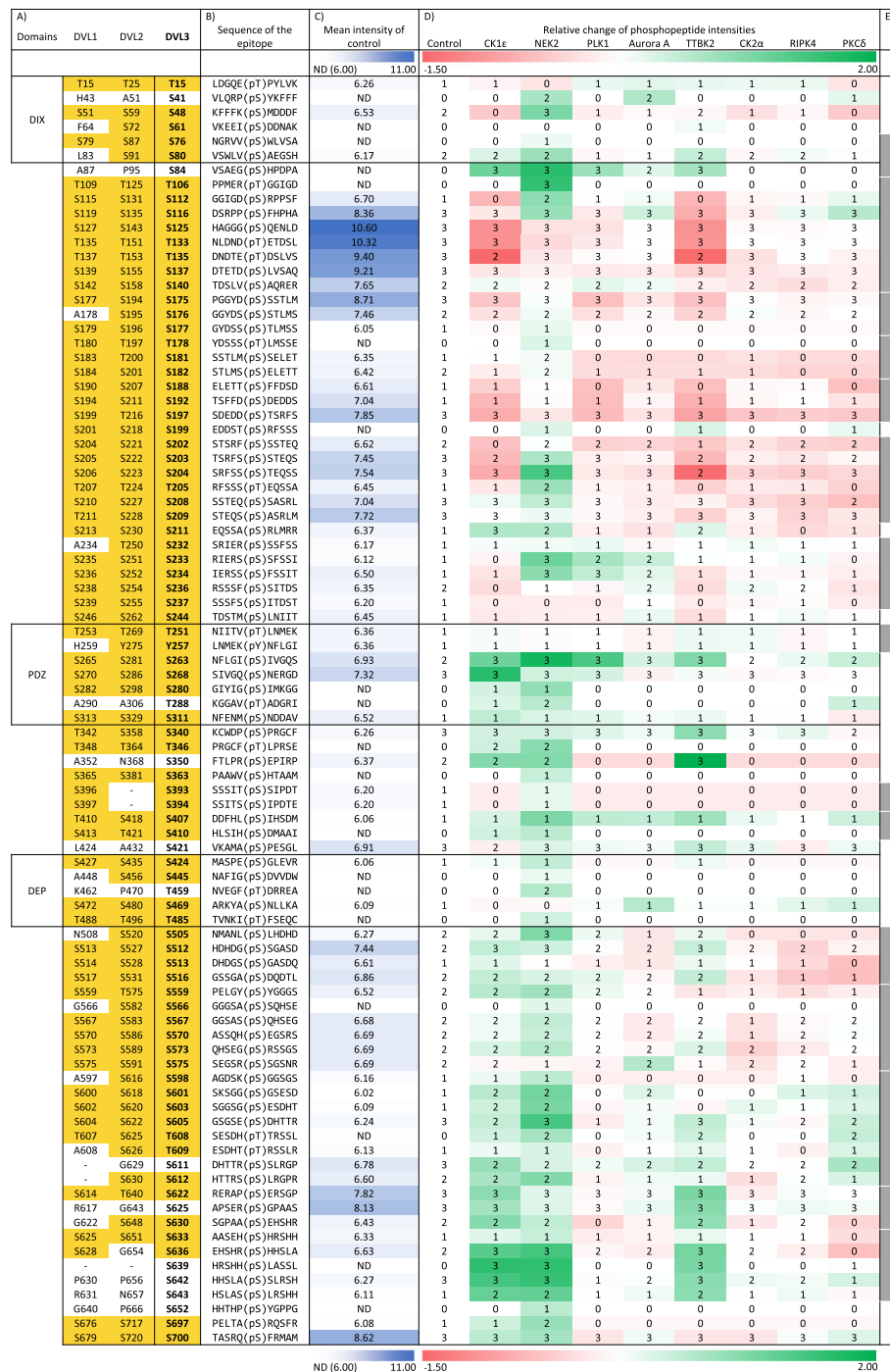
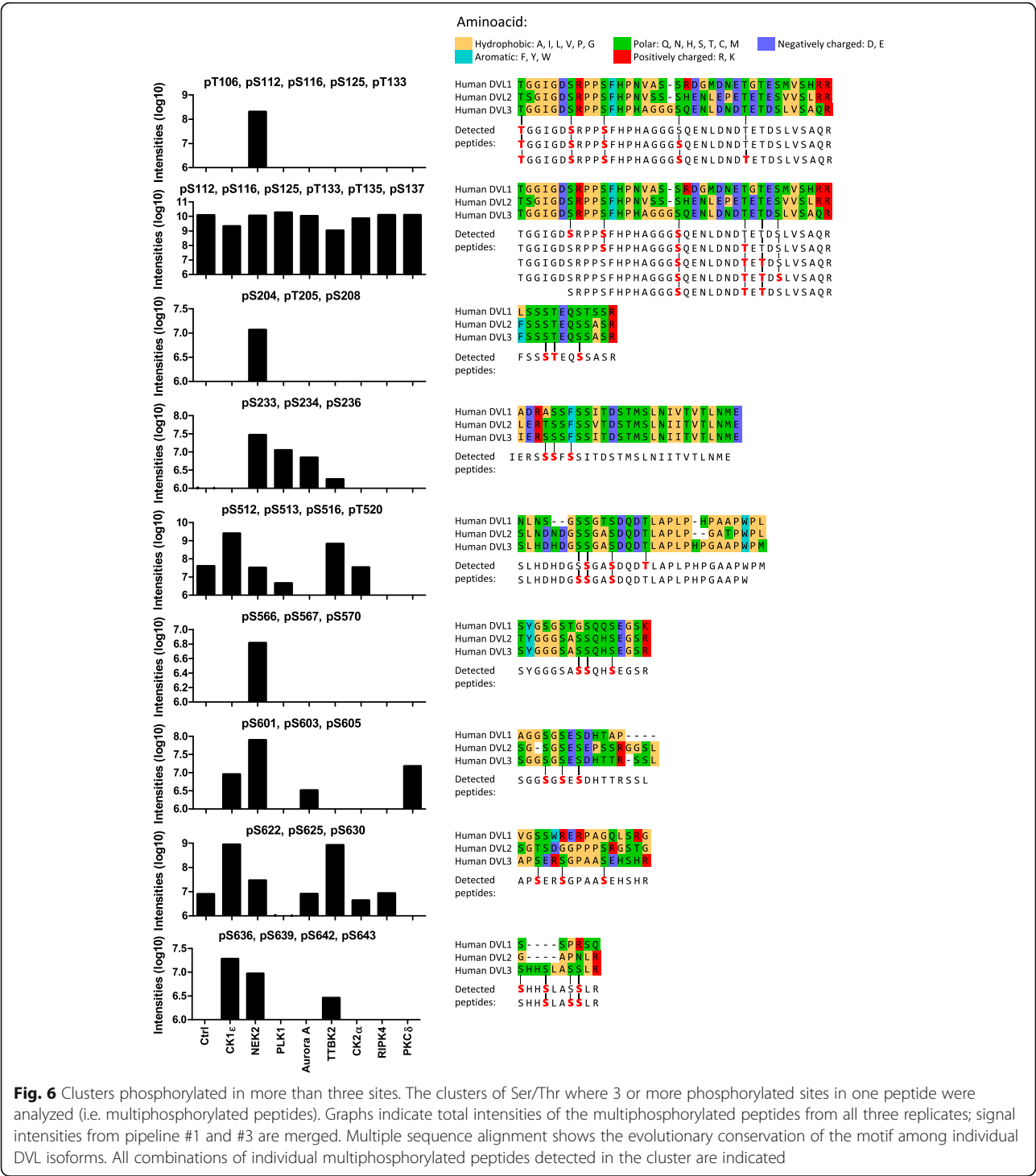


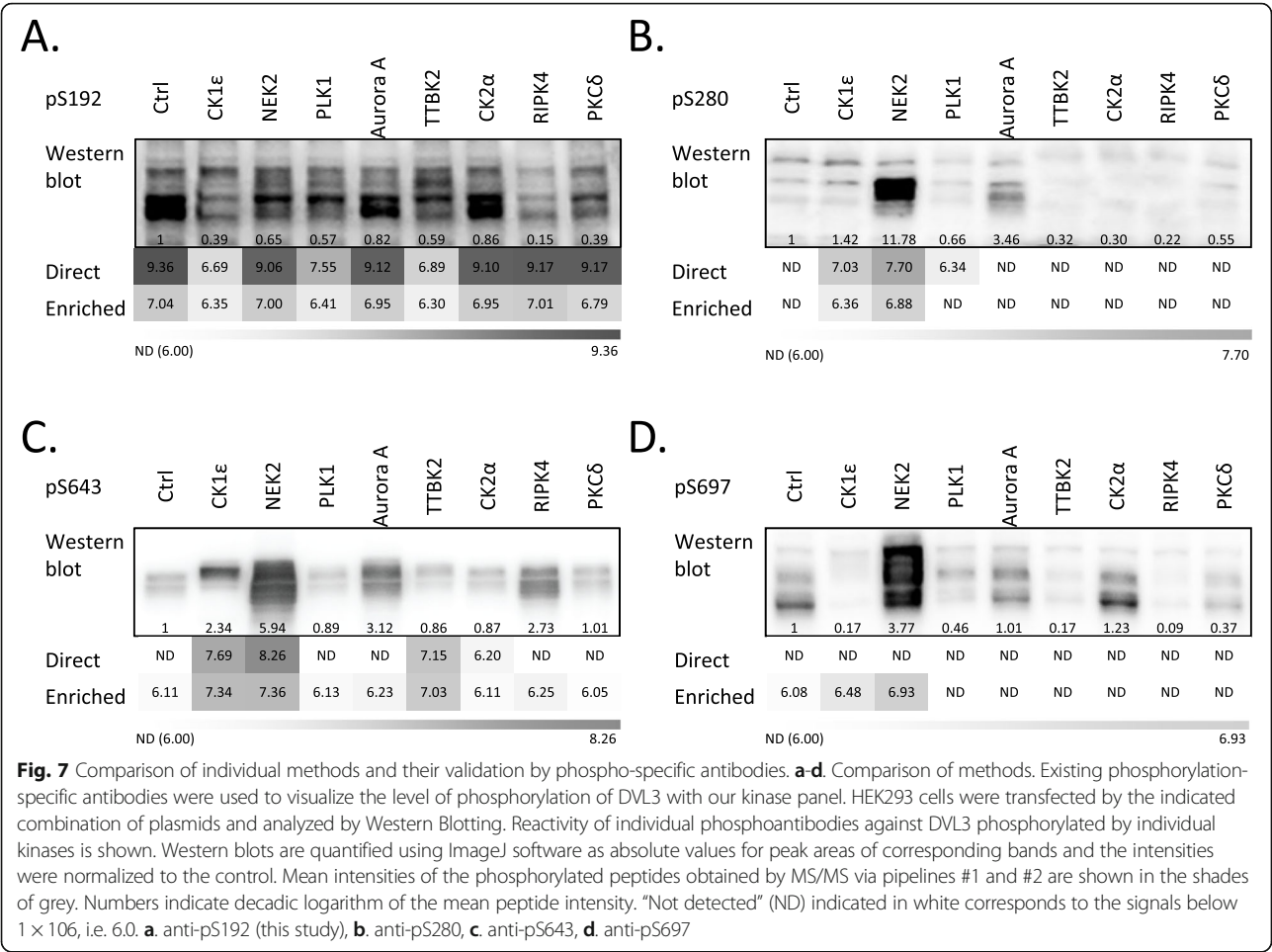
Fig. 5 Phosphorylation map of DVL3. All identified phosphorylation sites obtained from the pipeline #2 are visualized as a heatmap. Color intensities reflect relative change in the site phosphorylation (red – decrease, green – increase). Following additional information is also provided: **a)** Corresponding sites in human DVL1 and DVL2. Positions conserved in DVL1 and/or DVL2 either as Ser or Thr are highlighted in yellow. Position of the structured domains (DIX, PDZ and DEP) is indicated. **b)** The sequence of the phosphorylated epitope. Five amino acids before and after the identified phosphorylated site are shown. **c)** Mean absolute intensities of the phosphorylation sites in the control (DVL3 without exogenous kinase; $N=6$) are expressed in the shades of blue. Numbers indicate decadic logarithm of the mean. ND indicated in white corresponds means “not detected”. All signals lower than 1×10^5 , corresponding to log value 6.0 were considered as not detected. **d)** Nine columns represent heat map of relative change of phosphorylated peptide intensities (in log10 scale) obtained for individual kinases (relative to control). Numbers in the heatmap fields (0, 1, 2, 3) indicate the number of experimental replicates with the positive identification of the given phosphorylated site. **e)** Grey boxes indicate the position of clusters of sites analyzed also according to the pipeline #3 in the Additional file 2: Figure S2



Phosphorylation of S268 and S311 contributes to the activation of the Wnt/ β -catenin pathway

To associate any phosphorylation patterns with the function of DVL we compared individual kinases in their capacity to induce Wnt/ β -catenin-dependent transcription analyzed by the TopFlash reporter assay. In the absence of exogenous DVL3 only CK1 ϵ and RIPK4 significantly

activated TCF/LEF-driven transcription (Fig. 9a). When DVL3 was co-expressed, only CK1 ϵ , and to a lesser extent PLK1 (non-significant trend was observed also for CK2 α), could synergize with DVL3 to promote reporter activation (Fig. 9b). We could largely reproduce the reported effects: the capacity of CK1 ϵ and RIPK4 to activate TopFlash reporter [19, 48], and the synergistic behavior of DVL3 and



CK1ε in the TopFlash reporter [16]. Although, it has been proposed that RIPK4 activates Wnt/β-catenin also via phosphorylation of DVL [19] we have not observed any synergy with DVL3 which suggests that RIPK4 may act via other proteins in the Wnt/β-catenin pathway.

CK1ε stands unique among other kinases in its ability to efficiently induce Wnt/β-catenin downstream signaling in synergy with DVL3. We have thus analyzed the data reported in Figs. 4, 5 and Additional file 3: Figure S3 and identified S268 and S311 as candidate phosphorylation sites associated with the expression of CK1ε and activation of TopFlash reporter assay. In order to test to what extent phosphorylation of S268 and S311 participates in the activation of Wnt/β-catenin downstream signaling we mutated S268 alone or in combination with S311 to alanine and glutamic acid (S268A, S268E, S268A/S311A, S268E/S311E) and tested these DVL3 mutants for their capacity to rescue Wnt-3a signaling in DVL1/DVL2/DVL3-triple null HEK293 T-REx cells (D1/2/3 TKO cells) [47]. As shown in Fig. 9 C/D, DVL3 S268A and especially S268A/S311A are significantly less efficient in their ability to rescue Wnt-3a-induced activity. This data suggests that phosphorylation of DVL3 at S268 and S311 by CK1ε is one of the essential steps in the Wnt-3a-induced activation of β-catenin signaling.

Phosphorylation of S630-S643 mediates even localization of DVL3

Subcellular localization of DVL3 is dynamically regulated. Overexpressed DVL3, similarly to other DVL proteins, is localized in the “DVL punctae”; protein assemblies kept together via polymerization of DVL DIX domains [49]. These assemblies are dynamic and can be more compact (visible as puncta) or dissolved, resulting in the “even” distribution of DVL3 (examples of these two DVL states are presented in Fig. 10a). As shown in Fig. 10b, bottom panel, only three kinases – CK1ε, NEK2 and TTBK2 – were capable to promote even localization of DVL3.

In order to identify phosphorylation patterns associated with the even localization of DVL3 we analyzed common phosphorylation events induced by CK1ε, TTBK2 and NEK2. A cluster of the regularly spaced serines S630-S633-S636-S639-S642-S643 was the most obvious candidate for such function (see Figs. 4, 5

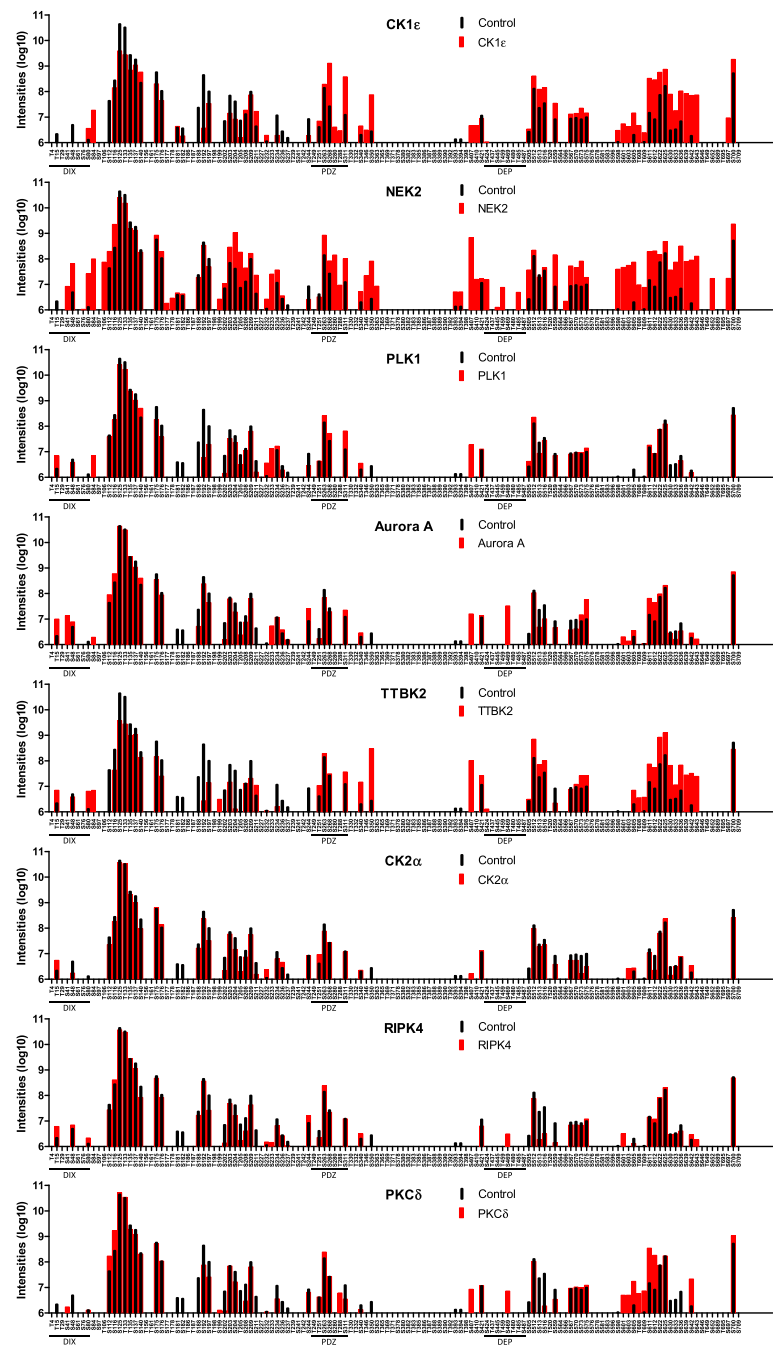


Fig. 8 Phosphoplots - phosphorylation barcodes of DVL3 with the individual kinases. Visualization of absolute intensity of phosphorylated peptides corresponding to the individual phosphorylated sites plotted on the primary sequence of DVL3 (only Ser and Thr are shown). Black bars represent a control condition, red bars the intensities in the presence of the kinase. Intensities are plotted on a log10 scale

and 6). Mutation of these residues to alanine (A) prevented the ability of CK1ε (Fig. 10c) to induce the even distribution of DVL3, in line with an earlier report [23]. Similar and even stronger effect was observed for TTBK2 suggesting that TTBK2 acts via a similar mechanism as CK1ε and that phosphorylation of S630-S643 is essential for TTBK2-induced even localization of DVL3.

Surprisingly, NEK2 efficiently promoted even localization of DVL3 in all DVL3 mutants (Fig. 10c, right). This suggested that although NEK2 strongly phosphorylates S630-S643 cluster, it is able to overcome the requirement for S630-S643 phosphorylation and efficiently induce even localization of DVL3 also via a different mechanism.

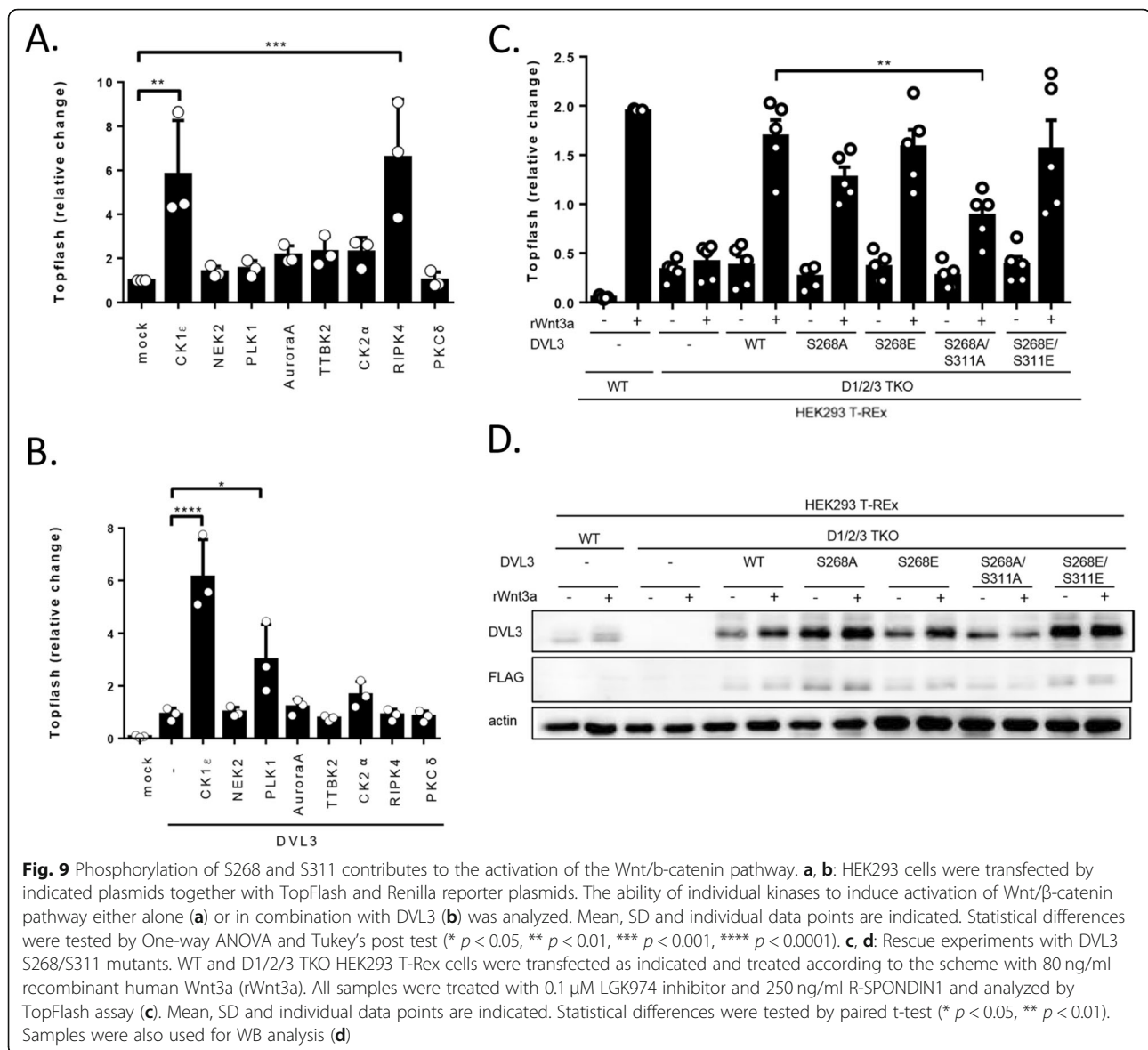


Fig. 9 Phosphorylation of S268 and S311 contributes to the activation of the Wnt/b-catenin pathway. **a, b:** HEK293 cells were transfected by indicated plasmids together with TopFlash and Renilla reporter plasmids. The ability of individual kinases to induce activation of Wnt/ β -catenin pathway either alone (**a**) or in combination with DVL3 (**b**) was analyzed. Mean, SD and individual data points are indicated. Statistical differences were tested by One-way ANOVA and Tukey's post test (* $p < 0.05$, ** $p < 0.01$, *** $p < 0.001$, **** $p < 0.0001$). **c, d:** Rescue experiments with DVL3 S268/S311 mutants. WT and D1/2/3 TKO HEK293 T-Rex cells were transfected as indicated and treated according to the scheme with 80 ng/ml recombinant human Wnt3a (rWnt3a). All samples were treated with 0.1 μ M LGK974 inhibitor and 250 ng/ml R-SPONDIN1 and analyzed by TopFlash assay (**c**). Mean, SD and individual data points are indicated. Statistical differences were tested by paired t-test (* $p < 0.05$, ** $p < 0.01$). Samples were also used for WB analysis (**d**)

Phosphorylation of S263 and S280 by NEK2 induces open conformation of DVL3

We have recently shown a correlation between the subcellular localization of DVL3 and DVL3 conformation [24]. DVL3 forms a closed conformation via an intramolecular interaction between the C-terminus and the PDZ domain [50]. To test whether a similar mechanism can overcome the requirement for phosphorylation of S630-S643 cluster by NEK2 we identified the phosphorylation sites in the PDZ domain uniquely induced by NEK2. S263 and S280 fit the criteria as the candidate sites for functional validation (see Fig. 4 and Fig. 5). In order to address the possible role of DVL3 phosphorylation-driven regulation involving S263 and S280 in vitro, we performed functional characterization by NMR. For this purpose, we exploited the well-characterized PDZ domain of human

DVL2 (aa 265–361) [51], in which S281 and S298 correspond to S263 and S280 of human DVL3. As seen in the crystal structure of the complex between DVL2 PDZ and an internal peptide ligand [52] the fully conserved S281 and S298 (Fig. 11a) reside at adjacent strands of the PDZ fold in close proximity to the peptide binding groove (Fig. 11b). From the NMR fingerprint spectra, we concluded that the phosphorylation-mimicking substitutions (S281E/S298E) did not affect the integrity of the PDZ fold (Additional file 4: Figure S4). Next, we assessed PDZ binding to a C-terminal peptide ligand derived from DVL3 (aa 698–716) by NMR titrations [24]. The residues in the binding loop region (L278 and G279) that serve as the H-bonding donors to the carboxyl sidechain of the peptide Asp sidechain undergo severe line broadening in wildtype PDZ, whereas in the phosphomimicking mutant

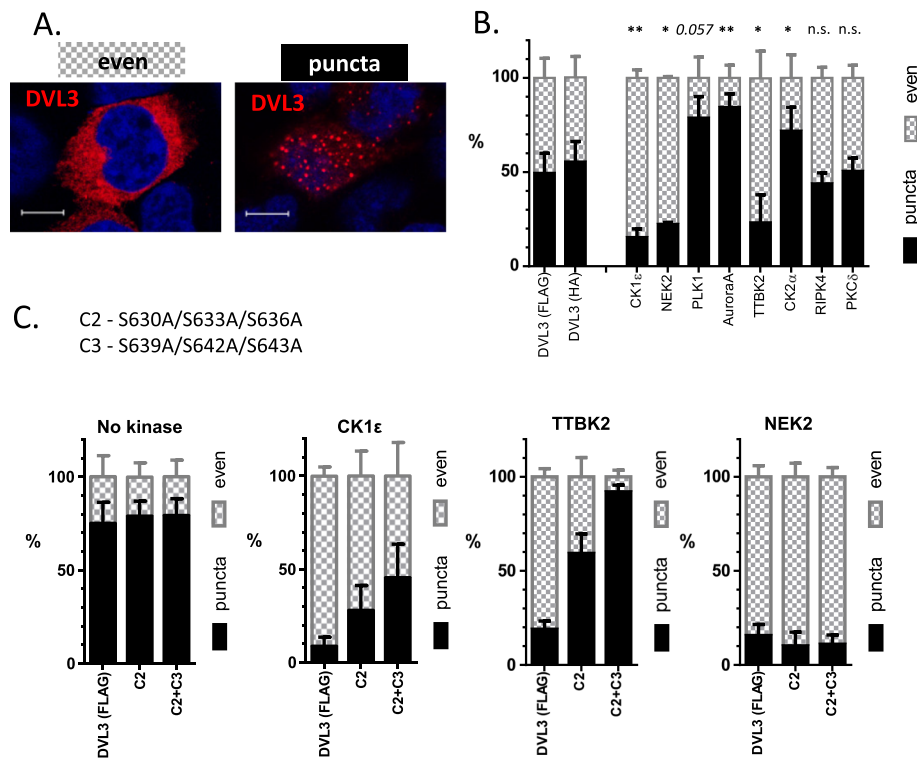


Fig. 10 Phosphorylation of S630-S643 promotes even localization of DVL3. **a:** HEK293 cells were transfected in the indicated combinations and the subcellular localization of DVL3 was assessed by immunocytochemistry. DVL3 was localized in two typical patterns – either in cytoplasmic puncta or evenly dispersed in the cytoplasm (upper panel). Scale bar, 7.5 μ m. **b:** The effects of individual kinases on DVL3 localization is shown in the bottom panel (HA-DVL3 was used for PLK1 and TTBK2, FLAG-DVL3 for the rest of kinases). **c:** Phosphorylation patterns associated with the even localization of DVL3 were analyzed by mutation of cluster of serine residues to alanine. Statistical data represent mean + SD from three independent experiments ($N = 3 \times 200$ cells). Statistical significance was confirmed by the comparison of the corresponding control (DVL3-FLAG or DVL3-HA without kinase) and DVL3 with individual kinases by One-way ANOVA and Tukey's post test (* $p < 0.05$, ** $p < 0.01$, n.s. - not significant)

experience fast exchange perturbation (Fig. 11c). Several other peaks (e.g. F277 and K301) that are largely perturbed in the course of the titration in wildtype remain unaffected in mutant (Fig. 11c). The qualitative analysis of the titration experiments indicates that the phosphomimicking S281E/S298E PDZ is insufficient in peptide binding as compared to wt PDZ (Fig. 11c). This suggests that phosphorylation of S263 and S280 (corresponding to S281 and S298 in DVL2) attenuates the capacity of PDZ domain to bind the C-terminus of DVL3 and therefore leads to open conformation of DVL3.

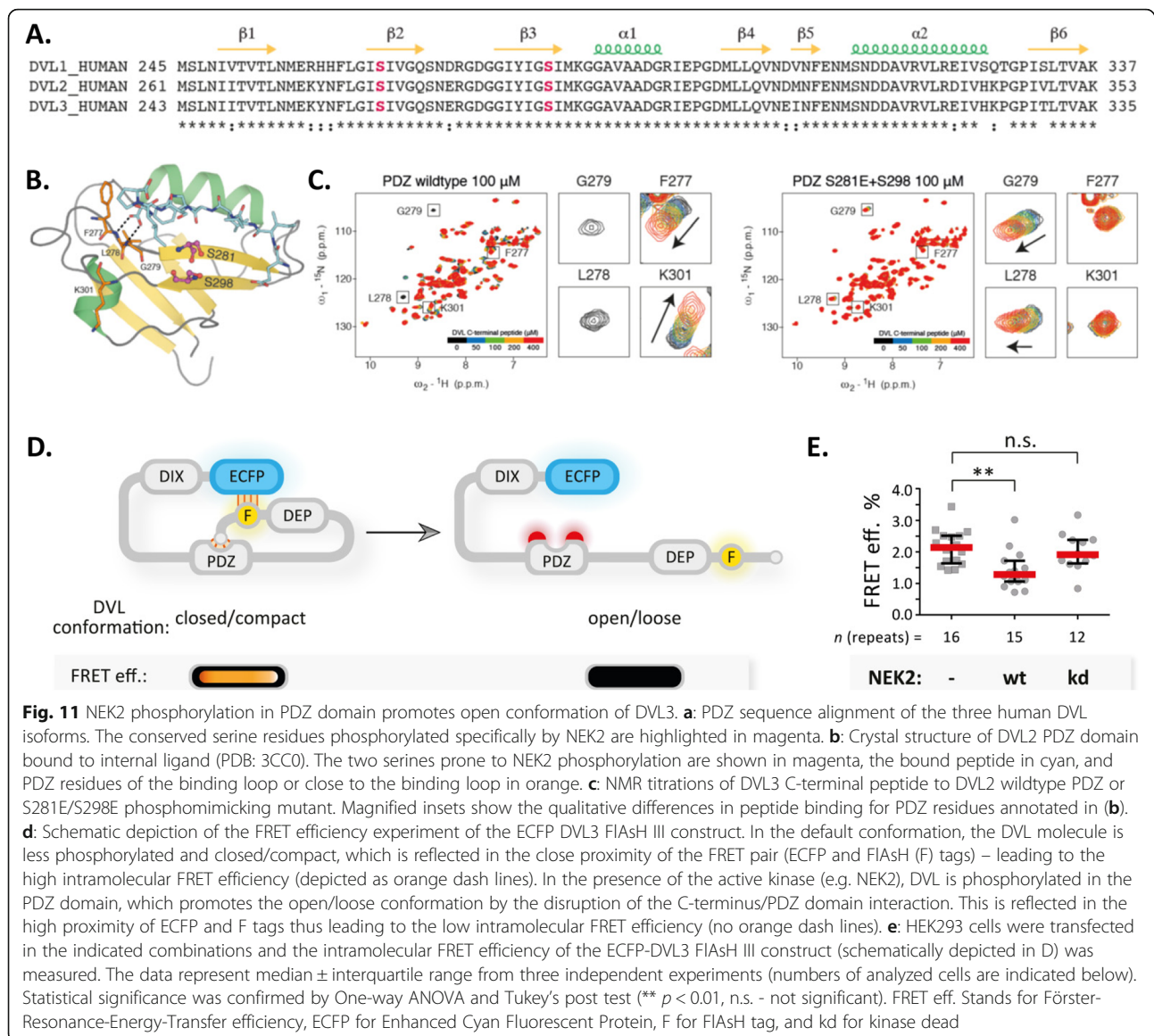
To directly test whether NEK2 indeed induces open conformation of DVL3 we employed the DVL3 FRET sensors [24]. Specifically, the ECFP-DVL3 FIAsH III sensor (schematized in Fig. 11d) was transfected in HEK293 cells either alone or in the presence of wild type (WT) and kinase dead (KD) NEK2 and subsequently, the intramolecular FRET efficiency was quantified. As shown in Fig. 11e, only WT (but not KD) NEK2 was able to lower the intramolecular FRET efficiency that depends on the proximity of the ECFP and FIAsH (F) tag. This result suggests that the kinase activity of NEK2 (and not the

presence of NEK2 itself as demonstrated by the KD variant) promotes the open conformation of DVL3. In summary with other data, we propose that NEK2-induced phosphorylation of S263 and S280 in human DVL3 prevents the interaction between DVL's C-terminus and PDZ domain, thus keeping DVL in the open conformation and more evenly distributed.

Discussion

Our study provides the first comprehensive description of DVL3 phosphorylation by most of the described DVL S/T kinases. Given the high sequence conservation of DVL3 and other DVL proteins it is an important reference point for the interpretation of published data as well as a benchmark for forthcoming studies focused on the regulation of DVL (and other proteins) function by kinases and phosphatases.

In this study we have identified TTBK2 and Aurora A as novel DVL kinases. For TTBK2 we propose a possible negative role in Wnt/ β -catenin signaling. TTBK2 is found to basal bodies or distal appendages, respectively. Indeed, DVL has been associated with centrosome and



basal bodies [6, 10, 53]. However, it does not seem to localize to distal appendages of mother centriole, where TTBK2 is recruited by CEP164 to trigger ciliogenesis [34, 40, 42–45]. It remains to be determined what is the possible interplay between TTBK2 activity and DVL3 phosphorylation by Aurora A, NEK2 and PLK1 and how these kinases together regulate DVL localization and functions in the individual phases of the cell cycle.

The parallel application of several pipelines for sample preparation and data analysis, in particular the newly introduced site occupancy analysis, demonstrated the potential to detect phosphorylation events that are biologically relevant. This approach identified S268 as signature site for CK1 ϵ , S280 as a signature site for NEK2 and S633–S643 cluster as a signature for CK1 ϵ , NEK2 and TTBK2. All these phosphorylation changes

have been validated by additional, more demanding proteomic pipelines and functional analysis.

The data collected by various approaches shown in Figs. 4, 5, 6, 7, provide a global view of DVL3 phosphorylation induced by kinases that were shown to control distinct functions of DVL. We can clearly observe codes of phosphorylated S/T in the structured domains – most typically in the PDZ domain at the fully conserved S263, S268, S280 and S311, and to a lesser extent also in the DIX and DEP domains. On the other hand, in the largely intrinsically disordered regions (IDRs) between the domains, we have detected conserved (see Fig. 6) multiphosphorylated sequences with specific phosphorylation patterns. Most intrinsically disordered proteins or regions are very S/T rich because these aa (together with A, R, G, Q, P, E and K) are

disorder-promoting. IDR-rich proteins (such as DVL) are essential components of multiple signal transduction pathways [54] and complex multiphosphorylation as shown for DVL can represent a shared and universal mechanism for the regulation of their function.

It is behind the scope of this study to test the functional consequences of all phosphorylation events. However, several interesting candidates for further analysis have been identified. For example, a striking phosphorylation pattern has been observed for two highly conserved regions between DIX and DEP domains – corresponding to S112–S140 and S188–S197. For the second cluster we were able to confirm the proteomic data by a phosphorylation-specific antibody targeted against pS192-DVL3. These sites showed high level of basal phosphorylation in the absence of any exogenously co-expressed kinase. Interestingly, expression of CK1 ϵ (and to a lesser extent TTBK2 and PLK1) dramatically reduced phosphorylation of these motifs. This suggests that there is a so far unidentified endogenous kinase that very efficiently phosphorylates these regions, and (ii) that the binding and/or phosphorylation by CK1 ϵ and TTBK2 interferes with this process or perhaps promotes removal of these phospho-moieties by activation of specific phosphatase(s). So far, only protein phosphatase 2A has been shown to have a positive function in the Wnt/ β -catenin signaling upstream of DVL [55, 56], which makes it an ideal candidate for such function.

Our functional analysis of PTMs that control subcellular localization of DVL3 showed that phosphorylation in the domains (namely PDZ) and in the IDRs can lead to the same outcome. CK1 ϵ , NEK2 and TTBK2, were the only kinases that could trigger the even distribution of DVL3 in the cytoplasm, in line with earlier reports [10, 12, 13] [20]. Interestingly, phosphorylation of the cluster S630–S643 was essential for the ability of CK1 ϵ and TTBK2 (but not of NEK2) to trigger even localization of DVL3. It appears that NEK2 uses a different mechanism dependent on the phosphorylation of S263 and S280 in the PDZ domain. Therefore, DVL C-terminus cannot bind to PDZ, which in turn stabilizes DVL3 in the open conformation. Importantly, despite the fact that the open conformation of DVL3 correlates with the even subcellular localization and more efficient recruitment to FZD receptors [24], it does not necessarily translate into the activation of the Wnt/ β -catenin signaling. Our data are rather compatible with the hypothesis that phosphorylation opens an auto-inhibited DVL conformation and then the kinase-specific barcode dictates the biological outcome. Phosphorylated S268 and S311 can be part of such barcode required for CK1 ϵ -induced activation of the Wnt/ β -catenin signaling [11, 13] whereas phosphorylated S263 and S280 are barcode components essential for the NEK2-controlled functions of DVL3 in the centrosome [10].

Conclusions

In summary, our study identified unique DVL3 phosphorylation barcodes associated with individual DVL kinases and DVL functions. Our data represent an important reference point and a toolbox for further analysis of DVL as exemplified by the functional analysis of the phosphorylation in the PDZ domain. From the more general point of view, our data pinpoint the importance of functional synergy between phosphorylation in the structured domains and in the unstructured IDRs that together dictate the biological outcome.

Supplementary information

Supplementary information accompanies this paper at <https://doi.org/10.1186/s12964-019-0470-z>.

Additional file 1: Figure S1. SDS-PAGE gels from three independent experiments. FLAG-DVL3 was overexpressed in HEK293, with or without the studied kinase, immunoprecipitated using the anti-FLAG antibody, separated on SDS-PAGE and stained with Coomassie Brilliant Blue. In red boxes are parts that were cut out.

Additional file 2: Figure S2. Phosphorylated clusters map of DVL3. All identified phosphorylated clusters obtained from the pipeline #3 are visualized as a heatmap. Mean absolute intensities of phosphorylation clusters in the control (DVL3 without exogenous kinase; six replicates) are expressed in the shades of blue. Numbers indicate decadic logarithm of the mean of 6 control samples. Nine columns represent heat map of relative change of phosphorylated peptide intensities (in log10 scale) obtained for individual kinases (relative to control). Numbers in the heat map fields (0, 1, 2, 3) indicate the number of experimental replicates with the positive identification of the given phosphorylated site.

Additional file 3: Figure S3. Cluster analysis of the individual phosphorylated sites/clusters and individual kinases. Mean phosphorylated peptide intensities (in log10 scale) standardized to control are used in the circular plot. Peptides expressed more intensively compared to control are in the shades of green, whereas less expressed peptides are in red. Dendrograms both for the kinases and the phosphosites are shown.

Additional file 4: Figure S4. NMR comparison of DVL2 PDZ wild-type and phosphorylation-mimicking mutant S281E + S298E. A. ¹H, ¹⁵N HSQC spectra of PDZ wild-type (blue) and phosphorylation-mimicking mutant S281E + S298E (red). All amide frequencies have been assigned unambiguously using 4D spectra. The e cross-peaks of wild-type and corresponding glutamic acids cross-peaks of the mutant are marked. B. Weighted chemical shift differences between PDZ wild-type and S281E + S298E mutant versus the protein sequence.

Additional file 5: Table S1. Intensities of the individual phosphorylated sites (raw data). Mean phosphorylated peptide intensities (in log10 scale) obtained for individual sample from direct (pipeline #1) and enriched analysis processed (pipeline #2) are expressed in the shades of blue. ND corresponds to not detected signals or signals with intensity below 1×10^6 .

Additional file 6: Table S2. Sequence coverage of DVL3 in the individual experiments. Sequence coverage of DVL3 obtained for individual kinases in each replicate, in individual sample (sum of all three replicates) and throughout the experiment.

Abbreviations

AB: Ammonium bicarbonate; CK: Casein kinase; DAPI: 4',6-diamidino-2-phenylindole; DMEM: Dulbecco's modified eagle's medium; DTT: Dithiotreitol; DVL: Dishevelled protein in human; ECFP: Enhanced cyan fluorescent protein; EDT: 1,2-ethanedithiol; FCS: Fetal calf serum; FIAsh: Fluorescein arsenical hairpin binder; GSK: Glycogen synthase kinase; HBSS: Hank's balanced salt

solution; HCD: Higher-energy collisional dissociation; IAA: Iodoacetamide; IDR: Intrinsically disordered region; NEK2: Nima-related kinase 2; PEG: Polyethyleneglycol; PEI: Polyethylenimine; PFA: Paraformaldehyde; PKC δ : Protein kinase C δ ; PLK1: Polo-like kinase 1; RIPK4: Receptor-interacting protein kinase 4; TCF/LEF: T-cell factor/lymphoid enhancer-binding factor; TTBK2: Tau tubulin kinase 2

Acknowledgements

We would like to thank Erich Nigg (Biozentrum, Basel) for sharing reagents, Lumir Krejci for access to DV Elite and Lucie Smyčková, Lenka Bryjová and Nada Bílá for excellent assistance.

Authors' contributions

OB, MK, MM, PP, LC and MR performed all cell-based assays, JH performed FRET assays, KH prepared samples for MS analysis and processed the data, DP performed LC-MS/MS analyses, PO performed the statistical analyses, JK performed NMR experiments and analysis, VB, KH, DP, LC, KT and ZZ planned the experiments, interpreted the data and wrote the manuscript. All authors have approved the final version.

Funding

The work was supported by grant from the Czech Science Foundation (19-28347X) to V.B., K.T. and Z.Z., and grants from Czech Science Foundation (16-03269Y and 19-05244S to L. C.); Swiss National Science Foundation (IZ11Z0_166533 to L.C.); Follow up research fund from Federation of Biochemical and Biophysical Societies (FEBS) to L.C.; M.K. was supported by Czech Science Foundation grant GA18-17658S. Furthermore, this research was supported by project CEITEC 2020 (no. LQ1601) with financial contribution from the MEYS CR and National Programme for Sustainability II to K.H. O.B. was supported by funds from the Faculty of Medicine MU to junior researcher. M.K., P.P. and J.K. were supported by Brno Ph.D. Talent Scholarship – Funded by the Brno City Municipality. CILSB research infrastructure project LM2015043 funded by MEYS CR is gratefully acknowledged for the financial support of the LC-MS/MS measurements at the Proteomics Core Facility and NMR measurements at CEITEC Josef Dadok National NMR Centre.

Availability of data and materials

Proteomic data are available via PRIDE.

Ethics approval and consent to participate

Not applicable.

Consent for publication

Not applicable.

Competing interests

The authors declare no competing interest.

Author details

¹CEITEC—Central European Institute of Technology, Masaryk University, Kamenice 5, 625 00 Brno, Czech Republic. ²National Centre for Biomolecular Research, Faculty of Science, Masaryk University, Brno, Czech Republic. ³Department of Experimental Biology, Faculty of Science, Masaryk University, Kotlářská 2, 611 37 Brno, Czech Republic. ⁴Department of Histology and Embryology, Faculty of Medicine, Masaryk University, Brno, Czech Republic. ⁵Institute of Biostatistics and Analyses, Faculty of Medicine, Masaryk University, Brno, Czech Republic. ⁶Department of Cytokinetics, Institute of Biophysics, Academy of Sciences of the Czech Republic, Brno, Czech Republic.

Received: 2 September 2019 Accepted: 22 October 2019

Published online: 23 December 2019

References

- Nusse R, Clevers H. Wnt/ β -catenin signaling, disease, and emerging therapeutic modalities. *Cell*. 2017;169(6):985–99.
- Semenov MV, Habas R, MacDonald BT, He X. SnapShot: noncanonical Wnt signaling pathways. *Cell*. 2007;131(7):1378.
- Schulte G, Bryja V. The frizzled family of unconventional G-protein-coupled receptors. *Trends Pharmacol Sci*. 2007;28(10):518–25.
- Sharma M, Castro-Piedras I, Simmons GE, Pruitt K. Dishevelled: a masterful conductor of complex Wnt signals. *Cell Signal*. 2018;47(July):52–64.
- Almuedo-Castillo M, Salo E, Adell T. Dishevelled is essential for neural connectivity and planar cell polarity in planarians. *Proc Natl Acad Sci U S A*. 2011;108(7):2813–8.
- Park TJ, Mitchell BJ, Abitua PB, Kintner C, Wallingford JB. Dishevelled controls apical docking and planar polarization of basal bodies in ciliated epithelial cells. *Nat Genet*. 2008;40(7):871–9.
- Lee KSH, Johmura Y, Yu L-R, Park J-E, Gao Y, Bang JK, et al. Identification of a novel Wnt5a-CK1 ϵ -Dvl2-Plk1-mediated primary cilia disassembly pathway. *EMBO J*. 2012;31(14):3104–17.
- Fumoto K, Kikuchi K, Gon H, Kikuchi A. Wnt5a signaling controls cytokinesis by correctly positioning ESCRT-III at the midbody. *J Cell Sci*. 2012;125(Pt 20):4822–32.
- Kikuchi K, Niikura Y, Kitagawa K, Kikuchi A. Dishevelled, a Wnt signalling component, is involved in mitotic progression in cooperation with Plk1. *EMBO J*. 2010;29(20):3470–83.
- Cervenka I, Valnohova J, Bernatik O, Harnos J, Radsetoul M, Sedova K, et al. Dishevelled is a NEK2 kinase substrate controlling dynamics of centrosomal linker proteins. *Proc Natl Acad Sci*. 2016;113(33):9304–9.
- Peters JM, McKay RM, McKay JP, Graff JM. Casein kinase I transduces Wnt signals. *Nature*. 1999;401(6751):345–50.
- Bryja V, Schulte G, Rawal N, Grahn A, Arenas E. Wnt-5a induces Dishevelled phosphorylation and dopaminergic differentiation via a CK1-dependent mechanism. *J Cell Sci*. 2007;120(4):586–95.
- Cong F, Schweizer L, Varmus H. Casein kinase I epsilon modulates the signaling specificities of dishevelled. *Mol Cell Biol*. 2004;24(5):2000–11.
- Bryja V, Schambony A, Čajánek L, Dominguez I, Arenas E, Schulte G. β -Arrestin and casein kinase 1/2 define distinct branches of non-canonical Wnt signalling pathways. *EMBO Rep*. 2008;9(12):1244–50.
- Willert K, Brink M, Wodarz A, Varmus H, Nusse R. Casein kinase 2 associates with and phosphorylates dishevelled. *EMBO J*. 1997;16(11):3089–96.
- Bernatik O, Ganji RS, Dijksterhuis JP, Konik P, Cervenka I, Polonio T, et al. Sequential activation and inactivation of Dishevelled in the Wnt/ β -catenin pathway by casein kinases. *J Biol Chem*. 2011;286(12):10396–410.
- Schertel C, Huang D, Bjorklund M, Bischof J, Yin D, Li R, et al. Systematic screening of a Drosophila ORF library in vivo uncovers Wnt/Wg pathway components. *Dev Cell*. 2013;25(2):207–19.
- Kinoshita N, Iioka H, Miyakoshi A, Ueno N. PKC delta is essential for Dishevelled function in a noncanonical Wnt pathway that regulates Xenopus convergent extension movements. *Genes Dev*. 2003;17(13):1663–76.
- Huang XD, McGann JC, Liu BY, Hannoush RN, Lill JR, Pham V, et al. Phosphorylation of dishevelled by protein kinase RIPK4 regulates Wnt signaling. *Science*. 2013;339(6126):1441–5.
- Bernatik O, Sedova K, Schille C, Ganji RS, Cervenka I, Trantírek L, et al. Functional analysis of dishevelled-3 phosphorylation identifies distinct mechanisms driven by casein kinase 1 and frizzled5. *J Biol Chem*. 2014;289(34):23520–33.
- Yanfeng WA, Berhane H, Mola M, Singh J, Jenny A, Mlodzik M. Functional dissection of phosphorylation of dishevelled in Drosophila. *Dev Biol*. 2011;360(1):132–42.
- Etheridge SL, Ray S, Li S, Hamblet NS, Lijam N, Tsang M, et al. Murine dishevelled 3 functions in redundant pathways with dishevelled 1 and 2 in normal cardiac outflow tract, cochlea, and neural tube development. *PLoS Genet*. 2008;4(11):e1000259.
- Bernatik O, Šedová K, Schille C, Ganji RS, Červenka I, Trantírek L, et al. Functional analysis of dishevelled-3 phosphorylation identifies distinct mechanisms driven by casein kinase 1 ϵ and Frizzled5. *J Biol Chem*. 2014;289(34):23520–33.
- Harnoš J, Cañizal MCA, Jurásek M, Kumar J, Holler C, Schambony A, et al. Dishevelled-3 conformation dynamics analyzed by FRET-based biosensors reveals a key role of casein kinase 1. *Nat Commun*. 2019;10(1):1–18.
- Lee KH, Johmura Y, Yu LR, Park JE, Gao Y, Bang JK, et al. Identification of a novel Wnt5a-CK1 ϵ -Dvl2-Plk1-mediated primary cilia disassembly pathway. *EMBO J*. 2012;31(14):3104–17.
- Angers S, Thorpe CJ, Biechele TL, Goldenberg SJ, Zheng N, MacCoss MJ, et al. The KLHL12-Cullin-3 ubiquitin ligase negatively regulates the Wnt- β -catenin pathway by targeting Dishevelled for degradation. *Nat Cell Biol*. 2006;8(4):348–57.
- Foldynová-Trantírková S, Sekyrová P, Tmejová KK, Brumovská E, Bernatik OO, Blankenfeldt W, et al. Breast cancer-specific mutations in CK1epsilon inhibit

- Wnt/beta-catenin and activate the Wnt/Rac1/JNK and NFAT pathways to decrease cell adhesion and promote cell migration. *Breast Cancer Res.* 2010; 12(3):1–14.
28. Fry AM, Meraldi P, Nigg EA. A centrosomal function for the human Nek2 protein kinase, a member of the NIMA family of cell cycle regulators. *EMBO J.* 1998;17(2):470–81.
 29. Golsteyn RM, Schultz SJ, Bartek J, Ziemiecki A, Ried T, Nigg EA. Cell cycle analysis and chromosomal localization of human Plk1, a putative homologue of the mitotic kinases *Drosophila polo* and *Saccharomyces cerevisiae Cdc5*. *J Cell Sci.* 1994;107(Pt 6):1509–17.
 30. Meraldi P, Honda R, Nigg EA. Aurora-a overexpression reveals tetraploidization as a major route to centrosome amplification in p53–/– cells. *EMBO J.* 2002;21(4):483–92.
 31. Turowec JP, Duncan JS, French AC, Gyenis L, St. Denis NA, Vilk G, et al. Protein kinase CK2 is a constitutively active enzyme that promotes cell survival: strategies to identify CK2 substrates and manipulate its activity in mammalian cells. *Methods Enzymol.* 2010;484:471–93.
 32. Kajimoto T, Sawamura S, Tohyama Y, Mori Y, Newton AC. Protein kinase C (delta)-specific activity reporter reveals agonist-evoked nuclear activity controlled by Src family of kinases. *J Biol Chem.* 2010;285(53):41896–910.
 33. Bertrand MJM, Lippens S, Staes A, Gilbert B, Roelandt R, De Medts J, et al. cIAP1/2 Are Direct E3 Ligases Conjugating Diverse Types of Ubiquitin Chains to Receptor Interacting Proteins Kinases 1 to 4 (RIP1–4). *Gartel AL, editor. PLoS One.* 2011;6(9):e22356.
 34. Čajánek L, Nigg EA. Cep164 triggers ciliogenesis by recruiting tau tubulin kinase 2 to the mother centriole. *Proc Natl Acad Sci U S A.* 2014;111(28):E2841–50.
 35. Yan X, Habedanck R, Nigg EA. A complex of two Centrosomal proteins, CAP350 and FOP, cooperates with EB1 in microtubule anchoring. *Mol Biol Cell.* 2006;17(2):634–44.
 36. Hoffmann C, Gaietta G, Bünnemann M, Adams SR, Oberdorff-Maass S, Behr B, et al. A FRET-based approach to determine G protein-coupled receptor activation in living cells. *Nat Methods.* 2005;2(3):171–6.
 37. Evangelidis T, Nerli S, Nováček J, Brereton AE, Karplus PA, Dotas RR, et al. Automated NMR resonance assignments and structure determination using a minimal set of 4D spectra. *Nat Commun.* 2018;9(1):384.
 38. Stejskal K, Potěšil D, Zdráhal Z. Suppression of peptide sample losses in autosampler vials. *J Proteome Res.* 2013;12(6):3057–62.
 39. Chaki M, Airik R, Ghosh AKK, Giles RHH, Chen R, Slaats GGG, et al. Exome capture reveals ZNF423 and CEP164 mutations, linking renal ciliopathies to DNA damage response signaling. *Cell.* 2012;150(3):533–48.
 40. Goetz SC, Liem KF, Anderson KV. The spinocerebellar ataxia-associated gene tau tubulin kinase 2 controls the initiation of ciliogenesis. *Cell.* 2012;151(4):847–58.
 41. Tanos BE, Yang HJ, Soni R, Wang WJ, Macaluso FP, Asara JM, et al. Centriole distal appendages promote membrane docking, leading to cilia initiation. *Genes Dev.* 2013;27(2):163–8.
 42. Oda T, Chiba S, Nagai T, Mizuno K. Binding to Cep164, but not EB1, is essential for centriolar localization of TTBK2 and its function in ciliogenesis. *Genes Cells.* 2014;19(12):927–40.
 43. Xu Q, Zhang Y, Wei Q, Huang Y, Hu J, Ling K. Phosphatidylinositol phosphate kinase PIPKγ and phosphatase INPP5E coordinate initiation of ciliogenesis. *Nat Commun.* 2016;7:10777.
 44. Yang TT, Chong WM, Wang WJ, Mazo G, Tanos B, Chen Z, et al. Super-resolution architecture of mammalian centriole distal appendages reveals distinct blade and matrix functional components. *Nat Commun.* 2018;9(1):2023.
 45. Huang N, Zhang D, Li F, Chai P, Wang S, Teng J, et al. M-phase Phosphoprotein 9 regulates ciliogenesis by modulating CP110-CEP97 complex localization at the mother centriole. *Nat Commun.* 2018;9(1):4511.
 46. Bryja V, Červenka I, Čajánek L. The connections of Wnt pathway components with cell cycle and centrosome: side effects or a hidden logic? *Crit Rev Biochem Mol Biol.* 2017;52(6):614–37.
 47. Pačliková P, Bernatik O, Radaszkiewicz TW, Bryja V. The N-Terminal Part of the Dishevelled DEP Domain Is Required for Wnt/β-Catenin Signaling in Mammalian Cells. *Mol Cell Biol.* 2017;37(18).
 48. Kishida M, Hino SS, Michiue T, Yamamoto H, Kishida S, Fukui A, et al. Synergistic activation of the Wnt signaling pathway by Dvl and casein kinase Iε. *J Biol Chem.* 2001;276(35):33147–55.
 49. Schwarz-Romond T, Fiedler M, Shibata N, Butler PJ, Kikuchi A, Higuchi Y, et al. The DIX domain of Dishevelled confers Wnt signaling by dynamic polymerization. *Nat Struct Mol Biol.* 2007;14(6):484–92.
 50. Lee HJ, Shi DL, Zheng JJ. Conformational change of Dishevelled plays a key regulatory role in the Wnt signaling pathways. *Elife.* 2015;4:e08142.
 51. Gammons MV, Rutherford TJ, Steinhart Z, Angers S, Bienz M. Essential role of the Dishevelled DEP domain in a Wnt-dependent human-cell-based complementation assay. *J Cell Sci.* 2016;129(20):3892–902.
 52. Zhang Y, Appleton BA, Wiesmann C, Lau T, Costa M, Hannoush RN, et al. Inhibition of Wnt signaling by Dishevelled PDZ peptides. *Nat Chem Biol.* 2009;5(4):217–9.
 53. Gupta GD, Coyaude É, Gonçalves J, Mojarad BA, Liu Y, Wu Q, et al. A dynamic protein interaction landscape of the human centrosome-cilium Interface. *Cell.* 2015;163(6):1483–99.
 54. Wright PE, Dyson HJ. Intrinsically disordered proteins in cellular signalling and regulation. *Nat Rev Mol Cell Biol.* 2015;16(1):18–29.
 55. Yang J, Wu J, Tan C, Klein PS. PP2A:B56ε is required for Wnt/beta-catenin signaling during embryonic development. *Development.* 2003; 130(23):5569–78.
 56. Ratcliffe MJ, Itoh K, Sokol SY. A positive role for the PP2A catalytic subunit in Wnt signal transduction. *J Biol Chem.* 2000;275(46):35680–3.

Publisher's Note

Springer Nature remains neutral with regard to jurisdictional claims in published maps and institutional affiliations.

Ready to submit your research? Choose BMC and benefit from:

- fast, convenient online submission
- thorough peer review by experienced researchers in your field
- rapid publication on acceptance
- support for research data, including large and complex data types
- gold Open Access which fosters wider collaboration and increased citations
- maximum visibility for your research: over 100M website views per year

At BMC, research is always in progress.

Learn more biomedcentral.com/submissions



Appendix 11

Renzova T, Bohaciakova D, Esner M, Pospisilova V, Barta T, Hampl A, **Čajánek L***. Inactivation of PLK4-STIL Module Prevents Self-Renewal and Triggers p53-Dependent Differentiation in Human Pluripotent Stem Cells. *Stem Cell Reports*. 2018 Oct 9;11(4):959-972. doi: 10.1016/j.stemcr.2018.08.008. (JCR 2018, IF= 5.499, Q1 – Cell Biology)



Inactivation of PLK4-STIL Module Prevents Self-Renewal and Triggers p53-Dependent Differentiation in Human Pluripotent Stem Cells

Tereza Renzova,¹ Dasa Bohaciakova,¹ Milan Esner,^{1,2} Veronika Pospisilova,¹ Tomas Barta,¹ Ales Hampl,^{1,3} and Lukas Cajanek^{1,*}

¹Department of Histology and Embryology, Masaryk University, Faculty of Medicine, Brno 625 00, Czech Republic

²Cellular Imaging Core Facility, Central European Institute of Technology (CEITEC), Masaryk University, Brno 625 00, Czech Republic

³International Clinical Research Center, St. Anne's University Hospital, Brno 656 91, Czech Republic

*Correspondence: lukas.cajanek@gmail.com

<https://doi.org/10.1016/j.stemcr.2018.08.008>

SUMMARY

Centrioles account for centrosomes and cilia formation. Recently, a link between centrosomal components and human developmental disorders has been established. However, the exact mechanisms how centrosome abnormalities influence embryogenesis and cell fate are not understood. PLK4-STIL module represents a key element of centrosome duplication cycle. We analyzed consequences of inactivation of the module for early events of embryogenesis in human embryonic stem cells (hESCs) and human induced pluripotent stem cells (hiPSCs). We demonstrate that blocking of PLK4 or STIL functions leads to centrosome loss followed by both p53-dependent and -independent defects, including prolonged cell divisions, upregulation of p53, chromosome instability, and, importantly, reduction of pluripotency markers and induction of differentiation. We show that the observed loss of key stem cells properties is connected to alterations in mitotic timing and protein turnover. In sum, our data define a link between centrosome, its regulators, and the control of pluripotency and differentiation in PSCs.

INTRODUCTION

The centrosome, an organelle named by Theodor Boveri at the end of the 19th century, has been studied for a long time, but its functions and mechanisms of regulation are still incompletely understood. The centrosome typically acts as a microtubule organizing center (MTOC), taking part in cell division, cell shape organization, and cell motility (Conduit et al., 2015; Khodjakov and Rieder, 2001; Piel et al., 2001). Its core consists of two centrioles, microtubule-based structures with nine-fold radial symmetry, embedded in a protein matrix termed pericentriolar material (Bornens and Gönczy, 2014; Nigg and Stearns, 2011).

The centrosome duplicates once per cell cycle. As a cell divides, each daughter cell inherits one centrosome, so its number in the cells remains stable, similar to DNA content (Bornens and Gönczy, 2014; Nigg and Stearns, 2011). To date, hundreds of centrosomal proteins participating in centrosome biogenesis have been identified (Andersen et al., 2003; Gupta et al., 2015), with PLK4-STIL module having a pivotal role in the orchestration of centriole duplication (Arquint and Nigg, 2016; Bettencourt-Dias et al., 2005; Habedanck et al., 2005; Tang et al., 2011).

Overexpression of essential centrosome regulators, including PLK4, leads to centrosome amplification, whereas their depletion causes loss of centrosomes (Bazzi and Anderson, 2014; Bettencourt-Dias et al., 2005; Habedanck et al., 2005; Leidel et al., 2005; Strnad et al., 2007; Tang et al., 2011). Deregulation of the centrosome duplica-

tion cycle is implicated in the etiology of various disorders such as ciliopathies, microcephaly, primordial dwarfism, and cancer (Chavali et al., 2014; Gambarotto and Basto, 2016; Gönczy, 2015; Nigg et al., 2014). However, the consequences of centrosome abnormalities for cell fate have started to be revealed only recently. Inhibition of PLK4 depletes centrioles in various human somatic cell lines, leading to p53-dependent G₁ arrest (Lambrus et al., 2015; Wong et al., 2015). In contrast, *in vivo* study using *Drosophila* demonstrated that centrosomes are not required for a substantial part of fly embryogenesis (Basto et al., 2006). The requirement for correct embryo development has been further addressed in mice. Mouse embryos without centrosomes die during gestation (Bazzi and Anderson, 2014; Hudson et al., 2001; Israeli et al., 1999), and amplification of centrosomes after PLK4 overexpression in developing mouse brain leads to microcephaly-like phenotype (Marthiens et al., 2013). That being said, it is becoming clear that cellular outcomes of centrosome abnormalities differ between different models and perhaps even specific cell types (Basto et al., 2008; Levine et al., 2017; Marthiens et al., 2013; Vitre et al., 2015).

Human pluripotent stem cells (PSCs) encompassing both human embryonic stem cells (hESCs) and human induced pluripotent stem cells (hiPSCs) are able to self-renew and to differentiate into all cell types in the human body (Takahashi et al., 2007; Thomson et al., 1998). Pluripotency, governed by a network of transcription factors including OCT-4, SOX-2, and NANOG (Jaenisch and Young, 2008; Kashyap et al., 2009), is tightly connected to cell-cycle



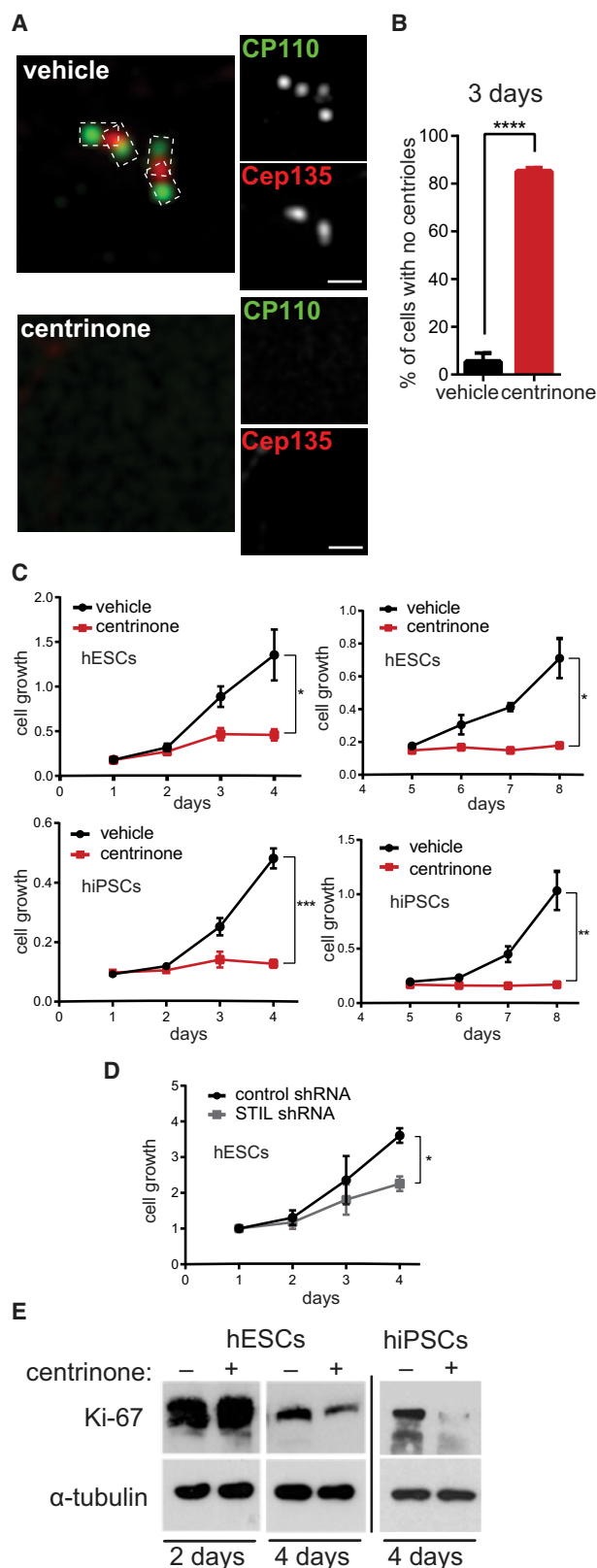


Figure 1. Blocking of PLK4 or STIL Leads to Centrosome Loss Followed by Decreased Proliferation of Stem Cells

(A and B) Immunofluorescence (A) of 3-day vehicle- and centrinone-treated hESCs: centrosomes were visualized by antibody staining of distal marker CP110 (green) and proximal marker Cep135 (red). Scale bars, 1 μ m. (B) Quantification of centrosome depletion, $N > 150$.

(C and D) Growth curves: cell number was measured at indicated time points by crystal violet assay, in vehicle- and centrinone-treated cells (C) or after STIL shRNA transfection (D).

(E) Western blot analyses of Ki-67 expression in 4-day vehicle- and centrinone-treated cells, with α -tubulin as a loading control.

Data are presented as mean \pm SEM (* $p < 0.05$, ** $p < 0.005$, *** $p < 0.001$, **** $p < 0.0001$). See also Figure S1.

regulation (Becker et al., 2006; Pauklin and Vallier, 2013). Importantly, hESCs/hiPSCs hold great promise to model both physiological and pathophysiological aspects of human embryogenesis (Lancaster et al., 2013; Park et al., 2008; Shahbazi et al., 2016). Noteworthy, early passages of human PSCs seem prone to centrosome abnormalities (Brevini et al., 2009; Holubcová et al., 2011). Given these unique properties, we elected to investigate the consequences of halted centrosome duplication cycle in early embryonic events using hESCs and hiPSCs.

Here, we present our analyses of molecular and functional consequences of the inactivation of PLK4-STIL module and centrosome loss for human PSCs. We show that upon centrosome loss, the cells are in principle still able to undergo cell division. Such acentrosomal mitosis is twice as long and leads to mitotic errors and p53 stabilization, which is reflected by gradual loss of self-renewal potential. Interestingly, the observed p53 increase does not lead to significant apoptosis, but to loss of pluripotency and induction of differentiation. Finally, our data demonstrate that the loss of pluripotency regulators after PLK4 inhibition is p53-independent and linked to altered protein turnover.

RESULTS

Blocking of PLK4 or STIL Leads to Centrosome Loss Followed by Decreased Proliferation of Stem Cells

To assess the role of centrosomes in PSCs we used a PLK4 inhibitor, centrinone (Wong et al., 2015). First, we examined the efficacy of centrosome depletion in hESCs following treatment with centrinone. Using immunofluorescence staining for proximal centriolar marker Cep135 (Kleylein-Sohn et al., 2007) and distal centriolar marker CP110 (Chen et al., 2002), we detected the loss of centrosomes in about 40% of hESCs after 2 days (Figures S1A and S1B), and after 3 days the centrosome was depleted in almost 85% of hESCs (Figures 1A and 1B). We were also able to deplete centrosomes in hESCs using PLK4 or STIL short hairpin RNA (shRNA) (Figures S1C and S1D).



It has been recently demonstrated that the loss of centrosomes is detrimental for proliferation of non-transformed human somatic cells, but has little effect on cancer cells (Fong et al., 2016; Lambrus et al., 2015; Meitinger et al., 2016; Mikule et al., 2007; Wong et al., 2015). Given reported similarities in cycle control between embryonic stem cells and cancer cells (Kim et al., 2010), we examined consequences of centrosome depletion for PSC proliferation. Intriguingly, centrinone-treated hESCs/hiPSCs showed impaired proliferation from day 2 and virtually halted their growth past day 5 (Figure 1C). In addition, we also observed a negative effect on proliferation of hESCs following STIL knockdown (Figure 1D). Noteworthy, the negative effect of centrosome loss on proliferation was even more pronounced in the case of hESC-derived neural stem cells (NSCs) (Figure S1E). On the other hand, centrinone treatment showed only a minor effect on proliferation of U2OS cells (Figure S1F), in agreement with the previous report (Wong et al., 2015), even though the efficiency of centrosome depletion was comparable with that of hESCs (Figure S1G).

To corroborate this result, we examined the expression of Ki-67, a marker of proliferating cells. As shown in Figure 1E, centrinone treatment reduced expression levels of Ki-67. In addition, a decrease in the number of Ki-67⁺ cells was detected in the centrinone condition also by immunofluorescence (Figure S1H, quantified in Figure S1I).

Centrosome Depletion Following PLK4 or STIL Blocking Leads to Prolonged Mitosis and Mitotic Defects

Centrosome loss has been reported to cause various mitotic defects in somatic cell lines (Sir et al., 2013; Wong et al., 2015). Indeed, we noted accumulation of rounded cells in the centrinone-treated cultures and following STIL knockdown (Figure 2A). Furthermore, our subsequent fluorescence-activated cell sorting (FACS) analysis proved that centrinone treatment leads to accumulation of hESCs/hiPSCs in G₂/M phase (Figures 2B and 2C).

Next, we analyzed the length of mitosis by live imaging of the reporter H2A-GFP line derived from the same paternal hESC line. As shown in Figure 2D, completion of mitosis between days 2 and 4 took for the treated cells approximately twice as long as controls. In addition, centrinone-treated hESCs showed 1.5-fold prolonged interphase on day 3 compared with control (Figure 2E). All these data indicated an intriguing possibility that centrosome-less hESCs are viable and able to divide, even though for a limited time for the latter. In agreement with this hypothesis we found bipolar mitotic spindles even in acentrosomal cells (Figure S2A). In addition, we quantified the number of cells successfully finishing mitosis in our live imaging experiments. We focused on mitoses past the third

day of centrinone treatment, when the majority of treated cells already lacks centrosomes (Figures 1A and 1B). Interestingly, we found 68.1% ± 1.9% of cells able to successfully go through mitosis within the 30-hr period we examined. This observation suggested that acentrosomal mitoses seem possible, but also confirmed our earlier observation (Figure 1C) that proliferation after centrosome loss is inefficient (note 1.5 times longer interphase of centrinone-treated cells; Figure 2E). In addition, we observed cytokinesis failure in approximately 15% of divisions (Figure S2D). To fully prove that acentrosomal hESCs can divide, we performed live imaging experiments with γ -tubulin-GFP hESCs following centrinone treatment (Figure S2G). To conclude, these data argue that centrosome-depleted hESCs are in principle able to successfully finish mitotic division and give rise to two daughter cells, albeit only for a limited time.

In the course of our experiments we noted that nuclei of centrinone-treated cells became bigger and acquired morphology different from control. In agreement with this, FACS analysis detected a modest increase of aneuploid cells after 3 days of centrinone treatment (Figures S2B and S2C). Since it is not possible to distinguish diploid cells residing in G₂/M phase from tetraploid cells residing in G₁ phase (Figures 2B and 2C) using this approach, it prompted us to quantify the chromosome number. The analysis was done at day 4, when the changes in cell morphology observed during live imaging were most pronounced. Previous work indicated that while centrosome loss during mouse embryogenesis does not lead to notable aneuploidy (Bazzi and Anderson, 2014), somatic cell lines show an increase in chromosomal abnormalities after the centrosome loss (Sir et al., 2013; Wong et al., 2015). Interestingly, our analyses revealed that centrinone treatment of hESCs/hiPSCs led to changes in chromosome number (Figure 2F), arguing that centrosome loss promotes genome instability in PSCs.

Next, to elucidate the survival potential of centrinone-treated cells, we assessed the number of early and late apoptotic cells by annexin V and propidium iodide (PI) staining. We found a modest difference in the number of viable (annexin V/PI negative) cells between centrinone condition and control (Figure 2G). Intriguingly, the proportion of apoptotic cells was notably elevated in hESC-derived NSCs following the centrinone treatment, in contrast to similarly treated cultures of hESCs/hiPSCs (Figure S2E). In addition, we compared the effects of centrinone with those of etoposide, a commonly used DNA-damage-inducing agent. Interestingly, while etoposide triggered a pronounced increase of apoptotic cells in hESC/hiPSC cultures, the percentage of apoptotic cells in centrinone-treated NSCs was similar to the NSC etoposide condition (Figure S2F).

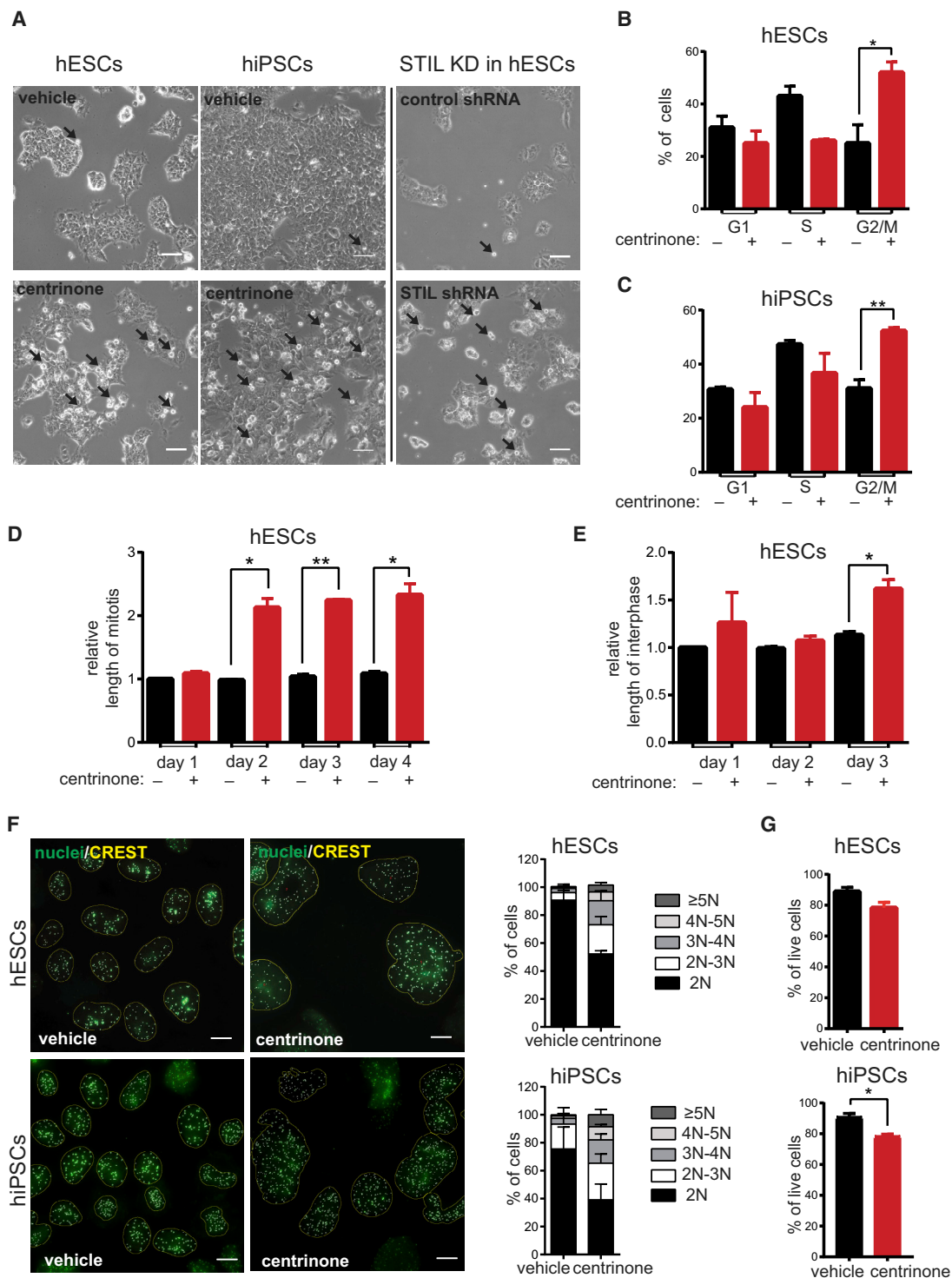


Figure 2. Centrosome Depletion Following PLK4 or STIL Blocking Leads to Prolonged Mitosis and Mitotic Defects

(A) Phase-contrast images of 2-day vehicle- and centrinone-treated hESCs and hiPSCs or 2 days after STIL shRNA transfection. Arrows indicate mitotic cells. Scale bars, 50 μ m.

(B–E) Cell-cycle distribution of 3-day vehicle- and centrinone-treated hESCs (B) or hiPSCs (C) analyzed by FACS. Measurement of relative length of mitosis (D) or interphase (E) by live imaging of H2A-GFP hESCs after indicated time of treatment. Data are normalized to the vehicle treatment condition on day 1 ($n = 2$, $N > 40$).

(legend continued on next page)



Blocking PLK4 or STIL Promotes Stem Cell Differentiation

Key aspects of PSC biology, the ability to self-renew and to differentiate, are intimately connected to cell-cycle regulation (Becker et al., 2006; Pauklin and Vallier, 2013). Given the phenotypes we found, we examined the impact of centrosome depletion after blocking PLK4 or STIL on those two features.

First, we observed that centrinone-treated cells lost typical stem cell morphology (Figure 3A), suggesting that centrosome loss affects stem cell differentiation. In agreement with this observation, we found a defect in polymerization of microtubules in centrosome-depleted hESCs (Figure S3A). Next, we examined expression of differentiation makers: ectodermal marker PAX-6, endodermal marker GATA-6, and mesodermal marker brachyury. Indeed, mRNA levels of all examined markers were upregulated after centrinone treatment (Figure 3B). Similar effects were confirmed also on the protein level (Figures 3C and S3B). Importantly, our analyses further revealed that protein levels of pluripotency markers OCT-4 and NANOG were decreased in centrinone-treated cells (Figures 3C and S3B). In addition, we detected higher protein levels of p53 in the centrinone conditions, thus confirming and extending previous observations on centrosome loss in somatic cells and mouse embryos (Bazzi and Anderson, 2014; Insolera et al., 2014; Lambrus et al., 2015; Mikule et al., 2007; Wong et al., 2015). Similar effects were also observed after PLK4/STIL shRNA (Figures S3C–S3E). Of note, we did not find a correlation between levels of aneuploidy and brachyury expression (Figures S3F and S3G).

Next, we examined centrinone effects in relation to those of retinoic acid (RA), a commonly used differentiation agent. Intriguingly, upregulation of p53 after centrosome loss was even higher than the effect of RA (Figure S3I). Furthermore, combination of centrinone and RA treatments enhanced PAX-6 protein levels, if compared with either RA treatment alone or untreated condition (Figure S3H).

In the course of our experiments we noted a temporal increase of Ser139 phosphorylated H2AX, a hallmark of DNA-damage response (DDR) (Rogakou et al., 1998) (Figure S3J). Given that DDR typically acts upstream of p53 activation (Brooks and Gu, 2010), we examined a possible role for DDR kinases in the observed increase of p53 levels. However, inhibition of ATM, ATR, and DNA-PK did not prevent the increase (Figure S3K). These data suggest that accumu-

lation of p53 after PLK4 or STIL blocking-induced centrosome loss in hESCs is independent of DDR signaling.

Given this result, we considered alternative routes of p53 upregulation. First, we found that knockdown of *dicer-1*, a key regulator of microRNA biogenesis, does not prevent p53 upregulation (Figure S3L), indicating that microRNA machinery is not involved in the p53 activation. Next, using cycloheximide (CHX) to block translation, we found that p53 protein moiety is stabilized following centrinone treatment (Figure 3D). Furthermore, we examined effect of prolonged mitosis on p53 stabilization. To mimic the effect of centrosome depletion on the mitotic length, we treated hESCs for 2 hr (Figure S3M) or hESCs/hiPSCs for 6 hr by nocodazole to arrest them in mitosis, isolated mitotic cells by shake-off, then released them by washout and analyzed them 2 days following release. Remarkably, we found upregulated p53, brachyury, and GATA-6 in cells that experienced temporal mitotic arrest (Figure 3E). Of note, we occasionally observed an increase also in PAX-6 levels (Figure 3E), perhaps reflecting requirement of concomitant downregulation of OCT4/NANOG for the efficient PAX-6 induction (see Figure S4B). Importantly, cells treated with nocodazole, but not passing through mitotic arrest (“Noco-leftover”), showed expression of examined markers at levels comparable with that of control. Thus, the data demonstrate that prolonged mitosis is sufficient to trigger p53 upregulation and cell differentiation.

Differentiation Induced by Blocking of PLK4 or STIL Is p53 Dependent

Previous studies linked p53 to induction of differentiation in PSCs (Jain et al., 2012; Lin et al., 2005; Qin et al., 2007; Zhang et al., 2014). On the other hand, there are contradictory reports about the expression and/or activity of p53 in hESCs/hiPSCs (Aladjem et al., 1998; Maimets et al., 2008; Momcilovic et al., 2009; Qin et al., 2007; Wang et al., 2016; Zhang et al., 2014). To examine the role of p53 in the differentiation observed in our experiments, we first downregulated it using small interfering RNA (siRNA) (Figure 4A). We found that the knockdown of p53 has no apparent effect on mitotic cell accumulation following centrinone treatment (Figure 4B). Importantly, downregulation of p53 expression by either siRNA in hESC cultures or CRISPR/Cas9 system (p53 low hESCs/hiPSCs) only partially rescued the proliferation defect seen after centrosome loss (Figure 4C). Thus, these results not only

(F) Immunofluorescence analyses of centromere number in 4-day vehicle- or centrinone-treated hESCs and hiPSCs. Centromeres were visualized by CREST staining (yellow), nuclei were counterstained by Hoechst (green). Scale bars, 10 μ m. Panels on the right show centromere quantification and corresponding intervals of chromosome numbers ($n = 2$, $N > 90$).

(G) Quantification of viability measurement by annexin V/PI staining in 2-day vehicle- and centrinone-treated hESCs and hiPSCs. Data are presented as mean \pm SEM (* $p < 0.05$, ** $p < 0.005$). See also Figure S2.

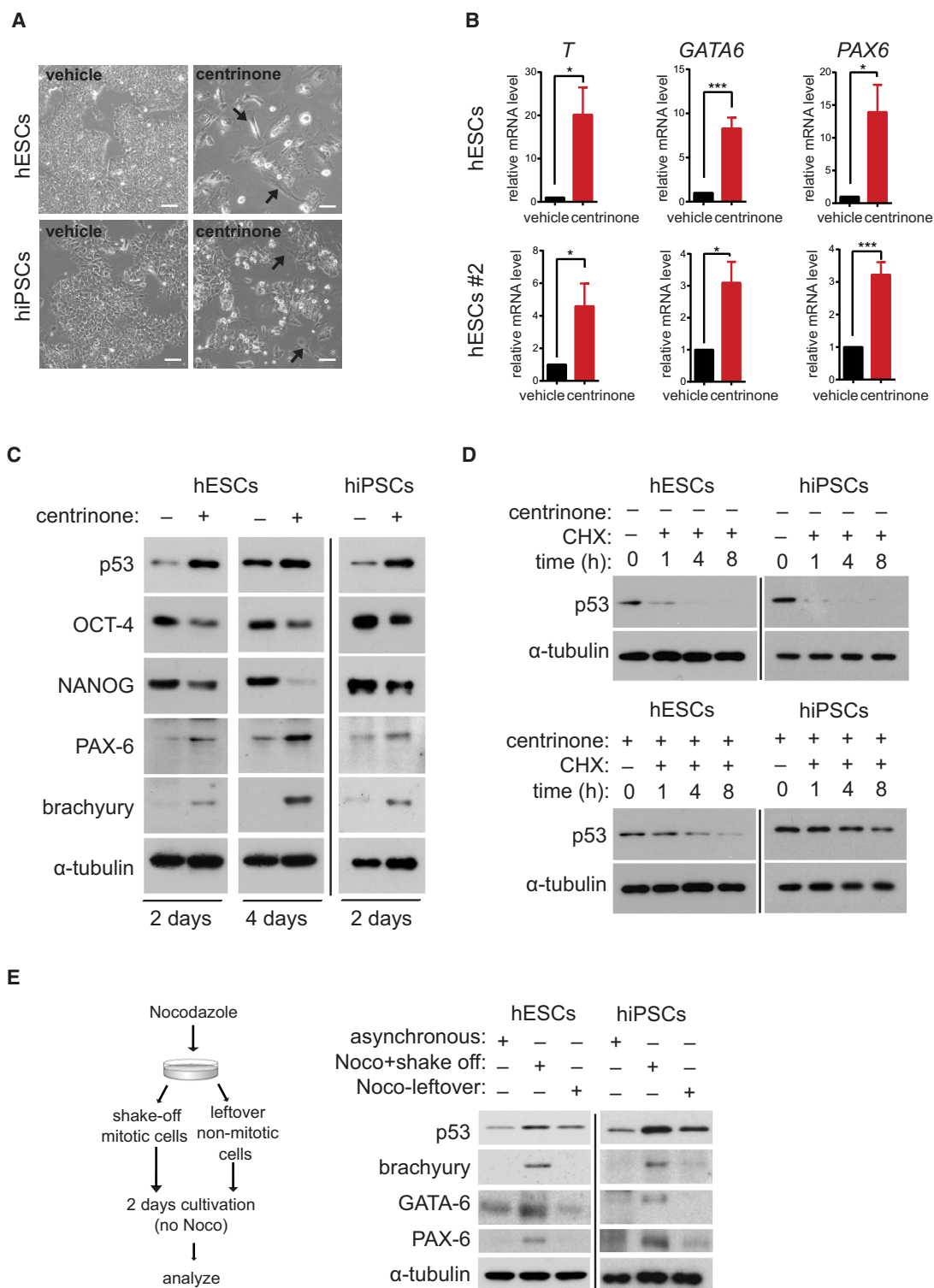


Figure 3. Blocking PLK4 or STIL Promotes Stem Cell Differentiation

(A) Phase-contrast images of hESCs or hiPSCs after 8 or 4 days of treatment, respectively. Arrows point to observed morphological changes. Scale bars, 50 μ m.

(B) Analyses of mRNA levels of *T*, *GATA6*, and *PAX6* in hESCs and hESCs #2 after 4 days of treatment. Data are presented as relative fold change over control.

(legend continued on next page)



confirmed and extended previous observations from somatic cells (Fong et al., 2016; Lambrus et al., 2016; Meitinger et al., 2016; Wong et al., 2015), but also suggested the interesting possibility that some of the phenotypes caused by centrinone treatment in hESCs/hiPSCs might be p53 independent. To this end, we examined the requirement of p53 for centrosome loss-induced differentiation of PSCs. We found that depletion of p53 prevented the upregulation of *T* and *PAX6* mRNA in hESCs (Figure 4D). Furthermore, centrinone treatment led to higher protein levels of brachyury in control condition, but not in cells with depleted p53 by siRNA (Figure 4E). Intriguingly, expression of OCT-4 was not rescued by p53 depletion. To corroborate this finding, we performed a similar experiment using p53 low hESCs/hiPSCs (Figures 4F and 4G). As expected, we found full dependency of the induction of brachyury expression on the presence of p53. Importantly, however, OCT-4 protein was downregulated even in conditions without detectable levels of p53 (Figure 4F). Thus, these data demonstrated that the induction of differentiation markers after centrinone-mediated centrosome loss requires p53, while the loss of pluripotency markers is p53 independent.

Loss of Pluripotency after PLK4 Inhibition and Centrosome Depletion Is Linked to Altered Protein Turnover

To elucidate the mechanism responsible for the downregulation of regulators of pluripotency after centrinone treatment, we first analyzed its effects on *POU5F1* and *NANOG* mRNA levels. Surprisingly, we found no difference in either *POU5F1* or *NANOG* mRNA levels (Figure S4A). This result indicated post-transcriptional regulation and prompted us to examine protein stability of OCT-4/*NANOG*. Interestingly, we found increased turnover of OCT-4/*NANOG* in the centrinone-treated hESCs (Figure 5A). Given that levels of p53 and β -catenin, included as controls in our experiments, did not follow the same trend as OCT-4/*NANOG*, these data confirmed the specificity of the effect. Next, we examined whether prolonged mitosis, induced by nocodazole, is sufficient to alter turnover of OCT-4/*NANOG*. However, in contrast to the effects seen on upregulation of p53 and other differentiation markers (Figure 3E), prolonged mitosis did not show an effect on OCT-4/*NANOG* turnover (Figure S4B).

To identify the degradation pathway responsible for turnover of OCT-4/*NANOG*, we used MG132 and chloroquine, inhibitors of proteasome and lysosome, respectively. While the treatment with chloroquine showed no effect (Figure S4C), addition of MG132 to CHX-treated cells showed a rescue effect on the drop in protein levels of OCT-4 and *NANOG*, indicating that these transcription factors are subjected to proteasomal degradation in both control and centrinone-treated cells (Figures 5B and S4C). As PLK4 was shown to regulate protein turnover of SAS-6 (Puklowski et al., 2011), we examined its possible direct role in turnover of OCT-4. First we tested that washing out centrinone is sufficient for reactivation of PLK4 in hESCs (Figures S4D–S4G), in agreement with previous reports on somatic cells (Lambrus et al., 2015; Wong et al., 2015). Importantly, however, restoring PLK4 activity in centrosome-depleted cells did not show any rescue effect on OCT-4 (Figure S4H).

We observed that the centrinone-treated cells were somewhat more sensitive, as they showed increased levels of cleaved poly(ADP ribose) polymerase (PARP) and cleaved caspase-3 (Figure 5B). Importantly, this phenomenon was triggered by the CHX treatment, as hESCs/hiPSCs treated only with centrinone showed no upregulation of apoptotic markers. Given these results, we hypothesized that the observed stress response of centrinone-treated cells to CHX treatment might reflect the accelerated loss of specific proteins in these cells. To this end, we aimed to test the causality between the observed priming of centrinone-treated stem cells to enter the apoptotic pathway and altered protein turnover. However, MG132 treatment, in agreement with its typical use in anti-tumor therapy (Goldberg, 2012), led to an increase of p53 and cell-death markers in hESCs/hiPSCs, indicated by the appearance of cleaved PARP and caspase-3 (Figure 5B). To bypass these undesired effects of MG132, we turned to p53 low hESCs. Interestingly, co-treatment of centrosome-depleted and CHX-treated hESCs with MG132 showed full rescue of the drop in OCT-4/*NANOG* levels (Figure 5C). Moreover, CHX treatment caused modest effects on cleaved PARP and caspase-3, respectively. Interestingly, those were fully rescued by the MG132 treatment. To corroborate our hypothesis, we tested the ability of MG132 to rescue the activation of the apoptotic pathway after centrosome loss in p53 low hESCs/hiPSCs. As expected, centrinone

(C–E) Western blot analyses of hESCs and hiPSCs after indicated time of treatment, with α -tubulin as a loading control. (C) Analyses of effects on pluripotency and differentiation by the indicated antibodies. (D) Analyses of effects of treatment (2 days) on protein turnover of p53 after indicated time (hours) of inhibition of translation by cycloheximide (CHX). (E) Analyses of the effect of temporal mitotic arrest by 6 hr of nocodazole treatment. Left panel shows scheme of the experiment. Controls (asynchronous cells) and treated samples (Noco+shake off, Noco-leftover) were probed for protein levels of p53, brachyury, GATA-6, and PAX-6 2 days after nocodazole washout. Noco-leftover condition represents non-mitotic nocodazole-treated cells. Data are presented as mean \pm SEM (* p < 0.05, *** p < 0.001). See also Figure S3.

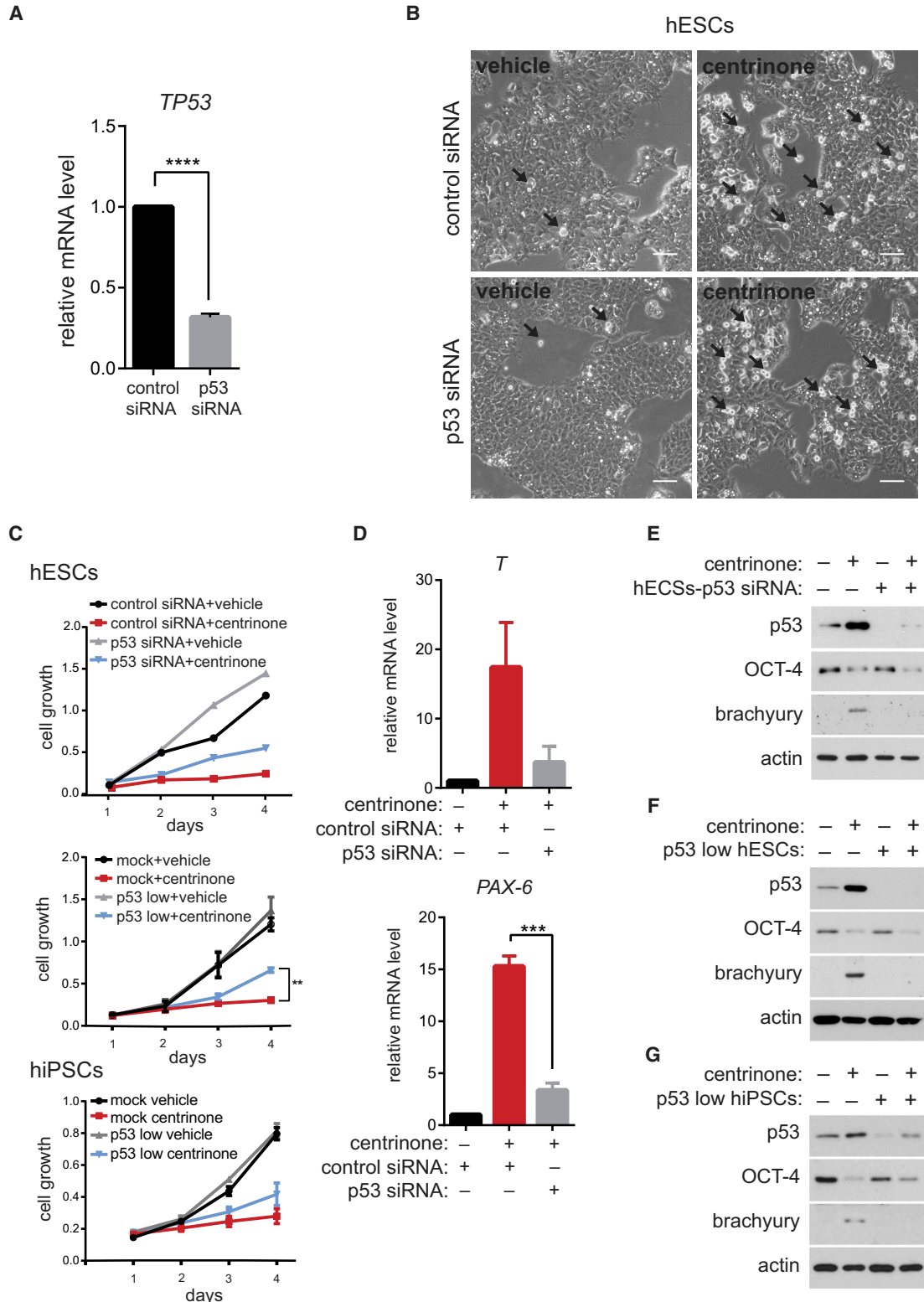


Figure 4. Differentiation Induced by Blocking of PLK4 or STIL Is p53 Dependent

Cells were transfected with either control or p53 siRNA, or the expression of p53 was permanently downregulated by CRISPR/Cas9 (p53 low cells) and subsequently treated as indicated.

(legend continued on next page)



treatment alone led to only a negligible fraction of early apoptotic cells, while co-treatment with CHX increased this fraction (Figure 5D). Remarkably, addition of MG132 was able to notably decrease the proportion of early apoptotic cells, specifically in centrinone + CHX conditions. Together, these results demonstrated that p53 is not necessary for the increased protein turnover of OCT-4/NANOG in centrinone-treated cells, and that block of excessive protein degradation in centrosome-depleted cells is sufficient to lower the stress response and priming of these cells to apoptosis.

DISCUSSION

Centrosome abnormalities are related to detrimental developmental defects. Here we have explored the link between the loss of centrosome and the cell fate in hESCs/hiPSCs and have shown that depletion/inhibition of PLK4 or depletion of STIL lead to centrosome depletion, and in turn to prolonged mitosis, which consequently leads to p53 upregulation and subsequent differentiation. We further established the PLK4 inhibition-mediated and/or centrosome depletion-mediated loss of pluripotency independent of p53 and linked to altered protein turnover.

Our data indicate that a large portion of acentrosomal hESCs/hiPSCs is able to divide. Importantly, our experiments further showed that centrosome loss promotes aneuploidy in hESCs/hiPSCs, a phenomenon usually seen in somatic/cancer cell lines but not *in vivo* in mouse embryos (Bazzi and Anderson, 2014; Insolera et al., 2014; Sir et al., 2013; Wong et al., 2015). It remains to be determined whether this “mouse embryo versus human cells” difference reflects specific aspects of cell culture or is linked to an acentrosomal period of early embryogenesis in mouse (Szollosi et al., 1972). Either way, our data establish that the loss of centrosome in hESCs/hiPSCs contributes to genome instability.

The proliferation rate of centrosome-less hESCs/hiPSCs was impaired, consistent with reports on human somatic cells (Lambrus et al., 2015; Wong et al., 2015) or mouse embryo (Bazzi and Anderson, 2014). Studies on somatic cells also proposed that the proliferation defect seen after centrosome loss is fully dependent on p53 (Lambrus et al., 2015; Wong et al., 2015). Interestingly, however, depletion of p53 by RNAi or CRISPR/Cas9 showed only moderate rescue of proliferation defect after centrosome loss, while it completely prevented the induction of differentiation markers. Even though we cannot formally exclude the effects of different experimental designs, we conclude that self-renewal defect in centrosome-depleted hESCs/hiPSCs following PLK4 or STIL blocking is dependent on p53 only partially.

Previous studies linked p53 to induction of differentiation in PSCs (Jain et al., 2012; Lin et al., 2005; Qin et al., 2007; Zhang et al., 2014). However, the ability of activated p53 to directly repress transcription of any gene has been recently challenged (Allen et al., 2014), and the possible role of p53 in direct repression of pluripotency factors is rather controversial (Aladjem et al., 1998; Maimets et al., 2008; Momcilovic et al., 2009; Qin et al., 2007; Wang et al., 2016; Zhang et al., 2014). In addition, a recent report by Gogendeau et al. (2015) postulated that aneuploidy-induced differentiation of NSCs in *Drosophila* is largely p53-independent. With all that said, our data clearly point out the requirement of p53 for the induction of differentiation markers after inactivation of PLK4-STIL module and centrosome loss. Importantly, however, loss of pluripotency markers upon centrinone treatment was not rescued by p53 depletion, suggesting that the loss of pluripotency is p53-independent. This is in agreement with recent reports on Nanog expression during differentiation of p53 null mouse ESCs (Shigeta et al., 2013; Wang et al., 2016) and work on p53-deficient mice reporting no developmental defects (Donehower et al., 1992). Furthermore, this model predicts that the control of pluripotency and the induction of differentiation following centrosome depletion are

(A) Analyses of mRNA levels of *TP53* after siRNA transfection in hESCs, showing the efficiency of p53 knockdown. Data are presented as relative fold change over control.

(B) Phase-contrast images of hESCs following siRNA transfection and 2 days of treatment; black arrows indicate mitotic cells. Scale bars, 50 μ m.

(C) Number of cells in described conditions was measured at indicated time points by crystal violet assay and plotted as growth curves. First panel shows siRNA data ($n = 1$), second panel shows analyses of p53 low hESCs and their respective controls ($n = 3$), and third panel shows p53 low hiPSCs ($n = 3$).

(D) Expression of differentiation markers (*T* and *PAX6*) after siRNA transfection and 4 days of treatment in hESCs, analyzed by qPCR. Data are presented as relative fold change over control (first column).

(E–G) Western blot analyses of rescue of the centrinone treatment-induced effects by p53 downregulation either by siRNA (2 days of treatment, E) or CRISPR/Cas9 (p53 low hESCs/hiPSCs; 3 days of treatment, F and G). Samples were probed with indicated antibodies, with actin as a loading control.

Data are presented as mean \pm SEM (** $p < 0.005$, *** $p < 0.001$, **** $p < 0.0001$).

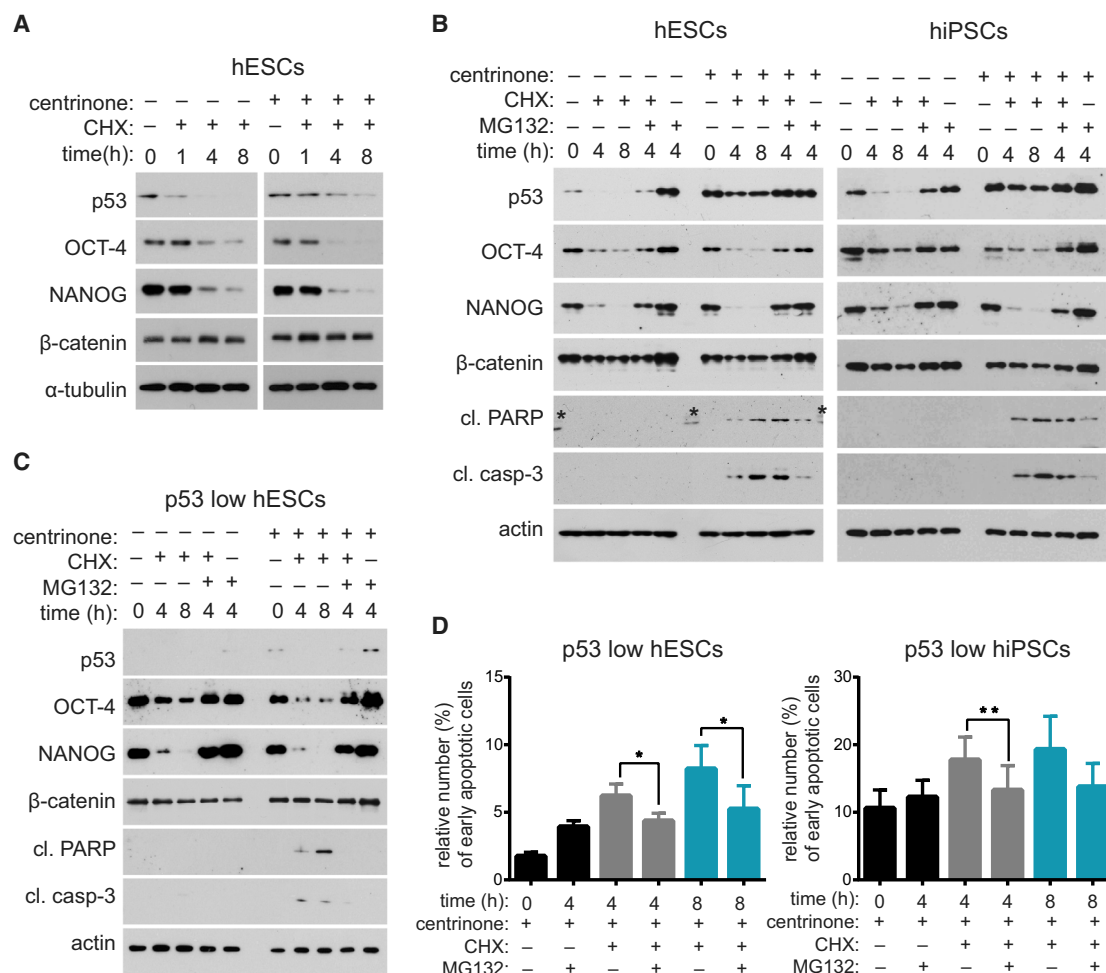


Figure 5. Loss of Pluripotency after PLK4 Inhibition and Centrosome Depletion Is Linked to Altered Protein Turnover

hESCs (mock: A and B, or p53 low: C and D) and hiPSCs (mock: B, or p53 low: D) were treated with centrinone (2 days) and indicated chemicals, and analyzed by western blot for protein expression (A–C) or by annexin V/PI staining for apoptosis (D).

(A) Western blot analyses of centrinone treatment effect on protein turnover after block of protein synthesis for indicated time by cycloheximide (CHX). Note the increased turnover of OCT-4 and NANOG, and the decreased turnover of p53 in centrinone conditions. β-Catenin was included in all depicted experiments as additional control for specificity; α-tubulin/actin served as loading controls.

(B and C) Analysis of rescue effects of inhibition of proteasome (MG132) on altered protein turnover following centrinone treatment (B). Where indicated, CHX was added together with MG132 for indicated time to analyze turnover rate of p53, OCT-4, NANOG, and β-catenin. Cleaved PARP and cleaved caspase-3 were used to probe for apoptosis (asterisks show non-specific antibody binding to marker). (C) Analysis of p53 low hESCs.

(D) Viability measurement by annexin V/PI staining of p53 low hESCs/hiPSCs in the indicated conditions (hESCs, n = 4; hiPSCs, n = 3). Data are presented as mean ± SEM (*p < 0.05, **p < 0.005). See also Figure S4.

interconnected but autonomously regulated phenomena, with p53 playing an instructive role in the latter. That being said, we speculate that the involvement of p53 in centrosome loss-driven differentiation explains why we and others (Amps et al., 2011; Ben-David et al., 2014; Taapken et al., 2011; Zhang et al., 2016) find no evidence for aneuploidy being the main driving force of upregulation of differentiation markers, as reported for p53-independent differentiation of *Drosophila* NSCs (Gogendeau et al., 2015).

Activation of p53 is a typical response to DDR. However, observations from us (this study) and others (Lambrus et al., 2015; Wong et al., 2015) demonstrate that the activation of p53 after centrosome loss is DDR-independent. Recent studies provided hints about events upstream of p53 activation in centrosome-less somatic cells by pointing out the requirement for TP53BP1 and USP28 (Fong et al., 2016; Lambrus et al., 2016; Meitinger et al., 2016). It is possible that this module operates also in PSCs. However,



the exact nature of the putative stress signal activating p53 remains elusive. Our data indicate that the prolonged mitosis, one of the earliest consequences of centrosome loss, is sufficient to trigger p53 upregulation and differentiation in hESCs/hiPSCs. This finding has two pertinent consequences. First, any experiments with PSCs involving mitotic drugs need to be interpreted with caution, as such treatment may directly interfere with their undifferentiated status. Furthermore, it raises a question about the role of prolonged mitoses following centrosome loss. As already mentioned, prolonged mitosis is sufficient to trigger differentiation via induction of p53. However, removal of p53 is not able to sustain self-renewal of centrosome-depleted hESCs/hiPSCs. In addition, we were not able to mimic the effect of PLK4 or STIL blocking on downregulation of OCT-4/NANOG by the prolongation of mitosis. Thus, it seems plausible that defects observed in hESCs/hiPSCs following inactivation of the PLK4-STIL module reflect impairment of both mitotic and non-mitotic function of the centrosome.

We found that the decrease of OCT-4/NANOG after centrinone treatment is caused by faster turnover of these proteins, independently of p53. The fact that active PLK4 is not able to rescue downregulation of OCT-4 in centrosome-depleted cells supports the conclusion that the enhanced turnover is a consequence of centrosome loss rather than inhibition of PLK4. We speculate that altered proteasomal activity, in combination with elevated stress response, might contribute to this phenomenon (Bryja et al., 2017; Gerdes et al., 2007; Vora and Phillips, 2015). In addition, the increased degradation of NANOG/OCT-4 could be a consequence of more complex metabolic changes. This prediction is supported by the rescue effect of MG132 treatment on induction of apoptosis in our experiments, possibly due to prevention of a loss of pro-survival factors upon block of protein synthesis (Portt et al., 2011).

In sum, our study defines a novel role for PLK4-STIL module and the centrosome in the regulation of key stem cell properties. It identifies both p53-dependent and -independent consequences of inactivation of the module in PSCs and connects them to alterations in mitotic timing and protein metabolism. Future studies on the links between centrosome, proteasome regulation, and apoptotic response could contribute to a better understanding of the pathology of centrosome-related diseases.

EXPERIMENTAL PROCEDURES

Cell Lines

hESCs (line CCTL14, <https://hpscereg.eu/cell-line/MUNie007-A>), hESCs 2 (CCTL12, <https://hpscereg.eu/cell-line/MUNie005-A>; “hESCs #2”) (Adewumi et al., 2007; Bohaciakova et al., 2017),

and hiPSCs (derived as described previously; Barta et al., 2016) were cultured, treated, and analyzed as described in detail in [Supplemental Experimental Procedures](#).

Statistical Analysis

All statistical analyses were done using Student's t test and graphically visualized in GraphPad Prism Software v. 6.0 (GraphPad Software, La Jolla, CA; www.graphpad.com). All data are presented as mean \pm SEM from three independent experiments, unless otherwise stated, and p values <0.05 were considered significant (*p < 0.05, **p < 0.005, ***p < 0.001, ****p < 0.0001 in figures).

Western Blots

Detailed protocol is described in [Supplemental Experimental Procedures](#); western blot quantifications and all independent repeats are shown in Supplemental Western Blot Data.

Additional experimental procedures are provided in [Supplemental Information](#). A list of used antibodies, primers, and shRNA constructs is provided in [Table S1](#).

SUPPLEMENTAL INFORMATION

Supplemental Information includes Supplemental Experimental Procedures, four figures, and one table and can be found with this article online at <https://doi.org/10.1016/j.stemcr.2018.08.008>.

AUTHORS CONTRIBUTIONS

T.R. designed and performed experiments, and analyzed and interpreted data; D.B. performed experiments, and analyzed and interpreted data; M.E. and V.P. performed experiments and analyzed data; T.B. and A.H. provided critical reagents; L.C. conceived and supervised the study, analyzed and interpreted data, and together with T.R. wrote the manuscript. All authors approved the final version of the manuscript.

ACKNOWLEDGMENTS

We thank Erich Nigg, Andrew Shiau, Borivoj Vojtesek, and Anthony Hyman for sharing reagents, Lumir Krejci for access to DV Elite, Pavlina Janovska for help with FACS analyses, Klara Koudelkova and Karolina Hanzakova for assistance, Vitezslav Bryja, Zdenek Andrysik, and members of the L.C. lab for critical comments and suggestions. We acknowledge the core facility CELLIM of CEITEC, supported by the MEYS CR (LM2015062 Czech-Bio-Imaging). This work was supported by grants from the SoMoPro II Program (project 4SGA8574), cofinanced by European Union and the South-Moravian Region; Czech Science Foundation (16-03269Y); Swiss National Science Foundation (IZ11Z0_166533); follow-up research fund from Federation of Biochemical and Biophysical Societies (FEBS); Grant Agency of Masaryk University (GAMU grant category E), and funds from Medical Faculty MU to Junior researcher (ROZV/24/LF2016) to L.C. D.B. and T.B. were supported by the Czech Science Foundation (15-18316Y, 16-24004Y, and 18-25429Y), and funds from Medical Faculty MU to Junior researcher (ROZV/25/LF2017, ROZV/24/LF2018 and MUNI/G/1131/2017). A.H. was supported by Czech Science Foundation (15-11707S) and by the project no. LQ1605 (MYES CR,



NPU II). The content of this publication reflects only the authors' views, and the European Union is not liable for any use that may be made of the information contained therein.

Received: June 6, 2017

Revised: August 8, 2018

Accepted: August 8, 2018

Published: September 6, 2018

REFERENCES

- Adewumi, O., Aflatoonian, B., Ahrlund-Richter, L., Amit, M., Andrews, P.W., Beighton, G., Bello, P.A., Benvenisty, N., Berry, L.S., Bevan, S., et al. (2007). Characterization of human embryonic stem cell lines by the International Stem Cell Initiative. *Nat. Biotechnol.* 25, 803–816.
- Aladjem, M.I., Spike, B.T., Rodewald, L.W., Hope, T.J., Klemm, M., Jaenisch, R., and Wahl, G.M. (1998). ES cells do not activate p53-dependent stress responses and undergo p53-independent apoptosis in response to DNA damage. *Curr. Biol.* 8, 145–155.
- Allen, M.A., Andrysiak, Z., Dengler, V.L., Mellert, H.S., Guarnieri, A., Freeman, J.A., Sullivan, K.D., Galbraith, M.D., Luo, X., Kraus, W.L., et al. (2014). Global analysis of p53-regulated transcription identifies its direct targets and unexpected regulatory mechanisms. *Elife* 3. <https://doi.org/10.7554/eLife.02200>.
- Amps, K., Andrews, P.W., Anyfantis, G., Armstrong, L., Avery, S., Baharvand, H., Baker, J., Baker, D., Munoz, M.B., Beil, S., et al. (2011). Screening ethnically diverse human embryonic stem cells identifies a chromosome 20 minimal amplicon conferring growth advantage. *Nat. Biotechnol.* 29, 1132–1146.
- Andersen, J.S., Wilkinson, C.J., Mayor, T., Mortensen, P., Nigg, E.A., and Mann, M. (2003). Proteomic characterization of the human centrosome by protein correlation profiling. *Nature* 426, 570–574.
- Arquint, C., and Nigg, E.A. (2016). The PLK4-STIL-SAS-6 module at the core of centriole duplication. *Biochem. Soc. Trans.* 44, 1253–1263.
- Barta, T., Peskova, L., Collin, J., Montaner, D., Neganova, I., Armstrong, L., and Lako, M. (2016). Inhibition of miR-145 enhances reprogramming of human dermal fibroblasts to induced pluripotent stem cells. *Stem Cells* 34, 246–251.
- Basto, R., Lau, J., Vinogradova, T., Gardiol, A., Woods, C.G., Khodjakov, A., and Raff, J.W. (2006). Flies without centrioles. *Cell* 125, 1375–1386.
- Basto, R., Brunk, K., Vinadogrova, T., Peel, N., Franz, A., Khodjakov, A., and Raff, J.W. (2008). Centrosome amplification can initiate tumorigenesis in flies. *Cell* 133, 1032–1042.
- Bazzi, H., and Anderson, K.V. (2014). Acentriolar mitosis activates a p53-dependent apoptosis pathway in the mouse embryo. *Proc. Natl. Acad. Sci. USA* 111, E1491–E1500.
- Becker, K.A., Ghule, P.N., Therrien, J.A., Lian, J.B., Stein, J.L., Van Wijnen, A.J., and Stein, G.S. (2006). Self-renewal of human embryonic stem cells is supported by a shortened G1 cell cycle phase. *J. Cell. Physiol.* 209, 883–893.
- Ben-David, U., Arad, G., Weissbein, U., Mandefro, B., Maimon, A., Golan-lev, T., Narwani, K., Clark, A.T., Andrews, P.W., Benvenisty, N., et al. (2014). Aneuploidy induces profound changes in gene expression, proliferation and tumorigenicity of human pluripotent stem cells. *Nat. Commun.* 5, 4825.
- Bettencourt-Dias, M., Rodrigues-Martins, A., Carpenter, L., Riparbelli, M., Lehmann, L., Gatt, M.K., Carmo, N., Balloux, F., Callaini, G., and Glover, D.M. (2005). SAK/PLK4 is required for centriole duplication and flagella development. *Curr. Biol.* 15, 2199–2207.
- Bohaciakova, D., Renzova, T., Fedorova, V., Barak, M., Kunova-Bosakova, M., Hampl, A., and Cajanek, L. (2017). An efficient method for generation of knockout human. *Stem Cells Dev.* 26, 1521–1527.
- Bornens, M., and Gönczy, P. (2014). Centrosomes back in the limelight. *Philos. Trans. R. Soc. Lond. B Biol. Sci.* 369. <https://doi.org/10.1098/rstb.2013.0452>.
- Brevini, T.A.L., Pennarossa, G., Antonini, S., Paffoni, A., Rebulli, P., Scanziani, E., De Eguileor, M., and Benvenisty, N. (2009). Cell lines derived from human parthenogenetic embryos can display aberrant centriole distribution and altered expression levels of mitotic spindle check-point transcripts. *Stem Cell Rev. Rep.* 5, 340–352.
- Brooks, C.L., and Gu, W. (2010). New insights into p53 activation. *Cell Res.* 20, 614–621.
- Bryja, V., Červenka, I., and Čajánek, L. (2017). The connections of Wnt pathway components with cell cycle and centrosome: side effects or a hidden logic? *Crit. Rev. Biochem. Mol. Biol.* 52, 614–637.
- Chavali, P.L., Pütz, M., and Gergely, F. (2014). Small organelle, big responsibility: the role of centrosomes in development and disease. *Philos. Trans. R. Soc. Lond. B Biol. Sci.* 369. <https://doi.org/10.1098/rstb.2013.0468>.
- Chen, Z., Indjeian, V.B., McManus, M., Wang, L., and Dynlacht, B.D. (2002). CP110, a cell cycle-dependent CDK substrate, regulates centrosome duplication in human cells. *Dev. Cell* 3, 339–350.
- Conduit, P.T., Wainman, A., and Raff, J.W. (2015). Centrosome function and assembly in animal cells. *Nat. Rev. Mol. Cell Biol.* 16, 611–624.
- Donehower, L.A., Harvey, M., Slagle, B.L., McArthur, M.J., Montgomery, C.A., Butel, J.S., and Bradley, A. (1992). Mice deficient for p53 are developmentally normal but susceptible to spontaneous tumours. *Nature* 356, 215–221.
- Fong, C.S., Mazo, G., Das, T., Goodman, J., Kim, M., O'Rourke, B.P., Izquierdo, D., and Tsou, M.F.B. (2016). 53BP1 and USP28 mediate p53-dependent cell cycle arrest in response to centrosome loss and prolonged mitosis. *Elife* 5. <https://doi.org/10.7554/eLife.16270>.
- Gambarotto, D., and Basto, R. (2016). Consequences of numerical centrosome defects in development and disease. In *The Microtubule Cytoskeleton: Organisation, Function and Role in Disease*, J. Lüders, ed. (Springer Vienna), pp. 117–149.
- Gerdes, J.M., Liu, Y., Zaghloul, N.A., Leitch, C.C., Lawson, S.S., Kato, M., Beachy, P.A., Beales, P.L., DeMartino, G.N., Fisher, S., et al. (2007). Disruption of the basal body compromises proteasomal function and perturbs intracellular Wnt response. *Nat. Genet.* 39, 1350–1360.
- Gogendeau, D., Siudeja, K., Gambarotto, D., Pennetier, C., Bardin, A.J., and Basto, R. (2015). Aneuploidy causes premature differentiation of neural and intestinal stem cells. *Nat. Commun.* 6, 8894.
- Goldberg, A.L. (2012). Development of proteasome inhibitors as research tools and cancer drugs. *J. Cell Biol.* 199, 583–588.



- Gönczy, P. (2015). Centrosomes and cancer: revisiting a long-standing relationship. *Nat. Rev. Cancer* 15, 639–652.
- Gupta, G.D., Coyaudo, É., Gonçalves, J., Mojarad, B.A., Liu, Y., Wu, Q., Gheiratmand, L., Comartin, D., Tkach, J.M., Sally, W.T., et al. (2015). A dynamic protein interaction landscape of the human centrosome-cilium interface. *Cell* 163, 1484–1499.
- Habedanck, R., Stierhof, Y.-D., Wilkinson, C.J., and Nigg, E.A. (2005). The Polo kinase Plk4 functions in centriole duplication. *Nat. Cell Biol.* 7, 1140–1146.
- Holubcová, Z., Matula, P., Sedláčková, M., Vínarský, V., Doležalová, D., Bárta, T., Dvořák, P., and Hampl, A. (2011). Human embryonic stem cells suffer from centrosomal amplification. *Stem Cells* 29, 46–56.
- Hudson, J.W., Kozarova, A., Cheung, P., Macmillan, J.C., Swallow, C.J., Cross, J.C., and Dennis, J.W. (2001). Late mitotic failure in mice lacking Sak, a polo-like kinase. *Curr. Biol.* 11, 441–446.
- Insolera, R., Bazzi, H., Shao, W., Anderson, K.V., and Shi, S.-H. (2014). Cortical neurogenesis in the absence of centrioles. *Nat. Neurosci.* 17, 1528–1535.
- Izraeli, S., Lowe, L.A., Bertness, V.L., Good, D.J., Dorward, D.W., Kirsch, I.R., and Kuehn, M.R. (1999). The *SIL* gene is required for mouse embryonic axial development and left–right specification. *Nature* 399, 691–694.
- Jaenisch, R., and Young, R. (2008). Stem cells, the molecular circuitry of pluripotency and nuclear reprogramming. *Cell* 132, 567–582.
- Jain, A.K., Allton, K., Iacovino, M., Mahen, E., Milczarek, R.J., Zwaka, T.P., Kyba, M., and Barton, M.C. (2012). p53 regulates cell cycle and microRNAs to promote differentiation of human embryonic stem cells. *PLoS Biol.* 10. <https://doi.org/10.1371/journal.pbio.1001268>.
- Kashyap, V., Rezende, N.C., Scotland, K.B., Shaffer, S.M., Persson, J.L., Gudas, L.J., and Mongan, N.P. (2009). Regulation of stem cell pluripotency and differentiation involves a mutual regulatory circuit of the NANOG, OCT4, and SOX2 pluripotency transcription factors with polycomb repressive complexes and stem cell microRNAs. *Stem Cells Dev.* 18, 1093–1108.
- Khodjakov, A., and Rieder, C.L. (2001). Centrosomes enhance the fidelity of cytokinesis in vertebrates and are required for cell cycle progression. *J. Cell Biol.* 153, 237–242.
- Kim, J., Woo, A.J., Chu, J., Snow, J.W., Fujiwara, Y., Kim, C.G., Cantor, A.B., and Orkin, S.H. (2010). A Myc network accounts for similarities between embryonic stem and cancer cell transcription programs. *Cell* 143, 313–324.
- Kleylein-Sohn, J., Westendorf, J., Le Clech, M., Habedanck, R., Stierhof, Y.-D., and Nigg, E.A. (2007). Plk4-induced centriole biogenesis in human cells. *Dev. Cell* 13, 190–202.
- Lambrus, B.G., Uetake, Y., Clutario, K.M., Daggubati, V., Snyder, M., Sluder, G., and Holland, A.J. (2015). P53 protects against genome instability following centriole duplication failure. *J. Cell Biol.* 210, 63–77.
- Lambrus, B.G., Daggubati, V., Uetake, Y., Scott, P.M., Clutario, K.M., Sluder, G., and Holland, A.J. (2016). A USP28-53BP1-p53-p21 signaling axis arrests growth after centrosome loss or prolonged mitosis. *J. Cell Biol.* 214, 143–153.
- Lancaster, M.A., Renner, M., Martin, C.-A., Wenzel, D., Bicknell, L.S., Hurles, M.E., Homfray, T., Penninger, J.M., Jackson, A., and Knoblich, J.A. (2013). Cerebral organoids model human brain development and microcephaly. *Nature* 501, 373–379.
- Leidel, S., Delattre, M., Cerutti, L., Baumer, K., and Gönczy, P. (2005). SAS-6 defines a protein family required for centrosome duplication in *C. elegans* and in human cells. *Nat. Cell Biol.* 7, 115–125.
- Levine, M.S., Bakker, B., Boeckx, B., Moyett, J., Lu, J., Vitre, B., Spierings, D.C., Lansdorp, P.M., Cleveland, D.W., Lambrechts, D., et al. (2017). Centrosome amplification is sufficient to promote spontaneous tumorigenesis in mammals. *Dev. Cell* 40, 313–322.
- Lin, T., Chao, C., Saito, S., Mazur, S.J., Murphy, M.E., Appella, E., and Xu, Y. (2005). p53 induces differentiation of mouse embryonic stem cells by suppressing Nanog expression. *Nat. Cell Biol.* 7, 165–171.
- Maimets, T., Neganova, I., Armstrong, L., and Lako, M. (2008). Activation of p53 by nutlin leads to rapid differentiation of human embryonic stem cells. *Oncogene* 27, 5277–5287.
- Marthiens, V., Rujano, M.A., Pennetier, C., Tessier, S., Paul-Gilloteaux, P., and Basto, R. (2013). Centrosome amplification causes microcephaly. *Nat. Cell Biol.* 15, 731–740.
- Meitinger, F., Anzola, J.V., Kaulich, M., Richardson, A., Stender, J.D., Benner, C., Glass, C.K., Dowdy, S.F., Desai, A., Shiau, A.K., et al. (2016). 53BP1 and USP28 mediate p53 activation and G1 arrest after centrosome loss or extended mitotic duration. *J. Cell Biol.* 214, 155–166.
- Mikule, K., Delaval, B., Kaldis, P., Jurczyk, A., Hergert, P., and Doxsey, S. (2007). Loss of centrosome integrity induces p38-p53-p21-dependent G1-S arrest. *Nat. Cell Biol.* 9, 160–170.
- Momcilovic, O., Choi, S., Varum, S., Bakkenist, C., Schatten, G., and Navara, C. (2009). Ionizing radiation induces ATM dependent checkpoint signaling and G2 but not G1 cell cycle arrest in pluripotent human embryonic stem cells. *Stem Cells* 27, 1822–1835.
- Nigg, E.A., and Stearns, T. (2011). The centrosome cycle: centriole biogenesis, duplication and inherent asymmetries. *Nat. Cell Biol.* 13, 1154–1160.
- Nigg, E.A., Čajánek, L., and Arquint, C. (2014). The centrosome duplication cycle in health and disease. *FEBS Lett.* 588, 2366–2372.
- Park, I.-H., Arora, N., Huo, H., Maherali, N., Ahfeldt, T., Shimamura, A., Lensch, M.W., Cowan, C., Hochedlinger, K., and Daley, G.Q. (2008). Disease-specific induced pluripotent stem cells. *Cell* 134, 877–886.
- Pauklin, S., and Vallier, L. (2013). The cell cycle state of stem cells determines cell fate propensity. *Cell* 155, 135–147.
- Piel, M., Nordberg, J., Euteneuer, U., and Bornens, M. (2001). Centrosome-dependent exit of cytokinesis in animal cells. *Science* 291, 1550–1554.
- Portt, L., Norman, G., Clapp, C., Greenwood, M., and Greenwood, M.T. (2011). Anti-apoptosis and cell survival: a review. *Biochim. Biophys. Acta* 1813, 238–259.
- Puklowski, A., Homsy, Y., Keller, D., May, M., Chauhan, S., Kossatz, U., Grünwald, V., Kubicka, S., Pich, A., Manns, M.P., et al. (2011). The SCF-FBXW5 E3-ubiquitin ligase is regulated by PLK4 and



- targets HsSAS-6 to control centrosome duplication. *Nat. Cell Biol.* 13, 1004–1009.
- Qin, H., Yu, T., Qing, T., Liu, Y., Zhao, Y., Cai, J., Li, J., Song, Z., Qu, X., Zhou, P., et al. (2007). Regulation of apoptosis and differentiation by p53 in human embryonic stem cells. *J. Biol. Chem.* 282, 5842–5852.
- Rogakou, E.P., Pilch, D.R., Orr, A.H., Ivanova, V.S., and Bonner, W.M. (1998). DNA double-stranded breaks induce histone H2AX phosphorylation on serine 139*. *J. Biol. Chem.* 273, 5858–5868.
- Shahbazi, M.N., Jedrusik, A., Vuoristo, S., Recher, G., Hupalowska, A., Bolton, V., Fogarty, N.M.E., Campbell, A., Devito, L.G., Ilic, D., et al. (2016). Self-organization of the human embryo in the absence of maternal tissues. *Nat. Cell Biol.* 18, 700–708.
- Shigeta, M., Ohtsuka, S., Nishikawa-Torikai, S., Yamane, M., Fujii, S., Murakami, K., and Niwa, H. (2013). Maintenance of pluripotency in mouse ES cells without Trp53. *Sci. Rep.* 3, 2944.
- Sir, J.H., Pütz, M., Daly, O., Morrison, C.G., Dunning, M., Kilmartin, J.V., and Gergely, F. (2013). Loss of centrioles causes chromosomal instability in vertebrate somatic cells. *J. Cell Biol.* 203, 747–756.
- Strnad, P., Leidel, S., Vinogradova, T., Euteneuer, U., and Gönczy, P. (2007). Regulated HsSAS-6 levels ensure formation of a single procentriole per centriole during the centrosome duplication cycle. *Dev. Cell* 13, 203–213.
- Szollosi, D., Calarco, P., and Donahue, R.P. (1972). Absence of centrioles in the first and second meiotic spindles of mouse oocytes. *J. Cell Sci.* 11, 521–541.
- Taapken, S.M., Nisler, B.S., Newton, M.A., Sampsell-Barron, T.L., Leonhard, K.A., McIntire, E.M., and Montgomery, K.D. (2011). Karyotypic abnormalities in human induced pluripotent stem cells and embryonic stem cells. *Nat. Biotechnol.* 29, 313–314.
- Takahashi, K., Tanabe, K., Ohnuki, M., Narita, M., Ichisaka, T., Tomoda, K., and Yamanaka, S. (2007). Induction of pluripotent stem cells from adult human fibroblasts by defined factors. *Cell* 131, 861–872.
- Tang, C.-J.C., Lin, S.-Y., Hsu, W.-B., Lin, Y.-N., Wu, C.-T., Lin, Y.-C., Chang, C.-W., Wu, K.-S., and Tang, T.K. (2011). The human microcephaly protein STIL interacts with CPAP and is required for procentriole formation. *EMBO J.* 30, 4790–4804.
- Thomson, J.A., Itskovitz-Eldor, J., Shapiro, S.S., Waknitz, M.A., Swiergiel, J.J., Marshall, V.S., and Jones, J.M. (1998). Embryonic stem cell lines derived from human blastocysts. *Science* 282, 1145–1147.
- Vitre, B., Holland, A.J., Kulukian, A., Shoshani, O., Hirai, M., Wang, Y., Maldonado, M., Cho, T., Boubaker, J., Swing, D.A., et al. (2015). Chronic centrosome amplification without tumorigenesis. *Proc. Natl. Acad. Sci. USA* 112, E6321–E6330.
- Vora, S., and Phillips, B.T. (2015). Centrosome-associated degradation limits β -catenin inheritance by daughter cells after asymmetric division. *Curr. Biol.* 25, 1005–1016.
- Wang, Q., Zou, Y., Nowotschin, S., Kim, S.Y., Li, Q.V., Soh, C.-L., Su, J., Zhang, C., Shu, W., Xi, Q., et al. (2016). The p53 family coordinates Wnt and nodal inputs in mesendodermal differentiation of embryonic stem cells. *Cell Stem Cell* 20, 70–86.
- Wong, Y.L., Anzola, J.V., Davis, R.L., Yoon, M., Motamedi, A., Kroll, A., Seo, C.P., Hsia, J.E., Kim, S.K., Mitchell, J.W., et al. (2015). Reversible centriole depletion with an inhibitor of Polo-like kinase 4. *Science* 348, 1155–1160.
- Zhang, M., Cheng, L., Jia, Y., Liu, G., Li, C., Song, S., and Bradley, A. (2016). Aneuploid embryonic stem cells exhibit impaired differentiation and increased neoplastic potential. *EMBO J.* 35, 2285–2300.
- Zhang, Z.N., Chung, S.K., Xu, Z., and Xu, Y. (2014). Oct4 maintains the pluripotency of human embryonic stem cells by inactivating p53 through sirt1-mediated deacetylation. *Stem Cells* 32, 157–165.

Appendix 12

Bohaciakova D, Renzova T, Fedorova V, Barak M, Kunova Bosakova M, Hampl A, Čajánek L*. An Efficient Method for Generation of Knockout Human Embryonic Stem Cells Using CRISPR/Cas9 System . *Stem cells and development*. 2017 Nov 1;26(21):1521-1527.
doi: 10.1089/scd.2017.0058. JCR 2017. IF= 3.315, Q2 – Hematology)

Published in final edited form as:

Stem Cells Dev. 2017 November 01; 26(21): 1521–1527. doi:10.1089/scd.2017.0058.

An efficient method for generation of Knock-out human embryonic stem cells using CRISPR/Cas9 system

Dasa Bohaciakova^{1,*}, Tereza Renzova¹, Veronika Fedorova¹, Martin Barak¹, Michaela Kunova Bosakova², Ales Hampl^{1,3}, and Lukas Cajanek^{1,*}

¹Department of Histology and Embryology, Masaryk University, Faculty of Medicine, Kamenice 3, 625 00, Brno, Czech Republic

²Department of Biology, Masaryk University, Faculty of Medicine, Kamenice 5, 625 00, Brno, Czech Republic

³International Clinical Research Center, St. Anne's University Hospital, Brno, Czech Republic

Abstract

Human embryonic stem cells (hESCs) represent promising tool to study functions of genes during development, to model diseases, and to even develop therapies when combined with gene editing techniques such as CRISPR/Cas9 system. However, the process of disruption of gene expression by generation of null alleles is often inefficient and tedious. To circumvent these limitations, we developed a simple and efficient protocol to permanently downregulate expression of a gene of interest in hESCs using CRISPR/Cas9. We selected *p53* for our proof of concept experiments. The methodology is based on series of hESC transfection, which leads to efficient downregulation of *p53* expression even in polyclonal population (*p53* Low cells), here proven by a loss of regulation of the expression of *p53* target gene, microRNA miR-34a. We demonstrate that our approach achieves over 80% efficiency in generating hESC clonal sublines that do not express *p53* protein. Importantly, we document by a set of functional experiments that such genetically modified hESCs do retain typical stem cells characteristics. In summary, we provide a simple and robust protocol to efficiently target expression of gene of interest in hESCs that can be useful for laboratories aiming to employ gene editing in their hESC applications/protocols.

Introduction

The development of efficient and reliable techniques to generate defined changes to the genome of human pluripotent stem cells is a long-standing goal in biomedical research. Their ability to unlimitedly self-renew allows them to be genetically modified, cloned, and expanded. Such genetically-modified clones can subsequently be differentiated into a variety of specialized cell types to analyze the effects of the introduced mutations. The ability to

*Corresponding authors: cajanek@med.muni.cz or dolezal@med.muni.cz, Tel: +420 549 49 6248 or +420 549 49 6051.

This is an Accepted Manuscript of an article published by Mary Ann Liebert, Inc. in *Stem Cells and Development* on 2 October 2017. Final publication is available from Mary Ann Liebert, Inc., publishers <http://dx.doi.org/10.1089/scd.2017.0058>

Disclosure of potential conflicts of interest

The authors indicate no potential conflicts of interest.

easily genetically modify human embryonic stem cells (hESCs) or induced pluripotent stem cells (iPSCs) also holds a great clinical promise for the disease-in-the-dish modelling and subsequent development of new gene therapies. Recently, a new tool based on a bacterial CRISPR-associated protein-9 nuclease (Cas9) has generated substantial interest due to its easy construction and low toxicity in human cells [1–3]. However, while immortalized human cancer cell lines as well as mouse ESCs have been edited with very high efficiency [4,5], much lower efficiency has been achieved in hESCs or hiPSCs [2,6]. Most of the studies on human ESCs or iPSCs show efficiencies ranging from generation 2–6% of only heterozygous mutants [7] to 2–10 % bi-allelic mutants (knockouts) in iPSCs [2,8,9].

In the present study, we describe an easy-to-use method of obtaining genetically modified hESCs using CRISPR/Cas9. Our data show that simple repeated transfection of undifferentiated hESCs leads to effective downregulation of expression of gene of interest (here *p53*) and very high efficiency (82%) of generation of knockout sublines. Our functional data further show that hESCs generated by this approach do retain their stem cell characteristics. We believe that our protocol can considerably simplify gene targeting in hESCs using CRISPR/Cas9 system.

Methods

Cell Culture, Cryopreservation, and Differentiation

Undifferentiated hESC line CCTL 14 ([10]; and Human Pluripotent Stem Cell Registry - hpscreg.eu) was used throughout this study. Undifferentiated hESCs were grown on gelatin-coated dishes in the presence of mitotically inactivated primary mouse embryonic fibroblasts (MEFs; derived from 12.5 days old mouse embryos, strain CF1; density 24,000 cells/cm²). Culture media Dulbecco's modified Eagle's medium (DMEM)/F12 was supplemented with 15% knockout serum replacement (KSR), 2 mmol/L L-Glutamine, 1× minimum essential medium non-essential amino acids (MEM-NEAA), 0.5% penicillin-streptomycin (all media components from Thermo Fisher Scientific), 100 µmol/L β-2 mercaptoethanol (Sigma-Aldrich), and 10 ng/mL human recombinant basic fibroblast growth factor-2 (FGF-2; PeproTech). Culture media was changed every day and cells were mechanically passaged every 4–5 days using StemPro™ EZPassage™ Disposable Stem Cell Passaging Tool (Thermo Fisher Scientific). For the repeated transfection experiments and clonal selection, hESCs were grown in feeder-free conditions on Matrigel™ hESC-qualified matrix (BD Biosciences) using MEF-conditioned hESC medium as described in [11].

Cryopreservation of cells was performed in the hESCs culture media supplemented with GIBCO® ES Cell Qualified Fetal Bovine Serum [FBS; 30% (Thermo Fisher Scientific)] and DMSO (10%). Cells were slowly frozen in ice-cold freezing media using Mr. Frosty™ Freezing Container (Thermo Fisher Scientific). During the thawing of hESCs, application of a selective Rho-associated kinase (ROCK) inhibitor Y-27632 (20 µM; Sigma-Aldrich) was used to increase survival of hESCs as described in [12].

Differentiation of hESCs was induced by Embryoid Body (EB) formation in non-adherent cell culture conditions in MEF media. Briefly, hESCs from feeder-free cell culture were cut into small pieces using StemPro® EZPassage™ Disposable Stem Cell Passaging Tool

(Thermo Fisher Scientific). These were then transferred to MEF culture medium (DMEM, 10% FBS, 1% L-Glutamine, 1% Non-Essential amino acids and 1% Penicillin/Streptomycin; all from Thermo Fisher Scientific) and left to form floating aggregates - EBs. Medium was changed every 3-4 days. All EBs were analyzed on the day 40.

Transfection of cells with Neon® Transfection System

Transfection experiments were carried out with plasmid px330-sgp53 (a generous gift from Oscar Fernandez-Capetillo, Karolinska Institute, Stockholm, Sweden), expressing both p53 gRNA (TGAAGCTCCCAGAATGCCAG) and Cas9 nuclease, using Neon transfection device (Thermo Fisher Scientific) according to manufacturer's instructions. Detailed experimental procedure is described in Results.

Western Blotting

For western blotting, harvested cells were washed three times with PBS, lysed in lysis buffer [50 mM Tris-HCl (pH 6.8), 1% sodium dodecyl sulfate (SDS), 10% glycerol] and stored at -80°C until use. The protein concentration was determined using the DC Protein Assay Kit (Bio-Rad) and lysates were supplemented with bromophenol blue (0.01%) and β -2 mercaptoethanol (1%). Equal amounts of total proteins were separated by SDS-polyacrylamide gel electrophoresis (PAGE) followed by transfer to a polyvinylidene fluoride (PVDF) membrane (Millipore). Proteins were immunodetected using the appropriate primary antibody followed by incubation with horseradish peroxidase (HRP)-conjugated secondary antibody. Amersham ECL Prime Western Blotting Detection Reagent (GE Healthcare Life Sciences) was used to visualize antibody-antigen complexes. The following primary antibodies were used in western blot analysis: Oct-4 (sc-5279; Santa Cruz Biotechnology); GATA6 (#5851), Brachyury (#81694), Nanog (#3580), phospho γ -H2A.X (#9718), and β -actin (#3700; all from Cell Signaling); GDF15 (07-217; Millipore); α -tubulin (11-250-C100; Exbio); mouse monoclonal antibody against p53 (DO-1) and mouse monoclonal antibody against MDM2 (2A9) were generously provided by Boivoj Vojtšek (Masaryk Memorial Cancer Institute, Brno, Czech Republic) and Stjepan Uldrijan (Department of Biology, Faculty of Medicine, Masaryk University, Brno, Czech Republic), respectively. Alpha-tubulin or β -actin were used as loading controls.

RNA isolation and qPCR

Total RNA was isolated using phenol-chloroform extraction. Harvested cells were washed with PBS and lysed in RNAlute reagent (Top-Bio) and immediately frozen and stored at -80°C . After thawing, BCP reagent (1-Bromo-3-chloropropan; Sigma-Aldrich) was added to lysate in ratio 1:10 and solution was vortexed extensively and centrifuged for 15 min at 8000g at $+4^{\circ}\text{C}$. Aqueous fraction containing RNA was transferred to a clean RNase free collecting tube and RNA was precipitated from the solution using 100% isopropanol for 20 minutes at -20°C . Precipitate was washed by 75% ethanol and eventually diluted in RNase free water. Concentration of RNA was measured using Nanodrop-1000 (Thermo Fisher Scientific) and stored at -80°C until use.

For the detection of microRNA expression, TaqMan microRNA Gene Expression Assays specific for selected mature microRNAs (hsa-miR-34a, hsa-mir-302a) were used according

to the manufacturers' protocols. Synthesis of cDNA for quantification of microRNAs was performed using the TaqMan MicroRNA Reverse Transcription Kit and PCR was performed using TaqMan® Fast Universal PCR Master Mix 2X (all reagents from Thermo Fisher Scientific). All samples were analyzed in triplicates, DNA amplification was detected using Roche Light Cycler 480 (Roche), and data were analyzed using LC480 software (Roche). The relative gene expression was calculated by normalization to small nucleolar RNA RNU38B expression.

FACS sorting

Cells growing on Matrigel™ were harvested by TrypLE Select (Thermo Fisher Scientific), washed with PBS, and resuspended in sterile FACS buffer containing PBS, 2% FBS and 1% EDTA. Cells were then pipetted through 40µm Corning Falcon™ Cell Strainer (Thermo Fisher Scientific) and sorted using BD FACS Aria™ cell sorter (BD Biosciences) as single cells per well into 96-well plate with fresh CM media supplemented with ROCK inhibitor (20µM) to improve cell survival [12].

Indirect Immunofluorescence

For immunodetection of Oct4 and Nanog proteins, cells were fixed in 4% paraformaldehyde (PFA) for 20 minutes on ice, washed 1x in PBS, permeabilized for 20 minutes with 0.1% Triton-X, blocked for 1 hour with 1% bovine serum albumin in PBS (pH 7.4) containing 0.05% Tween-20, and incubated overnight at 4°C with primary antibodies against Oct-4 (sc-5279; Santa Cruz Biotechnology), and Nanog (#3580; Cell Signaling). Final incubations with secondary antibodies were carried out for 1 hour at room temperature. Cell nuclei were counterstained with DAPI (Sigma-Aldrich), and cells were mounted in Mowiol mounting medium (Sigma-Aldrich). Microscopy was performed using an Olympus FluoView 500 laser scanning microscope (Olympus C&S Ltd., Prague, Czech Republic).

DNA Damage induction

For DNA damage induction, Etoposide diluted in DMSO was added to cell culture media for 8 hrs at the final concentration of 3.4 µM. Subsequently, all cells (including floating ones) were harvested and analyzed by Western blotting as described above. DMSO in dilution of 1:10000 was used as vehicle (negative) control.

Histology of Embryoid bodies

Embryoid bodies (EBs) were fixed in 4% PFA for 20 minutes, washed in PBS, and gently inserted into 3% ultra-low melting agarose (Sigma-Aldrich). Agarose containing EBs was embedded into paraffin, sectioned paraffin blocks were placed on Superfrost plus slides (Thermo Fisher Scientific), rehydrated and deparaffinised (Xylen-Ethanol). Antigen retrieval was performed in Target Retrieval Solution at pH 9 (Dako S2367; Agilent Technologies) at 92,5°C for 20 minutes. Sections were permeabilized in PBS with 0,025% Triton-X and incubated with primary antibodies diluted in TBS with 1% BSA at 4°C overnight. The day after, the sections were washed in TBS, shortly washed in PBS and incubated with secondary antibody diluted in TBS with 1% BSA for 1hr at 4°C. Following incubation, sections were extensively washed with PBS, cell nuclei were counterstained with DAPI, and

slides were mounted in Mowiol mounting medium. The following primary antibodies were used: GATA6 (#5851), Brachyury (#81694), Sox2 (#4900; all from Cell Signaling), and TUJ (kindly provided by Peter Andrews, University of Sheffield, UK).

Teratoma formation assay

The ability to differentiate *in vivo* was assessed in two clones of p53 KO hESC lines (clones #A9 and #A11). MOCK hESCs were used as a control. An inoculum of uniform clumps of undifferentiated hESCs (1×10^6 cells in 100 μ L culture medium) was injected into the hindlimb muscle of 8-week-old NOD/SCID/IL2Rg-null mice. When tumour diameter reached ~1cm, the mice were euthanatized by cervical dislocation. The tumours were dissected from the surrounding tissue, fixed in 4% PFA, embedded in paraffin, sectioned and stained with haematoxylin and eosin to visualize the tissue composition. All animal studies were carried out according to approved ethical guidelines (Project No. 02/2010).

Statistical analysis

All statistical analyses were performed using two-tailed paired t-test and graphically visualized using GraphPad Prism Software v. 5.0 (GraphPad Software, Inc., La Jolla, CA, www.graphpad.com). Unless otherwise stated, all data shown represent the results of at least three independent experiments and P-values < 0.05 were considered significant.

Results and discussion

Repeated transfection of hESCs using CRISPR/Cas9 system efficiently generates mixed population of cells with low expression of p53 protein while maintaining pluripotency

To rapidly and efficiently generate hESCs with disrupted expression of gene of interest (here p53), we used CRISPR/Cas9 construct expressing both Cas9 nuclease and gRNA (px330-sgp53). We initially performed transfections of hESCs using either Neon Transfection System (Neon TS) or Lipofectamine 3000 (L3000). However, transfection using L3000 proved to be inefficient (data not shown), therefore we only describe the procedure that employs Neon TS.

As schematized in Figure 1A, undifferentiated hESCs were grown in feeder-free conditions on MatrigelTM-coated culture dish. At the day of transfection, cells were enzymatically harvested, washed once with PBS, and re-suspended in R-buffer at the concentration 10,000 cells/ μ L. A total number of 100,000 cells (volume of 10 μ L) was mixed with 0.5 μ g of px330-sgp53 construct and incubated for 10 minutes at room temperature. In case of MOCK transfection, equal volume of vehicle was used. Electroporation was performed in the “E” electroporation buffer using 10 μ L Neon tip with one pulse set to the voltage of 1100V and 30ms width (Neon Optimization Program #6). Subsequently, cells were transferred to a new MatrigelTM-coated dish with fresh cell culture media. The entire above described procedure was then repeated in 3-4 day intervals before cells reached the confluency. Each time, only 100,000 cells were used for electroporation. The remaining cells were harvested for protein analyses. As shown in Figure 1B, our strategy resulted in notable downregulation of p53 protein already after two consecutive Neon transfections with the px330-sgp53 plasmid. The

knockdown efficiency was further improved after additional rounds of transfection (up to five consecutive transfections performed).

To assess both the efficiency and possible off-target activities of our protocol, following the fifth round of transfections the cells were passaged, approximately half of the total cell mass was harvested for analyses, while the rest was cryopreserved. Importantly, the expression of microRNA miR-34a, a direct transcriptional target of p53 protein [13], was significantly downregulated in those cells (Figure 1C), thus providing functional evidence that a process, normally controlled by p53, becomes abrogated in hESCs transfected by px330-sgp53 plasmid. These cells are further referred to as “p53 Low” hESCs.

CRISPR/Cas9 system typically offers higher specificity (less off-targets) over downregulation of gene expressing using RNAi strategies [14,15]. Nonetheless, prolonged expression of Cas9 nuclease might be associated with increased rate of off target effects [4,8]. Therefore, we aimed to verify that hESC sublines, produced here by our approach of repetitive transfections, remain pluripotent and do not undergo spontaneous differentiation. To this end, we assayed these cells for the presence and absence of markers of pluripotency (Oct4, Nanog, and microRNA miR-302a; Figure 1D & E) and differentiation (here represented by Brachyury and GATA6; Figure 1F), respectively, by qPCR and Western blotting. We found that in p53 Low cells the levels of all markers tested are about the same as in controls, thus verifying the undifferentiated phenotype of hESCs with downregulated p53 protein.

Given our experimental design, the resulting population retained some expression of p53 protein (Figure 1B). Most likely, this is due to the presence of small subpopulation of p53 heterozygotes [16]. Therefore, we decided to isolate individual clones of hESCs lacking expression of p53 (p53 knock out – p53 KO) in order to assess the efficacy of p53 targeting at single cell level.

Efficient clonal selection of p53 KO hESCs that retain their stemness

To select individual p53 KO clones from p53 Low hESC population, live cells were sorted to 96-well-plate using standard tabletop cell sorter (Figure 2A). Survival rate of hESCs at single cell level was around 20%, therefore within the range of clonal survival typically seen in such experiments [9]. Surviving clones (total number of 33) were subsequently expanded, passaged, approximately half of the total cell mass was harvested for protein analyses, while the rest was cryopreserved. Remarkably, out of the total number of clones analyzed, only 6 showed some minimal expression of p53 protein. The remaining 27 clones (82%) did not express any p53 protein as an evidence of efficient gene targeting and hence were considered p53 KO (Figure 2B and 2C).

Three individual p53 KO clones (numbered #A9, #A10, and #A11 in Figure 2B) were characterized further. Under the standard culture conditions on MEFs, both MOCK and p53 KO hESCs retained morphology typical for undifferentiated hESCs – round smooth colonies with distinct edges (Figure 2D, clone #A11, data for clones #A9 and #A10 not shown). Also, both MOCK and p53 KO hESCs contained the same amounts of Oct4 and Nanog as demonstrated by indirect immunofluorescence. To functionally verify the absence of p53

protein in p53KO hESCs, we have induced DNA damage to both MOCK and p53 KO hESCs by treatment with Etoposide for 8hrs. Results show that while the MOCK hESCs stabilized p53 protein and induced the expression of MDM2 and GDF15 proteins upon DNA damage, p53 KO hESCs failed to do so and the level of MDM2 and GDF15 proteins remained undistinguishable from the untreated cells (Figure 2E; MOCK and clone #A11, data for clones #A9 and #A10 not shown). Importantly, the level of phospho- γ H2AX, a hallmark of DNA damage induction, was increased in similar manner in both the MOCK and p53 hESCs after etoposide treatment.

Finally, to assess their overall differentiation propensity both *in vitro* and *in vivo*, we induced the p53 KO hESCs to differentiate towards embryoid bodies as well as injected them to NOD-SCID mice and evaluated their ability to form teratomas. As shown in Figure 2F, both MOCK and p53 KO hESCs formed EBs of comparable size, frequently with typical cavity inside. After 40 days of differentiation we also examined expression of differentiation markers in EBs derived from p53 KO cells. As determined by indirect immunofluorescence, EBs contained ectoderm-specific TUJ and SOX2, mesoderm-specific Brachyury, and endoderm-specific GATA6. Teratomas comprising all three germ layers developed *in vivo* from both MOCK hESCs and two p53 KO clones analyzed (Figure 2G; clone #A11, data for MOCK and clone #A9 not shown), further documenting uncompromised differentiation potential of hESCs derived by our protocol.

Conclusion

Altogether, our data show that repeated transfection of undifferentiated hESCs using Neon TS leads to dramatic downregulation of targeted protein (here p53) and provides an effective approach for establishment of p53 KO clones. We believe that our methodology represents an easy-to-use technique to obtain genetically modified hESCs, when the goal is to permanently disrupt expression of gene of choice. Given the increasing number of reports successfully and reproducibly utilizing CRISPR/Cas9 technology in high throughput screens [16–19], without reporting significant differences in targeting efficiency for individual loci, we are confident that our protocol can be easily adapted for targeting of any gene of interest. Even though we cannot formally exclude that prolonged expression of Cas9 nuclease might have led to additional cuts in genomic DNA, in addition to the targeted p53 locus, our functional data clearly show that hESCs generated by this approach do retain the key stem cell features.

Acknowledgement

Authors would like to acknowledge Oscar Fernandez-Capetillo, Peter Andrews, Lumír Krejčí, Stjepan Uldrijan, Boivoj Vojtěšek, and Karel Souček for sharing various reagents, Hana Kotasova for assistance with cell sorting, Milan Esner for assistance with microscopy, and Ondřej Bernatík, Michaela Kloucková, Klara Koudelková, Katerina Marecková, Veronika Sedláková, and Katerina Vasicková for technical support. This work was supported by funds from the Faculty of Medicine MU to junior researcher D.D. and L.C. (ROZV/24/LF/2016, ROZV/25/LF/2017), funds from Masaryk University to A.H. (Tissue Engineering 7; MUNI/A/1369/2016) and M.B. (MUNI/C/1709/2016), grants from Czech Science Foundation to D.D. (15-18316Y) and L.C. (16-03269Y), Follow up research fund from Federation of European Biochemical Societies (FEBS), and grant from Swiss National Science Foundation (IZ11Z0_166533) to L.C.

References

1. Cong L, Ran FA, Cox D, Lin S, Barretto R, Habib N, Hsu PD, Wu X, Jiang W, Marraffini LA, Zhang F. Multiplex genome engineering using CRISPR/Cas systems. *Science*. 2013; 339:819–823. [PubMed: 23287718]
2. Mali P, Yang L, Esvelt KM, Aach J, Guell M, DiCarlo JE, Norville JE, Church GM. RNA-guided human genome engineering via Cas9. *Science*. 2013; 339:823–826. [PubMed: 23287722]
3. Ding Q, Regan SN, Xia Y, Oostrom LA, Cowan CA, Musunuru K. Enhanced Efficiency of Human Pluripotent Stem Cell Genome Editing through Replacing TALENs with CRISPRs. *Cell Stem Cell*. 2013; 12:393–394. [PubMed: 23561441]
4. Fu Y, Sander JD, Reyon D, Cascio VM, Joung JK. Improving CRISPR-Cas nuclease specificity using truncated guide RNAs. *Nat Biotechnol*. 2014; 32:279–284. [PubMed: 24463574]
5. Wang H, Yang H, Shivalila CS, Dawlaty MM, Cheng AW, Zhang F, Jaenisch R. One-Step Generation of Mice Carrying Mutations in Multiple Genes by CRISPR/Cas-Mediated Genome Engineering. *Cell*. 2013; 153:910–918. [PubMed: 23643243]
6. Yang L, Guell M, Byrne S, Yang JL, De Los Angeles A, Mali P, Aach J, Kim-Kiselak C, Briggs AW, Rios X, Huang P-Y, et al. Optimization of scarless human stem cell genome editing. *Nucleic Acids Res*. 2013; 41:9049–9061. [PubMed: 23907390]
7. González F, Zhu Z, Shi Z-D, Lelli K, Verma N, Li QV, Huangfu D. An iCRISPR Platform for Rapid, Multiplexable, and Inducible Genome Editing in Human Pluripotent Stem Cells. *Cell Stem Cell*. 2014; 15:215–226. [PubMed: 24931489]
8. Hsu PD, Scott DA, Weinstein JA, Ran FA, Konermann S, Agarwala V, Li Y, Fine EJ, Wu X, Shalem O, Cradick TJ, et al. DNA targeting specificity of RNA-guided Cas9 nucleases. *Nat Biotechnol*. 2013; 31:827–832. [PubMed: 23873081]
9. Byrne SM, Mali P, Church GM. Genome editing in human stem cells. *Methods Enzymol*. 2014; 546:119–138. [PubMed: 25398338]
10. Adewumi O, Aflatoonian B, Ahrlund-Richter L, Amit M, Andrews PW, Beighton G, Bello PA, Benvenisty N, Berry LS, Bevan S, Blum B, et al. Characterization of human embryonic stem cell lines by the International Stem Cell Initiative. *Nat Biotechnol*. 2007; 25:803–816. [PubMed: 17572666]
11. Kunova M, Matulka K, Eiselleova L, Salykin A, Kubikova I, Kyrlyenko S, Hampl A, Dvorak P. Adaptation to robust monolayer expansion produces human pluripotent stem cells with improved viability. *Stem Cells Transl Med*. 2013; 2:246–254. [PubMed: 23486835]
12. Watanabe K, Ueno M, Kamiya D, Nishiyama A, Matsumura M, Wataya T, Takahashi JB, Nishikawa S, Nishikawa S, Muguruma K, Sasai Y. A ROCK inhibitor permits survival of dissociated human embryonic stem cells. *Nat Biotechnol*. 2007; 25:681–686. [PubMed: 17529971]
13. He L, He X, Lim LP, de Stanchina E, Xuan Z, Liang Y, Xue W, Zender L, Magnus J, Ridzon D, Jackson AL, et al. A microRNA component of the p53 tumour suppressor network. *Nature*. 2007; 447:1130–1134. [PubMed: 17554337]
14. Boettcher M, McManus MT. Choosing the Right Tool for the Job: RNAi, TALEN, or CRISPR. *Mol Cell*. 2015; 58:575–585. [PubMed: 26000843]
15. Evers B, Jastrzebski K, Heijmans JPM, Grønrum W, Beijersbergen RL, Bernards R. CRISPR knockout screening outperforms shRNA and CRISPRi in identifying essential genes. *Nat Biotechnol*. 2016; 34:631–633. [PubMed: 27111720]
16. McKinley KL, Cheeseman IM. Large-Scale Analysis of CRISPR/Cas9 Cell-Cycle Knockouts Reveals the Diversity of p53-Dependent Responses to Cell-Cycle Defects. *Dev Cell*. 2017; 40:405–420.e2. [PubMed: 28216383]
17. Fong CS, Mazo G, Das T, Goodman J, Kim M, O'Rourke BP, Izquierdo D, Tsou M-FB. 53BP1 and USP28 mediate p53-dependent cell cycle arrest in response to centrosome loss and prolonged mitosis. *eLife*. 2016; 5
18. Lambrus BG, Daggubati V, Uetake Y, Scott PM, Clutario KM, Sluder G, Holland AJ. A USP28-53BP1-p53-p21 signaling axis arrests growth after centrosome loss or prolonged mitosis. *J Cell Biol*. 2016; 214:143–153. [PubMed: 27432896]

19. Meitinger F, Anzola JV, Kaulich M, Richardson A, Stender JD, Benner C, Glass CK, Dowdy SF, Desai A, Shiau AK, Oegema K. 53BP1 and USP28 mediate p53 activation and G1 arrest after centrosome loss or extended mitotic duration. *J Cell Biol.* 2016; 214:155–166. [PubMed: 27432897]

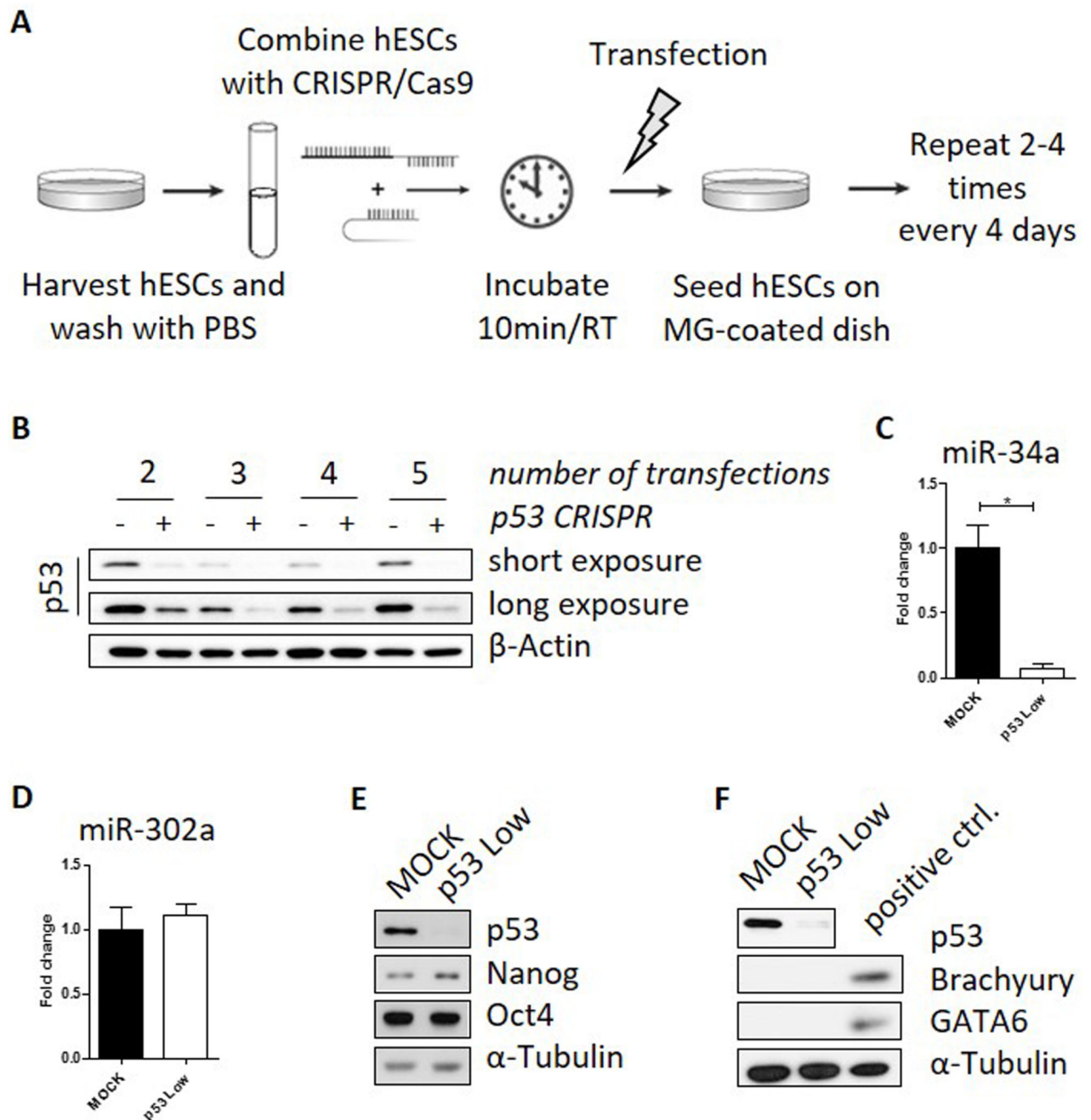


Figure 1. Repeated transfection of hESCs with p53-CRISPR/Cas9 shows efficient downregulation of p53 protein while maintaining pluripotency.

A) Scheme of repeated transfection using Neon Transfection System. B) Analyses of p53 protein expression by Western blot after 2-5 consecutive rounds of transfection. Alpha-tubulin was used as loading control. C) Relative expression of miR-34a, or miR-302a (D), as determined by qPCR. Protein levels of pluripotency markers (Oct4, Nanog; E) and differentiation-associated markers (GATA6, Brachyury; F) were analyzed in MOCK and p53 Low hESCs by Western blotting. Differentiating hESCs were used as positive control.

Alpha-tubulin was used as loading control. Mean data \pm SEM from at least three independent experiments are shown. (*) denotes $p < 0.05$.

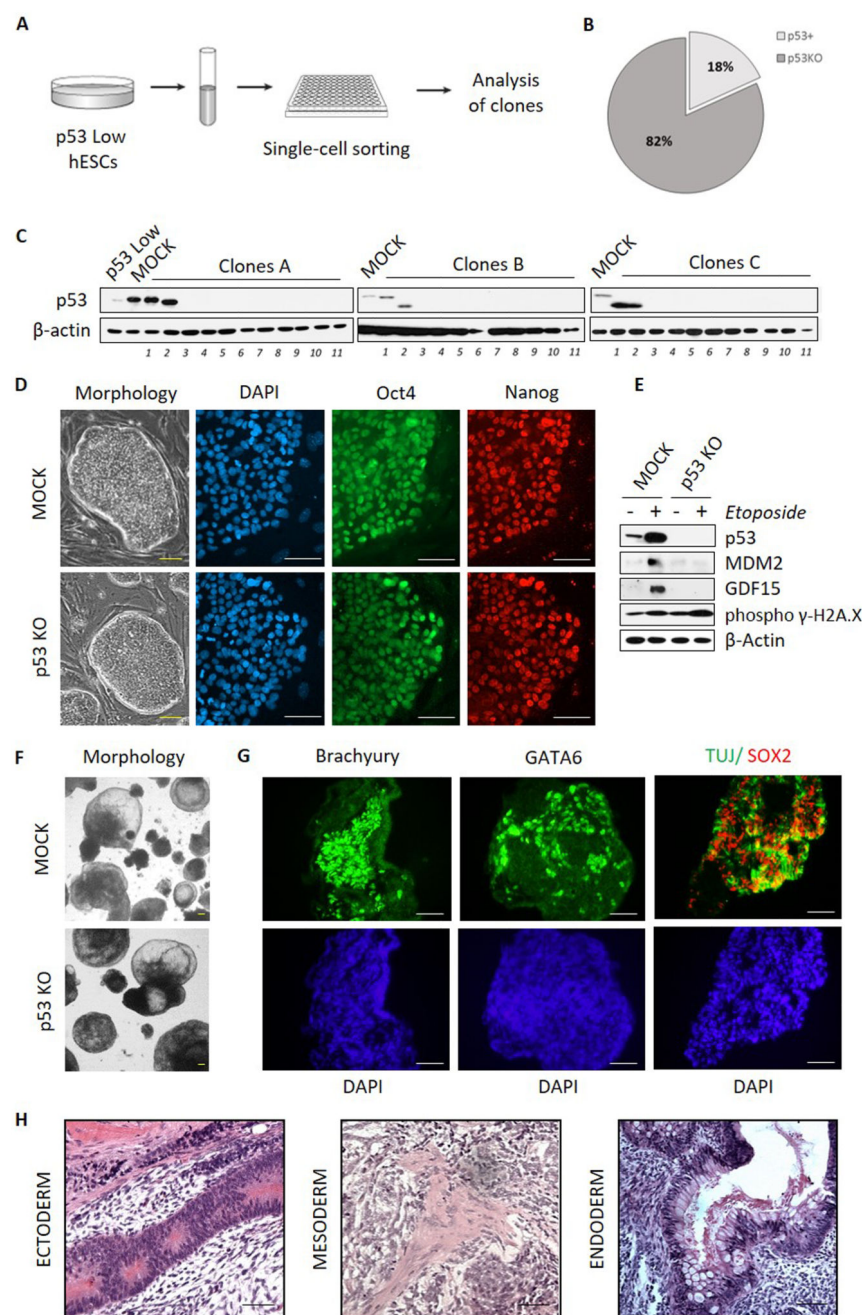


Figure 2. Efficient clonal selection of p53KO hESCs and evaluation of their stemness.

A) Experimental strategy of isolation of hESCs p53KO clones from p53 Low hESCs population. B, C) Isolated p53KO clones were analyzed by Western Blot for p53 expression, beta-actin antibody was used to verify equal loading. D) MOCK and p53 KO hESCs (clone #A11) were grown on MEFs and examined for the morphology of colonies (left) or the expression of pluripotency markers Oct4 (green) and Nanog (red) by microscopy. DAPI was used to visualize cell nuclei (blue). Scale bars = 100μm. E) MOCK and p53 KO hESCs (clone #A11) were treated either by 3.4 μM Etoposide to induce DNA damage or DMSO.

After 8 hrs, cells were harvested and analyzed by Western blot for p53 protein stabilization, and the expression of p53 downstream genes – MDM2 and GDF15. DNA damage induction is shown by the increase in phospho γ -H2A.X. F) Bright field microscopy images of MOCK and p53 KO hESCs (clone#A11) following differentiation into EBs. Scale bars = 200 μ m. G) EBs derived from p53 KO hESCs (clone#A11) were analyzed for the expression of the differentiation markers by antibody staining and confocal microscopy. DAPI (blue) was used to visualize cell nuclei. Ectoderm markers are represented by TUJ (green) and SOX2 (red), mesoderm is represented here by Brachyury (green), and endoderm is represented here by GATA6 (green). Scale bars = 200 μ m. H) Hematoxylin and eosin staining of teratoma tissue from SCID mouse injected with p53KO hESCs (representative data shown for clone #A9). Tissue sections show morphological structures typical for neuroectoderm, mesoderm, and endoderm. Scale bars = 200 μ m.

Appendix 13

Bryja V, Červenka I, **Čajánek L**. The connections of Wnt pathway components with cell cycle and centrosome: side effects or a hidden logic. *Crit Rev Biochem Mol Biol*. 2017 Dec;52(6):614-637. doi: 10.1080/10409238.2017.1350135. (JCR 2017. IF=5.279, Q1 - Biochemistry & Molecular Biology)

Published in final edited form as:

Crit Rev Biochem Mol Biol. 2017 December ; 52(6): 614–637. doi:10.1080/10409238.2017.1350135.

The connections of Wnt pathway components with cell cycle and centrosome: side effects or a hidden logic?

Vítězslav Bryja¹, Igor Šerpenka², and Lukáš Čajánek³

¹Department of Experimental Biology, Faculty of Science, Masaryk University, Brno, Czech Republic

²Molecular and Cellular Exercise Physiology, Department of Physiology and Pharmacology, Karolinska Institutet, Stockholm, Sweden

³Department of Histology and Embryology, Faculty of Medicine, Masaryk University, Brno, Czech Republic

Abstract

Wnt signalling cascade has developed together with multicellularity to orchestrate the development and homeostasis of complex structures. Wnt pathway components – such as β -catenin, Dishevelled, Lrp6, and Axin – are often dedicated proteins that emerged in evolution together with the Wnt signalling cascade and are believed to function primarily in the Wnt cascade. It is interesting to see that in recent literature many of these proteins are connected with cellular functions that are more ancient and not limited to multicellular organisms – such as cell cycle regulation, centrosome biology, or cell division. In this review, we summarize the recent literature describing this crosstalk. Specifically, we attempt to find the answers to the following questions: Is the response to Wnt ligands regulated by the cell cycle? Is the centrosome and/or cilium required to activate the Wnt pathway? How do Wnt pathway components regulate the centrosomal cycle and cilia formation and function? We critically review the evidence that describes how these connections are regulated and how they help to integrate cell-to-cell communication with the cell and the centrosomal cycle in order to achieve a fine-tuned, physiological response.

1 Wnt signaling pathways

Wnt signaling pathway is one of the key signaling cascades, essential for both correct embryo development and tissue homeostasis in adulthood. Research in Wnt signaling pathways started around 1980, when two groups independently reported new morphogenetic determinants in *Drosophila* and mouse, (Nusse and Varmus, 1982; Nusslein-Volhard and Wieschaus, 1980) respectively. Since then, Wnt signaling has been found to affect a myriad of aspects of cell behavior.

Declaration of Interest

The work in V. Bryja's lab is supported by the Czech Science Foundation (15-21789S, 17-16680S, 17-09525S), Masaryk University (MUNI/G/1100/2016) and Neuron – Fund for Support of Science. The Work in the Čajánek lab is supported by the Federation of European Biochemical Societies (Follow up research fund), funds from the Faculty of Medicine MU (ROZV/24/LF/2016), Czech Science Foundation (16-03269Y), and Swiss National Science Foundation (IZ11Z0_166533).

The Wnt signaling pathway is activated by Wnt ligands - secreted morphogens and drivers of embryogenesis that exert their influence over medium to long range distances. Nineteen homologs are present in the human genome and they are well conserved throughout the animal kingdom. Wnt proteins can activate several distinct pathways that are shortly introduced below.

1.1 Wnt/ β -catenin pathway

First discovered and best described, the Wnt/ β -catenin pathway, also referred to as the canonical pathway, influences cell fate, proliferation and self-renewal of stem and progenitor cells throughout the lifespan of metazoa (Korinek et al., 1998; ten Berge et al., 2011). It revolves around the transcriptional co-activator β -catenin, which is present in the cell in two distinct pools. It maintains the connection to actin cytoskeleton as a component of cadherin junctions and its soluble cytoplasmic pool serves as a signaling mediator. Cytoplasmic concentration of β -catenin in the cell is kept low by multiprotein complex consisting of Axin, Adenomatous polyposis coli (APC) and Glycogen synthase kinase-3 β (GSK-3 β). Without a Wnt signal, this destruction complex continually phosphorylates β -catenin and targets it for degradation using the ubiquitin proteasome pathway. For a scheme of the Wnt/ β -catenin pathway see Figure 1.

The pathway activation's beginning conforms to our view of standard signal transduction. Wnt protein binds the Frizzled receptor (Fz or Fzd) and Low-density-lipoprotein receptor-related proteins 5 and 6 (Lrp5/6) co-receptor forming a ternary complex. Cytoplasmic portion of this complex is phosphorylated, which prompts recruitment of Wnt cascade mediators. Dishevelled (DVL) protein binds to Fzd and initiates the phosphorylation of cytoplasmic tail of Lrp5/6 receptor, which then binds Axin. This renders the destruction complex inactive and stops the constant downregulation of β -catenin, which starts to accumulate in the cytoplasm. Upon reaching a certain threshold, β -catenin is translocated into the nucleus, where it couples with transcription factors from the T-cell-specific transcription factor/Lymphoid enhancer-binding factor (TCF/LEF) family. The final outcome of the signal cascade is the upregulation of genes connected to cell fate and cell proliferation, such as c-Myc, or Cyclin D1 and many others (Tetsu and McCormick, 1999; He et al., 1998).

1.1.1 Receptor complex – Frizzled and LRP5/6—Canonical Wnts require two receptor sets to propel the signal downstream. Frizzled are seven-pass transmembrane domain receptors belonging to class F of G-protein coupled receptors (GPCR) (Schulte and Bryja, 2007). Due to the fact that humans encode 10 Fzd receptors and 19 Wnts, their interaction, affinity, specificity and involvement in distinct cascades has been problematic to elucidate.

Lrp5/6 and *Drosophila* homologue Arrow are single-span transmembrane proteins that play a vital role as co-receptors in Wnt/ β -catenin signaling. The intracellular part of Lrp5/6 contains highly conserved PPPS/TPxS/T motif reiterated five times (Tamai et al., 2004) whose phosphorylation is required to activate downstream signaling as described in part 1.1.3.

1.1.2 Dishevelled—Dishevelled (DVL) is a key regulator of Wnt signaling connecting the receptor complex and downstream effectors. It also stands at the branching point between Wnt/ β -catenin and alternative pathways. Three DVL isoforms (DVL1, DVL2 and DVL3) are present in mammals and they have partially specific, partially overlapping functions. Even though many functions of DVL and its binding partners have been discovered and we have gained considerable insights into its regulation, the key question concerning its switching properties still remains unanswered.

DVL proteins possess a well-defined three-domain structure with interspersed unordered regions. DVL DIX domain (Dishevelled, aXin), which shares homology with a similar one present in Axin confers DVL the ability to assemble into homo- or hetero-oligomers. The ability to polymerize in a head-to-tail manner is required for Wnt/ β -catenin signaling (Schwarz-Romond et al., 2007). DVL DIX domain binding to Axin inhibits Axin function (Fagotto et al., 1999; Li et al., 1999; Smalley et al., 1999) in the destruction complex. PDZ domain (Post synaptic density, Disc large, Zonula occludens-1) is the most versatile when it comes to its array of binding partners. It interacts with both canonical and non-canonical activators alike, making it an ideal candidate for a switch (Wallingford and Habas, 2005). DEP domain was thought to function predominantly in alternative Wnt pathways (Axelrod et al., 1998) but recent evidence confirmed its critical importance also in the Wnt/ β -catenin pathway (Gammons et al., 2016; Paclikova et al., 2017). DEP domain helps with binding to Fzd and interacts with lipid moieties on the plasma membrane in order to stabilize this interaction (Pan et al., 2004; Tauriello et al., 2012).

DVL is a subject to a large array of post-translational modifications, as reviewed elsewhere (Bryja and Bernatik, 2014). The most important modification, with respect to its role in the Wnt pathway, is phosphorylation by casein kinase (CK1) δ/ϵ , required for Wnt pathway activation. CK1 δ/ϵ phosphorylates DVL in a two-step mechanism. Initial “switch on” phosphorylation is induced by Wnt signaling, followed by a second round of phosphorylation, which act as a shutoff mechanism (Bernatik et al., 2011; Bernatik et al., 2014). Other DVL kinases have been also reported and are discussed below.

1.1.3 Cytoplasmic events and activation of transcription—The clear sequence of events happening directly below the membrane after the Wnt initiation signal arrives has not yet been characterized; nevertheless, many facts are known. Lrp5/6 and Fzd are brought into close proximity, their association alone is sufficient for Wnt signal initiation. Fzd function is linked to DVL and DVL is required for Lrp6 phosphorylation. DVL and Axin contain homologous DIX domain which confers ability to form weak homo- or heterotypic interactions leading to aggregation (Bienz, 2014). DVL homo-oligomerization promotes Fzd-Lrp6 cluster creation and also recruits Axin to the membrane, facilitating Lrp6 phosphorylation by GSK-3 β and CK1 γ . It creates a positive feedback loop and amplifies the signal by phosphorylating all PPPSP motifs. This model for signal transduction has been dubbed 'initiation-amplification' (Zeng et al., 2008) and signaling component aggregation creates structures named 'signalosomes' (Bilic et al., 2007).

The key regulator of cytoplasmic β -catenin levels, destruction complex, consists of Axin, APC, GSK-3 β and several other proteins. Axin directly interacts with all other core

components of the destruction complex (β -catenin, APC, CK1 α , and GSK-3 β), thus being the central scaffold (Ikeda et al., 1998; Kishida et al., 1998; Sakanaka, Weiss, and Williams, 1998).

In the absence of a Wnt signal, the role of the destruction complex is to continually phosphorylate β -catenin and target it for ubiquitination and subsequent degradation, to prevent the expression of target genes. The phosphorylation is performed by GSK-3 β . In addition, CK1 α binds Axin and introduces priming phosphorylation on β -catenin's S45, which leads to it being recognized by GSK-3 β . GSK-3 β subsequently binds Axin as well and efficiently phosphorylates β -catenin on S33/S37/T41, which can be subsequently targeted for degradation by E3 ubiquitin ligase β -TrCP.

After deactivating the destruction complex, β -catenin is accumulated in the cytoplasm and shuttled to the nucleus by a mechanism that is not entirely understood (Henderson and Fagotto, 2002; Stadeli, Hoffmans, and Basler, 2006). When in the nucleus, β -catenin interacts with the TCF/LEF family of transcription factors, it replaces the transcriptional repressor Groucho (Daniels and Weis, 2005) and recruits co-activators such as BCL-9, Pygopus and other proteins, turning the whole complex into an activator.

1.2 β -catenin independent pathways

In addition to the Wnt/ β -catenin pathway, Wnts can also participate in the 'alternative' or also 'non-canonical' signaling branches. They do not employ β -catenin, but rather modify the cytoskeleton. The best known non-canonical Wnt pathway is Wnt/planar cell polarity (PCP) pathway, initially described in *Drosophila* (Fig. 2A). Planar polarity is determined by the asymmetric localization of so-called core PCP components. Two protein subsets are located on the opposite sides of cell-cell adherent junctions (Axelrod, 2009; Zallen, 2007). The Proximal subset consists of atypical cadherin Flamingo (Fmi), LIM domain protein Prickle (Pk) and four-pass Van Gogh transmembrane protein (Vang, also known as Strabismus; mammalian homologues: Van Gogh-like proteins, Vangl1 and Vangl2). Distal subset contains Fmi, serpentine receptor Frizzled (Fz), cytoplasmic protein Dishevelled (Dsh) and ankyrin repeat protein Diego (Dgo). The asymmetric localization of core PCP proteins stems from intracellular interactions between these subsets. They display self-organizing properties and the alignment between cells constructs itself and is propagated due to asymmetric cell-to-cell contacts (Fig. 2A).

Components of the PCP pathway – Fzd, DVL, Prickle, Vangl1/2 and Fmi homologues Celsr1-3 have fully conserved function also in vertebrates. However, additional proteins, namely atypical receptor kinases Ror1, Ror2 and PTK7 participate as co-receptors (Fig. 2B). Since PCP pathway activation usually results in cytoskeletal changes, its effectors in vertebrates mostly belong to the Rho family of GTPases and include RhoA and Rac1. RhoA interacts with DVL through protein Daam1 (Habas, Kato, and He, 2001) activating kinase ROCK, in turn mediating cytoskeletal rearrangements. The parallel pathway activates Rac1, leading to increased JNK activity (Fig. 2B). For a recent review on Wnt/PCP pathway see (Butler and Wallingford, 2017). In vertebrates, Wnts can in some cases activate release of intracellular calcium that subsequently triggers multitude of Ca²⁺ dependent events mediated via activation of CaMKII, PKC or calcineurin. This signaling cascade referred to

as Wnt/Ca²⁺ then triggers depending on the context NFAT-mediated transcription or cytoskeletal remodeling (Fig. 2C). For further reading we refer to the reviews on this topic (Kohn and Moon, 2005; Slusarski and Pelegri, 2007).

2 Cell cycle progression and cell division from a centrosome perspective - friends with benefits

Dividing a cell to giving rise to daughter cells is one of the most fundamental cellular processes for both unicellular and multicellular organisms. In fact, “to divide” is the true purpose of proliferating cells, such as stem cells or progenitors, in order to create a sufficient pool of cells from which more specialized cells differentiate. Such a task requires the coordination of cellular metabolism, duplication of DNA, and cytoskeletal rearrangements. To ensure timely action of the aforementioned processes, the cell deploys a sophisticated cell cycle regulatory machinery, centered on cyclin dependent kinases (CDKs) and additional specialized mitotic kinases, to control its progression through the cycle via a system of checkpoints (Nurse, 1997; Khodjakov and Rieder, 2009). That said, it is not surprising that organelle, thought to play a central role in many aspects of cell cycle and division, was given the fitting name “centrosome”. In fact, it was Theodor Boveri who coined that name more than hundred years ago when observing these organelles at the poles of the bipolar mitotic spindle. At that time, he also postulated its fundamental role in cell division (Boveri, 2008). The cell cycle and centrosomal cycle are tightly connected, as depicted in Figure 3.

The first experimental evidence for the centrosome’s directing role in cell division came from classical experiments with oocytes, demonstrating that injecting purified centrosomes was sufficient to trigger parthenogenetic development in frog or fish eggs (Klotz et al., 1990; Picard et al., 1987). It has become clear that centrosomes participate in mitotic spindle formation. Further, astral microtubules connect the cell cortex to the centrosome and specify in which position the mitotic spindle will form (Bornens and Gonczy, 2014). When the centrosome is absent, a bipolar spindle is formed through the action of small GTPases Ran (Kalab and Heald, 2008). Having no anchoring point due to the lack of astral microtubules, such spindles float freely in the cytoplasm and seem to adopt a random orientation (Louvét-Vallee, Vinot, and Maro, 2005; Khodjakov and Rieder, 2001). Centrosomes also affect the position of the cleave furrow during cytokinesis by affecting spindle orientation or perhaps also by acting directly on the cytokinetic apparatus (Khodjakov and Rieder, 2001; Piel et al., 2001; Oliferenko, Chew, and Balasubramanian, 2009). Some cell types can also divide asymmetrically, meaning that the daughter cells differ in size, fate, or eventually both (Doe, 2008; Knoblich, 2008). This is especially important during embryogenesis, when a stem cell gives rise to another stem cell to replenish the niche, and one progenitor which rapidly divides further. There is growing experimental evidence from both *Drosophila* and mice suggesting that spindle positioning and/or asymmetry in centrosome inheritance can directly affect the fate of daughter cells (Doe, 2008; Lancaster and Knoblich, 2012).

In addition, centrosomes might also fine tune additional aspects of cell cycle progression. Signaling cascade components implicated in regulating mitotic progression, namely PLK1, Aurora A, CDK1/Cyclin B, and CDC25 have been detected in centrosomes during G2/M

transition (Arquint, Gabryjonczyk, and Nigg, 2014). Further, CDK1/Cyclin B complex, essential for mitotic entry, requires a centrosome for its proper activation (Jackman et al., 2003). In addition, the actual destruction of CDK1/Cyclin B complex, marking the end of mitosis, also seems to be initiated at centrosome (Wakefield, Huang, and Raff, 2000).

2.1 Centrosome –basics

A centrosome is a non-membranous cytoplasmic organelle, formed around a core consisting of two microtubule-based cylindrical structures, the centrioles, which is surrounded by a layered protein matrix termed pericentriolar material (PCM). PCM contains proteins such as gamma-tubulin that help to organize and nucleate microtubules, explaining why centrosomes function as the main microtubule-organizing center (MTOC) in many cell types (Luders and Stearns, 2007). As the cell approaches mitoses, PCM undergoes marked changes. It significantly expands in size, but retains its inner organizations, with a pericentrin occupying layer most proximal to the centriole wall, while proteins such as CEP192 and CEP215/CDK5RAP2 are distributed in PCM's more distal elements (Mennella et al., 2014). Through the microtubules that it organizes and the proteins it recruits, the centrosome plays an important role not only during cell division, but also participates in regulation of cell polarity, migration, and cell trafficking (Conduit, Wainman, and Raff, 2015). In addition, the centrosome serves as a hub/scaffold for proteins involved in cell cycle regulation and cell signaling (Arquint, Gabryjonczyk, and Nigg, 2014). Protein assemblies found in the centrosome's vicinity are termed satellites, hypothesized to participate in centrosome biogenesis via transport or sequestration of key centrosome components (Tollenaere, Mailand, and Bekker-Jensen, 2014).

Centrosomes are typical for animal cells; they probably evolved from flagellar apparatus and possibly played an important role in transitioning to multicellular organisms (Bornens and Azimzadeh, 2007; Bornens, 2012). However centrosomes are not present in all multicellular organisms' cell types. Actually, plants do not have a centrosome at all, but have developed alternative structures and mechanisms to compensate for its absence. Interestingly, the centrosome is also absent in some vertebrate cells. A typical example is an oocyte, which loses centrosomes during its meiotic maturation. Centrosome loss is also a hallmark of final stage of myoblast or cardiomyocyte differentiation, characterized by relocating centrosomal proteins to the nuclear envelope (Bornens, 2012).

Even though a mammalian cell typically contains one or two centrosomes, some specialized cell types show a surprising variability in terms of centrosome numbers (Cunha-Ferreira, Bento, and Bettencourt-Dias, 2009). However, it would be very premature to conclude that the absolute centrosome number does not matter. Besides the rather extreme examples of cell specialization, the correct number of centrosomes in a proliferating cell is under strict surveillance (Holland et al., 2012; Fava et al., 2017; Wong et al., 2015; Bazzi and Anderson, 2014), since alterations in the number of centrosomes (called numerical centrosome aberrations) have profound effects on both development and homeostasis (Gonczy, 2015; Nigg, Cajanek, and Arquint, 2014; Godinho and Pellman, 2014; Bettencourt-Dias et al., 2011). Indeed, the presence of extra centrosomes is not only sufficient to trigger genome instability (Ganem, Godinho, and Pellman, 2009) but also to initiate tumor development

(Levine et al., 2017; Sercin et al., 2016; Basto et al., 2008). In addition, there is a growing body of evidence that alterations in centrosome numbers are linked to diseases such as primary microcephaly and primordial dwarfism (Nigg, Cajanek, and Arquint, 2014; Marthiens et al., 2013; Bettencourt-Dias et al., 2011).

2.2 Cilia

Cilia are microtubule-based organelles typically found protruding from the surface of non-dividing cells. They can be either motile or immotile, with immotile ones being called primary cilia. Primary cilia, given their non-motile character, were originally considered vestigial organelles. Importantly, however, an increasing number of studies appearing over the last 10-15 years have very much changed that view, and put the primary cilia into a position of important cellular antennas, with essential functions both during embryogenesis and tissue homeostasis, thanks to their employment in the Hh pathway or Calcium signaling (Goetz and Anderson, 2010; Singla and Reiter, 2006; Yoshida and Hamada, 2014). The importance of cilia has become perhaps even more appreciated when a group of diverse human diseases was linked to ciliary structural and/or functional defects, and hence collectively termed ciliopathies (Bettencourt-Dias et al., 2011; Mitchison and Valente, 2017; Braun and Hildebrandt, 2017).

Cells usually contain one mother centriole at a time, and therefore can form only one cilium. Multiciliated cells are an exception to this rule, typically found in airway epithelium or kidneys, for example. During the course of their differentiation, these cells are able to produce up to hundreds of extra centrioles, to serve as basal bodies (Brooks and Wallingford, 2014; Meunier and Azimzadeh, 2016).

The most prominent part of the cilium is the membrane-enclosed axoneme, see Fig. 4. It comprises of nine microtubule doublets surrounding a central pair – the so-called 9+2 arrangement is typically found in the motile cilia. The central pair is usually missing in primary cilia.

The first insight into ciliogenesis mechanisms was revealed in pioneering work by Sorokin (Sorokin, 1962), who postulated the docking of Golgi-derived vesicles to the mother centriole as one of the key steps in cilia formation. The current model expands on that notion, see again Fig. 4. Another crucial step towards the assembled cilium is the loss of protein CP110/CEP97 protein complex from the distal end of the mother centriole, which is predicted to allow outgrowth of axonemal microtubules (Schmidt et al., 2009; Spektor et al., 2007). The precise mechanism regulating this event is not known, but it requires activity from Tau tubulin kinase 2 (TTBK2) (Goetz, Liem, and Anderson, 2012; Cajanek and Nigg, 2014) and possibly also ciliary vesicle delivery (Lu et al., 2015). TTBK2 is also implicated in the recruitment of intraflagellar transport complexes (IFTs) to the basal body (Goetz, Liem, and Anderson, 2012; Cajanek and Nigg, 2014). IFT particles are essential for cargo delivery both in and out of the cilium (Rosenbaum and Witman, 2002; Bhogaraju et al., 2013), their actual movement with their cargo is performed by motor proteins, see Fig. 4. Intraflagellar transport mediates both the assembly and resorption of the cilium, and the trafficking of key signaling molecules; in its absence cells are not able to form cilia (Rosenbaum and Witman, 2002). The assembly of cilium as well as disassembly are tightly

interconnected with the cell cycle progression. The cells form primary cilia after exiting from mitoses, in G0/G1. Conversely, resorption of cilia typically starts upon the entry to the next cell cycle. Cilia need to be fully disassembled before mitosis. In fact, proteins implicated in controlling cilium disassembly involve many well established mitotic progression regulators, such as Aurora A, PLK1, or NEK kinase family (Sanchez and Dynlacht, 2016; Nachury and Seeley, 2010).

3 Crosstalk between centrosome-controlled events and Wnt signaling

Multiple reports have observed key Wnt pathway components localized in the centrosome/basal body and/or mitotic spindle. Centrosome can be a “sticky” organelle in the immunostainings and we thus reviewed only studies that use endogenous proteins and/or overexpression of proteins tagged with fluorescent proteins. These studies and their key observations, including the methodological weaknesses and strengths, are summarized in Table 1.

The commonly observed localization of Wnt pathway proteins in the centrosome/basal body raised a number of questions about the relationship between the Wnt pathway and centrosome-organized events. In the chapters below we attempt to critically summarize our current understanding of this crosstalk, and how it affects key events in Wnt signaling regulation and the centrosomal cycle.

3.1 To what extent is centrosome/cilium required for the Wnt/ β -catenin pathway?

Interestingly, over the years there have been an increasing number of reports arguing either for or against a possible role for centrosome, basal body or primary cilium in Wnt signaling. If one simply examines the reported localizations (Table 1), the argument of “guilty by being present” definitely applies here. This view is further supported by the reported protein-protein interactions between various Wnt pathway components (including β -catenin, DVL, Axin or APC) and bona fide centrosomal proteins that we summarize in Table 2. Recent proteomic studies that profile the protein composition of centrosomes and cilia provide additional evidence regarding the presence of Wnt pathway proteins (such as β -catenin or CK1 α and δ) in the centrosome (Jakobsen et al., 2011) or their interactions with core centrosomal proteins. The work of Pelletier lab, that used the BioID approach pinpointed the widespread nature of these physical contacts and identified more than a hundred of interactions between core centrosomal and Wnt pathway proteins, is especially informative. We list these interactions in Table 2 and refer the reader to the original publication (Gupta et al., 2015) for more details.

Given that possible connections between centrosomes/cilia and Wnt/PCP pathway have been identified earlier and discussed in several reviews (May-Simera and Kelley, 2012; Wallingford and Mitchell, 2011) primarily focus on the potential involvement of centrosome/basal body/primary cilium in the Wnt/ β -catenin signaling pathway in this chapter. Probably the first reported connection to Wnt/ β -catenin signaling was found in relation to *Inversin/Nephrocystin-2*, a mutation of which causes kidney defects (formation of cysts) typical for ciliopathies (Otto et al., 2003). Inversin was postulated to act as a molecular switch between Wnt signaling pathways, negatively regulating Wnt/ β -catenin

signaling (Simons et al., 2005). In addition, a later study showed that depleting Inversin increases expression of DVL1, but reduces levels of DVL2 and DVL3 at the ciliary base (Veland et al., 2013). However, the position of Inversin as a key negative regulator of the Wnt/ β -catenin pathway has been challenged by the work of Sugiyama and colleagues (Sugiyama et al., 2011). The authors failed to see any upregulation of the pathway in *inv* mutant mice, even though the ciliopathy phenotype was present. This example illustrates what will be discussed further - there is often compelling evidence providing an argument for both scenarios (does it or does it not influence Wnt signaling?), and it is not easy to reach a definitive conclusion. However, when the reported data allow alternative interpretations, we aim to provide them.

Knock-down of BBSome components (Bbs1, Bbs4, Mkks) was reported to hyperactivate Wnt/ β -catenin signaling (Gerdes et al., 2007). Furthermore, mutation/downregulation of additional regulators of ciliogenesis (Kif3a, Ift88, Odf1) were also shown to increase Wnt/ β -catenin signaling (Gerdes et al., 2007; Corbit et al., 2008; McDermott et al., 2010; Lin et al., 2003; Liu et al., 2014). However, *in vivo* analyses of mutants with ciliogenesis defects (IFT88, IFT172, Dync2h1, Kif3a) by other groups did not find any pronounced defects in Wnt/ β -catenin signaling, even though ciliogenesis and/or Hh pathway were severely hampered (Ocbina, Tuson, and Anderson, 2009; Huang and Schier, 2009). Possible explanation for such discrepancies is the different penetrance of some phenotypes (if there is indeed a defect in Wnt signaling seen, it is often modest), or cell type specificity. One also has to consider simple explanations such as off-target effects (especially if RNAi was employed and rescue experiments were not done) or different sensitivities of used readouts.

Alternatively, one could attempt to explain at least some of the phenotypes by distinguishing strictly between those caused by the absence of protein and those by the absence of organelle (centrosome or cilia, in this case), which is a consequence of the absent protein. This view is supported by the fact that some cilia regulators also give Wnt signaling phenotype while others do not. This implies that the signaling defects may not actually be related to defective ciliogenesis but rather arise due to some additional, cilia-unrelated functions of individual ciliary proteins, that may directly or indirectly translate into cross talk with Wnt/ β -catenin signaling. For illustration, several groups reported that knockdown/knockout of Kif3a, a subunit of kinesin2 molecular motor, lead to concomitant defects in ciliogenesis and Wnt/ β -catenin signaling (Gerdes et al., 2007; Corbit et al., 2008; Liu et al., 2014). Interestingly, Kif3a has been also shown to affect the orientation of basal bodies by interacting with kinase PAK, independently of its role in ciliary transport (Sipe and Lu, 2011). Moreover, work reporting Kif3a and β -arrestin interaction offers an even more attractive interpretation that altered Wnt signaling observed is due to the direct effects on the β -catenin destruction complex (Kim et al., 2016). Indeed, recent work from the Mlodzik lab (Balmer et al., 2015) has further supported this model in elegant experiments reporting the effects of several ciliary transport machinery components directly on the β -catenin level, independent of cilia formation.

Another plausible explanation of some of the conflicting results is based on well documented observation that β -catenin abundance is under the strict surveillance of proteasome machinery. Interestingly, active proteasomes have been reported to associate

with centrosomes/basal bodies (Gerdes et al., 2007; Wigley et al., 1999; Fabunmi et al., 2000; Gerhardt et al., 2015; Fuentealba et al., 2007; Vora and Phillips, 2015). In addition, E3 ubiquitin ligase Jade-1, which localizes to the centrosome/basal body, is able to ubiquitinate β -catenin and hence target it for destruction by proteasome. Jade-1 activity is controlled negatively by CK1 α and can be modulated by the transition zone protein Nephrocystin-4 (Chitalia et al., 2008; Borgal et al., 2014; Mollet et al., 2005). Thus, centrosome/basal body disruption could in principle lead to dysregulated proteasome/E3 ligase activity, and hence, altered Wnt/ β -catenin signaling (Gerdes et al., 2007; Vora and Phillips, 2015). Importantly, such an interpretation predicts that Wnt/ β -catenin signaling is fine-tuned by the membrane-anchored basal body or intact centrosome, not the presence or absence of cilium. However, there are several questions related to this model. It is not clear how relatively locally altered protein turnover (centrosome or its proximity) may lead to systemic effects on Wnt signaling.

In summary, despite some conflicting results, it seems that centrosomes/cilia are not required to activate the core Wnt/ β -catenin pathway – as indicated by grossly normal Wnt signaling in multiple mouse strains lacking cilia (Ocbina, Tuson, and Anderson, 2009; Huang and Schier, 2009). In support of this conclusion, experiments where centrosomes/basal bodies were genetically or pharmacologically ablated did not reveal striking effects on either the β -catenin protein turnover or Wnt/ β -catenin signaling (Wong et al., 2015; Basto et al., 2006; Bazzi and Anderson, 2014; Insolera et al., 2014). However, the possibility that centrosome/cilium fine tunes the Wnt pathway (i.e. via protein sequestration – see next chapters) and acts in a cell type-specific manner seem plausible but full understanding will require more experiments in the future.

3.2 Do Wnt pathway proteins control cell cycle progression and centrosomal cycle or vice versa?

As we have previously mentioned (see Table 1 and 2), almost all major Wnt/ β -catenin pathway components have been found in the centrosome. This arrangement may to some extent facilitate the proximity of the pathway regulators and in turn may influence Wnt pathway modulation. However, when seen from the opposite perspective, one can ask how centrosomal localization of the Wnt pathway components influences the progression of either the centrosome or cell cycle.

Historically, the Wnt signaling pathway and cell cycle have been connected by Wnt target gene expression: Cyclin D1 and c-myc that are required for progression via G1/S checkpoint were one of the first discovered Wnt target genes and are surely among the most intensively studied. Recently, however, we are witnessing that Wnt signaling, the centrosome and cell cycle are probably more closely intertwined than we previously thought. In this chapter, we would like to summarize the emerging interdependencies of Wnt-centrosome-cell cycle axis. The studies discussed below have two common denominators. The fact that Wnt pathway components localize to the centrosome/basal bodies and physically interact with the core centrosomal proteins and the fact that Wnt signaling components tend to change during the cell cycle and often peak during the G2/M cell cycle phase. Cell cycle associated protein

dynamics have been documented for almost all key Wnt pathway proteins (summarized in Table 3).

3.2.1 Cell cycle modulated Wnt signaling—The obvious question raised by the cycling behaviour of key Wnt pathway proteins is: Do cells respond to Wnt ligands differently while passing through the cell cycle? There is existing evidence that this is indeed the case and the issue was recently reviewed (Niehrs and Acebron, 2012; Acebron and Niehrs, 2016). We will thus sum up this topic only briefly and focus on the open questions.

The first observation suggesting that the response to Wnt ligands can be cell cycle dependent was the identification of Cyclin-Y/CDK14 complex as the kinase phosphorylating PPPSP motifs of Lrp6. This is the key event required for signal transduction and dissolution of the destruction complex. Cyclin-Y is a membrane bound protein and its expression is regulated based on the cell cycle, peaking in G2/M (Davidson et al., 2009). Another fact hinting at the same thing shows that the cells arrested during G2/M by knock-down of CDC25 increased Wnt/ β -catenin signaling (Lee et al., 2009).

Initially it was thought that this particular interaction and phosphorylation results in restricting β -catenin stabilization and thus signaling to the G2/M phase (Davidson et al., 2009). Further research suggested that this phosphorylation event is part of a signaling cascade dubbed Wnt/STOP (stabilization of proteins) signaling (Acebron et al., 2014). Wnt/STOP pathway, discovered and proposed as a signaling cascade in C. Niehrs's laboratory, is a Wnt-induced signaling cascade that results in the inhibition of GSK-3 β activity. GSK-3 β was proposed to phosphorylate multiple proteins in a conserved motif, degron (found also in β -catenin), and target them for degradation. As a consequence, activating Wnt/STOP increases the cell protein content in preparation for cell division. It was proposed that this pathway protects a variety of proteins from proteasome destruction and it is claimed that this is possible solely through the inhibition of GSK-3 β activity. As such, this has very interesting implications when we look at the Wnt-cell cycle connection from other angle. Although many studies reported increases in Wnt pathway molecules during the G2/M phase, little effort was invested in trying to decipher where G2/M-dependent stabilization comes from. Activating Wnt/STOP signaling offers itself as a very elegant solution, however not all Wnt pathway components are known to be targets for GSK-3 β mediated proteasome degradation.

Although the studies mentioned above provide an interesting explanation to some of the experimental findings, many questions still remain open. For example – in the meantime, many other kinases, in addition to CyclinY/CDK14, were shown to phosphorylate PPPSP motif of Lrp6. These include G-protein coupled receptor kinase 5 or 6 (GRK5, GRK6 (Chen et al., 2009) and multiple mitogen activated protein kinases such as p38, JNK or ERK (Cervenka et al., 2011). They were shown to influence Wnt/ β -catenin signaling amplitude (Cervenka et al., 2011; Krejci et al., 2012) which suggests that phosphorylating PPPSP motif in order to control the intensity of Wnt pathway activation can be affected by multiple factors – not only cell cycle phase but also mitogenic pathways or cellular stress activation. Similar questions accompany Wnt/STOP signaling and it has yet to be found if

GSK-3 is “the” kinase or other kinases can act in a redundant fashion. Analyzing GSK-3-null cells and mice can help to fully reconcile this question.

3.2.2 Wnt pathway proteins as regulators of centrosomal cycle—The next obvious question raised by the observations summarized in Tables 1-3 is the following: Are Wnt pathway proteins involved in the regulation of the cell or centrosomal cycle? And if so, which particular events during the centrosome cycle are under such control?

β -catenin, the molecule central to Wnt/ β -catenin signaling has probably been the most extensively documented when it comes to its centrosomal regulation. For the sake of simplicity, we can inspect it as a prototypic Wnt signaling component involved in the centrosome cycle, since many of the observations have been recapitulated with other proteins as well. β -catenin levels oscillate during cell cycle and peak in the G2/M phase (Olmeda et al., 2003). Reducing β -catenin levels lead to a prometaphase delay and increase in the proportion of monoastal spindles originating from unseparated centrosomes. During the interphase, β -catenin localizes to proximal centriole ends together with proteins comprising the flexible centrosomal linker – Rootletin and CNAP-1. As the cell nears mitosis and NEK2 activity peaks, both Rootletin and β -catenin are phosphorylated. Initial Rootletin-dependent localization of β -catenin to centrosome is switched to independent binding in mitosis, leading to centrosome separation (Bahmanyar et al., 2008). Interestingly, some of the β -catenin residues phosphorylated by NEK2 during these events seem to coincide with the S33/S37/T41 cluster phosphorylated by GSK-3 β . The results of these phosphorylations diverge, stabilizing β -catenin in the case of NEK2 and marking it for degradation in the case of GSK-3 β (Mbom 2014). Additionally, overactive β -catenin stabilization increases the formation of gamma-tubulin structures that resemble immature centrosomes, but are unable to nucleate microtubules (Bahmanyar et al., 2008).

Unlike the role of β -catenin, which seems to be confined to centrosome splitting, other key players in the Wnt pathway- namely DVL, Axin and APC - have more compound phenotypes. DVL was identified as localizing the centrosome, spindle poles and kinetochores during mitosis (Kikuchi et al., 2010; Cervenka et al., 2016). It was proposed that phosphorylation by PLK1 influences the orientation of the mitotic spindle and microtubule-kinetochore attachment. Depleting DVL reduces Mps1 autophosphorylation and localization of Bub1 and Bub1R to MT, possibly interfacing with a spindle assembly checkpoint (SAC) to mitigate the errors arising from improper chromosome segregation. Additionally, DVL acts as part of the machinery responsible for regulating centrosome cohesion. DVL localizes to the centrosome by its DIX domain, where it acts as a scaffold bridging together constituents of the intercentrosomal linker (Cervenka et al., 2016).

Maybe unsurprisingly, close DVL binding partner Axin, was found localized in the centrosome as well, both during interphase and mitosis (Fumoto et al., 2009; Kim et al., 2009). Axin2/Conductin, a negative regulator, increases during cell cycle and culminates at the G2/M boundary (Hadjihannas, Bruckner, and Behrens, 2010). Axin2/Conductin localization to the centrosome is also mediated by CNAP-1 and its loss leads to centrosome splitting due to interference with β -catenin stability and/or phosphorylation (Hadjihannas, Bruckner, and Behrens, 2010). The fact that both Axin and DVL bind to the centrosome

using their respective DIX domains indicates that the DIX domain is one of the general domain signatures that may target proteins to the centrosome. Unfortunately, involvement in centrosome-related processes is plagued by purely observational evidence and poor discrimination between its effects on the centrosome itself in contrast to microtubule kinetics. Overexpressing Axin seems to influence GSK-3 β and PLK1 localization, both of which have been implicated in phosphorylation cascades of β -catenin in relation to centrosome splitting (Kim et al., 2009). Although it seems to fit the bigger picture, the evidence relies heavily on antibody staining and seems slightly dubious. Moreover, Axin was itself found to be phosphorylated by PLK1 during mitosis. However, Axin phosphorylation also determines its affinity towards γ -tubulin and failure to do so leads to the formation of multi-centrosomes (Ruan et al., 2012). Other centrosome related functions of Axin, such as promotion of mitotic fidelity are rather coupled to its role in cytoskeletal dynamics as well (Poulton et al., 2013). Since changes in microtubule nucleation and astral microtubule positioning can cause defects in centrosome separation, stricter deconvolution of their individual contributions towards centrosome-related defects is needed.

Two important DVL kinases, CK1 δ and CK1 ϵ , have been described to localize to the centrosome, with C-terminal part as their localization signal (Greer and Rubin, 2011). As is often the case, their participation in centrosome related events is only observational with little mechanistic insight. So far, inhibiting CK1 δ in trophoblast cells was shown to result in a variety of centrosomal defects, such as multipolar spindles, centrosome amplifications and impairments in bipolar attachments as well as death by apoptosis after 24h of treatment due to mitotic failure (Greer et al., 2014).

In summary, the evidence, in line with the increased Wnt pathway protein levels in the G2/M phase, suggests that many proteins – such as β -catenin, Dishevelled and Axin - participate in the process of centrosome splitting that takes place at the end of the G2 phase. The described functions of Wnt pathway components and their regulation is schematized in Figure 5. The literature suggests that during the interphase, centrosome cohesion is maintained by the action of Axin2/Conductin and GSK-3 β that phosphorylates β -catenin (Bahmanyar et al., 2008; Hadjihannas, Bruckner, and Behrens, 2010). At the same time DVL interacts with distal appendage protein CEP164, perhaps to facilitate basal body docking in ciliated cells (Chaki et al., 2012). As the cell cycle progresses, DVL further accumulates in the centrosome, where it interacts with C-NAP1 (Cervenka et al., 2016). Localization of Axin and APC to the centrosome is probably mediated by microtubules. During the G2/M phase, phosphorylation cascade activates NEK2, which subsequently acts on several targets. Conductin is degraded by proteasome (Hadjihannas et al., 2012), β -catenin is protected from degradation by NEK2 phosphorylation and facilitates centrosome splitting (Bahmanyar et al., 2008). Concurrently, phosphorylation of DVL and C-NAP1 by NEK2 leads to an increase in their overall negative charge and subsequent release from the centrioles, severing the connection with Rootletin (Cervenka et al., 2016). Afterwards, the centrosomes can be pulled apart by the motor proteins' action. Axin is probably phosphorylated by PLK1, which affects microtubule dynamics during spindle formation (Ruan et al., 2012; Poulton et al., 2013).

3.2.3 Control of the cell-cycle dependent functions of Wnt pathway

components—The information provided above clearly indicates that individual Wnt pathway components perform multiple functions in distinct cell cycle phases. This implies that an individual Wnt pathway protein can exist in various “pools”. For the purpose of this review, we will define pool as a functional state of the protein that integrates a phosphorylation status, binding partner(s) in the complex, and subcellular localization. It is very likely that cells regulate such protein pools in a delicate manner, which subsequently allows precise control of time and space restricted activities in distinct protein pools. The characteristics of an individual protein in several cellular pools, e.g. three pools in the case of β -catenin (cytoplasmic, membrane and centrosomal) are just being discovered. Not surprisingly, pools are controlled by post-translation modifications and we summarize the available information regarding control of Wnt pathway protein pools by PTM in Table 4.

The barcoding of individual protein pools is only starting to emerge and currently most information about cell cycle-dependent regulation is available for β -catenin and DVL, which will be described in further detail. Not surprisingly, NEK2 kinase – a master regulator of centrosomal separation - has a key role in regulating the centrosomal pool and the function of both these proteins.

NEK2 phosphorylates and stabilizes β -catenin, and targets it to the spindle poles by independently phosphorylating the same residues as GSK-3 β (Bahmanyar et al., 2008). In direct contrast, Axin2/Conductin mediates β -catenin phosphorylation by GSK-3 β , but not by NEK2. However, although engaging both the same residues and same kinase, these phosphorylations do not lead to β -catenin destruction, but increase centrosome cohesion. It is the inhibition of phosphorylation that induces centrosome splitting (Hadjihannas et al., 2010). As recent studies point out, different pools of β -catenin or APC have varying degrees of mobility and stability, which subsequently restrict their biological activity (Kafri et al., 2016; Lui, Mok, and Henderson, 2016). Route for β -catenin transport from the membrane to the centrosome has recently been discovered (Kafri et al., 2016). It takes up to 90 minutes for β -catenin to reach the centrosome and the authors postulate that it is probably unphosphorylated β -catenin driving cell division that is transported this way. The β -catenin in the centrosome is especially short-lived when compared to other cellular compartments. If its rapid clearance (1.9 seconds) is necessary to both induce centrosome splitting and at the same time ensure its proper destruction without influencing Wnt signalling output remains to be seen. The same is true for the question as to how phosphorylation by NEK2 prevents β -catenin associating with β -TrCP and whether such stabilized β -catenin can also have signaling properties.

DVL was shown recently to be a substrate of NEK2 kinase (Cervenka et al., 2016; Schertel et al., 2013; Weber and Mlodzik, 2017). NEK2 can phosphorylate both DVL and centrosome linker proteins such as C-NAP1 or CDK5RAP2 on multiple sites – an almost unbelievable 82 (C-NAP1), 81 (CDK5RAP2) or 41 (DVL3) unique Ser/Thr sites were detected by mass spectrometry (Cervenka et al., 2016) which suggests that electrostatic repulsion or sterical exclusion proposed earlier for NEK2-driven removal of C-NAP1 from the centrosome (Hardy et al., 2014; Faragher and Fry, 2003), can represent a mechanism explaining centrosomal DVL release a complex with C-NAP1. Interestingly, NEK2-mediated DVL

release from the centrosome increases the availability of cytoplasmic DVL for the Wnt/ β -catenin pathway, where it has a crucial function as a component of signalosomes (Bilic et al., 2007). This effect of NEK2 on DVL pools explains the previously observed positive effects of NEK2 on Wnt/ β -catenin (Cervenka et al., 2016; Schertel et al., 2013) despite the fact that NEK2 is not sufficient to trigger the Wnt/ β -catenin pathway on its own. NEK2 is a substrate of anaphase-promoting complex/cyclosome (APC/C) that triggers it for degradation. It was shown that in fly retinal cells APC/C restricts retinal differentiation to the G1 phase by degradation of NEK2 and consequent time-restricted Wnt/ β -catenin suppression (Martins et al., 2017). The interference with NEK2 function can thus serve as a physiological mechanism that fine-tunes Wnt signaling.

Another mode how NEK2 can control Wnt pathway activation in a cell cycle-dependent manner was published recently (Weber and Mlodzik, 2017) and also builds on the fact that NEK2 is a substrate of APC/C. Weber and Mlodzik have found that NEK2 can reduce DVL stability and thus control the DVL levels required to establish planar cell polarity in the epithelium. All these examples suggest that NEK2 can act as a key integrator of DVL's multiple roles in Wnt/ β -catenin pathway, Wnt/planar cell polarity pathway, basal body docking and centrosome separation. Further tools – mainly phospho-specific antibodies and time-lapse imaging of DVL and other Wnt pathway proteins – holds the key towards the full understanding of these processes.

3.3 Role of Wnt pathway components in the regulation of (asymmetric) cell division

Another intriguing aspect we would like to discuss here is the possibility of Wnt pathway or its components to participate directly in the regulation of mitotic cell division – by the possible effects on either the centrosome or spindle positioning. These phenomena are best studied in *C. elegans* and *Drosophila*, thanks to powerful genetic tools combined with high resolution live imaging of intact, developing embryos, allowing high throughput phenotypic screening. Interestingly, such screens did indeed identify Wnt signaling components (e.g. *mom-1/porc*, *mom-3/fz*, *mom-5/?*, GSK3, APC, armadillo/ β -catenin, *kin-19/CK1*, *mig-5/DVL3*) as important regulators of mitotic spindle positioning (Schlesinger et al., 1999; McCartney et al., 2001; Zipperlen et al., 2001; Walston et al., 2004). While the genetic evidence is convincing, the molecular understanding is somewhat lagging behind, especially in comparison with what is known about the role of the Wnt/PCP pathway in the control of oriented cell division (here we again point our readers to recent reviews - (Sawa, 2012; Wallingford, 2012; Morin and Bellaiche, 2011)).

This chapter must be initiated by the short description of the function of APC (adenomatosis polyposis coli) in the cell cycle. APC is a large protein with multiple domains – some of its domains show homology with yeast proteins where they participate on cell division (eg. Kar9b in *Saccharomyces cerevisiae*) (Miller and Rose, 1998; Bloom, 2000). In contrast to other central Wnt pathway regulators (DVL, Axin, Fzd, Lrp6), it is thus likely that APC, or its ancient domains, functioned originally as regulators of microtubule function during cell division and only later attributed a role in the Wnt signaling. APC can interact with microtubules and multiple microtubule-associated proteins such as EB1, kinesin-associated protein 3 (KAP3) or Mitotic Centromere Associated Protein (MCAK) and is a crucial

regulator of mitosis. The key findings that described the capacity and the mode of interaction of APC with microtubules and its importance for mitosis and spindle assembly checkpoint are well reviewed (Bahmanyar, Nelson, and Barth, 2009; Caldwell and Kaplan, 2009; Zhang and Shay, 2017) and we do not further focus on the APC-mediated events in this review.

There is evidence for the role of Wnt/ β -catenin signaling components in oriented cell division also coming from vertebrate cells. Depleting β -catenin or DVL causes the formation of monopolar spindles (Kikuchi et al., 2010; Kaplan et al., 2004), which can be explained as a consequence of the role these proteins play in centrosome cohesion (Bahmanyar et al., 2008; Cervenka et al., 2016). Further, many other Wnt pathway components were reported to associate with spindle poles or the spindle itself (see Table 1). However, there is often only limited experimental evidence sufficiently explaining the possible functional consequences of such reported localizations for vertebrate mitosis. Moreover, one has to bear in mind that several of these observations are based purely on antibody staining, without appropriate controls (siRNA/ knock-out).

An obvious question here is if observations of Wnt components localizing to and/or affecting spindle/centrosome functions during mitoses means the direct involvement of the Wnt signaling pathway, or if these components act independently of the typical role in the Wnt pathway. In principle, both models seem plausible and, on the level of individual components, not mutually exclusive. Nonetheless, there is evidence supporting the possibility that some of the reported observations are direct consequences to events in the receptor-ligand complexes close to the cell membrane. First, spindle positioning during mitoses is affected if Wnt secretion is perturbed, either in *mom-1*/porcupine mutant or Wntless mutant, in *C.elegans*, (Schlesinger et al., 1999; Thorpe et al., 1997; Banziger et al., 2006). Moreover, a set of experiments in mouse embryonic stem cells (mESCs) demonstrated that locally distributed Wnt/beta catenin pathway ligand, Wnt3a, induced asymmetrical LRP6 and β -catenin distribution (of note, β -catenin was enriched mainly in the cell membrane, not in the nucleus), leading to effects on both the angle of mitotic division plane and the centrosome inheritance in asymmetrically dividing cells (Habib et al., 2013). In addition, recent work by (Stolz et al., 2015) showed that inhibiting Wnt/ β -catenin signaling by treatment with Dkk or SFRP effects the rate of microtubule polymerization in mitotic, but not interphase cells.

In summary, it is clear that we are still far from seeing the complete picture. However, based on both the genetic and biochemical evidence accumulated from experiments across different species and cell types, we argue that a hypothesis/model of Wnt/ β -catenin signaling directly regulating mitotic cell division is plausible.

3.4 Role of Wnt proteins for basal body docking and proper function/position of cilia

There is one more aspect we feel deserves a mention in regards to Wnt signaling and centrosome/primary cilium biology. Both monociliated and multiciliated cells need to dock their mother centrioles to the plasma membrane in order to initiate ciliogenesis. There is solid evidence from multiple model systems that this step relies directly or indirectly mainly on the action of the Wnt/PCP pathway and its components. Conversely, defects in the Wnt/PCP pathway lead to either complete failure to dock basal bodies, or cause defects in

cilia orientation. We have summarized current models of action for the Wnt/PCP pathway in different aspects of cilia biology in Figure 6. For a more thorough insight, we would like to point our readers to several excellent reviews comprehensively addressing this topic (May-Simera and Kelley, 2012; Wallingford and Mitchell, 2011; Carvajal-Gonzalez, Mulero-Navarro, and Mlodzik, 2016).

Nonetheless, there are still a few points, perhaps more speculative, which we would like to touch upon. One such case is whether the requirement of functional Wnt/PCP pathway for ciliogenesis lies in direct action of asymmetrically distributed PCP components, or if it rather reflects the consequences of the cytoskeletal rearrangement, downstream of the core Wnt/PCP toolkit. To this end, there is some evidence arguing that disrupting PCP does not always translate to defects in ciliogenesis (Antic et al., 2010; Borovina et al., 2010). Furthermore, many PCP proteins are involved in Rho-mediated apical actin assembly or the regulation of correct Rho localization, which may explain the reported effects on cilia basal body docking or vesicular traffic impairment in many PCP mutants (Oishi et al., 2006; Park et al., 2008; Park, Haigo, and Wallingford, 2006; Gray et al., 2009). Interestingly, recent work from the Mlodzik lab has demonstrated that actin polymerization, mediated via PCP effectors such as Inturned or Fuzzy regulate basal body docking to apical membranes via action of Rho GTPases. Conversely, centriole positioning is then one of the evolutionally conserved downstream effects of Wnt/PCP signaling (Carvajal-Gonzalez, Roman, and Mlodzik, 2016), see also Figure 6A.

In nodal cilia, two Wnt pathways interact to bring about proper cilia functioning and subsequently left-right asymmetry determination (Figure 6B). At the beginning, it is not PCP, but Wnt/ β -catenin signaling, acting probably through the Wnt8-Fzd8 complex that upregulates Foxj1 expression and initiates ciliogenesis (Caron, Xu, and Lin, 2012; Stubbs et al., 2008; Walentek et al., 2012; Walentek et al., 2013). Subsequently, in order to generate a proper directed laminar flow, Wnt/PCP signaling is activated by Wnt11b to control the posterior positioning of nodal cilium (Hashimoto et al., 2010; Walentek et al., 2013). This is dependent on DVL presence, demonstrated by the phenotype in DVL1/2/3 null mice (Ohata et al., 2014). However, it is yet unclear whether in this case the absence of DVL interferes again with vesicle trafficking, rather than PCP signaling. Another study confirmed that the planar polarity established by Vangl1 and Prickle influences proper cilia positioning, which in turn generates leftward flow, leading to the induction of left-right asymmetry by expressing homeobox gene Pitx2 (Antic et al., 2010).

In agreement with the model of Wnt/PCP signaling acting upstream of ciliogenesis, DVL was also demonstrated as crucial for basal bodies docking in multiciliated cells (Park et al., 2008). DVL has been further shown to be responsible for cell-autonomous cilia orientation (Mitchell et al., 2009). The role of DVL in this type of polarity has been partially attributed to its stability, which is controlled among others by APC/C, Inversin or Rpgrip11 (Simons et al., 2005; Ganner et al., 2009; Mahuzier et al., 2012) (Figure 6C). Intriguingly, DVL2 was also proposed to play a role in resorption of primary cilia (Lee et al., 2012). In the work by Lee and colleagues, DVL2 RNAi in Retinal pigment epithelial (RPE-1) cells did not cause defects in primary cilia formation, but prevented its resorption following cell cycle re-entry. The authors further identified CK1 ϵ and PLK1 as regulators of a cilia resorption event,

acting on the level of DVL2. As the formation of multiple cilia is linked to permanent cell cycle exit, it seems plausible that this function of DVL2 and its associated kinases is specific for monociliated cells. Another open question related to that is whether the link to control cilia resorption is specific for DVL2, or other DVL isoforms are involved as well. It certainly will not be a trivial task to track down all molecular processes involving DVL in the centrosome/basal body, given the numerous interactions with various centriolar and ciliary proteins (Gupta et al., 2015; Chaki et al., 2012; Gao and Chen, 2010).

Another player in the cilia formation is GSK3 β . GSK3 β has been identified as promoting the assembly of the ciliary membrane and hence the initiation of ciliogenesis after the mitotic exit (Zhang et al., 2015). The suggested mechanisms involve kinase activity-dependent control of PCM component Dzip and small GTPase Rab8 interactions. However, given the multiple functions assigned to GSK3 β , it is plausible it participates in ciliogenesis also by other means, as already proposed (Thoma et al., 2007).

Overall, the available evidence argues that removing PCP pathway components does typically disturb cilia formation. In most cases it seems to be linked to problems with basal body docking and vesicular transport. That being said, it should be noted that although evidence for PCP proteins participation is strong, not all studies provide sufficient mechanistic insights. For some proteins, such as DVL, CK1, or Inturned that are able to directly affect the organization of cytoskeletal apparatus, the molecular explanation seems straightforward. On the other hand, clarifying the exact role of some of the core membrane PCP proteins will require additional follow-ups to complete the picture.

4 Conclusions and open questions

The evidence for a dual role of Wnt pathway components is gradually increasing, but still remains too sporadic to formulate unifying conclusions. A lot of studies rely on antibody staining without using complementary knockdown/knockout controls for independent verification, so the results have to be taken with a grain of salt. Nevertheless, there are both interesting observations and instances of conflicting evidence available. Proteins such as DVL, Axin or APC are known scaffolds with multitude of binding partners and interact especially tightly with other Wnt pathway components. Explicit direct binding has not yet been clearly demonstrated and it is possible that the presence of one will recruit a plethora of other proteins.

In order to reach unifying conclusions one needs to carefully distinguish between the role of the organelle (cilium/centrosome) vs. protein required to form the organelle, or similarly between the pathway vs. the protein component of the pathway. Ignoring these differences often lead to oversimplification and seemingly conflicting results. However, recent advances in gene editing techniques combined with the revolution in imaging and proteomic techniques have created a platform that will help to speed up progress. Better control of experiments using Crispr/Cas9 generated knockout and analysis of cell phenotypes and protein-protein interactions in real time and in living cells gives hope that the connection between the cell and centrosomal cycle and major morphogenetic cascades will be fully elucidated in the near future.

Acknowledgements

We thank Lucie Smyková from the Bryja lab for a help with the preparation of tables used in this review.

References

1. Nusse R, Varmus HE. Many tumors induced by the mouse mammary tumor virus contain a provirus integrated in the same region of the host genome. *Cell*. 1982; 31:99–109. [PubMed: 6297757]
2. Nusslein-Volhard C, Wieschaus E. Mutations affecting segment number and polarity in *Drosophila*. *Nature*. 1980; 287:795–801. [PubMed: 6776413]
3. Korinek V, Barker N, Moerer P, van Donselaar E, Huls G, Peters PJ, Clevers H. Depletion of epithelial stem-cell compartments in the small intestine of mice lacking Tcf-4. *Nat Genet*. 1998; 19:379–83. [PubMed: 9697701]
4. ten Berge D, Kurek D, Blauwkamp T, Koole W, Maas A, Eroglu E, Siu RK, Nusse R. Embryonic stem cells require Wnt proteins to prevent differentiation to epiblast stem cells. *Nature cell biology*. 2011; 13:1070–5. [PubMed: 21841791]
5. Tetsu O, McCormick F. Beta-catenin regulates expression of cyclin D1 in colon carcinoma cells. *Nature*. 1999; 398:422–6. [PubMed: 10201372]
6. He TC, Sparks AB, Rago C, Hermeking H, Zawel L, da Costa LT, Morin PJ, Vogelstein B, Kinzler KW. Identification of c-MYC as a target of the APC pathway. *Science*. 1998; 281:1509–12. [PubMed: 9727977]
7. Schulte G, Bryja V. The Frizzled family of unconventional G-protein-coupled receptors. *Trends Pharmacol Sci*. 2007; 28:518–25. [PubMed: 17884187]
8. Tamai K, Zeng X, Liu C, Zhang X, Harada Y, Chang Z, He X. A mechanism for Wnt coreceptor activation. *Mol Cell*. 2004; 13:149–56. [PubMed: 14731402]
9. Schwarz-Romond T, Fiedler M, Shibata N, Butler PJ, Kikuchi A, Higuchi Y, Bienz M. The DIX domain of Dishevelled confers Wnt signaling by dynamic polymerization. *Nat Struct Mol Biol*. 2007; 14:484–92. [PubMed: 17529994]
10. Fagotto F, Jho E, Zeng L, Kurth T, Joos T, Kaufmann C, Costantini F. Domains of axin involved in protein-protein interactions, Wnt pathway inhibition, and intracellular localization. *The Journal of cell biology*. 1999; 145:741–56. [PubMed: 10330403]
11. Li L, Yuan H, Weaver CD, Mao J, Farr GH 3rd, Sussman DJ, Jonkers J, Kimelman D, Wu D. Axin and Frat1 interact with dvl and GSK, bridging Dvl to GSK in Wnt-mediated regulation of LEF-1. *Embo J*. 1999; 18:4233–40. [PubMed: 10428961]
12. Smalley MJ, Sara E, Paterson H, Naylor S, Cook D, Jayatilake H, Fryer LG, Hutchinson L, Fry MJ, Dale TC. Interaction of axin and Dvl-2 proteins regulates Dvl-2-stimulated TCF-dependent transcription. *Embo J*. 1999; 18:2823–35. [PubMed: 10329628]
13. Wallingford JB, Habas R. The developmental biology of Dishevelled: an enigmatic protein governing cell fate and cell polarity. *Development*. 2005; 132:4421–36. [PubMed: 16192308]
14. Axelrod JD, Miller JR, Shulman JM, Moon RT, Perrimon N. Differential recruitment of Dishevelled provides signaling specificity in the planar cell polarity and Wntless signaling pathways. *Genes & development*. 1998; 12:2610–22. [PubMed: 9716412]
15. Gammons MV, Rutherford TJ, Steinhart Z, Angers S, Bienz M. Essential role of the Dishevelled DEP domain in a Wnt-dependent human-cell-based complementation assay. *Journal of cell science*. 2016; 129:3892–902. [PubMed: 27744318]
16. Pačliková P, Bernatik O, Radaszkiewicz TW, Bryja V. N-terminal part of Dishevelled DEP domain is required for Wnt/beta-catenin signaling in mammalian cells. *Molecular and Cellular Biology*. 2017
17. Pan WJ, Pang SZ, Huang T, Guo HY, Wu D, Li L. Characterization of function of three domains in dishevelled-1: DEP domain is responsible for membrane translocation of dishevelled-1. *Cell Res*. 2004; 14:324–30. [PubMed: 15353129]
18. Tauriello DV, Jordens I, Kirchner K, Slootstra JW, Kruitwagen T, Bouwman BA, Noutsou M, Rudiger SG, Schwamborn K, Schambony A, Maurice MM. Wnt/beta-catenin signaling requires interaction of the Dishevelled DEP domain and C terminus with a discontinuous motif in Frizzled.

- Proceedings of the National Academy of Sciences of the United States of America. 2012; 109:E812–20. [PubMed: 22411803]
19. Bryja V, Bernatik O. Dishevelled at the crossroad of pathways Wnt signaling in Development and Disease: Molecular Mechanisms and Biological Functions Hoppler S, Moon RT, editors Wiley Publishers; 2014
 20. Bernatik O, Ganji RS, Dijksterhuis JP, Konik P, Cervenka I, Polonio T, Krejci P, Schulte G, Bryja V. Sequential activation and inactivation of Dishevelled in the Wnt/beta-catenin pathway by casein kinases. The Journal of biological chemistry. 2011; 286:10396–410. [PubMed: 21285348]
 21. Bernatik O, Sedova K, Schille C, Ganji RS, Cervenka I, Trantirek L, Schambony A, Zdrahal Z, Bryja V. Functional analysis of dishevelled-3 phosphorylation identifies distinct mechanisms driven by casein kinase 1 and frizzled5. The Journal of biological chemistry. 2014; 289:23520–33. [PubMed: 24993822]
 22. Bienz M. Signalosome assembly by domains undergoing dynamic head-to-tail polymerization. Trends Biochem Sci. 2014; 39:487–95. [PubMed: 25239056]
 23. Zeng X, Huang H, Tamai K, Zhang X, Harada Y, Yokota C, Almeida K, Wang J, Doble B, Woodgett J, Wynshaw-Boris A, et al. Initiation of Wnt signaling: control of Wnt coreceptor Lrp6 phosphorylation/activation via frizzled, dishevelled and axin functions. Development. 2008; 135:367–75. [PubMed: 18077588]
 24. Bilic J, Huang YL, Davidson G, Zimmermann T, Cruciat CM, Bienz M, Niehrs C. Wnt induces LRP6 signalosomes and promotes dishevelled-dependent LRP6 phosphorylation. Science. 2007; 316:1619–22. [PubMed: 17569865]
 25. Ikeda S, Kishida S, Yamamoto H, Murai H, Koyama S, Kikuchi A. Axin, a negative regulator of the Wnt signaling pathway, forms a complex with GSK-3beta and beta-catenin and promotes GSK-3beta-dependent phosphorylation of beta-catenin. EMBO J. 1998; 17:1371–84. [PubMed: 9482734]
 26. Kishida S, Yamamoto H, Ikeda S, Kishida M, Sakamoto I, Koyama S, Kikuchi A. Axin, a negative regulator of the wnt signaling pathway, directly interacts with adenomatous polyposis coli and regulates the stabilization of beta-catenin. The Journal of biological chemistry. 1998; 273:10823–6. [PubMed: 9556553]
 27. Sakanaka C, Weiss JB, Williams LT. Bridging of beta-catenin and glycogen synthase kinase-3beta by axin and inhibition of beta-catenin-mediated transcription. Proceedings of the National Academy of Sciences of the United States of America. 1998; 95:3020–3. [PubMed: 9501208]
 28. Henderson BR, Fagotto F. The ins and outs of APC and beta-catenin nuclear transport. EMBO Rep. 2002; 3:834–9. [PubMed: 12223464]
 29. Stadeli R, Hoffmans R, Basler K. Transcription under the control of nuclear Arm/beta-catenin. Curr Biol. 2006; 16:R378–85. [PubMed: 16713950]
 30. Daniels DL, Weis WI. Beta-catenin directly displaces Groucho/TLE repressors from Tcf/Lef in Wnt-mediated transcription activation. Nat Struct Mol Biol. 2005; 12:364–71. [PubMed: 15768032]
 31. Axelrod JD. Progress and challenges in understanding planar cell polarity signaling. Semin Cell Dev Biol. 2009; 20:964–71. [PubMed: 19665570]
 32. Zallen JA. Planar polarity and tissue morphogenesis. Cell. 2007; 129:1051–63. [PubMed: 17574020]
 33. Habas R, Kato Y, He X. Wnt/Frizzled activation of Rho regulates vertebrate gastrulation and requires a novel Formin homology protein Daaml. Cell. 2001; 107:843–54. [PubMed: 11779461]
 34. Butler MT, Wallingford JB. Planar cell polarity in development and disease. Nature reviews Molecular cell biology. 2017
 35. Kohn AD, Moon RT. Wnt and calcium signaling: beta-catenin-independent pathways. Cell calcium. 2005; 38:439–46. [PubMed: 16099039]
 36. Slusarski DC, Pelegri F. Calcium signaling in vertebrate embryonic patterning and morphogenesis. Developmental biology. 2007; 307:1–13. [PubMed: 17531967]
 37. Nurse P. Regulation of the eukaryotic cell cycle. European journal of cancer. 1997; 33:1002–4. [PubMed: 9376179]

38. Khodjakov A, Rieder CL. The nature of cell-cycle checkpoints: facts and fallacies. *Journal of biology*. 2009; 8:88. [PubMed: 19930621]
39. Boveri T. Concerning the origin of malignant tumours by Theodor Boveri. Translated and annotated by Henry Harris. *Journal of cell science*. 2008; 121(Suppl 1):1–84. [PubMed: 18089652]
40. Klotz C, Dabauvalle MC, Paintrand M, Weber T, Bornens M, Karsenti E. Parthenogenesis in *Xenopus* eggs requires centrosomal integrity. *The Journal of cell biology*. 1990; 110:405–15. [PubMed: 2298811]
41. Picard A, Karsenti E, Dabauvalle MC, Doree M. Release of mature starfish oocytes from interphase arrest by microinjection of human centrosomes. *Nature*. 1987; 327:170–2. [PubMed: 3106826]
42. Bornens M, Gonczy P. Centrosomes back in the limelight. *Philosophical transactions of the Royal Society of London Series B, Biological sciences*. 2014; 369
43. Kalab P, Heald R. The RanGTP gradient - a GPS for the mitotic spindle. *Journal of cell science*. 2008; 121:1577–86. [PubMed: 18469014]
44. Louvet-Vallee S, Vinot S, Maro B. Mitotic spindles and cleavage planes are oriented randomly in the two-cell mouse embryo. *Curr Biol*. 2005; 15:464–9. [PubMed: 15753042]
45. Khodjakov A, Rieder CL. Centrosomes enhance the fidelity of cytokinesis in vertebrates and are required for cell cycle progression. *The Journal of cell biology*. 2001; 153:237–42. [PubMed: 11285289]
46. Piel M, Nordberg J, Euteneuer U, Bornens M. Centrosome-dependent exit of cytokinesis in animal cells. *Science*. 2001; 291:1550–3. [PubMed: 11222861]
47. Oliferenko S, Chew TG, Balasubramanian MK. Positioning cytokinesis. *Genes & development*. 2009; 23:660–74. [PubMed: 19299557]
48. Doe CQ. Neural stem cells: balancing self-renewal with differentiation. *Development*. 2008; 135:1575–87. [PubMed: 18356248]
49. Knoblich JA. Mechanisms of asymmetric stem cell division. *Cell*. 2008; 132:583–97. [PubMed: 18295577]
50. Lancaster MA, Knoblich JA. Spindle orientation in mammalian cerebral cortical development. *Current opinion in neurobiology*. 2012; 22:737–46. [PubMed: 22554882]
51. Arquint C, Gabryjonczyk AM, Nigg EA. Centrosomes as signalling centres. *Philosophical transactions of the Royal Society of London Series B, Biological sciences*. 2014; 369
52. Jackman M, Lindon C, Nigg EA, Pines J. Active cyclin B1-Cdk1 first appears on centrosomes in prophase. *Nature cell biology*. 2003; 5:143–8. [PubMed: 12524548]
53. Wakefield JG, Huang JY, Raff JW. Centrosomes have a role in regulating the destruction of cyclin B in early *Drosophila* embryos. *Curr Biol*. 2000; 10:1367–70. [PubMed: 11084336]
54. Luders J, Stearns T. Microtubule-organizing centres: a re-evaluation. *Nature reviews Molecular cell biology*. 2007; 8:161–7. [PubMed: 17245416]
55. Mennella V, Agard DA, Huang B, Pelletier L. Amorphous no more: subdiffraction view of the pericentriolar material architecture. *Trends in cell biology*. 2014; 24:188–97. [PubMed: 24268653]
56. Conduit PT, Wainman A, Raff JW. Centrosome function and assembly in animal cells. *Nature reviews Molecular cell biology*. 2015; 16:611–24. [PubMed: 26373263]
57. Tollenaere MA, Mailand N, Bekker-Jensen S. Centriolar satellites: key mediators of centrosome functions. *Cellular and molecular life sciences : CMLS*. 2014
58. Bornens M, Azimzadeh J. Origin and evolution of the centrosome. *Advances in experimental medicine and biology*. 2007; 607:119–29. [PubMed: 17977464]
59. Bornens M. The centrosome in cells and organisms. *Science*. 2012; 335:422–6. [PubMed: 22282802]
60. Cunha-Ferreira I, Bento I, Bettencourt-Dias M. From zero to many: control of centriole number in development and disease. *Traffic*. 2009; 10:482–98. [PubMed: 19416494]
61. Holland AJ, Fachinetti D, Zhu Q, Bauer M, Verma IM, Nigg EA, Cleveland DW. The autoregulated instability of Polo-like kinase 4 limits centrosome duplication to once per cell cycle. *Genes & development*. 2012; 26:2684–9. [PubMed: 23249732]

62. Fava LL, Schuler F, Sladky V, Haschka MD, Soratroi C, Eiterer L, Demetz E, Weiss G, Geley S, Nigg EA, Villunger A. The PIDDosome activates p53 in response to supernumerary centrosomes. *Genes & development*. 2017; 31:34–45. [PubMed: 28130345]
63. Wong YL, Anzola JV, Davis RL, Yoon M, Motamedi A, Kroll A, Seo CP, Hsia JE, Kim SK, Mitchell JW, Mitchell BJ, et al. Reversible centriole depletion with an inhibitor of Polo-like kinase 4. *Science*. 2015; 348:1155–60. [PubMed: 25931445]
64. Bazzi H, Anderson KV. Acentriolar mitosis activates a p53-dependent apoptosis pathway in the mouse embryo. *Proceedings of the National Academy of Sciences of the United States of America*. 2014; 111:E1491–500. [PubMed: 24706806]
65. Gonczy P. Centrosomes and cancer: revisiting a long-standing relationship. *Nature reviews Cancer*. 2015; 15:639–52. [PubMed: 26493645]
66. Nigg EA, Cajanek L, Arquint C. The centrosome duplication cycle in health and disease. *FEBS letters*. 2014; 588:2366–72. [PubMed: 24951839]
67. Godinho SA, Pellman D. Causes and consequences of centrosome abnormalities in cancer. *Philosophical transactions of the Royal Society of London Series B, Biological sciences*. 2014; 369
68. Bettencourt-Dias M, Hildebrandt F, Pellman D, Woods G, Godinho SA. Centrosomes and cilia in human disease. *Trends Genet*. 2011; 27:307–15. [PubMed: 21680046]
69. Ganem NJ, Godinho SA, Pellman D. A mechanism linking extra centrosomes to chromosomal instability. *Nature*. 2009; 460:278–82. [PubMed: 19506557]
70. Levine MS, Bakker B, Boeckx B, Moyett J, Lu J, Vitre B, Spierings DC, Lansdorp PM, Cleveland DW, Lambrechts D, Fojer F, et al. Centrosome Amplification Is Sufficient to Promote Spontaneous Tumorigenesis in Mammals. *Developmental cell*. 2017
71. Serein O, Larsimont JC, Karambelas AE, Marthiens V, Moers V, Boeckx B, Le Mercier M, Lambrechts D, Basto R, Blanpain C. Transient PLK4 overexpression accelerates tumorigenesis in p53-deficient epidermis. *Nature cell biology*. 2016; 18:100–10. [PubMed: 26595384]
72. Basto R, Brunk K, Vinadogrova T, Peel N, Franz A, Khodjakov A, Raff JW. Centrosome amplification can initiate tumorigenesis in flies. *Cell*. 2008; 133:1032–42. [PubMed: 18555779]
73. Marthiens V, Rujano MA, Pennetier C, Tessier S, Paul-Gilloteaux P, Basto R. Centrosome amplification causes microcephaly. *Nature cell biology*. 2013; 15:731–40. [PubMed: 23666084]
74. Bettencourt-Dias M, Hildebrandt F, Pellman D, Woods G, Godinho SA. Centrosomes and cilia in human disease. *Trends in genetics : TIG*. 2011; 27:307–15. [PubMed: 21680046]
75. Goetz SC, Anderson KV. The primary cilium: a signalling centre during vertebrate development. *Nat Rev Genet*. 2010; 11:331–44. [PubMed: 20395968]
76. Singla V, Reiter JF. The primary cilium as the cell's antenna: signaling at a sensory organelle. *Science*. 2006; 313:629–33. [PubMed: 16888132]
77. Yoshida S, Hamada H. Roles of cilia, fluid flow, and Ca²⁺ signaling in breaking of left-right symmetry. *Trends in genetics : TIG*. 2014; 30:10–7. [PubMed: 24091059]
78. Mitchison HM, Valente EM. Motile and non-motile cilia in human pathology: from function to phenotypes. *The Journal of pathology*. 2017; 241:294–309. [PubMed: 27859258]
79. Braun DA, Hildebrandt F. Ciliopathies. *Cold Spring Harbor perspectives in biology*. 2017; 9
80. Brooks ER, Wallingford JB. Multiciliated cells. *Current biology : CB*. 2014; 24:R973–82. [PubMed: 25291643]
81. Meunier A, Azimzadeh J. Multiciliated Cells in Animals. *Cold Spring Harbor perspectives in biology*. 2016; 8
82. Sorokin S. Centrioles and the formation of rudimentary cilia by fibroblasts and smooth muscle cells. *The Journal of cell biology*. 1962; 15:363–77. [PubMed: 13978319]
83. Schmidt TI, Kleylein-Sohn J, Westendorf J, Le Clech M, Lavoie SB, Stierhof YD, Nigg EA. Control of centriole length by CPAP and CP110. *Current biology : CB*. 2009; 19:1005–11. [PubMed: 19481458]
84. Spektor A, Tsang WY, Khoo D, Dynlacht BD. Cep97 and CP110 suppress a cilia assembly program. *Cell*. 2007; 130:678–90. [PubMed: 17719545]

85. Goetz SC, Liem KF Jr, Anderson KV. The spinocerebellar ataxia-associated gene Tau tubulin kinase 2 controls the initiation of ciliogenesis. *Cell*. 2012; 151:847–58. [PubMed: 23141541]
86. Cajanek L, Nigg EA. Cep164 triggers ciliogenesis by recruiting Tau tubulin kinase 2 to the mother centriole. *Proceedings of the National Academy of Sciences of the United States of America*. 2014; 111:E2841–50. [PubMed: 24982133]
87. Lu Q, Insinna C, Ott C, Stauffer J, Pintado PA, Rahajeng J, Baxa U, Walia V, Cuenca A, Hwang YS, Daar IO, et al. Early steps in primary cilium assembly require EHD1/EHD3-dependent ciliary vesicle formation. *Nature cell biology*. 2015
88. Rosenbaum JL, Witman GB. Intraflagellar transport. *Nature reviews Molecular cell biology*. 2002; 3:813–25. [PubMed: 12415299]
89. Bhogaraju S, Cajanek L, Fort C, Blisnick T, Weber K, Taschner M, Mizuno N, Lamla S, Bastin P, Nigg EA, Lorentzen E. Molecular Basis of Tubulin Transport Within the Cilium by IFT74 and IFT81. *Science*. 2013; 341:1009–12. [PubMed: 23990561]
90. Sanchez I, Dynlacht BD. Cilium assembly and disassembly. *Nature cell biology*. 2016; 18:711–7. [PubMed: 27350441]
91. Nachury MV, Seeley ES. The perennial organelle: assembly and disassembly of the primary cilium. *Journal of cell science*. 2010; 123:511–18. [PubMed: 20144999]
92. Jakobsen L, Vanselow K, Skogs M, Toyoda Y, Lundberg E, Poser I, Falkenby LG, Bennetzen M, Westendorf J, Nigg EA, Uhlen M, et al. Novel asymmetrically localizing components of human centrosomes identified by complementary proteomics methods. *EMBO J*. 2011; 30:1520–35. [PubMed: 21399614]
93. Gupta GD, Coyaude E, Goncalves J, Mojarad BA, Liu Y, Wu Q, Gheiratmand L, Comartin D, Tkach JM, Cheung SW, Bashkurov M, et al. A Dynamic Protein Interaction Landscape of the Human Centrosome-Cilium Interface. *Cell*. 2015; 163:1484–99. [PubMed: 26638075]
94. May-Simera HL, Kelley MW. Cilia, Wnt signaling, and the cytoskeleton. *Cilia*. 2012; 1:7. [PubMed: 23351924]
95. Wallingford JB, Mitchell B. Strange as it may seem: the many links between Wnt signaling, planar cell polarity, and cilia. *Genes & development*. 2011; 25:201–13. [PubMed: 21289065]
96. Otto EA, Schermer B, Obara T, O'Toole JF, Hiller KS, Mueller AM, Ruf RG, Hoefele J, Beekmann F, Landau D, Foreman JW, et al. Mutations in INVS encoding inversin cause nephronophthisis type 2, linking renal cystic disease to the function of primary cilia and left-right axis determination. *Nat Genet*. 2003; 34:413–20. [PubMed: 12872123]
97. Simons M, Gloy J, Ganner A, Bullerkotte A, Bashkurov M, Kronig C, Schermer B, Benzing T, Cabello OA, Jenny A, Mlodzik M, et al. Inversin, the gene product mutated in nephronophthisis type II, functions as a molecular switch between Wnt signaling pathways. *Nat Genet*. 2005; 37:537–43. [PubMed: 15852005]
98. Veland IR, Montjean R, Eley L, Pedersen LB, Schwab A, Goodship J, Kristiansen K, Pedersen SF, Saunier S, Christensen ST. Inversin/Nephrocystin-2 is required for fibroblast polarity and directional cell migration. *PLoS One*. 2013; 8:e60193. [PubMed: 23593172]
99. Sugiyama N, Tsukiyama T, Yamaguchi TP, Yokoyama T. The canonical Wnt signaling pathway is not involved in renal cyst development in the kidneys of inv mutant mice. *Kidney international*. 2011; 79:957–65. [PubMed: 21248711]
100. Gerdes JM, Liu Y, Zaghloul NA, Leitch CC, Lawson SS, Kato M, Beachy PA, Beales PL, DeMartino GN, Fisher S, Badano JL, et al. Disruption of the basal body compromises proteasomal function and perturbs intracellular Wnt response. *Nat Genet*. 2007; 39:1350–60. [PubMed: 17906624]
101. Corbit KC, Shyer AE, Dowdle WE, Gaulden J, Singla V, Chen MH, Chuang PT, Reiter JF. Kif3a constrains beta-catenin-dependent Wnt signalling through dual ciliary and non-ciliary mechanisms. *Nature cell biology*. 2008; 10:70–6. [PubMed: 18084282]
102. McDermott KM, Liu BY, Tlsty TD, Pazour GJ. Primary cilia regulate branching morphogenesis during mammary gland development. *Curr Biol*. 2010; 20:731–7. [PubMed: 20381354]
103. Lin F, Hiesberger T, Cordes K, Sinclair AM, Goldstein LS, Somlo S, Igarashi P. Kidney-specific inactivation of the KIF3A subunit of kinesin-II inhibits renal ciliogenesis and produces polycystic

- kidney disease. *Proceedings of the National Academy of Sciences of the United States of America*. 2003; 100:5286–91. [PubMed: 12672950]
104. Liu B, Chen S, Cheng D, Jing W, Helms JA. Primary cilia integrate hedgehog and Wnt signaling during tooth development. *Journal of dental research*. 2014; 93:475–82. [PubMed: 24659776]
 105. Ocbina PJ, Tuson M, Anderson KV. Primary cilia are not required for normal canonical Wnt signaling in the mouse embryo. *PLoS One*. 2009; 4:e6839. [PubMed: 19718259]
 106. Huang P, Schier AF. Dampened Hedgehog signaling but normal Wnt signaling in zebrafish without cilia. *Development*. 2009; 136:3089–98. [PubMed: 19700616]
 107. Sipe CW, Lu X. Kif3a regulates planar polarization of auditory hair cells through both ciliary and non-ciliary mechanisms. *Development*. 2011; 138:3441–9. [PubMed: 21752934]
 108. Kim M, Suh YA, Oh JH, Lee BR, Kim J, Jang SJ. KIF3A binds to beta-arrestin for suppressing Wnt/beta-catenin signalling independently of primary cilia in lung cancer. *Scientific reports*. 2016; 6:32770. [PubMed: 27596264]
 109. Balmer S, Dussert A, Collu GM, Benitez E, Iomini C, Mlodzik M. Components of Intraflagellar Transport Complex A Function Independently of the Cilium to Regulate Canonical Wnt Signaling in *Drosophila*. *Developmental cell*. 2015; 34:705–18. [PubMed: 26364750]
 110. Wigley WC, Fabunmi RP, Lee MG, Marino CR, Muallem S, DeMartino GN, Thomas PJ. Dynamic association of proteasomal machinery with the centrosome. *The Journal of cell biology*. 1999; 145:481–90. [PubMed: 10225950]
 111. Fabunmi RP, Wigley WC, Thomas PJ, DeMartino GN. Activity and Regulation of the Centrosome-associated Proteasome. *Journal of Biological Chemistry*. 2000; 275:409–13. [PubMed: 10617632]
 112. Gerhardt C, Lier JM, Burmuhl S, Struchtrup A, Deutschmann K, Vetter M, Leu T, Reeg S, Grune T, Ruther U. The transition zone protein Rpgrip11 regulates proteasomal activity at the primary cilium. *The Journal of cell biology*. 2015; 210:115–33. [PubMed: 26150391]
 113. Fuentealba LC, Eivers E, Ikeda A, Hurtado C, Kuroda H, Pera EM, De Robertis EM. Integrating patterning signals: Wnt/GSK3 regulates the duration of the BMP/Smad1 signal. *Cell*. 2007; 131:980–93. [PubMed: 18045539]
 114. Vora S, Phillips BT. Centrosome-Associated Degradation Limits beta-Catenin Inheritance by Daughter Cells after Asymmetric Division. *Current biology : CB*. 2015; 25:1005–16. [PubMed: 25819561]
 115. Chitalia VC, Foy RL, Bachschmid MM, Zeng L, Panchenko MV, Zhou MI, Bharti A, Seldin DC, Lecker SH, Dominguez I, Cohen HT. Jade-1 inhibits Wnt signalling by ubiquitylating beta-catenin and mediates Wnt pathway inhibition by pVHL. *Nature cell biology*. 2008; 10:1208–16. [PubMed: 18806787]
 116. Borgal L, Rinschen MM, Dafinger C, Hoff S, Reinert MJ, Lamkemeyer T, Lienkamp SS, Benzing T, Schermer B. Casein Kinase 1 Alpha Phosphorylates the Wnt-Regulator Jade-1 and Modulates its Activity. *The Journal of biological chemistry*. 2014
 117. Mollet G, Silbermann F, Delous M, Salomon R, Antignac C, Saunier S. Characterization of the nephrocystin/nephrocystin-4 complex and subcellular localization of nephrocystin-4 to primary cilia and centrosomes. *Hum Mol Genet*. 2005; 14:645–56. [PubMed: 15661758]
 118. Basto R, Lau J, Vinogradova T, Gardiol A, Woods CG, Khodjakov A, Raff JW. Flies without centrioles. *Cell*. 2006; 125:1375–86. [PubMed: 16814722]
 119. Bazzi H, Anderson KV. Acentriolar mitosis activates a p53-dependent apoptosis pathway in the mouse embryo. *Proceedings of the National Academy of Sciences of the United States of America*. 2014; 111:E1491–500. [PubMed: 24706806]
 120. Insolera R, Bazzi H, Shao W, Anderson KV, Shi SH. Cortical neurogenesis in the absence of centrioles. *Nature neuroscience*. 2014; 17:1528–35. [PubMed: 25282615]
 121. Niehrs C, Acebron SP. Mitotic and mitogenic Wnt signalling. *EMBO J*. 2012; 31:2705–13. [PubMed: 22617425]
 122. Acebron SP, Niehrs C. beta-Catenin-Independent Roles of Wnt/LRP6 Signaling. *Trends in cell biology*. 2016; 26:956–67. [PubMed: 27568239]

123. Davidson G, Shen J, Huang Y-L, Su Y, Karaulanov E, Bartscherer K, Hassler C, Stannek P, Boutros M, Niehrs C. Cell Cycle Control of Wnt Receptor Activation. *Developmental cell*. 2009; 17:788–99. [PubMed: 20059949]
124. Lee G, White LS, Hurov KE, Stappenbeck TS, Piwnica-Worms H. Response of small intestinal epithelial cells to acute disruption of cell division through CDC25 deletion. *Proceedings of the National Academy of Sciences of the United States of America*. 2009; 106:4701–6. [PubMed: 19273838]
125. Acebron SP, Karaulanov E, Berger BS, Huang YL, Niehrs C. Mitotic wnt signaling promotes protein stabilization and regulates cell size. *Mol Cell*. 2014; 54:663–74. [PubMed: 24837680]
126. Chen M, Philipp M, Wang J, Premont RT, Garrison TR, Caron MG, Lefkowitz RJ, Chen W. G Protein-coupled receptor kinases phosphorylate LRP6 in the Wnt pathway. *The Journal of biological chemistry*. 2009; 284:35040–8. [PubMed: 19801552]
127. Cervenka I, Wolf J, Masek J, Krejci P, Wilcox WR, Kozubik A, Schulte G, Gutkind JS, Bryja V. Mitogen-activated protein kinases promote WNT/beta-catenin signaling via phosphorylation of LRP6. *Mol Cell Biol*. 2011; 31:179–89. [PubMed: 20974802]
128. Krejci P, Aklian A, Kaucka M, Sevcikova E, Prochazkova J, Masek JK, Mikolka P, Pospisilova T, Spoustova T, Weis M, Paznekas WA, et al. Receptor tyrosine kinases activate canonical WNT/beta-catenin signaling via MAP kinase/LRP6 pathway and direct beta-catenin phosphorylation. *PLoS One*. 2012; 7:e35826. [PubMed: 22558232]
129. Olmeda D, Castel S, Vilaro S, Cano A. Beta-catenin regulation during the cell cycle: implications in G2/M and apoptosis. *Mol Biol Cell*. 2003; 14:2844–60. [PubMed: 12857869]
130. Bahmanyar S, Kaplan DD, Deluca JG, Giddings TH Jr, O'Toole ET, Winey M, Salmon ED, Casey PJ, Nelson WJ, Barth AI. beta-Catenin is a Nek2 substrate involved in centrosome separation. *Genes & development*. 2008; 22:91–105. [PubMed: 18086858]
131. Kikuchi K, Niikura Y, Kitagawa K, Kikuchi A. Dishevelled, a Wnt signalling component, is involved in mitotic progression in cooperation with Plk1. *EMBO J*. 2010; 29:3470–83. [PubMed: 20823832]
132. Cervenka I, Valnohova J, Bernatik O, Harnos J, Radsetoulal M, Sedova K, Hanakova K, Potesil D, Sedlackova M, Salasova A, Steinhart Z, et al. Dishevelled is a NEK2 kinase substrate controlling dynamics of centrosomal linker proteins. *Proceedings of the National Academy of Sciences of the United States of America*. 2016; 113:9304–9. [PubMed: 27486244]
133. Fumoto K, Kadono M, Izumi N, Kikuchi A. Axin localizes to the centrosome and is involved in microtubule nucleation. *EMBO reports*. 2009; 10:606–13. [PubMed: 19390532]
134. Kim SM, Choi EJ, Song KJ, Kim S, Seo E, Jho EH, Kee SH. Axin localizes to mitotic spindles and centrosomes in mitotic cells. *Exp Cell Res*. 2009; 315:943–54. [PubMed: 19331826]
135. Hadjihannas MV, Bruckner M, Behrens J. Conductin/axin2 and Wnt signalling regulates centrosome cohesion. *EMBO Rep*. 2010; 11:317–24. [PubMed: 20300119]
136. Ruan K, Ye F, Li C, Liou YC, Lin SC, Lin SY. PLK1 interacts and phosphorylates Axin that is essential for proper centrosome formation. *PLoS One*. 2012; 7:e49184. [PubMed: 23155463]
137. Poulton JS, Mu FW, Roberts DM, Peifer M. APC2 and Axin promote mitotic fidelity by facilitating centrosome separation and cytoskeletal regulation. *Development*. 2013; 140:4226–36. [PubMed: 24026117]
138. Greer YE, Rubin JS. Casein kinase 1 delta functions at the centrosome to mediate Wnt-3a-dependent neurite outgrowth. *The Journal of cell biology*. 2011; 192:993–1004. [PubMed: 21422228]
139. Greer YE, Westlake CJ, Gao B, Bharti K, Shiba Y, Xavier CP, Pazour GJ, Yang Y, Rubin JS. Casein kinase 1 delta functions at the centrosome and Golgi to promote ciliogenesis. *Molecular biology of the cell*. 2014; 25:1629–40. [PubMed: 24648492]
140. Chaki M, Airik R, Ghosh AK, Giles RH, Chen R, Slaats GG, Wang H, Hurd TW, Zhou W, Cluckey A, Gee HY, et al. Exome Capture Reveals ZNF423 and CEP164 Mutations, Linking Renal Ciliopathies to DNA Damage Response Signaling. *Cell*. 2012; 150:533–48. [PubMed: 22863007]

141. Hadjihannas MV, Bernkopf DB, Bruckner M, Behrens J. Cell cycle control of Wnt/beta-catenin signalling by conductin/axin2 through CDC20. *EMBO Rep.* 2012; 13:347–54. [PubMed: 22322943]
142. Kafri P, Hasenson SE, Kanter I, Sheinberger J, Kinor N, Yunger S, Shav-Tal Y. Quantifying beta-catenin subcellular dynamics and cyclin D1 mRNA transcription during Wnt signaling in single living cells. *eLife.* 2016; 5
143. Lui C, Mok MT, Henderson BR. Characterization of Adenomatous Polyposis Coli Protein Dynamics and Localization at the Centrosome. *Cancers.* 2016; 8
144. Schertel C, Huang D, Bjorklund M, Bischof J, Yin D, Li R, Wu Y, Zeng R, Wu J, Taipale J, Song H, et al. Systematic screening of a Drosophila ORF library in vivo uncovers Wnt/Wg pathway components. *Dev Cell.* 2013; 25:207–19. [PubMed: 23583758]
145. Weber U, Mlodzik M. APC/CFzr/Cdh1-Dependent Regulation of Planar Cell Polarity Establishment via Nek2 Kinase Acting on Dishevelled. *Developmental cell.* 2017; 40:53–66. [PubMed: 28041906]
146. Hardy T, Lee M, Hames RS, Prosser SL, Cheary DM, Samant MD, Schultz F, Baxter JE, Rhee K, Fry AM. Multisite phosphorylation of C-Nap1 releases it from Cep135 to trigger centrosome disjunction. *Journal of cell science.* 2014; 127:2493–506. [PubMed: 24695856]
147. Faragher AJ, Fry AM. Nek2A kinase stimulates centrosome disjunction and is required for formation of bipolar mitotic spindles. *Mol Biol Cell.* 2003; 14:2876–89. [PubMed: 12857871]
148. Martins T, Meghini F, Florio F, Kimata Y. The APC/C Coordinates Retinal Differentiation with G1 Arrest through the Nek2-Dependent Modulation of Wntless Signaling. *Developmental cell.* 2017; 40:67–80. [PubMed: 28041905]
149. Schlesinger A, Shelton CA, Maloof JN, Meneghini M, Bowerman B. Wnt pathway components orient a mitotic spindle in the early *Caenorhabditis elegans* embryo without requiring gene transcription in the responding cell. *Genes & development.* 1999; 13:2028–38. [PubMed: 10444600]
150. McCartney BM, McEwen DG, Grevengoed E, Maddox P, Bejsovec A, Peifer M. Drosophila APC2 and Armadillo participate in tethering mitotic spindles to cortical actin. *Nature cell biology.* 2001; 3:933–8. [PubMed: 11584277]
151. Zipperlen P, Fraser AG, Kamath RS, Martinez-Campos M, Ahringer J. Roles for 147 embryonic lethal genes on *C.elegans* chromosome I identified by RNA interference and video microscopy. *The EMBO journal.* 2001; 20:3984–92. [PubMed: 11483502]
152. Walston T, Tuskey C, Edgar L, Hawkins N, Ellis G, Bowerman B, Wood W, Hardin J. Multiple Wnt signaling pathways converge to orient the mitotic spindle in early *C. elegans* embryos. *Dev Cell.* 2004; 7:831–41. [PubMed: 15572126]
153. Sawa H. Control of cell polarity and asymmetric division in *C. elegans*. *Current topics in developmental biology.* 2012; 101:55–76. [PubMed: 23140625]
154. Wallingford JB. Planar cell polarity and the developmental control of cell behavior in vertebrate embryos. *Annual review of cell and developmental biology.* 2012; 28:627–53.
155. Morin X, Bellaiche Y. Mitotic spindle orientation in asymmetric and symmetric cell divisions during animal development. *Developmental cell.* 2011; 21:102–19. [PubMed: 21763612]
156. Miller RK, Rose MD. Kar9p is a novel cortical protein required for cytoplasmic microtubule orientation in yeast. *The Journal of cell biology.* 1998; 140:377–90. [PubMed: 9442113]
157. Bloom K. It's a kar9ochore to capture microtubules. *Nature cell biology.* 2000; 2:E96–8. [PubMed: 10854334]
158. Bahmanyar S, Nelson WJ, Barth AI. Role of APC and its binding partners in regulating microtubules in mitosis. *Advances in experimental medicine and biology.* 2009; 656:65–74. [PubMed: 19928353]
159. Caldwell CM, Kaplan KB. The role of APC in mitosis and in chromosome instability. *Advances in experimental medicine and biology.* 2009; 656:51–64. [PubMed: 19928352]
160. Zhang L, Shay JW. Multiple Roles of APC and its Therapeutic Implications in Colorectal Cancer. *Journal of the National Cancer Institute.* 2017; 109

161. Kaplan DD, Meigs TE, Kelly P, Casey PJ. Identification of a role for beta-catenin in the establishment of a bipolar mitotic spindle. *The Journal of biological chemistry*. 2004; 279:10829–32. [PubMed: 14744872]
162. Thorpe CJ, Schlesinger A, Carter JC, Bowerman B. Wnt signaling polarizes an early *C. elegans* blastomere to distinguish endoderm from mesoderm. *Cell*. 1997; 90:695–705. [PubMed: 9288749]
163. Banziger C, Soldini D, Schutt C, Zipperlen P, Hausmann G, Basler K. Wntless, a conserved membrane protein dedicated to the secretion of Wnt proteins from signaling cells. *Cell*. 2006; 125:509–22. [PubMed: 16678095]
164. Habib SJ, Chen BC, Tsai FC, Anastassiadis K, Meyer T, Betzig E, Nusse R. A localized Wnt signal orients asymmetric stem cell division in vitro. *Science*. 2013; 339:1445–8. [PubMed: 23520113]
165. Stolz A, Neufeld K, Ertych N, Bastians H. Wnt-mediated protein stabilization ensures proper mitotic microtubule assembly and chromosome segregation. *EMBO reports*. 2015; 16:490–9. [PubMed: 25656539]
166. Carvajal-Gonzalez JM, Mulero-Navarro S, Mlodzik M. Centriole positioning in epithelial cells and its intimate relationship with planar cell polarity. *BioEssays : news and reviews in molecular, cellular and developmental biology*. 2016; 38:1234–45.
167. Antic D, Stubbs JL, Suyama K, Kintner C, Scott MP, Axelrod JD. Planar cell polarity enables posterior localization of nodal cilia and left-right axis determination during mouse and *Xenopus* embryogenesis. *PloS one*. 2010; 5:e8999. [PubMed: 20126399]
168. Borovina A, Superina S, Voskas D, Ciruna B. Vangl2 directs the posterior tilting and asymmetric localization of motile primary cilia. *Nature cell biology*. 2010; 12:407–12. [PubMed: 20305649]
169. Oishi I, Kawakami Y, Raya A, Callol-Massot C, Izpisua Belmonte JC. Regulation of primary cilia formation and left-right patterning in zebrafish by a noncanonical Wnt signaling mediator, *duboraya*. *Nature genetics*. 2006; 38:1316–22. [PubMed: 17013396]
170. Park TJ, Mitchell BJ, Abitua PB, Kintner C, Wallingford JB. Dishevelled controls apical docking and planar polarization of basal bodies in ciliated epithelial cells. *Nature genetics*. 2008; 40:871–9. [PubMed: 18552847]
171. Park TJ, Haigo SL, Wallingford JB. Ciliogenesis defects in embryos lacking inturnd or fuzzy function are associated with failure of planar cell polarity and Hedgehog signaling. *Nature genetics*. 2006; 38:303–11. [PubMed: 16493421]
172. Gray RS, Abitua PB, Wlodarczyk BJ, Szabo-Rogers HL, Blanchard O, Lee I, Weiss GS, Liu KJ, Marcotte EM, Wallingford JB, Finnell RH. The planar cell polarity effector Fuz is essential for targeted membrane trafficking, ciliogenesis and mouse embryonic development. *Nature cell biology*. 2009; 11:1225–32. [PubMed: 19767740]
173. Carvajal-Gonzalez JM, Roman AC, Mlodzik M. Positioning of centrioles is a conserved readout of Frizzled planar cell polarity signalling. *Nature communications*. 2016; 7 11135.
174. Caron A, Xu X, Lin X. Wnt/beta-catenin signaling directly regulates *Foxj1* expression and ciliogenesis in zebrafish Kupffer's vesicle. *Development*. 2012; 139:514–24. [PubMed: 22190638]
175. Stubbs JL, Oishi I, Izpisua Belmonte JC, Kintner C. The forkhead protein *Foxj1* specifies node-like cilia in *Xenopus* and zebrafish embryos. *Nat Genet*. 2008; 40:1454–60. [PubMed: 19011629]
176. Walentek P, Beyer T, Thumberger T, Schweickert A, Blum M. ATP4a is required for Wnt-dependent *Foxj1* expression and leftward flow in *Xenopus* left-right development. *Cell Rep*. 2012; 1:516–27. [PubMed: 22832275]
177. Walentek P, Schneider I, Schweickert A, Blum M. Wnt11b is involved in cilia-mediated symmetry breakage during *Xenopus* left-right development. *PLoS One*. 2013; 8:e73646. [PubMed: 24058481]
178. Hashimoto M, Shinohara K, Wang J, Ikeuchi S, Yoshida S, Meno C, Nonaka S, Takada S, Hatta K, Wynshaw-Boris A, Hamada H. Planar polarization of node cells determines the rotational axis of node cilia. *Nature cell biology*. 2010; 12:170–6. [PubMed: 20098415]
179. Ohata S, Nakatani J, Herranz-Perez V, Cheng J, Belinson H, Inubushi T, Snider WD, Garcia-Verdugo JM, Wynshaw-Boris A, Alvarez-Buylla A. Loss of Dishevelleds disrupts planar polarity

- in ependymal motile cilia and results in hydrocephalus. *Neuron*. 2014; 83:558–71. [PubMed: 25043421]
180. Mitchell B, Stubbs JL, Huisman F, Taborek P, Yu C, Kintner C. The PCP pathway instructs the planar orientation of ciliated cells in the *Xenopus* larval skin. *Curr Biol*. 2009; 19:924–9. [PubMed: 19427216]
 181. Ganner A, Lienkamp S, Schafer T, Romaker D, Wegierski T, Park TJ, Spreitzer S, Simons M, Gloy J, Kim E, Wallingford JB, et al. Regulation of ciliary polarity by the APC/C. *Proceedings of the National Academy of Sciences of the United States of America*. 2009; 106:17799–804. [PubMed: 19805045]
 182. Mahuzier A, Gaude HM, Grampa V, Anselme I, Silbermann F, Leroux-Berger M, Delacour D, Ezan J, Montcouquiol M, Saunier S, Schneider-Maunoury S, et al. Dishevelled stabilization by the ciliopathy protein Rpgrip11 is essential for planar cell polarity. *The Journal of cell biology*. 2012; 198:927–40. [PubMed: 22927466]
 183. Lee KH, Johmura Y, Yu LR, Park JE, Gao Y, Bang JK, Zhou M, Veenstra TD, Yeon Kim B, Lee KS. Identification of a novel Wnt5a-CK1 epsilon-Dvl2-Plk1-mediated primary cilia disassembly pathway. *The EMBO journal*. 2012
 184. Gao C, Chen YG. Dishevelled: The hub of Wnt signaling. *Cellular signalling*. 2010; 22:717–27. [PubMed: 20006983]
 185. Zhang B, Zhang T, Wang G, Wang G, Chi W, Jiang Q, Zhang C. GSK3beta-Dzip1-Rab8 Cascade Regulates Ciliogenesis after Mitosis. *PLoS biology*. 2015; 13:e1002129. [PubMed: 25860027]
 186. Thoma CR, Frew IJ, Hoerner CR, Montani M, Moch H, Krek W. pVHL and GSK3beta are components of a primary cilium-maintenance signalling network. *Nature cell biology*. 2007; 9:588–95. [PubMed: 17450132]
 187. Wakefield JG, Stephens DJ, M TJ. A role for glycogen synthase kinase-3 in mitotic spindle dynamics and chromosome alignment. *J Cell Sci*. 2003; 116(Pt 4):637–46. [PubMed: 12538764]
 188. Itoh K, Jenny A, Mlodzik M, Sokol SY. Centrosomal localization of Diversin and its relevance to Wnt signaling. *J Cell Sci*. 2009; 122:3791–98. [PubMed: 19789178]
 189. Alexandrova EM, Sokol SY. *Xenopus* axin-related protein: a link between its centrosomal localization and function in the Wnt/beta-catenin pathway. *Dev Dyn*. 2010; 239:261–70. [PubMed: 19842147]
 190. Sillibourne JE, Milne DM, Takahashi M, Ono Y, Meek DW. Centrosomal Anchoring of the Protein Kinase CK1δ Mediated by Attachment to the Large, Coiled-coil Scaffolding Protein CG-NAP/AKAP450. *Journal of Molecular Biology*. 2002; 322:785–97. [PubMed: 12270714]
 191. Zyss D, Ebrahimi H, Gergely F. Casein kinase I delta controls centrosome positioning during T cell activation. *The Journal of cell biology*. 2011; 195:781–97. [PubMed: 22123863]
 192. Firat-Karalar EN, Rauniyar N, Yates JR 3rd, Stearns T. Proximity interactions among centrosome components identify regulators of centriole duplication. *Current biology : CB*. 2014; 24:664–70. [PubMed: 24613305]
 193. Mick DU, Rodrigues RB, Leib RD, Adams CM, Chien AS, Gygi SP, Nachury MV. Proteomics of Primary Cilia by Proximity Labeling. *Developmental cell*. 2015; 35:497–512. [PubMed: 26585297]
 194. Andersen JS, Wilkinson CJ, Mayor T, Mortensen P. Proteomic characterization of the human centrosome by protein correlation profiling. *Nature*. 2003; 426:570–74. [PubMed: 14654843]
 195. Mbom BC, Siemers KA, Ostrowski MA, Nelson WJ, Barth AI. Nek2 phosphorylates and stabilizes beta-catenin at mitotic centrosomes downstream of Plk1. *Mol Biol Cell*. 2014; 25:977–91. [PubMed: 24501426]
 196. He XQ, Song YQ, Liu R, Liu Y, Zhang F, Zhang Z, Shen YT, Xu L, Chen MH, Wang YL, Xu BH, et al. Axin-1 Regulates Meiotic Spindle Organization in Mouse Oocytes. *PloS one*. 2016; 11:e0157197. [PubMed: 27284927]
 197. Dikovskaya D, Newton IP, Nathke IS. The adenomatous polyposis coli protein is required for the formation of robust spindles formed in CSF *Xenopus* extracts. *Molecular biology of the cell*. 2004; 15:2978–91. [PubMed: 15075372]

198. Lui C, Ashton C, Sharma M, Brocardo MG, Henderson BR. APC functions at the centrosome to stimulate microtubule growth. *The international journal of biochemistry & cell biology*. 2016; 70:39–47. [PubMed: 26556314]
199. Yamashita YM, Jones DL, Fuller MT. Orientation of Asymmetric Stem Cell Division by the APC Tumor Suppressor and Centrosome. *Science*. 2003; 301:1547–50. [PubMed: 12970569]
200. Fumoto K, Kikuchi K, Gon H, Kikuchi A. Wnt5a signaling controls cytokinesis by correctly positioning ESCRT-III at the midbody. *J Cell Sci*. 2012; 125:4822–32. [PubMed: 22825874]
201. Yang Y, Liu M, Li D, Ran J, Gao J, Suo S, Sun SC, Zhou J. CYLD regulates spindle orientation by stabilizing astral microtubules and promoting dishevelled-NuMA-dynein/dynactin complex formation. *Proceedings of the National Academy of Sciences of the United States of America*. 2014; 111(6):2158–63. [PubMed: 24469800]
202. Brockman JL, Gross SG, Sussman MR, Anderson RA. Cell cycle-dependent localization of casein kinase I to mitotic spindles. *Proceedings of the National Academy of Sciences of the United States of America*. 1992; 89:9454–58. [PubMed: 1409656]
203. Kaplan KB, Burds AA, Swedlow JR, Bekir SS, Sorger PK, Nathke IS. A role for the Adenomatous Polyposis Coli protein in chromosome segregation. *Nature cell biology*. 2001; 3:426–32.

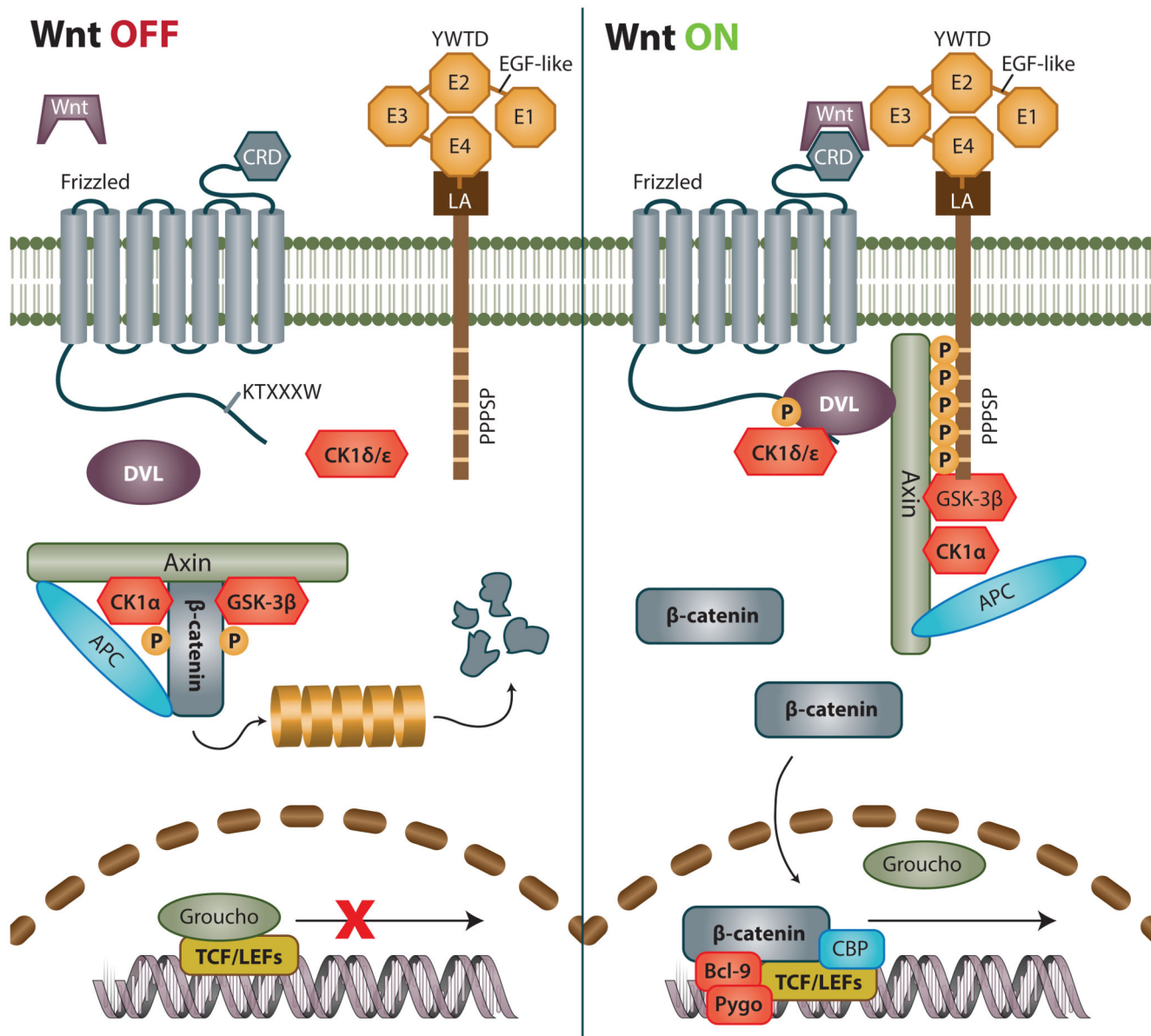


Figure 1. Current view of Wnt/β-catenin signaling in OFF and ON state.

During OFF state destruction complex consisting of Axin, APC and GSK-3β phosphorylates β-catenin and marks it for subsequent degradation via ubiquitin proteasome pathway. At the same time, transcription factors from the TCF/LEF family remain bound to repressors such as Groucho, blocking the transcription of Wnt target genes. Cascade is activated after binding of Wnt ligand to Frizzled (Fzd) receptor. Subsequently, both DVL and Lrp6 associate to Fzd. Intracellular residues of Lrp6 are phosphorylated and become a site of attachment for scaffold protein Axin, which can no longer serve as assembly site for destruction complex, which is thus desintegrated. It should be noted that phosphorylated Lrp6, DVL Axin together with other proteins form a structures dubbed signalosomes that 'attract' each other and amplify the Wnt signal. As a result, β-catenin is no longer degraded, and accumulates in the cytoplasm. After reaching a certain threshold, it is translocated to

nucleus where it binds to TCF/LEF family of transcription factors, replaces resident repressors thereby co-activating transcription of its target genes.

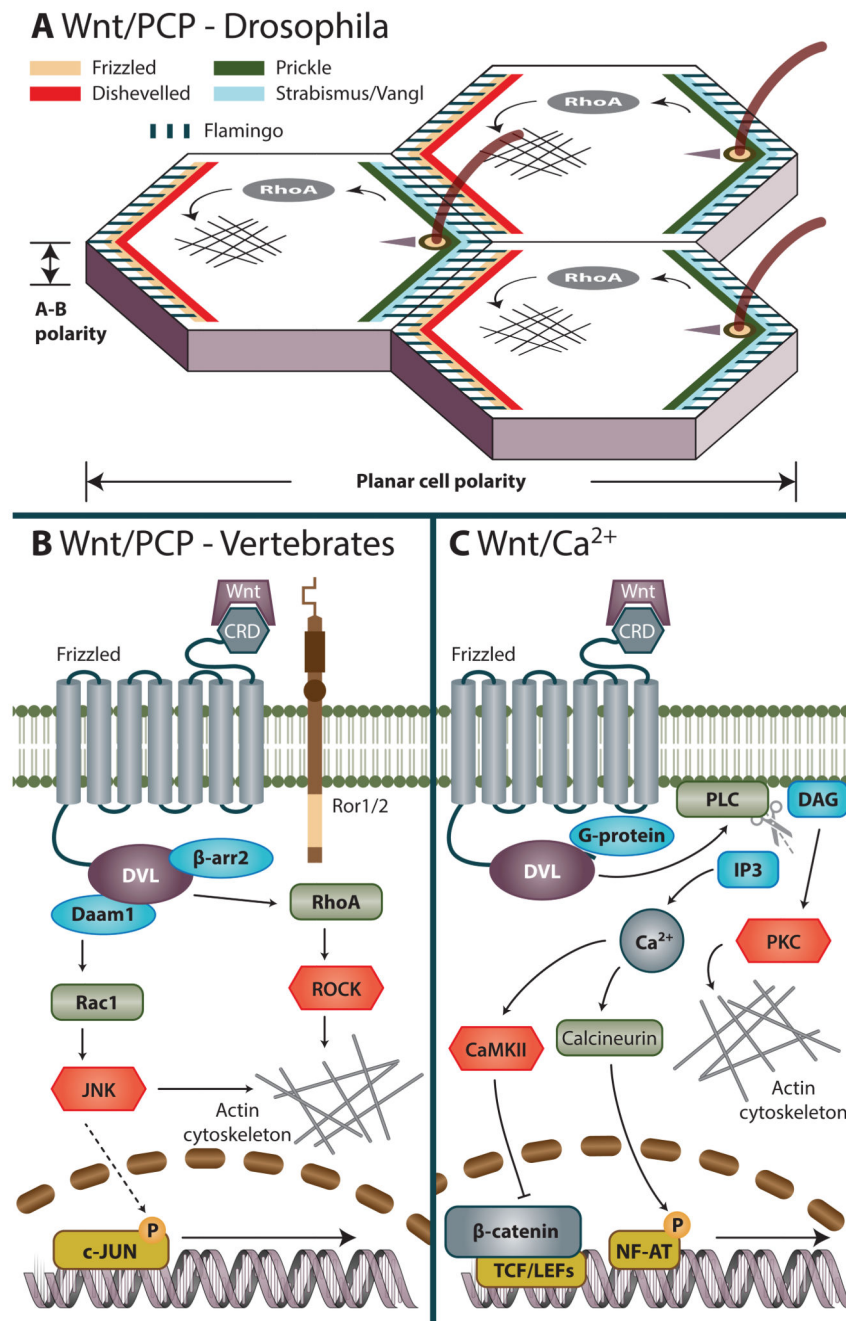


Figure 2. β -catenin-independent Wnt pathways.

A. Wnt/Planar cell polarity (PCP) in Drosophila is responsible for coordinated alignment of cells across a tissue plane. Figure shows configuration of asymmetric complexes of core PCP pathway components at the cell boundary after polarity has been established. Proximal site contains Frizzled-Dishevelled-Flamingo protein complexes and distal site contains Vangl-Prickle-Flamingo complexes. This asymmetric segregation arises from both intracellular cascades that perpetrate their mutual exclusion at either proximal or distal site and from their preferential heterotypic association extracellularly.

B. Wnt/PCP pathway in vertebrates. Activation of vertebrate PCP pathway is triggered by Wnt ligand (typically Wnt5a or Wnt11) that interact with Fzd and coreceptors (Ror1, Ror2, PTK7 or Ryk) and via DVL and β -arrestin activate members of Rho family of small GTPases. Coordinated activation of downstream effectors – JNK and ROCK – induces cytoskeletal rearrangements that in turn influence processes ranging from convergent extension movements to positioning of basal bodies or cilia.

C. Wnt/ Ca^{2+} pathway in vertebrates. Wnts were shown to induce release of intracellular Ca^{2+} stores that can activate a multitude of Ca^{2+} dependent effectors to modulate both transcription as well as actin cytoskeleton.

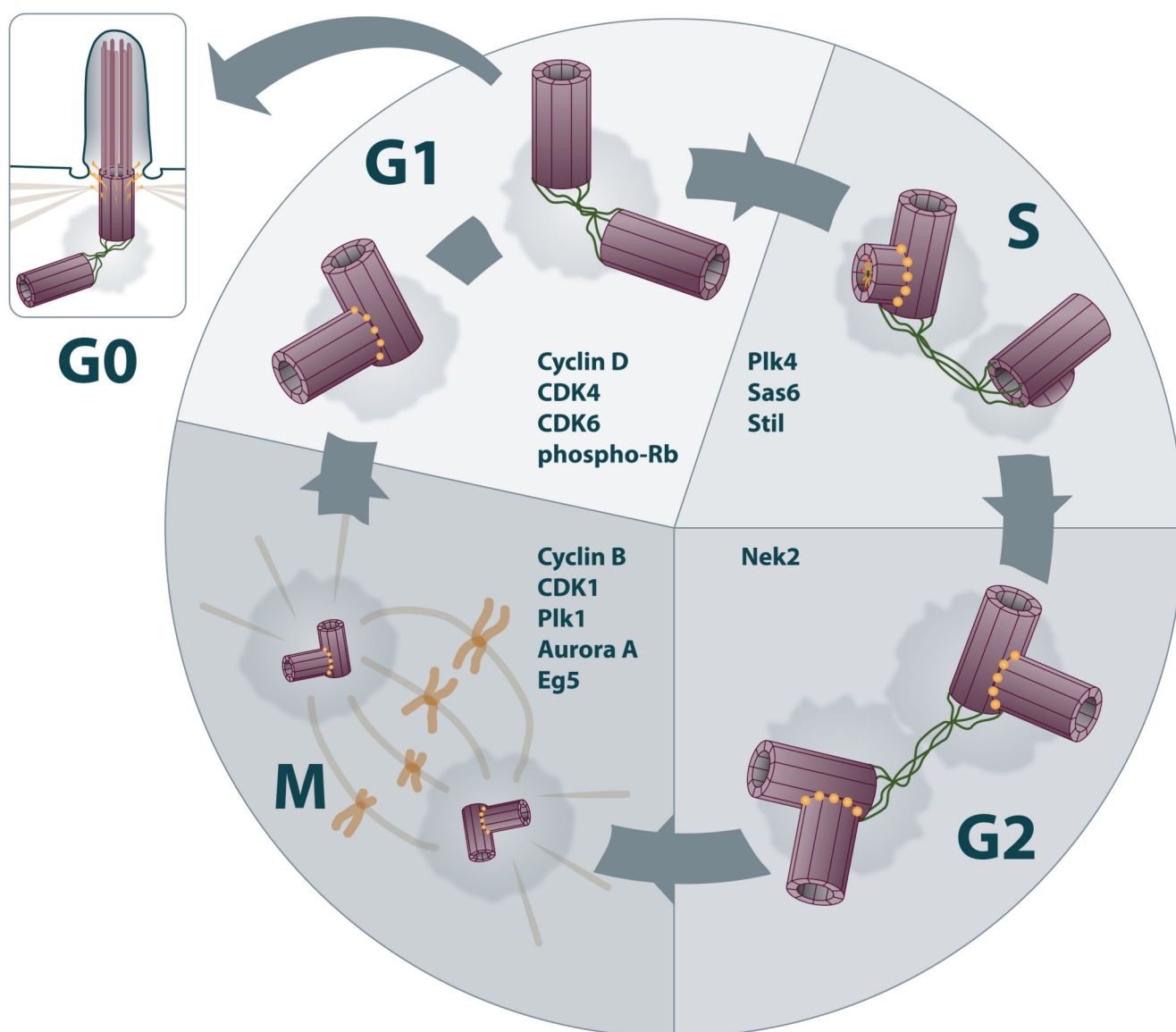


Figure 3. Coordination of cell cycle and centrosomal cycle.

The cell first needs to commit itself to enter new round of cell cycle (G1/S transition), then it replicates its DNA content (S phase), which is, after second gap (G2 phase) subsequently packed into chromosomes and divided into two daughter cells (M phase). Following the mitotic exit, cell typically forms primary cilium that is again disassembled before the new mitotic entry. First, cell needs to pass a 'restriction point' (G1/S) checkpoint at the end of the G1 phase. Key player regulating the G/S checkpoint is the Retinoblastoma tumor suppressor protein (Rb). Rb sequesters transcription factors that are essential for the cell cycle to progress to the S phase. Complexes of cyclin D-CDK4/6 phosphorylate Rb during early G1 phase. A cell in G1 phase typically contains one centrosome with two centrioles. After centrioles are disengaged, loose protein linker is established in-between. They are now in permissive state to duplicate. But they need to enter S phase to initiate centriole duplication. Biogenesis of new centrioles (procentrioles) is a semi-conservative process, which starts

next to the proximal end of each of the two pre-existing centrioles. Key steps in the initiation of centriole biogenesis are coordinated by proteins STIL, SAS-6, and kinase PLK4, leading to formation of assembly platform called 'cartwheel', which recruits microtubule dimers and dictates the typical 9 fold symmetry of centrioles.. Centrioles fully mature during subsequent cell cycle, by acquisition of protein assemblies termed distal and subdistal appendages, respectively. Only the mature centriole is capable to transform into basal body to serve as base of cilium or flagellum. Flexible linker, formed after centriole disengagement in anaphase, allows cohesion of the two centrosomes until the onset of next mitoses. Master regulator here is a kinase NEK2, which coordinates displacement of linker proteins at G2/M and subsequent centrosome separation via phosphorylation of several linker proteins. After linker elimination, centrosomes are physically separated by action of motors. The prominent role here has kinesin motor KIF11/Eg5, action of which is fine tuned by kinases Cdk1, PLK1, and NEK family. As the cell approaches mitosis, the centriolar pairs separate from each other and migrate to the opposite poles to help organizing the mitotic spindle. Cell that is about to divide usually uses an organized array of microtubules (spindle and astral microtubules) together with microtubule motors to generate pulling force to physically segregate chromosomes into two daughters. Entry into mitosis is triggered by activity of cyclin B-CDK1 complex. Cell division leaves each daughter cell with one centrosome containing two centrioles. These are originally kept in engaged mode which restrains their re-duplication. Subsequent centriole disengagement during mitoses is controlled by PLK1 and separase, and represents critical step for licensing of centriole to duplicate in the upcoming round of cell cycle. Enrolment of these mitotic regulators in the control of centriole disengagement hence elegantly interconnects the centrosome cycle with mitotic machinery and separation of chromatids, respectively, and ensures correct timing of these events.

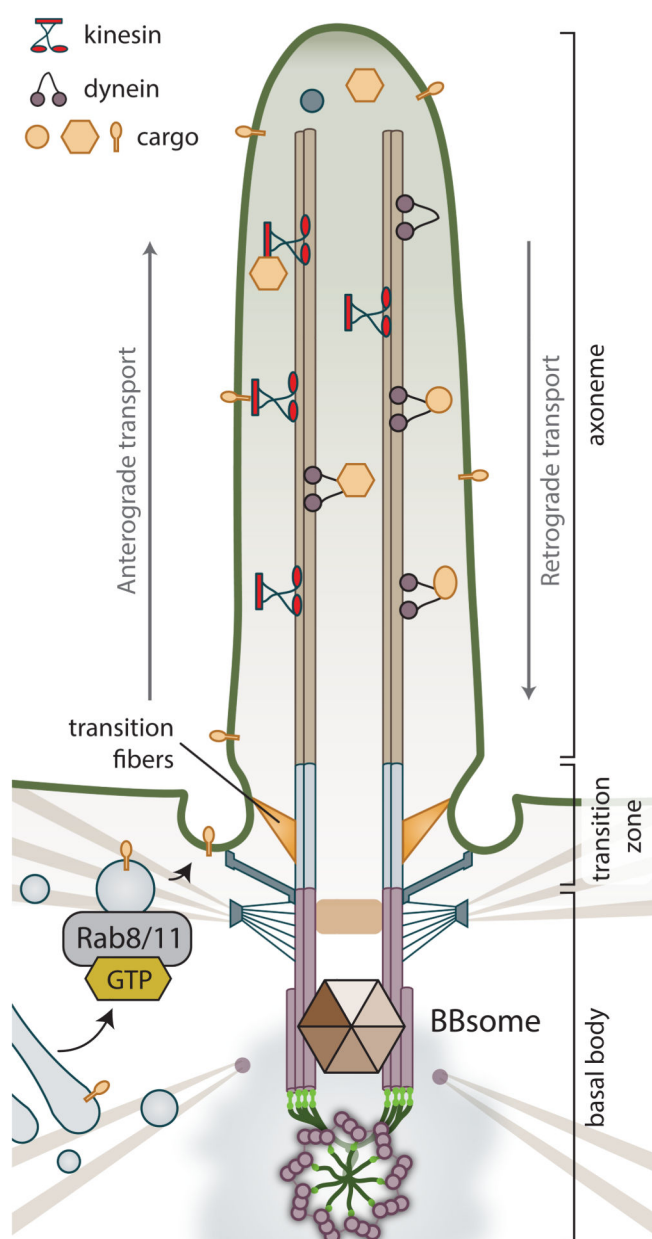


Figure 4. Cilium.

The axoneme stems from the mother centriole-derived basal body, anchored to the cell membrane via its distal appendages (subsequently called transition fibers). Transition fibers, connected both to microtubules and surrounding plasma membrane, contribute to formation of transition zone, which serves as a gate controlling sorting of molecules transported in the cilium. Depositioning of membrane to the mother centriole and formation of ciliary vesicle and subsequently ciliary shaft is coordinated by interactions of Rab11/Rabin8/Rab8 pathway, BBsome (Bardet-Biedl syndrome) protein complex, and components of distal

appendages. The ciliary cargo is transported along the axoneme loaded on IFT particles, which are moved by action of molecular motors. Specifically, kinesin-2 family motors mediate anterograde transport along the microtubules towards the tip of the cilium, while cytoplasmic dynein-2 mediates retrograde movement of intraflagellar transport complexes from the tip to the ciliary base.

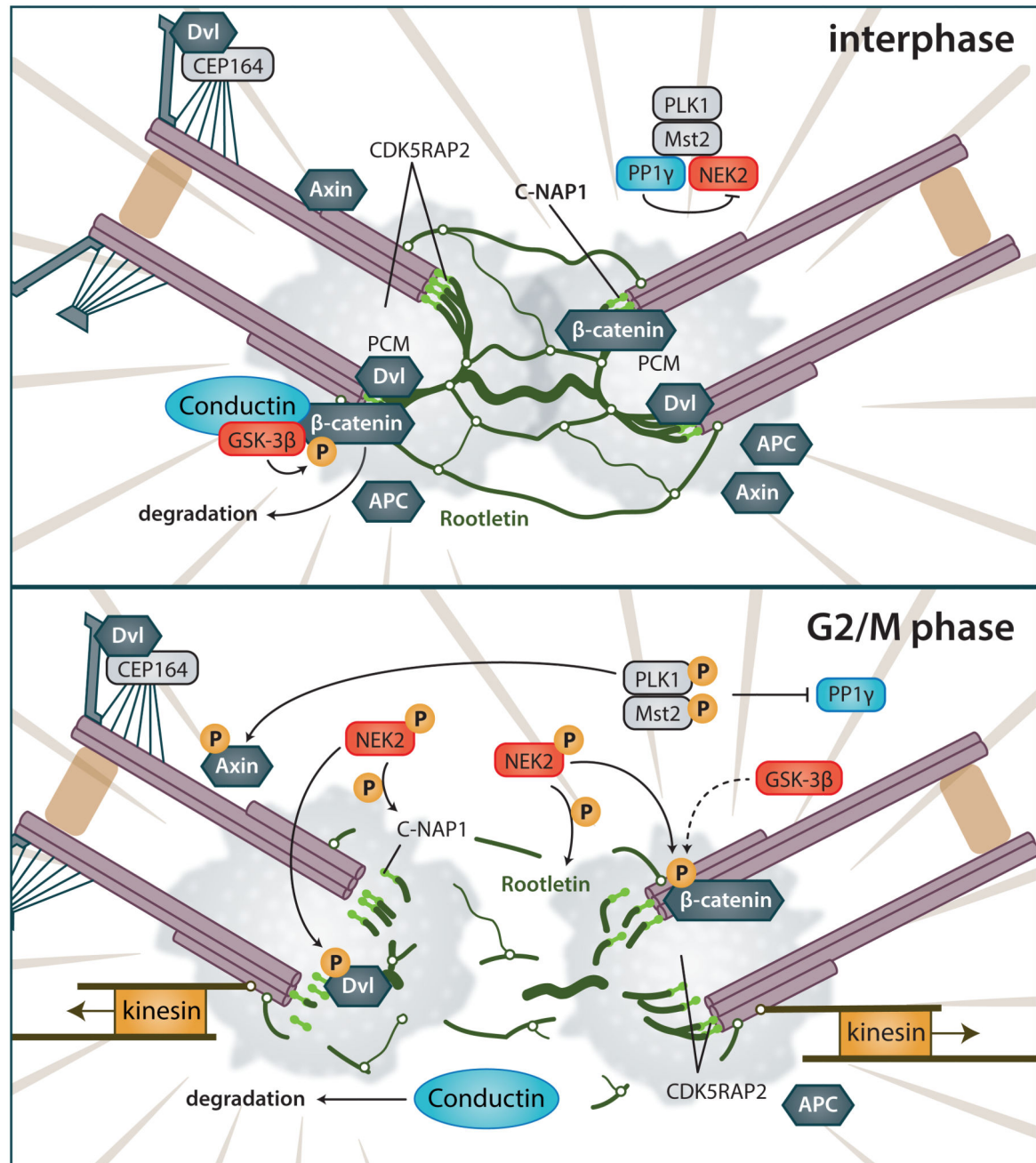
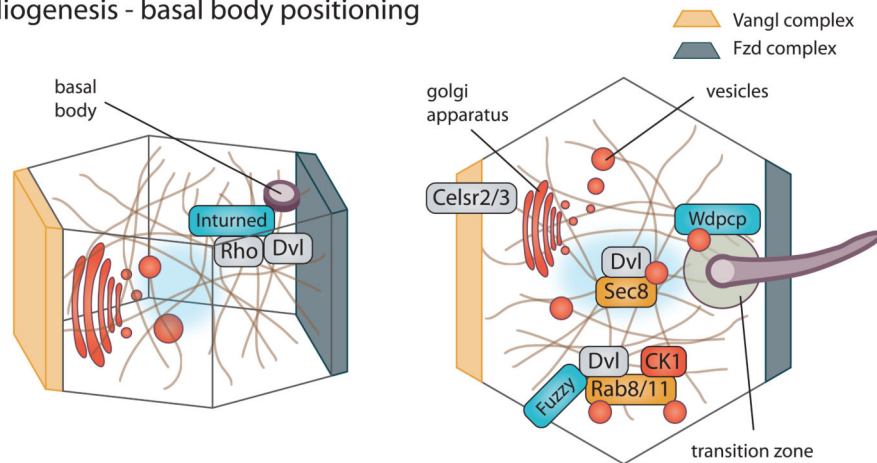


Figure 5. Effects of Wnt pathway components on the centrosome separation.

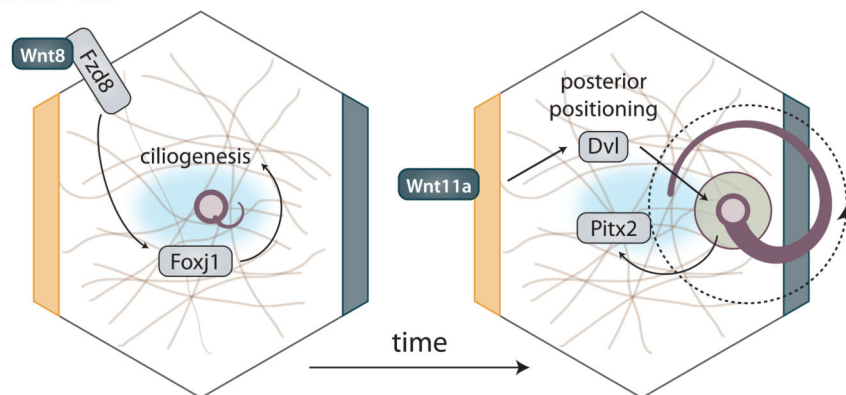
(Upper) Interphase cells. Centrosomes are connected by a linker that consists of fibrous Rootletin and is anchored to the proximal sides of centrioles by C-NAP1. During interphase, centrosome cohesion is maintained by action of Axin2/Conductin and GSK-3 β by phosphorylation of β -catenin. DVL in ciliated cells promote basal body docking, via interaction with CEP164 and other proteins. Axin and APC can be also found at centrosome, probably due to their microtubule interactions. NEK2 is kept inactive in complex with PLK1/MST2/PP1 γ . (Lower) G2/M phase. Phosphorylation cascade activates NEK2, which

subsequently acts on several targets. β -catenin is protected from degradation by NEK2 phosphorylation, and promotes centrosome separation; Axin2/Conductin is degraded by proteasome. Concurrently, phosphorylation of DVL and C-NAP1 by NEK2 leads to the increase in their overall negative charge and subsequent release from centrioles. Centrosomes can be subsequently pulled apart. Axin is phosphorylated by PLK1, which affects microtubule dynamics during spindle formation. For details and references see text.

A Ciliogenesis - basal body positioning



B Nodal cilia



C Multiciliated cells

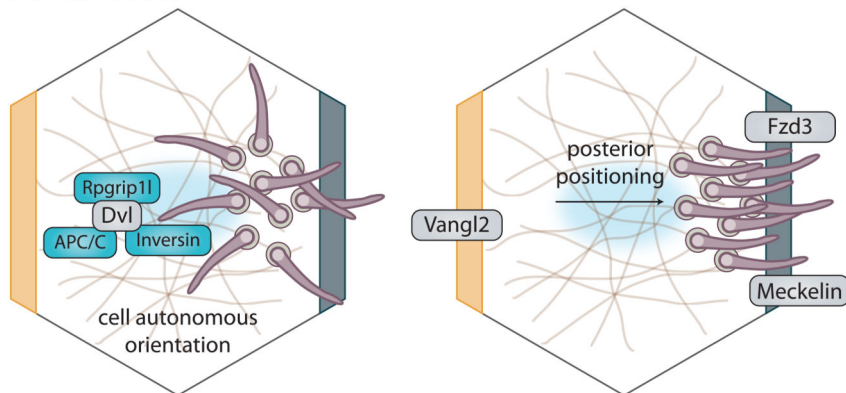


Figure 6. Modes of action of Wnt pathway components on cilia.

(A) Removal of PCP pathway components perturbs ciliogenesis and in most the cases it happens through interference with basal body docking and vesicular transport that is necessary during ciliary assembly. Side view of the cell (left) shows how PCP effector Inturned interacts with DVL in Rho-mediated actin assembly in apical positioning of basal body. At the same time in the top-down view (right), Celsr2/3, CK1, DVL and PCP effector Fuzzy influence vesicular transport towards basal body via interactions with Rab GTPases.

PCP effector protein Wdpcp, located at the transition zone, influences ciliogenesis by contributing to cargo sorting and restricting diffusion into ciliary compartment.

(B) Formation of nodal cilia is initiated by Wnt8 ligand binding to Fzd8 receptor, which in turn leads to upregulation of Foxj1, a transcriptional regulator of ciliogenesis. Over time, cilia are positioned towards posterior of the cell by action of cascade involving Wnt11a, DVL, and Pitx2. Only correctly formed and positioned nodal cilia can create leftward fluid flow that determines left-right asymmetry.

(C) Multiciliated cells in epithelia display cell-autonomous type of polarity that makes sure that all cilia are oriented in the same fashion. This event is influenced by stability of DVL, controlled by its interactors: Inversin, APC/C and Rpgrip11. On the other hand, tissue-wide posterior positioning is largely controlled by PCP pathway dependently on Vangl2 and Fzd3 with help of ciliary proteins, such as Meckelin.

Table 1
Summary of Localization of Key Wnt Pathway Components at the Centriole and/or Mitotic Spindle

Protein	Localization	Method ¹	Validation ²	Species/Cell Type	Note	References
DVL2	spindle poles, midbody	FP tagged protein	no	Hela	also weak kinetochore staining	Kikuchi et al. (2010)
DVL2	centrosome/basal body	ICC	no	Xenopus embryo, multiciliated cells	C-term sufficient	(Park et al., 2008)
DVL2/3	centrosome/basal body	ICC	yes CRISPR DVL1/2/3 TKO	Hek293T		(Cervenka et al., 2016)
β-catenin	spindle and spindle poles, midbody	ICC	no	L cells		(Kaplan et al., 2004)
β-catenin (phospho)	centrosome/basal body	ICC	no	MEFs	phospho Ser33/37/Thr41	(Hadjihannas, Bruckner, and Behrens, 2010)
β-catenin (phospho)	centrosome/basal body, midbody	ICC	no	rat and human fibroblasts	phospho Ser33/37/Thr41, total β-catenin not seen at centrosome	(Huang and Schier, 2009)
β-catenin	centrosome/basal body	ICC, EM	No, but multiple antibodies used	RPE-1, U2OS	localized to centriolar linker, armadillo repeat required	(Bahmanyar et al., 2008)
β-catenin (Sys1)	spindle poles	FP tagged protein	no	C.elegans	localization to PCM	(Vora and Phillips, 2015)
APC	centrosome/basal body	ICC	no	HaCa4 cells	only during mitoses	(Olmeda et al., 2003)
axin 1	centrosome/basal body	ICC	Yes, siRNA	HeLa, NIH3T3 and L cells	DIX domain dependent	(Butler and Wallingford, 2017)
axin 1	spindle and spindle poles	ICC	no	HaCaT cells		(Kim et al., 2009)
axin2/conductin	centrosome/basal body	ICC	no	MEFs, SW480, U2OS	localized to centriolar linker	(Hadjihannas, Bruckner, and Behrens, 2010)
GSK3	spindle poles and mitotic spindle	ICC	no	Hela	phospho Ser21/9	(Wakefield, Stephens, and M., 2003) (Itoh et al., 2009)
Diversin	centrosome/basal body	FP tagged protein	no	Xenopus animal cap cells		
Xenopus Axin-related protein	centrosome/basal body	ICC (overexp.)	no	Xenopus	DIX domain dependent	(Alexandrova and Sokol, 2010)
CK1δ	centrosome/basal body	ICC	no	TC-32 cells	C-term sufficient	(Greer and Rubin, 2011)
CK1δ	centrosome/basal body	ICC	no	SAOS-2, COS7		(Sillibourne et al., 2002)
CK1δ	centrosome/basal body	FP tagged protein	no	Jurkat cells	C-term required	(Zyss, Ebrahimi,

Protein	Localization	Method ¹	Validation ²	Species/Cell Type	Note	References
						and Gergely, 2011)

¹ICC (immunocytochemical staining of endogenous protein), FP tagged protein (protein of interest visualized by addition of fluorescent protein), EM – detection by immunogold electron microscopy

²Only validation based on the removal of the target protein via siRNA or Crispr/Cas9 was considered

Table 2
Protein Interactions of Wnt Pathway Components with Centrosomal/Ciliary Proteins - High Throughput Studies

Protein	Bait/Partner	Method of Detection	Cell Type/Species	Reference
DVL2	KIAA0753	BioID	U2OS	(Firat-Karalar et al., 2014)
DVL3, CK1e	NPHP3 (1-203)/cilia APEX	APEX	IMCD3	(Mick et al., 2015)
DVL1, DVL2, DVL3, β -catenin, Axin1, Lrp5, Lrp6, APC, β -arrestin, CK1 α , CK1 δ , CK1e	Cep290, Cep162, LCA5, MKS1, Nek8, NIN, NINL, NPHP1, Cep162, KIAA0753, Cep44, Cep63, Cep89, Cep97, CENT2, Centrobins, DCTN1, EVC2, NPHP1, NPHP4, Sas6, SCTL1, SPICE1, SSXIP, STIL, DYNLT1, TMEM17, TMEM216, RPF, ODF2, OFD1, PCM1, POC1a, RPGRIP1L, C3orf14, TCTN3, B9D1, CNTRL, Cep120, Cep128, Cep135, Cep152, Cep164, Cep170, Cep19, Cep104, AHI1, FBF1, B9D2, CC2D2A, Cep83, CP110, CENPJ, Cep290, TCTN1	BioID	Hek293T, RPE-1	(Gupta et al., 2015)
DVL3	Cep164	IP	Hek293T	(Chaki et al., 2012)
β -catenin, β -arrestin, CK1 α , CK1 δ	?	purified centrosomes	KE37 cells	(Alexandrova and Sokol, 2010; Andersen et al., 2003)

Table 3
Evidence for Cell Cycle Dependent Changes of Wnt Pathway Components

Protein	Cell Cycle/phase ¹	Note	Method ²	References
β-catenin	G2/M	phosphorylated by NEK2, regulates centrosome cohesion	IF, WB, synchronization	(Olmeda et al., 2003; Bahmanyar et al., 2008; Kaplan et al., 2004; Mbom et al., 2014)
β-catenin	G2/M	rapid centrosomal turnover by proteasome, centrosomal localization negatively regulates Wnt-dependent cell fate	IF	(Vora and Phillips, 2015)
DVL2/DVL3	G2/M	scaffold for centrosomal linker proteins	IF, WB, Fucci	(Cervenka et al., 2016)
DVL2	G2/M	regulates spindle orientation	IF	(Kikuchi et al., 2010)
DVL2	G0	controls planar polarization and apical docking of basal bodies	IF	(Park et al., 2008)
Axin2	G2/M, degraded after mitosis	alters β-catenin phosphorylation and centrosome cohesion	IF	(Hadjihannas, Bruckner, and Behrens, 2010)
Axin	G2/M, meiosis	regulated by Aurora A kinase, influence PLK1 and GSK3 activity	IF, FACS	(Kim et al., 2009)
Axin	meiosis	knockdown leads to abnormal meiotic spindles and misaligned chromosomes	IF	(He et al., 2016)
APC	G2/M	microtubule growth and elongation, stabilization of mitotic spindles, mitosis - stronger binding of APC to centrosome, slow and fast kinetics	IF	(Dikovskaya, Newton, and Nathke, 2004; Lui et al., 2016),
APC	G2/M	influences spindle orientation and asymmetric cell division	IF	(Yamashita, Jones, and Fuller, 2003)
APC2	G2/M	ensures mitotic fidelity, binding to Axin is important for cytoskeletal regulation, induces ectopic furrows	IF	(Poulton et al., 2013; McCartney et al., 2001)
Fz2	cytokinesis	together with DVL2, Wnt5a dependent	IF	(Fumoto et al., 2012)
LRP6	G2/M	phosphorylation by Cyclin Y/Ptk1	WB, IF, FACS	(Hadjihannas, Bruckner, and Behrens, 2010)
CYLD	G2/M	astral microtubule stabilization by dishevelled-NuMA-dynein/dynactin complex	synchronization, WB	(Yang et al., 2014)
CK1α	G2/M		IF	(Brockman et al., 1992)
CK1δ	G0	delta, blocks primary ciliogenesis, disrupts cis-Golgi organization	IF	(Greer et al., 2014)
GSK-3β	interphase, mitosis	phosphorylated in mitosis, inhibition affects astral microtubule length and chromosome alignment	IF, WB	(Mbom et al., 2014)

¹Indicates the cell cycle phase where the highest increase was observed

²Methods used for the detection of cell cycle dependent changes: IF (immunofluorescence), WB (Western blotting), FACS – flow cytometry, synchronization – chemical synchronization, Fucci - Fluorescent ubiquitination-based cell cycle indicator

Table 4
Wnt Pathway Components as Targets of Kinases Involved in the Regulation of cell cycle

Substrate	Kinase	Modified Residue	Function	Method of Detection ¹	Species ²	Ref.
β-catenin	NEK2	S33/S37/T41/T102/T556/S675	β-catenin stabilization, presence at mitotic centrosomes, promotion of centrosome disjunction, regulated upstream by Plk1	MS, WB	h	(Mbom et al., 2014)
APC	Bub1–Bub3, BubR1–Bub3 complexes	middle and C-terminal fragments	chromosome segregation, regulation of kinetochore-microtubule attachment (speculation)	IVP	h	(Kaplan et al., 2001)
Dsh	NEK2	Dsh 1–340 and Dsh 166–623 fragments	activation of Wnt/β-catenin signalling, regulation of Dsh half-life	IVP	d	(Schertel et al., 2013)
DVL	NEK2	T15/S280/S643/S679	separation of centrosomes, disengagement of centrosomal linker	MS, IVP, WB, IF	h	(Cervenka et al., 2016)
DVL2	PLK1	T206	spindle orientation, MT-KT attachment, SAC activation	IVP, WB	h	(Kikuchi et al., 2010)
LRP6	Cyclin Y/Ptk1	S1490	cell cycle dependent Wnt signalling activity	WB, IF	d, x, h	(Hadjihannas, Bruckner, and Behrens, 2010)
Axin	PLK1	S157	Axin-y-tubulin interaction, centrosome formation and segregation	MS, WB	h	(Mick et al., 2015)

¹ Methods of detection: MS (mass spectrometry), WB (Western Blotting), IVP (in vitro phosphorylation), IF (immunofluorescence with phospho-specific antibodies)

² Species: h – human, d – Drosophila, x – Xenopus

Appendix 14

Čajánek L, Nigg EA. Cep164 triggers ciliogenesis by recruiting Tau tubulin kinase 2 to the mother centriole. *Proc Natl Acad Sci U S A*. 2014 Jul 15;111(28):E2841-50. doi: 10.1073/pnas.1401777111. (JCR 2014. IF=9.674, Q1 - Multidisciplinary Sciences)

Cep164 triggers ciliogenesis by recruiting Tau tubulin kinase 2 to the mother centriole

Lukáš Čajánek and Erich A. Nigg¹

Biozentrum, University of Basel, 4056 Basel, Switzerland

Edited by Kathryn V. Anderson, Sloan-Kettering Institute, New York, NY, and approved June 6, 2014 (received for review January 28, 2014)

Primary cilia play critical roles in development and disease. Their assembly is triggered by mature centrioles (basal bodies) and requires centrosomal protein 164kDa (Cep164), a component of distal appendages. Here we show that loss of Cep164 leads to early defects in ciliogenesis, reminiscent of the phenotypic consequences of mutations in TTBK2 (Tau tubulin kinase 2). We identify Cep164 as a likely physiological substrate of TTBK2 and demonstrate that Cep164 and TTBK2 form a complex. We map the interaction domains and demonstrate that complex formation is crucial for the recruitment of TTBK2 to basal bodies. Remarkably, ciliogenesis can be restored in Cep164-depleted cells by expression of chimeric proteins in which TTBK2 is fused to the C-terminal centriole-targeting domain of Cep164. These findings indicate that one of the major functions of Cep164 in ciliogenesis is to recruit active TTBK2 to centrioles. Once positioned, TTBK2 then triggers key events required for ciliogenesis, including removal of CP110 and recruitment of intraflagellar transport proteins. In addition, our data suggest that TTBK2 also acts upstream of Cep164, contributing to the assembly of distal appendages.

primary cilium | centrosome

The primary cilium (PC) functions as an antenna-like signaling organelle typically found on postmitotic cells (1–3). It consists of a microtubule-based axoneme enclosed within a ciliary membrane, and its assembly is triggered at the basal body (4, 5). The basal body, in turn, is derived from one of the two centrioles that make up the centrosome, specifically the mature (or “mother”) centriole (M centriole) (6–9). Long erroneously considered a vestigial organelle, the PC has emerged as a key structure for sensing extracellular stimuli and hence plays crucial roles in cellular responses to both mechanical and chemical cues. In vertebrates, PC function has been linked to the regulation of many important aspects of embryonic development as well as tissue homeostasis in adulthood (2, 10); moreover, defects in ciliary assembly or function have been linked to a large number of human diseases known as ciliopathies (3, 6, 11–13).

PC structure and formation have long been studied at a morphological level (14, 15), but a molecular understanding of the regulation of PC assembly and resorption is only beginning to emerge (5, 7, 8, 16, 17). In cultured cells, PC formation generally occurs when cells exit the cell cycle to enter quiescence (Go), and, conversely, PCs are often resorbed when cells reenter the cell cycle. Thus, PC formation can readily be triggered by serum starvation of some cultured cells, including telomerase-immortalized retinal pigment epithelial (RPE-1) cells. Early steps in PC formation include the docking of membrane vesicles to centrioles (14, 18, 19), the removal of the capping protein CP110 from the distal part of the M centriole (20, 21), the recruitment of intraflagellar transport (IFT) protein complexes (22–24), the formation of a transition zone at the membrane (25, 26), and, finally, the outgrowth of the ciliary axoneme (27, 28).

An important role in PC formation resides with specific components of the M centriole, termed distal appendages (14, 15). These appendages are considered critical for the early docking of Golgi-derived membrane vesicles and the subsequent anchorage of the basal body underneath the plasma membrane.

Following the discovery of centrosomal protein 164kDa (Cep164), the first marker for distal appendages (29), several additional distal appendage proteins (DAPs) have recently been identified and functionally linked to ciliogenesis. These include centrosomal protein 83kDa (Cep83)/CCDC41, centrosomal protein 89kDa (Cep89)/CCDC123, SCLT1, and FBF1 (18, 19, 30, 31). The DAP Cep164 was discovered in a screen for components that are critical for PC formation (29). Subsequently, mutations in Cep164 were linked to ciliopathies, providing direct proof for the importance of this protein in human pathophysiology (32). At a mechanistic level, Cep164 was shown to be required at an early stage of PC formation, notably for the docking of membrane vesicles to the basal body (18). Moreover, two components of the vesicle transport machinery, the small GTPase Rab8 and its guanine-nucleotide exchange factor Rabin8, were identified as interaction partners of Cep164 (18). Despite this progress, the precise molecular functions of Cep164 remain to be fully understood.

Importantly, protein kinases have also been implicated in ciliogenesis and in cilia-related diseases. These include Nek1 and Nek8, two members of the family of NIMA-related kinases (33, 34), and Tau Tubulin Kinase 2 (TTBK2), a member of the casein kinase 1 family (35–37).

Here, we report that Cep164 and TTBK2 form a complex and that formation of this complex at M centrioles is essential for ciliogenesis. We show that the noncatalytic C-terminal domain of TTBK2 interacts with Cep164 and that formation of the complex critically depends on the WW domain within the N-terminal domain of Cep164. We also provide evidence that Cep164 is a likely physiological substrate of TTBK2. Use of chimeric TTBK2–Cep164 constructs in siRNA-rescue experiments leads us to conclude that a main function of Cep164 consists of the

Significance

The primary cilium is an organelle typically found on postmitotic vertebrate cells. Cilia serve as antennae to receive signals from extracellular space and thus play important roles in both development and disease. Understanding the mechanisms controlling their formation (ciliogenesis) is of great importance. Ciliogenesis is known to depend on basal bodies, but although major steps have been described at a morphological level, the underlying mechanism and its regulation remain poorly understood. In our study, we characterized Cep164, a key component of basal bodies that is crucial for ciliogenesis. We show that one major function of Cep164 is to recruit a protein kinase, TTBK2, to basal bodies. Once localized correctly, TTBK2 then functions in distal appendage assembly and primary cilia formation.

Author contributions: L.C. and E.A.N. designed research; L.C. performed research; L.C. analyzed data; and L.C. and E.A.N. wrote the paper.

The authors declare no conflict of interest.

This article is a PNAS Direct Submission.

¹To whom correspondence should be addressed. E-mail: erich.nigg@unibas.ch.

This article contains supporting information online at www.pnas.org/lookup/suppl/doi:10.1073/pnas.1401777111/-DCSupplemental.

recruitment of TTBK2 to M centrioles. Once localized correctly, TTBK2 is then in a position to trigger PC formation through phosphorylation of appropriate substrates. Interestingly, our data also reveal a role for TTBK2 in the assembly of distal appendages. Overexpression of active kinase in fact enhances not only the association of DAPs with existing appendages but also triggers their occasional recruitment to daughter centrioles (D centrioles).

Results

Loss of Cep164 Leads to Early Defects in Cilium Assembly. Cep164 is critical for ciliogenesis in human cells (18, 19, 29). This requirement can readily be demonstrated by siRNA-mediated depletion of Cep164 from RPE-1 cells, which results in strong suppression of PC formation (Fig. S1 *A* and *B*). To better understand the function of Cep164 in ciliogenesis, we first monitored the fate of two proteins previously implicated in the process, CP110 and IFT81. Whereas CP110 suppresses ciliogenesis and must be removed from M centrioles (19–21), the IFT complex component IFT81 is essential for ciliogenesis and must be recruited (38, 39). In serum-starved control cells, CP110 was virtually undetectable at M centrioles, but the protein persisted at all centrioles in most Cep164-depleted cells (Fig. 1 *A* and *B*). Conversely, IFT81 was recruited to M centrioles in controls, but not in Cep164-depleted cells (Fig. 1 *C* and *D*).

It has recently been demonstrated that Cep164 plays a role in vesicular docking, most likely through Rab8a activation (18). To determine whether the above phenotypes could be attributed to impaired Rab8a activity, we transiently expressed Flag-TBC1D30, a Rab8a GTPase-activating protein (GAP) known to interfere with Rab8a activity (40). Expression of the Rab8a GAP strongly suppressed PC formation (Fig. 1*F*), attesting to its functionality; however, IFT81 was still recruited to M centrioles (Fig. 1*E*), and CP110 was still removed (Fig. 1 *G* and *H*). We conclude that attenuation of Rab8a activity by expression of its GAP, TBC1D30, failed to phenocopy the defects observed after Cep164 siRNA depletion, indicating that initial IFT81 recruitment and CP110 removal occur independently of the Cep164/Rab8a pathway.

When considering alternative modes of action of Cep164, we were intrigued by a recent study implicating murine TTBK2 in ciliogenesis (35). Moreover, TTBK2 was found to bind Cep164 in a yeast two-hybrid screen (32). Thus, we decided to explore a possible functional connection between Cep164 and TTBK2. Reminiscent of Cep164 depletion, TTBK2-depleted RPE-1 cells failed to form PCs upon serum starvation (Fig. S1 *C* and *D*), and CP110 was not removed from M centrioles (Fig. S1*E*). Endogenous TTBK2 localized at M centrioles (Fig. 2*A*), confirming and extending previous results (35). Interestingly, in top views, TTBK2 showed a ring-like staining coincident with Cep164, consistent with appendage association (Fig. 2*A*). Localization of TTBK2 was dependent on the presence of Cep164 (Fig. 2 *B* and *C*) but not vice versa (Fig. 2 *D* and *E*). Exogenous Flag-tagged TTBK2 also colocalized with Cep164 (Fig. 2*F*), and, again, this staining was lost upon Cep164 depletion (Fig. 2*G*).

TTBK2–Cep164 Complex Formation and Cep164 Phosphorylation. Given the dependency of TTBK2 localization on Cep164 and a previously suggested interaction between the two proteins (32), we asked whether Cep164 and TTBK2 might form a complex. Indeed, Myc–Cep164 and Flag–TTBK2 could readily be coimmunoprecipitated from HEK293T cells (Fig. 3*A*). Furthermore, the electrophoretic mobility of Myc–Cep164 was retarded in the presence of Flag–TTBK2, suggesting that Cep164 undergoes TTBK2-mediated phosphorylation. In support of this conclusion, the TTBK2-induced mobility upshift of Myc–Cep164 was dependent on TTBK2 activity and sensitive to lambda phosphatase (Fig. 3*B*). It is noteworthy that TTBK2 itself also migrated more slowly than a kinase dead (kd) mutant [D163A (41)], and this

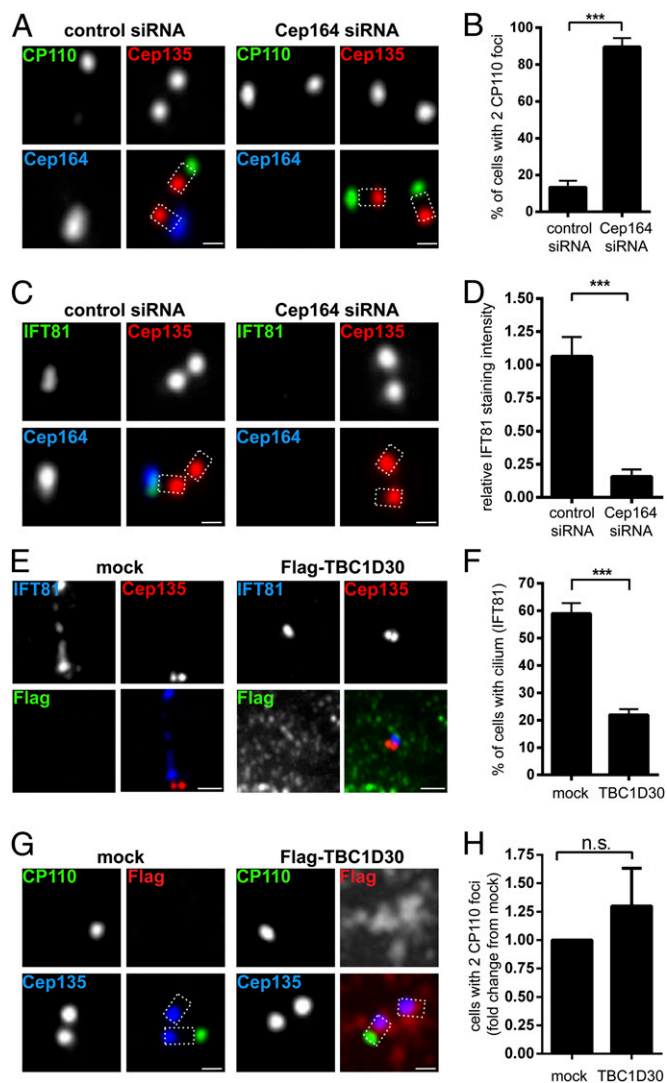


Fig. 1. Depletion of Cep164 impairs early events in ciliogenesis independently of Rab8. RPE-1 cells were transfected with the indicated siRNA oligonucleotides (*A–D*) or plasmids (*E–H*) and serum starved. After fixation and permeabilization, cells were stained with the indicated antibodies and examined by indirect immunofluorescence microscopy. Cep135 staining was used to label proximal ends of centrioles. Dashed lines in merged images outline the centrioles. [Scale bars: 0.5 μ m (*A*, *C*, and *G*) and 1 μ m (*E*).] (*A*) Depletion of Cep164 from RPE-1 cells prevents removal of distal centriolar protein CP110 from the M centriole. (*B*) Quantification of the effects of Cep164 depletion on CP110 removal. Graph represents the summary of three experiments. (*C*) Loss of Cep164 impairs the recruitment of IFT81 to the M centriole. (*D*) Quantification of the effects of Cep164 depletion on IFT81 recruitment. Graph represents the summary of two experiments. (*E*) Transient expression of TBC1D30 (Rab8 GAP) impairs ciliogenesis, but not IFT81 localization to M centriole. (*F*) Quantification of the effects of TBC1D30 expression on ciliogenesis. Graph represents the summary of three experiments. (*G*) Transient expression of TBC1D30 does not prevent removal of CP110 from M centrioles. (*H*) Quantification of the effects of TBC1D30 expression on the CP110 removal. Graph represents the summary of four experiments. ****P* < 0.001; n.s., not significant.

retarded migration was abolished by phosphatase treatment (Fig. 3*B*), indicating that TTBK2 undergoes autophosphorylation. Depletion of TTBK2 from RPE-1 cells caused a loss of higher migrating forms of endogenous Cep164 (Fig. S2*A*), supporting the conclusion that Cep164 is phosphorylated in a TTBK2-dependent manner in vivo.

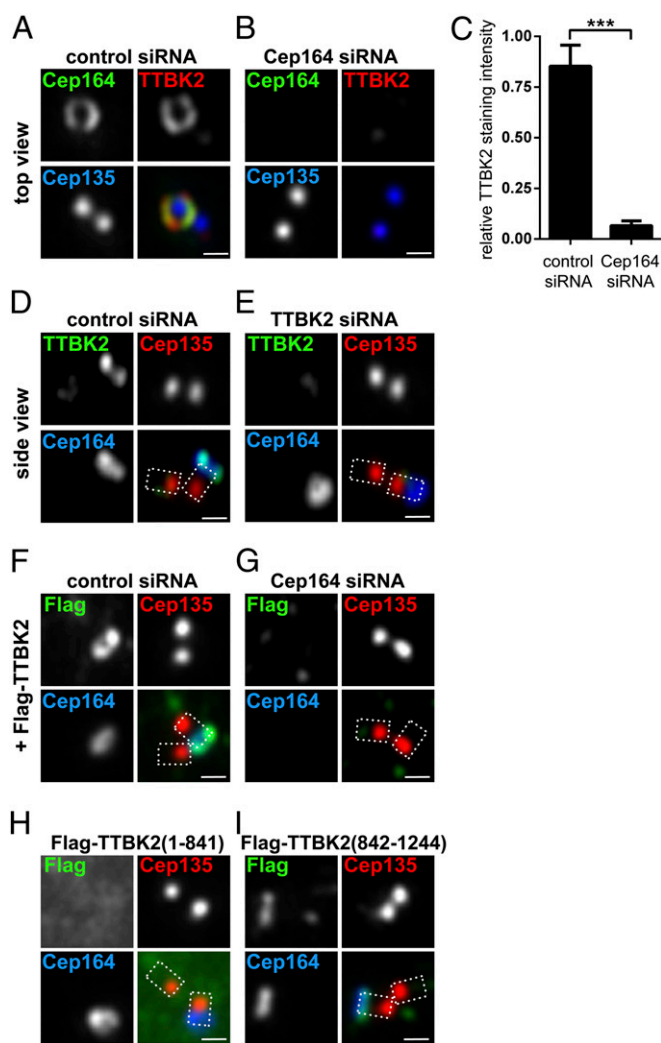


Fig. 2. Cep164 is required for TTBK2 localization to the M centriole. Transfection and immunofluorescence experiments were carried out as described in the Fig. 1 legend. Cep135 staining was used to label proximal ends of centrioles. (Scale bars: 0.5 μ m.) (A) Staining for endogenous Cep164 and TTBK2 reveals colocalization in a ring-like pattern at the M centriole, consistent with colocalization at distal appendages. (B) Depletion of Cep164 prevents recruitment of TTBK2 to the M centriole. (C) Quantification of the effects of Cep164 depletion on TTBK2 recruitment. Graph represents the summary of two experiments. *** $P < 0.001$. (D and E) Cep164 does not require TTBK2 for its localization to distal appendages of the M centriole. (F and G) Depletion of Cep164 prevents the recruitment of Flag-TTBK2 to the M centriole. (H) Flag-TTBK2 (1–841), lacking the Cep164 binding region (Fig. 3E), fails to localize to the M centriole. (I) Flag-TTBK2 (842–1244), containing the Cep164 binding region, localizes to the M centriole.

To explore a possible direct kinase–substrate relationship, we asked whether TTBK2 is able to phosphorylate Cep164 *in vitro*. Recombinant GST–TTBK2 (1–450; catalytic domain), but not the corresponding kd mutant construct (D163A), was indeed able to phosphorylate *in vitro*-translated Flag–Cep164 (Fig. 3C). *In vivo*, TTBK2 triggered a pronounced Cep164 upshift, not only when coexpressed with full-length protein, but also with Cep164 N-term, M-part, or C-term fragments, demonstrating the existence of multiple phosphorylation sites distributed throughout Cep164 (Fig. 3D). Together these results identify Cep164 as a likely physiological substrate of TTBK2. Analysis of the C-term fragment of Cep164 by mass spectrometry (MS) identified seven distinct phosphorylation sites (Fig. S2B); additional sites un-

doubtedly remain to be identified, both within the C-term fragment and the two other Cep164 moieties. Although the physiological consequences of Cep164 phosphorylation remain to be determined, we note that TTBK2 caused a striking accumulation of Cep164 full-length protein as well as C-term fragment (Fig. 3D). This finding raises the possibility that TTBK2-dependent phosphorylation triggers Cep164 stabilization (see also below).

To map the interaction domains between TTBK2 and Cep164, we performed coimmunoprecipitation experiments using deletion mutants of Cep164 and TTBK2, respectively. We identified the C-terminal noncatalytic region of TTBK2 (842–1244) and the N-terminal part of Cep164 (1–467) as being important for complex formation (Fig. 3E and F). Although phosphatase treatment clearly reduced phosphorylation of the interaction partners, it did not detectably affect the stability of the complex (Fig. S2C), arguing against a major regulatory role of phosphorylation in TTBK2–Cep164 complex formation.

Importantly, the C-terminal part of TTBK2 (842–1244) was sufficient for centriole localization, but the Flag–TTBK2 (1–841) mutant failed to localize (Fig. 2H and I), confirming and extending data obtained for murine TTBK2 (35). These results support our conclusion that the association of TTBK2 with M centrioles is mediated by direct binding to Cep164.

Cep164 N Terminus Suppresses Ciliogenesis Through Sequestration of TTBK2. Having established a physical interaction between Cep164 and TTBK2, we next asked to what extent this interaction might contribute to explaining the role of these two proteins in ciliogenesis. First, we examined the consequences of overexpression of various Cep164 constructs, either full-length or truncated. Overexpression of full-length Cep164, M part or C term did not detectably interfere with the formation of PCs, as monitored by staining for acetylated tubulin; in stark contrast, overexpression of Cep164 N term almost completely suppressed ciliogenesis (Fig. 4A and B). Virtually identical results were obtained when using alternative methods for assessing PC formation (Fig. S3A), demonstrating that these effects cannot be explained by an inhibitory influence of Cep164 on tubulin acetylation. We conclude that a strong correlation exists between the ability of Cep164 fragments to bind TTBK2 (Fig. 3F) and their ability to exert a dominant-negative effect on PC formation (Fig. 4B).

To determine whether the observed correlation might indicate causality, we next examined the consequences of expressing the above Cep164 constructs on TTBK2 localization in RPE-1 cells. Whereas endogenous TTBK2 localized to distal appendages of M centrioles in mock or Flag–Cep164 M-part transfected cells, the centriole association of this kinase was strongly diminished in cells transfected with Flag–Cep164 N term (Fig. 4C and D). Because Cep164 N term itself localizes diffusely throughout the cytoplasm (Fig. 4A; see also ref. 18); this result points to sequestration of TTBK2 away from centrioles, a conclusion confirmed by using Flag–TTBK2 (Fig. S3B). Interestingly, the N-terminal part of Cep164 contains a predicted WW domain (56–89) that has been suggested to play a role in ciliogenesis (18). Furthermore, the WW domains of other proteins have previously been implicated in protein–protein interactions (42, 43). Thus, we tested a possible involvement of the Cep164 WW domain in TTBK2 binding. A mutant version of Cep164 N term (WW_{mut}), in which two amino acid substitutions disrupt the structural integrity of the WW domain [(Y74AY75A) (18, 42)], failed not only to sequester TTBK2 away from centrioles (Fig. 4E and F), but also to coimmunoprecipitate GFP–TTBK2 (Fig. 4G). This result demonstrates that the WW domain of Cep164 is functionally important and required for efficient binding to TTBK2.

The above results suggested that the recruitment of TTBK2 to M centrioles might represent a key function of Cep164. If so, one would predict that the displacement of TTBK2 should phenocopy

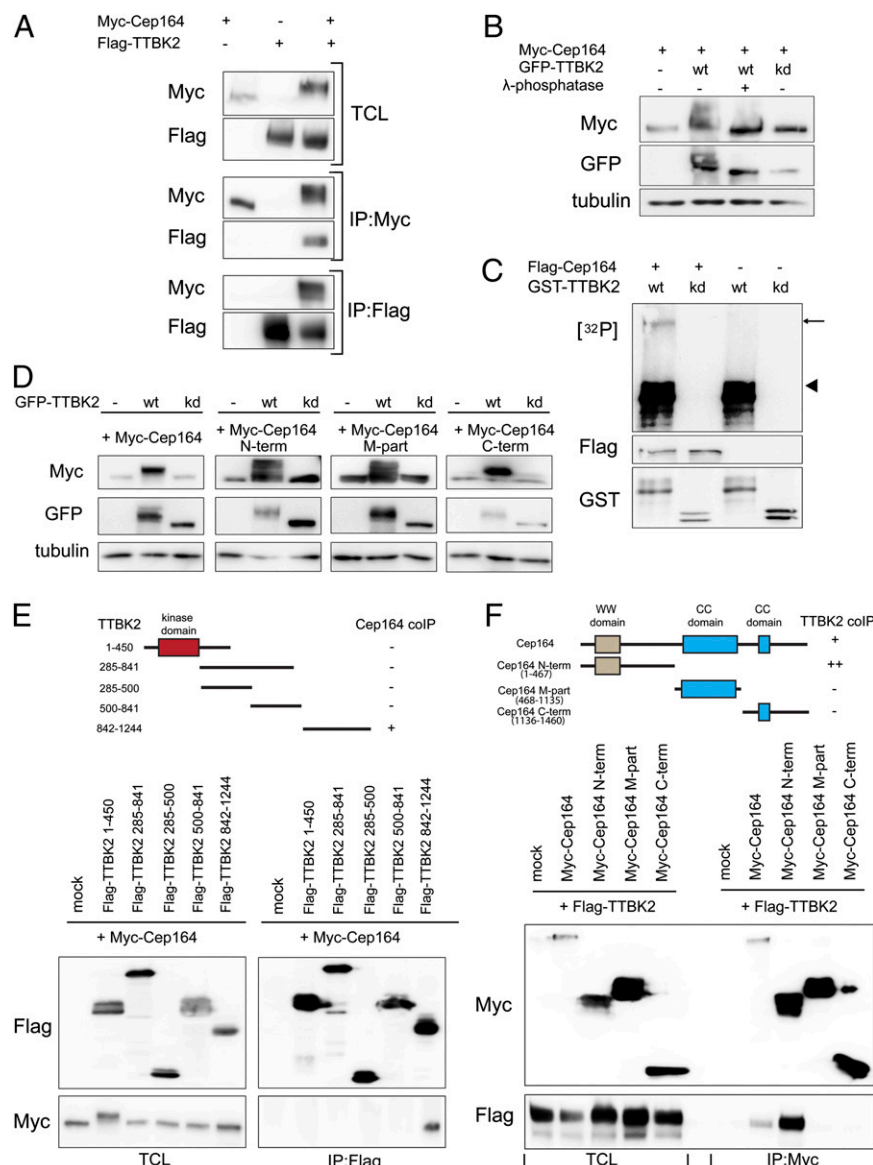


Fig. 3. Cep164 is a binding partner and substrate of TTBK2. (A) HEK293T cells were transfected with the indicated constructs and subjected to immunoprecipitation (IP)–Western experiments. *Upper* shows total cell lysate (TCL). Western blots were performed by using the anti-tag antibodies listed to the left, and IPs were performed by using either anti-Myc (Myc–Cep164; *Middle*) or anti-Flag antibodies (Flag–TTBK2; *Bottom*). (B) Protein extracts, prepared from HEK293T cells transfected with Myc–Cep164 and GFP–TTBK [wild-type (WT) or kinase dead (kd) mutant], were treated with or without λ -phosphatase and analyzed by Western blotting. Note that Cep164 undergoes TTBK2-mediated phosphorylation, as indicated by a mobility shift that is sensitive to λ -phosphatase treatment. (C) In vitro-translated Flag–Cep164 was immunoprecipitated by using anti-Flag antibody and subjected to a kinase assay in the presence of [γ - 32 P]ATP and recombinant GST–TTBK2 (1–450) WT or kd protein. Arrow and arrowhead point to phosphorylated Flag–Cep164 and autophosphorylated GST–TTBK2 (1–450), respectively. (D) Protein extracts of transfected HEK293T cells were analyzed by Western blotting. Note that expression of GFP–TTBK2, but not kd mutant, led to prominently retarded electrophoretic mobility of Myc-tagged Cep164, Cep164 N term, Cep164 M part, and Cep164 C term. Also, note concomitant increases in levels of Cep164 and Cep164 C term. (E and F) Transfected HEK293T cells were subjected to IP–Western experiments. (*Upper*) Schematic representations of the constructs used are shown, and the symbols +, ++, or – summarize the efficacy of coimmunoprecipitation for each combination. (E) Domain mapping of TTBK2 identifies the C-terminal part (842–1244) as sufficient for Cep164 binding. (F) Domain mapping of Cep164 identifies the N-terminal part (1–467) as sufficient for interaction with TTBK2.

the loss of Cep164. Although the overexpression of Flag–Cep164 N term in RPE-1 cells did not detectably affect either the levels or localization of endogenous Cep164 (Fig. S3 C and D), cells expressing Flag–Cep164 N term failed to trigger either removal of CP110 (Fig. S3E) or centriole recruitment of IFT81 (Fig. S3F). This result demonstrates that centriole-associated Cep164 cannot trigger these early steps of ciliogenesis when TTBK2 is mislocalized.

Functional Consequences of TTBK2–Cep164 Complex Formation. On the basis of the results described above, we hypothesized that

one of the key functions of Cep164 consists of the recruitment of TTBK2 to the appendages of M centrioles. This recruitment, mediated by the WW domain within the N terminus of Cep164, appears then to be sufficient to trigger both CP110 removal and IFT81 recruitment in preparation for ciliogenesis. To rigorously test this hypothesis, we carried out a series of siRNA-depletion and rescue experiments. The extent of Cep164 depletion achieved in these experiments is illustrated in Fig. S4A. Expression of a siRNA-resistant version of Cep164 (Cep164 RNAi-res) in

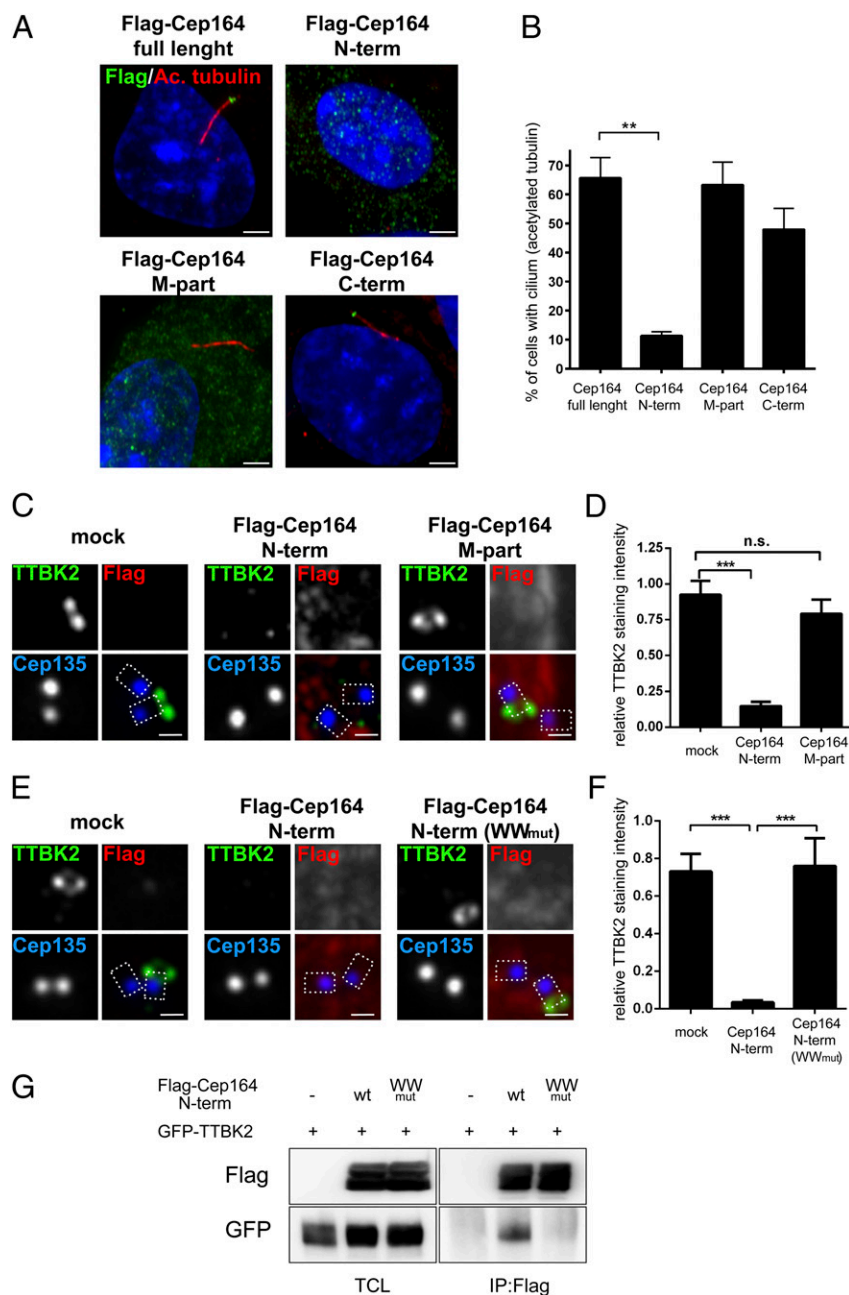


Fig. 4. Excess of Cep164 N-terminal fragment impairs cilia formation by WW domain-mediated sequestration of TTBK2. Transfections and immunofluorescence experiments were carried out as outlined in the Fig. 1 legend. Cep135 staining was used to label proximal ends of centrioles. [Scale bars: 2.5 μ m (A) and 0.5 μ m (C and E).] (A) Localizations and impact on ciliogenesis of Cep164 full-length and deletion mutants (N term, 1–467; M part, 468–1135; C term, 1136–1460). PCs were visualized by staining for acetylated tubulin; note the dominant-negative effect of Cep164 N term. (B) Quantification of the data shown in A. Graph represents the summary of three experiments. (C) Expression of Cep164 N term, but not Cep164 M part, prevents TTBK2 localization to M centrioles. (D) Quantification of the data shown in C. Graph represents the summary of two experiments. (E) Expression of the WW_{mut} mutant version of Cep164 N term (1–467) fails to impair M centriole localization of TTBK2. (F) Quantification of the data shown in E. Graph represents the summary of two experiments. (G) HEK293T cells were transfected with the indicated constructs and subjected to IP–Western experiments. Note that Cep164 N term (WW_{mut}) fails to coimmunoprecipitate TTBK2. *** P < 0.01; *** P < 0.001; n.s., not significant.

Cep164-depleted cells restored TTBK2 levels at M centrioles to ~70% of controls, and, importantly, this rescue required an intact WW domain within Cep164 (Fig. 5A and B). In parallel experiments, PC formation could be restored to Cep164-depleted cells by expression of Cep164 RNAi-res wild type (WT), but not the corresponding WW_{mut} construct (Fig. 5C and D).

To confirm the critical role of the N-terminal domain of Cep164 for TTBK2 recruitment and ciliogenesis, we examined the functionality of TTBK2–Cep164 fusion proteins. The struc-

tures of these chimeric proteins are illustrated in Fig. 5E. Remarkably, PC formation could be restored in Cep164-depleted cells by reexpression of two different fusion proteins in which TTBK2 is directly linked to C-terminal (appendage-targeting) domains of Cep164 (Fig. 5C and D and Fig. S4B). These results demonstrate that enforced M centriole targeting of TTBK2 via fusion to C-terminal fragments of Cep164 is sufficient to allow PC formation, even in the absence of full-length Cep164. To explore the possibility of a complete bypass of Cep164, we also

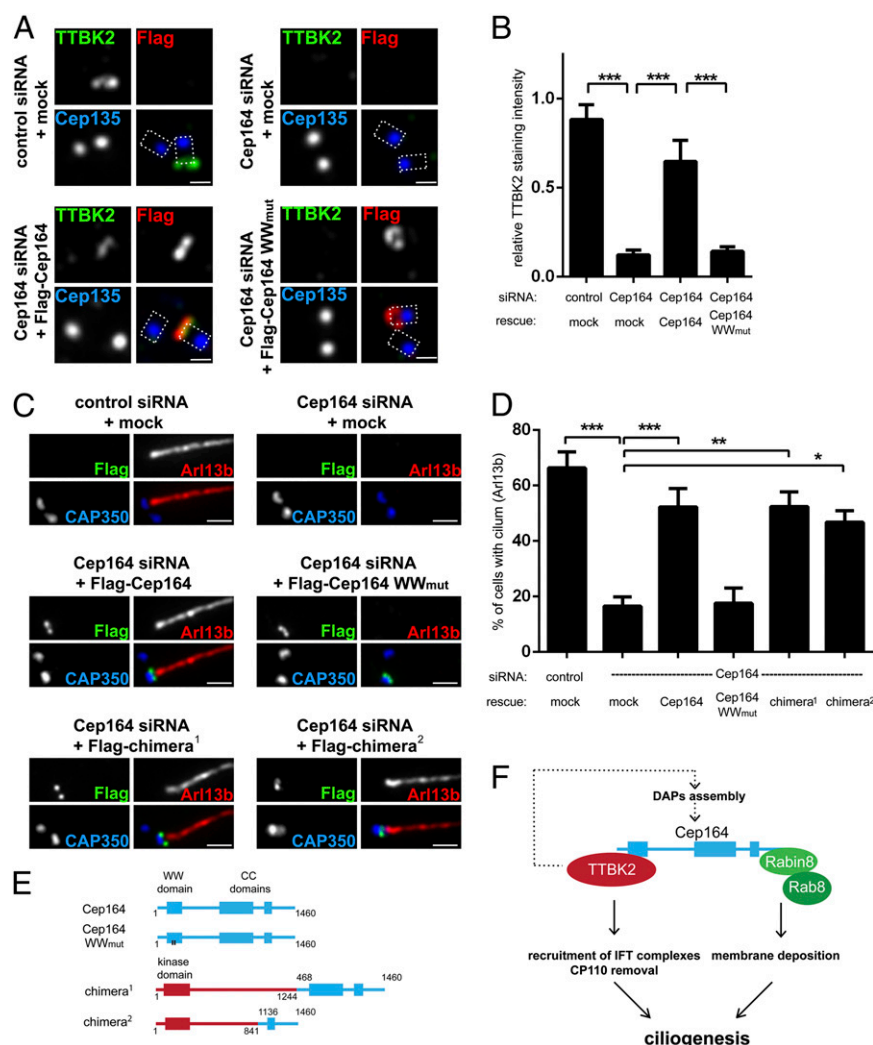


Fig. 5. Tethering of TTBK2 to M centrioles rescues ciliogenesis in the absence of full-length Cep164. (A–D) Transfections for siRNA-depletion/rescue experiments were carried out in RPE-1 cells, using the indicated siRNA oligonucleotides and rescue constructs; cells were then processed as outlined in the legend to Fig. 1. Cep135 staining visualizes proximal site of centrioles, and dashed lines in the merged images outline the centrioles. [Scale bars: 0.5 μ m (A) and 1 μ m (C).] (A) Expression of Cep164 full-length protein, but not the WW_{mut} mutant, restores TTBK2 levels at M centrioles in Cep164-depleted cells. (B) Quantification of the rescue data shown in A. Graph represents the summary of three experiments. (C) Representative images illustrating the ability of the indicated constructs to rescue ciliogenesis. Staining for CAP350 and Arl13b was used to visualize centrioles and PC formation, respectively. (D) Quantification of the rescue of the rescue data shown in C. Graph represents the summary of at least four experiments. (E) Schematic representations of chimeric constructs used for siRNA-depletion/rescue experiments. Cep164 moieties are depicted in blue, and TTBK2 moieties are in red. (F) Model summarizing the crucial functions of TTBK2 and Cep164 domains in PC formation (see also Discussion). * $P < 0.05$; ** $P < 0.01$; *** $P < 0.001$.

targeted TTBK2 to M centrioles via fusion to the DAP Cep89 (19, 31). However, although three different TTBK2–Cep89 chimeras (Fig. S4C) all conferred M centriole localization to TTBK2, none were able to restore ciliogenesis in Cep164-depleted cells (Fig. S4D). At face value, these negative results indicate that the C terminus of Cep164 is not dispensable, in line with a recent study identifying an essential role of this domain in the binding of Rab8a/Rabin and the recruitment of ciliary vesicles (18). We thus conclude that Cep164 comprises at least two functionally distinct domains: Whereas the C-terminal domain is crucial for centriole association and the recruitment of membrane vesicles (18), the N-terminal WW domain functions primarily to recruit TTBK2 to the M centriole; this kinase is then proposed to trigger at least two early steps in ciliogenesis, CP110 removal and IFT81 recruitment (Fig. 5F).

Evidence for an Additional Role of TTBK2 in the Assembly of Distal Appendages. The above model for the role of TTBK2 in ciliogenesis emphasizes kinase activities downstream of Cep164. However,

some of our results hint at additional activities upstream of Cep164. In particular, we had observed that coexpression of active TTBK2 with Cep164 resulted in the accumulation of Cep164, possibly reflecting stabilization (Fig. 3D). To follow up on this observation, we used immunofluorescence microscopy to monitor the localization of Cep164 and other DAPs in response to expression of exogenous TTBK2 in RPE-1 cells. Overexpression of TTBK2 WT, but not a kd mutant, markedly increased Cep164 levels at the M centriole (Fig. 6A and B), and similar effects were seen for the DAPs Cep83 (Fig. 6C and D) and Cep89 (Fig. S5A and B). Moreover, and most remarkably, we also observed the accumulation of GFP- or Flag-tagged TTBK2 at the distal ends of D centrioles (Fig. 6A and B). As quantified in Fig. 6E, this unexpected localization was accompanied by the concomitant recruitment of the DAPs Cep164 (Fig. 6A), Cep83 (Fig. 6C), and Cep89 (Fig. S5A). This finding strongly indicates that excess TTBK2 activity is able to trigger aspects of centriole maturation, notably the recruitment of DAPs to immature

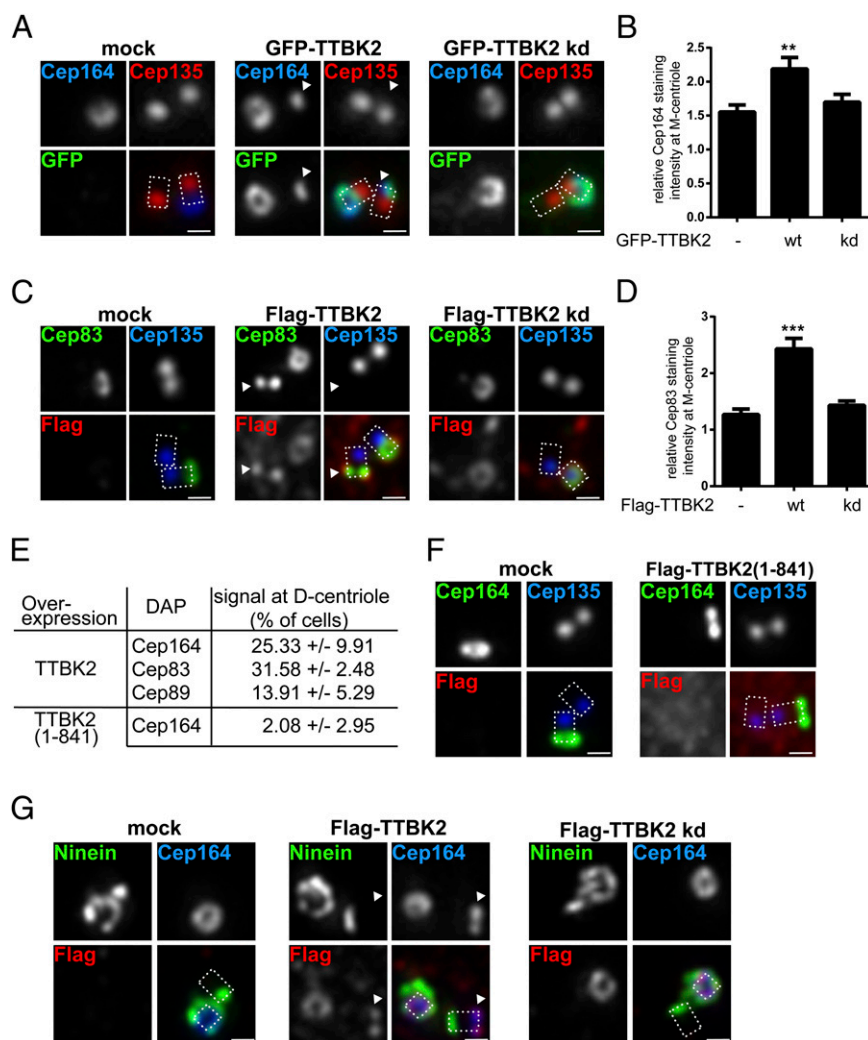


Fig. 6. TTBK2 promotes assembly of DAPs at both M and D centrioles. Transfections of RPE-1 cells and immunofluorescence experiments were carried out as outlined in the Fig. 1 legend. Cep135 staining was used to label proximal ends of centrioles, and dashed lines in merged images outline the centrioles. (Scale bars: 0.5 μ m.) Arrowheads point to distal parts of D centrioles. (A) Transient overexpression of GFP-TTBK2 promotes Cep164 localization to both M and D centrioles. (B) Quantification of the effects of TTBK2 overexpression on Cep164 levels at M centrioles. In cells where both centrioles showed Cep164 staining, the centriole showing more prominent Cep164 signal was considered as the M centriole. Graph represents the summary of two experiments. (C) Transient overexpression of Flag-TTBK2 promotes Cep83 localization to both M and D centrioles. (D) Quantification of the effects of TTBK2 overexpression on Cep83 levels at M centrioles. Graph represents the summary of two experiments. (E) Frequency of D centriole localizations of Cep164, Cep83, and Cep89 observed in transfected cells. Results were collected from at least two experiments. (F) Lack of influence of Flag-TTBK2 (1–841) overexpression on Cep164 localization. (G) Flag-TTBK2 promotes distal D centriole localization of Cep164 but not Ninein. Flag-TTBK2 kd is shown for control. ** $P < 0.01$; *** $P < 0.001$.

centrioles. Interestingly, a TTBK2 mutant (1–841) defective in Cep164 binding was impaired in its ability to induce ectopic assembly of DAPs at D centrioles, indicating that the C-terminal domain of TTBK2 is important for this function (Fig. 6E and F).

To exclude the possibility that the unexpected phenotype produced by excess TTBK2 activity might reflect generic effects on centriole structure and/or cell-cycle progression, we also examined the effects of TTBK2 overexpression on the localization of Ninein and Cep170, two proteins known to associate with both subdistal appendages (29, 44) and the proximal ends of centrioles (45, 46). Although Flag-TTBK2 promoted localization of Cep164 to the distal end of D centrioles, no recruitment to these ectopic sites was seen for either Ninein (Fig. 6G) or Cep170 (Fig. S5C). Likewise, the asymmetry in Ninein localization between M and D centrioles was maintained in cells in which Flag-TTBK2 localized to D centrioles (Fig. S5D). These experiments demonstrate that TTBK2 specifically promotes the assembly of distal

appendage components but not subdistal appendage proteins. We conclude that the range of activities of TTBK2 is not limited to events that occur downstream of Cep164. Instead, our data suggest that TTBK2 also contributes to the assembly of distal appendages, hinting at the existence of a positive feedback loop centered on the Cep164–TTBK2 complex (Fig. 5F).

Discussion

The appendage protein Cep164 plays a key role in the formation of PCs (18, 29). Here we have explored the mechanistic basis for this requirement. We demonstrate that a major role of Cep164 consists of the recruitment of a casein kinase I family member, TTBK2, to appendages of M centrioles. We show that Cep164 interacts via its N-terminal WW domain with the C-terminal domain of TTBK2 and that this interaction is required for both the recruitment of TTBK2 to appendages and for PC formation. The impairment of ciliogenesis in Cep164-depleted cells can be rescued by reexpression of Cep164 WT, but not a WW domain

mutant that is defective in TTBK2 binding. Furthermore, ciliogenesis can also be restored by reexpression of chimeric proteins in which TTBK2 is targeted to distal appendages via fusion to the C-terminal domain of Cep164. Once associated with appendages, TTBK2 is then in the appropriate place to trigger ciliogenesis by regulating both the recruitment of IFT components and the release of CP110 from M centrioles (see also ref. 35).

In a recent study, the C-terminal moiety of Cep164 was implicated in the binding of a Rab8a/Rabin complex, which in turn controls the docking of Golgi-derived vesicles to M centrioles (18). A role for Rab8a in ciliogenesis is well supported by data showing that GTP loading of Rab8a is important for both centrosome localization and vesicle trafficking (40, 47–49). By overexpression of TBC1D30, a Rab8a GAP, we could readily confirm that interference with Rab8a activity strongly suppresses PC formation. However, excess TBC1D30 did not detectably influence either the recruitment of IFT81 or the removal of CP110 from centrioles, arguing that these two key events are regulated independently of the Rab8a/Rabin interaction with Cep164.

As reported previously (18) and confirmed here, a N-terminal fragment of Cep164 exerts a dominant-negative effect on PC formation. Our finding that the N-terminal Cep164 fragment localizes to the cytoplasm and thus sequesters TTBK2 away from M centrioles provides an attractive explanation for the observed phenotype. Our siRNA-depletion/rescue experiments identified the WW domain within the N terminus of Cep164 as critical for TTBK2 recruitment and PC formation, clearly demonstrating the importance of the Cep164–TTBK2 interaction for ciliogenesis. This conclusion is strengthened further by our demonstration that PC formation could be restored to Cep164-depleted cells by chimeric proteins in which TTBK2 was fused to the C-terminal domain of Cep164. This finding strongly suggests that centriole recruitment of TTBK2 represents the key function of the N-terminal domain of Cep164, although it would be premature to exclude additional, perhaps more subtle, functions for this domain. The C-terminal moiety of Cep164, conversely, is both necessary and sufficient for correct localization to centriolar appendages. In addition, this domain has been implicated in the docking of Golgi-derived vesicles during early stages of PC formation (Fig. 5F) (18). This result provides a plausible explanation for the failure of our attempts at bypassing Cep164 through expression of TTBK2–Cep89 chimeras in Cep164-depleted cells.

Recently, information has begun to emerge on proteins that are likely to function upstream of Cep164 and TTBK2. These include Cep83/CCDC41 (19, 30) and C2CD3 (50–52). Although a strict requirement for Cep83/CCDC41 in Cep164 localization has been questioned (30), our data clearly demonstrate that Cep164 is both necessary and sufficient for M centriole association of TTBK2, in line with a model in which Cep83/CCDC41 acts upstream of Cep164 (19). C2CD3, a C2 domain protein required for ciliogenesis in mammals (50–52), has also been shown to be important for the recruitment of TTBK2 to basal bodies (52). This protein was reported to localize to centriolar satellites (52) as well as the distal ends of both M and D centrioles (51, 52). Furthermore, C2CD3 is required not only for ciliogenesis but also for centriole biogenesis (51), indicating that it functions hierarchically upstream in the assembly of appendages.

Our current understanding of TTBK2 function emphasizes events in ciliogenesis that are presumed to occur downstream of Cep164-mediated recruitment to distal appendages. However, in the course of our studies, we obtained evidence for an additional role of this kinase in the assembly of DAP complexes. In particular, we discovered that overexpression of TTBK2 led to the accumulation of Cep164 and the concomitant enrichment of Cep164 as well as other DAPs at the distal ends of M centrioles. In addition, and most surprisingly, excess TTBK2 was also able to trigger the recruitment of DAPs to the distal ends of D centrioles. Given that Cep164 is required to position TTBK2 for the

downstream functions of this kinase, as monitored by CP110 removal and IFT81 recruitment, the ability of overexpressed TTBK2 to enhance the recruitment of Cep164 and other DAPs to distal appendages may appear puzzling. If TTBK2 were strictly required for distal appendage formation, one might in fact have expected to see an impairment of Cep164 assembly in response to depletion or sequestration of TTBK2. However, this impairment was not observed in either this study (Fig. 2D and E and Fig. S3C and D) or elsewhere (19, 35). One possible explanation for this conundrum is that TTBK2 functions redundantly to other kinases, particularly members of the casein kinase 1 family, in DAP assembly. In addition, we consider it attractive to postulate the existence of a positive feedback loop centered on the TTBK2–Cep164 complex (Fig. 5F). A self-promoting recruitment mechanism may enhance the local concentration of this complex, leading to higher phosphorylation of substrates that are critical for DAP assembly. In support of this hypothesis, we emphasize that the induction of DAP recruitment by overexpressed TTBK2 required not only an intact catalytic domain but also the C-terminal domain that binds Cep164 (Fig. 6E and F). In light of a previous report on the regulation of TTBK2 activity (41), one could also argue that the C-terminal domain of TTBK2 may be required for regulation of kinase activity. Although we cannot rigorously exclude this possibility, we note that our rescue experiments with TTBK2–Cep164 chimeras demonstrate that constructs lacking the C-terminal part of TTBK2 exhibited sufficient kinase activity to restore ciliogenesis in Cep164-depleted cells (Fig. 5C and D and Fig. S4B).

Mutations in both Cep164 and TTBK2 are causally related to human disease. In particular, mutations in Cep164 have been implicated in the etiology of nephronophthisis-related ciliopathies, and a link to DNA-damage response signaling has been proposed (32). In line with this notion, the N terminus of Cep164 was proposed to interact with components of DNA damage pathways (53). Conversely, truncating mutations in human TTBK2 were identified as causative for the neurodegenerative disorder spinocerebellar ataxia type 11 (36, 54). Our domain-mapping experiments predict that the longest ataxia-associated TTBK2 truncation described, 450X (36), is unable to form a stable complex with Cep164 (Figs. 2H and 3E). Thus, the inability of ataxia-associated forms of TTBK2 to bind Cep164 provides a plausible explanation for the localization defects of these truncation mutants in murine cells (35). In consideration of the existence of the TTBK2–Cep164 complex characterized in this study, it is intriguing that mutations in the two proteins have been linked to different disease spectra, suggesting cell-type-specific functions and/or redundancies. Also, it might be rewarding to explore whether TTBK2 plays a role in nephronophthisis-related ciliopathies, and, conversely, whether Cep164 mutations can be found in ataxia patients.

TTBK2 was originally named for its ability to phosphorylate tau protein on two serine residues and thus regulate tau oligomerization (55). Tau is unlikely to be the only target, but little is presently known about the physiological substrates of TTBK2. It is interesting, therefore, that TTBK2 readily phosphorylates Cep164 in vitro and, most likely, in vivo. Given the colocalization of the two proteins and their intimately linked roles in ciliogenesis, Cep164 appears to be an attractive candidate substrate of TTBK2. Our preliminary analyses of Cep164 phosphorylation by TTBK2 point to a multitude of phosphorylation sites distributed throughout the protein, suggesting complex regulation. This finding notwithstanding, it will be interesting to explore the functional consequences of Cep164 phosphorylation in future studies. Furthermore, considering that TTBK2 controls the recruitment of IFT components as well as the dissociation of CP110 from M centrioles (ref. 35 and this study), these proteins, as well as their potential binding partners (20, 56, 57), represent attractive candidates for TTBK2 substrates. Understanding the functional consequences of substrate phosphorylation by TTBK2

as well as the interaction of TTBK2 with other kinases implicated in ciliogenesis (33, 34, 37) will undoubtedly be critical for a mechanistic understanding of ciliogenesis.

Materials and Methods

Cell Culture and Transfections. RPE-1 and HEK293T cells were propagated as described (21) and transfected with Lipofectamine LTX (Invitrogen) and TransIT-LT1 (Mirus), respectively. siRNA experiments were performed by using Oligofectamine (Invitrogen) and described control (GL2) and Cep164-specific oligonucleotides at concentrations of 50 nM (29). To knock down TTBK2, Silencer siRNA (Life Technologies; s44813 and s44814) was used at a concentration of 5 nM. Efficient knockdown was routinely verified by immunofluorescence staining and/or Western blotting. Following transfections of RPE-1 cells, ciliogenesis was promoted either by serum starvation for 24 h or, in the case of the experiments described in Fig. 4 A and B and Fig. S3A, the use of 0.5 μ M Cytochalasin D (Sigma).

Cloning. Insert-containing entry vectors for use in the GATEWAY system (Invitrogen) were generated by PCR, using Pfu Ultra II Fusion DNA polymerase (Agilent). Constructs were verified by sequencing and subsequently cloned into pDEST-Myc (58), pDEST-Flag (58), pDEST-GST (Invitrogen), or pg-LAP1 (Addgene plasmid 19702) GATEWAY destination vectors. The human cDNAs used here have been described: Cep164 (29), TTBK2 (35), TBC1D30 (40), and Cep89 (31). Inserts for TTBK2–Cep164/Cep89 fusions, containing a 3xGly linker, were constructed by overlapping PCR. Mutants were prepared by site-directed mutagenesis (Agilent). All primers are listed in Table S1.

Cell Lysis and Immunoprecipitation. At 24 h posttransfection, cells were washed in PBS and lysed in Lysis buffer [20 mM Tris-Cl, pH 7.4, 150 mM NaCl, 25 mM β -glycerol phosphate, 0.5% Triton-X-100, 0.5% Igepal CA630 (all from Sigma), and 1 \times Complete proteasome inhibitors (Roche)]. Following centrifugation (15,000 \times g for 10 min at +4 $^{\circ}$ C), cleared extracts were incubated (6 h at +4 $^{\circ}$ C in an orbital shaker) with anti-Myc (clone 9E10) or anti-Flag (clone M2) G protein Sepharose (GE Healthcare)-coupled antibodies. Immune complexes were pelleted, washed, and subsequently analyzed by SDS/PAGE and Western blotting. Where indicated, samples were treated with λ -phosphatase (New England BioLabs) (30 $^{\circ}$ C for 20–90 min). Luminescence was detected by using a SuperSignal Femto Maximum Sensitivity Substrate (Thermo Scientific) in the LAS3000 system (GE Healthcare). Where appropriate, contrast and/or brightness of images were adjusted by using Photoshop CS5 (Adobe). The following antibodies were used: rabbit anti-Cep164 (29), mouse anti-FLAG (clone M2; Sigma), mouse anti-Myc (clone 9E10), goat anti-GST (45-001-369; GE Healthcare), rabbit anti-GFP (ab290; Roche), rabbit anti-TTBK2 (HPA018113; Sigma), horseradish peroxidase (HRP)-conjugated goat anti-mouse and anti-rabbit secondary antibodies (BioRad), and HRP-conjugated donkey anti-goat secondary antibody (Santa Cruz Biotechnology).

Recombinant Protein Purification. BL21-RIL bacteria, transformed with appropriate plasmids, were grown overnight (37 $^{\circ}$ C) in LB medium (100 μ g/mL Ampicillin) and expanded the following day for another 3–5 h. Expression of recombinant proteins was induced by 0.2 mM IPTG (20 $^{\circ}$ C, 12 h). After centrifugation, bacteria were resuspended in 3 mL of Lysis buffer (20 mM Tris-Cl, pH 7.4, 150 mM NaCl, 1% Triton-X-100, 1 mM DTT, 1 \times Complete proteasome inhibitors) and repeatedly sonicated (2 \times , 20 s) and freeze-thawed. Following clearing of the extract (15,000 \times g for 10 min at +4 $^{\circ}$ C), GST-tagged recombinant proteins were purified (2 h at +4 $^{\circ}$ C in an orbital shaker) by using Glutathione Sepharose 4B (GE Healthcare), washed (20 mM Tris-Cl, pH 7.4, 300 mM NaCl, 1% Triton X-100, 1 mM DTT, 1 \times Complete proteasome inhibitors), eluted [50 mM Tris-Cl, pH 8, 50 mM NaCl, 10 mM Glutathione, 1 mM DTT, 5% (vol/vol) glycerol], and stored at -80° C. Chemicals were purchased from Sigma.

In Vitro Translation and Kinase Assay. Flag–Cep164 was obtained by using the in vitro translation TNT Quick system (Promega), mixed with Lysis buffer (see above; cell lysis), and subjected to anti-Flag immunoprecipitation (3 h at +4 $^{\circ}$ C

in an orbital shaker) and washing. In vitro kinase assays were performed in 50 mM Tris, pH 7.4, 10 mM MgCl₂, and 0.1 mM EGTA in the presence of 10 μ M ATP, 2 μ Ci of [γ -³²P]ATP and recombinant kinase (30 $^{\circ}$ C for 30 min). To terminate reactions, samples were mixed with 2 \times sample buffer, boiled for 5 min, and subjected to SDS/PAGE and PVDF membrane transfer. ³²P incorporation was detected by using Kodak BioMAX films (Sigma).

Immunofluorescence Microscopy. Methanol fixation, blocking, incubation with primary and secondary antibodies, and washing were performed as described (45). The antibodies used were as follows: mouse antiacetylated tubulin (6-11B-1; Sigma), mouse anti-glutamylated tubulin (GT335), rabbit anti-Arl13b (17711; Proteintech), mouse anti-Flag (M2; Sigma), rabbit anti-Cep83 (HPA038161; Sigma), rabbit Cep89 (31), rabbit anti-TTBK2 (HPA018113; Sigma; Alexa 488 or 647-labeled), goat anti-CAP350 (59) (Alexa 647-labeled), rabbit anti-Cep135 (60) (Alexa 555- or 647-labeled), rabbit anti-CP110 (60) (Alexa 488-labeled), rabbit anti-Cep164 (29) (Alexa 488- or 647-labeled), rat anti-IFT81 (38), Alexa 488 anti-rabbit, Alexa 488 anti-rat, Alexa 555 anti-mouse, and Alexa 555 anti-rabbit (all from Invitrogen). Direct labeling of primary antibodies was performed by using an Alexa-antibody labeling kit (Invitrogen). Imaging was performed on a DeltaVision system (Applied Precision) with a 60 \times /1.2 or 100 \times /1.4 Apo plan oil immersion objective. Image stacks were taken with a z distance of 0.2 μ m, deconvolved (conservative ratio, three to five cycles), and projected as maximal intensity images by using SoftWoRx (Applied Precision). Where appropriate, contrast and/or brightness were adjusted by using Photoshop CS5 (Adobe). For cell counts, 100 (siRNA experiments), 25–50 (transgene expression experiments), or 15–25 (siRNA rescue experiments) cells per condition and experiment were analyzed. Where indicated, a densitometry analysis within selected regions of interest was performed in 16-bit TIFF images by using ImageJ, analyzing 15–20 cells per experiment and condition. Data are presented as relative staining intensity (staining intensity of a protein of interest normalized to the staining intensity of the centriolar marker Cep135).

Rescue Experiments. At 4–5 h after transfection of RPE-1 cells, medium was changed to prevent cell death. At 26–30 h later, cells were transfected with appropriate siRNA oligonucleotides. At 72 h after the initial plasmid transfection, medium was changed (1% FBS) to promote the formation of PC for 24 h. Control experiments were carried out in parallel to verify efficient knockdown of Cep164 protein levels by Western blotting.

Phosphorylation Site Mapping by MS. Myc–Cep164 C-term protein complexes were immunoprecipitated from HEK293T cell extracts 24 h after transfection. Proteins were reduced, alkylated, digested with trypsin overnight, and then purified with C18 Microspin columns (Harvard Apparatus) according to manufacturer's instructions. Eluted peptides were separated by using an Easy-Nano-LC system, and liquid chromatography–tandem MS analysis was performed on a hybrid LTQ-Orbitrap mass spectrometer (both from Thermo Scientific). Obtained spectra were searched by Mascot against the human proteome database (UniProt). Carbamidomethylation was set as fixed modification. Oxidation and phosphorylation (Ser/Thr/Tyr) were considered as variable modification. Results were visualized and analyzed by using the Scaffold package (Proteome Software).

Statistical Analyses. Statistical analyses (Student t test and one-way ANOVA with multiple comparison tests) were performed by using Prism (Version 6; GraphPad Software). $P < 0.05$, $P < 0.01$, and $P < 0.001$ were considered as statistically significant differences. Results are presented as mean plus SEM.

ACKNOWLEDGMENTS. We thank Peter Jackson, Francis Barr, James Sillibourne, Kathryn Anderson, and Sarah Goetz for reagents; Elena Nigg, the staff of the Biozentrum Imaging facility (notably Alexia Ferrand) and the Proteomics core facility (Timo Glatzer) for assistance; and all members of the E.A.N. laboratory for helpful discussions. This work was supported by Swiss National Science Foundation Grants 31003A_132428 and 310030B_149641 and the University of Basel. L.C. was supported by a long-term fellowship from the Federation of European Biochemical Societies.

1. Singla V, Reiter JF (2006) The primary cilium as the cell's antenna: Signaling at a sensory organelle. *Science* 313(5787):629–633.
2. Goetz SC, Anderson KV (2010) The primary cilium: A signalling centre during vertebrate development. *Nat Rev Genet* 11(5):331–344.
3. Gerdts JM, Davis EE, Katsanis N (2009) The vertebrate primary cilium in development, homeostasis, and disease. *Cell* 137(1):32–45.
4. Satir P, Pedersen LB, Christensen ST (2010) The primary cilium at a glance. *J Cell Sci* 123(Pt 4):499–503.

5. Ishikawa H, Marshall WF (2011) Ciliogenesis: Building the cell's antenna. *Nat Rev Mol Cell Biol* 12(4):222–234.
6. Nigg EA, Raff JW (2009) Centrioles, centrosomes, and cilia in health and disease. *Cell* 139(4):663–678.
7. Seeley ES, Nachury MV (2010) The perennal organelle: Assembly and disassembly of the primary cilium. *J Cell Sci* 123(Pt 4):511–518.
8. Kobayashi T, Dynlacht BD (2011) Regulating the transition from centriole to basal body. *J Cell Biol* 193(3):435–444.

9. Nigg EA, Stearns T (2011) The centrosome cycle: Centriole biogenesis, duplication and inherent asymmetries. *Nat Cell Biol* 13(10):1154–1160.
10. Michaud EJ, Yoder BK (2006) The primary cilium in cell signaling and cancer. *Cancer Res* 66(13):6463–6467.
11. Bettencourt-Dias M, Hildebrandt F, Pellman D, Woods G, Godinho SA (2011) Centrosomes and cilia in human disease. *Trends Genet* 27(8):307–315.
12. Sharma N, Berbari NF, Yoder BK (2008) Ciliary dysfunction in developmental abnormalities and diseases. *Curr Top Dev Biol* 85:371–427.
13. Hildebrandt F, Benzing T, Katsanis N (2011) Ciliopathies. *N Engl J Med* 364(16):1533–1543.
14. Sorokin S (1962) Centrioles and the formation of rudimentary cilia by fibroblasts and smooth muscle cells. *J Cell Biol* 15:363–377.
15. Sorokin SP (1968) Reconstructions of centriole formation and ciliogenesis in mammalian lungs. *J Cell Sci* 3(2):207–230.
16. Anderson CT, Stearns T (2009) Centriole age underlies asynchronous primary cilium growth in mammalian cells. *Curr Biol* 19(17):1498–1502.
17. Kim J, et al. (2010) Functional genomic screen for modulators of ciliogenesis and cilium length. *Nature* 464(7291):1048–1051.
18. Schmidt KN, et al. (2012) Cep164 mediates vesicular docking to the mother centriole during early steps of ciliogenesis. *J Cell Biol* 199(7):1083–1101.
19. Tanos BE, et al. (2013) Centriole distal appendages promote membrane docking, leading to cilia initiation. *Genes Dev* 27(2):163–168.
20. Spektor A, Tsang WY, Khoo D, Dynlacht BD (2007) Cep97 and CP110 suppress a cilia assembly program. *Cell* 130(4):678–690.
21. Schmidt TL, et al. (2009) Control of centriole length by CPAP and CP110. *Curr Biol* 19(12):1005–1011.
22. Pazour GJ, et al. (2000) Chlamydomonas IFT88 and its mouse homologue, polycystic kidney disease gene tgc737, are required for assembly of cilia and flagella. *J Cell Biol* 151(3):709–718.
23. Qin H, Diener DR, Geimer S, Cole DG, Rosenbaum JL (2004) Intraflagellar transport (IFT) cargo: IFT transports flagellar precursors to the tip and turnover products to the cell body. *J Cell Biol* 164(2):255–266.
24. Rosenbaum JL, Witman GB (2002) Intraflagellar transport. *Nat Rev Mol Cell Biol* 3(11):813–825.
25. Garcia-Gonzalo FR, et al. (2011) A transition zone complex regulates mammalian ciliogenesis and ciliary membrane composition. *Nat Genet* 43(8):776–784.
26. Williams CL, et al. (2011) MKS and NPHP modules cooperate to establish basal body/transition zone membrane associations and ciliary gate function during ciliogenesis. *J Cell Biol* 192(6):1023–1041.
27. Pedersen LB, Rosenbaum JL (2008) Intraflagellar transport (IFT) role in ciliary assembly, resorption and signalling. *Curr Top Dev Biol* 85:23–61.
28. Reiter JF, Blacque OE, Leroux MR (2012) The base of the cilium: Roles for transition fibres and the transition zone in ciliary formation, maintenance and compartmentalization. *EMBO Rep* 13(7):608–618.
29. Graser S, et al. (2007) Cep164, a novel centriole appendage protein required for primary cilium formation. *J Cell Biol* 179(2):321–330.
30. Joo K, et al. (2013) CCDC41 is required for ciliary vesicle docking to the mother centriole. *Proc Natl Acad Sci USA* 110(15):5987–5992.
31. Sillibourne JE, et al. (2013) Primary ciliogenesis requires the distal appendage component Cep123. *Biol Open* 2(6):535–545.
32. Chaki M, et al. (2012) Exome capture reveals ZNF423 and CEP164 mutations, linking renal ciliopathies to DNA damage response signaling. *Cell* 150(3):533–548.
33. Upadhyay P, Birkenmeier EH, Birkenmeier CS, Barker JE (2000) Mutations in a NIMA-related kinase gene, Nek1, cause pleiotropic effects including a progressive polycystic kidney disease in mice. *Proc Natl Acad Sci USA* 97(1):217–221.
34. Liu S, et al. (2002) A defect in a novel Nek-family kinase causes cystic kidney disease in the mouse and in zebrafish. *Development* 129(24):5839–5846.
35. Goetz SC, Liem KF, Jr, Anderson KV (2012) The spinocerebellar ataxia-associated gene Tau tubulin kinase 2 controls the initiation of ciliogenesis. *Cell* 151(4):847–858.
36. Houlden H, et al. (2007) Mutations in TTBK2, encoding a kinase implicated in tau phosphorylation, segregate with spinocerebellar ataxia type 11. *Nat Genet* 39(12):1434–1436.
37. Kuhns S, et al. (2013) The microtubule affinity regulating kinase MARK4 promotes axoneme extension during early ciliogenesis. *J Cell Biol* 200(4):505–522.
38. Bhogaraju S, et al. (2013) Molecular basis of tubulin transport within the cilium by IFT74 and IFT81. *Science* 341(6149):1009–1012.
39. Taschner M, Bhogaraju S, Lorentzen E (2012) Architecture and function of IFT complex proteins in ciliogenesis. *Differentiation* 83(2):S12–S22.
40. Yoshimura S, Egerer J, Fuchs E, Haas AK, Barr FA (2007) Functional dissection of Rab GTPases involved in primary cilium formation. *J Cell Biol* 178(3):363–369.
41. Bouskila M, et al. (2011) TTBK2 kinase substrate specificity and the impact of spinocerebellar-ataxia-causing mutations on expression, activity, localization and development. *Biochem J* 437(1):157–167.
42. Macias MJ, Wiesner S, Sudol M (2002) WW and SH3 domains, two different scaffolds to recognize proline-rich ligands. *FEBS Lett* 513(1):30–37.
43. Ingham RJ, et al. (2005) WW domains provide a platform for the assembly of multi-protein networks. *Mol Cell Biol* 25(16):7092–7106.
44. Guarguaglini G, et al. (2005) The forkhead-associated domain protein Cep170 interacts with Polo-like kinase 1 and serves as a marker for mature centrioles. *Mol Biol Cell* 16(3):1095–1107.
45. Sonnen KF, Schermelleh L, Leonhardt H, Nigg EA (2012) 3D-structured illumination microscopy provides novel insight into architecture of human centrosomes. *Biol Open* 1(10):965–976.
46. Krauss SW, et al. (2008) Downregulation of protein 4.1R, a mature centriole protein, disrupts centrosomes, alters cell cycle progression, and perturbs mitotic spindles and anaphase. *Mol Cell Biol* 28(7):2283–2294.
47. Nachury MV, et al. (2007) A core complex of BBS proteins cooperates with the GTPase Rab8 to promote ciliary membrane biogenesis. *Cell* 129(6):1201–1213.
48. Hehnly H, Chen CT, Powers CM, Liu HL, Doherty S (2012) The centrosome regulates the Rab11-dependent recycling endosome pathway at appendages of the mother centriole. *Curr Biol* 22(20):1944–1950.
49. Westlake CJ, et al. (2011) Primary cilium membrane assembly is initiated by Rab11 and transport protein particle II (TRAPP II) complex-dependent trafficking of Rabin8 to the centrosome. *Proc Natl Acad Sci USA* 108(7):2759–2764.
50. Hoover AN, et al. (2008) C2cd3 is required for cilia formation and Hedgehog signaling in mouse. *Development* 135(24):4049–4058.
51. Balestra FR, Strnad P, Flückiger I, Gönczy P (2013) Discovering regulators of centriole biogenesis through siRNA-based functional genomics in human cells. *Dev Cell* 25(6):555–571.
52. Ye X, Zeng H, Ning G, Reiter JF, Liu A (2014) C2cd3 is critical for centriolar distal appendage assembly and ciliary vesicle docking in mammals. *Proc Natl Acad Sci USA* 111(6):2164–2169.
53. Sivasubramanian S, Sun X, Pan YR, Wang S, Lee EY (2008) Cep164 is a mediator protein required for the maintenance of genomic stability through modulation of MDC1, RPA, and CHK1. *Genes Dev* 22(5):587–600.
54. Bauer P, et al. (2010) Spinocerebellar ataxia type 11 (SCA11) is an uncommon cause of dominant ataxia among French and German kindreds. *J Neurol Neurosurg Psychiatry* 81(11):1229–1232.
55. Tomizawa K, Omori A, Ohtake A, Sato K, Takahashi M (2001) Tau-tubulin kinase phosphorylates tau at Ser-208 and Ser-210, sites found in paired helical filament-tau. *FEBS Lett* 492(3):221–227.
56. Tsang WY, Dynlacht BD (2013) CP110 and its network of partners coordinately regulate cilia assembly. *Cilia* 2(1):9.
57. Kobayashi T, Tsang WY, Li J, Lane W, Dynlacht BD (2011) Centriolar kinesin Kif24 interacts with CP110 to remodel microtubules and regulate ciliogenesis. *Cell* 145(6):914–925.
58. Arquint C, Sonnen KF, Stierhof YD, Nigg EA (2012) Cell-cycle-regulated expression of STIL controls centriole number in human cells. *J Cell Sci* 125(Pt 5):1342–1352.
59. Yan X, Habedanck R, Nigg EA (2006) A complex of two centrosomal proteins, CAP350 and FOP, cooperates with EB1 in microtubule anchoring. *Mol Biol Cell* 17(2):634–644.
60. Kleylein-Sohn J, et al. (2007) Plk4-induced centriole biogenesis in human cells. *Dev Cell* 13(2):190–202.

Appendix 15

Bhogaraju S, **Cajanek L**, Fort C, Blisnick T, Weber K, Taschner M, Mizuno N, Lamla S, Bastin P, Nigg EA, Lorentzen E. Molecular basis of tubulin transport within the cilium by IFT74 and IFT81. *Science*. 2013 Aug 30;341(6149):1009-12. doi: 10.1126/science.1240985. JCR 2013. IF= 31.477, Q1 - Multidisciplinary Sciences)

Published in final edited form as:

Science. 2013 August 30; 341(6149): 1009–1012. doi:10.1126/science.1240985.

Molecular Basis of Tubulin Transport Within the Cilium by IFT74 and IFT81

Sagar Bhogaraju¹, Lukas Cajanek², Cécile Fort³, Thierry Blisnick³, Kristina Weber¹, Michael Taschner¹, Naoko Mizuno¹, Stefan Lamla^{4,*}, Philippe Bastin³, Erich A. Nigg², and Esben Lorentzen^{1,†}

¹Department of Structural Cell Biology, Max Planck Institute of Biochemistry, Am Klopferspitz 18, D-82152 Martinsried, Germany. ²Biozentrum, University of Basel, Klingelbergstrasse 50/70, CH-4056 Basel, Switzerland. ³Trypanosome Cell Biology Unit, Institut Pasteur and CNRS URA2581, 25 Rue du Docteur Roux, 75015 Paris, France. ⁴Department of Cell Biology, Max Planck Institute of Biochemistry, Am Klopferspitz 18, D-82152 Martinsried, Germany.

Abstract

Intraflagellar transport (IFT) of ciliary precursors such as tubulin from the cytoplasm to the ciliary tip is involved in the construction of the cilium, a hairlike organelle found on most eukaryotic cells. However, the molecular mechanisms of IFT are poorly understood. Here, we found that the two core IFT proteins IFT74 and IFT81 form a tubulin-binding module and mapped the interaction to a calponin homology domain of IFT81 and a highly basic domain in IFT74. Knockdown of IFT81 and rescue experiments with point mutants showed that tubulin binding by IFT81 was required for ciliogenesis in human cells.

Cilia are microtubule-based organelles that function in motility, sensory reception, and signaling (1). Ciliary dysfunction results in numerous diseases and disorders commonly known as ciliopathies. Intraflagellar transport (IFT) is involved in cilium formation (2, 3) but also functions in other cellular processes, such as the recycling of Tcell receptors at the immune synapse (4). IFT relies on kinesin-2 and IFT-dynein molecular motors moving along the microtubule-based axoneme of cilia (5–7) and on the IFT complex, which contains at least 20 different protein subunits. Although ~600 proteins are known to reside in the cilium (8), we know very little about how they are recognized as ciliary cargo by the IFT machinery (9–11).

To identify potential cargo-binding sites on the IFT complex, we carried out bioinformatical and biochemical screening and identified conserved domains that were not required for IFT complex formation. We reasoned that such domains could protrude from the IFT particle-core structure and would thus be in a prime position for cargo recognition. The two IFT core

Copyright 2013 by the American Association for the Advancement of Science; all rights reserved.

[†]Corresponding author. lorentze@biochem.mpg.de.

^{*}Present address: Anni-Albers-Straße 11, D-80807 München, Germany.

Supplementary Materials www.sciencemag.org/cgi/content/full/341/6149/1009/DC1 Materials and Methods, Supplementary Text, Figs. S1 to S8, Table S1, References (24–47)

proteins IFT74 and IFT81 were found to possess N-terminal domains (IFT74N and IFT81N) that were not required for IFT complex formation or stability (fig. S1). Whereas IFT81N is highly conserved in sequence and predicted to be a folded domain, IFT74N was likely to be disordered and was highly basic with an isoelectric point (pI) > 12 (fig. S2). To characterize the properties of IFT74N and IFT81N, we purified recombinant *Homo sapiens* (Hs) IFT81N, *Chlamydomonas reinhardtii* (Cr) IFT81N, and a truncated HsIFT74/81 heterodimeric complex (fig. S3) (IFT74N alone degraded rapidly and could not be purified) and determined the crystal structure of CrIFT81N (Fig. 1, A to C; fig. S4, A to D; and table S1). The crystal structure revealed that IFT81N adopts the fold of a calponin homology (CH) domain with unexpected structural similarity to the kinetochore complex component NDC80 with microtubule (MT)–binding properties (12). Given that the cilium consists of a MT-based axoneme, IFT of large quantities of tubulin is required for cilium formation (13). We thus tested the tubulin-binding properties of HsIFT81N using affinity pull-downs (Fig. 1D and fig. S4E) and microscale thermophoresis (MST) with unpolymerized bovine $\alpha\beta$ -tubulin (Fig. 1, E and F). HsIFT81N bound tubulin with a dissociation constant (K_d) of 16 μ M via a highly conserved, positively charged surface patch, which was enhanced 18-fold by IFT74N (Fig. 1G and fig. S3). Because this result was unexpected, we also carried out MT sedimentation assays and electron microscopy (EM) to visualize IFT81 or IFT74/81 bound to MT (fig. S5). The IFT74/81 complex, but not IFT81N, at low μ M concentration cosedimented with MT during ultracentrifugation (fig. S5, D and E) and decorated MT (fig. S5F). Thus, the tubulin-binding module is formed by the IFT74/81 complex rather than by IFT81N alone.

To dissect the binding mode in the IFT74/81: $\alpha\beta$ -tubulin complex, samples were prepared from MT and unpolymerized $\alpha\beta$ -tubulin lacking the highly acidic C-terminal tails, often referred to as E-hooks (12) (fig. S5A). $\alpha\beta$ -tubulin lacking E-hooks had similar affinity for IFT81N as intact tubulin (fig. S5, B and C), which suggested that IFT81N recognizes the globular domain of $\alpha\beta$ -tubulin with no substantial interaction with the E-hooks. IFT74/81 displayed robust MT binding in sedimentation assays, which was, however, reduced to background levels in the absence of the β -tubulin E-hook (fig. S5E). Thus, IFT81N appears to bind the globular domain of tubulin to provide specificity, and IFT74N recognizes the β -tubulin tail to increase affinity (Fig. 1H).

To examine the role of tubulin binding by IFT74/81 in a cellular system, we transiently expressed Flag-HsIFT81 or Flag-HsIFT81 N in human RPE-1 cells and induced formation of primary cilia either by treatment with 0.5 μ M cytochalasin D (Fig. 2) (14) or serum starvation (fig. S6, A and D). In these experiments, centrioles were visualized by staining for CAP350 and cilia by staining for the small guanosine triphosphatase Arl13b or acetylated tubulin. We detected both Flag-HsIFT81 and Flag-HsIFT81 N at the tip of the primary cilium and, to a minor extent, also along the axoneme (fig. S6A), suggesting that IFT81N is not required for the transport of IFT81 within the primary cilium. Remarkably, however, the expression of Flag-HsIFT81 N had a strong negative impact on the extent of ciliogenesis (fig. S6, B to D), suggesting that excess IFT81 N caused a dominant-negative effect, presumably through formation of IFT complexes unable to bind tubulin.

To further investigate the function of the tubulin-binding domain of IFT81 in ciliogenesis, we carried out small interfering RNA (siRNA)–rescue experiments. siRNA-mediated depletion of IFT81 (fig. S6E) strongly reduced the percentage of ciliated cells (Fig. 2), which could be rescued by coexpression of an siRNA-resistant full-length IFT81, as expected. In contrast, none of the IFT81 mutants deficient in tubulin binding in vitro (HsIFT81mut¹ and HsIFT81mut²) compensated fully for the depletion of endogenous IFT81. Whereas expression of the deletion mutant (HsIFT81^N) or the mutant with reduced tubulin-binding ability (HsIFT81mut¹) resulted in partial rescue, expression of HsIFT81mut², in which the entire tubulin-binding patch was mutated, completely failed to rescue the siRNA-mediated knockdown of IFT81 (Fig. 2B). Thus, the entire negative effect on cilium formation by IFT81 depletion was recapitulated with a specific tubulin-binding–deficient mutant.

The fact that IFT81^N formed stable IFT core complexes (fig. S1) suggested that the ciliogenesis phenotype was because of reduced tubulin binding and not a general failure of IFT. To rule out whether mutation of the IFT81N CH domain resulted in general IFT deficiency, we turned to the unicellular protozoan parasite *Trypanosoma brucei*, where IFT has been well studied (15), and tested the effect of IFT81N CH-domain disruption on IFT. Yellow fluorescent protein (YFP)–tagged but otherwise normal IFT81 or mutant IFT81 (IFT81_{I46D,L47D}, Dm) where the CH domain was unfolded (fig. S7A) were expressed at wild-type levels. One of the two *IFT81* alleles was replaced with either YFP::IFT81 or YFP::IFT81Dm, leaving one WT *IFT81* allele unaltered (fig. S7B). Both the localization and the IFT speed of IFT81 and IFT81Dm were similar to that observed for other IFT proteins as judged by live-cell imaging and kymographic analysis (Fig. 3 and movies S1 and 2) (15). Thus, IFT81N is not required for IFT complex assembly or normal IFT in vivo, which corroborates that the ciliogenesis phenotype observed upon IFT81N CH-domain mutation (Fig. 2) was indeed because of tubulin-binding deficiency.

Axonemal precursors such as tubulin are added to the tip of the cilium in a length-dependent manner (16, 17). The removal of tubulin from the axonemal tip, on the other hand, appears to be constant, with no dependence on cilium length (17, 18). These observations inspired the balance-point model, in which the length of a mature cilium is the result of equal delivery and removal rates for axonemal precursors (17, 19). Furthermore, the concentration of tubulin in the cytoplasm influences ciliogenesis and cilium length in mammalian cells (20). Based on the measured affinity between IFT74/81 and tubulin ($K_d = 0.9 \mu\text{M}$) (Fig. 1G), we calculated the fraction of IFT complexes bound to $\alpha\beta$ -tubulin as a function of tubulin concentration (Fig. 4A). Because the cellular tubulin concentration is estimated to be in the low μM range (21) and tubulin expression is induced at the onset of ciliogenesis (22), the IFT74/81:tubulin affinity is optimal for regulating cilium length via tubulin transport (Fig. 4B). The prediction is thus that most IFT complexes are loaded with tubulin during early stages of ciliogenesis, whereas lower occupancies are found during steady-state cilium length (Fig. 4), which agrees well with previously obtained data demonstrating that tubulin transport in full-length cilia yields only faint traces on kymographs, likely due to low tubulin occupancy on IFT complexes (13). During cilium growth, both anterograde IFT complex

concentration and tubulin binding are negatively correlated with cilia length, resulting in a decreasing assembly rate as the cilium approaches steady-state length.

Here, we have shown that the two core IFT proteins IFT74 and IFT81 form a tubulin-binding module required for ciliogenesis, which suggests a role of IFT74/81 in the transport of tubulin within cilia. The fact that the high-affinity binding of tubulin occurs only for the IFT74/81 complex and not for IFT81 alone could help ensure that tubulin cargo only binds in the context of properly assembled IFT complexes. Because tubulin constitutes the backbone of all cilia, it makes sense that the tubulin has a dedicated cargo-binding site on the IFT core complex (23). We hypothesize that, although abundant ciliary cargo proteins such as tubulin may undergo IFT via dedicated transport modules, less abundant ciliary proteins are likely to compete for generic cargo-binding sites on the IFT complex.

Supplementary Material

Refer to Web version on PubMed Central for supplementary material.

Acknowledgments

We thank the staff at SLS for help with x-ray diffraction data collection; the crystallization facility of the Max Planck Institute of Biochemistry (Munich) for access to crystallization screening; the staff at Biozentrum Imaging Core Facility for assistance; C. Basquin for static light-scattering experiments; C. Jung for help with microscale thermophoresis; and S. Chakrabarti, A. Cook, and B. D. Engel for carefully reading and correcting the manuscript. B. D. Engel is additionally acknowledged for assistance with Fig. 4 and for many valuable discussions concerning ciliary length control. We thank the Plateforme d'Imagerie Dynamique for providing access to their equipment and Jean-Yves Tinevez for technical advice. We acknowledge M. Morawetz and M. Stiegler for technical assistance with molecular biology. This work was funded by an Emmy Noether grant (DGF; LO1627/1-1), the European Research Council (ERC grant 310343), and the European Molecular Biology Organization Young Investigator program. Work at the Institut Pasteur was funded by Agence Nationale de la Recherche grant ANR-11-BSV8-016. C.F. is funded by a fellowship from the Ministère de l'Enseignement et de la Recherche (ED387). E.A.N. acknowledges support from the University of Basel and the Swiss National Science Foundation (31003A_132428/1). M.T. is the recipient of an Erwin Schroedinger stipend granted by the Austrian Science Fund J3148-B12. S.B. was supported by the International Max Planck Research School for Molecular and Cellular Life Sciences (IMPRS), and L.C. was supported by the FEBS long-term fellowship. The authors declare that they have no conflict of interest. The data presented in this paper are tabulated in the main paper and the supplementary materials. Structural coordinates have been deposited at the Protein DataBank, accession nos. 4LVP and 4LVR.

References and Notes

1. Ishikawa H, Marshall WF. *Nat. Rev. Mol. Cell Biol.* 2011; 12:222–234. [PubMed: 21427764]
2. Kozminski KG, Johnson KA, Forscher P, Rosenbaum JL. *Proc. Natl. Acad. Sci. U.S.A.* 1993; 90:5519–5523. [PubMed: 8516294]
3. Rosenbaum JL, Witman GB. *Nat. Rev. Mol. Cell Biol.* 2002; 3:813–825. [PubMed: 12415299]
4. Finetti F, et al. *Nat. Cell Biol.* 2009; 11:1332–1339. [PubMed: 19855387]
5. Kozminski KG, Beech PL, Rosenbaum JL. *J. Cell Biol.* 1995; 131:1517–1527. [PubMed: 8522608]
6. Cole DG, et al. *J. Cell Biol.* 1998; 141:993–1008. [PubMed: 9585417]
7. Pazour GJ, Dickert BL, Witman GB. *J. Cell Biol.* 1999; 144:473–481. [PubMed: 9971742]
8. Pazour GJ, Agrin N, Leszyk J, Witman GB. *J. Cell Biol.* 2005; 170:103–113. [PubMed: 15998802]
9. Qin H, Diener DR, Geimer S, Cole DG, Rosenbaum JL. *J. Cell Biol.* 2004; 164:255–266. [PubMed: 14718520]
10. Hou Y, et al. *J. Cell Biol.* 2007; 176:653–665. [PubMed: 17312020]
11. Piperno G, Mead K. *Proc. Natl. Acad. Sci. U.S.A.* 1997; 94:4457–4462. [PubMed: 9114011]
12. Ciferri C, et al. *Cell.* 2008; 133:427–439. [PubMed: 18455984]

13. Hao L, et al. *Nat. Cell Biol.* 2011; 13:790–798. [PubMed: 21642982]
14. Kim J, et al. *Nature.* 2010; 464:1048–1051. [PubMed: 20393563]
15. Buisson J, et al. *J. Cell Sci.* 2013; 126:327–338. [PubMed: 22992454]
16. Johnson KA, Rosenbaum JL. *J. Cell Biol.* 1992; 119:1605–1611. [PubMed: 1281816]
17. Marshall WF, Rosenbaum JL. *J. Cell Biol.* 2001; 155:405–414. [PubMed: 11684707]
18. Song L, Dentler WL. *J. Biol. Chem.* 2001; 276:29754–29763. [PubMed: 11384985]
19. Marshall WF, Qin H, Rodrigo Brenni M, Rosenbaum JL. *Mol. Biol. Cell.* 2005; 16:270–278. [PubMed: 15496456]
20. Sharma N, Kosan ZA, Stallworth JE, Berbari NF, Yoder BK. *Mol. Biol. Cell.* 2011; 22:806–816. [PubMed: 21270438]
21. Hiller G, Weber K. *Cell.* 1978; 14:795–804. [PubMed: 688394]
22. Stephens RE. *Dev. Biol.* 1977; 61:311–329. [PubMed: 145385]
23. Lucker BF, et al. *J. Biol. Chem.* 2005; 280:27688–27696. [PubMed: 15955805]

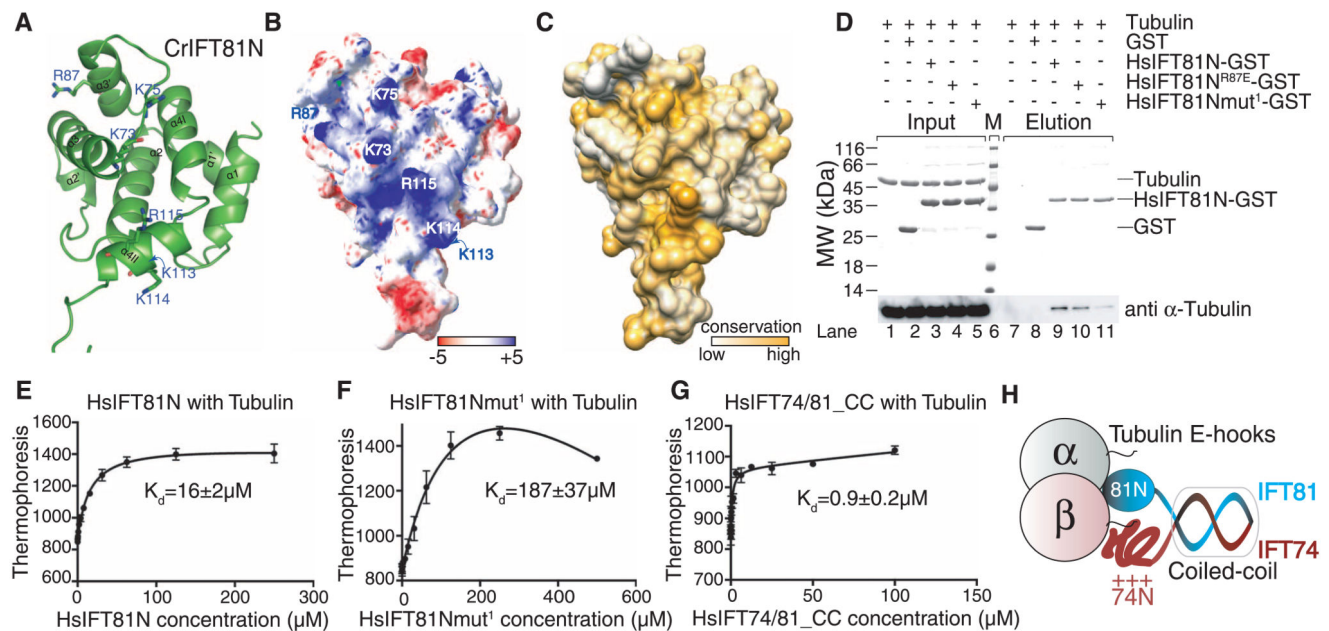


Fig. 1. IFT81 and IFT74 form a tubulin-binding module

(A) Cartoon representation of the crystal structure of CrIFT81N domain, with conserved lysines and arginines implicated in tubulin binding shown as sticks. (B) Electrostatic surface potential of IFT81N displaying the positively charged patch with the residues labeled according to the HsIFT81 sequence. (C) Surface conservation of IFT81N demonstrates that the basic patch is well conserved among different species (also see fig. S2). (D) Tubulin binding evaluated by glutathione (GSH) affinity pull-down of bovine $\alpha\beta$ -tubulin using glutathione S-transferase (GST)–HsIFT81N. Whereas tubulin does not bind the GSH beads and is not pulled down by GST alone, a substantial portion is pulled down by GST–HsIFT81N, demonstrating binding. Whereas the single-point mutation R87E does not strongly impair binding, the K73K75/EE double mutant (mut¹) results in reduced amounts of pulled-down tubulin, indicating reduced binding. (E) Quantification of tubulin binding to untagged HsIFT81N by microscale thermophoresis reveals a K_d of 16 μM . (F) The HsIFT81N mut¹ has drastically reduced binding with a K_d of 187 μM , showing that the basic patch is required for tubulin binding. (G) Microscale thermophoresis titration of tubulin with truncated HsIFT7481 complex reveals a K_d of 0.9 μM . The curves in (E), (F), and (G) are calculated for three independent experiments, and the error bars represent the mean \pm SD. (H) The experiments shown in (D) to (G), along with the data in fig. S5, suggest a model in which IFT81N recognizes the globular domain of tubulin, providing specificity, and IFT74N binds the acidic tail of β -tubulin, providing increased affinity.

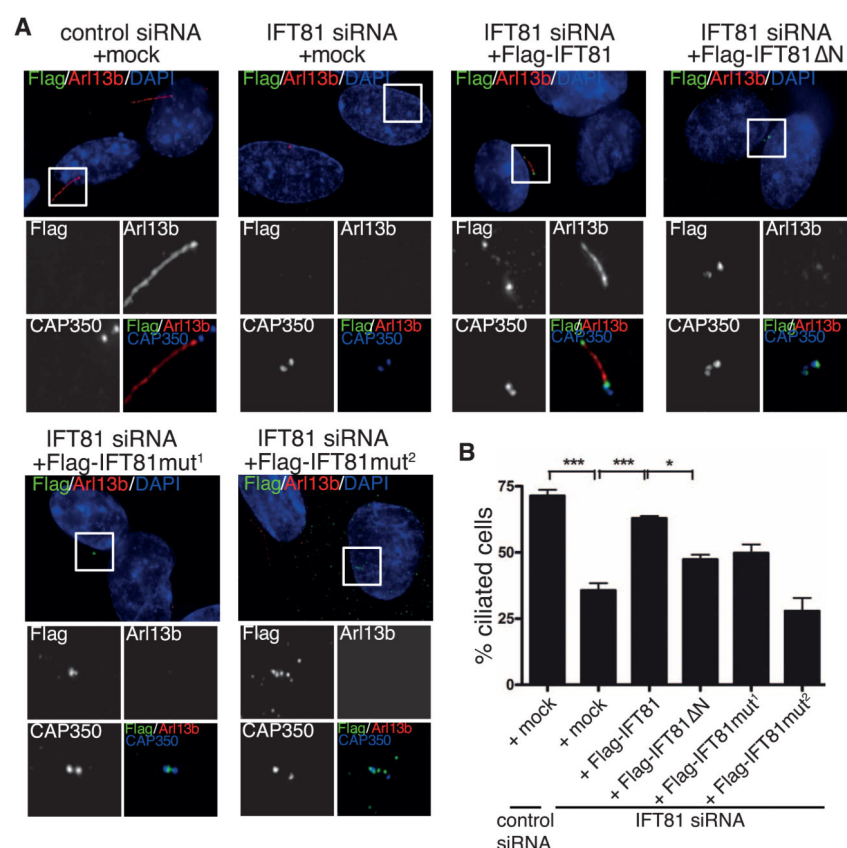


Fig. 2. Tubulin binding by IFT81 is required for ciliogenesis in human cells

(A) Transient expression of Flag-IFT81, but not the tubulin-binding-deficient IFT81 mutants (in green), rescues the ciliogenesis defect after IFT81 siRNA knockdown. Primary cilia formation was induced by 0.5 μ M cytochalasin D and detected by antibody to Arl13b (in red). CAP350 (in blue, inset images only) was used to visualize centrosomes. Mut¹ and Mut² are K73K75/EE and K73K75K113K114R115/EEEEEE tubulin-binding mutants, respectively. Scale bar, 5 μ m. (B) Quantification of the rescue experiment shown in (A). $n = 3$ independent experiments; statistical analyses by one-way analysis of variance.

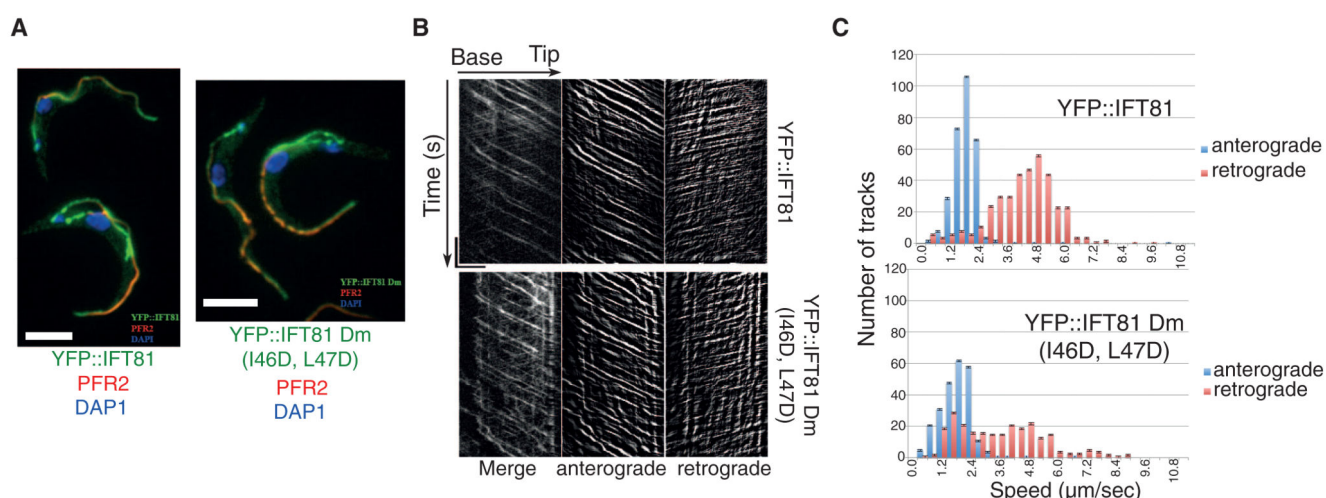


Fig. 3. IFT81N is not required for normal IFT

(A) Immunofluorescence analysis of methanol-fixed trypanosomes expressing the indicated YFP fusion proteins from the endogenous locus stained with an antibody to green fluorescent protein (GFP) (green) and with the antibody to PFR2 L8C4 to visualize the flagellum (red). The left panel corresponds to a control strain expressing YFP::IFT81 and the right panel to the mutant YFP::IFT81Dm, where the IFT81N CH domain is unfolded. Scale bar, 5 μ m. (B) Kymograph generation and separation of anterograde and retrograde traces. Kymographs were extracted from videos of cells expressing YFP::IFT81 (movie S1) or YFP::IFT81Dm (movie S2). Panels show the complete kymograph, anterograde events, and retrograde events (from left to right). The x axis corresponds to the length of the flagellum (horizontal scale bar, 5 μ m) and the y axis to the elapsed time (vertical scale bar, 5 s). (C) Quantitation of the kymograph analysis shown in (B). Anterograde (blue) and retrograde velocity (red) distribution of IFT particles are calculated from cells expressing YFP::IFT81 and YFP::IFT81Dm. The kymographic analysis reveals robust anterograde trafficking with a speed of $1.75 \pm 0.55 \mu\text{m/s}$ for YFP::IFT81 ($n = 294$ tracks from 15 cells) and $1.68 \pm 0.72 \mu\text{m s}^{-1}$ for YFP::IFT81Dm ($n = 244$ tracks from 15 cells). These values are in line with those reported for anterograde movement of GFP-IFT52 (15). Curiously, retrograde transport was slowed down in the case of YFP::IFT81Dm, where a second population of relatively slow trains was detected.

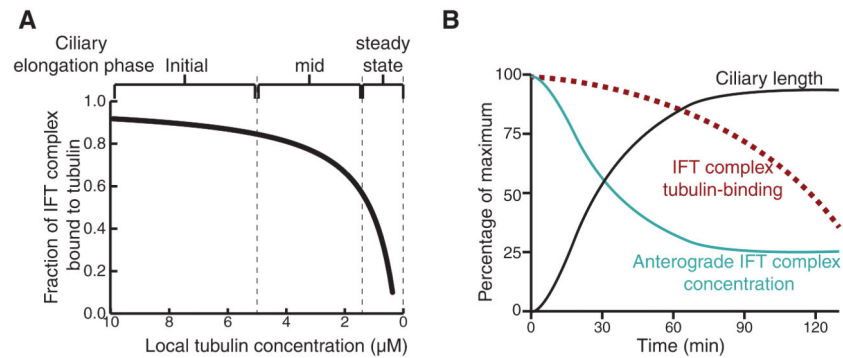


Fig. 4. Model for tubulin transport and ciliary length control

(A) Fraction of IFT complex bound to tubulin at varying tubulin concentrations is plotted using the equation $O_{\text{IFT}} = [\text{Tub}] / \{K_d + [\text{Tub}]\}$. O_{IFT} is the fraction of IFT bound to tubulin, K_d is the binding constant that is experimentally determined in this study as $0.9 \mu\text{M}$, and $[\text{Tub}]$ is the local concentration of free tubulin at the base of the cilium. (B) From the point of initiation of flagellar regeneration, the relationship between the ciliary length, the concentration of anterograde IFT particles, and O_{IFT} is plotted.